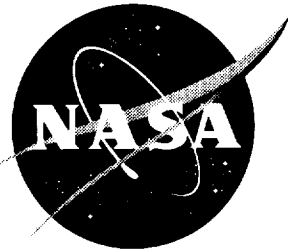


NASA/CP-2000-210291



Fifth International Symposium on Magnetic Suspension Technology

Edited by
Nelson J. Groom
Langley Research Center, Hampton, Virginia

Colin P. Britcher
Old Dominion University, Norfolk, Virginia

July 2000

The NASA STI Program Office . . . in Profile

Since its founding, NASA has been dedicated to the advancement of aeronautics and space science. The NASA Scientific and Technical Information (STI) Program Office plays a key part in helping NASA maintain this important role.

The NASA STI Program Office is operated by Langley Research Center, the lead center for NASA's scientific and technical information. The NASA STI Program Office provides access to the NASA STI Database, the largest collection of aeronautical and space science STI in the world. The Program Office is also NASA's institutional mechanism for disseminating the results of its research and development activities. These results are published by NASA in the NASA STI Report Series, which includes the following report types:

- **TECHNICAL PUBLICATION.** Reports of completed research or a major significant phase of research that present the results of NASA programs and include extensive data or theoretical analysis. Includes compilations of significant scientific and technical data and information deemed to be of continuing reference value. NASA counterpart of peer-reviewed formal professional papers, but having less stringent limitations on manuscript length and extent of graphic presentations.
- **TECHNICAL MEMORANDUM.** Scientific and technical findings that are preliminary or of specialized interest, e.g., quick release reports, working papers, and bibliographies that contain minimal annotation. Does not contain extensive analysis.
- **CONTRACTOR REPORT.** Scientific and technical findings by NASA-sponsored contractors and grantees.

- **CONFERENCE PUBLICATION.** Collected papers from scientific and technical conferences, symposia, seminars, or other meetings sponsored or co-sponsored by NASA.
- **SPECIAL PUBLICATION.** Scientific, technical, or historical information from NASA programs, projects, and missions, often concerned with subjects having substantial public interest.
- **TECHNICAL TRANSLATION.** English-language translations of foreign scientific and technical material pertinent to NASA's mission.

Specialized services that complement the STI Program Office's diverse offerings include creating custom thesauri, building customized databases, organizing and publishing research results . . . even providing videos.

For more information about the NASA STI Program Office, see the following:

- Access the NASA STI Program Home Page at <http://www.sti.nasa.gov>
- Email your question via the Internet to help@sti.nasa.gov
- Fax your question to the NASA STI Help Desk at (301) 621-0134
- Telephone the NASA STI Help Desk at (301) 621-0390
- Write to:
NASA STI Help Desk
NASA Center for AeroSpace Information
7121 Standard Drive
Hanover, MD 21076-1320

NASA/CP-2000-210291



Fifth International Symposium on Magnetic Suspension Technology

Edited by
Nelson J. Groom
Langley Research Center, Hampton, Virginia

Colin P. Britcher
Old Dominion University, Norfolk, Virginia

Proceedings of a workshop sponsored by the
National Aeronautics and Space
Administration, Washington, DC; the
National Aerospace Laboratory, Tokyo,
Japan; and the National High Magnetic Field
Laboratory, Tallahassee, Florida
and held in
Santa Barbara, California
December 1-3, 1999

National Aeronautics and
Space Administration

Langley Research Center
Hampton, Virginia 23681-2199

July 2000

The use of trademarks or names of manufacturers in this report is for accurate reporting and does not constitute an official endorsement, either expressed or implied, of such products or manufacturers by the National Aeronautics and Space Administration.

Available from:

NASA Center for AeroSpace Information (CASI)
7121 Standard Drive
Hanover, MD 21076-1320
(301) 621-0390

National Technical Information Service (NTIS)
5285 Port Royal Road
Springfield, VA 22161-2171
(703) 605-6000

INTRODUCTION

The Fifth International Symposium on Magnetic Suspension Technology was held at the Radisson Hotel Santa Barbara in Santa Barbara, California, on December 1-3, 1999. The Symposium was sponsored by the Guidance and Control Branch of the Langley Research Center, in coordination with NASA Headquarters, the National Aerospace Laboratory (NAL), Japan, and the National High Magnetic Field Laboratory (NHMFL) operated by Florida State University. The symposium was hosted by the University of California at Santa Barbara (UCSB) Center for Control Engineering and Computation.

The organizing committee and symposium committee consisted of the following people:

ORGANIZING COMMITTEE

Nelson J. Groom, Chair
NASA Langley Research Center
Hampton, VA 23681-2199
U.S.A.

Hideo Sawada
National Aerospace Laboratory
Chofu, Tokyo, 182
JAPAN

Hans Schneider-Muntau
National High Magnetic Field Laboratory
Tallahassee, FL 32306-4005
U.S.A.

SYMPOSIUM COMMITTEE

Nelson J. Groom, Symposium Co-Chair
NASA Langley Research Center
Hampton, VA 23681-2199
U.S.A.

Brad Paden, Symposium Co-Chair
University of California at Santa Barbara
Santa Barbara, CA 93106
U.S.A.

Sandy Johnson, Administrative Chair
NASA Langley Research Center
Hampton, VA 23681-2199
U.S.A.

An international steering committee assisted in selecting and reviewing submitted abstracts and in structuring the symposium sessions. The steering committee consisted of the following people:

Colin P. Britcher, Chair
Old Dominion University
Dept. of Aerospace Engineering
Norfolk, VA 23529-0247

Isaiah Blankson
NASA Glenn Research Center
MS/5-9
21000 Brookpark Road
Cleveland, OH 44135

David Trumper
Massachusetts Institute of Technology
77 Massachusetts Avenue
Cambridge, MA 02139

Jim Downer
Foster-Miller, Inc.
350 Second Avenue
Waltham, MA 02154

Alexander Kuzin
Moscow Aviation Technology Institute
Petrovka 27
Moscow, K-31, 103737
RUSSIA

Justin Schwartz
National High Magnetic Field Laboratory
1800 E. Paul Dirac
Tallahassee, FL 32306-4005

Raoul Herzog
MECOS Traxler
Industriestr. 26, CH 8404
Winterthur
SWITZERLAND

Atsushi Nakajima
National Aerospace Laboratory
7-44-1 Jindaiji-Higashi-machi
Chofu, Tokyo, 182
JAPAN

Jim Lauffer
Sandia National Laboratories

P.O. Box 5800
Albuquerque, NM 87185-0557

The goal of the symposium was to examine the state of technology of all areas of magnetic suspension and to review recent developments in sensors, controls, superconducting magnet technology, and design/implementation practices. The symposium included 18 sessions in which a total of 53 papers were presented. The technical sessions covered the areas of bearings, controls, modeling, electromagnetic launch, magnetic suspension in wind tunnels, applications, flywheel energy storage, rotating machinery, vibration isolation, and maglev. A list of attendees begins on page xiii.

The first symposium in this series was organized by NASA Langley Research Center and held at Langley Research Center, Hampton, Virginia, on August 19-23, 1991. The proceedings of the first symposium are available as NASA Conference Publication NASA CP-3152, Parts 1 and 2. The second symposium in the series, also organized by NASA Langley Research Center, was held at The Westin Hotel in Seattle, Washington, on August 11-13, 1993. The proceedings of the second symposium are available as NASA Conference Publication NASA CP-3247, Parts 1 and 2. The third symposium, organized by NASA Langley Research Center and hosted by the National High Magnetic Field Laboratory was held at The Holiday Inn Capital Plaza in Tallahassee, Florida on December 13-15, 1995. The proceedings of the third symposium are available as NASA Conference Publication NASA CP-3336, Parts 1 and 2. The fourth symposium, organized by NASA Langley Research Center, the National Aerospace Laboratory, Japan, the National High Magnetic Field Laboratory, and hosted by the National Aerospace Laboratory was held at The Nagaragawa Convention Center in Gifu City, Japan on October 30-November 1, 1997. The proceedings of the fourth symposium are available as NASA Conference Publication NASA/CP-1998-207654.

CONTENTS

Introduction	iii
List of Attendees.....	xiii

SESSION 1—Magnetic Bearings 1

Chairman: Nelson J. Groom, NASA LaRC

Comparison of Radial Magnetic Bearing Designs	3
Anthony S. Kondoleon and William P. Kelleher, Draper Laboratory	

Active Magnetic Bearings for 10kWh Flywheel Energy Storage System	15
Osamu Saito, Soichiro Une, and Hisayuki Motoi, Ishikawajima-Harima Heavy Industries Co., Ltd; Hironori Kamenno, Yasukata Miyagawa, Ryouichi Takahata, and Hirochika Ueyama, Koyo Seiko Co., Ltd.	

A Self-Healing Magnetic Bearing.....	25
H. Ming Chen, Foster-Miller Technologies, Inc.	

Magnetically Levitated Reaction Wheel for Space Application.....	35
Argondizza, S. Carabelli, G. Genta, and A. Tonoli Politecnico di Torino	

SESSION 2—Electromagnetic Launch/LSMs

Chairman: Hans Schneider-Muntau, NHMFL

Lateral Force Control Through Armature Currents in Superconducting LSM Maglev Vehicle.....	51
Tetsuzo Sakamoto, Kyushu Institute of Technology	

Sway and Yaw Motion Control Due to Reluctance Force in Controlled-PM LSM Maglev Carrier	63
Kinjiro Yoshida, Hiroshi Takami, and Kenji Shimamoto Kyushu University Yasunori Nakahashi, Fuji Electric Co., Ltd.	

Feasibility Study of Superconducting LSM Launcher System for Practical H-II Rocket.....	77
Kinjiro Yoshida, Kyushu University Takeshi Kawanami, Tokyo Electric Power Co., Inc.	

The NASA Inductrack Model Rocket Launcher at the Lawrence Livermore National Laboratory.....	93
L. S. Tung, R. F. Post, E. Cook, and J. Martinez-Frias Lawrence Livermore National Laboratory	

SESSION 3 – Controls 1
Chairman: Brad Paden, UCSB

Feedback Linearization Applied to a MIMO Active Magnetic Bearing: A Systematic Approach and Application to a Balance Beam.....	105
Michael Baloh, Gang Tao, and Paul Allaire, University of Virginia	
Identification and Control of a Magnetically Levitated Table.....	121
Koichi Matsuda, Yoichi Kanemitsu, and Shinya Kijimoto Kyushu University	
Non-Linear Fuzzy Logic Control for Magnetic Bearings in Large-Tip Clearance-Active Stall Control Approach	131
Shuliang Lei, Alan Palazzolo, Texas A&M University Albert Kascak, U.S. Army at NASA Glenn	
Iterative Control-Relevant Identification and Controller Enhancement of a MIMO Magnetic Bearing System.....	155
Dong-Chul Han, Sang-Wook Lee, Hyeong-Joon Ahn, and Sang-Ho Lee, Seoul National University	

SESSION 4 – Magnetic Suspension in Wind Tunnels
Chairman: Colin P. Britcher, ODU

Application of Magnetic Suspension and Balance Systems to Hypersonic Wind Tunnel Testing	171
Andrew K. Owen, University of Oxford	
Roll Motion Restraint System for NAL 0.6m MSBS (the 2nd report).....	185
Takashi Kohno, Hideo Sawada, and Tetsuya Kunimasu National Aerospace Laboratory (NAL)	

SESSION 5 – Modeling 1
Chairman: Kent R. Davey, American Maglev

A Frequency-Domain Model of Electromagnetic Actuators Composed of Solid Iron Cores With Hysteresis Effects.....	197
Satoru Fukata, Kyushu Institute of Design Yoshinori Kouya, Murakami Seiki Mfg. Co., Ltd. Shuang Ping Feng, Kyushu Institute of Design	
Modelling, Identification and Control of an AMB System for the Support of a High-Speed Flywheel.....	213
Z. Y. Wu, D. Howe, D. Peel, and C. M. Bingham, University of Sheffield	
Finite Element Design of Bearingless Permanent Magnet Motors	227
Wolfgang Amrhein, Siegfried Silber, and Klaus Nenninger, Johannes Kepler University	

A Comparison of Experimental and Theoretical Results for Magnetic Bearings	239
Robert I. Hibbs, Jr., Joseph K. Scharrer, Bonnie A. Galvin, and Mark W. Galvin, Rotordynamics-Seal Research	

SESSION 6 – Applications 1

Chairman: H. Ming Chen, Foster-Miller Technologies

Animal Trials of a Magnetically Levitated Left-Ventricular Assist Device	251
Brad Paden, University of California, Santa Barbara	
James Antaki, University of Pittsburgh	
Nelson Groom, NASA Langley Research Center	

Magnetic Suspension of an Artificial Heart Pump Using EM/PM Bearings (abstract only)	259
P. Allaire, J. Decker, M. Baloh, and J. Lee, University of Virginia	
J. Long, LDS Hospital	

Design of Magnetically Levitated Micro Operation Hands	261
Tatsuya Nakamura, Yoshiyuki Kogure, and Koichiro Shimamura, Tokyo Metropolitan University	

Design of a Magnetically Suspended Wheel for a Miniature Gyro Made Using Planar Fabrication Technologies	275
Charles R. Dauwalter, Milli Sensor Systems and Actuators, Inc.	

SESSION 7 – Flywheel Energy Storage

Chairman: Atsushi Nakajima, NAL

A 500-Wh Power Flywheel on Permanent Magnet Bearings	287
Johan K. Fremerey and Michael Kolk, KFA-IGV	

Development of 10kWh Flywheel Energy Storage System	297
Osamu Saito, Soichiro Une, and Hisayuki Motoi, Ishikawajima-Harima Heavy Industries Co., Ltd.	
Hironori Kamenno, Yasukata Miyagawa, Ryouichi Takahata, and Hirochika Ueyama, Koyo Seiko Co., Ltd.	

Application of Permanent Magnet Bias Magnetic Bearings to an Energy Storage Flywheel	309
Lawrence A. Hawkins, CalNetix, Inc.	
Brian T. Murphy and John Kajs, University of Texas	

SESSION 8 – Vibration Isolation

Chairman: Brad Paden, UCSB

Vibration Control on Active Magnetic Bearing Equipped Flywheel Rotor	327
Keiji Katsuno, Hiroki Okubo, Hiroyuki Fujiwara, and Osami Matsushita, The National Defense Academy	

A Design Method for Magnetic Suspension and Vibration Control Of Levitated Beams for Noncontact Processing.....	339
Ming-chih Weng and David L. Trumper, MIT	

SESSION 9 – Rotating Machinery Topics
Chairman: Raoul Herzog, Mecos Traxler AG

Touchdown/Launch-Lock Mechanism for Magnetically Suspended Control Moment Gyroscope	355
D. W. Smith, Honeywell Inc.	

Identification and Control of Unbalance and Sensor Runout on Rigid by Active Magnetic Bearing Systems	367
Yoichi Kanemitsu, Sinya Kijimoto, Koichi Matsuda, and Park Tea Jin, Kyushu University	

SESSION 10 – Modeling 2
Chairman: Colin P. Britcher, ODU

Linear and Nonlinear Analysis of Magnetic Bearing Bandwidth Due to Eddy Current Limitations	385
Andrew Kenny and Alan Palazzolo, Texas A&M University	

A Precise Force Measurement in Magnetic Bearings for Diagnosis Purposes	397
M. Aenis and R. Nordmann, Darmstadt University of Technology	

Nonlinear Stability Analysis of Active Magnetic Bearings.....	411
Norbert Steinschaden and Helmut Springer, Vienna University of Technology	

SESSION 11 – Controls 2
Chairman: Eric H. Maslen, UVA

Control System for Inside-Out Configuration Magnetic Bearings	431
Gregory Buckner, North Carolina State University Alan Palazzolo, Texas A&M University John Kajs, Brian Murphy, and Joe Beno, University of Texas at Austin	

Real Time Control of a Magnetic Bearing Suspension System for Flexible Rotors	443
Edgar F. Hilton, Marty Humphrey, John Stankovic, and Paul Allaire, University of Virginia	

Fuzzy Logic Control of Magnetic Bearings for Suspension of Vibration Due to Sudden Imbalance	459
Shuliang Lei and Alan Palazzolo, Texas A&M University Albert F. Kascak, U.S. Army at NASA Glenn	

SESSION 12 – MAGLEV

Chairman: Hans Schneider-Muntau, NHMFL

Prediction of Lift and Drag Forces in an EDS Maglev System	475
Kent Davey, American Maglev, Inc.	
Evaluation of Urban Magnetically Levitated Vehicles in Japan	487
Takeshi Mizuma, Ministry of Transport	
Concrete Guideways for Maglev Vehicles.....	501
Robert F. Mast, James S. Guarre, and Michael W. LaNier, BERGER/ABAM Engineers, Inc.	

SESSION 13 – Applications 2

Chairman: Paul E. Allaire, UVA

Simulation of Wind Tunnel Forces Using Magnetic Suspension Technology	515
R. Ralph Sinno, Thomas Price, Bert Nail, and Jason Melton Mississippi State University	
High-Tc Superconducting Accelerometer	527
Shigeharu Enkyo and Atushi Nakajima, National Aerospace Laboratory	
Design of a Hermetically Sealed Chemical Pump with Magnetic Bearings.....	531
J. Sobotzik, A. Hantke, and R. Nordmann, Darmstadt Univ. of Technology S. Brodersen, J. Gröschel, and B. Köhler, KSB AG	

SESSION 14 – Controls 3

Chairman: Hideo Sawada, NAL

Adaptive Model Following Control Method for Actively Controlled Magnetic Bearing Momentum Wheel	547
Y. C. Xie, Beijing Institute of Control Engineering H. Sawada, T. Hashimoto, K. Ninomiya, Institute of Space and Astronautical Science	
Achievable Robustness Comparison of Position Sensed and Self-Sensing Magnetic Bearing Systems.....	563
Nancy Morse Thibeault and Roy Smith, Univ. of California at Santa Barbara Brad Paden, Magnetic Moments; James Antaki, University of Pittsburg	
Adaptive Compensation of Sensor Runout for Magnetic Bearings With Uncertain Parameters: Theory and Experiments	575
Joga D. Setiawan and Ranjan Mukherjee, Michigan State University Eric H. Maslen, University of Virginia	

SESSION 15 – Magnetic Bearings 2

Chairman: Anthony S. Kondoleon, Draper Laboratory

Design of a Minimum Current Magnetic Bearing	593
C. Klesen, R. Nordmann, U. Schonhoff, Darmstadt Univ. of Technology	
Inside-Out Configuration Active Magnetic Bearing Actuators	611
M. A. Pichot, J. P. Kajs, R. J. Hayes, J. H. Beno, A. Ouroua, and B. M. Rech, University of Texas at Austin	
Development and Testing of a Four Pole Magnetic Bearing	625
Joe Imlach, Imlach Consulting Engineering	

SESSION 16 – Controls 4

Chairman: Nancy Morse Thibeault, UCSB

Integral Sliding Mode Controller for Magnetically Suspended Balance Beam: Theory and Experimental Evaluation	635
Jun-Ho Lee, Edgar F. Hilton, Xuerui Zhang, Gang Tao, and Paul E. Allaire, University of Virginia	
Self-Synchronous Detection Method for Magnetic Suspension Digital Control	645
Shin-ichi Moriyama, Kyushu Institute of Technology Katsuhide Watanabe and Takahide Haga, Ebara Research Co., Ltd.	

SESSION 17 – Magnetic Suspension in Wind Tunnels 2

Chairman: Nelson J. Groom, NASA LaRC

Status of MSBS Study at NAL.....	659
Hideo Sawada, Takashi Kohno, and Tetsuya Kunimasu, National Aerospace Laboratory	
Design of a Magnetic Suspension and Balance System for the Princeton/ONR High Reynolds Number Testing Facility	675
Colin P. Britcher, Oscar Gonzalez, Steven Gray, Oscar Gomeiz, James E. Barkley, and Adeel Jafri, Old Dominion University Alexander J. Smits, Princeton University	

SESSION 18 – Modeling 3

Chairman: Dennis Smith, Honeywell

Neural Network Based Fault Detection for Fault Tolerant Control of Systems with Multiple Magnetic Actuators and Sensors	689
Matthew O. T. Cole, Patrick S. Keogh, and Clifford R. Burrows University of Bath	
Possibility of Existence of Non-Linear Electromotive Force (EMF)	705
Osamu Ide, Clean Energy Laboratory	

LIST OF ATTENDEES

Frederick W. Adams
NASA Kennedy Space Center
Mail Stop MM-G2
Kennedy Space Center, FL 32899
407-867-9167
407-867-1603
Frederick.Adams-1@ksc.nasa.gov

Martin Aenis
University of Technology
Petersenstrasse 30
Darmstadt 64287
GERMANY
49-6151-162274
49-6151-165332
aenis@mesym.tu-darmstadt.de

Hyeong-Joom Ahn
Seoul National University
Kwanak-ku, Shilim-dong San 56-1
Seoul 151-742
KOREA
82-2-880-7153
82-2-882-3718
ahj@amed.snu.ac.kr

Paul E. Allaire
University of Virginia
MANE Dept./Thornton Hall
Charlottesville, VA 22901
804-924-6209
804-982-2037
pea@virginia.edu

Wolfgang Amrhein
University of Linz
Inst. of Automatic Contro
Altenbergerstr. A-4040 Linz
AUSTRIA
43-732-2468-9715
43-732-2468-9719
amrhein@mechatronik.uni-linz.ac.at

Vatche Artinian
CALNETIX
363 Van Ness Way #401
Torrance, CA 90501
310-782-8306
310-782-6335
advmotor@earthlink.net

Dorna Baumann
Magnetic Moments
5735 Hollister Avenue
Suite B
Goleta, CA 93117
805-683-9659
805-683-9671
Dorna@mmsb.com

Borij B. Bhargava
Ashman Technologies
4596 Sierra Madre Drive
Santa Barbara, CA 93110
805-964-2104
805-683-1011

Christopher Bingham
University of Sheffield
Mappin Street
Sheffield, United Kingdom
S1 3JD
ENGLAND
44 1142225195
44 1142225196

Dale V. Bloodgood
Old Dominion University
Dept. of Aerospace Engineering
Norfolk, VA 23529-0247
757-683-3720
757-683-3200
dvv1002@aero.odu.edu

Colin P. Britcher
Old Dominion University
Dept. of Aerospace Engineering
Norfolk, VA 23529-0247
757-683-4916
757-682-3200
c.p.britcher@larc.nasa.gov

Stefano Carabelli
Politecnico di Torino
Dip. Di Automatica e Info
Corso Duca degli Abruzzi 24
1-10129 Torino
ITALY
39-11-564-7058
39-11-564-7099
carabelli@polito.it

H. Ming Chen
Foster-Miller Technologies
431 New Karner Rd.
Albany, NY 12205-3833
518-456-9919 ext 104
518-456-8020
mchen@fosmiltech.com

Charles R. Dauwalter
Milli Sensor Systems & Ac
93 Border Street
West Newton, MA 02465-2013
617-965-1346 ext 2020
617-965-4872

Dr. Kent R. Davey
American Maglev Techn
2275 Turnbull Bay Road
New Smyrna Beach, FL 32168-5941
904-427-6643
904-427-2067
davey@ucnsb.net

Andreas Fleischli
Sulzer Electronics AG
Technoparkstrasse 1
CH 8005 Zuerich
SWITZERLAND
41-1-445-1353
41-1-445-1393

Johan K. Fremerey
Forschungszentrum Juelich
D-52425
Juelich
GERMANY
49-1-2561-61-3083
49-1-2461-61-3907
j.k.fremery@fz-juelich.de

Satoru Fukata
Kyushu University of Design
Dept. of Engineering Design
4-9-1 Shiobaru
Minami-ku Fukuoka 815-8540
JAPAN
81-92-553-4538
fukata@kyushu-id.ac.jp

Christopher Gabrys
Toray Composites Inc.
190002 50th Ave. E.
Tacoma, WA 98446
253-856-1777
253-846-3163
gabrynator@uswest.net

Nelson J. Groom
NASA Langley Research Center
Mail Stop 161
Hampton, VA 23681-0001
757-864-6613
757-864-7797
n.j.groom@larc.nasa.gov

Norman Grum
Rolls Royce
P.O. Box 2000
Raynesway
Derby DE217XX England
GREAT BRITAIN
44-1332-661461 x5959
44-1332-622948
grum@btinternet.com

James S. Guarre
Berger/Abam Engineers
33301 Ninth Ave South
Suite 300
Federal Way, WA 98003-2600
206-431-2300
206-431-2250
guarre@abam.com

Dong-Chul Han
Seoul National University
Kwanakku Shinlimdong San 56-1
Seoul, Korea 151-1142
82-2-880-7139
82-2-883-1513
dchan@amed.snu.ac.kr

Larry A. Hawkins
Calnetix, Inc.
363 Van Ness Ave. #401
Torrance, CA 90501
310-782-2586
310-782-8335
larry@calnetix.com

Stuart P. Henderson
UK Ships Support Agency
ME244, B-Block, Foxhill
Bath, Avon BA15AB
44-1225-885147
44-1225-885137
admes@navynet.gbnet.gov.uk

Raoul Herzog
MECOS Traxler AG
Industriestr.26
CH 8404
Winterthur
SWITZERLAND
41-52-235-14-13
41-52-235-14-23
herzog@mecos.ch

Robert I. Hibbs, Jr.
Rotordynamics Seal Research
3628 Madison Ave.
Suite 20
North Highland, CA 95660
916-344-9500 ext. 22
916-344-8400

Osamu Ide
Clean Energy Laboratory
Minatoku
Mita 3-4-21-601
Tokyo 108-0073
JAPAN
81-3-544-4746
81-3-544-4746

Dr. Joe Imlach
I.C.E.
460 Falke Ct.
Anchorage, AK 99504
907-337-8954
907-337-8954
jiice@alaska.net

Sandra G. Johnson
NASA Langley Research Center
Mail Stop 162
Hampton, VA 23681-0001
757-864-6222
757-864-8320
s.g.johnson@larc.nasa.gov

Frank (Jigger) Jumonville
MAFI-Trench Corp.
3037 Industrial Pkwy
Santa Maria, CA 93455
805-925-5757
805-925-3861

John Kajs
University of Texas at Austin
Center for Electromechanics
Mail Code R7000
Austin, TX 78712
512-232-1637
512-471-0781
j.kajs@mail.utexas.edu

Hironori Kamenno
Koyo Seiko Co., Ltd.
No. 24-1 Kokubu-Higanjo-cho
Kashiwara, Osaka 582-8588
JAPAN
81-744-29-7044
81-744-29-7049
hironori_kamenno@koyo-seiko.co.jp

Daniel Kane
General Dynamics/Electr.
150 Avenel Street
Avenel, NJ 07001
732-636-9100 ext 282
732-636-4317

Dr. Yoichi Kanemitsu
Kyushu University
Dept. of Intelligent Mach
6-10-1 Hakozaki
Higashi-ku, Fukuoka
812-8581
81-92-642-3427
81-92-631-4789
Kanemitu@mech.kyushu-u.ac.jp

Keiji Katsuno
National Defense Academy
Mechanical Engineering
1-10-20 Hasirimiza
Yokosuka, Kanagawa 239-8686
JAPAN
81-468-41-310
81-468-44-5900
kkatsuno@cc.nda.ac.jp

Patrick S. Keogh
University of Bath
School of Mech. Engineering
Bath BA27AY
UNITED KINGDOM
44-1225-826826
44-1225-826928
p.s.keogh@bath.ac.uk

Jong-Moon Kim
Korea Electrotech Res. Institute
28-1 Sungjoo-dong
Changwon, Kyung Nam
641-120
KOREA
82-551-280-1443
82-551-280-1479
jmkim@keri.re.kr

Yoshida Kinjiro
Kyushu University
10-1 6-chome Hakozaki Higashi-ku
Fukuoka 812-8581
JAPAN
92-642-3905
92-633-2710

Christof Klesen
Darmstadt University of Tech
Dept. of Mechatronics
Petersenstrasse 30
64287 Darmstadt
GERMANY
49-6151-163971
49-6151-165332
klesen@mesym.tu-darmstadt.de

Kurt J. Kloesel
NASA Dryden Flight Research Center
P.O. Box 273
Edwards, CA 93523
661-258-3121
661-258-2010

Takashi Kohno
National Aerospace Laboratory
7-44-1 Jinchijihigashi-machi
Chofu-shi, Tokyo 182-8522
JAPAN
81-422-40-3225
81-422-40-3234
kohno@nal.go.jp

Anthony S. Kondoleon
The Charles Stark Draper
Mail Stop 23
555 Technology Square
Cambridge, MA 02139-3563
617-258-1537
617-258-4656
kondo@draper.com

Marc S. LeDuc
MAFI-Trench Corp.
3037 Industrial Parkway
Santa Maria, CA 93455
805-938-5757
805-925-3861

Jun-Ho Lee
University of Virginia
Mechanical Engineering
Thornton Hall
Charlottesville, VA 22903-2442
804-982-2110
804-982-2037
j17e@virginia.edu

Sang-Wook Lee
Seoul National University
San 56-1, Shinlim-Dong
Kwanaki-ku
Seoul, Korea 463-480
82-2-880-7153
82-2-882-3718
swlee@amed.snu.ac.kr

Shuliang Lei
Texas A&M University
College Station, TX 77843-3123
409-845-5280
409-845-3081

Prof. Richard E. Markert
Darmstadt University of Tech
Hochschulstrabe 1
Darmstadt 64289
GERMANY
49-6151-16-2785
49-6151-16-4125

Eric H. Maslen
University of Virginia
Mech., Aero & Nuclear E
Thornton Hall
Charlottesville, VA 22903
804-924-6227
804-982-2037
ehm7s@virginia.edu

Koichi Matsuda
Kyushu University
Dept. of Intelligent Mach
6-10-1 Hakozaki
Fukuoka 812-8581
JAPAN
81-92-642-3429
81-92-631-4789
matsuda@mech.kyushu-u.ac.jp

Dr. Osami Matsushita
The National Defense Academy
Dept. of Mechanical Eng.
1-10-20 Hashirimizu
Yokosuka 239-8686
JAPAN
81-468-41-3810 x2326
81-468-44-5900
osami@cc.nda.ac.jp

William G. Meeker
Nat'l Transportation Safety Board
490 L'Enfant Plaza East, S.W.
Washington, DC 20594
703-451-1106
703-451-1106
meekerw@ntsb.gov

Takeshi Mitzuma
Traffic Safety & Nuisance
Ministry of Transport
6-38-1 Shinkawa
Mitaka-city, Tokyo 181-0004
JAPAN
81-422-41-3210
81-422-76-8602
mizuma@tsnri.go.jp

Shin-ichi Moriyama
Kyushu Institute of Tech
Dept. of Control Eng. & Sc.
Kawazu 680-4
Itzuka, Fukuoka 820
JAPAN
81-948-29-7700
81-948-29-7709
moriyama@ces.kyutech.ac.jp

Nancy Morse Thibeault
University of California at Santa Barbara
Dept. of Mechanical Eng.
Santa Barbara, CA 93106-5070
805-893-7785
805-893-8651

Atsushi Nakajima
National Aerospace Laboratory
7-44-1 Jindaiji-Higashi-machi
Chofu, Tokyo 182
JAPAN
81-442-47-5911 x2548
81-422-49-8813
nakajima@nal.go.jp

Prof. Tatsuya Nakamura
Tokyo Metropolitan Univ.
Dept. of Precision
1-1 Minami-Ohsawa
Hachioji-shi, Tokyo 192-0397
JAPAN
81-426-77-2727
81-426-77-2717
t-nakam@ecomp.metro-u.ac.jp

Prof. Yoshihiro Nakamura
Hosei University
Dept. of Mech. Eng.
3-7-2 Kajino-cho
Koganei 184-8584
JAPAN
81-42-387-6143
81-42-387-6121

Prof. Francesco Negrini
Universita di Bologna
Istituto di Elettrotecnica
Viale Risorgimento, 2
40136 Bologna 40136
ITALY
0039-51-2083575
0039-51-585700

Steve Nichols
SatCon Technology Corp.
161 First Street
Cambridge, MA 02142
617-349-0116
617-661-3373

Keiken Ninomiya
Institute of Space & Astronautical Science
3-1-1 Yoshinodai, Sagamihara 8510
JAPAN
81-42-759-8307
81-42-759-8473

Dr. Rainer Nordmann
MESYM
University of Technology
Petersenstrabe 30
Darmstadt 6428
GERMANY
49-6151-162074
49-6151-165332
nordmann@mesym.tu-darmst.de

Vladimir Odessky
General Dynamics/Electr
150 Avenel Street
Avenel, NJ 07001
732-636-9100 ext 368
732-636-4317

Andrew K. Owen
University of Oxford
Dept. of Engineering Sci
Parks Road
Oxford OX13PJ
UNITED KINGDOM
44-1865 288748
44-1865 288756

Prof. Brad Paden
University of California at SB
Dept. of Mechanical Eng.
Santa Barbara, CA 93106
805-893-8165

Nick J. Patz
Lawrence Livermore Nat
112 Mustang Dr. #302
San Luis Obispo, CA 93405
805-782-0548

Scott Penfield
Technology Insights
6540 Lusk Blvd.
Suite C-102
San Diego, CA 92121-2767
615-735-2666
615-735-3340

Jose O. Perez-Morales
NASA Kennedy Space Center
Mail Stop MM-H-A
Kennedy Space, FL 32899
407-867-2133
407-867-2960
jose.perez-maroles-1@ksc.nasa.gov

Mark Pichot
University of Texas at Austin
Center for Electromech.
PRC Bldg. 133, Mail Code R7000
Austin, TX 78712
512-232-1609
512-471-0781

Richard F. Post
Lawrence Livermore Nat
P.O. Box 808, MS L-644
7000 East Avenue
Livermore, CA 94550
510-422-9853
510-423-2395
post3@llnl.gov

Thomas E. Price
Mississippi State Univ.
Dept. of Civil Eng.
P. O. Box 9546
Mississippi State Univ., MS 39762
662-325-7191
662-325-7189

Gene M. Randich
Portland Cement Asso.
5420 Old Orchard Road
Skokie, IL 60077-1083
847-966-6200
847-966-9781

Nigel D. Reece
UR Ministry of Defense
ME231 Room 114
B Block
Foxhill, Bath BA15AB
ENGLAND
44-1225-885484
44-1225-883891

Tetsuzo Sakamoto
Kyushu Institute of Technology
Department of Control Engineering
Tobata, Kitakyushu 804-8550
JAPAN
81-93-884-3182
81-93-861-1159
sakamoto@cntl.kyutech.ac.jp

Hideo Sawada
National Aerospace Laboratory
7-44-1 Jindaijihigashi-machi
Chofu-shi
Tokyo 182
JAPAN
81-0422-47-5911
81-0422-49-0793
sawada@nal.go.jp

Mr. Hideyuki Sawada
Institute of Space & Astro.
3-1-1 Yoshinodal
Sagamihara
Kanagawa 229-8510
JAPAN
427-59-8312
427-59-8473
sawada@nnl.isas.ac.jp

Hans Schneider-Muntau
National High Magnetic Fields
Laboratory (NHMFL)
1800 E. Paul Dirac Drive
Tallahassee, FL 32306-4005
904-644-0863
904-644-0867

Koichiro Shimamura
Tokyo Metropolitan Univ.
Dept. of Precision Eng.
1-1 Minami-Ohsawa
Hachioji-shi, Tokyo 192-0397
JAPAN
81 426 77 1111
81 426 77 2717

Prof. Ralph Sinno
Mississippi State University
P. O. Box 9546
Dept. of Civil Engineering
Mississippi State Univ., MS 39762
662-325-3737
662-325-7189

Norbert Skricka
Darmstadt University of Tech
Hochschuistrabe 1
Darmstadt 64289
GERMANY
49-6151-16-4184
49-6151-16-4125

Dennis Smith
Honeywell Satellite Systems
P. O. Box 52199
Phoenix, AZ 85072-2199
602-822-3237
602-822-3963
dsmith@space.honeywell.com

Joachim F. Sobotzik
Technical University of Darmstadt
Petersenstrasse 30
Darmstadt D-64287
GERMANY
49-6151-163973
49-6151-165332
sobotzik@mesym.tu-darmstadt.de

Gregory A. Spencer
NASA Dryden Flight ResearchCenter
P. O. Box 273
Edwards, CA 93523
661-258-3319
661-258-2010

Norbert Steinschaden
Vienna University of Technology
Wiedner Hauptstrabe 8-10/E303
A-1040 Vienna
AUSTRIA
43-1-58801-30322
41-1-58801-30399
norbert.steinschaden@tuwien.ac.at

Ron J. Sun
NASA Dryden Flight Research Center
P. O. Box 273
Edwards, CA 93523
661-258-3121
661-258-2010

Louann S. Tung
The Lawrence Livermore
P. O. Box 808
Livermore, CA 94551-0808
925-422-1274
925-424-3532

Soichiro Une
IHI
1-15 Toyosu, 3-chome
Koto-ku, Tokyo 135-8732
JAPAN
81-3-3534-3351
81-3-3534-3322
soichiro_une@ihi.co.jp

Ming-Chih Weng
MIT
Mechanical Engineering
77 Mass Ave., Room 35-030
Cambridge, MA 02139
617-258-6098
617-258-9652
mingchih@mit.edu

Kinjiro Yoshida
Kyushu University
10-1, 6-Chome, Hakozaki
Higashi-ku
Kukuoka 812
JAPAN
92-641-1101 ext 5307
92-633-2710

Robert C. Youngquist
NASA Kennedy Space Center
Mail Stop MM-G2
Kennedy Space Center, FL 32899
407-867-1829
407-867-1177
robert.youngquist-1@ksc.nasa.gov

Edward S. Zorzi
American Flywheel System
P. O. Box 449
Medina, WA 98039
425-454-2888
425-455-9623
ed.zorzi@amflywheel.com

*2nd number in address is fax number
where applicable

Session 1 -- Magnetic Bearings 1

Chairman: Nelson J. Groom
NASA Langley Research Center

COMPARISON OF RADIAL MAGNETIC BEARING DESIGNS

Anthony S. Kondoleon

William P. Kelleher

Draper Laboratory

555 Technology Square

Cambridge, Ma 02139

ABSTRACT

The initial design of an active magnetic bearing actuator is critical for a successful magnetic suspension. The sizing of the stators and rotors is a vital step for maintaining a favorable weight to load capacity ratio for the magnetic suspension. Sizing the stators and rotors for minimum running losses during high-speed operation is a challenge all designers face. This paper presents results from recently completed analyses for running loss determination in radial magnetic bearings, and presents how these results are used in the initial design phase for radial magnetic bearings. Comparisons of flux density versus speed for various heteropolar radial flux distribution designs and a comparison of rotating loss versus load for various radial pole counts are also presented.

INTRODUCTION

Designing a radial magnetic bearing actuator for low loss and high load capacity is a challenge. Tests carried out (ref. 1) have provided insight into the nature of rotating losses in these actuators. Combining these results with design procedures (ref. 2) provides a means for determining the basic parameters of the radial bearing actuator for the initial design tradeoff comparisons. The basic design and analysis of a radial magnetic bearing actuator is presented along with magnetic FEM results. The results from the rotating loss tests and the basic equations used to determine rotor losses are then explained. The two procedures are combined for first order calculation of bearing sizing and rotor loss determination required in any initial design tradeoff study. Results are presented from this procedure as it relates to both rotor loss and bearing capacity determination.

MAGNETIC BEARING ACTUATOR SIZING

The basic equation (ref. 3) used to determine the pole area required to magnetically support an object is:

$$\text{Pole Force (F)} = 8260 * \text{Pole Area (A)} * B^2 \quad [1]$$

where F is in Newton, A is in mm^2 and B is in Tesla. Assuming B in the air gap and the B in the material are approximately the same, then the following equation (4) holds:

$$N * I = B * g_o / \mu_o \quad [2]$$

where g_o is the air gap length (meters), $\mu_o = 4\pi * 10^{-7}$ (Henrys / meter), N is the number of turns and I is the current (amps). The inductance of a coil and the relationship of inductance, voltage and current are:

$$L = N^2 * \mu_o * A / g_o \quad [3]$$

$$V / L = dI / dt \quad [4]$$

where L is in Henrys, V is in volts and t is in seconds.

These four equations when used together are the first steps in determining the size of a magnetic actuator. These equations also show that while all the equations are independent, when some parameters are chosen, then others become dependent. As an example, if the pole force and the maximum flux density are chosen, then the pole area is calculated using [1]. For a given air gap and flux density, the required NI is calculated using [2]. Given a maximum current, the number of turns is determined using [2] and with the number of turns the inductance of the coil is calculated using [3]. For a given voltage, the maximum slew rate of the actuator is calculated using [4].

RADIAL MAGNETIC ROTOR LOSSES

Rotor losses can be separated into three families, losses due to eddy currents, losses due to rotating hysteresis and losses due to alternating hysteresis effects. These three effects are influenced by the magnetic flux density in the material, the shape of the magnetic field, the type of material, mass of the rotor and the lamination thickness. Kasarda (ref. 1) has proposed the following equations for these three losses.

The equation for power loss in a rotor due to eddy currents is:

$$P_e = \frac{\pi^2 d^2 B_{max}^2 f_{eff}^2 M_{vec} (10^{-6})}{6\rho} \left(\text{watts / cm}^3 \right) \quad [5]$$

d = rotor lamination thickness (meters), ρ = resistivity ($\Omega\cdot\text{m}$) and M_{vec} is the effective volume coefficient. The effective frequency is determined by the rotational speed of the rotor times the number of pole edges:

$$f_{eff} = \frac{N \times n_e}{60} \quad [6]$$

where N = rotational speed of the rotor in rpm and n_e = number of stator pole edges, 32 for a 16 pole configuration and 16 for an 8 pole configuration.

The equation for the alternating hysteresis power loss component is:

$$P_{ha} = 10^{-7} \eta f_{eff} (10000 \times B_{max})^k M_{vah} \left(\text{watts / cm}^3 \right) \quad [7]$$

The hysteresis coefficient, η , has a proposed value of approximately 0.00046 and the exponent, k , has an approximate value of 1.6 for flux densities (B) in the range of 0.15 to 1.20 Tesla.

The proposed equation for the rotational hysteresis power loss component is:

$$P_{hr} = 10^{-7} [3000.0 \times B_{max} - 500.0] f_r M_{vrh} \left(\text{Watts/cm}^3 \right) \quad [8]$$

Where B_{max} is the maximum flux density in Tesla, f_r is the effective frequency in Hz, and M_{vrh} is the effective volume coefficient for the rotational hysteresis calculation. The effective frequency for the rotational hysteresis is:

$$f_r = \frac{N \times n_l}{60} \quad [9]$$

where N = rotational speed of the rotor in rpm and n_l = the number of flux loops experienced by the journal during one revolution, 8 for 16 pole configuration, 4 for an 8 pole configuration.

The above equations show a basic fact of magnetic bearing design: the loss in the bearing is a function of both maximum flux density and the mass of the rotor. While flux density on the rotor surface produces force, flux density inside the rotor produces loss. Reducing the flux density level inside the bearing and reducing the mass of the rotor at the same time will produce a design which will be low in loss and weight efficient.

RADIAL BEARING FLUX PATHS

The flux paths for a four-pole heteropolar radial bearing are shown in Figure 1. As shown by Figure 1, the flux leaving or entering the pole is twice that of the back iron and the rotor. If the flux density in all the material is desired to be at the same level, then the poles should be twice the cross sectional areas of the rotor and the back iron.

When the actuator poles become greater than four, the flux paths will differ depending on the polarity of the pole configurations. Two heteropolar actuator configurations used are the alternating pole (NSNS) and the pole pair (NNSS) configurations. The flux paths for these two eight-pole configurations, in the bias condition ($NI = 200$), are shown in Figures 2 and 3.

RADIAL BEARING FINITE ELEMENT MODELING

Finite element modeling was performed on the hetero-polar configurations shown in Figures 2 and 3. The dimensions of the design modeled are shown in Table I. While the flux density on the rotor surface is the same in the bias condition for the two configurations under the poles, (Figures 4 and 5), the pattern of the flux density is vastly different. Figures 6 and 7 show the flux density at the middle of the rotor for the two configurations. Both configurations have the same maximum flux density in and on the rotor, but with a different profile. Figures 8 and 9 show the flux density in the stator between poles 1 and 8. While the flux density under the poles on the rotor is the same, the flux density in the stator is approximately 200% higher for the pole pair configuration than the alternating pole configuration.

Figures 10 and 11 show FEM results of the flux paths for the two configurations in the maximum force condition ($NI = 450$), four poles on and four poles off. Figures 12 to 15 show the FEM results for the flux density on and in the rotor for the maximum force condition. As in the bias condition, the flux density levels are the same for the two configurations, but the patterns are again different. Figures 16 and 17 shown the flux density in the stator between poles 1 and 8. The flux density in the pole pair configuration is approximately 25% higher than the alternating pole configuration.

COMPARING FINITE ELEMENT MODELING AND POWER LOSS MEASUREMENTS

Kasarda (ref. 1) has shown that at speeds above 3,000 rpm, the loss in the rotors for the two configurations is approximately the same. Below 3,000 rpm, the pole pair configuration had less loss than the alternating pole configuration. This suggests that at high frequencies, the flux density level is more important than the flux density frequency pattern on or in the rotor.

DISTRIBUTED FLUX BEARING DESIGN

From the above analysis, the pole configuration at the same flux density level produces the same loss in the rotors. Reducing the loss by reducing the mass of the rotor is attempted by the distributed flux configuration magnetic bearing shown in Figure 18. The dimension of the magnetic bearing modeled for this configuration is shown in Table I. Figures 19 to 21 show the results of the FEM the flux density levels for this configuration in the bias condition ($NI = 200$). Figure 22 shows the flux pattern for the maximum force condition ($NI = 450$) for this configuration. In this configuration, three upper poles are in the full on state, the two horizontal poles are set half the NI value of the full on poles and the last three poles are off. Figures 23 to 25 show the results of the FEM for the flux density levels of this configuration in the full force condition.

COMPARING FINITE ELEMENT CONFIGURATION MODELS

Comparing the FEM results on the rotor for this configuration and the two previous designs, the pattern and the maximum levels of flux density for the bias condition are the same. For the maximum force condition, the levels are the same but the pattern is slightly different. The distributed flux condition produces a more efficient design than the other two hetero-polar designs.

POWER LOSS CALCULATIONS

Using equations 5 to 9, power loss calculations were carried out for the three configurations. For a speed of 30,000 rpm and a flux density level of 1.5 Tesla and a one-inch long rotor, the alternating pole and the pole pair configuration produced a power loss of 420 watts. The same length rotor for the flux distribution configuration produced a power loss of 250 watts.

The effective volume coefficient (ref. 1) had a uniform bias field at the poles with a small control flux superimposed at the poles for stability. When a heteropolar bearing is fully energized for maximum load capacity, the flux distribution is changed. In the maximum condition, approximately 50% of the bearing contains flux and approximately 50% is flux free. Modification of the preceding effective volume coefficients to account for these conditions was carried out for a series of first order parametric studies. The conditions held constant in the study were the outside diameter of the stator, the inside diameter of the rotor, the magnetic air gap, and the material properties of the rotor and stator.

For a 445 Newton load capacity bearing, Figure 26 shows the effect which setting the flux density to a maximum has on a four-pole design. Since load capacity changes as the square of the flux density, but the rotor mass changes linearly with flux density, the losses go down as the flux goes up. This type of comparison would be useful when a choice of material is required in the design phase of a program, with the only difference being in the flux saturation limit of the materials in question.

Applying the distributed flux configuration to stators with pole counts of 4, 8, 12, and 16, a comparison of rotor loss versus bearing load was made. For a given speed and control flux density (60,000 rpm and 2 Tesla), Figure 27 shows the influence which pole count in the stator has on rotor losses. The higher the pole count, the less rotor mass is required and the rotor losses go down even with increased effective frequency of the magnetic field in the rotor. The limit to the number of poles, which can be designed into a bearing is a function of the skin effect (ref. 7), the volume required for the coils and the overall volume of the bearing.

SUMMARY

This paper presents a first order attempt to size radial bearings for typical applications. A comparison of test data results to proposed rotor loss equations were presented. The use of these equations to understand the different stator pole configurations was shown. As more data become available on the true nature of rotating losses in magnetic bearings, the equations used in this procedure will be updated.

REFERENCES

1. Kasarda, M. E., "The Measurement and Characterization of Power Losses in High Speed Magnetic Bearings", Ph.D. Thesis, University of Virginia, January 1997
2. Kondoleon, A. S., Kelleher, W. P., "Magnetic Bearings at Draper Laboratory", NASA Publication, CP-3336, July 1996
3. Pearman, P. A., *Electrical Machinery and Transformer Technology*, Saunders College Publishing
4. Fitzgerald, A. E., *Electric Machinery*, McGraw-Hill, 5th edition
5. Kondoleon, A. S., Kelleher, W. P., "A Magnetic Bearing Suspension System for High Temperature Gas Turbine Applications", ASME Publication, 97-GT-114, June 1997
6. Hoole, S. H., *Computer Aided Analysis and Design of Electromagnetic Devices*, 1989 Elsevier Publishing
7. Bozorth, R. M., *Ferro-Magnetism*, Van Nostrand Company, 1964, 8th edition

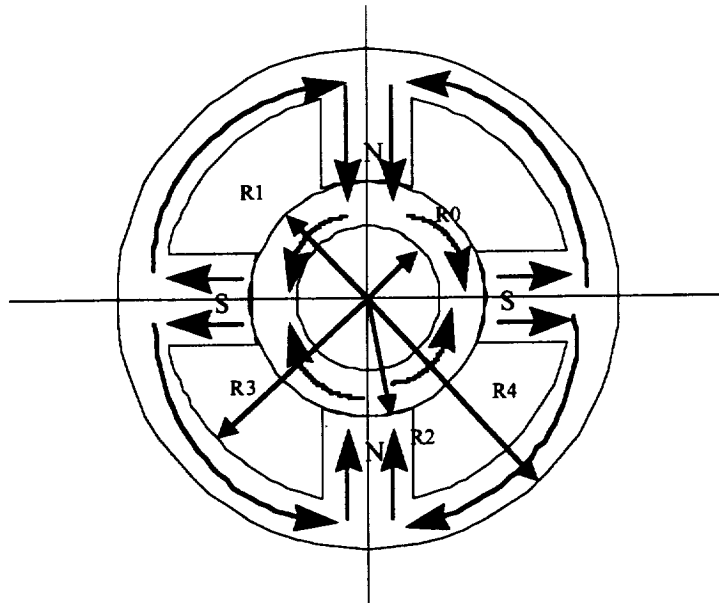


Figure 1 Flux Path for a Four Pole Radial Bearing

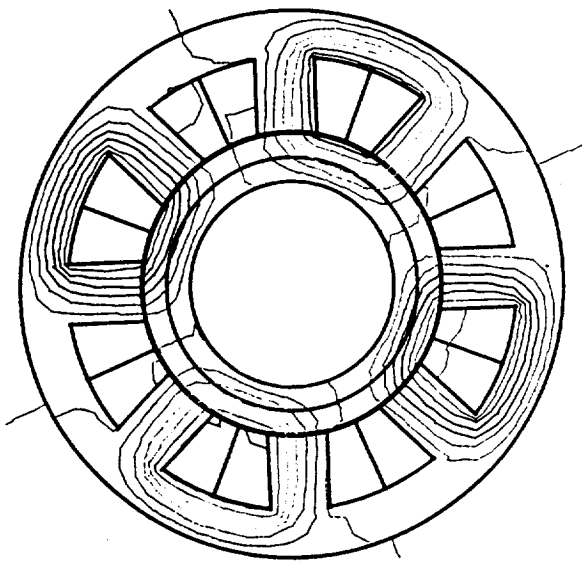


Figure 2 Flux Path for 8 Pole Pair Bias Configuration

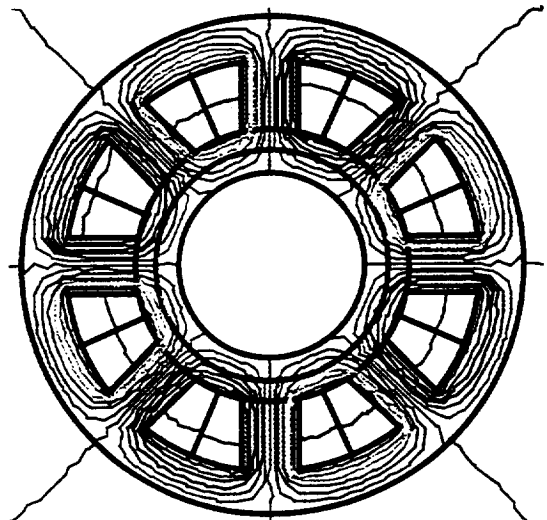


Figure 3 Flux Path for Alternating 8 Pole Bias Configuration

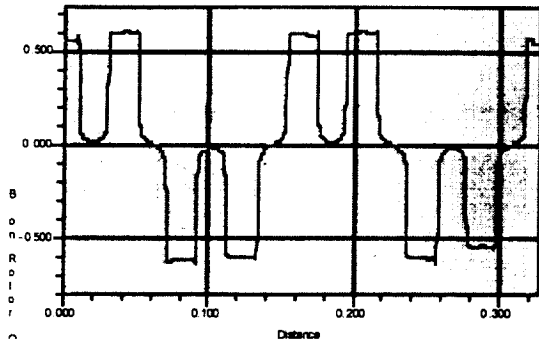


Figure 4 Flux Density on Rotor 8 Pole Pair Bias Configuration

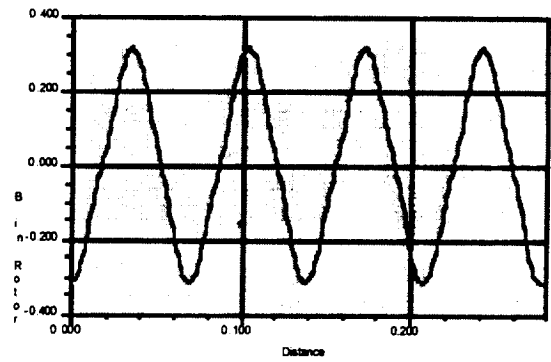


Figure 7 Flux Density in Rotor Alternating 8 Pole Bias Configuration

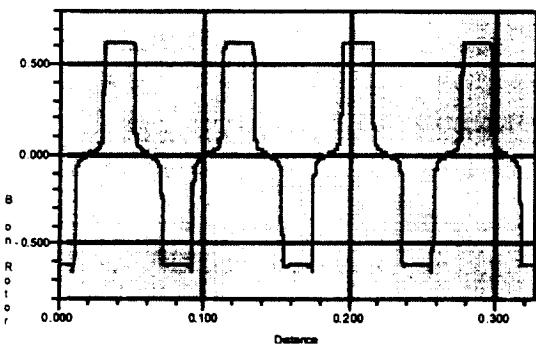


Figure 5 Flux Density on Rotor Alternating 8 Pole Bias Configuration

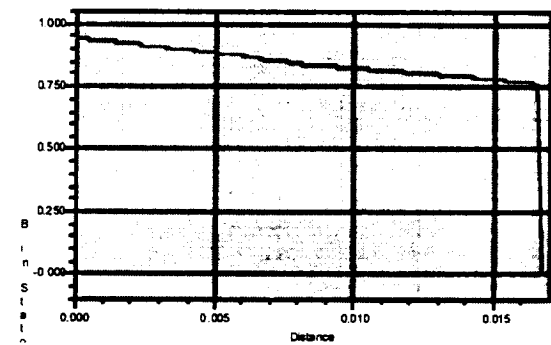


Figure 8 Flux Density in Back Iron 8 Pole Pair Bias Configuration

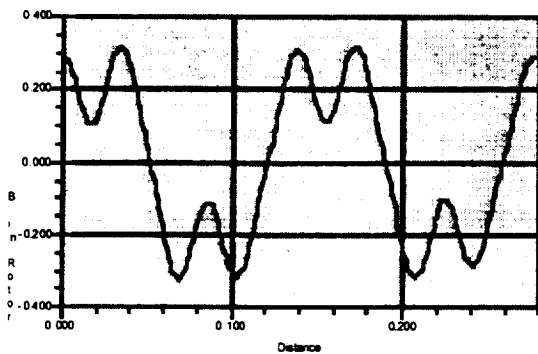


Figure 6 Flux Density in Rotor 8 Pole Pair Bias Configuration

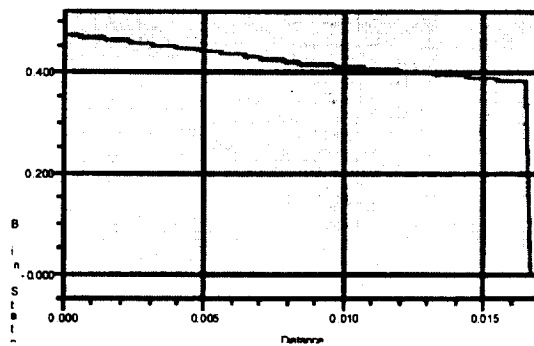


Figure 9 Flux Density in Back Iron Alternating 8 Pole Bias Configuration

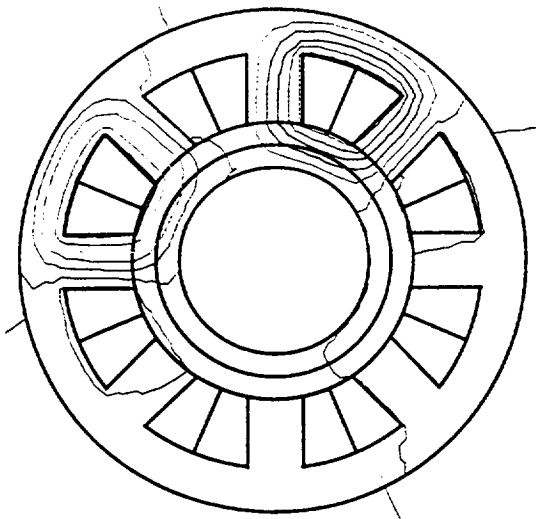


Figure 10 Flux Path for 8 Pole Pair Full Force Configuration

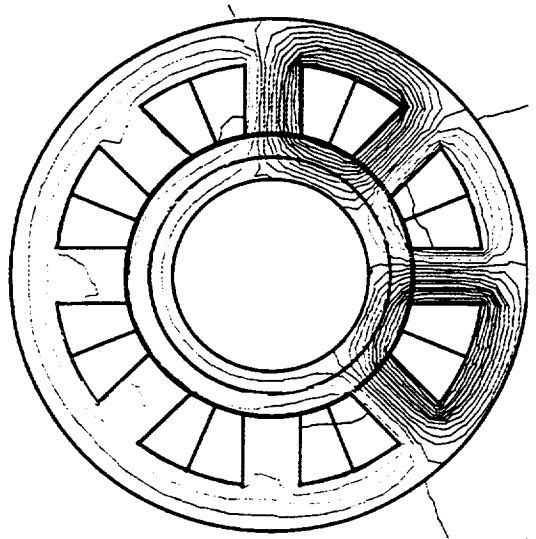


Figure 11 Flux Path for Alternating 8 Pole Full Force Configuration

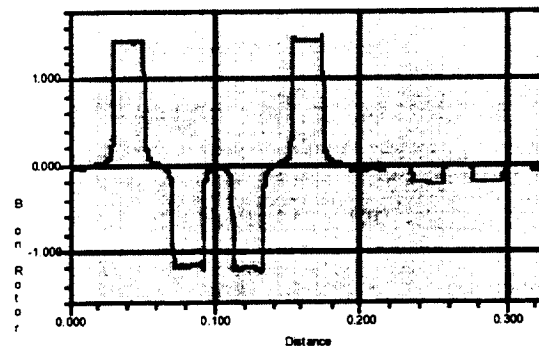


Figure 12 Flux Density on Rotor 8 Pole Pair Full Force Configuration

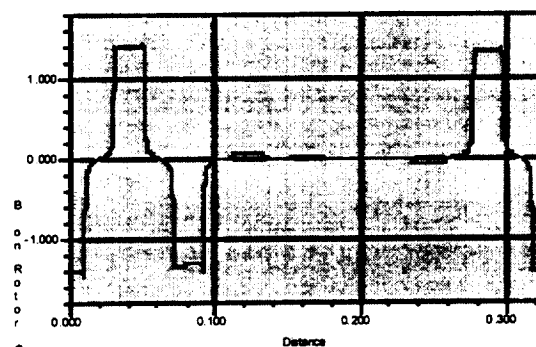


Figure 13 Flux Density on Rotor Alternating 8 Pole Full Force Configuration

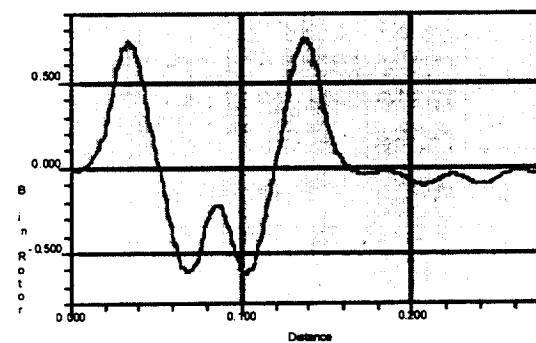


Figure 14 Flux Density in Rotor 8 Pole Pair Full Force Configuration

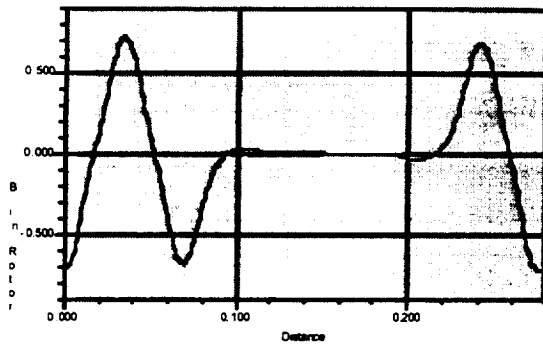


Figure 15 Flux Density in Rotor Alternating 8 Pole Full Force Configuration

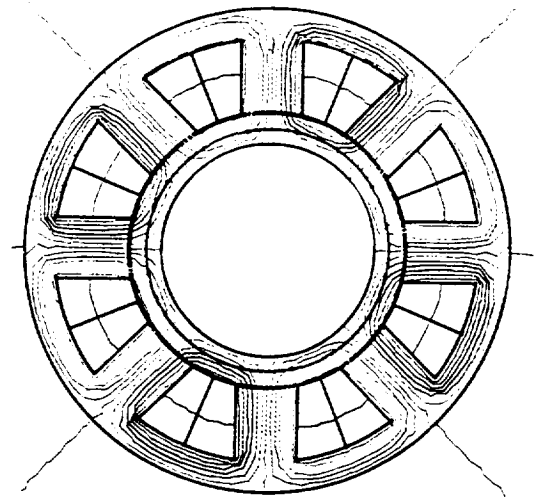


Figure 18 Flux Path for 8 Pole Distributed Bias Flux Configuration

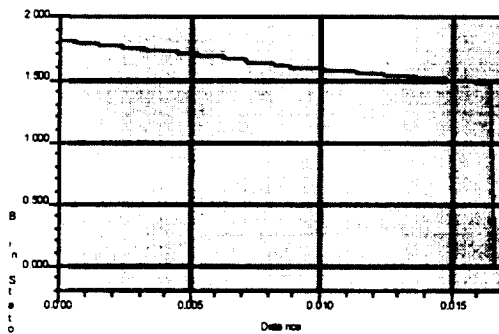


Figure 16 Flux Density in Back Iron 8 Pole Pair Full Force Configuration

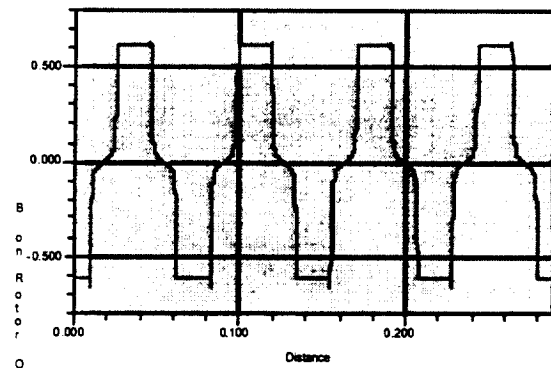


Figure 19 Flux Density on Rotor 8 Pole Distributed Bias Flux Configuration

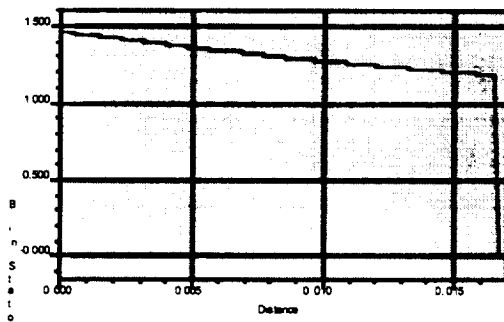


Figure 17 Flux Density in Back Iron Alternating 8 Pole Full Force Configuration

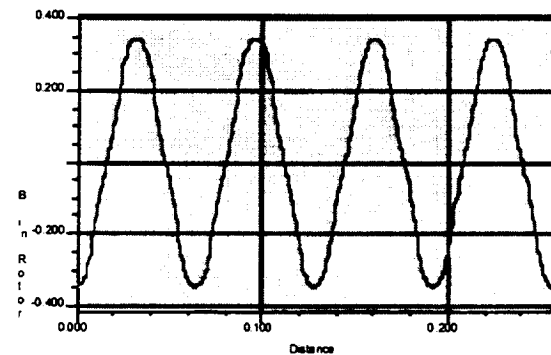


Figure 20 Flux Density in Rotor 8 Pole Distributed Bias Flux Configuration

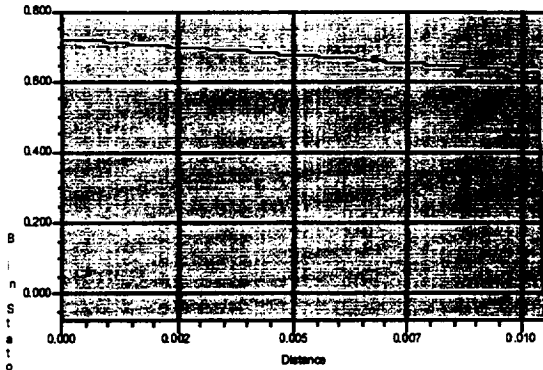


Figure 21 Flux Density in Back Iron 8 Pole Distributed Bias Flux Configuration

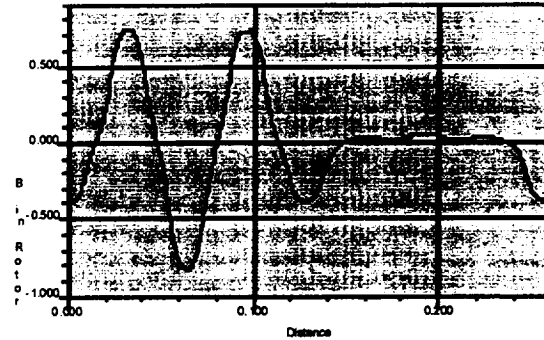


Figure 24 Flux Density in Rotor 8 Pole Distributed Flux Full Force Configuration

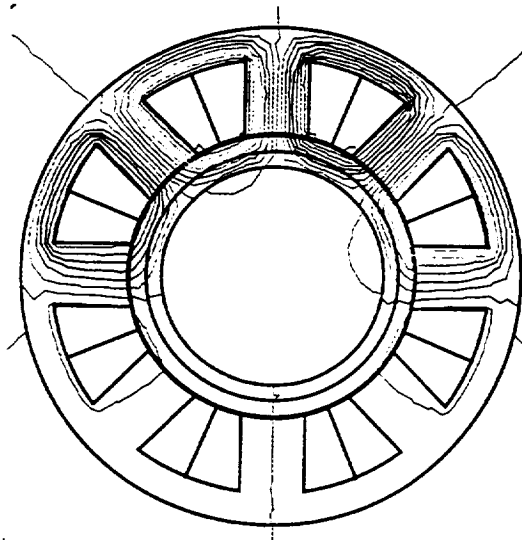


Figure 22 Flux Path for 8 Pole Distributed Flux Full Force Configuration

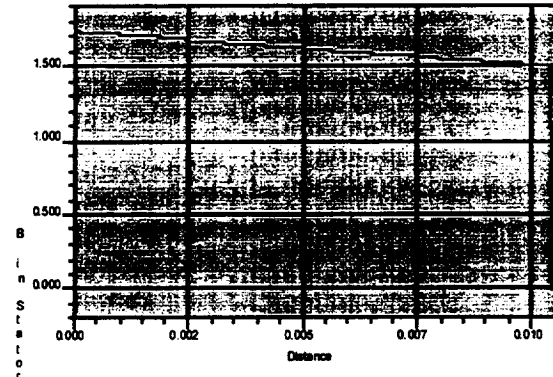


Figure 25 Flux Density in Back Iron 8 Pole Distributed Flux Full Force Configuration

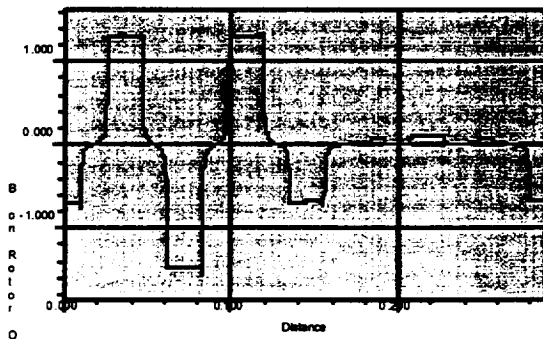


Figure 23 Flux Density on Rotor 8 Pole Distributed Flux Full Force Configuration

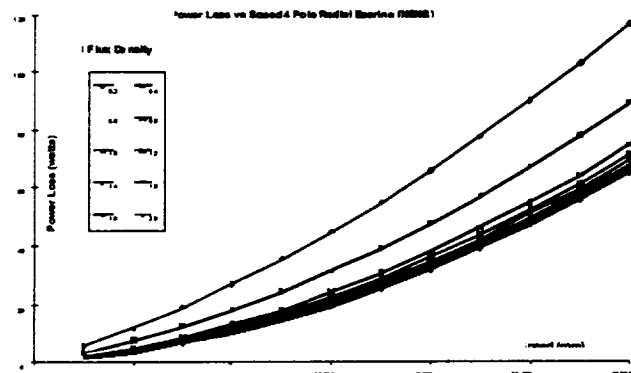


Figure 26 Rotor Loss vs Maximum Control Air Gap Flux Density

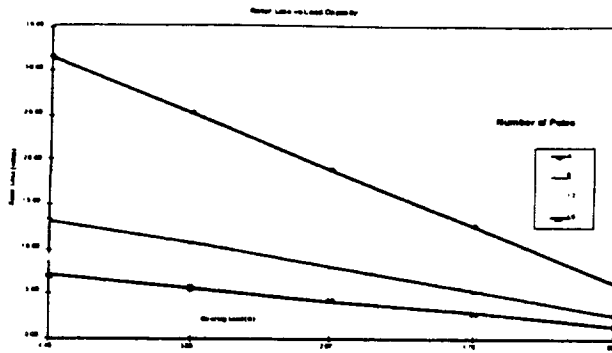


Figure 27 Rotor Loss vs Load Capacity, Speed = 60,000 rpm, Control B = 2.0 Tesla

Table I
8 Pole Magnetic Bearing Dimensions (inches)

	8 Pole Alternating Configuration	8 Pole Pair Configuration	8 Pole Distributed Flux Configuration
R0	1.40	1.40	1.40
R1	2.055	2.055	1.815
R2	2.070	2.070	1.830
R3	3.095	3.095	2.790
R4	3.75	3.75	3.20
Pole Width	.82	.82	.82

Active Magnetic Bearings for 10kWh Flywheel Energy Storage System

Osamu Saito, Soichiro Une, Hisayuki Motoi
Ishikawajima-Harima Heavy Industries Co.,Ltd
1-15,Toyosu 3 chome, Koto-ku, Tokyo 135-8732, Japan

Hironori Kamenno , Yasukata Miyagawa , Ryouichi Takahata , Hirochika Ueyama
R&D Center, KOYO SEIKO CO., LTD.
No.333, Toichi-chou, Kashihara, Nara 634-0008, Japan

SUMMARY

As the demand for electric power has been increasing steadily, a flywheel energy storage system (FESS) using magnetic bearings is needed in order to level daily load of electric power. We have succeeded to suspend a flywheel of 385kg in total weight which has a 1,000mm diameter carbon fiber reinforced plastics (CFRP) rotor performing as 10kWh FESS by means of 5 axis controlled active magnetic bearings (A.M.B.).

This paper presents the A.M.B. used in the above system controlled by digital signal processor (DSP). The switching power amplifiers of the A.M.B. can supply maximum current of 8A per channel driven by 300V supply voltage. The radial electromagnets were designed as so called homopolar type in order to reduce rotational loss due to eddy current. The decentralized controller was designed for upper and lower radial bearings using bias current system linearization. On the other hand, an axial electromagnet was designed as a permanent magnet biased (non-linear) actuator.

It is possible not only to monitor the displacement of the rotor and control currents in the electromagnet but also to change control parameters of each axis from personal computer by means of serial communication, including telephone line with modem, accessing directly to the DSP.

The paper also reports the system information of the FESS and measured data during stand still and rotation by means of above mentioned serial communication.

INTRODUCTION

In a flywheel energy storage system (FESS), the electric energy is stored as the kinetic energy of the rotating flywheel and it is taken out as electric energy if needed. In past studies, it had been considered that it was difficult to supply the energy more than one hour because the rotational loss of ball bearing was very large. Furthermore, there was no suitable material for flywheel which has high tensile strength against its density.

By the way, there were only a few reports about the flywheel rotor supported by contact free A.M.B. which can be accelerated up to a certain high speed practically. One of the reasons seems to be that it is very difficult to control and stabilize the natural frequency vibration of the rotor by A.M.B. Additionally, large gyro effect due to large moment of inertia around rotational axis increase such difficulties.

Recently, it was revealed that a high-Tc superconductor ($\text{YBa}_2\text{Cu}_3\text{O}_{7-x}$) which has a strong pinning force was used in magnetic bearings [1] and the rotational loss of superconducting magnetic bearings was very small [2]. In these conditions, it is expected that the superconducting magnetic bearings could be used for large scale FESS. Also, the development of CFRP for FESS rotor has advanced remarkably.

In Japan, a national research and development project of FESS using superconducting magnetic bearings was started in 1995. In this project, a small type model of 0.5kWh class FESS system was assembled, tested and discussed about its rotor dynamics in 1998 [3]. Currently, as a further step, a middle type model of 10kWh class FESS which rotor was suspended by A.M.B. (without superconducting magnetic bearing) has been tested in order to verify the developed know how in rotor dynamics for FESS.

STRUCTURE OF FESS ROTOR

Figure 1 shows a structure of 10kWh flywheel system and Table 1 shows a specification of the system respectively. It is necessary to place the rotor and bearings in a vacuum housing in order to minimize aerodynamic drag (windage loss). A flywheel (FW) made of carbon fiber reinforced plastic (CFRP) was shrunk-fitted to an aluminum hub connected on a main hollow shaft. A synchronous motor rotor was installed in the inside of main hollow shaft in order to perform energy input (acceleration) and output (deceleration). Two lamination cartridges of radial rotor core made by silicon steel plate for the radial active magnetic bearings (RaAMB) were also shrunk-fit to each end of the main shaft. In addition, a ring shaped disk for the axial active magnetic bearings (AxAMB) was attached to the upper end of the main shaft. The rotor assembly was levitated by RaAMB and AxAMB without mechanical contact in all directions. When the radial/axial vibration or displacement exceeds the control limit of the A.M.B.s, the main shaft touches the inner race of the emergency ball bearings in order to prevent

the rotor from being damaged. For future study in this project, it is possible to install permanent magnet in the inner side of main hollow shaft rotor for radial type superconducting magnetic bearings[4].

DESIGN OF ACTIVE MAGNETIC BEARINGS

The electromagnets of RaAMBs are homo-polar type in order to reduce drag torque due to eddy current loss in the radial rotor core. Table 2 shows the specification of A.M.B.s for this system.

The RaAMBs and AxAMB are totally controlled by Digital Signal Processor (DSP) TMS320C50. Thanks to the digitally controlled system, it is possible to monitor the displacement of the rotor and current of the A.M.B.s from a personal computer through serial communication. The autonomous scheduled diagnosis including residual unbalance of the rotor, running orbit analysis, etc are easily implemented by monitor software. Using modem and a telephone line as shown figure 2, it is also possible to access to the A.M.B. controller from any long distance place. (ex. From Santa Barbara to Tokyo). The PWM (Pulse Width Modulation) switching power amplifiers of the A.M.B.s, which switching frequency is 100KHz, can supply maximum peak current of 8A per channel driven by 300V supply voltage. The inductance type displacement sensors for radial direction are used and eddy current type displacement sensor are used for axial direction.

ANALYSIS OF ROTOR DYNAMICS

The entire rotor assembly consisting of shaft, hub and FW, as shown Figure 3, was modeled by means of the Finite Element Method (FEM). Finally a State-Space expression was used for mathematical rotor model which is easily used for total system analysis including feedback structure of A.M.B.s.

Figure 4 (a) shows a modeled entire rotor assembly used in this analysis. As a result, first 3 natural frequencies and corresponding bending mode shape at stand still were calculated as shown in figure 4 (b),(c) and (d). Figure 4 (b) and (c) show 1st and 2nd bending mode mainly due to the deformation of hub and FW. Contrary, figure 4(d) shows 3rd bending mode of rotor, which is resulted from 1st bending mode of main shaft. In the above natural frequency analysis, RaAMBs were expressed as simple spring element.

Figure 5 shows analysis results of natural frequencies of first 2 rigid mode of 1R, 2R, and above mentioned 1B, 2B and 3B including frequency response of upper and lower RaAMBs. The natural frequency of the rigid mode are results from the characteristics of RaAMB (resonance of A.M.B. stiffness and mass, rotating moment of inertia of the rotor) and 1B, 2B, 3B show natural frequency of bending mode caused by the elasticity of the rotor. It is indicated that each natural

frequency value is split in two branches (forward and backward) by increase of the rotational speed due to gyroscopic effect. The rotor speed is shown as a straight line in figure 5. At intersection of each natural frequencies and the line, the rotor can be expected to vibrate by resonance (critical speed). For accelerating the rotor at system target speed of 17,200rpm, the rotor has to pass through resonant frequency of backward 1B at 12,500rpm after passing resonant frequencies of 1R,2R. The controller of the RaAMBs has to be designed to stabilize these vibration mode and to pass the critical speed.

RESULT OF ROTATIONAL TEST

After the rotor was successfully suspended by AMB, the dynamic stiffness could be measured indirectly as the reciprocal of the sensitivity transfer function of the controller which has the input of the disturbance force to the rotor and output of the displacement of the rotor. These measurements can be easily carried out by developed built-in function of DSP. Figure 7 shows the dynamic stiffness measured in upper and lower RaAMB and AxAMB. Measured values of natural frequencies were nearly equal to calculated values in figure 4. The 3B bending mode was not found clearly in measured data, because this mode was thought to be damped quite well.

The rotor was accelerated up to 8,000rpm in this step. The actual natural frequencies were obtained from dynamic stiffness data measured during rotation. Figure 6 shows the measured results of interesting natural frequencies. The branch of measured 1B was larger than that of calculated value. But except for it, the whole branch of measured natural frequencies were predicted well by that of calculated results.

Figure 8 shows the results of measured run-out (orbit) in radial direction and axial direction at 8,000rpm. The run-out was approximately less than 5 μ m and the rotor vibration were damped well by RaAMBs. The rotor will be accelerated up to the target speed of 17,200rpm in near future.

CONCLUSIONS

The prototype of 10kWh class flywheel energy storage system which has the flywheel rotor of diameter 1,000mm and rotor weight of 385kg was supported by the Active Magnetic Bearings without mechanical contact. The whole rotor assembly could be successfully accelerated up to 8,000rpm. As a result, kinetic energy of the system was achieved about 2kWh. This energy storage value will become larger in near future by reaching more higher speed step by step, and will be finally achieved 10kWh at 17,200rpm.

In this study, the rotor dynamics of the flywheel energy storage system whose rotor had large gyroscopic effect including RaAMB dynamics were analyzed in detail, and the rotor vibration due to natural frequencies was damped well by RaAMBs.

This study was funded by the New Energy and Industrial Technology Development Organization (NEDO) in Japan, as a part of the Japanese national project "High-Temperature Superconducting Flywheel Energy Storage System."

REFERENCES

- [1] R.Takahata, H.Higasa, H.Ueyama, Y.Miyagawa, H.Kameno and F.Ishikawa ; "Trial Manufacturing of 0.2kWh Class Flywheel Rotor Supported by superconducting Magnetic Bearing, T.IEE, Vol.117-D, No.9, 1132_1138(1997) in Japanese
- [2] H.J.Bornemann, T.Ritter, C.Urban, O.Zaitsev, K. Weber and H.Rietschel _ "Low Friction in A Flywheel System with Passive Superconducting Magnetic Bearings", Applied Superconductivity Vol.2,No.7/8,439_447(1994)
- [3] Y.Miyagawa, H.Kameno R.Takahata, and H.Ueyama; "A 0.5kWh Flywheel Energy Storage System using A High-Tc Superconducting Magnetic bearing", IEEE Transaction on Applied Superconductivity, Vol..9, No.2 996_999(1999)
- [4] H.Kameno Y.Miyagawa, R.Takahata, and H.Ueyama; "A Measurement of Rotation Loss Characteristics of High-Tc Superconducting Magnetic bearing and Active Magnetic bearings", IEEE Transaction on Applied Superconductivity, Vol..9, No.2 972_975(1999)

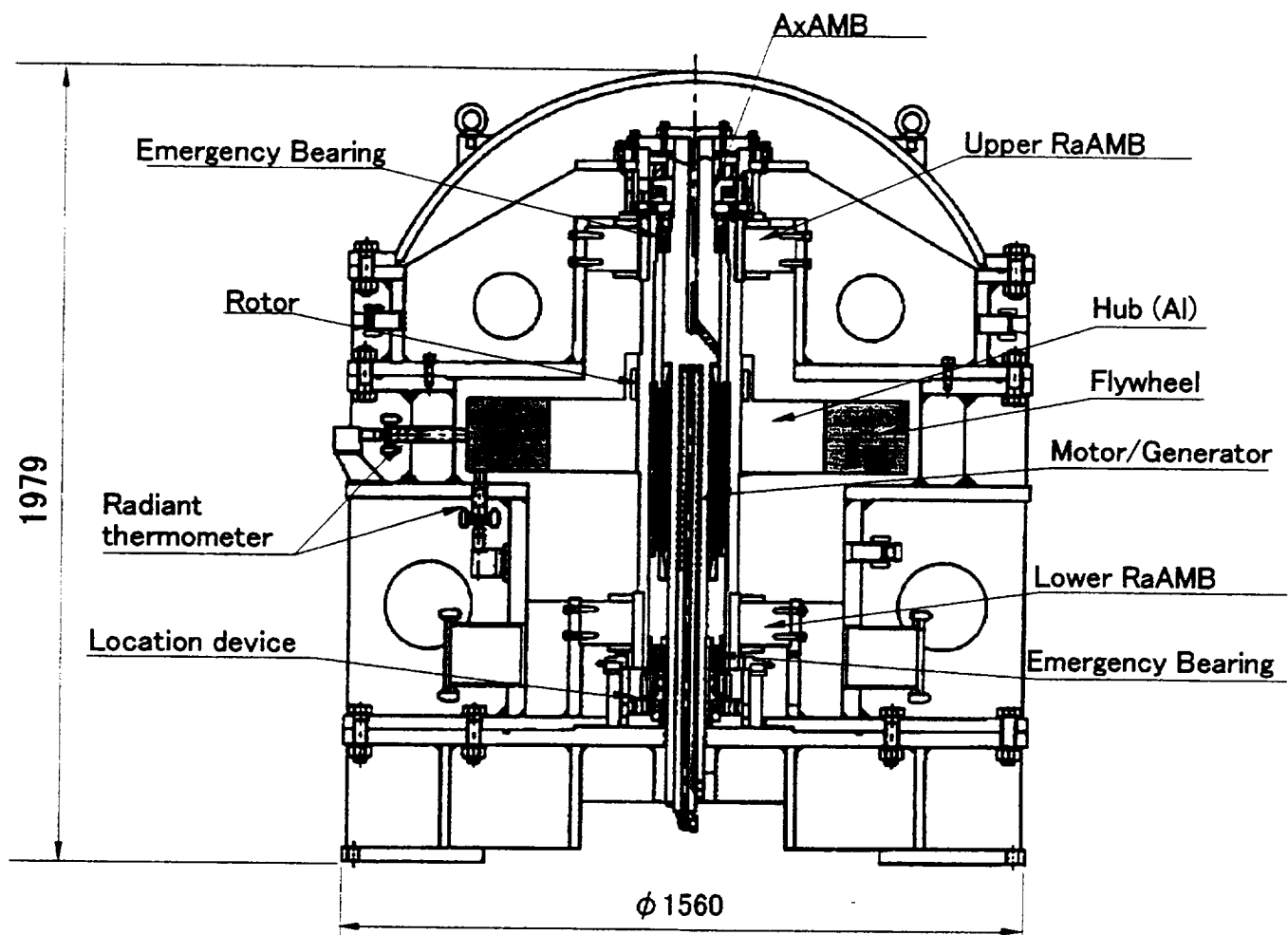


Figure 1 Structure of 10kWh flywheel system

Table 1 Characteristics of 10kWh flywheel system

Pressure	Less than 0.14 Pa (0.001 Torr)
Storage Energy	10kWh (at 17,200rpm)
Rotation Speed	17,200 rpm (target) 8,000rpm (achievement)
Inertia moment	$2.79 \times 10^8 \text{gcm}^2$
Length of Rotor	1,060 mm
Mass of Rotor	385 kg
Flywheel	CFRP $\phi 1000 \times \phi 625 \times 165$
Motor/Generator	Synchronous type 2kW

Table 2 Data of Active Magnetic Bearings

Control method	Digital control
Bias Current of RaAMB	1.5 A
Bias Current of AxAMB	3.0A
Air gap at AxAMB	0.4mm (axial direction)
Air gap at RaAMB	0.4mm (radial direction)
Air gap at emergency bearing	0.2mm (axial direction) 0.2mm (radial direction)
Type of electromagnet (RaAMB)	Homopolar type Inner diameter : 240.8mm
Material of rotor (RaAMB)	Super-E core(NKK) (0.1mm thick)

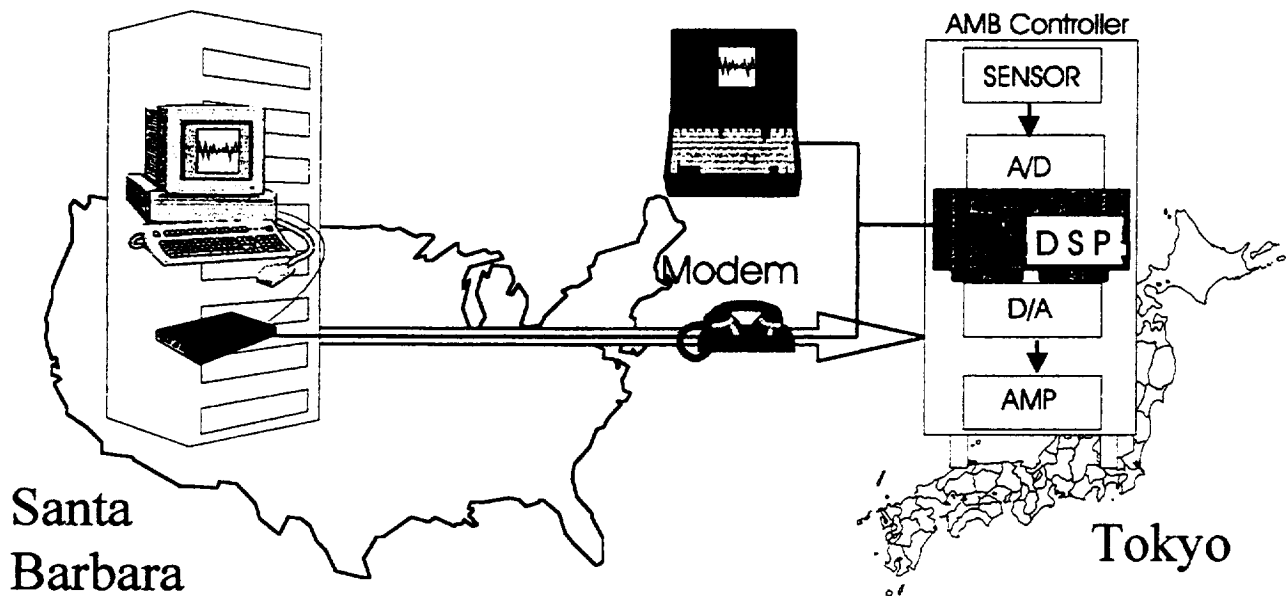


Figure 2 Remote control of AMB controller

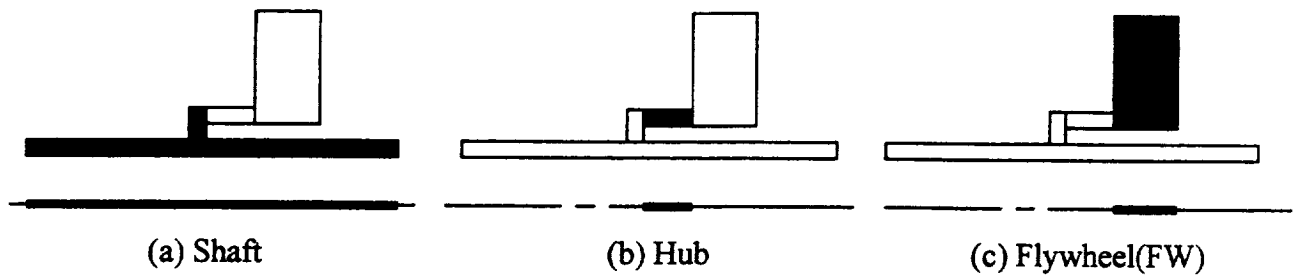
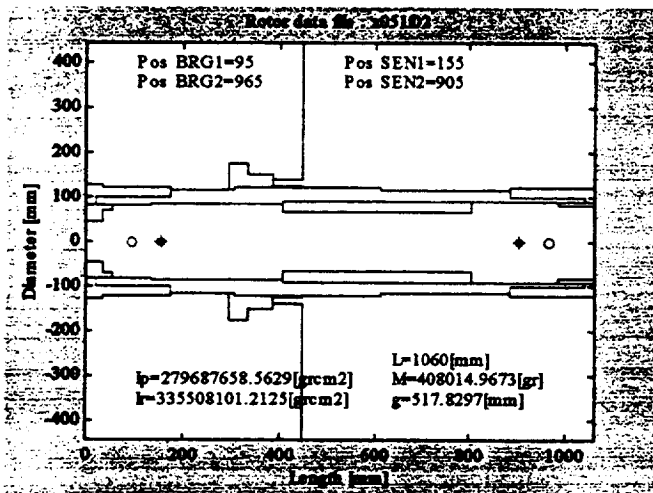
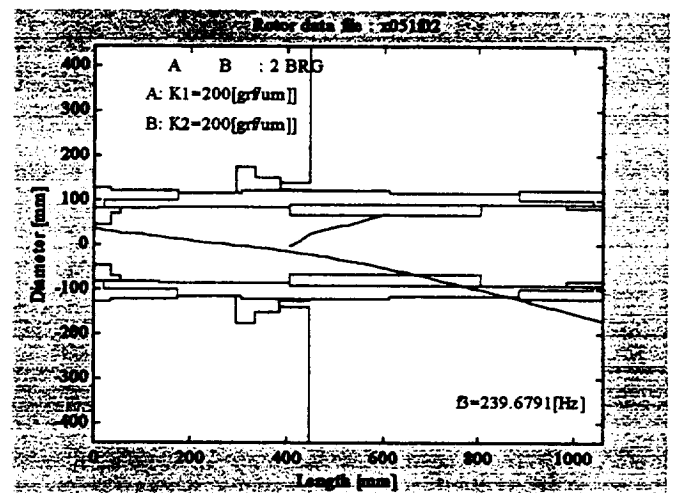


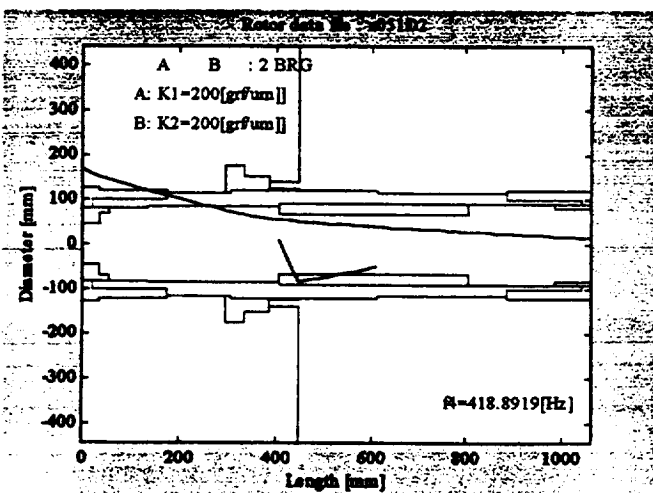
Figure 3 Modeling structure of the rotor consist of a shaft, hub and flywheel



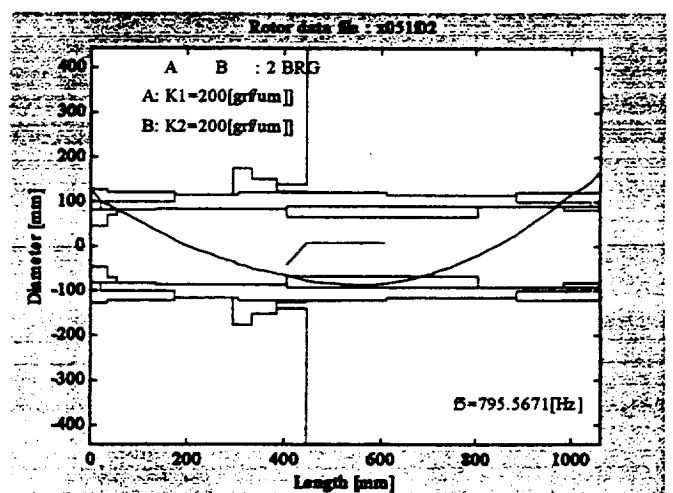
(a) Modeling structure of the rotor



(b) 1st bending mode mainly due to hub and FW

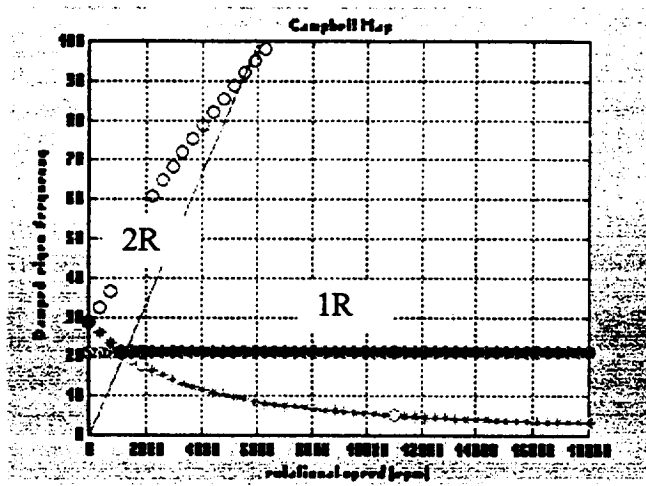


(c) 2nd bending mode mainly due to hub and FW

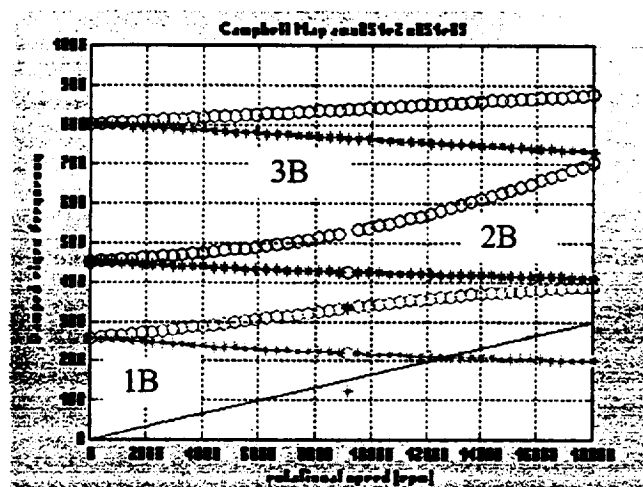


(d) 3rd bending mode mainly due to shaft

Figure 4 Analyzed results of natural frequency of the rotor

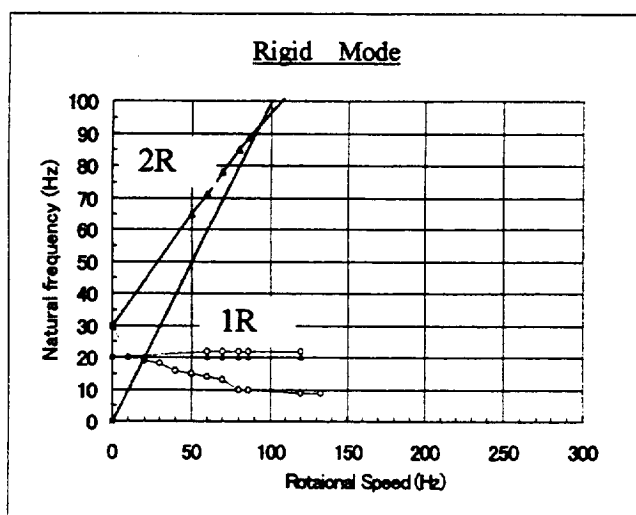


(a) 2 rigid mode natural frequency

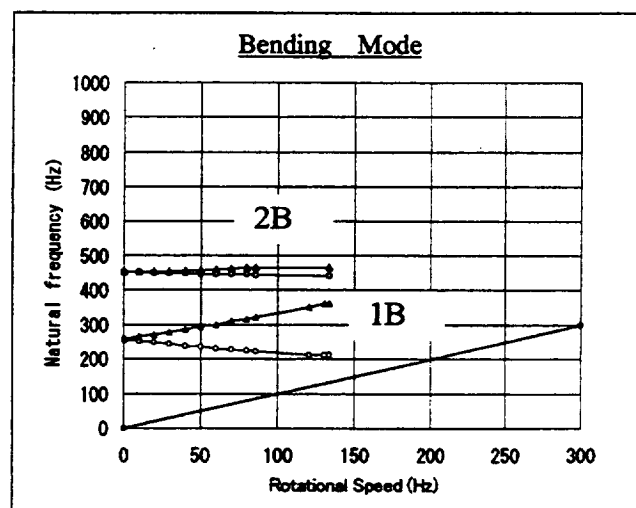


(b) 3 bending mode natural frequency

Figure 5 Analyzed results of natural frequency of the rotor

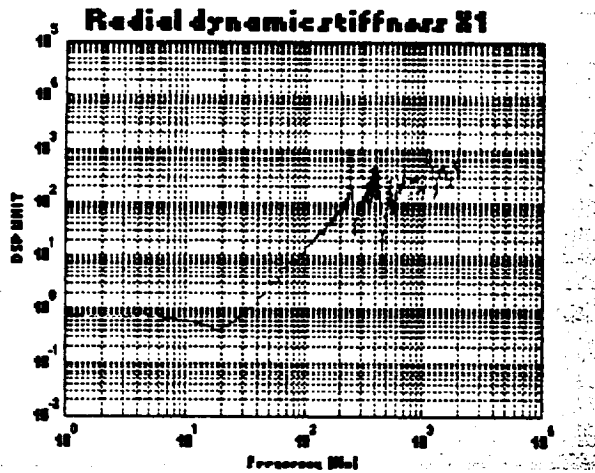


(a) 2 rigid mode natural frequency

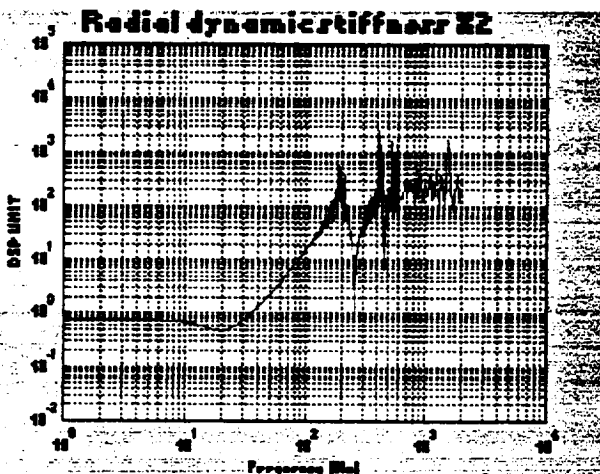


(b) 2 bending mode natural frequency

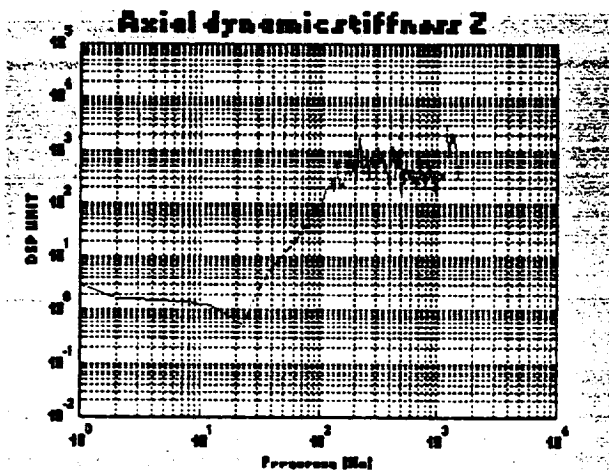
Figure 6 Measured results of natural frequency of the rotor



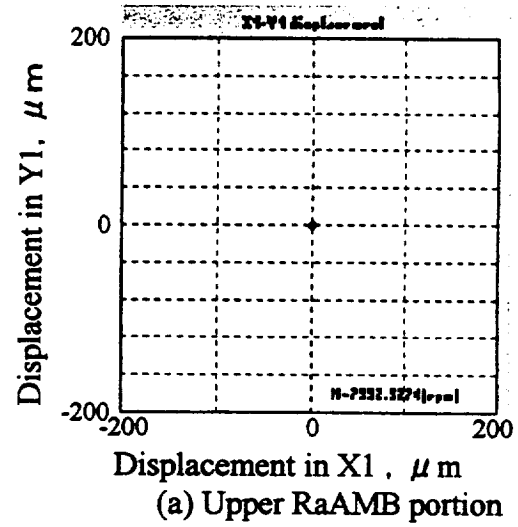
(a) Upper RaAMB portion



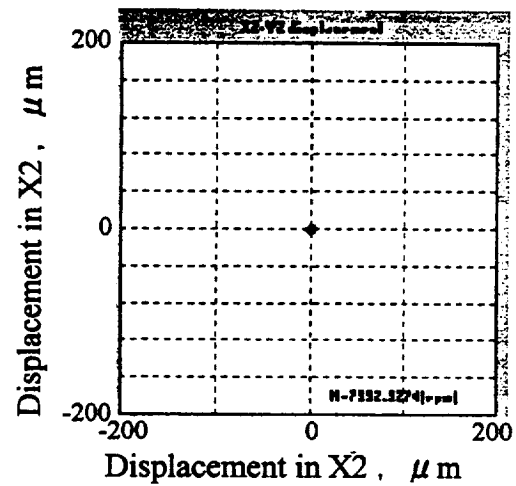
(b) Lower RaAMB portion



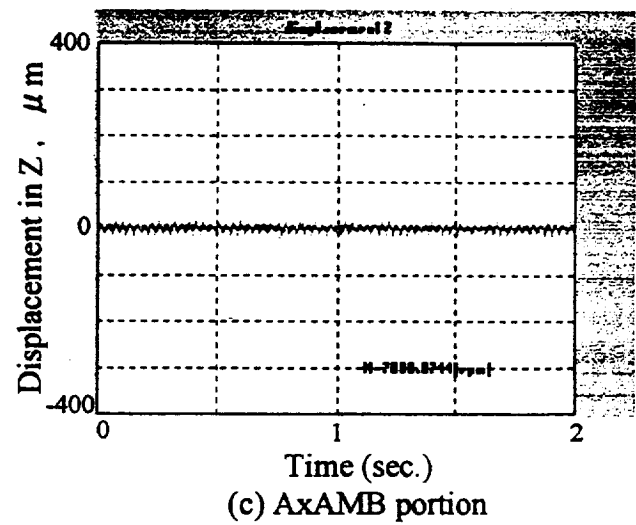
(c) AxAMB portion



(a) Upper RaAMB portion



(b) Lower RaAMB portion



(c) AxAMB portion

Figure.7 Dynamic stiffness of each AMB(measured) Figure.8 runout of the rotor in each AMB portion

A SELF-HEALING MAGNETIC BEARING

H. Ming Chen
Foster-Miller Technologies, Inc.
Albany, NY

SUMMARY

A fault tolerant magnetic bearing control scheme, which independently controls each stator pole using a proportional-integral-derivative (PID) displacement feedback, has been analytically tested. The scheme was applied to a 16-pole magnetic bearing with a load capacity of 6000 lb and a static load of 4000 lb. Transient response simulation of pole failures (such as those caused by power amplifier failure or coil short circuit) demonstrated that the rotor recovered its bearing center position in a fraction of a second after two consecutive failures of the two top load-carrying poles. The scheme does not require on-line current monitoring to determine the pole failure patterns or storage of precalculated control data to counteract pole failures.

INTRODUCTION

Conventional magnetic bearings share one common trait that impacts system reliability — if a single component fails, the entire system fails. For example, in a large turbine-generator supported by three radial magnetic bearings and one thrust magnetic bearing, a bearing system malfunction could occur due to burned-out electronic switches in one power amplifier out of thirty. Such unreliability is inherent to the method used to control the bearing. Consider the typical 8-pole bearing configuration shown in Figure 1. The conventional control method separates the poles into four pairs and uses two opposite pairs of poles (1-2 and 5-6) to control shaft motion in the vertical direction (y), and the other pair of poles (3-4 and 7-8) to control shaft motion in the horizontal direction (x). For each pair of poles, their coils are connected in series and driven by a power amplifier. If any of the four power amplifiers or coils fails, control of the associated direction or axis would usually fail due either to loss of static load-carrying capacity or when the system becomes dynamically out of tune. When one axis fails, the bearing cannot function, and the entire system must be shut down.

This paper addresses this deficiency of conventional magnetic bearing technology. Other methods have been developed to introduce redundancy into the control but all have certain limitations. Lyons, et al., [1] have designed and tested a fault-tolerant magnetic bearing system in which each radial bearing has three magnetically isolated control axes, any two of which can maintain control of the rotor position. However, with this approach, there is only one redundant control axis. Maslen, et al., [2] have taken a distributed approach that independently controls each pole-coil set by determining the coil currents for given required

magnetic forces. The multi-pole force-to-current relationship needed for feedback control is not unique and requires complex computation of a matrix relationship that is stored digitally in look-up tables. For the failure of a specific coil or a combination of coils, a specific matrix exists for the application of the servo control, and on-line monitoring of the coil currents is required to identify the pattern of coil failure.

As shown in Figure 2 for an 8-pole configuration, this author also uses the same distributed approach to independently control each pole-coil set (hereinafter called "pole"), but does not use the precalculated matrix method. Instead, a special set of bias currents and PID constants are assigned to each pole. These special values are determined by an engineering design analysis of the magnetic actuator, considering possible current and flux saturation, and overload due to different pole failure patterns. This new control scheme proves to be amazingly resilient to pole failures and shows a "self-healing" characteristic [3]. Specifically, when pole failures occur, the remaining poles work in unison and adjust current individually to regain control of the rotor. There is no need to monitor the pole failure pattern or provide precalculated current control parameters.

MULTI-POLE CONTROL MODEL

The self-healing control method is applicable to magnetic cores of heteropolar or homopolar configurations with any number of poles greater than three. To keep the discussion simple, we will concentrate on those bearings with uniform or identical poles in heteropolar configurations. The cross-sectional areas of magnetic flux paths at poles, rotor, and stator are all equal as with conventional active magnetic bearings. Each pole has a single coil driven by a dedicated power amplifier. Heteropolar bearings usually do not use separate bias currents, and the current in each coil may vary from zero to the maximum amperage but never change sign. Note that the flux variation or redistribution is no longer limited locally in a quadrant of poles. The current or air gap variation of one pole not only changes the flux density of that pole and the opposite quadrants, but also affects the perpendicular quadrants. Assuming negligible core metal reluctance, the flux distribution is calculated using the model in Figure 3 with an 8-pole example and the following matrix equation [2].

$$\mathbf{R}\phi = \mathbf{N}\mathbf{I} \quad (1)$$

where:

- ϕ = magnetic flux vector = $\{\phi_1, \phi_2, \dots, \phi_n\}^t$
- \mathbf{I} = current vector = $\{I_1, I_2, \dots, I_n\}^t$
- R_i = $g/\mu_0 A$ = air gap reluctance at i^{th} pole
- g_i = air gap at i^{th} pole
- A = pole area
- μ_0 = air permeability
- n = number of poles
- N = number of coils per pole

$$R = \begin{bmatrix} R_1 & -R_2 & 0 & \dots & 0 \\ 0 & R_2 & -R_3 & \ddots & \vdots \\ \vdots & \ddots & \ddots & \ddots & 0 \\ 0 & \dots & 0 & R_{n-1} & -R_n \\ 1 & 1 & 1 & 1 & 1 \end{bmatrix} \quad \text{and} \quad N = \begin{bmatrix} N & -N & 0 & \dots & 0 \\ 0 & N & -N & \ddots & \vdots \\ \vdots & \ddots & \ddots & \ddots & 0 \\ 0 & \dots & 0 & N & -N \\ 0 & 0 & \dots & 0 & 0 \end{bmatrix}$$

The current vector, \mathbf{I} , includes the bias currents and the modulating or dynamic currents from the displacement feedback control. The bias currents are set at equal amounts for all poles before the servo control starts. Once the control starts, the bias currents will be redistributed according to the bearing static load. The bias currents are set, for example, at the half value of the maximum allowable continuous current of the power amplifiers. The neighboring poles are assigned with alternate signs to avoid magnetic flux saturation at local cores. The dynamic current of each independently controlled pole is:

$$i = -C_p D - C_i \int D dt - C_d dD/dt \quad (2)$$

where:

- C_p, C_i, C_d = proportional, integral, derivative constants
- D = $x \cos(\theta) + y \sin(\theta)$
- x, y = displacement measurements in X, Y directions
- θ = pole angle
- t = time

Only two orthogonal displacement measurements are required as for conventional magnetic bearings. No sensor redundancy is assumed in the above formulation. The determination of the PID constants follows a linear system method for the magnetic bearing control [3], which is not elaborated on here. Additional filtering for phase and gain compensation to eliminate system resonance, for example, may be imposed on the dynamic current, i , if needed.

Once the flux vector, ϕ , is calculated using Equation 1, the pole force at the i^{th} pole can be calculated by:

$$F_i = p \phi_i^2 \quad (3)$$

where p is a constant depending on the units. The magnetic bearing rotor is thus subjected to n of these pole forces, equally spaced around the circumference.

Our interest is to know how the magnetic bearing behaves during pole failures. The transient behavior was simulated using the above nonlinear formulation, including the magnetic flux saturation in cores and the current limit of the power amplifiers. The formulation has been implemented into a commercial rotordynamics program, DyRoBeS, as a special bearing [4, 5]. Using this program, a rotor-bearing system including one or more self-healing magnetic bearings can be analyzed for its transient response by assigning pole failures in a time sequence.

TRANSIENT RESPONSE SIMULATION OF POLE FAILURES

The self-healing control method was simulated using a large-size magnetic bearing. Shown in Figure 4, this bearing has 16 poles, runs at 3600 rpm, supports a 4000-lb rotor weight, and has a load capacity of 6000 lb. Other important bearing parameters include:

Axial Length	$L = 5.5$ in.
Journal OD	$JD = 18.95$ in.
Saturation Flux	$B = 90,000$ Maxwell/in. ²
Air Gap	$g = 0.030$ in.
Coil Turns	$N = 65$
Pole Area	$A = 15$ in. ²

The proposed test rotor weighs about 8500 lb and is supported by two bearings: one rolling element bearing and a self-healing magnetic bearing, with a bearing span of 6 ft. The mathematical model for this rotor from DyRoBeS is presented in Figure 5. The lower half of the model is drawn with the rotor stiffness diameters and the top half with the mass diameters. The self-healing magnetic bearing is at the condensed model station no. 4. The following pole failure time sequence was assumed:

- At time = 0.35 sec, the top pole #5 fails.
- At time = 0.60 sec, another top pole #4 also fails.
- At time = 0.85 sec, the horizontal pole #1 also fails.

To present a clear picture of transient response, only gravity force was considered. No unbalance or other excitations were included. Figures 6 and 7 present the transient displacements at the bearings due to the pole failures. Figure 6 shows the displacements for the ball bearing, which has a static rotor load of 4500 lb and an assigned stiffness of 1×10^6 lb/in. The x (horizontal) and y (vertical) time traces are very flat and uneventful, because the bearing is relatively stiff. In the Y-direction, there is an average of 0.0045 in. of deflection as expected. Figure 7 presents the behavior of the self-healing magnetic bearing due to the pole failures. As the rotor position approaches steady-state position, the top pole #5 fails at 0.35 sec. The rotor drops vertically about 0.0055 in. and recovers its position in less than 0.25 sec. At 0.60 sec, when another top pole (#4) fails, the self-healing magnetic bearing loses more load-carrying capacity, and the rotor dips further down to 0.010 in. However, it also recovers its levitated position in 0.25 sec. Since #4 is an inclined pole, its failure also slightly affects the horizontal position of the rotor. The horizontal pole #1, which fails at 0.85 sec, affects both directions only slightly, because no horizontal static force exists. Figure 7 shows that the self-healing bearing can apparently correct for the pole failures in a fraction of a second and continue to function.

Figures 8 and 9 present the transient coil currents. As shown in Figure 8, as the top poles fail, the remaining top poles, noticeably #3 and #6, pick up more current to support the 4000-lb static load, which becomes a consideration for the design of power amplifiers for the self-healing bearing. Slight current saturation of the #3 and #6 coils occur when the #5 and #4 poles both fail. For the bottom poles, Figure 9 clearly shows that #11, #12, #13, #14 and #15 poles may all be eliminated without much impact on the dynamics for this application.

CONCLUSION

Power amplifier and coil failures can be catastrophic for rotor systems using magnetic bearings. A magnetic bearing control scheme that copes with this type of failure has been described, including a nonlinear formulation of the magnetic bearing dynamics based on this scheme and the transient simulation of rotor responses when the failures occur. The scheme independently controls each magnetic bearing pole without requiring on-line monitoring of failures or use of any precalculated, stored control data. When pole failures occur, the remaining poles work in unison and adjust current individually to regain control of the rotor, demonstrating the characteristics of a self-healing magnetic bearing.

REFERENCES

1. Lyons, J. P., et al.: "Design and Control of a Fault-Tolerant Active Magnetic Bearing System for Aircraft Engines." *Proceedings of 4th ISMB*, Zurich, Switzerland, pp. 449-454, August 23-26, 1994.
2. Maslen, E. H., et al.: "A Fault Tolerant Magnetic Bearing System." *Proceedings of MAG'97*, Alexandria, Virginia, pp. 231-240, August 21-22, 1997.
3. Chen, H. M.: "Self-Healing Magnetic Bearings." *Proceedings of 53rd Meeting of the Society for Machinery Failure Prevention Technology*, Virginia Beach, Virginia, April 19-22, 1999.
4. Eigen Technologies: "*DyRoBeS(c) User's Manual - Version 5.0.*" Eigen Technologies, Inc., Kentucky, 1999.
5. Chen, W. J.: "A Note on Computational Rotor Dynamics." *ASME Journal of Vibration and Acoustics*, Vol. 120, pp. 228-233, January 1998.

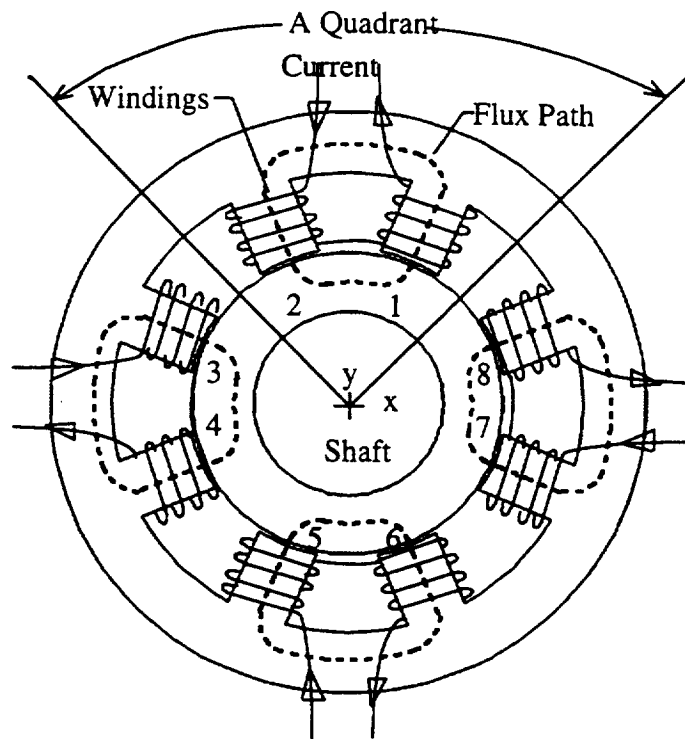


Figure 1. Conventional magnetic bearing coil arrangement

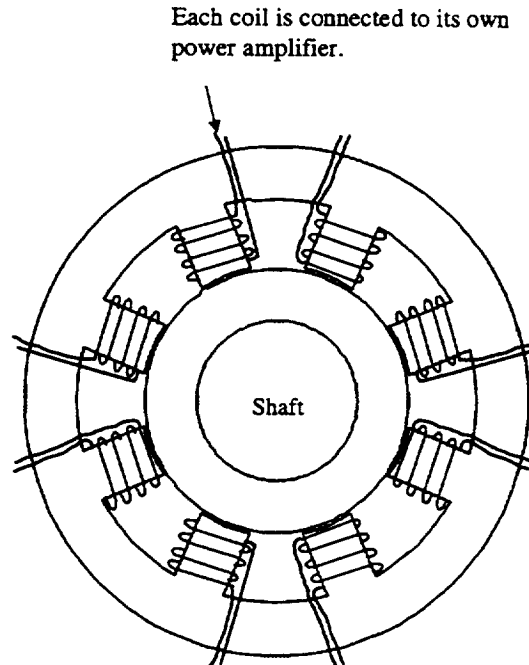


Figure 2. Self-healing magnetic bearing coil arrangement

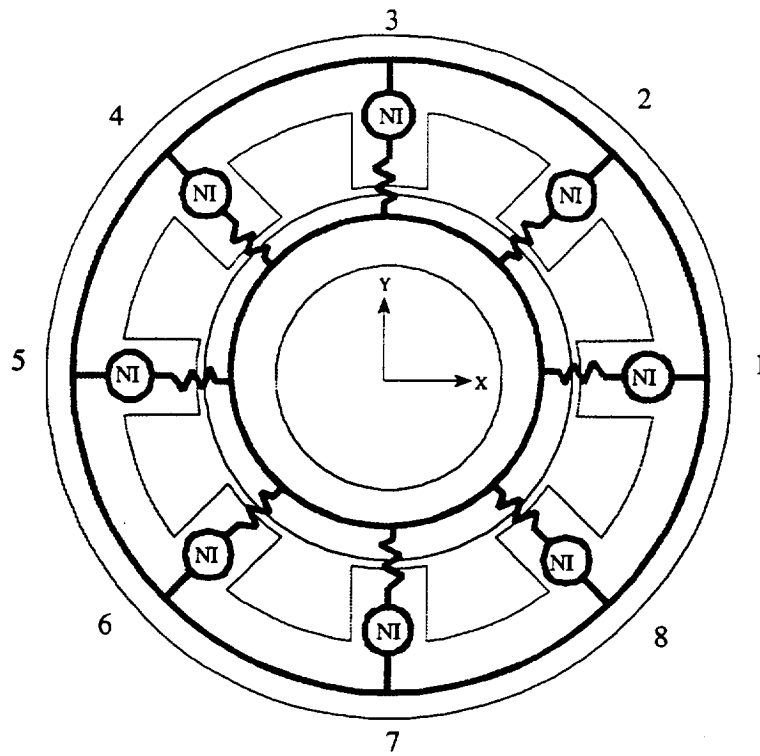


Figure 3. Self-healing magnetic bearing mathematical model

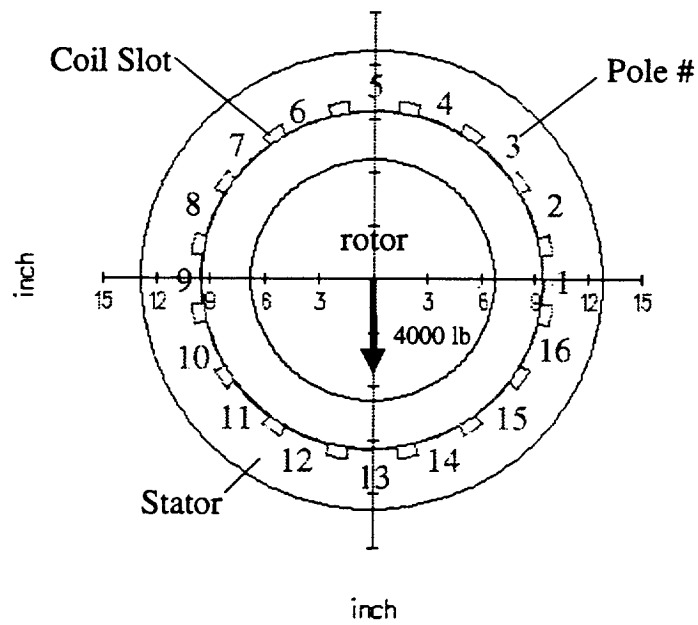


Figure 4. A 16-pole self-healing magnetic bearing

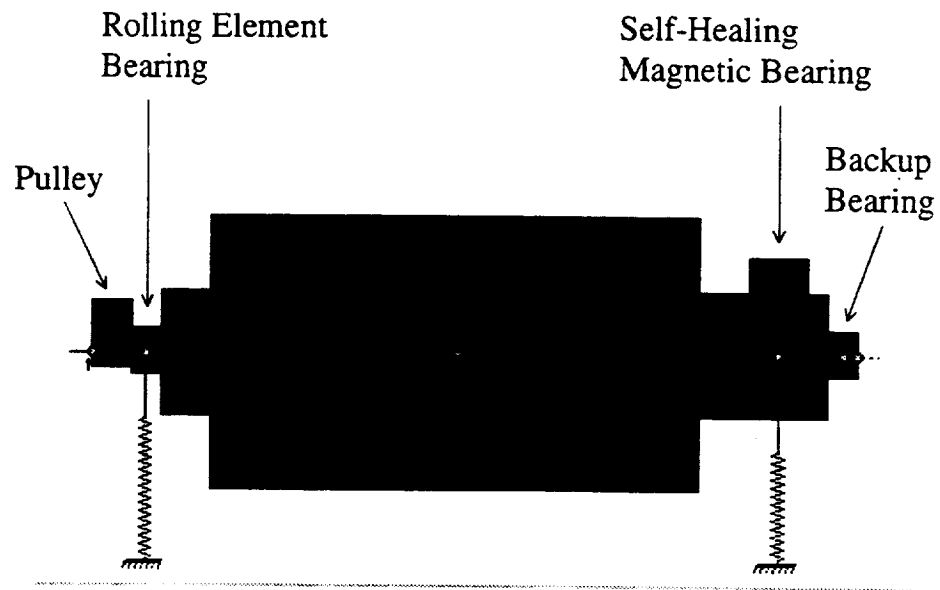


Figure 5. Test rotor mathematical model

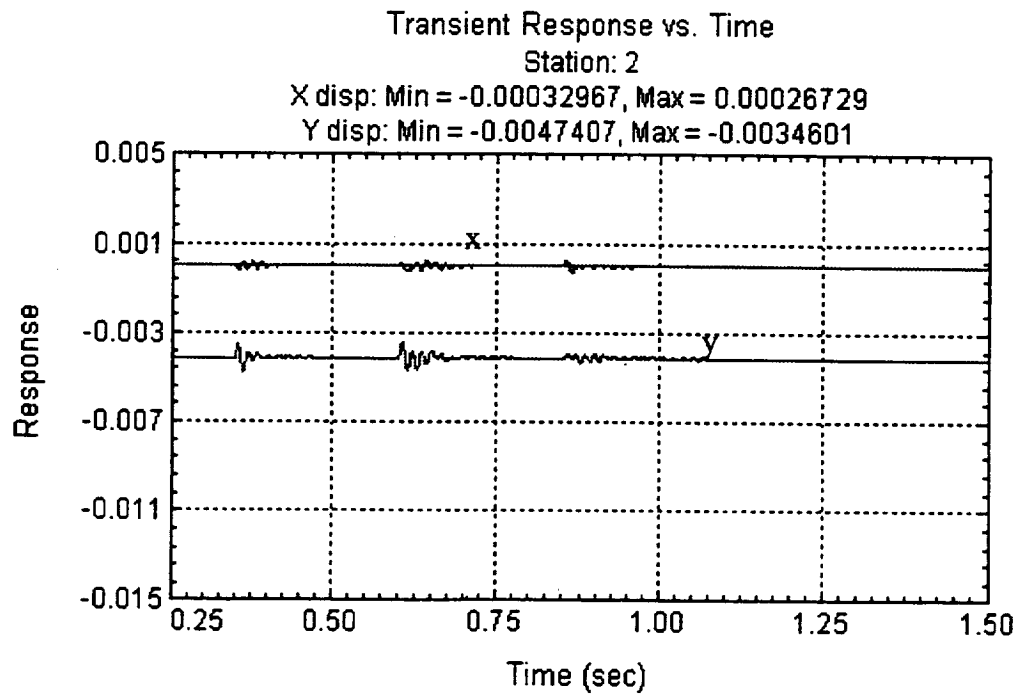


Figure 6. Simulated transient response at rolling element bearing due to pole failures

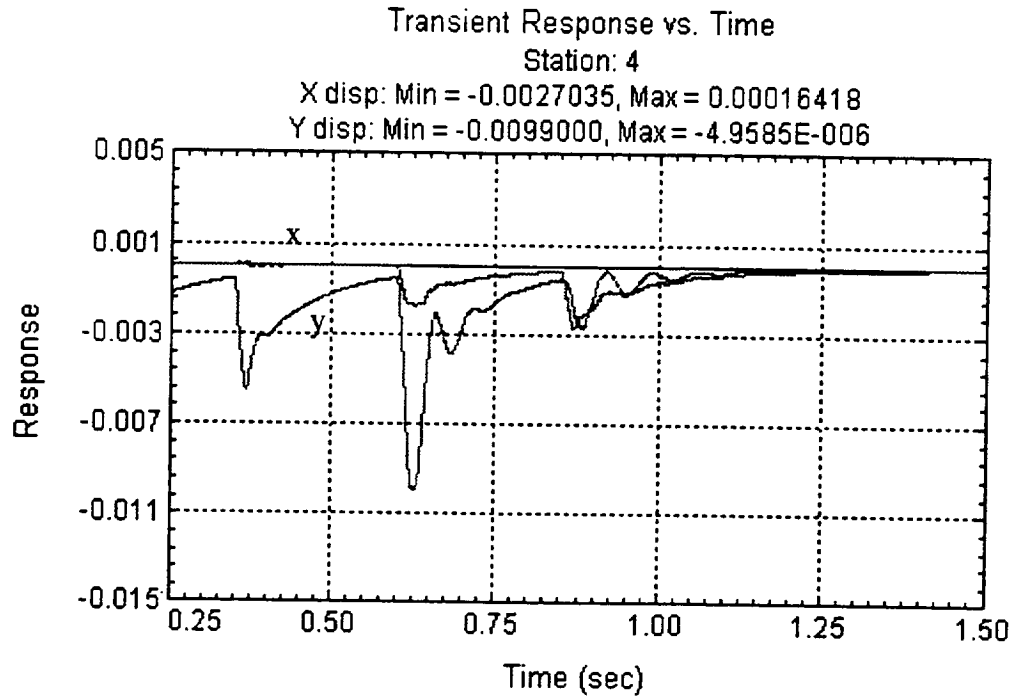


Figure 7. Simulated transient response at self-healing bearing due to pole failures

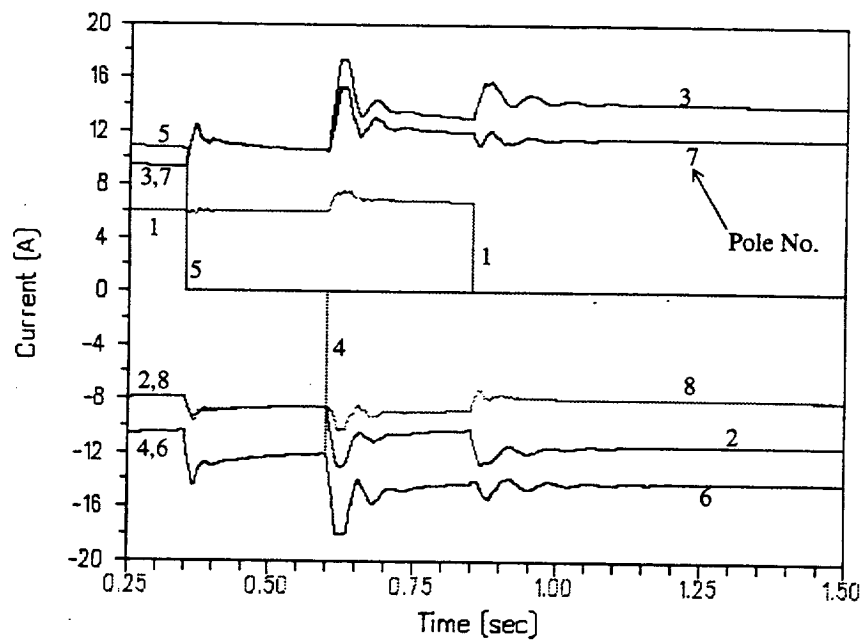


Figure 8. Simulated transient top-pole coil currents due to pole failures

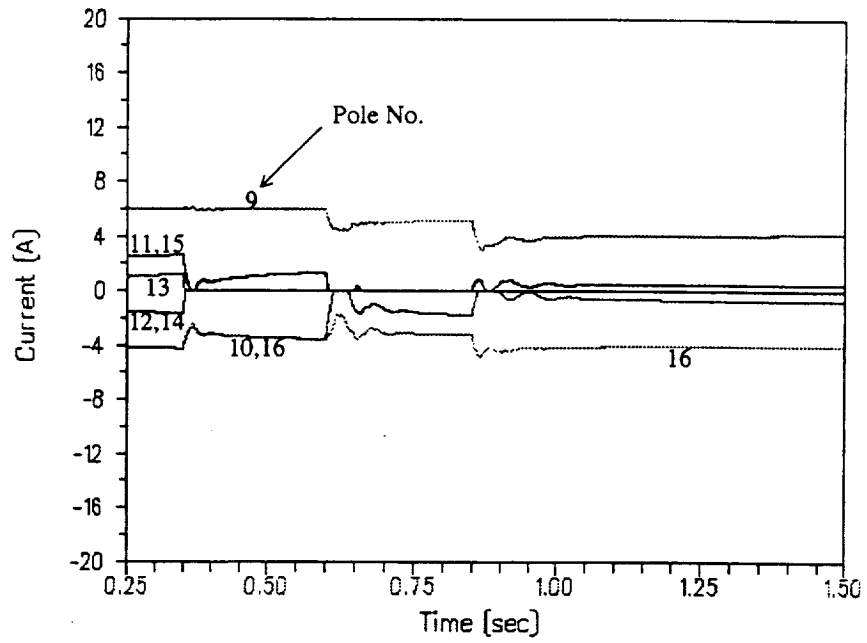


Figure 9. Simulated transient bottom-pole coil currents due to pole failures

Magnetically levitated reaction wheel for space application

A. Argondizza, S. Carabelli, G. Genta, A. Tonoli

Mechatronics Laboratory – Centro Servizi di Prototipazione
Politecnico di Torino
Corso Duca degli Abruzzi, 24
I-10129 Torino, Italy

Summary

The content of the present study is the feasibility assessment of a reaction wheel on active magnetic bearings (AMB) to be followed by the design of a fully operational engineering model¹, which is presently under construction. The stress is laid mainly on the demonstration that a small, simple reaction wheel on AMB can be built and operated reliably with power requirements which are not in excess than those characteristic of conventional units.

A reaction wheel is usually a part of a complex system whose task is the attitude control of a spacecraft and in some cases also the storage of energy in the form of kinetic energy in the rotor. Here the work is concentrated only on the reaction wheel component, intended as a torque actuator. No attempt to address the problems related to the global system or to the possibility of using the reaction wheel as an energy storage device is performed.

AMB technology is at present a well known technology in high speed rotating machinery. Several prototypes of machines of various kinds in which the rotor is magnetically suspended have been built and in some cases are on the market. Several applications of reaction wheels have been studied and many reaction wheels operating on AMB have been built, starting from the seventies². The present study is intended to address some specific problems, mostly related with low power consumption, high system integration and design compactness.

General architecture

The starting requirements were limited to those listed in table 1 in order to leave many open choices to the designer. In particular the maximum torque that the motor must supply to the wheel and the operational speed range have not been explicitly stated. The requirement on the maximum torque has no impact on the design of the wheel itself but is related to the power consumption, not only while producing torque but also while spinning in no torque conditions as the size of the motor influences the power losses in all conditions.

¹The feasibility study has been accomplished under contract 730-08-06527 from University of Houston (USA).

²A number of papers are available in the proceedings of the conferences on flywheel energy storage (San Francisco 1976, Scottsdale 1978), on active magnetic bearings (Zurich 88, Tokyo 90, Alexandria 92, Zurich 94, Kanazawa 96) and on magnetic suspension (sponsored by NASA). Other related papers were presented at the flywheel energy storage sessions of IECEC.

Angular momentum	≥ 3.5	$\text{kg m}^2 \text{s}^{-1}$
Wheel mass	≤ 1	kg
Wheel diameter	≤ 200	mm
Wheel thickness	≤ 60	mm
Five active axes magnetic suspension		
DC brushless motor		
Digital integrated AMB, controller and motor drive		

Table 1: General requirements given at the contract formalization.

Torque and power requirements together affect the choice of the working speed range. For the parameters not explicitly stated, a torque of 0.03 N m over a speed range of $\pm 10,000$ rpm were assumed as design objectives.

Wheel configuration In order to obtain the required angular momentum at a fairly low speed, a pierced disc with rim and central hub configuration has been chosen. The higher stress level, if compared with other configurations, is of no concern here as the peripheral velocity is very low.

Active magnetic bearings In order to limit the axial thickness of the rotor, a conical configuration for the magnetic bearings has been chosen. The conical bearings allow radial and axial forces to be produced without the need for a separate axial bearing. Moreover, the conical bearings are "O" mounted to improve the bearings load capability in order to compensate for the gyroscopic torque.

To keep to a minimum the number of power drives, each AMB actuator includes three horseshoe shaped electromagnets. The resulting six magnetic forces are enough to constrain the five degrees of freedom of the rotor.

An optical solution for colocated displacement sensors is proposed. Its main advantages are: integration within the magnetic actuator, low sensitivity from electromagnetic interferences and simple signal electronics.

Motor In order to limit the axial thickness of the system, a DC brushless motor with external rotor has been devised. The rotating permanent magnets are actually installed in the flywheel hub. The internal stator with the motor windings is mounted on the central shaft. The motor is driven to provide a constant torque in either directions.

Electronic control unit In order to obtain an electronic control unit as integrated as possible, a number of highly integrated components has been chosen. The computing unit is a fixed point digital signal processor (DSP) with integrated PWM outputs, A/D and capture inputs. Moreover, the power electronics for AMB and motor drives have been chosen to be directly interfaced to the DSP outputs.

Housing and locking The wheel, the bearings and the motor are in vacuum, together with the sensors and the sensor electronics. The electronic control unit is in a separate housing, not vacuum tight, to be mounted either on the wheel housing or at a certain distance from the main unit.

Whenever the wheel is in non operating conditions, one of the conical bearing can be used together with the landing bearings to lock the wheel against high vibrations or accelerations.

Reaction wheel

A minimum value of speed and moment of inertia of the reaction wheel can be easily assessed:

$$J_{\max}\omega_{\max} \geq M_a \quad (1)$$

where ω_{\max} is the minimum value of the top speed, M_a is the stated angular momentum and J_{\max} is the maximum moment of inertia compatible with the mass and the external envelope constraints. The shape which uses at best the allowed envelope is a circular hollow cylinder.

The higher the speed, the lighter the wheel can be. This consideration is limited by the allowable strength of the material (centrifugal stressing grows with the square of the peripheral speed) and by the maximum speed at which the chosen bearings can work. However, while this consideration is very important in the cases in which the angular velocity (or, better, the peripheral velocity) can be chosen without strict constraints and the limitations come only from the allowable strength of the material, as in the case of energy storage flywheels, in the present case the peripheral velocity is limited by the requirement of limiting the maximum power P needed to produce a given reaction torque T :

$$P = T\omega \quad (2)$$

As a trade-off between the mass of the wheel and the power of the motor generator, a value of 10,000 rpm is assumed for the maximum spin speed. The wheel must then have a moment of inertia

$$J = 0.00334 \text{ kg m}^2 \quad (3)$$

To exert the required torque of 0.03 Nm at 10,000 rpm, the motor must therefore supply a power

$$P = 31.4 \text{ W} \quad (4)$$

Rotor design

The ratio between the angular momentum $J\omega$ and the mass m of the rotor can be expressed as

$$\frac{J\omega}{m} = 2K \frac{\sigma_{\max}}{\rho\omega} \quad (5)$$

where K and σ_{\max} are the shape factor, depending only on the geometry of the rotor, and the maximum stress present in the material. At equal speed ω , maximum strength and material density ρ , the shape which allows the maximum value of the ratio between the angular momentum and the mass is that which is characterized by the maximum value of the shape factor, namely the constant stress disc. The stressing of the flywheel can thus not be the limiting factor and a disc-with-rim rotor can have performances exceeding those of a constant stress disc.

In the present case, a shape which minimizes the mass for the chosen momentum J and for the given external envelope constraints has been selected. The values of the stresses will be shown to be fairly low and a shape which maximizes the radius of inertia can be used. A disc with rim configuration has then been chosen. A pierced disc configuration has the added advantage of allowing the location of the motor inside the wheel, reducing the axial length of the system.

To reduce the mass of the disc without resorting to a very thin wall and to reduce centrifugal stressing, a light alloy has been chosen for the wheel. The stub shafts are made in one piece with the wheel.

The total mass and the moment of inertia of the wheel are 0.459 kg and 0.00349 kg m². Slightly higher values are to be expected owing to the presence of fillets at the disc-rim interface. The hub, the bearings and the rotating parts of the motor further increase the rotor mass.

The inertia properties of the wheel assembly, including the rotating parts of the magnetic bearings and motor are reported in table 2.

Rotordynamic analysis

The rotordynamic analysis of the wheel is aimed to verify that no critical speed linked to the wheel deformation modes falls in the working range of the machine. A free-free finite element model of the wheel, with its integral shaft, the laminations of the magnetic bearings and the rotor of the electric motor has been built. As usual, the laminations of the bearings and the permanent magnets of the motor have been modelled as distributed inertias located on the stub shafts, which has been considered as the only element which provides stiffness.

To take into account possible deformation modes of the wheel disc, the wheel has been modelled using suitable deformable disc elements, which take into account both centrifugal stiffening and gyroscopic effects. The model includes 17 nodes, 9 Timoshenko beam elements, 7 disc elements and one shaft-disc transition element. The total number of complex degrees of freedom is 50, then reduced to 17 after performing Guyan reduction.

The first critical speed related to deformation modes is 98,500 rad/s = 941,000 rpm and the analysis of its mode shows that it is due to shear deformation of the stub shafts. It is definitely outside the working range. The first two natural frequencies of the free-free rotor (Figure 1) at standstill and at the maximum speed of 10,000 rpm are reported in table 3.

The modes corresponding to the lowest natural frequencies are related to bending deformations of the disc. The very strong gyroscopic effect is clear: the disc deformation modes do not yield any critical speed, as conical modes are very much affected by the speed. The first mode which is mainly a cylindrical one has a natural frequency which is very high.

The rotor works in the low subcritical range, with respect to deformation modes, and its dynamics is that of a rigid rotor with very high gyroscopic effect (high ratio between polar and transverse moments of inertia) supported on magnetic bearings.

Load conditions

No requirements regarding external loads or gyroscopic moments have been explicitly stated. The inertia wheel has to operate in a microgravity environment but the engineering model must be tested on the ground. It is therefore reasonable to require that the wheel is able to operate under a gravitational acceleration load of 1 g in all directions. This value of the load, augmented by a suitable safety factor, will be used in designing the bearings. This choice leads

Mass	0.796	kg
Polar moment of inertia	0.00364	kg m ²
Transversal moment of inertia	0.00188	kg m ²

Table 2: Reaction wheel: inertial properties.

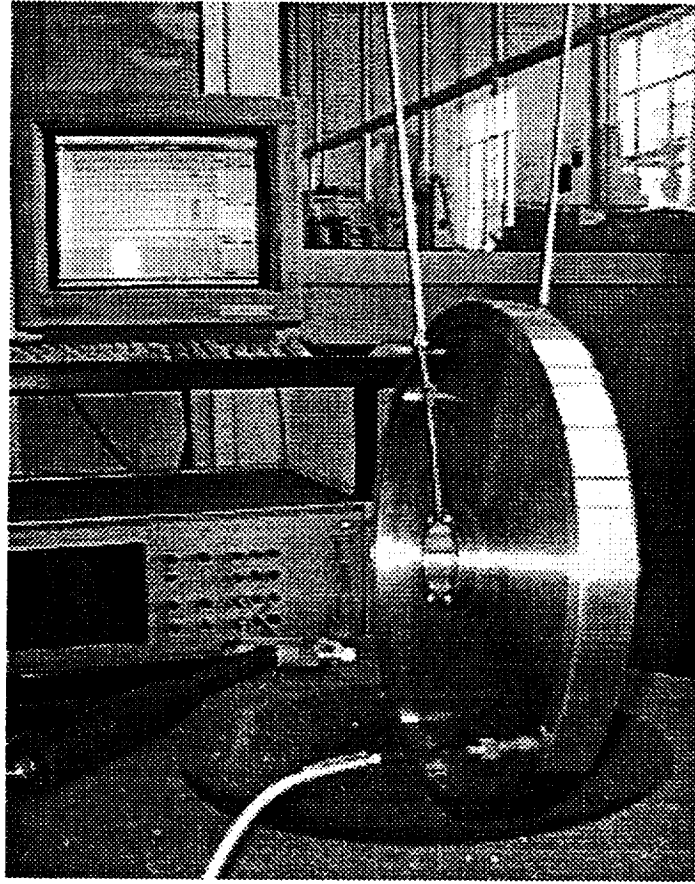


Figure 1: Free-free test for the validation of the FE model of the wheel.

to an overdesign of both the electromechanical parts and the power electronics relative to the microgravity operating conditions. However this has little effect on the power consumption and the mass of the systems and has two advantages: the bearings operate with very low magnetic induction, and hence with very low eddy current drag. In addition, severe requirements regarding acceleration and gyroscopic moments can be met by the engineering model. The no-torque power consumption while operating in 1 g environment will be greater than that which will occur in actual microgravity operation.

Mode	at standstill		at 10,000 rpm	
	[rad/s]	[Hz]	[rad/s]	[Hz]
1st Forward	3130	498	4120	656
1st Backward	3130	498	2780	443
2nd Forward	16330	2599	17960	2859
2nd Backward	16330	2599	15920	2534

Table 3: Free-free rotor: first two deformable body natural frequencies.

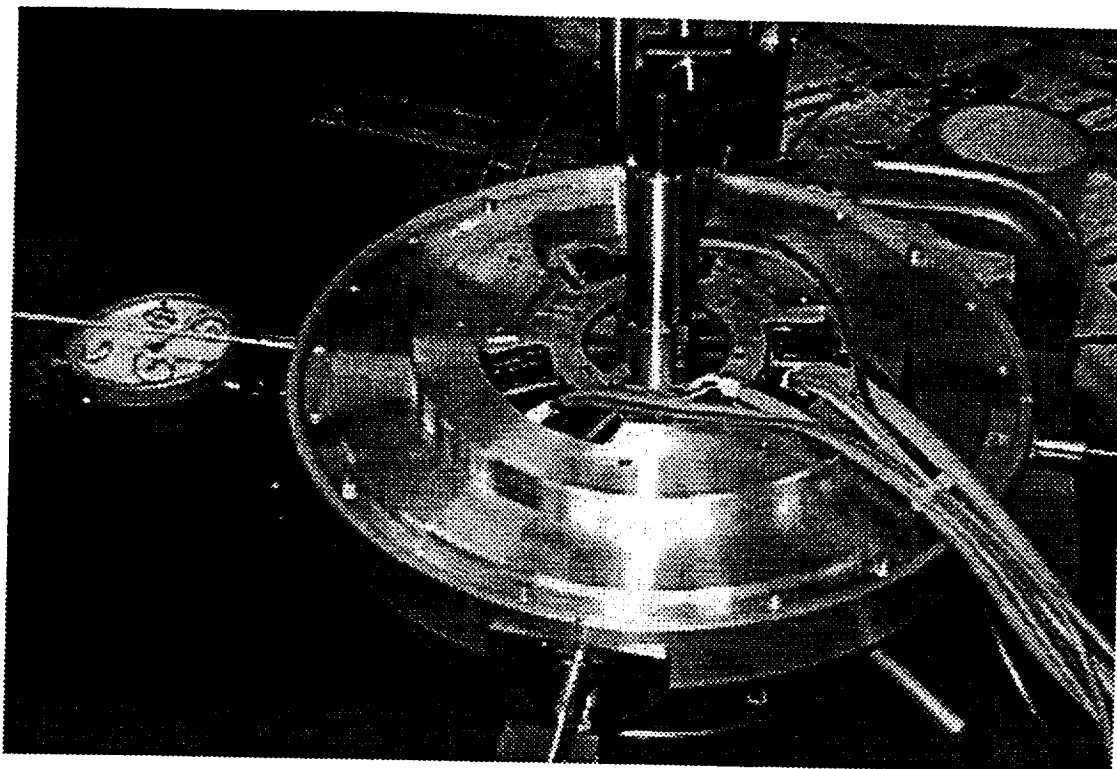


Figure 2: Reaction wheel under radial force tests.

Stator design

The main housing must contain the wheel in a vacuum environment. To allow an easy mounting and registration of all the internal components, the design includes two separate halves, which carry the bearing magnetic circuits and coils, the sensors and related local electronics, and two covers which, at the center, are connected by a central and nonrotating shaft, carrying the motor stator.

The electronic control unit is located in a separate housing, not vacuum tight. It is axially attached to the main one and cylindrically shaped to fit the wheel housing. Alternatively, it can be located at a certain distance from the main unit.

A vacuum connection will be located on the housing for evacuating the housing during laboratory tests. The simplest location for a vacuum flange is at the center of the left cover: the air can be pumped out through the central hollow shaft and the holes in the covers used to pass the cables.

Active magnetic bearings

In order to operate the active magnetic bearings, several **subsystems** must be properly designed and integrated: the AMB electromechanics made by the magnetic circuits and the coils, the rotor displacement sensors, the power electronics to drive the electromagnets, and the stabilizing controllers.

In non conical AMB configurations, each mechanical degree of freedom can be separately actuated, sensed and, most of the times, controlled. The AMB configuration here adopted

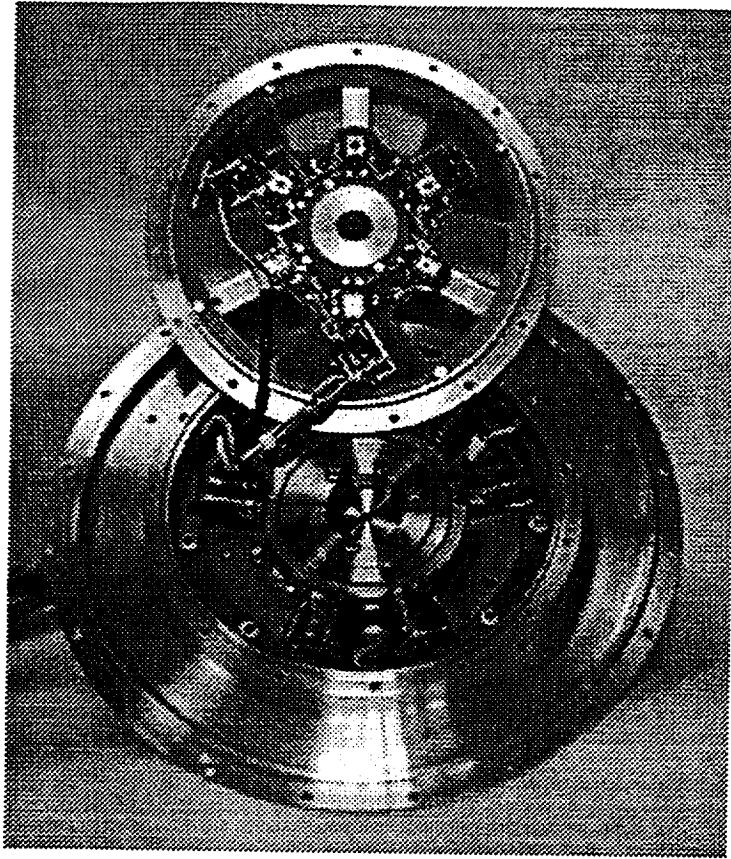


Figure 3: Reaction wheel in exploded view of optical sensors and electromagnets.

(Figure 3) includes two conical bearings with three electromagnets each to control the five degrees of freedom of the rotor. It should be noted that this layout intrinsically couples the radial and axial behaviors: each electromagnet produces a radial as well as an axial force at the same time.

The analog to digital converters integrated in the DSP (see 6) allows the sampling of two signals at a time. This is compatible with both the aforementioned sensor configurations in terms of computation efficiency, but only in the case of decentralized control.

Optical displacement sensors

Optical displacement sensors based on the measure of the light flux passing through the gap between the stator and the rotor are here used to measure the rotor to stator relative displacements. The light flux is related to the amplitude of the gap, its measure allows therefore to determine the relative position of the rotor. Each sensor is made of a light source, namely a light emitting diode (LED) and a light measuring device, namely a photodiode (for example Burr Brown OPT210P [1]). They are installed on opposite sides of each electromagnet so that the light emitted by the LED passes through the gap and illuminates the corresponding photodiode.

Six displacement sensors are installed on each AMB with a 60° angular spacing. Their angular location is the same where the forces produced by the three magnetic actuators are acting.

This setup has been chosen for the following reasons:

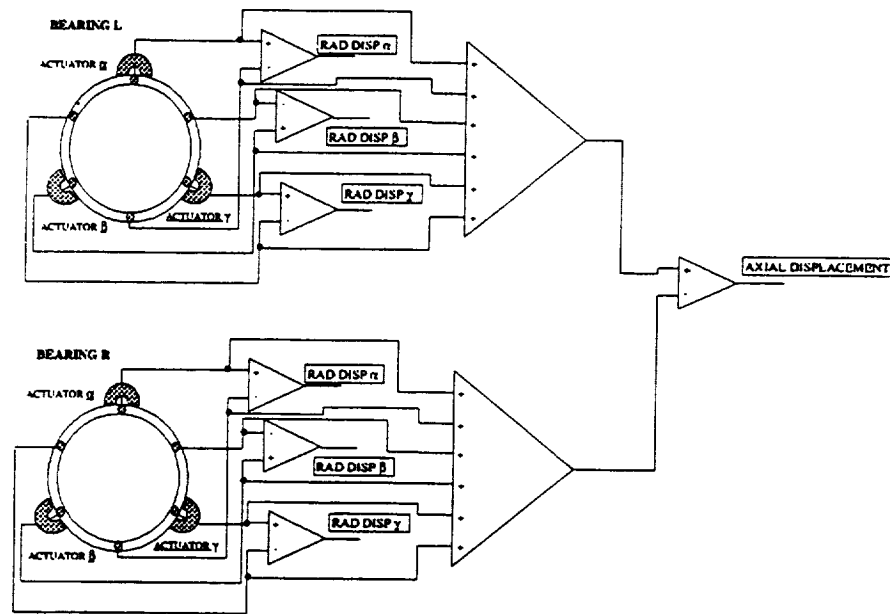


Figure 4: Block diagram of the signal electronics for the optical displacement sensor.

- redundancy: in the case a single sensor fails, the sensor located at 180° can be used instead of it with minimum system reconfiguration;
- flexibility: several connection schemes between the single sensors are possible with this configuration, this allows the adoption of different controller architectures;
- colocation: the sensors allow to measure the displacements along the directions where the AMB forces act.

A possible connecting configuration is shown in figure 4. The differential connection of the sensors at 180° is used to obtain a measure of the displacement along the diameter connecting the two sensors. This measure is decoupled from the axial displacements and from the displacements in a direction perpendicular to the diameter. The summing connection of the same sensors is used to obtain a measure of the axial displacements which is decoupled from the radial displacements.

The optical sensors used here are intrinsically collocated with the actuators, i.e. each of them measures the displacement in the same direction of the force produced by the corresponding electromagnet. In their simplest configuration, they can be directly used to implement a fully decentralized control, i.e. each measurement is fed back to a separate control that computes the driving command to be applied to the corresponding (collocated) actuator.

Electromagnets

Under the assumptions of

- no magnetic saturation in the iron core and
- no flux leakage out of the magnetic circuit in the air gap,

Maximum force (~ 2 g)	19	N
Maximum current	3	A
Pole cross section at the air gap	60	mm ²
Nominal air gap t_0	0.3	mm
Number of turns	95	
Coil resistance	0.19	Ω
Maximum field in iron	0.85	T
Bias current i_0	0.1	A
Nominal current density	0.2	A mm ⁻²
Nominal dissipated power	19	mW
Coil inductance L	1.1	mH
Force/current factor = $L \frac{i_0}{t_0}$	0.38	N A ⁻¹
Force/displacement factor = $L \left(\frac{i_0}{t_0} \right)^2$	127	N m ⁻¹

Table 4: Active magnetic bearing: main characteristics.

the force F_m generated by each electromagnet depends only on the induced magnetic field B and on the magnetic circuit cross section in air S_{air}

$$F_m = \frac{S_{air} B^2}{\mu_0} \quad (6)$$

where μ_0 is the magnetic permeability. The iron cross section along the magnetic circuit is relevant only as far as it does not induce saturation of the induced magnetic field. In order to avoid saturation, a geometrical relation of 1:1 is usually applied for the iron pole width and lamination radial width with respect to the pole width at the air gap. In case a lower ratio is needed for design reasons, a local check of the magnetic field must be carried out. The saturation limit is here assumed conservatively to 1 T.

The radial dimensions of the bearing slot depends on the characteristic of the coils it is supposed to house. A compromise must be found between the copper (or aluminum) wire section in order to have low thermal dissipation and the overall weight of copper and iron parts. Under steady state operation, a bias current of 100 mA is here supposed for each coil with a relatively low current density of around 0.2 A/mm² for a total heat dissipation of 20 mW for each coil. This value must be kept low because the dissipation is possible only by radiation since the bearing stator is under vacuum.

The main parameters of the designed electromagnets are summarized in table 4.

Control

The general scheme for the electromagnet control subsystem is sketched in figure 5. The presence of two analog to digital converters allows to sample simultaneously the current and the position signals for each electromagnet. With a decentralized control algorithm, it is possible to compute the command to set the PWM output while waiting for the conversion of the sampled current and position signals for the next multiplexed electromagnet.

The differential configuration of the optical sensors provides 6 decoupled purely radial displacement measurements and 1 purely axial displacement measurements. This set of measurements is intrinsically redundant to control the five degrees of freedom that fully characterize the rotor behavior.

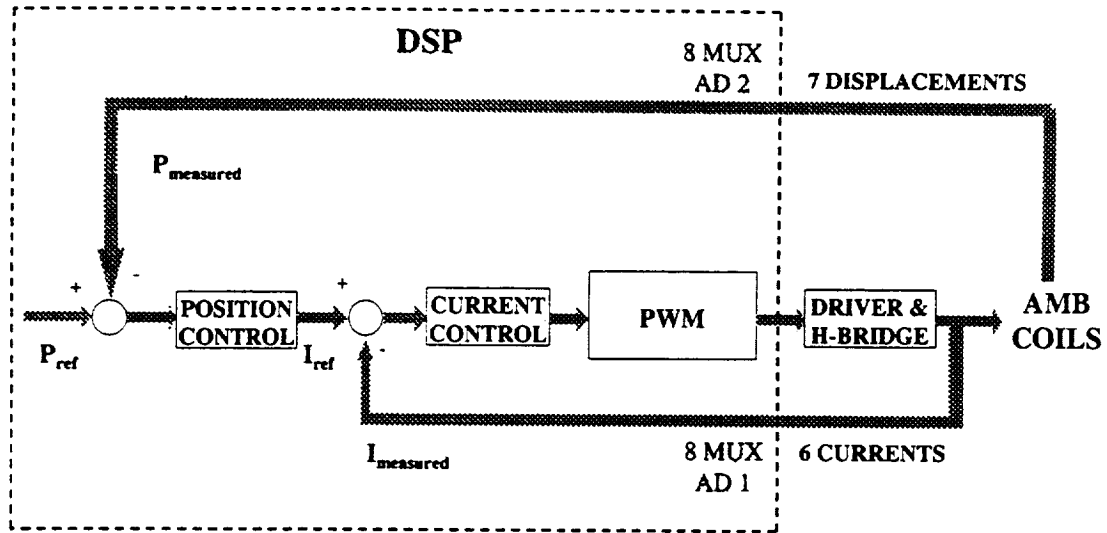


Figure 5: Block diagram for the electromagnet control subsystem.

It should be noted that, if a centralized control is adopted, every control output is setting a value to all the PWM outputs to the coils. A radial command usually drives three different coils to obtain a bidirectional force. In addition because of the conical shape of the bearing, any radial command also produces an axial action that can be compensated by equally actuating the three electromagnets on the opposite bearing. Actually, the PWM settings are updated after the computation of each control but the PWM commands are sent to the drivers of the power amplifier bridge only at the end of every sampling period.

Electronic control unit

The electronic control unit (ECU) is based on a digital signal processor (DSP), that manages all the system operations. The ECU also includes the external memories, the programmable logic and the AMB and motor power drives (figure 6).

The DSP choice strongly influences the overall machine layout: actually the use of the TMS320F240 DSP [2], that provides on a single chip the A/D converters, the PWM generation, the capture inputs, along with the timers and the computing unit, yields to a very compact ECU design, with a minimum amount of external components. Moreover, in the power electronics components selection, attention was paid to find integrated devices so as to reduce the total component number.

The system must be able to operate as a stand-alone machine and to be connected to a local and/or a remote interface. At power up the DSP is reset and the execution starts from the on-chip flash memory, programmed to load the code from the external nonvolatile RAM (NVRAM) into the external fast static RAM (SRAM). Once the code is loaded into the SRAM, the program execution starts. A programmable logic device (PLD) is responsible for the address decoding, the wait state generation to access the slow NVRAM and the reset logic.

To accomplish the need for an external interface, without DSP overloading, a dual port RAM (DPRAM) has been chosen. This allows to easily give accessibility to the relevant control and system parameters and variables, both for monitoring and tuning on-the-fly. If a dedicated bus

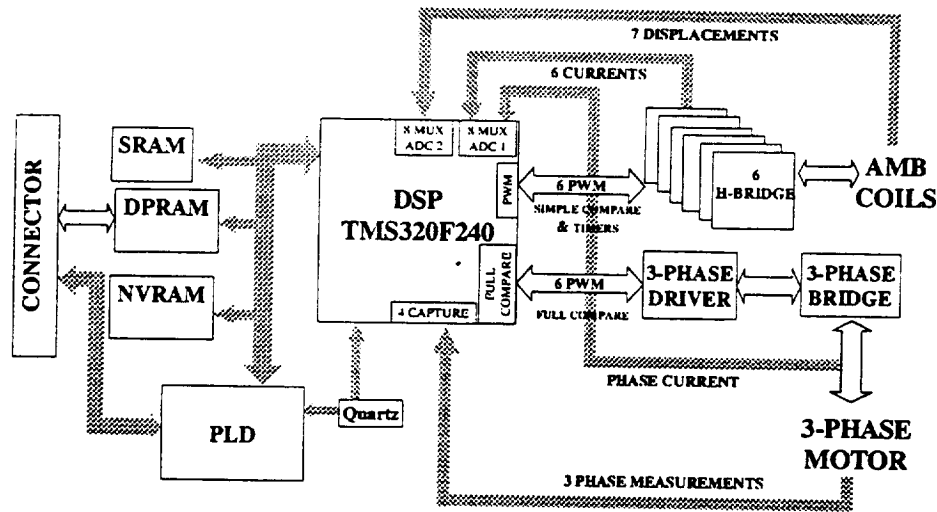


Figure 6: Electronic control unit functional block scheme.

is selected to interface the system to a host, then a PLD is needed to handle the interface. A single or two separate PLDs can be used to perform the ECU strictly necessary tasks and the bus interfacing: in the former case a larger device is necessary, but some redundancy is avoided, in the latter case a more compact solution for the ECU can be achieved.

The power to the AMB coils can be supplied by either linear or switching amplifiers: in the present case, to reduce the power consumption, the latter drives are selected. The DSP is able to directly provide the PWM signals necessary to drive the power stage that supplies the coil with the control current. An integrated H-bridge (including an internal current sense) has been found suitable for the AMB control [3] and has been tested at very low voltage supply (less than 15 V).

The brushless DC motor windings must be supplied by a 3-phase driver. An integrated device, suitable for the present application, is an SGS-Thomson 3-phase motor driver [4], with a high current capability (4 A) and a large supply voltage range; assuming a supply voltage of 15 V it can supply the motor with the requested power. Its inputs are directly connected to the DSP PWM outputs.

Conclusions

The present feasibility study shows the design configuration of a small, lightweight, highly integrated, low consumption reaction wheel based on the active electromagnetic bearing technology. The characteristics of the inertia wheel are summarized in table 5.

The main characteristics of the design are the following. It uses conical active bearings with the minimum number of coils, obtaining a five active-axis suspension with just six coils instead of the usual ten. The configuration used allows to positively lock the wheel against vibration and high accelerations when not rotating without resorting to a separate grabber system. Optical differential sensors are used instead of the more common eddy current or inductive sensors, with

System	Angular momentum	3.81	$\text{kg m}^2\text{s}^{-1}$
	Torque	0.03	N m
	Speed range	$\pm 10,000$	rpm
	Diameter	220	mm
	Length (including ECU)	78	mm
	Length (ECU not included)	67	mm
Reaction wheel	Mass	0.796	kg
	Moment of inertia	0.00364	kg m^2
	Diameter	100	mm
	Thickness (at the hub)	36	mm
	Material	Light alloy (2014)	
Motor	Poles	6	
	Slots	9	
	Phases	3	
AMB	Bearings	2	
	Electromagnets	6	
	Maximum radial load	19	N
	Maximum axial load	15	N
Power consumption	Full torque	~ 40	W
	No torque	~ 6	W

Table 5: Reaction wheel: main characteristics.

notable advantages for what the actuator-sensor colocation, the electrical disturbance rejection and the overall cost is concerned. State-of-the-art digital electronics and purposely developed circuitry and software are used.

The whole system is very compact, with some of the electronics located within the wheel housing and the ECU with the power electronics located in a separate housing, axially to the wheel. All the subsystems are designed with ample margins, allowing the possibility of upgrading the performance, particularly where the maximum angular momentum and maximum torque is concerned. The detailed analysis of all components will lead to reductions in mass.

The so-called engineering model is currently under construction and will be ready for testing in the first part of next year.

References

- [1] "OPT210 Monolithic Photodiode and Amplifier 300 kHz Bandwidth at $R_f = 1 \text{ M}\Omega$ - Data Sheet." Burr-Brown, December 1995.
- [2] "TMS320C240, TMS320F240 DSP Controllers - Data Sheet." Texas Instruments, December 1997.
- [3] "LMD18200 3A, 55V H-Bridge - Data Sheet." National Semiconductor, September 1996.
- [4] "L6234 Three Phase Motor Driver - Data Sheet." SGS-Thomson Microelectronics, March 1998.

Appendix: Drawing and main parts

The basic layout drawing of the system is reported in figure 7 . The main parts are identified and labelled; other parts as screws, seals, etc. are just indicated or omitted. With reference to the included layout, the main parts are as follows:

1. Wheel. Material: aluminum alloy, tentatively 2014. Owing to the low stress levels, the exact material choice is not critical. A constant thickness disc with rim and central hub configuration has been chosen. The stub, hollow shaft is integral with the wheel.
2. Left housing. Material: aluminum alloy, tentatively 2014. Main part of the housing, carrying the left magnetic bearing. The housing protrudes inwards to carry the circuit board with the LEDs of the position sensors.
3. Left cover. Material: aluminum alloy, tentatively 2014. Housing cover, carrying the central non-rotating shaft (part 9) and the motor.
4. Left magnetic bearing electronics. Two printed circuit boards, containing the main left bearing sensor components and the relevant electronics. The cables to this board run in the hollow shaft (part 9) and through a hole in left cover (part 3).
5. Left magnetic bearing stator. It is made of 3 horseshoe electromagnets. The magnetic circuit is laminated. The cables to the coils run in the hollow shaft (part 9) and through a hole in (part 3).
6. Left magnetic bearing rotor. It includes the laminated magnetic circuit, plus the inner flange. The flange is of steel, but aluminum can be used to save weight.
7. Left landing bearing support. Material: steel. The support acts also as outer flange for the bearing rotor.
8. Sleeve. Material: aluminum alloy. It carries the left landing bearing and keeps in position the motor windings.
9. Central shaft. Material: steel. It is attached to the right housing cover (part 11), and is restrained from rotating by a pin set into the left housing cover (part 3). The cables to the left bearing and the motor run through the shaft.
10. Left landing bearing. Standard deep groove ball bearing with O.D. 24 mm, I.D. 15 mm, thickness 5 mm.
11. Right housing. Material: aluminum alloy, tentatively 2014.
12. Right cover. Material: aluminum alloy, tentatively 2014. Similar to part 3, left cover, except for the fact that it carries the vacuum tight connector for all cables connecting the motor and the magnetic bearings.
13. Right magnetic bearing stator. Same as the left one (part 5).
14. Right magnetic bearing electronics. Same as the left one (part 4), but the cables are directly attached to the connector on part 12.
15. Right magnetic bearing rotor. Same as the left one (part 6).
16. Motor permanent magnet. Cylindrical permanent magnet with six poles.
17. Right landing bearing. Same as the left one (part 10).
18. Washer. Material: aluminum alloy.
19. Motor laminations. The magnetic circuit with 9 slots is laminated. The cables to the coils run in the hollow shaft (part 9) and through a hole in the right cover (part 12).
20. Right landing bearing support. Same as the left one (part 7), but with the provision for allowing a larger displacement of the wheel to the left (locked wheel conditions).
21. Nut. To lock the central shaft to the right cover.
22. Electronic control unit housing. Material: aluminum alloy. It is not vacuum tight.

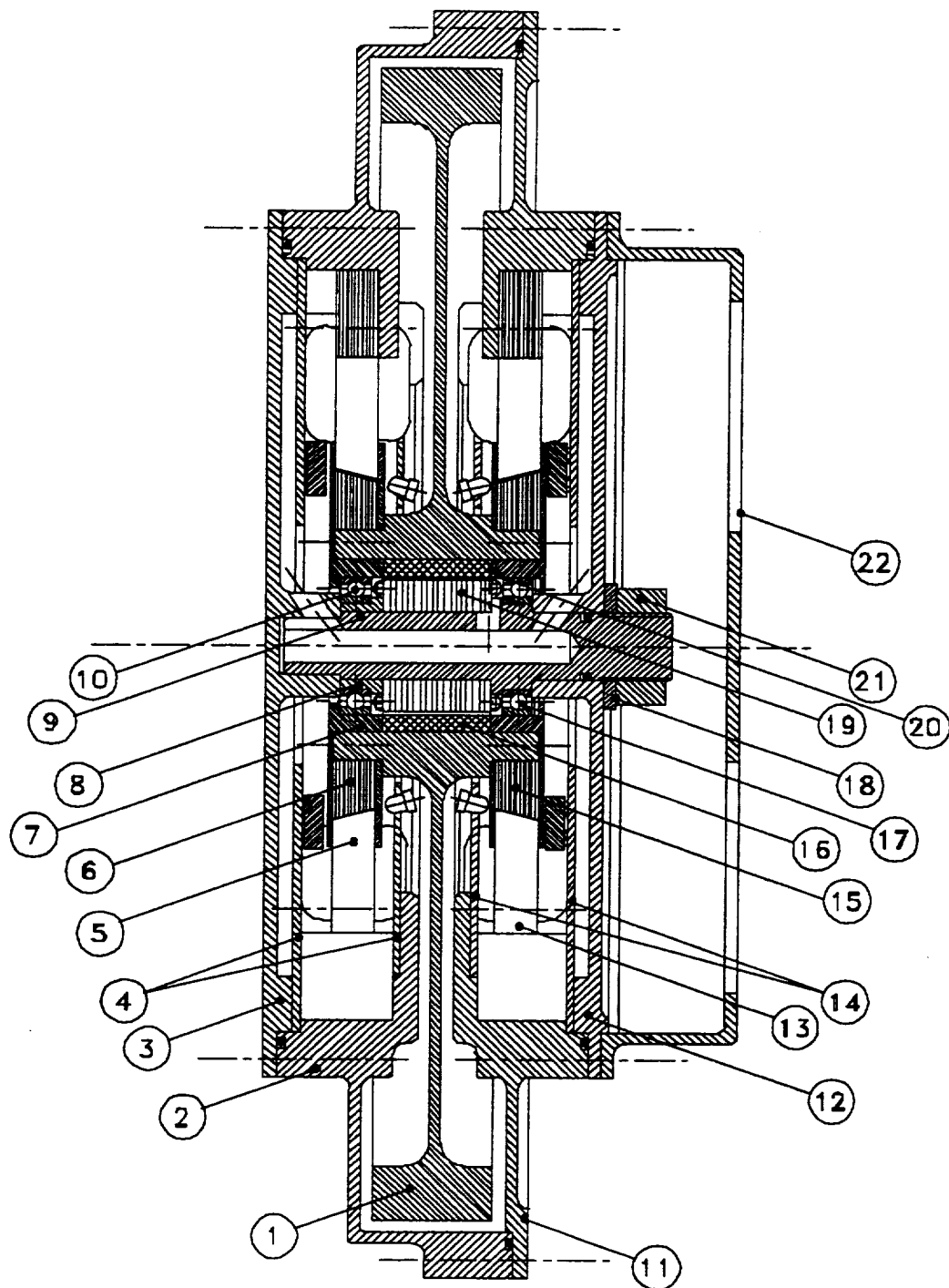


Figure 7: Reaction wheel section drawing (not to scale) with part numbers.

Session 2 -- Electromagnetic Launch/LSMs

Chairman: Hans Schneider-Muntau
National High Magnetic Field Lab (NHMFL)

LATERAL FORCE CONTROL THROUGH ARMATURE CURRENTS IN SUPERCONDUCTING LSM MAGLEV VEHICLE

Tetsuzo Sakamoto.

Department of Control Engineering, Kyushu Institute of Technology
Tobata, Kitakyushu 804-8550, Japan

SUMMARY

The ride comfort or stability of the superconducting maglev vehicle is still the area to be investigated for commercial implementation. This paper proposes a method to get the vehicle guidance forces for a superconducting EDS maglev with LSM propulsion. The author has previously proposed a methodology of analysis using dq0 transformation with space harmonics included, and obtained the exact expression for the propulsion force in terms of q-axis component. It is shown that the d-axis components of the LSM armature currents result in lateral forces, and we show the formulation and design the vehicle motion regulator system, demonstrating the high performance by computer simulations.

INTRODUCTION

Superconducting magnetically levitated vehicle is suitable for super high-speed ground transport in terms of both electrical and dynamical characteristics. It includes three fundamental elements for producing propulsion, levitation and guidance forces with no contact. The vehicle of Japan Railway in Yamanashi is being tested for gathering data for a possible commercial operation in the near future. A traveling magnetic field generated by the linear synchronous motor (LSM) windings on the ground interacts with onboard superconducting magnets (SCMs), resulting in propulsion forces. The magnetic field of SCMs on the vehicle induces emfs in levitation-guidance coils on the ground, and the forces of levitation and guidance are produced.

One of the problems of the vehicle is that the ride comfort has not yet been gained as much as the designer expects. The spring constant in the lateral direction can be specified at the design stage, while the damping forces cannot be obtained satisfactorily. The actual damping relies on the uncertain phenomenon that could not be estimated. This causes a slight vibration with amplitudes of less than 10mm [1]. Moreover the minimum levitating speed should be preferably set as low as possible, but it is limited because even the spring constant is very weak at low speeds. These problems strongly motivate the study for additional guidance forces.

The author has previously proposed a methodology of formulation for the superconducting linear synchronous motor with the space harmonics of magnetic field included exactly, and then defined the thrust coefficient [2]. This formulation has now become the basis for studying the propulsion system quantitatively [3].

This paper presents the extension of our formulation to the lateral motion of the superconducting LSM, and a guidance force coefficient of the propulsion system is defined. The coefficients are calculated for the two types of feeding system: two-power converter system and three-power converter system. Then a method of generating desired lateral forces through propulsion coil currents is proposed, and the regulator system design methodology for the three-power converter system is proposed.

LATERAL FORCE AND ITS FORMULATION

It is convenient to consider the dq -frame when we discuss the electromagnetic forces for propulsion and guidance. Suppose the situation that the LSM armature coils, i.e. propulsion coils, and SCMs are positioned as shown in Figure 1(a). The symbols of dot and cross represent the positive directions for armature currents. If the armature currents have the values such that $i_U > 0, i_V > 0, i_W < 0$, then the currents, which can be replaced with the equivalent magnets, interact with the magnetic fields of SCMs. The forces are decomposed into the propulsion force and lateral force as shown in the figures (b) and (c), respectively. The arrow directing to the SCM indicates repulsive force while the opposite arrow means the attractive force. In this case, the phases V and W generate propulsion force, whereas the phase U generates the lateral force. On the dq -frame in which the d -axis is assigned to the field axis of SCMs, the former corresponds with the q -axis, and the latter with the d -axis. Therefore, it is found from these discussions that the q -axis and d -axis currents produce propulsion and lateral forces, respectively.

The magnetic coenergy stored between the armature and the SCMs is

$$W'_m = \begin{pmatrix} i_U \\ i_V \\ i_W \end{pmatrix}^T \begin{pmatrix} \psi_U \\ \psi_V \\ \psi_W \end{pmatrix} \quad (\text{J}) \quad (1)$$

where ψ_ζ ($\zeta = U, V, W$) is the flux linkage of the armature windings, which is the function of the relative displacements of SCMs to the armature windings. Now we define the map of physical variables from the 3-phase axis to the $dq0$ -axis

$$C = \sqrt{\frac{2}{3}} \begin{pmatrix} c_1 & c_2 & c_3 \\ -s_1 & -s_2 & -s_3 \\ \frac{1}{\sqrt{2}} & \frac{1}{\sqrt{2}} & \frac{1}{\sqrt{2}} \end{pmatrix} \quad (2)$$

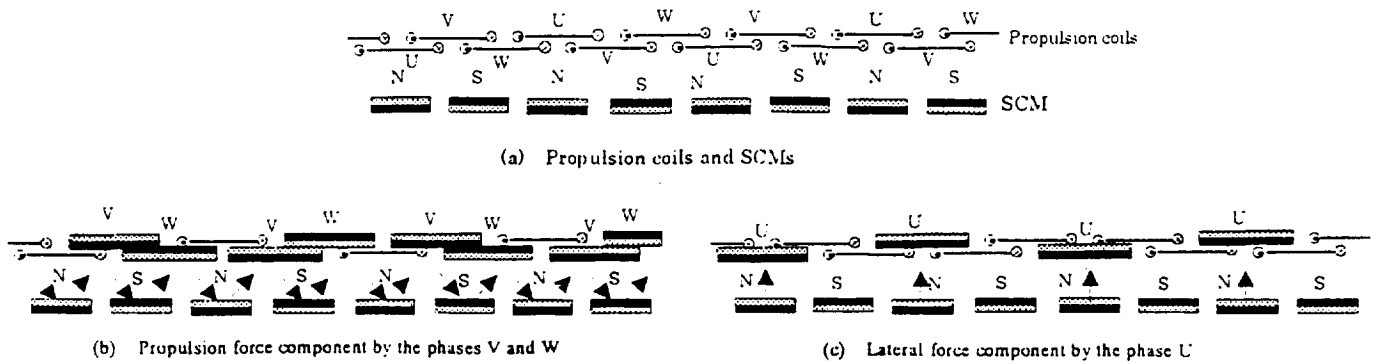


Figure 1. Principles of forces by propulsion
coil currents ($i_U > 0, i_V > 0, i_W < 0$)

where

$$c_1 = \cos \theta_{dq}, c_2 = \cos(\theta_{dq} - \frac{2\pi}{3}), c_3 = \cos(\theta_{dq} + \frac{2\pi}{3}), s_1 = \sin \theta_{dq}, s_2 = \sin(\theta_{dq} - \frac{2\pi}{3}), s_3 = \sin(\theta_{dq} + \frac{2\pi}{3}), \theta_{dq} = \frac{\pi x_1}{\tau}$$

Substituting this into (1), we have

$$W'_m = \begin{pmatrix} i_d \\ i_q \\ i_0 \end{pmatrix}^T \begin{pmatrix} \psi_d \\ \psi_q \\ \psi_0 \end{pmatrix} \quad (J) \quad (3)$$

where

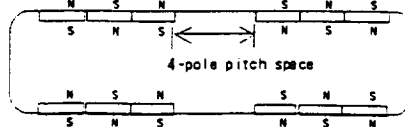
$$\begin{pmatrix} i_d \\ i_q \\ i_0 \end{pmatrix} = C \begin{pmatrix} i_U \\ i_V \\ i_W \end{pmatrix}, \quad \begin{pmatrix} \psi_d \\ \psi_q \\ \psi_0 \end{pmatrix} = C \begin{pmatrix} \psi_U \\ \psi_V \\ \psi_W \end{pmatrix}, \quad x_1 = v_x t, \quad v_x : \text{Vehicle speed}$$

Since we have obtained the energy in terms of currents and displacements, the lateral forces can be written by using the lateral displacement of the vehicle $y_1 (y' - y; y', y : \text{lateral axes fixed to the guideway and the vehicle, respectively})$ as follows

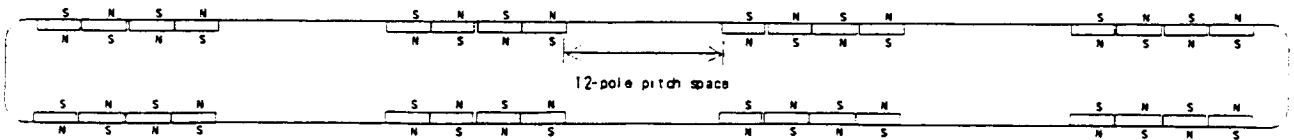
$$F_{Gpu} = \frac{\partial W'_m(i_d, i_q, i_0, y_1)}{\partial y_1} = i_d \frac{d\psi_d}{dy_1} + i_q \frac{d\psi_q}{dy_1} + i_0 \frac{d\psi_0}{dy_1} \quad (N) \quad (4)$$

Now we take up two models: one is a short vehicle equipped with the two-power converter system shown in Figure 2(a) and Figure 3(a), and the other is a long vehicle with the three-power converter system shown in Figure 2(b) and Figure 3(b). The flux linkages of the armature windings for one feeding section are given in the following equations:

$$\psi_U = \sum_{k=1,3,\dots}^{\infty} \sum_{m=1,3,\dots}^{\infty} \Psi_{km} e^{\beta_{km} y_1} \left[k_{ni} e^{\beta_{km} c_a / 2} \sin \left\{ \alpha_k \left(x_1 + \frac{3\tau}{2} \right) \right\} + k_{no} e^{-\beta_{km} c_a / 2} \sin \left\{ \alpha_k \left(x_1 - \frac{\tau}{2} \right) \right\} \right] \quad (Wb) \quad (5)$$



(a) A short length vehicle with double-feeding system (model-1)



(b) A long length vehicle with triple-feeding system (model-2)

Figure 2. Schematic diagram of the vehicle models

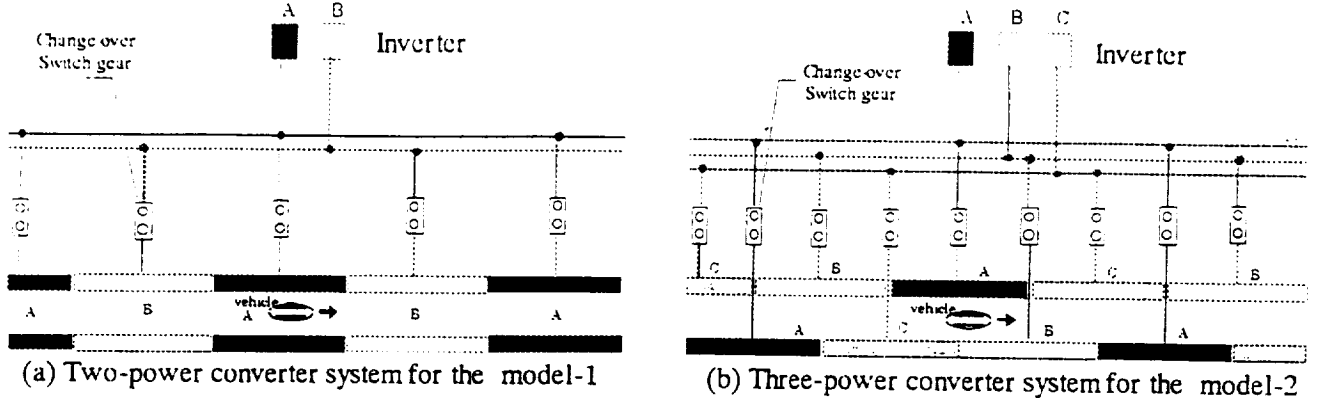


Figure 3. Feeding system

$$\psi_V = \sum_{k=1,3,\dots}^{\infty} \sum_{m=1,3,\dots}^{\infty} \Psi_{km} e^{\beta_{km} y_1} \left[k_{ni} e^{\beta_{km} c_a / 2} \sin \left\{ \alpha_k (x_1 - \frac{7\tau}{6}) \right\} + k_{no} e^{-\beta_{km} c_a / 2} \sin \left\{ \alpha_k (x_1 + \frac{5\tau}{6}) \right\} \right] \quad (\text{Wb}) \quad (6)$$

$$\psi_W = \sum_{k=1,3,\dots}^{\infty} \sum_{m=1,3,\dots}^{\infty} \Psi_{km} e^{\beta_{km} y_1} \left[k_{ni} e^{\beta_{km} c_a / 2} \sin \left\{ \alpha_k (x_1 + \frac{\tau}{6}) \right\} + k_{no} e^{-\beta_{km} c_a / 2} \sin \left\{ \alpha_k (x_1 - \frac{11\tau}{6}) \right\} \right] \quad (\text{Wb}) \quad (7)$$

where

$$\Psi_{km} = 2n_a \mu_0 \frac{\beta_{km}}{\alpha_k \alpha_m} \sin(\alpha_k \frac{l_a}{2}) \sin(\alpha_m \frac{w_a}{2}) a_s(k, m) e^{-\beta_{km}(d_a - d_s)} \frac{\sin(N_a \alpha_k \tau)}{\sin(2\alpha_k \tau)} \cos \alpha_m z_1$$

$$a_s(k, m) = \begin{cases} \frac{32n_s I_s}{\pi^2 km} \sin(\alpha_k \frac{l_s}{2}) \sin(\alpha_m \frac{w_s}{2}) \frac{\cos(3\alpha_k \tau / 2)}{\cos(\alpha_k \tau / 2)} \sin(5\alpha_k \tau / 2) & (\text{model-1}) \\ \frac{64n_s I_s}{\pi^2 km} \sin(\alpha_k \frac{l_s}{2}) \sin(\alpha_m \frac{w_s}{2}) \frac{\sin(2\alpha_k \tau)}{\cos(\alpha_k \tau / 2)} \cos(16\alpha_k \tau) \cos(8\alpha_k \tau) & (\text{model-2}) \end{cases}$$

$\beta_{km} = \sqrt{\alpha_k^2 + \alpha_m^2}$, $k_{ni} = n_{ai} / n_a$, $k_{no} = n_{ao} / n_a$, $\alpha_k = \pi k / L$, $\alpha_m = \pi m / W$, N_a : number of cells in one feeding section

$n_s I_s$: mmf of SCM, l_s , w_s : length and width of SCM, τ : pole pitch

n_{ai} , n_{ao} , n_a : number of turn of inner armature coil, outer coil, and the average turn

n_a , c_a , l_a , w_a , d_a : number of turns, layer depth, coil length, coil width, position of armature windings

z_1 : center height difference between the armature and the SCMs

Combining (4) with (5), (6) and (7), we obtain the lateral force for the unit feeding section

$$F_{Gpu} = \sqrt{\frac{2}{3}} \sum_{k=1}^{\infty} \sum_{m=1}^{\infty} \beta_{km} \Psi_{km} e^{\beta_{km} y_1} \{ k_d(x_1) i_d + k_q(x_1) i_q + k_0(x_1) i_0 \} \quad (\text{N}) \quad (8)$$

where

$$k_d(x_1) = k_{ni} e^{\beta_{km} c_a / 2} (c_1 s_{u1} + c_2 s_{v1} + c_3 s_{w1}) + k_{no} e^{-\beta_{km} c_a / 2} (c_1 s_{u2} + c_2 s_{v2} + c_3 s_{w2})$$

$$k_q(x_1) = -k_{ni} e^{\beta_{km} c_a / 2} (s_1 s_{u1} + s_2 s_{v1} + s_3 s_{w1}) - k_{no} e^{-\beta_{km} c_a / 2} (s_1 s_{u2} + s_2 s_{v2} + s_3 s_{w2})$$

$$k_0(x_1) = k_{ni} e^{\beta_{km} c_a / 2} (s_{u1} + s_{v1} + s_{w1}) / \sqrt{2} + k_{no} e^{-\beta_{km} c_a / 2} (s_{u2} + s_{v2} + s_{w2}) / \sqrt{2}$$

$$s_{u1} = \sin \left\{ \alpha_k (x_1 + \frac{3\tau}{2}) \right\}, \quad s_{u2} = \sin \left\{ \alpha_k (x_1 - \frac{\tau}{2}) \right\}, \quad s_{v1} = \sin \left\{ \alpha_k (x_1 - \frac{7\tau}{6}) \right\}, \quad s_{v2} = \sin \left\{ \alpha_k (x_1 + \frac{5\tau}{6}) \right\}, \quad s_{w1} = \sin \left\{ \alpha_k (x_1 + \frac{\tau}{6}) \right\},$$

$$s_{w2} = \sin\left\{\alpha_k\left(x_1 - \frac{11r}{6}\right)\right\}$$

The lateral force consists of the three components: d -axis, q -axis, and 0-sequence forces. It is going to be demonstrated in the next section that the d -axis component is dominant and the other two components are very small compared to it. Accordingly, we can rewrite the equation as follows

$$F_{Gpu} = K_{Gp}(y_1, t)i_d + K_{Gpq}(y_1, t)i_q + K_{Gp0}(y_1, t)i_0 \quad (\text{N}) \quad (9)$$

where

$$K_{Gp}(y_1, t) = \sqrt{\frac{2}{3}} \sum_{k=1,3,\dots}^{\infty} \sum_{m=1,3,\dots}^{\infty} \beta_{km} \Psi_{km} e^{\beta_{km} y_1} k_d(x_1) \quad (10.a)$$

$$K_{Gpq}(y_1, t) = \sqrt{\frac{2}{3}} \sum_{k=1,3,\dots}^{\infty} \sum_{m=1,3,\dots}^{\infty} \beta_{km} \Psi_{km} e^{\beta_{km} y_1} k_q(x_1) \quad (10.b)$$

$$K_{Gp0}(y_1, t) = \sqrt{\frac{2}{3}} \sum_{k=1,3,\dots}^{\infty} \sum_{m=1,3,\dots}^{\infty} \beta_{km} \Psi_{km} e^{\beta_{km} y_1} k_0(x_1) \quad (10.c)$$

Since the d -axis component K_{Gp} is used to control lateral motions of the vehicle, we now call it the guidance force coefficient of the propulsion system.

CALCULATED RESULTS OF THE GUIDANCE FORCE COEFFICIENT

Figure 4(a) shows the guidance force coefficient for one feeding section at the left side as a function of time for the model-1 when the vehicle runs at 500km/h without lateral displacement ($y_1 = 0$). The transients arise because it is assumed to have only one single feeding section. The plot indicates that guidance force may contain some pulsated forces, although the amplitudes are not so significant. It is found out that the harmonics are made from the 5-th and 7-th space harmonic fields. However, the

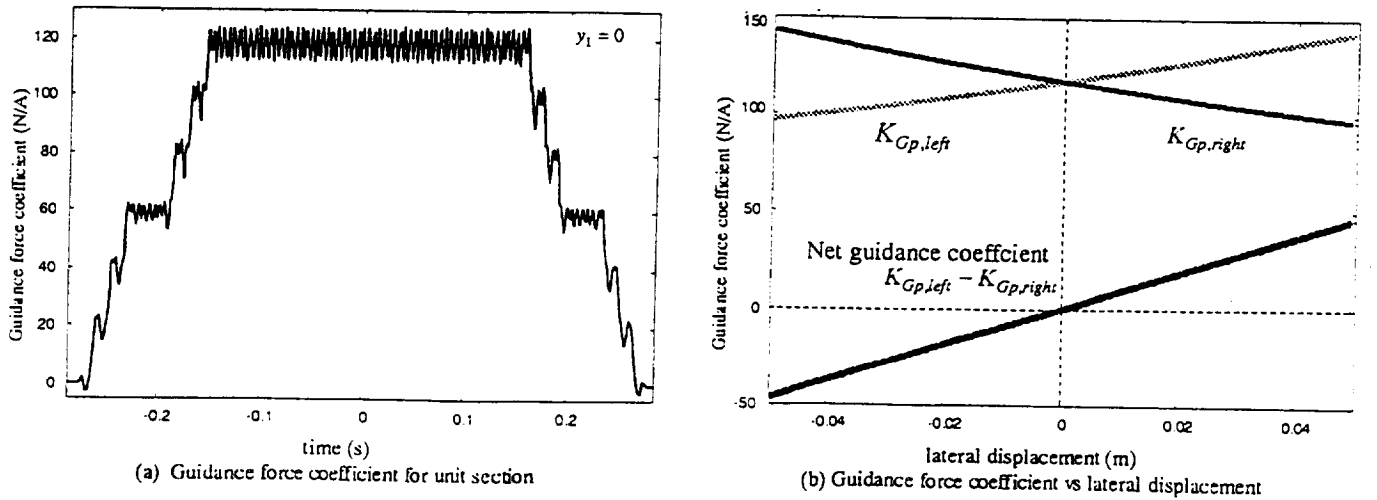
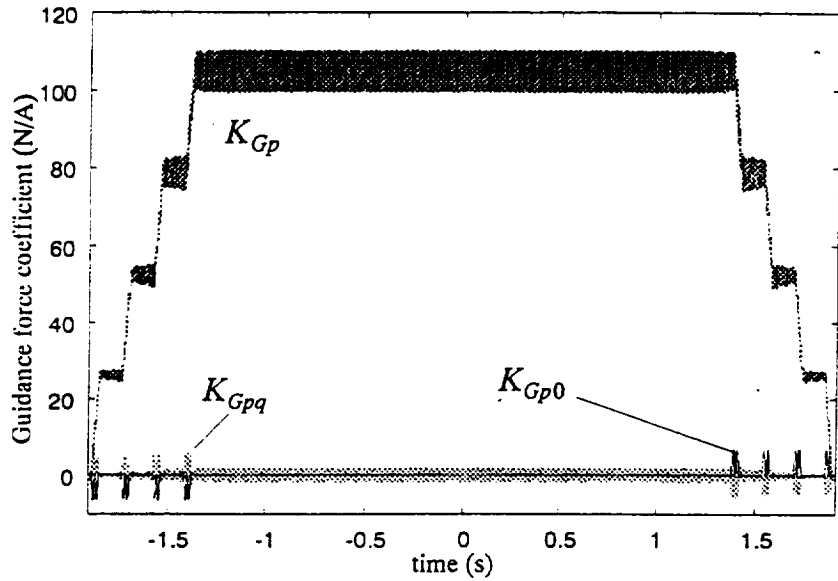


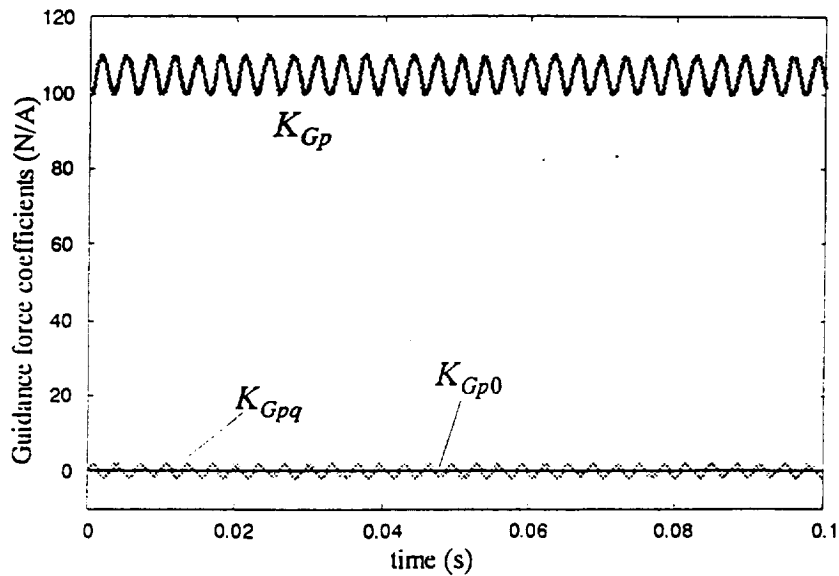
Figure 4. Guidance force coefficient (model-1; 500km/h)

model-1 has the two-power converter system, and accordingly the same armature current flows at both sides of feeding section. Therefore, the net guidance force coefficient is written as $K_{Gp, \text{left}} - K_{Gp, \text{right}}$, where the former is the one from the left side section, and the latter from the right section. This is shown in Figure 4(b). In this case, the vehicle guidance demands higher values of armature currents when the vehicle runs near the center of the guideway. To avoid this current capacity problem, the two sections at both sides of the vehicle should preferably be fed from different power supplies.

Figure 5 shows the calculated results for the model-2 with a three-power converter system, in which



(a) Guidance force coefficient for unit section



(b) Guidance force coefficients (close-up)

Figure 5. Guidance force coefficient
(model-2; 500km/h, $z_1=0.04\text{m}$)

every feeding section that faces the vehicle is supplied from a different source. The coefficients of (10) are plotted to compare the magnitudes. Positive value indicates that if the d -axis armature current is positive, the lateral force arises so that the lateral force y_1 increases, i.e., attractive force is generated between the armature and the SCMs. It is found that negative d -axis current should be supplied to the armature windings when the lateral displacement is positive. The q -axis has some ripples in the whole region, while the 0-sequence component is vanished except at the transient regions. Since the q -axis armature currents should be large enough to produce sufficient propulsion forces, rippled lateral forces may appear if only one side of q -axis current is especially enhanced. However, the same amplitude of q -axis armature currents is to be generated because propulsion force should be produced equally at both sides; there is no reason for enhancing one side of propulsion force. Therefore the both rippled forces cancel each other.

Figure 6 shows the coefficient as a function of lateral displacement. It is expected that the relation at the neighborhood of the center can be approximated by a linear function:

$$K_{Gp}(y_1, t) \cong K_{Gp0} + k_{Gp} y_1 \quad (11)$$

where

$$K_{Gp0} = K_{Gp}(0, t), \quad k_{Gp} = \left. \frac{\partial K_{Gp}(y_1, t)}{\partial y_1} \right|_{y_1=0}$$

LATERAL MOTION REGULATOR FOR VEHICLE

It was found out that the two-converter system might not fit into our guidance methodology using armature currents, and consequently our discussion for numerical simulations here for possible implementation is going to be focused on the model-2 with the three-converter system.

Our target is to build a regulator so that appropriate lateral guidance force is generated by armature

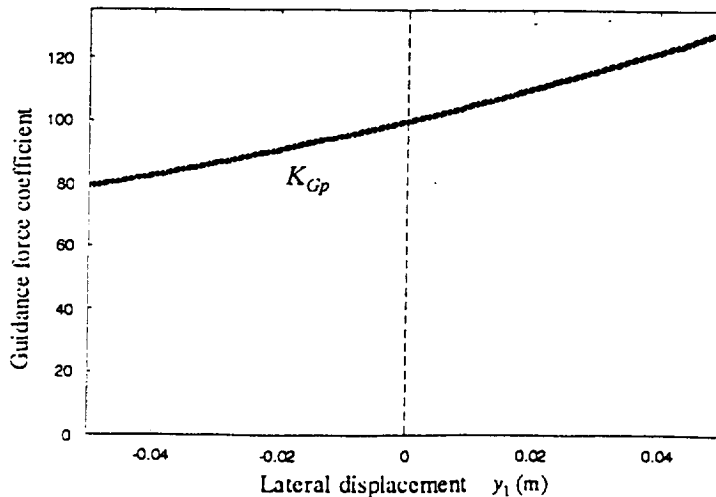


Figure 6. Guidance force coefficient of propulsion system as a function of lateral displacement

windings when the vehicle begins lateral motions triggered by some disturbances such as strong wind, guideway irregularities, etc. Figure 7 shows the concept of the regulator, where M is the vehicle mass, F is the feedback gain matrix, and K_{yy} is the spring constant of the levitation-guidance coils, which are installed along with the propulsion coils on the guideway. When the state vector comprised of lateral displacement and its time derivative has moved away from the equilibrium point, the state vector can be moved back by using a negative feedback of the vector to cancel the motions.

The regulator block diagram is shown in Figure 8, where the system has three controlled power sources corresponding to the three feeding sections. Instead of using the combination of the state feedback and feedback gain matrix, an output feedback is employed with a dynamic compensator $C(s)$: the negative feedback is given by

$$i_d = -Fx = -(f_1, f_2)(y_1, \frac{dy_1}{dt})^T = -f_1 y_1 - f_2 \frac{dy_1}{dt} \quad (12)$$

Using the Laplace transform, we have

$$I_d(s) = -(f_1 + f_2 s)Y_1(s) = -K_c(1 + T_{cd}s)Y_1(s) = -C(s)Y_1(s) \quad (13)$$

where $C(s) = K_c(1 + T_{cd}s)$.

If a feeding section is located on the left side of the vehicle, positive d -axis currents produce attractive

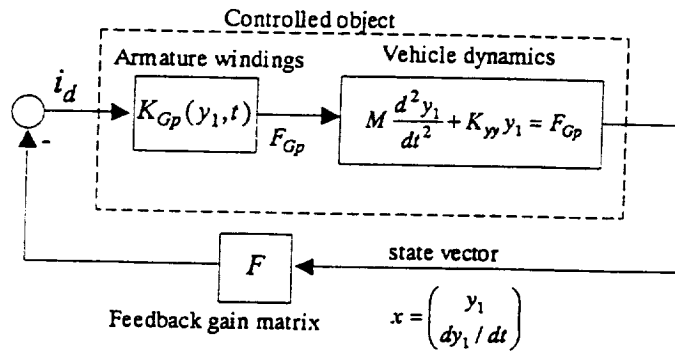


Figure 7. Concept of lateral motion regulator

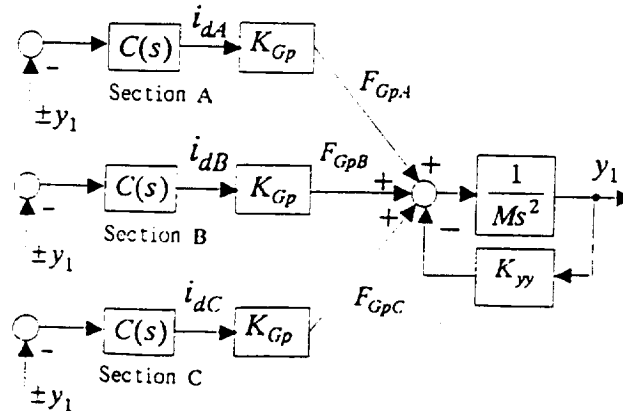


Figure 8 Vehicle lateral motion regulator system

force, i.e., positive force so that lateral displacement increases. When the feeding section is on the right side, it becomes a negative force. Therefore the guidance force coefficient K_{Gp} has different sign and function depending on which side of the vehicle the feeding section is located. Moreover a positive value of lateral displacement means that the vehicle is coming closer for the left side section, but moving away for the right side section. Then the control actions to cancel the vehicle motion should be the opposite from each other. The signs of y_1 in the figure indicate this situation.

The block diagram of Figure 8 is simplified to the diagram of Figure 9, being used for designing the dynamic compensator. Since the two sections at both sides of the vehicle are expected to generate the guidance force at the same time, one of them produces half the necessary force. Then the dynamic equation of the regulator observed from one section is written as

$$\frac{d^2 y_1}{dt^2} + \frac{1}{M'} K_{Gp0} K_c T_{cd} \frac{dy_1}{dt} + \frac{1}{M'} (K'_{yy} + K_{Gp0} K_c) y_1 = 0 \quad (14)$$

where $M' = M/2$, $K'_{yy} = K_{yy}/2$

This equation has the form of the standard second-order system

$$\frac{d^2 y_1}{dt^2} + 2\zeta\omega_n \frac{dy_1}{dt} + \omega_n^2 y_1 = 0 \quad (15)$$

As the result, our specification work for the regulator design has just become determining the damping factor and natural frequency. This is practically useful because we know the characteristics well. The spring constant of the levitation-guidance coils K_{yy} varies as the vehicle running speed changes. Accordingly, the proportional gain of the compensator K_c is to be altered based on a scheduling data if the natural frequency should be kept constant.

Assuming that $K_{yy} \approx 0$ at very low speed, the proportional gain is obtained by specifying the natural frequency ω_n as follows

$$K_c = \frac{M' \omega_n^2}{K_{Gp0}} \quad (16)$$

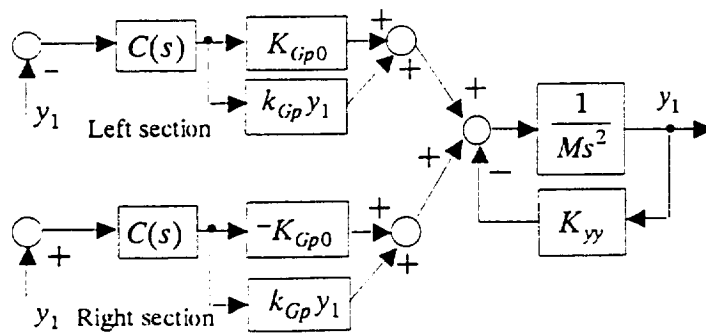


Figure 9. Simplified block diagram of the regulator

The derivative time is then determined by specifying the damping factor ζ , i.e.

$$T_{cd} = \frac{2\zeta\omega_n M'}{K_{cp0}K_c} \quad (17)$$

To avoid a noise problem for sensing the lateral displacement, the addition of a low pass filter to the derivative term may be useful. If we consider the derivation frequency range to be less than ω_{der} (rad/s), then the dynamic compensator is finally constructed as

$$C(s) = K_c \left(1 + \frac{T_{cd}s}{1 + s/\omega_{der}} \right) \quad (18)$$

Figure 10 shows the simulations for the proposed regulator system using the block diagram of Figure 9. The assumed natural frequency is 10 (rad/s) with the damping factor of 0.5, 1 and 2. The vehicle was assumed to have a lateral disturbance force of 10,000 (N) as shown in the figure, which is equivalent to 20 (m/s) of lateral wind. From the results, the regulator works very well to suppress the vehicle motion in less than about 1(mm). Since the currents of the two sections have almost the same amplitude with an opposite sign, only the currents of the left side are depicted here. The currents are required only around 100(A) at most. The desirable damping factor may be 1 as expected.

CONCLUSIONS

The paper has presented the formulation of lateral forces resulting from the interactions between the armature coil currents and the SCMs, and proposed the vehicle guidance system by using the d -axis currents. The guidance force coefficient of the propulsion system was then defined. And the lateral motion regulator system was proposed together with the design methodology, where the design formula has become the problem of determining the damping factor and natural frequency of lateral vehicle motion. Finally the numerical demonstration has shown that the system works very well.

REFERENCES

1. H.Yoshioka et al., Results of Running Tests and Characteristics of the Dynamics of the MLX01 Yamanashi Maglev Test Line Vehicles, Proc.MAGLEV'98, pp.225-230
2. T.Sakamoto, Analysis of a Superconducting Linear Synchronous Motor Propulsion in terms of dq variables, *Trans. IEE of Japan*, vol.116-D, No.2, pp.177-182, 1996
3. T.Sakamoto, Investigation of Superconducting Linear Synchronous Motor Propulsion Control via an Exact Mathematical Model, *Trans. IEE of Japan*, Vol.118-D, No.5, pp.572-578 (1998)

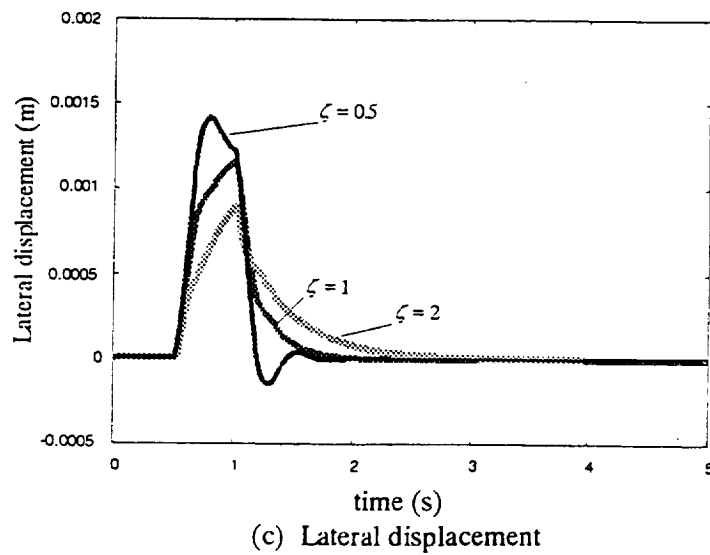
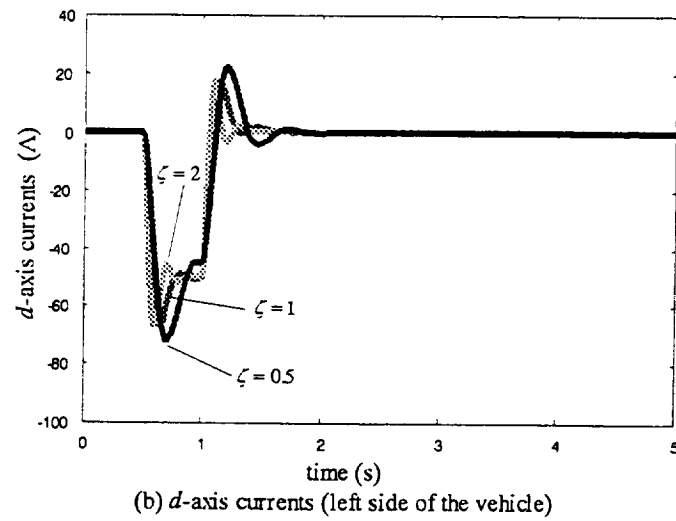
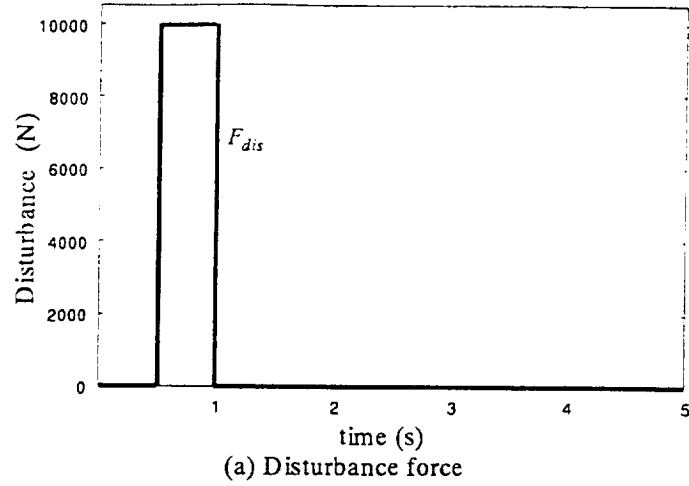


Figure 10. Regulator simulation

SWAY AND YAW MOTION CONTROL DUE TO RELUCTANCE FORCE IN CONTROLLED-PM LSM MAGLEV CARRIER

Kinjiro Yoshida*, Hiroshi Takami*, Yasunori Nakahashi**, Kenji Shimamoto*

* Department of Electrical and Electronic System Engineering,
Graduate School of Information Science and Electrical Engineering,
Kyushu University
10-1 6-chome Hakozaki Higashi-ku Fukuoka ,812-8581 Japan

** Fuji Electric CO.,LTD

SUMMARY

In controlled-PM LSM Maglev Carrier, four attractive-forces of four controlled-PM's fixed rigidly on the carrier can control heave, pitch and roll motions, by using an integral-control method. We have completed minimizing of electric power loss for its levitation. But it is very difficult to control guidance with the sway and yaw motions without any additional magnets and coils. For guidance control we have made successful use of a lateral reluctance-force which is produced between controlled-PM and armature iron rail.

INTRODUCTION

An experimental Maglev carrier in our laboratory (Fig. 1) has four controlled-PM's (CPM's) arranged rigidly at the four corners on the same plane of the bogie [1]. It is impossible to apply the local control method to the levitation problem for controlling simultaneously the four CPM's in the Maglev carrier system which includes six degrees of freedom. The integrated control method should be used to design the robust levitation control system for minimizing the electric power loss. The levitation control at standstill and propulsion motion combined with levitation have been carried out in our previous research without guidance control [2], [3]. The five degrees of freedom except propulsion motion can be controlled independently of the propulsion motion. The propulsion force due to LSM is treated as a disturbance for the heave, pitch, roll, sway and yaw motions. To control guidance with sway and yaw motions, a lateral force is required [4]. A reluctance force between CPM and armature iron rail can be used effectively.

This paper proposes a simple control method of using only *four* CPM's for the *five* degrees of freedom including sway and yaw motions as well as heave, pitch and roll ones. The method is based on using the lateral reluctance-force which is produced at both side-edges between CPM and armature iron rail. The restoring reluctance force is produced without any additional magnets and coils and depends on lateral displacement, airgap length and PM control current.

DYNAMICS MODELING OF MAGLEV CARRIER

Figure 1 shows a configuration of controlled-PM LSM Maglev Carrier in which the 2-pole-controlled PM's are arranged rigidly at the four corners on the same plane. The LSM armature guideway is also constructed rigidly. The levitation control system levitates the carrier stably while the propulsion control system propels the carrier by synchronizing the CPM with the travelling magnetic field produced by the stator armature current-carrying windings.

Figure 2 shows a rigid bogie model of Maglev carrier which has six degrees of freedom [5]. The heave motion is described as that of the center of the gravity (CG):

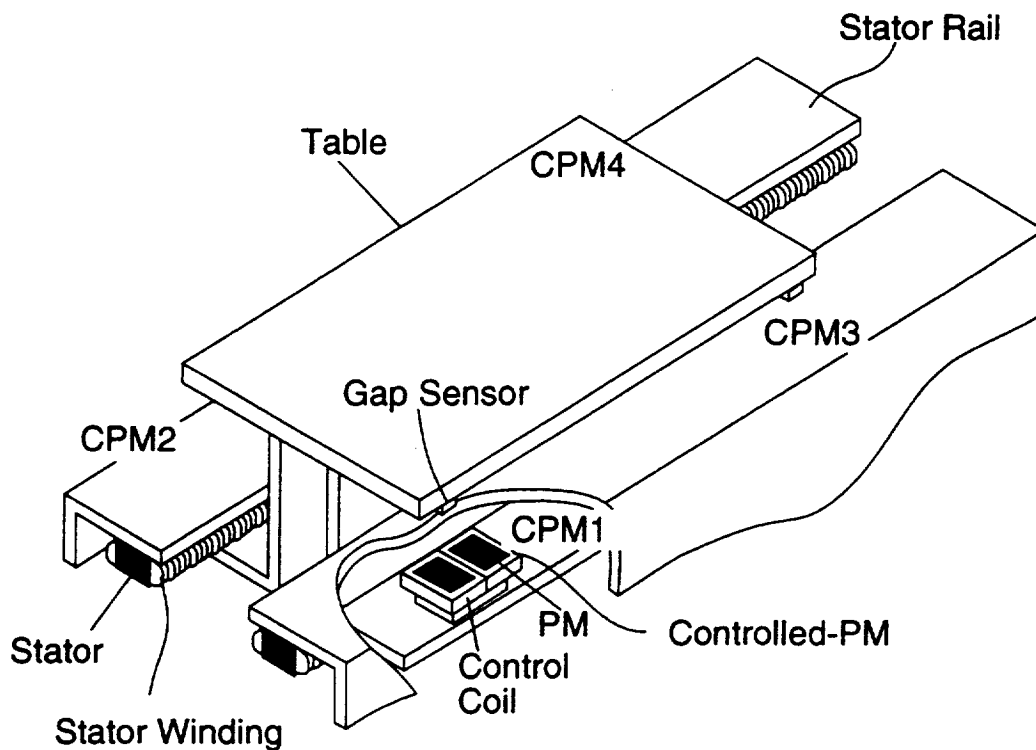


Figure 1. Controlled-PM Maglev Carrier.

$$M \frac{d^2 \Delta h_{Gz}}{dt^2} = F_{z1} + F_{z2} + F_{z3} + F_{z4} - Mg + F_{z,ex} \quad (1)$$

where M = the mass of carrier
 h_{Gz} = the height of the CG with respect to the reference plane, which is defined in the downward direction as shown in Fig.2
 $F_{zi} (i = 1,2,3,4)$ = the lift force produced in the CPM i ($i = 1,2,3,4$)
 $F_{z,ex}$ = the external force, such as aerodynamic drag force, and g is the acceleration of gravity

The roll motion is described as

$$I_\theta \frac{d^2 \theta}{dt^2} = (F_{z1} - F_{z2} + F_{z3} - F_{z4})l_y - (F_{y1} + F_{y2} + F_{y3} + F_{y4})l_z + N_{\theta,ex} \quad (2)$$

where I_θ = the moment of inertia around the x-axis
 θ = the roll angle, l_y and l_z the y- and z- directed distance between the CG and the PM's
 $F_{yi} (i = 1,2,3,4)$ = the guide force produced in the CPM i ($i = 1,2,3,4$), [4]
 $N_{\theta,ex}$ = the external moment around the x-axis

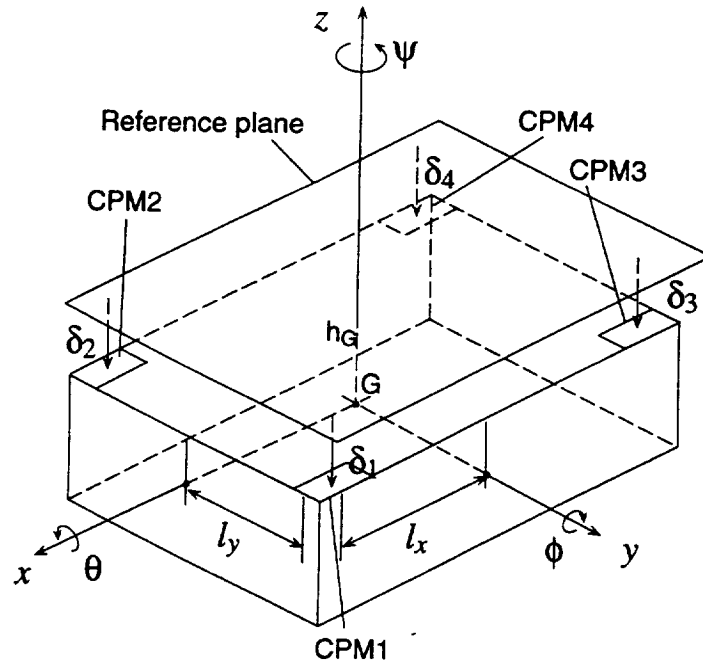


Figure 2. Rigid bogie model of carrier.

The pitch motion is described as

$$I_{\phi} \frac{d^2 \phi}{dt^2} = (-F_{z1} - F_{z2} - F_{z3} + F_{z4})l_x + (F_{x1} + F_{x2} + F_{x3} + F_{x4})l_z + N_{\phi,ex} \quad (3)$$

where I_{ϕ} = the moment of inertia around the y-axis
 ϕ = the pitch angle
 $F_{xi} (i = 1,2,3,4)$ = the thrust force produced in the CPMi ($i = 1,2,3,4$)
 l_x = the x-directed distances between the CG and the PM's
 $N_{\phi,ex}$ = the external moment around the y-axis

It is clear that equation (3) includes explicitly propulsion forces $F_{xi} (i = 1,2,3,4)$ and the pitch motion is affected directly by $F_{xi} (i = 1,2,3,4)$.

The sway motion is described as

$$M \frac{d^2 \Delta h_{Gy}}{dt^2} = F_{y1} + F_{y2} + F_{y3} + F_{y4} + F_{y,ex} \quad (4)$$

where h_{Gy} = the sway position of the CG with respect to the reference point
 $F_{y,ex}$ = the external force

The yaw motion is described as

$$I_{\psi} \frac{d^2 \psi}{dt^2} = (-F_{x1} + F_{x2} - F_{x3} + F_{x4})l_y + (F_{y1} + F_{y2} - F_{y3} - F_{y4})l_x + N_{\psi,ex} \quad (5)$$

where I_{ψ} = the moment of inertia around the z-axis
 ψ = the yaw angle
 $N_{\psi,ex}$ = the external moment around the z-axis

The self-inductance L_2 of the CPM coils are very large compared with the mutual inductance M between them and armature coils, so that terms associated with M can be neglected in the circuit equations of levitation control coils. They are described as

$$L_2 \dot{I}_{2i} + K_{\delta} \dot{\delta}_i + R_2 I_{2i} = e_{ci} \quad (i = 1,2,3,4) \quad (6)$$

where

- I_{2i} ($i = 1,2,3,4$) = an instantaneous current of the CPMi ($i = 1,2,3,4$) coils
 K_{δ} = the speed EMF coefficient due to the change in airgap
 R_2 = the equivalent resistance of control coil including additional resistance
 e_{ci} ($i = 1,2,3,4$) = the control voltage supplied to stabilize the levitation system according to the integrated control law

INTEGRATED-CONTROL DESIGN FOR MAGLEV CARRIER

At standstill when the Maglev carrier has no propulsion forces, i.e. $F_{xi} = 0$, the mutually cross-coupling levitation motion described by equations (1) - (5) and following equations (7) (8) that express the relationships of the airgaps δ_i between Δh_g , θ , ϕ and y_i between h_{Gy} , ψ can be transformed into five independent motions of the heave, roll, pitch, sway and yaw. They are expressed as follows.

$$\begin{bmatrix} \Delta\delta_1 \\ \Delta\delta_2 \\ \Delta\delta_3 \\ \Delta\delta_4 \end{bmatrix} = - \begin{bmatrix} 1 & 1 & -1 & -1 \\ 1 & -1 & -1 & 1 \\ 1 & 1 & 1 & 1 \\ 1 & -1 & 1 & -1 \end{bmatrix} \begin{bmatrix} \Delta h_{Gy} \\ l_y \theta \\ l_x \phi \\ 0 \end{bmatrix} = -T_1^T \begin{bmatrix} x_G \\ x_\theta \\ x_\phi \\ 0 \end{bmatrix} \quad (7)$$

$$\begin{bmatrix} \Delta y_1 \\ \Delta y_2 \\ \Delta y_3 \\ \Delta y_4 \end{bmatrix} = - \begin{bmatrix} -1 & -1 & -1 & 1 \\ -1 & -1 & 1 & -1 \\ -1 & 1 & -1 & -1 \\ -1 & 1 & 1 & 1 \end{bmatrix} \begin{bmatrix} h_{Gy} \\ r\psi \\ 0 \\ 0 \end{bmatrix} = -T_2^T \begin{bmatrix} h_{Gy} \\ r\psi \\ 0 \\ 0 \end{bmatrix} \quad (8)$$

$$M \frac{d^2 \Delta h_{Gz}}{dt^2} = F_{Gz} - Mg + F_{z,ex} \quad (9)$$

$$I_\theta \frac{d^2 \theta}{dt^2} = F_{G\theta} l_y + F_{\theta,ex} \quad (10)$$

$$I_\phi \frac{d^2 \phi}{dt^2} = F_{G\phi} l_x + F_{\phi,ex} \quad (11)$$

$$M \frac{d^2 \Delta h_{Gy}}{dt^2} = F_{Gy} + F_{y,ex} \quad (12)$$

$$I_{\psi} \frac{d^2 \psi}{dt^2} = F_{G\psi} \sqrt{l_x^2 + l_y^2} + F_{\psi,ex} \quad (13)$$

where $F_{Gz}, F_{z\theta}, F_{z\phi}, F_{yGy}, F_{y\psi}$ are derived from

$$\begin{aligned} & \begin{bmatrix} F_{Gz} & F_{z\theta} & F_{z\phi} & F_{zv} & F_{yGy} & F_{y\psi} & F_{yu} & F_{yw} \end{bmatrix}^T \\ &= T \begin{bmatrix} F_{z1} & F_{z2} & F_{z3} & F_{z4} & F_{y1} & F_{y2} & F_{y3} & F_{y4} \end{bmatrix}^T \end{aligned} \quad (14)$$

by using the following transformation matrix

$$T = \begin{bmatrix} T_1 & 0 \\ 0 & T_2 \end{bmatrix} \quad (15)$$

The linearizing equations (9) - (13) around the nominal operating point of $\delta_i = \delta_0$ ($i = 1, 2, 3, 4$), $I_{zi} = 0$ ($i = 1, 2, 3, 4$), the subsystem is obtained in the form of

$$M_j \frac{d^2 X_j}{dt^2} = -K_{FD} X_j + K_{FI} I_{2j} + F_{j,ex} \quad (j = G_z, \theta, \phi, G_y, \psi) \quad (16)$$

where

$$\begin{aligned} k_{FD} &= \left(\frac{\partial F_z}{\partial \delta} \right)_{\delta=\delta_0, I_{2i}=0}, \quad k_{FI} = \left(\frac{\partial F_z}{\partial I_z} \right)_{\delta=\delta_0, I_{2i}=0} \\ X_{Gz} &= \Delta h_{Gz}, \quad X_{\theta} = l_y \theta, \quad X_{\phi} = l_x \phi \\ X_{Gy} &= \Delta h_{Gy}, \quad X_{\psi} = \sqrt{l_x^2 + l_y^2} \psi \\ M_{Gz} &= M, \quad M_{\theta} = I_{\theta} l_y^{-2}, \quad M_{\phi} = I_{\phi} l_x^{-2} \\ M_{Gy} &= M, \quad M_{\psi} = I_{\psi} \sqrt{l_x^2 + l_y^2}^{-2} \end{aligned} \quad (17)$$

$$\begin{aligned} & \begin{bmatrix} I_{2Gz} & I_{2\theta} & I_{2\phi} & I_{2v} & I_{2Gy} & I_{2\psi} & I_{2u} & I_{2w} \end{bmatrix}^T \\ &= T \begin{bmatrix} I_{2z1} & I_{2z2} & I_{2z3} & I_{2z4} & I_{2y1} & I_{2y2} & I_{2y3} & I_{2y4} \end{bmatrix}^T \end{aligned}$$

In the same manner, the circuit equation (6) of the levitation system are given by

$$L_2 \frac{dl_{2j}}{dt} - 4k_\delta \frac{dx_j}{dt} + R_2 I_{2j} = e_{cj} \quad (j = G_z, \theta, \phi, G_y, \psi) \quad (18)$$

$$L_2 \frac{dl_{2j}}{dt} + R_2 I_{2j} = e_{cj} \quad (j = U, V, W) \quad (19)$$

where

$$\begin{aligned} & [e_{cGz} \ e_{c\theta} \ e_{c\phi} \ e_{cV} \ e_{cGy} \ e_{c\psi} \ e_{cU} \ e_{cW}]^T \\ & = T [e_{cz1} \ e_{cz2} \ e_{cz3} \ e_{cz4} \ e_{cy1} \ e_{cy2} \ e_{cy3} \ e_{cy4}]^T \end{aligned} \quad (20)$$

Equations (16) and (18) are three subsystems expressed as

$$\frac{dx_j}{dt} = A_j x_j + B_j u_j + d_j \quad (j = G_z, \theta, \phi, G_y, \psi) \quad (21)$$

$$x_j = [x_j \ \dot{x}_j \ I_{2j}]^T, \quad u_j = e_{cj} \quad (22)$$

$$A_j = \begin{bmatrix} 0 & 1 & 0 \\ -4k_{FD} / M_j & 0 & K_{FI} / M_j \\ 0 & 4k_\delta / L_2 & -R_2 / L_2 \end{bmatrix} \quad (23)$$

$$B_j = [0 \ 0 \ 1 / L_2]^T \quad (24)$$

Therefore, for each mode of motions, a stable levitation-control system is designed by applying the theory of linear optimal control.

DIGITAL CONTROL SYSTEM DESIGN

For the experimental Maglev carrier, an optimal digital levitation control system is designed to minimize the power loss in the control circuit. By descretizing the continuous subsystems of equation (21) by means of zero-hold with a sampling time, 1 type digital servosystem for three independent-motions are constructed as shown in Fig.3. Feedback gains K_1 , K_2 and K_3 are determined from optimizing the following performance index

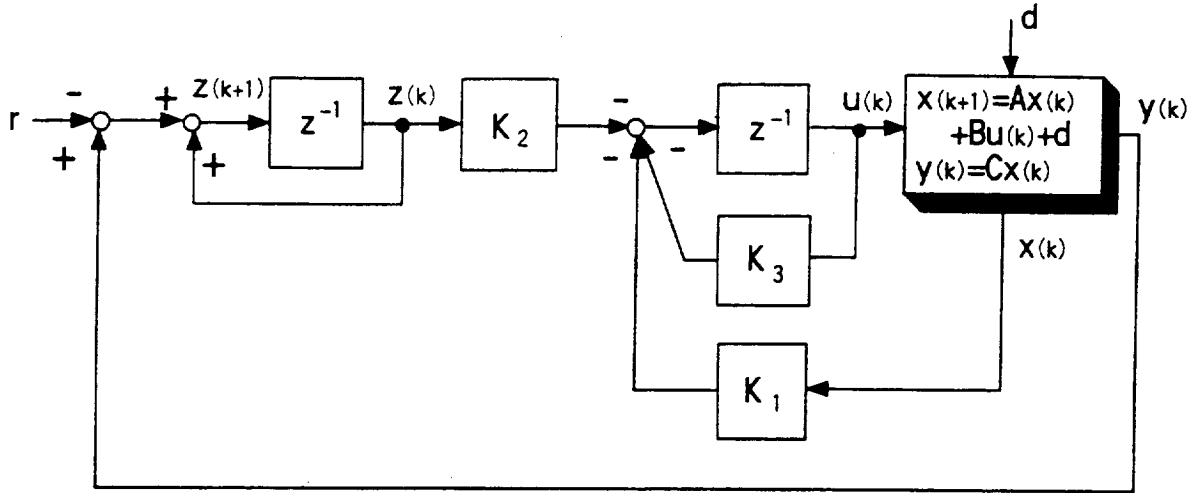


Figure 3. Servo system counting for sampling time.

$$J = \sum_{k=0}^{\infty} \{ \delta X(k) Q^T \delta X(k) + \delta u(k+2) R^T \delta u(k+2) \} \quad (25)$$

where

$\delta X(k), \delta u(k)$ = deflections from the steady-state values of X and u
 Q, R = weighting coefficient matrices

The digital control algorithm for minimizing levitation loss is achieved by choosing $c = [0 \ 0 \ 1]$ and outputs $y_j = I_{2j}$ ($j = G_z, \theta, \phi, G_y, \psi$). The control laws corresponding to the CPMi ($i = 1, 2, 3, 4$) are given by putting $e_{cv} = 0$ and by transforming inversely e_{ci} ($j = G_z, \theta, \phi, G_y, \psi$) by the help of the transformation matrix T , as follows:

$$e_{ci}(k+1) = K_{z1} \Delta \delta(k) + K_{z2} \Delta \dot{\delta}(k) - K_{z3} I_{2i}(k) - K_{z4} \sum I_{2i}(n) - K_{z5} e_{ci}(k) \quad (i = 1, 2, 3, 4) \quad (26)$$

where

K_{zm} ($m = 1, 2, 3, 4, 5$) = control gain matrices

$$\Delta \delta(k) = [\Delta \delta_1(k) \ \Delta \delta_2(k) \ \Delta \delta_3(k) \ \Delta \delta_4(k)]^T$$

SWAY AND YAW MOTION CONTROL STRATEGY AND DESIGN

Sway and yaw motions in phase of stable levitation of Maglev carrier can be damped by controlling reluctance force between stator iron and CPM's. The reluctance force is dependent on lateral displacement,

airgap length and PM control current [4]. When lateral displacement is increased with sway motion, a method to brake it effectively is to decrease airgap length and to increase control current. With respect to yaw motion, it is also true. However it is a problem how to do that by means of four lateral displacement y_i ($i = 1, 2, 3, 4$) caused due to sway and yaw motions. From some experiments, we have found a simple control method given in following equation:

$$\Delta e_{ci}(k+1) = \sum_{v=1}^4 \{K_{r1} \Delta y_v(k) + K_{r2} \Delta \dot{y}_v(k)\} \quad (i = 1, 2, 3, 4) \quad (27)$$

where

K_{r1} ($i = 1, 2, 3, 4$) = control gain for sway-motion control which is obtained by integrated control method

Δy_i ($i = 1, 2, 3, 4$) = lateral displacement of each CPM center of LSM guideway

$\Delta \dot{y}_i$ ($i = 1, 2, 3, 4$) = speed of lateral displacement of each CPM

Equation (27) is superposed on equation (26).

LEVITATION AND GUIDANCE CONTROL SYSTEM FOR EXPERIMENT

Figure 4 shows a configuration of levitation and guidance control system for the experiments. The gaps and current information from eight gap-sensors and four current-sensors are fed as a form of voltage to personal computer through A/D converters. The required control-voltages for each CPM's are calculated by personal computer according to equation (26). The control coil current is supplied with a sampling time of 1 ms by the PWM controllers.

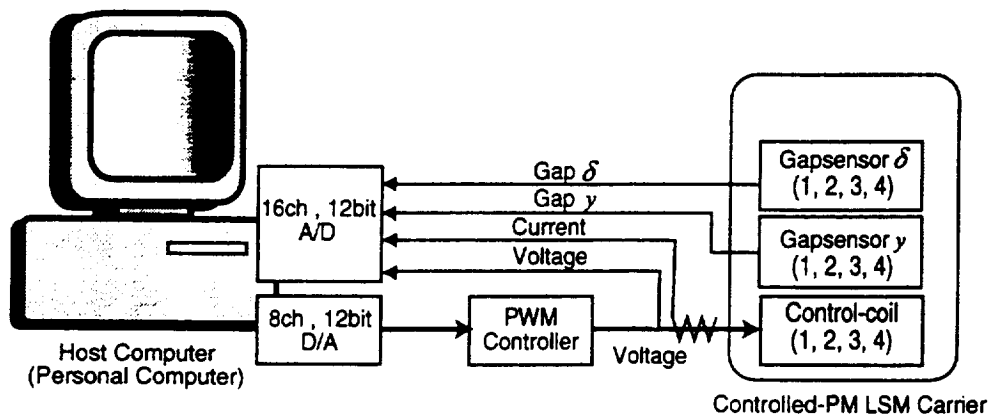


Figure 4. Levitation control system for experiment.

SWAY AND YAW CONTROL EXPERIMENTS

Figure 5 shows the experimental results of sway-and-yaw control by utilizing the lateral reluctance-force between CPM and armature iron rail during Maglev motion. The carrier takes off from initial height of 0.45mm limited mechanically by guide rollers and initial sway of about -2.2mm, and levitates at the standstill and stops from Maglev condition. Maximum control current is limited about 30A. Three-step-sway-control synchronizing the variation of sway motion is carried out effectively in order to suppress sway and yaw motions. Figures 5 (a) and (b) show the sway and yaw motions with sway-control (solid lines) and without sway-control (dotted line) *i.e.* free dynamics of sway and yaw motions, respectively. The halftone regions in the figures indicate intervals during which sway motion is controlled. Each control is started from a negative maximum value of sway motions and finished with 1.5 cycles of its oscillation. Though yaw motion becomes relatively large in only the regions of sway control, the sway and yaw motions are damped rapidly and the excellent sway-and-yaw motion control is achieved. On the other hand, sway and yaw motions without the control are oscillated continuously. Figures 5 (c) and (d) show control current i_{21} of CPM1 and heave motion h_{Gz} , respectively. In the sway control region, the control current and heave motion are varied similarly to oscillation of sway motion. Figures 5 (e) and (f) show the roll motion θ and pitch motion ϕ , respectively. Variations of these motions are very small and stable levitation control of carrier is realized and those with and without sway control are almost the same. The roll and pitch motions with sway control correspond almost to those without sway control. Figures 5 (g) - (i) show the control currents of CPM2, CPM3 and CPM4. These waveforms are the same as those in Fig.5 (c).

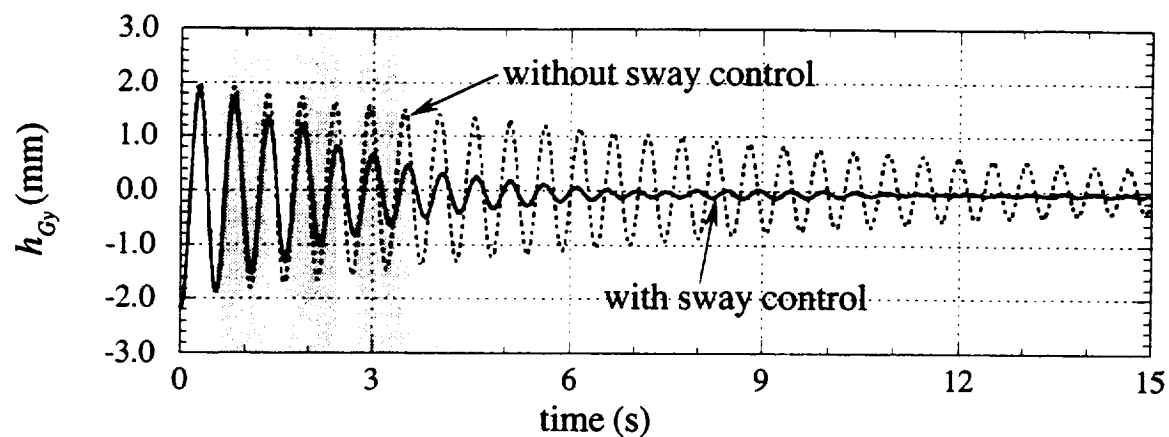
CONCLUSIONS

A simple control method for the five degrees of freedom including sway and yaw motions as well as heave, pitch and roll motions have been proposed for controlled-PM LSM Maglev carrier in our laboratory. By using the lateral reluctance-force which is produced at both side-edges between CPM and armature iron rail, oscillations of sway and yaw motions have been damped successfully by experiments without any additional magnets and coils. The results in this research leads to practical Maglev carrier system.

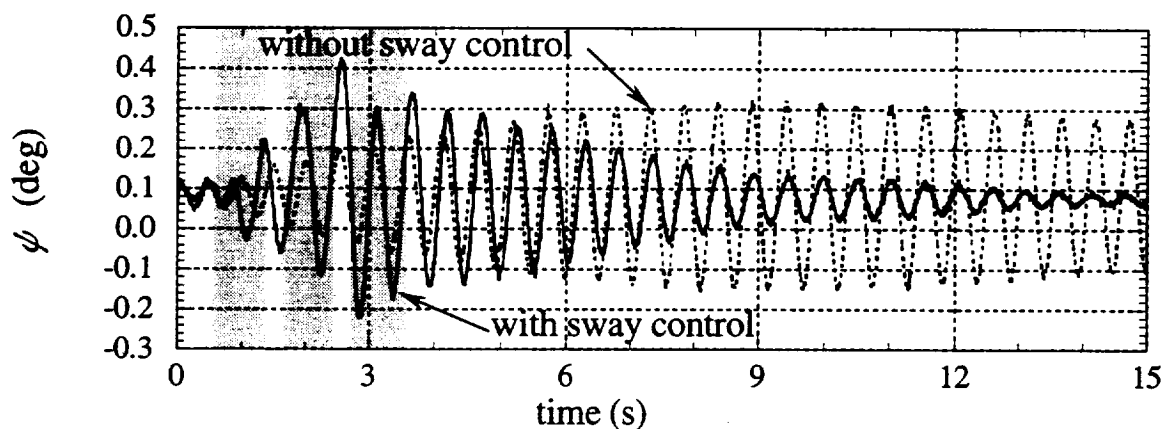
REFERENCES

1. K.Yoshida, E.Zen, H.Inoguchi, S.Sonoda and T.Nakano : Lift Force Analysis in a Controlled-PM LSM Maglev Carrier, Proc. of Int. Conf. on Magnetic Bearings, zurich June 1988, pp.103-163

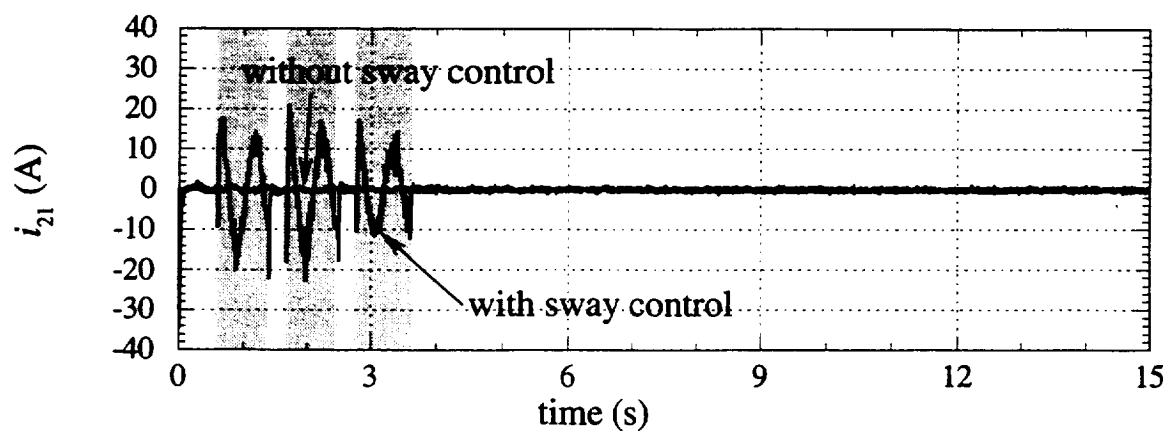
2. K.Yoshida, T.Yamashita and T.Jyozaki : Dynamics of Controlled-PM LSM Maglev Carrier, Proc. of the 4th Sym. on Dynamics related to Electromagnetic Forces, Invited 5-1, June 1992, pp.93-99
3. K.Yoshida, H.Takami, A.Hasuike, T.Hirakawa, J.Lee, T.Omura, A.Sonoda : Levitation and Propulsion motion control of Controlled-PM LSM Maglev Carrier, Proc. of Inter. Conf. on Electrical Machines, Sept. 1994, Vol.2, pp.21-26
4. K.Yoshida, J.Lee, T.Omura : Performance Analysis of Controlled-PM LSM Maglev Carrier with Lateral Displacement by 3-D FEM, Proc. of Int. Conf. on Linear Drives and Industry Application, May 1995, PP.215-218
5. K.Yoshida, T.Omura, J.Lee : Dynamics Simulations of Controlled-PM LSM Maglev Carrier, Taking into account Six Degree of Freedom, Advanced Computational and Design Techniques in Applied Electromagnetic Systems (book), 1995, Elsevier, PP.391-394



(a) Sway motion

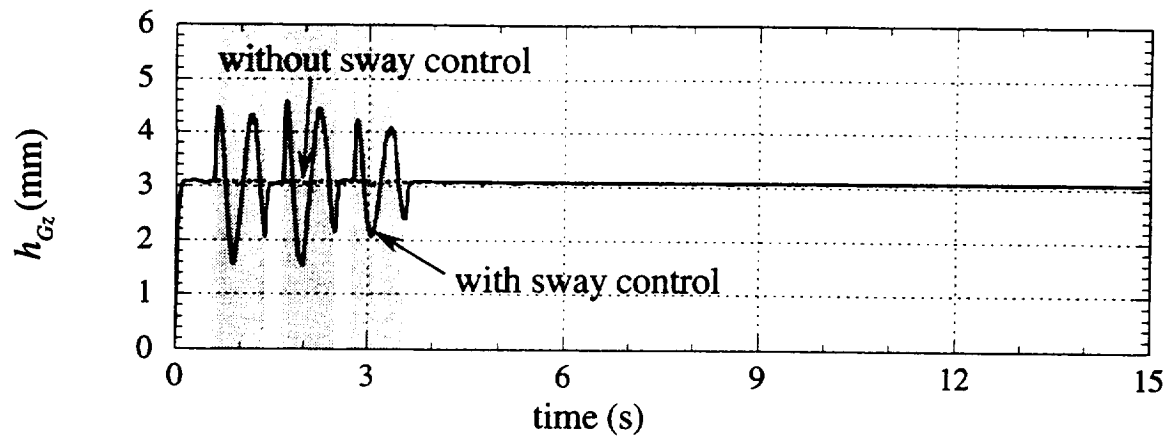


(b) Yaw motion

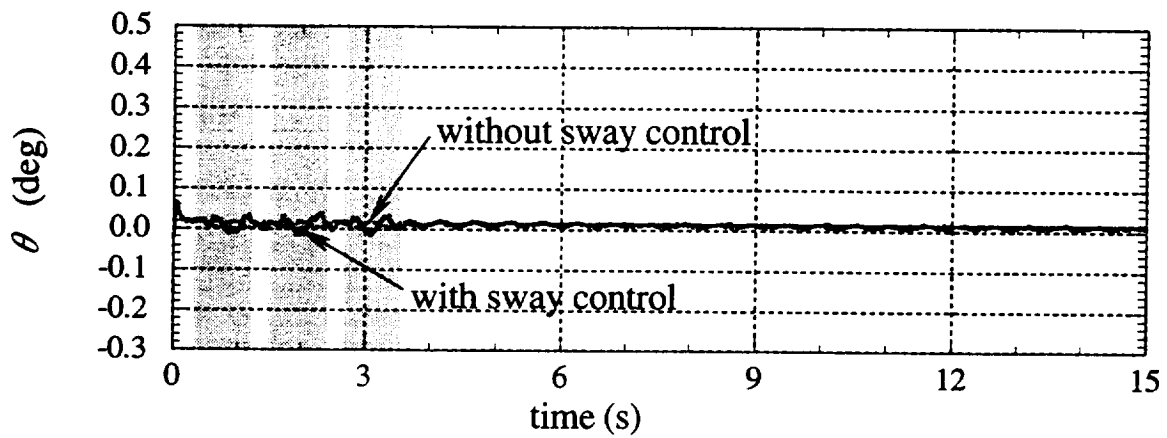


(c) Control current i_{21}

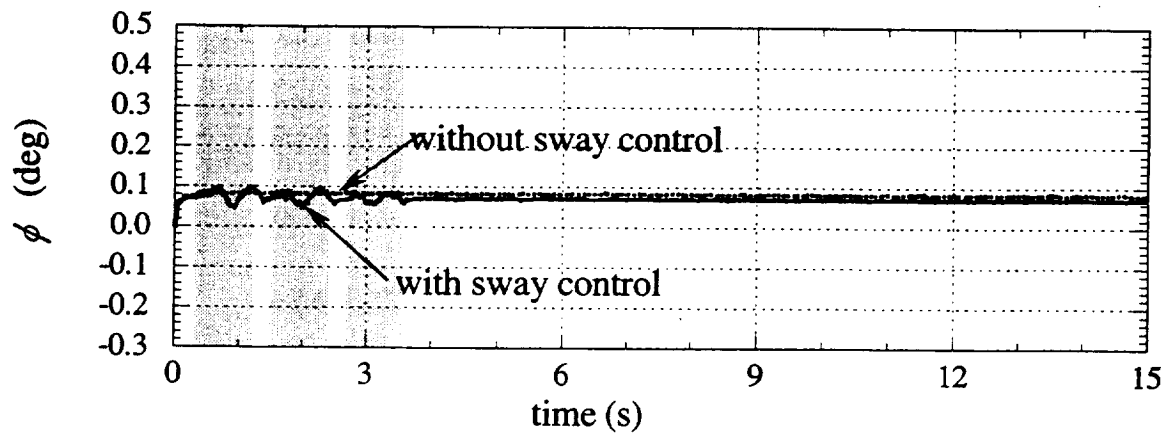
Figure 5. Experimental Results.



(d) Heave motion

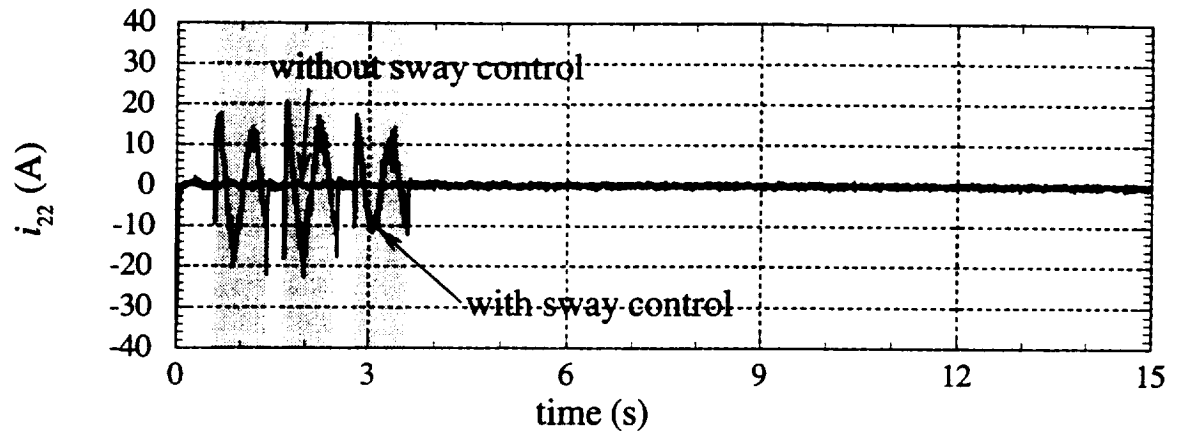


(e) Roll motion

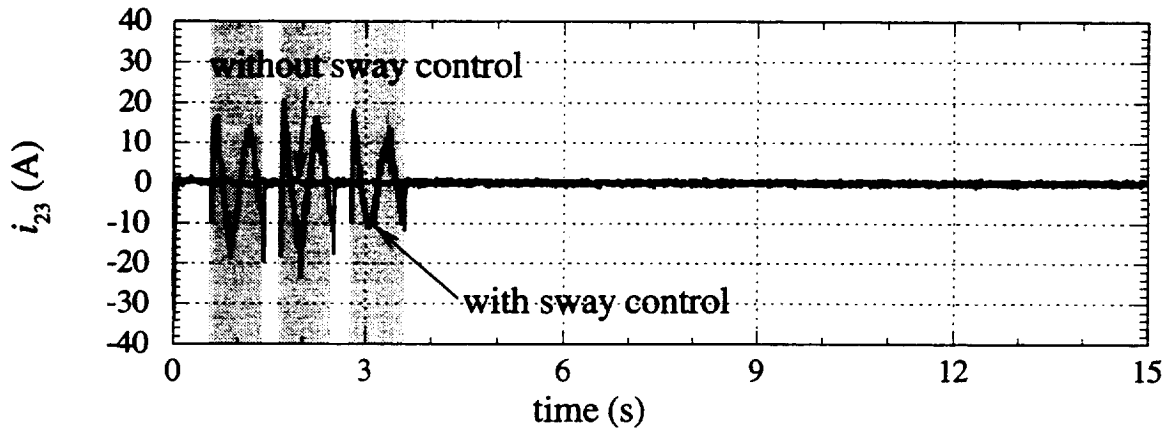


(f) Pitch motion

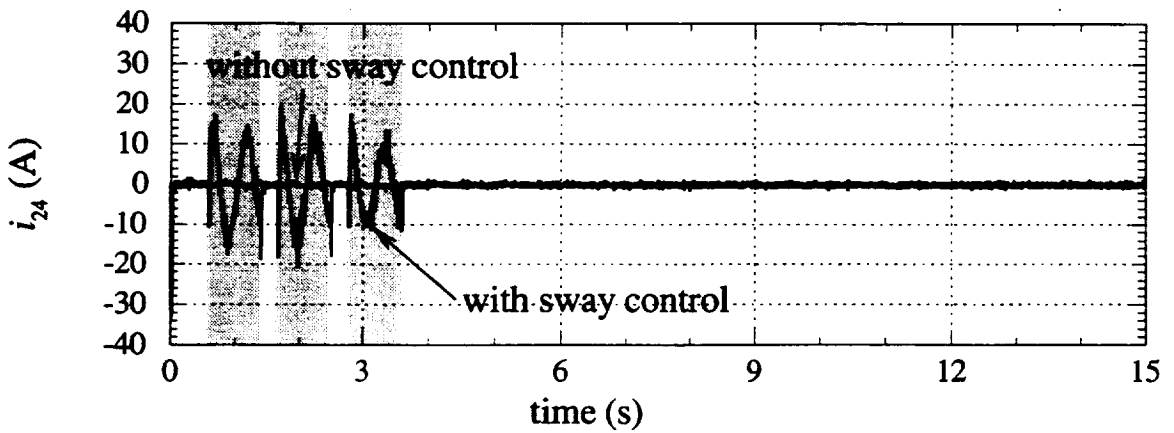
Figure 5. Experimental Results (cont.)



(g) Control current i_{22}



(h) Control current i_{23}



(i) Control current i_{24}

Figure 5. Experimental Results (cont.)

FEASIBILITY STUDY OF SUPERCONDUCTING LSM LAUNCHER SYSTEM FOR PRACTICAL H-II ROCKET

Kinjiro Yoshida*, Takeshi Kawanami**

* Department of Electrical and Electronic System Engineering,
Graduate School of Information Science and Electrical Engineering, Kyushu University
10-1 6-chome Hakozaki Higashi-ku Fukuoka, 812-8581 Japan

** Tokyo Electric Power Co., Inc.

SUMMARY

A practical feasibility study on superconducting linear synchronous motor (LSM) rocket launcher system for H-II rocket is presented on a basis of dynamic simulations of electric power energy, efficiency and power factor as well as ascending motions of the launcher and rocket. To decrease vastly maximum reactive power per section and to improve electrical efficiency and power factor, four-power-supply (A-B-C-D) system is introduced to shorten one section length as small as possible. It is made clear that the LSM rocket launcher system can obtain very high energy-efficiency of 94 %. It is found from very large instantaneous power at a peak speed and relatively low required-energy that initial cost is very high but operating cost is very low.

INTRODUCTION

We proposed a vertical type superconducting linear synchronous motor (LSM) rocket launcher system of which four acceleration guideways with double-layer armature windings are arranged symmetrically along a shaft of about 1,500 m under the ground. From our feasibility study, it is found that the linear launcher made the rocket attain the speed of 700 km/h at the height of 100 m above the ground, where the payload could be increased more than 15 % by substituting it for the first acceleration rocket. The linear launcher is brought to a stop at the ground surface by a quick control of deceleration. Superconducting LSM rocket launcher system was simulated to operate in an attractive-mode, controlling the Coriolis force [1]. Dynamics simulations of ascending the 4-ton-launcher with 1-ton-rocket were obtained to meet the same acceleration pattern of quick acceleration and deceleration rates as that of the repulsive-mode operation used in our previous papers [2], [3]. Electrical dynamics were simulated for electric powers, efficiency and power factor as well as ascending motions of launcher and rocket. It has been found that an optimal design of the 60-sections-length power supply system enable the system to obtain high efficiency and power factor [1].

This paper presents electromechanical dynamics simulations of ascending the launcher for H-II

rocket of practical size (length 48m , diameter 4m and weight 256 ton) which meet the same acceleration pattern of quick acceleration and deceleration rates as that of the attractive-mode operation used in our previous papers. After the rocket is released at a peak speed of about 900 km/h, the linear launcher is stopped for a very short time of 5 seconds by a rapid control of deceleration. To decrease vastly maximum reactive power per section and to improve electrical efficiency and power factor, four-power-supply (A-B-C-D) system is introduced to shorten one section length as small as possible. Electric power, energy, efficiency and power factor are evaluated qualitatively for more practical feasibility study. It is made clear that the LSM rocket launcher system with four-power-supply (A-B-C-D) system can obtain very high energy-efficiency of 94%.

SUPERCONDUCTING LSM ROCKET LAUNCHER SYSTEM FOR H-II ROCKET

Figure 1 shows a concept of a large-scale superconducting LSM-controlled rocket launcher system

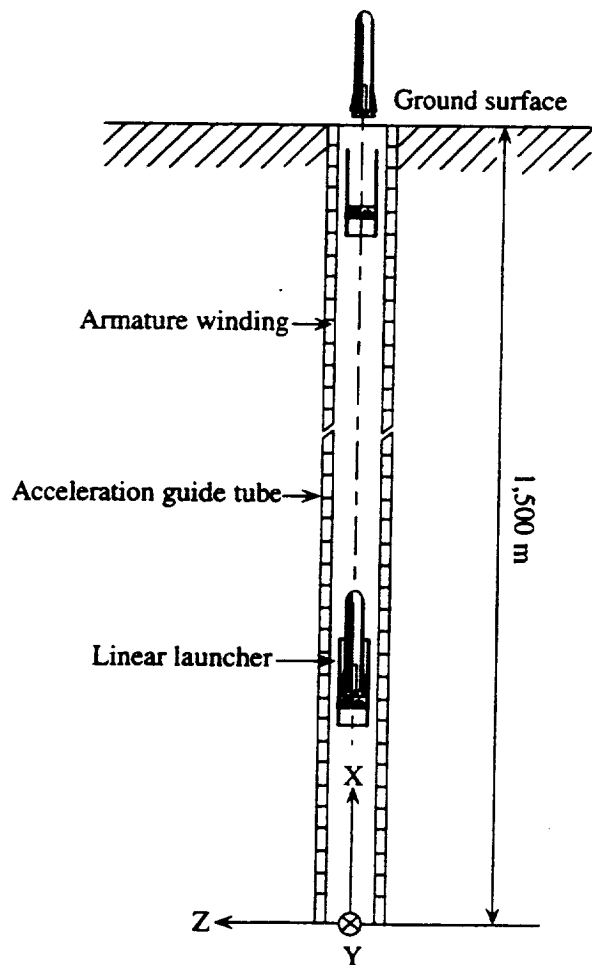


Figure 1. Vertical type superconducting-LSM controlled rocket launcher system for H-II rocket.

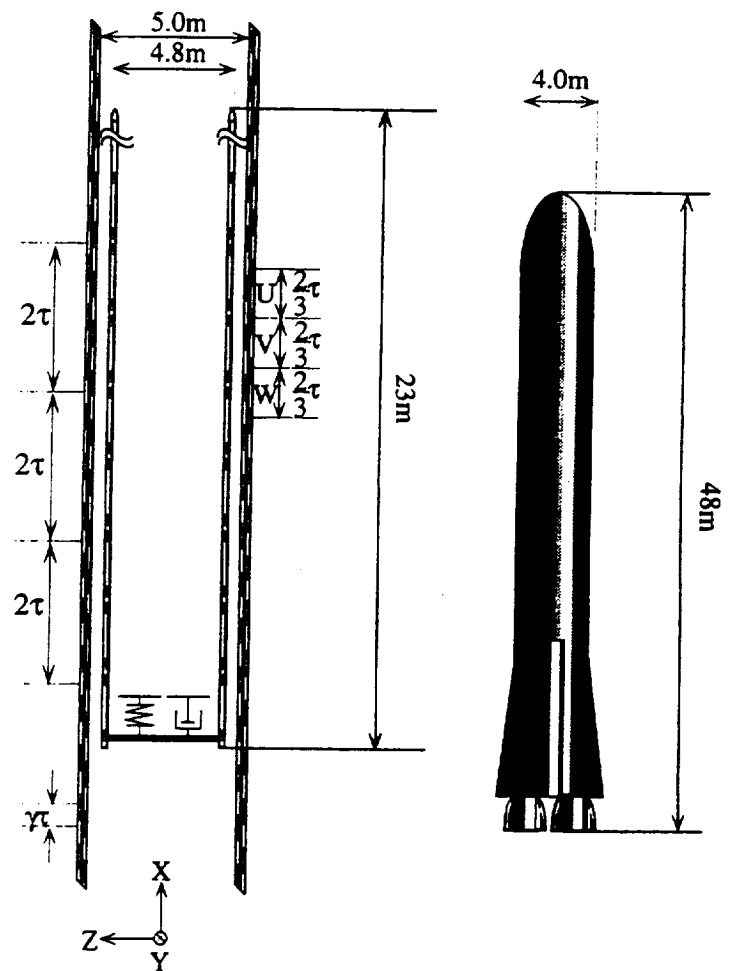


Figure 2. Acceleration guide tube of LSM armature and rocket launcher with superconducting magnets, and H-II rocket.

for H-II rocket, which has the acceleration guide tube of about 1,500 m deep under the ground. The concept is based on our theoretical work on a superconducting LSM-controlled ground-based zero-gravity facility with the drop shaft of about 800 m [4]. In Fig. 1, the LSM armature-windings which are installed all along the acceleration guide tube are used to drive and guide the linear launcher.

Figure 2 shows double-layer windings of the LSM armature which are composed of inside and outside coils, and the linear launcher on which the rocket is mounted through the use of passive suspension. The superconducting magnets are arranged with two poles facing the armature-windings in the front and rear portions of the linear launcher vehicle.

ASCENDING AND GUIDANCE MOTION CONTROL OF LINEAR LAUNCHER SYSTEM FOR H-II ROCKET

The linear launcher is accelerated to a peak speed, with the H-II rocket, and after releasing the rocket, it is decelerated with no-load to be brought to rest at the end of guide tube near the earth surface. On the other hand, during the acceleration phase, the rocket is fixed to the launcher through a passive suspension, but after separation from the launcher, it ascends freely in the guide tube. According to the armature-current control method proposed in Reference [1], the ascending motions in the X-direction of the launcher and the rocket are controlled together with the guidance motions in the Y-Z plane. When the Z-axis is assumed to be in an eastward direction, the Coriolis force can be taken into account as an external disturbance force in the Z-directed motions of the linear launcher and the rocket.

After the rocket is released from the launcher and takes off with a high initial-speed, the rocket continues to ascend with no control subject to the Coriolis force in the Z-direction under the force of gravity in the X-direction.

The effective values of armature-currents in four LSM systems are controlled independently for the launcher to meet the command acceleration pattern. The linear launcher should be controlled simultaneously to ascend at the synchronous speed V_{x0} of the travelling magnetic field, by producing total thrust force F_x due to all the four LSM-systems. The mechanical load-angle is controlled for all the four LSM's to produce the sufficiently strong attractive force due to the resultant guidance forces F_Y and F_Z . When the launcher receives any disturbance forces in the Y- and Z-directions, the LSM guidance forces can compensate them automatically and keep it at the center of the four LSM's.

ANALYSIS OF ELECTRICAL DYNAMICS

By applying vector analysis in the 3-phase armature-windings connected to satisfy the condition of $i_u + i_v + i_w = 0$, the terminal voltage per phase \dot{V} is derived in the following vector expression [1]:

$$\dot{V} = 2R\dot{i} + 2j\omega \left(L - M_2 + M_4 - \frac{M_5 + M_6}{2} \right) \dot{i} + \dot{E}_0 \quad (1)$$

with

$$\dot{E}_0 = E_0 e^{j(\pi/2 - \pi/\tau x_0)} \quad (2)$$

where R = resistance per phase of inside or outside armature-windings

L = self inductance per phase of inside or outside armature-windings

M_2 = mutual inductance between neighbouring inside and outside armature-windings

M_4 = mutual inductance between inside and outside armature-windings of the same phase

M_5, M_6 = mutual inductance between inside and outside armature-windings of lagging and leading phases

i = vector of phase current

\dot{E}_0 = vector of induced voltage

E_0 = effective value of induced voltage

x_0 = mechanical load-angle

$\omega = 2\pi f$ = angular velocity

f = supply frequency

The active power P_o , power loss P_l and the reactive power P_Q for each LSM system are described as follows:

$$P_o = 3E_0 I \sin \frac{\pi}{\tau} x_0 = F_x V_L \quad (3)$$

$$P_l = 6RI^2 \quad (4)$$

$$P_Q = 6\omega \left(L - M_2 + M_4 - \frac{M_5 + M_6}{2} \right) I^2 + 3E_0 I \cos \frac{\pi}{\tau} x_0 \quad (5)$$

where I = effective value of phase current

V_L = speed of launcher.

Apparent power P_a , the efficiency η and power factor $\cos \phi$ are thus calculated using equations (3) - (5).

$$P_a = \sqrt{(P_o + P_l)^2 + P_Q^2} \quad (6)$$

$$\eta = \frac{P_o}{P_o + P_l} \times 100 \quad (7)$$

$$\cos \phi = \frac{P_o + P_l}{P_a} \times 100 \quad (8)$$

Active electric energy E_M , electric loss energy E_l and energy-efficiency η_E are defined as follows:

$$E_M = \frac{1}{3600} \int_0^{t_M} P_M(t) dt \quad (\text{Wh}) \quad (9)$$

$$E_I = \frac{1}{3600} \int_0^{t_M} P_I(t) dt \quad (\text{Wh}) \quad (10)$$

$$\eta_E = \frac{E_M}{E_M + E_I} \times 100 \quad (11)$$

where t_M = total running time in seconds of the launcher which operates as a motor.

DESIGN OF POWER SUPPLY SYSTEM AND SECTION-LENGTH

Especially for the H-II rocket which is 220 times heavier than the rocket in previous papers [1], [2], power supply system design is one of the most important problems in reducing reactive power at a peak speed of 900 km/h as much as possible. By increasing number of power supply systems, one section-length of the long-stator along the guideway is made shorter, so that a large component of reactive power which is expressed by the first term in the right hand side of equation (5) is decreased in proportion to section-length. But with its increase, the total initial cost also increases. We have designed four-power supply (A-B-C-D) system which has four sets of inverters.

The section-length depends strongly on launcher speeds. Before the launcher enters the next section, the armature-current in the section is required to be at a steady state. The time constant is the same in all sections, so that the higher the speed of launcher increases, the longer one section-length should be. Figure 3 shows a design of total section-length which includes the 5 groups with 18-, 30-, 39-, 42- and 36-m-sections. The five kinds of section-lengths are determined considering the time (170 ms) required to converge switch-on transient phenomena, which is about three times larger than the time constant $\tau_c = 55.5$ ms as shown in Table 1. Tables 2 and 3 is for (A-B) and (A-B-C) systems.

Table 1. Resistance, inductances and time constant in each section for four-power-supply (A-B-C-D) system

section paramater	group (1) 6 sections of 18-m-section	group (2) 10 sections of 30-m-section	group (3) 8 sections of 39-m-section	group (4) 10 sections of 42-m-section	group (5) 10 sections of 36-m-section
R (Ω)	0.0706	0.1176	0.1529	0.1646	0.1411
$L - M_2 + M_4$ (mH)	3.936	6.560	8.528	9.184	7.872
$M_5 + M_6$ (mH)	0.0362	0.0604	0.0785	0.0846	0.0725
τ_c (ms)	55.5	55.5	55.5	55.5	55.5

Table 2. Resistance, inductances and time constant in each section
for two-power-supply (A-B) system

parameter \ section	group (1) 3 sections of 36-m-section	group (2) 5 sections of 60-m-section	group (3) 4 sections of 78-m-section	group (4) 5 sections of 84-m-section	group (5) 5 sections of 69-m-section
R (Ω)	0.1529	0.2352	0.3058	0.3293	0.2705
$L - M_2 + M_4$ (mH)	8.528	13.120	17.056	18.368	15.088
$M_5 + M_6$ (mH)	0.0785	0.1208	0.1570	0.1691	0.1389
τ_c (ms)	55.5	55.5	55.5	55.5	55.5

Table 3. Resistance, inductances and time constant in each section
for three-power-supply (A-B-C) system

parameter \ section	group (1) 5 sections of 27-m-section	group (2) 7 sections of 39-m-section	group (3) 7 sections of 54-m-section	group (4) 7 sections of 57-m-section	group (5) 7 sections of 45-m-section
R (Ω)	0.1058	0.1529	0.2117	0.2234	0.1764
$L - M_2 + M_4$ (mH)	5.904	8.528	11.808	12.464	9.840
$M_5 + M_6$ (mH)	0.0544	0.0785	0.1087	0.1148	0.0906
τ_c (ms)	55.5	55.5	55.5	55.5	55.5

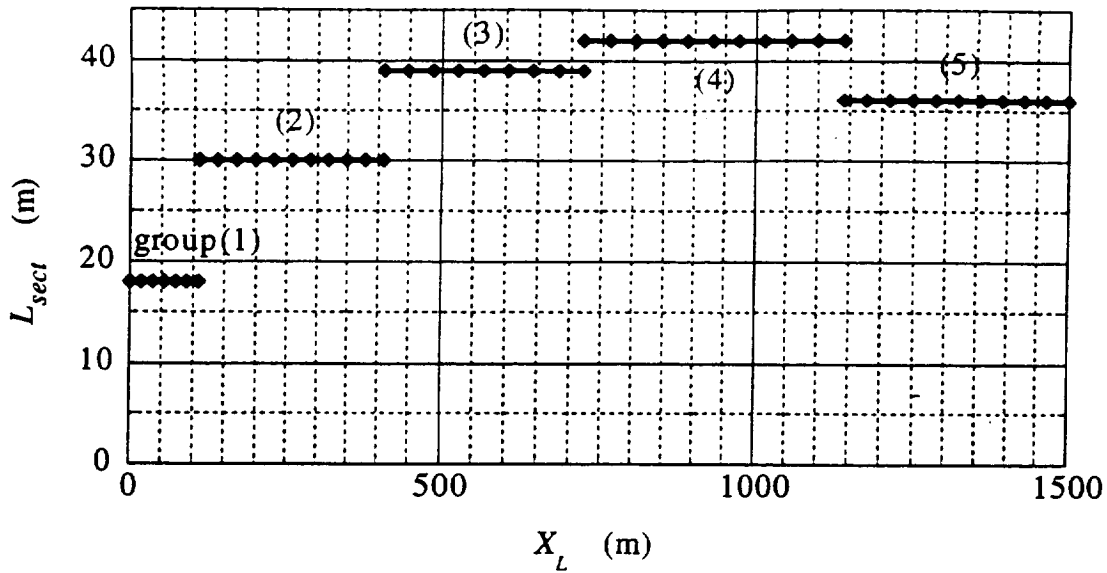


Figure 3. The 44 sections divided into five groups along the guideway

NUMERICAL EXPERIMENTS

The superconducting LSM rocket launcher system (see Table 4) is designed for the 1-ton rocket to attain a speed of 700 km/h at the height of 100 m above the ground. In the limited length of LSM armature guide tube, the linear launcher is controlled to meet the command acceleration pattern. It has the 6.6-s-acceleration-phase with a quick variation from zero to 4 G's for 0.5 s and 4 G's kept for 6.1 s, and the 4.67-s-deceleration-phase with a very quick variation from 4 G's to -7.5 G's for 1.3 s, -7.5 G's kept for 2.87 s and a very quick variation from -7.5 G's to zero for 0.5 s.

Table 4. Design data of superconducting LSM rocket launcher.

Guide Tube :		Total weight	15 ton
Total length	1,500 m	No. of Superconducting Magnets	60
Diameter	7 m	Superconducting Magnets per one LSM :	
LSM Armature Guide Tube :		No. of poles	15
Total length	1,500 m	Coil length	1.3 m
Inside diameter	5.0 m	Coil width	0.5 m
Outside diameter	5.1 m	MMF	700 kAT
No. of LSM Armature	4	Pole pitch	1.5 m
Coil length	0.8 m	Rocket :	
Coil width	0.6 m	Total weight	220 ton
Linear Launcher :		Clearance Gap :	
Total length	23 m	Electrical gap between coil centers	25 cm
Diameter	4.8 m	Mechanical gap	10 cm

Simulated Motions of LSM Launcher and Rocket

Figure 4 (a) and (b) show that the rocket is released from the launcher just after the peak speed at the height of 1,000 m from guideway tube bottom and launches with an initial speed of about 900 km/h. After the rocket ascends freely, receiving lateral force due to the Coriolis force in the guide tube, it flies out the LSM guide tube with a speed of about 720 km/h and then attains the command speed of 700 km/h at the height of 100 m above the ground. An instance at which the rocket is released is known from an instance for $\Delta H = 0$ in Fig. 4 (e). As shown in Fig. 4 (c), the launcher is controlled to follow very well the command acceleration pattern according to the command mechanical load-angle in Fig. 4 (f). The required armature-current and thrust force are shown in Figs. 4 (g) and (j).

Figure 4 (l) shows that the Coriolis force in the Z-direction is compensated completely using the guidance force in Fig. 4 (k) before the release point and after that the launcher itself is controlled quickly and stably in the center of the LSM guide tube. On the other hand the rocket is deflected in the reverse direction of the Z-axis, *i. e.* in the westward direction, by 3.75 cm at the flying-out point of the guide tube end. The deflection is sufficiently small compared with a mechanical clearance between the rocket and the inside coil of LSM armature, such that the rocket does not come into collision with the wall of the inside coils illustrated with shade in Fig. 4 (l). Figure 4 (l) shows that the launcher makes no motion in the Z-direction and the rocket is moved quite slowly in the westward direction due to the Coriolis force.

Electrical Dynamics Simulations

Figure 5 shows simulated results for terminal voltage, active-, reactive- and apparent-powers, power loss, efficiency and power factor per LSM for three cases of the power supply systems. They are power-supply system (PSS) (A-B), (A-B-C) and (A-B-C-D) which have two sets, three sets and four sets of inverters per LSM, respectively. Each terminal voltage per phase becomes a maximum value of 168 kV, 117kV and 93kV at a peak speed of 900 km/h, as shown in Fig. 5 (a). By using PSS (A-B-C-D) with four sets of inverters, the maximum voltage can be decreased to half value as compared with that of PSS (A-B) with two sets of inverters. The maximum active (output) power of about 1 GW is required as shown in Fig. 5 (b). Even in PSS (A-B-C-D), it is followed by the maximum power loss of 60 MW in Fig. 5 (c) and the maximum reactive power of 1.9 GVar in Fig. 5 (d) which result in the maximum apparent power of 2.4 GVA in Fig. 5 (e). However, very high efficiency of above 90 % is obtained during almost all operating phases of LSM launcher controlled by PSS (A-B-C-D), as shown in Fig. 6 (a). Power factor is also generally very high and its minimum value is above 50 % in Fig. 6 (b) especially in PSS (A-B-C-D).

According to equations (9), (10) and (11), active electric-energy E_M , power loss energy E_l and energy-efficiency η_E are calculated as shown in Table 5. Active electric-energy E_M due to active power P_o shown in Fig. 5 (b) is constant independently of three kinds of power supply systems. Its value is very small though the maximum power at the peak speed of 900 km/h is extremely high. It

is due to very short operating time of about 12 s. Power loss energy E_l is much smaller than electric-energy E_M and strongly dependent on three kinds of power supply systems as shown in Table 5, because the section-length and the armature coil resistance become smaller corresponding to PSS (A-B), (A-B-C) and (A-B-C-D). Consequently, energy-efficiency η_E is generally very high. Especially in PSS (A-B-C-D) very high value of 95 % is obtained.

Table 5. Active electric-energy, Power loss energy and energy-efficiency for three kinds of PSS

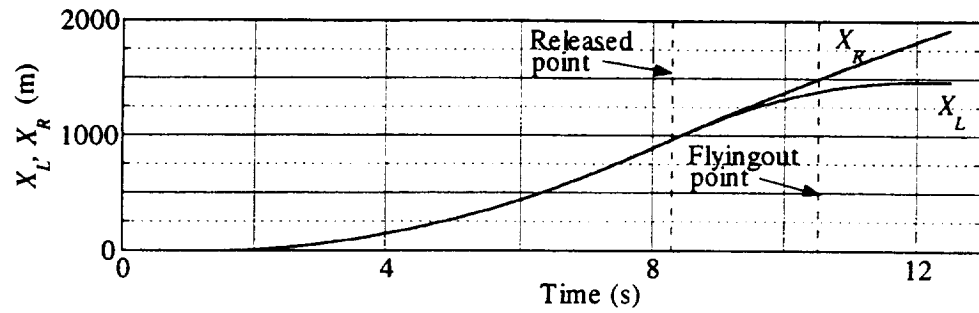
energy \ PSS	(A-B)	(A-B-C)	(A-B-C-D)
E_M (kWh)	929.45	929.45	929.45
E_l (kWh)	98.47	66.29	48.95
η_E (%)	90.42	93.34	94.99

CONCLUSIONS

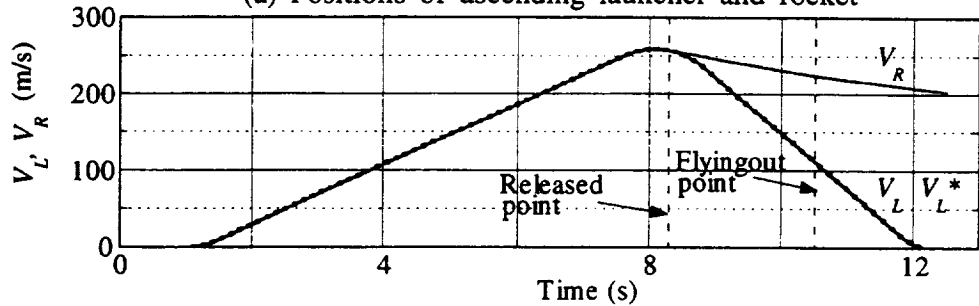
A vertical type superconducting LSM rocket launcher system under the ground which is operated in an attractive-mode is proposed to apply to full-size H-II rocket with the first acceleration rocket eliminated. To reduce maximum terminal phase-voltage and maximum reactive power and to improve efficiency and power factor, three kinds of power-supply systems with two sets, three sets and four sets of inverters are designed and evaluated for feasibility study.

The following results are obtained from the simulation study :

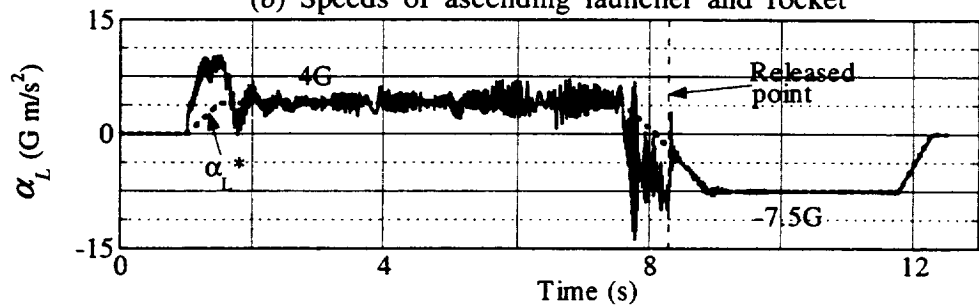
- (1) The novel armature-current control method proposed previously by us was successfully applied in an attractive-mode operation for the 15-ton-launcher with 220-ton-rocket to meet the 4 G acceleration pattern and for the launcher without the released rocket to meet 7.5 G deceleration pattern. The launcher is controlled quite stably with no deflection in the center of the guide shaft with compensating for the Coriolis's force as a lateral disturbance force.
- (2) Even when the designed power-supply (A-B-C-D) system with four sets of inverters is used and electric characteristics are improved to a large extent, the maximum terminal phase-voltage is about 90 kV, the maximum active (output) power about 1 GW, the maximum power loss 60 MW, the maximum reactive power 1.9 Gvar and the maximum apparent power 2.4 GVA for each LSM.
- (3) But efficiency is generally very high and power factor is also above 50 %. Active electric-energy is only 930 kWh, electric loss energy is only about 49 kWh which is about 5 % as compared with electric-energy, and very high energy-efficiency of 95 % is obtained.
- (4) The LSM rocket launcher system requires very high initial cost but relatively low operating cost. The launcher system is feasible technically.



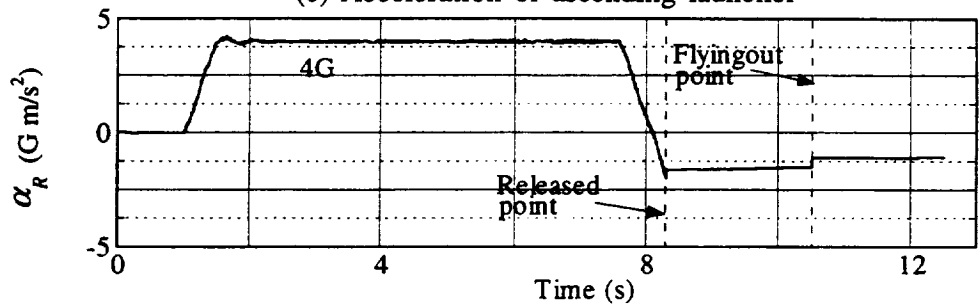
(a) Positions of ascending launcher and rocket



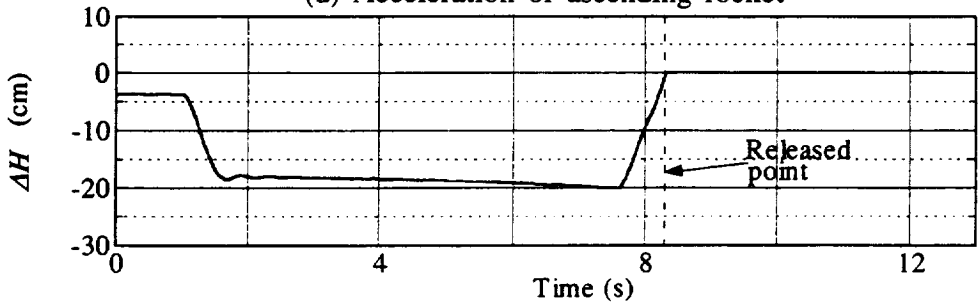
(b) Speeds of ascending launcher and rocket



(c) Acceleration of ascending launcher

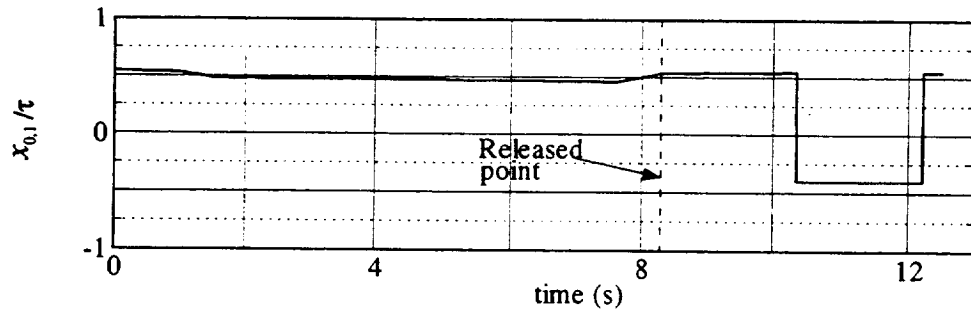


(d) Acceleration of ascending rocket

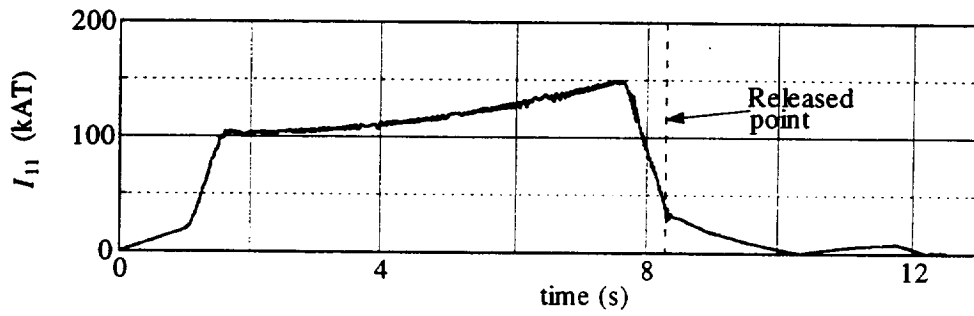


(e) Relative height between launcher and rocket

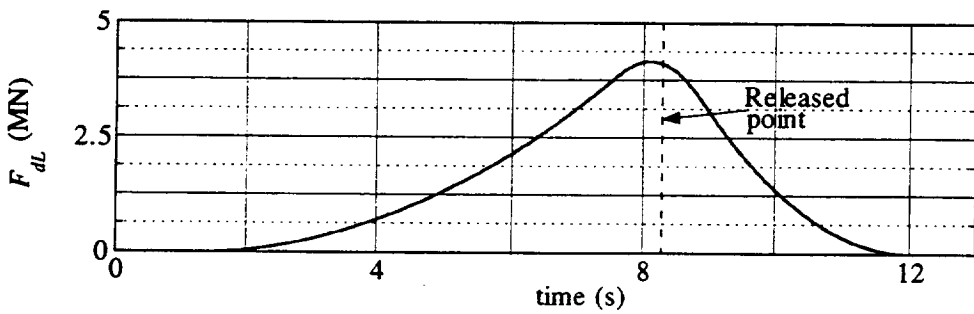
Figure 4. Ascending motion of LSM rocket launcher



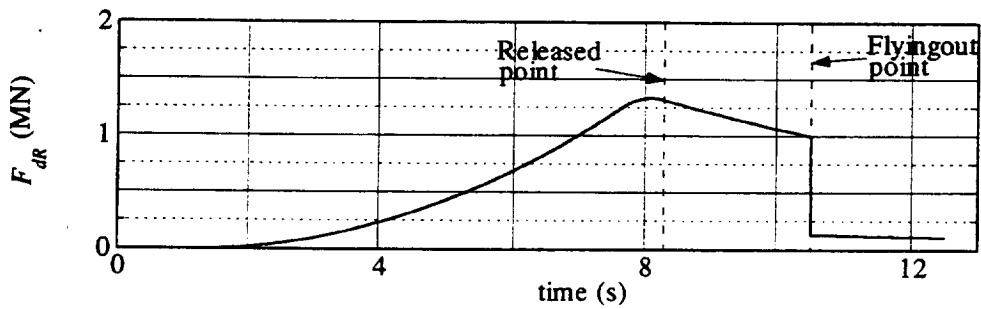
(f) Mechanical load-angle of inside armature winding



(g) Current of inside armature-winding in LSM ①

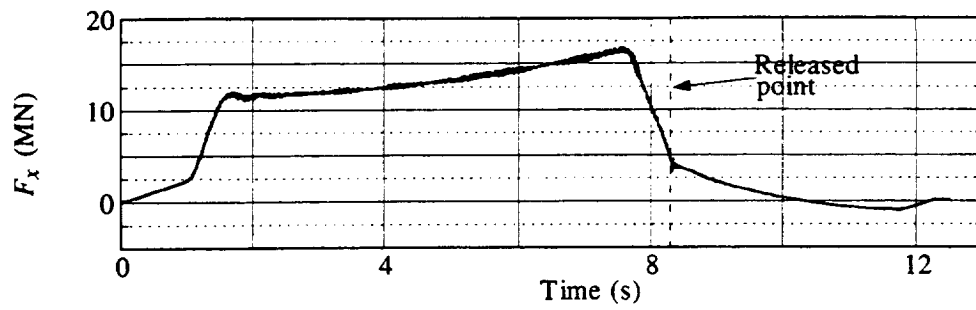


(h) Aerodynamic drag acting on launcher

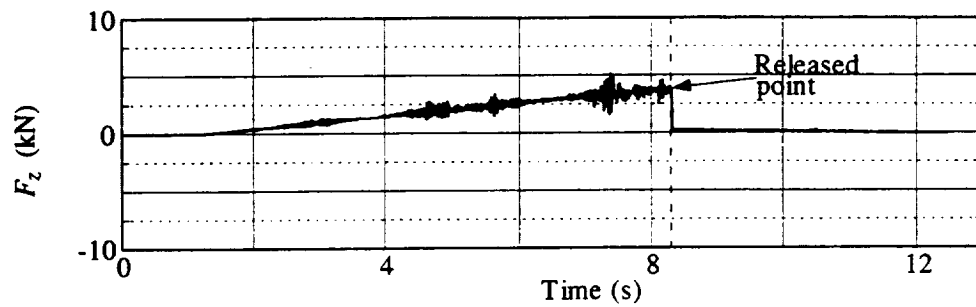


(i) Aerodynamic drag acting on rocket

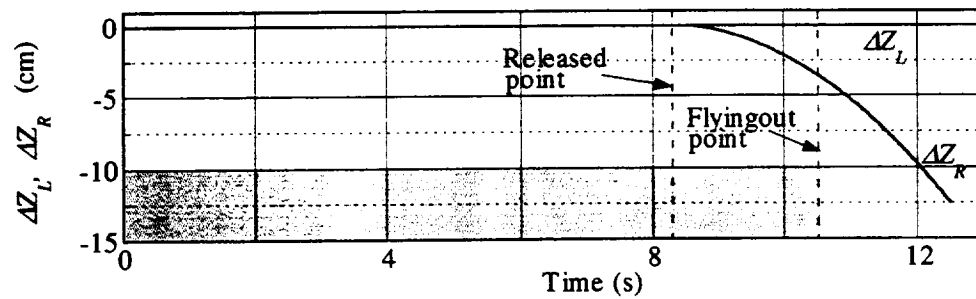
Figure 4. Ascending motion of LSM rocket launcher



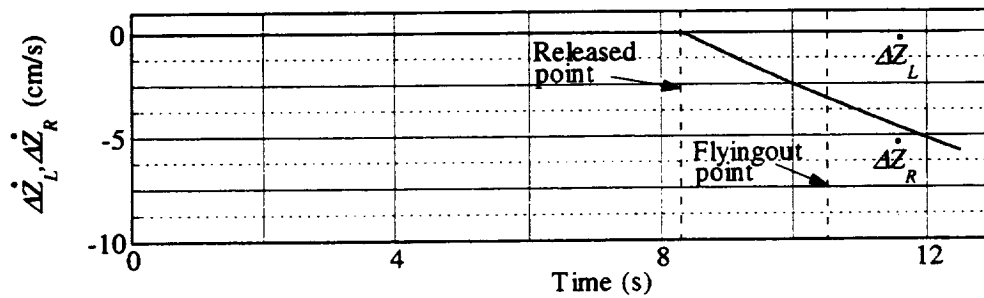
(j) Total thrust force in the X-direction



(k) Total guidance force in the Z-direction

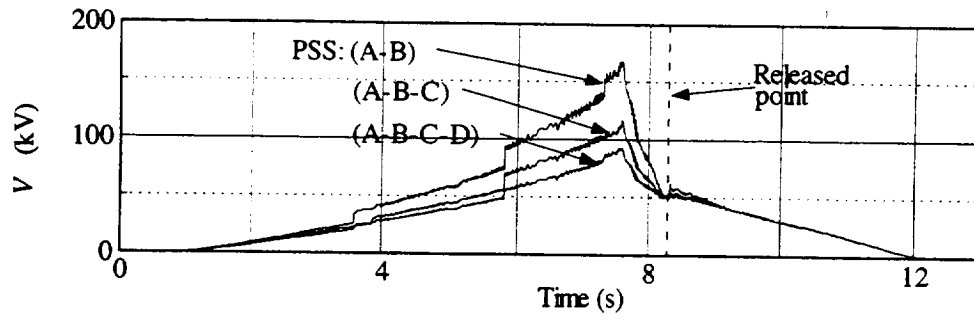


(l) Laucher and rocket deflections in the Z-direction

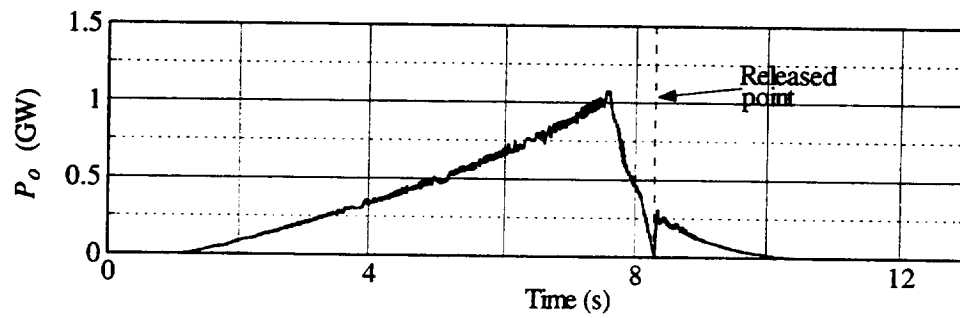


(m) Laucher and rocket speeds in the Z-direction

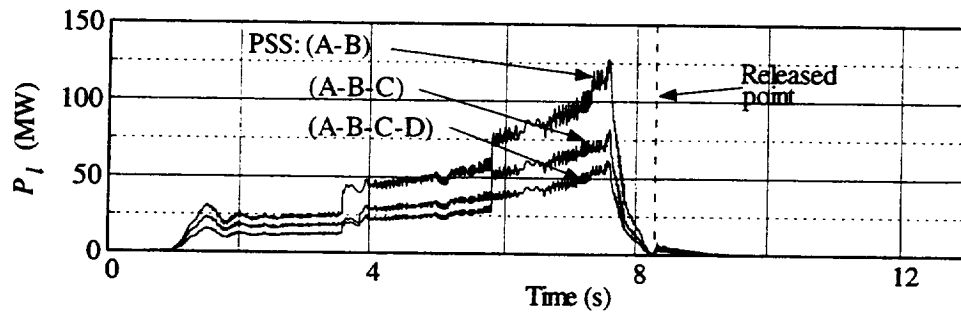
Figure 4. Ascending motion of LSM rocket launcher (cont.)



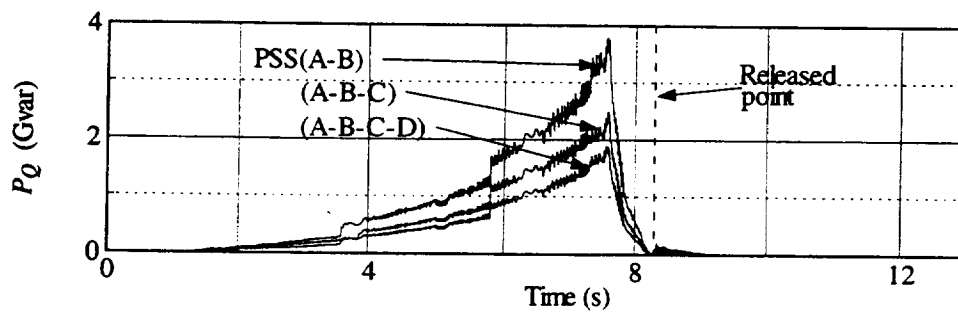
(a) Terminal voltage per phase



(b) Active power



(c) Power loss



(d) Reactive power

Figure 4. Ascending motion of LSM rocket launcher (cont.)

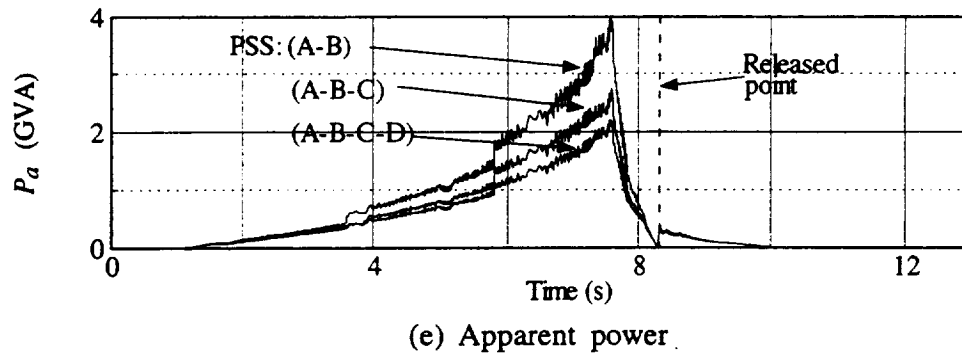


Figure 5. Terminal voltage and electric powers in three kinds of power supplies

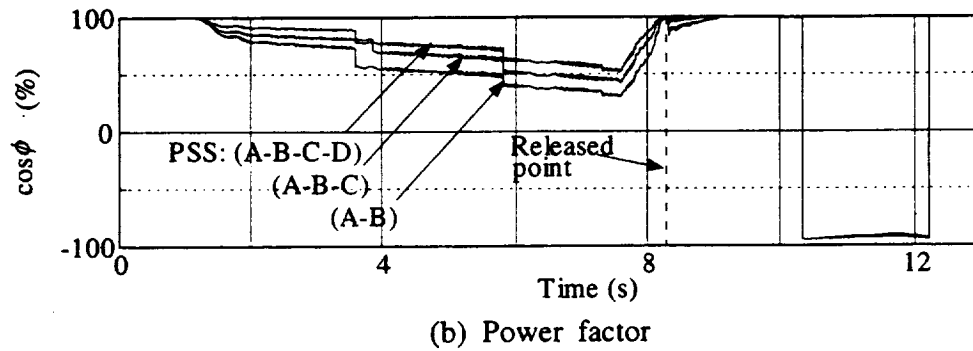
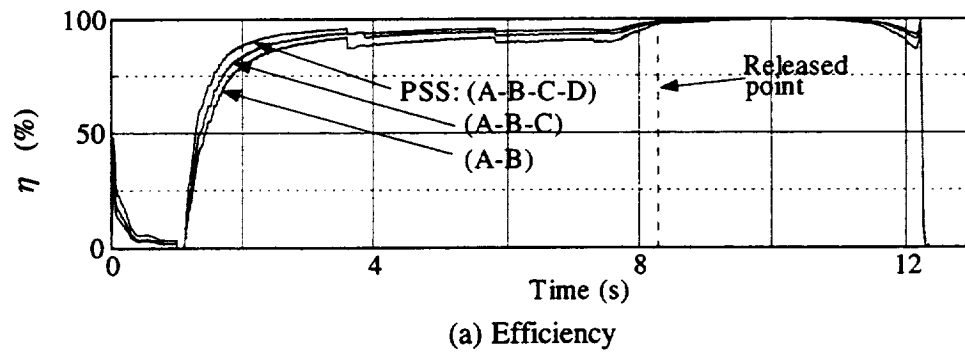


Figure 6. Efficiency and power factor for three kinds of power supplies

ACKNOWLEDGEMENTS

The authors gratefully acknowledge Mr. Yuji Asoh for his great help in making this paper.

REFERENCES

1. K. Yoshida, K. Hayashi and H. Takami : Electromechanical Dynamics of Superconducting LSM Rocket Launcher System in Attractive-Mode, NASA Conference Publication 3336 Part 2, July 1994, pp. 623 - 638
2. K. Yoshida, T. Ohashi, K. Shiraishi and H. Takami : Feasibility Study of Superconducting LSM Rocket Launcher System, NASA Conference Publication 3247 Part 2, May 1994, pp. 607 - 621
3. K. Yoshida, T. Ohashi, K. Shiraishi and H. Takami : Dynamics Simulations of Superconducting LSM Rocket Launcher System, J. of Space Tech. and Science, Vol.9 No.2, Autumn 1993, pp. 13 - 28
4. K. Yoshida, A. Kunihiro and T. Ohhashi : Superconducting LSM Dynamics in Ground - Based Zero - Gravity Facility, Proc. of Inter. Conf. on the Evolution and Modern Aspects of Synchronous Machines, Zurich, Aug. 1991, Part 3, pp. 797 - 802

THE NASA INDUCTRACK MODEL ROCKET LAUNCHER AT THE LAWRENCE LIVERMORE NATIONAL LABORATORY*

L. S. Tung, R. F. Post, E. Cook, and J. Martinez-Frias
Lawrence Livermore National Laboratory, Livermore, California

SUMMARY

The Inductrack magnetic levitation system, developed at the Lawrence Livermore National Laboratory, is being studied for its possible use for launching rockets. Under NASA sponsorship, a small model system is being constructed at the Laboratory to pursue key technical aspects of this proposed application. The Inductrack is a passive magnetic levitation system employing special arrays of high-field permanent magnets (Halbach arrays) on the levitating carrier, moving above a "track" consisting of a close-packed array of shorted coils with which are interleaved with special drive coils. Halbach arrays produce a strong spatially periodic magnetic field on the front surface of the arrays, while canceling the field on their back surface. Relative motion between the Halbach arrays and the track coils induces currents in those coils. These currents levitate the carrier cart by interacting with the horizontal component of the magnetic field. Pulsed currents in the drive coils, synchronized with the motion of the carrier, interact with the vertical component of the magnetic field to provide acceleration forces. Motional stability, including resistance to both vertical and lateral aerodynamic forces, is provided by having Halbach arrays that interact with both the upper and the lower sides of the track coils. In its completed form the model system that is under construction will have a track approximately 100 meters in length along which the carrier cart will be propelled up to peak speeds of Mach 0.4 to 0.5 before being decelerated. Preliminary studies of the parameters of a full-scale system have also been made. These studies address the problems of scale-up, including means to simplify the track construction and to reduce the cost of the pulsed-power systems needed for propulsion.

* Work performed under the auspices of the U. S. Department of Energy by the Lawrence Livermore National Laboratory under Contract W-7405-ENG-48

INTRODUCTION

The Inductrack concept uses passive magnetic levitation that is generated when a moving object holding an array of permanent magnets moves over shorted loops of wire embedded in a stationary track (ref. 1). The interaction of the magnetic field moving over the wires induces currents in the wire. Above a critical speed, the induced current interacts with the magnetic field to generate a repulsive force that levitates the object above the track. There are many potential applications of this concept that range from magnetic bearings in motors to levitating a cradle that carries a payload or a trainload of people. In particular, under NASA sponsorship at Lawrence Livermore National Laboratory, we are building a prototype to demonstrate the feasibility of this concept for initiating rocket launches. At this phase of the project, our goal is to demonstrate acceleration in excess of 10g's with stable levitation. (The high acceleration – higher than would be needed for magnetic launching – is dictated by our need to limit the track length and costs.)

The basic concept of passive magnetic levitation has already been demonstrated at LLNL (ref. 2). In that experiment, a 20-kg cart was accelerated (at about 1 g) to 12 m/s, a speed which was about 6 times greater than the critical speed needed for levitation. Following initial acceleration, the cradle entered the region of shorted coils, levitated, and coasted to a stop on its auxiliary wheels at the end of the 20-m track. Except for initial transients, which damped out in flight, the cradle behaved stably.

THEORY

Levitation

The Inductrack concept for passive magnetic levitation uses a special configuration of high strength permanent magnets. This configuration, called a Halbach array, has an array of permanent magnets with a direction of magnetization that is rotated by 90° with respect to adjacent magnets (ref. 3). Figure 1 shows the contours of constant magnetic flux around a 5-bar array that is similar to that used in the Inductrack experiment. Without the horizontally-polarized magnets, the flux would be equal on the top and bottom.

An infinite number of bar magnets in a Halbach configuration would produce a sinusoidal variation of field at a constant distance from the bottom of the array. For the five magnets, the field parallel to the bottom of the array (B_x) and the field normal to the bottom of the array (B_y) are nearly sinusoidal in the x direction, parallel to the bottom of the array. Figure 2 shows these field profiles as generated using ANSYS (ref. 4) for our array that is 1-cm thick, 13-cm (5 bars) wide, and 12-cm long. The remanent field of these magnets, composed of NdFeB, is 1.23 T. The field is 0.26 T at 1-cm from the array surface, which is the expected levitation height above the shorted coils.

The sinusoidal variation in $B_x(x)$ and $B_y(x)$ is critical to provide the proper time-variation in magnetic field experienced by the stationary wires as the magnets move by. As the field cuts through the nearest upper conductors in the track, the time-variation in magnetic field acts as a voltage source in each closed loop of wire. The effective circuit of this wire is just an inductor L and resistor R in series so that the levitation forces can be predicted through standard circuit theory. The excitation frequency ω of the circuit is $\omega = k v$ where $k = 2 \pi / \lambda$, v is the array velocity (m/s), and λ is the array wavelength (0.1-m as

seen in figure 2). When $\omega \gg R/L$ the phase of the current is shifted 90° with respect to the voltage so that the current is in phase with the flux which maximizes the force in the $+y$ direction to provide lift and minimizes the drag force. For velocities much greater than the transition speed of

$$v_t = (\lambda R)/(2 \pi L) \text{ m/s}, \quad (1)$$

the cradle will lift off the track. For lesser velocities, the drag force, acting in the $-x$ direction, will decelerate the cradle. At a speed of v_t , the levitation and drag forces are equal.

The current I_L induced in each closed loop is a function of the flux ϕ enclosed so that

$$I_L = \phi / L = \lambda B_0 / (2 \pi L) w \exp(-2 k y_1) \sin(k x) \text{ A} \quad (2)$$

where B_0 is the theoretical surface field for a Halbach array, w = length of the excited wire and y_1 = gap between the array and wire. This surface field, as given by Halbach, is

$$B_0 = B_r (1 - \exp(-k d)) \sin(\pi / M) / (\pi / M) \text{ T} \quad (3)$$

where d = array thickness and M = the number of magnets per wavelength (4 in the present case). The levitating force, averaged over x , is produced when the induced current is crossed with B_x so that the average levitating force per closed loop is

$$\langle F_y \rangle = \langle B_x(x) w I_L \rangle \text{ N}. \quad (4)$$

The theory and assumptions behind equations 1-4 can be found in other articles (refs. 1, 2).

Acceleration

Acceleration is provided to the cradle through the use of an impulsive current provided to drive coils that turn on when the peak of the B_y field is present (refer to figure 2). Because the drive loop generates a local field that could affect the induced current in the nearby levitation coils, there is also a flux-canceling coil that is co-planar with the drive coil. The wire layout is configured so that the return path for current is far from the magnets yet creates a flux pattern that yields a zero net flux in the adjacent circuits.

The peak value of acceleration can be estimated from the peak strength of B_y so that

$$B_{y,max} = B_0 \exp(-k (y + d/2)) \text{ T} \quad (5)$$

where d_c is the conductor thickness. Then the peak force F_x , dependent on the drive current I_D is given by

$$F_x = B_{y,max} w I_D \quad N. \quad (6)$$

Experiment

Mechanical

In the present phase of development, the Inductrack test track is 30-m long. Mechanical acceleration, e.g. a compressed air cylinder, will be used to launch the cradle. This should provide acceleration to 10 m/s within the first meter. Mechanical acceleration is considerably less expensive than electrical drive during this launch phase. The next 16 meters is the acceleration/levitation section of track. Here the drive coils are interleaved with the levitation coils every 5 cm. The levitation coils are 1-cm wide and the levitation coils are 4-cm wide. The remaining track length has a non-magnetic stainless steel sheet that provides deceleration caused by the eddy currents in the conducting sheet that are generated when the magnets move by.

The cradle, pictured in figure 3, is composed of carbon-fiber composite material and has a length of 64 cm. A 3d ANSYS (ref. 4) computer simulation aided in the development of this design. The analysis was used to minimize the weight yet withstand 40 g's of acceleration. It was also used to design the structure necessary to keep the cradle from "opening" due to the repulsion of the magnets away from the track and to calculate the natural frequencies of the cradle structure. The cradle has arms that extend past the track and surround the guide rails. As seen in the photo of the Inductrack model in figure 4, the C-guides on these arms are needed to prevent the track from touching the fragile magnets on the inside of the cradle prior to levitation. The cradle without the magnets weighs 3 kg.

There are three arrays of magnets on the front and three on the back of the cradle. These magnets are located next to the track inside the cradle ribs as pointed out in figures 3 and 4. The lower magnets oppose the force in the upper magnets. The upper magnets have a width of 12-cm and the lower a width of 8-cm. Because the lower magnets are at a 45° angle to the upper magnets, only 6% of the repulsive force from the top magnets balances the weight of the cradle and magnets. The remainder is used to center the cradle about the track to provide stability. The total weight of the cradle and magnets is 8.5 kg.

Electrical

Within each set of levitation coils, which are 4-cm wide, are close-packed loops of #10 wire. The perimeter of each loop is 56-cm. Each loop has a resistance of $1.5 \times 10^{-3} \Omega$ and inductance of 2.6×10^{-6} H. Applying these values to equation 1, one finds the transition speed for our levitation coils is 11 m/s. Thus mechanical acceleration produces levitation just after the first meter of track.

The NdFeB magnets with a $B_r = 1.2$ T have a thickness d of 1-cm and $M = 4$ magnets per wavelength (as seen in figure 2). According to equation 3 then the field at the surface (if the array were infinitely long) would be $B_0 = 0.52$ T. We anticipate that the cradle will levitate at $y_1 = 1$ cm above the track. We also assume that the lateral arrays will levitate at 1-cm above the track. Thus, using equation 2, one finds that the current generated in each loop by the presence of the three, moving Halbach arrays, that have a total length of $w = 12+2*8$ cm, is 570 A. The total repulsive force provided by just the top array is 1450 N. With 94% of this force contributing to stability, the remaining lifting force provided by all six arrays is 166 N. This should provide sufficient lift with some operating margin for the 8.5-kg cradle assembly.

The drive coils comprise a single turn of # 6 square insulated magnet wire. The drive coils are separated by 5-cm to align with the peaks in $B_y(x)$ seen in figure 2. Note that because $B_y(x)$ changes sign, the current pulse must also switch directions to still produce a forward force. Thus six drive coils (3 front and 3 back) are energized simultaneously to provide acceleration. A pulse of 7000 A with a fixed width of 600 micro-seconds is expected to produce a maximum cradle speed of around 50 m/s at the end of the driven section of the track. Using equations 5 and 6, one can estimate that the maximum acceleration will be about 3000 N or 36 g's. Although a variable pulse width could provide optimal acceleration in a shorter distance, this option is very expensive because of the number of high current switches required.

The drive circuitry is triggered pairs of infrared detector/emitters mounted along the track. The infrared beam sends a trigger signal when an arm attached to the cradle blocks the beam. This signal will also be used as a diagnostic to measure cradle velocity. A series inverter is used as an ac switch for each group of drive coils. When triggered, the series inverter both energizes the desired group of coils and creates the half-sine wave pulse of fixed amplitude and time. The pulse width and amplitude depend on the inductance and resistance of the coils, the capacitance of the resonant capacitor, and the dc bus voltage. The pulse width can be varied in discrete intervals along the track by changing the value of the resonant capacitor.

FUTURE

The simplest diagnostic will be that of using the trigger signal to measure velocity. We also plan to add an on-board laser to project down the track in order to measure the pitch, roll, and yaw of the cradle. If necessary vibration dampers may also be added around the C-clamps to mitigate instabilities at the slower speeds. The next phase of this project is to extend the track to 100 meters in length and achieve peak speeds of Mach 0.4 to 0.5.

ACKNOWLEDGMENTS

Contributions from William Kent -Lead technician, Dan Shimer - Electrical engineer, Ernie Schwarz - Electrical designer and scrounger, Nick Patz - Summer student analyst and cradle builder, and Brian Smith - Summer student technician are gratefully acknowledged. A special appreciation is extended to YLA of Benicia, CA who donated the materials and equipment needed to build the cradle. This work is being funded under NASA contract number # H27814D.

REFERENCES

1. R. F. Post, "Magnetic Levitation for Moving Objects," U.S. Patent No. 5,722,326.
2. Accepted for publication in the IEEE Transactions on Applied Superconductivity (Proc. of the 16th International Conf. on Magnetic Technology, Sept. 1999).
3. K. Halbach, "Application of permanent magnets in accelerators and electron storage rings," *Journal of Applied Physics*, vol. 57, p. 3605, 1985.
4. ANSYS User's Manual Revision 5.5, Vol. 1, Procedures, Swanson Analysis Systems, Inc. 1998.

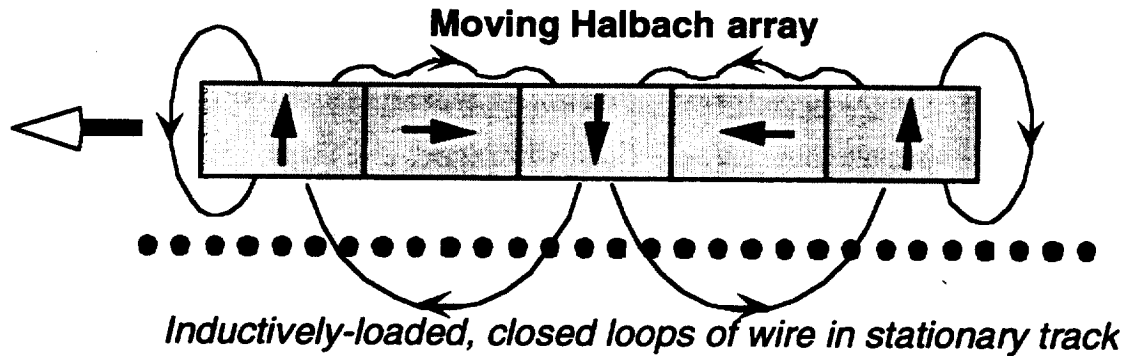


Figure 1. Sketch of passive magnetic levitation using a Halbach array of magnets. The horizontally-polarized magnets concentrate the flux on one side of the array and help to form the sinusoidal flux shape.

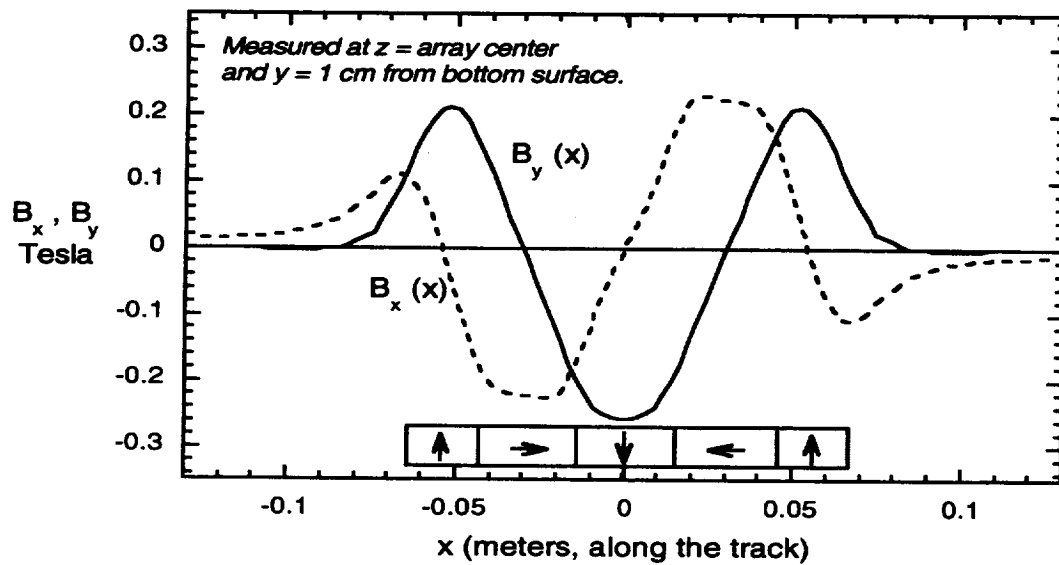


Figure 2. Variation of B_x and B_y along the track (in x) indicating the nearly sinusoidal behavior. Results are calculated from a 3d model of the Halbach array using ANSYS.

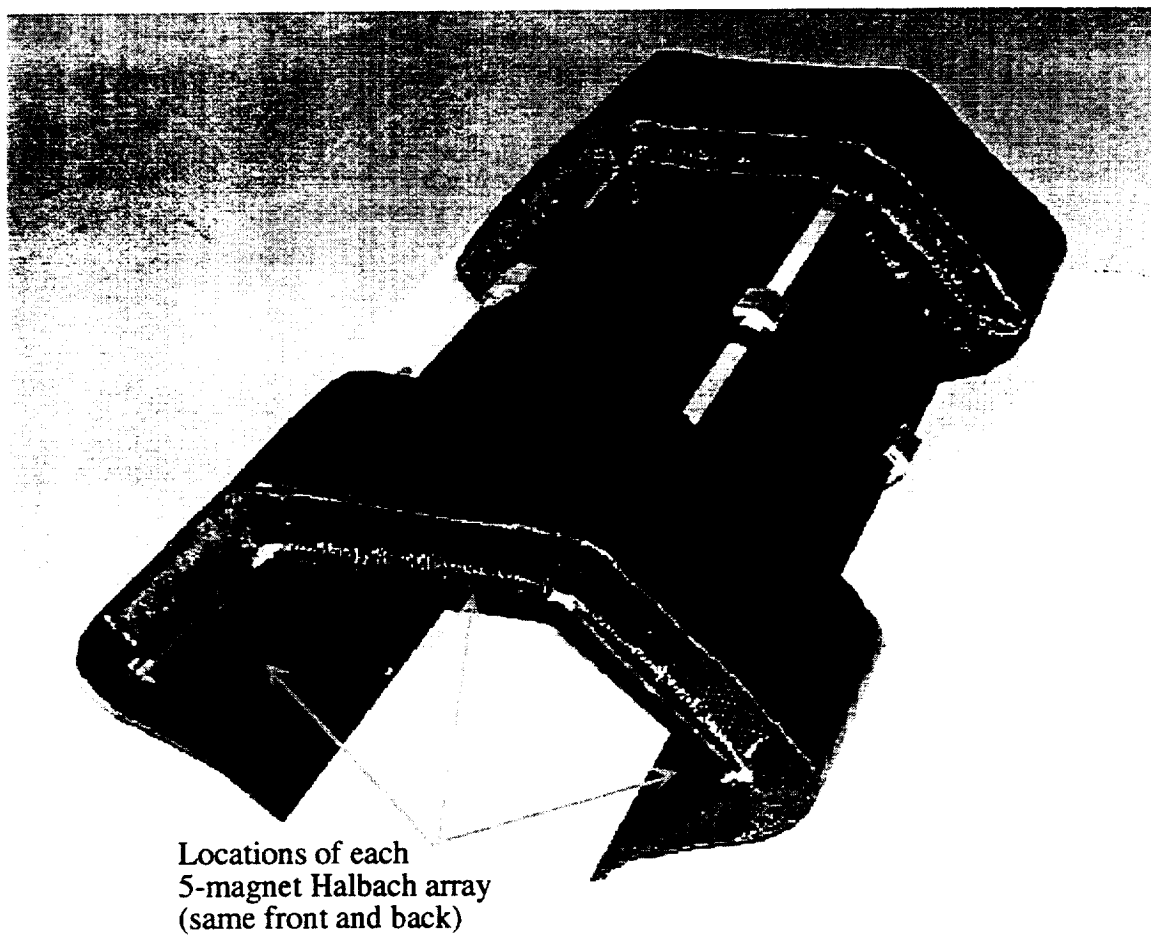


Figure 3. Photo of carbon fiber cradle (magnets not shown). The length is 64 cm.

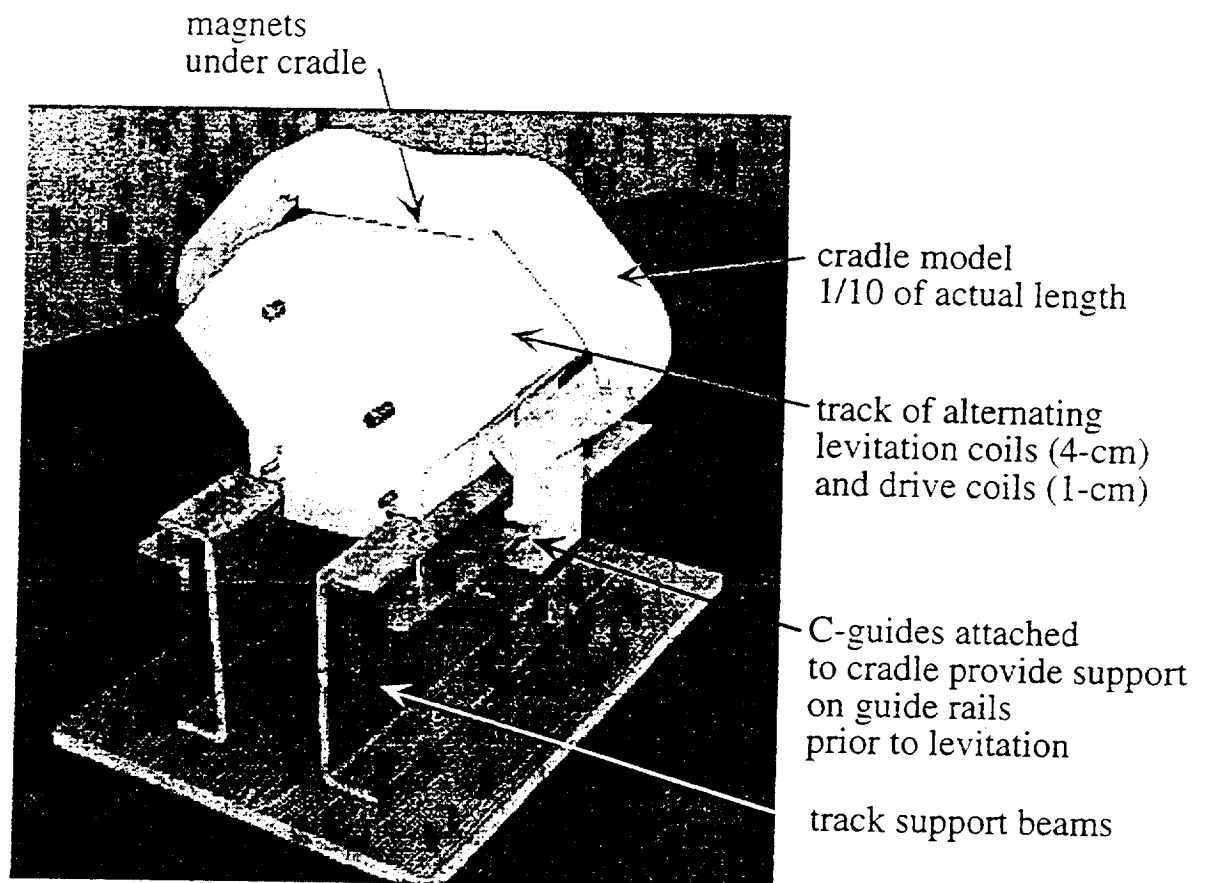


Figure 4. Photo of the model of the drive and levitation coil assembly.

Session 3 -- Controls 1

Chairman: Brad Paden
University of California at Santa Barbara (UCSB)

Feedback Linearization Applied to a MIMO Active Magnetic Bearing: A Systematic Approach and Application to a Balance Beam

Michael Baloh, Gang Tao, and Paul Allaire ^{*†}

Abstract

This paper illustrates a systematic approach to feedback linearization for a magnetic bearing system. This method relies upon the construction of a nonlinear coordinate transformation that insures a unique feedback linearization law exists which has several practical properties: the linearizing feedback is guaranteed regular; the resulting linearized system is guaranteed controllable; and beam angular position regulation is achievable. Moreover, the construction of a diffeomorphism allows the control engineer to assert operating constraints on the actuator fluxes. In particular, this paper investigates constant flux sum and constant product constraints and compares their relative merits.

1 Introduction

Magnetic bearings are nonlinear devices, but normally they are modeled using Jacobian linearization about a fixed operating point (of both position and magnetization) [6]. However, there are many instances when the bearing system must operate away from the linearization neighborhood. For example, magnetic bearings typically have large clearances and in some cases the rotor must operate reliably over the entire clearance space. A particular application where this is true is the magnetic bearing suspended impeller for an artificial heart pump, which does not have back-up bearings and must sometimes operate near the bearing clearance limit [9]. Similarly, actuator fluxes might also deviate far from nominal conditions, compromising both performance and stability. Feedback linearization avoids these problems by providing an exact linearization over the entire operating clearance of the actuator.

On the other hand, many applications require a minimum control effort, while still achieving a specified performance [3]. One objective is to keep the bias flux as low as possible to

^{*}Michael Baloh and Gang Tao are with the Electrical Engineering Department of the University of Virginia, Charlottesville, Virginia, USA. E-mail: mjb5s@Virginia.EDU and gt9s@ral.ee.virginia.edu, respectively

[†]Paul Allaire is with the Mechanical, Aerospace, and Nuclear Engineering Department of the University of Virginia, Charlottesville, Virginia, USA. E-mail: pea@virginia.edu

limit coil current induced ohmic losses. However, the flux ϕ governs the force slew rate \dot{F} of the actuator, placing restrictions on bearing performance. Mathematically,

$$\dot{F} \propto \frac{d}{dt}\phi^2 \propto \phi \frac{v}{N} \quad (1)$$

where N and v are the coil turns and voltage respectively. Therefore, with decreased bias fluxes, the actuator's dynamic capacity gradually diminishes until it is zero at the origin. Feedback linearization provides a method of constraining actuator fluxes independently of rotor position, which allows the control designer to implement low power biasing strategies.

Several works have considered solutions to the above mentioned difficulties. Levine *et. al.* [10] employed a polynomial to define the flux constraints on a magnetic bearing in order to keep the bias flux low but still avoid zero bias flux and the resulting loss of stability. Kim and Kim [14] explored the use of gain scheduled controllers over a range of actuator motion. Trumper *et. al.* [5] applied feedback linearization to the magnetic suspension of a ball with resulting improvement in tracking and stability away from the nominal operating point. A globally linearized current control law in controllability canonical form was developed which was linear with ball position and proportional to the square root of the acceleration to be applied to the mass. Mittal and Menq [15] investigated the use of a geometric feedback linearization technique about the origin for a suspended ball similar to that of [5]. They noted that their method is subject to uncertainty errors due to parameter variations and external disturbances but that these effects can be overcome with good nonlinear control design methods with resulting robust control. The conventional linearized model destabilizes under certain conditions that the feedback linearized controller can still control, such as large ball motions. Lindlau [4] investigated a feedback linearization approach to dynamic biasing. Recently, Li [12] as well as Li and Mao [13] discussed exact linearization using several different control configurations: constant voltage sum (CVS), constant current sum (CCS) and constant flux sum (CFS). They showed better tracking properties of the magnetic bearing with these control algorithms.

While several authors have discussed exact linearization, no systematic method of developing the approach has been presented in the literature for MIMO magnetic bearings to date. This paper discusses a very general special coordinate transformation developed by Nijmeijer [8] and Isidori [1] that can be used to evaluate various control strategies for magnetic bearings and applies this method to some particular magnetic bearing systems. Slotine and Li [11] discuss a similar approach. It is well known that an infinite number of transformations can be found to linearize a nonlinear system. However, a very specific one must be constructed, called a diffeomorphism, that twists the original system into a new one with specific properties: unique feedback linearization that is regular and guarantees controllability. This mathematical technique provides an unambiguous way of obtaining the coordinate transformation and a natural way of placing constraints on the actuator fluxes.

2 System Description

Figure 1 illustrates the system to be considered in this paper. Essentially, a rigid beam of moment J is simply supported at its center of mass by a pivot designated by O . At

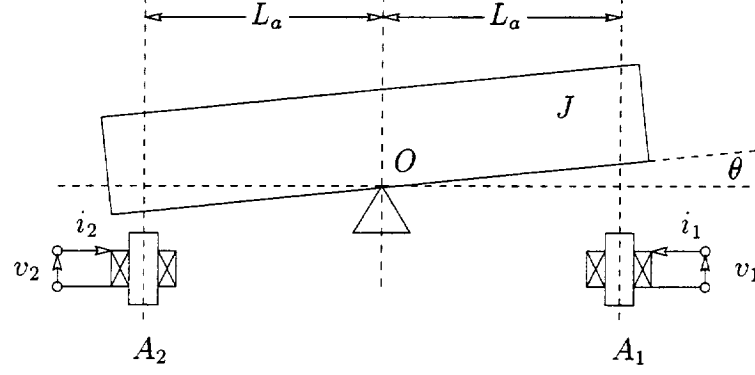


Figure 1: Symmetric balance beam with magnetic bearings.

a length L_a to either side of the pivot are horse-shoe electromagnets labeled $A1$ and $A2$, which produce forces F_1 and F_2 . Each actuator has a voltage input v_1 and v_2 and flux state variables ϕ_1 and ϕ_2 . The remaining two states of the system are the beam angle, θ , and angular velocity, $\dot{\theta}$. The system can be adequately described by the following differential equation

$$J\ddot{\theta} = \tau_m(\phi, \theta) + d(t) \quad (2)$$

where $\tau_m(\phi, \theta)$ is the magnetic actuator torque and $d(t)$ is an unknown external moment.

We now calculate the function $\tau_m(\phi, \theta)$ assuming the coil voltage as input. Begin by noting the that the flux linkage, λ , and flux, ϕ , are related by the number of wire turns, N , in the actuator coil

$$\lambda = N\phi$$

Then from Faraday's Law we have that

$$v = \frac{d\lambda}{dt} + Ri = N\frac{d\phi}{dt} + Ri \quad (3)$$

where R and i are the coil resistance and current respectively. However, Ampere's Law gives the current, i , in terms of flux ϕ , as

$$i = \frac{1}{N}\mathcal{R}(\theta)\phi$$

where the actuator reluctance, $\mathcal{R}(\theta)$, for actuators $A1$ and $A2$ is

$$\mathcal{R}_1(\theta) = \frac{2(g_0 \pm L_a\theta)}{\mu_0 A}$$

Here g_0 and A are the nominal air gap length and air gap area, respectively. When combined with Eq. (3) this gives

$$v_1 = N\frac{d\phi_1}{dt} + \frac{2R}{\mu_0 NA}(g_0 + L_a\theta)\phi_1 \quad \text{and} \quad v_2 = N\frac{d\phi_2}{dt} + \frac{2R}{\mu_0 NA}(g_0 - L_a\theta)\phi_2 \quad (4)$$

which expresses the relationship from voltage to actuator flux. A corresponding force between the stator and rotor components develops in response to the flux between them. This relationship between force and flux can be approximated by evaluating the magnetic energy present within the actuator given variations in beam displacement. Neglecting magnetic fringing and leakage the magnetic energy stored in the actuator is [2]

$$E(\theta) = \frac{1}{2} \mathcal{R}(\theta) \phi^2$$

Differentiation of the reluctance with respect to beam angle provides the force expression

$$F = -\frac{\partial E}{\partial \theta} = -\frac{1}{2} \frac{\partial \mathcal{R}}{\partial \theta} \phi^2$$

Then, given a torque arm of length L_a , the actuator torque for $A1$ and $A2$ becomes

$$\tau_2 = F_2 \cdot L_A = \mp \frac{L_a}{\mu_0 A} \phi_2^2 \cdot L_a \quad (5)$$

Finally, in state space form the nonlinear dynamic equations describing the magnetic bearing system become

$$\frac{d}{dt} \begin{Bmatrix} \phi_1 \\ \phi_2 \\ \theta \\ \dot{\theta} \end{Bmatrix} = \begin{Bmatrix} -c_2(g_0 + L_a\theta)\phi_1 \\ -c_2(g_0 - L_a\theta)\phi_2 \\ \dot{\theta} \\ c_1(\phi_2^2 - \phi_1^2) \end{Bmatrix} + \begin{Bmatrix} \frac{1}{N} \\ 0 \\ 0 \\ 0 \end{Bmatrix} v_1 + \begin{Bmatrix} 0 \\ \frac{1}{N} \\ 0 \\ 0 \end{Bmatrix} v_2 \quad (6)$$

$$\frac{dx}{dt} = f(x) + g_1 v_1 + g_2 v_2 \quad (7)$$

For convenience we have defined $c_1 = \frac{L_a^2}{J\mu_0 A}$ and $c_2 = \frac{2R}{\mu_0 N^2 A}$. This system has two inputs and at most two outputs. One output will be the beam angle $h_1 = \theta$. The other, h_2 , will not be chosen until later because its selection will profoundly affect the construction of a diffeomorphism that makes feedback linearization possible. As stated earlier the diffeomorphism twists the nonlinear system described by (7) so that its nonlinear components can be algebraically canceled. Although one might construct a feedback linearization in an “ad hoc” approach there is no guarantee that the resulting linear system would be controllable and implementable. In the next section the controllability of system (7) will be investigated to prove that the system is feedback linearizable.

3 Nonlinear Controllability

This section will be to show that the system exhibits the properties of strong accessibility and feedback invariance. Conceptually, we are interested in the overlap of the input space and the state space defined by $f(x)$. If the overlap is the same dimension as the state space then some type of controllability exists for the system (7). To explore this concept further, define \mathcal{C}_0 as the smallest Lie algebra which contains g_1 and g_2 and also satisfies $[f, X] \in \mathcal{C}_0$ for all $X \in \mathcal{C}_0$. Using the above definition we generate a corresponding distribution

$$\mathcal{C}_0(x) = \text{span}\{X(x) | X \text{ vector field in } \mathcal{C}_0\}$$

In the literature, \mathcal{C}_0 is the *accessibility algebra* and C_0 the *accessibility distribution*. With these definitions we posit the following

Theorem 1 *The system (7) is said to have the property of strong accessibility from the point x_e if*

$$\dim C_0(x_e) = n$$

where n is the system order.

Readers interested in the proof of the above theorem are referred to [8]. Note that for linear systems this reduces to the Kalman Rank Condition. For the system (7), g_1 and g_2 are constant, therefore the distribution spanned by the vector fields g_1 and g_2 is trivially involutive¹. so that the accessibility distribution for the system does not contain brackets of g_1 and g_2 . Hence, the accessibility distribution for system (7) becomes

$$C_0(x_e) = \text{span} \{g_1, g_2, [f, g_1], [f, g_2], [f, [f, g_1]], [f, [f, g_2]], [f, [f, [f, g_1]]], [f, [f, [f, g_2]]], \dots\} \quad (8)$$

where the maximum *possible* dimension of C_0 is the dimension of the state space described by (7), in this case four. Examination of C_0 shows that we need only take

$$C_0(x_e) = \text{span} \{g_1, g_2, [f, g_1], [f, g_2], [f, [f, g_1]], [f, [f, g_2]]\} \quad (9)$$

to achieve a dimension of four because additional vector combinations are redundant. Given this information, we select Eq. (9) as the definition of the accessibility distribution for this particular system. Interestingly, strong accessibility vanishes when the equilibrium point of the system is chosen to be $x_e = (0, 0, 0, 0)$, which agrees with intuition based on Eq. (1). However, for an equilibrium point in the open set $\mathbb{R}^4 - \mathbf{0}$, say $x_e = (\epsilon, \epsilon, 0, 0)$, $\dim C_0(x_e) = 4$ so that the system exhibits strong accessibility by Theorem 1. This suggests that the system described by (7) must have at least a very small bias flux to be controllable.

Now we may use the following theorem of Nijmeijer [8] to determine feedback linearizability.

Theorem 2 *Given the system $\dot{x} = f(x) + g_1 u_1 + g_2 u_2$ is strongly accessible in x_e and $f(x_e) = 0$ the system is feedback linearizable² if and only if the distributions*

$$D_k(x) = \text{span}\{ad_f^r g_1, \dots, ad_f^r g_2 | r = 0, \dots, k-1\}, k = 1, 2, 3, 4$$

¹A distribution G is involutive if the lie bracket $[\beta_1, \beta_2]$ of any pair of vectors fields β_1 and β_2 belonging to G is a vector field belonging to G . Mathematically,

$$\beta_1 \in G, \beta_2 \in G \Rightarrow [\beta_1, \beta_2] \in G$$

²Briefly, $\dot{x} = f(x) + g(x)v$ is feedback linearizable if the following statements are true:

- (i) a diffeomorphism, $z = \Phi(x)$ is defined around x_e
- (ii) regular feedback is defined

such that the nonlinear system $\dot{x} = f(x) + g(x)v$ can be written in the form $\dot{z} = Az + Bu$

are involutive and of constant dimension in the neighborhood x_e ³. Furthermore, the resulting linear system is controllable.

In the case of system (7), the distributions are in fact all involutive, thus satisfying the first condition of Theorem 2. The next condition is that the dimensions of these distributions are constant (i.e. feedback invariant). This test is performed by evaluating the dimension of the distributions at x and at $x + \delta$, where δ is a state perturbation. Performing this test shows the distributions D_1, D_2, D_3, D_4 have invariant dimensions 2, 3, 4, 4 respectively, and so satisfy the second condition of Theorem 2. As with controllability, the system fails the feedback invariance criterion at an equilibrium point $x_e = (0, 0, 0, 0)$ such that the distributions D_1, D_2, D_3, D_4 have invariant dimensions 2, 3, 3, 3. This further emphasizes the ill-defined nature of the system at the origin (without bias).

4 Construction of Diffeomorphism

In the previous section system (7) was shown to be feedback linearizable. Consequently, a coordinate transformation $z = \Phi(x)$ exists such that its application will twist the original system into Byrnes-Isidori normal form. Here $\Phi(x)$ represents a function in \mathbb{R}^n and is called a *global diffeomorphism* when the following conditions are satisfied:

- (i) $\Phi^{-1}(z)$ exists such that $\Phi^{-1}(\Phi(x)) = x$ (invertible)
- (ii) $\Phi(x)$ and $\Phi^{-1}(z)$ both have continuous partial derivatives of any order (smooth mappings).

Application of the diffeomorphism to the description of the nonlinear system can be calculated as

$$\begin{aligned}\dot{z} &= \hat{f}(z) + \hat{g}(z)v \\ y &= \hat{h}(z)\end{aligned}$$

where

$$\hat{f}(z) = \left. \frac{d\Phi}{dx} f(x) \right|_{x=\Phi^{-1}(z)} \quad \hat{g}(z) = \left. \frac{d\Phi}{dx} g(x) \right|_{x=\Phi^{-1}(z)} \quad \hat{h}(z) = h(x)|_{x=\Phi^{-1}(z)} \quad (10)$$

We wish to construct a diffeomorphism that twists the nonlinear system into a specific form (i.e. normal form). Let us begin by considering the normal form of the system described by Eq. (7) given relative degree $r = 3, 1$

$$\begin{aligned}\dot{z}_1 &= z_2 \\ \dot{z}_2 &= z_3 \\ \dot{z}_3 &= \beta_{11}(z)v_1 + \beta_{12}(z)v_2 + \alpha_1(z) \\ \dot{z}_4 &= \beta_{21}(z)v_1 + \beta_{22}(z)v_2 + \alpha_2(z)\end{aligned} \quad (11)$$

³A convenient shorthand notation for the k -th recursive bracketing of f with g is $ad_f^k g(x) = [f, [f, \dots [f, g] \dots]]$

Let us elaborate on each equation of system (11) beginning with the uppermost

$$\dot{z}_1 = \frac{d\Phi_1}{dt} = \frac{\partial\Phi_1}{\partial x} \frac{\partial x}{\partial t} = \frac{\partial\Phi_1}{\partial x} (f(x) + g_1(x) + g_2(x)) = z_2$$

and then set the first channel of the coordinate transformation to be the first output, mathematically

$$\Phi_1 = z_1 = h_1 \quad (12)$$

where h_1 is the first output. Then the previous equation for \dot{z}_1 becomes

$$\dot{z}_1 = L_f h_1 + L_{g_1} h_1 + L_{g_2} h_1$$

Here $L_f(\cdot)$ is the Lie derivative⁴. Now, inspection of the system (11) shows that the input should not appear in the first equation. Therefore, the following must be true

$$L_{g_1} h_1 = 0 \quad \text{and} \quad L_{g_2} h_1 = 0$$

so that

$$\dot{z}_1 = L_f h_1 = z_2 \quad (13)$$

Continuing onto the second equation of system (11) and using the fact that $z_2 = \Phi_2 = L_f h_1$ we have

$$\begin{aligned} \dot{z}_2 = \frac{d\Phi_2}{dt} = \frac{\partial\Phi_2}{\partial x} \frac{\partial x}{\partial t} &= L_f h_1 (f(x) + g_1(x) + g_2(x)) \\ &= L_f^2 h_1 + L_f L_{g_1} h_1 + L_f L_{g_2} h_1 = z_3 \end{aligned}$$

Once again, inspection of the system (11) shows that the input should not appear yet. As such

$$L_f L_{g_1} h_1 = 0 \quad \text{and} \quad L_f L_{g_2} h_1 = 0$$

then

$$\dot{z}_2 = L_f^2 h_1 = z_3 \quad (14)$$

in similar fashion \dot{z}_3 is calculated

$$\begin{aligned} \dot{z}_3 = \frac{d\Phi_3}{dt} = \frac{\partial\Phi_3}{\partial x} \frac{\partial x}{\partial t} &= L_f^3 h_1 (f(x) + g_1(x) + g_2(x)) \\ &= L_f^3 h_1 + L_f^2 L_{g_1} h_1 + L_f^2 L_{g_2} h_1 \end{aligned}$$

⁴This differential operation $L_f \lambda(x)$ is called the Lie derivative of λ along f where λ is a real-valued function and f a vector field and is calculated as

$$\langle d\lambda(x), f(x) \rangle = \frac{\partial \lambda}{\partial x} f(x) = \sum_{i=1}^n \frac{\partial \lambda}{\partial x_i} f_i(x)$$

where product of the Lie derivative is a new real-valued function.

Since the output must appear in this equation to satisfy the normal form we have that

$$L_f^2 L_{g_1} h_1 \neq 0 \quad \text{and} \quad L_f^2 L_{g_2} h_1 \neq 0$$

Having exhausted the output h_1 by this process, we proceed to calculate z_4 using the output h_2 . The results of Isidori [1] explain that if the number of differentiations before an input appears is r for each output h such that $r_1 + \dots + r_m = n$ (where there are m inputs and the system is n^{th} order), then a coordinate transformation exists that is both nonsingular and twists the nonlinear system into normal form. Thus, since the first output was differentiated three times before the input was allowed to appear, $r_1 = 3$, we desire to differentiate the second output only once before the input may appear, $r_2 = 1$. From a geometric perspective, we desire to maximize the dimension of the system manifold such that the zero dynamics sub-manifold must be 0-dimension. The zero dynamics manifold represents the “internal” dynamics of the system which for specific input and initial conditions constrains the output to be identically zero. For linear systems, the zero dynamics are those eigenvalues of the system which coincide with the zeros of the transfer function. If possible, we avoid zero dynamics by proper selection of the output. Hence we select the fourth channel of the coordinate transformation to be

$$\Phi_4 = z_4 = h_2 \tag{15}$$

and since this is the last equation of the system, the input must appear so that $r_1 + r_2 = 4 = n$

$$\dot{z}_4 = \frac{d\Phi_4}{dt} = \frac{\partial \Phi_4}{\partial x} \frac{\partial x}{\partial t} = L_f h_2 + L_{g_1} h_2 + L_{g_2} h_2$$

and thus

$$L_{g_1} h_2 \neq 0 \quad \text{and} \quad L_{g_2} h_2 \neq 0$$

Several conditions were placed on equations for \dot{z}_1 through \dot{z}_4 to ensure that the coordinate transformation results in normal form with no zero-dynamics. Summarizing

$$L_{g_j} L_f^k h_i(x) = 0 \tag{16}$$

for all $1 \leq j \leq m$, for all $1 \leq i \leq m$, and for all $k \leq r_i - 1$. In addition, the following matrix must be nonsingular:

$$\begin{bmatrix} L_{g_1} L_f^2 h_1 & L_{g_2} L_f^2 h_1 \\ L_{g_1} h_2 & L_{g_2} h_2 \end{bmatrix} \tag{17}$$

The above conditions are in fact the definition of the *relative degree* $\{r_1, r_2\}$ of this system[1].

Although the framework for building a coordinate transformation that twists the nonlinear system described by (7) has been provided by the previous analysis, i.e.

$$\begin{aligned} \Phi_1 &= h_1 \\ \Phi_2 &= L_f h_1 \\ \Phi_3 &= L_f^2 h_1 \\ \Phi_4 &= h_2 \end{aligned}$$

the outputs h_1 and h_2 have not been chosen. It is clear that the conditions (16)-(17) place restrictions on the choice of output such that normal form can be achieved. Consider the primary control objective for the system, which is that $\theta(t) \rightarrow 0$ as $t \rightarrow \infty$. As such, one output must be θ . Recall that the first output, θ , must be differentiated three times before an input appears. To satisfy the condition $r_1 + r_2 = n = 4$, we must only differentiate the second output once before the input appears. Inspection of system (7) shows that *any* smooth function $F(\phi_1, \phi_2)$ satisfies this condition. In this paper two functions for h_2 will be considered: $h_2 = (\phi_1 + \phi_2)/2$ and $h_2 = \phi_1\phi_2$. The first choice offers the possibility of controlling the nominal flux dynamically, while the second dismisses the concept of biasing altogether in favor of complimentary flux control. Either choice satisfies the conditions of relative degree imposed by conditions (16)-(17) at the equilibrium of the system, $x_e = (\epsilon, \epsilon, 0, 0)$ where $\epsilon > 0$.

5 Feedback Linearization

Having satisfied all mathematical preliminaries, we proceed to calculate the coordinate transformation for system (7) with the choice $h_2 = (\phi_1 + \phi_2)/2$. Based on Eqs. (12), (13), (14), and (15), the coordinate transformation for this system becomes

$$\begin{aligned}\Phi_1 &= h_1 = \theta \\ \Phi_2 &= L_f h_1 = \dot{\theta} \\ \Phi_3 &= L_f^2 h_1 = c_1(\phi_2^2 - \phi_1^2) \\ \Phi_4 &= h_2 = \frac{1}{2}(\phi_1 + \phi_2)\end{aligned}\tag{18}$$

where $\Phi(x) = \text{col}(\Phi_1, \Phi_2, \Phi_3, \Phi_4)$ and whose Jacobian is

$$\frac{d\Phi}{dx} = \begin{bmatrix} 0 & 0 & 1 & 0 \\ 0 & 0 & 0 & 1 \\ -2c_1\phi_1 & 2c_1\phi_2 & 0 & 0 \\ \frac{1}{2} & \frac{1}{2} & 0 & 0 \end{bmatrix}$$

Application of the chain rule gives

$$\dot{z} = \begin{bmatrix} \dot{\theta} \\ c_1\phi_2^2 - c_1\phi_1^2 \\ \frac{2c_1}{N}(\phi_2v_2 - \phi_1v_1) + 2c_1c_2((g_0 + L_a\theta)\phi_1^2 - (g_0 - L_a\theta)\phi_2^2) \\ \frac{1}{2N}(v_1 + v_2) - \frac{c_2}{2}((g_0 + L_a\theta)\phi_1 + (g_0 - L_a\theta)\phi_2) \end{bmatrix}$$

We place the above result into the form of system (11) where we define β and α as

$$\beta = \frac{1}{N} \begin{bmatrix} -2c_1\phi_1 & 2c_1\phi_2 \\ \frac{1}{2} & \frac{1}{2} \end{bmatrix} \quad \alpha = \begin{bmatrix} 2c_1c_2((g_0 + L_a\theta)\phi_1^2 - (g_0 - L_a\theta)\phi_2^2) \\ -\frac{c_2}{2}((g_0 + L_a\theta)\phi_1 + (g_0 - L_a\theta)\phi_2) \end{bmatrix}\tag{19}$$

Finally, the nonlinear system in new coordinates (11) is linearized with the feedback law

$$\begin{bmatrix} v_1 \\ v_2 \end{bmatrix} = \beta^{-1} \left(\begin{bmatrix} u_1 \\ u_2 \end{bmatrix} - \alpha \right)\tag{20}$$

where $\text{col}(u_1, u_2)$ are the new input into the linearized system and β^{-1} is

$$\beta^{-1} = \frac{N}{(\phi_1 + \phi_2)} \begin{bmatrix} -\frac{1}{2c_1} & 2\phi_2 \\ \frac{1}{2c_1} & 2\phi_1 \end{bmatrix}, \phi_1 + \phi_2 \neq 0$$

As defined, the feedback law of Eq. (20) is regular since both β^{-1} and α are smooth and always finite.

Now consider the diffeomorphism defined with outputs $h_1 = \theta$ and $h_2 = \phi_1\phi_2$. Then the bottom most channel of Eq. (18) becomes $\Phi_4 = \phi_1\phi_2$ so that Jacobian of $\Phi(x)$ is

$$\frac{d\Phi}{dx} = \begin{bmatrix} 0 & 0 & 1 & 0 \\ 0 & 0 & 0 & 1 \\ -2c_1\phi_1 & 2c_1\phi_2 & 0 & 0 \\ \phi_2 & \phi_1 & 0 & 0 \end{bmatrix}$$

Consequently,

$$\dot{z} = \begin{bmatrix} \dot{\theta} \\ c_1\phi_2^2 - c_1\phi_1^2 \\ \frac{2c_1}{N}(\phi_2v_2 - \phi_1v_1) + 2c_1c_2((g_0 + L_a\theta)\phi_1^2 - (g_0 - L_a\theta)\phi_2^2) \\ -2c_2g_0\phi_1\phi_2 + \frac{1}{N}(\phi_2v_1 + \phi_1v_2) \end{bmatrix}$$

which when placed in the form of system (11) gives β and α as

$$\beta = \frac{1}{N} \begin{bmatrix} -2c_1\phi_1 & 2c_1\phi_2 \\ \phi_2 & \phi_1 \end{bmatrix} \quad \alpha = \begin{bmatrix} 2c_1c_2((g_0 + L_a\theta)\phi_1^2 - (g_0 - L_a\theta)\phi_2^2) \\ -2c_2g_0\phi_1\phi_2 \end{bmatrix} \quad (21)$$

Like the previous linearization, the well behaved form of β^{-1} and α implies regular feedback.

$$\beta^{-1} = \frac{N}{(\phi_1^2 + \phi_2^2)} \begin{bmatrix} -\frac{\phi_1}{2c_1} & \phi_2 \\ \frac{\phi_2}{2c_1} & \phi_1 \end{bmatrix}$$

Regardless of the choice of outputs h_2 , the feedback linearization results in the linear system of the general form

$$\begin{aligned} \begin{bmatrix} \dot{z}_1 \\ \dot{z}_2 \\ \dot{z}_3 \\ \dot{z}_4 \end{bmatrix} &= \begin{bmatrix} \begin{bmatrix} 0 & 1 & 0 \\ 0 & 0 & 1 \\ 0 & 0 & 0 \end{bmatrix} & \begin{bmatrix} 0 \\ 0 \\ 0 \\ 0 \end{bmatrix} \\ \begin{bmatrix} 0 & 0 & 0 \\ 0 & 0 & 0 \end{bmatrix} & [0] \end{bmatrix} \begin{bmatrix} z_1 \\ z_2 \\ z_3 \\ z_4 \end{bmatrix} + \begin{bmatrix} 0 & 0 \\ 0 & 0 \\ 1 & 0 \\ 0 & 1 \end{bmatrix} \begin{bmatrix} u_1 \\ u_2 \end{bmatrix} \\ &= Az + Bu \end{aligned} \quad (22)$$

where the linearized system decomposes into two subsystems, the top left of A into a 3×3 system and the bottom right of A into a 1×1 system. For the first subsystem, the equations simplify to

$$\ddot{z}_1 = \ddot{\theta} = u_1$$

while the second subsystem becomes

$$\dot{z}_4 = \dot{\phi}_1 + \dot{\phi}_2 = u_2$$

This implies that the first input can be used to control the beam angle, θ , while the second input can be used to constrain the actuator fluxes independently of one another.

The flux constraint we use has serious repercussions on the total power consumption of the magnetic bearing system. Consider the flux constraint $h_2 = (\phi_1 + \phi_2)/2 = r(t)$, where $r(t)$ is a “dynamic bias” reference signal. The ability to alter the bias flux to achieve better performance is highly desirable for two reasons. First, the bias flux is proportional to bias current, greatly affecting I^2R losses. Second, the force slew capacity of the actuator is directly proportional to the bias flux. Thus, a small bias can be selected during low disturbance periods and a higher bias during greater disturbance periods, thus limiting power losses while maintaining actuator dynamic capacity. Unfortunately, the process of selecting the bias reference trajectory, $r(t)$, doesn’t appear to be simple and will require an entirely new layer of control artifice.

On the other hand, the flux constraint $h_2 = \phi_1\phi_2 = \epsilon$, where ϵ is a small constant alluded to in Section 3, discards this problem altogether. With this constraint the flux trajectory behaves parabolically so that both fluxes always have the same sign, while the actuators react nearly complementarily providing an almost optimal suspension depending on the choice of ϵ . More precisely, the value of ϵ is dictated by dynamic requirements and hardware limitations. For instance the maximum flux density allowed in either actuator is related to magnetic saturation of the iron core of the actuators B_{sat} . On the other hand, the minimum flux allowed must be such that actuator slew capacity is sufficient. Therefore, ϵ must be selected based on hardware limitations. This can be summarized mathematically as

$$\epsilon \geq \phi_{max}\phi_{min} = \left(\frac{\phi_{max}}{A}\right) \left(\frac{NA}{2c_1V_{ps}}\right) \dot{F}_{min} = B_{sat}\dot{F}_{min} \left(\frac{NA}{2c_1V_{ps}}\right) > 0 \quad (23)$$

Here \dot{F}_{min} is the minimum slew rate allowed based on a knowledge of the possible disturbance $d(t)$ (See Eq. (2)), and V_{ps} is the power supply voltage of the amplifiers and represents the maximum voltage available for control. Note, since $\epsilon > 0$, we conveniently avoid the origin (i.e. uncontrollability) automatically.

6 Simulation

The purpose of this simulation is to ascertain the performance of the feedback linearization in a realistic manner. First, we acknowledge that the flux, ϕ , is not directly available for measurement, but instead must be estimated in some way. Therefore it seems necessary to first simulate the system in terms of current and displacement, then to use that information to construct a feedback linearized system. From these “measurements”, gap fluxes are estimated and then used to build the linearized feedback of Eqs. (20) and (22). For instance, under ideal circumstances the flux can be derived as

$$\phi_1 = \frac{\mu_0 AN i_1(\phi_1, \theta)}{2(g_0 + L_a \theta)}, \quad \phi_2 = \frac{\mu_0 Aa Ni_2(\phi_2, \theta)}{2(g_0 - L_a \theta)} \quad (24)$$

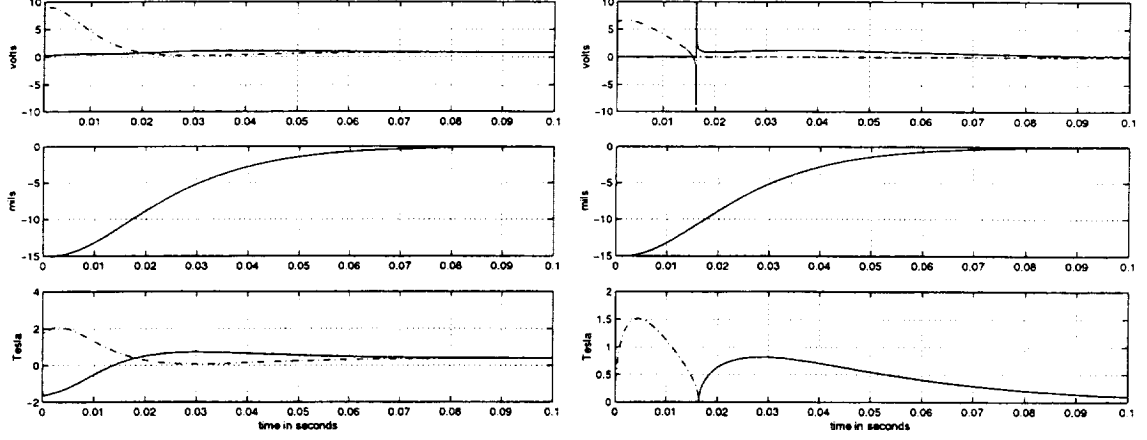


Figure 2: Startup of beam with $h_2 = (\phi_1 + \phi_2)/2$, (left), and $h_2 = \phi_1\phi_2$, (right) with $A1(-)$ and $A2(-)$

where the coil currents $i_{1,2}$ and beam angle θ are available experimentally. In practice, estimating ϕ is not very simple (Keith [7]).

The system as described has been simulated for both outputs, h_2 , described in this paper. In each case, a pole placement controller with identical feedback gains was used to stabilize the linear system. For the linearized system with $h_2 = 1/2(\phi_1 + \phi_2)$, the bias flux was set at a constant of $r(t) = 0.4T$, although, a dynamic bias might just as well have been used. For the linearized system with output $h_2 = \phi_1\phi_2$, ϵ was selected using Eq. (23) such that the steady state flux density is about $0.01T$ ($\epsilon = 10^{-4}$) for each actuator. This choice insures that at *all times* the actuators provide sufficient slew rate to react to any possible disturbances.

Figure (2) shows a startup sequence for the beam system with initial conditions of zero voltage, current, and flux, but leaning against actuator $A1$. The mechanical response of the system was independent of the output employed. Even so, the system with bias required greater startup flux and voltages than the system with constant product. Also, the startup flux for the biased case crosses the 0-axis which **tends** to destabilize the beam since $F \propto \phi^2$. Any dynamic biasing system must avoid this situation. Please note that the flux trajectories for the system with output $h_2 = \phi_1\phi_2$ are at times obscured by the zero axis even though they are slightly positive. Also, note that Eq. (23) guarantees slew performance during these periods. Figure (3) illustrates the system with initial conditions all zero, but with a sinusoidal disturbance torque, $d(t)$, of amplitude 0.8N-m and frequency 2Hz. Again, the mechanical performance in either case was nearly identical. The difference rests with the voltage and flux used to achieve that performance. For instance, the net RMS flux for the biased system was $0.4 \times 2 = 0.8T$ while for the unbiased system the net RMS was about $0.32T$. Lastly, Figure (4) shows the actuators fluxes plotted against one another for both biased and unbiased systems. The fluxes begin at the origin at startup and quickly approach their desired trajectories where they remain indefinitely.

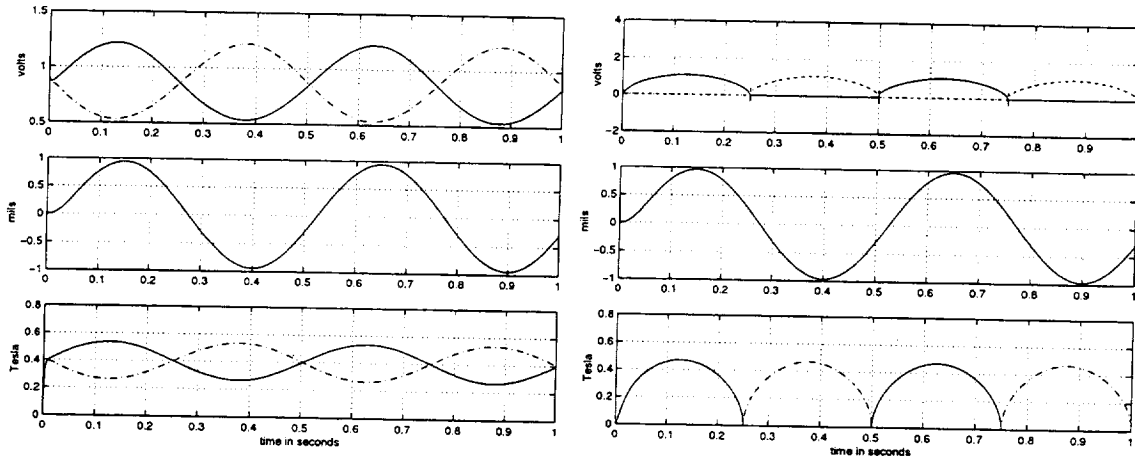


Figure 3: Sinusoidal disturbance for beam with $h_2 = (\phi_1 + \phi_2)/2$, (left), and $h_2 = \phi_1\phi_2$, (right) with $A1(-)$ and $A2(-)$

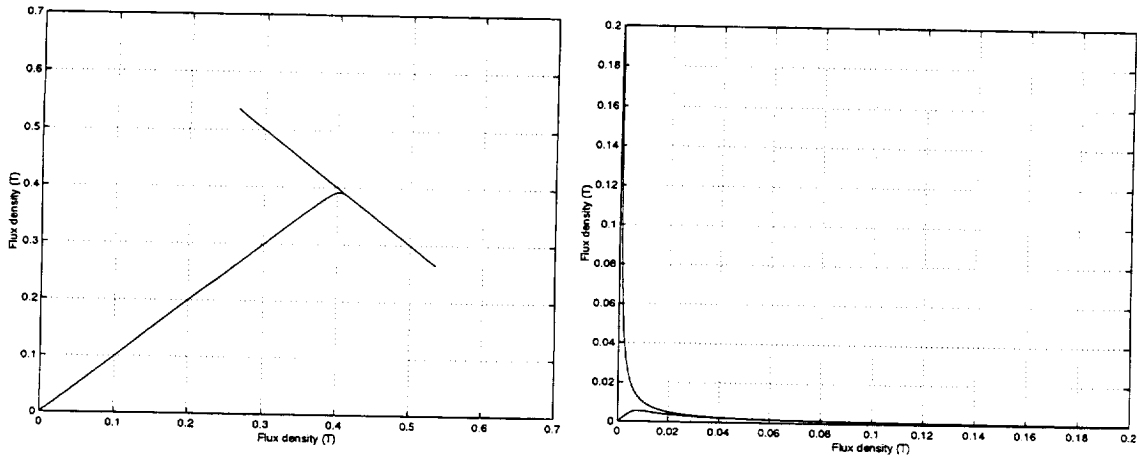


Figure 4: Flux trajectory for beam with $h_2 = (\phi_1 + \phi_2)/2$, (left), and $h_2 = \phi_1\phi_2$, (right) with $A1(-)$ and $A2(-)$

7 Conclusions

In this paper a systematic and formal mathematical procedure was used to feedback linearize a magnetic bearing system. This procedure is a direct application of the methods illustrated by Isidori [1] and Nijmeijer [8]. Consequently, the resulting linearization had three favorable properties:

- (i) linearizing feedback was smooth and finite, i.e. regular;
- (ii) the resulting system was controllable; and
- (iii) beam angular position and flux regulation achievable.

The generality of the method allows it to be applied to almost any magnetic bearing system. As an additional benefit of the linearization, beam and flux control were decoupled. Specifically, the system decoupled into a third and first order system governing the beam angle and actuator flux respectively (Eq. 22). For the output $h_2 = (\phi_1 + \phi_2)/2$ a dynamic bias was possible. However, there are many difficulties in choosing the trajectory of a dynamic bias: what signals are to be measured to determine reference and do they exist? If these signals are available, how are they processed? how do we optimize the bias trajectory while avoiding slew deprivation? In other words, how do we specify the behavior of the second output h_2 ? Thus, several barriers must be overcome before dynamic biasing becomes practical. Perhaps, the problem of dynamic biasing is not well posed. Ultimately, our goal is not to achieve dynamic biasing, but instead to achieve some sense of optimization regarding the use of force. If we minimize net force, power losses will necessarily be minimized, motivating the choice of output $h_2 = \phi_1\phi_2$. Constant flux product becomes more appealing since the reference value ϵ can be chosen based on well known actuator properties and the dynamic requirements of the plant.

Future work will consider the application of linear optimal control theory to the linearized system. However, it will be necessary to establish the relation of optimality in the z state and optimality in the x state. If this can be done, then the vast body of literature developed for linear optimal control will be applicable.

References

- [1] Isidori A. *Nonlinear Control Systems*. Springer-Verlag, New York, New York, 1989.
- [2] Karnopp D. C., Margolis D. L., and Rosenberg R. C. *System Dynamics, A Unified Approach*. John Wiley & Sons, Inc, New York, New York, 1990.
- [3] Knospe C.R. and Collins E.G. Introduction to the special issue on magnetic bearing control. *IEEE Transactions on Control Systems and Technology*, pages 481–483, 1996.
- [4] Lindlau J. D. Dynamic biasing of active magnetic bearing via feedback linearization. Master's thesis, University of Virginia, Department of Mechanical, Aerospace, and Nuclear Engineering, 1999.

- [5] Trumper D., Olson S., and Subrahmanyam P. Linearizing control of magnetic suspension systems. *IEEE Transactions on Control Systems and Technology*, pages 427–438, 1997.
- [6] Allaire P. E., Maslen E. H., Humphris R. R., Knospe C. R., and Lewis D. W. *Handbook of Lubrication and Tribology*, volume III, chapter Magnetic Bearings, pages 577–600. CRC Press, 1994.
- [7] Keith F. *Implicit Flux Feedback Control for Magnetic Bearings*. PhD thesis, University of Virginia, 1993.
- [8] Nijmeijer H. and van der Schaft A.J. *Nonlinear Dynamical Control Systems*. Springer-Verlag, New York, New York, 1990.
- [9] Baloh M. J., Allaire P. E., Hilton E. F., and et al. Magnetic bearing system for continuous flow ventricular assist device. *Journal of the American Society for Artificial Internal Organs*, 45(5), 1999.
- [10] Levine J., Lottin J., and Ponsart J. A nonlinear approach to the control of magnetic bearings. *IEEE Transactions on Control Systems and Technology*, pages 524–544, 1996.
- [11] Slotine J. and W. Li. *Applied Nonlinear Control*. Prentice Hall, Englewood Cliffs, New Jersey 07632, 1991.
- [12] Li L. Linearizing magnetic bearing actuators by constant current sum, constant voltage sum, and constant flux sum. *IEEE Transactions on Magnetics*, 35(1), 1999.
- [13] Li L. and Mao J. Feedback linearization of magnetic bearing actuators for uniform upper bound of force slew rate. *IEE Proc. -Electr. Power Appl.*, 146(4), 1999.
- [14] Proceeding of American Control Conference. *Gain Scheduled Control of Magnetic Suspension Systems*, 1994.
- [15] Mittal S. and Menq C. H. Precision motion control of a magnetic bearing suspension actuator using a robust nonlinear compensation scheme. *IEEE/ASME Transactions on Mechatronics*, 2(4), 1997.

IDENTIFICATION AND CONTROL OF A MAGNETICALLY LEVITATED TABLE

Koichi Matsuda, Yoichi Kanemitsu, and Shinya Kijimoto

Department of Intelligent Machinery and Systems

Kyushu University

6-10-1 Hakozaki, Fukuoka 812-8581, JAPAN

SUMMARY

A new vibration isolation system is developed. A table is levitated by an active magnetic bearing and isolated from any external vibration. Subspace identification methods are used to find a state-space model for this system from input-output data. A PID controller is designed to levitate the table, and a random signal is used to excite the system in addition to the controller inputs. This paper points out some problems when subspace methods are used for identification of closed-loop systems. Although three subspace methods are applied to the present problem, only one of them works well. Two subspace methods are not able to find a model with order of a reasonable value. We present one of the reasons why those subspace methods do not work

INTRODUCTION

Vibration isolation is an important topic in a lot of engineering fields such as manufacturing a semiconductor or micro-scale observation using an electron microscope. Vibration-proof rubber, coil spring, or air bearings are used for passive vibration isolation. However, those passive methods are not yet able to achieve a working environment required by the preceding engineering fields. As an alternative to the passive methods, magnetic bearings are used for active vibration isolation¹⁻³. A table is levitated by an active magnetic bearing and isolated from any external vibration. This system is expected to achieve good vibration isolation when compared with the preceding passive methods. Traditional controllers for magnetic bearings are designed to regulate the relative displacement between a levitated object and a base; those bearings are fixed on the base. In order to isolate the table from external disturbance, we have to redesign a controller to regulate the absolute displacement of the levitated table in an inertial coordinate system. Moreover, it would be necessary to obtain a precise model of the controlled system in order to design a good controller. One of the excellent ways to get a precise model would be the one based on the input and output data of the controlled system. From this philosophy, many methods have been developed for the system identification based on the input and output data. In particular, subspace identification methods⁴ have been proven to be a valuable alternative to classical prediction-error methods. Unlike the classical methods they do not suffer from such problems as a priori parameterizations, initial estimates and nonlinear optimizations. Subspace methods are used to find a state-space model for the present system from input-output data. Since this system is essentially unstable, we first design a PID controller to levitate the table and then add a random signal to the controller inputs in order to excite the system for a frequency region of interest. So, the system identification is made owing to closed-loop data of the inputs and the outputs.

This paper points out some problems when subspace methods are used for identification of closed-loop systems. Although three subspace methods are applied to the present problem, only one of them works

well. Subspace methods determine the state-space dimension owing to the singular value decomposition of a matrix; the state dimension is the number of the singular values different from zero. The singular values could be different between the methods. In other words, the state dimension might be different between the subspace methods. In particular, two subspace methods are not able to find a model with order of a reasonable value. We present one of the reasons why those subspace methods do not work.

HARDWARE DESCRIPTION

A table (a rectangular plate) is levitated by electromagnets in order to isolate it from external disturbance such as floor vibration. Here the system configuration is shown in figure 1. The system contains a table to be isolated from any disturbance, three electromagnets, and a base; the base supports those actuators and table and fixed on the floor of our laboratory. The table motion is vertically limited to 0.35 mm, that is, gap width of the electromagnetic actuator. The electromagnetic actuators are able to generate an attractive force upward and downward in order to levitate the table. An eddy-current-type displacement sensor is built in each electromagnetic actuator to measure the relative displacement of the table to the floor, neglecting mechanical flexibility of the base. Moreover, three acceleration sensors are located on the table to measure the table motion in an inertial coordinate system.

Here we present the control system for the preceding sensors and actuators. A digital controller is implemented on a digital signal processor (DSP) built in a PC. All the sensor outputs are amplified, passed through an anti-aliasing filter, and put into the DSP through an analog-to-digital converter (16 bit resolution). The controller input is calculated by the digital controllers and put out of the PC through a digital-to-analogue converter (12 bit resolution). Moreover, the input is passed through a smoothing filter and a Pulse-Width-Modulation (PWM) circuit and converted into an electric current driving the electromagnetic actuator.

IDENTIFICATION SCHEME

Subspace methods are used to find a state-space model for the present system from input-output data. The control system for the levitated table is essentially unstable if it is in open loop, although the clearance of the magnetic bearings would limit the table motion. Since we assume a state-space model should describe the system, input and output data are necessary for the identification such that the table moves not contacting the clearance limits. Thus, we first design a PID controller to levitate the table in that way and then add a random signal to the controller inputs to excite the system for a frequency region of interest. In other words, the system identification is made owing to closed loop data of the inputs and the outputs.

The configuration of the inputs and the outputs for this system is shown in figure 2. If the open-loop plant is given by the state-space realization: $P(z) = C(zI - A)^{-1}B + D$, the system is written in a state-space form:

$$\begin{aligned} x_{k+1} &= Ax_k + Bu_k, & y_k &= Cx_k + Du_k \end{aligned} \quad (1)$$

$$u_k = v_k - w_k \quad \text{with } v_k = K(z)y_k \quad (2)$$

Here, x_k is an n -dimensional state-vector, the matrix A is $n \times n$, B is $n \times m$, C is $l \times n$ and D is $l \times m$; $K(z)$ is a PID controller, and w_k is a random signal. Now the controller input u_k is completely measurable, and we don't account for measurement noise, process noise, model mismatch, and so on. In other words, the present system is completely deterministic. The problem is now to find the system matrices, A , B , C , and D , from the input and output data, u_k 's and y_k 's. Subspace identification methods are applied to this problem, although it is known that these methods don't work in closed-loop stochastic system. Although many subspace methods have been proposed⁴, we have applied three methods (Intersection Method⁵, N4SID⁶, and Balanced-basis method^{6,7}) to the present problem, and only one of the three works well. Since this successful method has received little attention as far as the authors know, we would like to present a part of the algorithms in order to point out the differences between the three subspace methods.

Subspace methods start with introducing a block Hankel matrix such as

$$U_{0i-1} = \begin{pmatrix} u_0 & u_1 & \cdots & u_{j-1} \\ u_1 & u_2 & \cdots & u_j \\ \cdots & \cdots & \cdots & \cdots \\ u_{i-1} & u_i & \cdots & u_{i+j-2} \end{pmatrix} \quad (3)$$

where the subscript of U denotes the subscripts of the first and last element of the first column. A block Hankel matrix formed with the output is defined as Y_{0i-1} in the same way. Intersection methods continues to introduce the singular value decomposition of the following matrix:

$$H = \begin{pmatrix} H_1 \\ H_2 \end{pmatrix} = \begin{pmatrix} U_{11} & U_{12} \\ U_{21} & U_{22} \end{pmatrix} \begin{pmatrix} \Sigma_1 & 0 \\ 0 & 0 \end{pmatrix} V^T \quad \text{with } H_1 = \begin{pmatrix} Y_{0i-1} \\ U_{0i-1} \end{pmatrix} \text{ and } H_2 = \begin{pmatrix} Y_{i|2i-1} \\ U_{i|2i-1} \end{pmatrix} \quad (4)$$

It is easily found that the following relation holds for the intersection of the row space of the matrices H_1 and H_2 :

$$U_{12}^T H_1 = -U_{22}^T H_2 \quad (5)$$

If we introduce the state-vector sequence $X_2 = (x_i \quad x_{i+1} \quad \cdots \quad x_{i+j-1})$, it is proved in reference 5 that the row space of X_2 is equal to the row space of $U_{12}^T H_1$ or $U_{22}^T H_2$. Therefore, a sequence of state vectors can be determined by the intersection of the Hankel matrices up to within a similarity transformation. Moreover, the sequence of the state vectors is used to find the system matrices⁵, although the state dimension and basis have been determined already.

On the other hand, the other two methods, N4SID and Balanced-Basis method, continues to the optimal projection of a Hankel matrix as follows:

$$Z_i = Y_{i/2i-1} / \begin{pmatrix} U_{0i-1} \\ U_{i/2i-1} \\ Y_{0i-1} \end{pmatrix} \equiv L_i^1 U_{0i-1} + L_i^2 U_{i/2i-1} + L_i^3 Y_{0i-1} \quad (6)$$

where $A/B = AB^T(BB^T)^{-1}B$, that is, the optimal projection of the row space of A onto the row space of B . Equation (6) gives the projection of the future outputs onto the past and future inputs and the past outputs. The extended observability matrix is defined as

$$\Gamma_i^T = \begin{pmatrix} C^T & (CA)^T & \dots & (CA^{i-1})^T \end{pmatrix} \quad (7)$$

It is shown in Ref that the column space of Γ_i coincides with the column space of the following matrices:

$$T_1 = L_i^1 U_{0i-1} + L_i^3 Y_{0i-1}, \quad T_2 = L_i^1 + L_i^3 L_i^2 \quad (8)$$

where N4SID and Balanced-basis method take T_1 and T_2 , respectively, as a matrix with the same column space as that of Γ_i . Therefore, we can put $\Gamma_i = U_1 \Sigma_1^{1/2}$ when the singular value decomposition of T_1 or T_2 is given by

$$T_k = (U_1 \quad U_2) \begin{pmatrix} \Sigma_1 & 0 \\ 0 & 0 \end{pmatrix} V^T \quad (9)$$

Moreover, we can observe $\Gamma_{i-1} = \underline{U}_1 \Sigma_1^{1/2}$ owing to the definition of equation (7), where \underline{U}_1 is defined as U_1 without the last l rows. If the relation, $\text{rank}(\Gamma_i) = \text{rank}(\Gamma_{i-1})$, holds, the two subspace methods work. Here the state-vector dimension is the number of the singular values different from zero, whereas the state basis has been fixed by selecting a matrix with the same column space of Γ_i . Furthermore, Γ_i is used to find the system matrices as shown in reference 6.

In theory the difference between the two subspace methods is the state-space basis, which constitutes a similar transformation connecting the two state space models. In practice, the state dimension n could be different between the two methods because it is determined by counting the singular values larger than a threshold value; those singular values might be different between the two methods. In order to clarify this point, let us consider a problem reducing a model of order n to a model of order r by truncating the singular values σ_k 's of T_1 . The following relation then holds for N4SID⁷:

$$\| (P(z) - \hat{P}(z)) S_u(z) \|_{\infty} \leq 2 \sum_{k=r+1}^n \sigma_k (1 + \alpha) \quad (\alpha > 0) \quad (10)$$

where $\hat{P}(z)$ is the reduced model of order r ; $S_u(z)$ is the spectral factor of $U(z)$. Equation (10) shows that

the error of the reduced model would be small where the frequency content of the input is large. In other words, a lot of input energy in a certain frequency region leads to an accurate model in that region. The similar relation to equation (10) holds for Balanced-Basis method⁷:

$$\|P(z) - \hat{P}(z)\|_{\infty} \leq 2 \sum_{k=r-1}^n \sigma_k \quad (11)$$

Here, σ_k is a singular value of T_2 . This reduction cannot depend on a spectrum of input energy. Judging from equations (10) and (11), the state-space dimension n might be different between the two methods unless the input is white noise.

EXPERIMENTAL RESULT

Although three subspace methods are introduced in the preceding chapter, those subspace methods are used to identify the control system for the table levitated by the electromagnetic actuators. Those subspace methods are implemented in MATLAB, whereas all the programs for controlling the table system are written in C language. An M-sequence (maximum length null sequence) signal of 15th order is used to excite the table as a random input w_k . This M-sequence is generated by a PC and keeps its power spectral density constant up to a given frequency. The input and output data for the identification test are sampled 15000 times into the PC through an analog-to-digital converter; the sampling rate is 3000 Hz.

Although we have applied the three subspace methods to the present system, we show the calculated results here. The column number of the Hankel matrices is 14800 through all the calculation for system identification. When using the Intersection method, we are not able to find the intersection up to order of 50. This number of the model order is the upper limit in our PC. Since the smallest singular values of equation (4) is 6.9 even at $i = 50$, the matrices U_{12} and U_{22} don't exist, that is, there is no intersection of those two Hankel matrices. Therefore, the Intersection method does not work well in the present case. When we take N4SID to identify the present system, we encountered a problem similar to the problem we have already observed. The matrix T_1 is always of full rank with respect to the column up to 90; the smallest singular value is 3.1×10^{-2} at $i = 90$. Since Γ_i is then of full rank, $\text{rank}(\Gamma_i)$ cannot be equal to $\text{rank}(\Gamma_{i-1})$ due to the definition, which means the state dimension n is not constant. Therefore, N4SID subspace method does not work, either. Finally, Balanced-Basis method is used to identify this table system and works well. The smallest singular value of T_2 is 5.9×10^{-5} at $i = 42$. By truncating the singular values larger than 1.0×10^{-4} , we get a state-space model of order 40. The transfer function $P(z)$ is computed owing to the identified system matrices (Figure 3).

Let us consider the reason why N4SID does not work well whereas Balanced-Basis method works. As shown in equations (10) and (11), the two methods would yield the same system matrices within up to a similar transformation if the input is white noise. However, it would be difficult to cause the input to be white noise in closed-loop settings because the input absolutely contains the frequency content to stabilize the system, in the present case, v_k . It would be possible to solve the problem by passing the input sequence through a filter if the spectral factor S_u is invertible.

CONCLUSION

A new vibration isolation system is developed. A table is levitated by an active magnetic bearing and isolated from any external vibration. Subspace identification methods are used to find a state-space model for this system from input-output data. A PID controller is designed to levitate the table, and a random signal is used to excite the system in addition to the controller inputs. This paper points out some problems when subspace methods are used for identification of close-loop systems. Although three subspace methods are applied to the present problem, only one of them works well. Two subspace methods are not able to find a model with order of a reasonable value. We present one of the reasons why those subspace methods do not work

REFERENCES

1. Y. Kanemitsu et al., "Control of Levitation and Vibration of Magnet Bearing Type Isolator for Absolute Gravimeter," Proceedings of the 6th International Symposium on Magnetic Bearing, Cambridge, USA, August 1998, pp. 67-76.
2. K. Watanebe et al., "Combination of H^∞ and PI control for an Electromagnetically Levitated Vibration Isolation System," Proceedings of the 35th Conference on Decision and Control, Kobe, JAPAN, December 1996, pp. 1223-1228.
3. W. Cui, K. Nonami, and Y. Kanemitsu, "Isolation Performance of Hybrid Isolation System by H^∞ Control and Disturbance Cancellation Control," Proceedings of the 3rd International Conference on Motion and Vibration Control, Chiba, JAPAN, September 1996, pp. 7-12.
4. M. Viberg, "Subspace-based Methods for the Identification of Linear Time-Invariant Systems," Automatica, Vol. 31, No. 12, 1995, pp. 1835-1851.
5. M. Moonen et al., "On- and Off-line Identification of Linear State-Space Models," International Journal of Control, Vol. 49, No. 1, 1989, pp. 219-2325.
6. P.V. Overschee and B.D. Moor, "N4SID: Subspace Algorithms for the Identification of Combined Deterministic-Stochastic Systems," Automatica, Vol. 30, No. 1, 1994, pp. 75-93.
7. P.V. Overschee and B.D. Moore, "Choice of State Space Basis in Combined Deterministic-Stochastic Subspace Identification," Automatica, Vol. 30, 1995, pp. 75-93.

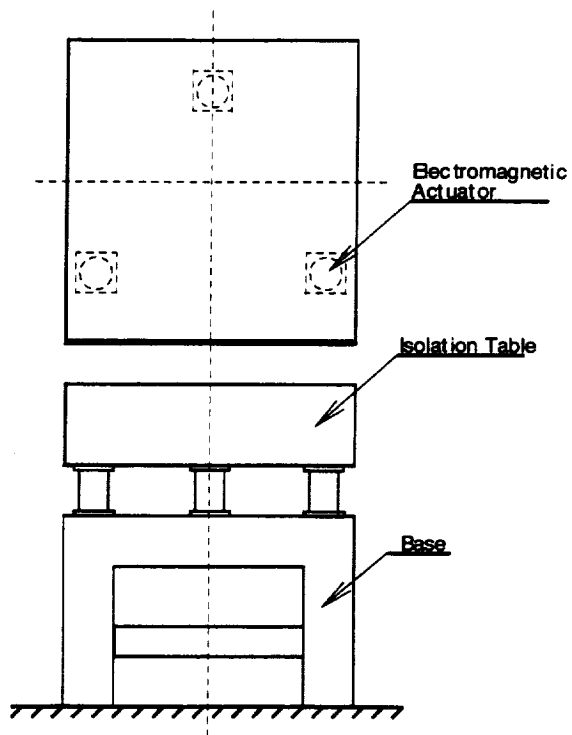


Figure 1. Vibration isolation system using electromagnetic actuators

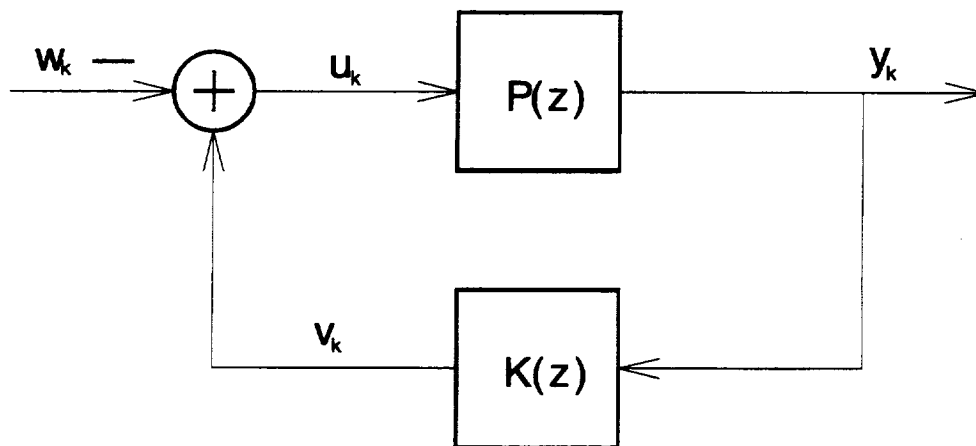


Figure 2. Block diagram for identification tests

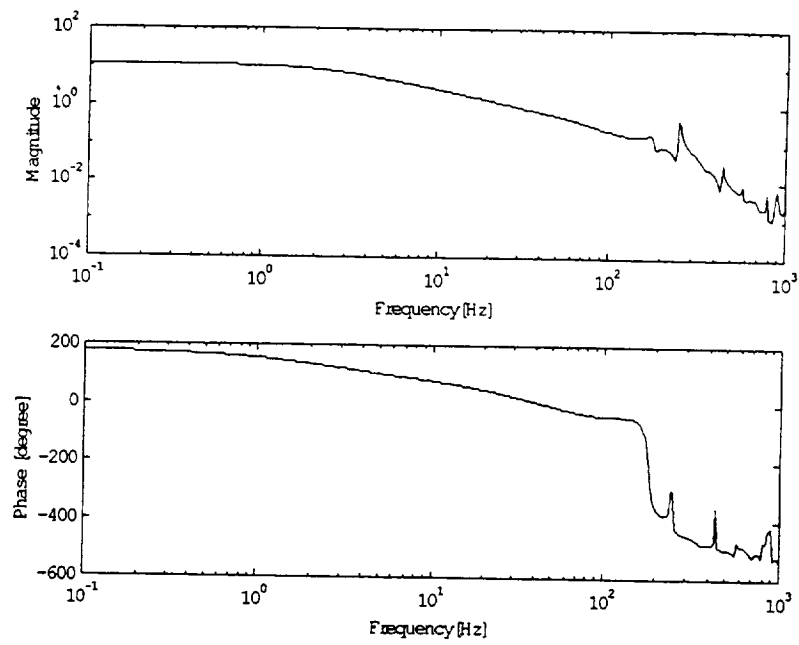


Figure 3 Calculated transfer function using the estimated state-space model

NON-LINEAR FUZZY LOGIC CONTROL FOR MAGNETIC BEARINGS IN LARGE-TIP CLEARANCE- ACTIVE STALL CONTROL APPROACH

SHULIANG LEI, ALAN PALAZZOLO

Texas A&M University, Department of Mechanical Engineering, College Station, TX 77843-3123, USA

ALBERT KASCAK

U. S. Army at NASA Glenn, 21000 Brookpark RD, Cleveland, Ohio 44135, USA

In this paper a prescribed large motion control using active magnetic bearings in a proposed active stall control test rig was developed. A finite element method is employed to model and to synthesize the flexible shaft in a closed loop system. A linearized model of the stall rig using conventional PD controllers to 16 magnetic poles (4 opposing C-cores) yields stability and frequency responses. In the mean time the nonlinear model is studied to consider the Ampere's Law, Faraday's Law and the Maxwell stress tensor. A fuzzy logic control system is then designed to show the advantages over the conventional controllers with the fully nonlinear model.

1. INTRODUCTION

The development of magnetic bearings in rotating machinery has increased significantly due to its low power loss with high-speed operations. Since the shaft and the bearing assembly have no contact between one another, frictional loss, which grows drastically with speed increase, is nearly eliminated. Active magnetic bearings require closed loop feedback, which offers a way to support the rotating shaft as well as to control the vibration. In most industrial applications, the feedback system includes a linear PID controller with compensators, power amplifiers, magnetic actuators and inductive eddy current or optical sensors [1]. In addition to the widely applied PID controllers, advanced control strategies such as optimal control [2], μ -synthesis control [5], H_∞ control [6,8] can be found in some applications. All these methods are based on linear systems theory and need linear models. Nonlinear control techniques were also applied to active magnetic bearings. Sliding mode control and fuzzy logic based control can be found in several papers.

In the applications of aircraft engines, in order to suppress rotating stall in a high-speed compressor wheel, it is desired to shake the wheel at a large amplitudes while maintaining the rotor system stable. Electromagnetic shakers and magnetic bearings have been used for actuators in vibration control. In the case of magnetic shaker with the nonlinear models, there are some difficulties to obtain large whirl orbits because of system instability. By carefully designing a PD controller the shaking orbit radius can be increased but only to a limited value in the stable region.

Motivated by the capability of dealing with nonlinearities of the problem, fuzzy logic has been introduced for control of magnetic bearing system. Although sliding mode control can yield robust performance against modeling error, it is difficult to achieve fast switching required. Fuzzy logic theory was first established in Zadeh's seminal paper [9] in 1965. Since then it has been considered as an effective means in various control problems. An idea of applying fuzzy logic to dynamics systems was introduced in early 70's by Mamdani [10]. The Mamdani architecture of fuzzy logic controller is build up based on qualitative and empirical knowledge of human beings. Later Takagi and Sugeno established a fuzzy model [11], called Takagi-Sugeno model, which can be more easily used for analytical purpose.

The AMB nonlinear model considers the three cases: nonlinear B-H curve, Ampere's Law and Maxwell stress tensor. Fuzzy logic control is constructed by designing a rule base to implement a non-linear control strategy. The antecedent and consequent of each rule operate on the positions of input and output variables in predefined membership functions. These membership functions possess qualitative descriptions which generalize the notion of assigning a single degree to a specific response severity or corrective action level. Researchers in the area of AMB using fuzzy logic control are mainly based on

simple model such as lumped mass model or rigid body model [12] [13]. Some application needs to recursively tune the rules to achieve better performances [14]. While these results are absorbing, they can not deal with a flexible shaft with a dimension of over hundreds of structural states plus control variables. The stall-rig model consists of a rotating shaft with a compressor wheel. Finite element method is used to describe the flexible rotor in designing a suitable control and analyzing the system behavior. The front bearing is an active magnetic bearing system, which includes feedback between non-collocated sensors and actuators, via controllers. The shaft is divided into 23 elements and at node 17, an oil film bearing is employed to support the rotor system. The magnetic bearing is located at node 9. The non-collocated sensors are placed at node 7 and have outputs directed PD controllers. The control signals are then directed to power amplifiers to produce control currents, which drive the coils of the magnetic bearings to control the rotor system. The shaking voltages are applied to a summing point at the control output to force the shaft to execute motions that alter the compressor wheel's tip clearance and inhibit stall cell formation.

Fuzzy logic controllers for active magnetic bearings are synthesized and designed for suppression of imbalance vibration and to increase the shaking orbit radius. The main objective of this paper is to develop robust controllers for maintaining magnetic bearing system stability against imbalance and external shaking forces or voltages for linear and nonlinear models. Applying the basic magnetic bearing theory yields a fully nonlinear model. Based on the nonlinear magnetic bearing model, linearization is carried out to formulate a complete linear model for analysis. The PD controller and the fuzzy logic controllers based on Mamdani architecture are synthesized and designed. The superiority of nonlinear fuzzy logic control over linear PD control is also shown. Simulation results for each type of controllers are provided and their performance specifications can be compared accordingly.

2. SYSTEM MODEL

2.1. MAGNETIC BEARING FORCE

Consider the 2 opposing magnetic C-cores shown in figure 1:

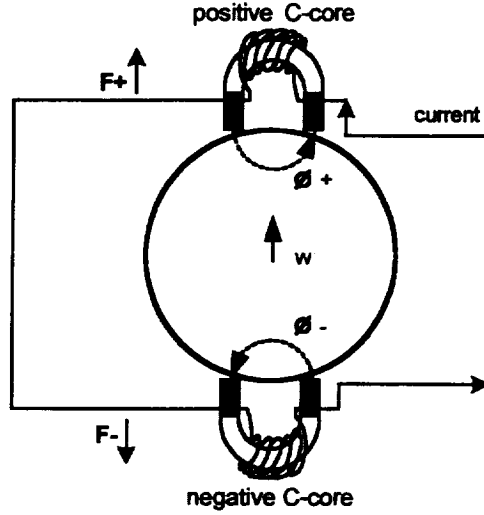


Figure 1. Schematic of 2 opposing C-cores

According to Ampere's law, the magnetic flux density ϕ^+ in the positive C-core is

$$\phi^+ = \frac{(N_B i_B + N_c i)}{2w^+} \mu_0 A_a = \frac{(N_B i_B + N_c i)}{2(g_0 - w)} \mu_0 A_a \quad (1)$$

The magnetic flux density ϕ^- in the negative C-core is

$$\phi^- = \frac{(N_B i_B - N_c i)}{2w^-} \mu_0 A_a = \frac{(N_B i_B - N_c i)}{2(g_0 + w)} \mu_0 A_a \quad (2)$$

where g_0 is the air gap of the magnetic bearing and w is the displacement of the rotor in positive direction. The corresponding flux density in the positive magnetic path and the negative magnetic path can then be written as:

$$B^+ = \frac{\phi^+}{A_a} = \frac{(N_B i_B + N_c i)}{2(g_0 - w)} \mu_0, \quad B^- = \frac{\phi^-}{A_a} = \frac{(N_B i_B - N_c i)}{2(g_0 + w)} \mu_0 \quad (3)$$

Note that Ampere's Law yields flux expressions that are nonlinear functions of the shaft displacement w .

A second nonlinearity occurs when the Maxwell stress tensor formula is applied to obtain the resultant electromagnetic force of the two opposing C-cores:

$$F = [(B^+)^2 \frac{A_a}{\mu_0} - (B^-)^2 \frac{A_a}{\mu_0}] \cos \delta \quad (4)$$

where

$$(B^+)^2 = \frac{(N_B i_B + N_c i)^2}{4(g_0 + w)^2} \mu_0^2, \quad (B^-)^2 = \frac{(N_B i_B - N_c i)^2}{4(g_0 + w)^2} \mu_0^2 \quad (5)$$

This yields:

$$F = \eta^2 \cos \delta \frac{A_a \mu_0}{4} \left[\left(\frac{N_B i_B + N_c i}{g_0 + w} \right)^2 - \left(\frac{N_B i_B - N_c i}{g_0 + w} \right)^2 \right] \quad (6)$$

The related parameters for the example considered are :

$$\mu_0 = 4\pi \times 10^{-7}$$

$$A_a = \frac{6}{39.37^2} (m^2) , \text{ area per pole}$$

$$g_0 = \frac{0.02}{39.37} (m) , \text{ air gap}$$

$$\delta = 360^\circ / (16 \times 2) = 11.25^\circ , \text{ half angle between poles}$$

$$\eta = 0.9 \text{ derate factor}$$

$$i_B = 30(A) , \text{ bias current}$$

$$N_B = 40 (\text{turns per C-core}), \text{ bias coil}$$

$$N_c = 16 (\text{turns per C-core}), \text{ control coil}$$

2.2. COIL INDUCTANCE AND VOLTAGE

According to Faraday's law, the coil voltage in each C-core can be written as follows:
positive C-core

$$V_L^+ = N_c \frac{d\phi^+}{dt} = \frac{N_c^2 \mu_0 A_a}{2} \frac{d}{dt} \left(\frac{i}{w^+} \right) \quad (7)$$

negative C-core

$$V_L^- = N_c \frac{d\phi^-}{dt} = \frac{N_c^2 \mu_0 A_a}{2} \frac{d}{dt} \left(\frac{i}{w^-} \right) \quad (8)$$

or:

$$\begin{aligned}
 V_L^+ &= \frac{N_c^2 \mu_0 A_a}{2w^+} \frac{di}{dt} + \frac{N_c^2 \mu_0 A_a}{2} i \frac{d}{dt} \left(\frac{1}{w^+} \right) \\
 &= L^+ \frac{di}{dt} + \frac{N_c^2 \mu_0 A_a}{2} i \frac{d}{dt} \left(\frac{1}{g_0 + w} \right)
 \end{aligned} \tag{9}$$

and

$$\begin{aligned}
 V_L^- &= \frac{N_c^2 \mu_0 A_a}{2w^-} \frac{di}{dt} + \frac{N_c^2 \mu_0 A_a}{2} i \frac{d}{dt} \left(\frac{1}{w^-} \right) \\
 &= L^- \frac{di}{dt} + \frac{N_c^2 \mu_0 A_a}{2} i \frac{d}{dt} \left(\frac{1}{g_0 + w} \right)
 \end{aligned} \tag{10}$$

where

$$L^+ = \frac{N_c^2 \mu_0 A_a}{2} \left(\frac{1}{g_0 - w} \right), \quad L^- = \frac{N_c^2 \mu_0 A_a}{2} \left(\frac{1}{g_0 + w} \right) \tag{11}$$

are the non-linear inductances of the coils on the two opposing C-cores.

Considering the coil resistance R , the voltage drop across the power amplifier output terminals for two opposing C-cores becomes:

$$V = 2Ri + L^+ \frac{di}{dt} + \frac{N_c^2 \mu_0 A_a}{2} i \frac{d}{dt} \left(\frac{1}{g_0 - w} \right) + L^- \frac{di}{dt} + \frac{N_c^2 \mu_0 A_a}{2} i \frac{d}{dt} \left(\frac{1}{g_0 + w} \right) \tag{12}$$

Eqs. 10-12 show the nonlinearity that is contained in the voltage expression obtained from Faraday's Law.

2.3. FLUX DENSITY SATURATION

Due to the non-linear property of the ferromagnetic materials, the flux density in the magnetic circuit will saturate with increase of exciting coil current. The AMB forces saturate accordingly due to the saturation of the magnetic field.

For simplicity , suppose the maximum flux density is 2 Teslas:

$$B_{\max}^+ = B_{\max}^- = 2 \text{ (Teslas)} \quad (13)$$

Then we have for the maximum AMB forces expressed as:

$$F_{\max}^- = F_{\max}^+ = \eta^2 \cos \delta (B_{\max}^+)^2 \frac{A_a}{\mu_0} = 4\eta^2 \cos \delta A_a \mu_0 \quad (14)$$

The saturation of flux density B limits the maximum force :

$$F_{\max} = (B_{\max}^+)^2 \frac{A_a}{\mu_0} \quad (15)$$

The above result is valid for each opposing C-core pair (2 opposing C-cores).

2.4. CLOSED LOOP SYSTEM

The basic configuration of one control channel is shown in Figure 2.:

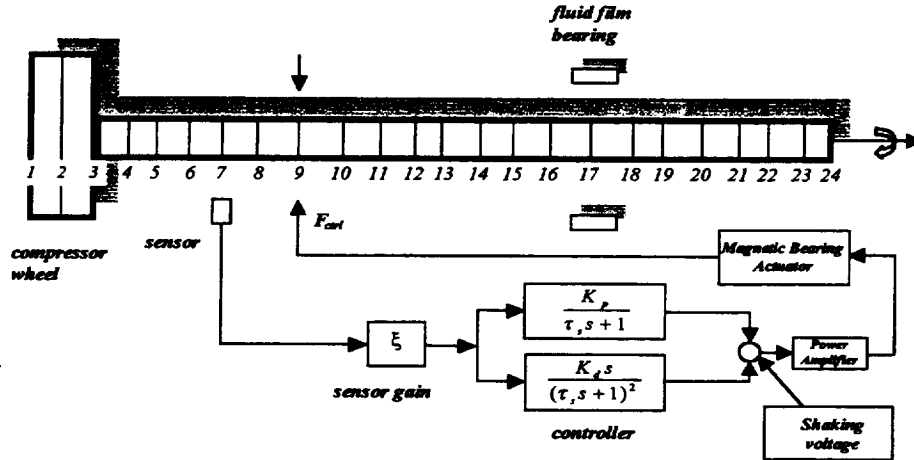


Figure 2. Finite element model of shaft plus feedback control path

In this diagram, we use PD controllers in the feedback loop. A more elegant nonlinear fuzzy logic controller will be described later. It can be seen from this configuration that the shaft is divided into 23 elements. Dimensional data for this model are given in the Appendix. The sensor is located at node 7 and the actuator is located at node 9: this is a non-collocated system. An oil film bearing is placed at node 17 to support the other end of the shaft (see Appendix). The sensor measures the displacement signal of the rotor and feeds the signal to the controller. The controller synthesizes the input signal to generate output voltage to the power amplifier (P.A.), which in turn produces the control current for the magnetic bearing coil to support the rotor. The compressor wheel is located in the first two elements and the operating rotor spinning rate is set to $\Omega=17000 \text{ rpm}$

3. LINEAR ANALYSIS

3.1. LINEARIZATION

The magnetic bearing used to support and shake the rotor has 16 poles, which constitutes 4 C-core -pairs. The 4 magnetic bearing system consists of 8 C-cores distributed around the circle at uniform angles of 45 degrees. Each C-core has 2 poles, N and S, two opposing C-cores have 4 poles. Totally the system has 16 poles evenly distributed at an angle of 22.5 degrees. Figure 3 shows the configuration of the 4 C-core-pairs.

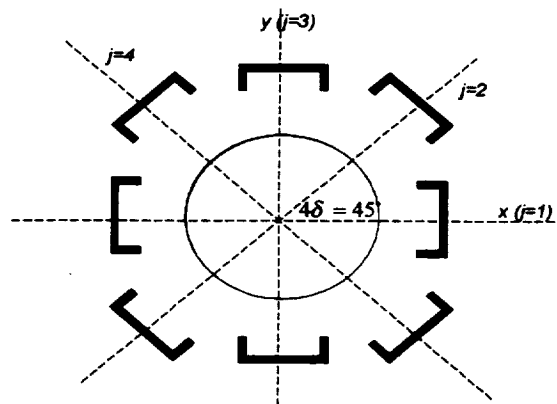


Figure 3. Configuration of the 4 C-core-pairs

Rewrite F for the j-th ($j=1,2,3,4$) C-core pole pair as

$$F = \eta^2 \cos \delta \frac{A_a \mu_0}{4} \left[\left(\frac{N_B i_B + N_c i}{g_0 - w} \right)^2 - \left(\frac{N_B i_B - N_c i}{g_0 + w} \right)^2 \right] \quad (16)$$

$$= k_\alpha \left[\left(\frac{N_B i_B + N_c i}{g_0 - w} \right)^2 - \left(\frac{N_B i_B - N_c i}{g_0 + w} \right)^2 \right]$$

where

$$k_\alpha = \eta^2 \cos \delta \frac{A_a \mu_0}{4} \quad (17)$$

Linearize the force at $i=0$ and $w=0$:

$$\frac{dF}{di} = 2k_\alpha \left[\frac{(N_B i_B + N_c i) N_c}{(g_0 - w)^2} + \frac{(N_B i_B - N_c i) N_c}{(g_0 + w)^2} \right] \Big|_{i=0, w=0} = 4k_\alpha \frac{i_B^2}{g_0^2} N_B N_c \quad (18)$$

$$\frac{dF}{dw} = 2k_\alpha \left[\frac{(N_B i_B + N_c i)^2}{(g_0 - w)^3} + \frac{(N_B i_B - N_c i)^2}{(g_0 + w)^3} \right] \Big|_{i=0, w=0} = 4k_\alpha N_B^2 \frac{i_B^2}{g_0^3} \quad (19)$$

Therefore,

$$\mathbf{F} = [F_x(x, y, i_x, i_y), F_y(x, y, i_x, i_y)]$$

$$= \begin{bmatrix} \frac{\partial F_x}{\partial g_1} & \frac{\partial F_x}{\partial g_2} & \frac{\partial F_x}{\partial g_3} & \frac{\partial F_x}{\partial g_4} \\ \frac{\partial F_y}{\partial g_1} & \frac{\partial F_y}{\partial g_2} & \frac{\partial F_y}{\partial g_3} & \frac{\partial F_y}{\partial g_4} \end{bmatrix} \begin{bmatrix} \frac{\partial g_1}{\partial x} & \frac{\partial g_1}{\partial y} \\ \frac{\partial g_2}{\partial x} & \frac{\partial g_2}{\partial y} \\ \frac{\partial g_3}{\partial x} & \frac{\partial g_3}{\partial y} \\ \frac{\partial g_4}{\partial x} & \frac{\partial g_4}{\partial y} \end{bmatrix} \begin{bmatrix} x \\ y \end{bmatrix} + \begin{bmatrix} \frac{\partial F_x}{\partial i_x} & \frac{\partial F_x}{\partial i_y} \\ \frac{\partial F_y}{\partial i_x} & \frac{\partial F_y}{\partial i_y} \end{bmatrix} \begin{bmatrix} i_x \\ i_y \end{bmatrix} \quad (20)$$

Geometric consideration of the 4 C-core pairs gives the following relations:

$$\begin{aligned} g_1 &= x \\ g_2 &= x \cos(\pi/4) + y \sin(\pi/4) \\ g_3 &= y \\ g_4 &= x \cos(3\pi/4) = y \sin(3\pi/4) \end{aligned} \quad (21)$$

Then,

$$\begin{aligned} \mathbf{F} &= [F_x(x, y, i_x, i_y), F_y(x, y, i_x, i_y)] \\ &= \begin{bmatrix} \frac{\partial F_x}{\partial g_1} & \frac{\partial F_x}{\partial g_2} & \frac{\partial F_x}{\partial g_3} & \frac{\partial F_x}{\partial g_4} \\ \frac{\partial F_y}{\partial g_1} & \frac{\partial F_y}{\partial g_2} & \frac{\partial F_y}{\partial g_3} & \frac{\partial F_y}{\partial g_4} \end{bmatrix} \begin{bmatrix} 1 & 0 \\ \sqrt{2}/2 & \sqrt{2}/2 \\ 0 & 1 \\ -\sqrt{2}/2 & \sqrt{2}/2 \end{bmatrix} \begin{bmatrix} x \\ y \end{bmatrix} + \begin{bmatrix} \frac{\partial F_x}{\partial i_x} & \frac{\partial F_x}{\partial i_y} \\ \frac{\partial F_y}{\partial i_x} & \frac{\partial F_y}{\partial i_y} \end{bmatrix} \begin{bmatrix} i_x \\ i_y \end{bmatrix} \end{aligned} \quad (22)$$

After algebraic manipulations:

$$\mathbf{F} = K_{pos} \begin{bmatrix} 1 & 0 \\ 0 & 1 \end{bmatrix} \begin{bmatrix} x \\ y \end{bmatrix} + \begin{bmatrix} \frac{\partial F_x}{\partial i_x} & \frac{\partial F_x}{\partial i_y} \\ \frac{\partial F_y}{\partial i_x} & \frac{\partial F_y}{\partial i_y} \end{bmatrix} \begin{bmatrix} i_x \\ i_y \end{bmatrix} \quad (23)$$

where $K_{pos} = 8k_\alpha \frac{i_B^2}{g_0^3} N_B$ is the position stiffness.

For the current stiffness, note that

$$\begin{aligned} i_1 &= i_x \\ i_2 &= i_x \cos(\pi/4) + i_y \sin(\pi/4) \\ i_3 &= i_y \\ i_4 &= i_x \cos(3\pi/4) + i_y \sin(3\pi/4) \end{aligned} \quad (24)$$

Therefore:

$$\begin{bmatrix} \frac{\partial F_x}{\partial i_x} & \frac{\partial F_x}{\partial i_y} \\ \frac{\partial F_y}{\partial i_x} & \frac{\partial F_y}{\partial i_y} \end{bmatrix} = N_B N_c 8k_\alpha \frac{i_B}{g_0^2} \begin{bmatrix} 1 & 0 \\ 0 & 1 \end{bmatrix} \quad (25)$$

where $K_i = N_B N_c 4k_\alpha \frac{i_B}{g_0^2}$ is the current stiffness.

The total linearized resultant force is:

$$\mathbf{F} = K_{pos} \begin{bmatrix} 1 & 0 \\ 0 & 1 \end{bmatrix} \begin{bmatrix} x \\ y \end{bmatrix} + K_i \begin{bmatrix} 1 & 0 \\ 0 & 1 \end{bmatrix} \begin{bmatrix} i_x \\ i_y \end{bmatrix} \quad (26)$$

To obtain the linear electric load, we ignore the coil inductance difference in the two opposing C-cores due to the radial displacement of the rotor, that is, let

$$w^+ = w^- = g_0$$

Then $L^+ = L^- = L$, where

$$L = \frac{N_c^2 \mu_0 A_a}{2g_0} \quad (27)$$

For two opposing C-cores, the linear electric load is

$$V = 2Ri + 2L \frac{di}{dt} \quad (28)$$

3.2. STABILITY AND STEADY STATE ANALYSIS

The linearized closed loop equation is expressed as:

$$\dot{\mathbf{Z}} = \mathbf{A} \mathbf{Z} + \mathbf{B} \mathbf{u} \quad (29)$$

where

$\mathbf{Z} = [x_1 \ y_1 \ \theta_{x1} \ \theta_{y1} \ x_2 \ y_2 \ \theta_{x2} \ \theta_{y2} \ \dots \ x_N \ y_N \ \theta_{xN} \ \theta_{yN}]^T$ is the state variable vector of the

closed loop system,

$\mathbf{B} \mathbf{u}$ represents external disturbances, i.e. imbalance and shaking input

\mathbf{A} = closed loop system matrix where the feedback control forces are included.

The system stability property is determined by the eigenvalues of the closed loop system matrix A . If all the real parts of the eigenvalues of A are negative, i.e. the complex eigenvalues are all located on the left half plane, the system is stable. For a stable system, the steady state solution is given as follows:

$$U = \hat{U} e^{j\omega t} \quad \text{where } \omega = \text{shaking frequency}$$

This lead to

$$\begin{aligned}\hat{U}j\omega e^{j\omega t} &= A\hat{U}e^{j\omega t} + \hat{F}e^{j\omega t} \\ \Rightarrow j\omega\hat{U} &= A\hat{U} + \hat{F} \\ \Rightarrow (j\omega - A)\hat{U} &= \hat{F} \\ \Rightarrow \hat{U} &= (j\omega - A)^{-1} \hat{F}\end{aligned}$$

Figure 4 show the amplitude of the compressor wheel (node 2 and node9) with respect to the shaking frequency.

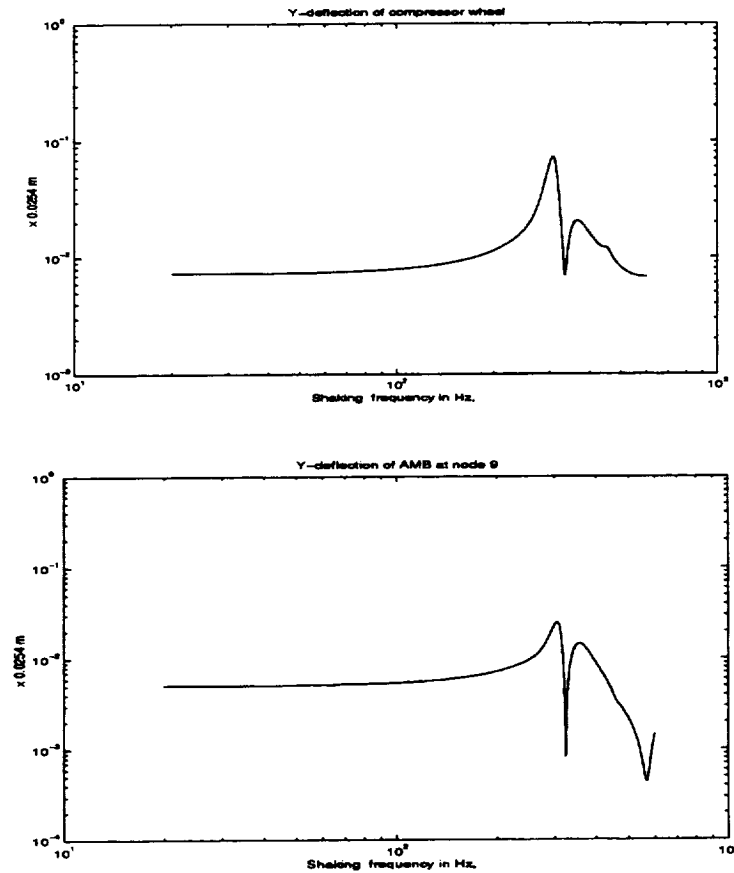


Figure 4. Compressor wheel amplitude vs. shaking frequency

The frequency responses are obtained with the following conditions:

Shaking frequency varies from 20 Hz to 600 Hz, shaking voltage=66 v

Rotor spinning rate $\Omega=17000$ rpm

The following table shows the steady state displacements in the x and y directions at node 2, node 5, node 9 and node 17, when the shaking frequency =200 Hz, respectively:

Node number	2	5	9	17
Displacement (mm)	0.292	0.241	0.178	0.0355

Note that this is a linear response prediction and the nonlinear response amplitudes were less than 0.254mm.

4. TRANSIENT RESPONSE SIMULATION WITH PD CONTROLLERS

The simulation was carried out with the following parameters:

PD controllers:

Proportional control path: $\frac{K_p}{\tau_s s + 1}$, Derivative control path: $\frac{K_d s}{(\tau_s s + 1)^2}$

where $K_p = 65$, $K_d = 0.008$, $\tau_s = \frac{1}{2\pi \times 5000}$

Power amplifier DC gain = 1

Sensor gain : $\xi = 200$

Rotor spin rate: $\Omega = 17000$ rpm

Shaking voltage frequency: 200Hz

SIMULATION WITH LINEAR MODEL:

Results for the linear model are shown in Table 1

Table 1. Linearized model forced response results

V(shaking)	Radius of orbit	Power amplifier	Power amplifier
	At node 2 (mm)	voltage (v)	current (A)
20	0.0889	50	16
45	0.2032	110	35
80	0.3556	180	62

It can be seen that the radius of the orbit at node 2 is proportional to the magnitude of the shaking voltage. The magnitude of the shaking voltage increases linearly with time until it reaches the desired steady state value. Figure 5 shows a linear system shaking orbit and power amplifier voltage for $V_{shaking}=80$ v:

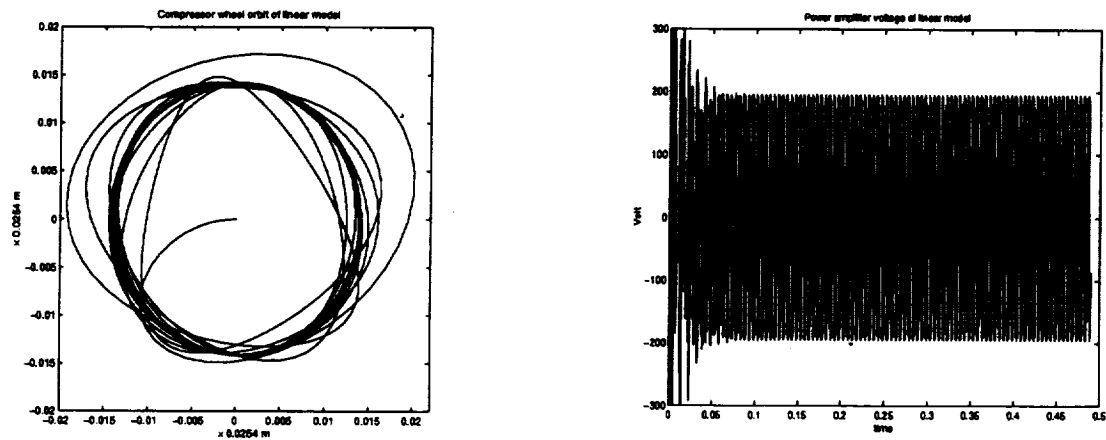


Figure 5. Linear model vibration response at node 2

SIMULATION WITH NON-LINEAR MODEL:

In the non-linear model, we include the nonlinear magnetic bearing forces, the nonlinear electric load expression and the saturation of the flux density. The following table summarizes the simulation result:

V(shaking) (v)	Radius of orbit At node 2 (mm)	Power amplifier voltage (v)	Power amplifier current (A)
20	0.0635	17	5
30	0.0965	25	8
45	0.1524	40	12
46	0.1549	46	14
50	diverge		

Figure 6 shows a shaking orbit and power amplifier voltage for the fully non-linear model when $V_{shaking}=46v$. Not ethat the target of $0.25mm$ could not be achieved with a PD control. This was true even over an exhaustive range of K_p and K_d values.

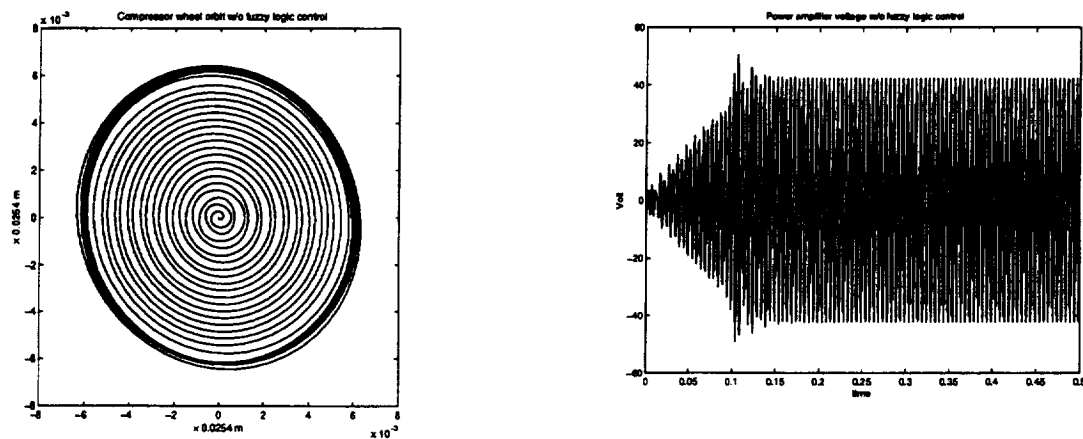


Figure 6. Nonlinear model vibration response of node 2

5. FUZZY LOGIC CONTROL

From the simulation results, it can be seen that with the linear model, the radius of the shaking orbit can be easily made greater than $0.25mm$. For the nonlinear model, the maximum radius is $0.16mm$ at a shaking voltage of $46v$. Further increase of the shaking voltage leads to system divergence.

For the active stall control studies, it is desired to obtain a shaking radius of $0.25mm$ to reduce the stall of the compressor wheel. This target can not be attained with the PD controller. A fuzzy logic controller is introduced in the control loop to overcome this difficulty. The $0.25mm$ shaking radius can be reached by adding fuzzy logic controllers with Mamdani architecture.

Fuzzy logic is an intuitive way to map an input space to an output space. In our case, the input space is position voltage v_p and the rate of change voltage v_d , and the output space is the control voltage v_c . To employ a fuzzy logic controller, we define input and output membership functions which describe the truth of any statement as a matter of degree. More precisely, a membership function is a curve that defines how each point in the input space is mapped to a membership value between 0 and 1. Then based on experts' heuristic knowledge about how to control a system, a rule base is formulated holding the knowledge of how to best control the system.

The fuzzy logic controller is formed as follows:

The 2 inputs called v_p and v_d , and one output denoted as v_c . Triangular and trapezoidal shapes are used to define the membership functions.

The 3 input membership functions for v_p are: *neg, zero, pos*

The 3 input membership functions for v_d are: *neg, zero, pos*

The 5 output membership functions for v_c are: *vneg, neg, zero, pos, vpos*

The following figures depict the input and output membership functions:

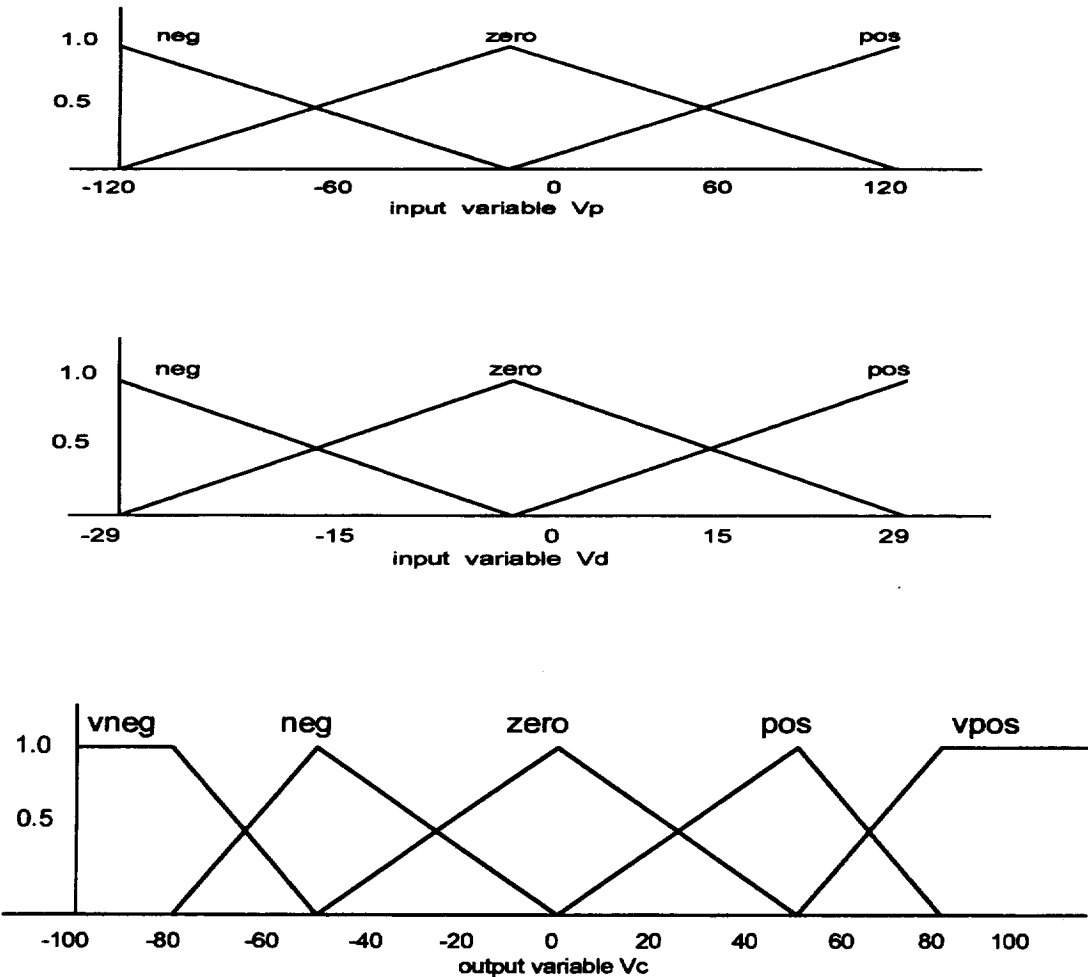


Figure 7. Input and output membership functions

The rule base can be described in the following compact form:

Inputs	v_p : <i>neg</i>	v_p : <i>zero</i>	v_p : <i>pos</i>
v_d : <i>neg</i>	<i>vneg</i>	<i>neg</i>	<i>zero</i>
v_d : <i>zero</i>	<i>neg</i>	<i>zero</i>	<i>pos</i>
v_d : <i>pos</i>	<i>zero</i>	<i>pos</i>	<i>vpos</i>

The above table formulates 9 rules. For example, the first rule is:

if v_p is neg and v_d is neg , then v_c is vneg.

Schematically, the closed loop system with fuzzy logic controller is depicted in Figure 8:

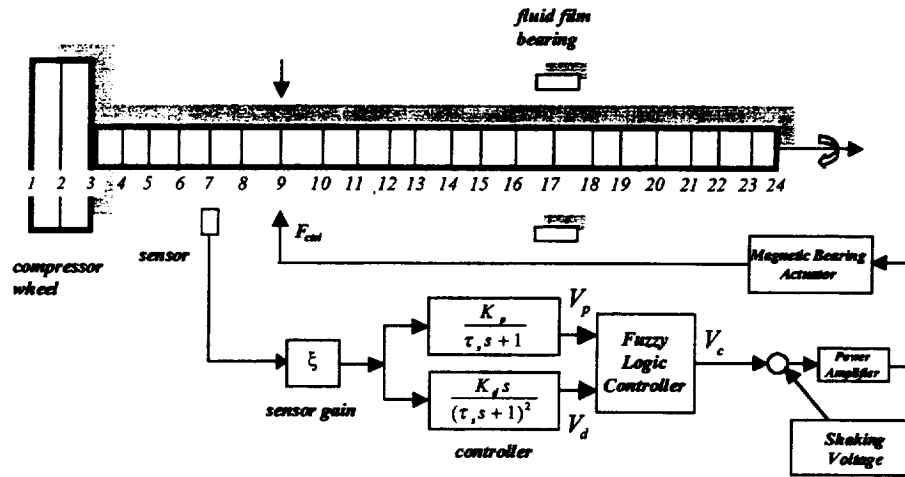


Figure 8. PD controllers with fuzzy logic control stage

The results with the fuzzy logic controller are

$V_{\{shaking\}}$ (v)	Radius of orbit	Power amplifier volt. (v)	Power amplifier current(A)
45	0.25 mm	220	70

It can be seen that the cost paid for the larger shaking radius is higher power amplifier voltage and current. However, these are within the allowable limits for the selected power amplifier. Figure 9 shows the wheel orbit and the power amplifier voltage with the fuzzy logic control stage.

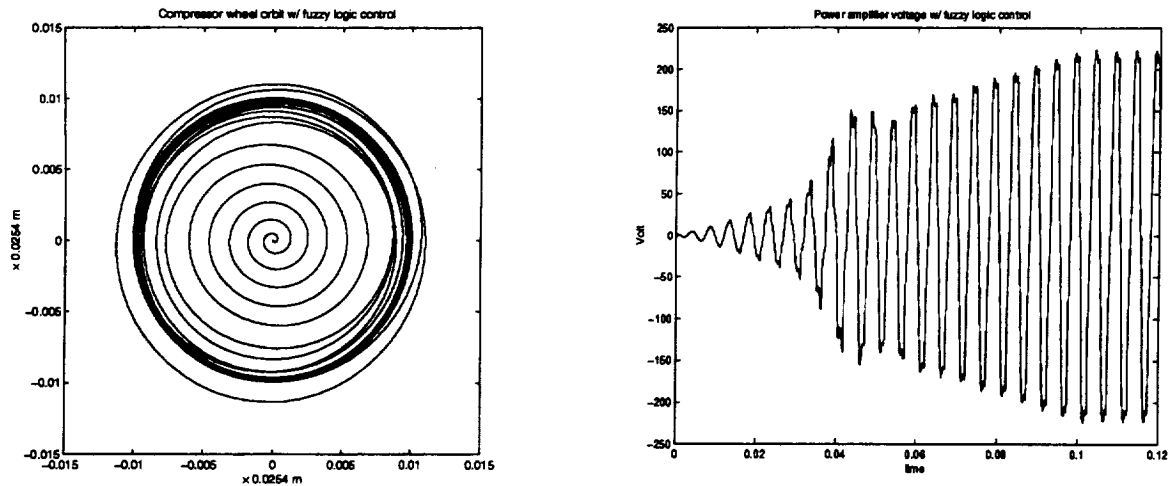


Figure 9. Shaking voltage response with fuzzy logic control stage

6. CONCLUSION

In the closed loop analysis, frequency response with the shaking voltage of 66 v is given for the magnetic front bearing system. When the shaking frequency is 200 Hz, the shaking radius of node 2 reaches 0.29 mm with the designed PD control.

We have also shown that in the transient simulation, the linear model can reach higher shaking orbit radius. When the shaking voltage is as high as 80 volts, the simulation still converges and the orbit radius at node 2 is greater than 0.25 mm. However the linearized force assumptions are shown to be invalid by comparing the results between the linear and nonlinear models.

For the full nonlinear case it is impossible to reach 0.25mm radius with conventional PD controllers. Further increase of the shaking voltage will result in simulation divergence. However, the large shaking amplitudes required for the NASA stall-rig necessitates a fully nonlinear model. Although a linear approach can be used as a preliminary means to analyze the system, it is not appropriate for obtaining accurate results. By employing a fuzzy expert system, it has been shown that the shaking orbit

radius may be increased 50% greater than that with the conventional PD controllers. The fuzzy rule base system used in this approach is very simple and direct, so it is easy to implement on a real time basis.

REFERENCES

- [1] C. Kim, A. B. Palazzolo *et al* 1995 *Transactions of the ASME* 117, 162-170. Eddy current effects on the design of rotor-magnetic bearing systems.
- [2] Ho-seop Jeong *et al* 1994 *Proceed. International Symposium on Mag. Bearings* 4, 23-28. Modeling and control of cone-shaped active magnetic bearing system.
- [3] F. Matsumura *et al* 1986 *IEEE Transactions Magnetics* MAG-22 3, 196-203. System modeling and control design of a horizontal shaft magnetic bearing system.
- [4] Y. Zhuravlyov 1998 *Proceed. International Symposium on Mag. Bearings* 6, 587-596. Linear quadratic optimal control of active magnetic bearings for high speed rotor.
- [5] K. Nonami *et al* 1994 *Proceed. International Symposium on Mag. Bearings* 4, 73-78. μ -Synthesis flexible rotor magnetic bearing control.
- [6] F. Carrere *et al* 1994 *Proceed. International Symposium on Mag. Bearings* 4, 65-72. H^∞ control design of flexible rotor magnetic bearings.
- [7] M. Fujita *et al* 1993 *IEEE Control System Magazine* 13-4, 57-65. Loop shaping based robust control of a magnetic bearing.
- [8] F. Matsumura *et al* 1996 *IEEE Trans. Control System Tech.* 4-5, 484-493. Application of gain scheduled H^∞ robust controllers to a magnetic bearing.
- [9] L. Zadeh 1965 *Information and Control* 8-3, 338-353. Fuzzy sets.
- [10] E. Mamdani 1976 *Int. J. Man-Machine Stud.* 6, 669-678. Advances in the linguistic synthesis of fuzzy controllers.
- [11] K. Tagaki and M. Sugeno 1985 *IEEE Trans. Syst., Man, Cybern.* 15, 116-132. Fuzzy identification of systems and its application to modeling and control.
- [12] H. Koskinen *et al* 1994 *Proceed. International Symposium on Mag. Bearings* 4, 89-93. Fuzzy logic in active magnetic bearing control.
- [13] B. Weidemann *et al* 1994 *Proceed. International Symposium on Mag. Bearings* 4, 59-64. A nonlinear fuzzy control for magnetic bearings without premagnetization.

- [14] J. Hung 1995 *IEEE Trans. on Industry Applications* 31-6, 1492-1497. Magnetic bearing control using fuzzy logic.

APPENDIX

Finite Element Model of Stall-Rig:

No. of Element	DO	DI	E	G	RHO	LEN
1	14 ×25.4	0	2.07e10	6.9e11	7.8	0.7×25.4
2	14 ×25.4	0	2.07e10	6.9e11	7.8	0.7×25.4
3	5.25 ×25.4	3×25.4	2.07e10	6.9e11	7.8	1.25×25.4
4	3.75×25.4	1×25.4	2.07e10	6.9e11	7.8	1.0×25.4
5	3.75×25.4	1×25.4	2.07e10	6.9e11	7.8	1.25×25.4
6	3.75×25.4	1×25.4	2.07e10	6.9e11	7.8	0.5×25.4
7	4.25×25.4	1×25.4	2.07e10	6.9e11	7.8	5/8×25.4
8	8.25 ×25.4	4.8×25.4	2.07e10	6.9e11	7.8	2.5×25.4
9	8.25 ×25.4	4.8×25.4	2.07e10	6.9e11	7.8	3.0×25.4
10	8.25 ×25.4	4.8×25.4	2.07e10	6.9e11	7.8	0.5×25.4
11	6.20 ×25.4	4.8×25.4	2.07e10	6.9e11	7.8	3.0×25.4
12	6.20×25.4	4.8×25.4	2.07e10	6.9e11	7.8	3.0×25.4
13	6.20×25.4	4.8×25.4	2.07e10	6.9e11	7.8	3.0×25.4
14	6.20×25.4	4.8×25.4	2.07e10	6.9e11	7.8	2.75×25.4
15	6.20×25.4	0	2.07e10	6.9e11	7.8	5/8×25.4
16	3.30×25.4	0	2.07e10	6.9e11	7.8	1.75×25.4
17	3.30 ×25.4	0	2.07e10	6.9e11	7.8	1.5×25.4
18	3.30×25.4	0	2.07e10	6.9e11	7.8	1.75×25.4
19	7.30×25.4	0	2.07e10	6.9e11	7.8	5/8×25.4
20	7.30×25.4	0	2.07e10	6.9e11	7.8	5/8×25.4
21	3.50×25.4	0	2.07e10	6.9e11	7.8	1.25×25.4
22	3.50×25.4	0	2.07e10	6.9e11	7.8	0.75×25.4
23	8.25 ×25.4	0	2.07e10	6.9e11	7.8	1.25×25.4

where DO outer diameter, mm
DI inner diameter, mm
E Young's modulus, N/m^2
G elastic shear modulus, N/m^2
RHO mass density, kg/cm^3
LEN length of element, mm

Total number of elements: 23

Total number of nodes: 24

ITERATIVE CONTROL-RELEVANT IDENTIFICATION AND CONTROLLER ENHANCEMENT OF A MIMO MAGNETIC BEARING SYSTEM

Dong-Chul Han, Sang-Wook Lee, Hyeong-Joon Ahn and Sang-Ho Lee

School of Mechanical & Aerospace Engineering, Seoul National University

SUMMARY

The magnetic bearing systems are intrinsically unstable, and need the feedback control of electromagnetic forces with measured displacements. So the controller design plays an important role in constructing high performance magnetic bearing system. In case of magnetic bearing systems, the order of identified model can be high because of unknown dynamics included in closed loop systems - such as sensor dynamics, actuator dynamics - and non-linearity of magnetic bearings. "Identification for control" – joint optimization of system identification and controller design - is proposed to get the limited-order model which is suited for the design of high-performance controller. We applied the joint identification/controller design scheme to MIMO rigid rotor system supported by magnetic bearings. First, we designed controller of a nonlinear simulation model of MIMO magnetic bearing system with this scheme and proved its feasibility. Then, we performed experiments on MIMO rigid rotor system supported by magnetic bearings, and the results shows that the performance of the closed-loop system is gradually improved during the iteration.

INTRODUCTION

Active magnetic bearing (AMB) systems have been widely used for their unique advantages such as: non-contact, lubricant-free operation, the possibility of high rotational speed, and the controllability of the bearing characteristics. Since AMB systems always require the feedback control of magnetic force for stable levitation of a rotor, the characteristics of AMB system is mainly determined by the feedback controller. Therefore, the design of controller plays a significant role in building high performance AMB system.

Since nominal models of AMB systems are generally constructed ignoring the non-linearity of magnetic force, dynamics of sensors and actuators, and the spill-over of a rotor, the identification of AMB systems is

essential to enhance the performance of whole system. So far, identifications of AMB systems have been performed to get experimental values of specific physical parameters, which were current stiffness and displacement stiffness of AMB or poles of open-loop plant. However, the estimation of system parameters in the sense of controller design law is required to achieve better performance.

In these days, the control-relevant identification has become more and more important area of control researchers. An idea has been raised that the model identification and controller design is not performed independently. This has led to the iterative design of model-based controller. While conventional identification methods put emphasis upon getting accurate model, the objective of the control-relevant identification is to get the nominal model that is suitable for the design of a high-performance controller. Various control-relevant identification schemes [1-2] were proposed recently and achieved good results in many industrial applications [3-4].

This paper presents the iterative identification and controller design of a MIMO rigid rotor AMB system. A theoretical model of the system is derived, and the iterative scheme based on LQG criterion is suggested. We verified the feasibility of this scheme through simulations, and performed experiments on a MIMO rigid rotor AMB system. The performance of the closed-loop system is enhanced successively during iterative designs.

MATERIAL AND METHOD

Active Magnetic Bearing

The magnetic force equation near the operating point is approximated by

$$F = k_i \cdot i + k_z \cdot z \quad (1)$$

$$k_i = \frac{\mu_0 N_c^2 A}{g_0^3} i_b, \quad k_z = \frac{\mu_0 N_c^2 A}{g_0^3} i_b^2 \quad (2)$$

where displacement is given by z , input current by i , permittivity in vacuum by μ_0 , the number of coil turns by N_c , the area of actuator pole by A , nominal gap by g_0 , and bias current by i_b , respectively.

A configuration of rigid rotor AMB model is shown in Figure 1 and the theoretical model of a rigid rotor

AMB system using magnetic force equation (1) is described as follows

$$M_b \ddot{z}_b + C_b \dot{z}_b + K_b z_b = f_b \quad (3)$$

$$M_b = \begin{bmatrix} (ml_2^2 + J_x)/(l_1 + l_2)^2 & (ml_1 l_2 - J_x)/(l_1 + l_2)^2 & 0 & 0 \\ (ml_1 l_2 - J_x)/(l_1 + l_2)^2 & (ml_1^2 + J_x)/(l_1 + l_2)^2 & 0 & 0 \\ 0 & 0 & (ml_2^2 + J_y)/(l_1 + l_2)^2 & (ml_1 l_2 - J_y)/(l_1 + l_2)^2 \\ 0 & 0 & (ml_1 l_2 - J_y)/(l_1 + l_2)^2 & (ml_1^2 + J_y)/(l_1 + l_2)^2 \end{bmatrix}$$

$$C_b = \begin{bmatrix} 0 & 0 & 1 & -1 \\ 0 & 0 & -1 & 1 \\ 1 & -1 & 0 & 0 \\ -1 & 1 & 0 & 0 \end{bmatrix} J_z \Omega, \quad K_b = \begin{bmatrix} -K_{x1} & 0 & 0 & 0 \\ 0 & -K_{x2} & 0 & 0 \\ 0 & 0 & -K_{y1} & 0 \\ 0 & 0 & 0 & -K_{y2} \end{bmatrix}, \quad z_b = [x_1 \ x_2 \ y_1 \ y_2]^T$$

$$f_b = [K_{ix1} i_{x1} \ K_{ix2} i_{x2} \ K_{iy1} i_{y1} \ K_{iy2} i_{y2}]^T$$

where m denotes rotor mass, J_x, J_y, J_z polar and diametrical moment of inertia, K_b displacement stiffness of AMB, Ω rotating speed, f_b bearing force and z_b displacement at bearing location.

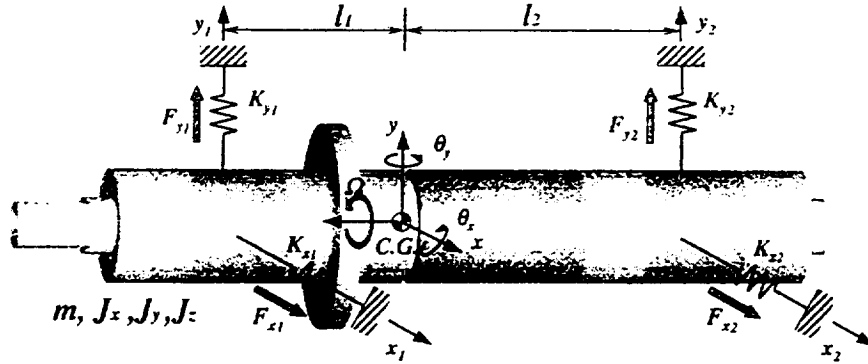


Figure 1. The model of a rigid rotor AMB system

Ignoring the gyroscopic effects, theoretical model above has 4 rigid body modes and these modes give 4 double poles in real-axis, which are symmetric to imaginary-axis.

Control-relevant identification

The basic principle of the control-relevant identification problem is described by the following triangle inequalities, as considered by Schrama [5]:

$$\|J(G_i, C)\| \leq \|J(\hat{G}, C)\| + \|J(G_0, C) - J(\hat{G}, C)\| \quad (4)$$

$$\|J(G_0, C)\| = J^{ach} : \text{the achieved performance} \quad (4-a)$$

$$\|J(\hat{G}, C)\| = J^{des} : \text{the desired performance} \quad (4-b)$$

$$\|J(G_0, C) - J(\hat{G}, C)\| = J^{id} : \text{the identification criterion} \quad (4-c)$$

where G_0 means true plant, \hat{G} estimated model of true plant, and C the controller.

Basically, the objective of all controller design is the minimization of cost function (4-a), which is the left part of equation (4). But, that is unrealizable since the exact description of a true plant G_0 is not available. The aim of the control-relevant identification is the minimization of the right part of equation (4), which means the upper bound of the achieved performance cost (4-a). It can be done by the minimization of both (4-b) and (4-c), but the simultaneous minimization of equations (4-b) and (4-c) is impossible by ordinary identification and control-design method. Therefore, separate optimizations over \hat{G} and over C are performed in an iterative way. The model and controller of i^{th} iteration are obtained by

$$\hat{G}_{i+1}(\theta) = \arg \min_{\theta} \|J(G_0, C_i) - J(\hat{G}(\theta), C_i)\|, \quad C_{i+1} = \arg \min_C \|J(\hat{G}_{i+1}(\theta), C)\| \quad (5)$$

where θ denotes the parameter vector that is estimated in the identification procedure and i means the iteration step.

The iterative identification and control design procedure described above will be modified for LQ criterion. The state-space model of an LQG controller is described as

$$\dot{\hat{x}} = A_c \hat{x} + Hy, \quad u = -K\hat{x} \quad (6)$$

where \hat{x} is estimated state, y system output, H Kalman filter gain, K LQ gain and A_c augmented system matrix, individually.

The control design procedure for LQ criterion minimizes a following cost function.

$$J_{LQG} = \lim_{N \rightarrow \infty} \frac{1}{N} \sum_{t=0}^{N-1} E \{ \hat{x}^T Q \hat{x} + u^T R u \} \quad (7)$$

The identification procedure with LQG criterion minimizes

$$J^{id} = \lim_{N \rightarrow \infty} \frac{1}{N} \sum_{t=0}^{N-1} \{ W_z(z)(y(t) - \hat{y}(t, \theta)) \}^T \{ W_z(z)(y(t) - \hat{y}(t, \theta)) \} \quad (8)$$

, which is equivalent to equation (9) in frequency domain

$$J^{id} = \| W(j\omega)(G_0(j\omega) - \hat{G}(j\omega, \theta)) \|_2^2 \quad (9)$$

$W(s)$ is a control-relevant weighting function in frequency domain and is calculated as

$$W(s) = W_{CR}(s)(I + \hat{G}(s, \theta)C(s))^{-1} \quad (10)$$

where $W_{CR}^T(s)W_{CR}(s) = H^T(sI - A_c)^{-T}(Q + K^T R K)(sI - A_c)^{-1}H$ can be calculated by Schur decomposition.

A flow chart of the iterative identification and control design procedure is described in Figure 2.

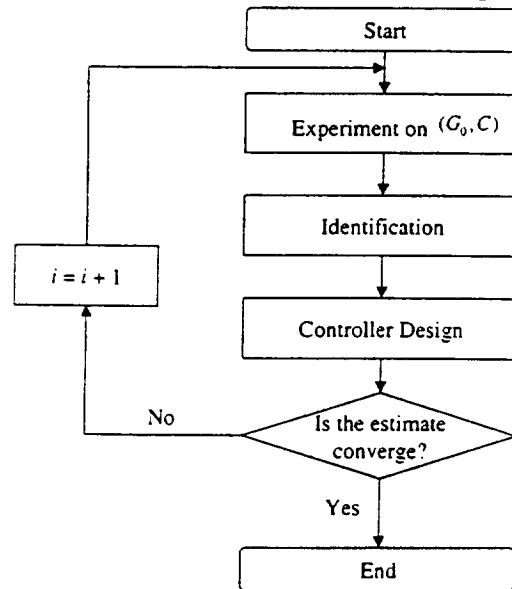


Figure 2. A flow chart of the iterative identification and control design procedure

Frequency domain identification

The averaged frequency spectra of input and output signals are used to get the frequency response function (FRF) of a plant. Experiments are done with 8 different excitation signals. The frequency spectra of input and output signals are $U^{(i)}(j\omega) \in C^{nu \times 1}$, $Y^{(i)}(j\omega) \in C^{ny \times 1}$, $i = 1, 2, \dots, 8$ and nu, ny the number of input and output, respectively. The entire input/output data are defined as

$$Y(j\omega) = [Y^{(1)}(j\omega) Y^{(2)}(j\omega) \dots Y^{(8)}(j\omega)]^T \in C^{ny \times 8} \quad (11)$$

$$U(j\omega) = [U^{(1)}(j\omega) U^{(2)}(j\omega) \dots U^{(8)}(j\omega)]^T \in C^{nu \times 8} \quad (12)$$

Then non-parametric transfer function matrix $G(j\omega) \in C^{ny \times nu}$ can be obtained by [6]

$$G(j\omega) = Y(j\omega)U(j\omega)^+ \quad (13)$$

where superscript + denotes the Moore-Penrose pseudo-inverse.

Frequency-domain curve fitting algorithm using polynomial matrix fractional descriptions (MFD) is used for the identification of MIMO system. The transfer function $\hat{G}(\omega, \theta)$ is described via left MFD.

$$\hat{G}(\omega, \theta) = A(\omega, \theta)^{-1} B(\omega, \theta) \quad (14)$$

A and B denote polynomial matrices as follows.

$$B(\xi, \theta) = \sum_{i=d}^{d+a_b-1} B_i p(\xi)^i, \quad B_i \in R^{ny \times nu}, \quad A(\xi, \theta) = I_{ny \times ny} + \xi \sum_{i=d}^{d+a_a-1} A_i p(\xi)^i, \quad A_i \in R^{ny \times ny} \quad (15)$$

where polynomial matrices are written in terms of a (scalar) polynomial basis

$$p(\xi) \equiv p_0 + p_1 \xi + p_2 \xi^2 + \dots + p_n \xi^n \quad (16)$$

The parameters are estimated via minimizing 2-norm of each element of weighted error matrix

$$\hat{\theta} = \arg \min_{\theta \in \mathcal{R}} \sum \|E^w(\theta)\|_F^2 \quad (17)$$

The $(i, j)^{th}$ component of weighted error matrix is parameterized as follows.

$$E^{ij}(\omega, \theta) = [W_{oi}(\omega)A(\omega, \theta)^{-1}]^T [G^{im}(\omega) - \bar{A}^{ij}(\omega, \theta)G^{jm}(\omega) - B^{im}(\omega, \theta)]W_{oj}(\omega) \quad (18)$$

where $A(\xi, \theta) = I_{n \times n} - \bar{A}$, $\bar{A}^{ij}(\omega_k) = \phi(\omega_k) \cdot [A_0^{ij} \ A_1^{ij} \ \dots \ A_{n_s}^{ij}]$, $B^{ij}(\omega_k) = \psi(\omega_k) \cdot [B_0^{ij} \ B_1^{ij} \ \dots \ B_{n_s}^{ij}]$
 $\psi(\omega_k) = [p^0(\xi(\omega_k)) \ p^1(\xi(\omega_k)) \ \dots \ p^{n_s}(\xi(\omega_k))]$, $\phi(\omega_k) = -\xi(\omega_k) [p^0(\xi(\omega_k)) \ p^1(\xi(\omega_k)) \ \dots \ p^{n_s}(\xi(\omega_k))]$

The equation (17) above are converted to general least squares form.

$$\hat{\theta} = \arg \min_{\theta \in \mathbb{R}} \sum \|Y_{wt} - P_{wt} \cdot \theta\|_F^2 \quad (19)$$

Y_{wt} is denoted by

$$Y_{wt}(\omega_k) = \begin{bmatrix} \{Y_w^{1*}(\omega_k)\}^T \\ \vdots \\ \{Y_w^{p*}(\omega_k)\}^T \end{bmatrix}, \text{ where } Y_w^{ij} = [W_{wt}^{i1} \ W_{wt}^{i2} \ \dots \ W_{wt}^{in}], \begin{bmatrix} G^{11} & G^{12} & \dots & G^{1n} \\ G^{21} & G^{22} & \dots & G^{2n} \\ \vdots & \vdots & \ddots & \vdots \\ G^{p1} & G^{p2} & \dots & G^{pn} \end{bmatrix} \cdot \begin{bmatrix} W_i^{1j} \\ W_i^{2j} \\ \vdots \\ W_i^{nj} \end{bmatrix} \quad (20)$$

and P_{wt} is

$$P_{wt}(\omega_k) = \begin{bmatrix} \{P_w^{1*}(\omega_k)\}^T \\ \vdots \\ \{P_w^{p*}(\omega_k)\}^T \end{bmatrix} = W_{wt} \otimes [(W_i)^T \otimes \psi \ (G \cdot W_i)^T \otimes \phi] \quad (21)$$

where $W_{wt}(\omega_k) = W_o(\omega_k)A(\xi, \theta)^{-1}$, $\{P_w^{i*}(\omega_k)\}^T = W_{wt}^{i*} \otimes [(W_i)^T \otimes \psi \ (G \cdot W_i)^T \otimes \phi]$, \otimes is Kronecker product.

First, SK algorithm based on QR factorization [7-8] estimates the approximate value of system parameter. Then, using this approximate estimate as the initial value, nonlinear least square problem is solved with MATLAB optimization toolbox function [9].

RESULT

Simulations

Eight different excitation signals are generated using multi-sine of random phases. In general, the amplitude of an excitation signal should be as large as possible to ensure sufficient signal-to-noise ratio (SNR). Except safety or economic reasons, there are two important limitations of input amplitude on AMB – linearity region and slew rate of magnetic actuator. The slew rate of magnetic bearing rotor system can be described by (22)

$$\frac{di}{dt} = \frac{2g_0}{\mu_0 N_c A} [V_s - (i_b + i)(R_c + R_f + R_{FET})] \quad (22)$$

where V_s is supply voltage, R_c coil resistance, R_f the resistor connected to FET, and R_{FET} FET resistance.

A nonlinear AMB rotor model is constructed by using MATLAB Simulink and the proposed control-relevant identification scheme is applied through the flow chart of Figure 2. Estimated model parameter converges as iterations are repeated. Although **identified model** differs from theoretical model, it can be considered as the approximated model that is suitable in the control-design point of view. The eigenvalues of identified plant are given in Table 1 and the values of cost function J^{uch} and J^{id} at each iteration are shown in Table 2.

Table 1. Eigenvalue of identified system matrix \hat{A} (Simulation)

	1 st eigenvalue	2 nd eigenvalue	3 rd eigenvalue	4 th eigenvalue
Nominal	627.68	-627.58	493.05	-493.05
Step1	649.27	-737.29	550.50	-608.09
Step2	648.83	-791.93	552.66	-633.86
Step3	648.83	-791.93	552.63	-633.87

Table 2. The cost function value (Simulation)

	Step1	Step2	Step3
J^{uch}	4.69	4.58	4.58
J^{id}	0.63	0.58	0.58

The parameters of identified plant converge in 3rd step, and the cost function value of the achieved closed-loop performance J^{ach} decreases. This results from the reduction of the identification cost function, J^{id} .

The number of iteration is only two, which is relatively small in general control-relevant identification scheme. This is because control-relevant schemes are effective in case that high-order plant should be approximated to low-order model for the design of reduced-order controller. The simulated plant can be sufficiently described as the model of 2nd order, so the decrease of cost function is not drastic. But the enhancement of performance still can be shown.

Experiment

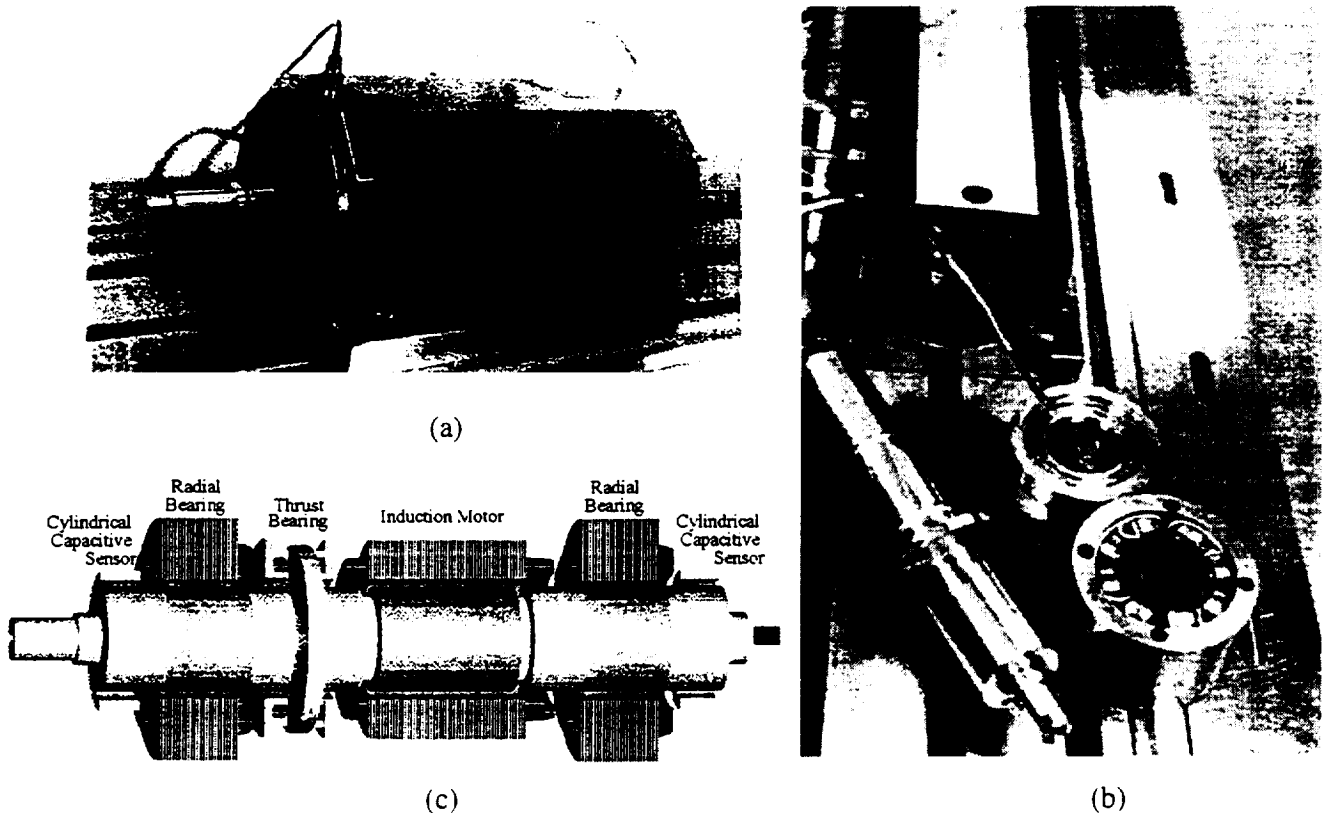


Figure 3. Rigid rotor AMB system (a) assembly (b) elements (c) schematics

A rigid rotor AMB experimental setup consists of two AMB units with built-in cylindrical capacitive sensor, thrust bearing, rigid rotor, and induction motor, as shown in Figure 3 [10]. The AMB unit is designed for ease of assembly like a commercial bearing. The cylindrical capacitive sensor and electromagnetic actuator are embedded in the housing of the AMB unit as shown in Figure 3(b). In case of wiring, small connectors are used for the convenience of assembling and machining. The rotor has outer radius of 39mm at the AMB unit and the maximum rotational speed is 60000 rpm. The water jacket is embedded around 3kW induction motor. TMS320C44 40MHz DSP board with 8 ch. 16 bit, 200kHz AD/DA is used.

Experiments are performed through the same procedure as simulation. The eigenvalues of the identified system matrix are shown in Table 3, and cost function values are shown in Table 4.

Table 3. Eigenvalue of identified system matrix \hat{A} (Experiment)

	1 st eigenvalue	2 nd eigenvalue	3 rd eigenvalue	4 th eigenvalue
Nominal	627.58	-627.58	493.05	-493.05
Step1	629.12	-618.82	559.66	-565.99
Step2	612.84	-588.46	533.88	-544.18
Step5	613.82	-588.07	541.99	-533.62
Step8	616.58	-587.55	535.76	-537.47
Step10	615.90	-592.75	534.38	-533.95

Table 4. The cost function value (Experiment)

	Nominal	Step1	Step2	Step5	Step8	Step10
J^{ach}	9.33	7.28	7.26	7.24	7.24	7.22
J^{id}	1.25	0.813	0.591	0.544	0.551	0.539

Measured FRF and identified transfer functions are shown in Figure 4. Because of unknown dynamics of rotor system and other factors, nominal transfer function is not matched well with measured FRF of system. As shown in Figure 4, the identified model (step 7) with the control-relevant scheme does not look better than the model estimated without control-relevant weighting (step 1). But the decrease of the achieved cost function J^{ach} (Table 4) proves that the identified model is appropriate for high-performance controller design. Figure 5 shows the relative error of the closed-loop transfer function, $T(s)$ between real and identified plant. The relative error decreases as the iteration steps increase. The experimental results confirm the simulation results that the iterative scheme can enhance system performance.

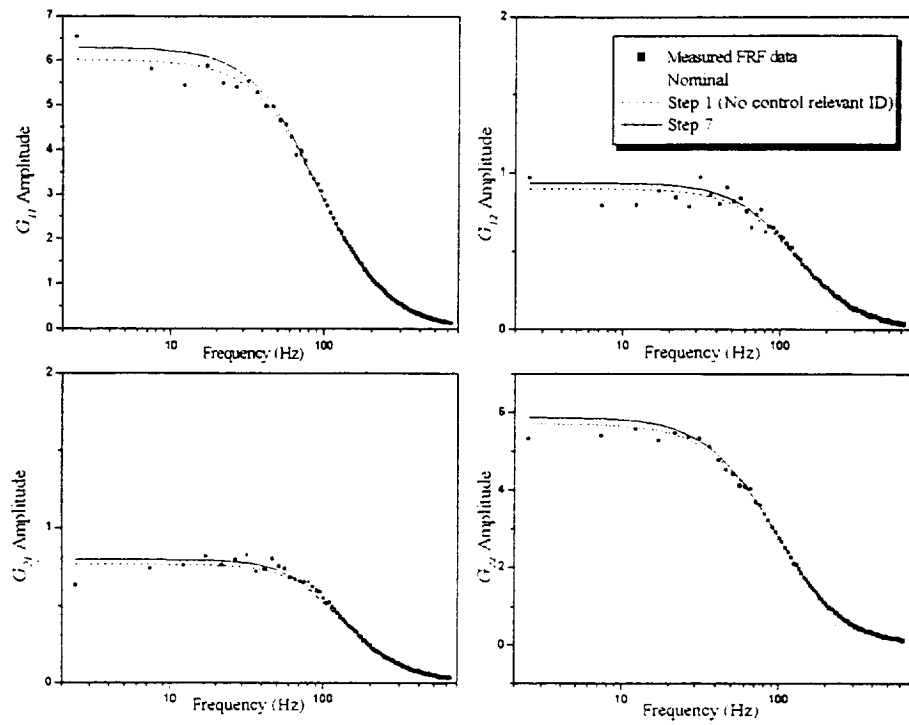


Figure 4. Measured FRF and identified models

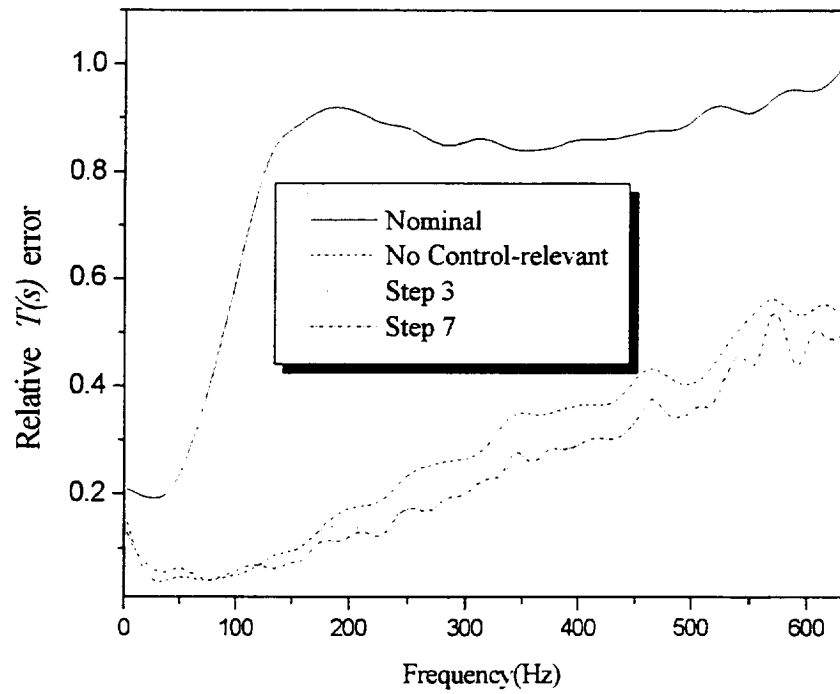


Figure 5. Relative errors of closed-loop transfer function

CONCLUSION

We applied the joint identification/controller design scheme to MIMO rigid rotor system supported by magnetic bearings and the performance of the closed-loop system is improved sequentially during the iteration. Although the rigid rotor AMB system is not significantly high-order plant, the control-relevant identification method gives better performance. In case of high-order system, such as flexible rotor supported by AMB, the improvement of performance may be more conspicuous.

For the future work, the control-relevant identification with other robust control design scheme – H_∞ or μ control synthesis – will be developed. Also a considerable amount of work is needed to apply this scheme to a flexible rotor AMB system.

ACKNOWLEDGEMENT

This work is supported by Turbo and Power Machinery Research Center and Institute of Advanced Machinery and Design in Seoul National University.

REFERENCE

1. Z. Zang; R. Bitmead; and M. Gevers: "Iterative Weighted Least-squares Identification and Weighted LQG Control Design", *Automatica*, 1995
2. R. G. Hakvoort; R. J. P. Schrama; and P. M. J. Van den Hof: "Approximate Identification with Closed-loop Performance Criterion and Application to LQG Feedback Design", *Automatica*, 1994
3. R. A. de Callafon; P. M. J. Van den Hof; and M. Steinbuch: "Control Relevant Identification of a Compact Disc Pick-up Mechanism", *Proc. of the IEEE Conference on Decision and Control*, 1993
4. P. Michelberger; J. Bokor; L. Palkovics; E. Nandori; and P. Gaspar: "Iterative Identification and Control Design for Uncertain Parameter Suspension System", *IFAC Transportation Systems*, 1997

5. R. J. P. Schrama: "Approximate Identification and Control Design with Application to a Mechanical System", Ph.D. Thesis, Delft University of Technology, 1992
6. R. Pintelon; P. Guillaume; G. Vandersteen; and Y. Rolain: "Analyses, Development, and Applications of TLS Algorithms in Frequency Domain System Identification", SIAM J. Matrix Anal. Appl., 1998
7. D. S. Bayard: "High-order Multivariable Transfer Function Curve Fitting: Algorithms, Sparse Matrix Methods and Experimental Results", Automatica, 1994
8. R. A. de Callafon; D. de Roover; and P. M. J. Van den Hof: "Multivariable Least Squares Frequency Domain Identification Using Polynomial Matrix Fraction Descriptions", Proc. of IEEE Conference on Decision and Control, 1996
9. MATLAB Optimization Toolbox: User's Guide, MathWorks, 1997
10. H. Ahn; S. Lee; and D. Han: "Precision AMB Spindles with Cylindrical Capacitive Sensors", Proc. of 10th World Congress on TMM, 1999

Session 4 -- Magnetic Suspension in Wind Tunnels

Chairman: Colin P. Britcher
Old Dominion University (ODU)

APPLICATION OF MAGNETIC SUSPENSION AND BALANCE SYSTEMS TO HYPERSONIC WIND TUNNEL TESTING

Andrew K. Owen
Department of Engineering Science
University of Oxford
Oxford, UK

SUMMARY

Wind tunnel model sting and shroud interference effects can be significant especially when testing small slender models which are required to simulate higher Knudsen number flows. Indeed, the presence of a sting of any size complicates all flowfield calculations since the model/sting geometry must also be numerically modeled.

Thus, in an attempt to generate reliable low density aerothermodynamic data on test models in flows closer to the flight test ideal, the University of Oxford Low Density Wind Tunnel was recommissioned for an extensive series of experiments in which a magnetic suspension and balance system was used to obtain sting and shroud free model data. Test data were obtained over wide ranges of freestream Mach ($M = 6 - 9$) Knudsen numbers (.001-0.3) on a wide variety of half angle cones at angle of attack, axially aligned cylinders of varying aspect ratio, and a model of the NASA Aerobrake vehicle.

In this paper, the critical components and functions of the magnetic suspension and balance system along with the levitation and test measurement procedures will be described. Techniques used to achieve model stability through the active control of lift, pitch and drag, and lateral stability, including suitable shaping of the magnetic field, and strategic placement of ferromagnetic material within the test section will be discussed. Coil placement, coil current control loop, and the interactive magnetic field and optical control procedures required for successful levitation will also be described. Details of the optical model position detection and feedback system which were developed for both conical and axisymmetric model levitation and testing will also be presented along with the procedures developed for drag calibration and measurement. Some of the data that were acquired during the program will also be presented and they include: Aerodynamic heat transfer and recovery factor measurements on slender cones, and the drag data obtained for the NASA Aerobrake vehicle.

MAGNETIC SUSPENSION SYSTEM DESCRIPTION

The Oxford University magnetic suspension and balance system in its basic form was designed and built by Haslam-Jones ('78) to measure cone drag in the Oxford University Low Density Wind Tunnel (Figure 1).

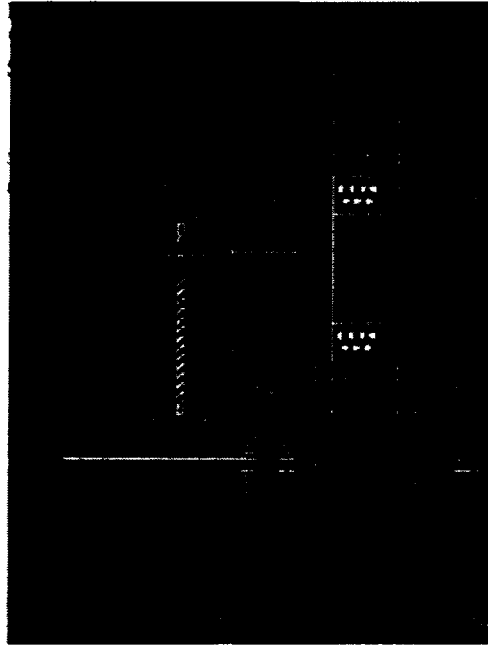


Figure 1 Magnetic Suspension System and Traversing Mechanism

A view of a levitated cone is shown in Figure 2. This view is looking at an angle of 45° towards the upstream direction with the cone in the centre of the test section. There was active control of lift pitch and drag, together with an inherent lateral stability due to suitable shaping of the magnetic field. This shaping was performed by the strategic placement of a ferromagnetic material within the test section resulting in a component of field towards the centre of the test section. This material can be seen at the corners of test section in Figure 2. The drag coils were split into front coils and rear coils which typically had 30 amps divided between them.

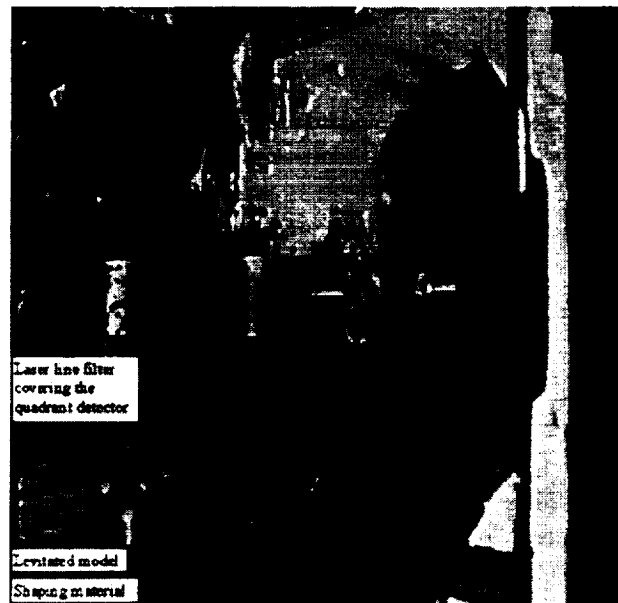


Figure 2 Cone Levitated in Test Section

They are located around the test section and were used to magnetise the model and maintain its axial location. The difference between the front and rear drag coil currents produced an axial gradient of the axial field component, while maintaining constant magnetisation of the model. With the drag coils magnetising the model, the lift and pitch coils, all located on the same horseshoe shape steel core, acted on the model as a magnetic dipole (Figure 3).

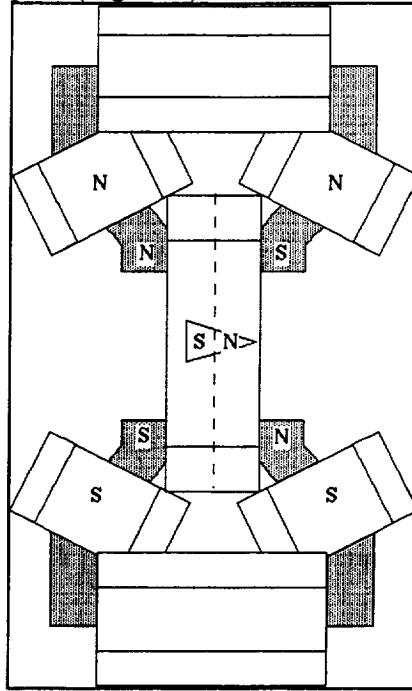


Figure 3 Magnetic fields

The pitch coils produced a uniform vertical field creating a pitching moment and the lift coils superimposed a horizontal gradient on this vertical field component to produce lift. The magnetic fields were controlled by Proportional, Integral, Differential (PID) analogue electronics with feedback provided by optical detection of the model position.

Within the vacuum chamber there is no effective inherent cooling other than radiation, therefore all of the magnetic coils were enclosed in water tight casings, and cooling water was continuously flowing through the system, preventing the coils from overheating.

This basic magnetic field coil construction was built by Haslam-Jones, as already mentioned, and essentially remained unaltered. In addition, the PID electronics was also that originally employed. However, the model detection system was completely renewed in order to perform the more advanced experiments undertaken by the author. This was made possible due to the new opto-electronic devices now available.

OPTICAL DETECTION SYSTEM

The original optical detection system consisted of 4 individual photodiodes arranged in the pattern shown in Figure 4.

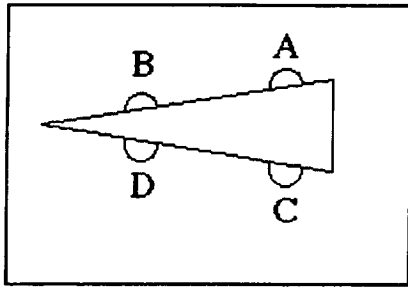


Figure 4 Original Detection System

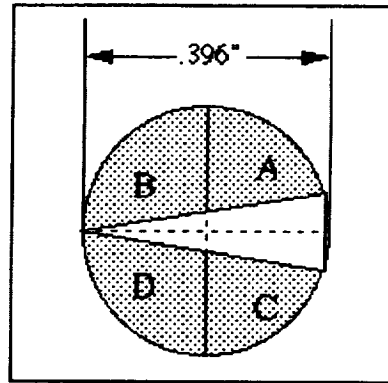


Figure 5 Modified Detection System

The physical size of the photodiodes restricted the size of cones which could be suspended. By replacing the existing 4 photodiodes with one quadrant photodiode, there was virtually no restriction on the minimum model size (Figure 5), and since the new detector worked in the same manner as the original individual photodiodes, no complex modification of the control circuits was required. The original incandescent light source was replaced with a low power (1 mWatt) class III laser diode ($\lambda = 570 \text{ nM}$), and the quadrant detector was covered by a laser line filter, which eliminated the interference from ambient light which was a problem with the original incandescent light source. Since the laser diode is a source of unvarying light intensity, there was no longer a requirement to monitor the light intensity.

The laser beam traversed through the test section and over the model by a series of mirrors as shown in Figure 6. The model position was found by comparing the signals of the quadrant detector illuminated by the laser.

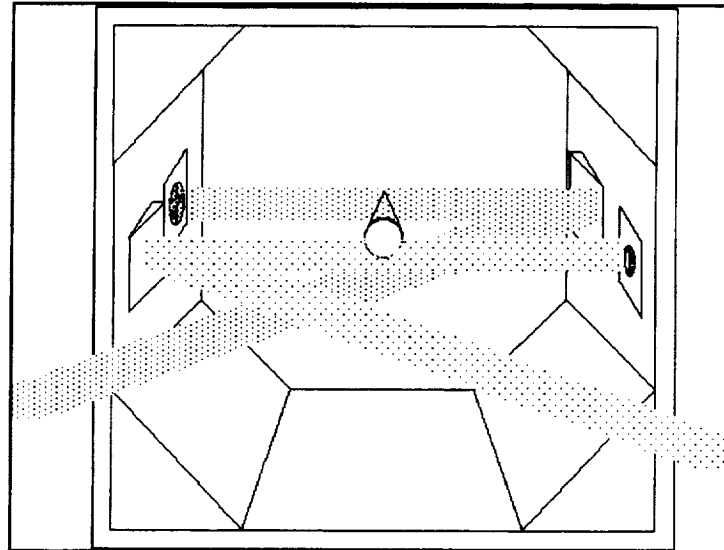


Figure 6 Test Section

Using the notation in Figure 5, the model was said to be in the null position when there was an equal signal from all four quadrants. This position was set by placing the model in approximately the right position and adjusting the potentiometers associated with each quadrant until equal outputs were observed. Axial movement of the model affected all four quadrants similarly, ie backward movement showed an increase in light signal on all four, while a forward movement showed a decrease in light level. For solely vertical movement, the outputs of the two lower quadrants were equal as were the

outputs of the two upper diodes, ie upward movement decreases the signal from the top two diodes, while increasing the lower ones. Pitching caused opposite pairs to behave the same way, ie pitching upwards caused the output of the front top quadrant and the rear bottom quadrant to decrease, with the output of the other two diodes increasing. The original control signals were as follows:

Drag	$A + B + C + D + E$
Lift	$(A + B + 5E) - (C + D)$
Pitch	$(B + C + 5E) - (A + D)$

The fifth diode (E) was used to monitor the overall light level intensity, and was replaced with a constant voltage signal since the laser is a source of essentially constant intensity.

The additional benefit of this new system is that it enables position detection

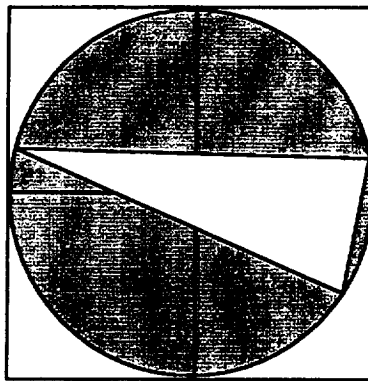


Figure 7 Model at Non-Zero Angle of Attack

of cones at non-zero angles of attack. Figure 7 shows the orientation of a model at non-zero angle of attack. Following the nomenclature of Figure 5, and the control signals described above, it can be seen that the same criteria apply. The maximum angle of attack was therefore limited by the pitch coil current distribution. This distribution is discussed in the appendix on the operational procedure of the Magnetic Suspension System.

NON-CONICAL MODELS

The optical system also has a removable second laser diode, and single photodiode detector for use with non-conical models (Figure 8).

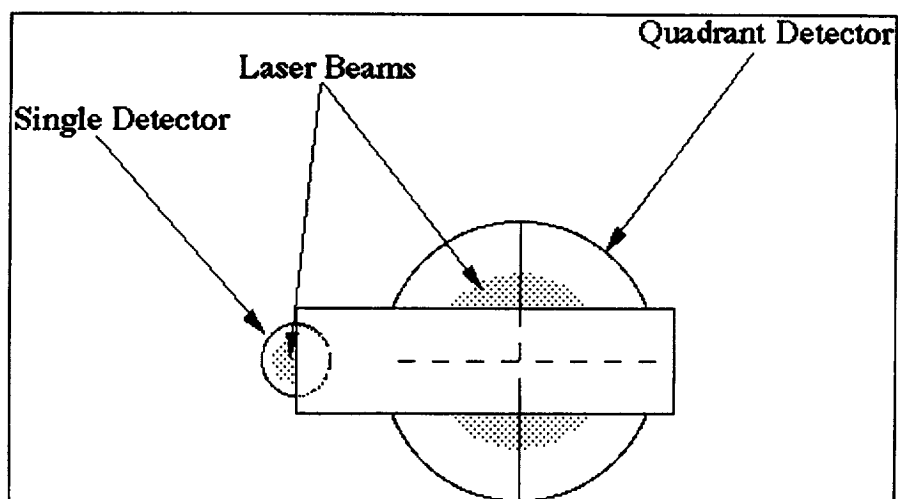


Figure 8 Non-Conical Model Position Sensing

This additional system was used to detect the rear of the model and replaced the above mentioned drag control signals with the output from the single photodiode.

MODEL STABILITY

The Magnetic Suspension System has active control of drag lift and pitch. There was no active control of yaw, roll, or lateral position. Yaw was stabilised by the drag coils creating a field in the axial direction. This field induces a moment and magnetic field within the model which produced a stabilising yaw moment if the model axis was misaligned with the balance axial direction. Roll was seen to be of little consequence to the bodies of revolution tested, and was, therefore, not controlled at all. However, roll could be used to determine viscous terms by monitoring the roll speed as a function of time whilst the model was suspended. The lateral position was maintained by suitable shaping of the axial magnetic field. By placing ferromagnetic material in strategic positions in the test section, a component of force was created towards the centre.

CALIBRATION TECHNIQUE

The magnetic suspension and balance system is used to measure the aerodynamic forces applied to a model under test conditions. The forces on a suspended model are balanced by the magnetic force required to hold the model in a stationary position relative to the flow. This magnetic force comes about from a change in the distribution of current in the two drag coils. A calibration procedure is required to relate the coil currents to the forces applied to a model. Previously, the calibration procedure entailed glueing the end of a light thread to a model and then tying small weights to the other end which was draped over a pulley, thus applying an axial force on the model. This procedure is quite straightforward and, although laborious, produces a fairly accurate calibration. The drawbacks are that this technique inevitably suffers from the effects of friction and pendulum movements of the hanging weights. A new technique was developed that has no errors due to friction.

The entire balance is tilted with a hydraulic jack so that the mass of the model itself is used in the calibration, both techniques are shown in Figure 9.

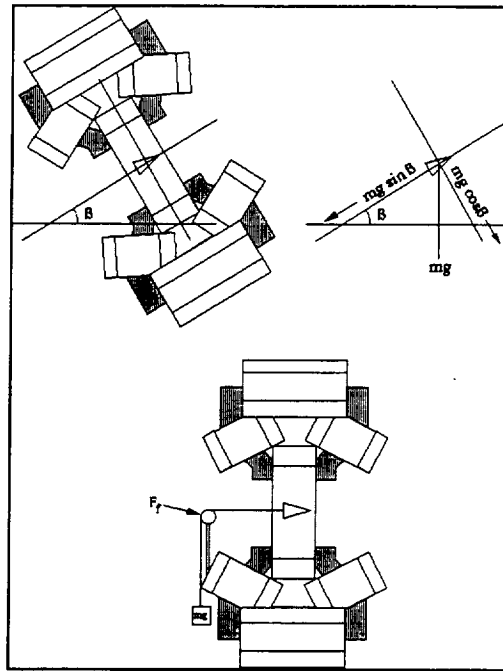


Figure 9 Calibration Methods

The angle to which the balance is rotated is measured on an inclinometer fixed to the balance and has an accuracy of one minute. The angle and the difference in the two drag coils are logged in the data acquisition system. The procedure is repeated at several different angles and a calibration is taken from the slope of the resulting line. A comparison of the two techniques is shown in Figure 10.

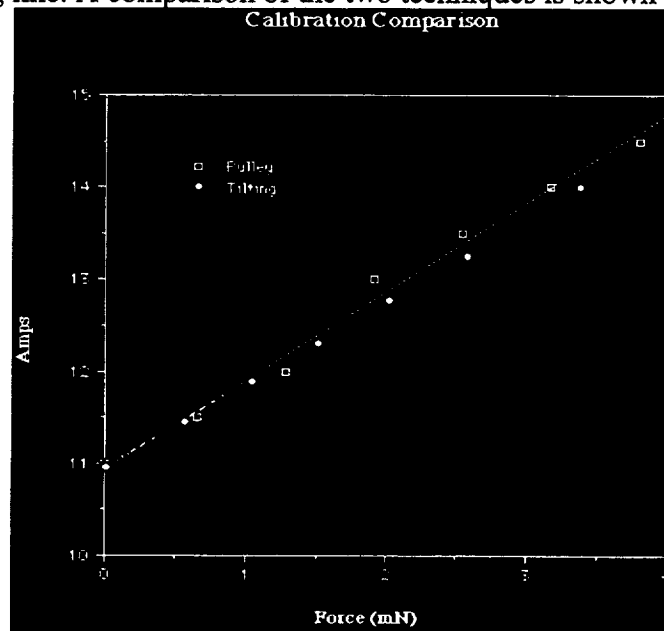


Figure 10 Calibration Comparison

It can be seen that there is a very small difference in the two procedures. However there is little scatter in the tilting calibration, and this procedure proved to be more practical.

A typical calibration done before and after a run is shown Figure 11, which demonstrates the repeatability of the drag calibration procedure.

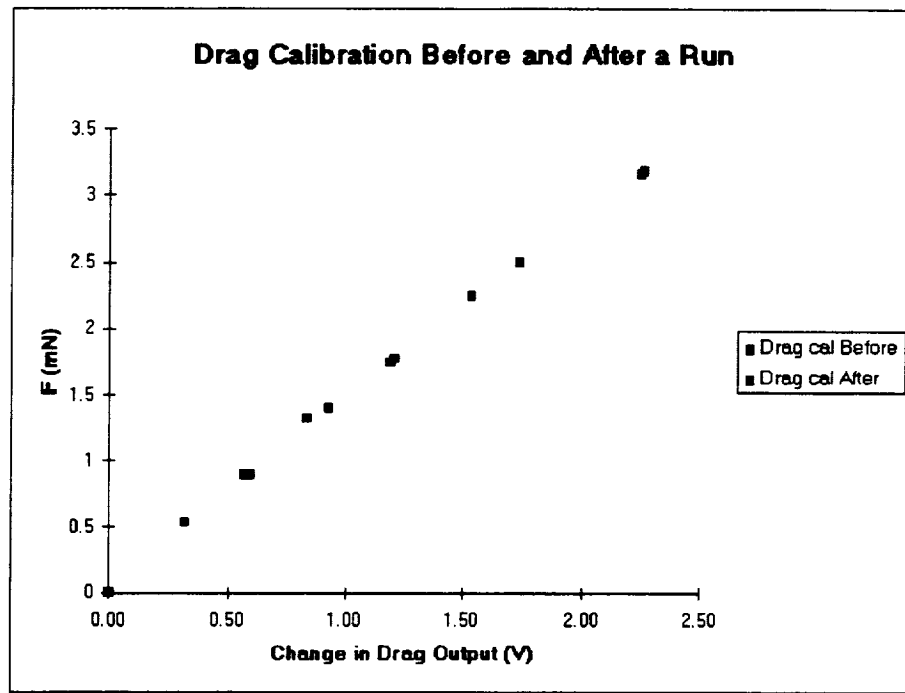


Figure 11 Drag Calibration Before and After a Run

A comparison of calibrations obtained for a cone at varying angle of attack is shown in Figure 12.

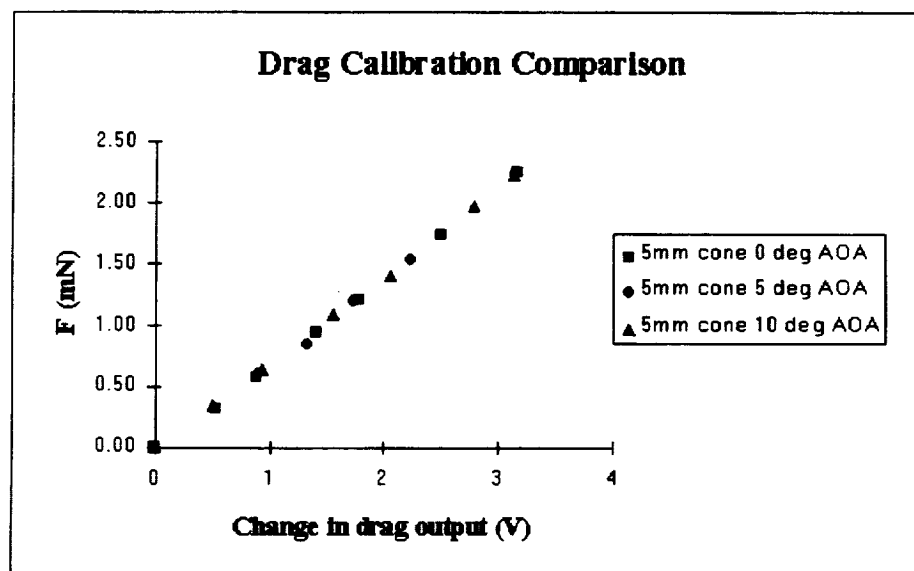


Figure 12 Calibration comparison of a cone at 3 different angles of attack

It can be seen that there is essentially no difference in the calibration with the different angles of attack. This was taken to be true on all subsequent testing of cones at angles of attack.

HEAT TRANSFER AND RECOVERY TEMPERATURE MEASUREMENTS

The total heat transfer and recovery temperature of a cone have been measured while the model was suspended. The heat transfer was to be measured using calorimetry techniques whereas the recovery temperature was found from the equilibrium temperature. The model temperature was measured remotely utilising liquid crystals.

The following technique was used to measure the convective and radiative heat transfer rates using the temperature sensitive liquid crystals. The model temperature was measured by observing the colour of the liquid crystal on the cone as previously stated. The model was suspended in the magnetic balance and then heated in a vacuum to a temperature above the colour play of the liquid crystals. The cone models had a good thermal conductivity so their internal temperature was essentially uniform and the models acted as calorimeters. With the test section at the operating background pressure and with no flow established, the heater was removed and the model was allowed to cool radiatively. Using the liquid crystal calibration, a comparison was made with the cooling experiment to determine accurate model temperature. With this procedure it was possible to obtain a history of model temperature against time, Figure 13. With a relatively simple analysis, the radiative and convective heat transfer coefficients can be calculated.

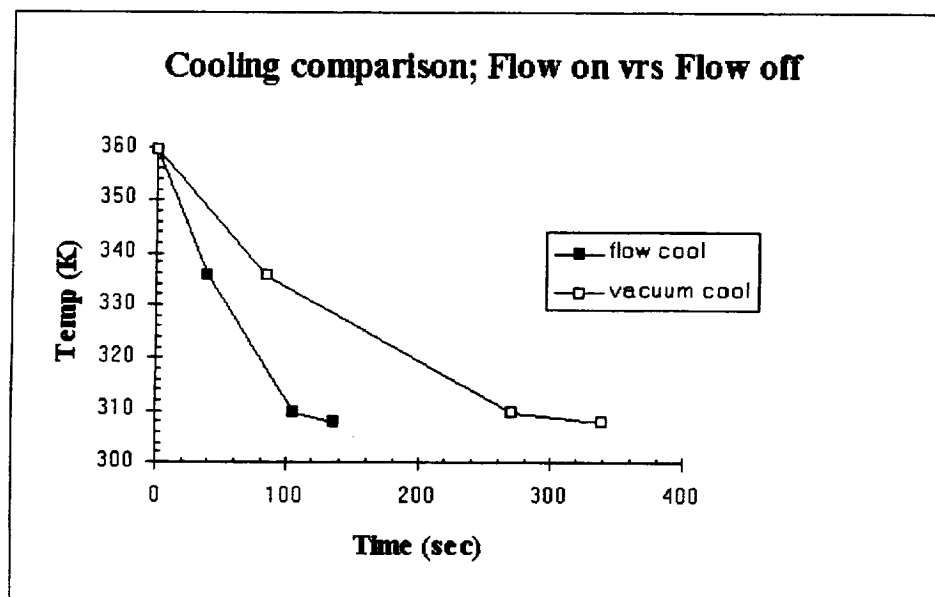


Figure 13 Cooling Rates

A technique for determining the recovery temperature of a levitated cone has also been developed. The procedure involves coating the model with temperature sensitive liquid crystals having colour play temperatures around those of the expected recovery temperature.

In the present experiments, the recovery factor for a 6.5 degree half angle silver steel cone has been found in a low density nitrogen flow at both zero incidence and at 10 degrees angle of attack in a Mach 5.4 flow. The cone base was covered with three temperature sensitive liquid crystals, with colour play temperatures of 10, 15, and 22 degrees C. The stagnation chamber was heated until the 22 degree crystal colour play had been exceeded so that the model temperature was above 25 degrees C. The flow stagnation chamber was then allowed to cool and the model temperature decreased accordingly. By monitoring the liquid crystal colour changes, along with the corresponding stagnation temperature, the recovery factor could be deduced. The model temperature corresponds to the colour of the liquid

crystals during their color play. A graph of stagnation temperature vs. model temperature is shown in Figure 14 for the two models tested at zero and 10° angles of attack (AOA).

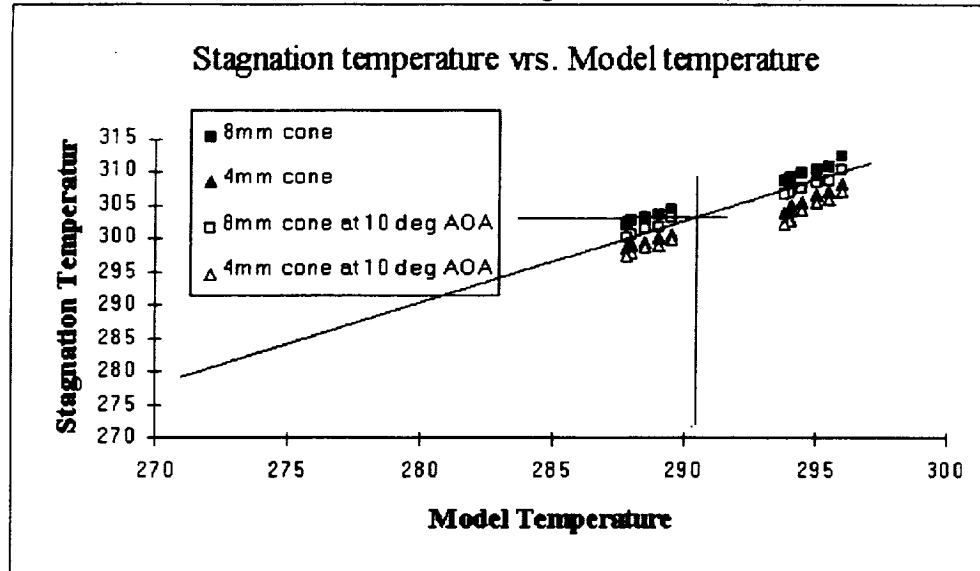


Figure 14 6.5 degree cone model cooling in heated Mach 5.4 flow

To find the recovery factor, shown in Figure 14, a point on the line where the model temperature is equal to the chamber wall temperature is taken. This is done so that there is no effect of radiation to or from the chamber wall.

NASA AEROBRAKE

Aero-assisted space transfer vehicles have three primary components: the aerobrake, the payload, and the propulsion unit. Flowfield interaction with and between these elements can have significant effects on drag, vehicle stability, and allowable payload size and shape. Of particular importance is the interaction of the near wake with the payload compartment. Consequently, precise determination of drag and wake structure are critical issues for aerobrake design. Unfortunately, the heating and aerodynamic forces which result from the interactions between the payload and the near wake are not well understood. Also, available experimental data are not sufficient for design purposes nor sufficient to validate CFD models. The few data which are available are contaminated to unknown degrees by sting or shroud interference or model wire suspension effects. In particular, the most recent direct simulation Monte Carlo (DSMC) calculations of Moss et al ('95) indicate that considerable sting/wake interference effects call into question conventional sting mounted model experimental data obtained in low density hypersonic wind tunnels at CNRS Meudon and DLR Gottingen. These data, generated in support of AGARD Working Group 18, are known to be influenced by model support interference. As a result, additional calculations are needed to explore the sensitivity of the wake to sting effects. Reliable experimental and prediction design methods will be essential to the success of future space missions. This will require new interference free test results which will provide unique test cases for the validation of DSMC calculations and predictions generated by solutions of the rarefied forms of the Navier-Stokes equations.

The Aerobrake model used for testing is shown in Figure 15.



18 mm base diameter of the Aerobrake model. This more than satisfied the AGARD guidelines for sting interference, and set the Knudsen number, based on model base diameter, in the range between

0.005 and 0.01. The Aerobrake was made of a light non-ferromagnetic material, balsa wood, and the afterbodies were constructed of mild steel. A picture of the Aerobrake in suspension can be seen in Figure 16. This view of the Aerobrake is taken from a downstream location through the test section. The present results of the drag on the Aerobrake are shown in Figure 17, and are compared with DSMC results of Gilmore et. al. ('94) for the same configurations. A unique feature is the decrease in C_d with increasing Kn , evident in both the experimental data and the DSMC predictions. This trend is opposite to that which has been experienced with the slender cones, and is attributed to a negative shear component acting along the sting. This shear component is a result of the recirculating region reattaching along the sting, and acts in an upstream direction. The trend could also be associated with an increase in base pressure.

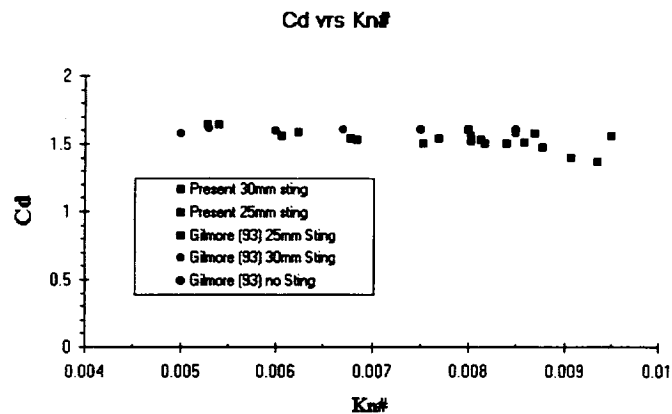


Figure 17 Experimental Aerobrake Drag Results Compared with DSMC Predictions

In Figure 18 the data are compared with C_d results for the Mars Pathfinder calculated from the data collected during its decent into the Martian atmosphere in July 1997.

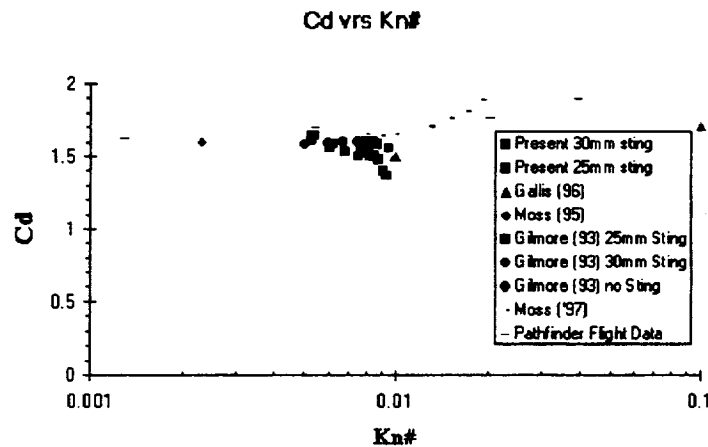


Figure 18 Experimental Aerobrake Drag Results Compared with Mars Pathfinder Flight Data

The decrease in C_d with increasing Knudsen number is also evident in the drag coefficient shown in Figure 19 computed from the Viking 1 pressure and acceleration data. Viking 1 also had a 70 degree blunt nose cone and entered the Martian atmosphere in June, 1976. This effect on Viking has been attributed, by NASA, to a departure from chemical equilibrium with the increase in altitude which results in a reduction in pressure coefficient and corresponding decrease in drag coefficient. This explanation was concluded in 1975 from experiments in the Langley Expansion Tube facility by C.

Miller, (Blanchford et. al. ('97)). At even higher altitudes rarefied-flow effects begin to dominate and C_D rises again.

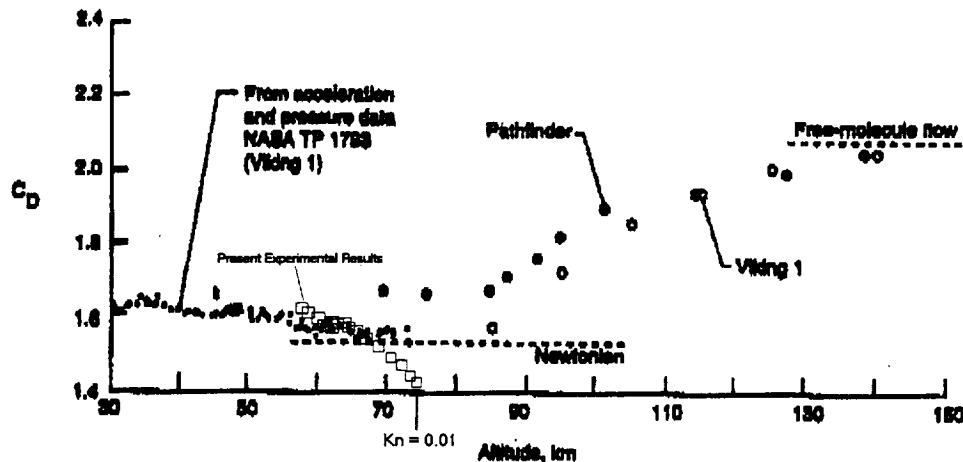


Figure 19 Viking 1 drag coefficient vs altitude from flight measurements and DSMC simulations along with Pathfinder drag coefficient predictions from DSMC simulations (from Blanchford et al '97) and including the present experimental results

The present data shows a decreasing C_D with increasing Kn over the range tested and this appears to be consistent with available flight data both from Pathfinder and Viking. The present experimental C_D values are a little below those of the CFD. However, this trend appears to be supported. The mechanism for the decrease is still the subject of investigation, although from the low enthalpy results here, and the CFD predictions, it does appear that it is more of an aerodynamic effect rather than an effect due to chemical non-equilibrium.

REFERENCES

1. Haslam-Jones, T.F. (1978) "*Measurements of the Drag of Slender Cones in Hypersonic Flow at Low Reynolds Numbers Using a Magnetic Suspension and Balance*," Oxford University Report 1235/78
2. Moss, J.N., Price, J.M., and Dogra, V.K.(1995) "*DSMC Calculations for a 70 degree blunted cone at 3.2 km/s in nitrogen*," NASA TM 109181
3. Gilmore, M.R., Owen, A.K., and Jones, T.V. (1994) "*70° Aerobrake Vehicle plus Afterbody in Hypersonic Rarefied Nitrogen Flow*," Rarefied Gas Dynamics, 19th Symposium
4. Blanchard, R.C., Wilmoth, R. G., Moss, J. N. (1997) "*Aerodynamic Flight Measurements and Rarefied-Flow Simulations of Mars Entry Vehicles*," J. of Spacecraft and Rockets, Vol.34, No. 5

ROLL MOTION RESTRAINT SYSTEM FOR NAL 0.6m MSBS - the 2nd report -

Takashi KOHNO, Hideo SAWADA, Tetsuya KUNIMASU

National Aerospace Laboratory
7-44-1, Jindaijihigashi-machi, Chofu-shi, Tokyo 182 JAPAN

SUMMARY

Suspending the wind tunnel model and controlling its motion in 5 degrees of freedom are realized in the NAL 0.6m MSBS but the roll motion of the model is not controlled yet. So a mechanical roll motion control system is designed for NAL 0.6m MSBS. This system has worked well in the test with the free rotation model hung by the string vertically and applied to the model suspended by MSBS. A wireless communication system between the system inside the model and the observer out of the test section has also been designed.

INTRODUCTION

Magnetic Suspension and Balance System (MSBS) is a new technique for the wind tunnel tests that suspends the testing model by the magnetic force. It enables to avoid the support interference problem and has many other advantages in the future wind tunnel tests. At National Aerospace Laboratory (NAL), a MSBS for the 0.1m x 0.1m test section (0.1m MSBS) has been developed and succeeded in suspending the cylindrical model and controlling its motion in 6 degrees of freedom. And a MSBS for 0.6m x 0.6m test section (0.6m MSBS) has been designed to apply the techniques proved at 0.1m MSBS to the larger test section.

Figure-1 shows the arrangement of the electromagnets of NAL 0.6m MSBS. A model containing a cylindrical magnet is at the center of the test section and the magnetic field from the electromagnets surrounding the test section causes the lifting force that suspends the model. The position of the model and its attitude around y-axis and z-axis are measured by the optical position sensor and controlled by modifying the current supplied to each electromagnet by digital automatic control. Figure-1 also shows the outlook of the 0.6m MSBS. As shown here, it has already attached to the low speed wind tunnel and succeeded in suspending the model in the wind tunnel flow. The flow

velocity is up to 28m/sec.

However, in this system, the magnetization of the model is equal around the x-axis so the motion around x-axis (roll motion) of the model causes no change of the magnetic force acting on the model. So the roll motion cannot be controlled by modifying the current supplied to each electromagnet. In the wind tunnel testing, some roll moment acting on the model from the wind tunnel flow must be considered, so some means to restrain the roll motion is necessary.

Containing some magnets besides the main magnet (the magnet to obtain the lifting force that suspends the model) or using the main magnet that is not cylindrical gives the gradient of magnetization in the direction perpendicular to x-axis and enables to control the roll motion by modifying the surrounding magnetic field. Such a way to control the roll motion is realized in some facilities successfully.(Ref. 1, 2) At NAL 0.1m MSBS, Sawada et al succeeded in control the motion in 6 degree of freedom by using the model containing 4 small magnets besides the main magnet. (Ref. 3) Figure-2 shows the model used in the 0.1m MSBS and the test of the roll motion control.

However, when the MSBS and the models become larger, the required current to the electromagnet increases proportionally to the increasing size of the test section in such a way to control the roll motion. And when magnetic field from the main magnet becomes stronger it deducts the effect of radius magnetization for the roll control and make the required electric supply larger. In addition, such a system has another problem that it causes the coupling between the roll motion and other mode of motions.

On the other hand, when the MSBS becomes larger, using the large models makes it easier to contain some mechanical system inside the model. So a mechanical system that is contained in the model and controls the roll motion is designed for the large scale MSBSs.

GENERAL IDEA & PROTOTYPE

Figure-3 shows the general idea of the mechanical roll motion restraint system. In this system, the roll rate of the model is measured by the gyro contained in the model and the roll rate is fed to the control circuit. The control signal from the control circuit drives the DC motor with flywheel to cancel the roll motion of the model. According to an approximate numerical simulation, such a system will control the roll motion well with simple P-I compensator.

This system has two problems that are to be solved. One is that it creates counter-torque by changing the rotation of the flywheel, so when the constant moment from

wind tunnel flow is acting on the model, the rotation will increase continuously to the maximum rotation of the motor. Increasing the mass of the flywheel increases the capacity of the constant moment acting on the model, but the weight of the flywheel is limited by the payload of the MSBS.

Another problem is that when the flywheel is rotating, the gyro moment changes the force required to change the attitude of the model and influences the control of the motions besides the roll motion. In the prototype designed, the mass of the part that is rotating in the model is only 1-2% of the total mass of the model, so it is expected that the gyro moment caused by the rotating flywheel has little effect on the whole control systems.

A prototype of the mechanical roll motion restraint system is designed for the $\phi 55\text{mm}$ diameter cylindrical model used in NAL 0.6m MSBS. Figure-4 shows the arrangement in the system. In order to avoid the unexpected force from the surrounding magnetic field, a fiber optic gyro (FOG) and coreless DC motor are used and the frame is made of aluminum. Because we could not get the FOG that can be contained in the $\phi 55\text{mm}$ model, the system is contained in a $\phi 75\text{mm}$ diameter and 150mm long cylindrical frame and attached to the model with the longitudinal axes in common. The difference in diameter is of course intolerable for the wind tunnel tests. But it is only because of the size of the FOG and not an essential problem of such a system. Some smaller FOG that will be developed in future or further enlargement of the MSBS will solve the problem. A $\phi 90\text{mm}$ diameter super-conducting solenoid model has been introduced to NAL 0.6m MSBS already so this test makes sense as the preparation for applying this system to the $\phi 90\text{mm}$ super-conducting solenoid model. The FOG used in this system is TA7319N1 produced by Tamagawa Seiki Co., Ltd.

In order not to spoil the advantage of the MSBS that it has no support interference, no connection for the power supply between the model and the external power source is allowed. So the power source also must be contained in the model and must have the capacity to keep driving all through the wind tunnel test. A 9V dry cell on the market is used and DC-DC converter is used to produce required constant voltage. The dry cells are magnetic bodies so it's not desirable to use it actually. According to the experiments below, some effect to the MSBS control has been considered.

Figure-5 shows the outlook of the prototype of the roll motion restraint system. The lifting ability of the NAL 0.6m MSBS with its $\phi 55\text{mm}$ diameter model is limited to 700g so the system has been made as light as possible. Finally the weight of the system is 650g with the communication system mentioned below.

COMMUNICATION SYSTEM

In the wind tunnel tests, no wire connection for data communication is allowed because it spoils the advantage of the MSBS that it has no support interference. So a wireless communication system for the MSBS is required. It must work under strong magnetic field and its interference, and strong electric noise caused by power amplifiers for MSBS and should be small and light in order to be contained in the model.

As a prototype of such a wireless communication system for the MSBS, an infrared (IR) communication system is designed for NAL 0.6m MSBS. Figure-6 shows the outlook of the IR communication system. An IR communication system has been chosen instead of conventional radio telemetry system because it is expected to have required anti-noise performance. It has one analog input and converts the data to 12 bit digital data and sends it to the PC with IR communication. It also has a 12 bit digital IR input from the PC and converts it to analog voltage output. It can keep driving for 60 minutes with conventional dry cells.

At first, a system that sends the roll rate from the FOG to the PC and receives the calculated control signal from PC was planned. But because the designed communication system does not have enough sampling rate to control the roll motion, an analog PID compensation electric circuit has been designed and implemented to control the roll motion of the model. Figure-7 shows the control circuit. So the communication system was used only to monitor the roll rate and to change the reference value of the roll rate.

Such a system can be used not only for the communication to control the motion of the model but also sending the data measured by the sensors contained in the model, such as temperature, pressure, etc. It will be a useful tool in future wind tunnel tests. However, it requires more channel numbers and further accuracy including anti-noise performance.

EXPERIMENTS

Before applying the roll motion restraint system to the model suspended in the MSBS, a test by the vertically hung model is carried out to prove the possibility of restraining the roll motion under the influence of the magnetic field caused by the main magnet of the model. The model with mechanical roll motion restraint system is hung by a string and can rotate around x-axis. First, the test was carried out without control circuit. The FOG and the motor were connected by wire to the PC and the PC calculates the control signal that drives the motor after the roll rate from the FOG. After that, the test with the analog control circuit in the model was carried out. In this system the

control loop is closed in the model and the PC was used only for the monitor.

Figure-8 shows the time trajectory of the roll rate ($d\phi$) in degree per second and the roll (ϕ) in degree and control command in voltage. The initial value of the roll rate is given and the system works to restrain the roll rate to the zero value. Because of the elasticity of the string suspending the model, the roll motion is reduced without any control as shown in the upper chart (Fig.-8.1). But the results of the test shown in the lower chart (Fig.-8.2) shows that the roll control system reduces the roll motion much faster. The magnetic field by the main magnet contained in the model did not cause any influence on the performance of this system. The required time to restrain the roll motion is longer than expected by the numerical simulation. This is probably because of the capacity of the circuit that drives the DC motor. This circuit has been refined when it was combined to the inner control circuit, so there exists the possibility of some improvement in the response speed between the system with wire and the system with inner control circuit.

Figure-9 shows the picture of the roll motion restraint system attached to the cylindrical model actually suspended in the MSBS, but with no wind tunnel flow. The IR communication system was attached to the model but could not perform as expected probably because of the heavy electric noise from the power amplifiers of the MSBS. So in the experiments below, it is replaced by a wire connection temporarily. But the P-I control loop itself was implemented as the analog control circuit contained in the model and closed in the model.

At first, the roll motion restraint system also could not perform as expected because of the heavy electric noise from the power amplifiers of the MSBS. So the test was carried out again by the system whose anti-noise performance is enhanced by strictly shielding the electric circuits. Figure-10 shows the time trajectory after some initial roll rate. The initial rate is not accurately the same but it is clear that the roll motion restraint system works to reduce the roll rate much faster. The position of the model and its attitude around y-axis and z-axis changed little while the roll motion restraint system was reducing the initial roll rate. This means that there exists little coupling with the roll motion control.

As mentioned before, this system works to restrain the roll rate to the reference value, so was not designed to control the roll value itself. The easiest way to know the roll angle is to integrate the roll rate but it did not work well when the roll rate value is affected by the electric noise. So the position sensor of 0.6m MSBS was refined to be able to measure the roll angle and modify the reference value of the roll rate to control the roll angle. The reference value of the roll rate is fed to the control system once a second from the external PC by the IR communication system. Figure-10 also shows that the roll angle is kept the same as that before the impulse has been given in spite of the outer moment given as the initial roll rate.

CONCLUDING REMARKS

A mechanical roll motion restraint system is designed for use in the large scale MSBS that requires strong magnetization of the model. A prototype of the roll motion restraint system and the IR communication system has been designed. This prototype is temporarily larger than the model in diameter but this problem can be solved for larger MSBS.

Some tests by the model hung vertically was carried out. The results showed that this system control led the roll motion in the constant magnetic field. Further tests have been carried out with the model actually suspended in the MSBS. The system restrained the roll motion from outer force in the strong magnetic field and its fluctuation by the MSBS. But the IR communication system could not perform as expected probably because of the heavy electric noise from the power amplifiers of the MSBS. It should be refined in the near future because this system is very important not only for control but also for data acquisition such as pressure and temperature.

As mentioned before the tests were carried out under the no flow condition. The next step is to increase the performance enough to control the roll motion of a cylindrical model in the wind tunnel flow with this roll motion restraint system. It requires that the cylindrical model completely contain the mechanical roll motion restraint system in it and further improvement in accuracy and reliability of this system.

REFERENCE

- 1) M. J. Goodyer : "THE GENERATION OF ROLLING MOMENTS WITH THE SUPERCONDUCTING SOLENOID MODEL", NASA CR-172520, 1985.
- 2) M. J. Goodyer : "Roll Control Techniques on Magnetic Suspension Systems", Aeronautical Quarterly, Vol.18, Feb. 1967, Pt. 1, pp.22~42.
- 3) H. Sawada : "Rolling Moment Control in the NAL 10cm x 10cm Magnetic Suspension and Balance System", NAL TR-1164, 1992.
- 4) T. Kohno; H. Sawada; T. Kunimasu : "Roll Motion Restraint System for NAL 0.6m MSBS", Proc. 4th International Symposium on Magnetic Suspension Technology, pp.141~150, NASA/CP-1998-207654, May, 1998

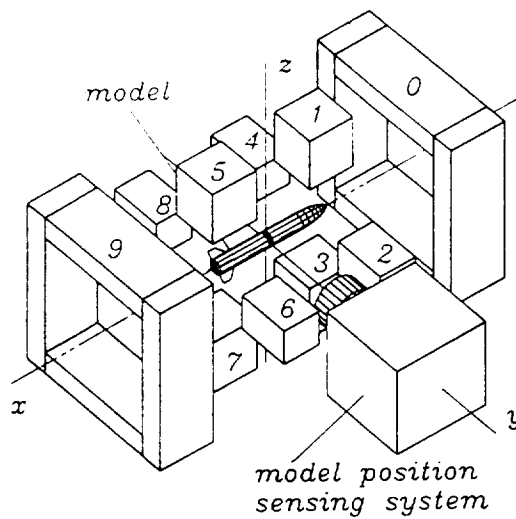


Fig.-1 : arrangement & outlook of the NAL 0.6m MSBS

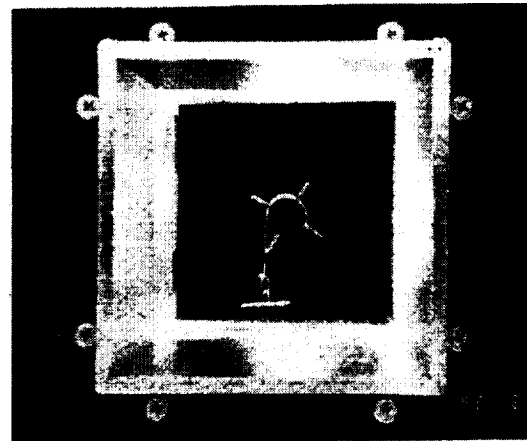
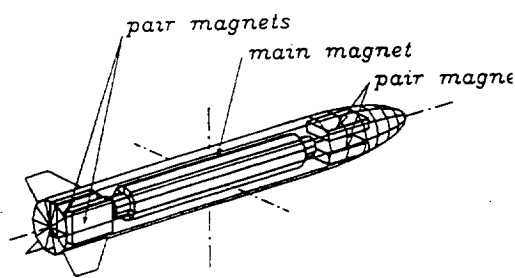


Fig.-2 : roll motion control in NAL 0.1m MSBS

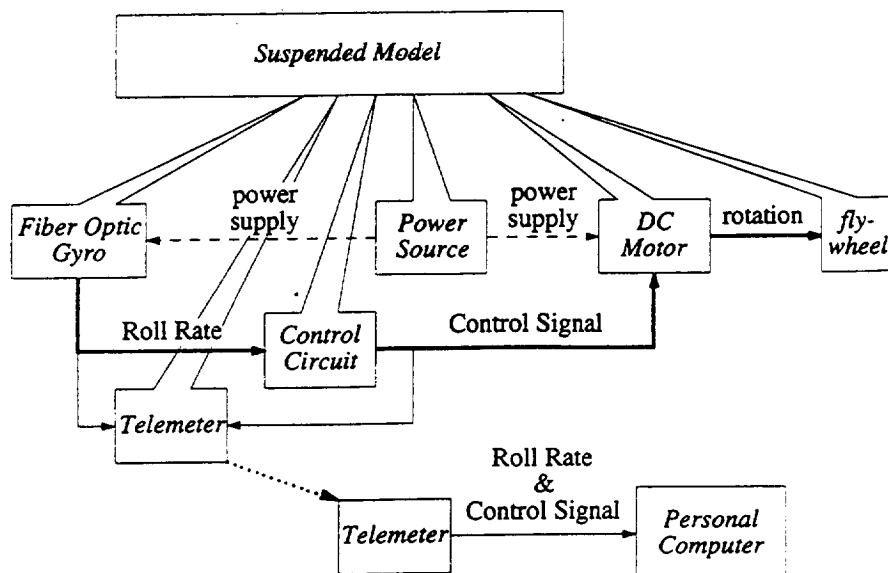


Fig.-3 : general idea of the mechanical roll motion restraint system

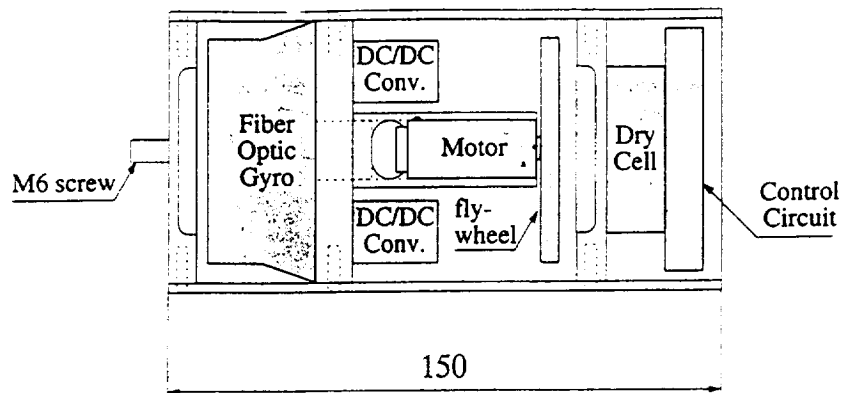


Fig.-4 arrangement of the mechanical roll motion restraint system

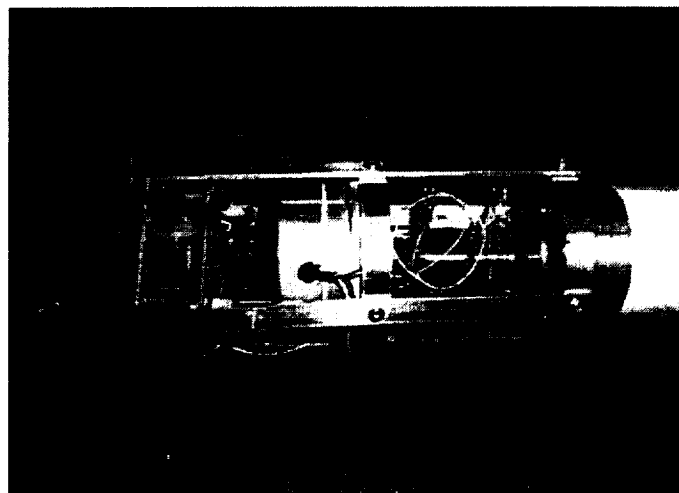


Fig.-5 : outlook of the mechanical roll motion restraint system



Fig.-6 : outlook of the IR communication system

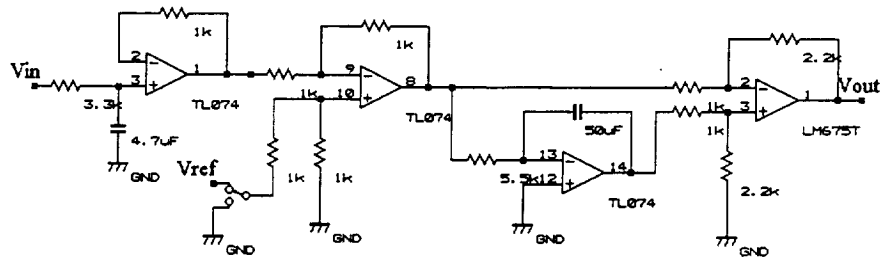


Fig.-7 : analog control circuit of the roll motion restraint system

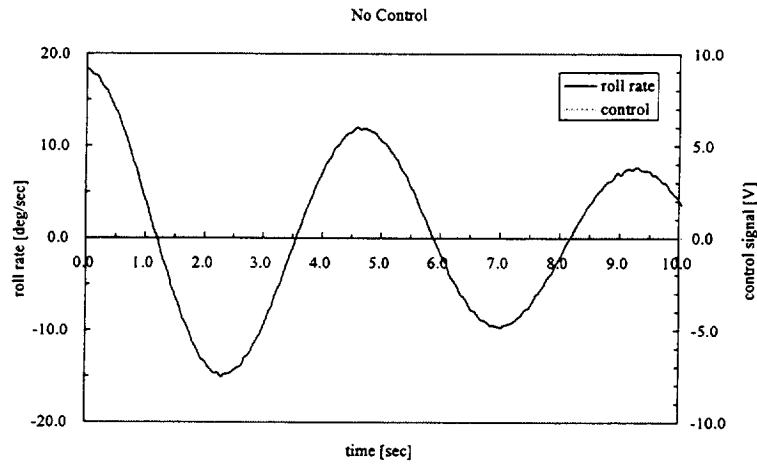


Fig.-8.1 : Trajectory of the roll rate (with no control)

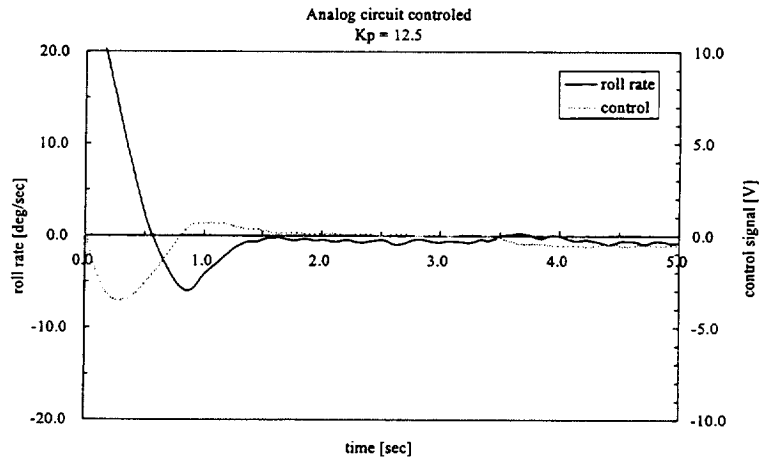


Fig.-8.2 : Trajectory of the roll rate (controlled)

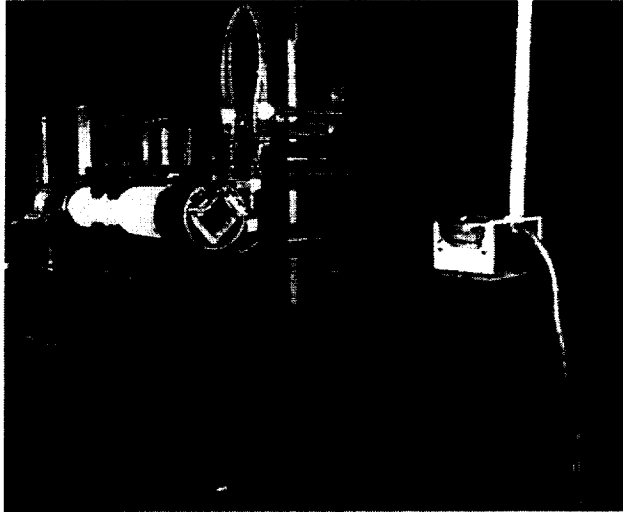


Fig.-9 : roll motion restraint system in the MSBS

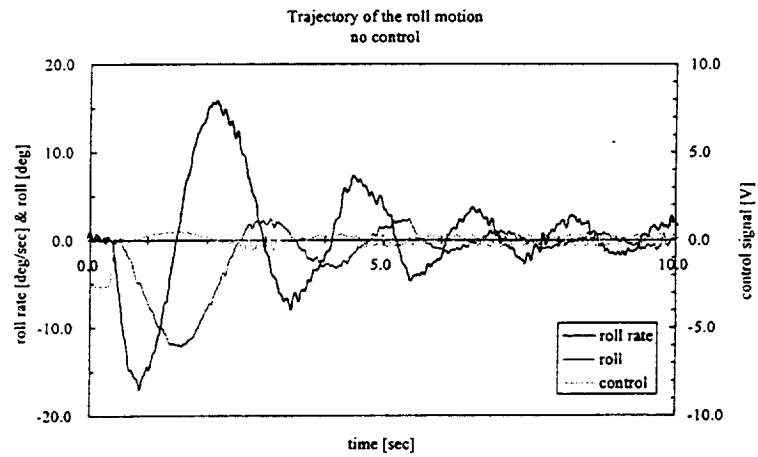


Fig.-10.1 : Trajectory of the roll rate (with no control)

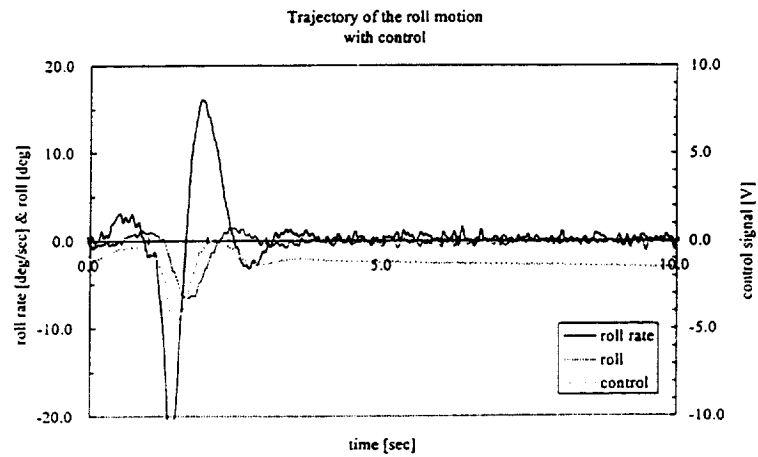


Fig.-10.2 : Trajectory of the roll rate (controlled)

Session 5 -- Modeling 1

Chairman: Kent R. Davey
American Maglev

A FREQUENCY-DOMAIN MODEL OF ELECTROMAGNETIC ACTUATORS COMPOSED OF SOLID IRON CORES WITH HYSTERESIS EFFECTS

FUKATA Satoru

Department of Industrial Design, Kyushu Institute of Design
4-9-1, Shiobaru, Minamiku, Fukuoka 815-8540, Japan
e-mail: fukata@kyushu-id.ac.jp

KOUYA Yoshinori

Murakami Seiki Mfg. Co., Ltd.
1-1, Kukikatamachi, Yahatanishiku, Kitakyushu 807-0811, Japan

FENG Shuang Ping

Graduate Student, Kyushu Institute of Design, Japan

SUMMARY

A model in the frequency domain is considered and checked with experimental results for the dynamic characteristics of magnetic actuators with solid iron core. First, an analytical magnetic reluctance based on a two-dimensional analysis is approximated in a simple form with a half-power of frequency and an accompanying complex number. This approximation is used to describe the dynamic characteristics of the electromagnet system with a C-shaped stator. Magnetic hysteresis effect is considered with a simple phase shift and with the conception of a complex value of permeability; leakage flux is ignored. The model is given by relations in the form of Laplace transform with the variation of working air-gap. For the symmetric electromagnet system with a uniform cross-sectional area, the frequency responses are compared with the experimental results when the working air-gap is fixed.

INTRODUCTION

When solid iron cores are used in electromagnets, eddy currents induced in the iron cores degrade and complicate the dynamic characteristics of the actuators. Several approaches have been presented to the analysis of eddy current effects, and distributive models have been derived (refs. 1-5). These are described by a transcendental function of the Laplace transform variable. There are two ways to obtain a lumped parameter model from the distributive models. One is to expand the transcendental functions into an infinite sum of lumped parameter systems and truncate them by several terms (refs. 6-8). The other one is to identify the parameters for a prescribed system in a range of frequency (ref. 9). The first method is very simple but may fail with a low-order system. The parameter identification method, in contrast, is generally reliable but requires a complicated computational procedure.

On the other hand, Feeley (ref. 10) proposed a simple distributive form to approximate an analytical one-dimensional model. This form is equivalent to the description with the half-power of the Laplace transform variable, \sqrt{s} . The approximation has been proven effective in very low and higher frequencies. This form may be useless in the time-domain analysis but presents few problems in the frequency-domain analysis. Britcher et al. (ref. 11) recommend an alternative form with a term such as $\sqrt{1 + \tau s}$, where τ is a time constant.

In addition, magnetic hysteresis in iron cores has effects on the generation of the magnetic flux. The

shape of the hysteresis loop is complex, in general; several models have been proposed in precise but very complicated forms (ref. 12). A simple treatment was devised by Aspden (ref. 1) with the conception of a complex value of permeability. This approach may have a difficulty in understanding the static hysteresis loop.

In this paper, we adopt an approximation similar to Feeley's and apply it to a theoretical magnetic reluctance of iron cores based on a two-dimensional analysis. With hysteresis effects, we take an approximated elliptical form for the static loop and apply it to the dynamic behaviors in its original form. The model considers the variation of working air-gap, but ignore's leakage flux. We check the validity of the proposed model with the experimental results when the working air-gap is fixed.

SYMBOLS AND NOTATIONS

- A : Cross-sectional area of iron core.
- a : Width of iron core.
- B : Magnetic flux density.
- b : Thickness of lamination.
- b_m : Increment of B .
- H : Magnetic field intensity in iron core.
- H_s : H -value on the surface of iron core.
- h_s : Increment of H_s .
- I : Magnet-coil current.
- i : Increment of I .
- j : $= \sqrt{-1}$.
- k_b : Gain of magnetic-flux density to coil current.
- k_i : Gain of coil current to input voltage.
- l_a : Mean length of air-gap.
- l : Mean length of iron core.
- N_k : Magnet-coil turns.
- N : Total magnet-coil turns.
- q : Incremental variable equivalent to magnetic flux.
- R : Magnetic reluctance of iron core.
- R_a : Magnetic reluctance of working air-gap.
- r_a : Increment of R_a .
- s : Laplace transform variable.
- T : Time constant.
- t : Time.
- Φ : Magnetic flux.
- ϕ : Increment of Φ .
- μ : Permeability of iron core.
- μ_0 : Permeability of free space.
- σ : Conductivity of iron core.
- ω : Angular frequency.

APPROXIMATION OF MAGNETIC RELUCTANCE OF SOLID CORE

Assumptions

We make the following assumptions.

- (A1) There is no leakage flux.
- (A2) Magnetomotive force is uniform on the surface of iron core.
- (A3) The distribution of magnetic flux is uniform in working air-gaps.
- (A4) Magnetic material parameters are uniform and constant (no saturation).
- (A5) The increments of flux and working air-gap are sufficiently small.

Eddy Current Effects

We consider a magnetic-flux path of length l and of constant cross-sectional area A , and assume the flux distribution is two-dimensional with assumption (A4). Eddy current effects complicate the flux distribution. We consider a rectangular iron core of width a and thickness b ($a \geq b$). For the sinusoidal excitation of the magnetic intensity on the surface, a two-dimensional analysis derives the following equation as an expression of the amplitude of the induced flux (refs. 5 and 6).

$$\Phi(\omega) = \mu A H_s p(\omega) \quad (1)$$

where

$$p(\omega) = p_1(\omega) + p_2(\omega) \quad (2)$$

$$p_1(\omega) = \frac{\tanh(\alpha b / 2)}{\alpha b / 2} \quad (3)$$

$$p_2(\omega) = \sum_{k=1}^{\infty} \frac{8}{[(2k-1)\pi]^2} \frac{\alpha^2}{\beta_k^2} \frac{\tanh(\beta_k a / 2)}{\beta_k a / 2} \quad (4)$$

$$\alpha = \sqrt{j\mu\sigma\omega}, \quad \beta_k^2 = \alpha^2 + \left[\frac{(2k-1)\pi}{b} \right]^2 \quad (5)$$

and where H_s is the amplitude of the input intensity on the surface, and ω an angular frequency. Equation (1) is rewritten as

$$H_s l = R(\omega) \Phi(\omega) \quad (6)$$

where

$$R(\omega) = \frac{R_0}{p(\omega)}, \quad R_0 = \frac{l}{\mu A} \quad (7)$$

Approximation of Magnetic Reluctance

If the thickness is much smaller than the width ($b \ll a$), then the first term is dominant in eq. (2). To approximate this term, a low-order lumped parameter model is simple but not always successful because its series expansion has poor convergency. Feeley (ref. 10) proposed a distributive model described by the half-power frequency with the approximation

$$\tanh(x) \approx \frac{x}{1+x} \quad (8)$$

This approximation is very good in very low and high frequencies but fairly poor in the intermediate frequencies.

For real x , we note that the function $\tanh(x)/x$ monotonically decreases with increasing x . In this case, if we replace the second and higher-order terms by the first approximation, then we have an overestimation. Neglecting them, we have an underestimation. Taking the overestimation, we approximate the infinite sum of eq. (4) as

$$p_2(\omega) = \begin{cases} 0 & \text{for } \omega < \omega_{b1} \\ \frac{\tanh(\alpha a/2)}{\alpha a/2} & \text{for } \omega \gg \omega_{b1} \end{cases} \quad (9)$$

where

$$\omega_{b1} = \frac{1}{\mu\sigma} \left(\frac{\pi}{b} \right)^2$$

In this case, for high frequencies, we have an approximation to eq. (2) as

$$p(\omega) \approx \frac{1}{\alpha b/2} + \frac{1}{\alpha a/2} = \left(1 + \frac{b}{a} \right) \frac{1}{\alpha b/2} \quad (10)$$

Considering the static value of unity, we give a rough approximation to the magnetic reluctance as

$$\frac{R(\omega)}{R_0} \approx \bar{r}_2(\omega) = 1 + \alpha \frac{b'}{2}, \quad b' = \frac{b}{1 + \frac{b}{a}} \quad (11)$$

To check the approximation, we take up a iron core of $a=20\text{mm}$ and $b=8\text{mm}$ ($b/a=0.4$) with the material parameters in Table 1 given later. The absolute value and argument are shown in Fig. 1 by broken lines (notation \bar{r}_2), and compared with the theoretical values shown by thick filled lines (\bar{r}_0). The approximation is very good in higher frequencies but fairly poor in lower frequencies. The comparison for different values of width and material parameters is given only against a scaled frequency axis. The approximation becomes better with the increase of the ratio b/a (≤ 1).

To improve the approximation in lower frequencies, we may modify eq. (11) as

$$\bar{r}_3(\omega) = \frac{1}{1 + \frac{b}{a}} \left(1 + \alpha \frac{b}{2} \right) \quad (12)$$

by ignoring the accuracy in the statics. The evaluation is shown by thin filled lines with \bar{r}_3 in Fig. 1. This modification improves the first approximation in lower frequencies but is poor in very low frequencies. We note $\bar{r}_3(0) = 1/(1 + b/a) < 1$, while the first approximation gives the accurate value of unity.

The frequency characteristics with fixed working air-gap may be expressed by the transfer function

$$G(s) = \frac{1}{1 + c_{R0} \bar{r}(s)}, \quad c_{R0} = \frac{R_0}{R_{a0}} \quad (13)$$

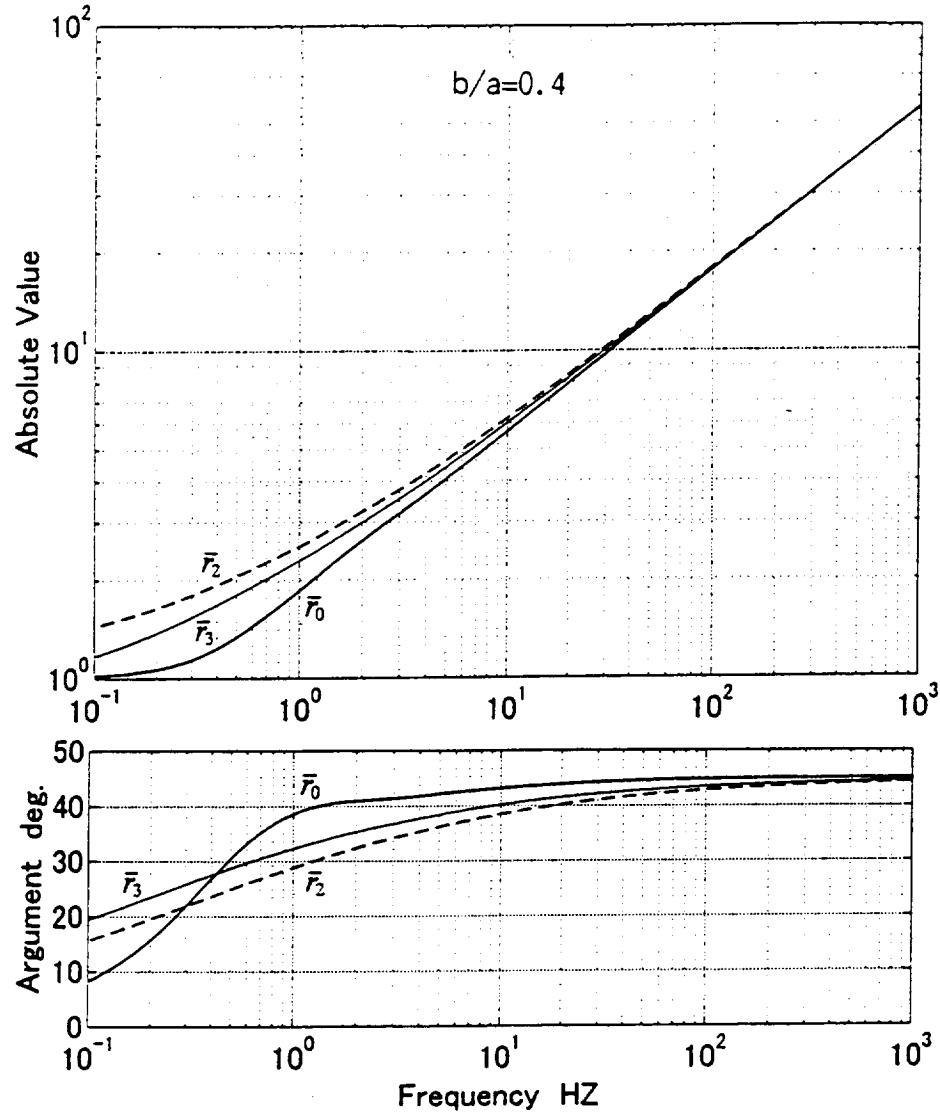


Figure 1. Approximation of magnetic reluctance.

In the equation, R_0 is the static magnetic reluctance of iron core and R_{a0} that of working air-gap. Figure 2 shows the frequency responses for the approximations when $c_{R0}=0.1$.

MODEL OF ELECTROMAGNETIC ACTUATORS WITH C-SHAPED STATOR

Magnetic Circuit Model

Figure 3 illustrates in the left-hand part a configuration of electromagnetic actuators composed of a C-shaped stator and an I-shaped rotor. Two coils are set on the two pole legs and connected in series. Actually, the magnetic flux is distributive with leakage along the flux path. When the effects of eddy currents are combined, the leakage fluxes increase with frequency; hence the dynamics become more complicated.

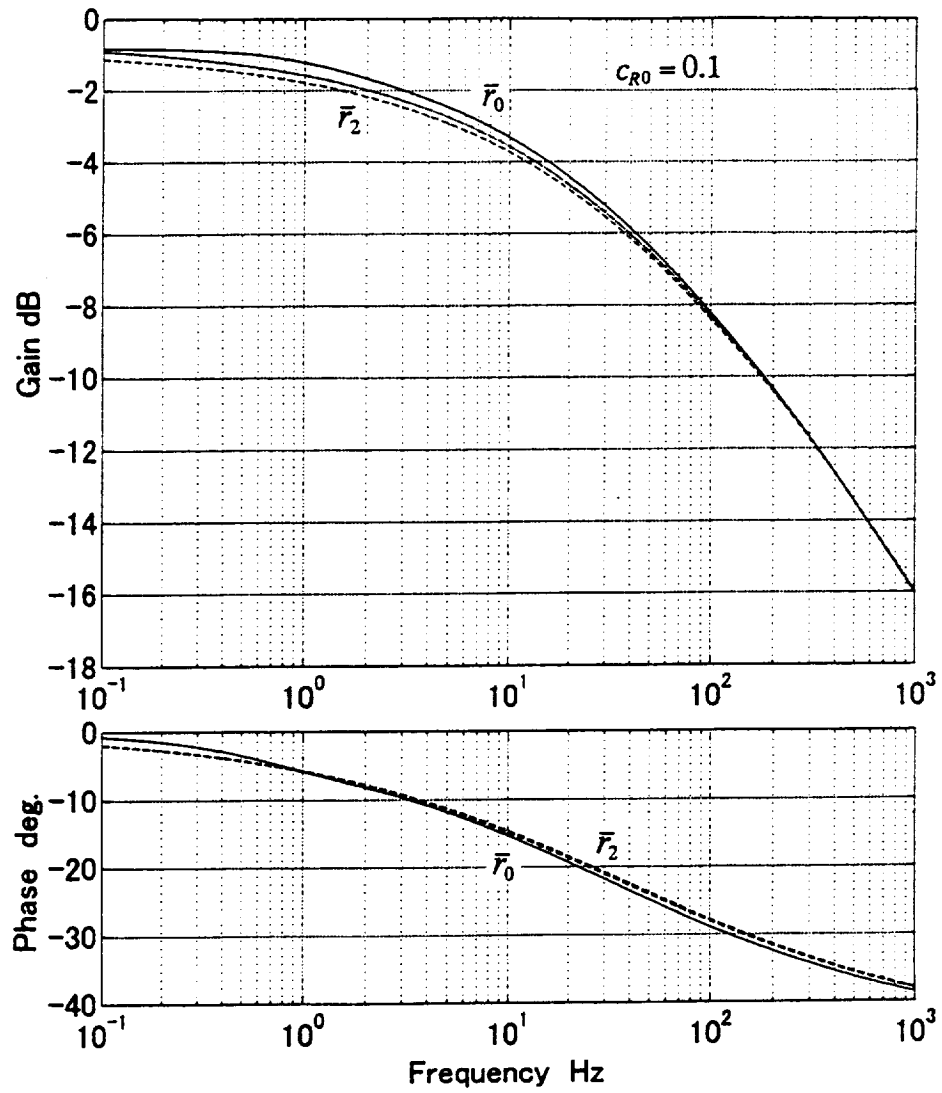


Figure 2. Frequency characteristics with approximated reluctance.

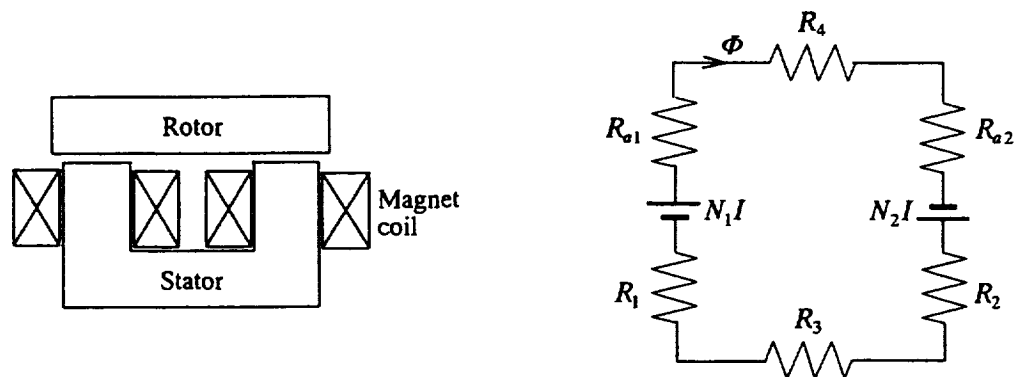


Figure 3. Configuration of magnetic actuator and magnetic circuit model.

If we neglect the leakage fluxes, the magnetic system is modeled by an equivalent magnetic circuit, as shown in the right-hand part of Fig. 3. In this figure, $N_i I$ are the magnetomotive forces, and R_{ak} and R_k are the magnetic reluctances in the working air-gaps and in the iron cores, respectively.

Relation of Magnetic Flux to Coil Current

For a loop along the surface of the iron cores in the magnetic system, Ampere's loop law gives the relation

$$H_a l_a + H_s l = NI \quad (14)$$

where H_a and l_a are the field intensity and the path length, respectively, associated with the working air-gap, H_s and l are those with the iron cores, N the turns of magnet coil and I the coil current. The length l is given by the mean on Assumption (A2). Concerning the working air-gap, with Assumption (A3) we have the relation

$$H_a l_a = R_a \Phi \quad (15)$$

where

$$R_a = \frac{l_a}{\mu_0 A_a}, \quad \Phi = A_a B_a$$

where A_a is an effective area of the working air-gap, B_a the flux density assumed to be uniform over the area, and μ_0 the permeability of air. Concerning the iron cores, in the steady state, the flux distribution is uniform; hence, we have the simple relation

$$H_{s0} l = R_0 \Phi_0, \quad R_0 = \frac{l}{\mu A} \quad (16)$$

where A is the cross sectional area and μ the permeability. This gives the steady-state value of the flux. In the unsteady state, another approach is required.

For the increment of coil current and for the variation of working air-gap length, we consider the resulting increments of the field intensity and the flux.

$$I = I_0 + i, \quad R_a = R_{a0} + r_a, \quad H_s = H_{s0} + h_s, \quad \Phi = \Phi_0 + \phi \quad (17)$$

Substituting these into eq. (14) with eqs. (15) and (16) and neglecting the second-order term, $r_a \phi$, we obtain the equation of the increments

$$R_{a0} \phi + h_s l = Ni - \Phi_0 r_a \quad (18)$$

The Laplace transform of the above relation is given by

$$R_{a0} \phi(s) + h_s(s) l = Ni(s) - \Phi_0 r_a(s) \quad (19)$$

where the variables with the argument s denote the Laplace transform of the corresponding variable, for example, $\phi(s)$ of ϕ , with the initial values of zero.

Now, we apply the result of eq. (1) to eddy current effects in the magnet core. In a similar way to the

derivation of eq. (1), from the Laplace transform of the original equation under some conditions for the associated functions, we can obtain a similar equation

$$R(s)\phi(s) = lh_s(s) \quad (20)$$

where $R(s)$ is given by the relation in eq. (7) where $j\omega$ is replaced by s in the term α in eq. (5). We set the initial values of the variables to be zero. Then, eq. (19) results in

$$[R_{a0} + R(s)]\phi(s) = Ni(s) - \Phi_0 r_a(s) \quad (21)$$

If we use a variable for the flux, defined by

$$q = \frac{R_{a0}}{N} \phi \quad (22)$$

then eq. (21) is written by

$$[1 + \bar{r}(s)] q(s) = i(s) - I_0 \bar{r}_a(s) \quad (23)$$

where

$$\bar{r}(s) = \frac{R(s)}{R_{a0}}, \quad \bar{r}_a = \frac{r_a}{R_{a0} + R_0} = \frac{1}{1 + \bar{r}_0} \frac{r_a}{R_{a0}}, \quad \bar{r}_0 = \frac{R_0}{R_{a0}} \quad (24)$$

and where we used the steady-state relation in the term with $\bar{r}_a(s)$.

Equations with Input Voltage

We take a power amplifier with coil-current control. In this case, the electric circuit gives an equation to the incremental voltage between the ends of magnet coil, v , as

$$v = p(k_i' e - i) = R_c i + N \frac{d\phi}{dt} \quad (25)$$

where e is an incremental voltage input to the power amplifier, k_i' a constant, p the loop gain of current feedback, and R_c the resistance of the magnet coil. Then, the above equation is simplified with eq. (22) as

$$i + T_0 \frac{dq}{dt} = k_i' e \quad (26)$$

where

$$k_i = \frac{pk_i'}{p + R_c}, \quad T_0 = \frac{N^2}{(p + R_c)R_{a0}}$$

Substituting the Laplace transform of eq. (26) into eq. (23), we obtain the relation between the magnetic flux and the input voltage

$$[1 + Ts + \bar{r}(s)] q(s) = k_i' e(s) - I_0 \bar{r}_a(s) \quad (27)$$

For the coil current, we have

$$[1 + T_0 s + \bar{r}(s)] i(s) = [1 + \bar{r}(s)] k_i e(s) + I_0 T_0 s \bar{r}_a(s) \quad (28)$$

Effects of Magnetic Hysteresis

The conception of complex permeability allows us to consider the hysteresis effects with an approximate elliptical relation (ref. 1). This approach is simple and can be applied to the results obtained above only by use of the complex permeability $\mu e^{-j\varphi}$ in place of the real permeability μ . This approach, however, presents difficulties with regard to giving a reasonable understanding to the experimental static hysteresis.

If we slowly change the value of magnet-coil current I with amplitude i_0 around a bias current I_0 , then the magnetic flux forms a hysteresis loop with the current. Concerning the magnetic flux density, B_0 is the mean value of the upper and lower values at the bias current and b_{m0} the resulting amplitude. With the increments i and b_m around I_0 and B_0 , respectively, we approximate the hysteresis loop with the elliptical function and consider the transfer function with a phase shift

$$\frac{b_m(s)}{i(s)} = k_b e^{-j\varphi} \quad (29)$$

where the phase shift φ determines the swell of the ellipse; $\varphi = 0$ gives the linear relation $b_m = k_b i$, where k_b is the gradient of the long axis and given by

$$k_b = \frac{b_{m0}}{i_0} \quad (30)$$

The hysteresis loop brings another effect, in general, that the current-flux gain k_b varies with the variation of the amplitude of coil current. In the steady states without hysteresis effects, eq. (21) gives the flux $\phi_{TH}(s)$

$$\frac{\phi_{TH}(s)}{A_a} = k_{TH} \left[i(s) - \frac{\Phi_0}{N} r_a(s) \right], \quad k_{TH} = \frac{N}{(R_{a0} + R_0)A_a} = \frac{\mu_0 N}{(1 + \bar{r}_0)l_a} \quad (31)$$

The term in the square brackets in the above equation is a magnetomotive force, corresponding to the coil current in eq. (29). Hence, a corresponding equation with the hysteresis effects is written by a similar form

$$\phi(s) = \bar{k}_b e^{-j\varphi} \phi_{TH}(s), \quad \bar{k}_b = \frac{k_b}{k_{TH}} \quad (32)$$

Combining eq. (32) with eq. (21), we have the equations

$$[1 + \bar{r}(s)] q(s) = \bar{k}_b e^{-j\varphi} [i(s) - I_0 \bar{r}_a(s)] \quad (33)$$

$$\{[1 + \bar{r}(s)] e^{j\varphi} + Ts\} q(s) = \bar{k}_b [k_i e(s) - I_0 \bar{r}_a(s)] \quad (34)$$

$$[1 + \bar{r}(s) + Tse^{-j\varphi}] i(s) = [1 + \bar{r}(s)] k_i e(s) + I_0 Tse^{-j\varphi} \bar{r}_a(s) \quad (35)$$

where

$$T = \bar{k}_b T_0 \quad (36)$$

We note that the time constant T_0 was replaced by $\bar{k}_b T_0$. This is a result of the decay of back electromotive force in the magnet coil.

Special Case with Fixed Working Air-gap

The approximations of magnetic reluctance are applicable to iron cores composed of different cross-sectional dimensions or different materials. If the material and the dimensions are common, then the total reluctance has a simple form. When the working air-gap is fixed, i.e. $\bar{r}_a(s)=0$, if eq. (11) is applied to the magnetic reluctance of the iron core, then eqs. (33) to (35) are written by the very simple transfer functions:

$$\frac{q(s)}{i(s)} = \frac{\bar{k}_b e^{-j\varphi}}{1 + \bar{r}_0(1 + \sqrt{\tau s})} \quad (37)$$

$$\frac{i(s)}{e(s)} = k_i \frac{1 + \bar{r}_0(1 + \sqrt{\tau s})}{1 + \bar{r}_0(1 + \sqrt{\tau s}) + T s e^{-j\varphi}} = \frac{k_i}{1 + \frac{T s}{1 + \bar{r}_0(1 + \sqrt{\tau s})} e^{-j\varphi}} \quad (38)$$

$$\frac{q(s)}{e(s)} = \frac{k_i \bar{k}_b e^{-j\varphi}}{1 + \bar{r}_0(1 + \sqrt{\tau s}) + T s e^{-j\varphi}} \quad (39)$$

where τ is a time constant given by

$$\sqrt{\tau} = \frac{1}{1 + b/a} \sqrt{\mu \sigma} \frac{b}{2} = \sqrt{\mu \sigma} \frac{b'}{2} \quad (40)$$

EXPERIMENTAL RESULTS

Experimental Setup

Figure 3 shows the dimensions of the magnet-iron cores; the cross-sectional area perpendicular to the flux path is uniform. The rotor is longer by 5mm than the width of the stator, and sticks out by 2.5mm from the pole legs on each side. The material is a soft iron. The magnet coils have the same turns and are excited with a PWM power amplifier with current feedback control. Two pieces of cardboard are put between the pole-leg faces and the rotor core to set the working air-gap length. We set the air-gaps to 1mm and the bias current to 1.5A. The primary specifications and data are summarized in Table 1.

Magnetic Hysteresis Loop

Hysteresis loop of the flux density against the coil current was measured with a gaussmeter in the working air-gap when the coil current was changed through the input voltage with the bias current. To obtain the static hysteresis loop, we applied a sinusoidal input at a frequency of 0.0125Hz, and had the

data of two periods. The results are shown in Fig. 4 for three amplitudes; the hysteresis is very small. The loops are approximated with a phase shift of about $\varphi = 0.03 \text{ rad.}$ ($= 1.7 \text{ deg.}$) in eq. (29). This phase shift is so small that we will neglect it in the calculations below. The argument of permeability, θ , has a small effect on the static loop when we calculate it with eq. (37). Hence, it may be difficult to estimate the value of θ from the static loop.

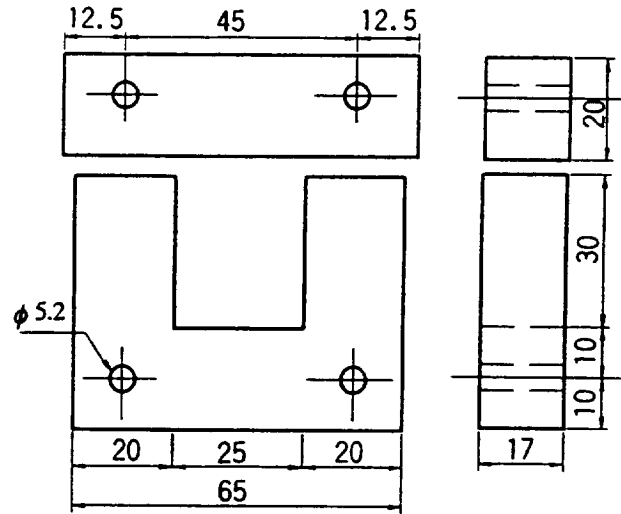


Figure 3. Iron cores of experimental setup

Table 1 Specifications and Data of Experimental Setup

Thickness of iron core	$b = 17 \times 10^{-3}$	m
Width of iron core	$a = 20 \times 10^{-3}$	m
Airgap length	$l_a/2 = 1.0 \times 10^{-3}$	m
Permeability of air	$\mu_o = 4\pi \times 10^{-7}$	H/m
Permeability of iron core	$\mu = 3\,000\,\mu_o$	
Conductivity of iron core	$\sigma = 1.0 \times 10^7$	$1/\Omega \cdot \text{m}$
Magnet coil: turns	$N/2 = 200$	turns/pole
resistance (at 21 °C)	$R_c = 1.40$	Ω
Mean length of iron core:		
Pole leg	$l_1 = l_2 = 30 \times 10^{-3}$	m
Connecting stator, Rotor	$l_3 = l_4 = 65 \times 10^{-3}$	m
Current gain	$k_i = 0.95$	A/V
Control loop gain	$p = 140$	
Time constant	$T = 0.24 \times 10^{-3}$	s
Phase shift	$\varphi = 0$	rad.
Gain	$\bar{k}_b = 1.0$	

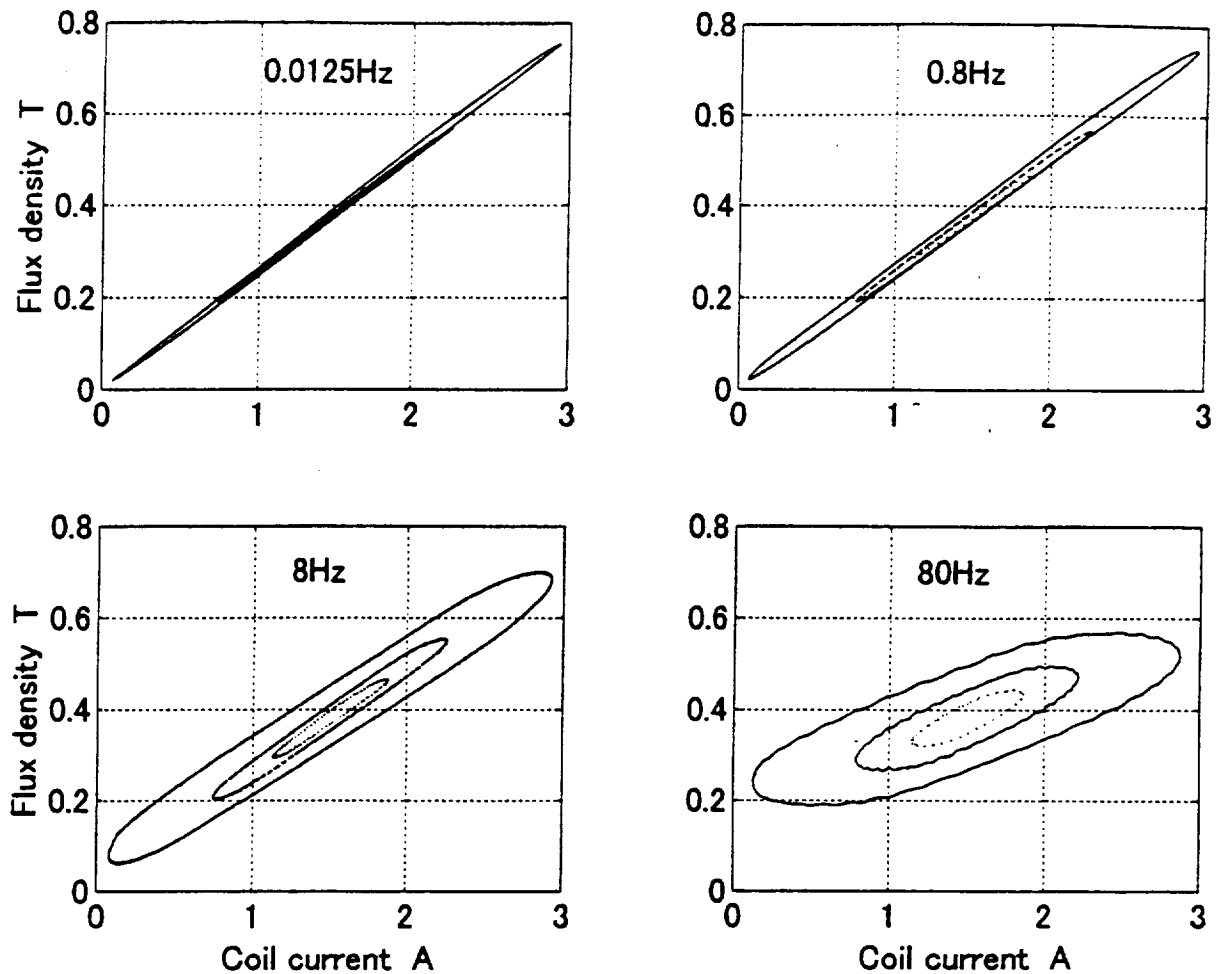


Figure 4. Magnetic hysteresis loop.

We checked that the measurement may be reliable in frequencies below about 100Hz; we measured the hysteresis loops in several frequencies; the results are shown in Fig. 4. We see that the amplitude-dependency of the current-flux gain (k_b in eq. (30)) is very small in low frequencies. In higher frequencies, the loops in each frequency may be similar in shape, but have a larger gradient for a smaller amplitude. The swell of the loop is a result of the time lag mainly due to eddy current effects.

Frequency Response of Flux to Coil-current

The frequency response of magnetic flux to coil current is independent of the characteristics of the power amplifier. To detect the incremental flux, a search coil of two turns was wound around two pole legs, one turn in each, near the pole faces. We input a biasing sinusoidal voltage to the power amplifier, and measured the coil current and the induced voltage between the ends of the search coil to obtain the frequency response between them. From the numerical operation of dividing the response by pure complex numbers $j\omega$, we obtained the response of the incremental flux. The amplitude of the input voltage was taken to give a statical amplitude of the coil current of about 25, 50 and 75% of the bias current. The results are shown by the filled lines in Fig. 5, indicated with the corresponding amplitude of the input voltage. The dependency on the input amplitude is very small in lower frequency; this was

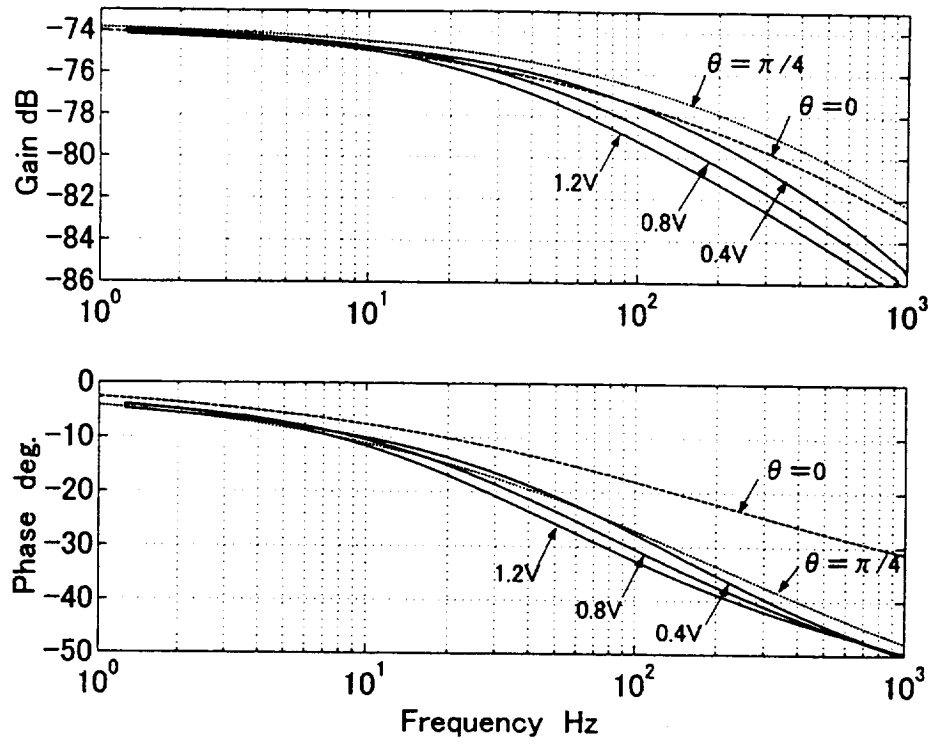


Figure 5. Frequency responses of magnetic flux to coil current.

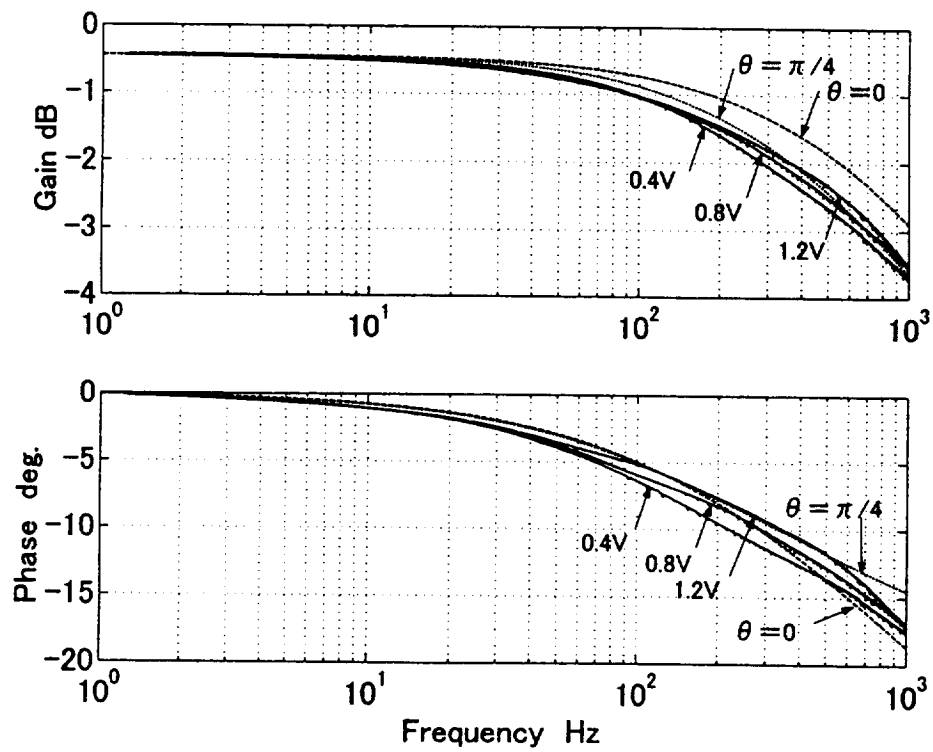


Figure 6. Frequency responses of coil current to input voltage.

expected from the static hysteresis loop. The gain characteristics, however, decays more for a larger amplitude above about 10Hz. This decay is probably because a part of the magnetic flux saturates in some parts of the iron core where the flux takes a short cut.

Numerical results based on eq. (37) with $\bar{k}_b=1$ and $\varphi=0$ are shown in the figure by broken and dotted lines when we assumed $\theta=0$ and $\theta=\pi/4$ rad. We shifted these gains up by 2.0dB (1.26 in magnitude) for simplicity of comparison (such a shift is valid because the fringing effect in the working air-gaps increases the flux). With the agreement to the experimental results, the parameter $\theta=0$ gives a better result than $\theta \neq 0$ in the gain, but opposite in the phase. We note that the numerical gain becomes larger for the permeability of a complex number. Anyway, the agreement to the experimental results is unsatisfactory in higher frequencies. This may be mainly due to the flux saturation in the experimental results and also due to defects of the model.

Frequency Response of Coil-current to Input Voltage

The filled lines in Figure 6 shows the experimental frequency responses of coil current to input voltage. The amplitude dependency is much smaller than the response of the flux to the coil current, and the gain increases with input-amplitude in higher frequencies. The latter fact seems contrary to an experience, in general, that the output current decays with the increasing input-amplitude in higher frequencies, as a result of dynamic characteristics of the power amplifier. The experimental result is probably a result of smaller eddy current effects with a smaller magnetic flux.

The broken and dotted lines in the figure show the numerical results of eq. (38). The agreement to the experimental results is much better than the results in Fig. 5; $\theta=\pi/4$ rad. Equation (38) may give an explanation for the experimental results with the amplitude dependency, mentioned in the preceding paragraph: the time constant T given by eq. (36) is related to the output amplitude through k_b in eq. (30), and proportional to the output amplitude (gain).

CONCLUSIONS

We presented a simple model in the frequency domain for electromagnetic actuators composed of C-shaped stators of solid iron core with magnetic hysteresis but without leakage flux. The proposed model is described by the half-power of the Laplace transform variable with eddy current effects and a phase shift of the static hysteresis effects in addition to the complex permeability. The agreement to the experimental results is unsatisfactory in higher frequencies. This may be mainly a result of flux saturation in the experiment. Leakage flux may be another factor: the leakage has a little effect on the characteristics of the actuators in lower frequencies, but may be large in higher frequencies.

REFERENCES

1. Aspden, H.: Eddy-Currents in Solid Cylindrical Cores Having Non-Uniform Permeability, *J. Applied Physics*, **23**-5, pp. 523-528, 1952.
2. Kesavamurthy, N., and Rajagopalan, P. K.: Effects of Eddy Currents on the Rise and Decay of Flux in Solid Magnetic Cores, *Proc. IEE*, Vol. 109 C, pp. 63-75, 1961.
3. Subba Rao, V.: Equivalent Circuits of Solid Iron Core for Impact Excitation Problem, *Proc. IEE*, Vol. 111, No. 2, pp. 349-357, 1964.

4. Silvester, P., Eddy Current Models in Linear Solid-Iron Bars, *Proc. IEE*, Vol. 112, No. 8, pp. 1589-1594, 1965.
5. Stoll, R. L.: *The Analysis of Eddy Currents*, pp. 34-40, Clarendon Press, Oxford, 1974.
6. Zmood, R. B., Anand, D. K., and Kirk, J. A.: The Influence of Eddy Currents on Magnetic Actuator Performance, *Proc. IEEE*, 75-2, pp. 259-260, 1987.
7. Leon, F. de, and Semlyen, A.: Time Domain Modeling of Eddy Current Effects for Transformer Transients, *IEEE Trans. Power Delivery*, 8-1, pp. 271-277, 1993.
8. Meeker, D. C., Maslen, E. C., and Noh, M. D., An Augmented Circuit Model for Magnetic Bearings Including Eddy Currents, Fringing, and Leakage, *IEEE Trans. Magnetics*, Vol. 32, No. 4, pp. 3219-3227, 1996.
9. Kucera, L., and Ahrens, M.: A Model for Axial Magnetic Bearings Including Eddy Currents, *NASA CP-3336, Third Inter. Sympo. on Magnetic Suspension and Technology*, Part 2, pp. 421-436, 1996.
10. Feeley, J. J.: A Simple Dynamic Model for Eddy Currents in a Magnetic Actuators, *IEEE Trans. on Magnetics*, Vol. 32, No. 2, pp. 453-458, 1996.
11. Britcher, C. P., and Bloodgood, D. V.: Eddy Current Influences on the Dynamic Behaviour of Magnetic Suspension Systems, *NASA CP-1998-207654, Fourth Inter. Sympo. on Magnetic Suspension and Technology*, pp. 273-284, 1998.
12. Vistin, A. Edit.: *Models of hysteresis*, Longman Scientific & Technical, 1993.

MODELLING, IDENTIFICATION AND CONTROL OF AN AMB SYSTEM FOR THE SUPPORT OF A HIGH-SPEED FLYWHEEL

Wu Z Y, Howe D, Peel D & Bingham C M
Department of Electronic and Electrical Engineering
The University of Sheffield, Mappin Street, Sheffield S1 3JD, UK
E-mail: ellwzy@stoat.shef.ac.uk

SUMMARY

The paper describes the modelling, closed-loop identification, and control of an active magnetic bearing (AMB) system to support a high-speed flywheel in an energy storage/peak power buffer system. Experimental frequency-domain data is applied to a model-order reduction procedure, based on μ -synthesis, to provide the open-loop transfer function of the AMB's. Loop-shaping is subsequently used to design a compensator to impart robust stability and desired dynamic stiffness attributes to the system, based on QFT templates. Experimental results are included to demonstrate the real-time dynamic behaviour of the AMB's, and thereby validate the modelling, identification and controller design procedure.

INTRODUCTION

Due to their frictionless nature, lubricant-free operation, and low electromagnetic losses, AMBs are being employed increasingly for high-speed applications spanning different market sectors. This paper investigates the theoretical modelling, identification, and robust control of an AMB system to support a high-speed fibre composite flywheel rim in a peak power buffer unit which is being developed for electric vehicles [Howe, et. al. 1999].

Although simple rigid-body dynamic models of an AMB derived from a purely theoretical viewpoint may exhibit significant inaccuracies, they are often useful for providing an initial physical insight into their operational characteristics, and as an aid to bearing controller design [Matsumura 1986, Schweitzer et. al. 1994]. However, to account for features which are not accommodated by these simple models, such as under-damped flexible modes of vibration, system identification together with robust controller synthesis is often required. This paper employs closed-loop frequency-domain identification of the dominant AMB dynamics, and, based on state-variable models of rigid and flexible modes, results in a reduced order model of the system via the application of μ -synthesis techniques. Based on the outcome of the modelling and identification procedure, loop-shaping is used to impart desirable stability and performance attributes to the closed-loop system.

MODEL OF MAGNETIC BEARING

In the flywheel unit under consideration, the magnetic bearing system is comprised of two radial active bearings, and two passive axial bearings, as shown schematically in Figure 1. Kinetic energy is converted to electrical energy, and vice-versa, via an integral motor/generator. Initially, the central hub, comprising the AMB and electrical machine stators, and the flywheel rim, which carries the AMB and electrical machine rotors, are considered as rigid-bodies, and the free space motion of the rim in the radial direction, ie. two translational motions and two rotational motions, is analysed. The effect of the flexible modes of vibration of the rotor and stator assembly is subsequently incorporated in the model.

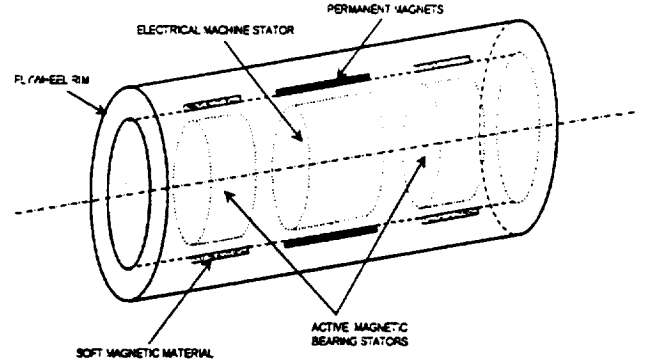


Figure 1. Schematic of fibre composite flywheel, with integral magnetic bearings and electrical machine

Rigid Body Equations Describing Flywheel Rim

A simplified representation of the horizontally mounted, magnetically suspended flywheel rim is shown in Figure 2, in which x and y are the horizontal and vertical displacements, f_x and f_y are the component forces exerted on the rim, θ and ϕ are the rotational angles, T_θ and T_ϕ are the torque components acting on the rim, and l is the distance between the electromagnets of the AMBs and the centre of the rim. Subscripts '1' and '2' denote the right and left-hand ends of the flywheel, respectively.

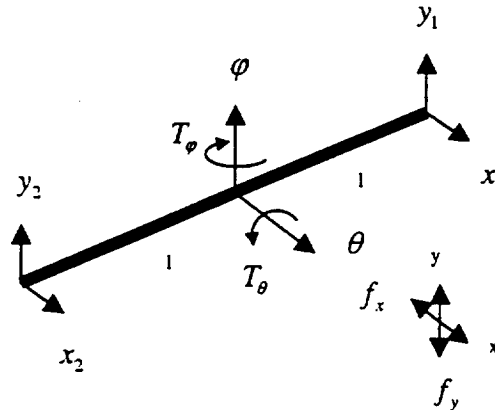


Figure 2. Illustration of rim and definition of variables.

For a linear AMB, in which both the horizontal and vertical axes comprise two opposing electromagnets each carrying a bias current i_0 , the net electromagnetic force that results on each axis is given by:

$$f = k_i i + k_x x$$

where

$$k_i = 4k_f \frac{i_o^2}{x_o^2}, \quad k_x = -4k_f \frac{i_o^2}{x_o^3}, \quad k_f = \mu_o N^2 A_p$$

x_o is the nominal air-gap length, N is the number of turns on each of the electromagnet coils, A_p is the effective pole-face area of each electromagnet, and μ_o is the permeability of free space. k_x and k_i are normally referred to as the bearing natural stiffness and bearing current sensitivity, respectively. The resultant force and torque components acting on the rim can be expressed as:

$$\begin{cases} f_x = f_{x1} + f_{x2} \\ f_y = f_{y1} + f_{y2} + mg \end{cases}, \quad \begin{cases} T_\theta = (f_{y1} - f_{y2})l \\ T_\phi = (f_{x2} - f_{x1})l \end{cases}$$

where f_{x1} , f_{x2} , f_{y1} and f_{y2} are the forces generated by the magnetic bearings on the x_1 , x_2 , y_1 and y_2 axes, respectively, and mg is the force exerted on the flywheel rim due to gravity.

The Newton-Euler motion equations for the magnetic bearing can be written as,

$$\begin{cases} m\ddot{x} = -f_x \\ m\ddot{y} = -f_y \end{cases}, \quad \begin{cases} J_x\ddot{\theta} + J_z\omega\dot{\phi} = -T_\theta \\ J_y\ddot{\phi} - J_z\omega\dot{\theta} = -T_\phi \end{cases}$$

where J_x , J_y and J_z are the polar moments of inertia along the x-, y- and z-axes, respectively, and ω is the rotational speed of the rim.

Denoting the state vector, X , the input force vector, F , and the output displacement vector, Y , as:

$$X = [x \quad y \quad \theta \quad \phi]^T, \quad F = [f_{x1} \quad f_{y1} \quad f_{x2} \quad f_{y2}]^T, \quad Y = [x_1 \quad y_1 \quad x_2 \quad y_2]^T$$

the equations of motion can be expressed in state-space form, viz:

$$\begin{aligned} \frac{d}{dt} \begin{bmatrix} X \\ \dot{X} \end{bmatrix} &= \begin{bmatrix} 0 & I \\ A_1 & A_2 \end{bmatrix} \begin{bmatrix} X \\ \dot{X} \end{bmatrix} + \begin{bmatrix} 0 \\ -B_1 \end{bmatrix} F + \begin{bmatrix} 0 \\ W \end{bmatrix} \\ Y &= [C_1 \quad 0] \begin{bmatrix} X \\ \dot{X} \end{bmatrix} \end{aligned}$$

where:

$$\begin{cases} x_1 = x - l\phi \\ y_1 = y + l\theta \\ x_2 = x + l\phi \\ y_2 = y - l\theta \end{cases}, \quad A_1 = 0, \quad A_2 = \begin{bmatrix} 0 & 0 & 0 & 0 \\ 0 & 0 & 0 & 0 \\ 0 & 0 & 0 & -J_z/J_x\omega \\ 0 & 0 & J_z/J_y\omega & 0 \end{bmatrix}$$

$$B_1 = \begin{bmatrix} 1/m & 0 & 1/m & 0 \\ 0 & 1/m & 0 & 1/m \\ 0 & l/J_x & 0 & -l/J_x \\ -l/J_y & 0 & l/J_y & 0 \end{bmatrix}, \quad W = [0 \quad g \quad 0 \quad 0]^T, \quad C_1 = \begin{bmatrix} 1 & 0 & 0 & -l \\ 0 & 1 & l & 0 \\ 1 & 0 & 0 & l \\ 0 & 1 & -l & 0 \end{bmatrix}$$

Model of Magnetic Bearing Including Flexible Modes of Rim and Hub

In addition to the dominant rigid-body dynamics of the rim, there are significant vibration modes associated with the flexibility of the system. Whilst the frequency of these flexible modes can be predicted theoretically, for instance, by using either the lumped parameter or finite element methods, reliable estimates of the effective damping ratio of the modes is often difficult to obtain using these methods, and experimental techniques are normally employed [Meirovitch, 1975]. A typical measured frequency response of the flywheel AMB is shown in Figure 3, where two dominant vibration modes are evident, viz; at 1440 rad/s (230 Hz) and 13200 rad/s (2.1 kHz), respectively. The low frequency mode is due to the first bending mode of the stator, whilst the high frequency mode is due to the first bending mode of the rotor. An estimate of the undamped natural frequency and damping ratio of each mode is:

$$\begin{cases} \omega_{n1} = 1440 \\ \xi_1 = 0.0161 \end{cases} \quad \begin{cases} \omega_{n2} = 13200 \\ \xi_2 = 0.0002 \end{cases}$$

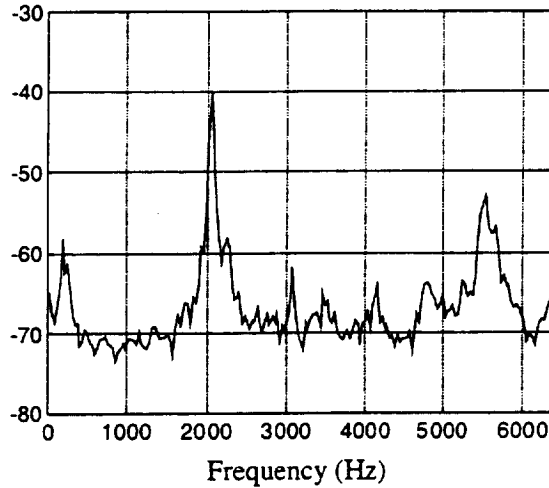


Figure 3. Measured frequency response of magnetic bearing system.

It has been shown, [Yocum 1978], that the influence of flexible modes with low damping on the overall positional displacement can be modelled as additive terms to the displacement dynamics due to the rigid-body mode alone, Figure 4.

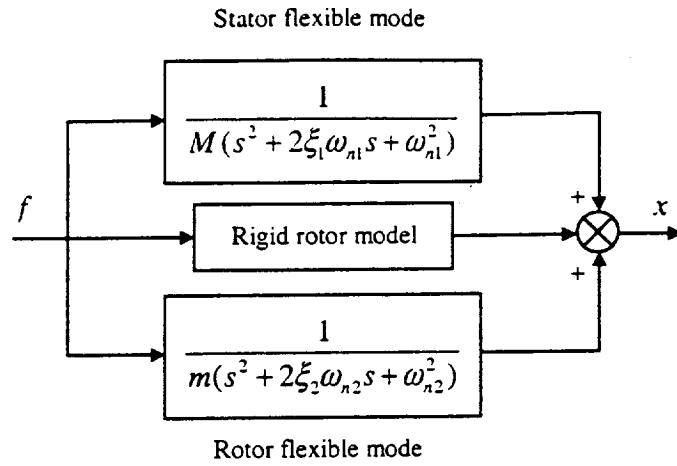


Figure 4. Model of magnetic bearing incorporating structural flexibility.

The equations describing the stator flexible mode can be expressed in state-variable form as:

$$\frac{d}{dt} \begin{bmatrix} X' \\ \dot{X}' \end{bmatrix} = \begin{bmatrix} 0 & I \\ A'_1 & A'_2 \end{bmatrix} \begin{bmatrix} X' \\ \dot{X}' \end{bmatrix} + \begin{bmatrix} 0 \\ B'_1 \end{bmatrix} F$$

where

$$X' = [x'_1 \quad y'_1 \quad x'_2 \quad y'_2]^T, \quad A'_1 = -\omega_{n1}^2 I, \quad A'_2 = -2\zeta_1 \omega_{n1} I, \quad B'_1 = \frac{1}{M} I$$

Similarly, a state-variable description of the rotor flexible mode takes the form:

$$\frac{d}{dt} \begin{bmatrix} X'' \\ \dot{X}'' \end{bmatrix} = \begin{bmatrix} 0 & I \\ A''_1 & A''_2 \end{bmatrix} \begin{bmatrix} X'' \\ \dot{X}'' \end{bmatrix} + \begin{bmatrix} 0 \\ B''_1 \end{bmatrix} F$$

where:

$$X'' = [x''_1 \quad y''_1 \quad x''_2 \quad y''_2]^T, \quad A''_1 = -\omega_{n2}^2 I, \quad A''_2 = -2\zeta_2 \omega_{n2} I, \quad B''_1 = \frac{1}{m} I$$

The superposition of the rigid body and flexible modes yields the combined position displacement vector:

$$\begin{aligned} Y &= [x_1 \quad y_1 \quad x_2 \quad y_2]^T \\ &= [x - l\varphi + x'_1 + x''_1 \quad y + l\theta + y'_1 + y''_1 \quad x + l\varphi + x'_2 + x''_2 \quad y - l\theta + y'_2 + y''_2]^T \end{aligned}$$

Denoting the combined state vector, Z, as follows:

$$Z = [X \quad \dot{X} \quad X' \quad \dot{X}' \quad X'' \quad \dot{X}'']^T$$

the complete AMB model, relating force to position displacement, is:

$$\begin{aligned}\dot{Z} &= A Z + B F \\ Y &= C Z\end{aligned}$$

where

$$A = \begin{bmatrix} 0 & I & & & & \\ A_1 & A_2 & & & & \\ & & 0 & I & & \\ & & A_1' & A_2' & & \\ & 0 & & & 0 & I \\ & & & & A_1'' & A_2'' \end{bmatrix}, \quad B = [0 \quad -B_1 \quad 0 \quad B_1' \quad 0 \quad B_1'']^T, \quad C = [C_1 \quad 0 \quad I \quad 0 \quad I \quad 0]$$

Model Relating Control-Current to Position Displacement

For controller design purposes, it is convenient to employ a dynamic model which relates the coil currents to the rim displacement dynamics. Under the assumption that the power amplifier current-controller will have a much greater bandwidth than the desired position displacement controller, the winding current can be assumed to be approximately equal to the current demanded by the position displacement controller output. By defining the current vector:

$$i = [i_{x1} \quad i_{y1} \quad i_{x2} \quad i_{y2}]^T$$

the force vector can be expressed as,

$$F = K_I i + K_X Y$$

where

$$K_I = \begin{bmatrix} k_{ih} & 0 & 0 & 0 \\ 0 & k_{iv} & 0 & 0 \\ 0 & 0 & k_{ih} & 0 \\ 0 & 0 & 0 & k_{iv} \end{bmatrix}, \quad K_X = \begin{bmatrix} k_{xh} & 0 & 0 & 0 \\ 0 & k_{xv} & 0 & 0 \\ 0 & 0 & k_{xh} & 0 \\ 0 & 0 & 0 & k_{xv} \end{bmatrix}$$

Thus, a model relating the control currents to the position displacements takes the form:

$$\begin{aligned}\dot{Z} &= (A + BK_X C)Z + BK_I i \\ Y &= CZ\end{aligned}$$

Analysis of Magnetic Bearing Model

The derived state-variable model is to be used for describing the dominant dynamic characteristics of the flywheel magnetic bearing system. The lumped parameters of the AMB are given in Table. 1.

	Symbol	Units
Stator mass	M	18 kg
Rotor mass	m	12 kg
Length from bearing to centre of rim	l	0.19 m
Inertia along z-axis	J_{zz}	0.071 kg m ²
Inertia along x-axis	J_{xx}	0.42 kg m ²
Inertia along y-axis	J_{yy}	0.42 kg m ²
Stator flexible natural frequency	ω_{n1}	1440 rad/s
Stator flexible damping coefficient	ξ_1	0.0161 N s/m
Rotor flexible natural frequency	ω_{n2}	13200 rad/s
Rotor flexible damping coefficient	ξ_2	0.0002 N s/m
Electromagnet pole-face area : vertical axis	A_{pv}	$2.6 \times 10^{-4} \text{ m}^2$
Electromagnet pole-face area : horizontal axis	A_{ph}	$1.3 \times 10^{-4} \text{ m}^2$
Number of turns/coil	N	40
Nominal air-gap length	x_0	0.4 mm
Bias current	i_0	5 A

Table 1. Parameters for flywheel AMB's

Influence of Rotational Speed on Dynamic Characteristics

From the theoretical state-variable AMB model, Figures 5(a),(b) show the estimated frequency responses of the magnetic bearings for zero speed and 60,000rpm, respectively, together with corresponding pole-zero maps. It is observed that, in addition to the highly under-damped vibration modes and an unstable pole, RHP zeros are present which contribute to controller design difficulties. As the rotational speed increases, the magnetic bearing dynamics begin to exhibit characteristics commensurate with gyroscopic coupling. From Figure 5, it is observed that the RHP zero moves away from the imaginary axis as speed increases, and, consequently, the control constraints due to the RHP zero become less significant. However, the dynamics due to rotor imbalance, which is not discussed in this paper, become increasingly significant with increased rotational speed.

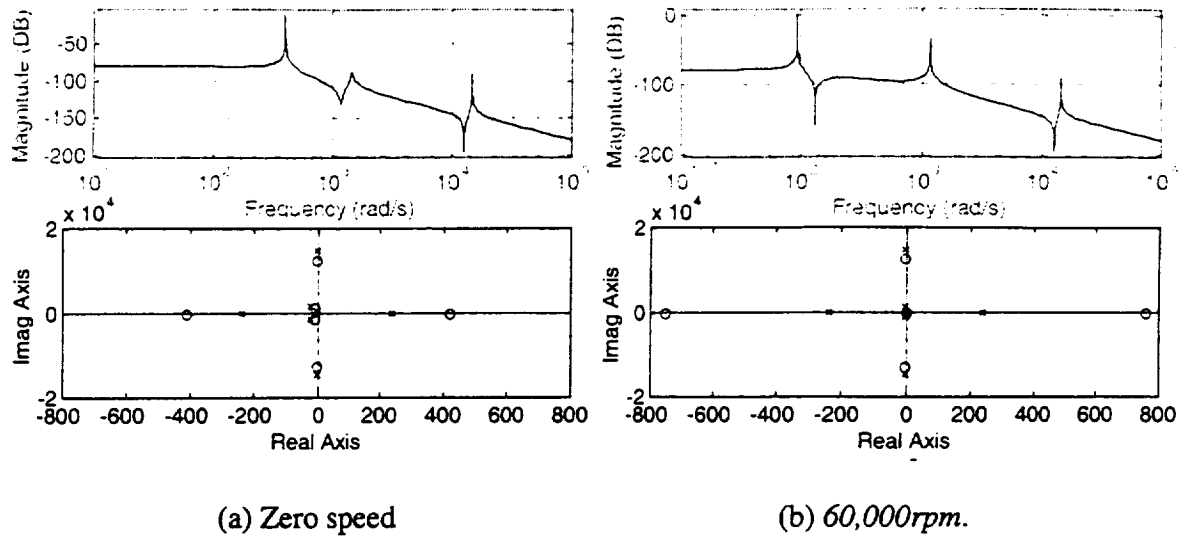


Figure 5. Frequency response of AMB from state-variable models

De-coupled SISO Control or Multi-variable Control

From the state-variable model, Figures 6(a),(b) show the predicted de-coupled and cross-coupled frequency responses of the AMB's, respectively, for zero speed and $10,000rpm$. It can be seen that at low speed, the cross-coupling between axes is negligible compared to the de-coupled responses, and a SISO controller may be adequately employed. However, as the rim speed is increased, the cross-coupling between axes becomes more significant, and a multi-variable controller will often be required to impose desired closed-loop performance attributes.

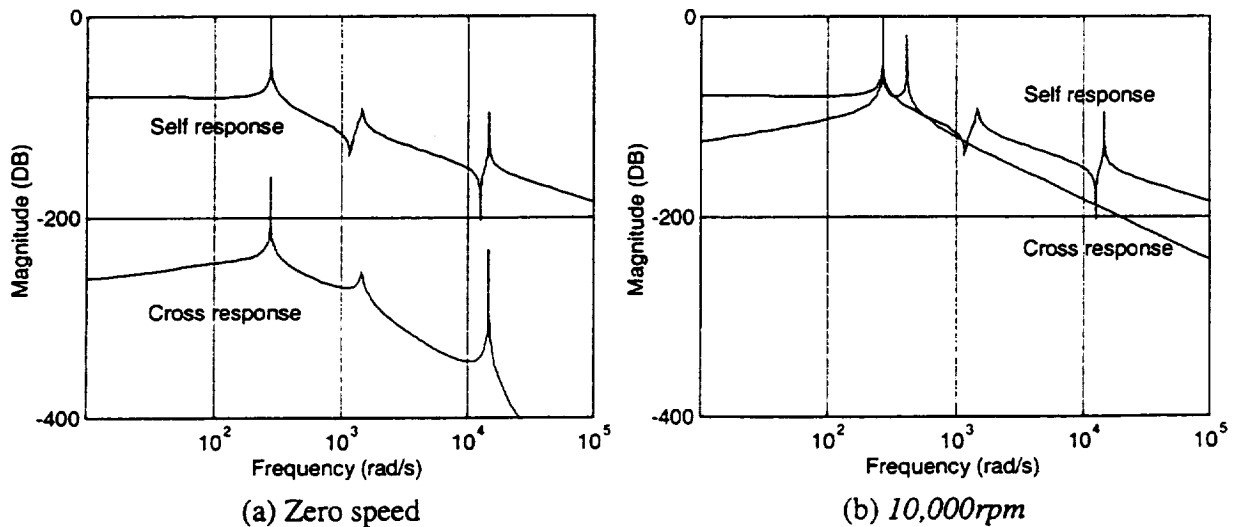


Figure 6. Self and cross-frequency responses of magnetic bearings.

SYSTEM IDENTIFICATION FOR AMB's

Since AMB's are inherently unstable, data obtained from the bearing for the purpose of determining its transfer function must be measured whilst the bearing is subject to stable closed-loop control. Consequently, conventional open-loop system identification techniques are of limited use, and a closed-loop system identification technique should be employed.

Closed-Loop Identification

One of the key challenges to system identification is to estimate the system transfer function in the presence of noise. In the case of identification of stable plants, the transfer function can be obtained directly from the input and output signals, Figure 7(a) and Eq. (1), under the assumption that the additive noise exhibits Gaussian, zero-mean, white-noise characteristics (since the effect of noise will be averaged out):

$$G = \frac{y}{u} \quad (1)$$

However, if the same technique is applied to a closed-loop system, Figure 7(b), the transfer function G cannot be obtained simply from Eq. (1), due to correlation between the noise, n , and the input signal, u .

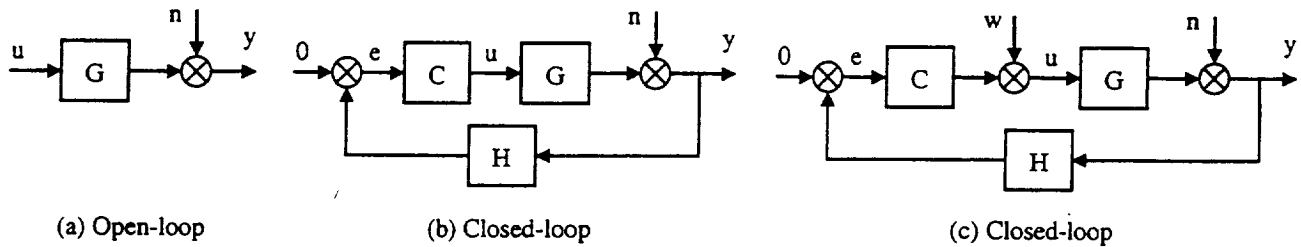


Figure 7. Configurations for system identification.

To address this issue, a test signal, typically a band-limited chirp or white-noise source, can be injected at the input to the plant. The input and output dynamics of the plant can then be obtained by noting that:

$$y = \frac{G}{1 + CHG} w + \frac{1}{1 + CHG} n$$

$$u = \frac{1}{1 + CHG} w - \frac{CH}{1 + CHG} n$$

Since the injected signal, w , and the noise, n , are no-longer correlated, the plant open-loop transfer function can be obtained from the relationship:

$$G = \frac{y/w}{u/w} \quad (2)$$

AMB System Identification

To instigate a system identification procedure for the AMB, it is first necessary to design a closed-loop position displacement compensator to stabilize the AMB at its nominal position. Typically, a PID controller whose parameters are tuned manually, or are obtained by an appropriate robust control design methodology, is employed. During stable operation of the magnetic bearing, a chirp signal, w , having an appropriate magnitude and frequency range, is superimposed on the controller's current demand. The frequency response from the test signal, w , to the input signal, u , and from the test signal, w , to the output signal, y , are recorded. By appropriate manipulation, Eq.(2), the AMB open-loop frequency response characteristic can be obtained, Figure 8.

Derivation of AMB Transfer Function; μ - Synthesis

Although the AMB open-loop frequency response characteristic can be used directly for control system design, it is often convenient to have a parametric model for investigation of the system properties, and for application of advanced control techniques.

Here, μ -synthesis is employed to derive a reduced order model, based on a best-fit to the experimental frequency response data. A weighting function is used to attenuate the effects of high frequency noise picked up during the measurements. The resulting estimate of the plant transfer function is:

$$G(s) = \frac{0.024(s^2 + 199s + 1.212 \times 10^6) \cdot (s^2 + 30s + 3.5 \times 10^6) \cdot (s^2 - 1787s + 7.06 \times 10^6)}{(s + 1804) \cdot (s + 190) \cdot (s - 178) \cdot (s^2 + 53s + 1.931 \times 10^6) \cdot (s^2 + 140s + 4.617 \times 10^6) \cdot (s^2 + 5s + 2.171 \times 10^8)} \quad (3)$$

Figure 8 compares the frequency response of the estimated $G(s)$, Eq.(3), with the experimental frequency response. The high degree of correlation between the two descriptions confirms the effectiveness of the μ -synthesis method.

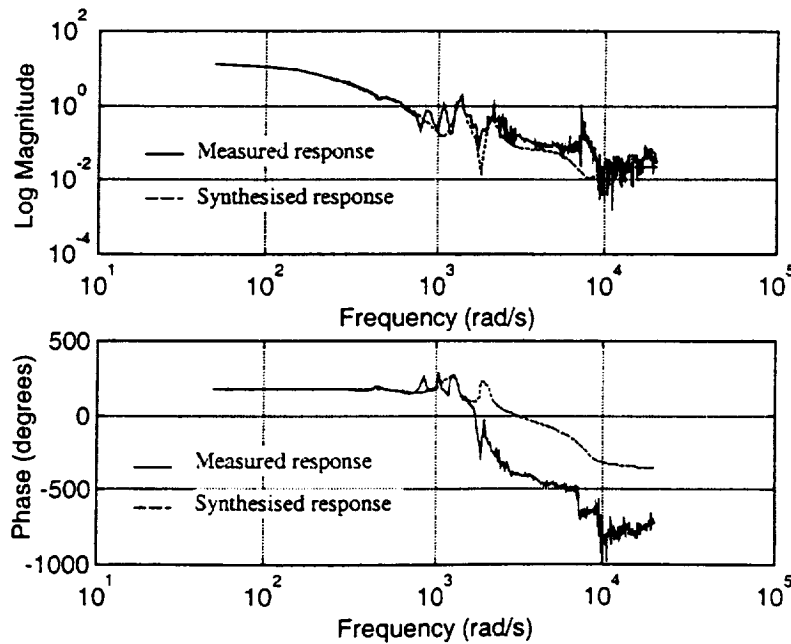


Figure 8. Identified AMB open-loop frequency response, and corresponding μ -synthesis model.

APPLICATION OF MODEL FOR AMB CONTROLLER DESIGN

The identified model of each axis of the AMB system is now used as a basis for the design of a decoupled SISO position displacement controller. Although there are numerous methods that could be used, this paper employs a QFT approach to achieve robust stability and other desired performance attributes from the closed-loop system, such as dynamic stiffness. The performance specifications that are used as a basis for the design of a compensator are summarised below:

- (a) Robust stability/Robust gain-margin. This criteria is ensured by placing an upper bound on the complementary sensitivity function, for example:

$$\left| \frac{PG}{1+PG} \right| < 1.7, \quad \forall \omega$$

provides a gain margin >1.6 and a phase margin $>33^\circ$, and, classically, should provide transient characteristics with an effective damping ratio ≥ 0.3 .

- (b) Control effort constraint.

$$\left| \frac{U}{Y} \right| < 50, \quad \omega < 400$$

This limits the control maximum controller demand to the maximum power electronic amplifier capability when the rim is subjected to maximum displacement.

- (c) Zero steady-state position error. This is achieved by the incorporation of integral action, which also influences the static stiffness of the AMB.

- (d) Robust output disturbance rejection

$$\left| \frac{Y}{D} \right| < |0.009\omega|, \quad \omega < 100$$

- (e) Robust input disturbance rejection

$$\left| \frac{Y}{V} \right| < 0.001, \quad \omega < 100$$

which can be interpreted as a bearing dynamic stiffness of 10^8 N/m over 0 to 100 rad/s .

Using QFT and loop-shaping, Figure 9, the performance specifications are satisfied by the compensator:

$$C(s) = \frac{41600(s+1281)(s+918.8)(s+16.7)}{s(s+2.958e004)(s+8000)}$$

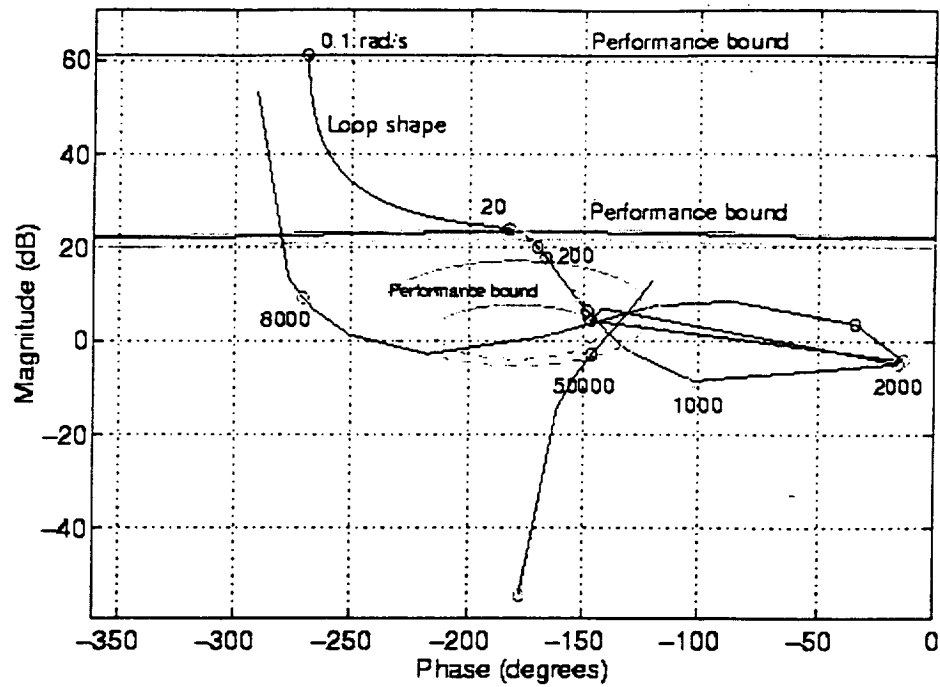


Figure 9. QFT design for AMB controller.

A simulated step response using the identified model and the controller designed using QFT, is shown in Figure 10. It can be seen that the transient responses are commensurate with a damping ratio of ≈ 0.3 , and a bandwidth $\approx 100 \text{ rad/s}$, as specified by the design criterion.

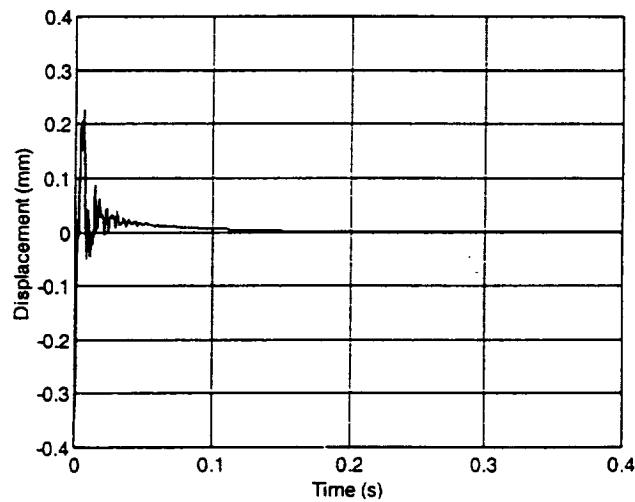


Figure 10. Simulated step response using the identified model and the QFT designed controller

EXPERIMENTAL CONTROL OF THE FLYWHEEL AMBs

The prototype flywheel and magnetic bearing system is shown schematically in Figure 11. The two active radial magnetic bearings that are used to support the rim have a homopolar magnetic circuit topology, and the peak force capability being 1600N in the vertical direction and 800N in the horizontal

direction. Eddy current position sensors are used to monitor the displacement of the rim from its quiescent position on both the horizontal and radial axes. For position control of the active bearing, the sensors have a resolution of $1\mu\text{m}$, a linearity of 1% of full scale, and a bandwidth of 5kHz . The electromagnets of each bearing are supplied from current-controlled switched-mode power amplifiers, and the controllers are implemented using the DSPACE/TMS320C40-based hardware development platform.

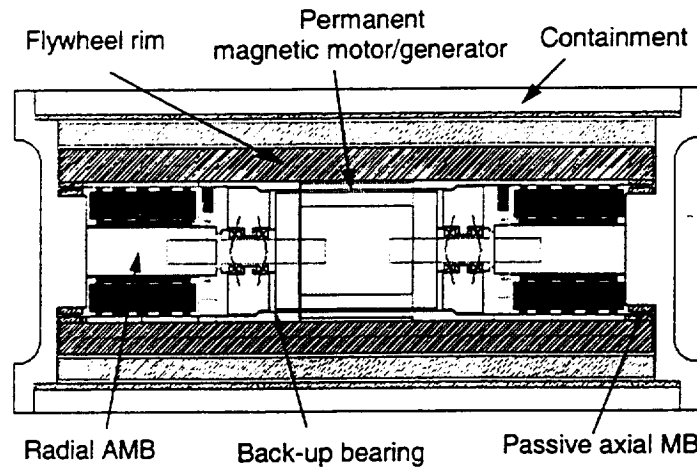


Figure 11. Magnetic bearings for a flywheel energy storage unit.

Figure 12 shows the initial excitation responses when both of each radial magnetic bearing are excited simultaneously, with the flywheel rim initially resting on the touch-down/backup bearings. The results verify theoretical performance predictions, and, in particular show characteristics consistent with a robust gain margin >1.6 , and phase margin $>33^\circ$, as desired.

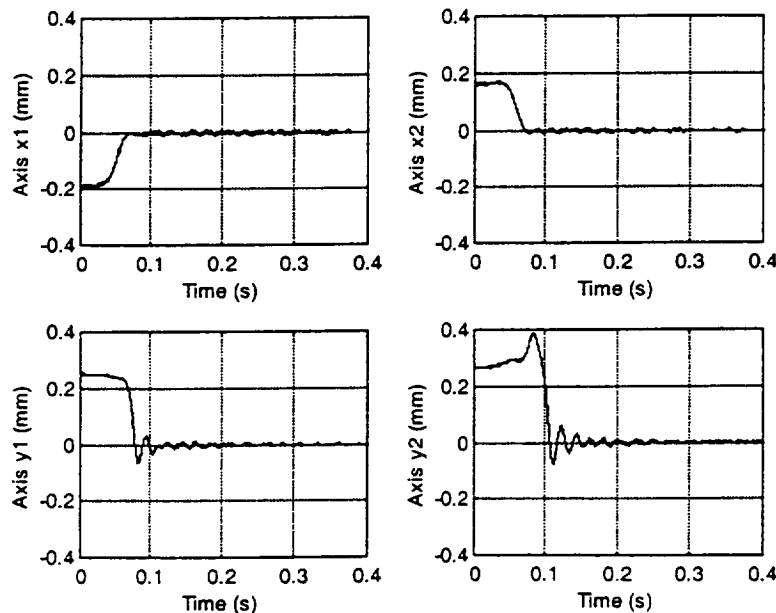


Figure 12. Initial response of flywheel magnetic bearing control system.

CONCLUSIONS

The paper has described the modelling, closed-loop identification, and control of an AMB system to support the rim of a high-speed flywheel peak-power buffer for an electric vehicle.

State-variable models incorporating rigid-body and flexible modes of vibration have been derived, and used to demonstrate the effects of increasing rim speed on the poles and zero's of the AMB transfer function. Experimental data has been used to validate the theoretical predicted dominant rigid-body and flexible modes of the system.

Closed-loop identification has subsequently been employed together with μ -synthesis to obtain a reduced order model of the AMB system from experimental frequency response data. The resulting model has been used as a basis for controller design to satisfy desired stability robustness and performance attributes, via the adoption of a QFT design methodology. Experimental results verify the resulting controller induced closed-loop dynamics of the AMB system.

ACKNOWLEDGEMENTS

The authors gratefully acknowledge the provision of funding from the European Commission, under the BRITE-EURAM and JOULE-THERMIE programmes, to support research on energy storage flywheel systems for use in electric vehicles, of which the work reported in the paper forms a small part.

REFERENCES

- Howe D., Mason P. E., Mellor P. H., Wu Z. Y. and Atallah K.: 'Flywheel peak power buffer for electric/hybrid vehicles'; IEEE International Electric Machines and Drives Conference , IEMDC'99, Seattle, Washington, USA, May 9-12, 1999, pp. 508-510.
- Matsumura F and Yoshimoto T.; 'System modelling and control design of a horizontal shaft magnetic bearing system'; IEEE Trans. on Magnetics, 22(3), 1986.
- Meirovitch L.; 'Elements of vibration analysis'; McGraw-Hill, Inc. 1975.
- Schweitzer G., Bleuler H. and Traxler A.: 'Active magnetic bearings, basic, properties and applications'; Zurich, Switzerland, vdf Hochschulverlag AG, 1994.
- Yocum J F and Slafer L I.; 'Control system design in the presence of severe structural dynamics interactions'; Journal of Guidance and Control, Vol.1, No.2, 1978.

FINITE ELEMENT DESIGN OF BEARINGLESS PERMANENT MAGNET MOTORS

Wolfgang Amrhein, Siegfried Silber, Klaus Nenninger
Johannes Kepler University
Department of Power Electronics and Electrical Drives
Altenberger Straße 69
A-4040 Linz, Austria

SUMMARY

In high performance applications with high demands on speed range, lifetime, cleanness or tightness, magnetic bearing systems can provide substantial advantages to classical drive systems using ball or sliding bearings. Some of these applications like pumps, blowers or fans require only three actively controlled degrees of freedom and can be supported by four coil bearingless permanent magnet motors. In these cases three degrees of freedom are passively stabilized by the tensile force of permanent magnets.

Depending on the particular application an interior or exterior rotor design of the bearingless motor may be advantageous. A finite element analysis is used to show the interactions between the current density distributions of the stator and the excitation fields of the rotor. Different permanent magnet magnetization forms are examined. It is shown that the results of the interior rotor design differ significantly from the results achieved by exterior rotor design.

INTRODUCTION

In high performance applications with high demands on speed range, lifetime, cleanness or tightness, classical drive systems using ball or sliding bearings can get technical problems. Typical applications are spinning drives, high speed cutting milling machines, turbo compressors, blowers for mainframes, or pumps for the medical or chemical industry. In most of these high technology applications magnetic bearing systems are already used. Depending on the required number of actively controlled degrees of freedom magnetic bearing systems can be equipped with separate devices like radial bearings, axial bearings and motors or as in the case of only three actively controlled degrees of freedom with merely one bearingless drive.

In the last ten years a lot of research work has been done to work out different conceptions for bearingless drives, i.e. drives with integrated winding systems for generating torque as well as radial forces. There are several proposals based on the principle of induction machines, reluctance machines and synchronous permanent magnet motors [3]-[11].

In applications with only three actively controlled degrees of freedom and especially in pump applications, where the non-ferromagnetic pump housing is placed inside the motor air gap, a significant magnetization is necessary to establish the air gap field. In these cases, it is more efficient to use permanent magnet motors instead of electrically excited induction or reluctance motors. Figure 1 shows two examples of a bearingless pump design with an interior and exterior permanent magnet rotor.

In [1], [2] new bearingless permanent magnet motor types were presented by the authors. These motors use only four coils to generate both the radial levitation forces and the torque. In contrast to former proposals with considerably higher numbers of coils, there are some significant differences concerning the design and the functional principle. Table 1 shows a comparison of the two concepts with their substantial differences.

Table 1. Comparison of Bearingless Motors: Classical and Single-Phase Design

	classical bearingless motor	single-phase bearingless motor
winding concept	one winding (radial force control) one winding (torque control)	only one winding
number of phases	three phases (radial force control) three phases (torque control)	four phases (radial force and torque control)
armature fields	rotatory field (radial force control) rotatory field (torque control)	rotatory field (radial force control) alternating field (torque control)
field harmonics	suppressed by chorded and distributed windings	concentrated windings
armature currents	separate currents for radial force and torque control	current components superposed in the current controller
number of coils	depending on the motor design, but much higher than four (typically about 20)	four coils
radial force vector locus curve	radial force amplitude independent from the rotor angle (circular shape)	amplitude depends on the rotor angle (non-circular shape)

Figure 2 presents the constructional principle of the built and tested prototype in exterior rotor design [2], which is characterized by the features mentioned in the last row of table 1.

For the design of the bearingless motor it is very useful to get information about the specific force and torque characteristic using analytical [1,2] or finite element calculation methods. Depending on the application an interior or exterior rotor design can be more advantageous. The following part of the paper will show main differences between these two construction variants. The analysis has been done under the support of the finite element calculation program FEMAG.

FIELD AND FORCE COMPUTATIONS

For time-invariant field problems the system of Maxwell equations can be described by two electrostatic and two magnetostatic equations. The magnetostatic part is defined by the following set of equations

$$\nabla \times \mathbf{H} = \mathbf{J} \quad (1)$$

$$\nabla \cdot \mathbf{B} = 0 \quad (2)$$

where \mathbf{H} defines the magnetic field intensity, \mathbf{J} the electric current density and \mathbf{B} the magnetic flux density.

Further the interaction between \mathbf{B} and \mathbf{H} has to be defined by a material specific equation

$$\mathbf{B} = \mu \mathbf{H} + \mathbf{M} \quad (3)$$

where \mathbf{M} denotes the magnetization of the material.

Since $\nabla \cdot \mathbf{B} = 0$, \mathbf{B} can be represented as a curl of the vector potential \mathbf{A}_p

$$\nabla \times \mathbf{A}_p = \mathbf{B}, \quad (4)$$

i. e. if vector potential \mathbf{A}_p is known the flux density \mathbf{B} can be calculated using (4).

The vector potential is solved numerically by

$$\nabla \times \frac{1}{\mu} \nabla \times \mathbf{A}_p = \nabla \times \mathbf{H} = \mathbf{J}. \quad (5)$$

The numerical computation of the forces acting on the rotor or the stator of the bearingless motor uses Maxwell's force tensor.

Using Maxwell's force tensor, it is supposed that the magnetic field intensity \mathbf{H} is known on the surface enclosing the body. It's also supposed that this body is located in air with $\mu = \mu_0$.

With a differential area ds on the surface and an unit vector \mathbf{n} normal to the surface (with $d\mathbf{s} = \mathbf{n}ds$) Maxwell's tensor is defined by the general expression

$$d\mathbf{F} = -\frac{\mu_0}{2} H^2 d\mathbf{s} + \mu_0 (\mathbf{H} \cdot d\mathbf{s}) \mathbf{H}. \quad (6)$$

or as magnetic pressure

$$\frac{d\mathbf{F}}{ds} = -\frac{\mu_0}{2} H^2 \mathbf{n} + \mu_0 (\mathbf{H} \cdot \mathbf{n}) \mathbf{H} \quad (7)$$

The total force acting on the body is given by the integration of the magnetic pressure over the whole surface.

SIMPLIFICATION OF THE MOTOR MODEL

The magnetic circuit of the motor shown in figure 2 can be simplified by the use of a slotless motor design with an infinite thin current layer at the stator surface in the air gap. The magnetomotive force distribution of the air gap winding should have equivalent values as in the slotted design. The proposed simplification usually shows a good correspondence between calculations and measurements concerning radial forces and the mean value of the torque. Angle dependent torque variations due to the slotting of the stator don't occur in the motor model and therefore have to be neglected.

The forces acting on the rotor or the stator model can be divided into two parts: the Lorentz force components acting on the current layer and the Maxwell components acting on the ferromagnetic material.

For two-dimensional field problems with the condition for the ferromagnetic permeability $\mu_{fe} \gg \mu_0$ the two components can be derived from (7) in the following way

$$\frac{d\mathbf{F}(\varphi)}{ds} = \begin{pmatrix} \frac{B_n^2(\varphi)}{2\mu_0} \\ 0 \\ 0 \end{pmatrix} + \begin{pmatrix} -\frac{1}{2}\mu_0 A^2(\varphi) \\ A(\varphi)B_n(\varphi) \\ 0 \end{pmatrix}. \quad (8)$$

with B_n as normal component of the flux density B and A as the current density distribution along the stator surface. In (8) the first row of the vectors denotes the normal and the second row the tangential pressure components. Usually the normal component of the Lorentz vector can be neglected.

INTERIOR ROTOR DESIGN

Depending on the specifications of the application, the decision about the motor design either with interior or exterior rotor has to be made. As the following analyses will show there are differences not only in the mechanical design but also from the magnetic point of view.

Figure 3 presents an example of a motor model in interior rotor design. The stator comprises four concentrated coils. The rotor is equipped with four cylindrical permanent magnets which provide approximately a rectangular magnetic field distribution in the air gap. Depending on the phase currents a two pole armature field as well as a four pole armature field can be produced by the stator windings. According to the supposed motor design the two pole field is used for levitation force and the second field for torque control.

For the computation of the characteristic levitation force locus curve it is supposed that the rotor is turned while the phase currents are constant and the currents in two opposite slots compensate each other whereas the currents in the other two slots have the same amplitude and direction. In this case we get the two pole armature configuration.

Figure 4 shows the force vectors computed using (8) for different rotor angle steps. The force amplitudes in the two main axes of the diagram differ significantly. This effect is also demonstrated by figures 5 and 6 which show the flux density distribution of the motor in two orthogonal positions (rotor angle $\delta_1=0^\circ$; $\delta_2=90^\circ$). There are different reasons which are responsible for this behavior. One reason is the substantial influence of harmonics in the current and field distribution. The magnetic conditions are not comparable to idealized conditions with sinusoidal current and field distributions which would lead to a circular levitation force locus curve. Another reason are the different directions of rotation concerning the Lorentz and the Maxwell force vectors. Figure 7 and 8 illustrate the two force components separately.

A better performance can be achieved by a sinusoidal permanent magnet field distribution. The corresponding levitation force curve is presented in figure 9. In this case the force locus curve has an elliptical shape. With appropriate corrective currents in the motor windings the levitation forces can be produced in all directions. This would not be possible using the motor design with rectangular magnetic field distribution shown in figure 3.

EXTERIOR ROTOR DESIGN

The corresponding motor model design of figure 3 is shown in figure 10. The only difference is that in this motor design the rotor is outside the stator. The dimensions of the air gap diameter and the magnet height as well as the current distribution are the same. In contrast to the interior rotor results of figure 4 the force vector of figure 11 describes a curve which is not very far away from an ideal circular shape. An advantage of this design is the common direction of rotation of the Lorentz and the Maxwell force vectors (figures 12 and 13). In the superposition the two (non ideal) components complement each other to a curve with a relatively small amplitude variation. From the mechanical point of view the exterior rotor design can lead to better motor performance concerning torque ripple and cogging torque. Owing to the higher inertia the dynamic behavior of course is worse than in the interior rotor variant.

CONCLUSIONS

Owing to the integration of both the torque and the levitation force, windings in the stator bearingless permanent motors are distinguished by a very compact motor construction. In some applications like pumps, fans or blowers with no special demands on the starting torque a single-phase motor can be well suited for low cost devices.

The proposed motor design with only four concentrated coils leads to non-circular force locus curves. The shape of these curves is formed by Lorentz and Maxwell force components acting on the current layers and on the surface of the ferromagnetic materials. Finite element calculations show that the force characteristic is strongly influenced by the rotor design. The exterior rotor design shows better results than the interior rotor variant. An advantage of the exterior design is the common direction of rotation of the Lorentz and the Maxwell force vectors. In the superposition the two (non ideal) components complement each other to a curve with a small variation of the force amplitude.

ACKNOWLEDGMENT

The project was kindly supported by the Laboratory for Electrical Engineering Design (EEK) of Swiss Federal Institute of Technology, Zurich (ETH Zurich) and Sulzer Electronics AG, CH-Winterthur.

REFERENCES

- [1] W. Amrhein, S. Silber, "Bearingless Single-Phase Motor with Concentrated Full Pitch Windings in Interior Rotor Design", Proc. ISMB-6, Cambridge, MA USA, pp. 486-496, August 1998.
- [2] S. Silber, W. Amrhein, "Bearingless Single-Phase Motor with Concentrated Full Pitch Windings in Exterior Rotor Design," Proc. ISMB-6, Cambridge, MA USA, pp. 476-485, August 1998.
- [3] R. Schöb, N. Barletta, "Principle and application of a bearingless slice motor", Proc. ISMB-5, Kanazawa, Japan, pp. 313-318, Aug. 1996.
- [4] R. Schöb, Beiträge zur lagerlosen Asynchronmaschine, Dissertation, ETH Zürich, 1993
- [5] J. Bichsel, Beiträge zum lagerlosen Elektromotor, Dissertation, ETH Zürich, 1990.
- [6] R. Schöb, J. Bichsel, "Vector control of the bearingless motor", Proc. 4th Int. Symp. Magn. Bearings, Zurich, Switzerland, 1994
- [7] H. Bleuler, H. Kawakatsu, W. Tang, W. Hsieh, D.K. Miu, Y. Tai, F. Moesner, M. Rohner, "Micromachined active magnetic bearings", Proc. ISMB-4, Zürich, Switzerland, pp. 349-352, August 1994.
- [8] T. Ohishi, Y. Okada, K. Dejima, „Analysis and design of a concentrated wound stator for synchronous-type levitated motor", Proc. ISMB-4, Zürich, Switzerland, pp. 201-206, August 1994.
- [9] M. Oshima, S. Miyazawa, T. Deido, A. Chiba, F. Nakamura, T. Fukao, "Characteristics of a Permanent Magnet Type Bearingless Motor", IEEE Trans. Ind. Applic., vol. 32/2, pp. 363-369, March/April 1996.

- [10] Y. Okada, S. Miyamoto, T. Ohishi, "Levitation and Torque Control of Internal Permanent Magnet Type Bearingless Motor", IEEE Trans. on Control Syst. Techn., vol. 4/5, pp. 565-571, September 1996.
- [11] M. Ooshima, A. Chiba, T. Fukao, M. A. Rahman, "Design and Analysis of Permanent Magnet-Type Bearingless Motors", IEEE Trans. on Indus. Electr., vol. IE-43, no. 2, pp. 292-299, April 1996.

FIGURES

Figure 1. Bearingless motor in a pump application (interior and exterior rotor design).

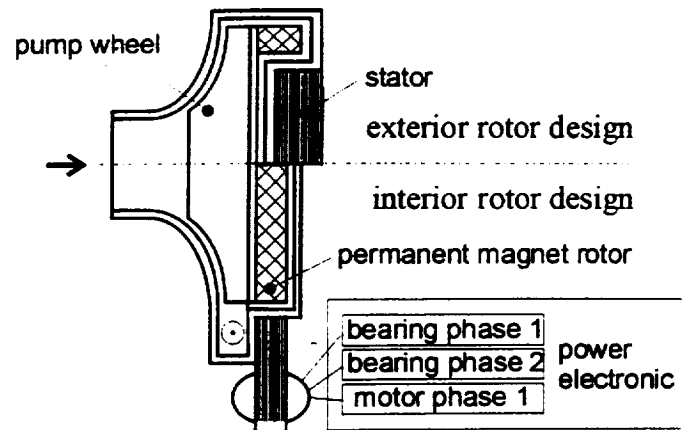


Figure 2. Principle construction of the bearingless motor in exterior rotor design.

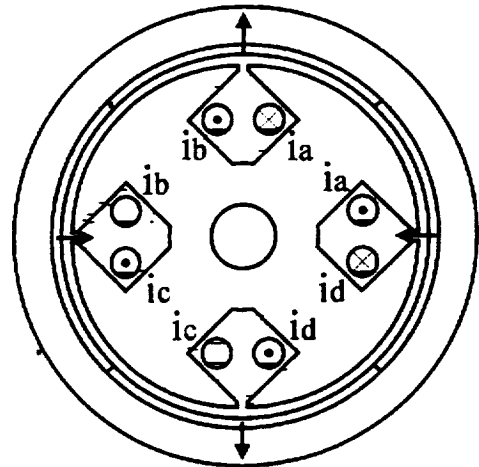


Figure 3. Simplified motor model in interior rotor design.

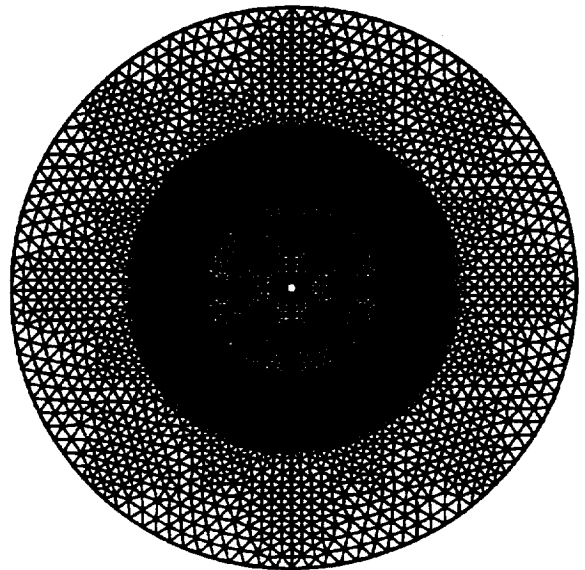


Figure 4. Force locus curve of the motor in interior rotor design (rectangular flux density distribution).

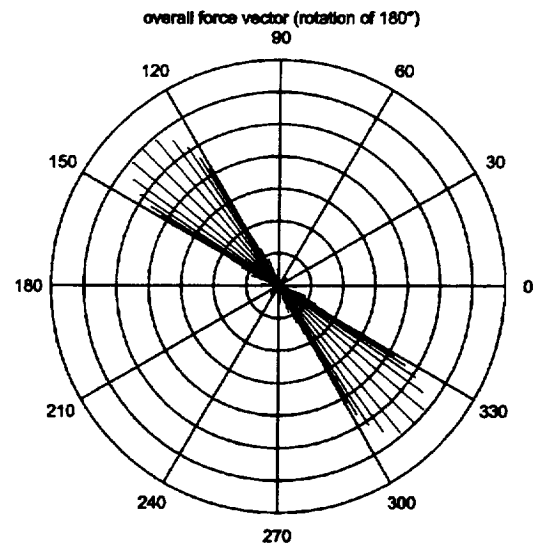


Figure 5. Field distribution for rotor position $\delta=0^\circ$.

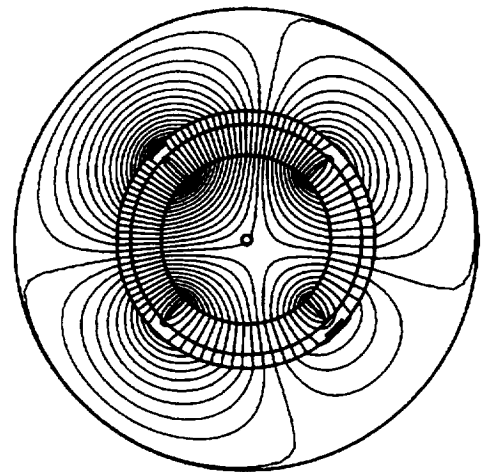


Figure 6. Field distribution for rotor position $\delta=90^\circ$.

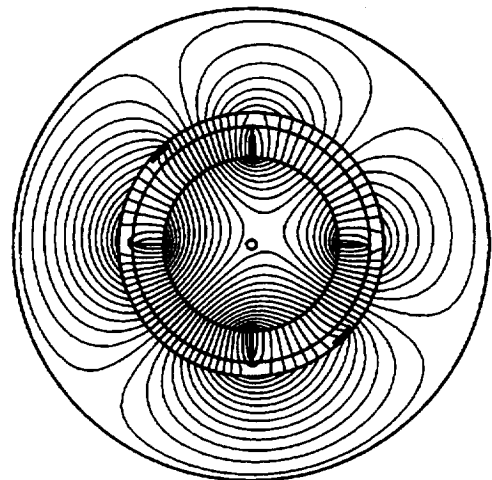


Figure 7. Lorentz forces of figure 4.

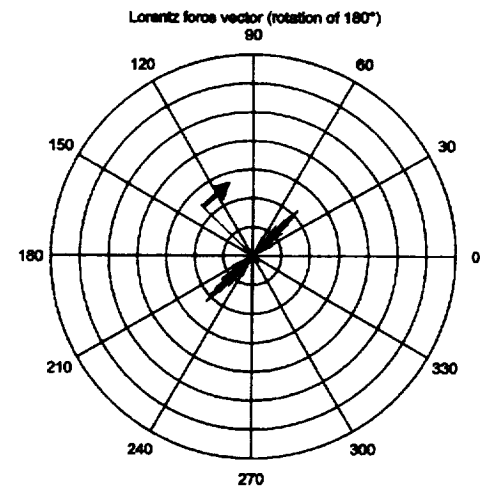


Figure 8. Maxwell forces of figure 4.

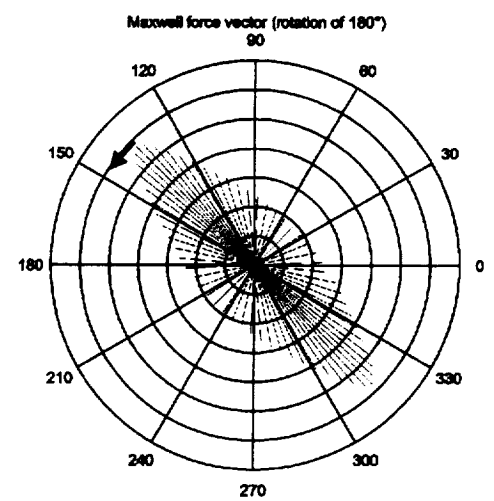


Figure 9. Force locus curve of the motor in interior rotor design (sinusoidal flux density distribution).

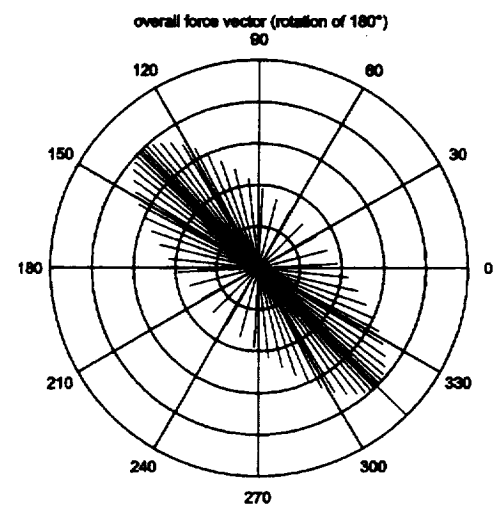


Figure 10. Simplified motor model in interior rotor design.

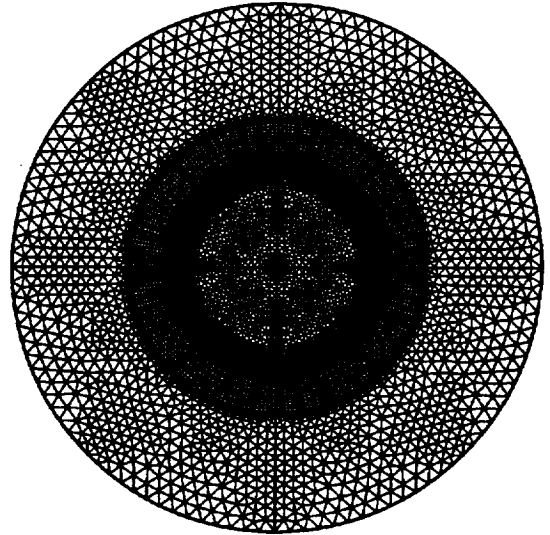


Figure 11. Force locus curve of the motor in exterior rotor design (rectangular flux density distribution).

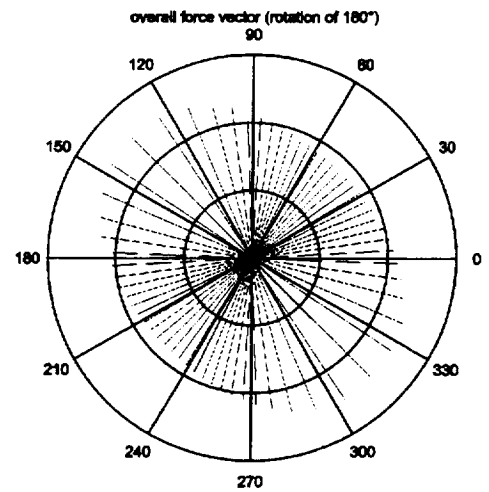


Figure 12. Lorentz forces of figure 11.

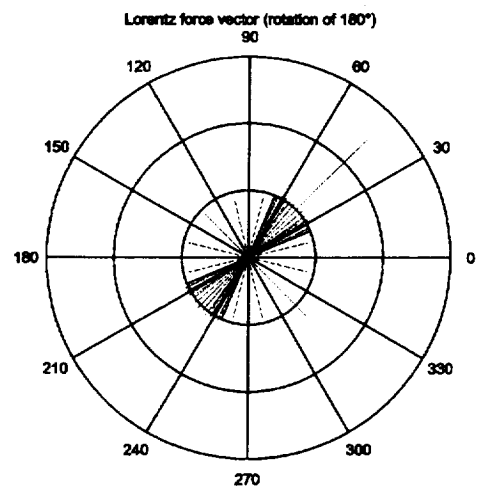
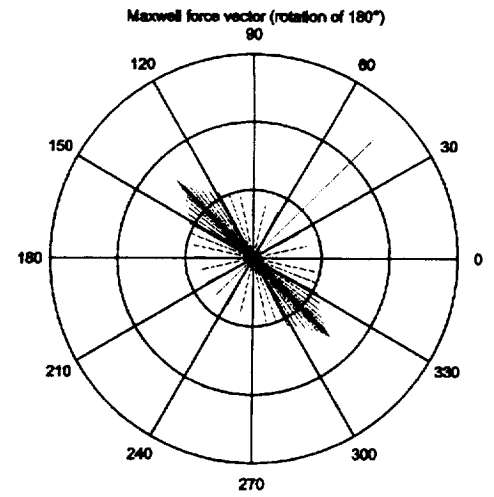


Figure 13. Maxwell forces of figure 11.



A COMPARISON OF EXPERIMENTAL AND THEORETICAL RESULTS FOR MAGNETIC BEARINGS*

Robert I. Hibbs, Jr.
Joseph K. Scharrer
Bonnie A. Galvin
Mark W. Galvin
Rotordynamics-Seal Research
North Highlands, CA 95660

ABSTRACT

A comprehensive program was undertaken to experimentally characterize the static and dynamic characteristics of a heteropolar magnetic bearing and to develop nonlinear theoretical models capable of accurately predicting magnetic bearing performance. This paper presents the results for the static characteristics of the magnetic bearing and a comparison with the predictions from the analytical model. The results indicate that the nonlinear theoretical model can accurately predict the static characteristics of the magnetic bearing.

SYMBOLS AND ABBREVIATIONS

A	- magnetic vector potential
B	- flux density
F	- force
H	- field intensity
I	- current
J	- current density
ν	- reluctivity of the material
σ	- conductivity of the material

subscripts

x,y,z - spatial coordinates

* This work was partially sponsored by NASA Lewis Research Center under contract NAS3-27827 and NASA Marshall Space Flight Center under contract NAS8-40584.

INTRODUCTION

The magnetic bearing holds great promise for product lubricated and non-lubricated rotating machinery. Although the potential benefits in terms of bearing friction losses, condition monitoring, and active control are many, there is a great price to be paid in terms of increased complexity. The complexity and lack of fundamental understanding of magnetic bearing static and dynamic performance characteristics have limited its application in both aerospace and industrial machinery.

One important application where detailed knowledge of magnetic bearing force characteristics is required is their use as force measurement devices in rotordynamic test rigs^{1,2,3,4,5}. Scharrer et al.¹ showed that use of magnetic bearings for this application requires accurate calibration of the magnetic bearing's static characteristics and transfer function in order to obtain acceptable measurement uncertainty. Without such a calibration, the data from the test apparatus will be questionable at best.

To better understand magnetic journal bearing technology, a number of researchers have attempted to characterize them both analytically and experimentally. Hibbs and Scharrer⁶ and Scharrer and Powers⁷ review previous efforts in magnetic bearing actuator analysis and rotordynamic analysis, respectively.

There are basically two experimental approaches to the characterization of journal bearings (magnetic or otherwise), rotor model-matching and direct component measurement. Rotor model matching involves the building of a test rotor with somewhat known properties and mounting the rotor in a housing with two of the bearings of interest. Test data for rotor displacement is measured and through comparison with rotor static and dynamic analysis predictions, journal bearing performance is inferred. This technique has been utilized in the past with many kinds of fluid film and mechanical bearings with the same result: large uncertainty and misleading results. This technique has also recently been utilized for magnetic bearings^{8,9}. No attempt at predicting the uncertainty was made in either case.

Accurate results for journal bearing characteristics are best obtained through direct component measurement. This technique requires the complete isolation of the test bearing so that all forces are reacted through the test bearing and measured directly. Imlach et al.¹⁰ reported the first component measurements of static force characteristics for a heteropolar magnetic bearing. A closed loop controller was employed. The measurements were somewhat indirect in that a load was applied at the end of the shaft and analytically corrected to adjust for the offset relative to the bearing's actual position. The authors reported stiffness as a function of shaft eccentricity. No experimental uncertainty was reported.

Knight et al.¹¹ tested a heteropolar magnetic journal bearing without a controller. Loads were applied to one actuator at a time. The authors reported force of the single actuator as a function of position. Experimental uncertainty was reported.

The present effort is focused on measurement of the force versus current characteristics of a full heteropolar bearing with closed loop control.

ANALYTIC MODEL

The current model⁶ is focused on the actuator design and characterizes the following nonlinearities of magnetic bearings.

- Nonlinear stator/rotor core permeability
- Nonlinear force/ flux relationship
- Magnetic leakage and fringing effects
- Air gap non-uniformity (eccentricity)
- Eddy current effects - rotational and control current frequency

Slew rate and other controller dependent effects are modeled separately as discussed by Scharrer and Powers⁷. The two dimensional magnetic bearing analysis solves the harmonic vector potential equation. Derivation continues from Maxwell's field equations:

$$\frac{\partial}{\partial x} \left(\nu_z \frac{\partial A_z}{\partial x} \right) + \frac{\partial}{\partial y} \left(\nu_y \frac{\partial A_y}{\partial y} \right) = \sigma \frac{\partial A_z}{\partial t} - J_z \quad (1)$$

The transient term is further split into a rotational and control current term. The control current is assumed to harmonically vary so that $J_z = J_z e^{j\omega t}$ that requires the magnetic vector potential to vary similarly, $A_z = A_z e^{j\omega t}$. A novel approach is used to solve for the vector potential.

Nonlinear magnetic flux - magnetomotive force relationship is included in the analysis by allowing the reluctivity to vary with the magnetic flux such that $\nu = \nu(B)$. The medium is assumed to be isotropic ($\nu_x = \nu_y$). The periodic boundary condition was used between the actuators on the magnetic bearing, and zero vector potential was set at the inner radius of the rotor and the outer radius boundary.

TEST APPARATUS

The test apparatus employed for this effort is shown in figure 1. The test rig can support the test article either horizontally or vertically. For this effort, the test article was supported vertically in order to eliminate gravity effects and difficulties associated with determination of the zero position control current¹⁰.

In the vertical position, the test article is supported by four flexures that connect to the test article through a ring attached at the mid-plane. The stiffness of the flexures was small. Calibration of the flexure stiffness was accomplished to account for its contribution to the measurement uncertainty. For this test the shaft was nonrotating and hard mounted to the support structure. Four SKF proximity probes were mounted at each end of the test article. The proximity probes had a range of 1.3 mm and were specially calibrated for this application to insure that the magnetic field would not interfere with the measurement accuracy. SKF had the only product found to be suitable for this application. The load was applied through a loading rod connected on one end to the mounting ring and at the other end to a strain-gauged load bolt from A. L. Design. The capacity of the load bolt was 9200 N. All displacement, current, and load data was acquired using a Pemtech data acquisition system. The sample rate used was 100 Hz.

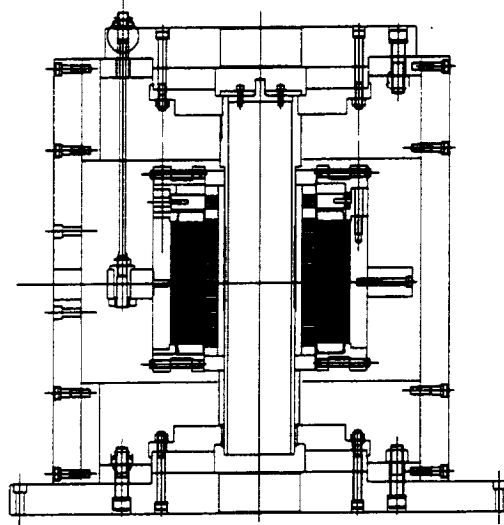


Figure 1. Magnetic bearing test rig

TEST BEARING

The test bearing was a four pole, E-sector heteropolar magnetic bearing from Revolve Technologies. The bearing geometry and material properties are given in Tables 1 and 2, respectively. A representative magnetization curve for Hiperc 50 with a rotor anneal is shown in figure 2.

Table 1. Bearing Geometry

Stator Stack Length (mm)	152.400
Stator OD (mm)	226.081
Stator ID (mm)	140.716
Rotor OD (mm)	139.700
Rotor Lamination ID (mm)	105.973
Nominal Gap (mm)	0.508
Small Pole Width (mm)	16.060
Pole Height (mm)	25.819
Slot Width (at ID) (mm)	15.277
Pole Centerline Angle (radians)	0.224

Table 2. Material Properties

Rotor Material	Hiperco 50
Stator Material	Hiperco 50
Sat. Flux Density, Tesla	1.80
Rotor Lam. Thickness (mm)	0.3556
Stator Lam. Thickness (mm)	0.3556
Mat. Resistivity ($\mu\text{ohm}\cdot\text{mm}$)	48.0
Density (N/cu.cm)	0.07

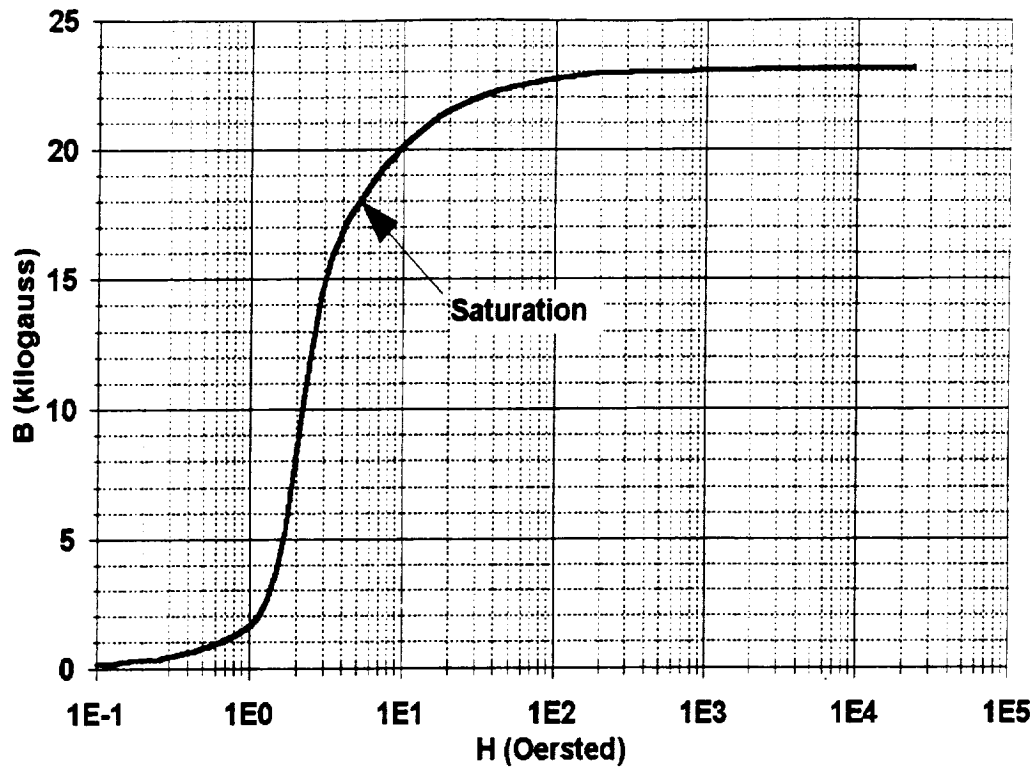


Figure 2. Magnetization curve for Hiperc 50

UNCERTAINTY ANALYSIS

The uncertainty analysis was performed using the methods outlined by Coleman and Steele¹². End to end calibration of the entire system (i.e., transducer to D/A) was conducted to obtain the necessary inputs to the uncertainty analysis. The calculated uncertainties in the force and current measurements were 10.5 N and 0.25 mA, respectively.

RESULTS AND COMPARISON

Using the loading rod, the bearing was incrementally loaded over the range 0-8000 N. The bearing load was increased in 222 N increments. Data was taken continuously as the load was increased and decreased over the complete range. The loading was applied through the center of the actuator pole and between actuator poles. The bearing maintained a centered position for all load points. The results of the on pole loading are shown in figure 3. The figure shows that the nonlinear predictions are much closer to the test data and have the same characteristic curvature as the test data. The linear predictions are in error as much as 20% when compared to the test data. Figure 4 shows the load between pole data. Again, the nonlinear predictions are much closer to the test data than the linear predictions. The curvature in the data and the nonlinear prediction is much less pronounced.

The current shown in the graphs is twice the control current. Beyond around 5 amps on the graphs, the loaded actuator becomes saturated. Bias current in the actuator gives a maximum magnetic flux around 17 kG which is in the upper part of the linear range of the magnetization curve (see figure 2). This indicates that the bearing is operating in the nonlinear range of material properties.

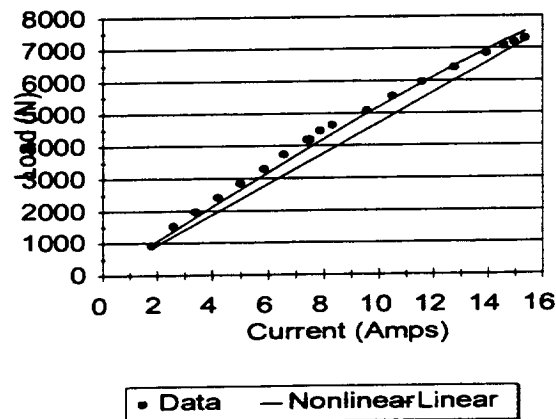


Figure 3. Load on pole data

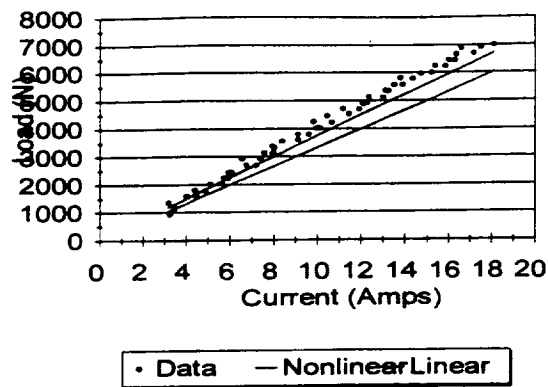


Figure 4. Load between poles data

CONCLUSIONS

New experimental data for the force versus current characteristics of a heteropolar magnetic bearing were presented. The data indicate that the force characteristics are nonlinear. Results from a previously developed nonlinear analysis technique were compared to the test data. The agreement between theory and experiment was good.

REFERENCES

- ¹Scharrer, J., Mosher, P., and Greenhill, L., "Pump Impeller Test Method Using Dynamically Calibrated Magnetic Bearings," AIAA Paper 95-2406, 1995.
- ²Gahler, C. and Forch, P., 1994, "A Precise Magnetic Bearing Exciter for Rotordynamic Experiments," Proceedings, Fourth International Symposium on Magnetic Bearings, pp. 193-200.
- ³Guinzburg, A. and Buse, F., 1994, "Axial and Radial Forces on a Pump Impeller Obtained with a Magnetic Bearing Force Measurement Rig," Proceedings, Fourth International Symposium on Magnetic Bearings, pp. 537-542.
- ⁴Matros, M. and Nordmann, R., 1996, "Dynamic Characteristics of a Hydrostatic Bearing Identified by Active Magnetic Bearings," Rotordynamic Instability Problems in High Performance Turbomachinery, proceedings of a workshop held at Texas A&M University.

⁵Wagner, N. and Steff, K., 1996, "Dynamic Labyrinth Coefficients from a High-Pressure Full-Scale Test Rig Using Magnetic Bearings," Rotordynamic Instability Problems in High Performance Turbomachinery, proceedings of a workshop held at Texas A&M University.

⁶Hibbs, R. and Scharrer, J., "Nonlinear Magnetic Bearing Analysis," AIAA paper 97-3101, 1997.

⁷Scharrer, J. and Powers, R., "Transient, Nonlinear Rotordynamic Analysis of a Cryogenic Turbopump with Magnetic Bearings," AIAA Paper 96-2739, 1996.

⁸Gahler, C. and Herzog, R., "Identification of Magnetic Bearing Systems," Proceedings, Fourth International Symposium on Magnetic Bearings, pp. 293-298, 1994.

⁹Lee, C.W., Ho, Y.H., and Kim, C.S., "Identification of Active Magnetic Bearing System Using Magnetic Force Measurement," Proceedings, Fourth International Symposium on Magnetic Bearings, pp. 305-3309, 1994.

¹⁰Imlach, J., Blair, B., and Allair, P., "Measured and Predicted Force and Stiffness Characteristics of Industrial Magnetic Bearings," ASME paper 90-TRIB-70, 1990.

¹¹Knight, J.D., Xia, Z., McCaul, E., and Hacker Jr., H., "Determination of Forces in a Magnetic Bearing Actuator: Numerical Computation with Comparison to Experiment", Journal of Tribology, v114, pp. 784-788, 1992.

¹²Coleman, H. and Steele, W., Experimentation and Uncertainty Analysis for Engineers, 1989, John Wiley and Sons, New York.

Session 6 -- Applications 1

Chairman: H. Ming Chen
Foster-Miller Technologies

Animal Trials of a Magnetically Levitated Left-Ventricular Assist Device

Brad Paden¹, James Antaki², and Nelson Groom³

Abstract

The University of Pittsburgh/Magnetic Moments mag-lev left-ventricular assist devices (LVADs), the Streamliner HG3b and HG3c, have successfully been implanted in calves. The first was implanted for 4 hours on July 10, 1998 (Figure 1) and the second for 34 days on August 24, 1999 respectively. The tests confirmed the feasibility of low power levitation (1.5 watts coil power) and very low blood damage in a mag-lev ventricular assist device. In this paper, we describe the unique geometry of this pump and its design. Key features of this LVAD concept are the passive radial suspension and active voice-coil thrust bearing.

I. Introduction

The University of Pittsburgh's McGowan Center for Artificial Organs and Magnetic Moments, LLC, have brought a mag-lev LVAD to the *in vivo* animal testing stage. The first test was 4-hours long and was conducted with the polycarbonate HG3b version of the Streamliner on July 10, 1998 (Figure 1). Following this initial demonstration of feasibility and low blood damage, the titanium HG3c was fabricated and tested for 34 days in a calf following implantation on August 24, 1999. The Streamliner design affords low-power levitation (1.5 watts of levitation coil power) and very high reliability. These successful trials mark a turning point in the efforts of many researchers to devise such a magnetically levitated pump.

The research effort to develop a reliable mag-lev LVAD is motivated by a tremendous human need. In the U.S. alone, 700,000 deaths per year are attributed to heart diseases such as myocardial infarction and cardiomyopathy [Hogness 1991]. It is estimated that at least 35,000 to 70,000 of these lives can be saved with a mechanical cardiac assist device. Further, the worldwide need is an overwhelming 200,000 per year. Technologies for mechanical circulatory support, particularly left-ventricular assist devices (LVADs) have evolved to commercially viable medical devices. However, a *long-term* implantable LVAD has been elusive due to mechanical wear and limited biocompatibility. These two problems can be addressed through

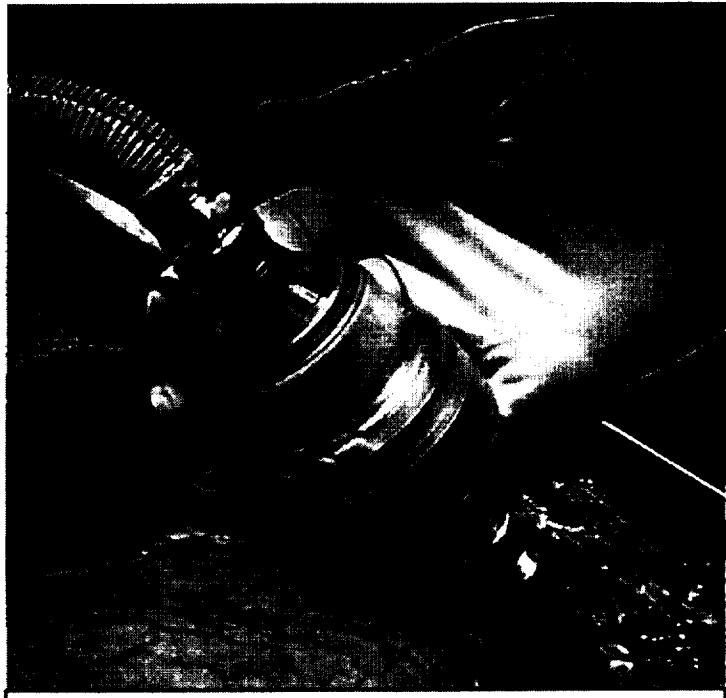


Figure 1. HG3b implant in a calf (July 10, 1998)

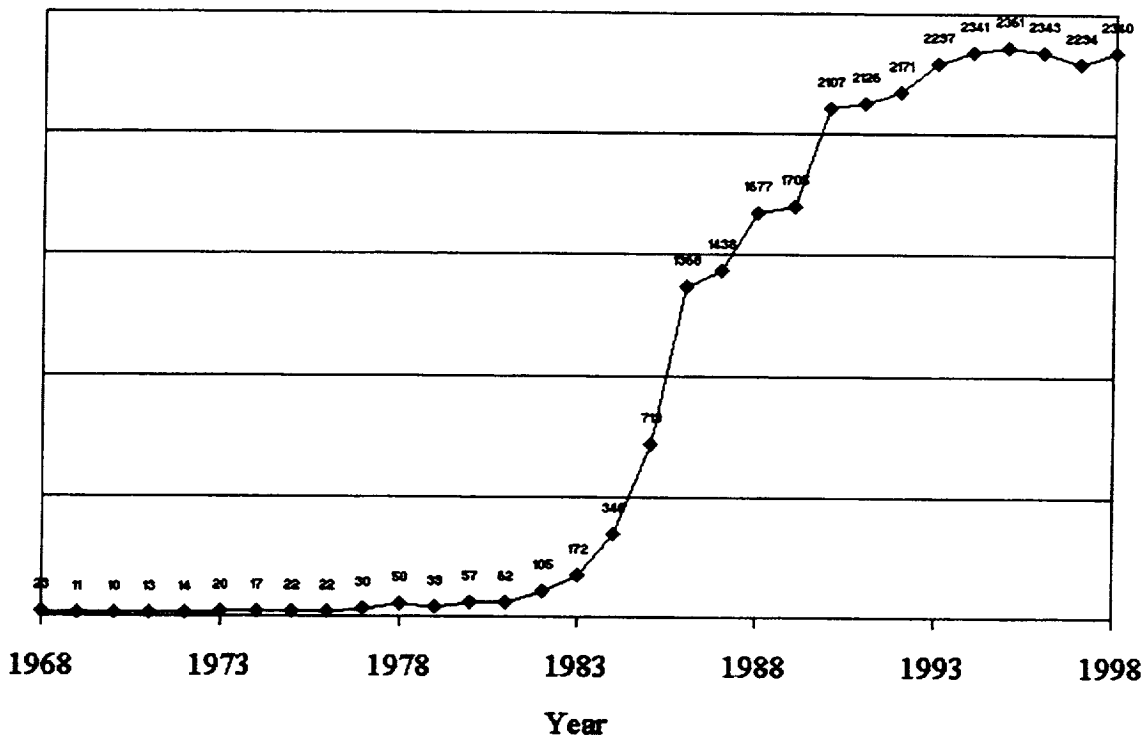
¹ Department of Mechanical and Environmental Engineering, University of California, Santa Barbara, 93106, paden@engineering.ucsb.edu, and Magnetic Moments, LLC, Goleta, CA.

² Department of Surgery, University of Pittsburgh.

³ NASA Langley Research Center.

Figure 2.

Number of Heart Transplants in years 1968-1998



the application of magnetic suspension technology. Basic mag-lev research at Magnetic Moments in collaboration with NASA, and hemodynamics and pump research at the University of Pittsburgh on the Streamliner artificial heart have created an LVAD capable of meeting the needs of a tremendous number of patients.

The supply of human hearts for transplant is limited to 2,500 per year in the U.S. at best. Once anti-rejection drugs were developed making heart transplantation practical, the treatment grew exponentially, doubling about every year in the mid 1980's until limits in supply capped the growth (see Figure 2). It is reasonable to expect that long-term LVAD use will follow a similar growth curve, but will not be limited by supply. The application of LVADs is much broader than that for transplants, and patients do not need immunosuppressive anti-rejection drugs.

Mechanical circulatory support has a long background with many device types explored and much gained in basic knowledge. The first approach applied in human clinical trials was the total artificial heart (TAH). This is the conceptually simple removal of the human heart and replacement with two mechanical pumps to simulate both the left and right ventricles. Dr. Jarvik, a veterinarian, is credited with the design of the first artificial heart, which sustained a patient for 112 days



Figure 3. Clockwise from upper left: Jarvik-7, Baxter/Novacor LVAD, Streamliner HG3a

[Marshall 91]. His Jarvik-7 TAH (upper left in Figure 3) was used in 3 more patients with limited success. The Jarvik-7 has found a niche as a temporary TAH implanted for interim use while patients and surgeons await a human heart for transplant. This bridge-to-transplant application of assist devices is a beneficial use of mechanical circulatory support, and is seen as a stepping stone market for long-term use for our device. The Baxter/Novacor LVAD (upper right in Figure 3) is the first to receive approval for permanent implantable use, and was granted preliminary market approval (PMA) in 1998 by the FDA. The first Streamliner prototype is shown in the lower center of the Figure 3.

The applications of LVADs can be apportioned into four areas. The term of use for each application varies a great deal:

Post-Cardiotomy (1-2 weeks): Numerous short-term disposable devices currently serve this application. It is therefore not an ultimate target market for the Streamliner LVAD.

Bridge-to-Transplant (BTT) (< 1 year): The maximum number of heart transplants in the U.S. is approximately 2,500 per year. Simultaneously, roughly 30,000 patients are awaiting a heart transplant. Thus, for those who are critically ill, it may be advisable to use an LVAD temporarily while the patients await a transplant. Bridge-to-transplant use may become "chronic support" use by default if a transplant does not become available.

Bridge-to-Recovery (< 1 year): Remarkably, some patients who receive a ventricular assist device experience marked recovery from their heart failure. In some cases the VAD has been removed and the patient discharged from the hospital.

Chronic Support (> 1 year): An estimate of the patient pool needing chronic support with an LVAD is approximately 35,000-70,000 per year in the U.S. This patient group is now served by the Baxter/Novacor LVAD that is only suitable for use up to 2 years due to thrombus and thromboembolism.

It is clear that there are a multitude of patients and applications requiring a high-performance implantable LVAD. By 2005, implantable LVAD's may be as common as pacemakers are today.

II. Background

The HG3 mag-lev LVAD was the first fully magnetically-suspended pump to be implanted as in an *in-vivo* animal trial on July 10, 1998. A second titanium pump was implanted for a 34-day trial in August 24, 1999. Both animal trials were performed at the McGowan Center for Artificial Organs at the University of Pittsburgh. One of the key technical achievements of this design was the efficient magnetic levitation scheme requiring only 1.5 Watts of levitation coil power while pumping. Further the pump design and motor have optimized designs enabling low-power operation.

The Streamliner's success in fully implanted *in vivo* studies follows a number of major contributions by researchers in the area of mag-lev LVADs. Bramm, Novak and Olsen [Bramm 81] appear to be the first to advocate magnetic suspension in LVADs in the literature. Subsequently, a prototype device was successfully levitated as reported by Bramm and Olsen [Bramm 85]. Akamatsu et al [Akamatsu 89, 92, 94] tested a magnetically suspended centrifugal pump in the laboratory. This pump has a magnetically levitated centrifugal impeller magnetically coupled to a conventional bearing supported motor.

The University of Utah/University of Virginia team (P. Allaire, E. Maslen, H. Kim, D. Olsen, and G. Bearnson) developed a fully-levitated LVAD prototype (CFVAD 2) and tested it in water achieving 6 L/min and 100mmHg at 2,400 RPM and 50 Watts of levitation power [Allaire 95, 96]. A subsequent prototype (CFVAD III) has a much more efficient levitation system requiring only 8 watts of power [Hilton 97], [Allaire 98].

There are a number of patents on magnetically levitated blood pumps listed in Figure 4. These are easily accessible at the IBM Patent server site (the current URL is www.patents.ibm.com).

US Patent #	Date	Inventors
4,688,998	08/25/87	Olsen, Bramm, and Novak
4,763,032	08/09/88	Bramm and Novak

4,779,614	10/25/88	Moise
4,994,748	07/31/90	Bramm and Olsen
5,078,741	01/07/92	Bramm and Olsen
5,112,202	05/12/92	Oshima, Nakazeki, Akamatsu, and Niki
5,195,877	03/23/93	Kletschka
5,326,344	07/05/94	Bramm and Olsen
5,385,581	01/31/95	Bramm and Olsen
5,443,503	08/22/95	Yamane
5,470,208	11/28/95	Kletschka
5,507,629	04/16/96	Jarvik
5,695,471	12/09/97	Wampler
5,725,357	03/10/98	Nakazeki
5,840,070	11/24/98	Wampler
5,928,131	07/27/99	Prem
6,015,272	01/13/00	Antaki, Paden, Burgreen and Groom

Figure 4. US Patents on Fully Magnetically Levitated Blood Pumps

III. System Description

The preferred Streamliner LVAD implant configuration is shown in Figure 5 and consists of

- Inflow and outflow cannulae, which connect the pump to the left ventricle and aorta respectively.
- Internal controller, which controls and monitors the pump.
- Small internal battery, which powers the pump for limited periods, allowing complete mobility (such as when taking a shower).
- External controller, for programming and monitoring the pump.
- External battery, which recharges the internal battery and powers the pump for extended periods.
- Transcutaneous energy transmission system (TETS), which transmits power through the skin to recharge the internal battery and/or power the pump.

The TETS also carries the control signals between the external and internal controllers. Therefore, the system is fully implantable and fully self-contained—there are no wires or ports that penetrate the skin. Except for the need to periodically recharge the battery, this system would provide extremely high mobility and quality of life for the patient.

A cross section of the pump is shown in Figure 6 together with a table of parts. The key suspension components are fore and aft passive permanent magnet bearings and the voice-coil thrust actuator. The advantage of this design is that the blood shear is low in the relatively small diameter gap on the inner pump stator section. Note that the rotor is hollow and supported on a fixed shaft supported by the inlet and outlet hubs.

Streamliner Ventricular Assist System

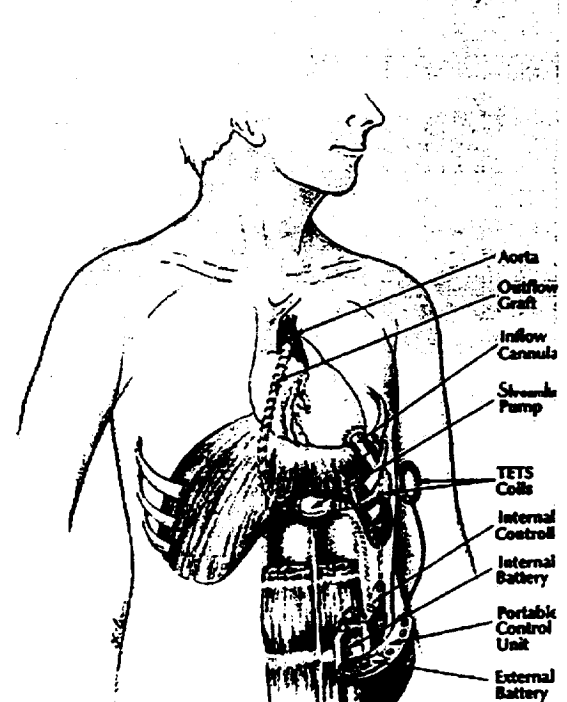
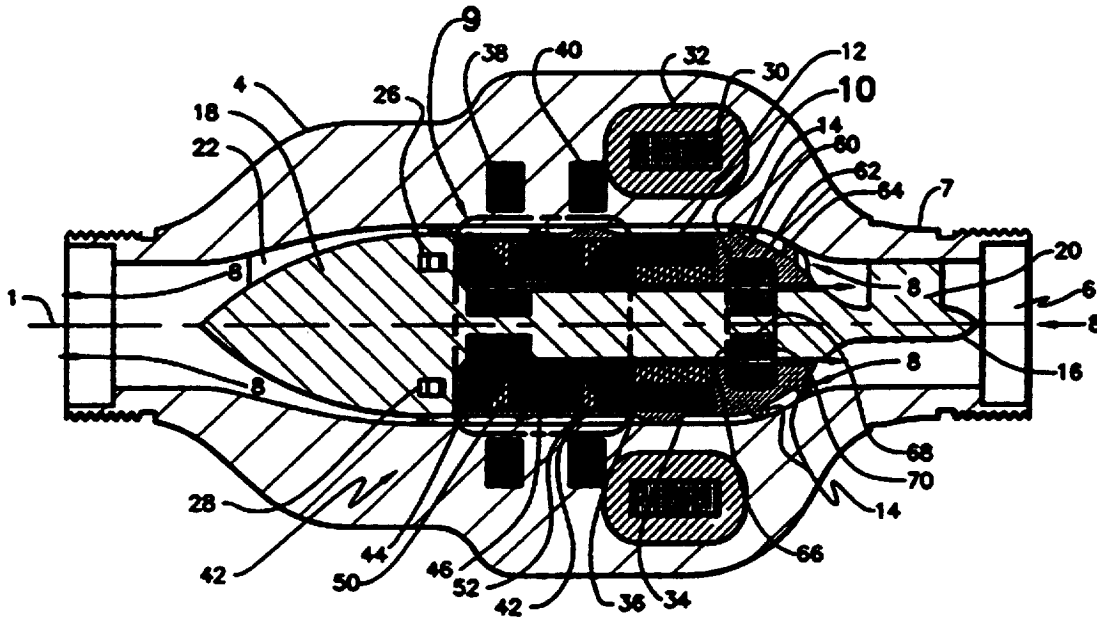


Figure 5. System Configuration

Figure 6. Cross section of HG3c and parts list.



part #	description
1	pump axis of symmetry
4	aft housing
6	inlet
7	fore housing
8	primary blood flow path
9	aft magnet assemblies (two parts). The inner bearing stack forms the inner race of permanent magnet bearing. The outer magnets and pole iron stack serves two purposes: a) it is the outer race of the aft PM bearing, and b) it is the magnet structure for the axial actuator – it interacts with the coils 38 and 40 to provide thrust force.
10	fore PM bearing stacks
12	magnetically levitated impeller (hollow)
14	impeller blades
16	inlet hub
18	outflow hub
20	inlet stator blade and support
22	outflow stator blade, converts rotational kinetic energy in the blood in to pressure
30	slotless iron laminations of motor stator
32	toroidal winding on slotless 2-pole DC brushless motor stator
34	2-pole DC brushless motor magnet

36	motor rotor iron
38	thrust actuator coil
40	thrust actuator coil
26, 28	axial position sensor, used for feedback control of the rotor axial position.
42,44,46	voice-coil actuator magnets. The aft two magnets also serve as the outer race of the aft PM bearing
50,52	iron focusing poles direct field toward coils 38 and 40.
60,62,64	outer bearing race magnet
66, 68, 70	inner race magnet rings

IV. Passive bearings

The design of the passive radial bearings was facilitated with the development of design formulae for passive PM bearings. For passive magnetic bearings with dimensions shown in Figure 7, we derived design equations for the radial restoring force per unit of journal cross section

$$\frac{F(x,g,d)}{2LR} = \frac{4B_r}{\pi\mu_0} \sum_{\substack{n=1 \\ \text{odd}}}^{\infty} \frac{1}{n^2} (1 - e^{-n2\pi d/\lambda}) e^{-n2\pi g/\lambda} I_1(n2\pi x/\lambda)$$

where the left-hand side of the equation is the radial restoring force divided by the journal cross section. The right-hand side depends on the remanance, B_r , of the magnetic material and the bearing geometry as given in the Figure 7. The function I_1 is the modified Bessel function of order 1.

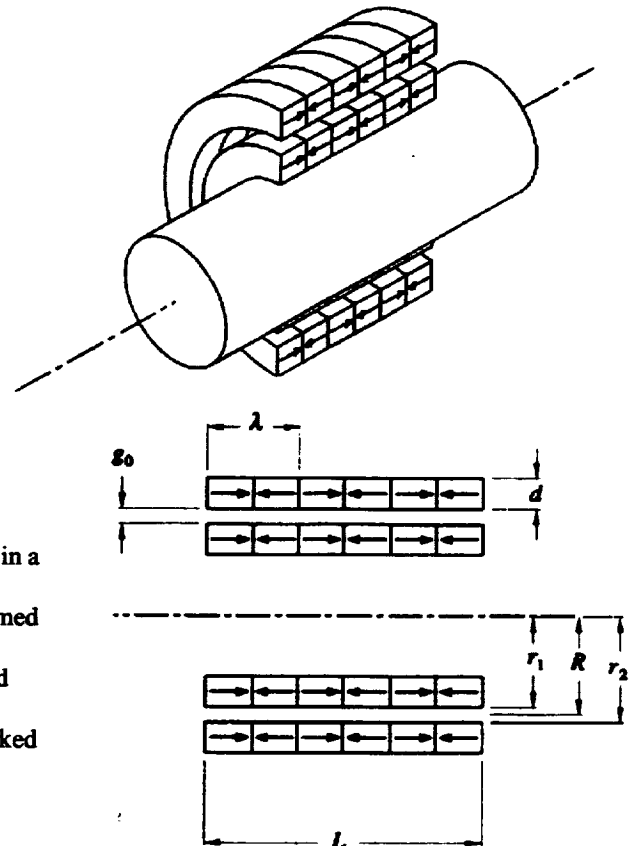
Figure 7. PM bearing geometry

V. Thrust Bearing and Controller

The active thrust bearing was designed without any stator iron to minimize negative stiffness effects. Once we chose the two-coil structure the dimensions of both the coils and the magnets were optimized using ANSYS. The objective function was the force per root watt for the actuator, and constraints were placed on the dimensions and geometry. The feedback controller is a virtually zero power type loop. Thus as the pump pressure changes, the equilibrium position of the impeller moves several thousandths of an inch. The rotor position is detected with a low-noise Magnetic Moments ECS98S eddy-current sensor.

VII. Conclusion

The HemoGlide HG3b pump (polycarbonate housing) was implanted in a calf for four hours on July 10, 1998 at the University of Pittsburgh's McGowan center for artificial organs. The levitation coils only consumed 1.5 Watts of power not including amplifier losses. Very low blood damage was observed. A second titanium pump, HG3c, was implanted for a 34-day trial in September 1999 in a calf. The pump components showed very minor thrombus formation and the levitation system worked reliably. The titanium HG3c pump is depicted in figure 8 with the housings removed.



References

- [Allaire 95] Allaire, P., Maslen, E., Kim, H., Olsen, D., and Bearnson, G., "Prototype Ventricular Assist Device Supported on Magnetic Bearings, Proceedings of MAG '95, Alexandria, VA; Technomic Publishing, Lancaster, pp. 63-76, 1995.
- [Allaire 96] P. E. Allaire et al, "Prototype Continuous Flow Ventricular Assist Device Supported on Magnetic Bearings," *Artificial Organs*, 20(6): 582-590, 1996.
- [Allaire 98] P. E. Allaire et al, "Performance of a Continuous Flow Ventricular Assist Device: Magnetic Bearing Design, Construction, and Testing," *Artificial Organs*, 22(6), pp. 475-480, 1998.
- [Bramm 81] Bramm, G. Novak, P. and Olsen, D., "Blood Pump for Long Term Application with Magnetically Suspended Rotor to Reduce Blood Trauma," 2nd International Workshop of the Austrian Society of Artificial Organs," Vol. 11, pp. 26-29, 1981.
- [Hart 96] T. M. Hart et al, "A Magnetically Suspended and Hydrostatically Stabilized Centrifugal Blood Pump," *Artificial Organs*, 20(6): 591-596, 1996.
- [Hilton 97] Hilton, E. Allaire, P., Baloh, M. et al. "Magnetic suspension controls for continuous flow ventricular assist device CFVAD III," *ASAIO Journal* 43(5), pp. 598-602, 1997.
- [Hogness 91] Hogness, J. R. and VanAntwerp, Eds. "The Artificial Heart: Prototypes, Policies, and Patients," Institute of Medicine, National Academic Press: Washington, DC, 1991.
- [Khanwilkar 96] P. Khanwilkar et al, "Using Hybrid magnetic Bearings to Completely Suspend the Impeller of a Ventricular Assist Device," *Artificial Organs*, 20(6): 5597-604, 1996.
- [Marshall 91] Marshall, E. "Artificial Heart: The Beat Goes On," *Science*, Vol. 253, pp. 500-502, 2 August 1991.
- [Olsen 85] Olsen, D. and Bramm, G., "Blood Pump with Magnetically Suspended Impeller," *Transactions of the American Society of Artificial Internal Organs*, Vol. 31, pp. 395-401, 1985.

Figure 7. (Continued)

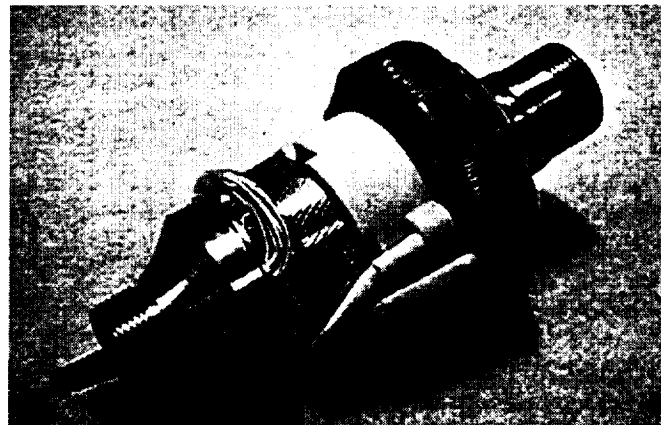
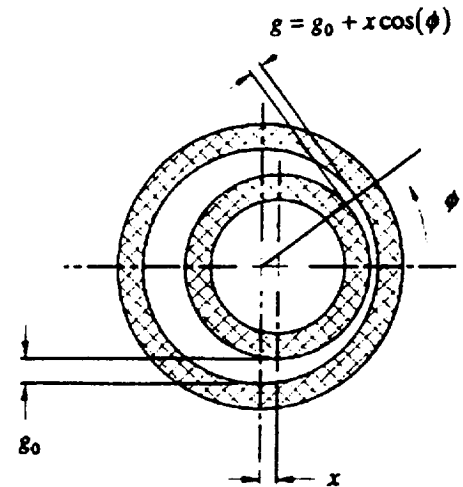


Figure 8. HG3c with housings removed

(Editors Note: Only the abstract of this paper is available since the text of the paper was not received by the time of publication of the proceedings.)

MAGNETIC SUSPENSION OF AN ARTIFICIAL HEART PUMP USING EM/PM BEARINGS

P. Allaire, Wade Professor
J. Decker, Research Scientist
M. Baloh, Research Associate*
J. Lee, Post Doctoral Fellow

Mechanical and Aerospace Engineering
*Electrical Engineering
University of Virginia
Charlottesville, VA, USA

J. Long, Cardiac Surgeon
LDS Hospital
Salt Lake City, UT, USA

ABSTRACT

An artificial heart pump is under development for use as a ventricular assist device. This paper describes a fourth generation prototype pump of diameter 68 mm (2.62 in) and axial length 33.5 mm (1.32 in). The pump is a small centrifugal pump with a shaftless impeller fully supported in magnetic bearings. It is desired that the magnetic support system have high load capacity, be very compact, and have very low power consumption. A hybrid electromagnet/permanent magnet bearing design has been developed and tested. The bearings consist of two identical rings, one placed on the inlet side of the centrifugal impeller and one placed on the discharge side of the impeller. Each ring has eight poles, four radial and four axial, to control the pump impeller in five axes (x, y, z, α, β) – three displacements and two angular displacements relative to the x, y axes. The bearings have a radial load capacity of 9.65 N (2.16 lbf) and an axial load capacity of 19.3 N (4.33 lbf). The dynamic model of the impeller in the magnetic bearings is developed. The estimated coil ohmic power loss in normal operation is less than 5 watts.

DESIGN OF MAGNETICALLY LEVITATED MICRO OPERATION HANDS

Tatsuya Nakamura, Yoshiyuki Kogure and Koichiro Shimamura
Tokyo Metropolitan University
Department of Precision Engineering
1-1, Minami-Ohsawa, Hachioji-shi, Tokyo 192-0397, Japan

SUMMARY

Application of magnetic levitation technology to mechatronics has a possibility of compact design of machine, since no transmission mechanism is required. Furthermore, because of non-friction, force control is easy to implement and high accuracy is expected in position control. These features are also effective in robotics. In our research, mechanism and control of micro operation hands are investigated. The hand consists of two finger rods each of which has three degrees of freedom and is controlled by an independent finger subsystem. To realize this finger subsystem two models are considered: a hybrid (magnetic and mechanical) suspension model and a full levitation model. A novel magnetic actuator composed of a permanent magnet and an air-core coil is used for actuation and suspension in the models. The basic characteristics of the actuator is analyzed and it is shown that it has a good property for motion control. Also it is shown that the actuator works as a useful passive suspension component which is used in the full levitation model. Finally, results of a task of micro drawing using the hybrid model are presented.

INTRODUCTION

Research on applications of magnetic levitation technology to manufacturing areas are conducted recently. One feature of the technology used in this area is the manipulation capability of objects in vacuum environments such as clean rooms in semiconductor industry[1,2]. Another feature is the low friction and force control capability[3]. For such applications in robotics a robotic hand with magnetic bearing, a haptic interface[4], that is, a magnetically levitated joystick, by which the operator can sense force feedback, etc. are developed. Recently, research on devices for micro operation in a biological / medical area and a micro machine area are a center of attraction. In such areas, devices by which operators can do dexterous operations for biological cells, a human body or mechanical parts are required[5,6]. Force control is considered to be effective to these dexterous operations even in the micro world, where tasks of assembly and machining such as cutting objects are necessary. Up to this time, a ball screw mechanism driven by electrical motors or a link mechanism driven by piezoelectric actuators are developed. Force control is difficult to implement using these mechanisms. However magnetic suspension type devices have not been developed yet for these tasks.

In our research, mechanisms and controls of micro operation hands are investigated. The hand consists of two finger rods each of which has three degrees of freedom and is controlled by an independent finger subsystem. Fig.1 shows a concept of micro operation by a two-finger micro operation hand which is attached to a macro robot. The macro robot is used to position the micro operation hand roughly in a large work space. Therefore, the workspace of the micro operation hand considered is more than the volume of 10_10_10 mm, since the size of micro machine is defined as this size. Operations considered are machining

and assembly. The two fingers are used as a gripper for the assembly application. If a micro tool, such as a drill or a knife, is attached, drilling or cutting processes can be done. The operator observes the operations through a microscope and performs a task using an interface such as a joystick. To realize this finger subsystem two models are considered. (1) A hybrid (magnetic and mechanical) suspension model and (2) a full levitation model are considered. The model (1) uses a link mechanism with mechanical bearings to constrain the finger motion. Each degree of freedom is driven directly by a magnetic actuator. A lever mechanism was tested to realize the model (1). The model (2) can be used for fine operations in the environment where mechanical suspension is not suitable. Passive suspension components are investigated to simplify the control and the preliminary test was conducted.

To develop these models, a novel but simple magnetic actuator composed of a permanent magnet and a air-core coil is proposed for actuation and suspension. A magnetic field inside a coil is almost constant near the center of the coil and, if the pole of the permanent magnet is there, an actuator with linear characteristics suitable for motion control is obtained. Another feature of the actuator is that a magnetic force acts outward of the coil on a pole of the magnet and it can be used as a spring at the position away from the center. Then the design of two models are presented and illustrated how to use the actuators, although current states of prototype development are in different phase in each model.

Finally the results of a task of micro drawing are presented using a prototype of the lever mechanism, where a position control is conducted in the direction tangential to the contact surface and a force control in the direction normal to the surface. The position controller uses a disturbance observer which is robust against model errors and disturbances, and its effectiveness is shown experimentally.

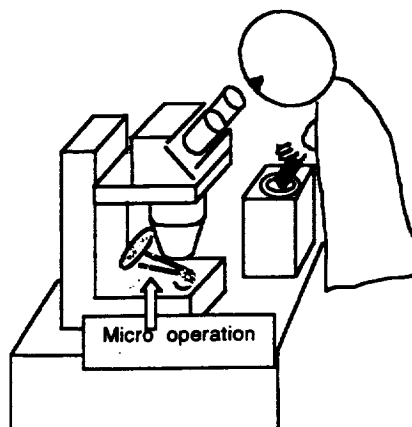


Fig.1 Concept of a micro operation hand

MAGNETIC ACTUATOR

The actuator proposed for micro operation hands consists of an air-core coil and a permanent magnet as shown in Fig.2. The permanent magnet is attached to the finger rod and the coil is fixed in the base frame. The actuation is done in the axial direction of the coil. The inner diameter of the coil is large enough for the pole of the permanent magnet to move around in the volume corresponding to the workspace. Apparently, there is a magnetic force in the radial direction at the place away from the axis. However if the radial force is small compared with the axial force, the problem is not significant for the control of the finger rod. The axial force is almost constant at the position near the center of the coil and proportional to the coil current, and this is a property suitable for motion control.

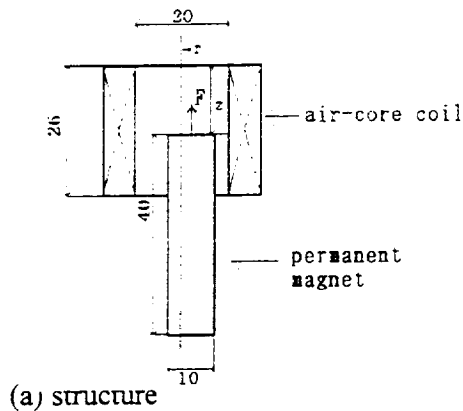


Fig.2 Magnetic actuator

Driving Force

A conventional type actuator is multiple electromagnets as used in magnetic bearing. Driving force of our actuator is compared with that of the conventional type actuator under the same condition with respect to the size and current of the coil. Magnitudes of driving force are estimated using the models in Fig.3, where (a) is a conventional type and (b) is ours. Assume that the conventional type contains an iron

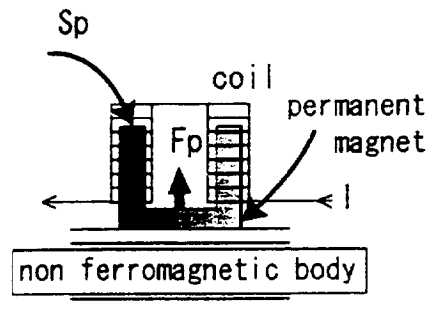
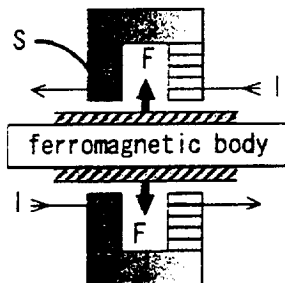


Fig.3 Comparison of two types of actuator

core inside a coil, while our type contains a permanent magnet. Let $S[\text{m}^2]$, $I[\text{A}]$ and $n[\text{1/m}]$ be the cross-sectional area, the electrical current and the number of windings per unit length of the coil respectively. Then the magnetic field H is given by

$$H = n I \quad (1)$$

Let us estimate maximum forces for both types. Suppose the gap is very small for the conventional type. Then the magnetic force F is given by

$$F = 2\mu H^2 S \quad (2)$$

where μ is a magnetic permeability of the object. Consider our type. Let the area of the cross-section of the permanent magnet be S_p . Both poles of the magnet are assumed to be inside the coil. Then the magnetic force F_p is

$$F_p = 2HS_pM \quad (3)$$

where M is the magnetization of the permanent magnet used.

Let us compare F and F_p . Typical values of the parameters are $\mu=0.002[\text{NA}^{-2}]$ for an iron and $M=0.8[\text{T}]$ for a rare earth magnet.

$$S_p < S \quad (4)$$

But our type can generate a larger force than the conventional type for small H , since $M > \mu H$. For large H , the magnetization is saturated. It depends on the material and the saturated magnetization is about $0.8[\text{T}]$ at $H=105[\text{A/m}]$ for silicon steel. But the linear region of the B-H curve shows $M < 0.6[\text{T}]$. If the gap between the object and the electromagnetic pole is small enough for the conventional type,

$$F \doteq F_p \quad \text{for a small gap.} \quad (5)$$

However, the magnetic force decreases rapidly as the gap increases. Therefore our type is significantly stronger as a whole.

Linear Characteristics

Consider a multi-layer cylindrically wound coil. Let r and z be the radial and axial distances from the center of the coil as shown in Fig.2. Let $H_r(r, z)$ and $H_z(r, z)$ be radial and axial components of the magnetic field H at the position (r, z) as shown in Fig.4. Magnetic intensity on the axis $H_z(0, z)$ is given by

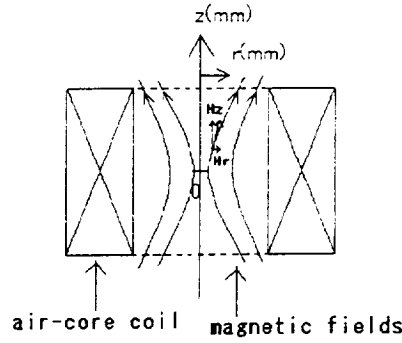


Fig.4 Magnetic field inside the air-core coil

$$H_z(0, z) = \frac{nl}{2(a_2 - a_1)} \left\{ (b+z) \ln \frac{a_2 + \sqrt{a_2^2 + (b+z)^2}}{a_1 + \sqrt{a_1^2 + (b+z)^2}} + (b-z) \ln \frac{a_2 + \sqrt{a_2^2 + (b-z)^2}}{a_1 + \sqrt{a_1^2 + (b-z)^2}} \right\} \quad (6)$$

where

- a_1 : an inner diameter of the coil,
- a_2 : an outer diameter,
- b : half length of the coil,
- n : the number of windings per unit length,
- I : coil current.

The theory was compared with the measurement. Magnetization of the permanent magnet and coil current were assumed to be 0.8[T] and 0.2[A] respectively. The results are shown in Fig.5 and 6. Theory and measurement give similar results but the z -values which gives a maximum magnetic force are different. The reason for this is that the effect of the pole of the other side of the permanent magnet is not taken into consideration in the theory.

The magnetic field at the position away from the axis can be theoretically calculated using the magnetic equations inside the coil.

$$\text{Div } \mathbf{H} = 0 \quad (7)$$

$$\text{Curl } \mathbf{H} = 0 \quad (8)$$

From Eq.(8), \mathbf{H} is a potential. H_r and H_z are obtained from Eq.(7) by using a potential function approximated up to the second order with respect to r and z in its Taylor series expansion.

$$H_z(r, z) = H_z(0, z) - \frac{1}{4} r^2 \left(\frac{\partial^2 H_z}{\partial z^2} \right) (0, z) \quad (9)$$

$$H_r(r, z) = -\frac{1}{2} r \left(\frac{\partial H_z}{\partial z} \right) (0, z) \quad (10)$$

Eq.(10) shows that the radial component of H_r is small near the center of the coil and the actuator can be used to drive the permanent magnet in the direction of z .

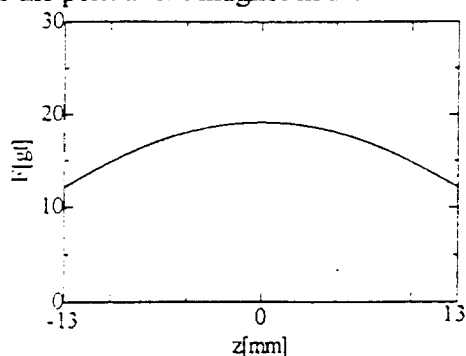


Fig.5 H_z on the z -axis (theory)

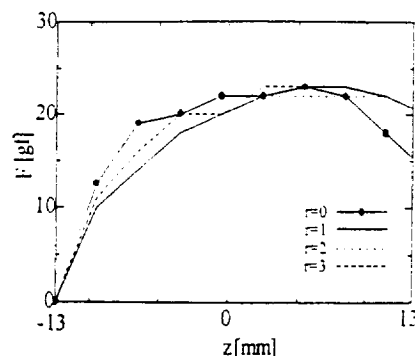


Fig.6 H_z on and off the z -axis (experiment)

Passive Magnetic Spring

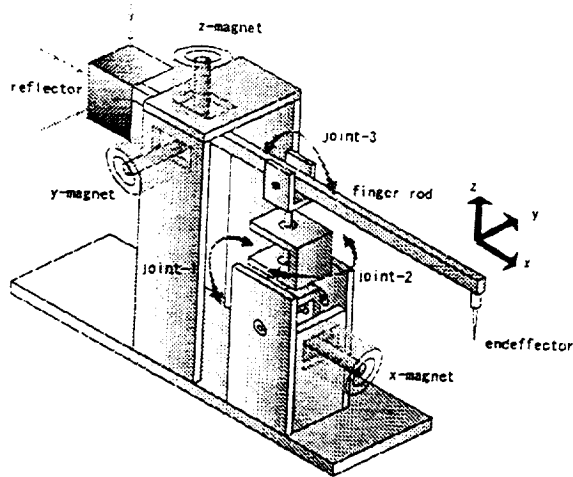
The distribution of magnetic field along the axis shows that the actuator works as a spring without control if a positive magnetic pole is placed at $z > 0$ inside the coil. Therefore, if a positive magnetic pole is placed at $z > 0$, the magnetic pole is levitated at the position where the magnetic and gravitational forces balance. Although it contacts with the internal surface of the coil, the radial force is not significant so that it can be used as a passive suspension component. This magnetic spring is effective to reduce the degree of freedom actively controlled.

DESIGN OF MICRO OPERATION HANDS

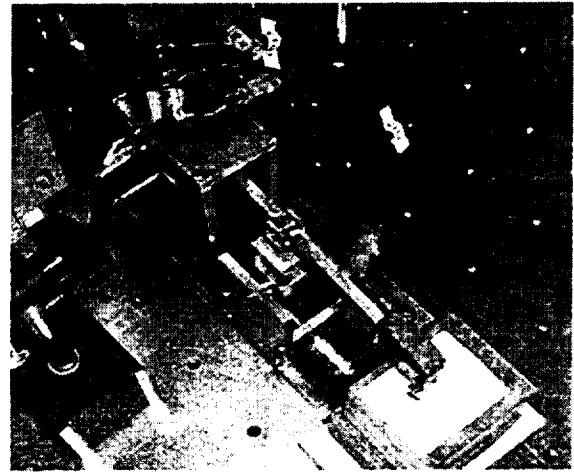
We propose two models for one finger subsystem of a micro operation hand; (1) a hybrid (magnetic and mechanical) suspension model and (2) a full levitation model.

Hybrid Model

A prototype with a lever mechanism was developed and tested for micro drawing. Its structure and photograph are shown in Fig. 7. A finger is constrained with a three DOF link mechanism and three motions of rotations around joints 1, 2 and 3 are allowed. Rotations around these joints generate approximate straight line motions of the finger tip in x , y and z directions due to the relatively longer lever compared with the size of the workspace. Three DOF positions are measured at the opposite side of the finger with laser displacement sensors. Magnetic actuators are placed apart by enough distances not to interfere at this side. This mechanism has the following features:



(1)structure



(2)photograph

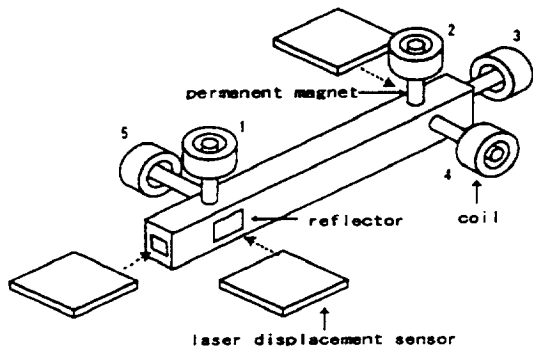
Fig.7 Prototype of the hybrid model (lever mechanism)

- (1) (Near) line motions of the finger tip are possible using a MAGLEV technique.
- (2) Gravity is decoupled by using counter balances for various postures of the micro hand.
- (3) Effects of the joint frictions is minimized for fine motions.
- (4) The mechanism is rigid in a constrained DOF motion
- (5) Compact and light weighted design is possible. Specifications of the prototype are as follows:
[link mechanism]

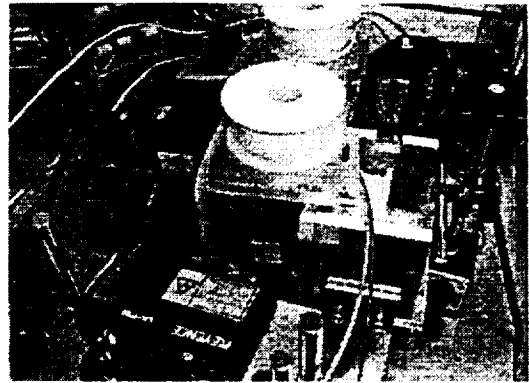
size:	L320 × H110 × W175 mm
weight:	1 kg
workspace:	10 × 10 × 10 mm
[sensor]	
type:	Keyence LK-2000
range of measurement:	±5 mm
resolution:	1 μm
response time:	512 μs
[coil]	
size:	φ20 mm(internal diameter)×26 mm(length)
windings:	550 turns with wire of φ0.5 mm
force:	120 gf /A

Full Levitation Model

A full levitation model has diverse potential applications because of the simplicity of the mechanism. Especially a compact design of hands might be possible in the applications which do not require large operational forces. At the beginning, the feasibility was tested using the model illustrated in Fig.8(a) and experimental apparatus shown in Fig.8(b). The actuators 1 and 2 are used as passive springs and the upward magnetic forces balance with the gravity force. Other actuators 3, 4 and 5 are actively controlled using the corresponding laser displacement sensors. Fig.8 shows the experimental apparatus.



(a) structure



(b) experimental apparatus

Fig. 8 Full levitation model for feasibility test

The sensors are the same as the ones used in the hybrid models but more powerful coils are used for actuators. The specifications of the coil are as follows:

size:	$\phi 25 \text{ mm}(\text{internal diameter}) \times 26 \text{ mm}(\text{length})$
windings:	1000 turns with wire of $\phi 0.7 \text{ mm}$
force:	250 gf / A

An aluminum regular prism of $18 \times 18 \times 260 \text{ mm}$ with a weight of 500 gf including permanent magnets was easily levitated using a simple PID control for the actuators 3, 4 and 5.

TASK OF MICRO DRAWING USING A HYBRID MODEL

The results of a task of micro drawing are presented in this section, where the prototype of the hybrid model is used and a pen is attached to the finger tip to draw figures on a paper parallel to the x-y plane, where x, y and z axes are defined in Fig.7. A position control is conducted in the direction tangential to the contact surface, that is x and y directions in this case. At the same time, a force control is conducted in the direction normal to the surface, that is z direction. The position controller is designed using a disturbance observer which is robust against model errors and disturbances, and its effectiveness is evaluated experimentally.

Control System

A position and force control is used for the contact motion control. However the force control is simply an open loop control since the coil current is proportional to the normal force applied to an object, while the position control suffers from disturbances such as friction. It also suffers from modeling errors when a linear controller like PID is used. Recently, a disturbance observer is known for its robustness against disturbances and modeling errors, and it is implemented in various motion controls.

For these reasons, we applied a disturbance observer to the position control. Assume that the x, y and z motions of the end effector are decoupled. Since the mechanical time constant is longer than the electrical constant, the end effector motion in a direction is formulated as follows:

$$\frac{dv}{dt} = \frac{p'q'}{R'}u - f_{dis} \quad (11)$$

where u is a control, f_{dis} is a disturbance, and p' , q' and R' are nominal values of parameters p , q and R :

p : amplification rate of the amplifier
 q : force constant of the actuator
 R : resistance of the coil

The principle of disturbance observers [8] is stated as follows: "If \dot{v} and u are known values, we can estimate the disturbance from Eq.(11). Then, by adding the corresponding value to u we can cancel the disturbance." In our system, velocity \dot{v} is not measured thus \dot{v} has to be estimated from the displacement, say x , where

$$v = \dot{x} \quad (12)$$

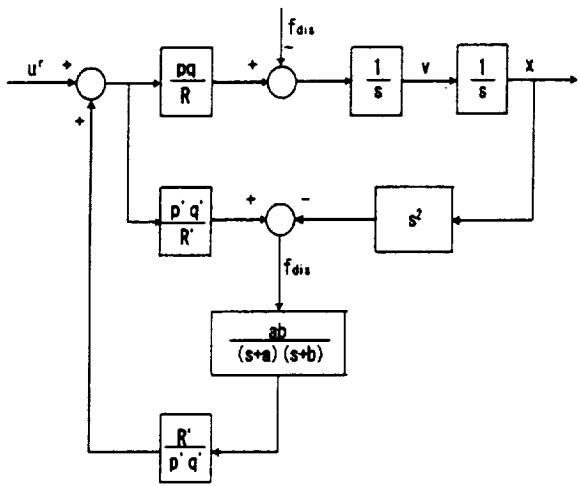
Fig.9(a) describes this principle in the form of block diagram, where a low pass filter is added to reject noises.

$$\frac{ab}{(s+a)(s+b)} \quad (13)$$

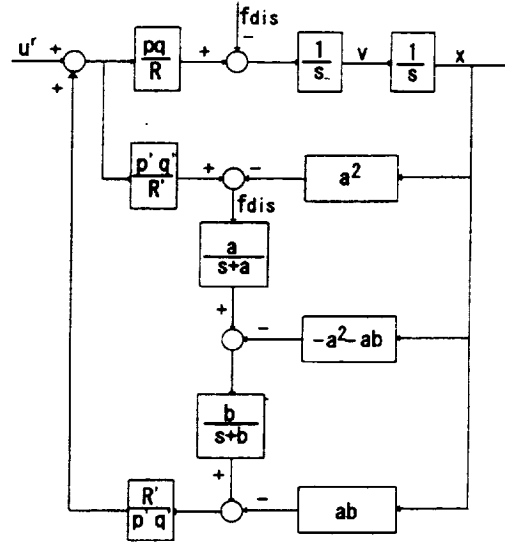
However, Fig.9(a) is not desirable since derivative operations are included. But Fig.9(a) can be converted to the diagram as shown in Fig.9(b) which contains no derivative operation. The reference u^r of the control can be determined by PID control law.

$$u^r = K_p(x_d - x) + K_i \int (x_d - x) dt + K_d(v_d - v)$$

where K_p , K_i and K_d are PID gains, and x_d and v_d are desired values of x and v .



(a) a form including derivative operations



(b) a form without derivative operations

Fig. 9 Disturbance observer for position control

Experiments

In the experiments, a pen and a counter balance were attached to the tip of the finger rod. The total weight of the finger rod is 120 [gf] including the weights of permanent magnets, the counter balance and the pencil. Using this experimental setup, the effectiveness of the disturbance observer was experimentally investigated by drawing small circles in the air in case of free motion and on a paper placed in case of contact motion. In both cases, the circles are parallel to the x-y plane. In the free motion, x , y and z are position controlled. In contact motion, x and y are position controlled, and the force in z -direction is open-controlled. The discrete-time form of the controller described above was derived by approximation and implemented on a computer. Sampling time of 1[ms] was used. This value is related with the resolution of the measurement and the derivative operation of the PID control law.

Free Motion

Fig. 10 shows the trajectories formed from the data of the laser displacement sensor outputs where references are circles with radii of 300 and 500 [μm] and the operational time $t=13.6[\text{s}]$. In this figure, (a) results in case of without disturbance observer and (b) with disturbance observer are shown. Comparing these figures significant differences can not be observed. On the other hand, Fig. 11 shows the results with $t=0.72[\text{s}]$. In this case, the non-linearity of the actuator and the dynamics can not be cancelled with the integral operation of PID. So the result without disturbance observer deviates from the reference circle.

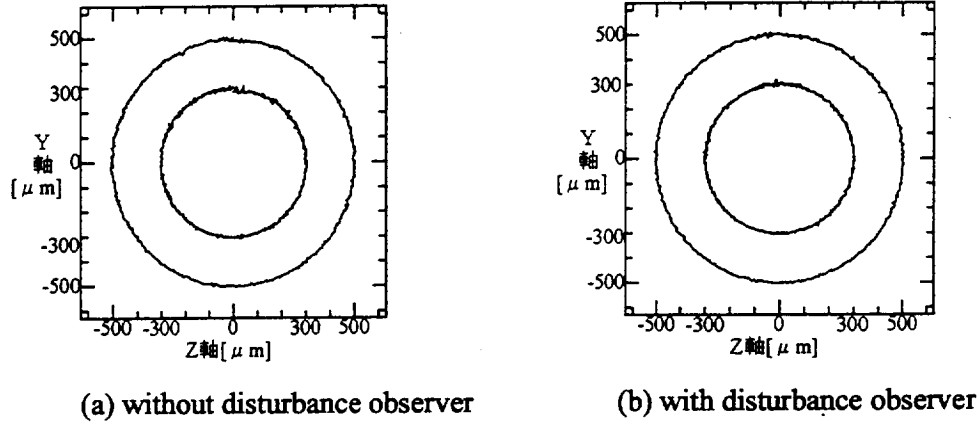


Fig.10 Experimental results in free motion ($t=13.6$)

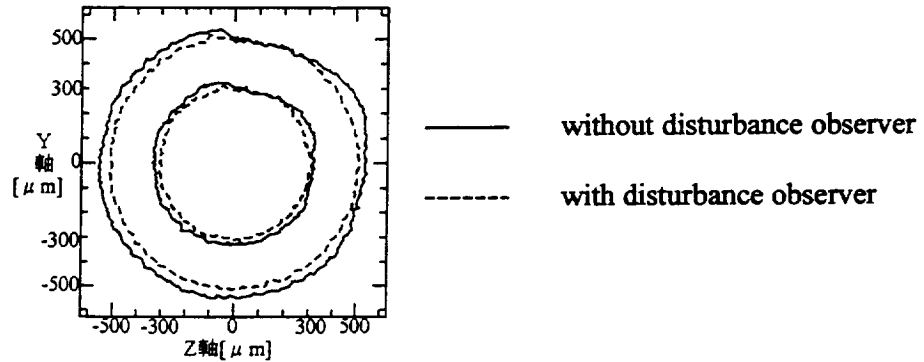


Fig.11 Experimental results in free motion ($t=0.72$)

Contact Motion

Fig.12 shows the results in contact motion where references are circles of radii 300 and 500 [μm] and $t=13.6[\text{s}]$. Force enough to draw circles on the paper was applied to the z-direction. The applied force was 24 [gf]. (a) is the results without disturbance observer and (b) is the ones with disturbance observer.

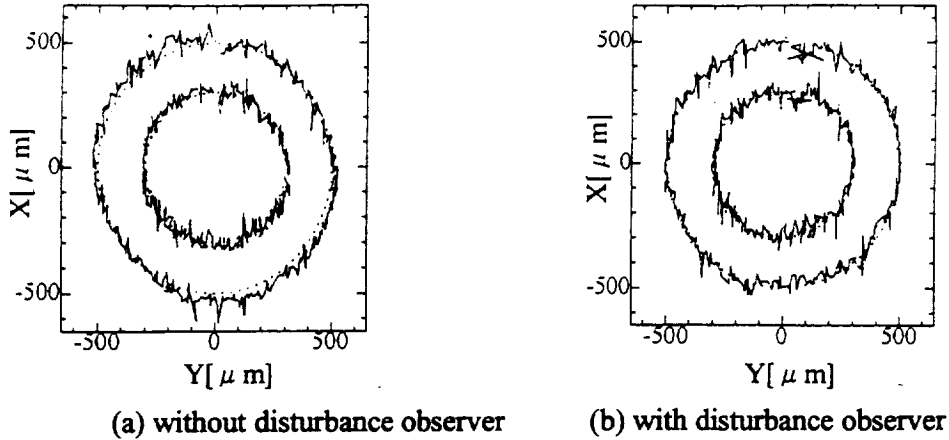


Fig.12 Experimental results in contact motion ($t= 13.6$)

Both results show the stick-slip motions of the endeffector. However (a) shows smaller stick-slip motions. This tendency is obvious from the graph $y(t)$ of the straight line contact motion with applied force of 100[gf] as shown in Fig. 13. Moreover, Fig.12 shows that (a) deviates from the reference circle but (b) is on the reference circles in average.

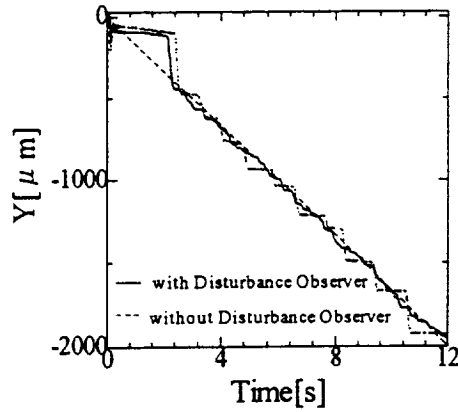


Fig.13 $y(t)$ in the experiments of straight line contact motion

CONCLUSIONS

This paper proposed a micro operation hand. Finger subsystems with a hybrid model and full levitation model were presented. Our idea is a novel actuator which consists of a permanent magnet and an air-core coil to realize a magnetically levitated micro operation hand. Characteristics of the actuator was analyzed and it was shown that it has a linear characteristics suitable for the control. It can also be used as a passive suspension component without control. The effectiveness of the actuator was verified by making a prototype and a feasibility test model. Finally the hybrid model was applied to a task of micro drawing and the performance was evaluated experimentally. Especially, the effectiveness of a disturbance observer was tested, where disturbances are friction in a contact motion and some nonlinear terms in the equation of

motion of the mechanism and the actuator characteristics. The experimental results show that the disturbance observer is effective for disturbance rejection.

The applied task was micro drawing in this paper but our goal is to apply a micro operation hand to various tasks. A two-finger micro operation hand each finger of which is constrained with a parallel link mechanism is also being made for assembly and machining of micro products. It will be presented in the near future. Also we are going to develop a prototype of the full levitation model with a compact size in future. We are considering that this model is effective to biological or medical applications.

Finally, authors would like to thank Mr. Tetsuharu Kohkaki for his help in preparing this manuscript.

REFERENCES

- [1] R.E.Perline, "Maglev Microrobotics: An Approach Toward Highly Integrated Small-Scale Manufacturing Systems", Proc. IEEE/CHMT '89 IEMT Symposium, pp.273-276, 1989.
- [2] T.Nakamura and B.M.Khamesee, "A Prototype Mechanism for Three-Dimensional Levitated Movement of a Small Magnet", IEEE/ASME Trans. On Mechatronics, Vol.2, No.1, pp.41-50, 1997.
- [3] R.L.Hollis, S.E.Salcudean and A.P.Allen, "A Six-Degree-of-Freedom Magnetically Levitated Variable Compliance Fine-Motion Wrist: Design, Modeling and Control", IEEE Trans. On Robotics and Automation, Vol.7, No.3, pp.320-332, 1991
- [4] P.J.Beckelman, Z.J.Butler and R.L.Hollis, "Design of a hemispherical magnetic levitation haptic interface device", Proc. ASME Symposium on Haptic Interface, (Atlanta), November 17-22, 1996.
- [5] T.Sato, K.Koyano, M.Nakano and Y. Hatamura: "Novel Manipulator for Micro Object Handling as Interface between Micro and Human World", IROS '93, pp.1674-1681, 1993
- [6] M.C.Carrozza, P.Dario, A.Menciassi and A.Feno, "Manipulating Biological and Mechanical Micro-Objects Using LIGA-Microfabricated End-Effectors", ICRA '98, pp.1811-1816, 1998
- [7] T. Kohno: Applied Electro Magnetism, (in Japanese), Byhukan, 1991
- [8] K. Ohnishi et al. "Microprocessor-Controlled DC Motor for Load Insensitive Position Servo System", IEEE Trans. On Ind. Elec. Vol. IE-34, pp.44-49 (1987)

DESIGN OF A MAGNETICALLY SUSPENDED WHEEL FOR A MINIATURE GYRO MADE USING PLANAR FABRICATION TECHNOLOGIES*

Charles R. Dauwalter
Milli Sensor Systems and Actuators, Inc.
93 Border Street
West Newton, MA 02465-2013

SUMMARY

The technical feasibility of a magnetically suspended rotating wheel for miniature gyro and other applications, which was first investigated under a NASA SBIR contract, was assessed in much greater detail under a BMDO SBIR administered by DTRA. The configuration is amenable to economical and highly reproducible batch fabrication using the rapidly emerging planar fabrication technologies. The actuator for the wheel magnetic suspension was optimized for improved performance by exploring the design space through over 600 configuration variations using a finite difference magnetic circuit analysis technique implemented in a spreadsheet environment. Normal and tangential magnetic force components of circumferentially slotted rotors and stators were determined over a range of air gaps, slot width to tooth width ratios, slot depth to tooth pitch ratios and tangential displacements

INTRODUCTION

The work described herein is an extension of work reported at the 3rd International Symposium on Magnetic Suspension Technology[1]. The principal objective of the new work was to optimize the design of the magnetic actuator for the magnetically suspended wheel, maximize the support force capability, minimize power dissipation and provide approximately equal capability to support accelerations both in the plane of the wheel and perpendicular to it. Secondary objectives were to develop a specific design of variable reluctance drive motor; and determine the maximum feasible rotational speed consistent with allowable stresses in the wheel material.

Our group is pursuing the development of inertial instruments, such as gyros and accelerometers, that can be fabricated through the use of many of the technologies widely used for micro-devices, but adapted for application to larger devices. We have termed these fabrication technologies "millimachining"; they were discussed in the previous paper[2]. Briefly, millimachining is a design philosophy and fabrication approach that MSSA is developing from a merging of the traditional technologies and the emerging micro-machining technology, and applying it to devices in the size range between macro and micro. Millimachined inertial instruments are expected to realize higher performance than micro instruments due to larger angular momentum. Millimachined devices can also be expected to be less expensive and more reliable than conventionally fabricated macro-sized instruments because they can take advantage of the economy and reproducibility of batch processing and dispense with most of the expensive, time consuming and unreliable hands-on human labor.

*The work described was performed under BMDO SBIR Contract DTRA01-96-C-0138

MAGNETICALLY SUSPENDED WHEEL CONFIGURATION

The wheel and actuator configuration that we are pursuing is shown in Figure 1, which shows the wheel assembled with the magnetic suspension actuator quadrants and the "U"-shaped segments of the drive motor stator. This configuration and associated control system are the subject of a recently issued patent[3].

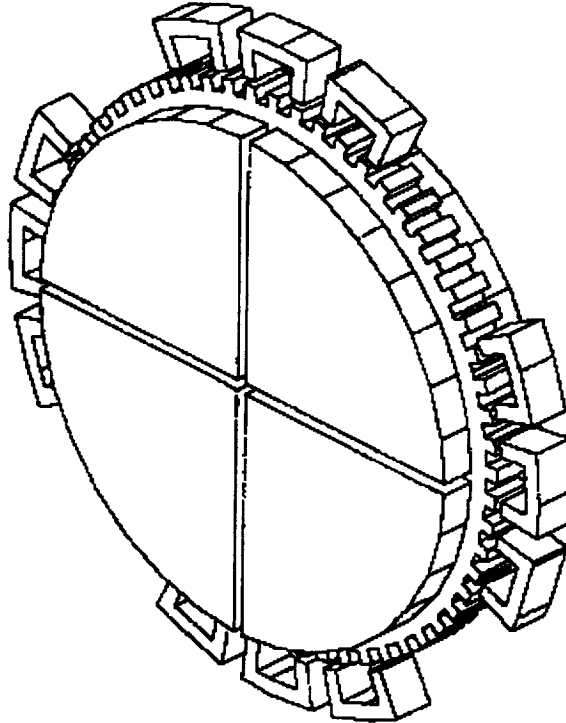


Figure 1. Magnetically suspended wheel and actuator configuration.

Figure 2 shows the assembly with a group of 4 magnetic suspension actuator stators swung away from the wheel. As shown in Figure 2, the wheel has circumferential grooves that enable the generation of forces that are parallel to the actuator/wheel plane, in addition to the forces normal to that plane usually utilized in electromagnetic actuators. The circumference of the wheel has notches, or "teeth" which, in conjunction with the "U"-shaped motor stator segments (the electrical conductors used to excite the cores are not shown in the illustration), constitute a multi-phase variable reluctance motor to drive the wheel in rotation.

Each of the actuator quadrants has matching circumferential grooves which have electrical conductors imbedded in (and electrically insulated from) them. The current in adjacent grooves flows in opposite directions. Passage of electric current through the conductors makes the actuator quadrants electromagnets, which magnetically attract the wheel to the actuator quadrants. Radial forces (parallel to the plane of the actuators) are also produced due to the slight intentional misalignment of the actuator grooves with the wheel grooves. This misalignment can be seen in Figure 3, which is a partial crosssection of the wheel and a facing actuator quadrant showing the details of the construction. The grooves in the actuator quadrant are displaced laterally from those of the wheel by approximately $1/2$ of the slot pitch, P , (slot pitch is the distance from one edge of a slot to the corresponding edge of the adjacent slot; tooth pitch is similarly defined where the teeth are the projecting portions adjacent to the slots). This is shown more clearly in Figure 4, a crosssection view of half of the wheel with its actuators. The misalignment of the teeth (or slots) causes tangential forces (parallel to the air gap; this is in the radial direction of the wheel) as well as normal forces (perpendicular to the air gap) to be generated by the passage of electrical current through the conductors. The tangential forces result from the tendency for the actuator and wheel teeth to become aligned under the influence of the

magnetic field, because the position of minimum magnetic energy, for a given air gap, is when the wheel and actuator teeth are perfectly aligned.

Eight actuator sectors, 4 on each side of the wheel, are provided to generate the forces necessary to support the wheel in 5 degrees of freedom; rotation about the axis of symmetry of the wheel is the sixth degree of freedom. Each actuator sector is capable of generating forces both normal and parallel to the surface facing the wheel.

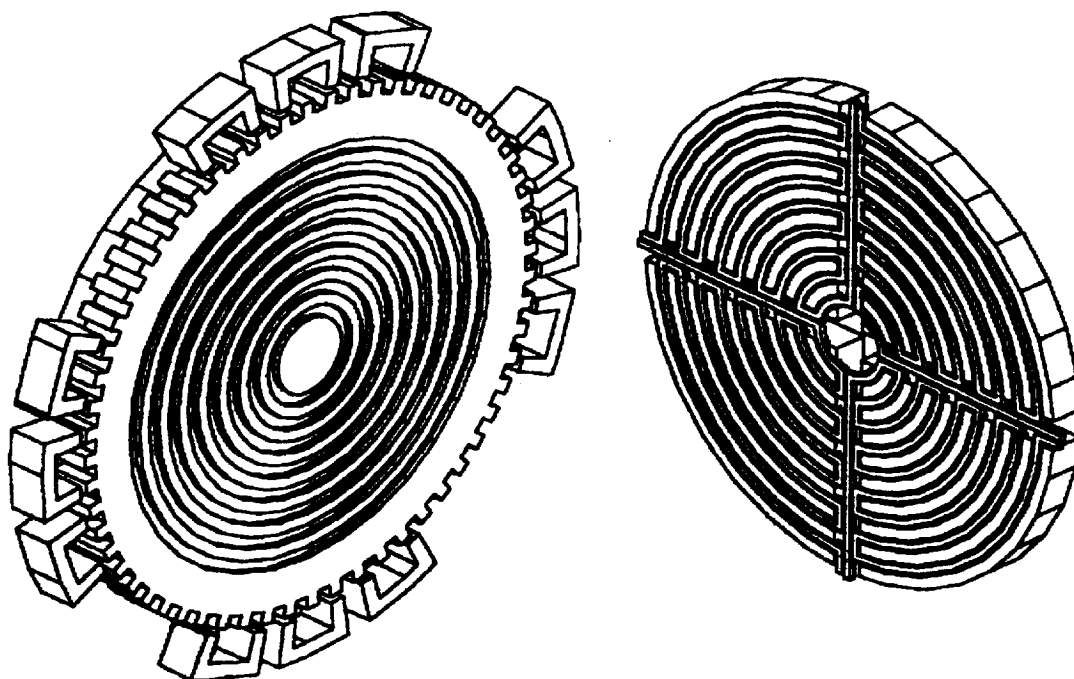


Figure 2. Magnetically suspended wheel and actuator configuration, exploded.

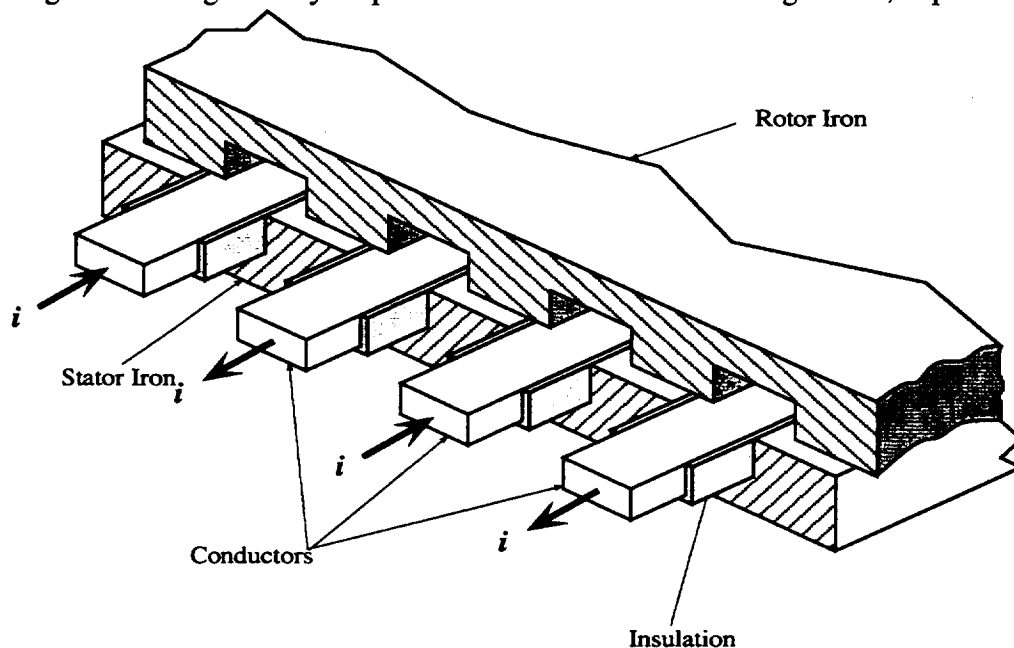


Figure 3. Actuator details.

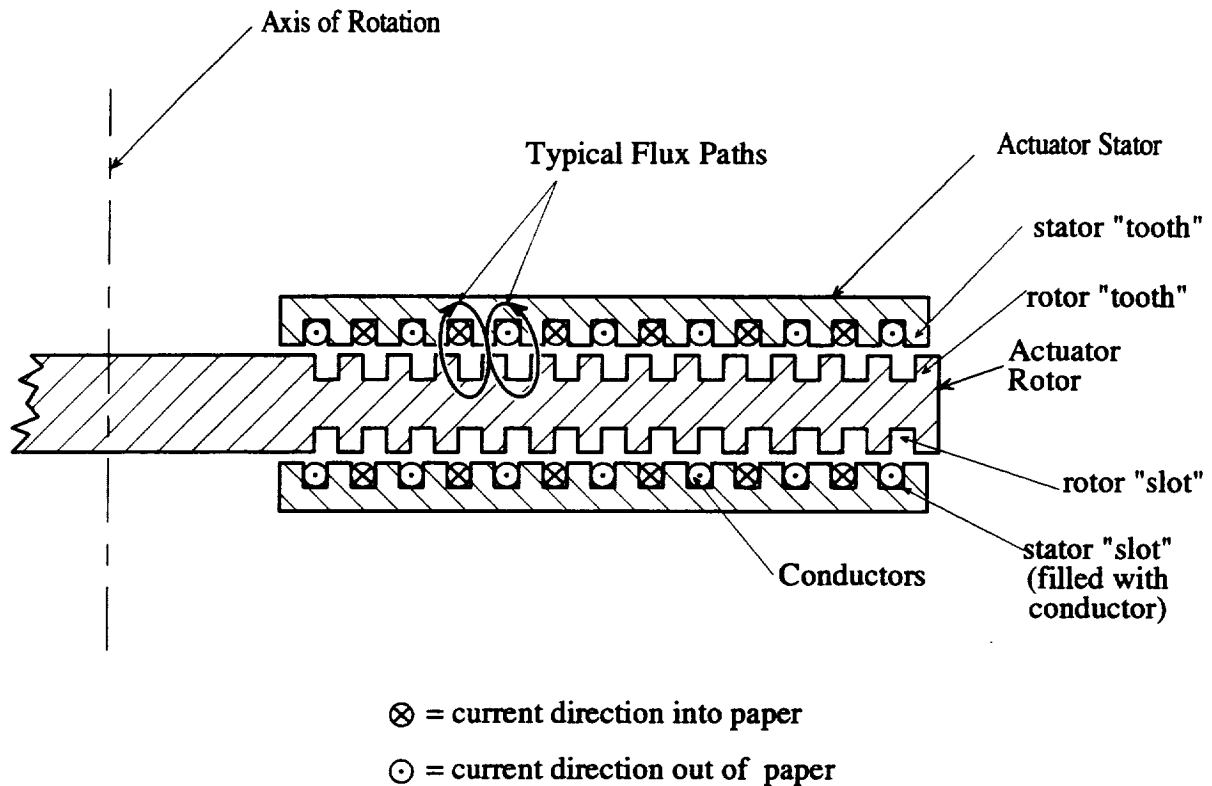


Figure 4. Wheel and actuator crosssection.

PREVIOUS RESULTS

In the previous work, the radial and tangential forces were both found to vary approximately sinusoidally with tangential (parallel to the actuator plane) displacement with a period of the slot pitch, P . The normal and tangential forces are phase shifted by about $\pi/2$, or $1/4$ of the slot pitch. Consequently, the normal force is maximum (or minimum) at the tangential displacement at which the tangential force is zero and the tangential force is maximum (or minimum) when the normal force is midway between its extrema. As might be expected, the normal forces were much larger than the tangential forces, resulting in a wheel that had much lower force capabilities (thus linear acceleration capability) in the plane of the wheel than normal to it. In most applications, equal capability in all directions would be necessary, or at least advantageous. With this in mind, the present work was initiated to, among other things, optimize the suspension configuration to achieve, as nearly as possible, equal suspension capabilities in all directions.

PRESENT WORK

Suspension Capability Optimization

The previous work explored the normal and tangential force capability of the actuator configuration in which both the rotor and stator pole widths and slot widths were the same, namely, half of the slot pitch, P . The stator slot depth was $0.25P$ and the rotor slot depth was $0.375P$, and the air gap was varied from

0.09375P to 0.25P. The present work set out to explore the design space more fully in search of a more optimum configuration. To this end, the tooth width to slot width ratio, $w_{\text{tooth}}/w_{\text{slot}}$, was varied from 0.1428P to 1.666P, the stator slot width, $w_{\text{slot,stator}}$, was varied from 0.25P to 0.75P, the rotor slot width, $w_{\text{slot,rotor}}$, was varied from 0.125P to 0.5P, and the air gap, g , was varied from 0.09375P to 0.25P. Over these ranges of parameter values, approximately 600 models were formulated and solved for normal and tangential forces. For most of these models, a slot current value of 1.0 ampere was used, although, as expected, the forces scale as the slot current squared and results from models with other current values could easily be converted to equivalent values at 1.0A.

Results

Force vs. Slot Depths Figure 5 shows the tangential (F_x) and normal (F_y) forces with $w_{\text{tooth}}/w_{\text{slot}}=1$ as a function of the rotor and stator slot depths at two different tangential displacements. All of this data was generated with $w_{\text{tooth}}/w_{\text{slot}}=1$. The displacement, $x=8$, for Figure 5a and Figure 5b are for the rotor displaced $P/4$ from the condition when the rotor and stator teeth are aligned. This is the displacement where F_x is approximately maximum and F_y is approximately midway between its extrema.

The displacement, $x=16$, for Figure 5c and Figure 5d are for the rotor displaced $P/2$ from the condition when the rotor and stator teeth are aligned, that is, for the rotor teeth centered over the stator slots. Here, F_x is essentially zero and F_y has its minimum value (note that in Figure 5c, the force scale has been magnified to show the shape more clearly). In all of these cases, the force dependence on the stator slot depth is negligible. The force dependence on the rotor slot depth is also not very large in any of these cases. For this reason, the stator and rotor slot depths were held at $12/32=0.375$ and $8/32=0.25$ for exploration of the force dependencies on the $w_{\text{tooth}}/w_{\text{slot}}$ ratio.

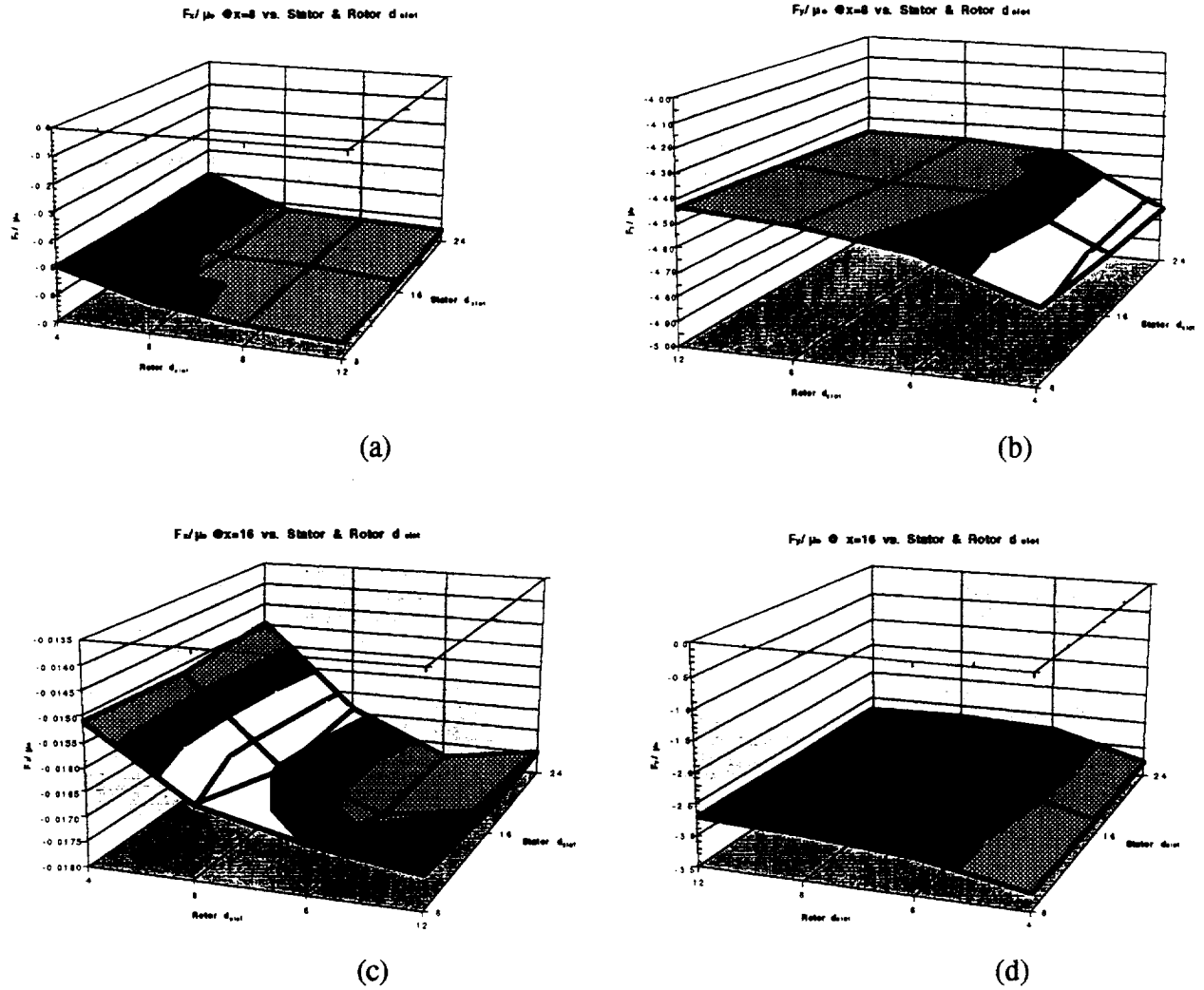


Figure 5. Normal and tangential forces vs. rotor & stator slot depths, 1.0 A slot current.

Force vs. $\frac{w_{\text{tooth}}}{w_{\text{slot}}}$ ratio While the tangential and normal forces vs. air gap were determined for 6 values of the air gap, ranging from 0.09375P to 0.25P, only the results for $g=0.125P$ are presented here because of space limitations. Figure 6 shows the tangential force vs. x at a slot current of 1.0A for the 8 values of $\frac{w_{\text{tooth}}}{w_{\text{slot}}}$ that were used. While the variation vs. x for all the $\frac{w_{\text{tooth}}}{w_{\text{slot}}}$ values is roughly sinusoidal, the displacements at which the peak values occur are shifted towards zero, compared to the value at $\frac{w_{\text{tooth}}}{w_{\text{slot}}}=1$, as the values of $\frac{w_{\text{tooth}}}{w_{\text{slot}}}$ both increase and decrease from 1. Some of the peak values are larger than for $\frac{w_{\text{tooth}}}{w_{\text{slot}}}=1$, but only about 20%. Figure 7 shows the normal force vs. x for the same

conditions. Here, all values consistently increase as the slot width is increased and the curves become flatter near the minima as $w_{\text{tooth}}/w_{\text{slot}}$ becomes both larger and smaller than 1.

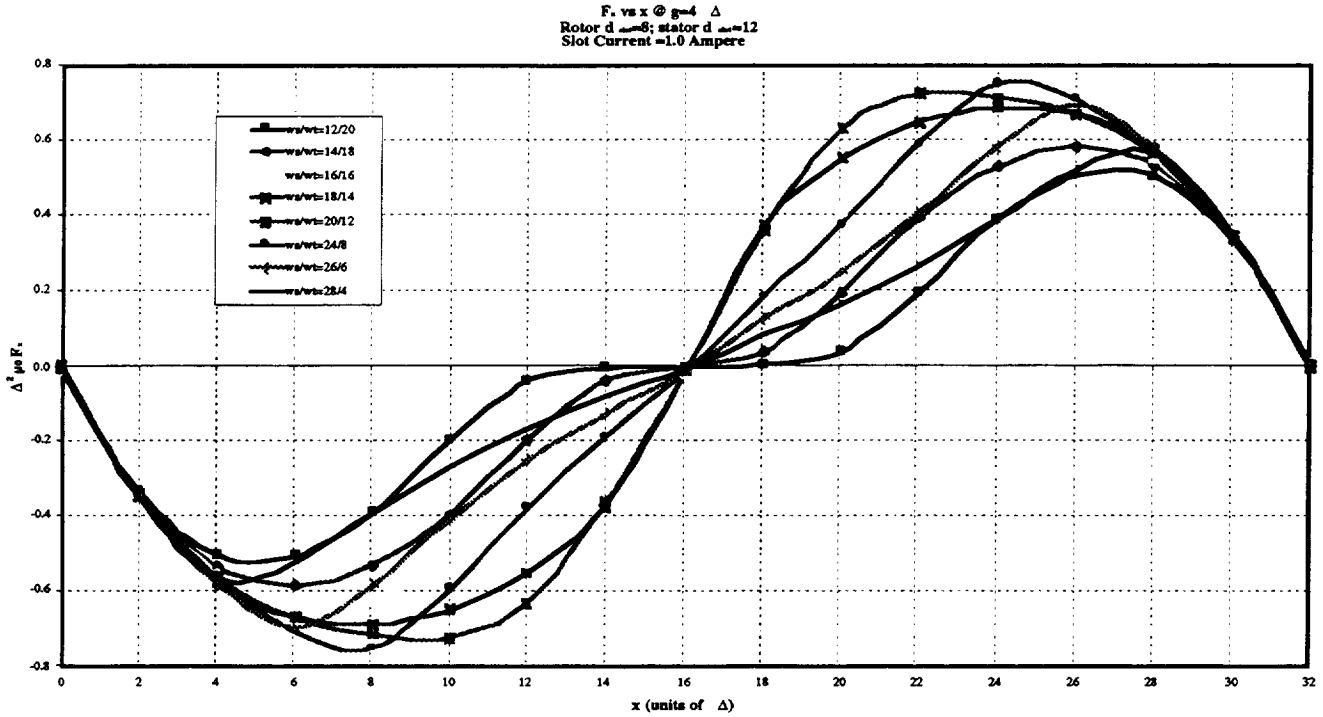


Figure 6. Tangential force vs. x for various $w_{\text{tooth}}/w_{\text{slot}}$ and $I_{\text{slot}}=1.0\text{A}$.

F_x/F_y vs. $w_{\text{tooth}}/w_{\text{slot}}$ ratio Figure 8 shows the ratio of tangential to normal force vs. x . Note that $F_x/(-F_y)$ is plotted to allow easier comparison with the curves for F_x . Recall that the motivation for this work was to increase this ratio so as to make the maximum suspension force capability as nearly equal in the radial and axial directions as practical. Figure 8 shows that the force ratio, $F_x/(-F_y)$, consistently increases as $w_{\text{tooth}}/w_{\text{slot}}$ is increased. The maximum value, -0.69, occurs near $P/4$ (tangential displacement of

approximately 8 in the graphs) and is 4.95 times larger than the maximum of -0.14 at $w_{\text{tooth}}/w_{\text{slot}}=1$ as calculated in the earlier work. Achieving such an increase was one of the principal motivations for the work.

Force vs. $w_{\text{tooth}}/w_{\text{slot}}$ ratio Changing the slot width while maintaining the slot current constant, also has the effect of changing the power dissipation, J^2/ρ , since changing the slot area changes J . A useful basis on which to compare various configurations might be the power density on the exposed surface of the device, since both conductive and convective heat transfer depend on the surface area. The temperature rise in the device depends on the heat transfer coefficient as well as the power dissipation. Maintaining the surface power density constant while varying device parameters has the effect of maintaining the device temperature rise constant across the parameter variations. Figure 9 and Figure 10 show the tangential and normal force variations vs. displacement for various $w_{\text{tooth}}/w_{\text{slot}}$ values, with the surface power density maintained at the same value as for $w_{\text{tooth}}/w_{\text{slot}}=1$, the value used in the earlier work.

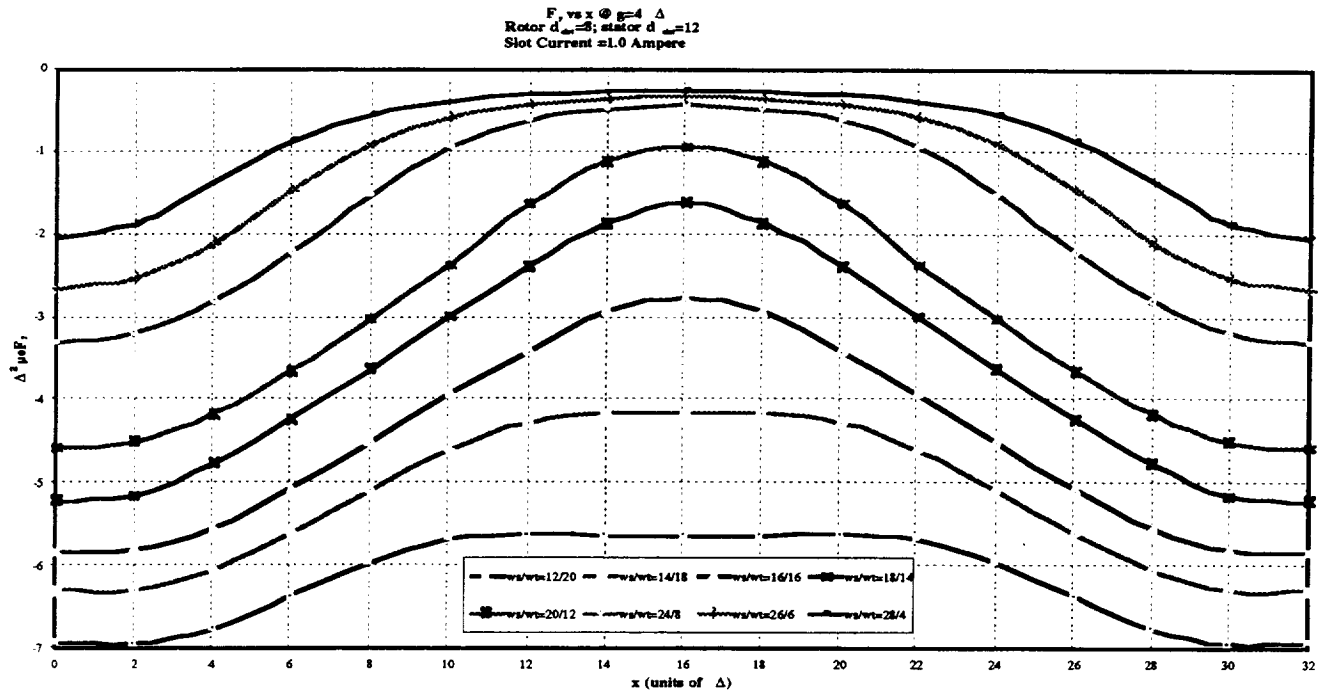


Figure 7. Normal force vs. x for various $w_{\text{tooth}}/w_{\text{slot}}$ and $I_{\text{slot}}=1.0\text{A}$.

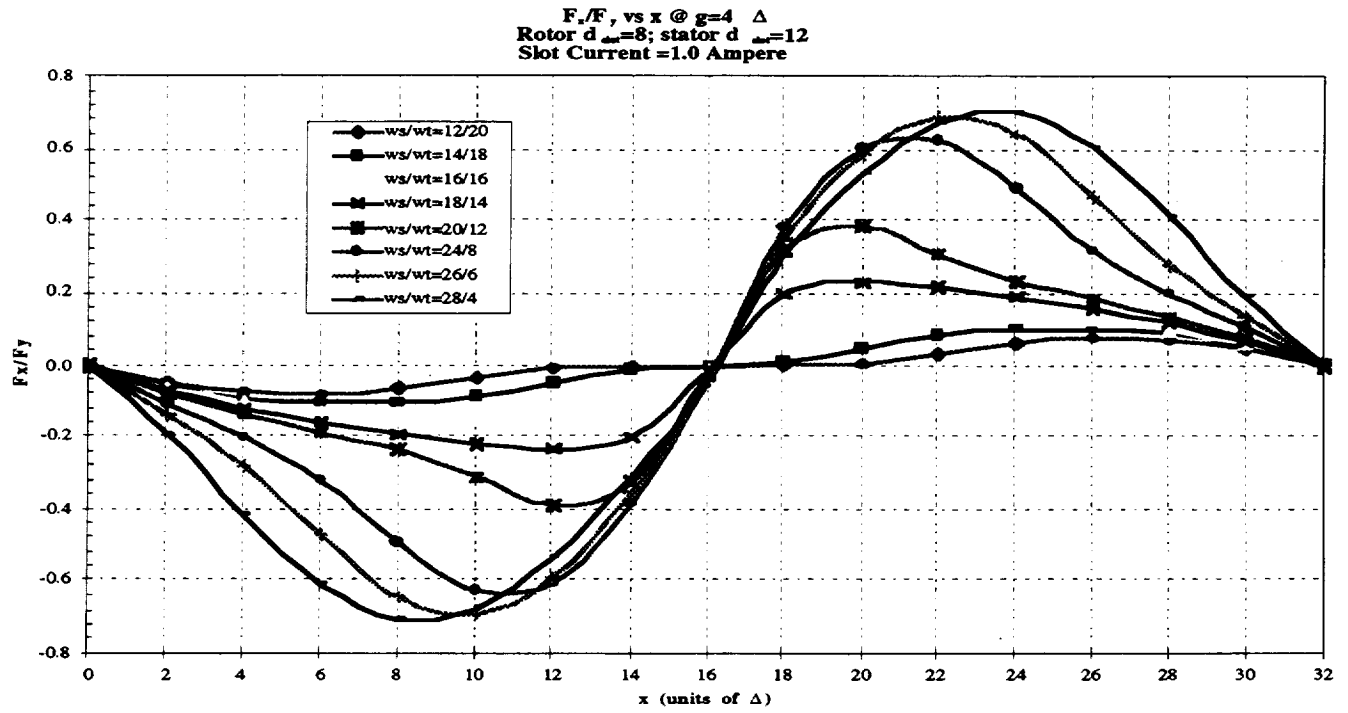


Figure 8. F_x/F_y vs. x for various $w_{\text{tooth}}/w_{\text{slot}}$ and $I_{\text{slot}}=1.0\text{A}$.

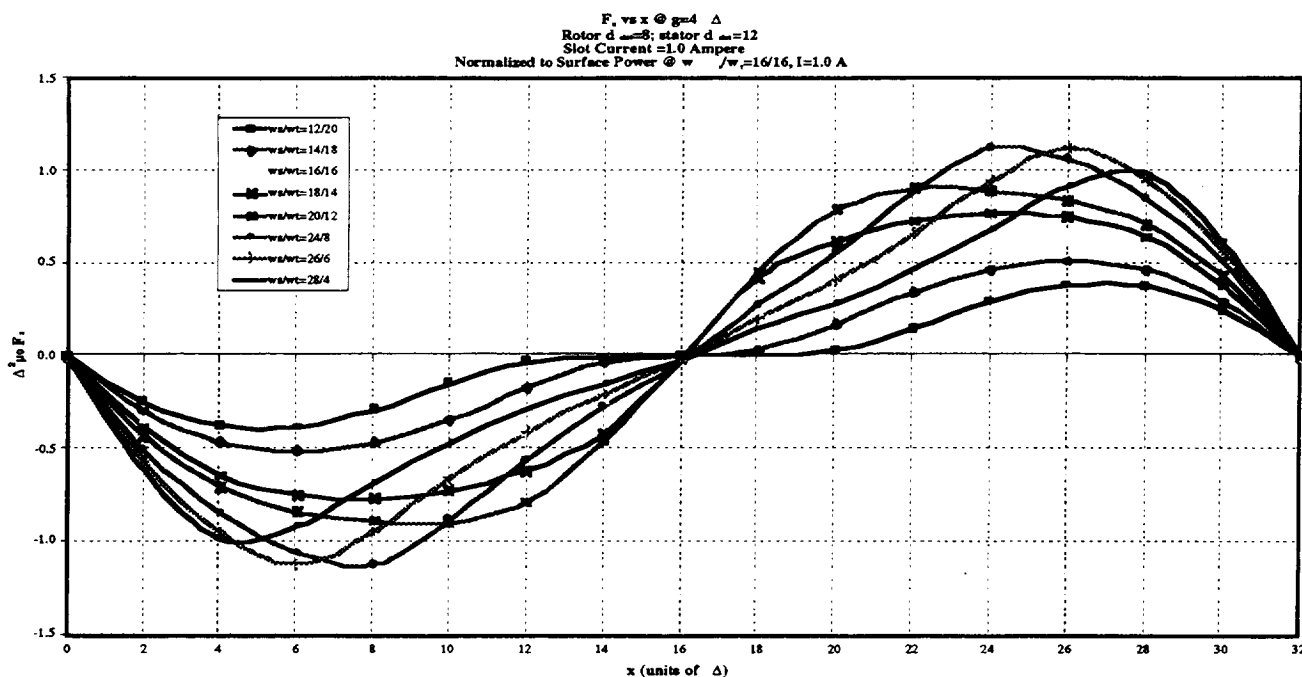


Figure 9. Tangential force vs. x for various $w_{\text{tooth}}/w_{\text{slot}}$ and I_{slot} normalized to $P_{\text{surface}}/A = \text{constant}$.

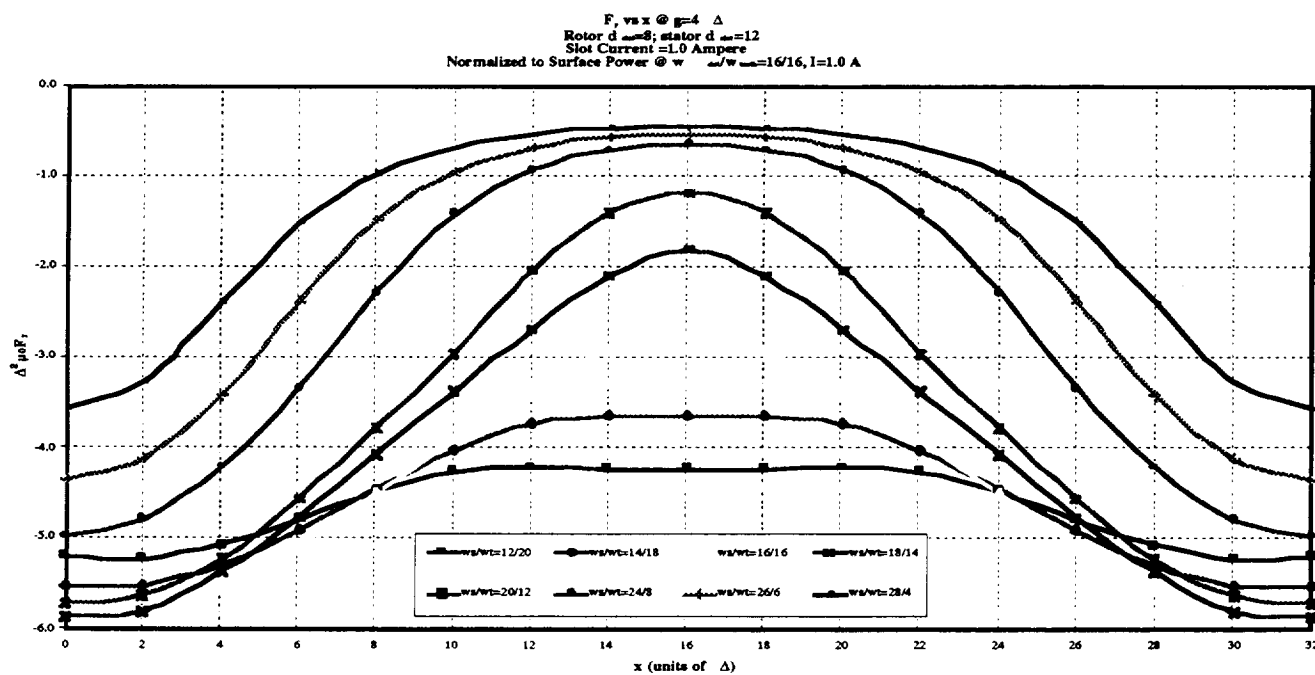


Figure 10. Normal force vs. x for various $w_{\text{tooth}}/w_{\text{slot}}$ and I_{slot} normalized to $P_{\text{surface}}/A = \text{constant}$.

CONCLUSION

The work described thoroughly explored the design space of the magnetic actuator for a magnetically suspended wheel for a miniature gyro and determined the tangential and normal forces for a wide range of design parameter values, including air gap, rotor and stator slot depths and stator and rotor slot widths. The results allow increasing the ratio of tangential to normal force to nearly unity, an improvement of almost a factor of 5 over that of the previous work. This will allow the construction of a magnetically suspended wheel with approximately equal acceleration withstanding capability in all directions, which was one of the principal motivations for the work.

REFERENCES

1. Dauwalter, Charles R., Design of a Magnetically Suspended Wheel for a Miniature Gyro Made Using Planar Fabrication Technologies, Proc. 3rd International Symposium on Magnetic Suspension Technology, Tallahassee, FL, Dec. 1995
2. *ibid.*, pg. 2.
3. U.S. Patent 5,959,382, Magnetic Actuator and Position Control System, Charles R. Dauwalter

Session 7 -- Flywheel Energy Storage

Chairman: Atsushi Nakajima
National Aerospace Laboratory (NAL)

A 500-Wh POWER FLYWHEEL ON PERMANENT MAGNET BEARINGS

Johan K. Fremerey
Forschungszentrum Jülich
D-52425 Jülich, Germany

Michael Kolk
Strubbergstraße 3
D-60489 Frankfurt, Germany

SUMMARY

A 500-Wh disk-and-shaft power flywheel test prototype for possible application in uninterruptible power supply (UPS) systems is described. The system was set up in order to evaluate the stability of a passive radial permanent-magnet bearing system under static and dynamic power load of the integrated motor generator. Preliminary tests have been run under up to 15-kW transient discharge power load with no significant effect on the bearing stability.

INTRODUCTION

Flywheels have been in use for energy storage since the early history of mankind. The potter's wheel is a standard example for discontinuous-in, continuous-out energy conversion. Early steam engines as well as modern internal-combustion, piston-type engines use flywheels in a similar manner.

High-speed flywheels on the basis of carbon-fibre reinforced plastics material (CFRP) and magnetic suspensions have been developed for energy storage [1-3], in particular, for possible replacement of electro-chemical batteries in UPS systems, electric car drives and space applications. One specific advantage of a flywheel storage is that its total energy content can be discharged within less than a minute without injury to the system. Chemical batteries would not survive under similar conditions. When running on non-contacting, preferably magnetic bearings, a flywheel provides freedom of bearing friction and virtually unlimited life time.

For optimum reliability and power saving, *permanent-magnet* bearings (PMB) have been the preferred choice in space flight applications [4,5] as these are operable at "zero-power" stabilization conditions [6,7]. PMB technology has also been introduced to and commercialized in a variety of earth-born applications during the last two decades on the basis of some special bearing concepts developed at Forschungszentrum Jülich [8]. One of these [9] has been implemented in the flywheel system described in the present paper. The system was designed in the early 90's as a basic study for possible commercial applications in UPS and electric car drives.

A first unit was realized and tested [10] in order to investigate the stability of a passive radial PMB system under dynamic load conditions of the integrated power generator. We regard the outcome of this investigation as a milestone on the way of introducing the PMB technology into the field of heavy machine construction.

TECHNICAL DESCRIPTION

The flywheel system test prototype is shown in figure 1. The functional components are displayed in the sectional view of figure 2. The complete rotor system is encapsuled in a vacuum-tight aluminum housing that also serves as a safety containment. The system is designed for operation at a fixed vertical axis.

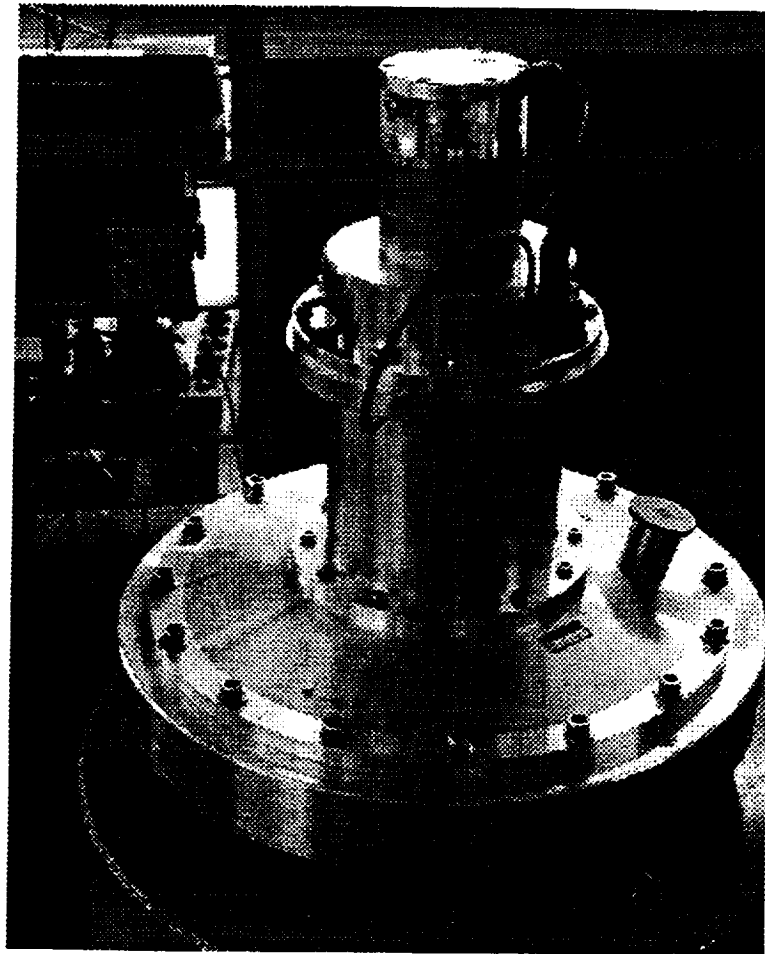


Figure 1. Flywheel system

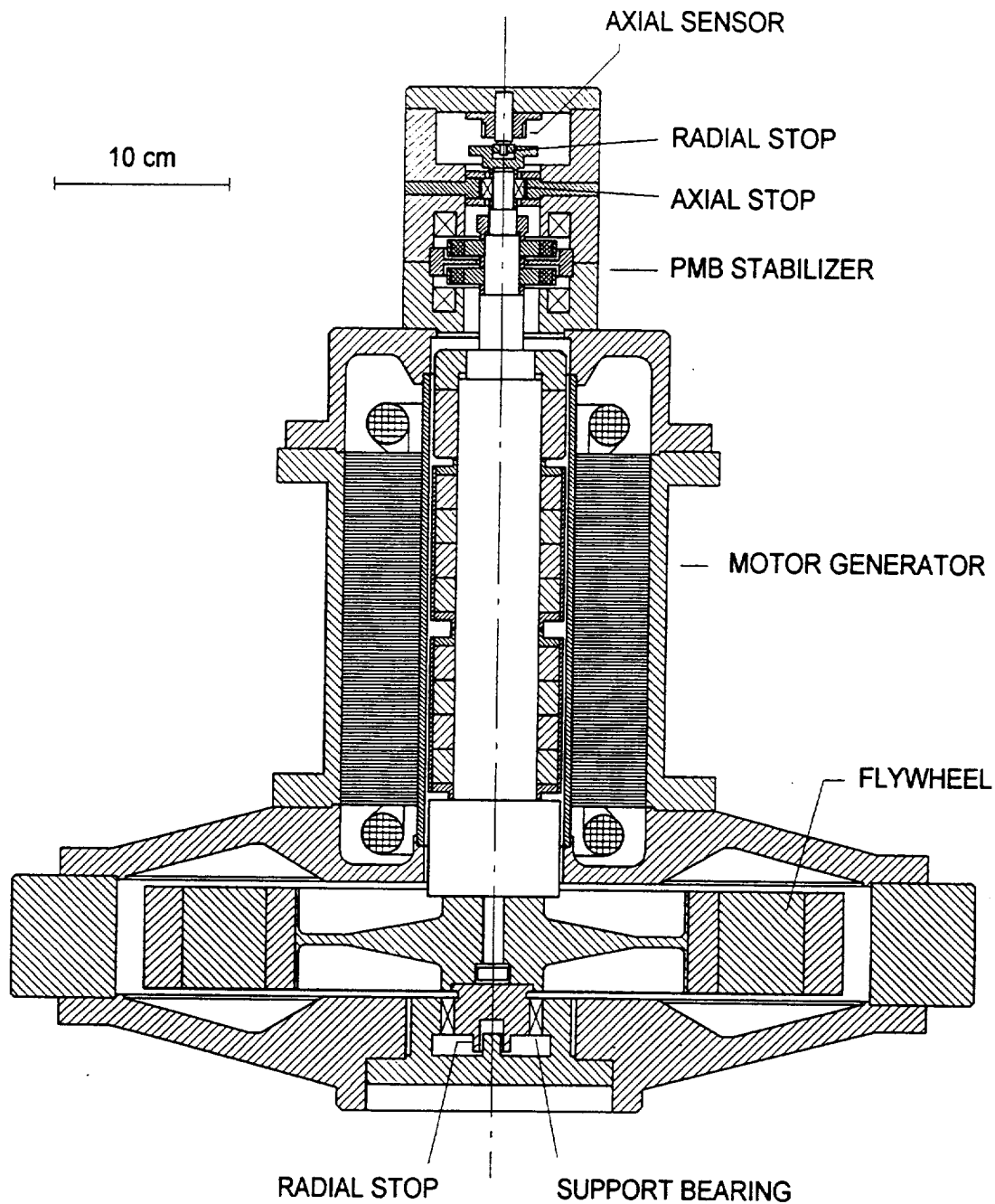


Figure 2. Sectional view of the flywheel system

The flywheel itself consists of three press fit annular components. The outermost ring is made of high-modulus M46J CFRP, the next one is standard T300 CFRP and the inner one is aluminum. An aluminum hub with elastic collars provides tight mechanical coupling between the ring package and the driving shaft where the hub is fixed by a central high-strength bolt.

The shaft carries two sets of permanent magnets made of plastic bound NdFeB material with diametrical magnetization. The magnets are part of a motor generator with a nominal power of 50 kW at 40,000 rpm of rotor speed. The annular magnets fit into centrifugal belts made of T300 CFRP. The magnet packages are fixed to the shaft by an axial thrust nut. The motor generator stator is mounted outside the vacuum enclosure. The latter passes through the magnetic gap of the motor generator.

The PMB system comprises a support bearing located just below the flywheel and a stabilizer assembly located on top of the motor generator.

The support bearing is shown in more detail in figure 3. This bearing contains four double-ring permanent magnets with attractive polarization [11] giving the rotor a net upward pull thus balancing its total mass of 23 kg. The mass of the permanent magnet material contained in the support bearing amounts to 184 g which is 0.8 % of the rotor mass.

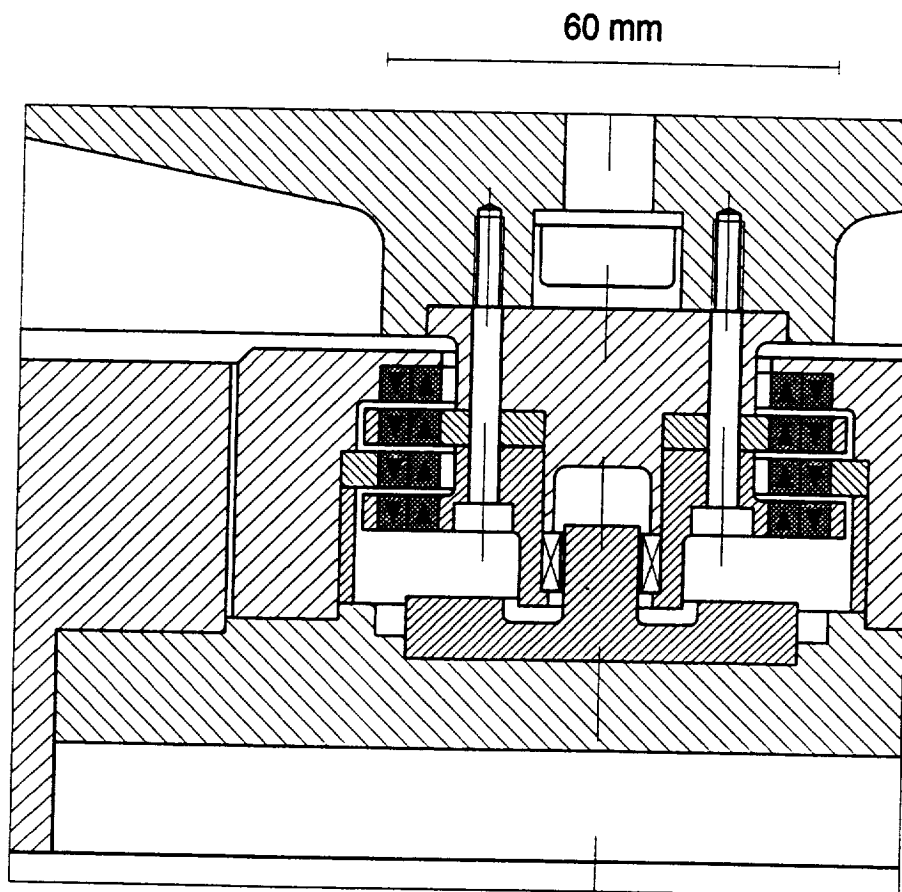


Figure 3. Close-up view of support bearing and lower radial stop assembly

Each double ring is made of two rings with opposite polarity. The forces between the magnets are attributed to surface currents as visualized in figure 4. These currents are built up from elementary currents associated with the electron spin at an atomic scale. All elementary currents within the magnet material cancel, as schematically indicated by loops at the axial surfaces, except those at the cylindrical surfaces where counterrotating neighbours are missing. The magnitude of the surface current of a given magnet equals the coercive force of the magnet material hence can be read from the corresponding data sheet. The NdFeB material presently used provides a coercive force of about 850 kA/m. With a magnet height of 4.7 mm we have about 4 kA of surface current on each of the cylindrical surfaces. The resulting currents are surprisingly high and could never be established in electric conductors of similar size. By fitting the double rings with opposite magnetization the surface currents sum up to 8 kA at their contact surface instead of cancelling each other. As the magnetic pull between parallel currents grows according to the product of their magnitudes, the 8-kA contact surfaces of the double rings provide four times as much pull across the axial gaps of the support bearing as the 4-kA bare surfaces on the in- and outsides. Thus, the four double-rings magnets provide 50% more pull than eight single rings of similar volume.

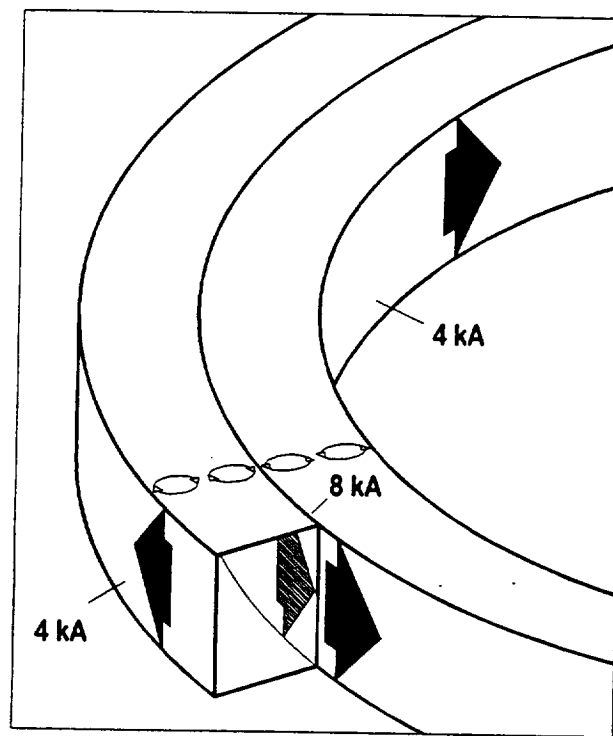


Figure 4. Double-ring permanent magnet with associated surface currents

The total surface current contained in a given PMB system may be regarded as a key parameter for characterization of its load capacity. The support bearing described here carries about 64 kA of surface current. This remarkably high current and the corresponding forces are steadily available without energy loss and without any obvious time limitation. For this reason it is proposed to

attribute a permanent magnet the quality of a superconductor, not even a "high-temperature" superconductor but rather an "ambient-" or "room-temperature" superconductor. In fact, the practicable temperature range of permanent magnets extends up to several hundred degrees C for certain magnet materials. At higher temperatures the magnetization weakens due to thermally induced disorder at an atomic scale. The demagnetization is enhanced in PMB applications based on a repulsive magnet configuration.

In the present attractive PMB configuration the currents not only provide the axial mass support of the rotor but also tend to align the rotor and stator magnets in the radial directions thus giving the rotor a radial stability. The radial stiffness is about 220 N/mm.

Along the axial direction, the currents tend to pull the gaps tight. The system is intrinsically unstable along the axial direction. The instability is specified by a negative stiffness which for geometrical reasons is about twice the magnitude of the radial stiffness. Axial stabilization is achieved by the stabilizer located at the upper end of the driving shaft (see figure 2). This type of stabilizer was developed for both, axial and radial stabilization functions [12]. The stabilizer is contained in an iron case. Two electric coils fixed inside the stabilizer case and a pair of permanent magnets on the rotor enable axial force actuation of the rotor. The coils are fed from a bidirectional DC power source (not shown) which is controlled by an axial position sensor located opposite to the upper end face of the driving shaft. The sensing circuit is automatically adjusted such as to drive the rotor to the axial position where the magnetostatic and gravitational forces acting on the rotor cancel. At this point the coil current approaches zero. Axial stabilization of the system is achieved at "zero-current" conditions. In fact, a small stand-by current (typically on the order of one watt of electric power) is required to keep the electronics alive for immediate action in case of axial force disturbances of the rotor. The power capability of the axial actuator system is adequately dimensioned to supply the lift-off force required on system start for pulling the rotor out of its axial rest position.

The stabilizer further provides radial centering and damping forces for the rotor. Centering is achieved by annular extensions of the iron case which penetrate the axial coils ending up at a close distance in front of the rotating magnets. As with the support bearing radial stability is provided by attraction forces. The radial stiffness of the present system at the stabilizer site is about 20 N/mm. Radial damping is achieved by eddy currents induced by radial rotor vibration in a copper disk extending into the gap between the rotating magnets. The damping force is about 27 Ns/m.

The weight support and attitude control functions are provided by two separate assemblies (support bearing and stabilizer) with quite different features at two distant locations. The system stabilization mechanism is thus comparable to the typical wing-and-tail-plane air craft design concept [9].

Axial and radial excursions of the rotor assembly are limited by mechanical stops (often termed touch-down or catcher bearings). The bidirectional axial stop is located on top of the stabilizer. It consists of a double ball bearing fixed to the shaft and a pair of axial disks on the stator giving the rotor a free axial play of ± 0.2 mm with respect to the axial equilibrium position. Radial stops on either end of the rotating system are designed for tangentially contacting the rotor at an inner cylindrical surface. In case of mechanical contact due to backward conical motion (precession) the tangential friction associated with the mechanical contact brings the rotor axis back to the central

position [13,10]. The upper radial stop consists of a ball bearing fixed to the housing that fits into an axial bore at the rotor with a radial play of ± 0.2 mm. The lower radial stop is a simple pivot-and-sleeve type friction bearing with similar radial play.

RESULTS AND DISCUSSION

The present flywheel system was designed as a test prototype for operation up to 40,000 rpm of rotor speed. The preliminary test program, however, was stopped in view of safety aspects at 33,000 rpm when we observed a sudden alteration of the rotor balance. At this maximum test speed the energy content of the wheel was about 430 Wh.

The main goal of the investigation has been achieved by demonstrating that a “*passive*” radial PMB system is capable of matching the forces associated with a power motor generator under static as well as under dynamic load conditions. The maximum pulsed power extracted from the system before the test stop was 15 kW at 30,000 rpm of rotor speed. At this and all preceding points of observation the rotor excursions excited by pulse power load were very small compared to the free play of the rotor shaft within the limits given by the mechanical stops.

The discharge power was drained into a power resistor network. A discharge efficiency of 97.4% was measured during 15-kW pulsed power extraction at 30,000 rpm.

System testing was originally planned for a maximum power load of 50 kW at 40,000 rpm. Under these target conditions the current and associated force load on the rotor would have increased by a factor of 2.5 with respect to the maximum realized load. We were able to extract currents of this magnitude by short circuiting the motor generator leads by a high current switch. This was done at 4,200 rpm maximum in view of the switch ratings. By this action excitation of the lowest precessional motion of the rotor system became significant. The radial amplitudes, however, were still well within the free radial play of the rotor shaft.

The design of the present flywheel system has been made in view of application in an UPS system. In order to ensure undelayed power supply from the system the motor generator was equipped with a permanent-magnet rotor. Idling losses have been recorded up to the maximum tested speed of 33,000 rpm where the losses reached about 200 W. The almost linear frequency dependence identifies the losses as being mainly of hysteresis type. Extrapolating to 40,000 rpm we expect about 250 W of idling losses which is 0.5% of the nominal 50-kW output power.

Evaluation of the magnetic bearing related losses is difficult as these are very small compared to the motor losses. An upper limit of the bearing losses was determined after replacing the motor permanent magnets with a steel tube and running the motor in an asynchronous mode. About 0.2 W of idling losses were determined at 4,200 rpm in this configuration. In an earlier investigation of a 12-kg neutron beam chopper suspended by a similar bearing system but with the rotation axis horizontal [8] we determined about 3 W of idling losses at 20,000 rpm under high-vacuum conditions (no air friction). We further found a linear increase of the idling losses with rotor speed. This implies the predominance of hysteresis losses. By linear extrapolation of our present results we

expect about 2 W of bearing related losses at the nominal flywheel speed of 40,000 rpm. This figure is in agreement also with theoretical considerations [10].

After fixing the rotor balance failure that terminated the preliminary test phase the system is intended for power tests up to full speed. The system is also considered as a basic test unit in view of day-and-night cycle energy storage application with the present motor generator replaced by a 5-kW machine and up to three more stacked flywheel assemblies on the rotor. Even on maintaining the present motor generator design with a permanent-magnet rotor, the self-discharge time constant of that energy storage system would be several days. A non-iron or externally excited type of motor generator would contribute to a further reduction of the idling losses with a corresponding further increase of the run-down time constant.

By modification and investigation of the present system towards more compact dimensions and higher speeds we expect to extend our knowhow also in view of possible car-drive and other mobile applications.

ACKNOWLEDGEMENT

The authors gratefully acknowledge the kind support of the project by Professor George Comsa.

REFERENCES

1. Post, R. F. and Post, S. F., "*Flywheels*", Scientific American 229, 17 (1973)
2. Kirk, J. A., "*Flywheel Energy Storage Part I - Basic Concepts*", Int. J. of Mech. Science, 19, 223 (1977)
3. Kirk, J. A. and Studer, P. A., "*Flywheel Energy Storage Part II - Magnetically Suspended Superflywheel*", Int. J. of Mech. Science, 19, 233 (1977)
4. Henrikson, C. H., Lyman, J. and Studer, P. A., "*Magnetically Suspended Momentum Wheels for Spacecraft Stabilization*", AIAA Paper No. 74-128 (1974)
5. Sabnis, A. V., Dendy, J. B. and Schmitt, F. M., "*Magnetically Suspended Large Momentum Wheels*", AIAA Paper No. 74-899 (1974)
6. Gilbert, R. G., "*Magnetic Suspension*", U.S. Patent 2,946,930 (July 26, 1960, *filed* June 20, 1955)
7. Boden, K. and Scheffer, D., "*Bearing Systems*", U.S. Patent 3,650,581 (March 21, 1972); German Patent 1750602 (*filed* May 17, 1968),

8. Boden, K. and Fremerey, J. K., "*Industrial Realization of the 'SYSTEM KFA-JÜLICH' Permanent Magnet Bearing Lines*", Proceedings MAG'92 Magnetic Bearings, Magnetic Drives and Dry Gas Seals Conference, Alexandria, Virginia, July 29-31, 1992 (TECHNOMIC PUBLISHING CO.)
9. J. K. Fremerey, "*Radial Shear Force Permanent Magnet Bearing System with Zero-Power Axial Control and Passive Radial Damping*", in "*Magnetic Bearings*", Proceedings of the First International Symposium, ed. G. Schweitzer, pp. 25-31, Springer-Verlag Berlin Heidelberg 1989
10. Kolk, M. "*Ein Schwungrad-Energiespeicher mit permanentmagnetischer Lagerung*", Thesis, Berichte des Forschungszentrums Jülich Jül-3470, 1997 (in German)
11. Fremerey, J. K., "*Axially stabilized magnetic bearing having a permanently magnetized radial bearing*", U.S. Patent 5,126,610 (June 30, 1992); German Patent 3808331 (*filed* March 12, 1988)
12. Fremerey, J. K. and Weller, A., "*Magnetic bearing having triaxial position stabilization*", U.S. Patent 4,620,752 (November 4, 1986); German Patent 3409047 (*filed* March 13, 1984)
13. Innerhofer, G., Sindlinger, R., Auer, W. and Schneider, W., German Patent Application 2741062 (September 13, 1977, *layed open* March 22, 1979)

Development of 10kWh Flywheel Energy Storage System

Osamu SAITO, Soichiro UNE and Hisayuki MOTOI
Ishikawajima-Harima Heavy Industries Co., Ltd.
15, Toyosu, 3 Chome, Koto-ku, Tokyo 135-8732, Japan

Hironori KAMENO, Yasukata MIYAGAWA, Ryouichi TAKAHATA and Hirochika UYEYAMA
R&D Center, KOYO SEIKO Co., Ltd.
No. 24-1, Kokubu, Higanjo-cho, Kashiwara, Osaka 582-0023, Japan

SUMMARY

We have designed and manufactured a flywheel energy storage system (FESS). The system has a flywheel made of carbon fiber reinforced plastics (CFRP) of the diameter of 1m supported by active magnetic bearings (AMB) of low energy loss. The flywheel rotor can be accelerated to 17,200rpm by a synchronous motor. The rated capacity of the energy storage system is 10kWh.

The energy loss of AMB is measured by using a test rig, which is designed to minimize the energy loss of AMB. Results obtained by free-running tests up to 12,000rpm show that the energy loss of the homopolar AMB is smaller than that of the heteropolar AMB. The energy loss of the homopolar AMB is found to be about 75W for one unit of the AMB with the bias current of 1.5A at 12,000rpm.

The present paper shows details of the energy loss of the test rig equipped with three types of the AMB, and also presents some of the measured data of the 10kWh FESS.

INTRODUCTION

Recently, energy storage systems at distributing substations are needed in order to level off daily fluctuations of loads on electric power, because of increasing electric power demands. A FESS is believed to be one of potential systems. Although there were some studies on FESS, these systems were difficult to store energy for long time. This reason was that they were equipped with ball bearings which induced higher energy loss, furthermore, that the flywheels were made of alloys leading lower rotation speed with lower storage capacities.

On the other hand, it was revealed that a high- T_c superconductor $\text{YBa}_2\text{Cu}_3\text{O}_{7-x}$ that had a strong pinning force was used in a magnetic bearing [1] and the energy loss of superconducting magnetic bearings (SMB) has been very small. Also the development of CFRP advanced. In these conditions, it is expected that the SMB can be used for large scale FESS.

The present investigation is conducted for designing and manufacturing a medium-sized 10kWh FESS mounted with a CFRP flywheel of the diameter of 1m in order to verify the rotor dynamics realizing a large-sized 10MWh class FESS with high temperature SMB. The flywheel rotor of this system is supported by two radial AMB and one thrust AMB without SMB to verify the energy loss and the rotor dynamics of the system. The flywheel system is anticipated to store the energy of 10kWh by rotating the flywheel up to 17,200rpm with a synchronous motor by the end of March 2000.

The flywheel rotor of the developed system is supported by AMB without contact to enable stable rotation at higher speed with lower mechanical loss. In order to develop the AMB of extremely low loss, a test rig for testing a low energy loss type AMB applicable to a medium-sized 10kWh FESS is developed in the present investigation. Thus, three types of AMB are tested on the test rig with measuring energy loss.

The present paper reports (1) low energy loss AMB developed, and (2) the medium-sized 10kWh FESS and results of rotation tests.

LOW ENERGY LOSS AMB

Structure of the test rig

Figure 1 shows the low energy loss AMB test rig designed and manufactured, and table 1 summarizes the basic specifications for the test rig. The test rotor is an outer rotor type, and a permanent magnet type synchronous motor is mounted inside the rotor. The whole mass of the rotor is supported by a spherical spiral groove bearing (spherical SGB) situated at the lowest position of the rotor. The radial vibration of the rotor is restricted by two AMB situated one at the top and the other at the bottom. Rotation tests are conducted in a vacuum chamber to reduce effects of windage loss as low as possible.

Tested AMB

The AMB designed and manufactured in the present investigation are, (a) a homopolar AMB, (b) a heteropolar AMB, and (c) a homopolar AMB with a permanent magnet (PM) [2]. These AMB are shown in figure 2. All types of the AMB have structures of laminated magnetic steel sheets of 0.35mm thick (stator side) to reduce eddy current loss induced by the rotating rotor. Similarly, opposing parts on a rotor to the AMB (rotor side) have structures of laminated magnetic steel sheets (containing 6.5% silicon) of 0.1mm thick. Usually, an AMB is required to have a certain amount of continuous bias current, and the energy for the current is not so small as to be neglected. Then, the AMB of the type (c) is designed and manufactured. The type (c) substitutes the PM for the bias flux generated by the bias current. The bias flux generated by the PM can be varied by adjusting gap adjustment screws as shown in figure 2(c).

Results of free running

Each pair of the AMB is mounted on the test rig. The rotor is accelerated to 12,000rpm by a motor, and then, the motor current is cut off to let the rotor to rotate freely (free running) for measuring energy loss. The energy loss of the homopolar AMB and the heteropolar AMB at the bias current of 1.5A is shown in figure 3. Here, the effect of windage loss is subtracted from the measured values according to the following equation [3], [4].

$$P_w = C (1 + 2.3 t / R) \rho^{0.8} n^{2.8} R^{4.5} \mu^{0.2}$$

Here,

P_w :	windage loss	(kW)
T :	height	(m)
R :	outer radius	(m)
ρ :	density of air	(kg/m ³)
n :	rotation speed	(rpm)
μ :	viscosity of air	(10 ⁻³ Ns/m ²)

The energy loss of the motor and of the spherical SGB is also shown in figure 3. The figure shows that the energy loss of only the homopolar AMB is about 150W (75W per one unit of AMB) with the bias current of 1.5A at 12,000rpm. Similarly, that of only the heteropolar AMB is about 380W (190W per one unit of AMB). This energy loss corresponds to as much as 2.5 times to that of the homopolar AMB.

The energy loss of the homopolar AMB and the heteropolar AMB in case of changing bias current into 1.5A, 1.0A and 0.5A is shown in figure 4. The figure shows that the energy loss gets small as the bias current is small for both AMB, and the changing rate of the homopolar AMB is smaller than that of the heteropolar AMB. Furthermore the energy loss of the homopolar AMB with the bias current of 1.5A is smaller than that of the heteropolar AMB with the bias current of 0.5A.

The results shown above indicate the superiority of the homopolar AMB over heteropolar AMB with respect for attaining low energy loss. An estimated the energy loss of the homopolar AMB on the medium-sized 10kWh FESS at the rated rotation speed (17,200rpm) is about 320W (160W per one unit of AMB).

Figure 5 shows measured the energy loss of the homopolar AMB with PM. The bias flux from the PM is adjusted to be equivalent to that with the bias current of 1.5A. The energy loss of the homopolar AMB with the bias current 1.5A is also shown in figure 5. The figure shows that the energy loss is equivalent to that of the homopolar AMB with the bias current of 1.5A. Thus, the homopolar AMB with PM is found to reduce energy loss equivalent to the bias current, leading to energy saving of a storage system.

MEDIUM-SIZED 10kWh FESS

Structure of 10kWh FESS

Table 2 summarizes the basic specifications for the medium-sized 10kWh FESS. Figure 6 shows structures of the mechanical parts of the apparatus, and figure 7 shows the system diagram.

The main body of the flywheel is made of light weight and high tensile CFRP, and is fixed to a center of an outer rotor with an aluminum hub of handle shape. The rotor is to be driven by a synchronous motor/generator equipped with permanent magnets and mounted on a stationary shaft inside the rotor. The stator of the motor/generator is cooled by cooling water flowing inside the stationary shaft.

Two radial AMB are mounted on the top and bottom ends of the rotor for restricting radial vibration of the rotor (unbalanced vibration and earthquake, etc.) [5]. These AMB are same sized homopolar AMB which were verified superior on the energy loss in the previous chapter. A thrust AMB equipped with permanent magnets is mounted at the top of the rotor for supporting the whole mass of the rotor without contact. This thrust AMB not only supports the mass of the rotor, but also restricts vertical vibration. The whole rotor system is enclosed in a vacuum chamber for reducing windage loss during rotation as low as possible. The rotor can be cooled only by radiation here, thus, two infrared radiation thermometers are mounted for monitoring temperature rises of the CFRP flywheel during rotation. Each one of angular ball bearings and of carbon rings as auxiliary touchdown bearings are equipped at upper and lower ends of the stationary shaft to cope with accidental contacts between the rotor and any stationary parts as to be caused by AMB failure. Another equipment is a location device mounted on the lower part of the rotor to lift the rotor to an active range of the thrust AMB. The rotor mounted on the test apparatus can be rotated to 17,200rpm by a synchronous motor in the vacuum chamber for storing the rated energy of 10kWh.

Results of rotation tests

Figure 8 shows the energy loss measured on the test apparatus. The chamber is evacuated to 10^{-3} torr, and the rotation speed is 8,000rpm. The figure also contains the energy loss induced by the motor/generator. The figure indicates that the total energy loss is about 280W. The estimated loss at 17,200rpm based on the measured energy loss is about 700W. Here, the energy loss resulting from only the radial AMB is about 400W (including the thrust AMB energy loss of about 18W, and windage loss of about 10W). This value is larger than the estimated value mentioned in the previous section based on the measured value at low energy loss AMB tests (about 320W) by about 25%, although these values could be thought to be almost the same.

CONCLUSIONS

The results obtained in the present investigation are summarized.

- 1) The energy loss induced by the homopolar AMB and the heteropolar AMB was measured and compared. The energy loss of the homopolar AMB was found to be smaller than that of the heteropolar AMB. The energy loss of both of the homopolar AMB and the heteropolar AMB got small as the bias current was small, and the changing rate of the homopolar AMB was smaller than that of the heteropolar AMB.
- 2) The energy loss induced by the homopolar AMB and the homopolar AMB with PM was measured and compared. The homopolar AMB with PM was found to be beneficial in reducing energy consumption of the FESS.
- 3) A medium-sized 10kWh FESS was designed and manufactured. Some test runs were conducted up to 8,000rpm, and the energy loss was measured. The measured energy loss at 8,000rpm was found to be comparable to that obtained on the low energy loss AMB test rig.

Rotation tests on the medium-sized 10kWh FESS of the rated speed of 17,200rpm will be performed. Results thus obtained will be utilized for further reducing the energy loss of FESS.

ACKNOWLEDGMENTS

The present investigation is conducted as a contract research project with NEDO as a part of "The research and development program for high temperature superconducting flywheel energy storage systems" under the industrial science and technology development system conducted by the Agency of Industrial Science and Technology of MITI. The authors are greatly thankful to many useful advice and cooperations of NEDO and related people.

REFERENCES

- [1] Y. Miyagawa, et. al.: A Trial Manufacturing of Flywheel Energy Storage System using a High-Tc Superconducting Magnetic Bearing, Preprint of Applied Superconductivity Conference, 1998
- [2] K. Nonami, et. al. Discrete Time Sliding Mode Control of Zero Power Magnetic Bearing System, Transactions of the Japan Society of Mechanical Engineers, 62-592, C, 1996
- [3] Anderson, N. E. and Loewenthal, S. H., Spur-Gear-System Efficiency at Part and Full Load, NASA TP 1622, 1980
- [4] Loewenthal, S. H. and Scibble, H. W., Operating Characteristics of a 0.87 kW-hr Flywheel Energy Storage Module, 20th Intersoc. Energy Convers. Eng. Conf., No.2, 1985,p.2.361.
- [5] O. Saito, et. al.: Active Magnetic Bearings for 10 kWh Flywheel Energy Storage System, 5th International Symposium on Magnetic Suspension Technology, 1999

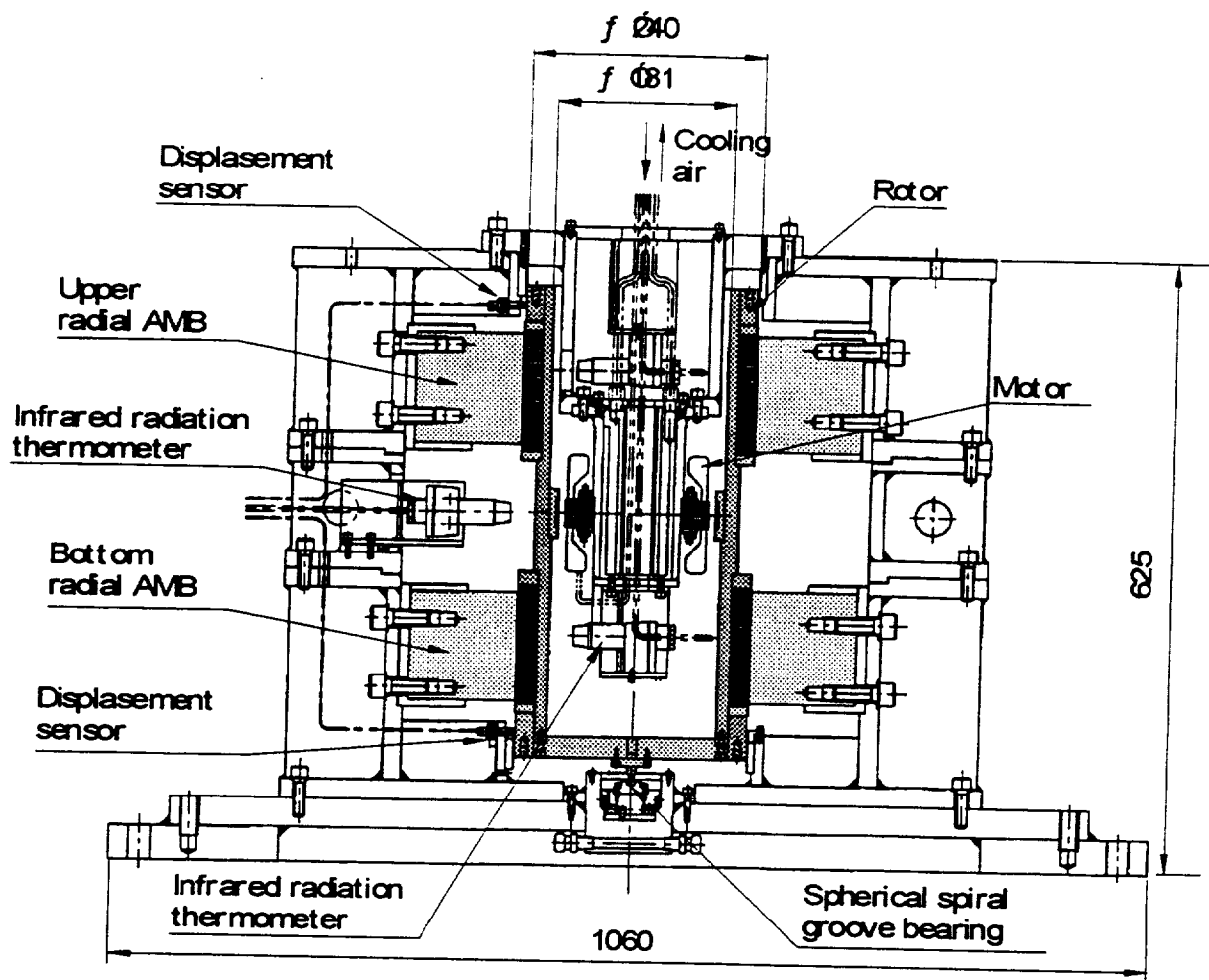


Figure 1. Low energy loss AMB test rig

Table 1. Basic specifications for low energy loss AMB test rig

Max. rotation speed		17,200 rpm (target)
Energy storage		0.34 kWh
Rotor	Inertia	0.75 kgm ²
	Mass	72 kg
	Diameter	ϕ 240 mm
	Length	465 mm
Pressure		Less than 0.1 torr

Rotor side : Magnetic steel sheet ($t = 0.1 \text{ mm}$, $\text{Si} = 6.5 \%$)

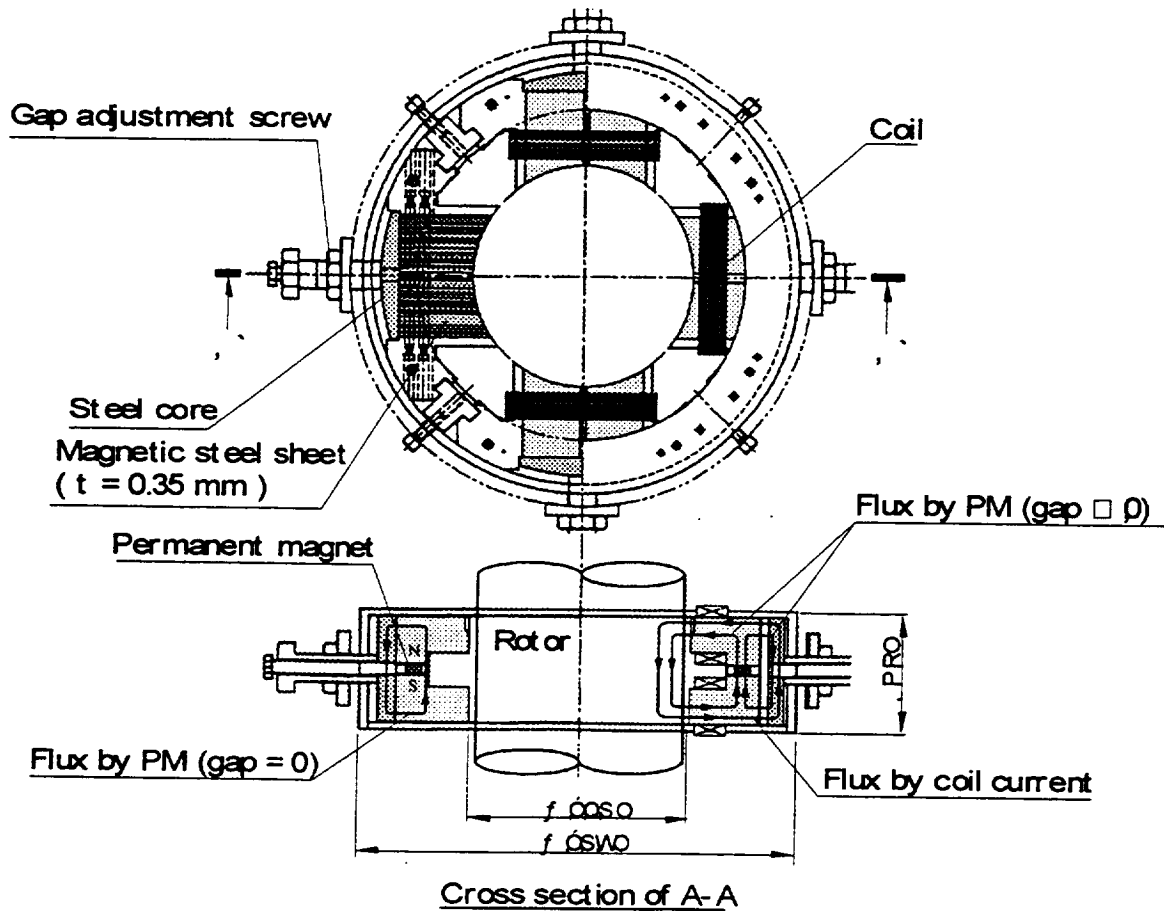
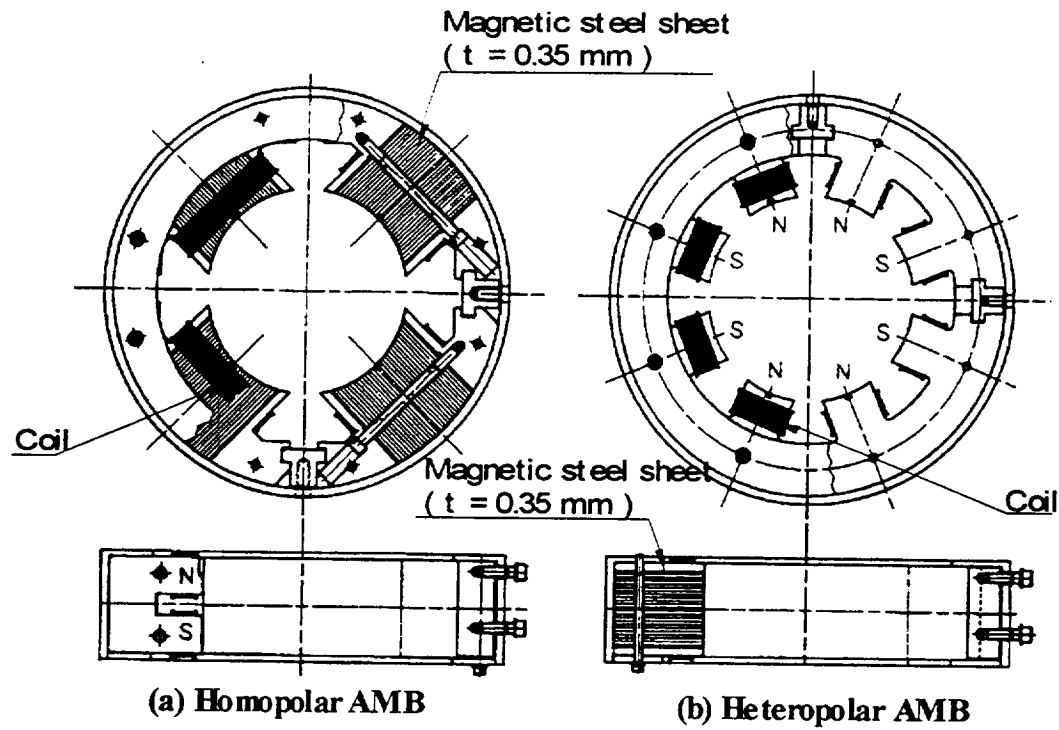


Figure 2. Tested AMB

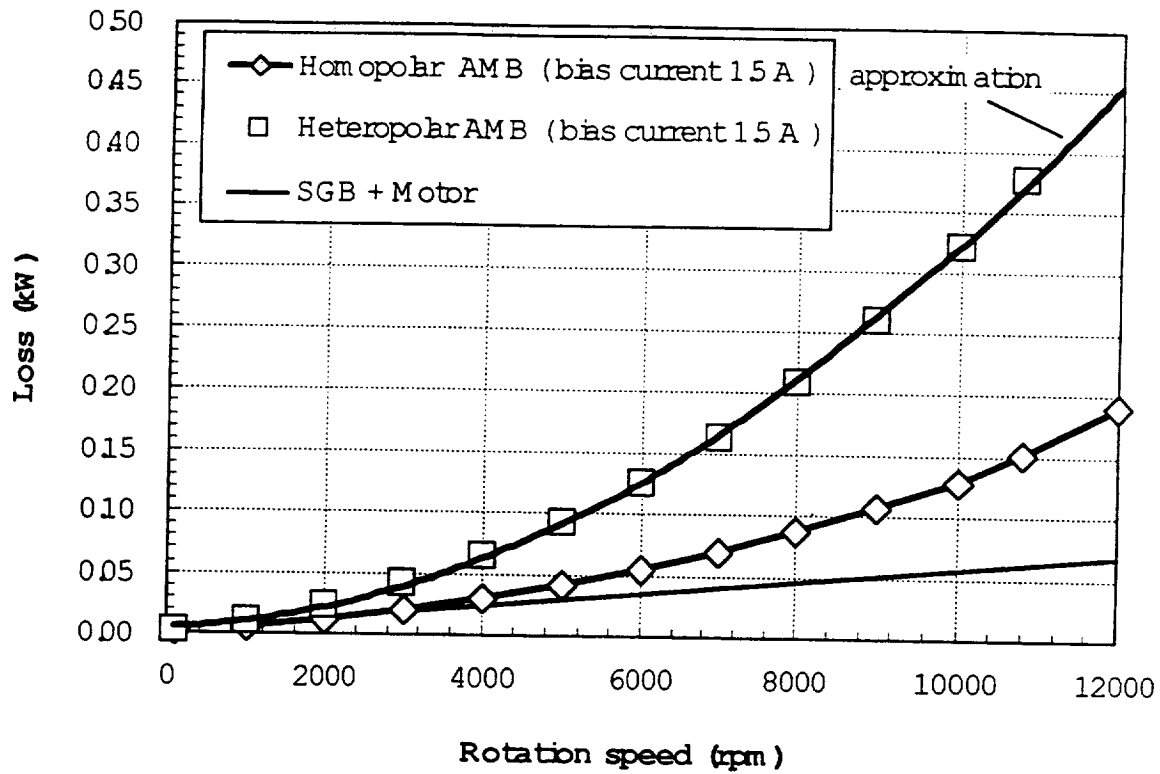


Figure 3. Energy loss of homopolar and heteropolar AMB with the bias current 1.5 A

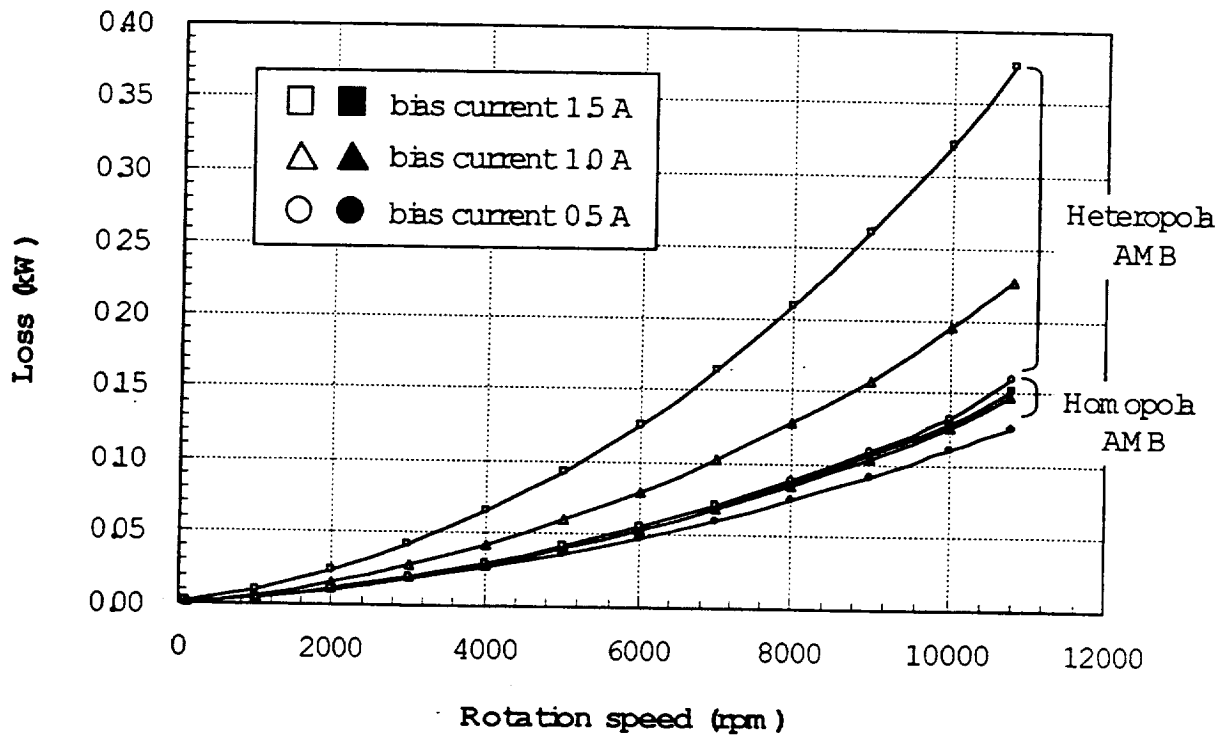


Figure 4. Energy loss of homopolar and heteropolar AMB in case of changing the bias current

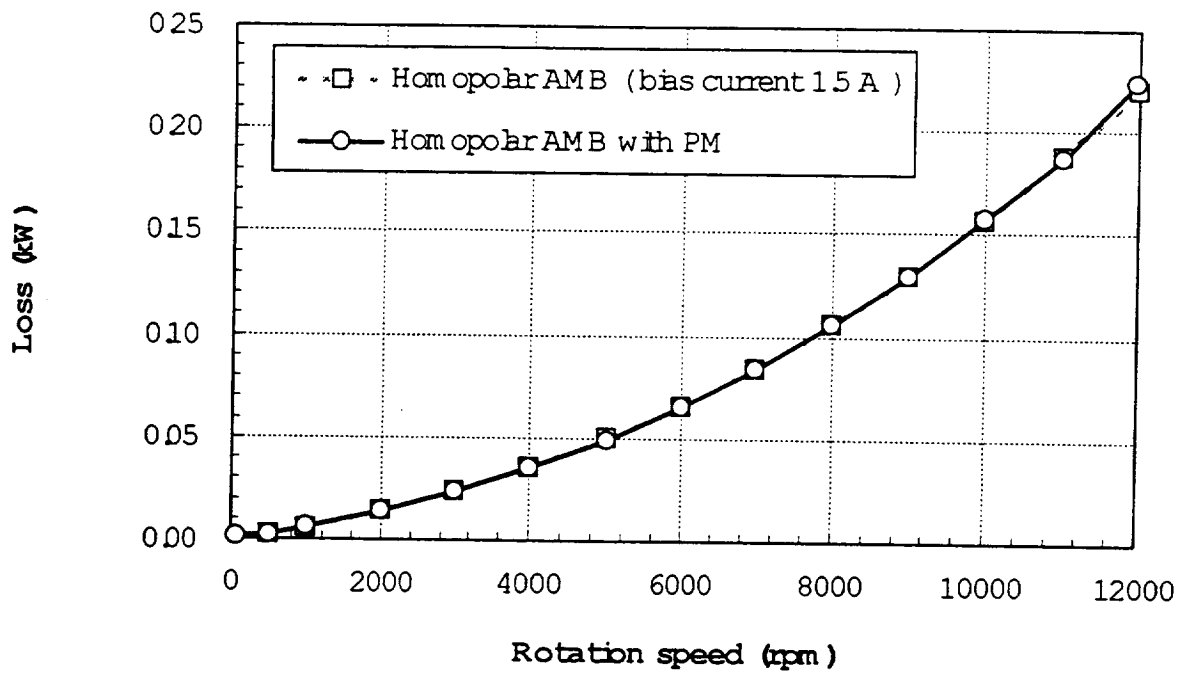


Figure 5. Energy loss of homopolar AMB with PM

Table 2. Basic specifications for the medium-sized 10 kWh FESS

Rotation speed		17,200 rpm (target)
Energy storage		10 kWh
Rotor	Inertia	$2.79 \times 10^{-3} \text{ kgm}^2$
	Mass	385 kg
		flywheel 123 kg
		rotor 207 kg
	Length	1040 mm
		Less than 1×10^{-3} torr

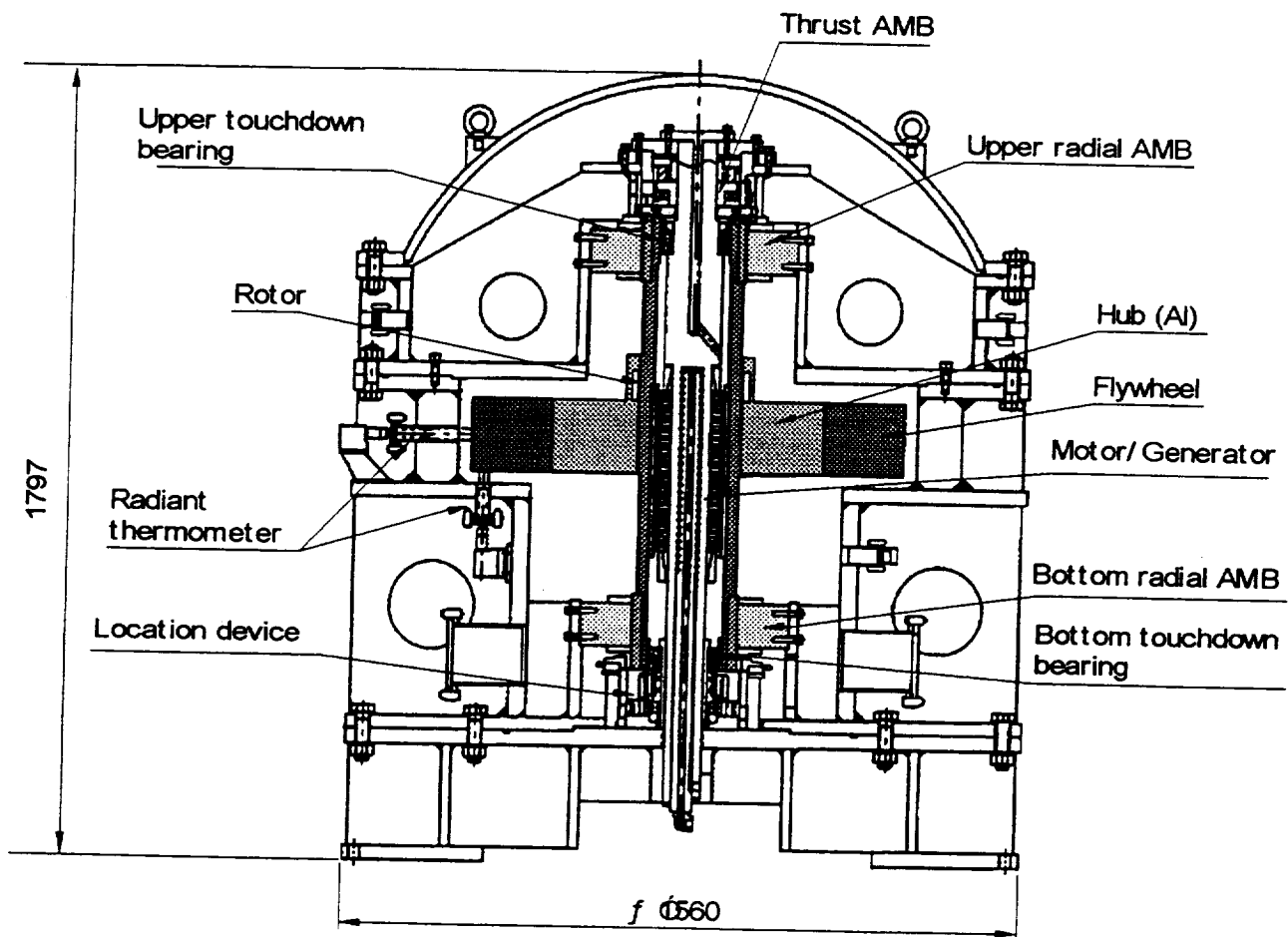


Figure 6. Structure of the medium-sized 10 kWh FESS

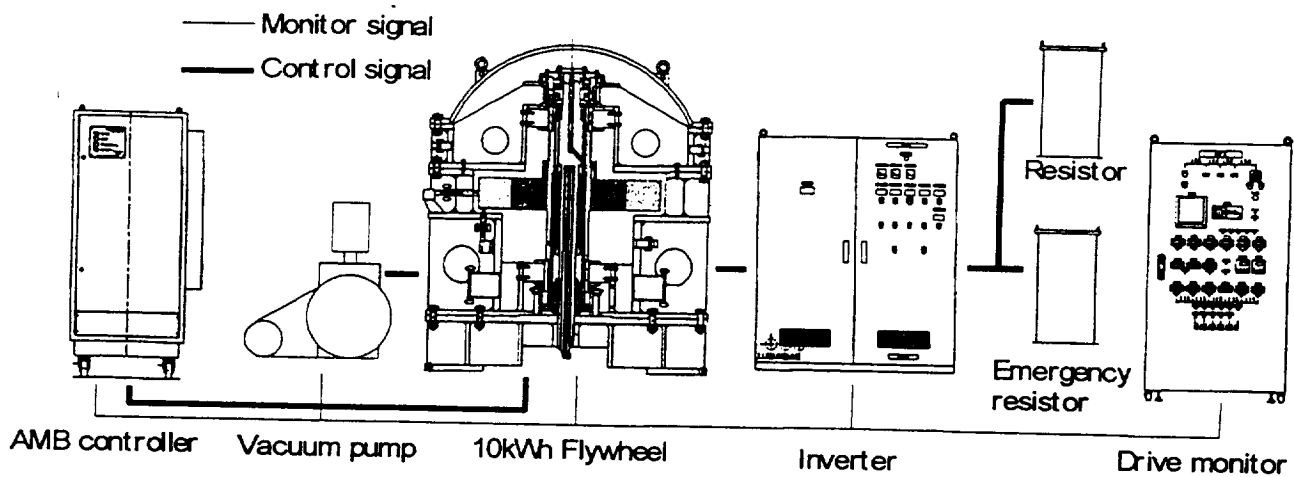


Figure 7. System diagram

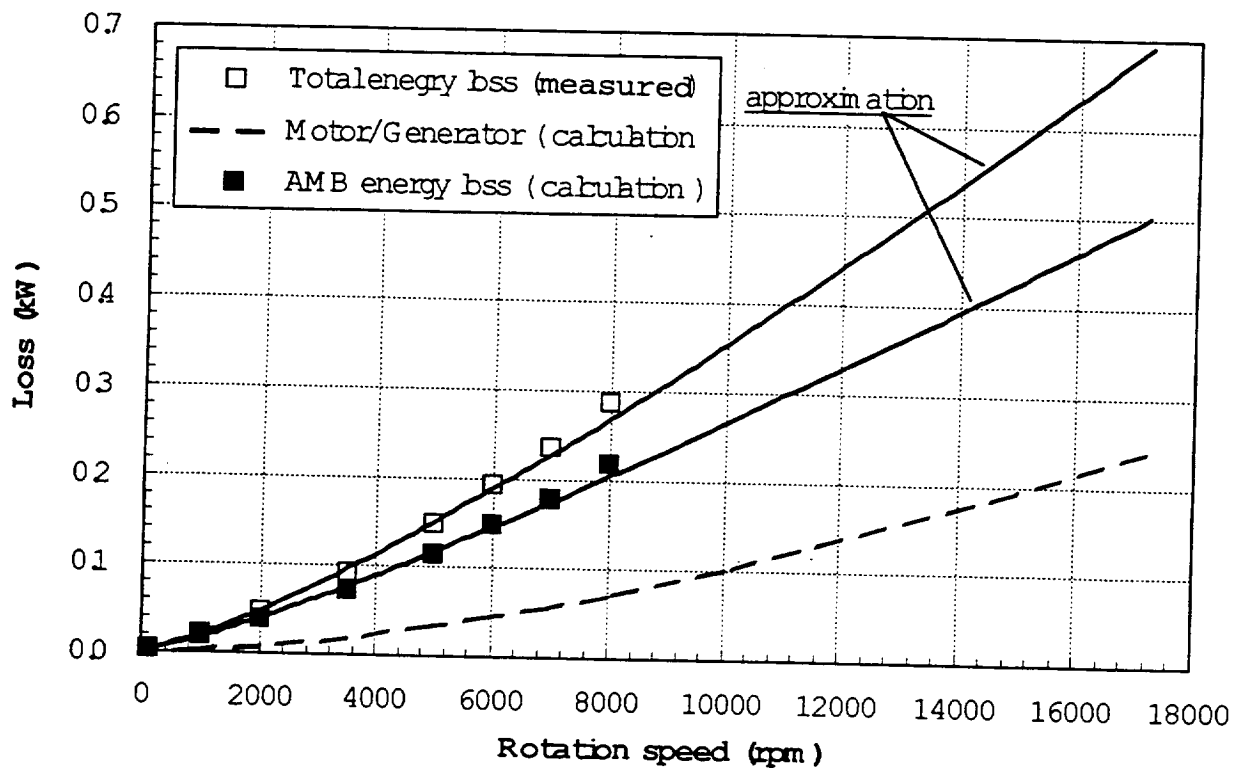


Figure 8. Energy loss measured on the medium-sized 10 kWh FESS

APPLICATION OF PERMANENT MAGNET BIAS MAGNETIC BEARINGS TO AN ENERGY STORAGE FLYWHEEL

Lawrence A. Hawkins
CalNetix, Inc.
Torrance, CA 90501

Brian T. Murphy
John Kajs
Center for Electromechanics
University of Texas
Austin, TX 78712

ABSTRACT

The design and initial testing of a five axis magnetic bearing system in an energy storage flywheel is presented. The flywheel is under development at the University of Texas Center for Electromechanics (UT-CEM) for application in a transit bus. CalNetix performed the system dynamic analysis, developed the magnetic bearing control algorithms, and developed the digital control hardware to meet the needs of the flywheel system. The bearing system for the prototype features two types of homopolar, permanent magnet bias magnetic bearings: a combination radial/thrust bearing and a pure radial bearing. The backup bearing system features a viscously damped, compliant mount. The system has been successfully tested to the maximum design speed of 42,000 rpm. A gain-scheduled, MIMO control algorithm was required to control the system modes affected by rotor gyroscopics. The implementation and basis for this control scheme is discussed. Dynamic test results are discussed relative to the rotordynamic and control system design.

INTRODUCTION

UT-CEM is developing a flywheel energy storage system, conveniently referred to as a flywheel battery (FWB), for use in a power-averaging role in a hybrid electric bus [1,2]. Energy generated during vehicle braking is converted to mechanical energy by using a motor/generator to drive the FWB. During vehicle acceleration, the motor/generator extracts energy from the FWB, completing the storage/recovery cycle. FWBs are ideal for this application because they have significantly higher power densities and longer life than other types of batteries [3]. The system, shown in Figure 1, is designed to store 2 kWh at 40,000 rpm, and produce 110 kW of continuous power (150 kW peak).

The goal of maximizing energy density leads to carbon fiber composites as the material of choice for modern high performance flywheels. These materials can operate safely at surface speeds of 1,000 m/s, as opposed to only 200-300 m/s for metals. The high surface speeds result in unacceptable windage losses unless the rotor operates in a vacuum. Thus rotor heat removal must be accomplished through radiation, making minimization of rotor heating a major design consideration. Consequently, low-loss homopolar, permanent magnet bias magnetic bearings and a permanent magnet motor/generator were chosen to reduce rotor heating. Initial testing was performed with a titanium flywheel rotor having a 9.9 inch outer diameter. This allowed for safe evaluation of the magnetic bearings and motor/generator. Now that the bearings and motor/generator are fully functional, complete thermal testing is underway. When thermal tests are complete, the titanium rotor will be machined down and composite rings added to bring the outer diameter up to 17.5 inches. This change to the rotor will alter its weight and polar-to-transverse inertia ratio, I_p/I_t . At that time the magnetic bearing control algorithms will require additional refinement for the reconfigured rotor.

In order to achieve the target operating speed, a gain scheduled MIMO control approach was developed. Similar approaches have been applied to magnetic bearings for other applications [4,5]. These features were applied in a limited way for the current system with titanium flywheel. Future testing of the composite flywheel will probably require additional sophistication, such as that provided by the more recent Linear Parameters Varying (LPV) approach [6,7].

FLYWHEEL BATTERY

The vertically mounted flywheel battery (Figure 1) uses a pancake flywheel placed below a separate motor/generator on the same shaft. This partially integrated configuration was chosen to allow integration of an existing, proven motor/generator with a robust flywheel design [1]. Although the composite flywheel section has a high I_p/I_t , the rigid body I_p/I_t for the entire flywheel rotor is significantly less than 1.0 (0.45 for the rotor in Figure 1) due to the size of the high-power density motor/generator. The motor/generator utilizes a diametrically polarized permanent magnet rotor (two pole) designed by AlliedSignal Aerospace. The magnet is captured radially by a thick inconel sleeve, which also provides the structural connection to the rest of the flywheel rotor. A beryllium copper sleeve is shrunk over the inconel sleeve to reduce rotor eddy current losses. The three phase, two pole toothless stator is ring wound with non-potted Litz wire, allowing minimum end turn length and excellent flow-through liquid cooling of the stator winding.

The magnetic bearings are placed immediately above the motor/generator and immediately below the flywheel. Rolling element backup bearings are placed outboard of the magnetic bearings. The magnetic bearings are inboard of the backup bearings for two distinct reasons: 1) this is the best bearing location from a rotordynamic standpoint, and since the backup bearings are intended for use only during rare events (preferably never) they are naturally placed in a less optimal location, and 2) the backup bearings are not

capable of operation at the same high surface speeds as the magnetic bearings, so they are placed outboard where the shaft diameter can be reduced to lower the surface speed.

Magnetic Bearing

The magnetic bearings use a homopolar, permanent magnet bias topology. Homopolar refers to the direction of the bias flux, which is oriented either uniformly into or uniformly out of the shaft at any circumferential location. This topology significantly reduces rotor eddy current losses compared to conventional designs. A permanent magnet is used to produce the bias flux for the bearing, resulting in several advantages compared to electromagnetic bias: 1) less power is consumed by the magnetic bearings, 2) the bearing has a more linear force/displacement characteristic due to the contribution of the large, fixed reluctance of the permanent magnet to the bias flux path, and 3) only one amplifier is required per axis, increasing reliability and reducing cost compared to conventional designs that use two amplifiers per axis.

The combo bearing in Figure 1 is a three-axis combination radial/thrust bearing. A combination bearing is more compact axially than separate radial and axial magnetic bearings. This increases the frequency of the rotor bending modes, making the magnetic bearing control design less difficult. This combination bearing, shown in more detail in Figure 2, uses a single radially polarized permanent magnet ring to provide bias flux for both the radial and axial flux paths. Three separate pairs of control coils allow individual control of each axis (two radial and one axial).

The radial (Brg 2) bearing is a two-axis radial bearing. The basic operation of this bearing was described in [8]. Some characteristics of the magnetic bearings are given in Table 1.

Table 1. Magnetic Bearing Characteristics.

Bearing	Combo Bearing (Radial)	Radial Bearing	Combo Bearing (Axial)
Bearing Reference Name	Brg 1	Brg 2	Thrust
Channel Names	1,2	3,4	5
Coordinate Names	x1,y1	x2,y2	Z
Load Capacity, N (lbf)	1115 (250)	670 (150)	2230 (500)
Force Constant, N/A (lbf/A)	156 (35)	94 (21)	303 (68)
Negative Stiffness, N/mm (lbf/in)	1751 (10,000)	963(5500)	3502 (20,000)
Air Gap, mm (in)	0.508 (.020)	0.508 (.020)	0.508 (.020)
Maximum Current, A	7.1	7.1	7.4

Backup Bearings

The backup bearings have radial and axial clearances of 0.010 inches (one-half of the magnetic air gap) between the bearing inner races and the shaft. The backup bearings are expected to carry load in the following cases: 1) when the system is at rest and the

magnetic bearings are turned off, 2) in the event of a substantial shock transient that exceeds the capacity of the magnetic bearings, and 3) in the event of a component failure that causes the loss of one or more axes of control for the magnetic bearing.

The backup bearing system consists of a duplex pair of angular contact ball bearings at each end of the shaft. The lower backup bearing also acts as a backup thrust bearing due to the inclusion of thrust collars on the rotor. The bearing materials are 440C inner and outer races, SiN₃ balls, composite cage, and dry film lube (MoS₂). Lead bronze sleeves are used for the rotor contacting surfaces. This material provides a touchdown surface with low friction characteristics at the expense of long wear life.

A radially compliant backup bearing support in parallel with a sealed viscous damper contains the backup bearings. The nominal stiffness and damping characteristics selected for the support were 100,000 lb/in and 150 lb-s/in respectively. These values were defined by a parametric study using a transient, nonlinear drop and spin down rotordynamic analysis. The selection criteria were to minimize deflection and load during critical speed traverse on the spin down, and to minimize static deflection and load during drop impact transient and at rest.

SYSTEM MODELLING

Rotordynamic Model

The rotordynamic structural model is shown in Figure 3. The top half shows the stiffness model and the lower half the mass model. The actuator and sensor locations and the first free/free, zero-speed bending mode are superimposed on the plot. Notice that the sensor and actuator modal displacements are lower at Brg 1 compared to Brg 2 in the first bending mode. The first four bending modes are included in the system analysis. The frequencies of those modes at zero speed are: 745 hz, 1425 hz, 1990 hz, and 3590 hz.

The rotordynamic equation of motion for the plant, which is in general a coupled, flexible rotor/casing system with conventional bearings, is:

$$[M]\{\ddot{q}\} + [C]\{\dot{q}\} + [K]\{q\} = \{f\} \quad (1)$$

Where q represents the physical coordinate degrees of freedom, f represents external forces, and the mass matrix is represented by M . The passive negative stiffness of the magnetic bearing is included in the bearing stiffness matrix, K . The terms representing gyroscopic effects are part of the rotor partition of the damping matrix, C .

For the flywheel, each rotor bending mode was given a static internal damping ratio, $\xi_{ns}=0.5\%$. This is a reasonable value for a rotor with sleeves if no modal test data is

available. The dynamic internal damping for rotor modes is reduced as speed increases by:

$$\xi_n = \xi_{ns} \left(\frac{\omega_n - \omega_{spin}}{\omega_n} \right) \quad (2)$$

Where ω_n represents the natural frequency of the mode, and ω_{spin} represents the spin frequency. The basis for this circular whirl approximation can be derived from the discussion of internal rotor damping by Childs [9].

For system analysis with magnetic bearings, the plant represented by Eqn. (1) is transformed to modal coordinates, μ , and converted to state space form:

$$\begin{aligned} \{\dot{\mu}_p\} &= [A_p] \{\mu_p\} + [B_p] \{f\} \\ \{q\} &= [C_p] \{\mu_p\} + [D_p] \{f\} \end{aligned} \quad (3)$$

Partitions of the characteristic matrix A_p contain the modal stiffness and damping matrices. The input and output matrices B_p and C_p contain mass normalized eigenvectors for modes selected for the system analysis. Some authors include the passive negative stiffness as part of the feed forward matrix D_p instead of as a bearing stiffness in K . These equations have been presented in detail by several authors; one recent example is Antkowiak [10].

Predicted and measured plant bode plots are shown in Figure 4 for zero speed. Both curves include the bearing and sensor dynamics because the plant must be measured in the installed system by taking the transfer function between the position sensor and the amplifier current monitor. The phase roll-off seen in Figure 4 beginning around 100 hz is due to the low pass filter (bandwidth of 3.4 kHz) in the position sensor demodulation electronics. The weak mode at about 30 hz in the measured transfer function is the rigid body mode of the system on the elastomeric housing supports. Due to its limited influence on the control of the rotor, the housing was not included as part of the plant model for this stage of the FWB analysis. Future application of this FWB to the transit bus platform will require inclusion of the housing and gimbal dynamics in the system model. Although the coherence of the measured result is poor above 800 hz, the first two bending modes at 750 and 1425 hz are apparent and consistent with model predictions.

System Analysis

The initial magnetic bearing transfer function for Brg 1 (x_1 and y_1) is given in Figure 5. The transfer function for Brg 2 is similar. For linear response and eigenvalues analysis, the magnetic bearing transfer functions are converted to state space form and coupled to the plant model of Eqn. (3). Figure 6 is a comparison of the predicted versus measured closed loop transfer function of the system. Overall, the agreement is reasonable; however, the predicted damping is somewhat high near the rigid body mode at about 150 hz. Again, the measurement coherence is poor above about 800 hz. Figure 7 is a plot of all predicted system natural frequencies below 1000 hz that have damping ratios (ξ) less

than 0.25. Well damped modes were left out because the large number of such modes in the system make this type of plot difficult to interpret. The strong gyroscopic influence is responsible for the rise of the second rotor rigid body mode with speed, as well as the spread of the forward and backward bending modes (see Figure 7).

CONTROL SYSTEM DEVELOPMENT

Speed Independent, SISO Control Approach

The original magnetic bearing system was designed and built by Avcon, a company that ceased operation just as the flywheel was initially assembled. Due to limited processing power of the DSP in the controller supplied with the system, the original control hardware allowed only SISO compensation with a maximum of six biquad filters per axis at a 10 kHz sample rate. No speed input was provided, thus a successful compensation would have to control all modes of the system from rest to 42,000 rpm. This task is readily achievable for some types of rotors; but not practical for a rotor with substantial gyroscopic effects such as this FWB. Stability of the rigid body conical mode and/or the backward first bending mode was marginal at all speeds above 30,000 rpm. The highest speed achieved with the SISO single speed controller was 37,000 rpm.

The SISO transfer function was shown in Figure 5. The control strategy used was to provide direct phase lead for the second rigid body mode, roll off the compensation quickly enough to again provide phase lead for the backward and forward components of the first bending mode. The backward bending mode needed phase lead throughout the operating range. However, the forward bending mode exits the positive phase lead region near 900 Hz. The mode is still stable due to the low gain of the transfer function at those frequencies. This strategy has a limit in that at higher speeds, the frequencies of the forward rigid body mode and the first backward bending mode become close enough that the phase cannot be transitioned quickly enough between the modes. That limit was reached at 37,000 rpm for this rotor and the original control hardware.

Gain Scheduled, MIMO Control Approach

Hardware Development

In order to bring the machine to full speed operation, CalNetix developed a new stand-alone control module based on the Texas Instruments TMS 320C6201 (C6x) digital signal processor (DSP). This control module provided a factor of 5 to 10 increase in processing speed, program memory and data memory. Whereas, the previous control module had to be programmed in assembly and used 80 μ s (80% of available processing time at a 10 kHz sample rate) to execute the desired set of transfer functions for the flywheel (a 12 state compensator for each radial axis, 4 states for the axial), the new control module could execute the same set of transfer functions in about 15 μ s with a

control program written in C. Since a 10 kHz sample rate is suitable for most magnetic bearing supported turbomachinery, the new control hardware comfortably allows at least five times as many instructions as the previous hardware. The new control hardware also allowed the easy incorporation of a speed/phase detection scheme. Thus previously unavailable MIMO and gain scheduled control schemes could now be used.

Gain Scheduling Implementation

As an initial implementation of gain scheduled control, the control program was structured to access up to four independent sets of control parameters (filter coefficients and gains). Each set of control parameters is applied in a different rotor spin speed range. The speed ranges overlap so that the selected set of control parameters is prevented from toggling back and forth near a transition speed. The speed ranges for the FWB are indicated on the natural frequency map of Figure 7. When the spin speed moves into a new speed range, the coefficients for that speed range are made current. This feature allows the use of a transfer function that is optimized more closely to the plant requirements within a given speed range than can be accomplished with a single control structure. The choice of four speed ranges was made simply to address the (now) well-known needs of the titanium FWB. The only hard limit to the number of speed ranges imposed by the control module is the amount of data memory used, which is about 1 kB per speed range with the structure now in use. Since robust operation had been achieved to 30,000 rpm with a single set of control parameters, the initial implementation of gain scheduling focused on simple modifications to this compensation. Parameters for the first speed range were modified to provide more damping at the rigid body critical speeds. The resulting damping ratios were approximately: 0.38 and 0.32 respectively. The control parameters for the three higher speed ranges successively track the second forward rigid body mode and first backward bending mode, at the expense of reduced damping at 50-150 hz since the critical speeds have already been traversed.

Circumferential Cross-Coupling (MIMO) Implementation

In order to further improve the damping ratios of the troublesome modes, a simple MIMO control feature was added to the control program. For the test results presented in this paper, the MIMO feature was used only for the fourth speed range, but it can easily be used in any or all speed ranges as desired. As with the SISO controller, the magnetic bearing control commands are calculated from a series of cascaded biquad filters that produce the desired transfer functions. Five direct axis transfer functions are used to represent the normal SISO control for a five-axis system. SISO implies that each axis is controlled independently of the others. In the MIMO implementation employed here, up to four additional transfer functions are provided which can be used with independently selectable input and output axes. The intended use for this feature is for circumferential (x,y) cross-coupling; however, the selection of input and output channels is general, allowing this feature to be used in other ways.

Description of Circumferential Cross-Coupling

Circumferential cross-coupling is well suited to the flywheel because it allows the application of a phase lead to a specific region of the frequency spectrum with less influence on other parts of the spectrum. The forces that are applied by the cross-coupled terms can be understood in the following way. Consider a radial bearing to have two orthogonal axes, x and y . In a SISO controlled magnetic bearing, the bearing reaction force, F , along a given axis is due to motion only along that same axis. That is, if the rotor moves in the x axis direction, this produces a bearing force along only the x axis. This is illustrated in Eqn. (4):

$$\begin{Bmatrix} F_x \\ F_y \end{Bmatrix} = - \begin{bmatrix} H_{xx} & 0 \\ 0 & H_{yy} \end{bmatrix} \begin{Bmatrix} x \\ y \end{Bmatrix} \quad (4)$$

For magnetic bearings, the H are called transfer functions, and are generally functions of frequency. The frequency dependence in a magnetic bearing is defined by the control compensation in conjunction with the dynamic characteristics of other parts of the system such as the position sensor, power amplifier, and magnetic actuator. In a MIMO controlled magnetic bearing, the off-diagonal terms can be nonzero. This is called *circumferential* cross-coupling since the x and y axes within one radial bearing are being coupled. In this case, motion in one axis, say x , produces forces in *both* the x and y axes. This is illustrated in Eqn. (5):

$$\begin{Bmatrix} F_x \\ F_y \end{Bmatrix} = - \begin{bmatrix} H_{xx} & H_{xy} \\ H_{yx} & H_{yy} \end{bmatrix} \begin{Bmatrix} x \\ y \end{Bmatrix} \quad (5)$$

The H_{xy} and H_{yx} are the circumferential cross-coupling transfer functions. Another potentially attractive type of cross-coupling would be between the x axes (or y axes) of two radial bearings working in tandem to support a rotor.

Two of the four cross-coupled transfer functions used for the FWB are given in Figures 9 - 10. Both of these transfer functions include the dynamics of the position sensor, amplifier and magnetic actuator, and a Pade approximation of the calculation phase delay. These elements are part of the magnetic bearing transfer function. Figure 9 is the transfer function between input 2 and output 1 (H_{xy} for Brg 1). The transfer function between input 1 and output 2 (H_{yx} for Brg 1) is the same except that the gain term carries the opposite sign, making the phase different by 180° . The phase inversion between the two cross-coupled transfer functions is necessary to produce consistent forces at the two axes (either both leading or both lagging). Together with the opposite signed H_{yx} , the transfer function of Figure 9 produces a stabilizing force on forward modes (and a destabilizing force on backward modes) with frequencies up to about 300 hz (21,000 cpm). For modes above 300 Hz, the force is destabilizing for forward modes and stabilizing for backward modes.

The Figure 10 is the transfer function between input 4 and output 3 (H_{xy} for Brg 2). H_{yx} for Brg 2 is the same as H_{xy} , except that, again, the gain term carries the opposite sign,

making the phase different by 180° . The cross-coupled transfer function applied at Brg 2 is designed specifically to provide a stabilizing force for the first backward bending mode of the rotor, which is near 30,000 cpm when the rotor speed is in the range of 35,000 to 42,000 rpm.

DYNAMIC TEST DATA

Figures 11 - 13 show dynamic data collected from a full-speed rundown of the machine. During rundown, the motor/generator is used to decelerate the rotor from 42,000 rpm to rest in approximately 90 seconds. Figure 11 is a plot of synchronous displacements taken from the magnetic bearing position sensors during the spin-down. There is a spike at about 1,500 rpm on all sensors due to the traverse of the housing support mode. A significant displacement at Brg 2 occurred near the expected traverse of the second rotor rigid body mode at 8,000 rpm. There is also significant displacement at Brg 1, near the traverse of a lightly damped system mode at 15,000 - 18,000 rpm. This mode is closely related to the second rigid body mode and the compensator pole that provides phase lead for the mode. These response peaks agree well with the mode locations in Figure 7. The synchronous displacements also begin to rise again between 30,000 and 42,000 rpm as the net direct stiffness of the bearing falls. Figure 12 is a plot of synchronous coil current for each bearing. The magnetic bearing control current diminishes between 30,000 and 42,000 rpm in tandem with the rise in rotor displacements. This is because the stiffness (gain) of the bearing transfer function drops significantly in this frequency range (see Figure 5). Note that the current curves exhibit steps at 24,000, 30,000, and 35,000 rpm. These are the switching points for the gain scheduling when the rotor is spinning down in speed.

A waterfall plot for the $X1$ axis (Brg 1, input 1) position sensor is shown in Figure 13. The waterfall shows the frequency spectrum for a large number of spin speeds during the spin down from 42,000 rpm to 5,000 rpm. Two decades of the amplitude spectrum are shown, and the clearly dominant signal is the rotor synchronous displacement (700 hz at 42,000 rpm). The forward and backward bending modes are intermittently visible; at approximately 560 hz and 920 hz at 42,000 rpm, converging to 750 hz at low speed. The mode visible near 250 hz (42,000 rpm spin speed) is the second rigid body mode. This mode drops to about 150 hz at rest. The locations of these modes are in agreement with the predicted natural frequencies in Figure 7. The speed independent response at 720 hz is a noise frequency.

CONCLUSION

System development and analysis of a permanent magnet bias, magnetic bearing system for an energy storage flywheel was described. Development and implementation of a gain-scheduled, MIMO digital control scheme was discussed. Because the needs of the test flywheel system were moderate, the new control features have been applied in only a limited way to date. The capability of the control system will be more fully utilized in the

future application to the composite rotor flywheel. Dynamic test data from full speed testing of the system showed good performance from the bearings and control system. Good agreement was found between the system analysis and test data.

REFERENCES

1. Hayes, R.J., Kajs, J.P., Thompson, R.C., Beno, J.H., "Design and Testing of a Flywheel Battery for a Transit Bus", SAE 1999-01-1159, 1998.
2. Murphy, B.T., Beno, J.H., Bresie, D.A. "Bearing Loads in a Vehicular Flywheel Battery", PR-224, SAE Int. Congress and Exp., Detroit, 1997.
3. Reiner, G., "Experiences with the Magnetodynamic (Flywheel) storage System (MDS) in Diesel Electric and Trolley Busses in Public Transport Service," Pres. at Flywheel Energy Storage Technology Workshop, Oak Ridge, TN, 1993.
4. Matsumura, F., Namerikawa, T., Hagiwara, K., and Fujita, M., "Application of Gain Scheduled H_{∞} Robust Controllers to a Magnetic Bearing," IEEE Transactions on Control Systems Technology, Vol. 4, no. 5, pp. 484-492, 1996.
5. Sivrioglu, S. and Nonami, K., "LMI Approach to Gain Scheduled H_{∞} Control Beyond PID Control for Gyroscopic Rotor-Magnetic Bearing Systems," Proc. 35th Conf. On Decision and Control, pp. 3694-3699, Kobe, Japan, 1996.
7. Tsiotras, P. and Knospe, C., "Reducing Conservatism for Gain-Scheduled H_{∞} Controllers for AMB's", Proc. of MAG'97, p. 290-299, Alexandria, VA, 1997.
6. Apkarian, P. and Adams, R.J., "Advanced Gain-Scheduling Techniques for Uncertain Systems," IEEE Transactions on Control Systems Technology, Vol. 6, no. 1, pp. 21-32, 1997.
8. Meeks, C.R., DiRusso, E., Brown, G.V., "Development of a Compact, Light Weight Magnetic Bearing", AIAA/SAE/ASME/ASEE 26th Joint Propulsion Conference, Orlando, 1990.
9. Childs, D.W., "Turbomachinery Rotordynamics", J. Wiley, New York, p. 25, 1993.
10. Ankowiak, B.M., Nelson, F.C., "Rotordynamic Modeling of An Actively Controlled Magnetic Bearing Gas Turbine Engine", ASME 97-GT-13, 1997 IGTI Turbo-Expo, Orlando, 1997.

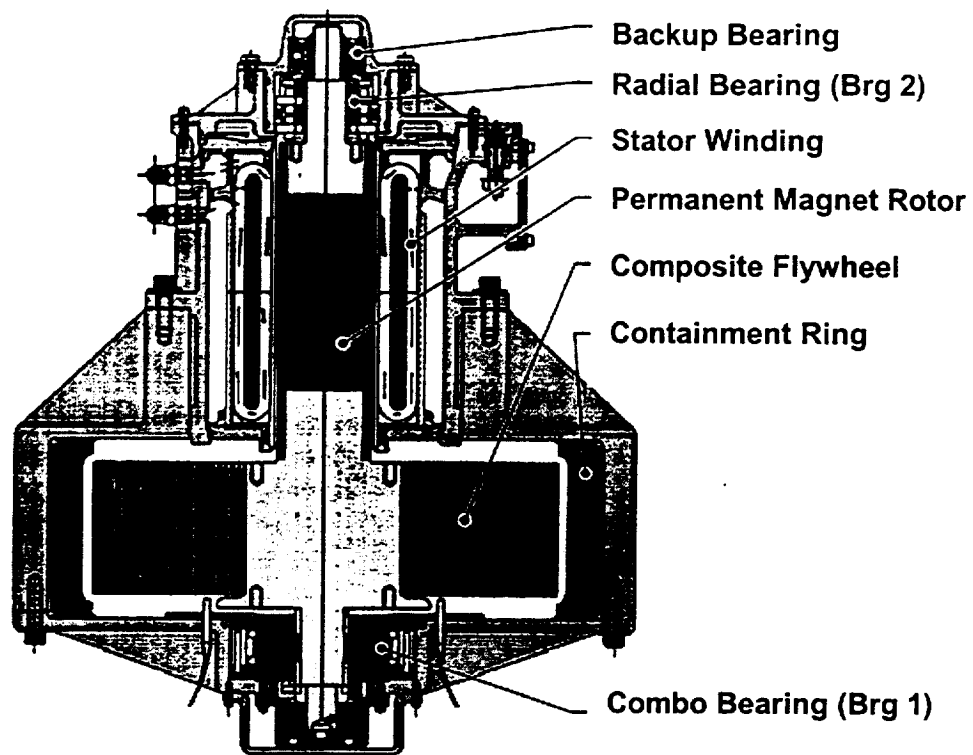


Figure 1. UT-CEM Flywheel Battery Designed for a Transit Bus.

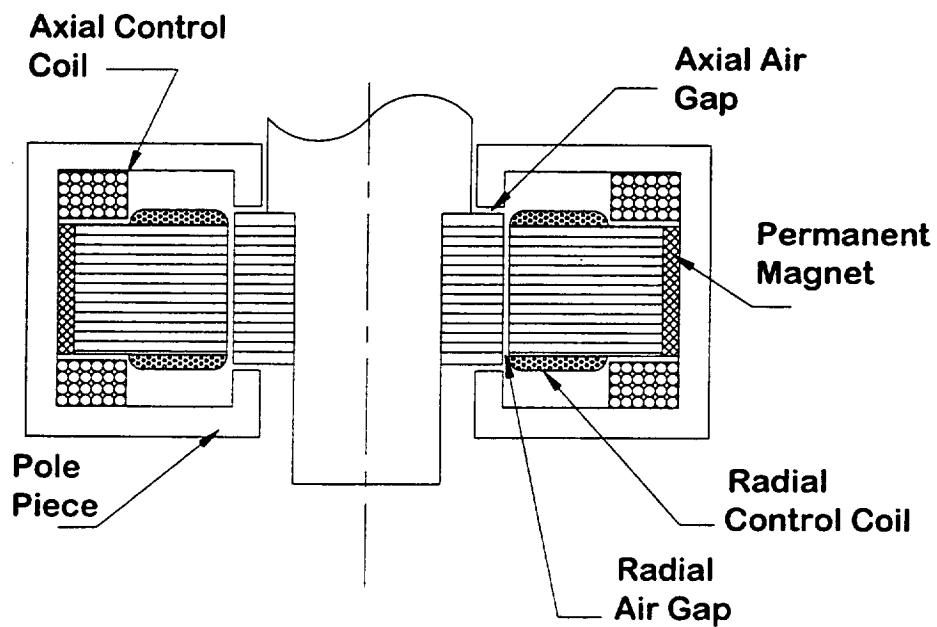


Figure 2. Combination radial/thrust permanent magnet bias bearing (Combo Bearing).

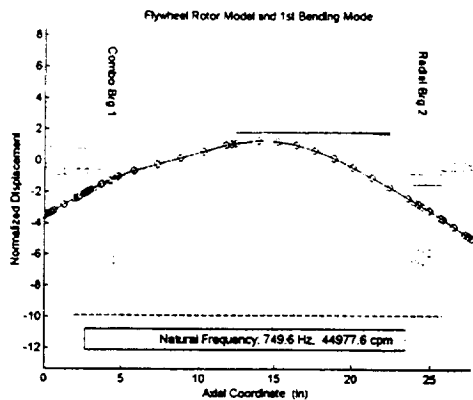


Figure 3. Rotordynamic Structural Model with First Bending Mode.

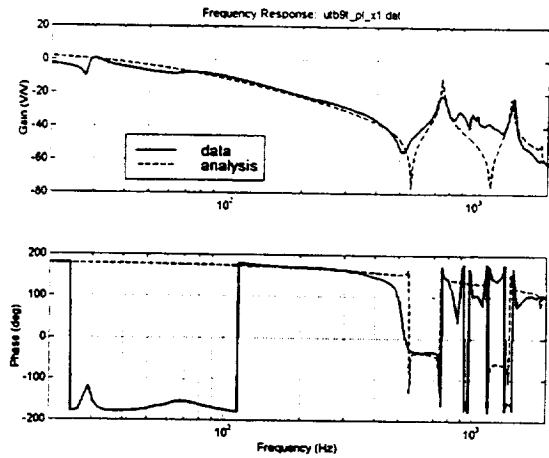


Figure 4. Predicted vs. Measured Actuator/Plant/Sensor Bode Plot (x1 axis).

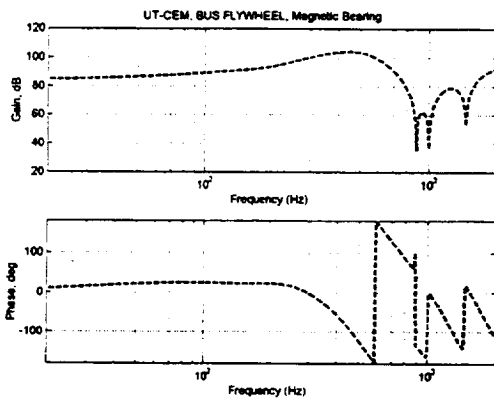


Figure 5. Single Speed SISO Mag Bearing Transfer Function, includes Sensor/Compensator/Amplifier/Actuator

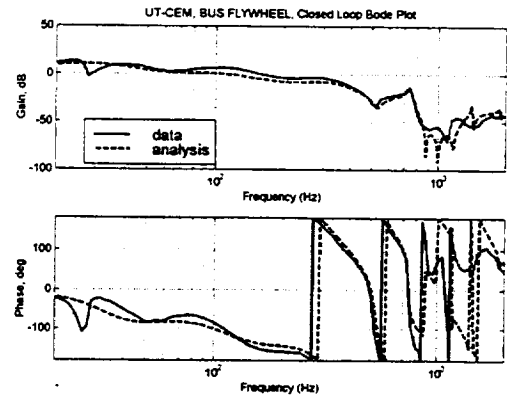


Figure 6. Predicted vs. Measured Closed Loop Bode Plot (x1 ref input, x1 sensor output).

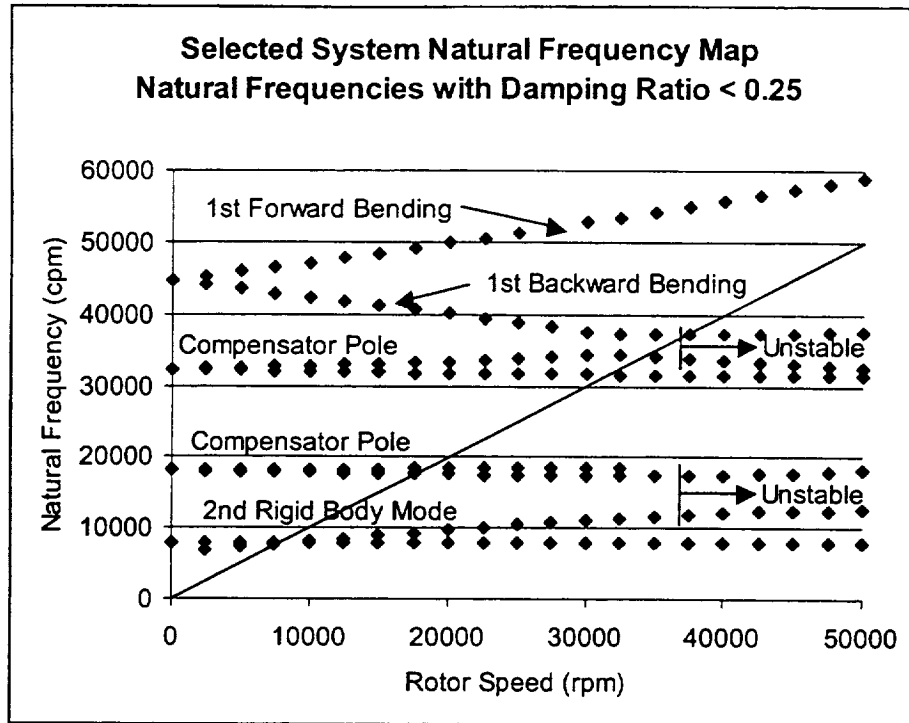


Figure 7. Selected System Natural Frequencies ($\xi < 0.25$), with Speed Independent SISO Controller

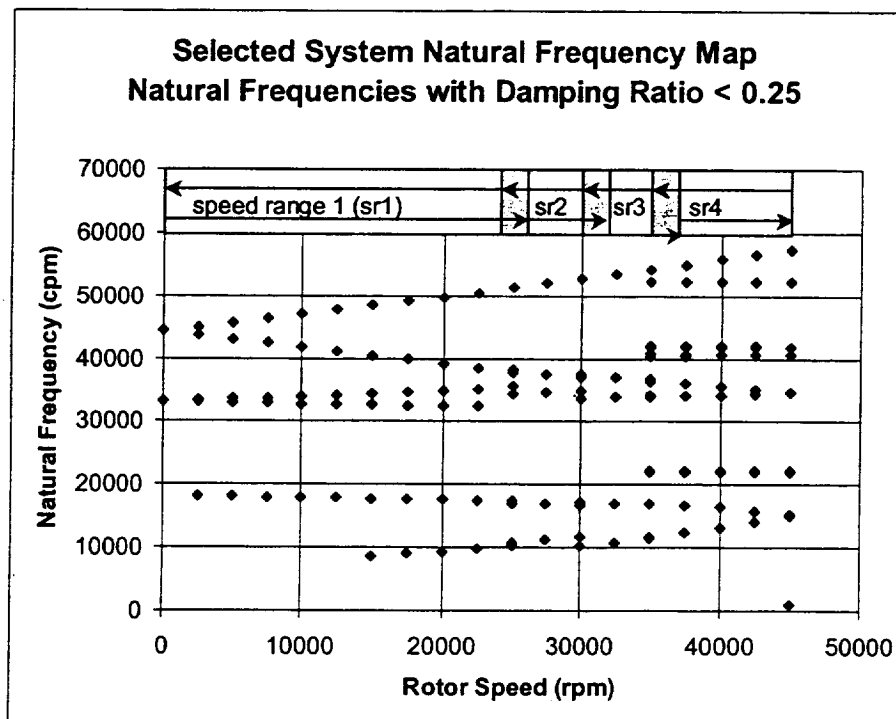


Figure 8. Selected System Natural Frequencies ($\xi < 0.25$), with Gain Scheduled MIMO Controller (speed ranges shown at top).

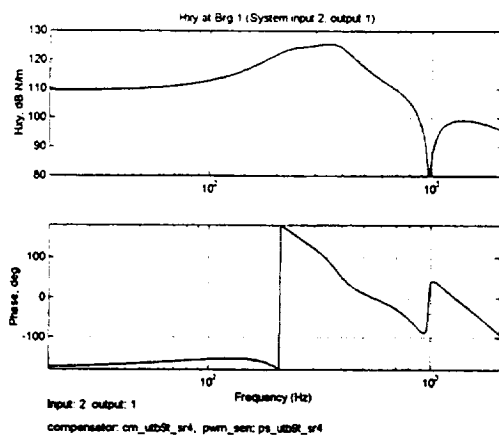


Figure 9. Hxy at Brg 1: (a) gain and phase,
(b) Kxy and ωC_{xy}

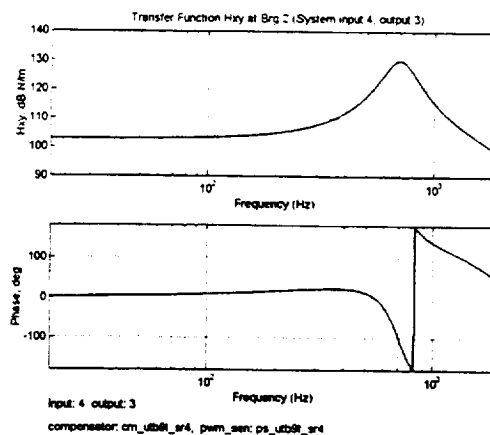


Figure 10. Hxy at Brg 2: (a) gain and phase,
(b) Kxy and ωC_{xy}

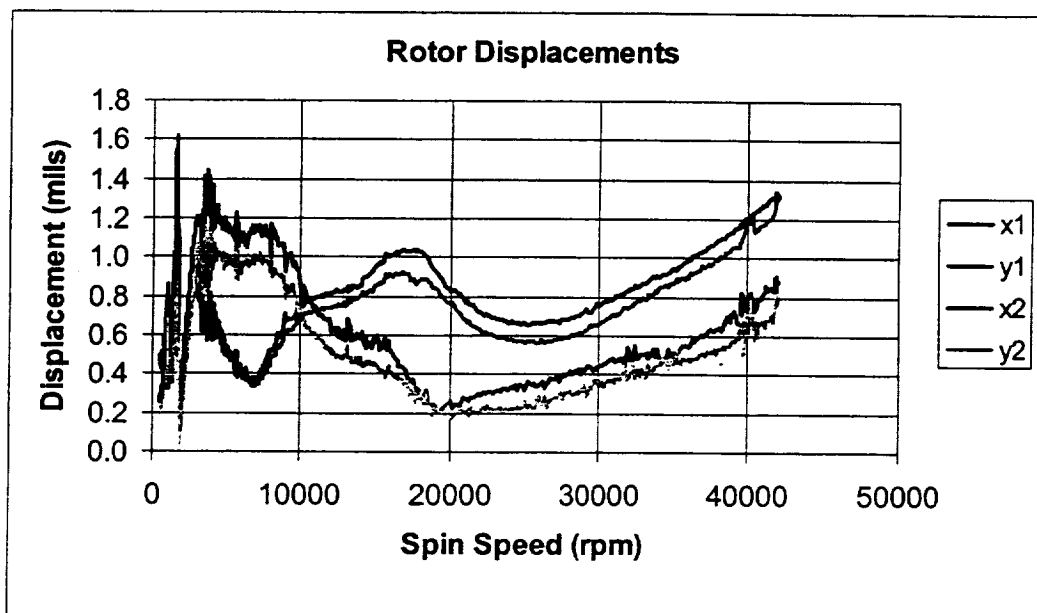


Figure 11. Synchronous Displacements during Spin Down from Full Speed

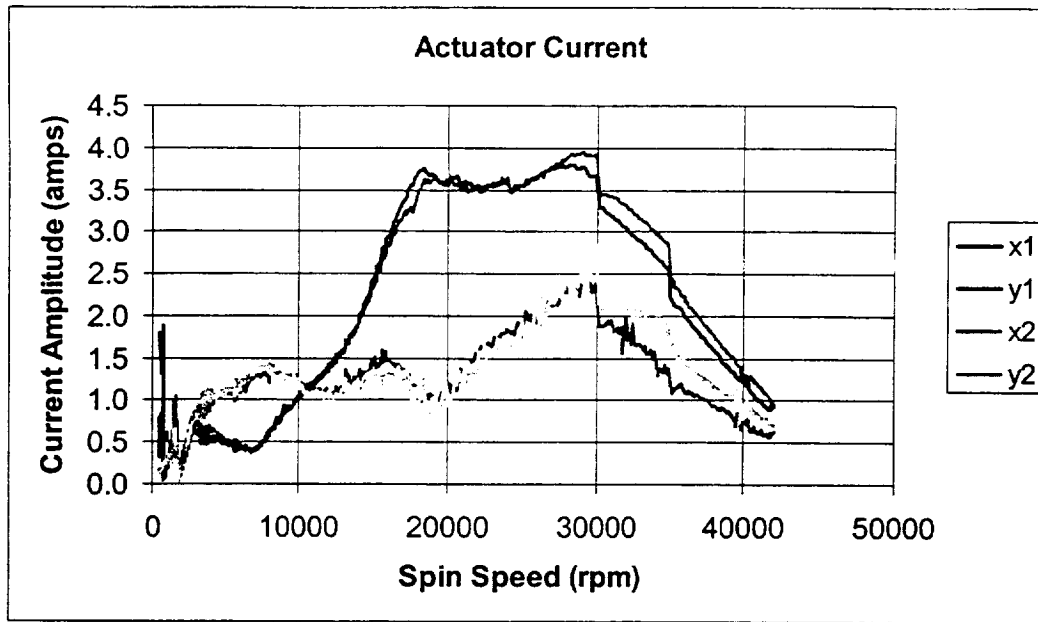


Figure 12. Synchronous Coil Current during Spin Down from Full Speed.

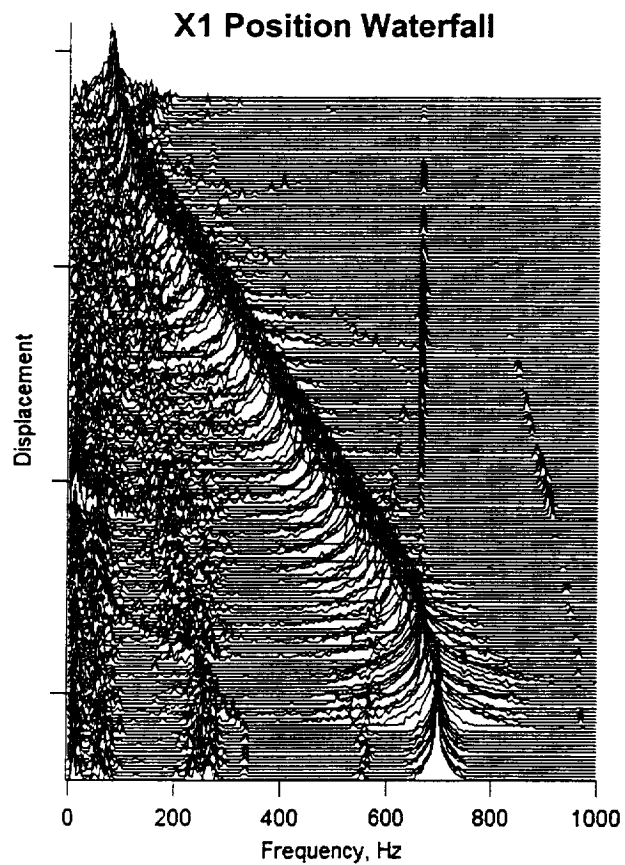


Figure 13. Waterfall plot, from x1 position sensor during spindown from 42,000 rpm to 5,000 rpm.

Session 8 -- Vibration Isolation

Chairman: Brad Paden

University of California at Santa Barbara (UCSB)

VIBRATION CONTROL ON ACTIVE MAGNETIC BEARING EQUIPPED FLYWHEEL ROTOR

Keiji Katsuno, Graduate student

Department of Mechanical Engineering, The National Defense Academy
Hasirimizu, Yokosuka, Kanagawa, Japan

Hiroki Okubo, Lecturer, Dr.

Department of Mechanical Engineering, The National Defense Academy

Hiroyuki Fujiwara, Research Associate, Dr.

Department of Mechanical Engineering, The National Defense Academy

Osami Matsushita, Professor, Dr.

Department of Mechanical Engineering, The National Defense Academy

ABSTRACT

Flywheel technology has been developing for an effective and clean means of energy storage techniques. From the point of view of the improvement for the stable rotation during high speed revolution, we employed the active magnetic bearing (AMB) to apply it to a flywheel test rotor. Our AMB equipped flywheel rotor is levitated without mechanical contact by five-axis controllers in the decentralized manner: three positions to vertically suspend this flat rotor and two X and Y rotations to maintain the rotor at a neutral position.

In this paper, we propose several ideas in numerical simulations concerning the AMB control method for the stability improvement of this flywheel rotor. An equivalent reduced model of the rotor is first completed from the quasi-modal method. The traditional PID control is mainly applied to the standstill levitation. This PID controller is not able to cover the stability in the entire speed range, because natural frequencies split into two ways due to the strong gyroscopic effect: the increase of the forward eigenfrequency and the decrease of the backward eigenfrequency. In order to compensate the destabilization caused by this split, we recommend the addition of an optional technique of the cross stiffness control. The simulation proves that the cross stiffness control should be combined with a band-pass filter for selecting the forward eigenmode vibration and a low pass filter for tuning the backward mode vibration. We also consider the spillover instability due to the flexibility of the flywheel disk.

1 INTRODUCTION

Flywheel has been used for a long time. It has attracted the attention as an energy storage system^{(1),(2),(3)}. Large flywheel with low rotation has already put into practical use in several instances. The small flywheel with high speed rotation used for more than eight hours has been developing. Several dynamic problems still remain, e.g., energy loss of bearing, high-speed rotation, rotor vibration and noise. The vibration control of the flywheel with active magnetic bearing is being studied for gyroscopic stability of artificial satellite^{(4),(5)}.

There are different control types of AMB, the axial direction (one degree of freedom; 1DOF) control, the radial direction (2 or 4 DOF) control and the omni-directional (5 DOF) control⁽⁶⁾. The omni-directional control type of AMB, which is analyzed in this paper, can control the motion of the center of gravity (3 DOF) and the declination around the center of gravity (2 DOF). The control system has to take into account the dynamics of rotor-disk coupled system, that is, the low frequency backward instability and high frequency forward instability due to strong gyroscopic effect. The study of the stability using cross stiffness control has been reported^{(4),(7)}.

In this paper, an equivalent reduced model of the rotor is completed from the quasi-modal method. The obtained model is applied to design and evaluation of the rotor dynamics combined with the servo feedback control theory of the AMB system.

The PID control theory is popular in practical engineering and we employed it for the levitation control. Due to the gyroscopic effect at high-speed rotation, the natural frequencies are split into two ways: the backward motion is low and forward motion is high. The prepared PID controller is then not able to cover the stability in the entire speed range. In order to compensate this insufficiency of the PID controller, the introduction of the cross stiffness control is successfully demonstrated with the combination of a band-pass filter for tuning the high frequency vibration of the forward mode and a low-pass filter for low frequency backward mode.

We also take into account the rotor-disk coupled dynamics due to disk bending flexibility which made the system stabilization difficult. According to the simulations, our PID control method combined with optional techniques made the stabilization control and the reduction of unbalance vibration level for global conditions of standstill and rotation.

2 MODEL

2.1 Flywheel

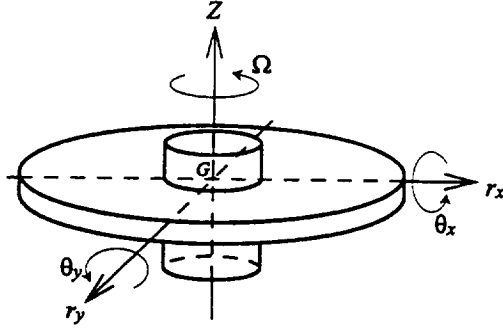


Fig.1 Rotor coordinate system

Fig.1 shows the structure of the flywheel model and the coordinate system. The equation of motion of the flywheel and AMB neglecting the damping term can be expressed as follows⁽⁶⁾:

$$\text{Axial : } M\ddot{Z} + K_a Z = -Q_{AMBa} \quad (1a)$$

$$\text{Tilting : } I_d \ddot{\theta} - i\Omega I_p \dot{\theta} + K_\theta \theta = -l Q_{AMBa} \quad (1b)$$

$$\text{Radial : } Mr + Kr = -Q_{AMB r} \quad (1c)$$

Where:

Z : the displacement in the axial direction

M : the rotor mass matrix

K_a : the stiffness matrix in the axial direction

Q_{AMBa} : the axial AMB control force matrix

I_d : the tilting inertia moment

θ : the complex declination angle($\theta_x + i\theta_y$)

I_p : the inertia moment of flywheel

K_θ : the tilting stiffness matrix

l : the length from geometrical center of the flywheel to geometrical center of axial AMB

r : the complex displacement($r_x + ir_y$)

K : the stiffness matrix

$Q_{AMB r}$: the radial AMB control force

The modeling is analyzed by quasi-modal model based on the component mode synthesis⁽⁸⁾. The flywheel consists of a motor-rotor and an elastic disk. The coupled vibration of the rotor-disk is shown in Table1⁽⁹⁾. We can see there are only two coupled vibration in Table 1(see the O). Therefore the model is included eigenmodes of the disk, the coupled axial mode of the rigid motor-rotor δ_a with one nodal circle mode ϕ_a and the coupled tilting mode of the rigid motor-rotor δ_t with one nodal diameter mode ϕ_t ⁽¹⁰⁾. These modes in the axial direction and the tilting direction are shown in Fig.2. The axial and the tilting motion are considered as independent.

Table 1 Coupled Vibration of Rotor-disk System

Disk Modes (Flexible)	Nodal-Diameter	0	1	2
	Nodal-Circule	1	0	0
Rortor Modes (Rigid)	Axial Z	○	×	×	×	×
	Tilting θ	×	×	○	×	×
	Radial r	×	×	×	×	×

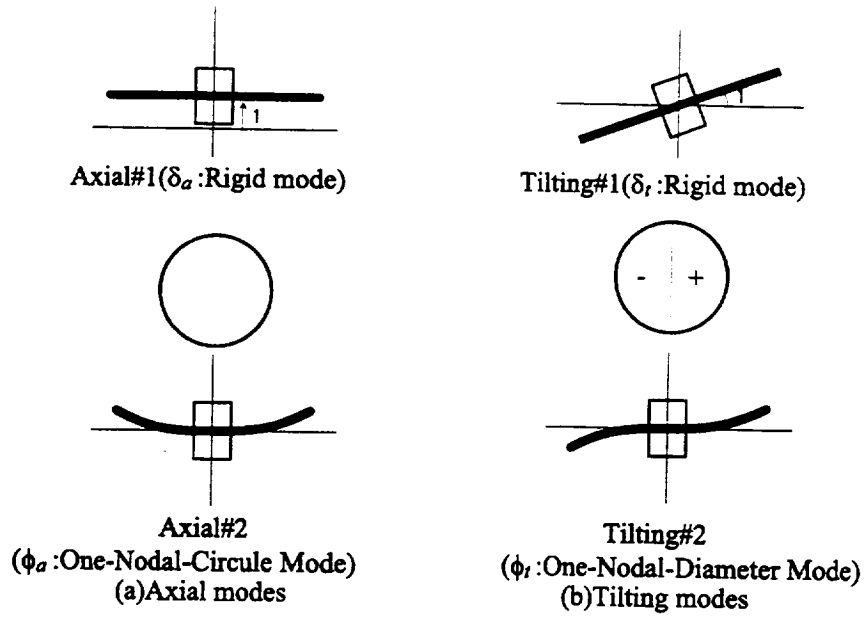


Fig.2 Flywheel Rotor Displacement Modes

The displacement vector, absolute displacement of the rotor; Z_1 , θ_1 , and internal displacement of the disk; Z_2 , θ_2 , can be expressed in terms of the rotor Z_1 , θ_1 and the relative displacement of disk η_a , η_t by the following formula:

$$Z = \begin{bmatrix} Z_1 \\ Z_2 \end{bmatrix} = \begin{bmatrix} 1 & 0 \\ \delta_a & \phi_a \end{bmatrix} \begin{bmatrix} Z_1 \\ \eta_a \end{bmatrix} = \Phi_a \begin{bmatrix} Z_1 \\ \eta_a \end{bmatrix} \quad (2a), \quad \theta = \begin{bmatrix} \theta_1 \\ \theta_2 \end{bmatrix} = \begin{bmatrix} 1 & 0 \\ \delta_t & \phi_t \end{bmatrix} \begin{bmatrix} \theta_1 \\ \eta_t \end{bmatrix} = \Phi_t \begin{bmatrix} \theta_1 \\ \eta_t \end{bmatrix} \quad (2b)$$

where, Φ_a , Φ_t are the component mode synthetic conversion matrix. Substituting Eq.(1a) and Eq.(1b) for Eq. (2a) and Eq.(2b), and the transposed matrix of Φ_a , Φ_t multiplied from the front in order to make the quadratic form, the equation of motion of the rotor can be obtained as in Eq.(3a) and (3b).

$$\text{Axial : } \begin{bmatrix} m & m_{ca} \\ m_{ca} & m_D^* \end{bmatrix} \begin{bmatrix} \ddot{Z}_1 \\ \ddot{\eta}_a \end{bmatrix} + \begin{bmatrix} k_a & \\ & k_{aD} \end{bmatrix} \begin{bmatrix} Z_1 \\ \eta_a \end{bmatrix} = - \begin{bmatrix} Q_{AMBa} \\ 0 \end{bmatrix} \quad (3a)$$

$$\text{Tilting : } \begin{bmatrix} I_d & i_{dc} \\ i_{dc} & i_{dD}^* \end{bmatrix} \begin{bmatrix} \ddot{\theta}_1 \\ \ddot{\eta}_t \end{bmatrix} - i\Omega \begin{bmatrix} I_p & i_{pc} \\ i_{pc} & i_{pD}^* \end{bmatrix} \begin{bmatrix} \dot{\theta}_1 \\ \dot{\eta}_t \end{bmatrix} + \begin{bmatrix} k_\theta & \\ & k_{\theta D} \end{bmatrix} \begin{bmatrix} \theta_1 \\ \eta_t \end{bmatrix} = - \begin{bmatrix} lQ_{AMBa} \\ 0 \end{bmatrix} \quad (3b)$$

m : total mass

$m_D^* = m_D \phi_a^2$: modal mass of disk, $i_{dD}^* = i_{dD} \phi_t^2$: modal tilting inertia moment of disk

m_D : mass of disk, i_{dD} : tilting inertia moment of disk

m_{ca} : mass compound terms, i_{dc}, i_{pc} : inertia compound terms

Eq.(3a) and (3b) represents the disk bending modes by the relative displacement. The absolute displacement of the bending modes are indicated by ξ_a and ξ_t . It is assumed with ξ_a - Z_1 and ξ_t - θ_1 in proportion to η_a and η_t . We define the quasi-modal matrix T .

$$\begin{bmatrix} Z_1 \\ \eta_a \end{bmatrix} = T \begin{bmatrix} Z_1 \\ \xi_a \end{bmatrix} = \begin{bmatrix} 1 & 0 \\ -a_a & a_a \end{bmatrix} \begin{bmatrix} Z_1 \\ \xi_a \end{bmatrix} \quad (4a)$$

$$\begin{bmatrix} \theta_1 \\ \eta_t \end{bmatrix} = T \begin{bmatrix} \theta_1 \\ \xi_t \end{bmatrix} = \begin{bmatrix} 1 & 0 \\ -a_t & a_t \end{bmatrix} \begin{bmatrix} \theta_1 \\ \xi_t \end{bmatrix} \quad (4b)$$

where a_a and a_t are determined to cancel the mass compound terms in Eq(3a),(3b).

$$a_a = \frac{m_{ca}}{m_D} = \frac{m_D \phi_a}{m_D \phi_a^2} \quad (5a)$$

$$a_t = \frac{i_{dc}}{i_{dD}} = \frac{i_{dD} \phi_t}{i_{dD} \phi_t^2} \quad (5b)$$

Finally, the equation of motion of the quasi-modal model is as Eq.6 and the quasi-modal model is shown Fig.3.

$$\begin{bmatrix} m_m + \Delta m_D & m_{Deq} \\ m_{Deq} & m_{Deq} \end{bmatrix} \begin{bmatrix} \ddot{Z}_1 \\ \ddot{\xi}_a \end{bmatrix} + \begin{bmatrix} k_a + k_{Deq} & -k_{Deq} \\ -k_{Deq} & k_{Deq} \end{bmatrix} \begin{bmatrix} Z_1 \\ \xi_a \end{bmatrix} = - \begin{bmatrix} Q_{AMBa} \\ 0 \end{bmatrix} \quad (6a)$$

$$\begin{bmatrix} I_{dm} + \Delta i_{dD} & i_{dDeq} \\ i_{dDeq} & i_{dDeq} \end{bmatrix} \begin{bmatrix} \ddot{\theta}_1 \\ \ddot{\xi}_t \end{bmatrix} - i\Omega \begin{bmatrix} I_{pm} + \Delta i_{pD} & i_{pDeq} \\ i_{pDeq} & i_{pDeq} \end{bmatrix} \begin{bmatrix} \dot{\theta}_1 \\ \dot{\xi}_t \end{bmatrix} + \begin{bmatrix} k_\theta - k_{D\theta eq} & -k_{D\theta eq} \\ -k_{D\theta eq} & k_{D\theta eq} \end{bmatrix} \begin{bmatrix} \theta_1 \\ \xi_t \end{bmatrix} = - \begin{bmatrix} lQ_{AMBt} \\ 0 \end{bmatrix} \quad (6b)$$

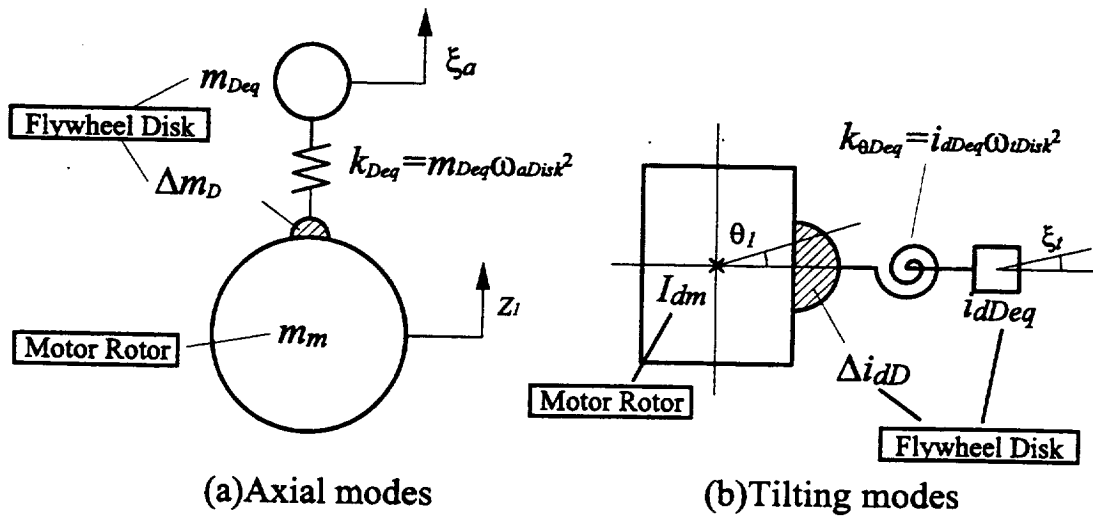


**Fig.3 Quasi-modal Models
(Equivalent Reduction System)**

2.2 Flywheel Test Rotor System

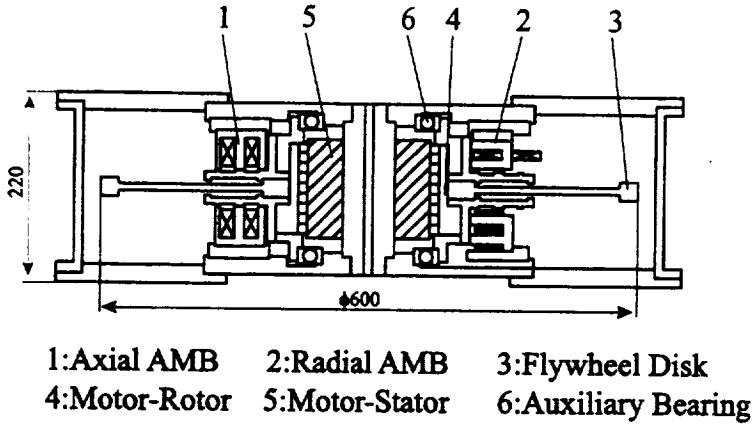


Fig.4 Schematic of Flywheel

Schematic of flywheel test rotor is shown in Fig.4. The main characteristics of the flywheel is as follows:

Flywheel Diameter : 0.6m
Rotor mass : 36kg
Inertia moment : 0.69kgm²
Max. rotational speed : 200rps

2.3 Active Magnetic Bearing(AMB)

The coordinate system and outline of the magnetic bearings are shown in Fig.5 and 6, respectively. The axial AMB has three displacement sensors arranged at each actuator and feeds back the sensing data directly. Displacement output Z_a , Z_b , Z_c measured by each sensor is changed into declination θ and displacement Z_1 of the axis center of gravity by conversion matrix $T_{z\theta}$ shown in Eq.(7).

$$\begin{bmatrix} Z_a \\ Z_b \\ Z_c \end{bmatrix} = T_{z\theta} \begin{bmatrix} Z_1 \\ \theta_x \\ \theta_y \end{bmatrix} = \begin{bmatrix} 1 & -l & 0 \\ 1 & l \sin 30^\circ & l \sin 30^\circ \\ 1 & l \sin 60^\circ & -l \sin 60^\circ \end{bmatrix} \begin{bmatrix} Z_1 \\ \theta_x \\ \theta_y \end{bmatrix} \quad (7)$$

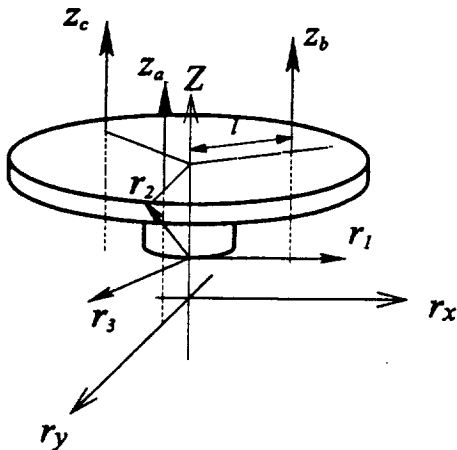


Fig.5 Coordinate Frame of AMB

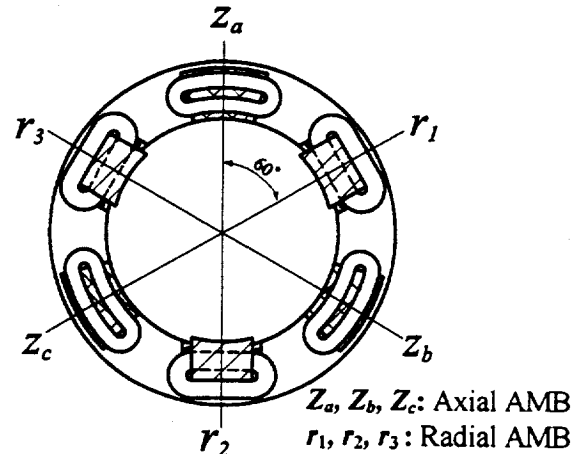
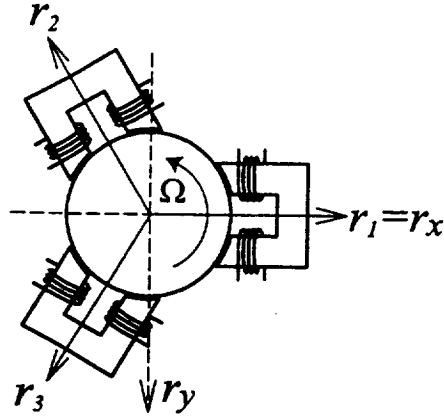


Fig.6 AMB Actuator Assembly

Radial displacement sensors have been installed in the 2 directions of r_x and r_y (Fig. 7). The three directional deviations, which is used to control radial direction, are computed from two deviations between the AMB reference inputs and exact gaps using the conversion matrix T_r , shown in Eq. (8).



**Fig.7 Active Magnetic Bearing Actuator
(6pole Type Radial AMB)**

$$\begin{bmatrix} r_1 \\ r_2 \\ r_3 \end{bmatrix} = T_r \begin{bmatrix} r_x \\ r_y \end{bmatrix} = \begin{bmatrix} 1 & 0 \\ -\cos 60^\circ & -\cos 30^\circ \\ -\cos 60^\circ & \cos 30^\circ \end{bmatrix} \begin{bmatrix} r_x \\ r_y \end{bmatrix} \quad (8)$$

Using this conversion, it is possible to control three actuators independently. The whole composition of AMB is shown in Fig. 8 and the main specification is shown in table 2.

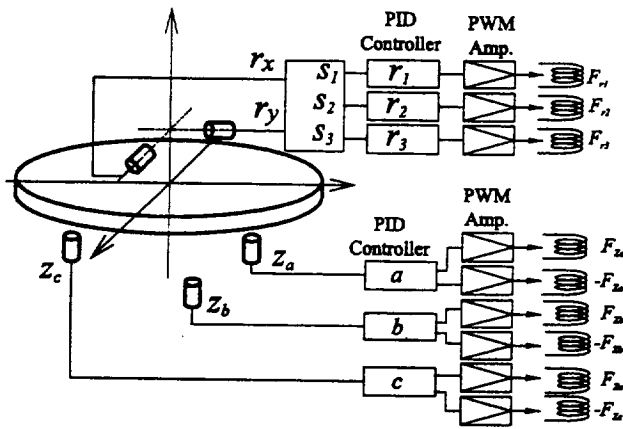


Fig.8 Block Diagram of The Electronics System

Table 2 Main Parameter of AMB

	Axial AMB	Radial AMB
Load Capacity	557 N	332 N
AMB Clearance	$0.3 \times 10^{-3} \text{ m}$	$0.5 \times 10^{-3} \text{ m}$
Sensor Gain	10000 V/m	10000 V/m
Power Amp. Gain	2 A/V	2 A/V

3 EIGENVALUE ANALYSIS

3.1 Critical Map

The critical map of this rotor system is shown in Fig. 9. The horizontal axis is the stiffness of AMB and the vertical axis is the natural frequency. Each line indicates the natural frequency of the first rigid mode (Axial), the second rigid mode (Tilting), the first bending mode (Axial) and the second bending mode

(tilting) from downward to upward, respectively. When the stiffness of AMB is set to 3×10^5 N/m, the natural frequency of the rigid mode (Axial) is fixed about 30 Hz. The resonance oscillated by a disturbance, e.g., earthquakes, is prevented using this tuning (setting the natural frequency to less than 10 Hz).

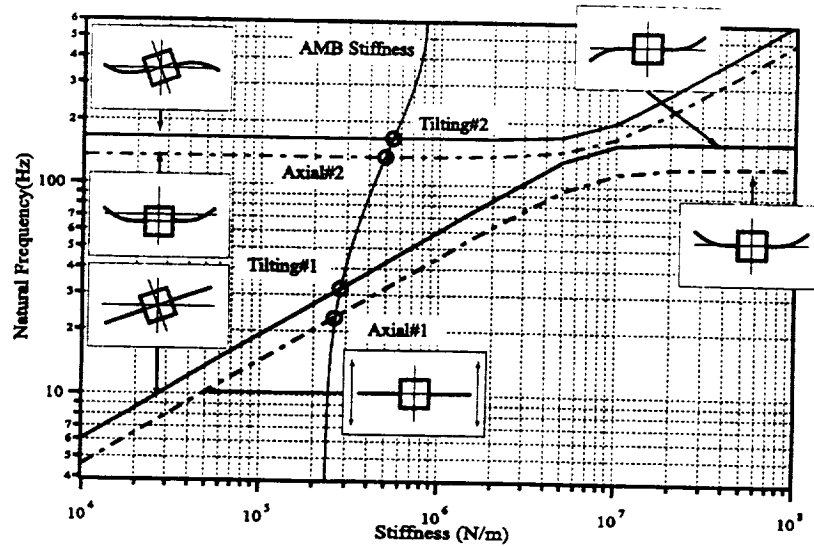


Fig.9 Critical map with AMB Stiffness (Standstill)

3.2 Eigenvalue Map

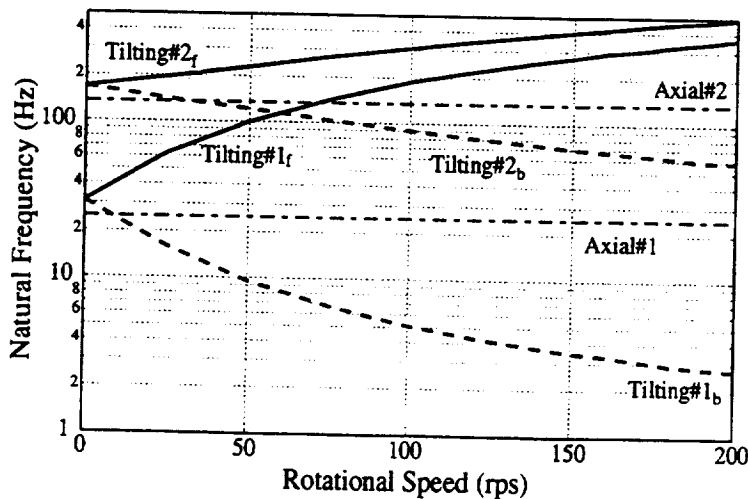


Fig.10 Eigenvalue Map

The eigenvalue map (Campbell diagram) is shown in Fig. 10. The horizontal axis is the rotational speed of flywheel and the vertical axis is a frequency. The solid lines indicate the natural frequency of the first and the second forward tilting (Tilting#1 and #2) mode, the dashed lines indicate the natural frequency the first and the second backward tilting (Tilting#1b and #2b) mode and the dot-dashed lines indicate the natural frequency of axial (Axial#1 and #2) mode. The axial natural frequencies are constant (the rigid mode is 23 Hz and the bending mode is 137 Hz) because no gyroscopic force is affected to the axial

direction. However, the tilting natural frequency changes with the rotational speed due to the effect of gyroscopic force. The natural frequency of the forward motion is more than 400 Hz at 200 rps and the natural frequency of the backward motion is less than 10 Hz.

4 DESIGN OF CONTROL SYSTEM

4.1 Control System

The control system of the experimental device is shown in Fig.11. The AMB levitates the flywheel with the feedback control using the signal from the displacement sensor without the mechanical contact. The control system executes analog PID control in the axial and radial directions. The phase progress is up to 200 rps in the transfer function, allowing damping addition against the unbalance vibration. The phase progress is from 10Hz to 400Hz by the characteristics of the PID controller and PWM amplifier. The bode diagram is shown in Fig.12.

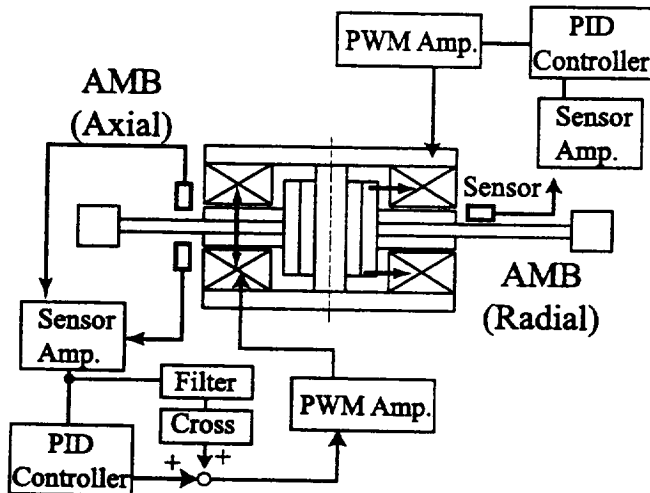


Fig.11 Block Diagram of AMB Control System (with Cross Stiffness)

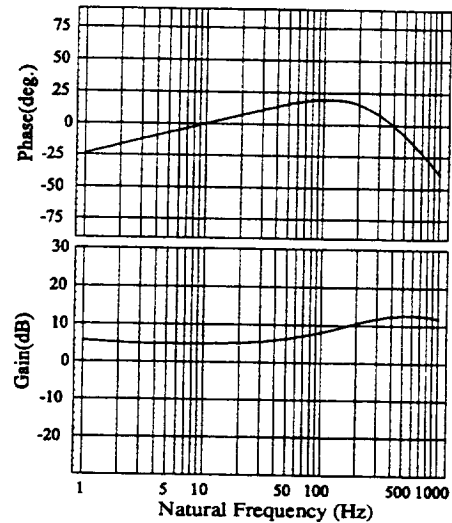


Fig.12 Basic Control Low (PID Controller)

4.2 Stability Analysis and Design of Controller

We simulate the flywheel rotation test including the controller in the axial, tilting and radial direction. It is expected not to be stable with only PID control. The controller is added against the forward motion and the backward motion due to tilting gyroscopic effect.

4.2.1 Control in the tilting direction

The tilting natural frequency changes by gyroscopic effect. The natural frequency of the forward motion is more than 400Hz with 200 rps rotation speed and the frequency of the backward is less than 10Hz. The PID controller does not have the damping in more than 400 Hz because of the phase lag. It is unstable below 10 Hz because of integral compensation which removes the steady error. The stability using cross stiffness control is useful for these cases^{(4),(7)}. However, the cross stiffness to stabilize one makes the other unstable.

We use two types of displacement cross stiffness control in the unstable area. In order to compensate this insufficiency of PID controller, we recommend the addition of optional techniques such as, Band-Pass-Filter(BPF) and Low-Pass-Filter(LPF) cross stiffness control for tilting mode. The BPF cross stiffness control for more than 150rps rotational speed completes the stabilization against the forward motion. The transfer function is as follows:

$$G_{BPFCross}(s) = G_{BPF}(s) \cdot (-ik_c), \quad G_{BPF}(s): \text{The Transfer Function of BPF} \quad (9)$$

The LPF cross stiffness control completes the stabilization against the backward motion. The transfer function is as follows:

$$G_{LPFCross}(s) = \frac{ik_c}{\tau s + 1}, \quad \tau = \frac{1}{2\pi \times 6} \quad (10)$$

Therefore, the controller gives the stability against the forward and backward motion due to tilting gyroscopic effect.

4.2.2 Control in the radial direction

The natural frequency is about 30Hz in the radial direction. There is no gyroscopic effect. Therefore the stability is given by the PID controller only. Because there is only the rigid mode within the operational speed, addition of N-Cut control⁽¹¹⁾ is able to prevent the instability caused by unbalance vibration after passing of the rigid mode.

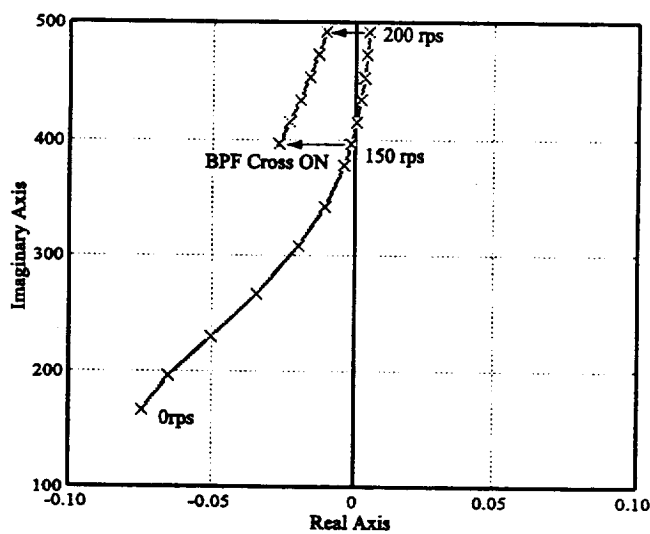
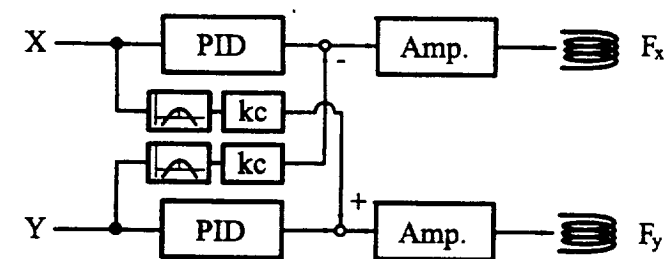


**Fig.13 Root Locus with BPF Cross Stiffness
(Tilting#2 Forward Whirl)**

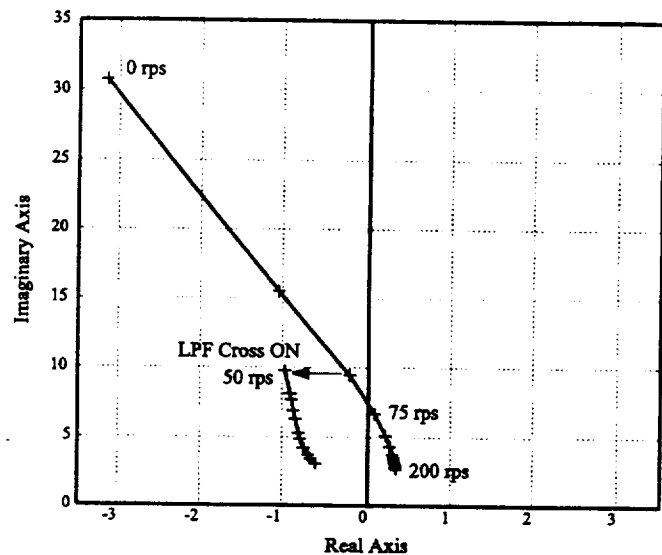
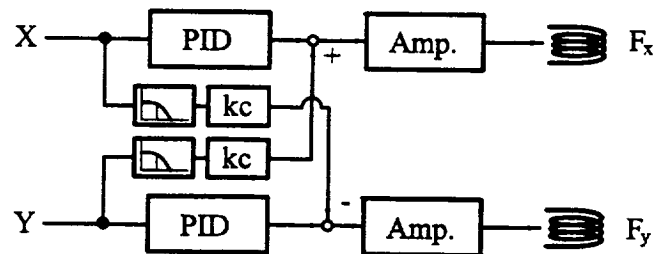


**Fig.14 Root Locus with LPF Cross Stiffness
(Tilting#2 Backward Whirl)**

5 CONCLUSION

We discussed the stability improvement by the AMB control system including the design review of our flywheel test rotor.

- (1) Our AMB equipped flywheel is featured by a 5DOF control of three axes for the vertical suspension control and two axes for radial positioning control.
- (2) A reduced model is obtained by quasi-modal modeling, which considers the gyroscopic effect and disk bending flexibility.
- (3) The instability induced by the strong gyroscopic effect for flat disk and the compensation by the cross stiffness control is evaluated. The cross stiffness in combination with the filter to select only unstable vibrations is strongly recommended by the simulation.
- (4) The spill over instability due to the disk flexibility is eliminated by preparing wide control frequency domain covering the disk bending eigenfrequencies..
- (5) The design review of our flywheel test rotor is achieved.

REFERENCES

- (1) Stienmier, J. D. et al., Analysis and control of a flywheel energy storage system with a hybrid magnetic bearing, *Trans. ASME, J. Dyn. Syst. Meas. Control*, vol.119, no.4(1997), p.650
- (2) Higasa, H. et al., Technical Problems of Superconducting Magnetic Bearing and Construction of Flywheel Power Storage System, *Proc. of ISS'93(1993)* p.1231
- (3) Jayaraman, C. P. et al., Rotor dynamics of flywheel energy storage systems, *Trans. ASME, J. Sol. Energy Eng.*, vol.113, no.1(1991), p.11
- (4) Inoue, M., High-speed test and the gyroscopic stability of the magnetically suspended wheel, *Trans. Soc. Instrum. & control Eng. (In Japanese)*, vol.23, no.3(1987), p.294
- (5) Ohshima, T. et al., Stabilization of satellite equipped with a magnetically suspended momentum wheel, *Trans. Soc. Instrum. & control Eng. (In Japanese)*, vol.27, no.2(1991), p.192
- (6) Higuti, T. et al., Control system design for totally active DC-type Magnetic bearing, *Trans. Soc. Instrum. & control Eng. (In Japanese)*, vol.18, no.5(1982), p.79
- (7) Matsushita, O. et al., Cross stiffness control of electromagnetic damper for flow-induced rotor instability, *Proc. of Elastic Aero Hydrou Engineering'99(1999)*
- (8) Matsushita, O., Modering; Free from boundary condition, *Jpn. Soc. Prec. Eng. (In Japanese)*, vol.54, no.5(1988),p.44
- (9) Irretier, H. et al., Numerical and experimental investigations of coupling effects in an isotropic elastic rotors, *Proc. of IFToMM Conf. on Rotor Dynamics 1998*, p.296
- (10) Matsushita, O. et al., An equivalent reduced system for coupled vibration analysis, *Trans. Jpn. Soc. Mech. Eng.*, vol.54, no.499,C, p.587
- (11) Matsushita, O. et al., Optional techniques for active magnetic bearing equipped flexible rotors, *Proc. of IFToMM Conf. on Rotor Dynamics 1998*

A DESIGN METHOD FOR MAGNETIC SUSPENSION AND VIBRATION CONTROL OF LEVITATED BEAMS FOR NONCONTACT PROCESSING

Ming-chih Weng, David L. Trumper
Department of Mechanical Engineering
Massachusetts Institute of Technology
Cambridge, MA 02139, USA

SUMMARY

This paper presents an integrated approach to magnetic suspension of flexible beams for non-contact processing. The challenges of designing such systems are mainly due to the lightly-damped vibration modes of the suspended structures. Our design goal is to make the suspension robustly stable for beams with varying boundary conditions. In this paper, we propose general design procedures for systems with different dimensions and properties, including structural modelling, sensor design, actuator design, sensor/actuator positioning, and controller design. We demonstrate our proposed ideas in a scaled-down experiment, in which we successfully suspend a 3 m long, 6.35 mm diameter steel tube with varying boundary conditions by using 8 sensors and 8 actuators.

INTRODUCTION

Many industrial operations center on processing of elongated translating elements, such as steel rolling, plastic film production, paper production, coating, and painting. Noncontact handling of the elements can be advantageous for these existing processes [1] [2] [3], and may serve as the underpinnings for new classes of manufacturing methods. Figure 1 shows an idea developed by Dr. Conrad Smith [4] with the assistance of the second author for the production of painted metal handles for brooms and mops. The challenges of designing such magnetic suspension stages are mainly due to the lightly-damped vibration modes of suspended structures.

In this paper, we focus on the magnetic suspension of ferromagnetic beams for non-contact processing. Our goal is to design a new control system to robustly suspend the object with varying boundary conditions. In the following sections, we develop a generalized method to design such systems, including structural modelling and uncertainty envelope, sensor design, actuator design, sensor/actuator averaging positioning method, and controller design.

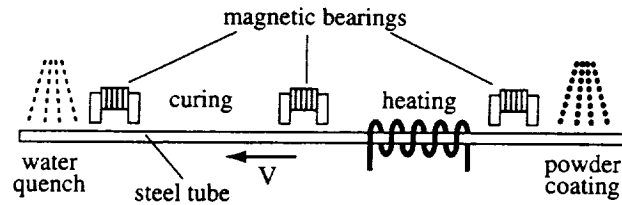


Figure 1: Non-contact coating process

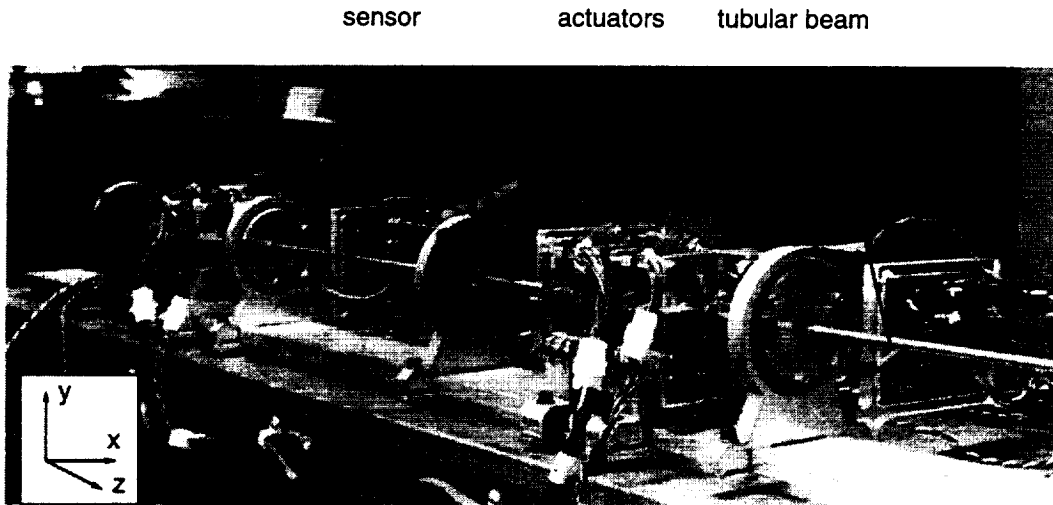


Figure 2: Experimental setup for beam suspension

We demonstrate our proposed ideas in a scaled-down experiment in our lab as shown in Figure 2. We use 8 position sensors and 8 electromagnet actuators to suspend a 3 m long, 6.35 mm diameter steel tube. The experimental results show that the suspended beam is robustly stable under varying boundary conditions, including free, hinged, and clamped boundaries.

DESIGN REQUIREMENTS AND SYSTEM PROPERTIES

To start designing the system, we first specify the design requirements and system properties. Based on this information, we can then model the system, and design/scale the parameters for sensors, actuators, sensor/actuator positioning, and controllers.

1. Design requirement: sufficient suspension dc stiffness K , closed-loop bandwidth ω_{BW} , phase margin within bandwidth ϕ_{PM} , and airgap g .
2. Robustness requirement: varying boundary types (free, hinged, or clamped) and varying boundary positions.

3. Beam properties: bending stiffness EI , material density ρ , cross-sectional area A , axial tension T , total length L , wall thickness W , axial moving velocity V , modal damping ratio ζ , electric conductivity σ , magnetic permeability μ , and magnetic saturation flux density $(B_{sat})_{steel}$.
4. Sensor properties: low-pass dynamics $H_s(s)$, and nonlinear position to voltage relationship.
5. Actuator properties: force function of input current and air gap $F(i, g)$, low-pass dynamics $H_a(s)$, maximum current i_{max} due to limited heat dissipation, and magnetic saturation flux density $(B_{sat})_{lamination}$.
6. Controller speed: calculation time t_c and sampling time t_s for digital control. (time delay $\approx t_c + 0.5t_s$)

BEAM DYNAMICS AND UNCERTAINTY ENVELOPE

To design the control system, we first model the structural dynamics of beams. We will analyze the beam dynamics by modal analysis, and further derive the uncertainty envelope for varying boundary conditions. Assuming constant bending stiffness EI , constant axial tension force T , and axial velocity V , the dynamic equation of a slender beam can be modelled as a Euler-Bernoulli Beam [5]

$$EI \frac{\partial^4 u}{\partial z^4} - T \frac{\partial^2 u}{\partial z^2} + \rho A \frac{\partial^2 u}{\partial t^2} + 2\rho A \frac{\partial^2 u}{\partial z \partial t} V + \rho A \frac{\partial^2 u}{\partial z^2} V^2 = f, \quad (1)$$

where z is axial coordinate, u is transverse deflection, ρ is material density, A is cross-sectional area, and f is transverse force density. In this paper, we neglect the axial moving velocity V and axial tension force T , and thus obtain the simplified beam equation

$$EI \frac{\partial^4 u}{\partial z^4} + \rho A \frac{\partial^2 u}{\partial t^2} = f. \quad (2)$$

The resulting beam dispersion equation

$$EI\lambda^4 = \rho A\omega^2 \quad (3)$$

shows the relation between wavenumber λ and frequency ω for beams. By modal analysis, the beam equation can be decoupled, and the solution can be represented by the superposition of an infinite number of orthogonal modal shapes

$$u(z, t) = \sum_{n=1}^{\infty} \eta_n(t) \phi_n(z), \quad (4)$$

where η_n is modal coordinate, and $\phi_n(z)$ is the n -th modal shape

$$\phi_n(z) = C_{n1}\cos\lambda_n z + C_{n2}\sin\lambda_n z + C_{n3}\cosh\lambda_n z + C_{n4}\sinh\lambda_n z. \quad (5)$$

The frequency response of the n -th mode can be represented as

$$\frac{\eta_n(s)}{N_n(s)} = \frac{1}{M_n(s^2 + 2\zeta_n\omega_n s + \omega_n^2)}, \quad (6)$$

where N_n is the modal force, M_n is the modal mass, ζ_n is the modal damping ratio, and ω_n is the mode natural frequency. The first two terms above are defined as

$$N_n(t) = \int_0^L f(z, t)\phi_n(z)dz, \quad (7)$$

$$M_n = \int_0^L \rho A \phi_n^2(z)dz. \quad (8)$$

Combining Equations 4, 6 and 7, if we have a point force input F at z_a and position feedback y at z_s , the frequency response from input F to output y can be derived as

$$G(s) = \frac{y(s)}{F(s)} = \sum_{n=1}^{\infty} \frac{\phi_n(z_s)\phi_n(z_a)}{M_n(s^2 + 2\zeta_n\omega_n s + \omega_n^2)}. \quad (9)$$

This shows that the modal shape at sensor $\phi_n(z_s)$ determines the modal observability, and the modal shape at actuator $\phi_n(z_a)$ determines the modal controllability.

To include uncertainty into our beam model, we look at the envelope of the resonance peaks. For a lightly-damped system, the resonance peaks can be approximated by

$$G(j\omega_r) \approx \frac{\phi_r(z_a)\phi_r(z_s)}{2M_r\zeta_r\omega_r^2}. \quad (10)$$

Assuming a normalized sinusoidal modal shape, modal mass M_r can be calculated as

$$M_r = \int_0^L \rho A \phi_r^2 dz = \rho A \int_0^L \sin^2\left(\frac{x}{L}n\pi\right)dz = \frac{1}{2}\rho AL = \frac{1}{2}m, \quad (11)$$

where m is the total mass of the beam. Assuming the worst case that both $\phi_r(z_a)$ and $\phi_r(z_s)$ are 1, the resonance peak envelope can then be obtained by

$$\boxed{G_{envelope}(\omega) = \frac{1}{m\zeta\omega^2}}. \quad (12)$$

Figure 3 shows the derived peak envelope and the frequency response of a free-free beam model and a hinged-free beam model. Both models assume modal damping ratio $\zeta = 0.005$. This result shows that the peak envelope covers the uncertainty for beams with varying boundary conditions.

We will use the peak envelope in our controller design to include the uncertainty of varying boundary conditions. An important result from Equation 12 is that the designed suspension stiffness will be mainly limited by the beam's total mass m and damping ratio ζ .

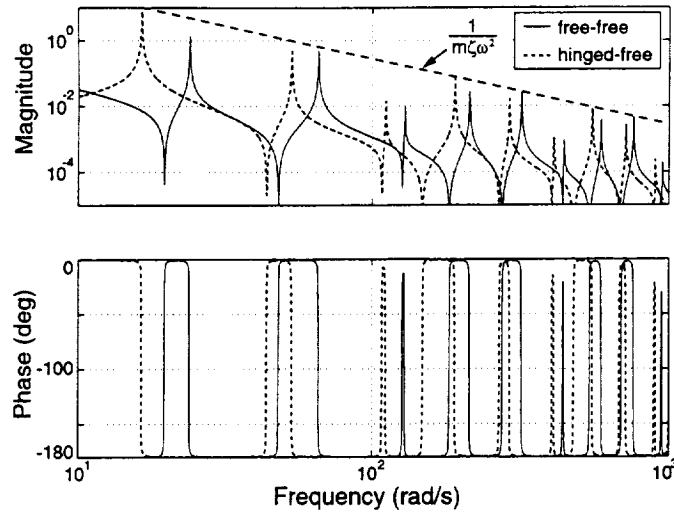


Figure 3: Bode plots of beam models, from force input $F(s)$ to position output $y(s)$: free-free boundaries, hinged-free boundaries, and uncertainty envelope

SENSOR DESIGN

We have designed a two-dimensional position sensor for the suspension of tubular beams in the form of a two-dimensional variable differential transformer. The reason for choosing this operating principle is that it is robust with respect to surface coatings and dusty environments. The schematic design is shown in Figure 4, the details can be found in [6]. The three primary coils on the poles generate a 6 kHz rotating magnetic field. The

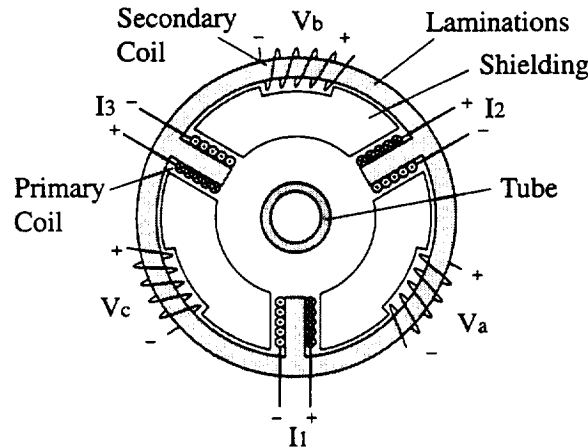


Figure 4: Sensor schematic design

three secondary coils are the outputs that read the magnetic flux rate of change. The x and y positions of the tube are obtained by synchronously detecting the output voltages

V_a , V_b and V_c as

$$V_x = \sqrt{3}(V_a \text{sgn}(I_3) - V_c \text{sgn}(I_2))H_s(s), \quad (13)$$

$$V_y = (2V_b \text{sgn}(I_1) - V_a \text{sgn}(I_3) - V_c \text{sgn}(I_2))H_s(s). \quad (14)$$

Here $\text{sgn}(u)$ is the signum function equal to ± 1 depending on the sign of u , and $H_s(s)$ is a low-pass filter with 1 kHz bandwidth. We need to make sure that sensor bandwidth well exceeds the control bandwidth, and the phase lag due to $H_s(s)$ within the control bandwidth must be small to avoid causing difficulties in stabilizing the system.

ACTUATOR DESIGN

In designing the actuators, we want to obtain the force as a function of current and airgap $F(i, g)$. We also need to predict the maximum force, which is usually limited by coil current due to heat dissipation, and by magnetic flux saturation in the core and in the steel target.

We consider an U-shaped electromagnet made of laminations as shown in Figure 5. To

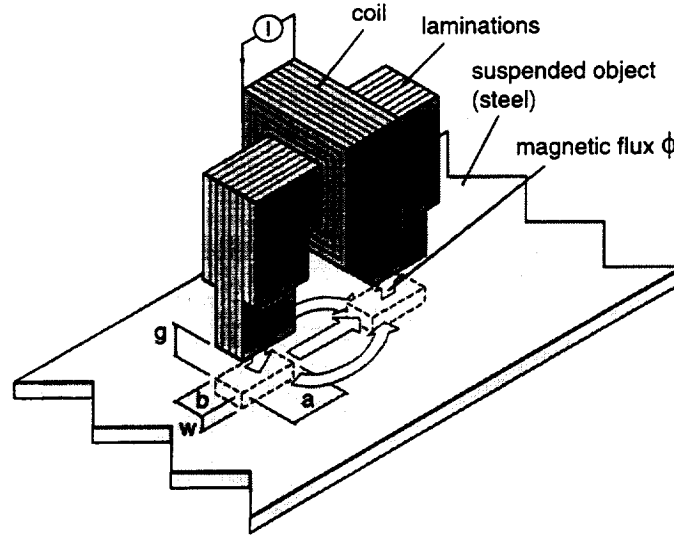


Figure 5: Actuator design

estimate the force function, we neglect fringing field and use a simplified magnetic circuit model. The magnetic flux B and applied force F can be derived as

$$B = \mu_0 \frac{Ni}{2g}, \quad i < i_{max}, \quad (15)$$

$$F = 2ab \frac{B^2}{2\mu_0} = \frac{\phi^2}{\mu_0 ab}, \quad \phi < \phi_{max}, \quad (16)$$

where $\mu_0 = 4\pi \times 10^{-7}$ H/m is permeability of air, N is number of turns of coil, i is current input, and ab is cross-sectional area of actuator pole face. A more accurate model can also be derived by solving for the magnetic field distribution analytically or numerically. In our scaled experiment, we predict $F(i, g) = 18i^2/g^2$ from this magnetic circuit model, where F is in Newton, i is in Amp, and g is in mm. In reality we experimentally measure $F(i, g) = 30i^2/g^2$; the difference comes from the neglected fringing field due to the large airgap.

To estimate the maximum force, we first examine the current limit due to heat dissipation in the coil. Air cooled motors usually operate at a thermally-limited current density of about 5×10^6 A/m² [7]. For example, a 26 gauge wire has 0.13mm² cross sectional area, and has a current limit of about 0.7 Amp. From the required force, we can decide the wire gauge and turns of coils to use for the actuators.

We further examine the force limit due to magnetic saturation, which can happen inside the actuator or the suspended object. We can follow the magnetic flux loop to find the bottleneck. The saturating flux density B_{sat} is about 1 to 2 Tesla for both Si-Fe laminations and the target steel. For our actuator model, ϕ_{max} is limited by $(ab)B_{sat}$ and $(2aW + 2bW)B_{sat}$. We can avoid magnetic saturation by increasing the size of the actuator cores and by increasing the number of actuator poles. In reality, due to the fringing field, the middle part of the actuator core tends to saturate easier than actuator poles.

In this paper, we consider actuators with large air gaps and neglect the eddy currents in the steel target. The reason is that the air reluctance is much larger than material reluctance over the control bandwidth if the airgap is large, hence the magnetic flux is mainly determined by coil current and air reluctance. For actuators with small airgaps, we need to consider the dynamic behavior by including the induced eddy currents at high frequencies, and we will further study it and present the results in a later publication.

SENSOR/ACTUATOR POSITIONING

One of the greatest problems with the suspension of flexible elements is to maintain stability of high frequency modes. We have developed *sensor interpolation*, *sensor averaging*, and *actuator averaging* methods to address this problem. These methods are derived in [6] and [8]. In fact, our experiment of free-free beam suspension was not stable until we developed the filtering effect of sensor averaging and actuator averaging.

For the sensor interpolation method, we place 2 actuators in between 2 sensors in close proximity, interpolate 2 sensor outputs to estimate the beam deflections at the actuators, in order to reduce sensor/actuator non-collocation problems.

For sensor averaging method, we place 1 actuator at the center between 2 sensors, and average the 2 sensor outputs to estimate the deflection at the actuator. By doing so, we not only eliminate non-collocation problems, we can also adjust the sensor distance to attenuate undesired resonance modes. Assuming a sinusoidal modal shape, with sensors located at $z_1 = (z_0 - d_s)$ and $z_2 = (z_0 + d_s)$, the averaged output is

$$u_{ave}(z_0, t) = \frac{1}{2}(u(z_1, t) + u(z_2, t)) = \sum_{n=1}^{\infty} \eta_n(t) \phi_n(z_0) \underline{\cos(\lambda_n d_s)}. \quad (17)$$

This averaging effect creates a modal band-stop filter of $\cos(\lambda_n d_s)$, which has low gain when $\lambda_n d_s \approx \pi/2$. The cosine effect $\cos(\lambda_n d_s)$, combined with beam dispersion equation $EI\lambda^4 = \rho A\omega^2$, is demonstrated in Figure 6 for the value $d_s = 0.15$ m. The result shows a

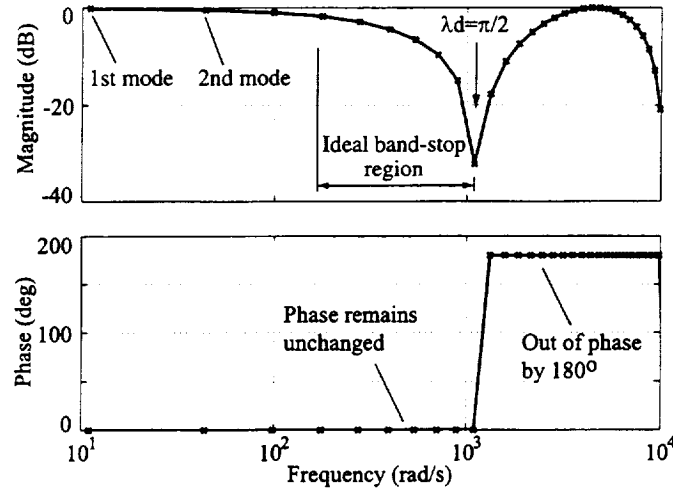


Figure 6: Cosine effect from sensor averaging: a broad notch attenuates several resonance modes, and phase remains unchanged until $\lambda d_s > \pi/2$.

broad notch that attenuates several resonance modes that have wavenumbers near $\pi/2d_s$, and the phase remains unchanged until $\lambda d_s > \pi/2$. Furthermore, this modal filtering effect of $\cos(\lambda_n d_s)$ is a function of beam properties and sensor distance, and is independent of boundary conditions and beam position.

Similarly, for actuator averaging, we place two actuators apart by $2d_a$, and apply the same force on each actuator. We can thereby create another modal band-stop filter of $\cos(\lambda_n d_a)$. Physically the sensor averaging method attenuates the modal observability at the associated frequency range, and actuator averaging method attenuates the modal controllability.

By using this averaging method, we can place the filters near designed cross-over frequency, and hence improve the gain margin without adversely affecting the phase. This averaging effect will be shown in the experiment results in a subsequent section.

CONTROLLER DESIGN

To deal with the lightly-damped vibration modes of the suspended beam, we design a *slow roll-up lead compensator*, which is a SISO multiple-lead compensator. This compensator has the following structure:

$$H(s) = K_p \frac{(s + m)(s + 4m)(s + 16m) \dots}{(s + 2m)(s + 8m)(s + 32m) \dots} \quad (18)$$

The controller frequency response is shown in Figure 7. This controller will provide phase margin of about 30 degrees for the frequencies of interest. It has gain rolling up at an average slope of 10 dB/decade to avoid over-amplifying resonance peaks at high frequencies. Depending on the design requirement and structural damping ratio, the ratio of the zero-pole locations can be designed to have more phase margin or slower roll-up rate.

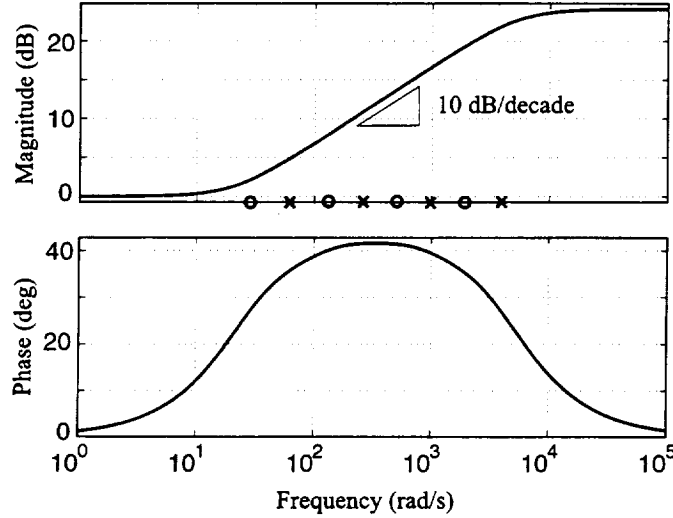


Figure 7: Bode Plots of slow roll-up lead compensator

SCALED EXPERIMENT

In this section, we describe the design procedures of our beam experiment. Two experimental results are shown. The first experiment uses 2 sensors and 2 actuators to suspend a single point of the beam with clamped-clamped boundaries. The second experiment uses 8 sensors and 8 **actuators** to suspend the beam in 4 units with sensor and actuator averaging within each unit. We also show that the suspension is stable under varying boundary conditions. We first summarize the system properties:

1. Design requirements: suspension dc stiffness $K = 0.4 \text{ N/mm}$, bandwidth $\omega_{BW} = 100 \text{ Hz}$, airgap 3 mm, and varying boundary conditions.
2. Beam: $E = 200 \text{ GPa}$, $I = 58.4 \text{ mm}^4$, $\rho = 7800 \text{ kg/m}^3$, $A = 15 \text{ mm}^2$, $L = 3 \text{ m}$, $\zeta = 0.001$, $\sigma = 7.5 \times 10^6 \text{ mhos/m}$, and $\mu = 5 \times 10^3 \mu_0 \text{ H/m}$.
3. Sensor: bandwidth of 1 kHz.
4. Actuator: $a = 13 \text{ mm}$, $b = 3 \text{ mm}$, $c = 25 \text{ mm}$, $N = 1200$, 26 gauge wire, current limit $i_{max} = 0.7 \text{ A}$, and bandwidth 500 Hz.
5. Controller: $t_s = 250 \mu\text{s}$ and $t_c = 220 \mu\text{s}$. (delay $\approx 345 \mu\text{s}$)

From the beam properties, we can derive the structure peak envelope. Assuming proportional control of gain K , the loop transfer function becomes

$$KG_{envelope}(\omega) = \frac{K}{m\zeta\omega^2} = \frac{2800K}{\omega^2} \cdot \left(= \frac{K}{140} \text{ at } 100 \text{ Hz} \right) \left(= \frac{K}{400} \text{ at } 170 \text{ Hz} \right) \quad (19)$$

This result shows how the design of control bandwidth and stiffness is constrained to the mass and damping ratio of the beam. It suggests that if we choose dc stiffness $K = 140 \text{ N/m}$, we will have resonance peaks below 0 dB when frequencies are higher than 100 Hz, and thus we need positive phase margin at least up to 100 Hz. Similarly, if we choose dc stiffness $K = 400 \text{ N/m}$, we will need positive phase margin up to 170 Hz. From the two design requirements of $\omega_{BW} \geq 100 \text{ Hz}$ and $K \geq 400 \text{ N/m}$, we choose $K = 400 \text{ N/m}$ to meet both requirements.

Furthermore, we arrange sensor averaging to attenuate the vibration modes around 170 Hz. From the beam dispersion equation, we have

$$EI\lambda^4 = \rho A\omega^2 \Rightarrow \lambda^2 = 0.1\omega \Rightarrow \lambda = 10.3 \text{ at } 170 \text{ Hz}, \quad (20)$$

therefore we place 2 sensors apart by $2d_s$ with $d_s = \frac{\pi}{2\lambda} = 0.15 \text{ m}$.

In our first experiment, we used 2 sensors and 2 actuators to control one point ($z_0 = 1.12 \text{ m}$) of a clamped-clamped beam. We compared the two positioning methods of sensor interpolation and sensor averaging. In the first arrangement, we placed 2 actuators in between 2 sensors in close proximity and used sensor interpolation method. we were almost able to stabilize the system, except there is a limit cycle vibration at 1100 rad/s. In the second arrangement, we used sensor averaging by placing two sensors at $\pm 0.15 \text{ m}$ from the center, and used the same controller. We were able to stabilize the system and avoid the limit cycle. Figure 8 shows the loop transfer function of both experiments. The loop has 30° phase margin for all vibration modes below 500 rad/s. Below 1000 rad/s, we have an alternating pole-zero pattern, which means each resonance mode is in phase, and hence shows there is no non-collocation problem. Above 1000 rad/s, the modes become

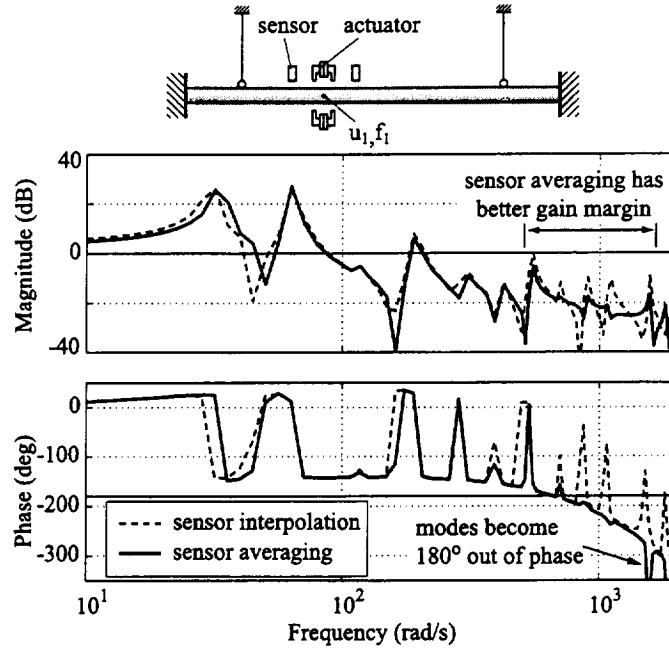


Figure 8: Experimental setup and experimental Bode plots of loop transfer function $H(s)G(s)$, sensor interpolation and sensor averaging

out of phase due to sensor averaging when $\cos(\lambda d_s) < 0$. The sensor averaging shows its advantage around the cross-over frequency, where it attenuates the vibration modes without affecting the phase, and hence improves the stability robustness by increasing the gain margin.

In our second experiment, we used 8 sensors and 8 actuators to control 4 points of the beam with varying boundary conditions. We compared two different arrangements: sensor averaging only, and both sensor/actuator averaging. In the first arrangement, we used the sensor averaging method only, and were able to stabilize the beam with loosely clamped boundaries. However, when the beam was released to free-free boundaries, a vibration at 800 Hz builds up and destabilizes the system in a few seconds. In the second arrangement, we added actuator averaging to the previous sensor averaging arrangement. To attenuate vibration modes around 800 Hz, we placed two actuators apart by $2d_a$ with $d_a = 0.07$ m, and we were able to suspend the beam with varying boundary conditions, including clamped, hinged, and free boundaries. The Bode plots of $H(s)G_{22}(s)$ for a suspended free-free beam is shown in Figure 9, where $G_{22}(s)$ is the open-loop dynamics of the 2nd control point at $z_0 = 1.12$ m. The result shows the damping ratio of the beam is below 0.001. An interesting observation is that the free-mass dynamics of $1/(ms^2)$ is not observed in the Bode plots. That is because the measured horizontal dynamics are coupled to vertical dynamics, and the low frequency dynamics are determined by a pendulum mode with natural frequency of 20 rad/s, which appears as a small bump in Figure 9.

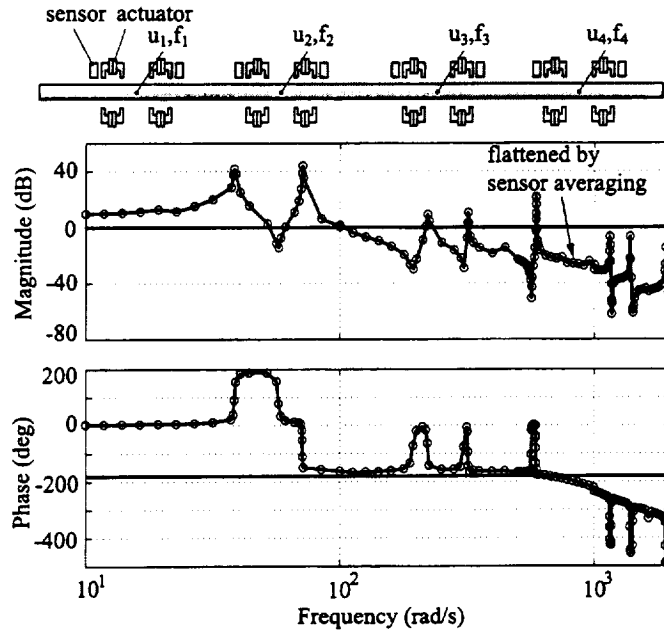


Figure 9: Experimental setup and experimental Bode plots of $H(s)G_{22}(s)$ for free-free beam suspension

CONCLUSION

This paper presents general design procedures for magnetic suspension of elongated beams for noncontact processing. We derived the uncertainty envelope that represents the beam dynamics with varying boundary conditions, and used it to guide the controller design. We developed sensor and actuator averaging methods to attenuate undesired resonance modes without adversely affecting phase. We also built a scaled experiment to suspend a tubular beam, and demonstrated the effectiveness of our proposed design method. In the future, we plan to further study the effects of beam axial velocity V and axial tension T . We will also investigate the dual problem of electrostatic levitation, and the suspension of different structures, including strings, membranes, and plates.

ACKNOWLEDGMENTS

This research is sponsored by the National Science Foundation under Grant Award Number DMI-9700973. The authors wish to acknowledge Professor Jeffrey H. Lang and Professor Samir Nayfeh at MIT for their helpful comments.

References

- [1] Y. Oshinoya and T. Shimogo "Electro-magnetic Levitation Control of an Elastic Plate," in *Proc. Maglev '89*, pp. 435-440, 1989.
- [2] H. Hayasiya, H. Ohsaki, and E. Masada "Magnetic Levitation Control of Elastic Steel Plate for Steel Making Process," in *Proc. ICEE '95*, 1995.
- [3] J. Jin, T. C. Yih, T. Higuchi, and J. U. Jeon, "Direct Electrostatic Levitation and Propulsion of Silicon Wafer," *IEEE Trans. Industry Applications*, vol. 34, No. 5, pp. 975-984, 1998.
- [4] American Metal Handle, Vulcan Dr., Birmingham, AL, USA.
- [5] J. A. Wickert and C. D. Mote, Jr., "Classical Vibration Analysis of Axially Moving Continua," *Journal of Applied Mechanics, Transactions of the ASME*, Vol. 57, pp.738-744, September 1990.
- [6] D. L. Trumper, M. C. Weng, and R. J. Ritter, "Magnetic Suspension and Vibration Control of Beams for Non-contact Processing," *Proc. of the 1999 IEEE International Conference on Control Applications*, pp. 551-557, 1999.
- [7] M. K. Liebman, "Thermally Efficient Linear Motor Analysis & Design," Chapter 3, Master's Thesis, MIT Dept. of Mechanical Engineering, 1996.
- [8] M. C. Weng and D. L. Trumper, "Vibration Control of Flexible Structures Using Sensor Averaging and Actuator Averaging Methods," submitted to the *IEEE Transactions on Control Systems Technology*.

Session 9 -- Rotating Machinery Topics

Chairman: Raoul Herzog
Mecos Traxler AG

TOUCHDOWN/LAUNCH-LOCK MECHANISM FOR MAGNETICALLY SUSPENDED CONTROL MOMENT GYROSCOPE

D.W. Smith - Honeywell Inc., Satellite Systems Operation

ABSTRACT

In the event of power failure in a magnetically suspended Control Moment Gyroscope (CMG), a mechanical touchdown bearing is required to prevent contact between the rotor and various magnetic actuators. Additionally, a launch-lock system must be provided to suspend the rotor during launch, when power is not applied to the CMG. Honeywell Inc. has incorporated both of these functions into one system.

This paper describes the patented system, including pertinent design details, and summarizes bench- and brass-board CMG testing results. Described in design information is an essential aspect of the bearing design, a conical clutch that acts as both contact interface and launch-lock mechanism. Test results summarize materials used for critical interface between the touchdown system and rotor, as well as results of durability tests (1000 touchdowns at various loads) in a bench test rig, and planned and unplanned touchdowns in the CMG test bed.

Predominant lessons learned include the discovery of:

- At least one successful material combination for high-speed, high-load contact
- The affect of lubrication on contact interfaces
- How grease lubricated bearings work at very high acceleration rates to speeds up to 1.1×10^6 DN
- Unexpected reasons for over designing bearing load capacities, for this type of application

INTRODUCTION

In the quest for achieving minimum emitted disturbances and maximum life from a CMG, Honeywell is developing a large, magnetically suspended device capable of a torque output of 43.8 N-m (3100 ft-lbf). No one has built such a large, magnetically suspended CMG, although the Soviets have flown a low-output, 2.1 N-m (150 ft-lbf) CMG on the Mir Space Station.

Any magnetically suspended device requires a backup system in case of primary suspension failure; generally, this takes the form of mechanical bearings. The touchdown system prevents damage to magnetic actuators and other components in the event of power loss or other magnetic suspension failures. The most common touchdown system consists of a mechanical bearing, through which a shaft feature extends from the rotor. Adequate clearance is provided between the shaft and bearing Inside Diameter (ID) to allow the magnetic suspension to function normally. Should a magnetic suspension failure occur, the shaft will contact the bearing ID before contacting the actuators. An axial-thrust bearing is added to this radial bearing to prevent excess axial excursions. The mechanical bearings that contain shaft excursions are most commonly ball bearings, although roller or sleeve bearings may also be used.

While most mechanically suspended momentum devices take launch vibration loads through bearings making a separate launch-lock system unnecessary, a unique problem posed by a magnetically suspended CMG occurs during launch when suspension is not powered up and normal operating clearances provide an unacceptable opportunity for the rotor to rattle around. Left unchecked, this leads to high-impact loads and damage during launch vibration. Additionally, if magnetic suspension fails during operation, the rotor would continue to rattle around for the remainder of the mission, causing significant shock and vibration whenever the vehicle moved. Therefore, a magnetically suspended CMG requires a locking system to support the rotor during launch.

Launch-lock systems are commonly used on many types of space hardware, usually taking the form of a device that clamps hardware to a structural member by means of an actuator. Common actuators include pyrotechnics, paraffins, solenoids, and motors. A magnetically suspended CMG's rotor is quite massive (86 kg, 190 lbm), and common launch-lock techniques would be heavy and complex.

DESIGN

The design objective was to combine functions of touchdown bearings and the launch-lock device into one system, reducing weight and complexity. The solution, illustrated in Figure 1, was designing a female conical feature at each end of the rotor that mates with male conical housings supported by duplexed pairs of angular contact ball bearings. In normal operation, the rotor is suspended by magnetic actuators (not illustrated in Figure 1). A sufficient gap is available between female cones of the rotor and male cones of the touchdown system to allow the rotor to move within operational range of the magnetic suspension system. Should magnetic suspension fail, or loads are applied to it that are beyond capacity, the rotor will traverse the gap and the cones will touch. When this occurs, the male cone suspended by ball bearings is accelerated to rotor speed.

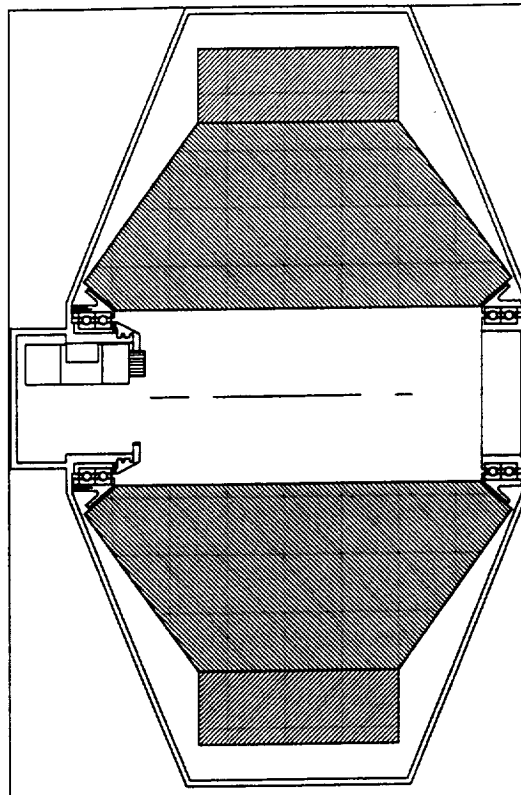


Figure 1. Touchdown/Launch-lock System

Acceleration rate is dependent on the bearing's drag torque, mass inertia of the male cone-bearing assembly, friction coefficient between the two cones, and contact force. Between the time that initial contact is made, and the time that the male cone assembly matches rotor speed, sliding occurs between the two cones. Because of sliding, it is important to select wear-resistant surfaces for both cones. There are two particularly significant effects of this wear. First, static or dynamic rotor balance may be affected by removing material from, or adding material to, the female cone that is part of the rotor. Second, excess wear will produce debris that must be contained.

This system serves as a touchdown system and a method of supporting the rotor during launch including occurrences when magnetic suspension is inoperative. In Figure 1, the fixed bearing-cone assembly is solidly mounted to the structural housing. A floating bearing-cone assembly is mounted to a shaft-like feature of the structural housing. This allows the floating bearing-cone assembly to be translated axially until the rotor is captured between fixed and floating bearing-cone assemblies.

While axial actuation may be accomplished by a number of methods, the method illustrated in Figure 1 uses a motor-driven, threaded actuator. In this implementation, a gear motor turns the floating bearing-cone assembly through a planetary gear. The inboard end of the floating bearing-cone assembly interfaces with the structural housing through an ACME thread. As the motor turns the planetary gear, the floating bearing-cone assembly moves axially by means of the ACME thread.

Once the launch-lock feature is engaged, the rotor is free to turn about its rotational axis on touchdown bearings. Touchdown bearings have an adequate load capacity to withstand launch vibration in all three axes and the impact loads that might be encountered if magnetic suspension fails when the CMG is gimbaled.

CONICAL CLUTCH DESIGN

Material selection was the most difficult part of conical clutch design. Design criteria dictated that the clutch had to endure 1000 touchdowns with a minimum of debris generation and weight change on the rotor (female) side. Soft materials (e.g., brake and clutch friction materials) were considered and abandoned because of the quantity of debris generated. Facing unlimited choices of hard materials and coatings, yet limited time and budget, candidates were narrowed to five.

In early design stages, it appeared that the selection of female cone material was going to be limited by rotor design considerations; therefore, Maraging 250 became the first test material. Maraging 250 is very soft (Rc50), so a hard coating over the Maraging was chosen as the second candidate. Titanium Nitride (TiN) coating was selected because of the considerable experience base available using this material. A hard bearing material, 440C, was selected as one of the mating candidates. The 440C material was chosen over other bearing materials because of its relatively high corrosion resistance, and the community experience in applying surface treatments to it. The fourth candidate was 440C, plated with chromium, followed by nitrogen ion implantation. While there are many implantation candidates, this choice was primarily dictated by budgetary considerations. The final choice was Nitronic 60, an austenitic stainless steel that was developed for wear resistance.

The only reasonable way to choose among candidates was to perform a comparative test series. These tests, called the contact interface tests, are described later in this paper.

In terms of the physical geometry of the conical clutch, the angle of conical surfaces was most critical. Selection of this angle was based on clearance requirements for axial and radial actuators. In this case, radial actuators are most significant for CMG performance, and axial actuator gap may be varied with less impact to the system, allowing there was a range of acceptable angles. Within this range, the following two considerations dominated the decision:

1. The amount of force required to disengage the launch-lock system is a function of the friction coefficient between the cones and cone angle. If the cone angle is less than 45deg, then it is possible that axial force will be required to disengage the cones unless the friction coefficient is low enough to do so. If the friction coefficient is less than the value of the tangent of half the cone angle, then the disengagement force will be zero. In terms of disengagement, the larger the cone angle, the better.
2. The force required to engage the launch-lock system when the shaft is horizontal in a 1g field is a function of rotor weight, cone angle, and friction coefficient. The lower the cone angle for a given rotor weight and friction coefficient, the better.

BEARING DESIGN

Selection of bearing size was driven by accommodation requirements for magnetic suspension system components. These components dictated relatively large, thin-section bearings. It was, therefore, easy to provide plenty of load capacity margin from the start. This allowed flexibility to incorporate certain design

features that would help in other areas. Silicone Nitride (Si_3N_4) balls were selected because of low mass, as compared to steel. This minimized ball group inertia and, subsequently, the amount of skidding during rapid acceleration. Additional advantages of using Si_3N_4 balls include a substantial reduction in bearing component wear by the elimination of adhesive wear between ball and raceway, and the reduction of outer ring loading, as the greatly reduced ball mass minimizes ball centripetal force.

M50 tool steel was chosen for the rings due to a superior resistance to sliding wear (compared with 52100) and common availability. Since this project was completed, substantial development work has been done with Vim CRU 20 tool steel for bearings of this type, ref. 1. This material is much harder than M50 (Rc 66 compared to Rc 60), has a higher modulus (34 E6 psi compared to 30 E6 psi), substantially lower wear rates, and at least five-times fatigue life.

An inertially biased phenolic cage was designed to provide optimum stability throughout speed range, with minimum mass inertia. Curvature ratios were kept relatively tight to maintain low stress levels, even under maximum loads, and to consider differences in moduli between the steel ring and ceramic balls. Rheolube 2000 grease was selected for the lubricant because of low vapor pressure and drag torque. Minimum grease quantity was required because bearings are only used intermittently and minimizing the viscous drag component at these very high DN numbers is desirable. The low vapor pressure of Rheolube 2000 allows low lubricant quantities without concern for excessive lubricant loss.

Because of concerns over ball skidding under very rapid accelerations, a series of bearing acceleration tests were planned. Later, these tests were combined with contact interface tests by installing a sensitive speed-measuring system that measured the rate of acceleration during contact tests. This system, along with test results, is described in the Contact Interface/Bearing Acceleration Testing section of this paper.

LAUNCH-LOCK ENGAGEMENT SYSTEM DESIGN

The launch-lock engagement system consists of a multi-pass gear drive motor that drives a pinion to engage an internal gear. The principle parameters that trade off in this system design are weight, power, engagement time, and size. Of these, size and weight are dominant. Power is not critical because the drive motor uses only a small fraction of the CMG allotment. Engagement time is not critical because the touchdown system is designed to work with the launch lock completely disengaged. The launch-lock system is functionally independent of the touchdown system and, thus, devoid of time constraints.

The motor was sized on the basis of output torque required to translate the floating system axially in a 1g field with the rotor in any orientation. The rotor weight resists this translation by acting through gear friction, ACME thread, cartridge/shaft interface, and conical clutch interface. The current motor provides adequate power to engage the launch-lock system in approximately 15 seconds.

CONTACT INTERFACE / BEARING ACCELERATION TESTING

As the design of the magnetic CMG touchdown system evolved, two areas of concern emerged. The first was the contact interface between the female conical feature on the rotor and the male conical housing of the touchdown bearings. With the wheel spinning at 6000 rpm and gimbaling as rapidly as 2.25 radians-per-second (assuming a control system failure), the touchdown is violent with great potential for cone damage or wear. The second concern was the bearings' acceleration rate. Calculation at touchdown proved that the bearing may be called upon to accelerate from 0 to 6000 rpm in as little time as 40 ms, depending on the

friction coefficient at conical interface. Although the bearing was designed with light-weight Si_3N_4 balls and a phenolic cage to minimize ball set inertia, including preload selected to impede ball skidding, a test was still needed. A fixture was designed that would spin a female cone while forcing a male cone, supported by touchdown bearings, against it. A series of tests were conducted using various materials and loads at 6000 rpm. Later in the program, consideration was given to increasing rotor speed to 9000 rpm, and additional tests were conducted at that speed with a commensurate increase in applied loads.

TEST SETUP

The test fixture, depicted in Figure 2, consists of a 1/2 hp synchronous motor that turns a shaft at either 6000 or 9000 rpm, depending on the toothed belt's pulley ratio. The shaft is mounted on a set of angular contact ball bearings: a single 206-size bearing at belt end and a 209-size bearing at test cone end. The female test cone is bolted to the shaft flange. A massive shaft, supporting the touchdown bearings and male cone, is mounted on a pivot so that when it is pulled down by the hydraulic ram, it will contact the female cone with both conical surfaces parallel.

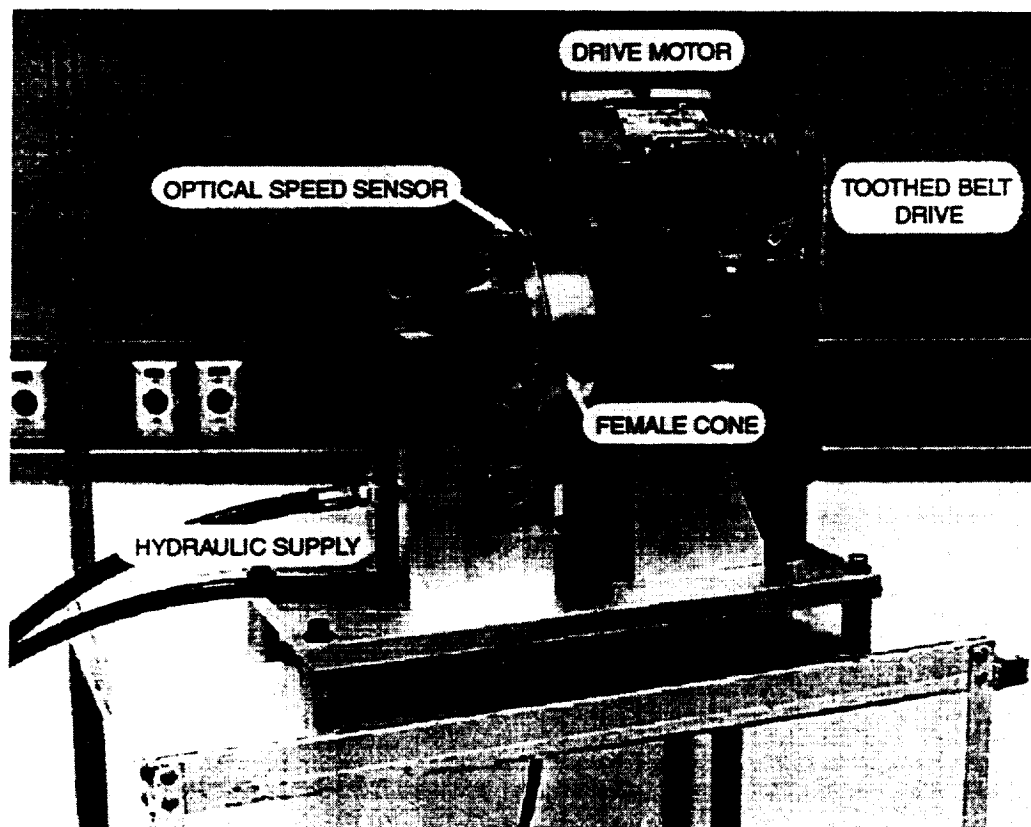


Figure 2. Touchdown Test Setup

Figure 2. Touchdown Test Setup

Contact force is adjustable by varying hydraulic pressure to the ram. A light-emitting diode and photo-diode, straddling an aluminum disk containing 360 equally spaced holes, measures rotational speed of the male cone by marking time on a running clock each instance the light of a passing hole strikes the photo-diode. Acceleration rate is obtainable from the speed-versus-time plot.

TEST PROCEDURE

Prior to any touchdown, a profilometer was used to record axial surface geometry, and three, equally spaced Tallyronds™ were taken to define the roundness of each part.

In early tests, the fixture was configured as previously described with 6000 rpm pulleys in place. With cones of the desired material installed, hydraulic pressure was adjusted and the female cone brought up to speed. Once shaft speed stabilized and the speed-measuring computer program was zeroed, the solenoid valve was actuated to command the hydraulic ram to pull the male cone down into contact with the female cone. Tests were performed at various loads, from 150 to over 2000 lbf, to simulate touchdowns under different gimbaling conditions. When speed again stabilized, the motor was turned off and the rotating assembly was allowed to decelerate and stop. The hydraulic ram was then reversed to disengage the male cone. The male cone/touchdown bearing/shaft assembly was removed from the fixture and conical surfaces examined. Profile and roundness measurements were repeated to determine the dimensions of observed surface features.

As the testing program progressed, more load cycles were applied to test specimens before examination. Eventually, hundreds of touchdowns were performed between inspections.

After down selecting the material combination, an additional test was run at 9000 rpm. Tests were run with applied radial loads of 150 and 3500 lbf.

TEST DESCRIPTION

Initial tests were run using high loads, due to concerns about bearing acceleration. Acceleration times were measured at roughly 140 ms with high loads; this was three times the minimum calculated time, and caused no observed damage to the bearing. The opposite end of the spectrum was then investigated with contact forces of 150 lbf. This was the most difficult load range from the standpoint of damage to conical surfaces because of the duration of sliding at the interface. Acceleration times at 150 lbf were on the order of 500 ms.

Different material combinations were tried, as summarized in Table I, in an effort to find the combination that showed least wear. When combinations were found to show promise, multiple load cycles were performed between inspections. It was during this extended testing that some of the bearings' grease was expelled and migrated, by centrifugal force, onto the cone surface. It was discovered, when the test was stopped for a routine inspection after ten touchdowns, that the lubricated zone covered about one-third of the cone area. The inspection revealed almost no wear in the lubricated region and substantial wear over the remainder of the cone.

Tests that followed used only Pennzane 2000 oil, and Rheolube 2000 and Apiezon T grease. The application of lubricants increased run-up times considerably, affecting wear rates by various amounts (refer to Table I).

After the final candidate was selected, a separate set of tests was run at 9000 rpm to prove that the entire system would operate satisfactorily at that speed as well. A thousand touchdowns were performed at each of the radial loads tested (150 and 3500 lbf).

TEST RESULTS

Table I is a summary of the 6000 rpm test results. Table II is a summary of the 9000 rpm test results.

Table I. 6000 rpm Contact Interface/Bearing Acceleration Test Results

Test Number	Female	Male	Lube?	Results
1	Maraging	440C	No	Narrow contact zone – fixture alignment significant wear
2	TiN Maraging	440C	No	Significant wear – TiN removed
3	Nitronic 60	440C	No	Marks at two contact points
4	Nitronic 60	440C	Pennzane 2000	Wear similar to Test 3
5	Nitronic 60	CY-N 440C	No	Removed CY-N
6	Nitronic 60	Nitronic 60	Pennzane 2000	Separate wear bands
7	Nitronic 60	440C TCP	No	Lower wear – gummy debris
8	440C	TiN 440C	Rheolube 2000	All TiN removed by 1000 cycles 0.002 maximum wear 0.002 maximum buildup at 1000 touchdowns
9	Nitronic 60	440C	Rheolube 2000	Low wear with grease (first 50 touchdowns) 0.0035 maximum wear - 0.0032 maximum buildup at 1000 touchdowns bearings – like new
10	TiN 440C	440C	Apiezon T	More wear and sparks

Table II. 9000 rpm Contact Interface/Bearing Acceleration Test Results

Test Number	Female	Male	Lube	Results
11	Nitronic 60	440C	Rheolube 2000	Low wear (0.0016 maximum wear after 1000 150 lbf touchdowns, 0.0163 maximum wear after an additional 1000 touchdowns at 3500 lbf)

TEST CONCLUSIONS

After examining the test results, the following predominant conclusions emerged,:

- The design was found adequate to support over 1000 touchdowns with at least two different material combinations. Bare 440C against TiN-coated 440C and bare 440C against Nitronic 60 tests endured 1000 touchdowns.

- Proper lubrication with grease also helped. At least 50 touchdowns were applied to grease-lubricated cones without observable wear. This was true for both material combinations that endured 1000 touchdowns.
- The test that ran 440C against TiN-coated 440C exhibited less total wear than the 440C against Nitronic 60 test.
- The test that ran Nitronic 60 against 440C had more wear but less debris than the 440C tested against TiN-coated 440C. This is due to material transferring from the Nitronic 60 and building up on the 440C. The transfer appeared to be uniform around the cone's circumference and should, therefore, have minimal effect on rotor balance.

By using a low-friction contact interface, a reduction in bearing-rate acceleration occurred. This effectively transfers the challenge of bringing the touchdown system up to speed from the bearing design to the clutch design. Additionally, skidding between the two conical surfaces continues for a longer time. This has the benefit of distributing wear more evenly around the circumference of contacting surfaces.

The system using a Nitronic 60 female cone against a 440C male cone with a Rheolube 2000 grease film on each performed equally well at 9000 rpm.

CMG TEST BED RESULTS

Having made the final material selection based on contact interface testing, the system was designed into a CMG test bed. This unit evaluated all mechanical and electrical components, as well as control laws and overall system operation. As one might expect on such a complex system, everything did not work correctly the first time. Principle complexities existed in the control system, and every time the control system failed to control the suspended rotor, the touchdown system was tested. During the next year of testing, the CMG touchdown system was tested well over 1000 times. It was estimated that, when fully developed, a flight CMG would experience on the order of 10 touchdowns in a lifetime.

Three significant touchdown system issues arose during this testing period. The first was the loss of an engagement motor, which was caused by operation at its rated load for too long a period. The motor selected was not rated for continuous operation or vacuum operation. The combination of high duty cycle and vacuum operation burned up a set of brushes. The solution was simple, a space-rated motor is available in the same chassis size.

The second problem appeared more significant. A thin, plastic film was applied to inner surfaces of magnetic actuators and, during a period of significant touchdown activity, plastic was transferred to the rotor, suggesting that the touchdown system failed to prevent contact with actuators. The ensuing investigation revealed that a control system instability had caused actuators to be energized in phase with rotor oscillations, causing touchdown loads that were twice the maximum design loads. Structural deflections caused by these loads were adequate to allow contact between rotor and actuators. No damage was done to the structure or touchdown system, partially due to a substantial bearing-load-capacity margin. Improvements in the control system prevented sympathetic actuator energizing, eliminating the possibility of overloading the touchdown system.

The third problem dealt with engagement and disengagement of the launch-lock system. The engagement motor provided substantial torque by using a high-ratio, gear box. This torque was necessary in order to engage the system in a gravity field, should the movable cone be located directly below the rotor. In the original design, however, no rotational stop existed, and the cone continued to move until the drive motor stalled. At this point, the cone driven into the rotor generated axial thrust that produced compressive strain in the rotor and engagement drive system, and tensile strain in the support structure. When a disengagement command was then given to the motor, it had to overcome increased friction in the ACME thread caused by

engagement strain, proving too much for the drive motor. The solution was to install a limit stop to allow the driven cone to just engage the rotor, and hit the limit before being driven hard against the rotor cone.

SUMMARY

A unique system was designed to combine touchdown and launch-lock functions for a magnetically suspended CMG. The principle challenge encountered in this design implementation was selecting material for the conical clutch surfaces. Testing several material combinations produced an acceptable candidate, and proved that bearings can withstand required acceleration rates. This touchdown/launch-lock system has been included in a magnetically suspended CMG design, and a prototype successfully tested under actual operating conditions.

OBSERVATIONS AND RECOMMENDATIONS

While this system was developed for a CMG application that has unique requirements, it would be useful in other applications.

From the vantage of a touchdown function, the philosophy of separating contact surface function from bearing function is a key to success. Controlling contact interface [i.e., area (pressure), geometry, materials, and lubrication] separately from bearing design allows more optimum solutions to both.

While the material combination selected for contact interface surfaces worked satisfactorily for this application, the possibility remains that other material combinations may prove more successful. While examining a new application, consideration should be given to newer materials, for example, REX20 (CRU20), that have greater wear resistance.

Coatings on contact interfaces should be avoided. Contact interface is a violent environment, and coatings only complicate tribology and add new failure mechanisms and costs.

REFERENCES

1. Smith, D.W., Leveille, A.R., Hilton, M.R., Ward, P.C., Rex 20 / Si₃N₄ CMG Bearing Development, 32nd Aerospace Mechanisms Symposium, May 1998.
2. Park, W., Hilton, M.R., Leveille, A.R., Ward, P.C., McClintock, D.E., Smith, D.W., Microstructure, Fatigue Life, and Load Capacity of PM Tool Steel REX20 for Bearing Applications, 1998 AME / STLE International Tribology Conference, October 1998.

Identification and Control of Unbalance and Sensor Runout on Rigid by Active Magnetic Bearing Systems

Yoichi Kanemitsu, Sinya Kijimoto, Koichi Matsuda, Park Tea Jin

Department of Intelligent Machinery and systems, Graduate School of Engineering,
Kyushu University, JAPAN E-mail:kanemitu@mech.kyushu-u.ac.jp

ABSTRACT

In this paper, we propose a new identification method of the sensor runout and the unbalance on a rigid rotor supported by active magnetic bearings applying the incremental least square on-line method and perform some numerical simulations and experiments on the their identification applying to a rigid rotor model of a turbo-molecular pump. The paper also presents some results of the experiment on the identification accuracy and effects of the rotor model error. From the numerical simulations and the experiments, we conclude that the proposed identification method is effective for the simultaneous identification of the unbalance of rotor and the sensor runout.

1 INTRODUCTION

An active magnetic bearing(AMB) is non-contact, frictionless and has the ability to actively control the bearing force and the journal eccentricity in the bearing. The application of AMB also has a possibility to compensate the mass unbalance on the rotor.

Two methods are generally adopted to reduce the unbalance vibration of the rotor levitated by AMB. One method is called the peak-gain method (PG method), in which the feedback gain of the AMB controller is extremely high only at the rotating speed frequency. Another method is called the feed forward method (FF method)⁽¹⁾ in which the unbalance on the rotor is estimated from the measured vibration signals by the AMB proximity sensor and a compensating magnetic pull from the AMB is added to the rotor in opposite direction of the unbalance force so as to cancel out the mass unbalance force. The FF Method is better than the PG method from the viewpoint of system stability. But it is essential to estimate the unbalance correctly for the FF method.

In a magnetically levitated rotor by AMB, the clearance between rotor and stator is usually measured by the eddy current type proximity sensor, which is sensitive to circumferential irregularity of conductivity and permeability of sensor target material on the rotor. The measured signal by the sensor is called electrical sensor runout⁽²⁾. The proximity sensor runout enters into the control circuit of the AMB and then the magnetic pull induced by the runout signal whirls the rotor supported the AMB just as an unbalance on the rotor does. And moreover the undesirable sensor runout saturates the control current from the power source.

It is necessary for realization of minimal rotor whirl by the FF method to identify the sensor runout and the unbalance at the same time, compensate the unbalance force by the FF method and eliminate the sensor runout from the measured proximity signal of the AMB simultaneously. It is recommended for minimization of the control current to use the modified proximity signal without the runout for the AMB levitation control.

2. EQUATION OF MOTION OF RIGID ROTOR SUPPORTED BY ACTIVE MAGNETIC BEARINGS

A simple AMB model is shown in figure 1. AMB levitates a rotor by regulating the current in magnetic coil and holding the bearing clearance (gap) constant. An attractive force from AMB is formulated as Equation(1).

$$f = -\frac{\mu_0 S N^2}{8} \cdot \left(\frac{i_{p0} + i}{x_{p0} + x} \right)^2 + \frac{\mu_0 S N^2}{8} \cdot \left(\frac{i_{n0} - i}{x_{n0} - x} \right)^2 = \frac{\mu_0 S N^2}{8} \cdot \left\{ -\left(\frac{i_{p0} + i}{x_{p0} + x} \right)^2 + \left(\frac{i_{n0} - i}{x_{n0} - x} \right)^2 \right\} \quad (1)$$

Equation (1) is linearized with respect to the control current i and the gap change x as follows:

$$f = -Fi + Gx$$

where

$$F = \frac{\mu_0 S N^2}{4} \left\{ \frac{i_{p0}}{x_{p0}^2} + \frac{i_{n0}}{x_{n0}^2} \right\}, \quad G = \frac{\mu_0 S N^2}{4} \left\{ \frac{i_{p0}^2}{x_{p0}^3} + \frac{i_{n0}^2}{x_{n0}^3} \right\}$$

F, G are called AMB control stiffness and negative position stiffness respectively.

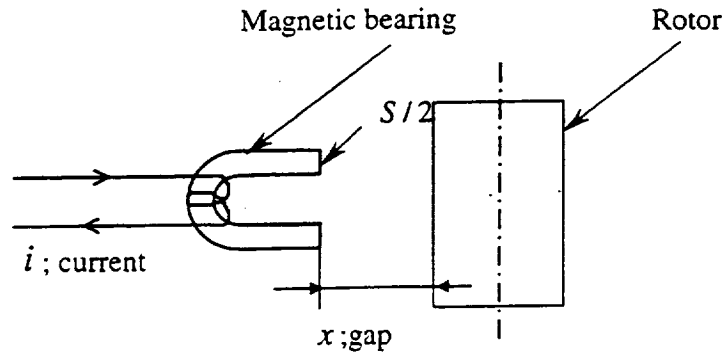


Figure 1 A Model of Active Magnetic Bearing

In this paper, we try to identify the unbalance and the sensor runout on a rotor of a small turbo-molecular pump levitated by AMB, of which photograph is shown in figure 2.

In order to make a numerical model of AMB, the transfer function of the controller has been measured and approximated with PID type controller which is represented as Equation (2) and the measured and the esti-

mated transfer functions are shown in figure 3. The solid line and the dotted line represent the measured transfer function and the approximated one. The estimated PID gain is also tabulated in table 1.

$$i = k_p \hat{x} + k_i \int \hat{x} dt + k_d \frac{d\hat{x}}{dt} \quad (2)$$

The rotor of the turbo-molecular pump is levitated by 2 AMBs and has a massive cylinder with rotor blades on the top end. Now the cylinder is replaced by a disk for the convenience of the verification experiment of the proposing identification method. The tested rotor is drawn in figure 4.

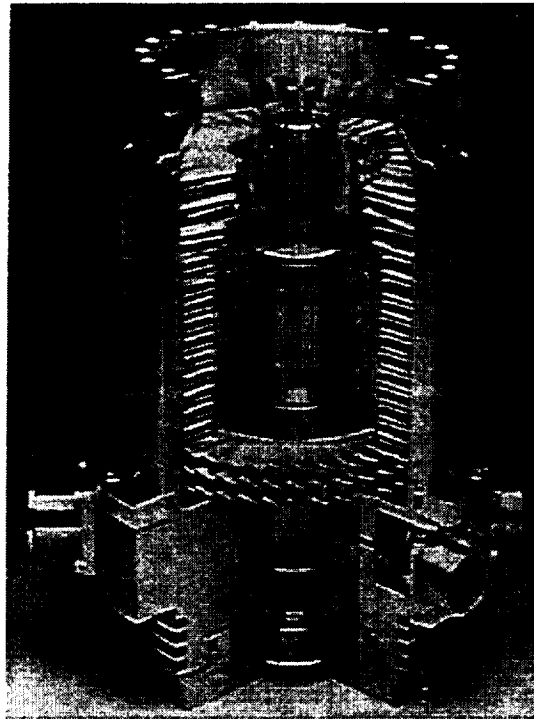


Figure 2 Photograph of the turbo molecular pump rotor

Table 1 Estimated control gain of AMB from measured transfer function

	Bearing 1	Bearing 2
k_p (A/m)	7810	6950
k_i (A/ms)	98300	49300
k_d (As/m)	9.83	4.4

Equation of motion of the rigid rotor shown in figure 4 and levitated by 2 AMBs is given as following equation.

$$M\ddot{x} + \omega M_1 \dot{x} + F_i + Gx_i = U_i \quad (3)$$

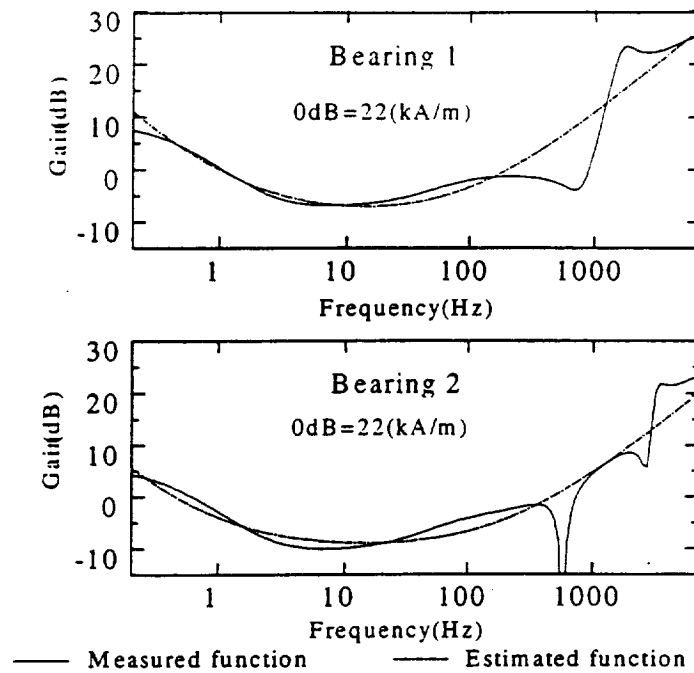


Figure 3 Measured and estimated transfer function

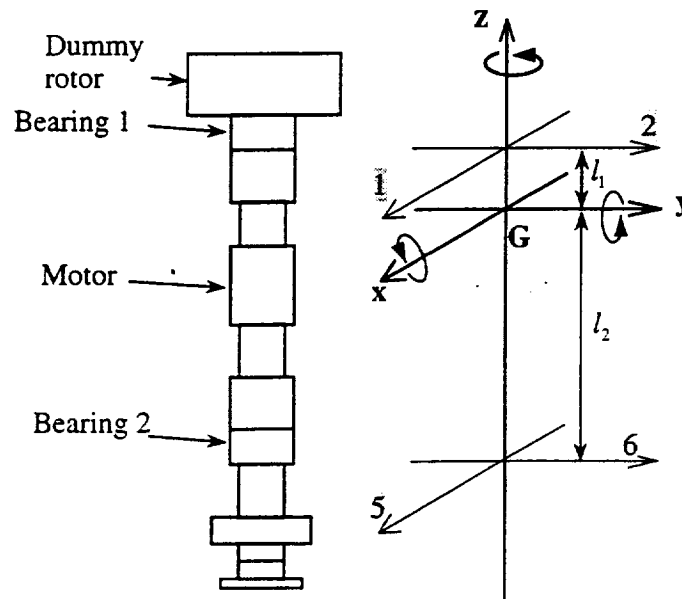


Figure 4 Rotor Model of Turbo-molecular Pump

(1,2,5,6 indicate the upper bearing in x direction and y-direction and the the lower bearing x-direction and y-direction respectively. G is the center of gravity of the rotor)

where $\mathbf{x}, \mathbf{x}_s, \mathbf{x}_r, \mathbf{i}$ are the actual rotor displacement vector, the measured displacement vector at AMB sensor, the sensor runout vector and the AMB control current vector. $\mathbf{M}, \mathbf{M}_1, \mathbf{U}_i, \mathbf{F}, \mathbf{G}$ are the mass matrix, the gyro-moment matrix, the rotor unbalance matrix, the control stiffness matrix and the negative position stiffness matrix.

$$\begin{aligned}\mathbf{x} &= [x \quad y \quad \theta_x \quad \theta_y]^T, \mathbf{x}_s = [x_1 \quad x_2 \quad x_5 \quad x_6]^T \\ \mathbf{x}_r &= [x_{1r} \quad x_{2r} \quad x_{5r} \quad x_{6r}]^T, \hat{\mathbf{x}} = [\hat{x}_1 \quad \hat{x}_2 \quad \hat{x}_5 \quad \hat{x}_6]^T \\ \mathbf{i} &= [i_1 \quad i_2 \quad i_5 \quad i_6]^T \\ \mathbf{M} &= \begin{bmatrix} m & 0 & 0 & 0 \\ 0 & m & 0 & 0 \\ 0 & 0 & I_d & 0 \\ 0 & 0 & 0 & I_d \end{bmatrix}, \mathbf{M}_1 = \begin{bmatrix} 0 & 0 & 0 & 0 \\ 0 & 0 & 0 & 0 \\ 0 & 0 & 0 & I_p \\ 0 & 0 & -I_p & 0 \end{bmatrix} \\ \mathbf{F} &= \begin{bmatrix} F_1 & 0 & F_5 & 0 \\ 0 & F_2 & 0 & F_6 \\ 0 & -F_2 l_1 & 0 & F_6 l_2 \\ F_1 l_1 & 0 & -F_5 l_2 & 0 \end{bmatrix}, \mathbf{G} = \begin{bmatrix} -G_1 & 0 & -G_5 & 0 \\ 0 & -G_2 & 0 & -G_6 \\ 0 & G_2 l_1 & 0 & -G_6 l_2 \\ -G_1 l_1 & 0 & G_5 l_2 & 0 \end{bmatrix}, \mathbf{U}_i = \begin{bmatrix} m\epsilon\omega^2 \cos(\omega t + \phi) \\ m\epsilon\omega^2 \sin(\omega t + \phi) \\ -(Id - Ip)\tau\omega^2 \sin(\omega t + \psi) \\ (Id - Ip)\tau\omega^2 \cos(\omega t + \psi) \end{bmatrix}\end{aligned}$$

$$\hat{\mathbf{x}} = \mathbf{x}_s + \mathbf{x}_r \quad (4)$$

The shaft displacement at the center of gravity and the sensor position of the AMBs is given from the geometrical relation of the shaft as follows:

$$\begin{aligned}\mathbf{x} &= \mathbf{L}\mathbf{x}_s = \mathbf{L}(\hat{\mathbf{x}} - \mathbf{x}_r) \\ \mathbf{L} &= \frac{1}{l_1 + l_2} \begin{bmatrix} l_2 & 0 & l_1 & 0 \\ 0 & l_2 & 0 & l_1 \\ 0 & -1 & 0 & 1 \\ 1 & 0 & -1 & 0 \end{bmatrix}\end{aligned} \quad (5)$$

As we have assumed the controller of the AMB to be the PID controller, the control current of the AMB are described as follows:

$$\mathbf{i} = \mathbf{K}_D \dot{\hat{\mathbf{x}}} + \mathbf{K}_P \hat{\mathbf{x}} + \mathbf{K}_I \int \hat{\mathbf{x}} dt \quad (6)$$

where

$$\mathbf{K}_D = \begin{bmatrix} K_{D1} & 0 & 0 & 0 \\ 0 & K_{D2} & 0 & 0 \\ 0 & 0 & K_{D5} & 0 \\ 0 & 0 & 0 & K_{D6} \end{bmatrix}, \mathbf{K}_P = \begin{bmatrix} K_{P1} & 0 & 0 & 0 \\ 0 & K_{P2} & 0 & 0 \\ 0 & 0 & K_{P5} & 0 \\ 0 & 0 & 0 & K_{P6} \end{bmatrix}, \mathbf{K}_I = \begin{bmatrix} K_{I1} & 0 & 0 & 0 \\ 0 & K_{I2} & 0 & 0 \\ 0 & 0 & K_{I5} & 0 \\ 0 & 0 & 0 & K_{I6} \end{bmatrix}$$

Now we adopt the estimated values in table 1 as the controller gain k_{Di}, K_{Pi}, K_{Ii} ($i = 1, 2, 5, 6$).

Substituting equations (4)(5)(6) for $\mathbf{x}_s, \mathbf{x}, \mathbf{i}$ of equation (3), we obtain a following equation of motion:

$$ML\ddot{\mathbf{x}} + (\omega\mathbf{M}_1\mathbf{L} + \mathbf{FK}_D)\dot{\mathbf{x}} + (\mathbf{FK}_P + \mathbf{G})\mathbf{x} + \mathbf{FK}_I \int \dot{\mathbf{x}} dt = \mathbf{U}_i + \mathbf{ML}\ddot{\mathbf{x}}_r + \omega\mathbf{M}_1\mathbf{L}\dot{\mathbf{x}}_r + \mathbf{G}\mathbf{x}_r \quad (7)$$

The unbalance matrix \mathbf{U}_i is represented as follows:

$$\mathbf{U}_i = \omega^2 \mathbf{M}_2 \begin{bmatrix} \varepsilon \cos(\omega t + \phi) \\ \varepsilon \sin(\omega t + \phi) \\ -\tau \sin(\omega t + \psi) \\ \tau \cos(\omega t + \psi) \end{bmatrix} \quad (8)$$

where

$$\mathbf{M}_2 = \begin{bmatrix} m & 0 & 0 & 0 \\ 0 & m & 0 & 0 \\ 0 & 0 & I_d - I_p & 0 \\ 0 & 0 & 0 & I_d - I_p \end{bmatrix}$$

ε, ϕ are mass eccentricity and its phase, τ, ψ are inclination of the central principal axis of inertia and its phase and ω is rotating speed.

The sensor runout vector \mathbf{x}_r is represented as follows:

$$\mathbf{x}_r = \begin{bmatrix} \lambda_1 \cos(\omega t + \phi_1) \\ \lambda_1 \sin(\omega t + \phi_1) \\ \lambda_2 \cos(\omega t + \phi_2) \\ \lambda_2 \sin(\omega t + \phi_2) \end{bmatrix} \quad (9)$$

where λ, ϕ are the sensor runout and its phase and subscripts 1,2 identify 2 radial bearings.

3. IDENTIFICATION METHOD

The identification method is as follows:

(1). Laplace transforms of the Equation of motion

Taking Laplace transforms of equation (7), we obtain the left-hand term of the equation as

$$\left[\mathbf{ML}s^2 + (\omega\mathbf{M}_1\mathbf{L} + \mathbf{FK}_D)s + (\mathbf{FK}_P + \mathbf{G}) + \mathbf{FK}_I \frac{1}{s} \right] \hat{\mathbf{X}}(s)$$

where $L[\bullet]$ is the Laplace transforms and $L(\hat{\mathbf{x}}) = \hat{\mathbf{X}}(s)$.

The right-hand term of equation (7) by the Laplace transforms is given as follows:

First term of the right-hand term

$$L[\mathbf{U}_i] = \frac{\omega^2}{s^2 + \omega^2} \mathbf{M}_2 \begin{bmatrix} \varepsilon(s \cos \phi - \omega \sin \phi) \\ \varepsilon(\omega \cos \phi + s \sin \phi) \\ -\tau(\omega \cos \psi + s \sin \psi) \\ \tau(s \cos \psi - \omega \sin \psi) \end{bmatrix} = U(s) \omega \mathbf{M}_2 \begin{bmatrix} s & -\omega & 0 & 0 \\ \omega & s & 0 & 0 \\ 0 & 0 & -\omega & -s \\ 0 & 0 & s & -\omega \end{bmatrix} \begin{bmatrix} \varepsilon \cos \phi \\ \varepsilon \sin \phi \\ \tau \cos \psi \\ \tau \sin \psi \end{bmatrix}$$

$$= \mathbf{M}_2 \left[s\omega \begin{bmatrix} 1 & 0 & 0 & 0 \\ 0 & 1 & 0 & 0 \\ 0 & 0 & 0 & -1 \\ 0 & 0 & 1 & 0 \end{bmatrix} + \omega^2 \begin{bmatrix} 0 & -1 & 0 & 0 \\ 1 & 0 & 0 & 0 \\ 0 & 0 & -1 & 0 \\ 0 & 0 & 0 & -1 \end{bmatrix} \right] U(s)\mathbf{E}_0 = \mathbf{M}_2 [s\omega \mathbf{H}_{01} + \omega^2 \mathbf{H}_{02}] U(s)\mathbf{E}$$

where

$$U(s) = L[\sin(\omega t)] = \frac{\omega}{s^2 + \omega^2}, \quad \mathbf{E} = \begin{bmatrix} \mathbf{E}_0 \\ \mathbf{E}_1 \end{bmatrix}; \quad \mathbf{E}_0 = \begin{bmatrix} \varepsilon \cos \phi \\ \varepsilon \sin \phi \\ \tau \cos \psi \\ \tau \sin \psi \end{bmatrix}, \quad \mathbf{E}_1 = \begin{bmatrix} \lambda_1 \cos \phi_1 \\ \lambda_1 \sin \phi_1 \\ \lambda_2 \cos \phi_2 \\ \lambda_2 \sin \phi_2 \end{bmatrix}$$

$$\mathbf{H}_{01} = \begin{bmatrix} 1 & 0 & 0 & 0 \\ 0 & 1 & 0 & 0 \\ 0 & 0 & 0 & -1 \\ 0 & 0 & 1 & 0 \end{bmatrix}, \quad \mathbf{H}_{02} = \begin{bmatrix} 0 & -1 & 0 & 0 \\ 1 & 0 & 0 & 0 \\ 0 & 0 & -1 & 0 \\ 0 & 0 & 0 & -1 \end{bmatrix}$$

$\mathbf{0}$ is 4×4 zero matrix.

Second term of the right-hand term

$$\mathbf{M} \mathbf{L} \mathbf{L}[\ddot{\mathbf{x}}_r] = \frac{-\omega^2}{s^2 + \omega^2} \mathbf{M} \mathbf{L} \begin{bmatrix} \lambda_1 (s \cos \phi_1 - \omega \sin \phi_1) \\ \lambda_1 (\omega \cos \phi_1 + s \sin \phi_1) \\ \lambda_2 (s \cos \phi_2 - \omega \sin \phi_2) \\ \lambda_2 (\omega \cos \phi_2 + s \sin \phi_2) \end{bmatrix} = \mathbf{M} \mathbf{L} [s\omega \mathbf{H}_{11} + \omega^2 \mathbf{H}_{12}] U(s)\mathbf{E}$$

where

$$\mathbf{H}_{11} = \begin{bmatrix} -1 & 0 & 0 & 0 \\ 0 & -1 & 0 & 0 \\ 0 & 0 & -1 & 0 \\ 0 & 0 & 0 & -1 \end{bmatrix}, \quad \mathbf{H}_{12} = \begin{bmatrix} 0 & 1 & 0 & 0 \\ -1 & 0 & 0 & 0 \\ 0 & 0 & 0 & 1 \\ 0 & 0 & -1 & 0 \end{bmatrix}$$

Third term of the right-hand term

$$\omega \mathbf{M}_1 \mathbf{L} \mathbf{L}[\dot{\mathbf{x}}_r] = \frac{\omega^2}{s^2 + \omega^2} \mathbf{M}_1 \mathbf{L} \begin{bmatrix} -\lambda_1 (\omega \cos \phi_1 + s \sin \phi_1) \\ \lambda_1 (s \cos \phi_1 - \omega \sin \phi_1) \\ -\lambda_2 (\omega \cos \phi_2 + s \sin \phi_2) \\ \lambda_2 (s \cos \phi_2 - \omega \sin \phi_2) \end{bmatrix} = \omega U(s) \mathbf{M}_1 \mathbf{L} \begin{bmatrix} -\omega & -s & 0 & 0 \\ s & -\omega & 0 & 0 \\ 0 & 0 & -\omega & -s \\ 0 & 0 & s & -\omega \end{bmatrix} \mathbf{E}_1$$

$$= \omega \mathbf{M}_1 \mathbf{L} [s\mathbf{H}_{21} + \omega \mathbf{H}_{22}] U(s)\mathbf{E}$$

where

$$\mathbf{H}_{21} = \begin{bmatrix} 0 & -1 & 0 & 0 \\ 1 & 0 & 0 & 0 \\ 0 & 0 & 0 & -1 \\ 0 & 0 & 1 & 0 \end{bmatrix}, \mathbf{H}_{22} = \begin{bmatrix} -1 & 0 & 0 & 0 \\ 0 & -1 & 0 & 0 \\ 0 & 0 & -1 & 0 \\ 0 & 0 & 0 & -1 \end{bmatrix}$$

Fourth term of the right-hand term

$$\begin{aligned} \mathbf{GL}[\mathbf{x}_r] &= \frac{1}{s^2 + \omega^2} \mathbf{G} \begin{bmatrix} \lambda_1 (s \cos \phi_1 - \omega \sin \phi_1) \\ \lambda_1 (\omega \cos \phi_1 + s \sin \phi_1) \\ \lambda_2 (s \cos \phi_2 - \omega \sin \phi_2) \\ \lambda_2 (\omega \cos \phi_2 + s \sin \phi_2) \end{bmatrix} = \frac{U(s)}{\omega} \mathbf{G} \begin{bmatrix} s & -\omega & 0 & 0 \\ \omega & s & 0 & 0 \\ 0 & 0 & s & -\omega \\ 0 & 0 & \omega & s \end{bmatrix} \mathbf{E}_1 \\ &= \mathbf{G} \left[s \frac{1}{\omega} \mathbf{H}_{31} + \mathbf{H}_{32} \right] U(s) \mathbf{E} \end{aligned}$$

where

$$\mathbf{H}_{31} = \begin{bmatrix} 1 & 0 & 0 & 0 \\ 0 & 1 & 0 & 0 \\ 0 & 0 & 1 & 0 \\ 0 & 0 & 0 & 1 \end{bmatrix}, \mathbf{H}_{32} = \begin{bmatrix} 0 & -1 & 0 & 0 \\ 1 & 0 & 0 & 0 \\ 0 & 0 & 0 & -1 \\ 0 & 0 & 1 & 0 \end{bmatrix}$$

In the end, we obtain the Laplace transforms of equation (7) as follows:

$$\left[\mathbf{M} \mathbf{L} s^2 + (\omega \mathbf{M}_1 \mathbf{L} + \mathbf{F} \mathbf{K}_D) s + (\mathbf{F} \mathbf{K}_P + \mathbf{G}) + \mathbf{F} \mathbf{K}_I \frac{1}{s} \right] \hat{\mathbf{X}}(s) = [\mathbf{H}_1(\omega) s + \mathbf{H}_2(\omega)] U(s) \mathbf{E} \quad (11)$$

where

$$\mathbf{H}_1(\omega) = \omega \mathbf{M}_2 \mathbf{H}_{01} + \omega \mathbf{M} \mathbf{L} \mathbf{H}_{11} + \omega \mathbf{M}_1 \mathbf{L} \mathbf{H}_{21} + \frac{1}{\omega} \mathbf{G} \mathbf{H}_{31}$$

$$\mathbf{H}_2(\omega) = \omega^2 \mathbf{M}_2 \mathbf{H}_{02} + \omega^2 \mathbf{M} \mathbf{L} \mathbf{H}_{12} + \omega^2 \mathbf{M}_1 \mathbf{L} \mathbf{H}_{22} + \mathbf{G} \mathbf{H}_{32}$$

(2) Discrete-time system from continuous time system using the Bilinear z transformation

Substituting equation (12) to equation (11) to take the bilinear z transform of equation (11), we obtain the equation in the z plane as equation (13):

$$s = 2(1 - z^{-1}) / T(1 + z^{-1}) \quad (12)$$

$$[\mathbf{W}_0 + \mathbf{W}_1 z^{-1} + \mathbf{W}_2 z^{-2} + \mathbf{W}_3 z^{-3}] \hat{\mathbf{X}}(z) = [\mathbf{U}_0 + \mathbf{U}_1 z^{-1} + \mathbf{U}_2 z^{-2} + \mathbf{U}_3 z^{-3}] U(z) \mathbf{E} \quad (13)$$

where

$$\begin{cases} \mathbf{W}_0 = 8\mathbf{M} \mathbf{L} + 4T(\omega \mathbf{M}_1 \mathbf{L} + \mathbf{F} \mathbf{K}_D) + 2T^2(\mathbf{F} \mathbf{K}_P + \mathbf{G}) + T^3 \mathbf{F} \mathbf{K}_I \\ \mathbf{W}_1 = -24\mathbf{M} \mathbf{L} - 4T(\omega \mathbf{M}_1 \mathbf{L} + \mathbf{F} \mathbf{K}_D) + 2T^2(\mathbf{F} \mathbf{K}_P + \mathbf{G}) + 3T^3 \mathbf{F} \mathbf{K}_I \\ \mathbf{W}_2 = 24\mathbf{M} \mathbf{L} - 4T(\omega \mathbf{M}_1 \mathbf{L} + \mathbf{F} \mathbf{K}_D) - 2T^2(\mathbf{F} \mathbf{K}_P + \mathbf{G}) + 3T^3 \mathbf{F} \mathbf{K}_I \\ \mathbf{W}_3 = -8\mathbf{M} \mathbf{L} + 4T(\omega \mathbf{M}_1 \mathbf{L} + \mathbf{F} \mathbf{K}_D) - 2T^2(\mathbf{F} \mathbf{K}_P + \mathbf{G}) + T^3 \mathbf{F} \mathbf{K}_I \end{cases}$$

$$\begin{cases} U_0 = 4TH_1(\omega) + 2T^2H_2(\omega) \\ U_1 = -4TH_1(\omega) + 2T^2H_2(\omega) \\ U_2 = -4TH_1(\omega) - 2T^2H_2(\omega) \\ U_3 = 4TH_1(\omega) - 2T^2H_2(\omega) \end{cases}$$

T is the sampling period

As z is unit delay, following relations are given:

$$\begin{aligned} z^{-i}\hat{\mathbf{X}}_k(z) &= \mathbf{X}_{k-i}(z) = \hat{\mathbf{x}}(k-i) \\ z^{-i}U_k(z) &= U_{k-i}(z) = u(k-i) \end{aligned}$$

Substituting the upper equations to equation (13), we obtain the equation in the discrete-time system

$$\begin{aligned} & \mathbf{W}_0\hat{\mathbf{x}}(k) + \mathbf{W}_1\hat{\mathbf{x}}(k-1) + \mathbf{W}_2\hat{\mathbf{x}}(k-2) + \mathbf{W}_3\hat{\mathbf{x}}(k-3) \\ &= [\mathbf{U}_0u(k) + \mathbf{U}_1u(k-1) + \mathbf{U}_2u(k-2) + \mathbf{U}_3u(k-3)]\mathbf{E} \end{aligned} \quad (14)$$

Replacing the left-hand term and the parenthesized term in the right-hand term of equation (14) by $\mathbf{W}(k)$, $\mathbf{U}(k)$ and substituting $\mathbf{W}(k)$, $\mathbf{U}(k)$ to equation (14), we obtain equation (15).

$$\begin{aligned} \mathbf{W}(k) &= \mathbf{W}_0\mathbf{x}(k) + \mathbf{W}_1\mathbf{x}(k-1) + \mathbf{W}_2\mathbf{x}(k-2) + \mathbf{W}_3\mathbf{x}(k-3) \quad \mathbf{U}(k) = \mathbf{U}_0u(k) + \mathbf{U}_1u(k-1) + \mathbf{U}_2u(k-2) + \mathbf{U}_3u(k-3) \\ \mathbf{W}(k) &= \mathbf{U}(k)\mathbf{E} \quad (k=1 \dots n) \end{aligned} \quad (15)$$

In equation (15), the left-hand term $\mathbf{W}(k)$ is determined from the dynamic parameters of the rotor and AMB, the sampling period and the measured shaft displacement including the sensor runout and also the $\mathbf{U}(k)$ in the right-hand term is determined from the dynamic parameters of the rotor and AMB, the sampling period and the rotating speed. \mathbf{E} is an unknown vector, of which element are unknown unbalance and sensor runout and can be identified by the incremental least-square method.

(3) the incremental least-square method

As we may use n sets of $\mathbf{W}(k)$, $\mathbf{U}(k)$ ($k=1 \dots n$) and get $4n$ equations in equation (16) to identify the unknown vector \mathbf{E} so that we employ the incremental least-square method to estimate the unbalance and the sensor runout.

$$\mathbf{W} = \mathbf{U}\mathbf{E} \quad (16)$$

where

$$\mathbf{W} = [\mathbf{W}(1) \quad \mathbf{W}(2) \quad \dots \quad \mathbf{W}(n)]^T, \quad \mathbf{U} = [\mathbf{U}(1) \quad \mathbf{U}(2) \quad \dots \quad \mathbf{U}(n)]^T$$

In order to minimize the estimation error, a following quadratic cost function J is introduced and \mathbf{E} is determined by minimizing the cost function J .

$$J = \mathbf{R}^T \mathbf{R}$$

where $\mathbf{R} = \mathbf{W} - \mathbf{U}\mathbf{E}$ is the estimation error.

Its minimum satisfies

$$\frac{\partial J}{\partial \mathbf{E}} = -2\mathbf{U}^T \mathbf{W} + 2\mathbf{U}^T \mathbf{U} \mathbf{E} = 0$$

, which gives

$$\mathbf{E} = (\mathbf{U}^T \mathbf{U})^{-1} \mathbf{U}^T \mathbf{W}$$

provided of course the inverse $(U^T U)^{-1}$ exists.

The incremental least square on-line method is applied to identify. The incremental least square on-line algorithm^(13,14) is given as follows:

$$\hat{E}(k) = \hat{E}(k-1) + P(k)U^T(k)q(k) \quad (17)$$

where

$$q(k) = W(k) - U(k)\hat{E}(k-1), \quad Q(k) = [I + U(k)P(k-1)U^T(k)]^{-1}$$

$$P(k) = P(k-1) - P(k-1)U^T(k)Q(k)U(k)P(k-1)$$

5. IDENTIFICATION RESULTS USING SIMULATION DATA

Numerical simulation of the rotor vibration excited by the unbalance and levitated by the AMB including the measurement error caused by the AMB sensor runout is carried out to evaluate the proposed method for estimation of the unbalance and the sensor runout on the rotor. The Runge-Kutta method is employed and the condition of the numerical simulation is tabulated in table 2. 1000 data on the rotor displacement are calculated at each bearing at 500rpm and 1500rpm. Sampling period is set to be 1.7msec. The calculated vibrations at both bearings are shown in figure 5

Table. 2 Condition of numerical simulation

	Rotating speed (rpm)	Sampling period (m sec)	Number of data
First data	500	1.7	500
Second data	1500	1.7	500

The unbalance and the sensor runout are identified by the algorithm in equation (17) using the simulated vibration data. The convergent process of the identification of the unbalance and the sensor runout is shown in figure 6. In this figure, the left side figures and the right side figures show the amplitude and the phase angles of the unbalance and the sensor runout respectively and the abscissa shows sampled data number. Solid lines indicate the identified values of the identifying parameters and dotted straight lines are given values, namely static unbalance $\varepsilon = 2.0\mu\text{m}$, coupled unbalance $\tau = 0.6 \times 10^{-4}\text{rad}$, sensor runout of bearing 1 $\lambda_1 = 1.1\mu\text{m}$ and sensor runout of bearing 2 $\lambda_2 = 2.2\mu\text{m}$.

Just after a change of the rotating speed from 500rpm to 1500rpm, all gains and phase angles of the identified parameters converge to the given values rapidly. From this numerical result, we confirm that the unbalance and the sensor runout on the AMB rotor may be identified by the proposed rotor model and the incremental least-square method.

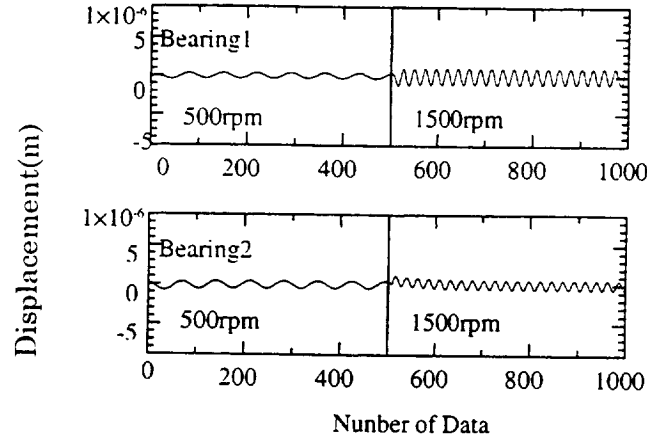


Fig.5 Time series data of calculated rotor displacement

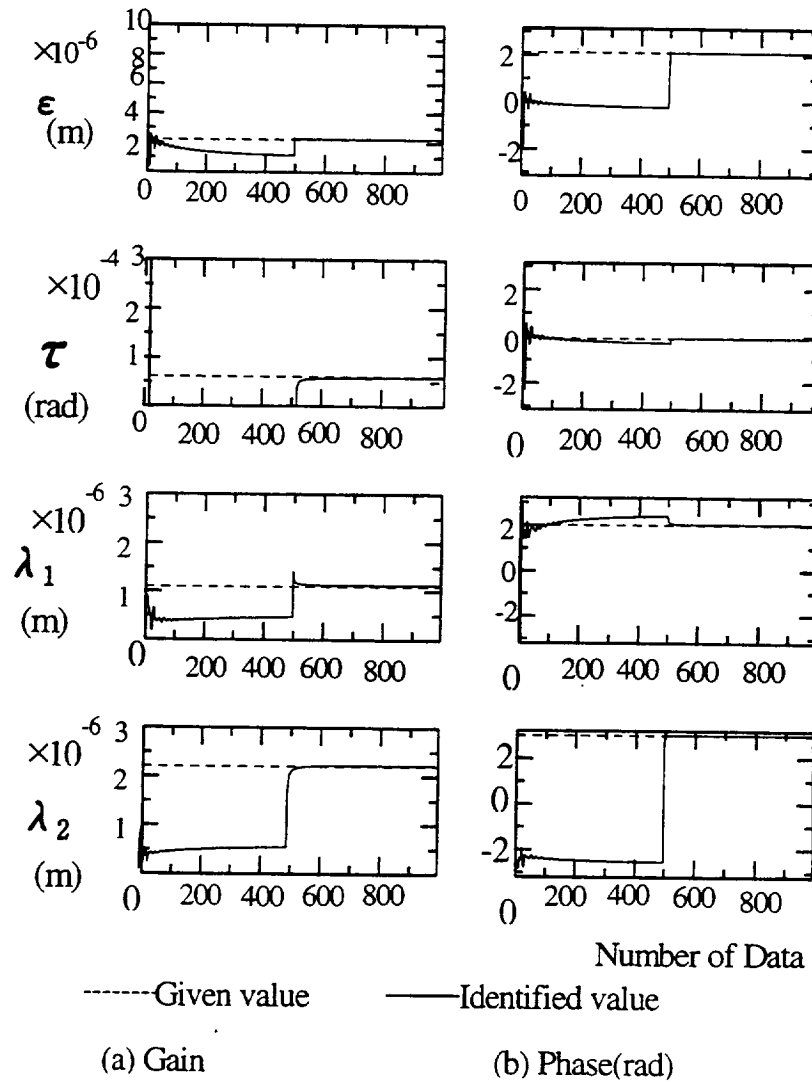


Fig 6 Identification process using the numerical simulation results.

6. IDENTIFICATION RESULTS USING MEASURED DATA OF TMP ROTOR

Figure 7 shows measured rotor vibration at the upper bearing(1) and the lower bearing(2) at 496rpm and 1498rpm. The sampling period is set to be 1.668ms and 1000 data of shaft vibration at both AMB are sampled and used for the identification.

In the figure these time series data seem to include high-order component caused by high-order component of the sensor runout. But in this study, the high-order components in the vibration data are ignored and only the synchronous component of the sensor runout is identified in the identification algorithm because the effect of the high-order components of sensor runout does not have any effect on the synchronous vibration and the high-order component may be estimated separately. We will propose a method for identifying the high-order component in next paper.

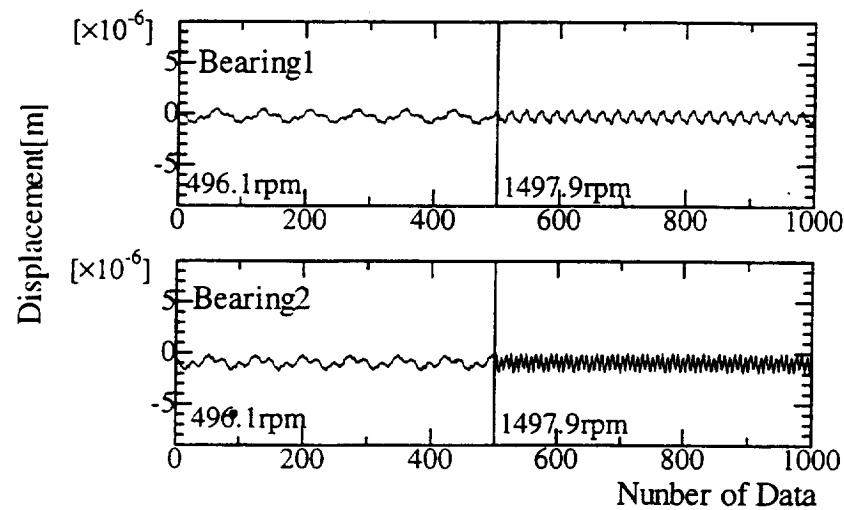


Fig. 7 Measured shaft vibration of the tested rotor before attaching trial weight

Table.3 Data of attached unbalance

Mass m_0 (g)	0.53
Distance from x axis l_0 (mm)	59.5
Distance from z axis r_0 (mm)	51.0

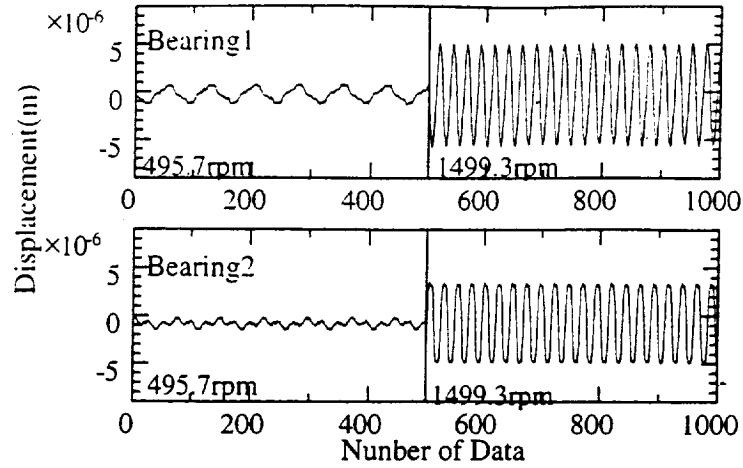


Fig. 8 Measured shaft vibration of the tested rotor after attaching trial weight

Figure 9 shows converging process of the identification of the static unbalance ε , coupled unbalance τ , bearing1 runout τ_1 and bearing2 runout τ_2 . The identified gain and phase angle of the initial unbalance and the initial sensor runout are presented by slender solid lines in figure 9.

Unfortunately, we could not measure the initial unbalance of the tested rotor and the runout of the AMB sensor, so we try to identify the change of the unbalance between before and after attaching a known trial weight on outer surface of the dummy disk. The weight and the location of the attached unbalance is tabulated in table 3.

The measured time-series data of the vibration at the bearing 1 and 2 are measured in the same condition as figure 7 and are illustrated in figure 8. The identified gain and phase angle of the unbalance and the sensor runout are presented by bold solid lines in figure 9 using these data measured after attaching the trial weight.

In figure 9 dotted lines indicate the gain and phase angle of the parameters obtained by **vectorial** addition of the identified unbalance before attaching the weight and the attached weight so the difference between the bold solid lines and the dotted lines indicates the identification error. As we do not change the sensor runout especially so the estimated sensor runout after the attachment of the trial weight is reasonably same as before the attachment. In figure 9, the gains and the phase angles of λ_1 and λ_2 after attachment of the trial weight coincide with that before attachment so the sensor runout is identified correctly by the proposed method.

On the other hand as to the identification of the both unbalance ε and τ , there is a slight difference between the bold solid lines and the dotted lines in figure 9.

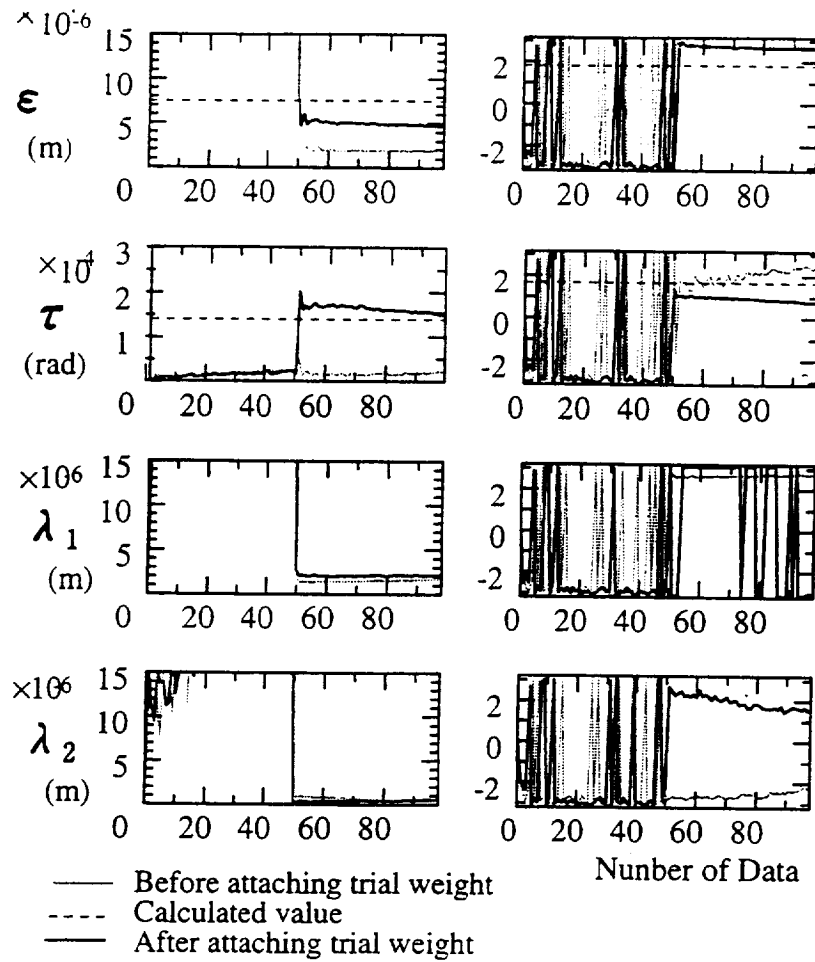


Fig 9 Identification process using the experimental results.

7. CONCLUSIONS

We have developed the equation of motion of the rigid rotor supported by active magnetic bearings in consideration of the static and coupled unbalances and the sensor runout and proposed an identification method of the unbalance and the sensor runout simultaneously.

The numerical simulations and the experiments carried out here on unbalance response of the rotor have shown that the proposed method is effective for identifying the unbalance and the sensor runout on the AMB rotor.

REFERENCES

- (1) Y.Kanemitsu, Non-contact Sensor of Shaft Vibration and its Problem,
Journal of JSME, Vol.80, No.706,(1977)
- (2) Y.Kanemitsu, et.al., Real Time Balancing of a Flexible Rotor supported by magnetic bearing,
proc. 2nd int. symp.on magnetic bearings,(1990)
- (3) S.Sagara, et al., System Identification, SICE (1981)
- (4) T.Nakamizo, Signal Analysis and System Identification, korona-sya (1988)
- (5) S.Beale, et al., Adaptive Forced Balancing for Magnetic Bearing Systems,
Rpoc. 3rd int. symp.on magnetic bearings (1992)

Session 10 -- Modeling 2

Chairman: Colin P. Britcher
Old Dominion University (ODU)

LINEAR AND NONLINEAR ANALYSIS OF MAGNETIC BEARING BANDWIDTH DUE TO EDDY CURRENT LIMITATIONS

Andrew Kenny
Dr. Alan Palazzolo
Department of Mechanical Engineering
Vibration Control and Electromechanics Laboratory
Texas A&M University
College Station, TX 77840

SUMMARY

Finite element analysis was used to study the bandwidth of alloy hyperco50a and silicon iron laminated rotors and stators in magnetic bearings. A three dimensional model was made of a heteropolar bearing in which all the flux circulated in the plane of the rotor and stator laminate. A three dimensional model of a plate similar to the region of a pole near the gap was also studied with a very fine mesh. Nonlinear time transient solutions for the net flux carried by the plate were compared to steady state time harmonic solutions. Both linear and quasi-nonlinear steady state time harmonic solutions were calculated and compared. The finite element solutions for power loss and flux bandwidth were compared to those determined from classical analytical solutions to Maxwell's equations.

INTRODUCTION

Several commercial finite element codes which solve electromagnetic problems include both a steady state time harmonic solver and a time transient solver. Both of these include the induced eddy currents in the solution. Analysis with a time harmonic solver has the advantage that a single solution predicts the response at given frequency. For a magnetic bearing supporting a shaft running at a steady speed, the time harmonic solver would be the most desirable choice since the time transient solver requires many solutions in the form of time steps for at least one period of the control signal.

The purpose of this study was to determine how much the time harmonic solver's inability to accurately model nonlinear flux saturation would affect the bandwidth and power loss predictions for most cases of magnetic bearing analysis. It was expected that flux saturation might affect the solution in two ways. The first would be due to the concentration of flux near the laminate surfaces due to eddy current skin effect. Second, magnetic bearings generally run with a control flux superposed on a bias flux. Time harmonic solvers can't include the effect of the DC bias flux.

NOMENCLATURE

α = parameter defined by skin depth
 δ = skin depth of eddy current
 μ = material permeability
 σ = material conductivity
 ω = frequency in radians per second
 d = laminate thickness
 B = time varying magnetic flux density
 E = time varying electric field intensity
 H = time varying magnetic field
 \tilde{H} = complex magnitude and phase of time harmonic magnetic field
 J_f = time varying free conducting electron current density
 \tilde{J}_f = complex magnitude and phase of time harmonic current density

THEORY

Magnetic bearings may be expected to support shafts turning at 120,000 rpm or more. This frequency of 2,000 Hz is low enough that the displacement current term, dD/dt , in Ampere's Law may be neglected. For this reason the four quasistatic Maxwell's equations given by equations 1 to 4 are used to model the induced field and eddy current in magnetic bearings [1].

$$\nabla \times \bar{H} = \bar{J}_f \quad (1)$$

$$\nabla \times \bar{E} = -\frac{\partial \bar{B}}{\partial t} \quad (2)$$

$$\nabla \cdot \bar{B} = 0 \quad (3)$$

$$\nabla \cdot \bar{J}_f = 0 \quad (4)$$

The analysis of eddy currents induced in a laminate by a changing magnetic field begins with the derivation of the diffusion equation [2,3]. This is done by combining the constitutive material laws, $B=\mu H$, and $J_f=\sigma E$, with equations (1) to (4), and then taking the curl of Equation (1) as given by equation (5).

$$\nabla \times \nabla \times \bar{H} = \nabla(\nabla \cdot \bar{H}) - \nabla^2 \bar{H} = \nabla \times J_f \quad (5)$$

After the substitutions this becomes the diffusion equation given by (6).

$$\nabla^2 \bar{H} = \mu\sigma \frac{\partial \bar{H}}{\partial t} \quad (6)$$

The solution to equation (6) is used to compute the induced eddy currents by using equation (1).

Equations (1) and (2) are intertwined by the material constitutive laws so that in a conductive material, the induced eddy currents cause their own magnetic fields which cancel the original external field and effectively shield deeper material from any magnetic field. The effect is that the magnetic flux and eddy currents are concentrated on the surface. To get a quantitative estimate of this effect in the laminates of magnetic bearings, equation (6) can be solved with the boundary conditions of a flat plate.

Figure 1 shows a conducting laminate in which the magnetic and electric fields are induced by a sinusoidal external magnetic field. The internal field must be the solution to equation (6) reduced to one dimension as shown by equation (7).

$$\frac{\partial^2 H_y}{\partial x^2} = \mu\sigma \frac{\partial H_y}{\partial t} \quad (7)$$

The general solution to equation (7) is equation (8) where H tilde has both a magnitude and phase. The spatial variation of H tilde depends on both the initial conditions and the boundary conditions. For the two sided plate shown in Figure 1 the magnetic field is given by equation (9). It follows from equation (1) that the eddy currents are described by equation (10). Alpha is defined in terms of the skin thickness, delta, as given by equations (10) and (11)

$$H_y = \tilde{H}_y(x) e^{j\omega t} \quad (8)$$

$$\tilde{H}_y(x) = H_o \frac{\cosh(\alpha x)}{\cosh(\alpha d/2)} \quad (9)$$

$$\tilde{J}_z(x) = \alpha H_o \frac{\sinh(\alpha x)}{\cosh(\alpha d/2)} \quad (10)$$

$$\alpha = \frac{1+j}{\delta} \quad (11)$$

$$\delta = \sqrt{\frac{2}{\omega\mu\sigma}}$$

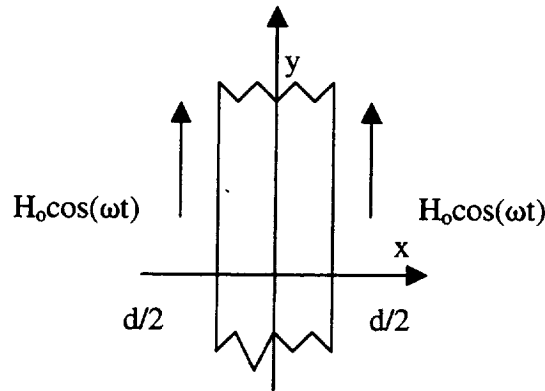


Figure 1. Sketch of Infinite Plate and Magnetic Fields

The eddy current losses per unit area of the laminate can be calculated from the integral given by equation (13). The star indicates complex conjugate. Utilizing the current density distribution given by equation (10) and performing the integration results in the power loss expression of equation (14). A plot of the power loss in a laminate of alloy Hyperco50a is given in Figure 2.

$$P = \frac{1}{2} \int_{-\frac{d}{2}}^{\frac{d}{2}} \frac{\tilde{J}_z \tilde{J}_z^*}{\sigma} dx \quad (13)$$

$$P = \frac{H_o^2}{\sigma \delta} \left[\frac{\sinh\left(\frac{d}{\delta}\right) - \sin\left(\frac{d}{\delta}\right)}{\cosh\left(\frac{d}{\delta}\right) + \cos\left(\frac{d}{\delta}\right)} \right] \quad (14)$$

There are two regions to the curve given by figure (2). For laminates less than about 2 skin depths thick, the eddy currents are too low to cause their own magnetic field and reduce the magnetic field penetrating the conductor. In this region of the curve, the power loss is called resistance limited and is proportional to the cube of the laminate thickness.

For laminates with a ratio of laminate thickness to skin depth of more than four, the field induced by surface eddy currents shields the deeper volume of the laminate from the external field. Since the power loss is reduced by the induced eddy currents on the surface, the power loss for thick laminates is termed inductively limited.

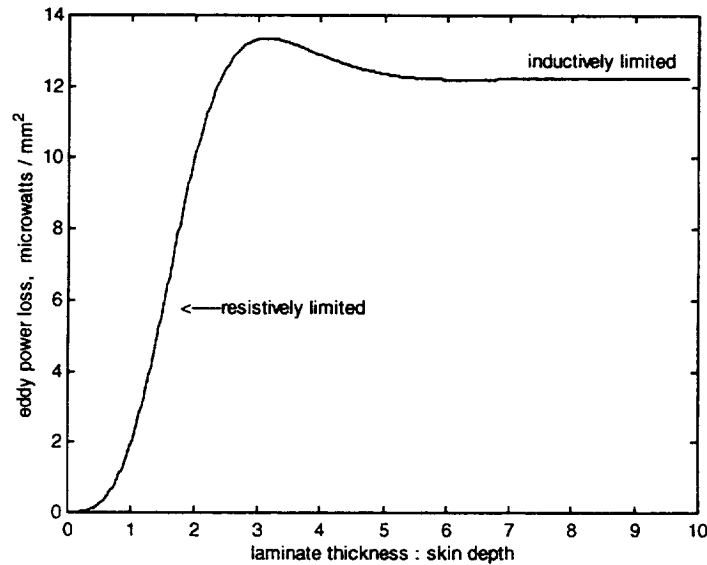


Figure 2. Eddy current loss in Hyperco50a (relative permeability 7500, conductivity 2500 /(ohm*mm)).

FINITE ELEMENT ANALYSIS RESULTS

The eddy current losses in a heteropolar magnetic bearing were analyzed. A bearing of this type is shown in Figure 3. There are several planes of normal and tangential flux symmetry in this bearing. These were taken advantage of to make a finite element model with fewer nodes, finer mesh density, and better aspect ratio. Figure 4 shows the finite element model of the heteropolar bearing used for this study.

The material modeled was a silicon iron with a conductivity of 5500/(ohm-mm) and a relative permeability of 1214. The coil excitation frequency was 100 Hz. At this frequency, the skin depth was .616 mm. The thickness of the laminate was varied from half a skin depth (0.308 mm) to four times the skin depth (1.232 mm). These thicknesses were in the resistive region of the power loss curve, which is where a magnetic bearing would be expected to be operating.

The power loss for the heteropolar bearing includes the stator and rotor laminates. Figure 5 shows the power loss calculated using the steady state ac solver which used a constant relative permeability to calculate the solution. The power loss calculated with the analytical flat plate formula given by equation (14) is shown on the same graph for comparison. The main reason the plots are not the same is that in the heteropolar laminate the value of the magnetic field, H_0 , varies. It is less at the outer circumference of the path and higher near the inner corners. Equation (14) indicates the power loss is very sensitive to the chosen level of the field.

In addition to causing power loss, the eddy currents also causes the magnetic flux to lag the control current as evident in equation (9). The force the bearing exerted on the shaft is proportional to the square of the flux in the air gap. The magnitude and phase of the gap flux was determined from the finite element analysis. Since there are no eddy currents in the gap, the magnitude and phase of the flux in the gap is uniform throughout. Figure 6 shows the effect of laminate thickness on gap flux. Better than 99 percent of the maximum obtainable flux in the gap is reached when the laminate has been reduced to two skin thicknesses.

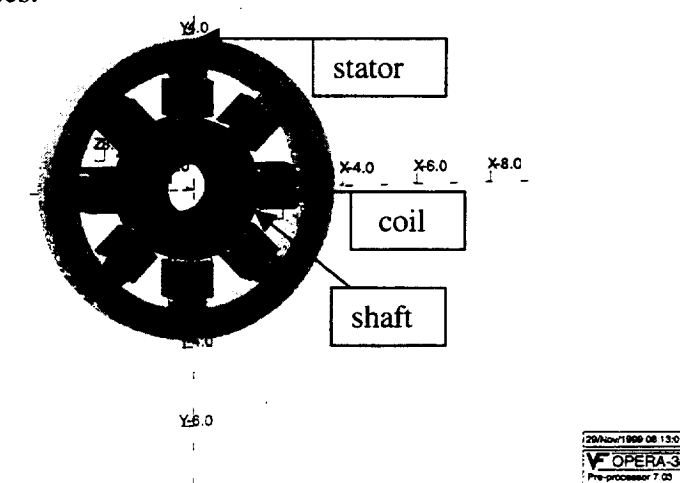


Figure 3. Heteropolar Magnetic Bearing

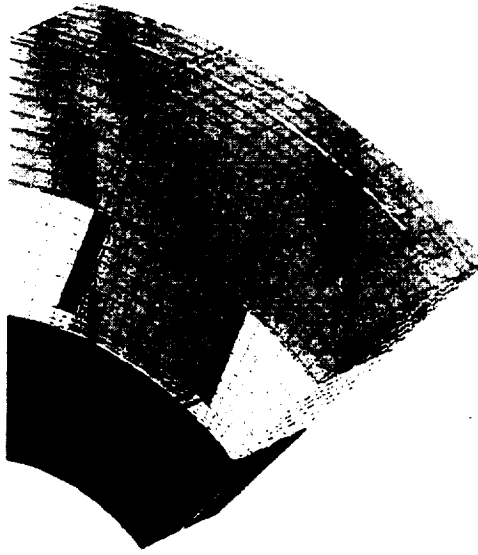


Figure 4. Finite Element Model of Heteropolar Magnetic Bearing. 32000 Nodes, Maximum Element Edge Aspect Ratio 32:1.

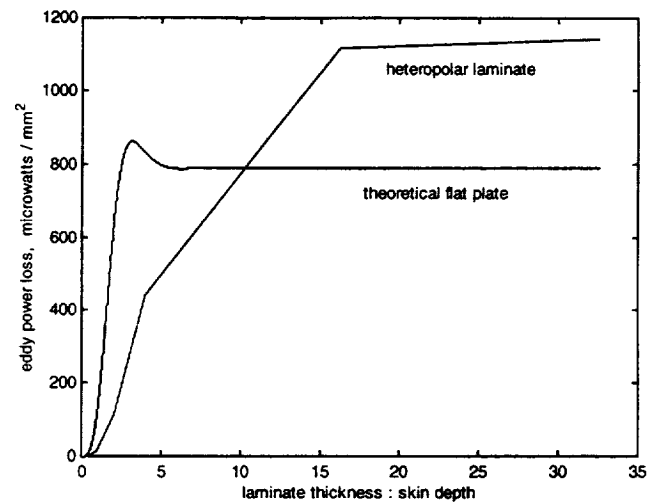


Figure 5. Power Loss in Laminate of Heteropolar Bearing Versus Laminate Thickness. Results of Steady State AC Solver with Constant Relative Permeability. [100 Hz, Peak gap flux .5 T]

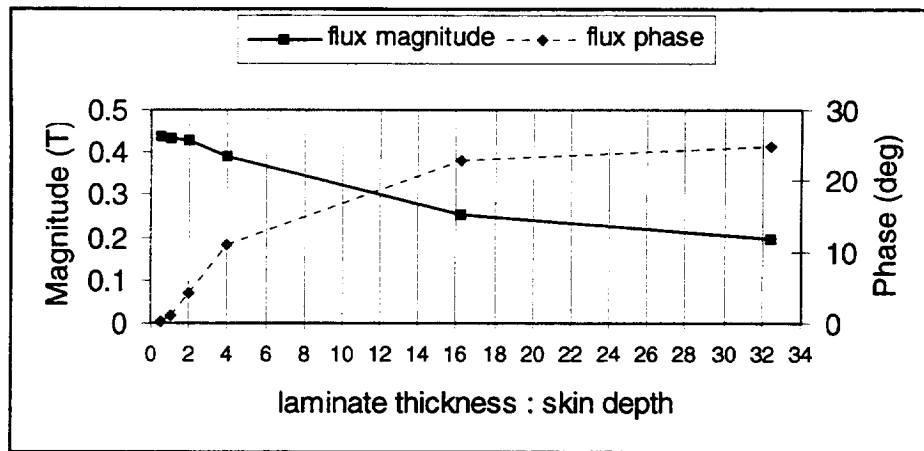


Figure 6. Magnitude and Phase of Flux in Gap of Heteropolar Magnetic Bearing Versus Laminate Thickness.

One of the major motivations for this work was the difficulty in obtaining time transient results using a nonlinear BH curve. For a model as large as that of the heteropolar bearing shown in Figure 4, a linear steady state ac solution could be obtained in a few hours of computer calculation. A time transient model of 64 time steps over two cycles of the control current would take days or weeks. A new model was designed to estimate what the sacrifice in the accuracy of the power loss and flux frequency response would be if the linear steady state ac analysis was performed.

Figure 7 was the new finite element model. It was a plate with zero electrical conductivity butted to a conducting plate. The purpose of this geometry was to transmit an even flux distribution in through the edge of the conducting plate in a similar fashion to flux entering the edge of a stator pole from an air gap.

This model covered a very small area. Each plate is only 5 mm x 5 mm. Only 14000 nodes were needed to model the entire plate with brick elements with an edge length equivalent to the skin depth. For a distance of two skin depths from the plate edges, there were eight elements and the edge length was reduced to one fourth the skin depth for a distance two skin depths. The plate thickness was two skin depths (.734 mm) at 100 Hz with the properties of alloy hyperco50a. Because of symmetry only half the plate thickness needed to be modeled. There were four elements through the half thickness of the model. Therefore, there were four elements through all the outer skin regions. Analyses with successively finer meshes showed this model to produce precise results.

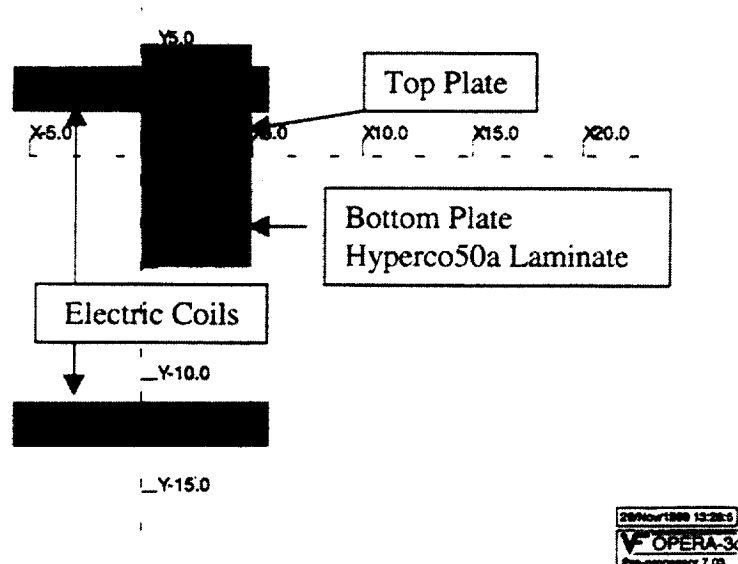


Figure 7. Two Plate, One Fourth Symmetry, Model With Drive Coils.

The power loss and average flux density in the conducting laminate was calculated using three different solvers. First was the steady state linear ac solver, second was the quasi-nonlinear solver, and finally was the time transient nonlinear solver with 50 time steps each equal to one thirty-second of a period of 100 Hz. The quasi-nonlinear solution has the magnetic flux density and magnetic field in phase like similar to the linear solution, but the quasi-nonlinear solver utilizes the nonlinear BH curve and limits the flux from exceeding saturation [4].

The current in the drive coils was set to produce a peak alternating flux of about one tesla. For the steady state analyses this meant the maximum flux was about 1 T and the minimum was -1 T. The time transient analysis included a DC bias flux of 1 T as would be typical in a magnetic bearing. In that case the maximum flux was about 2 T and the minimum about 0 T. Figure 8 shows the nonlinear BH curve used for alloy hyperco50a.

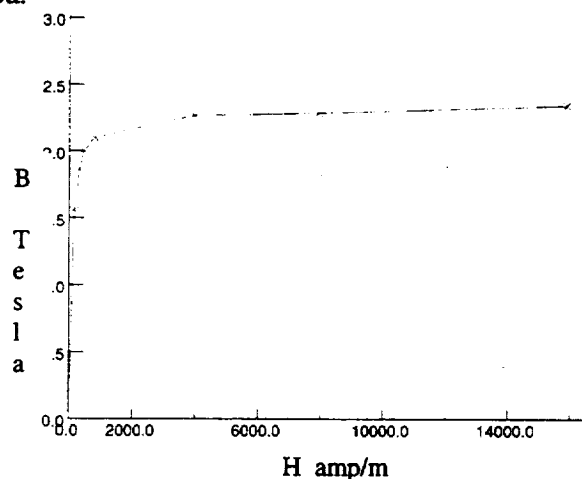


Figure 8. Alloy hyperco50a nonlinear BH curve [5].

A table comparing the energy loss per cycle calculated by each of the three different solvers is shown below. The difference between any of the three solution methods is less than one tenth of one percent. This is especially remarkable considering the plot of the power loss calculated by the nonlinear time transient solution method over one period of the coil current (shown in Figure 9). Although the power loss is only shown over one period of the coil current, further time steps showed these two power loss humps to repeat themselves. The first peak is higher because the flux starts at near zero tesla and reaches a faster rate of change than when the flux decreases from its peak value which is slightly lowered by saturation. The energy loss per cycle was calculated by integrating the area underneath the repeating peaks.

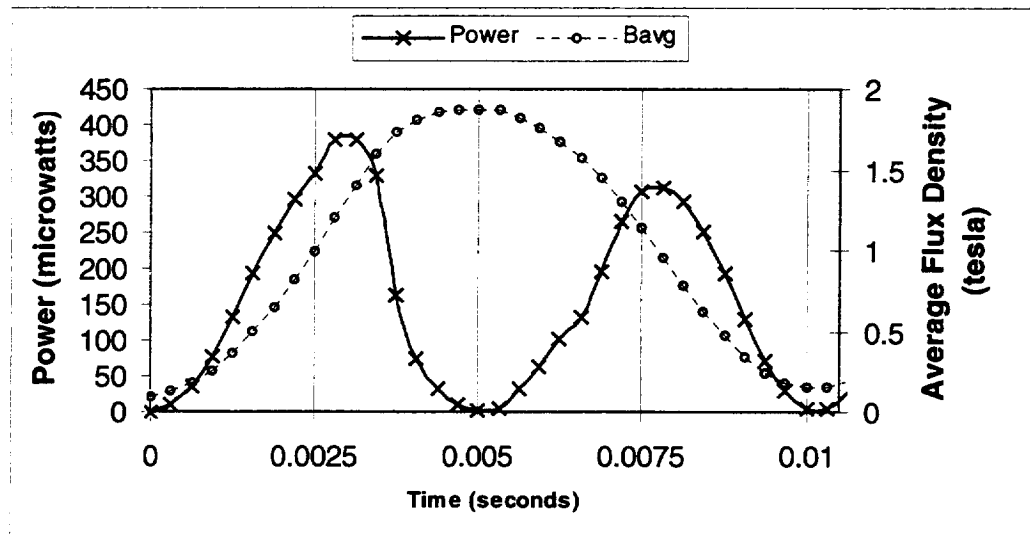


Figure 9. Nonlinear Time Transient Analysis on Two Skin Depth Thick Laminate .

Table 1. Comparison of Eddy Current Energy Loss Per Cycle Computed by Three Methods.

<u>Nonlinear Time Transient</u>	<u>Quasi-nonlinear Steady State</u>	<u>Linear Steady State</u>
1.585 micro Joules	1.579 micro Joules	1.586 micro Joules

Finally the average flux density carried by the conducting plate is shown in the table below as calculated by the three different methods. The average flux density times the plate cross section is the total flux the plate can transport and directly affects the force that can be applied by a laminated heteropolar bearing. Nonlinear saturation reduces the peak flux density calculated by the nonlinear time transient and quasi-nonlinear steady state solvers by 4.6 to 3.2 percent compared to the linear steady state analysis. The phase lag of the average flux density calculated by the time transient analysis varied from zero degrees when increasing to four degrees after peaking and decreasing.

Table 2. Comparison of Average Flux Density Computed by Three Methods.
[Magnitude and Phase Lag].

<u>Nonlinear Time Transient</u>	<u>Quasi-nonlinear Steady State</u>	<u>Linear Steady State</u>
.978 T; 0 to 4 degrees	.965 T; 3.69 deg	1.01 T; 3.66 deg

CONCLUSIONS

A laminate of a heteropolar bearing stator and shaft was modeled with three dimensional finite elements. For laminate thicknesses below two skin depths, both the finite element solution and the theoretical assumption showed the power loss to increase as a resistively limited loss. The finite element linear ac analysis showed that better than 99 percent of the maximum obtainable flux in the gap was achieved with laminates two or less skin depths thick.

A fine mesh model was made to simulate a small section of a laminate in a heteropolar bearing. In the skin regions, element edges were just one fourth of a skin depth in length. The power loss calculated by the nonlinear time transient solver was compared to that computed by a linear steady state ac solver and a quasi-nonlinear steady state ac solver. The comparison showed that the power loss predicted by the steady state ac solvers was the same as the average energy loss per cycle predicted by the nonlinear time transient solver. The nonlinear time transient solver and the quasi-nonlinear steady state ac solver predicted peak values of the AC flux magnitude that differed by just 1.3 percent.

ACKNOWLEDGEMENT

The authors gratefully acknowledge the technical and funding support provided by NASA Glenn Space Power and Dynamics Branch (Albert Kascak, Raymond Beach, and Gerold Montague) and the Office of Naval Research – Naval Surface Warfare Center (Tom Calvert, Lyn Peterson, and Glenn Bell).

BIBLIOGRAPHY

- [1] Wiley Encyclopedia of Electrical and Electronics Engineering, Volume 6, Eddy Currents, 163-178, Eddy Currents, John Wiley, New York, 1999.
- [2] Stoll, R.L., The Analysis of Eddy Currents, Clarendon Press, Oxford, 1974.

- [3] Lammeraner J. , Stafle, M., Eddy Currents, CRC Press, 1964.
- [4] Opera-3d Users Guide, Chapter 3, Time Variation in Electra, Vector Fields Ltd, Oxford, 1999.
- [5] Carpenter Magnetic Alloys, Carpenter Technology Corporation, Carpenter Steel Division, 1995.

A PRECISE FORCE MEASUREMENT IN MAGNETIC BEARINGS FOR DIAGNOSIS PURPOSES

M. Aenis, R. Nordmann
Darmstadt, University of Technology
Department of Mechatronics
aenis@mesym.tu-darmstadt.de
nordmann@mesym.tu-darmstadt.de

ABSTRACT

The aim of the presented project sponsored by the DFG (German Research Council) is to use active magnetic bearings for the diagnosis of centrifugal pumps. Therefore, active magnetic bearings are integrated in a single-stage respectively four-stage pump substituting the conventional ball bearings. The diagnosis procedures are based on evaluating frequency response functions where the active magnetic bearings operate as actuators and as sensors to measure the displacements and the forces induced in the rotating structure. Simulation results of an exemplarily fault applied to the pump system are presented.

For this type of diagnosis using transfer functions, an accurate force measurement is crucial. The paper compares force measurement results and achievable accuracies of a radial magnetic bearing using different measurement techniques over a large operating range. Furthermore, a finite-element model is used to investigate fringing and leakage effects to improve the different measurement techniques. The finite element model allows eccentric rotor positions and non-symmetrical coil current distributions with nonlinear material properties of the stator and rotor part of the magnetic bearing.

INTRODUCTION

Nowadays, the industrial applications of turbomachines demand higher reliability and availability. Therefore, an integrated failure detection becomes increasingly more important in the case of these machines.

Up to now, the monitoring systems are normally not an integral component of turbomachines. They must be additionally acquired by the operators of such machines. In the case of these failure detection systems, the relative and/or absolute motions of the rotor are measured as output signals. After signal processing, certain features (threshold values, orbits, frequency spectra and so forth) are created from the measured data. With the deviations of these features from a faultless initial state, the diagnosis attempts to recognize possible faults. The problem with these procedures is that the causes of the modifications of the

output signal can not be detected clearly. They can either lie in a change of the process or in a modification of the system itself.

An improvement of the existing diagnostic techniques is possible through the use of active magnetic bearings (AMB) in turbomachines (fig. 1). The active magnetic bearings are able to excite rotating shafts without contact and to measure simultaneously the required forces and displacements very precisely. Consequently, frequency response functions (stiffness or compliance frequency responses) can be determined from the measured input and output signals, of which the physical parameters (mass, damping, stiffness) or modal parameters (natural frequencies, eigenmodes, modal damping) of the system are identified.

In the presented project of the Special Research Program (SFB 241) supported by the German Research Council (DFG), it is examined how faults in turbomachines can be diagnosed experimentally with active magnetic bearings. An important role of the development of the fault diagnosis is the precise measurement of the input/output values (motions and forces). The measurement of the displacements by means of the utilised Eddy current probes have reached a sufficient precision. That is not the case for the measurement of the forces applied to rotating structures. In the following, results of different force measurements using magnetic bearings (i-s-method, reluctance network method, Hall sensor method) are compared.

Afterwards, the method of the model based diagnosis is then presented briefly by means of simulation of a selected fault applied to the single-stage pump representing the turbomachine system. Parallel to the numeric computations, a test rig of the single-stage pump (fig. 2) is under construction. This test rig is used to verify and to demonstrate the performance of the developed diagnosis methods. The pump is located between two active magnetic bearings levitating

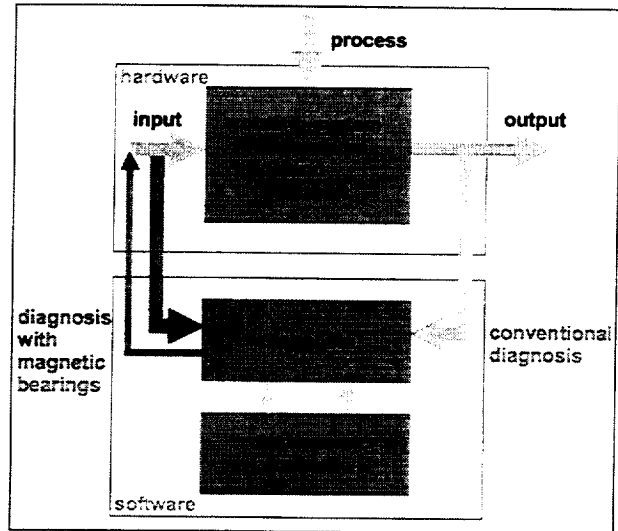


Figure 1. Failure diagnosis with active magnetic bearings.

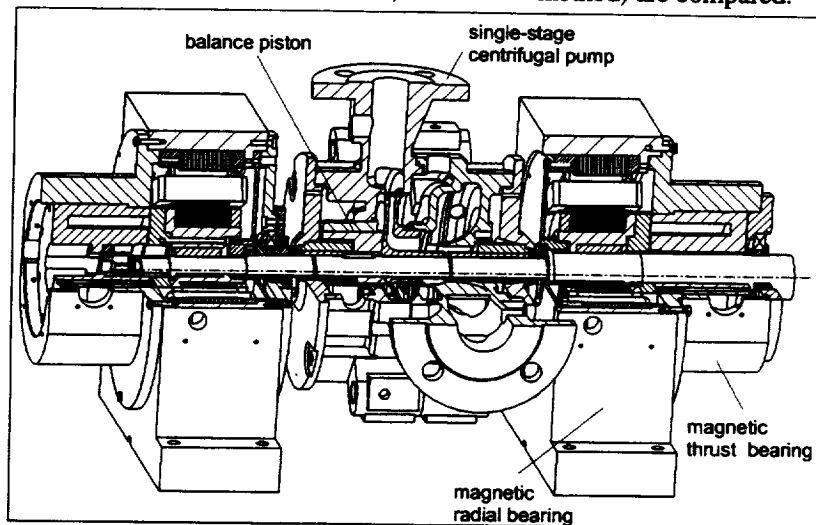


Figure 2. Scheme of the test rig of the single-stage centrifugal pump in active magnetic bearings.

the rotor in five degrees of freedom. Besides the replacement of the conventional roller bearings with the active magnetic bearings, the original pump system remains unchanged. In addition to the two mechanical seals sealing up the hydraulic part, the pump contains two contactless annular seals. One is placed at the suction side and one at the pressure side of the impeller, which is the balance piston. The modular design of the test rig enables an easy extension of the single-stage to a four-stage pump system for future investigations.

FORCE MEASUREMENT WITH MAGNETIC BEARINGS

Description of the Active Magnetic Bearings

Unlike conventional bearing systems, the rotor is carried by a magnetic field. In this case, sensors and controllers are necessary to stabilize the unstable open loop state of the rotor. Therefore, essential dynamic characteristics like stiffness and damping properties are influenced by the controller. The rotor can be moved on almost arbitrarily chosen trajectories independently of the rotation. These can either be harmonic motions in one plane, forward or backward whirls. Additionally, an imbalance compensation can be performed.

A magnetic bearing system consists of four basic components: magnetic actuator, controller, power amplifier, and shaft position sensor. To keep the rotor in the bearing center, the position sensor signal is used as input for an electronic control circuit to adequately adjust the coil currents. As shown in fig. 3, the stator component is normally composed of horseshoe-shaped magnets and the rotor component is a ring

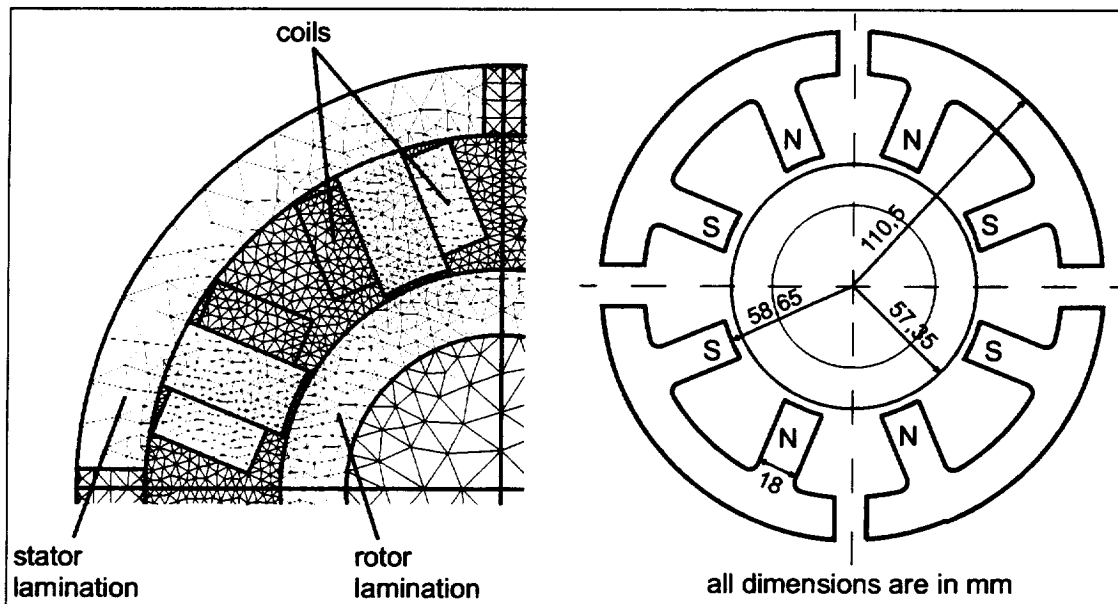


Figure 3. FE-Model and the main dimensions of the stator and rotor laminations of the magnetic bearing.

of magnetic material to complete the magnetic path. The bearing configuration is operated in the so-called differential driving mode [10], where one magnet is driven with the sum of bias current i_0 and control current i_x , and the other one with the difference. Consequently, if the magnetization of the iron is neglected, a linear force-current-displacement relation is obtained. The operation point of the magnetic bearing is determined by the bias current (here $i_0 = 4A$), which is half of the maximum coil current. Figure 3 shows the main geometric data of the bearings used. The material carrying the magnetic flux consists of SiFe-laminations with typically nonlinear soft magnetic material behavior.

Force-Current-Displacement Characteristic of the Magnetic Bearings

The setup for the measurements to compare the different measurement techniques is shown in figure 4 and is explained in detail in the work done by Knopf et al. [6]. An external load cell is used to obtain a reference force F_{ref} . While the rotor is floating in the active magnetic bearings, different external static forces F_{ref} are applied (starting with positive maximum force until negative and back). This procedure is performed for different rotor positions. The data of the external forces, coil currents, and rotor positions are recorded simultaneously. Figure 5 shows the resulting measured static force-current-displacement characteristic for one axis of the radial magnetic bearing. Dynamic effects like eddy currents are neglected in this paper and will not be considered in the following.

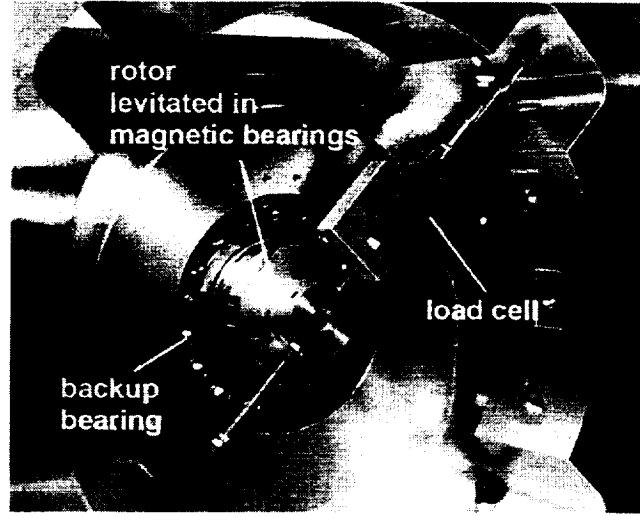


Figure 4. Setup for the force measurement of the external loads applied to the levitated rotor.

The necessary magnetic bearing forces F_{AMB} to compensate the externally applied forces F_{ref} are determined in different ways. In general, the magnetic force F_{AMB} can be computed from

$$\vec{F}_{AMB} = \frac{A_{pole}}{2\mu_0} \sum_k \vec{B}_{pole_k}^2, \quad (1)$$

assuming a uniform flux density in every flux-carrying cross-section and no flux fringing at the tip of the poles. In equation (1), A_{pole} stands for the cross-section of the poles carrying the flux densities B_{pole_k} . Where B_{pole_k} are the fluxes at the different magnetic poles. μ_0 means the magnetic permeability of vacuum. Hence, the entire force of the radial bearing results from the sum of the individual forces of each pole.

i-s-Method

Using magnetic bearings in differential driving mode [10], equation (1) can be linearized leading to the well-known equation

$$F_x = k_i i_x + k_s s_x \quad (2)$$

where i_x is the control current in the x-direction, s_x is the rotor displacement in the x-direction, and N represents the number of coil turns. The linearization constants k_i , k_s depend on the chosen design point of the magnetic bearings (i_0 , s_0) and are computed using the following equations

$$k_i = \frac{\mu_0 N^2 A_{pole} \cos(\pi/8) i_0}{s_0^2} \quad (3)$$

$$k_s = \frac{\mu_0 N^2 A_{pole} (\cos(\pi/8))^2 i_0^2}{s_0^3} \quad (4)$$

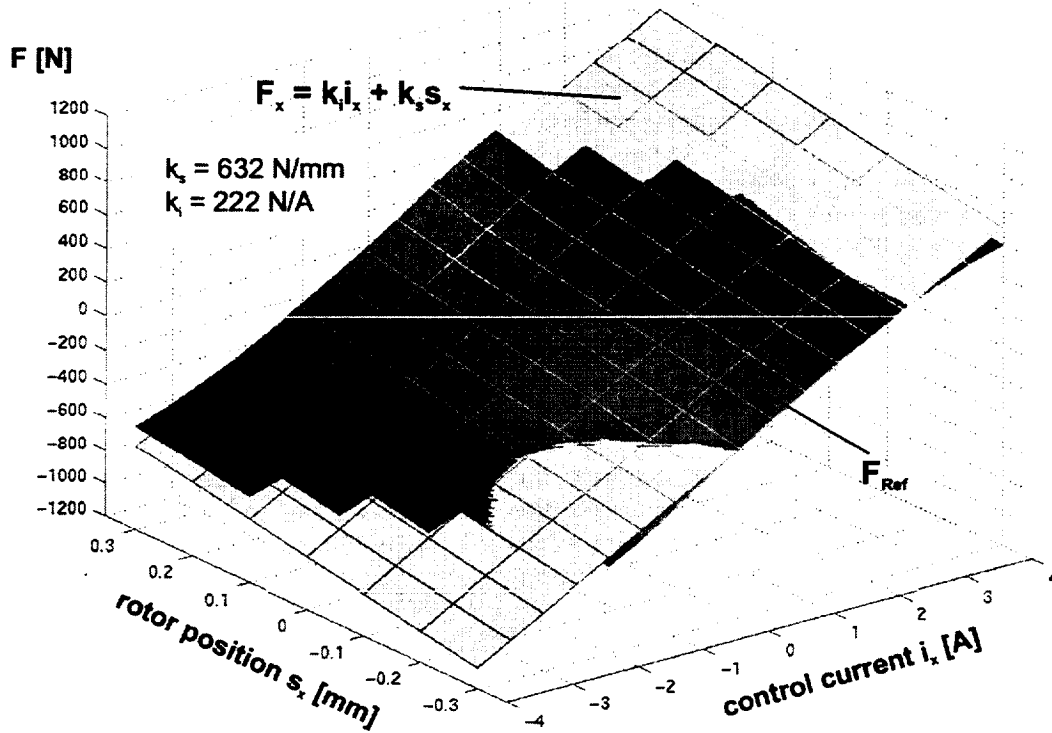


Figure 5. Measured and linearized force-current-displacement characteristic for one magnetic bearing axis.

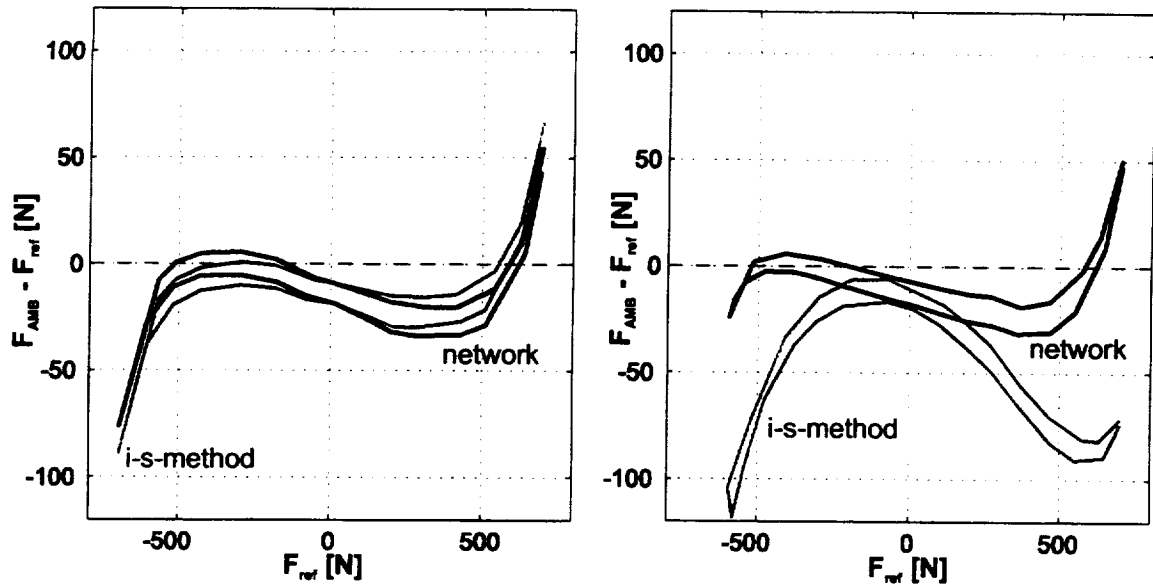


Figure 6. Force error of the i-s-method and network method without calibration for a centric ($s_x=0\text{mm}$, $s_y=0\text{mm}$) and an eccentric ($s_x=0.3\text{mm}$, $s_y=0\text{mm}$) rotor position.

Figure 5 shows the linearized force-current-displacement characteristic using equation (2) with the analytically computed k_i - k_s -values. This method assumes a uniform flux density in the air gap and neglects flux paths in the iron part, fringing and leakage effects.

The resulting force error of the i-s-method is demonstrated in figure 6 for a centric rotor position ($s_x=0\text{mm}$, $s_y=0\text{mm}$) and for an eccentric rotor position ($s_x=0.3\text{mm}$, $s_y=0\text{mm}$). In case of a centric rotor position, the error significantly increases with high external loads due to the nonlinear material properties (BH-curve) which are neglected with this method. Furthermore, the influence of the hysteresis of the soft magnetic material behavior can be seen, which results in a splitting up of 10N. The right side of figure 6 shows the significant dependence of the force error on the rotor position due to the neglected nonlinear material behavior and additional fringing effects.

Summarizing, in an operating range of $\pm 0.3\text{mm}$ (that is 23% of the nominal air gap) and $\pm 700\text{ N}$ (that is 100% of the maximum bearing force) the force error calculated with the i-s-method is about 17%. An increase in the accuracy can be reached with calibration, which is performed with a least-square fit of the k_i - k_s -plane to the measured data. The resulting value for k_i is 217 N/A and for k_s is 759 N/mm. Then, the force error of the chosen operating range is less than 9%. Figure 7 shows the corresponding force errors after calibration for the same two rotor positions. It should be mentioned that the calibration of k_i , k_s is strongly dependent on the chosen operating range. By limiting the working range of the bearings, the accuracy of the measurement method could be increased.

The i-s-method is simple and often used for on-line computation of the magnetic bearing forces because information about the coil currents and rotor positions is available during digital control and no additional sensors are needed. The disadvantage of the i-s-method is the neglect of the material properties of iron, leakage and fringing effects.

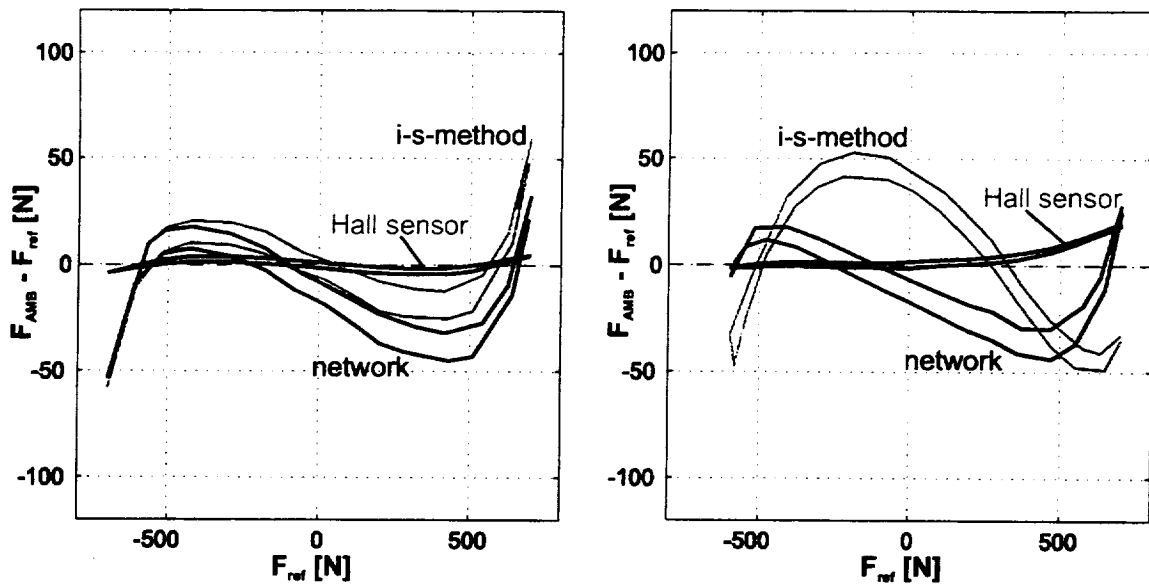


Figure 7. Force error of the different force measurement methods with calibration for a centric ($s_x=0\text{mm}$, $s_y=0\text{mm}$) and an eccentric ($s_x=0.3\text{mm}$, $s_y=0\text{mm}$) rotor position.

Reluctance Network Model

The second force measurement method is based on a reluctance network. The entire bearing is modelled as a multi-node network of variable reluctances (air gaps, pole legs, and back-iron paths of the stator) located between the model node points as it is described in Gähler [3]. Magnetic networks can be computed in a similar way to electric networks. The magnetic flux Φ corresponds to the electric current i and the magnetic potential ($\Delta V = Ni$) to the electric voltage U . The reluctance is then similar to the electric resistor $R = (\Delta V)/\Phi$. The reluctance depends on the length, the cross-section and the material constant of the flux carrying material. Applying Ampere's Law to the magnetic network leads to a set of algebraic equations $\Phi = R^{-1}\Delta V$, which can be solved for the unknown magnetic fluxes. With $B_{pole} = \Phi/A_{pole}$ and equation (1) follows the entire force of the magnetic bearing. For a given magnetic bearing geometry and material property, the network input data are the coil currents and the rotor positions. The analysis is computed using the assumptions of no flux fringing, no flux leakage and a uniform flux density in every flux-carrying cross-section. An advantage of this measurement technique is the extendability to consider nonlinear material behavior and hysteresis effects as described in e.g. Meeker et al. [8], Springer et al. [12]. Furthermore, additional sensors are again not necessary. However, the complexity of this method increases the computation time significantly. Hence, the method is only applicable for on-line implementation.

The resulting force error for this method can be seen in figure 6 for the same operation range as described above. The error is about 11%. As for the i-s-method, the main reason for the inaccuracies at higher loads are that the non-linearities of the magnetic material are not modelled. Hence, the network-method is

not superior to the i-s-method for the rotor in centric position, but is for eccentric rotor positions as clearly demonstrated in figure 6. When calibrating the network procedure the error can be further reduced to 8% as pictured in figure 7. The calibration is done by applying a constant correction factor minimizing the maximum force error in the entire operating range.

Hall Sensor Method

The most accurate method of determining the magnetic bearing forces is the direct measurement of the flux density B_{pole_k} by means of Hall sensors at each pole. Therefore, Hall sensors have been placed at each pole of the magnetic bearing in the air gap. The necessary calibration procedure of the Hall sensors is described in Knopf et al. [6]. Knopf reported a force error of 5% for the entire working range considered here. He further mentioned that the substantial part of the remaining force error results from an offset depending on the rotor position. Therefore, a rotor position dependent factor ($k_{offset} = 75\text{N/mm}$) is introduced to correct this offset error. Hence, the resulting force error is reduced to a maximum of 2.8% (fig. 7). If the rotor is only operated in the nominal center of the bearing, the force error of this method will lie clearly below 1%.

Non-linearities of the material, hysteresis effects, and saturation have almost no influence on the measurement error unlike the i-s-method, because these effects are causing a change of the flux density, and hence being accounted for. Another advantage is that the measurement location is much closer to the location where the force is actually acting. This means that influences of the amplifiers, coils, etc. are not falsifying the measurement. The entire computation can be performed on-line, again. On the other hand, additional sensors as well as an enlargement of the air gap are required. As a consequence of this, the maximum applicable magnetic force is reduced.

FE-MODEL

For a more detailed knowledge about the magnetic flux density distribution in the magnetic bearings a Finite-Element model is generated using a commercial software package (FLUX2D). The deviations of the computed magnetic bearing forces compared to the measured ones are less than 5.6% for the same load cases applied before (fig. 8). These agreements confirm a good quality of the model. A further improvement of this performance requires an experimental determination of the exact material behavior (BH-curve), which is modelled so far based on manufacturer's specifications without hysteresis effects.

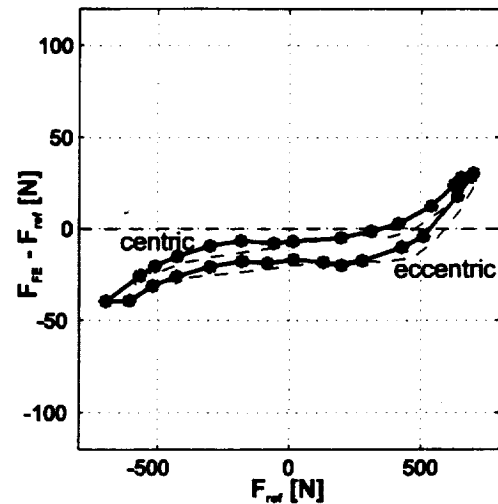


Figure 8. Force error of the FE-simulation for a centric ($s_x=0\text{mm}$, $s_y=0\text{mm}$) and an eccentric ($s_x=0.3\text{mm}$, $s_y=0\text{mm}$) rotor position.

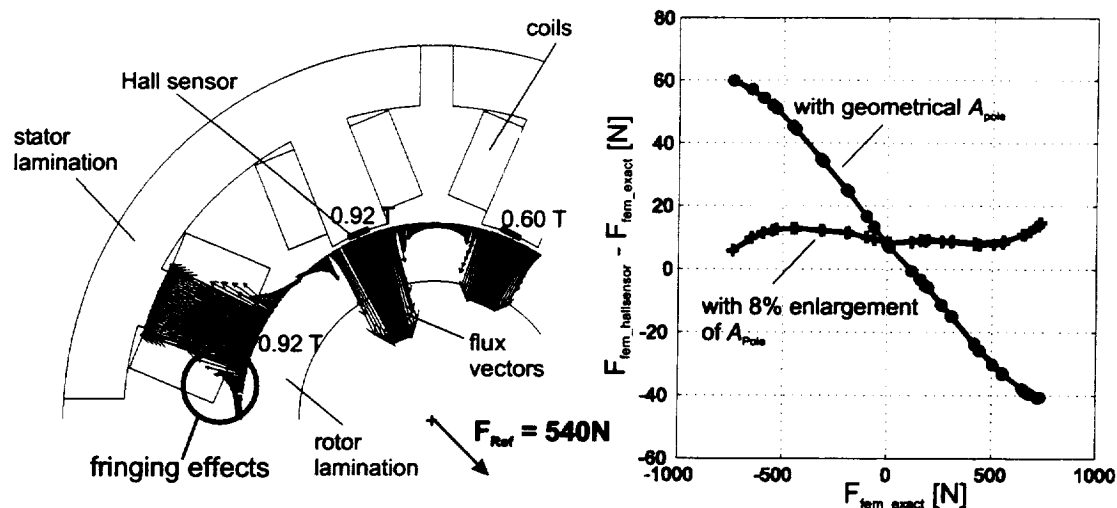


Figure 9. Left side: The magnetic flux distribution along the rotor lamination for an external force of 540N and centric rotor position shows the fringing effects.
Right side: Force measurement error of the simulated Hall sensor method for different external loads and centric rotor position.

With the FE-model the Hall sensor measurement technique is simulated. On one hand, the magnetic force is calculated from the integral of the flux values along the rotor. On the other hand, the magnetic force is computed using equation (1) from eight single flux values from the FE-simulation maintained at the Hall sensor locations. Assuming that the first calculation leads to the correct forces, the difference between both force computations represents the force error of the Hall sensor method. This error is shown in figure 9 for the centric rotor. If equation (1) is used with the geometrically calculated area of the magnetic poles, the resulting force error will be 9%. For getting more accurate results the pole area has to be increased by 8% due to the fringing effects in the air gap. This enlargement, independent of the load case and rotor position is accounted for through calibration and reduces the error significantly. The resulting error characteristic in the right picture of figure 9 agrees well with the one of the Hall sensor method in the left picture of figure 7. Only a general offset of about 10N yet remains in the FE-simulations. The dependence of the Hall sensor method on the rotor position could be observed, but with a smaller extend than with the measurement.

The different measurement techniques will now be used to diagnose various faults brought into the pump test rig. Especially, the accuracy obtained by the Hall sensor method seems to be sufficient for the diagnosis method, which is demonstrated in the following.

MODELING AND IDENTIFICATION

For many machines with rotating shafts the dynamic behavior can be described by linear models with time invariant system parameters. In these models the relation between input- and output quantities are

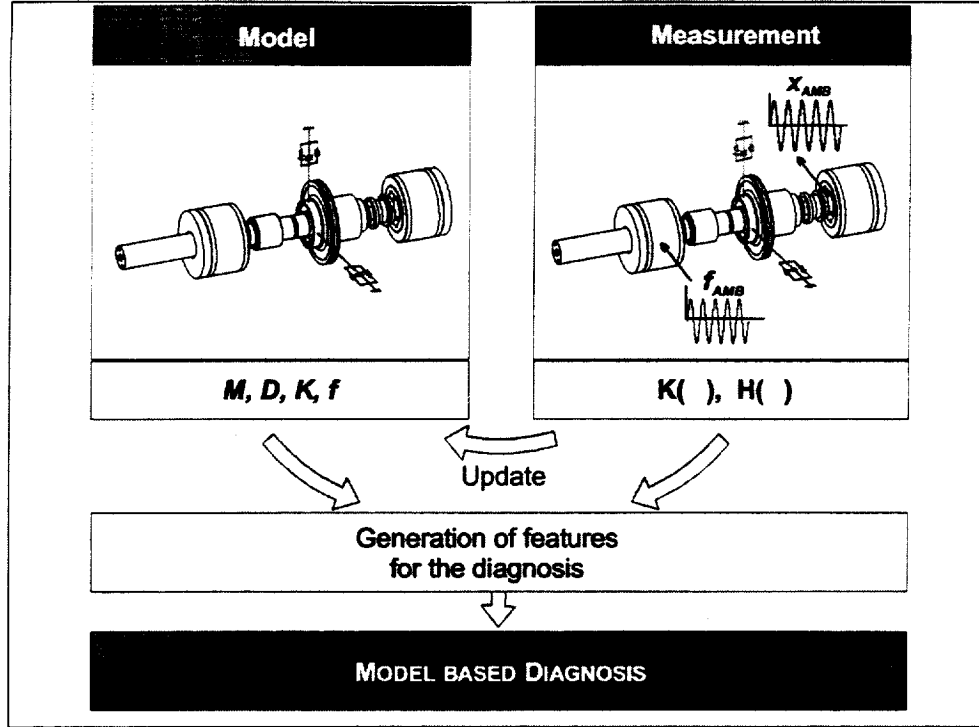


Figure 10. The procedure of the model based diagnosis using active magnetic bearings

given in terms of differential equations, expressing the dynamic equilibrium of inertia-, damping-, stiffness- and external forces:

$$M\ddot{x} + D\dot{x} + Kx = f. \quad (5)$$

The physical mass, damping and stiffness parameters, assembled in the $n \times n$ -system matrices M , D , K , (n number of degrees of freedom), characterize the dynamic behaviour of the system. The determination of the physical parameters M , D , K is possible either by calculations or by measurements. The measurement procedure is known as identification. More precisely, if the structure of the rotordynamic model is already known, e.g. by equation (5), and only the parameters are not known and have to be identified, this is called parameter identification.

From the measured input and output signals the dynamic characteristics can be calculated from well-known input/output relationships in the time or in the frequency domain. In this paper only frequency domain relations will be treated. When input-output relations are considered, the following complex frequency response functions can be introduced

$$\hat{f}(\Omega) = (K - \Omega^2 M + j\Omega D)\hat{x}(\Omega) = \bar{K}(\Omega)\hat{x}(\Omega), \quad (6)$$

$$\hat{x}(\Omega) = (K - \Omega^2 M + j\Omega D)^{-1} \hat{f}(\Omega) = \bar{H}(\Omega)\hat{f}(\Omega), \quad (7)$$

where $\bar{K}(\Omega)$ is the stiffness and $\bar{H}(\Omega)$ is the compliance frequency response function, respectively. From a practical point of view, in most rotating systems it is more easy to measure compliance functions instead of stiffness functions. On the other hand, concerning the parameter estimation, there is a very sim-

ple linear relation between the physical parameters and the stiffness frequency function. The objectives of the measurement task are to excite a rotordynamic system artificially by force or kinematic excitation, to measure input and output signals and to process functions that are used for the parameter estimation and hence for the model updating (see fig. 10). In case of linear systems the frequency domain functions (equation (6) and (7)) are often used.

When input/output functions of the system have been measured, corresponding model functions are fitted to the measured ones in order to estimate the unknown physical parameters. In general, parameter estimation procedures like least squares method, instrumental variables, maximum likelihood can be used for this task.

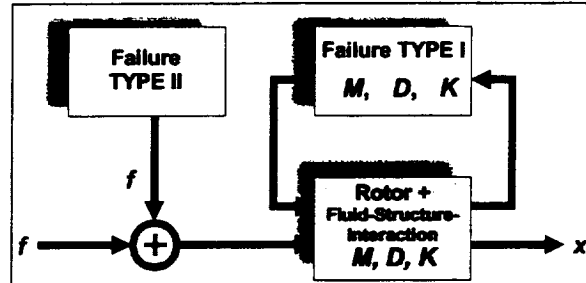


Figure 11. Scheme of the two different fault types being investigated

FAULT DETECTION AND DIAGNOSIS

Within this project several faults in the pump system will be identified. The aim of the project is to find out when a fault occurs and to determine the fault's type, location, and extent.

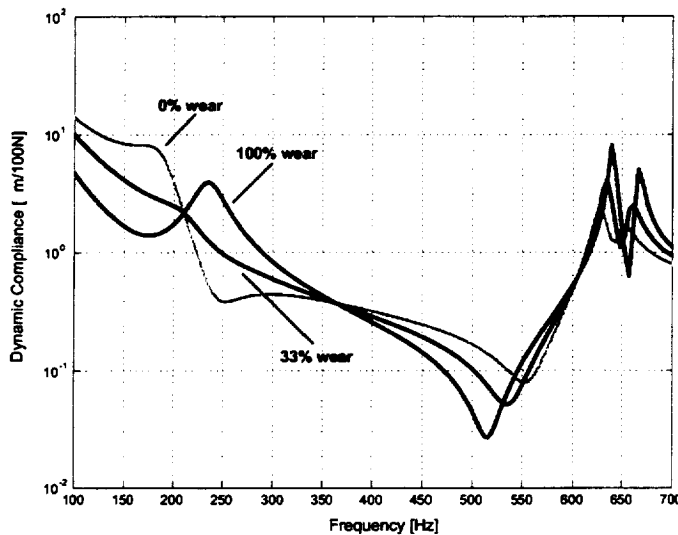


Figure 12. Change of the compliance function $H(\Omega)$ due to different wear states of the balance piston.

In general, the faults brought into the system are subdivided in two cases. Faults of type I (see fig. 11) are altering the system matrices. These are for example a crack in the rotor, the wear of the seals, loosening parts, etc. Faults of type II are caused by changing external loads like an increase of the imbalance, cavitation, etc.

Exemplarily, some simulation results of the pump with different worn out states of the balance piston are presented. The different states are a seal with a clearance of 0.2mm (new), 0.3mm (33% wear), and 0.5mm (100% wear). The corresponding mass, stiffness, and damping coefficients for the simulation are calculated with validated programs, which are described in detail in [11].

Based on the models, it is possible to compute the resulting compliance functions $H(\Omega)$ including the different seal states. Corresponding results are presented in figure 12. From this figure it can be derived that with an excitation amplitude of about 100N corresponding responses of about $5\mu\text{m}$ in the vicinity of the first and second eigenfrequencies can be expected. Hence, the location of the eigenfrequencies can be identified from the measured compliance function. Repeating this procedure for the different worn out

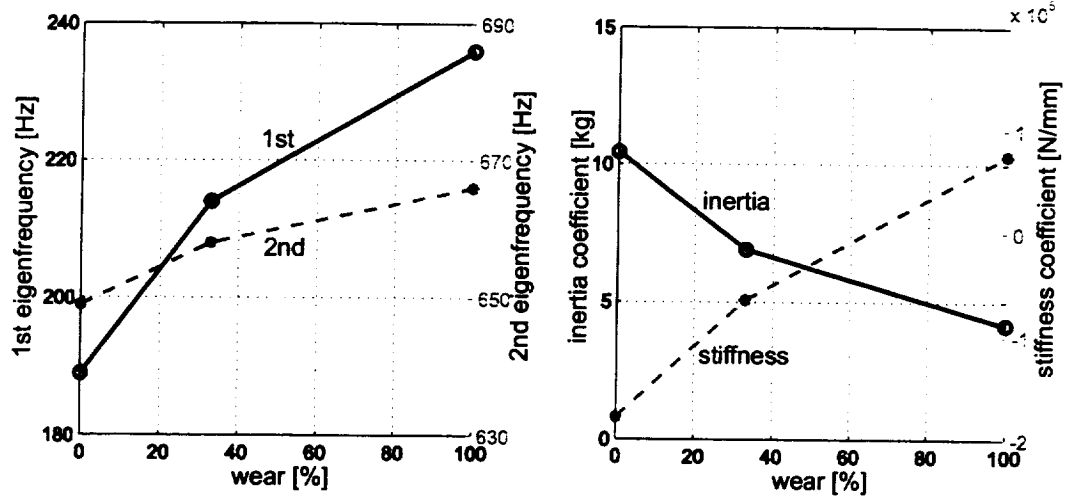


Figure 13. The change of two features characterizing the wear of the balance piston. On the left side, the increase of the first and second bending eigenfrequencies and on the right side, the altering of the identified inertia and stiffness coefficients.

states of the balance piston leads to the left picture in figure 12. The eigenfrequencies clearly increase with a wearing out piston due to decreasing inertia and damping forces in the seal.

Furthermore, with the parameter estimation using the compliance function $H(\Omega)$ the seal coefficients can directly be derived. Exemplarily, the stiffness- and inertia coefficient are shown in the right picture of figure 13. With increasing wear of the balance piston the inertia coefficient decreases while the stiffness coefficient increases.

CONCLUSION AND OUTLOOK

In this paper the model based diagnosis using active magnetic bearings in a centrifugal pump is introduced. For this type of diagnosis using frequency response functions an accurate force measurement is crucial. The paper compares force measurement results and achievable accuracies of a radial magnetic bearing using different measurement techniques over a large operating range. The different techniques investigated are the i-s-method, a reluctance network method, and a Hall sensor method. For each method the accuracy as well as the ability for on-line computation and the improvement through calibration is presented. The most accurate method is the Hall sensor method. Additionally, a finite element model is generated to simulate this measurement technique. As a result of the simulation a rotor position dependent factor is introduced to account for the fringing effects. A future improvement of the Hall sensor measurement technique could be the development of a correction factor depending on the coil current and the rotor position for each pole instead of one for the whole bearing. Exemplarily, simulation results of a worn out balance piston of a single-stage pump are presented. The simulation shows that the accuracy of the force measurement achieved will enable the diagnosis of this fault in the pump system.

ACKNOWLEDGEMENT

The presented paper is a result from the work of the Special Research Program (SFB 241) sponsored by the German Research Council (DFG).

REFERENCES

- [1] **D.O. BAUN, R.D. FLACK:** *A Plexiglas Research Pump With Calibrated Magnetic Bearings/Load Cells For Radial And Axial Hydraulic Force Measurement*. ASME Fluids Engineering Division Summer Meeting, FEDSM'97, June 22 -26, 1997.
- [2] **P. FÖRCH:** *Dynamische Untersuchungen an rotierenden Strukturen mittels Magnetlagern*. Diss. Technische Universität Darmstadt. Darmstadt: 1998
- [3] **C. GAEHLER:** *Rotor Dynamic Testing and Control with Active Magnetic Bearings*. Diss. Swiss Federal Institute of Technology Zürich. Zürich: 1998
- [4] **R. ISERMANN** (Hrsg.): *Überwachung und Fehlerdiagnose*. Düsseldorf: VDI-Verl., 1994.
- [5] **E. KNOFF, M. AENIS, R. NORDMANN:** *Aktive Magnetlager zur Identifikation der dynamischen Eigenschaften von mediumgeschmierten Gleitlagern*. thema FORSCHUNG, Volume 1/99, S. 80f, Hrsg. Präsident der TU-Darmstadt, Verlag für Marketing und Kommunikation, Worms, 1999.
- [6] **E. KNOFF, R. NORDMANN:** *Active Magnetic Bearings for the Identification of Dynamic Characteristics of Fluid Bearings*, 6th International Symposium on Magnetic Bearings, Massachusetts Institute of Technology, Cambridge, USA, 1998
- [7] **S. LEONHARDT:** *Modellgestützte Fehlererkennung mit neuronalen Netzen - Überwachung von Radaufhängungen und Diesel-Einspritzanlagen*. Diss. TH Darmstadt. Fortschritt-Berichte VDI Düsseldorf: VDI-Verlag, 1996.
- [8] **D.C. MEEKER, E.H. MASLEN, D.N. MYOUNGGYU:** *A Wide Bandwidth Model For The Electrical Impedance of Magnetic Bearings*. NASA conference publication No. 3336/PT2, 1996.
- [9] **R. NORDMANN:** *New Identification Techniques in Rotordynamics Using Motion and Force Control*. MOVIC'98, Zurich, Switzerland, Aug. 25-28, 1998.
- [10] **G. SCHWEITZER, H. BLEULER, A. TRAXLER:** *Magnetlager*, Springer Verlag, Berlin Heidelberg, 1994
- [11] **J. SOBOTZIK, R. FONGANG, R. NORDMANN:** *Experimental Investigations on Fluid-Structure Interaction-Effects of a High- N_s Impeller*. Third International Conference on Pumps and Fans, Tsinghua University Beijing, Oct. 13 - 16, 1998.
- [12] **H. SPRINGER, G. SCHLAGER, T. PLATTER:** *A Nonlinear Simulation Model For Active Magnetic Bearing Actuators*, 6th International Symposium on Magnetic Bearings, Massachusetts Institute of Technology, Cambridge, USA, 1998

NONLINEAR STABILITY ANALYSIS OF ACTIVE MAGNETIC BEARINGS

Norbert Steinschaden and Helmut Springer
Institute for Machine Dynamics and Measurements,
Vienna University of Technology,
Wiedner Hauptstraße 8-10 / E303, A-1040 Vienna, Austria.

ABSTRACT

In order to get a better understanding of the dynamics of active magnetic bearing (AMB) systems under extreme operating conditions a nonlinear model for a radial AMB system is investigated. Instead of the common way of linearizing the magnetic forces at the center position of the rotor with respect to rotor displacement and coil current, the fully nonlinear force to displacement and force to current characteristics are used. The nonlinear model employed in this investigation is an advanced version of a simple nonlinear model, which has already been published and discussed in [Steinschaden, Springer, 1999]. Magnetic saturation effects, saturation of the amplifier and limitations of the control currents are additional nonlinear components modeled in this work.

The AMB system is excited by unbalance forces of the rotor. Especially for the case of large rotor eccentricities, causing large rotor displacements, the behaviour of the system is discussed. A path-following analysis of the equations of motion shows that for some combinations of parameters well-known nonlinear phenomena may occur.

INTRODUCTION

AMBs represent modern mechatronical systems. The avoidance of any lubrication systems and lubricants, the absence of material wear and almost no friction losses, as a consequence of no mechanical or fluidic contact between the rotor and the stator, are significant advantages resulting in high life time and low maintenance requirements, see [Schweitzer, et al., 1993]. If magnetic bearings are used, no additional equipment will be needed for diagnosis and permanent monitoring tasks during machine operation. Stiffness, damping and force characteristics of the bearing can be adapted to actual machine operating conditions by adaptive control strategies easily implemented into the feedback control device, see [Lang, et al., 1995]. As the area of industrial applications of AMB systems grows, there is a growing demand of highly reliable systems at any operating conditions. This requires a deep and complete understanding of the dynamics of rotor-AMB systems.

For a rigid rotor supported by two lubricated journal bearings Moser has investigated the nonlinear stability and bifurcation behaviour in terms of three important dimensionless bifurcation parameters, [Moser, 1993]. They correspond to the rotor speed, the static load and the unbalance eccentricity of the rotor. For magnetic bearings, there are only a few papers available that partially deal with the problem of nonlinear modeling, stability and bifurcation. Hebbale investigated a four-magnet AMB system with linear state variable control and pole placement design, [Hebbale, 1985, Hebbale, Taylor, 1986]. A two degrees of freedom single-mass rotor with nonlaminated (solid) ferromagnetic flux paths was considered which generates speed dependent eddy current effects due to rotation of the rotor. By applying the center manifold theory, see [Troger, Steindl, 1991], a subcritical Hopf bifurcation was detected in terms of the rotor speed being the bifurcation parameter. Furthermore, in [Hebbale, 1985, Hebbale, Taylor, 1986] the influence of rotor unbalance on the stability was investigated by numerical simulation studies.

Mohamed and Emad investigated a rigid rotor in two radial AMBs with a linear state variable voltage controller, [Mohamed, Emad, 1993]. Nonlinear force to magnetic flux relationships were considered along with speed dependent gyroscopic effects of the rotor. A subcritical Hopf bifurcation was found for a static equilibrium state in terms of the rotor speed being the distinguished bifurcation parameter.

Wang et al. investigated a single-mass rotor (with and without unbalance) supported by an AMB with linear voltage PD-controller, [Wang, et al., 1994]. They considered nonlinear force to air gap and nonlinear force to coil current characteristics. Applying the center manifold theory, bifurcations were found in terms of the controller feedback gain parameters.

Ecker, Knight and Virgin found pitchfork and torus bifurcations for the vibrational amplitudes of an AMB-supported single-mass rotor with unbalance excitation in terms of the rotor speed as the distinguished bifurcation parameter, [Ecker, et al., 1997, Knight, Ecker, 1996, Virgin, et al., 1994]. Since they used flux control with a linear feedback law, the only nonlinearities were conservative cross coupling forces acting between two pairs of orthogonal oriented electromagnets, see [Knight, et al., 1993, Knight, et al., 1992].

Chinta et al. investigated the effects of cross-coupling forces using current control, where the nonlinear force to displacement and the nonlinear force to coil current characteristics are additionally active, [Chinta, et al., 1996]. Again an AMB system with a single-mass rotor excited by unbalance forces is considered. They used the tool of numerical simulation method. Quasiperiodic and period-2 solutions for the rotor vibration were found.

Beside the above discussed references several authors applied the classical methods of harmonic balance, describing function and perturbation theory to autonomous or non-autonomous AMB systems, see [Hoffmann, et al., 1997, Knight, et al., 1993, Nataraj, 1995, Sinha, 1990]. Moreover, stable limit cycles as response to speed synchronous unbalance excitation were found by the tool of numerical simulation. see [Haferl, Springer, 1991, Jeong, et al., 1994, Knight, Ecker, 1996, Knight, et al., 1993, Satoh, et al., 1990, Springer, et al., 1990].

This paper discusses the dynamic characteristics of an AMB-supported single-mass rotor with speed synchronous unbalance excitation. The mathematical model includes nonlinear force to displacement and force to coil current relationships. Nonlinear saturation effects of the magnetic materials as well as limitations, of the power amplifier and of the control current are considered in the present model. Effects of coil inductance combined with an underlying current controller are included as well.

AMB SYSTEM MODEL

Magnetic Force Model

The calculation of the magnetic forces generated by AMB-actuators is based on the commonly used one-dimensional model for the magnetic flux, see [Schweitzer, et al., 1993].

Leakage and fringing effects, are neglected. The permeability within the iron paths is considered to be finite and constant. Thus, the mathematical formulation of the magnetic force of one radial actuator can be presented as

$$f = k \frac{i^2}{4g^2 \left(1 + \frac{\mathcal{R}_{mi}}{\mathcal{R}_g} + \frac{\mathcal{R}_{m2}}{\mathcal{R}_g}\right)^2}, \quad (1)$$

where k is a constant value depending on the actuator properties, i is the coil current of the actuator and g is the radial air gap length between rotor and stator. \mathcal{R}_g is the reluctance of the air gap and \mathcal{R}_{mi} is the reluctance of an iron path i , which can be written as

$$\mathcal{R}_g = \frac{2g}{\mu_0 A_g}, \quad \mathcal{R}_{mi} = \frac{l_{mi}}{\mu_0 \mu_{r,mi} A_{mi}}, \quad (2)$$

respectively, where μ_0 is the permeability of air, A_g is the cross section area of the air gap, l_{mi} is the length, $\mu_{r,mi}$ is the relative permeability and A_{mi} is the cross section area of iron path i .

Magnetic saturation effects within the iron paths are modeled by an approximation of the anhysteretic curve of the magnetic materials. Hysteresis effects are not considered in this investigation. Therefore, there is a definite relationship between magnetic flux density and magnetic field strength. The relative permeability of a magnetic material is a function of the magnetic flux density and is calculated from the empirical relation

$$\mu_{r,mi} = \frac{1 - \mu_{r,mi,0}}{\pi} \arctan \left(K_{M,mi} \frac{|B_{mi}| - B_{mi,max}}{B_{mi,max}} \right) + \frac{1 + \mu_{r,mi,0}}{2}, \quad (3)$$

where $\mu_{r,mi,0}$ is the relative permeability well below the saturation value $B_{mi,max}$, B_{mi} is the actual magnetic flux density and $K_{M,mi}$ is a shaping factor of the anhysteretic curve.

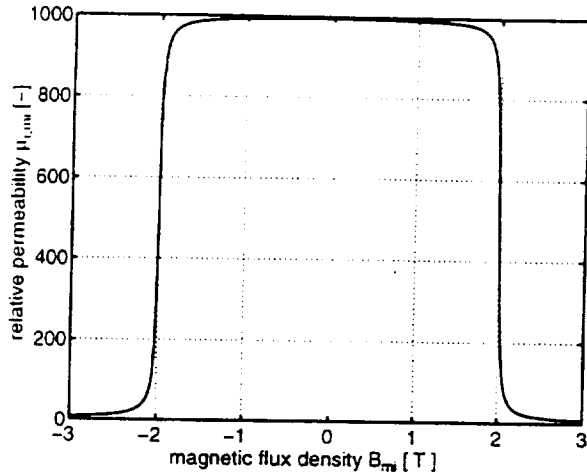


Figure 1: Relative permeability as a function of the magnetic flux density for the parameter values $\mu_{r,mi,0} = 1000$, $K_{M,mi} = 100$ and $B_{mi,max} = 2.0\text{T}$.

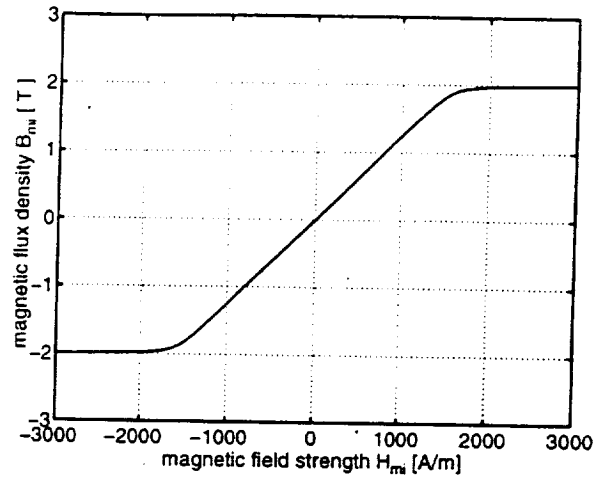


Figure 2: B-H curve for the parameter values $\mu_{r,mi,0} = 1000$, $K_{M,mi} = 100$ and $B_{mi,max} = 2.0\text{T}$.

Figure 1 shows the calculated relative permeability $\mu_{r,mi}$ as a function of the magnetic flux density B_{mi} . The corresponding approximation for the anhysteretic curve is shown in Fig. 2.

There is no specific parameter which determines the slope of the B-H curve above the saturation value. Instead, the slope is specified by the choice of the shaping factor $K_{M,mi}$. Equ. 3 allows a qualitatively good approximation within the range of interest of the magnetic flux density. It should be mentioned that this formulation should not be used in the case of very high values of the magnetic flux density far above the saturation value. However, such high values of magnetization are not achieved in common magnetic bearing systems.

The relatively simple structure of this mathematical formulation of the magnetic saturation characteristic is very useful for a successful application of the employed numerical solution method which allows a calculation of stable and unstable periodic solutions. See the section entitled 'Numerical Solution Methods.'

Magnetic Bearing Model

Figure 3 shows a schematic diagram of the axial view of an active magnetic bearing. The shaft is plotted in the center position ($x = 0$, $y = 0$, $g = g_0$). The magnetic bearing considered consists of two pairs of orthogonally oriented electromagnets. The magnet pairs are controlled independently. Any coupling effects between the directions x and y are neglected.

For each magnet pair one collocated displacement sensor measures the rotor position in the x -

and y -direction, respectively. The displacement signal is the input for the PID-current controller where the integral feedback gain eliminates steady state deviations from the center position of the rotor. According to the output of the controller, the amplifier supplies the voltage to produce the appropriate magnetic force in the actuator.

In order to achieve a stable damped system, a bias current, i_b , which has a static, predefined value, is supplied in each actuator and a control current, which corresponds to the controller output, is superimposed. It is very common to apply a so-called 'differential control', which means that one magnetic actuator input consists of the bias current plus the control current, while the input of the opposite actuator consists of the bias current minus the control current. Thus, the coil currents calculated by the controller for the actuators acting in x - and y -directions, respectively, are given by

$$\begin{aligned} i_{C,x,+} &= i_b - G_P x - G_D \dot{x} - G_I \int_0^t x dt \\ i_{C,x,-} &= i_b + G_P x + G_D \dot{x} + G_I \int_0^t x dt \\ i_{C,y,+} &= i_b - G_P y - G_D \dot{y} - G_I \int_0^t y dt \\ i_{C,y,-} &= i_b + G_P y + G_D \dot{y} + G_I \int_0^t y dt, \end{aligned} \quad (4)$$

where G_P is the proportional feedback gain, G_D is the differential feedback gain and G_I is the integral feedback gain. The subscripts '+' and '-' identify the actuators located at the positive and negative axes, respectively (see Figure 3). In the special case, when the bearing does not carry a steady lateral load, the bias currents i_b will be equal in all actuators, which is assumed in the following.

This investigation includes the effects of coil inductance and requires an additional state variable for each magnetic flux. As a consequence of inductance the coil current does not instantaneously follow the voltage applied by the power amplifier. Instead, the voltage drop u in each actuator coil has to be calculated from

$$u = Ri + N\dot{\Phi}, \quad (5)$$

where R is the electric resistance of the coil, i is the coil current, N is the number of coil turns and Φ is the magnetic flux of the actuator. In order to achieve a better dynamic behaviour of the magnetic bearing an underlying current controller is implemented. For that task a simple P-controller is employed. As a result the applied voltage is then given by

$$u = Ri_b + RG_{P,I}(i_b \mp i_c - i), \quad (6)$$

where $G_{P,I}$ is the proportional feedback gain of the underlying current controller, i_c is the control current calculated by the main PID-controller and i is the actual coil current.

Any power amplifier has an upper and a lower limit for the voltage which can be applied to the electromagnet. If the voltage determined by the underlying current controller exceeds the limited

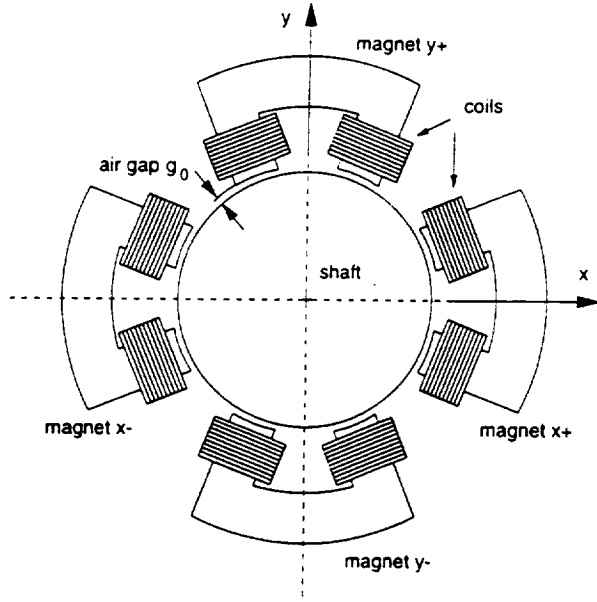


Figure 3: Schematic diagram of an 8-pole active magnetic bearing with the shaft in center position.

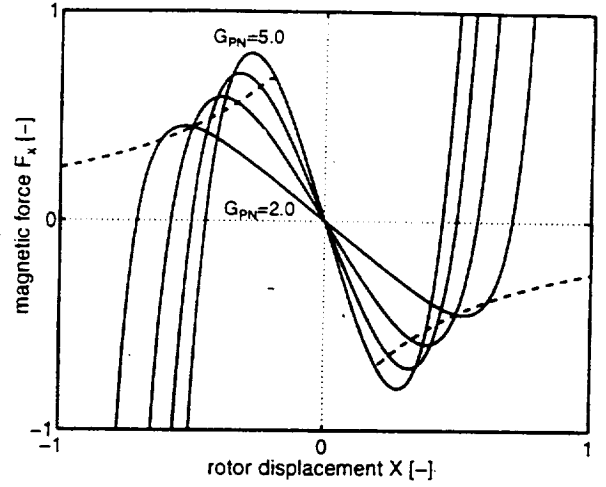


Figure 4: Nonlinear magnetic force exerted on the rotor for the quasistatic case. The proportional feedback $G_{P,N}$ is varied from 2.0 to 5.0.

range of voltage, the required voltage cannot be fully supplied. This results in a reduced slew rate of the coil currents and consequently of the magnetic forces. The saturation effect of the amplifier may cause poor dynamical behaviour of the magnetic bearing. It can be modeled by the empirical equation

$$u_a = u_n + \left[\frac{1}{2} + \frac{1}{\pi} \arctan \left(K_U \frac{u_n - u_{max}}{u_{max}} \right) \right] (u_{max} - u_n) - \left[\frac{1}{2} - \frac{1}{\pi} \arctan \left(K_U \frac{u_n + u_{max}}{u_{max}} \right) \right] (u_{max} + u_n), \quad (7)$$

where u_n is the nominal voltage given by the underlying current controller, u_{max} is the maximum voltage which can be supplied by the power amplifier, and u_a is the actual voltage. K_U is a shaping factor. Figure 5 shows the actual voltage u_a versus nominal voltage u_n according to Equ. 7.

It is very common to limit the control current, i_c , so that the coil current i_C calculated by the main PID-controller, given by

$$i_C = i_b \mp i_c, \quad (8)$$

may vary only between zero and a maximum value. This can be modeled similar to Equ. 7 by

$$i_{C,a} = i_{C,n} + \left[\frac{1}{2} + \frac{1}{\pi} \arctan \left(K_I \frac{i_{C,n} - i_{C,max}}{i_{C,max}} \right) \right] (i_{C,max} - i_{C,n}) - \left[\frac{1}{2} - \frac{1}{\pi} \arctan \left(K_I \frac{i_{C,n}}{i_{C,max}} \right) \right] i_{C,n}, \quad (9)$$

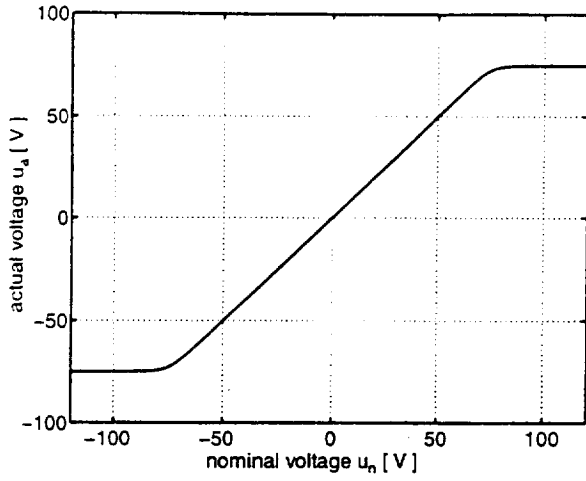


Figure 5: Actual voltage versus nominal voltage for the parameter values $u_{max} = 75.0\text{V}$ and $K_U = 10.0$.

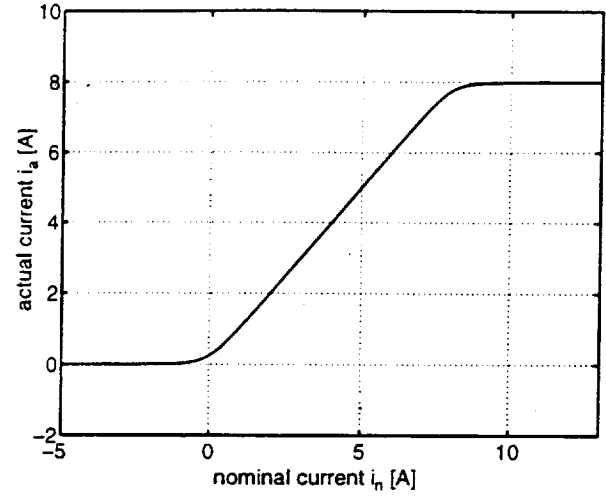


Figure 6: Actual current versus nominal current for the parameter values $i_{c,max} = 8.0\text{A}$ and $K_I = 10.0$.

where $i_{C,n}$ is the nominal coil current calculated by the main PID-controller, $i_{C,max}$ is the saturation value and $i_{C,a}$ is the actual current value at the input of the underlying current controller. K_I is a shaping factor. Figure 6 shows the actual PID-controller output $i_{C,a}$ versus the nominal current $i_{C,n}$ according to Equ. 9.

Rotor Model

The rotor is represented as a lumped mass with two degrees of freedom supported by two opposed magnetic actuators in both x - and y -directions, see Figure 3. The rotor is excited by speed synchronous unbalance forces, which are caused by the mass imbalance eccentricity e . Thus, the equations of motion have the simple form

$$\begin{aligned} m\ddot{x} &= f_{x,mag} + me\omega^2 \cos(\omega t) \\ m\ddot{y} &= f_{y,mag} + me\omega^2 \sin(\omega t), \end{aligned} \tag{10}$$

where m is the rotor mass, $f_{x,mag}$ is the resulting magnetic force exerted on the rotor by both actuators in the x -direction and $f_{y,mag}$ is the resulting magnetic force exerted on the rotor by both actuators in the y -direction. Further, ω is the angular velocity of the rotor and t is the physical time.

Equations of Motion

A dimensionless formulation of the equations of motion can be introduced by the following dimensionless variables

$$\begin{aligned}
 X &= \frac{x}{g_0} & G_{PN} &= \frac{G_P g_0}{i_b} & L_{mi} &= \frac{\mathcal{R}_{mi}}{\mathcal{R}_{g_0}} & U_j &= \frac{u_j}{R i_b} \\
 Y &= \frac{y}{g_0} & G_{DN} &= \frac{G_D \omega_0 g_0}{i_b} & L_{mi,0} &= \frac{\mathcal{R}_{mi,0}}{\mathcal{R}_{g_0}} & I_j &= \frac{i_j}{i_b} \\
 E &= \frac{e}{g_0} & G_{IN} &= \frac{G_I g_0}{i_b \omega_0} & \Phi_{N,j} &= \frac{\Phi_j}{\Phi_b} & \dot{R}_N &= \frac{2g_0 R}{k \omega_0} \\
 \tau &= \frac{\omega}{2\pi} t & \Omega &= \frac{\omega}{\omega_0},
 \end{aligned} \tag{11}$$

where g_0 is the radial air gap length between the rotor and the stator at the rotor center position. The above definition of a dimensionless time τ maps one excitation period into the interval $[0, 1]$, which is useful for the formulation of the boundary value problem, see section 'Numerical Solution Methods'. \mathcal{R}_{g_0} is the reluctance of the air gap for the center position of the rotor and $\mathcal{R}_{mi,0}$ is the reluctance of an iron path i valid for the linear range of the anhysteretic curve. They can be written as

$$\mathcal{R}_{g_0} = \frac{2g_0}{\mu_0 A_g} \quad \text{and} \quad \mathcal{R}_{mi,0} = \frac{l_{mi}}{\mu_0 \mu_{r,mi,0} A_{mi}}. \tag{12}$$

The magnetic flux is normalized by its bias value

$$\Phi_b = \frac{k i_b}{2g_0 N (1 + L_{m1,0} + L_{m2,0})}. \tag{13}$$

The natural frequency of the linearized system is given by

$$\omega_0 = \sqrt{k \frac{i_b^2}{m g_0^3 (1 + L_{m1,0} + L_{m2,0})^2} \left(\frac{G_{P,I}}{1 + G_{P,I}} G_{PN} - \frac{1}{1 + L_{m1,0} + L_{m2,0}} \right)}, \tag{14}$$

and the damping ratio ζ can be written as

$$\zeta = \frac{\frac{G_{P,I}}{1 + G_{P,I}} G_{DN}}{2 \left(\frac{G_{P,I}}{1 + G_{P,I}} G_{PN} - \frac{1}{1 + L_{m1,0} + L_{m2,0}} \right)}. \tag{15}$$

Finally, the dimensionless equations of motion have the form

$$\begin{aligned}
 X'' &= \left(\frac{2\pi}{\Omega} \right)^2 \left[\frac{1 + L_{m1,0} + L_{m2,0}}{4 [G_{PN} (1 + L_{m1,0} + L_{m2,0}) - 1]} (\Phi_{N,x,+}^2 - \Phi_{N,x,-}^2) + E \Omega^2 \cos(2\pi\tau) \right] \\
 Y'' &= \left(\frac{2\pi}{\Omega} \right)^2 \left[\frac{1 + L_{m1,0} + L_{m2,0}}{4 [G_{PN} (1 + L_{m1,0} + L_{m2,0}) - 1]} (\Phi_{N,y,+}^2 - \Phi_{N,y,-}^2) + E \Omega^2 \sin(2\pi\tau) \right]
 \end{aligned} \tag{16}$$

and

$$\Phi'_{N,x,+} = \frac{2\pi}{\Omega} R_N [(1 - L_{m1,0} + L_{m2,0}) U_{x,+,a} - \Phi_{N,x,+} (1 - X + L_{m1,x,+} + L_{m2,x,+})] \quad (17)$$

$$\Phi'_{N,x,-} = \frac{2\pi}{\Omega} R_N [(1 + L_{m1,0} + L_{m2,0}) U_{x,-,a} - \Phi_{N,x,-} (1 + X + L_{m1,x,-} + L_{m2,x,-})],$$

where the primes denote the derivatives with respect to the dimensionless time τ , and

$$L_{mi,x,+} = L_{mi,0} \frac{\mu_{r,mi,0}}{\left[\frac{1-\mu_{r,mi,0}}{\pi} \arctan \left(K_{M,mi} \frac{|\Phi_{N,x,+}| - \Phi_{N,mi,max}}{\Phi_{N,mi,max}} \right) + \frac{1+\mu_{r,mi,0}}{2} \right]} \quad (18)$$

represents the magnetic saturation effect. The actual voltage is calculated from

$$\begin{aligned} U_{x,+,a} &= G_{P,I} (I_{C,x,+,a} - I_{x,+}) + 1 \\ &+ \left[\frac{1}{2} + \frac{1}{\pi} \arctan \left(K_U \frac{G_{P,I} (I_{C,x,+,a} - I_{x,+}) + 1 - U_{max}}{U_{max}} \right) \right] \\ &\quad \left[U_{max} - G_{P,I} (I_{C,x,+,a} - I_{x,+}) - 1 \right] \\ &- \left[\frac{1}{2} - \frac{1}{\pi} \arctan \left(K_U \frac{G_{P,I} (I_{C,x,+,a} - I_{x,+}) + 1 + U_{max}}{U_{max}} \right) \right] \\ &\quad \left[U_{max} + G_{P,I} (I_{C,x,+,a} - I_{x,+}) + 1 \right] \end{aligned} \quad (19)$$

with

$$\begin{aligned} I_{C,x,+,a} &= I_{C,x,+,n} + \left[\frac{1}{2} + \frac{1}{\pi} \arctan \left(K_I \frac{I_{C,x,+,n} - I_{C,max}}{I_{C,max}} \right) \right] [I_{C,max} - I_{C,x,+,n}] - \\ &- \left[\frac{1}{2} - \frac{1}{\pi} \arctan \left(K_I \frac{I_{C,x,+,n}}{I_{C,max}} \right) \right] I_{C,x,+,n}. \end{aligned} \quad (20)$$

The actual coil currents are given by

$$\begin{aligned} I_{x,+} &= \frac{1 - X + L_{m1,x,+} + L_{m2,x,+}}{1 + L_{m1,0} + L_{m2,0}} \Phi_{N,x,+} \\ I_{x,-} &= \frac{1 + X + L_{m1,x,-} + L_{m2,x,-}}{1 + L_{m1,0} + L_{m2,0}} \Phi_{N,x,-}. \end{aligned} \quad (21)$$

The nominal coil currents calculated by the main PID-controller are given by

$$\begin{aligned} I_{C,x,+,n} &= 1 - G_{PN} X - G_{DN} \frac{\Omega}{2\pi} X' - G_{IN} \frac{2\pi}{\Omega} \int_0^\tau X d\tau \\ I_{C,x,-,n} &= 1 + G_{PN} X + G_{DN} \frac{\Omega}{2\pi} X' + G_{IN} \frac{2\pi}{\Omega} \int_0^\tau X d\tau. \end{aligned} \quad (22)$$

Because of the limited space only the most important equations are presented here. In order to obtain the whole set of equations the indices must be varied. In Equ. 17 to 22 the index 'x' may be substituted by 'y'. Additionally, in Equ. 18 to 20 the index '+' may be substituted by '-'.

Magnetic Force Characteristics

Defining dimensionless forces by

$$F_k = f_k \frac{g_0^2}{k i_b^2} \quad (23)$$

and considering the quasistatic case without any saturation effects the dimensionless magnetic force in x -direction produced by the magnet pair is given by

$$F_x = \frac{1}{4(1 + L_{m1,0} + L_{m2,0})^2} (\Phi_{N,x,+}^2 - \Phi_{N,x,-}^2), \quad (24)$$

where

$$\begin{aligned} \Phi_{N,x,+}^2 &= \frac{1}{(1 + G_{P,I})^2} \left[\frac{1 + L_{m1,0} + L_{m2,0}}{1 - X + L_{m1,0} + L_{m2,0}} (1 + G_{P,I} (1 - G_{PN}X)) \right]^2 \\ \Phi_{N,x,-}^2 &= \frac{1}{(1 + G_{P,I})^2} \left[\frac{1 + L_{m1,0} + L_{m2,0}}{1 + X + L_{m1,0} + L_{m2,0}} (1 + G_{P,I} (1 + G_{PN}X)) \right]^2. \end{aligned} \quad (25)$$

In Figure 4 the force function in x -direction $F_x(X)$ is plotted for various values of the proportional feedback gain G_{PN} . The effects of all saturation types presented become identical in the quasistatic case. Moreover, beyond the saturation value the resulting magnetic force is independent of the proportional feedback gain, which is plotted as a dashed line in Fig. 4.

Model Limitations

Fringing and leakage of the magnetic flux as well as magnetic flux paths, coupling different magnets, are not considered. Therefore, flux densities in different magnets are calculated from independent magnetic circuits. Any coupling between different coordinate directions is neglected. Therefore, the system is completely symmetric since no lateral static load is imposed to the shaft.

NUMERICAL SOLUTION METHODS

Nonlinear mathematical models concerning AMBs have already been investigated by several authors employing the tool of numerical simulation. However, a simulation approach, based on the Initial Value Problem (IVP) has the disadvantage that a sufficiently high number of transient cycles must be allowed to decay before a steady-state response is reached. This makes such an approach quite

cumbersome and slow, in particular near stability limits of the system. Furthermore, unstable solutions of limit cycles cannot be calculated by numerical simulation. However, a positive aspect of the simulation approach via IVP is that it is not restricted to periodic solutions and any kind of quasi-periodic or even chaotic solutions can be found.

Another widely used approach is the so-called Harmonic Balance method, which is rather an analytical than a numerical approximation. It has the advantage that both stable and unstable solutions can be obtained. However, the method does not yield stability characteristics. Since an approximation of the original system is solved, there is always the question about the validity of the results obtained.

In this investigation the numerical simulation method is an additional tool only, primarily used for verification and for calculating time response plots. It is obvious that the steady-state response of the system is basically periodic with the period T of one rotor revolution. Therefore, numerical integration is used, but formulated as a Boundary Value Problem (BVP). By employing periodic boundary conditions $z(0) = z(T)$ and solving the BVP numerically by an appropriate method any kind of stable or unstable periodic solutions can be calculated. To track solutions for a certain parameter variable, in our case the exciting unbalance frequency Ω , a smart continuation (path-following) method has to be employed. This becomes very important if so-called turning points occur during the continuation process.

The following results were obtained using the subroutine collection BIFPACK, see [Seydel, 1996]. BIFPACK provides a multiple shooting routine to solve boundary value problems, it possesses a sophisticated continuation algorithm and it can investigate the stability of a periodic solution, as outlined before. Beside other useful features the package offers a branch switching option to calculate new starting points on emanating solutions near a bifurcation.

NUMERICAL RESULTS

Solving the BVP as mentioned for the non-autonomous system with speed synchronous unbalance excitation, bifurcation diagrams can be produced with the rotor speed Ω as the chosen bifurcation parameter. Numerical simulation is used for verification and interpretation of the obtained stable or unstable periodic solutions.

In the following, system responses are discussed for certain parameter values in order to show the most interesting results of this research. Since a fully symmetrical problem is discussed, all diagrams are valid for both x - and y -direction. Figure 7 shows the steady-state amplitudes of the rotor vibration in x - and y -direction, respectively, versus the dimensionless excitation frequency Ω . Stable periodic solutions are represented by solid lines, unstable periodic solutions by dashed lines. All presented solutions are calculated for the parameter values $G_{PN} = 3.0$, $G_{DN} = 1.34$, $I_{C,max} = 2.0$, and $E = 0.35$.

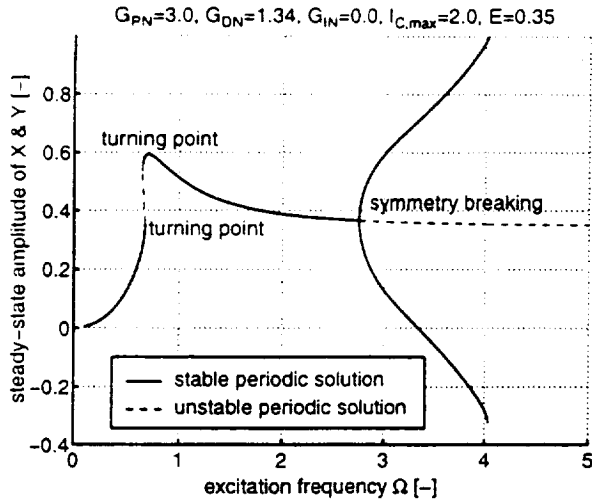


Figure 7: AMB System response without integral feedback gain.

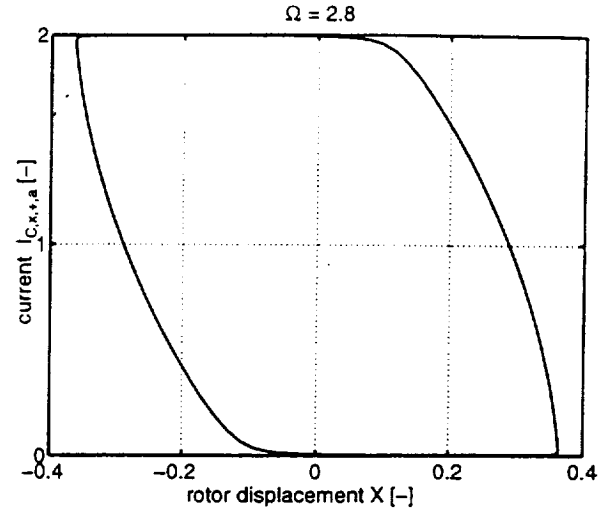


Figure 8: Saturation effect of the output of the main PID-controller in the neighborhood of the bifurcation point.

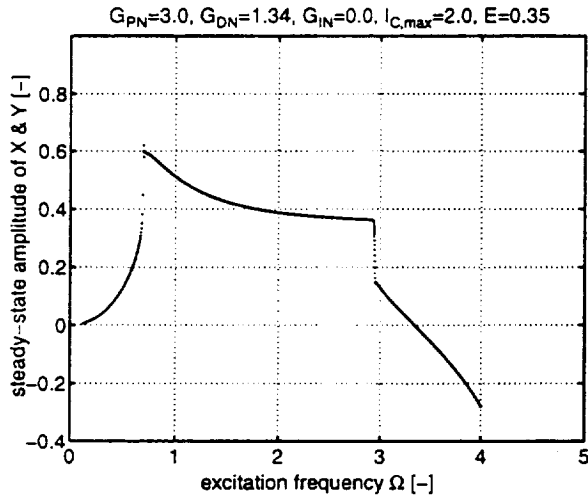


Figure 9: Numerical simulation results with stable lower unsymmetric branch.

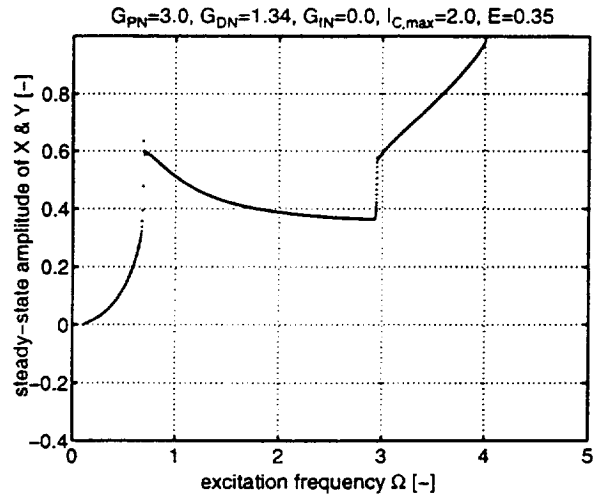


Figure 10: Numerical simulation results with stable upper unsymmetric branch.

The system response without integral feedback is shown in Fig. 7. Sweeping from low to high values of the excitation frequency, at $\Omega = 0.67$ a turning point occurs. Because of the softening spring characteristic of the system the resonant curve bends to the left until a second turning point at $\Omega = 0.64$ is reached. For all frequency values between these two turning points three coexisting periodic solutions exist, i.e. two stable solutions and one unstable solution. This causes jump and hysteresis phenomena when changing the excitation frequency across this region.

Increasing the frequency far beyond the eigenfrequency of the linearized system at $\Omega = 1.0$, another nonlinear phenomenon occurs. At $\Omega = 2.75$ symmetry breaking is detected. At this

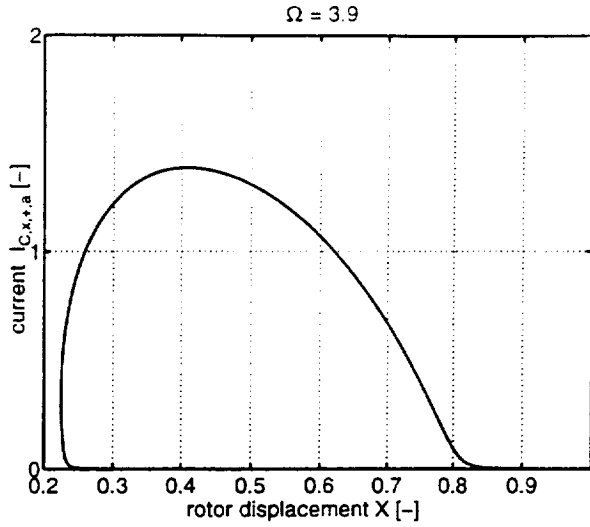


Figure 11: Output of PID-controller for electromagnet 'x,+' (on upper stable branch).

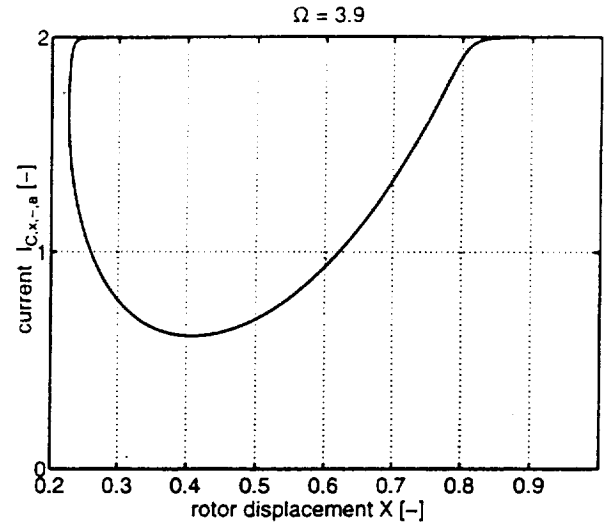


Figure 12: Output of PID-controller for electromagnet 'x,-' (on upper stable branch).

bifurcation point the symmetric periodic solution becomes unstable, when a stable unsymmetric solution emanates. The maximum and minimum values of the rotor vibrations are not equal in the case of an unsymmetric solution. However, four different stable rotor orbits are possible which are symmetric with respect to the x - or y -axis, respectively.

At $\Omega = 4.03$ the system response curve of both stable unsymmetric periodic solutions ends, because of contact between the rotor and the stator. However, the contact problem is beyond the scope of this work. Concerning the motion of a rotor with contact different types of bifurcations and nonlinear phenomena are discussed in [Ecker, 1997] and [Ecker, 1998], for example.

Note, that in Fig. 7 and subsequent diagrams rotor motion is considered only in one axis of the AMB. Therefore, maximum amplitudes at contact of $X_{max} = X_{cont} = 1.0$ are possible. In the case that both axes are considered maximum amplitudes in x - and y -direction at contact are limited according to $\sqrt{X_{cont}^2 + Y_{cont}^2} = R_{max} = 1.0$. In Fig. 7 this situation occurs at $\Omega = 3.63$.

The frequency value of the bifurcation point depends on the differential feedback gain. It can be shifted to lower frequencies by increasing the differential feedback gain G_{DN} . Symmetry breaking is caused by saturation of the nominal coil current required by the main PID-controller, see Fig. 8, 11 and 12.

In order to verify the results obtained by BIFPACK, additional numerical simulations are carried out. By slowly increasing the excitation frequency from $\Omega = 0.0$ to $\Omega = 4.0$ identical results are obtained, see Fig. 9 and 10. Each point of the plotted curve represents the maximum of rotor displacement during one period of unbalance excitation. Therefore, the transient behaviour of the jump phenomenon can be seen in Fig. 9 and 10. It depends on the initial conditions, which stable unsymmetric branch is picked by the system. Practically speaking the branches are randomly chosen

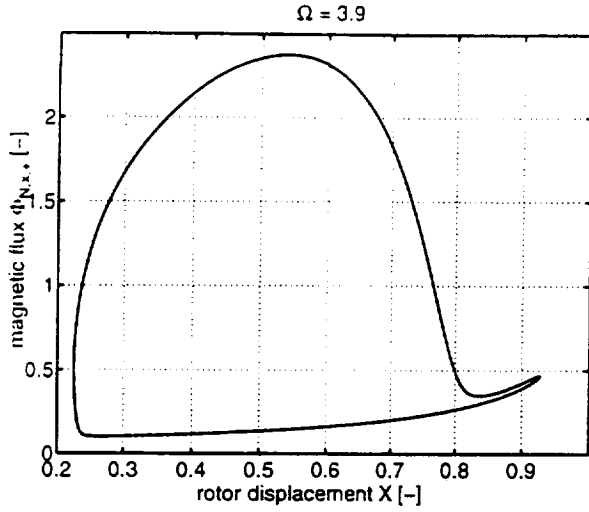


Figure 13: Magnetic flux for electromagnet 'x,+' (on upper stable branch).

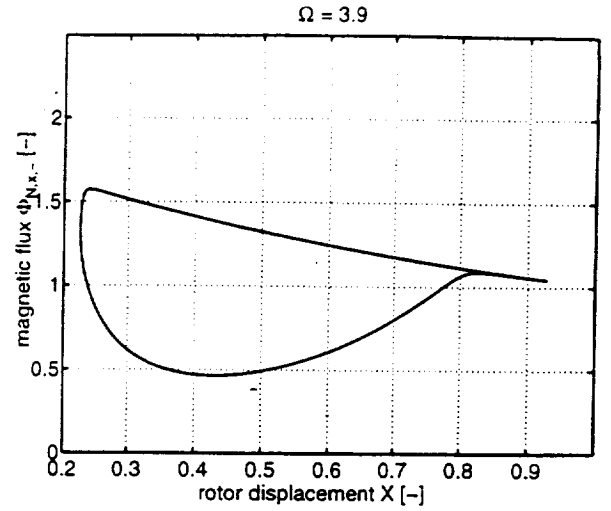


Figure 14: Magnetic flux for electromagnet 'x,-' (on upper stable branch).

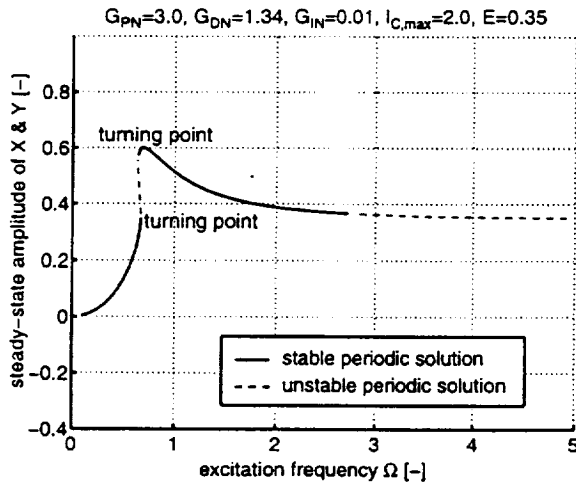


Figure 15: AMB system response with integral feedback gain.

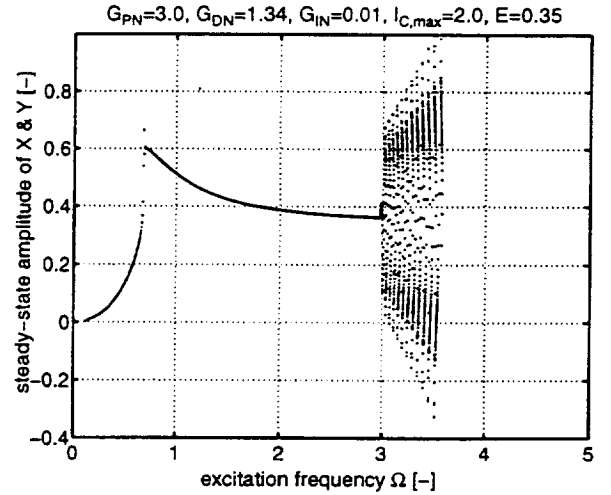


Figure 16: Numerical simulation results with integral feedback gain.

corresponding to arbitrary initial conditions.

Figure 11 and 12 show the coil currents calculated by the main PID-controller for the upper stable branch at $\Omega = 3.9$. The plots show a strong nonlinear characteristic caused by saturation. The magnetic flux for the same parameter set is plotted in Fig. 13 and 14 respectively.

For all results presented, only the output of the PID-controller exceeds the saturation value. Both the voltage of the power amplifier and the magnetic flux density remain well within the linear range.

Turning on the integral feedback gain G_{IN} stable periodic branches could not be found anymore

beyond the speed threshold of $\Omega = 2.75$, see Fig. 15. Instead, a quasiperiodic motion of the rotor occurs, which is detected by numerical simulation results, see Fig. 16. Because of symmetry breaking the integral part of the control current constantly increases the output of the PID-controller. Beyond the saturation value the influence of the proportional and differential feedback decreases almost down to zero-value. This would be changed by introducing a separate saturation level only for the integral part of the control current well below the saturation value for the whole output of the PID-controller.

CONCLUSION

AMB systems show important nonlinear phenomena if nonlinear components are included in the analysis. This investigation discusses vibration effects of saturation of the PID-controller output. Numerical results obtained by solving a boundary value problem combined with the path following method are presented. Stable and unstable periodic solutions are calculated. For specific parameter sets symmetry breaking and quasiperiodic solutions may occur. It is shown that important phenomena exist in AMB systems which are not predictable by linear methods. Future investigations will be carried out to discuss further interesting parameter sets. Higher sophisticated models including more components, as for example geometric coupling and static preload, will be investigated.

ACKNOWLEDGEMENT

The authors gratefully acknowledge the support of this project by the Austrian science foundation 'Fonds zur Förderung der wissenschaftlichen Forschung (FWF)'.

REFERENCES

- [Chinta, et al., 1996] Chinta, M., Palazzolo, A.B., Kascak, A., *Quasiperiodic Vibration of a Rotor in a Magnetic Bearing with Geometric Coupling*, Proc. of 5th Int. Symp. on Magnetic Bearings, Kanazawa, Japan, 1996.
- [Ecker, 1998] Ecker, H., *Nonlinear stability analysis of rigid single mass rotor contacting a rigid auxiliary bearing*, IFToMM Proc. of Fifth Int. Conf. on Rotor Dynamics, (Irretier, H., Nordmann, R., ed.), pp. 790-801, Darmstadt, Germany, Sept. 7-10, 1998.
- [Ecker, 1997] Ecker, H., *Steady-state orbits of an AMB-supported rotor contacting the backup bearings*, Proc. of Indust. Conf. of Magnetic Bearings MAG'97, (Allaire, P., ed.), pp. 129-138, Alexandria, VA, Aug. 21-22, 1997.
- [Ecker, et al., 1997] Ecker, H., Knight, J.D., Wu, L., *Nonlinear Dynamic Simulation of an Active Magnetic Bearing System with Non-symmetric Coordinate Coupling Forces*, Proc. of Int. Gas

- Turbine & Aeroengine Congress & Exhibition, Orlando, Florida, ASME Conf. paper No. 97-GT-113, 1997.
- [Haferl, Springer, 1991] Haferl, A., Springer, H., *Simulation von Magnetisierungsprozessen in Magnetlagern*, Proc. of 7. Symp. Simulationstechnik, ASVM-Tagung in Hagen, Verlag Vieweg, 1991.
- [Hebbale, 1985] Hebbale, K.V., *A Theoretical Model for the Study of Nonlinear Dynamics of Magnetic Bearings*, Ph.D. thesis, Cornell University, 1985.
- [Hebbale, Taylor, 1986] Hebbale, K.V., Taylor, D.L., *Nonlinear Dynamics of Attractive Magnetic Bearings*, Proc. of the Workshop on Rotordynamic Instability Problems in High-Performance Turbomachinery, Texas A&M-Univ., NASA-Conf. Publ. No. 2443, 1986.
- [Hoffmann, et al., 1997] Hoffmann, K.-J., Laier, D., Markert, R., *Nonlinear Control of Magnetically Supported Rotors*, Proc. of MAG'97 - Industrial Conference and Exhibition on Magnetic Bearings, Alexandria, VA, 1997.
- [Jeong, et al., 1994] Jeong, H.S., Kim, C.S., Lee, C.W., *Modelling and Control of Cone Shaped Active Magnetic Bearing Systems*, Proc. of 4th Int. Symp. on Magnetic Bearings, ETH-Zürich, 1994.
- [Knight, Ecker, 1996] Knight, J.D., Ecker, H., *Simulation of Nonlinear Dynamics in Magnetic Bearings with Coordinate Coupling*, Proc. of Summer Computer Simulation Conf., Portland, Oregon, 1996.
- [Knight, et al., 1993] Knight, J., Walsh, T., Virgin L., *Dynamic Analysis of a Magnetic Bearing System with Flux Control*, Proc. of 2nd Int. Symp. on Magnetic Suspension Technology, Seattle, WA, 1993.
- [Knight, et al., 1992] Knight, J.D., Xia, Z., McCaul, E.B., *Forces in Magnetic Journal Bearings: Nonlinear Computation and Experimental Measurement*, Proc. of 3rd Int. Symp. on Magnetic Bearings, Alexandria, VA, 1992.
- [Lang, et al., 1995] Lang, O., Wassermann, J., Springer, H., *Adaptive Vibration Control of a Rigid Rotor supported by Active Magnetic Bearings*, Proc. of Int. Gas Turbine and Aeroengine Congress and Exposition, Houston, Texas, 1995.
- [Mohamed, Emad, 1993] Mohamed, A.M., Emad, F.P., *Nonlinear Oscillations in Magnetic Bearing Systems*, IEEE Transactions on Automatic Control, Vol. 38, No.8, 1993.
- [Moser, 1993] Moser, F., *Stabilität und Verzweigungsverhalten eines nichtlinearen Rotor-Lager-Systems*, Ph.D. thesis, Vienna University of Technology, 1993.
- [Nataraj, 1995] Nataraj, C., *Nonlinear Analysis of a Rigid Rotor on Magnetic Bearings*, Proc. of Int. Gas Turbine and Aeroengine Congress and Exposition, Houston, ASME Conf. paper No. 95-GT-204, 1995.
- [Satoh, et al., 1990] Satoh, I., Murakama, C., Nakajima, A., Kanemitsu, Y., *A Self-Excited Vibration of Magnetic Bearing Systems with Flexible Structure*, Proc. of 2nd Int. Symp. on Magnetic Bearings, Tokyo, 1990.

- [Schweitzer, et al., 1993] Schweitzer, G., Traxler, A., Bleuler, H., *Magnetlager, Grundlagen, Eigenschaften und Anwendungen berührungsfreier, elektromagnetischer Lager*, Springer Verlag, Berlin, 1993.
- [Seydel, 1996] Seydel R., *BifPack, a Program Package for Continuation, Bifurcation and Stability Analysis*, Program documentation, University of Ulm, Germany, 1996.
- [Sinha, 1990] Sinha, A., *On the Design of Magnetic Suspension Systems*, Proc. of Gas Turbine and Aeroengine Congress and Exposition, Belgium, ASME Conf. paper No. 90-GT-239, 1990.
- [Springer, et al., 1990] Springer, H., Maslen, E.H., Humphris, R.H., *Nonlinear Hysteresis Effects in Electromagnetic Bearings*, Proc. of 3rd Int. Conf. on Rotordynamics, Lyon, (Ed. du CNRS), 1990.
- [Springer, et al., 1998] Springer, H., Schlager, G., Platter T., *A Nonlinear Simulation Model for Active Magnetic Bearing Actuators*, Proc. of 6th Int. Symp. on Magnetic Bearings, MIT Cambridge, MA, 1998.
- [Steinschaden, Springer, 1999] Steinschaden, N., Springer, H., *Some Nonlinear Effects of Magnetic Bearings*, Proc. of the 1999 ASME Design Engineering Technical Conferences, Las Vegas, Nevada, ASME Conf. paper No. DETC99/VIB-8063, 1999.
- [Troger, Steindl, 1991] Troger, H., Steindl, A., *Nonlinear Stability and Bifurcation Theory*, Springer Verlag, Wien - New York, 1991.
- [Virgin, et al., 1994] Virgin, L., Walsh, T.F., Knight, J.D., *Nonlinear Behavior of a Magnetic Bearing System*, Proc. of Int. Gas Turbine and Aeroengine Congress and Exposition, The Hague, Netherlands, ASME Conf. paper No. 94-GT-341, 1994.
- [Wang, et al., 1994] Wang, H., Wu, Z., Niu, X., *Dynamic Bifurcations of Active Magnetic Bearings Rotor Systems*, Proc. of 4th Int. Symp. on Magnetic Bearings, ETH-Zürich, 1994.

Session 11 -- Controls 2

Chairman: Eric H. Maslen
University of Virginia (UVA)

CONTROL SYSTEM FOR INSIDE-OUT CONFIGURATION MAGNETIC BEARINGS

Gregory Buckner¹, Alan Palazzolo², John Kajs¹, Brian Murphy⁴, Joe Beno³

¹ Department of Mechanical and Aerospace Engineering, North Carolina State University, Raleigh NC

² Department of Mechanical Engineering, Texas A&M University, College Station TX

^{3,4,5} Center for Electromechanics, The University of Texas at Austin, Austin TX

ABSTRACT

The University of Texas Center for Electromechanics (UT-CEM) in association with the Texas A&M Vibration Control Lab (TAMU-VCL) has developed an active magnetic bearing control system for use in a 5 MW, 25 MJ, 20,000 RPM flywheel alternator developed under the Combat Hybrid Power Systems (CHPS) program. The inside-out topology of this flywheel (i.e., the 650 lb (294 kg) flywheel rotor is positioned outside the stator) was dictated by the extreme power density and energy density requirements, and presented unique control challenges seldom encountered in conventional magnetic bearing applications. These challenges resulted from a large number of flexible modes in the rotor and stator, requiring a high-order flexible dynamic model and extensive rotordynamic analysis. A simulation-based design effort was implemented to accomplish the primary control objective: to provide robust, efficient magnetic levitation of the CHPS rotor over a wide range of operating speeds and disturbance inputs, while minimizing the occurrence of backup bearing touchdowns. Additionally, this design effort provided critical specifications for CHPS flywheel design and component selection. Details of the CHPS magnetic bearing design, prototyping, and testing are presented in a companion paper "Inside-Out Configuration Active Magnetic Bearing Actuators".

INTRODUCTION

Researchers at the University of Texas Center for Electromechanics (UT-CEM) have been actively involved in the design, fabrication, and testing of advanced flywheel energy storage systems for several years [1,2,3,4]. One example of this research is the recently-completed Combat Hybrid Power System (CHPS) Flywheel Design Program, which developed a 5 MW, 25 MJ, 20,000 RPM flywheel alternator for military applications under DARPA funding [5]. This flywheel system was designed to power multi-MW pulse loads and provide mobility load leveling over the 15-year life cycle of a combat vehicle. The power density and energy density requirements dictated an inside-out, fully-contained flywheel topology, meaning the 650 lb (294 kg) rotor is positioned outside the stator. This unique, state-of-the-art machine consists of a vacuum housing that supports a hollow, non-rotating shaft (stator), and a magnetically-levitated composite rotor (see

Figure 1). Critical to the success of this flywheel system was the development of inside-out radial and combination magnetic bearings that could accommodate the high speeds, heavy loads, and disturbance inputs with minimal frictional losses, nominal power consumption, and modest design complexity.

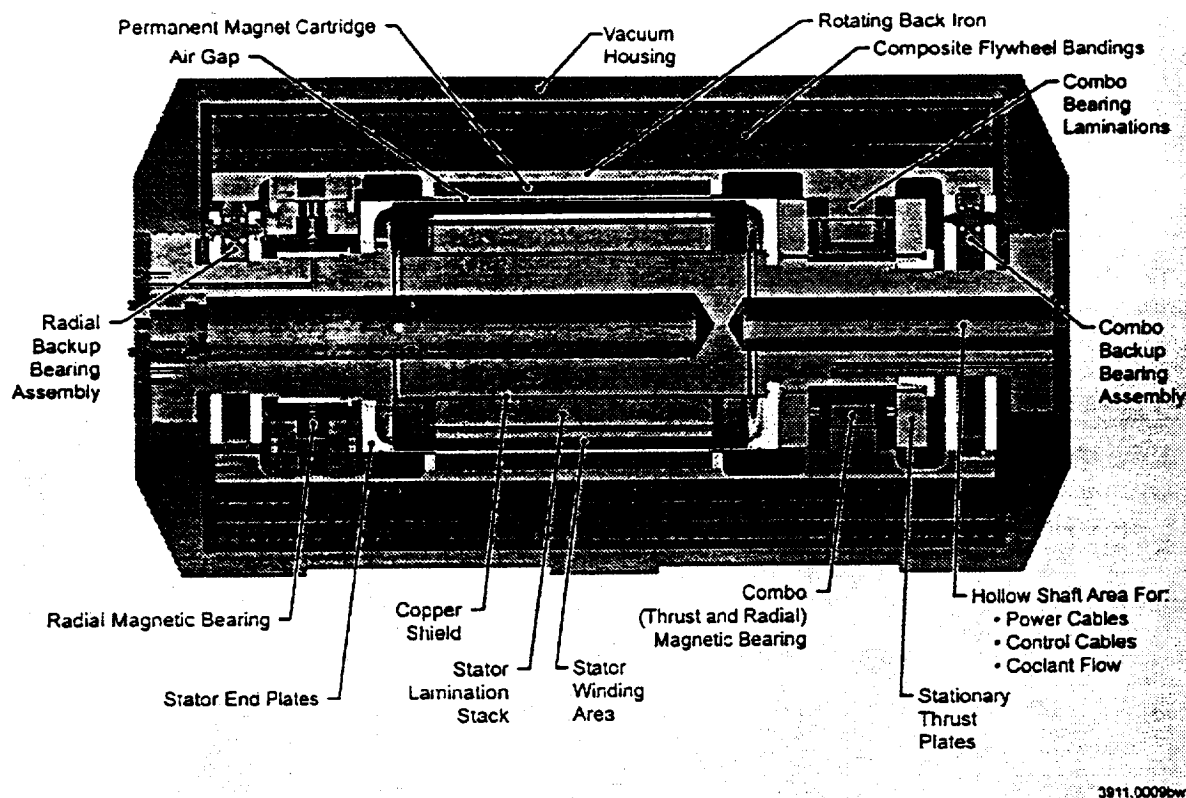


Figure 1: The UT-CEM CHPS Flywheel Design

The characteristics and capabilities of Active Magnetic Bearings (AMBs) in supporting high-speed rotors have been thoroughly documented in the literature [6,7]. For flywheel applications their most prominent features are high-speed capability, vacuum compatibility, low frictional losses, and lack of any required lubricant. Additionally, the control algorithms developed in recent years have addressed the complexities of flexible rotors and highly gyroscopic systems [8]. Modern DSP-based controllers can accommodate sophisticated control algorithms (multivariable, gain-scheduled, etc.) at high sampling rates (10-100kHz) and make magnetic bearings a viable option for demanding high-speed, flexible-rotor applications.

This paper describes a joint research effort between UT-CEM and the Texas A&M Vibration Control Laboratory (TAMU-VCL) to develop a control system for the inside-out radial magnetic bearings employed by the CHPS flywheel. The primary design objective was to provide robust, efficient magnetic levitation of the CHPS rotor over a wide range of operating speeds and disturbance inputs, while minimizing the occurrence of backup bearing touchdowns. This design effort required extensive rotordynamic analysis to determine the flywheel's critical speeds and mode shapes, and to answer

important questions that surfaced during the mechanical design of the rotor and stator, including: 1) Would passive stator damping need to be introduced? 2) Would enlarging the stator through-hole adversely affect system stability? Additionally, this controller development provided several important design specifications for the CHPS flywheel components: 1) Power amplifier selection (voltage and current requirements, wiring configurations), 2) Rotor and stator fabrication (runout and mass imbalance specifications), 3) Sensor selection (resolution and noise requirements), and 4) Digital controller selection (required processor performance, number of input/output channels, etc.).

The controller design approach followed a logical progression of steps, and relied heavily on good communication and cooperation between the two research centers. UT-CEM provided electromechanical characteristics of the bearings (inductance, resistance, current stiffness, position stiffness, etc.) and rotordynamic characteristics of the rotor, stator, and housing based on extensive Finite Element Analysis (FEA). TAMU-VCL conducted the controller design, beginning with rigid body models of the flywheel system. Later, high-order FEA models were used to study the closed-loop rotordynamic behavior, providing insight into the modal and inertial load responses. The large number of stator flexible modes, coupled with a bearing air gap that increases with speed, made the controller development particularly challenging. The final controller was optimized to provide stable operation over the entire speed range of the CHPS flywheel, and was robust to the specified levels of runout, noise, and mass imbalance.

ROTORDYNAMIC ANALYSIS

As in the case of standard rotor/stator configurations, AMB controller design is primarily concerned with critical vibration modes below the maximum operating speed (20,000 RPM, or 333 Hz for the CHPS flywheel). Additionally, modes above the operating speed can create control problems if they fall within the controller's bandwidth (3,000 Hz). For the CHPS flywheel (including the rotor, stator, and housing), there are at least 20 modes in this frequency range, thus a high-fidelity rotordynamic model was necessary for control design. To accommodate this need, a 548 degrees of freedom (DOF) model was developed at UT-CEM using TXRotor (a custom rotordynamic FEA package). This model provided a complete analysis of natural frequencies and mode shapes in the 0-3,000 Hz range, and was critical to successful controller development. Additionally, it enabled investigation of the benefits of additional stator damping in attenuating certain modes.

Figure 2 shows the CHPS rotordynamic model, a two-dimensional TXRotor finite element model made up of 3-node, cylindrically-shaped, isoparametric beam elements. Beam element models of this type are known to yield accurate estimates of lateral modes of vibration [9]. The model contains 137 nodes, 185 beam elements, and 548 DOF (4 DOF per node) — a level of detail more than adequate for this application. In addition to

the rotor (dark shaded elements), the model includes the stator through-shaft (cross-hatched elements), endplates and outer vacuum housing (light shaded elements).

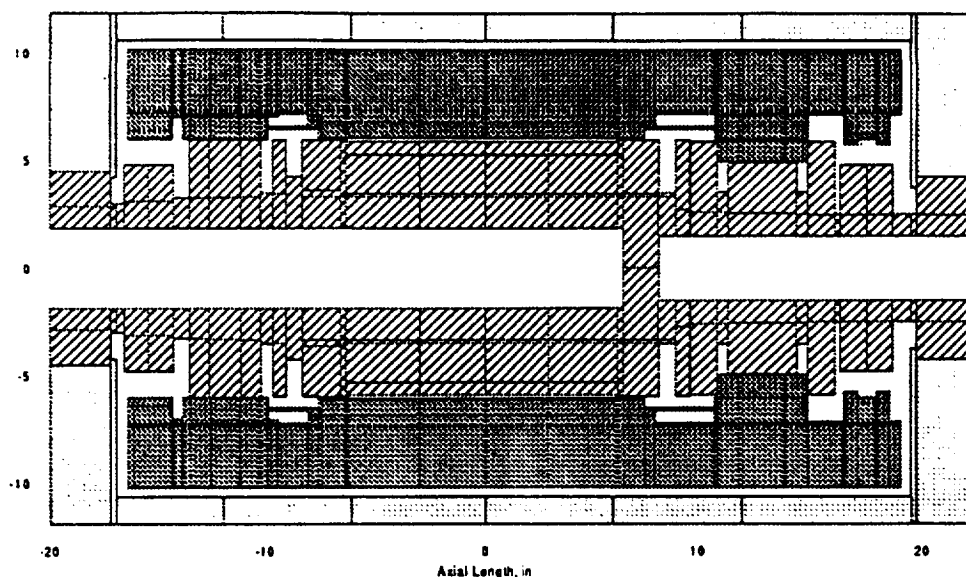


Figure 2: CHPS Rotordynamic FEA Model

The five lowest mode shapes associated with this model are shown in Figure 3. The four lowest modes occur at frequencies below the minimum operating speed of 15,000 RPM. These four modes all represent “rigid body modes”, as there is no appreciable bending of either the rotor or stator. The two lowest modes are the “bouncing” and “rocking” modes, respectively, of the entire machine with the rotor and stator moving in unison. The next two higher modes are “bouncing” and “rocking” modes of the rotor, with respect to the stator. That is, the rotor is moving more than the stator. These rigid body modes must be traversed while the rotor accelerates up to its operating speed range of 15,000-20,000 RPM. The fact that these modes involve no bending of the stator or rotor means they can be easily controlled by the magnetic bearings.

The first (i.e., lowest) flexible mode of vibration (illustrated as the fifth mode shape in Figure 3) occurs at 30,000 CPM, well above the maximum operating speed of 20,000 RPM. This mode shape is the fundamental bending mode of the stator, with the rotor moving very little. A key point is that the frequency of this first flexible mode is far above the maximum rotational speed of the machine. This wide separation margin means that the mode will not interfere with AMB controller as it maintains support of the rotor in its normal operating range.

The first (i.e., lowest) flexible mode of vibration (illustrated as the fifth mode shape in Figure 3) occurs at 30,000 CPM, well above the maximum operating speed of 20,000 RPM. This mode shape is the fundamental bending mode of the stator, with the rotor moving very little. A key point is that the frequency of this first flexible mode is far above the maximum rotational speed of the machine. This wide separation margin means that the mode will not interfere with AMB controller as it maintains support of the rotor in its normal operating range.

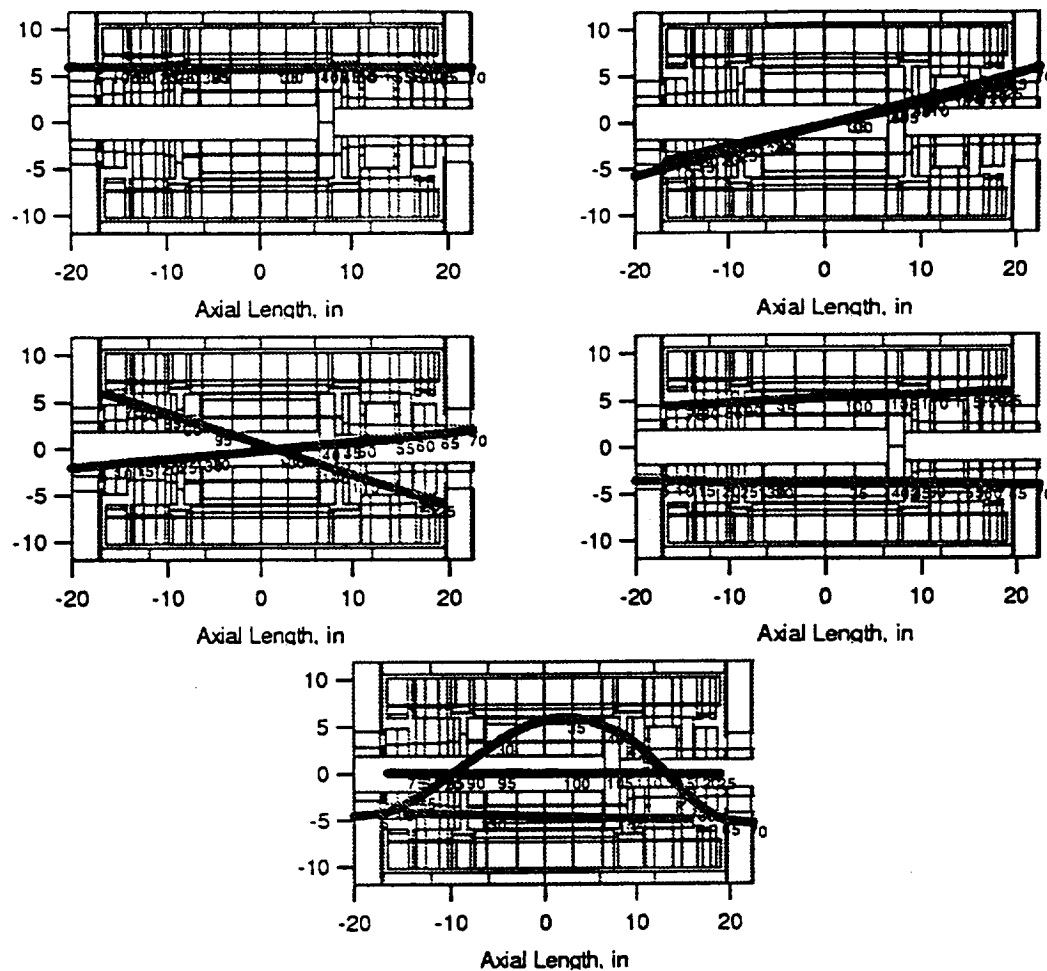


Figure 3: CHPS Rotordynamic Mode Shapes

Figure 4 is a natural frequency map, and shows that the modal frequencies actually change as the rotor speed changes. Note that the frequencies of the conical (or bounce) modes increase as speed increases. This is due to gyroscopic stiffening, which becomes stronger as the rotor spins faster. The hatched region on the plot labeled Operating Range covers the operating speed range on the horizontal axis, and on the vertical axis covers a frequency range from 20% below rotor speed to 20% above rotor speed. To avoid resonance and interference with the magnetic bearing controller while the flywheel is within its operating speed range, frequencies of all modes must lie outside this hatched region. The rigid rotor conical mode is seen to come closest to the Operating Range, but still lies outside it. More importantly, however, the first flexible mode is well removed from the Operating Range as it is well above 30,000 CPM. The results of this rotordynamic analysis indicate that the CHPS flywheel rotor is a good candidate for magnetic bearing support.

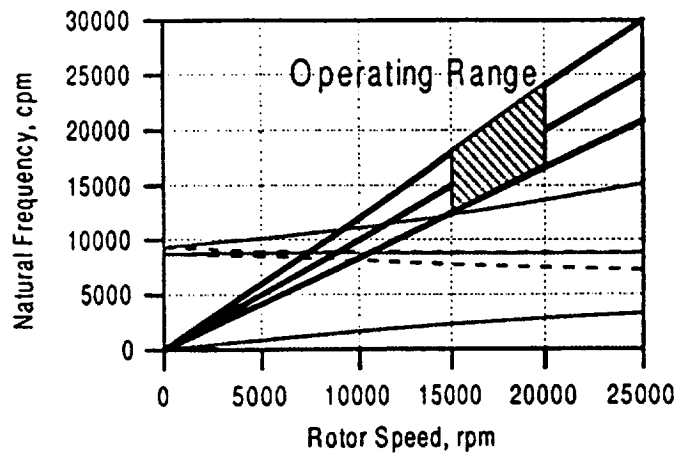


Figure 4: CHPS Natural Frequency Map

CONTROLLER DEVELOPMENT

One of the stated research objectives was to develop a straightforward AMB control system, hence controller development focused on decentralized, or Single-Input, Single-Output (SISO) approaches. In other words, the problem of controlling rotor position was simplified by assuming that radial displacements and forces at one end of the rotor were independent of displacements and forces at the other end. Additionally, displacements and forces acting in one radial direction of a bearing were independent from displacements and forces perpendicular to that direction within the same bearing. Despite the unique challenges associated with this design effort (extremely high-order rotordynamic model, large number of flexible modes, an air gap dependent on rotor speed, etc.) this design simplification has proven to be highly effective for lightly-coupled rotordynamic systems like the CHPS flywheel [6,10]. SISO development is generally more straightforward than multivariable development, requires less computational power, and provides greater flexibility when choosing a real-time processor.

Baseline PD Control

A Proportional+Derivative (PD) compensator was chosen to be the baseline controller for the CHPS flywheel. PD controllers have been selected for numerous AMB applications in the literature [6,7], primarily due to their intuitive appeal: Proportional control relates directly to bearing stiffness, while Derivative control relates to bearing damping. Independent PD controllers were selected for each measured displacement of the rotor (5 total: radial displacements at the thrust end (X and Y), radial displacements at the non-thrust end (X and Y), and thrust displacement at the thrust end (Z)). For the CHPS flywheel, each displacement sensor was co-linear with the axes of the control coils. The first step in tuning this controller was to determine a range of proportional gains (K_p) and derivative gains (K_d) that would result in stable levitation, based on the linear control system model of Figure 5. For reference purposes, a proportional gain of 16 was

determined to be equivalent to a static bearing stiffness of 88,377 lb/in (15,483,341 N/m) at the nominal operating conditions.

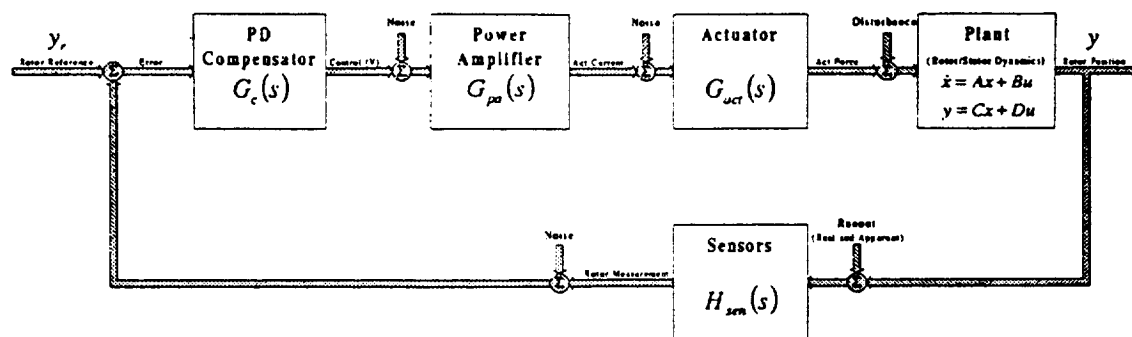


Figure 5: Linear Model of Baseline PD Control System

A linear stability analysis was conducted for a range of proportional gains ($0 \leq K_p \leq 80$) and derivative gains ($0 \leq K_d \leq 0.05$). Note that system stability also depends on controller bandwidth, as shown in Figure 6. If the bandwidth is limited to 1,000 Hz, the entire range of gains results in linear stability. If the bandwidth is increased to 2,000 Hz, all proportional gains greater than 40 destabilize the controller. For the CHPS application, a controller bandwidth of 3,000 Hz was anticipated (allowing approximately 10 control actions per rotation at full speed) resulting in a smaller range of stabilizing gains.

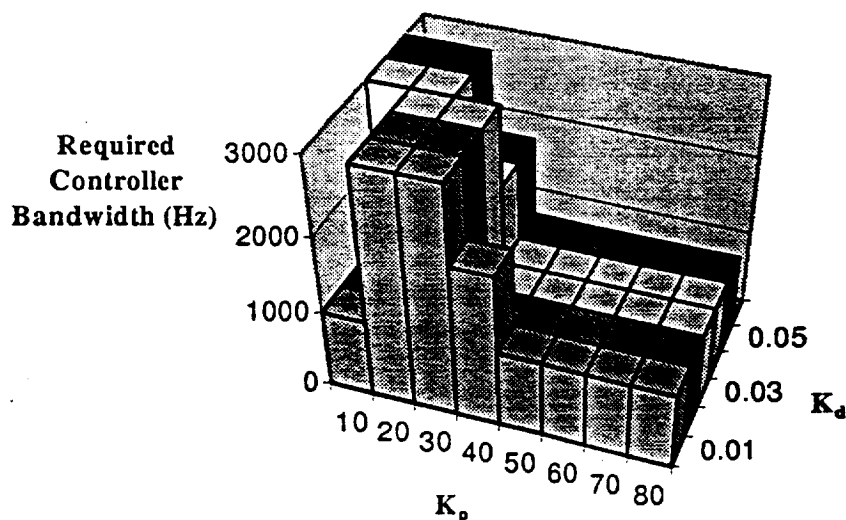


Figure 6: Linear Stability Map for Baseline PD Controller

Based on this linear stability analysis, PD controller gains were selected and controller performance was evaluated for a variety of operating conditions. Using a proportional gain of 10 and a derivative gain of 0.03, simulations confirmed AMB stability over the entire speed range (0-20,000 RPM). Figure 7 shows closed-loop orbits for one rotor mode (top) and one stator mode (bottom) at a rotor speed of 20,000 RPM. This PD controller was robust to modest values of mass imbalance and sensor runout, but the

required AMB coil voltages were excessive. At a rotor speed of 20,000 RPM, the controller required peak steady-state voltages of 50 V to compensate for a mass imbalance of 0.00001" and 150 V to compensate for a sinusoidal sensor runout of 0.0006". Clearly, controller refinements were needed to reduce this level of control effort. Furthermore, the controller was particularly sensitive to sensor noise and disturbances, indicating the need for more sophisticated control.

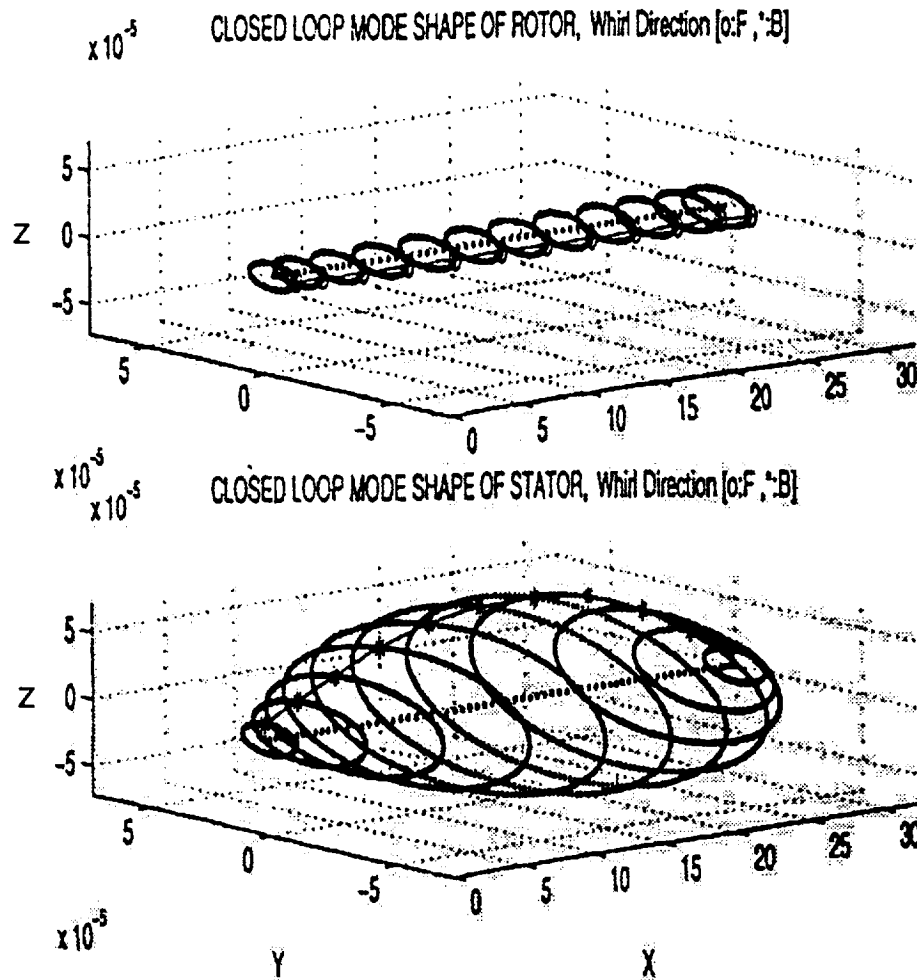


Figure 7: Closed-Loop Orbit Plots for PD Controller

Imbalance Compensation

The primary deficiency of the baseline PD controller resulted from synchronous (once per revolution) disturbances: mass imbalance and sensor runout. In each case, the controller required unacceptably high AMB coil voltages to compensate for these disturbances. To address this problem, a standard controller refinement called "imbalance compensation" was implemented [11,12]. Imbalance compensation introduces a cascaded band-reject notch filter (whose center frequency tracks the rotor speed) to attenuate controller responses to synchronous disturbances. In other words,

mass imbalance and synchronous runout are not controlled, which enables the rotor to spin about its inertial axis (instead of controlling it to spin about its geometric axis). Assuming adequate air gap exists, the rotor no longer transmits imbalance forces to the stator/housing (vibration and noise are reduced), and synchronous control effort is virtually eliminated.

Figure 8 illustrates the dramatic reductions in control effort achieved by introducing a tracking notch filter. Figure 8.a shows the peak coil voltages (which depend on rotor speed) required to compensate for a mass imbalance of $0.00001''$, with the notch filter fixed at 20,000 CPM. As the rotor speed approaches the filter's center frequency (20,000 RPM), the required coil voltage drops to nearly zero. Figure 8.b shows a time response of the required coil voltage, at a rotor speed of 20,000 RPM, as the fixed notch filter is inserted. For times $0 \leq t \leq 0.1$ seconds, the controller requires a peak voltage of 50 V to compensate for the imbalance. As the notch filter is inserted (at time $t=0.1$ seconds), the controller effort is dramatically reduced.

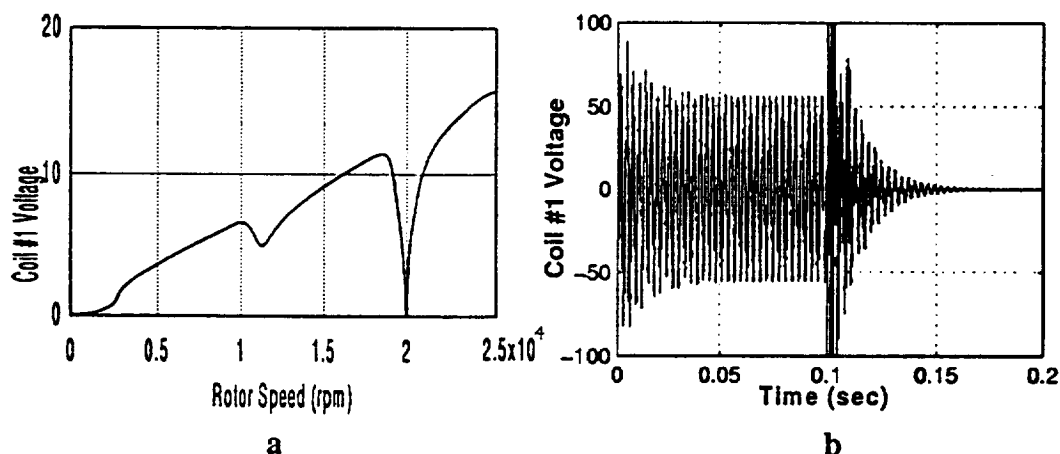


Figure 8: Coil Voltage Requirements for 20 kHz Imbalance Compensation:
a) Steady-State Peak Voltages b) Transient Voltage During Notch Introduction

Fixed-Frequency Notch Filtering

Although the introduction of a tracking notch filter significantly reduced the control effort and improved robustness to mass imbalance and synchronous runout, it had an undesirable impact on overall system stability. Certain high-frequency modes between 2,500 Hz and 3,000 Hz (within the controller bandwidth) became very poorly damped or even unstable as a result of this refinement. Some of these modes were associated with low stator damping, and prompted a rotordynamic analysis to investigate the benefits of adding passive stator damping. This analysis concluded no significant benefits could be achieved with increased damping, so additional controller refinements were needed.

To counteract these unstable modes, a series of fixed-frequency notch filters and a lead compensator were systematically cascaded with the existing controller, as shown in Figure 9. The resulting cascaded controller demonstrated acceptable performance over the operating range for a larger range of disturbances and noise.

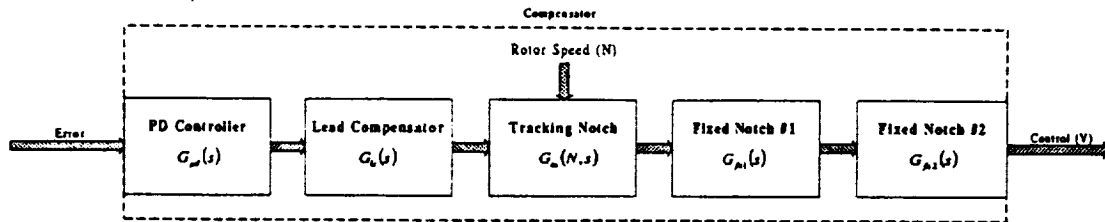


Figure 9: Final Cascaded Bearing Controller

CONTROL SYSTEM PERFORMANCE EVALUATION

An extensive series of dynamic simulations was conducted to assess system performance for a variety of operating conditions and disturbance inputs. Although the design effort relied on linear models of control system components (Figure 5) and simplified models of sensor runout, these final evaluations included realistic models of system nonlinearities and experimental runout data. The most significant nonlinearities were voltage and current limitations associated with the power amplifiers and AMB stiffness variations (position and current stiffness) associated with rotor speed (due to changes in the air gap with rotor speed). Because sensor runout was identified as being critical to overall system performance, UT-CEM fabricated an experimental test-rig to collect representative runout data using the same optical sensor hardware and unpolished materials planned for the CHPS Flywheel. This runout data, presented in Figure 10, provided authentic, “worst-case” disturbance information for control system evaluation.

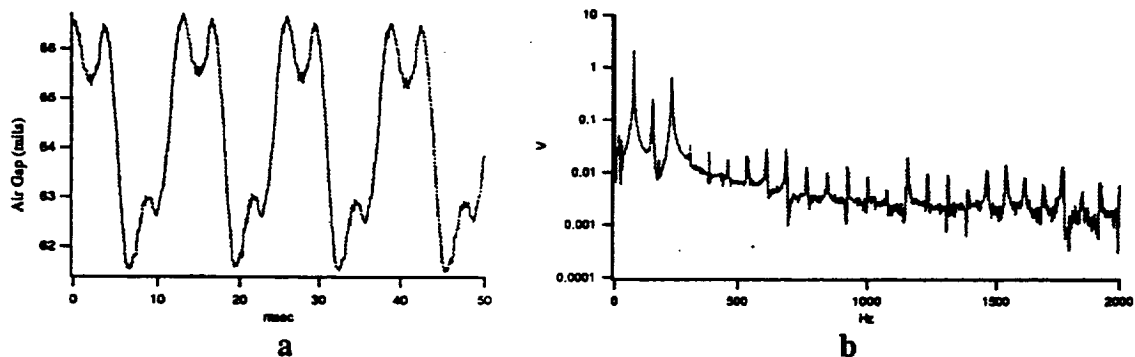


Figure 10: Experimental Air Gap Measurements for the CHPS Flywheel:
a) Optical Sensor Time Series b) Unfiltered FFT Showing Harmonic Content

The simulations confirmed the control system’s effectiveness with respect to the design objectives. Most importantly, this cascaded design maintained stable levitation of the

CHPS rotor over the entire speed range (0-20,000 RPM) for a variety of disturbance inputs, including authentic sensor runout, mass imbalance, sensor noise, and inertial loading (due to vehicle cornering and braking). Additionally, the peak coil voltages were within the design specifications for this system (150 V) and currents were within the specified limits for the selected power amplifiers, with adequate margin against clipping. Margin against saturation in the flux path circuit was also achieved. Finally, these simulations provided valuable design specifications for the power amplifiers, sensors, and machining tolerances.

CONCLUSIONS

Researchers from UT-CEM and TAMU-VCL have successfully developed a control system for the inside-out radial magnetic bearings employed by the CHPS flywheel. Although the SISO cascaded control architecture is straightforward, this controller conquered numerous design challenges (extremely large number of system states, lightly-damped flexible modes, air gap dependent on rotor speed, etc.) to meet or exceed each of the design objectives. Moreover, this design effort is the first known application of AMBs to inside-out configuration bearings. Extensive performance simulations confirmed that the control system provides robust, efficient magnetic levitation of the CHPS rotor over a wide range of operating speeds and disturbance inputs, while minimizing the occurrence of backup bearing touchdowns. Additionally, this design effort provided critical design specifications for CHPS flywheel design and component selection.

REFERENCES

1. R. Hayes, J. Kajs, R. Thompson, J. Beno, "Design and Testing of a Flywheel Battery for a Transit Bus", 1999 SAE International Congress and Exposition, March 1-4, 1999, Detroit, MI.
2. R. Thompson, R. Hayes, J. Beno, "The Flywheel Battery Containment Problem-Light Weight Solution", 1999 SAE International Congress and Exposition, March 1-4, 1999, Detroit, MI.
3. B. Murphy, J. Beno, D. Bresie, "Bearing Loads in a Vehicular Flywheel Battery", 1997 SAE International Congress and Exposition, Feb 24-27, 1997, Detroit, MI.
4. M. Pichot, J. Kramer, R. Hayes, R.C. Thompson, J. Beno, "The Flywheel Battery Containment Problem", 1997 SAE International Congress and Exposition, Feb 24-27, 1997, Detroit, MI.

5. M. Pichot, J. Kajs, A. Ouroua, J. Beno, R. Hayes, "Inside-Out Configuration Active Magnetic Bearing Actuators", 5th International Symposium on Magnetic Suspension Technology, 1999.
6. G. Schweitzer, H. Bleuler, A. Traxler, Active Magnetic Bearings: Basics, Properties and Applications of Active Magnetic Bearings, vdf Hochschulverlag AG, 1994.
7. R. Siegwart, R. Larsonneur, and A. Traxler, "Design and Performance of a High Speed Milling Spindle in Digitally Controlled Active Magnetic Bearings", Proceedings of 2nd International Symposium on Magnetic Bearings, Tokyo, 1990.
8. M. Ahrens, L. Kucera, and R. Larsonneur, "mu-Synthesis of Flexible Rotor-Magnetic Bearing Systems", IEEE Transactions on Control Systems Technology, Vol. 4, No. 5, September 1996.
9. J. M. Vance, Rotordynamics of Turbomachinery, John Wiley & Sons, 1998.
10. H. Bleuler, "Decentralized Control of Magnetic Bearing Systems", Dissertation, Eidgenössische Technische Hochschule, Zürich, 1984 (Diss. ETH Nr. 7573).
11. R. Herzog, B. Philipp, G. Conrad, L. Rene, "Unbalance Compensation Using Generalized Notch Filters in the Multivariable Feedback of Magnetic Bearings", IEEE Transactions on Control Systems Technology, Vol. 4, No. 5, pp. 580-586, September 1996.
12. Knospe, C.R., "Stability and Performance of Notch Filter Controllers for Unbalance Response", Proceedings of the International Symposium on Magnetic Suspension Technology, NASA Langley Research Center, Hampton VA 1991.

REAL TIME CONTROL OF A MAGNETIC BEARING SUSPENSION SYSTEM FOR FLEXIBLE ROTORS

Edgar F. Hilton, Research Associate*
Marty Humphrey, Research Assistant Professor†
John Stankovic, B.P. Professor and Chair‡
Paul Allaire, MacWade Professor§

University of Virginia
Charlottesville, VA 22901

November 30, 1999

Abstract

Suspension of a magnetic bearing system involves significant computational effort. Control systems based upon embedded Digital Signal Processors (DSP) boards often require specialized programming and development tools, may lack flexibility when computational requirements change, and are often relatively expensive. Magnetic bearing systems need 1) real time monitoring of the plant states, inputs, and outputs 2) real time plotting functions such as rotor position *vs.* time, Fast Fourier Transform (FFT) functions and user specified filters, 3) controller parameter updates, and 4) access to reference signals. It is desired to employ a hardware/software system which is low cost, easy to use, is extensible as more advanced versions of hardware/software become available, and distributable over local networks of DSPs. A system with all of the above desired characteristics has been implemented for control of a magnetic bearing supported flexible rotor using RT-Linux, a free modification of Linux, intended to support hard real-time computation. Experiences designing the software architecture, defining timing requirements of the control tasks, implementing the control tasks in RT-Linux, and measuring the predictability of RT-Linux for this application are discussed.

1 Introduction

An artificial barrier seems to exist that separates the implementation of complex automatic control systems on active magnetic bearings (AMBs) and basic scheduling theory as devised in computer

*efhilton@alum.mit.edu, Mechanical and Aerospace Engineering, Rotating Machinery and Controls Laboratory, UVA

†Department of Computer Science, UVA

‡Department of Computer Science, UVA

§Mechanical and Aerospace Engineering, Rotating Machinery and Controls Laboratory, UVA

science circles. This paper seeks to remove that barrier and discuss the priority driven scheduling algorithms that are needed to efficiently implement complex automatic controllers for AMBs.

AMBs now require multiple computational tasks such as (in order of importance) 1) periodic fixed rate closed loop suspension loops, 2) a spin rate measuring system, 3) open loop balancing controller, 4) data transfer and plotting tasks, 5) network transfer tasks, and 6) miscellaneous additional tasks such as screen refresh or shell programs. Commonly, each of these tasks is implemented digitally as a sequence of commands which are interpreted by a digital computer, one command at a time. Normally, all of these tasks are easily implemented if enough independent computational engines are available unless restricted by factors such as hard disk, network, or bus access times (Stankovic, 1988; Stankovic and Buttazzo, 1995).

However, many applications of AMBs have a need for highly efficient inter-task communications, controller weight limitations, controller size limitations, cost limitations, or other factors (Allaire et al., 1994). Thus, the solution is to implement all of these tasks in one single CPU by the use of Real Time systems, using some of the many optimal scheduling algorithms that are currently available in this field.

Full embedded control for an AMB system usually requires significant computational effort – especially for flexible rotors. This is caused by the inherent instability of all AMBs. That is, all AMBs are open loop unstable. Thus, the only way to stabilize an AMB system is via a properly designed closed loop controller. However, in order to correctly tune an AMB controller, the controls engineer needs to fully evaluate AMB performance via considerable access to plant input/output (I/O), controller states, and controller parameters. Most importantly, and for safety reasons, in high speed AMB applications the controls engineer needs to get access to this data from a safe location which may or may not necessarily be even in the same building.

The success of the AMB is heavily dependent on the design of the controller. In turn, the controller relies heavily on *a priori* knowledge of the plant dynamics. Thus, considerable modeling, characterization, and controller parameter calibration effort is necessary during the early controller implementation stages for a given AMB application. However, once the controller has been selected and tuned for the particular bearing, the controller is most often not revised.

An important aspect of real time computing for magnetic bearings is the effectiveness of resource allocation strategies so as to satisfy stringent timing-behavior requirements (Stankovic, 1988). The proper design of a real time control system requires solutions to many interesting problems - for example, specification and timing behavior, and programming languages semantics dealing with time, and the use of timing constraints. The correct functioning of the system depends upon an implementation which evaluates the logical power of different forms of timing constraints in solving various coordination problems and determines the least restrictive timing constraints sufficient for the control system. Unlike other combinatorial scheduling problems in operations research which mostly deal with one shot tasks, in real time control systems, the same task may recur very often, either periodically or at irregular intervals, and thus may have to synchronize or communicate with a number of other tasks (Stankovic and Buttazzo, 1995). This is the case with AMB systems such as magnetic bearing supported artificial hearts (Hilton et al., 1999; Baloh et al., 1999; Allaire et al., 1996) and high speed energy storage flywheels for powering communication satellites (Bartlett et al., 1999).

The primary objectives of real time systems design for automatic controls include 1) automation of the process by exploiting optimizing transforms and scheduling theory and 2) the synthesis of highly efficient code and customized resource schedulers from timing constraint specifications. Reliance on clever hand coding and difficult to trace timing assumptions are major sources of bugs in real-time

programming that can be avoided with recent advances in real time structured computing resources such as Linux and Real Time Linux. Real Time Linux is an add-on to the Linux operating system which converts the Linux OS into a hard real time environment by implementing any of many powerful Real Time scheduling algorithms.

The central idea in real time systems is to allocate resources judiciously to make certain that any critical timing constraints can be met with the available resources, assuming that the hardware/software functions correctly and the external environment does not stress the system beyond what it is designed to handle. This is best handled via powerful scheduling algorithms. The real time systems literature is filled with different types of scheduling algorithms, both static¹ and dynamic². This paper does not attempt to review all of these algorithms since some of these do not lend themselves too well for AMB applications. Instead, this paper concentrates on one of the so called “static” scheduling algorithms, the “Fixed Priority Scheduling”. This scheduling algorithm is especially useful for periodic tasks, as would be the case in the implementation of most fixed rate controller algorithms.

The following sections are broken up as follows. First, Real Time Systems and their associated basic scheduling results are presented. Second, the Real Time Controls Laboratory – a controls implementation platform developed and tested at the University of Virginia Rotating Machinery and Controls Laboratory – is presented along with the underlying Real Time Linux executive. Finally, suspension results are shown while using the Real Time Controls Laboratory.

2 Real Time Systems

“Real Time Systems”, are computer systems in which the temporal correctness of the system is at least as important as the logical correctness of those results. For example, in a high speed AMB, it is imperative that our fixed rate suspension controller maintains a strict sampling rate of 5 kHz, irrespective of whether or not the screen and graphical user interface have been fully refreshed. Failure to do so could cause our AMB to catastrophically fall out of suspension at the mere touch of the computer mouse.

Unfortunately, there are several misconceptions (Stankovic, 1988) regarding Real Time Systems which have inhibited the controls community from correctly implementing real time controllers in AMBs. Four of the perhaps most commonly cited misconceptions in our field are:

1. *faster hardware implies that all deadlines will be met*: while it may be true that faster hardware will minimize the mean response time of our system, it does not necessarily imply that the system will be predictable (Stankovic and Ramamritham, 1990), that is, that it will execute precisely at the requested sample rate.
2. *real time systems are equivalent to control systems programmed in assembly coding, interrupt programming, and complex device drivers*: one of the most important research aspects of real time systems is that researchers concentrate on developing powerful scheduling algorithms that will meet all hard timing constraints. Consequently, a real time system designer can now use high level code such as Ada and C instead of a more arcane and platform specific assembly language.

¹The scheduler has full knowledge of previous, present, and future tasks, as would be the case for a fixed rate controller.

²The scheduler has full knowledge of previous and current tasks, but does not know the time nor the number of tasks that will arrive in the future.

3. *real time systems are all developed in an ad hoc fashion*: real time systems research concentrates on developing powerful, flexible, and structured techniques that formalize the actual development and implementation of real time systems. Many structured tools now exist to help develop, validate, and simulate real time systems.
4. *real time is equivalent to fast computing*: “fast” is relative. That is, in the AMB community, a sampling rate of $100\ \mu s$ is considered “fast”. In the robotics community, a sampling rate of $1,000\ \mu s$ is already considered “fast”. In the geo-sciences community, a sampling rate of $86,400,000\ \mu s$ (1 day) is considered “fast”. In all three systems, it is imperative that tasks execute at *precisely* the given time or else the results may no longer be valid. Consequently, all three systems are categorized as “real time systems”.

The real time systems community focuses on many aspects of real time research. Namely, they consider real time hardware, software, validation, and simulation among others. We, as end users, normally do not attempt to understand all of these and rely on the Computer Science community to develop most of these technologies. However, it is imperative that we understand, as a minimum, some very powerful scheduling results which greatly aid in the design process of real time systems and consequently in the implementation of hard-timing control environments. These results are discussed in what follows.

2.1 Scheduling Theory

One of the first works on scheduling theory for computer systems appeared in 1967 by Conway, Maxwell, and Miller (Conway et al., 1967). In this work, they reference much scheduling work that up to that point had been primarily used in job shops across the country. They discuss results which are applicable to both what later became known as classical scheduling theory, and real time systems.

Classical scheduling theory – such as what would normally be seen in a regular multitasking operating system such as Unix – typically uses metrics such as minimizing the sum of completion times, minimizing the weighted sum of completion times, minimizing schedule length, or minimizing the number of processors required. Most of these metrics evolved in job shops during and immediately after World War II, where the main concern was of maximizing the throughput of a given machine, such as either a lathe or a milling machine.

Coffman and Denning (1973) showed that these metrics are not useful for Real Time Systems. For example, the sum of completion times is useless for time critical systems because there is no direct assessment of timing properties (deadlines or periods) in the metric. Thus this algorithm may be desirable for Unix, where the goal is to maximize the throughput or number of tasks that are executed in a given amount of time, but will not be desirable for a hard timing environment as would be the case of AMB control.

Real time researchers thus looked at the second results presented by Conway *et al.*. Namely, they cite a 1955 job-shop scheduling result by Jackson, where he states:

The maximum lateness and maximum job tardiness are minimized by sequencing the jobs in order of non-decreasing due dates

This algorithm, which is usually referred to as the “Earliest Deadline First” or simply EDF algorithm, has been shown to be optimal for uniprocessor systems, where optimality in real time scheduling algorithms is measured by the following:

An optimal scheduling algorithm is one that may fail to meet a deadline only if no other scheduling algorithm can meet it.

The Jackson result sparked much interest and consequently spawned two areas of real time scheduling research. Namely, it developed research in both *dynamic* and *static* scheduling, the latter of which is more applicable to AMB control. A scheduling algorithm is said to be “dynamic” when the algorithm has full knowledge of task properties³ of both previous and present tasks. However, it has no knowledge of future tasks, neither in the number of tasks nor in their start times.

A static scheduler, on the other hand, knows the task properties of all past, present, and future tasks and therefore it is possible to set up some scheduling parameters *a priori*. For example, suppose that an AMB will use a simple PID for thrust control and a plotting package for real time monitoring of plant states. We know *a priori* that the suspension controller must execute every 100 μs without fail, and that the plotting package will execute once every 14,000 μs , although we are not too concerned if one time it executes after 14k or after 50k μs . Consequently, we can assign, *a priori* some schedule parameters such as the next execution time (now + 100 μs and now + 14k μs), and a relative priority (it is more important that the suspension controller executes at its specified time).

A “fixed priority scheduler” (FPS) is a type of static scheduling algorithm where tasks are assigned – *a priori* – a priority, or relative importance, as shown in Figure 1. Each task has an associated start time at which the task is expected to begin its execution, an execution time, and a completion time. Thus, at both the start time and completion times of each of these tasks, the scheduler must make a decision. That is, it must decide which task should be allowed to execute in the CPU. Higher priority tasks are given precedence over lower priority tasks, and tasks having the same priority level are assigned into the CPU on a First In First Out (FIFO) scheme. Tasks may *preempt* lower priority tasks, only, and tasks in general are assumed to be completely independent of each other. Research in FPS algorithms is most heavy in optimal solutions to the priority assignment for each of these tasks, since depending on how priorities are assigned will determine if deadlines are met.

Liu and Layland (1973) developed the “Rate Monotonic Algorithm” (RMA). This algorithm assigns priorities to each of the tasks in the following fashion:

The priority of the task is inversely proportional to its period.

In other words, under this assignment policy, tasks having the smallest period (highest frequency) – as would be the case for a suspension controller in an AMB – would have the higher priority over a second task that executes with a larger period. Of most importance is that this algorithm was shown to be *optimal* among FPS algorithms for real time systems, and that it can be applied for any number n of tasks.

Unfortunately, the RMA algorithm was shown to be optimal only for periodic and *independent* tasks. However, since there is a large need for communication between controller tasks in an AMB (for example, controller effort from the suspension task are communicated to a second task which in turn transmits this information over the network), the RMA algorithm can be shown to be limiting for real time applications. Consequently, research ensued which tried to relax this independence assumption, necessary for RMA.

³example: execution time, start time, number of tasks

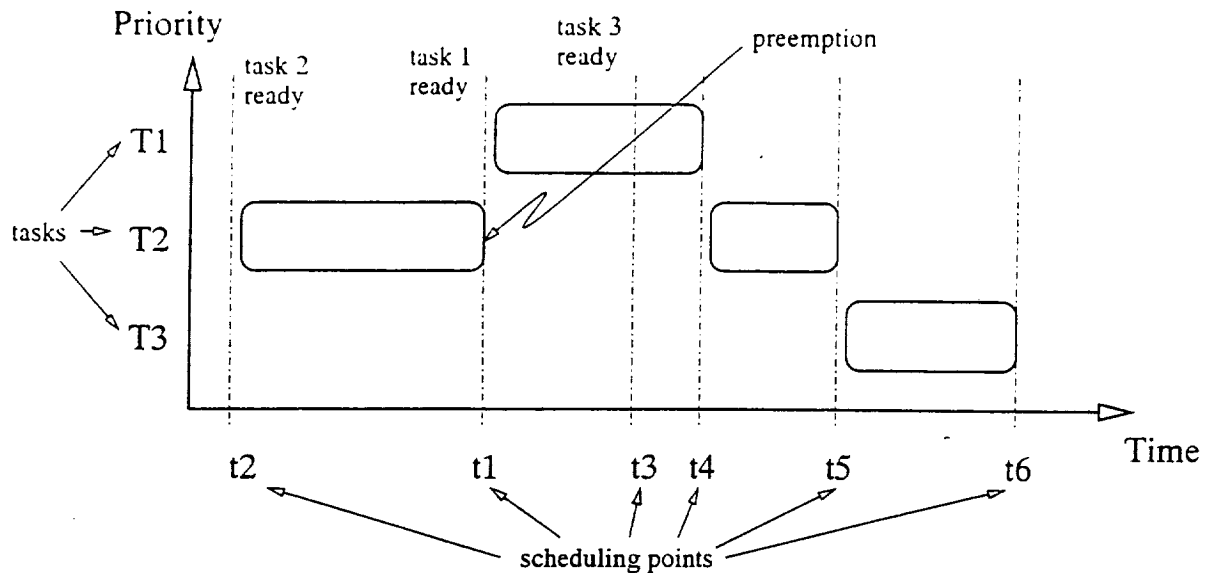


Figure 1: Fixed priority scheduling algorithm example. For illustration purposes, let T_1 denote a suspension controller, T_2 an anti-imbalance controller, and T_3 a plotting package.

The direct application of a simple *semaphore*⁴, or synchronization variable, for sharing critical data between tasks may result in a high priority task being blocked by a lower priority task for an unbounded amount of time. More importantly, this may potentially lead to missed deadlines. This type of unbounded blocking is usually referred to as *priority inversion*, and is exemplified in Figure 2.

Priority inversion usually occurs when there are three or more tasks present, and data is shared between both the highest and lowest priority tasks. Generally, the lowest priority task may get hold of the semaphore and begin accessing data. Then, sometime later, the highest priority task will attempt to access the semaphore but will find that it is already locked by the lowest priority task, and therefore the highest priority task is blocked by the lowest priority task. At this time the lowest priority task resumes execution. However, some time later, the medium priority task begins executing and preempts the lowest priority task. Consequently, the highest priority task not only needs to wait for the medium priority task to finish, but also for the lowest priority task to release the semaphore. The problem becomes more acute when there are more than one medium priority tasks. Consequently, the highest priority task will have to wait for an undetermined amount of time until all intermediate priority tasks complete, and the lowest priority task releases its semaphore.

A powerful solution to this problem was introduced by Sha et al. (1990) under the name of “priority inheritance protocols” (PIPs). PIPs are a series of protocols in which the lower priority tasks that may be blocking a higher priority task will, while blocking the higher priority task, automatically inherit the priority of the highest priority task that the offending task blocks. Two protocols were presented: a basic priority inheritance protocol and a priority ceiling protocol. In both cases, priority inversion

⁴A semaphore is a “lock” which is shared between several tasks. Semaphores are primarily useful in protecting shared data – or critical sections of code –, where a requesting task may first lock the semaphore, access the data, and then release the semaphore. Only one task at a time may enable a semaphore. If any other tasks try to enable the semaphore, they will be put to sleep until the task currently owning the semaphore releases the semaphore, at which time one waiting task will be able to lock the semaphore and all other waiting tasks will continue to sleep.

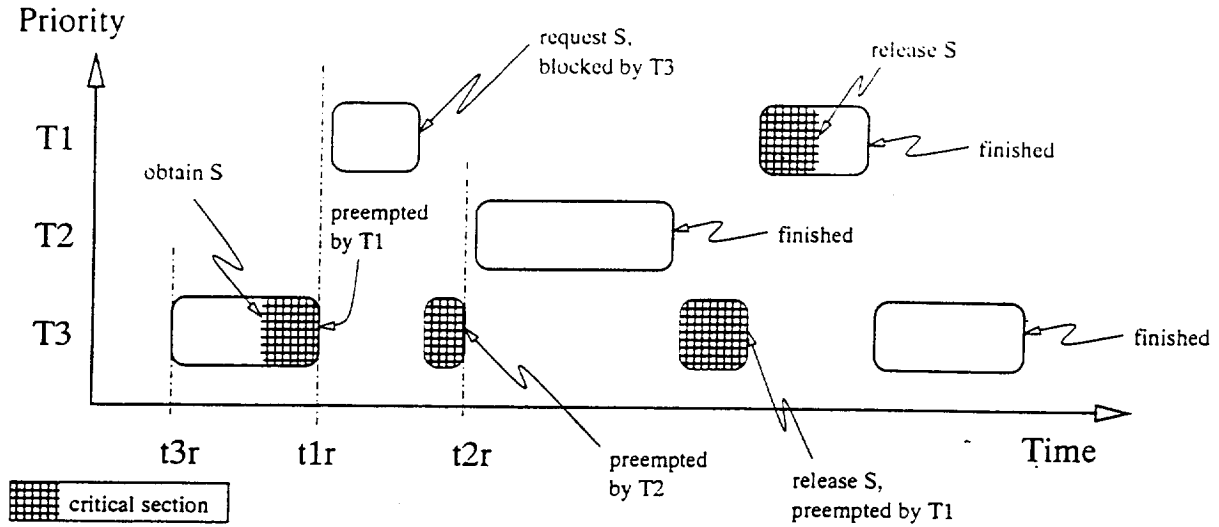


Figure 2: Fixed priority scheduling algorithm example. For illustration purposes, let T_1 denote a suspension controller running at a period of $100 \mu s$, T_2 an anti-imbalance control algorithm, and T_3 a plotting algorithm. Tasks T_1 and T_3 share data, of which T_1 produces the data and T_3 plots it to screen. T_1 and T_3 share semaphore S which is used to protect the integrity of the data.

will be solved by effectively *bounding* the maximum amount of time that the highest priority tasks will be blocked by the lower priority tasks. The former will block the higher priority task by *at most* the duration of one critical section from *each* of the lower tasks which share semaphores with the higher priority tasks, while the latter will block the higher priority task by *at most* the duration of *one* shared segment from any of the lower priority tasks. Thus, by the application of either of these protocols, one can know, *a priori* the worst case execution time of any tasks.

2.2 Schedulability Analysis

Real time scheduling of periodic tasks (such as AMB controllers) often uses the rate-monotonic algorithm (Liu and Layland, 1973; Stankovic and Buttazzo, 1995). This algorithm has been shown to be optimal in the literature for uniprocessor systems and periodic tasks. The most important feature about this algorithm is that it introduces the ability to find, *a priori*, whether or not a given set of tasks will be schedulable – that is, whether or not they will meet all their deadlines.

Liu and Layland showed that for n independent tasks – all of which have the same start time at some point in time, whose execution time is smaller than their deadline, and which, most importantly, are completely independent one of the other – all tasks are schedulable if the following is true:

$$\sum_{i=1}^n \frac{C_i}{P_i} \leq n(2^{1/n} - 1) \quad (1)$$

where C_i is the worst case execution time of the task, P_i is the period of the task, and the left hand side of (1) is called the total CPU utilization. Of most use is the fact that:

$$\lim_{n \rightarrow \infty} \sum_{i=1}^n \frac{C_i}{P_i} \leq 69.34\% \quad (2)$$

or equivalently, if CPU utilization is less than 69.3%, all tasks will meet their deadlines. This relation describes a worst case sufficient condition for a rate-monotonic algorithm and is thus pessimistic. An exact characterization was obtained by Lehoczky, Sha, and Ding (Lehoczky et al., 1989) but is not quoted here due to its higher degree of complexity.

Equation (1) provides conditions under which a set of periodic tasks can be scheduled taking into account the effect of a task being preempted exclusively by higher priority tasks. However, (1) can be extended to include blocking of higher priority tasks by lower priority tasks (Sha et al., 1990). That is, assuming that the priority ceiling protocol is used to eliminate priority inversion, then (1) can be extended as:

$$\sum_{i=1}^n \frac{C_i}{P_i} + \max \left(\frac{B_1}{P_1}, \dots, \frac{B_{(n-1)}}{P_{(n-1)}} \right) \leq n(2^{1/n} - 1) \quad (3)$$

where B_j denotes the worst case blocking time that may occur from any of the lower priority tasks (where increasing j denotes tasks with decreasing priority).

The most important point to note about these scheduling tests is that we now have an effective method of selecting a CPU for a given application (or determining that no CPU will handle the given controller at the given sampling rate). That is, if we know the target execution periods (for example, a controller may repeat itself every 100 μs) and the worst case execution time for each of our control tasks (for example, the execution time of the aforementioned controller may be 80 μs), then by use of the aforementioned schedulability tests, we can scientifically select a computer that is appropriate for our application. Stated differently, if the left hand side of these tests is much smaller than the right hand side, then we know that the target CPU is much too fast for our application and thus we can select a lower cost system. Alternatively, if the left hand side is too large compared with the right, then we should either consider upgrading to a faster CPU or redesigning the controller given that our given CPU cannot compute this controller at the given rate). From our example and (1), we find that $80/100 = 0.8 \leq 1.0$, therefore our individual task is schedulable in this CPU and will meet all of its deadlines.

Real Time Systems literature is too vast to be summarized in this paper. Interested readers are encouraged to pursue further reading in many of the excellent papers on the subject.

In what follows, an AMB control solution has been implemented at the University of Virginia Rotating Machinery and Controls Laboratory in a novel controls implementation platform using Real Time Linux and a set of networked personal computers.

3 The Real Time Controls Laboratory, (RTiC-Lab)

Control of AMBs may require an exhaustive tuning process during the early stages of the AMB life. During this stage, the controls engineer performs thorough plant characterization and evaluation. Using this new-found information, the controls engineer can then proceed to tune the controller. For that,

the controls engineer needs soft real time access to plant I/O, controller states, controller parameters, and set points.

The *Real Time Controls Laboratory. RTiC-Lab*, is explicitly designed by the main author of this work to be used during these early stages of controller design, plant characterization, subsequent monitoring, and subsequent control. Designed and tested at the University of Virginia's Rotating Machinery and Controls Laboratory, it provides an environment in which to implement controller algorithms while providing real time access to controller states, plant outputs, controller actions, controller parameters, and other controller information. All this information can be plotted and filtered – via user defined filters – in soft real time. The user can further filter the necessary data either in real time or *post mortem*. Last and most importantly, the controller parameters can be updated in real time through a user-defined graphical user interface.

RTiC-Lab attempts to incorporate several of the most critical scheduling methods in order to make RTiC-Lab a powerful controls implementation platform for AMBs and any other system that can use both fixed rate and event driven controllers. Priority assignment has been employed with Liu and Layland's RMA scheduling algorithm. Data is synchronized via priority inheritance protocols, and is transmitted from the hard real time tasks to the graphical user interface via real time FIFOs.

RTiC-Lab has two very important features not found in any other real time controls implementation platforms. The first and most important one is that RTiC-Lab is and will be – as its underlying Linux and Real Time Linux platforms – Open Source Software. That is, users of RTiC-Lab can download the source code via the web from <http://www.people.virginia.edu/efh4v>, and are heavily encouraged to both add to, and improve this code⁵. The second feature is that RTiC-Lab is designed to be distributed over a common network of personal computers. That is, RTiC-Lab can be used over a common 10/100 Mb ethernet network.

In conclusion, RTiC-Lab has been designed to be free, extremely flexible, organic, and powerful enough to handle very large tasks. Its success is based on the hard timing capabilities of Real Time Linux and the Open Source design of Linux.

3.1 RTiC-Lab Design

The general scheme used in the design of the Real Time Controls Laboratory is shown in Figure 3. A devoted display or host computer (DHC) is networked via 10 or 100 Mb/s TCP/IP network to a set of devoted controls computers (DCCs).

The controls engineer sits at the DHC (which may or may not be at the same room or even building as the DCCs) and coordinates, codes, and synchronizes all DCCs from the DHC. Run time parameters, such as sampling rate, startup delay, and networking parameters can be set for each of the DCCs from the DHC.

Each of the DCCs is a stripped down computer system having no keyboard, mouse, video card, or monitor. These only have both the necessary I/O cards which are used to interface to the plant hardware and the necessary ethernet card to communicate with the DHC.

An AMB example of RTiC-Lab is shown in Figure 4. A single DHC interfaces with three DCCs which in turn interface to the AMB rotor system. The first DCC handles all radial control of the AMB, while a second (and slower) DCC controls the thrust direction of the AMB, and a third DCC is used to add either some excitation or synchronous forces to cancel out rotor imbalances at the midspan. Both

⁵Please send all code submissions to the main author of this paper.

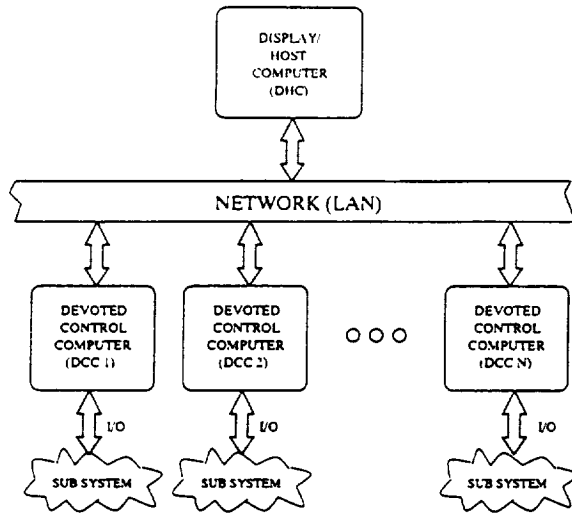


Figure 3: Overview of the Real Time Controls Laboratory network environment

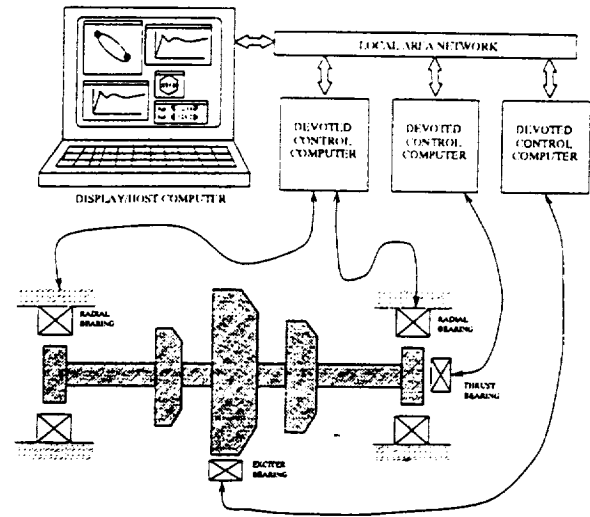


Figure 4: Example of the applicability of RTiC-Lab on an AMB system.

controller parameters can be updated through the graphical user interface, and all data is plotted in soft real time at the DHC.

In the event that the controlled plant is computationally simple enough to be handled exclusively in a single computer, then RTiC-Lab will collapse into one single computer to control the entire plant. Stated differently, the same computer is used to both plot all incoming data and to update controller parameters in soft real time.

In accordance with the RT-Linux paradigm, RTiC-Lab separates the AMB controller into the hard real time or “embedded” part and the soft real time or “reactive” part. The embedded part of the controller (resident exclusively in the DCCs) includes all tasks having hard timing constraints:

1. the AMB suspension controller(s) (both periodic and event driven),
2. a software watchdog, and
3. a set of interrupt service routines that are used for communication with the reactive task.

The reactive task (resident in both DHC and DCCs) is a multi-threaded, user-space application which runs within the Linux kernel. In a standalone system, the reactive task would perform the following functions:

1. communicate with the embedded tasks via RT-FIFOs,
2. display a graphical user interface for the user,
3. perform error checking of the user’s controller code,
4. send parameter updates to the embedded tasks as requested by user,
5. plot data to either screen, save to a file, or print to stdout,

Alternatively, in a multi-node environment, the DCCs' reactive system is charged with communicating with both the local embedded tasks via RT-FIFOs and with the remote DHC through the LAN. It would also be used to trap some vital errors from the local real time tasks, such as missed deadlines. The DHC – which does not necessarily have real time support – would then receive the incoming data through the network and would perform all of the necessary graphical duties as described above. In addition, the DHC would be used to coordinate all networked DCCs.

3.2 RTiC-Lab Proof of Concept

Figure 5 shows the rotor for the UVA/ROMAC controls test rig (CTR). Some salient points about this rotor system that make this system an excellent test bench for the Real Time Controls Laboratory are itemized as follows:

- rotor weight is 37 lbf, consequently emphasis is placed on minimization of rotor vibration and force transmissivity into the underlying frame and housing.
- $D/L \ll 1$, that is, this rotor is long and skinny and thus has many flexible modes that must be controlled during normal rotor operation.
- the surrounding housing and casing are relatively flexible and further introduce dynamics of their own.
- due to the high frequency content in the sensor and actuator wiring harnesses, all cabling must be kept as short as possible in order to minimize electrical noise in the system. This implies that the computational engine must be placed as close to the rig as possible. Yet for safety reasons, the controls engineer should remotely monitor the rig from any location outside of the test chamber.

As of the time of this writing, a single *Pentium II*, 450 MHz computer was used to implement a full five degree of freedom controller sampling at 5 kHz. The thrust direction is controlled using a strictly proper PID controller, and each of the remaining radial control currents (X and Y for an upper and lower magnetic bearing) are controlled using strictly proper PID controllers alongside four notch filters per channel, as shown in Figure 6. For this application, a total of 61 controller parameters could be updated in soft real time through RTiC-Lab.

The RTiC-Lab windows were exported (using the XWindow ability to do so) from the control computer to a second Linux computer housed in a remote location, from which we could safely both monitor the rotor system in the test chamber and control the embedded tasks in the controls computer. Consequently, the test chamber was evacuated during the rotor spin tests. All sampled data was stored in the control computer's harddrive and downloaded via ftp to the remote computer in "pseudo real time".

3.3 Suspension Results

Figures 7 and 8 show the suspension results of the controls test rig at 5,000 RPM. In the figures, the rotor vibrates less than 0.2 thousandths of an inch from its nominal location⁶. The first bending mode is expected at 8,000 RPM and presently measures are being taken to take the rotor up to 12,000 RPM before the end of the year.

⁶Note that as of the time of this writing, the rotor has not been formally balanced

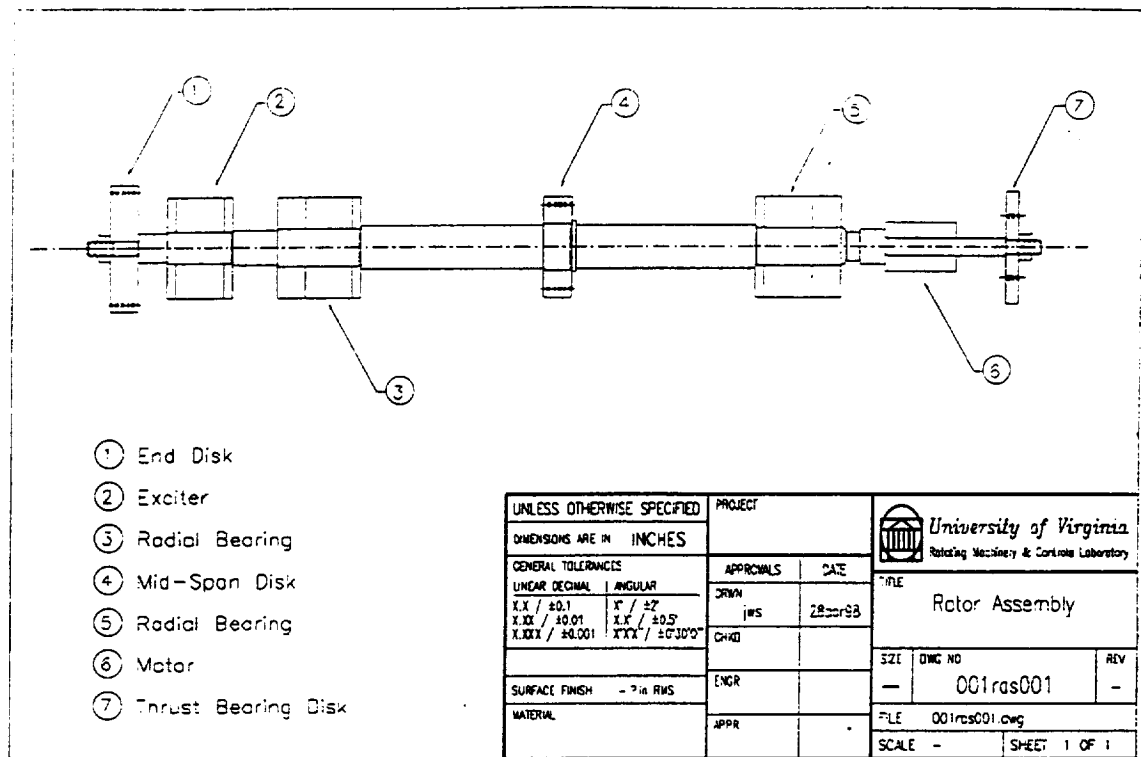


Figure 5: Detail of the rotor for the UVA/ROMAC controls test rig

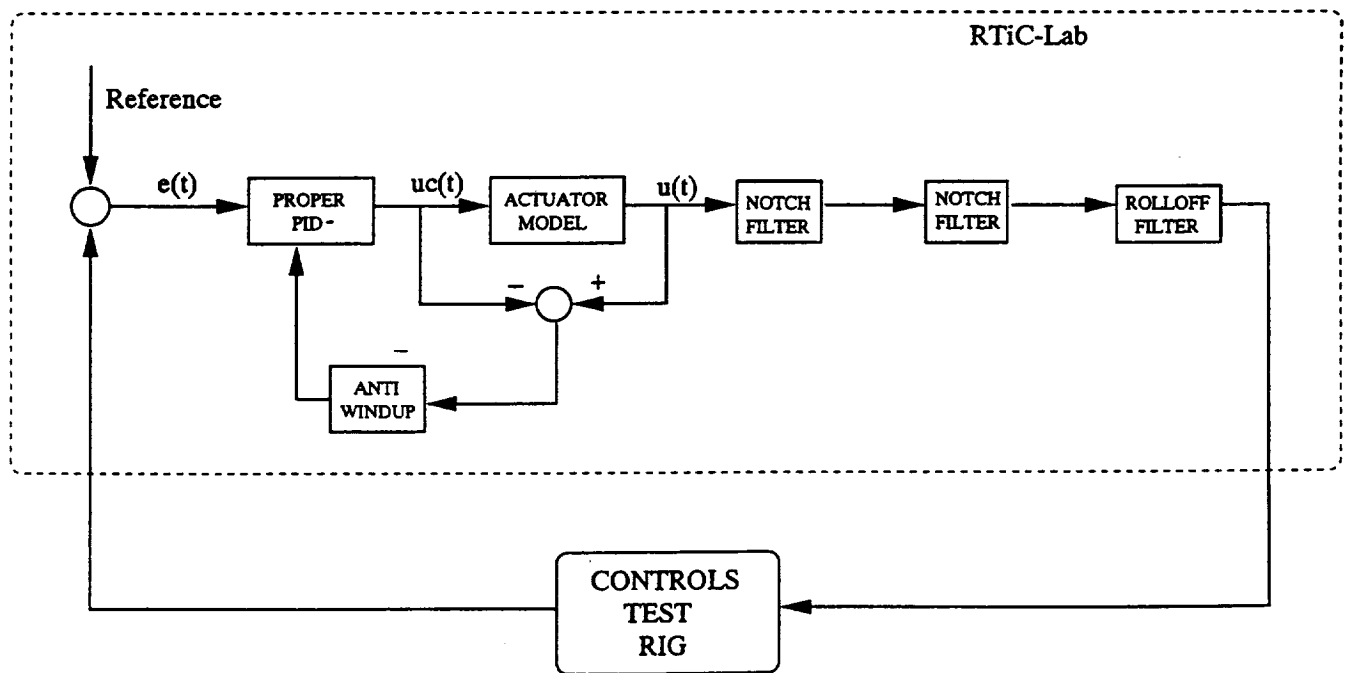


Figure 6: Detail of each of the axis controllers

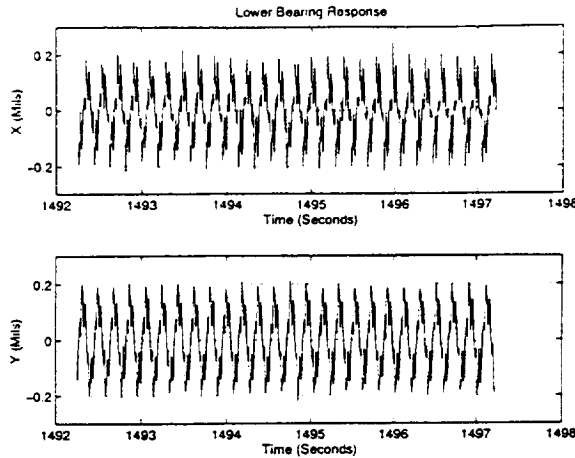


Figure 7: Lower bearing response at 5,000 RPM

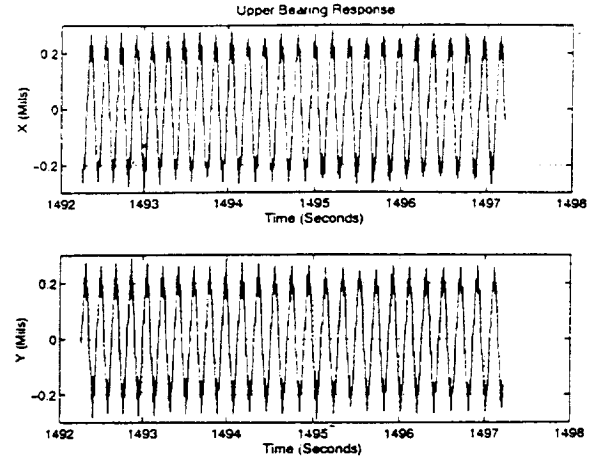


Figure 8: Upper bearing response at 5,000 RPM

Figure 9 shows the actual predictability of RT-Linux. Here, it is shown that the sampling error at 5 kHz sampling is small and bounded to less than a 0.6%. From (1), the CPU utilization of our DCC is 62% and well below its 69% bound.⁷

4 Conclusion

Basic understanding of Real Time Systems scheduling results is necessary towards efficient and successful implementation of *predictable* real time controllers for AMB systems. Namely, for periodic tasks, such as fixed rate controllers, it has been shown that priority assignment for a fixed priority scheduling algorithm via the Liu and Layland RMA will lead to predictable control systems for AMBs. Most importantly, via this priority assignment policy, it is possible to implement multiple tasks that are used not only for the actual suspension control but also for real time monitoring, data logging, data display, network communications, and controller parameter updates.

In order to simplify controller implementation by use of these scheduling techniques, the Real Time Controls Laboratory, or RTiC-Lab, was developed at UVA/ROMAC which aids in the controller implementation process. It uses both Linux and Real Time Linux as the implementation platform. And, consistent with the underlying operating system, RTiC-Lab is Open Source, which means that AMB controller developers who are interested in using this software are encouraged to download the software from <http://www.people.virginia.edu/~efh4v>, use it, and contribute to it by sending modifications to efhilton@alum.mit.edu.

References

P. E. Allaire, H. C. Kim, E. H. Maslen, G. B. Bearnson, and D. B. Olsen. Design of a magnetic bearing supported prototype centrifugal artificial heart pump. In *Tribology Transactions*, volume 39-3, pages

⁷Note that for this particular controller system, this level of utilization shows that our computer was properly sized for this controller algorithm although may be undersized for a more complex or higher order controller algorithm.

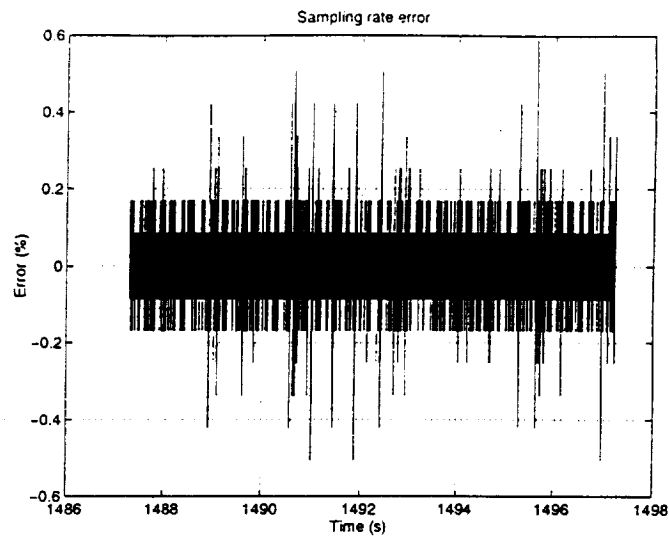


Figure 9: Sampling error of RTiC-Lab during rotor suspension at 5,000 RPM

663–669, July 1996.

- P. E. Allaire, E. H. Maslen, R. R. Humphris, C. R. Knospe, and D. W. Lewis. Magnetic bearings. In E. R. Boozar, editor, *CRC Handbook of Lubrication and Tribology*, volume 3, pages 577–600, 1994.
- M. Baloh, P. Allaire, E. Hilton, N. Wei, E. Maslen, D. Baun, and R. Flack. Magnetic bearing system for continous flow ventricular assist device. *J. of the ASAIO*, 45(5), 1999.
- R. Bartlett, J. Coyner, S. Djouadi, P. Allaire, E. Hilton, J. Luo, P. Tsiotras, F. Maher, and R. Strunce. A simulation of spacecraft energy momentum wheels using advanced **magnetic** bearing controllers. In *1999 Invitational NASA/Air Force Flywheel Workshop*, NASA Glenn Research Center, 1999. Accepted for Publication, Invited Paper.
- E.G. Coffman and P.J Denning. *Operating Systems Theory*. Prentice-Hall, 1973.
- R.W Conway, W.L. Maxwell, and Miller L.W. *Theory of Scheduling*. Addison-Wesley, 1967.
- E. Hilton, P. Allaire, M. Baloh, N. Wei, G. Bearnson, D. Olsen, and P. Khanwilkar. Test controller design, implementation, and performance for a magnetic suspension continous flow ventricular assist device. *Artificial Organs*, 23(8):785–791, 1999.
- J.P. Lehoczky, L. Sha, and Y. Ding. The rate monotonic scheduling algorithm: Exact characterization and average case behaviour. *Proceedings of the IEEE Real-Time Systems Symposium*, pages 166–171, 1989.
- C.L. Liu and J.W. Layland. Scheduling algorithms for multiprogramming in a hard real-time environment. *JACM*, 20(1):46–61, 1973.

- L. Sha, R. Rajkumar, and J. Lehoczky. Priority inheritance protocols: An approach to real-time synchronization. *IEEE Transactions on Computers*, 39(9), September 1990.
- J. Stankovic. Misconceptions about real-time computing. *IEEE Computer*, 21(10), October 1988.
- J. Stankovic and G. Buttazzo. Implications of classical scheduling results for real-time systems. *IEEE Computer*, 28(6), June 1995.
- J. Stankovic and K. Ramamritham. What is predictability for real-time systems? *J. Real-Time Systems*, 2:247–254, December 1990.

FUZZY LOGIC CONTROL OF MAGNETIC BEARINGS FOR SUSPENSION OF VIBRATION DUE TO SUDDEN IMBALANCE

Shuliang Lei* , Alan Palazzolo*
Albert F. Kascak**

1. Introduction

In recent years, the use of magnetic bearings in rotating machinery has received much interest due to its potential advantages. The non-contact magnetic bearing exhibits much better performance in high speed rotating machinery. While it is very important to suppress the vibration of the rotating body due to imbalance, active magnetic bearings offer a way to support the rotating shaft as well as to control the vibration. Sudden imbalance in rotating machinery usually results from partial or full blade loss or from sudden shedding of accumulated deposits. The resulting transient may cause severe internal rubs between stator and rotor. Damage from this action may have catastrophic consequences in terms of cost. Active magnetic bearings (AMB) provide the capability for adaptive control of shaft vibration via supervisory systems which detect the upset conditions or changes in operating parameters. Most AMB's utilize a linear PID controller with power amplifiers, magnetic actuators and inductive, eddy current or optical sensors. These electronic components act linearly up to a saturation limit. The linear controller usually does not include logic for maintaining accurate control with non-linear system behavior.

In this work, fuzzy logic control is constructed by designing a rule base to implement a non-linear control strategy. The antecedent and consequent of each rule operate on the positions of input and output variables in predefined membership functions. These membership functions possess qualitative descriptions which generalize the notion of assigning a single degree to a specific response severity or corrective action level. Fuzzy logic controllers for active magnetic bearings are synthesized and designed for suppression of sudden imbalance vibration. The rule base is constructed to provide nonlinear resistance with respect to the position of the rotor and the control current of the electromagnetic iron coil.

The main objective of this paper is to develop robust controllers for maintaining magnetic bearing control periods of sudden high force such as blade loss, flywheel partial burst, component loss, etc., to demonstrate superiority of nonlinear fuzzy logic control over linear control. Simplification of the nonlinear fuzzy logic algorithm for practical implementation on a DSP digital controller or on an analog controller is also performed. Section 2 briefly describes the basic theoretical background of the non-linear property of active magnetic bearings as well as our experimental result as a supplement to the understanding of the features of the heteropolar magnetic bearings under bipolar operating conditions. In Section 3 the linear quadratic regulator is implemented to the

* Texas A&M University, Mechanical Engineering, College Station, TX 77843-3123

** U.S. Army at NASA Lewis , 21,000 Brookpark RD., Cleveland, Ohio 44135 (216) 433-6024

linearized model of the system. Then fuzzy logic controllers based on Takagi-Sugeno are synthesized and designed with respect to different partitions of the input universe of discourse. Simulation results for each type of controllers are provided and their performance specifications can be compared accordingly. The effectiveness of the fuzzy logic controller is evaluated against the performance of the optimal linear controller. Finally in Section 4 conclusions are drawn and discussions with respect to the limitations and further study are presented.

2. Theory and Experiment

The electromagnetic force f_c acting on the rotor made up of ferromagnetic materials ($\mu_r \gg 1$) at the bearings is non-linear in both the displacement x and the active control current i_c , i.e. neglecting fringing and metal path reluctance;

$$f_c = k \left[\frac{(i_0 + i_c)^2}{(s_0 - x)^2} - \frac{(i_0 - i_c)^2}{(s_0 + x)^2} \right] \quad (1)$$

where i_0 is the bias current and s_0 is the air gap of the magnetic bearing, and

$$k = 0.25 \mu_0 n^2 A_a$$

is the magnetic force constant, in which

$$\mu_0 = 4\pi \times 10^{-7} \quad (N/A^2)$$

is the permeability of vacuum, n is the number of turns of the coil, and A_a is the area of the cross section of the magnetic iron.

Fig. 1 shows the nonlinear property of the magnetic force with respect to the control current and the rotor displacement from its original position.

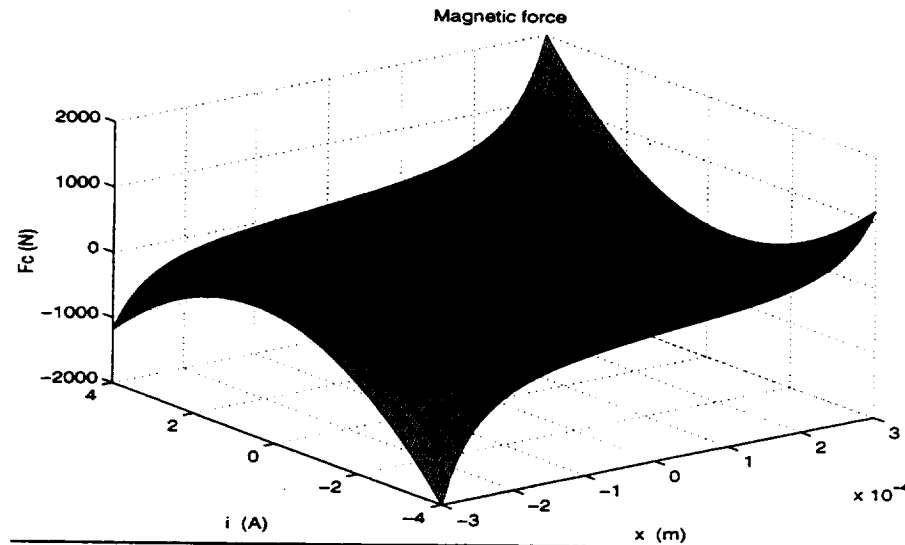


Fig. 1 Surface view of magnetic force

It can be seen from this figure that, as i_c and x increase, the control force f_c increases very sharply and goes to infinity when x reaches the air gap clearance.

Sudden imbalance in rotating machinery occurs in the case of blade loss, flywheel partial burst, component loss, etc., resulting in high vibrating force. The imbalance force f_u can be expressed as follows:

$$f_u = me\omega^2 \sin(\omega x)$$

where ω is the spin rate of the shaft, e is the offset of the center of gravity of the rotor due to imbalance, and m is the equivalent mass.

The rigid rotor model of the complete system is now written as

$$m\ddot{x} = k\left[\frac{(i_0 + i_c)^2}{(s_0 - x)^2} - \frac{(i_0 - i_c)^2}{(s_0 + x)^2}\right] + me\omega^2 \sin(\omega x) \quad (2)$$

The objective of the controller is to generate appropriate control current i_c fed to the coil of the electromagnetic iron to control the vibration. Basically there are two kinds of control schemes: linear control which is based on a linear approximation of the system, and non-linear control, which in our research, utilizes the fuzzy logic theory to stabilize the AMB system. Comparison of linear control and fuzzy logic control will be carried out and the superiority of the non-linear fuzzy logic control over linear control is demonstrated.

To fully understand the behavior of the active magnetic bearing, an experiment was carried out to study the relations of the flux density B vs. control current i_c for a heteropolar magnetic bearing. The objective of this experiment is to investigate the property of the magnetic bearing under bipolar working conditions. To show this, both positive current and negative current are fed to coils respectively and the flux density, which is measured through a Hall probe, is recorded. The experimental setup is shown in Fig. 2.

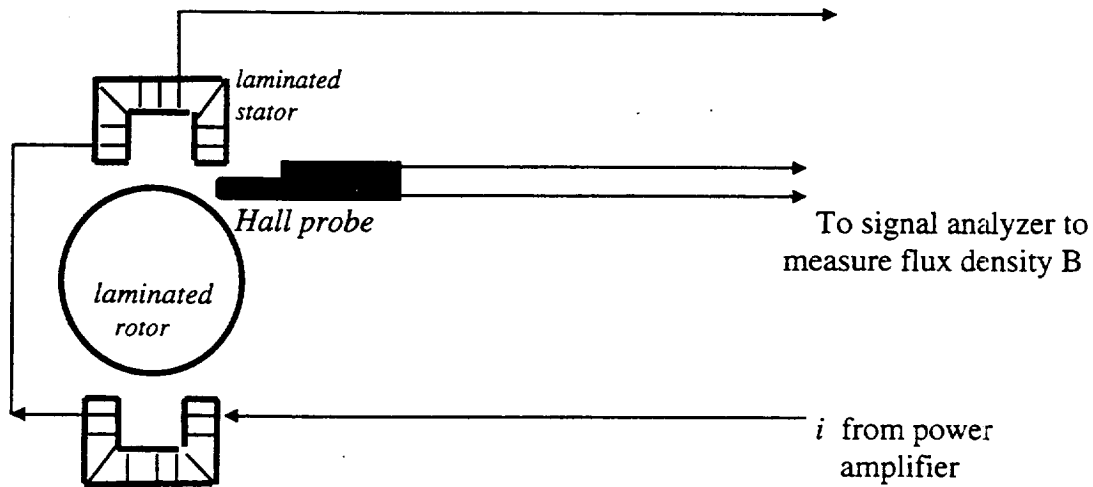


Fig. 2 Schematic diagram of the experimental setup

In this experiment, an operational amplifier (Kepco 72 v, 6A) generates a current i fed into the coils of the heteropolar magnetic bearing. A Hall probe is used to sense the flux density B . The following table records the test result:

Current i (A)	-3.1	-3.0	-2.5	-2.2	-1.6	-1.0	-0.76	-0.5	-0.26	-0.11
Flux density (Tesla)	1.17	1.17	1.12	1.02	0.75	0.46	0.33	0.22	0.11	0.046

Current i (A)	0.257	0.51	0.75	1.0	1.58	2.41	3.62	3.72
Flux density (Tesla)	-0.123	-0.23	-0.34	-0.47	-0.75	-1.02	-1.24	-1.24

Fig. 3 shows the relation between B and i .

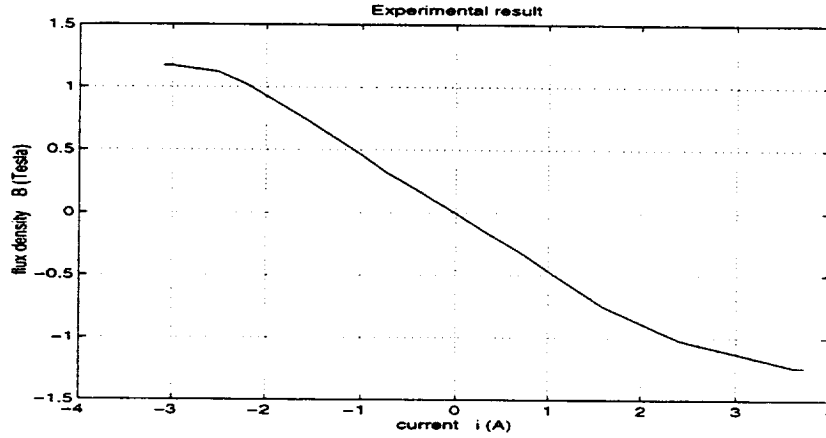


Fig. 3 Experimental result of flux-current relation

This result exhibits that for a heteropolar magnetic bearing, the reverse of the current polarity will have the same effect on the flux density, only with an opposite direction. We will use this result in our controller where negative input current $i = i_0 + i_c$ are allowed.

3. Controller Design and Simulation

3.1. Linear optimal controller

To apply a linear quadratic regulator to an active magnetic bearing system, first linearize the system around a chosen operating point. The system equation is rewritten as:

$$\begin{aligned}\dot{x}_1 &= x_2 \\ \dot{x}_2 &= k/m \left[\frac{(i_0 + i_c)^2}{(s_0 - x)^2} - \frac{(i_0 - i_c)^2}{(s_0 + x)^2} \right] \triangleq f(x_1, x_2, i_c)\end{aligned}\quad (3)$$

where we denote $x_1 = x$.

For the linearization of the system, the following partial derivatives are derived:

$$\begin{aligned}
\frac{\partial f}{\partial x_1} &= 2k/m \left[\frac{(i_o + i_c)^2}{(s_o - x)^3} - \frac{(i_o - i_c)^2}{(s_o + x)^3} \right] \\
\frac{\partial f}{\partial x_2} &= 0 \\
\frac{\partial f}{\partial i_c} &= 2k/m \left[\frac{(i_o + i_c)}{(s_o - x)^2} - \frac{(i_o - i_c)}{(s_o + x)^2} \right]
\end{aligned} \tag{4}$$

Therefore

$$\begin{bmatrix} \dot{x}_1 \\ \dot{x}_2 \end{bmatrix} = \begin{bmatrix} 0 & I \\ \frac{\partial f}{\partial x_1} & 0 \end{bmatrix} \begin{bmatrix} x_1 \\ x_2 \end{bmatrix} + \begin{bmatrix} 0 \\ \frac{\partial f}{\partial i_c} \end{bmatrix} i_c + \begin{bmatrix} 0 \\ f(x_1, x_2, i_c) \big|_* - \frac{\partial f}{\partial x_1} \big|_* x_1^* - \frac{\partial f}{\partial i_c} \big|_* i_c^* \end{bmatrix} \tag{5}$$

The above equation is in control canonical form. We can further write it in a more compact form:

$$\dot{\mathbf{x}} = \mathbf{A}\mathbf{x} + \mathbf{B}u + \mathbf{c} \tag{6}$$

where u denotes the control current i_c .

The general cost function J is

$$J = \int_0^{\infty} (\mathbf{x}^T \mathbf{Q} \mathbf{x} + u^T \mathbf{R} u) dt \tag{7}$$

where \mathbf{Q} and \mathbf{R} are weight matrices.

Solve the algebraic Riccati equation for \mathbf{P} :

$$\mathbf{P}\mathbf{A} + \mathbf{A}^T \mathbf{P} - \mathbf{P}\mathbf{B}\mathbf{R}^{-1} \mathbf{B}^T \mathbf{P} + \mathbf{Q} = 0 \tag{8}$$

and the state feedback gain matrix is

$$\mathbf{K} = \mathbf{R}^{-1} \mathbf{B}^T \mathbf{P} \tag{9}$$

Therefore, the closed loop system is

$$\dot{\mathbf{x}} = (\mathbf{A} - \mathbf{B}\mathbf{K})\mathbf{x} \tag{10}$$

Simulation:

As an example, the parameters used in the simulation are as follows:

$$\omega = 3000 \text{ (rpm)}, m = 1.0 \text{ (kg)}, s_o = 0.4 \text{ (mm)}, n = 150, A_a = 200 \text{ (mm}^2\text{)}, i_o = 5 \text{ (A)}.$$

Choose the operating point at $i_c^* = 0, x_1^* = 0$, then

$$\mathbf{A} = \begin{bmatrix} 0 & I \\ 1561.95 & 0 \end{bmatrix}, \mathbf{B} = \begin{bmatrix} 0 \\ 124.96 \end{bmatrix}$$

Choose the weight matrices as

$$\mathbf{Q} = \begin{bmatrix} 20 & 0 \\ 0 & 0.1 \end{bmatrix}, \mathbf{R} = 15$$

then the optimal feedback gains are

$$k_p = 20.05, k_d = 0.64$$

With the LQR applied, the system converges until the offset e reaches $86E-4(m)$. When $e \geq 86E-4(m)$, the system diverges. Fig. 4 shows the simulation result.

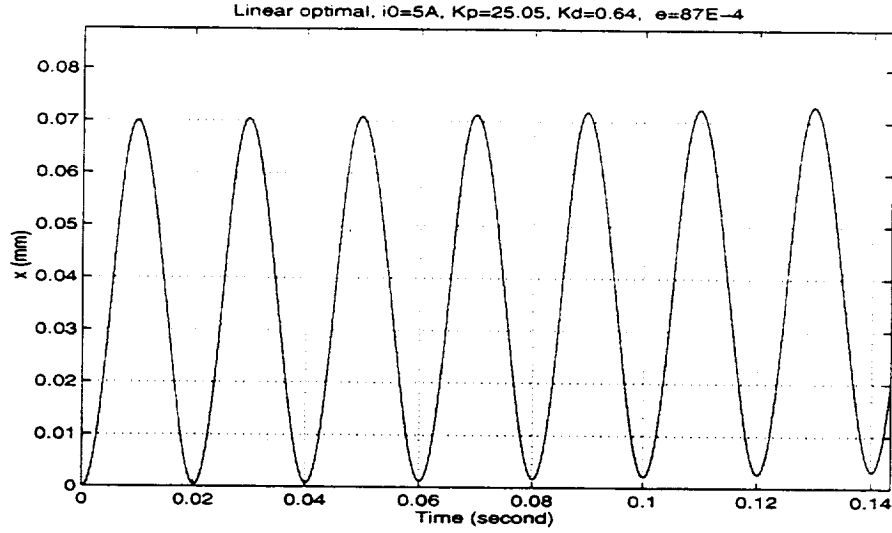


Fig. 4 Response of linear optimal control when offset $e=87E-4$

3.2 Fuzzy logic control

(1) Theoretical background

The fuzzy logic controller design is based on piece-wise linearization of the system. Pole placement method is applied to each subsystem to obtain the feedback gains. It has been proved that, if the poles of each subsystem is placed at the same location, the global non-linear system will be stable.

Generally, a SISO system can be described as

$$\begin{aligned}\dot{x}_1 &= x_2 \\ \dot{x}_2 &= x_3 \\ &\dots \dots \\ \dot{x}_n &= f(x_1, x_2, \dots, x_n, F)\end{aligned}\tag{11}$$

where F is the control force.

We introduce l operating points around which the system (11) is linearized as

$$\begin{bmatrix} \dot{x}_1 \\ \dot{x}_2 \\ \vdots \\ \dot{x}_n \end{bmatrix} = \begin{bmatrix} 0 & 1 & 0 & \dots & 0 \\ 0 & 0 & 1 & \dots & 0 \\ & \dots & & \dots & \\ -a_1^i & -a_2^i & -a_3^i & \dots & -a_n^i \end{bmatrix} \begin{bmatrix} x_1 \\ x_2 \\ \vdots \\ x_n \end{bmatrix} + \begin{bmatrix} 0 \\ 0 \\ \vdots \\ 1 \end{bmatrix} u^i + \begin{bmatrix} 0 \\ 0 \\ \vdots \\ d^i \end{bmatrix}, \quad i = 1, 2, \dots, l\tag{12}$$

or in a more compact form

$$\dot{\mathbf{x}} = \mathbf{A}_{op}^i \mathbf{x} + \mathbf{b}u^i + \mathbf{d}^i, \quad i = 1, 2, \dots, l$$

where the parameters a and d , appropriately indexed, are obtained as follows:

$$\begin{aligned} f(x_1, x_2, \dots, x_n, F) &\approx f(x_1^{i*}, x_2^{i*}, \dots, x_n^{i*}) + \left. \frac{\partial f}{\partial x_1} \right|_* (x_1 - x_1^{i*}) + \left. \frac{\partial f}{\partial x_2} \right|_* (x_2 - x_2^{i*}) + \dots \\ &\quad + \left. \frac{\partial f}{\partial x_n} \right|_* (x_n - x_n^{i*}) + \left. \frac{\partial f}{\partial F} \right|_* \Delta F^i \\ &= \left. \frac{\partial f}{\partial x_1} \right|_* x_1 + \left. \frac{\partial f}{\partial x_2} \right|_* x_2 + \dots + \left. \frac{\partial f}{\partial x_n} \right|_* x_n + \left. \frac{\partial f}{\partial F} \right|_* \Delta F^i \\ &\quad - \left(\left. \frac{\partial f}{\partial x_1} \right|_* x_1^{i*} + \left. \frac{\partial f}{\partial x_2} \right|_* x_2^{i*} + \dots + \left. \frac{\partial f}{\partial x_n} \right|_* x_n^{i*} \right) + f(x_1^{i*}, x_2^{i*}, \dots, x_n^{i*}) \\ &\triangleq [-a_1^i, -a_2^i, \dots, -a_n^i][x_1, x_2, \dots, x_n]^T + u^i + d^i, \quad i = 1, 2, \dots, l \end{aligned}$$

and $*$ denotes values of the relevant variables at the given operating points.

Therefore, for $i=1, 2, \dots, l$, we have

$$\begin{aligned} d^i &= -\left(\left. \frac{\partial f}{\partial x_1} \right|_* x_1^{i*} + \left. \frac{\partial f}{\partial x_2} \right|_* x_2^{i*} + \dots + \left. \frac{\partial f}{\partial x_n} \right|_* x_n^{i*} \right) + f(x_1^{i*}, x_2^{i*}, \dots, x_n^{i*}) \\ a_k^i &= \left. \frac{\partial f}{\partial x_k} \right|_* \\ u^i &= \left. \frac{\partial f}{\partial F} \right|_* \Delta F^i, \quad k = 1, 2, \dots, n \\ \Delta F^i &= F^i - F^{i*}, \quad F^{i*} = 0 \end{aligned} \tag{13}$$

Here F^i is the actual control architecture input to the plant. The last two expressions in (3) lead to $F^i = u^i / \left. \frac{\partial f}{\partial F} \right|_*$ where u^i will be drawn by the fuzzy inference process described below.

Based on the piece-wise linear model (12), state feedback control is employed to stabilize the given non-linear system:

$$u^i = -k_1^i x_1 - k_2^i x_2 - \dots - k_n^i x_n + k_0^{i*}, \quad i = 1, 2, \dots, l \tag{14}$$

Motivated by the Takagi-Sugeno model, the fuzzy rule base takes the following form:

Rule i ($i=1,2,\dots,l$):

If x_1 is S_1^i and x_2 is S_2^i and... x_n is S_n^i and u^i is U^i , then

$$\dot{\mathbf{x}} = \mathbf{A}_{op}^i \mathbf{x} + \mathbf{b}u^i + \mathbf{d}^i$$

and the control for the next step is

$$u^i = -k_1^i x_1 - k_2^i x_2 - \dots - k_n^i x_n + k_0^{i*}$$

where S_j^i and U^i are fuzzy sets centered at the i th operating point for variable x_j and control u .

With the implementation of the state feedback control law (14), the resulting closed loop system can be written, in terms of the Takagi-Sugeno architecture, as

Rule i ($i=1,2,\dots,l$):

If x_1 is S_1^i and x_2 is S_2^i and... x_n is S_n^i and u^i is U^i , then

$$\begin{bmatrix} \dot{x}_1 \\ \dot{x}_2 \\ \vdots \\ \dot{x}_n \end{bmatrix} = \begin{bmatrix} 0 & 1 & 0 & \dots & 0 \\ 0 & 0 & 1 & \dots & 0 \\ & \dots & & \dots & \\ -(a_1^i + k_1^i) & -(a_2^i + k_2^i) & -(a_3^i + k_3^i) & \dots & -(a_n^i + k_n^i) \end{bmatrix} \begin{bmatrix} x_1 \\ x_2 \\ \vdots \\ x_n \end{bmatrix} + \begin{bmatrix} 0 \\ 0 \\ \vdots \\ k_0^{i*} + d^i \end{bmatrix}$$

It can be seen that one of the design objectives is to use k_0^{i*} to cancel the linearized constant d^i , that is

$$k_0^{i*} = -d^i = \left(\frac{\partial f}{\partial x_1} \Big|_{x_1^{i*}} x_1^{i*} + \frac{\partial f}{\partial x_2} \Big|_{x_2^{i*}} x_2^{i*} + \dots + \frac{\partial f}{\partial x_n} \Big|_{x_n^{i*}} x_n^{i*} \right) - f(x_1^{i*}, x_2^{i*}, \dots, x_n^{i*})$$

Then we have for the i th subsystem the control canonical form:

$$\begin{bmatrix} \dot{x}_1 \\ \dot{x}_2 \\ \vdots \\ \dot{x}_n \end{bmatrix} = \begin{bmatrix} 0 & 1 & 0 & \dots & 0 \\ 0 & 0 & 1 & \dots & 0 \\ & \dots & & \dots & \\ -(a_1^i + k_1^i) & -(a_2^i + k_2^i) & -(a_3^i + k_3^i) & \dots & -(a_n^i + k_n^i) \end{bmatrix} \begin{bmatrix} x_1 \\ x_2 \\ \vdots \\ x_n \end{bmatrix} \quad (15)$$

Using the weighted sum to defuzzify the system, we have the closed loop system described as:

$$\begin{bmatrix} \dot{x}_1 \\ \dot{x}_2 \\ \vdots \\ \dot{x}_n \end{bmatrix} = \begin{bmatrix} 0 & 1 & 0 & \dots & 0 \\ 0 & 0 & 1 & \dots & 0 \\ \vdots & \vdots & \vdots & \ddots & \vdots \\ -\sum_{i=1}^l (w^i a_1^i + w^i k_1^i) & -\sum_{i=1}^l (w^i a_2^i + w^i k_2^i) & -\sum_{i=1}^l (w^i a_3^i + w^i k_3^i) & \dots & -\sum_{i=1}^l (w^i a_n^i + w^i k_n^i) \\ \sum_{i=1}^l w^i & \sum_{i=1}^l w^i & \sum_{i=1}^l w^i & \dots & \sum_{i=1}^l w^i \end{bmatrix} \begin{bmatrix} x_1 \\ x_2 \\ \vdots \\ x_n \end{bmatrix} \quad (16)$$

where w^i is the grade of membership of the input x with respect to the i th rule.

Now using triangular shaped membership functions with the following property:

$$\sum_{i=1}^l w^i = 1, \quad (17)$$

Eq. (16) is simplified to

$$\begin{bmatrix} \dot{x}_1 \\ \dot{x}_2 \\ \vdots \\ \dot{x}_n \end{bmatrix} = \begin{bmatrix} 0 & 1 & 0 & \dots & 0 \\ 0 & 0 & 1 & \dots & 0 \\ \vdots & \vdots & \vdots & \ddots & \vdots \\ -\sum_{i=1}^l (w^i a_1^i + w^i k_1^i) & -\sum_{i=1}^l (w^i a_2^i + w^i k_2^i) & -\sum_{i=1}^l (w^i a_3^i + w^i k_3^i) & \dots & -\sum_{i=1}^l (w^i a_n^i + w^i k_n^i) \\ \sum_{i=1}^l w^i & \sum_{i=1}^l w^i & \sum_{i=1}^l w^i & \dots & \sum_{i=1}^l w^i \end{bmatrix} \begin{bmatrix} x_1 \\ x_2 \\ \vdots \\ x_n \end{bmatrix} \quad (18)$$

This system model is in *control canonical form*. Therefore it is easy to apply linear control design techniques to stabilize the system and to obtain satisfactory performance.

Pole placement method is recommended to perform the design of the piece-wise linear subsystems. By choosing suitable feedback gains k_j^i for $i=1,2,\dots,l$ and $j=1,2,\dots,n$ such that all linear subsystems (15) have the *same set of eigenvalues*, a globally stable fuzzy controller can be obtained. In this design, the closed loop system behaves *uniformly* across the entire operating range.

(2) Fuzzy logic controller design and simulation

We choose 5 operating points for the displacement and the control current respectively, which results in a fuzzy logic controller of Takagi-Sugeno architecture with 25 rules.

The input membership functions are of triangular and trapezoidal shapes centered at the 5 operating points of each input universe of discourse. Fig. 5 depicts the input membership functions.

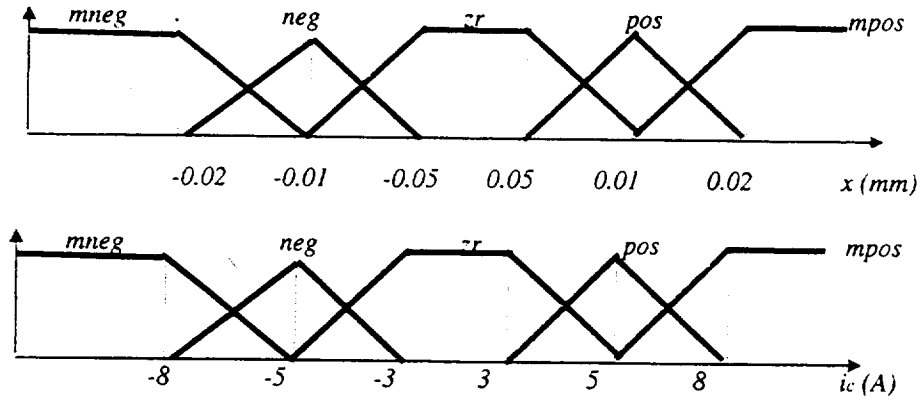


Fig. 5 Membership functions of input spaces

The output membership functions are formulated in terms of pole placement method for a piece-wisely linearized system where the closed loop poles are placed at $P_1=(60+6j)$, $P_2=(60-6j)$.

The rules base is formulated as:

*Rule i : If x is X_i and i_c is U_i
Then the control current is $-k_{pi} x - k_{di} \dot{x} + k_{oi}$
($i=1,2,...,25$)*

where X_i and U_i are membership functions in the x and i_c input spaces respectively. The control coefficients k_{pi} and k_{di} are obtained via pole placement method for each linear subsystem.

Fig.6 shows the simulation results with maximum unbalance offset $e=137E-4$ (m)

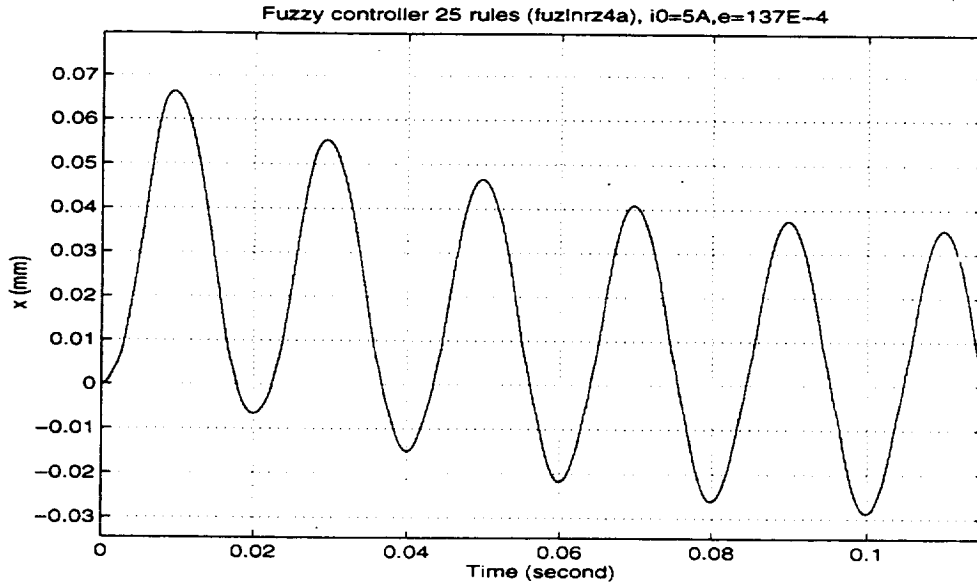


Fig. 6 Response in the presence of imbalance (25 rules)

To make the fuzzy controller capable of being implemented in a real time DSP controller, further simplification of the rule base is made to reduce the total number of rules from 25 to only 9, with little sacrifice of the maximum allowable offset from $e=137E-4$ (m) to $e=130E-4$ (m). The membership functions in this case are shown in Fig. 7.

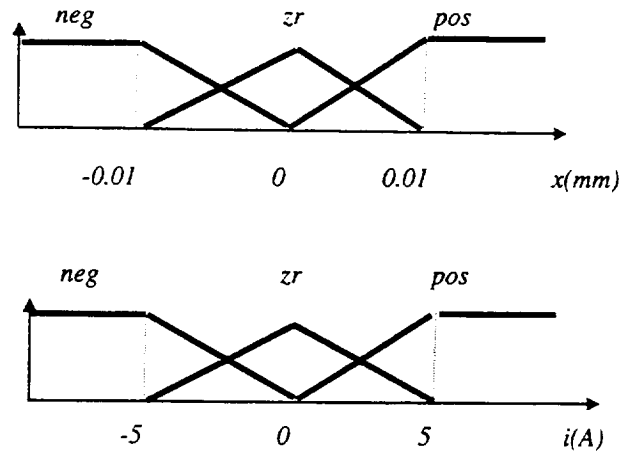


Fig. 7. Membership functions of input spaces

The output membership functions are formulated in a similar way as before and the poles of each linear subsystem are placed at the same locations: $P_1=(60+6j)$, $P_2=(60-6j)$

Fig. 8 shows that the system converges at a maximum unbalance offset of $e=130E-4$ (m)

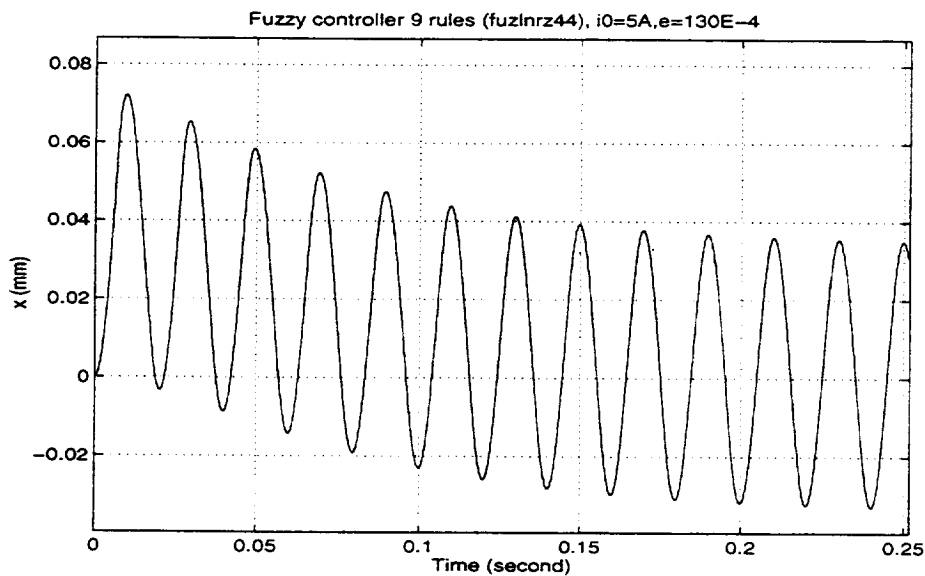


Fig. 8 Response in the presence of unbalance (9 rules)

4. Conclusion

This paper develops the use of fuzzy logic controller of active magnetic bearings for suppression of sudden imbalance generated vibration. Fuzzy logic controllers in terms of Takagi-Sugeno architecture are studied and designed. Their superiority over the best linear controller, i.e. linear quadratic regulators, is demonstrated. Moreover, the simplification of fuzzy logic controller by reducing the number of membership functions is performed, which makes the implementation on real time DSP control practical. Results show significant improvement in maximum controllable imbalance, resulting shaft excursions versus optimal linear control. In summary the largest stable unbalance eccentricity is $87e-4$ for the LQR based control and $137e-4$ for the non-linear fuzzy logic controller.

The work in this paper is based on rigid rotor model with lumped mass and adjustable mass eccentricity to represent the imbalance. Further study for an active magnetic bearing system which includes flexible shaft, non-collocated sensor and actuator, dynamics of the electronic processing circuit and the eddy current effect will be covered in our later research in terms of finite element studies.

Acknowledgment

The authors would like to express thanks to NASA Lewis Dynamics Branch - Structure Division and NASA Lewis Space Power Division (Mr. Raymond Beach) for their support of this research.

References

- [1] C. Kim, A. B. Palazzolo *et al.* Eddy current effects on the design of rotor-magnetic bearing systems, *Transactions of the ASME*, Vol. 117, June 1995.
- [2] P.Tang, A. B. Palazzolo *et al.* An electromechanical simulation method for the active vibration control of a magnetic bearing supported rotor. *Proceedings of the 1993 International Gas Turbine and Aeroengine Congress and Exposition*, Cincinnati, Ohio, May 24-27, 1993
- [3] Shuliang Lei and R. Langari. An approach to synthesis and approximation of stable fuzzy logic controllers, *Fifth IEEE International Conference on Fuzzy Systems*, New Orleans, Sept. 8-11, 1996.
- [4] K. Tanaka and M. Sugeno. Stability analysis and design of fuzzy control systems, *Fuzzy Sets and Systems*, 45 (1992) 135-156 North-Holland.
- [5] K. Tanaka and M. Sano. A robust stabilization problem of fuzzy control systems and its application to backing up control of a truck-trailer, *IEEE Transactions on Fuzzy Systems*, Vol. 2, No. 2 May 1994.

- [6] T. Takagi and M. Sugeno. Fuzzy identification of systems and its application to modeling and control, *IEEE Trans. Syst. Man Cyber.* Vol. SMC-15, No. 1, Jan/Feb, 1985.
- [7] A. El Hajjaji and A. Rachid. Analytic formulation of linguistic rules for fuzzy controller, *Fuzzy Sets and Systems*, 73 (1995) 219-225.
- [8] R. Langari and Shuliang Lei. Hierarchical fuzzy control of a double inverted pendulum, *Technical Report*, Center of fuzzy logic, robotics and intelligent systems research, Texas A&M University, Collage Station, TX 77843.
- [9] Gerhard Schwitzer *et al.* *Active magnetic bearings*, Hochschulverlag AG an der ETH Zurich, 1994
- [10] J. Doyle, B. Francis and Tannenbaum. *Feedback control theory*, Macmillan, 1991.
- [11] D. Filev. Polynomial approach to the synthesis of stable fuzzy systems, *1996 Biennial Conference of the North American Fuzzy Information Processing Society - NAFIPS*, June 1996.
- [12] M. Gopal. *Modern Control System Theory*, John Wiley & Sons, 1993.
- [13] M. Anderson. Lyapunov optimal feedback control of a nonlinear inverted pendulum, *Tran. AMSE, Vol. 111*, p. 554, Dec. 1989.
- [14] J. Cruz, Jr. Feedback in systems, *Feedback systems*, McGraw-Hill Co., New York, 1972
- [15] Terano. *Fuzzy Systems Theory and Its Applications*, Academic Press, 1987.

Session 12 – MAGLEV

Chairman: Hans Schneider-Muntau
National High Magnetic Field Lab (NHMFL)

Prediction of Lift and Drag Forces in an EDS Maglev System

Kent Davey

American Maglev, Inc.

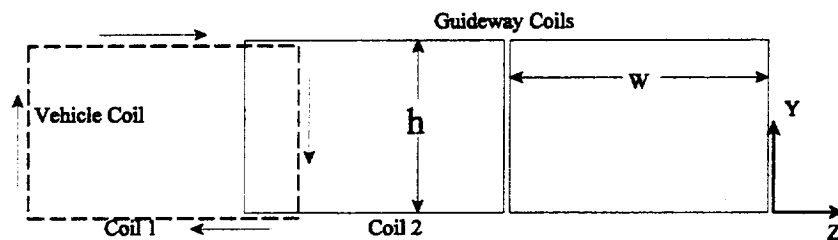
2275 Turnbull Bay Rd., New Smyrna Beach, FL 32168-5941, davey@ucnsb.net

July 27, 1999

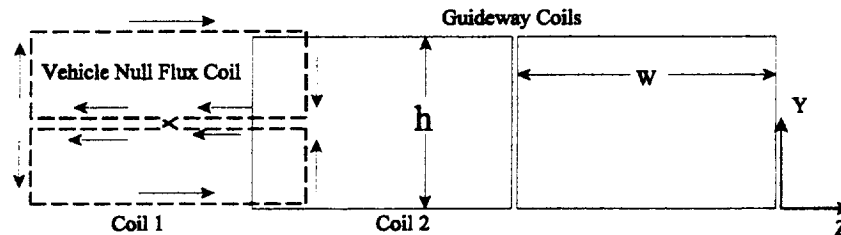
Abstract

This document examines the tradeoffs of choosing a null flux excitation system versus a simple coil excitation. In both cases the guideway is considered to be a simple "O" shaped coil positioned vertically on the track. An analysis of both shows that the null flux excitation provides equivalent lift to the open coil system with less drag; further the lift is stabilizing in both directions for the null flux excitation. The full rectangular excitation coil proves to be excellent for guidance especially if the vehicle magnets/coils on either side are arranged in repulsion. The rectangular coils in attraction prove to be expensive for drag production and unable to produce downward restoring forces.

Introduction



(a) Rectangular shaped excitation coil translating past "O" shaped guideway coils.



(b) Null flux excitation vehicle coil sweeping past fixed guideway coils.

Figure 1 Rectangular (a) and null flux (b) vehicle coils sweeping past fixed guideway coils.

The innovation of null flux coils in Maglev systems goes back to 1966 when Danby and Powell suggested their use in the first EDS system with superconducting magnet coils [1][2]. The dynamic stability of such systems have been studied experimentally and through mutual inductance approaches by Rote [3][4]. The mutual inductance coupling approach for the prediction of forces in such systems is adopted in this study. EDS systems that do not use flux canceling techniques have also been proposed and tested (e.g. Magneplane [5]), but these

systems have a much poorer lift to drag ratio. Perhaps the best review of the state of the art for this type of system is found through the Japanese Rail program in Japan where these techniques have demonstrated 550 kph operation in the Japanese rail test prototype [6].

The goal of this paper is to compare the null flux excitation to a full O coil excitation and then predict the lift and drag generally for a null flux excitation. Figure 2 shows the two options being compared along with the guideway coils. The full rectangular coils in inset (c) experience a repulsive force away from the guideway coils with any displacement. One way to make such a system stable is to place a second set of guideway coils vertically over the first set. The full rectangular system coils will experience a downward force by this second set of coils.

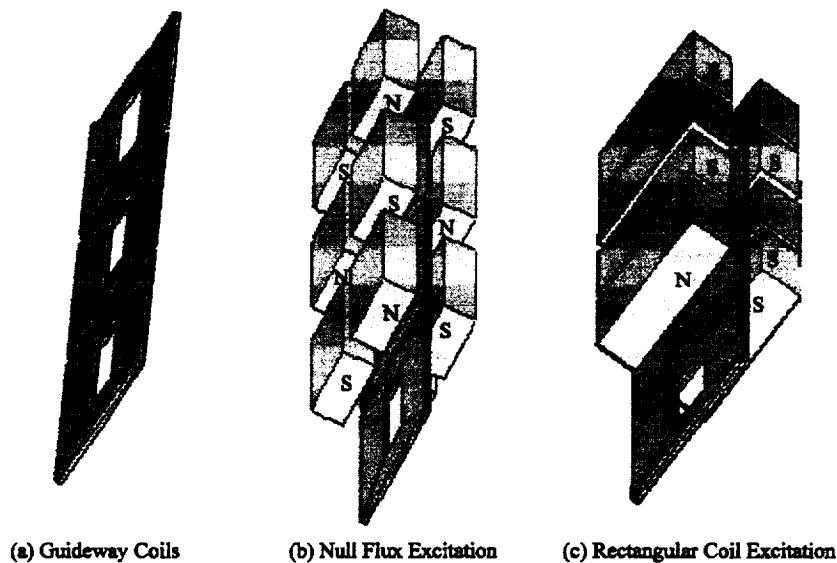


Figure 2 Null flux and rectangular excitation of O shaped guideway coils.

Geometry

Designers seek advantages for different coil configurations; Comparative assessment of coil configurations can only be obtained quantitatively. An electrodynamic O shaped coil guideway system is considered in this paper. A simple cost effective guideway structure consists of "O" shaped conducting coils placed vertically in the guideway as depicted in Figure 1(a). The dotted rectangular excitation coil can be considered a simple coil, a superconducting loop, or a permanent magnet. As it sweeps past the guideway coils, it induces a current which attempts to oppose the flux change. When the coil is offset vertically in the y direction, a force is generated to further push it off center.

This system will be contrasted with the null flux system shown in Figure 1(b). The excitation coil supports oppositely directed flux through the upper and lower portions of the windows of the coil. When the coil is centered vertically, no current is induced in the guideway coils. When the excitation coil is displaced in the y direction, a current is induced which does the

opposite of that in Figure 1(a). The induced current from the null flux coil exerts a force on the coil to restore it to its centered position. This is the well known benefit of the null flux geometry and why it has become so popular.

Analysis

To perform a useful comparison of these two systems, it is useful to make some approximations to pertinent quantities. One of the most important quantities is the mutual inductance coupling between the vehicle coil 1 and the fixed guideway coil 2. Let $z=0$ refer to the position in which the vehicle and guideway coil directly overlap. Let $z=0$ refer to the position in which the window of the guideway coil matches the vertical position of the window of the vehicle coil. The vehicle coil straddles the guiderail, and is wound in series, so it can be thought of as a single coil. In this embodiment, the mutual coupling of the rectangular coil in Figure 1(a) is

$$M_R = M_0(x) \cos\left(\frac{\pi}{2h}y\right) \cos\left(\frac{\pi}{2w}z\right) \equiv M_0 \cos\left(\frac{\pi}{2h}y\right) \cos(kz). \quad (1)$$

The mutual coupling of the null flux coil in Figure 1(b) with the guideway coil is approximately

$$M_N = \frac{M_0(x)}{2} \sin\left(\frac{\pi}{h}y\right) \cos\left(\frac{\pi}{2w}z\right) \equiv \frac{M_0}{2} \sin\left(\frac{\pi}{h}y\right) \cos(kz). \quad (2)$$

The x dependence is omitted from these expressions, but it commonly is a linear function that starts with zero when the coil is centered laterally, and grows linearly as the vehicle coil gets closer to the guideway coil on one side.

Regardless of which system is employed, the current induced in the shorted guideway coil 2 depends on M , the self inductance of the guideway coil L_2 , and the resistance of the guideway coil R_2 as

$$L_2 \frac{dI_2}{dt} + R_2 I_2 + \frac{d}{dt} (MI_1) = 0. \quad (3)$$

The induced current in the low and high frequency limit become

$$I_2 = - \begin{cases} \frac{M(y)I_1 \cos(kvt)}{L_2}; & \text{low frequency} \\ \frac{M(y)I_1 kv \sin(kvt)}{R_2}; & \text{high frequency} \end{cases}. \quad (4)$$

Equation (4) assumes that the vehicle speed is v , so that $z=vt$, and $M(y)$ is either the cosine in (1) or the sine in (2). The current I_1 is assumed fixed, being the representative current of the superconducting coil or magnet. Equation (4) can be written for any speed by allowing $\omega=kv$, and writing the result in phasor format as

$$I_2 = - \frac{j\omega M(y)I_1}{(j\omega L_2 + R_2)} e^{j\omega t}. \quad (5)$$

Of interest are the forces generated on the vehicle coil as it sweeps past the guideway coils at speed v . These forces are easily derived through the derivative in the various directions of the coenergy

$$W' = MI_1 I_2 \quad (6)$$

holding the respective currents constant during the spatial derivative. The average of the z directed drag force is

$$\hat{F}_z = \frac{1}{2} \Re \left(\frac{\partial M}{\partial z} I_1 I_2^* \right). \quad (7)$$

Inserting (5) and (6) into (7) yields for the rectangular vehicle coil

$$\begin{aligned} \hat{F}_z &= \frac{1}{2} \Re \left\{ \frac{jkM_0 \cos(\frac{\pi}{2h}y) (e^{j\omega t})^* I_1 \left(-j\omega M_0 \cos(\frac{\pi}{2h}y) I_1 e^{j\omega t} \right)}{(j\omega L + R)} \right\} \\ &= \frac{1}{2} \Re \left\{ \frac{k\omega (M_0 \cos(\frac{\pi}{2h}y) I_1)^2}{(j\omega L + R)} \right\}. \end{aligned} \quad (8)$$

When the same procedure is performed on the null flux system, the result is

$$\begin{aligned} \hat{F}_z &= \frac{1}{2} \Re \left\{ \frac{jk \frac{M_0}{2} \sin(\frac{\pi}{h}y) (e^{j\omega t})^* I_1 \left(-j\omega \frac{M_0}{2} \sin(\frac{\pi}{h}y) I_1 e^{j\omega t} \right)}{(j\omega L + R)} \right\} \\ &= \frac{1}{8} \Re \left\{ \frac{k\omega (M_0 \sin(\frac{\pi}{h}y) I_1)^2}{(j\omega L + R)} \right\}. \end{aligned} \quad (9)$$

Of central importance is the ratio of the drag with the rectangular non-null flux system and the null flux system,

$$\frac{\hat{F}_{zR}}{\hat{F}_{zN}} = \frac{\left[M_0 \cos(\frac{\pi}{2h}y) \right]^2}{\left[\frac{M_0}{2} \sin(\frac{\pi}{h}y) \right]^2} \approx \begin{cases} \left(\frac{2h}{\pi y} \right)^2 & \text{for small } y \\ 4 & \text{at their maximum positions} \end{cases} \quad (10)$$

The drag force is substantially larger than it is with the rectangular non-null flux coil system for small y . As will be shown shortly, the rectangular system reaches a lift force maximum at $y=h/2$, and is stable for $h/2 < y < h$. The null flux system reaches a lift force maximum at $y=h/4$, and is stable for $0 < y < h/4$. At these respective maximums the rectangular system has four times the drag of the null flux system. This is not the total story since the other component forces should be investigated.

The y component of the rectangular coil system is

$$\hat{F}_y = \frac{1}{2} \Re \left(\frac{\partial M^*}{\partial y} I_1 I_2 \right) = \frac{1}{4} \Re \left\{ j\omega (M_0 I_0)^2 \frac{\pi}{h} \frac{\cos(\frac{\pi}{2h}y) \sin(\frac{\pi}{2h}y)}{(j\omega L_2 + R_2)} \right\}. \quad (11)$$

Similarly, the average lift force from the null flux system is

$$\hat{F}_y = \frac{1}{2} \Re \left(\frac{\partial M^*}{\partial y} I_1 I_2 \right) = -\frac{1}{8} \Re \left\{ j\omega (M_0 I_0)^2 \frac{\pi}{h} \frac{\sin(\frac{\pi}{h}y) \cos(\frac{\pi}{h}y)}{(j\omega L_2 + R_2)} \right\}. \quad (12)$$

The null flux system has a sign reversal from the derivative of the cosine rather than the sine; this sign reflects its inherent stability. The rectangular system has to have a different initial positioning for repulsion to work. Stability for the rectangular system is achieved if the rectangular coil is positioned above the maximum lift position $y \geq h/2$. The null flux coil system delivers maximum lift at $y=h/4$; any vertical displacement after that point becomes unstable. The all important ratio of these two lift forces is

$$\frac{\hat{F}_{yR}}{\hat{F}_{yN}} = \frac{2 \sin(\frac{\pi}{2h}y) \cos(\frac{\pi}{2h}y)}{\sin(\frac{\pi}{h}y) \cos(\frac{\pi}{h}y)} \approx \begin{cases} 1 & \text{for small } y \\ 2 & \text{at their respective maximum positions} \end{cases}. \quad (13)$$

The two systems can generate the same lift forces in a stable configuration, but the drag for the rectangular system is horrendously bad. The mutual coupling M is low for the null flux system, while the derivative $\frac{\partial M}{\partial y}$ is low for the rectangular system; the two compensate. At their

respective maximums, the rectangular system generates twice the lift of the null flux system, and as shown in (10), four times the drag.

The lateral guidance forces are the last to compare. The lateral derivative on the mutual coupling enters prominently in the calculation. Consider the null flux geometry displayed in Figure 3. Stacked magnets are used to simulate a null flux excitation. The “O” shaped guideway coil is shown as comprised of thirteen individual conductors as it must to minimize eddy current losses. Two identical coils are shown side by side. The two pairs can be connected together in series to emulate a single coil, or they can be cross-connected so that their flux cancels. The later embodiment is of little value as will be witnessed shortly.

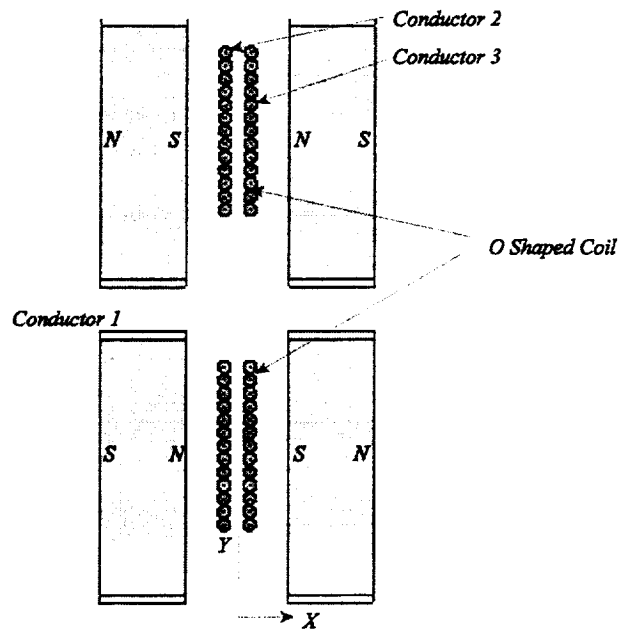


Figure 3 Null flux excitation (end view) acting against two "O" shaped coils.

The gap between magnets is 6.03 cm (2.375"). Of interest is the mutual inductance change as the guideway coils are displaced 1.52 cm (0.6") to the right. Treat the magnets as blocks with surface current on the sides. The mutual inductances M_{12} and M_{13} are shown in Figure 4. Since the guideway coils are displaced to the right, the right coil 3 continues to grow much more rapidly than the left coil coupling.

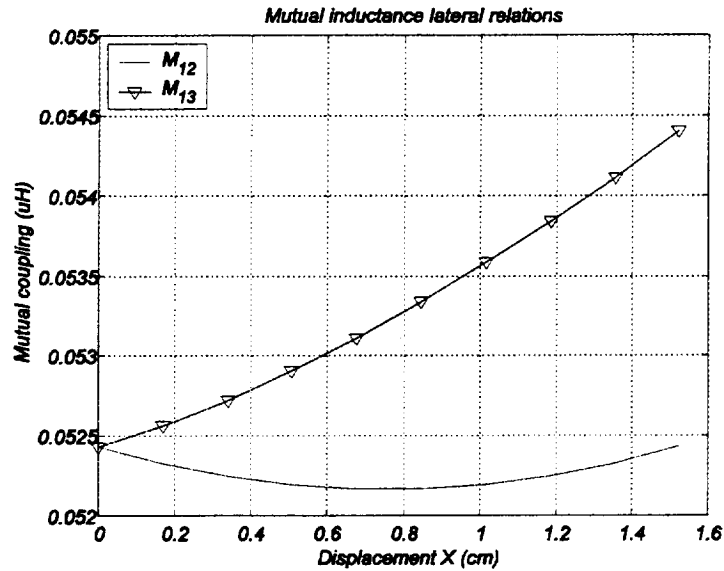


Figure 4 Mutual inductances M_{12} and M_{13} as a function of displacement.

If the coils are connected additively in series, the resultant coupling should be the sum of the two inductances in Figure 4. Conversely if they are connected to subtract in series, the mutual coupling should be the difference of these two quantities. A cross-connecting affecting this subtraction is not useful when the coils are in close proximity as they are here. Shown in Figure 5 are the results of these computations. As expected, subtracting the left and right mutuals results in a zero starting inductance, which grows with displacement.

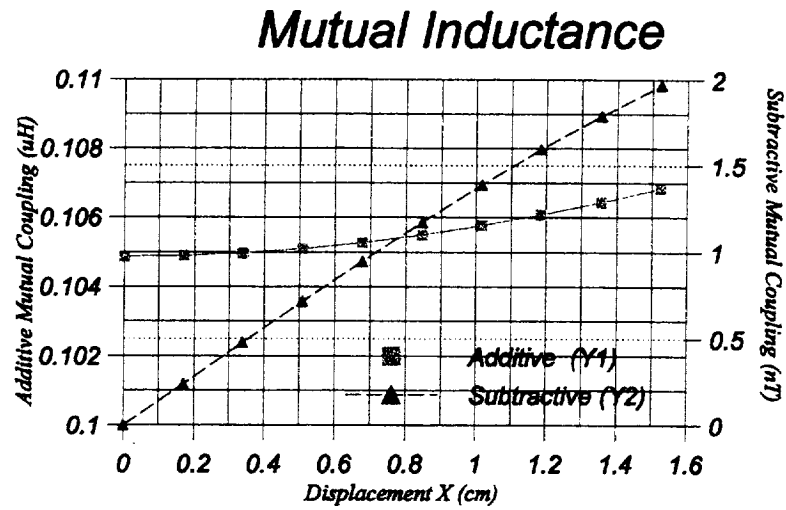


Figure 5 Mutual inductance when the left and right coils are connected additively in series versus subtractive.

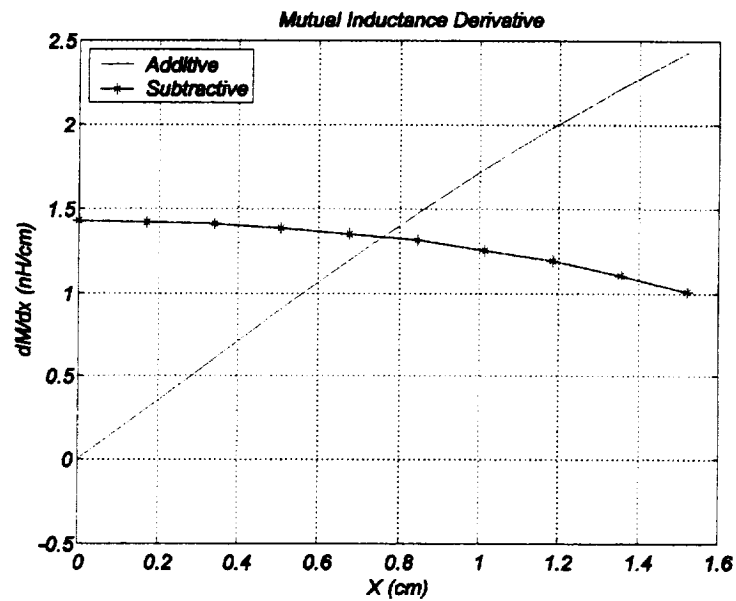


Figure 6 Mutual inductance derivative for additive and subtractive cross-connections.

Of central importance is the derivative of these inductances with displacement, X . This derivative is shown in Figure 6. The derivative of the subtractive curve is incorrect at $x=0$. The $x=0$ point corresponds to the top of a peak for which the derivative is actually undefined. But the

value jumps immediately off the peak to a value superior to the additive cross-connection. What is more noteworthy is the fact that the additive cross-connection soon catches up and exceeds the subtractive cross-connection. No real advantage is gained by cross connecting the coils.

The analysis for lateral guidance parallels that for lift. The average x directed force is

$$\hat{F}_x = \frac{\Re}{2} \left[\frac{\partial M^*}{\partial x} I_1 I_2 \right]. \quad (14)$$

The mutual coupling is written either as (1) or (2), and I_2 from (5) gives

$$\begin{bmatrix} \hat{F}_{xR} \\ \hat{F}_{xN} \end{bmatrix} = -\frac{\Re}{2} \frac{\partial M_0}{\partial x} I_1^2 \left(\frac{jM_0\omega}{j\omega L_2 + R_2} \right) \begin{bmatrix} \cos(\frac{\pi}{2h}y) \\ \frac{1}{2}\sin(\frac{\pi}{h}y) \end{bmatrix}. \quad (15)$$

The derivative $\frac{\partial M_0}{\partial x}$ scales with M_0 for either the rectangular or the null flux system. The all important ratio of these two forces becomes

$$\frac{\hat{F}_{xR}}{\hat{F}_{xN}} = \left(\frac{\cos(\frac{\pi}{2h}y)}{\frac{1}{2}\sin(\frac{\pi}{h}y)} \right)^2 \approx \begin{cases} \left(\frac{2h}{\pi y} \right)^2 & |_{small\ y} \\ 4 & |_{at\ their\ maximum\ positions} \end{cases}. \quad (16)$$

A full coil rectangular excitation gains in lateral guidance exactly what it lost in drag. Since the rectangular excitation generates more lift, less units are required for levitation. But in addition to greater drag, the rectangular coil has another disadvantage, that of providing no restoring force to the vehicle should the vehicle be lifted by a gust of wind or in rising over the crest of a hill. The return path for the field also must be made in the z direction. This sometimes forces the use of more back iron for reasonably long pole pitches.

Is there a way to use the larger guidance force generated by the full rectangular coil? When the magnets are in repulsion as suggested in Figure 7, the mutual coupling for the coils themselves drops by an order of magnitude. When the fields repel one another, the drag induced will be much smaller since the mutual coupling is smaller. Note that this is a top view of the rectangular system, unlike Figure 3 in which an end view is pictured for the null flux magnets.

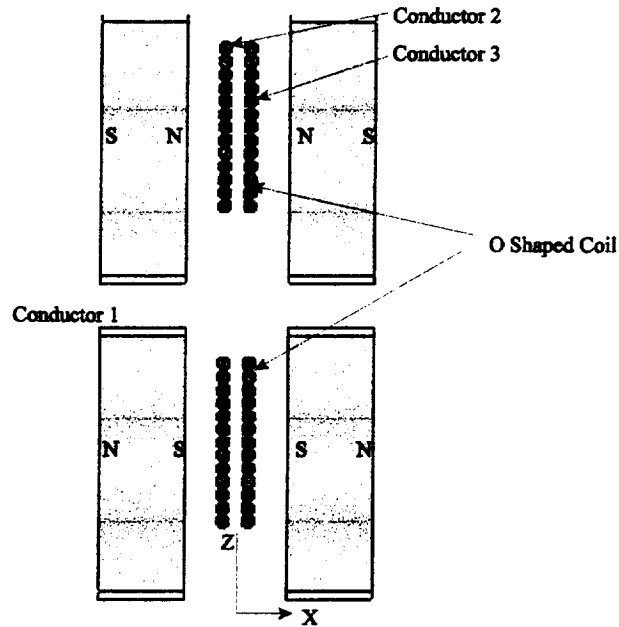


Figure 7 Guidance magnets (top view) are arranged in repulsion to minimize drag.

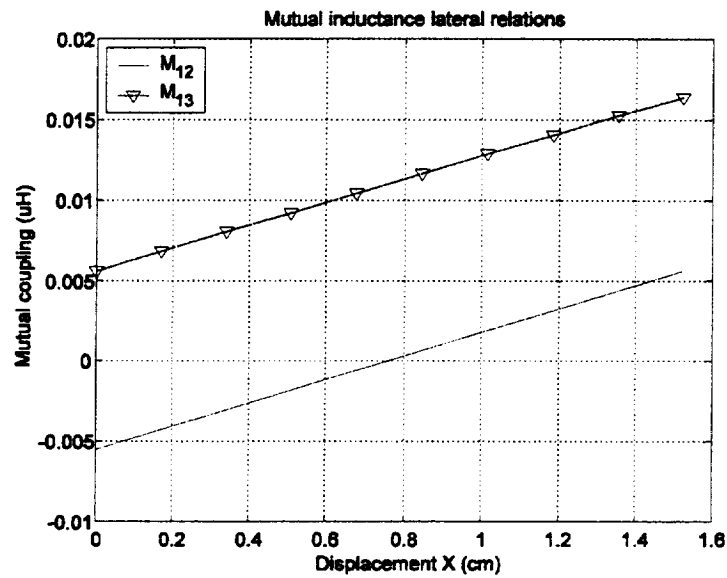


Figure 8 Mutual coupling M_{12} and M_{13} for a repulsive field arrangement.

For this repulsion arrangement the mutual coupling equivalent to Figure 4 results in the mutual coupling of Figure 8. Note that these mutual couplings are an order of magnitude smaller than those in Figure 4. But the rate of change of these quantities is also much larger.

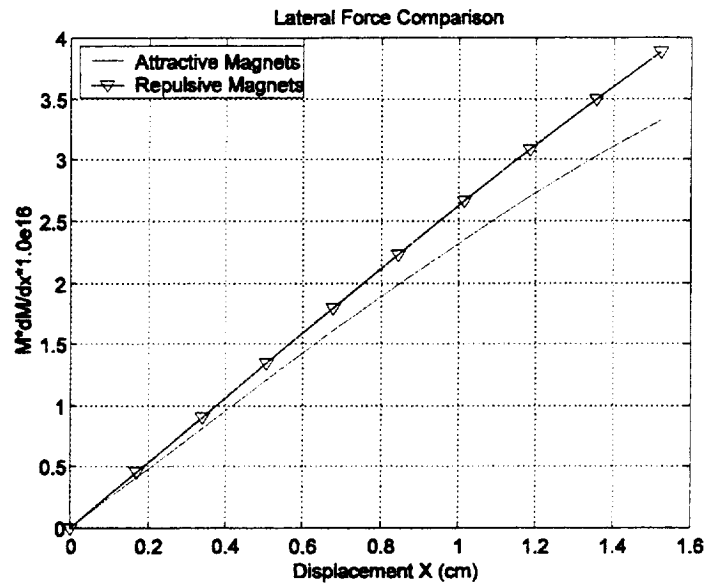


Figure 9 Comparison of the guidance force from repulsive and attractive magnets.

The actual number to compare, evident from (15), is the product $M \frac{\partial M}{\partial x}$. Figure 9 shows that the derivative more than makes up for the smaller mutual coupling, yielding a higher product. So a repulsive magnet arrangement has a small drag penalty, but yields a high guidance force. The optimal excitation appears to be a combination of these two excitations to get lift and drag simultaneously. The configuration shown in Figure 10 shows what may be the best combination.

Conclusions

Null flux excitation systems are preferred over full coil excitation. Null flux coil excitation systems have the following advantages:

- ! Provision of lift force in both directions.
- ! Less drag.

The following disadvantages are also noted:

- ! Poor lateral guidance force production.
- ! Slightly smaller lift generation capability than a full coil excitation.

Both continue to improve their lift / drag ratio with speed. Drag force continues to decrease with speed. Attempting to cross-connect identical guideway coils is not an effective means of enhancing guidance forces. One effective means is to use full coil excitations oriented in repulsion. This arrangement has a smaller drag due to the diminished net coupling with the repulsion magnets. Excitation coils in repulsion yield the same guidance forces as attractive excitation coils, yet the former have less drag. The objective for lift or guidance is to maximize

the mutual derivatives, and minimize the mutual inductance, since the latter contributes drag.

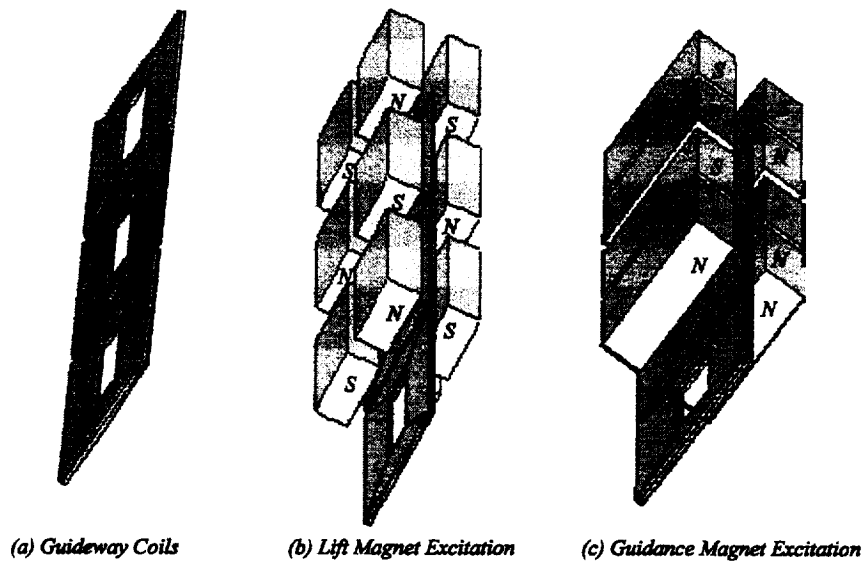


Figure 10 Using null flux magnets for lift and repulsive rectangular magnets for guidance appears optimal.

References

1. J. R. Powell and G.R. Danby, "Magnetically Suspended Trains for Very High Speed Transport", *Proceedings of the Fourth Intersociety Engineering Conference*, Washington, Sept. 22-26, 1969, pp. 953-963.
2. J.R. Powell and G.R. Danby, "High Speed Transport by Magnetically Suspended Trains", *ASME Publication No. 66, WA/RR5*, December, 1966.
3. Y. Cai, D. M. Rote, T.M. Mulcahy, Z. Wang, S.S. Chen, and S. Zhu, "Dynamic Stability of Repulsive-Force Maglev Suspension Systems", Argonne National Laboratory report ANL-96/18, November 1996.
4. J.L. He, D.M. Rote, and H.T. Coffey, "Study of Japanese Electrodynamic-Suspension Maglev Systems", *Argonne National Laboratory report ANL/ESD-20*, April 1994.
5. H.H. Kolm and R.D. Thornton, "The Magneplane: Guided Electromagnetic Flight", *Proceedings of the 1972 Applied Superconductivity Conference*, May 1-3, 1972.
6. H. Soejima and K. Isoura, "Development of the Maglev System in Japan, Past, Present, and Future", *The 15th International Conference on Magnetically Levitated Systems and Linear Drives*, April 15-18, 1998, Mt. Fuji, Yamanashi, Japan, pp. 8-11.

Takeshi MIZUMA

Traffic Safety and Nuisance Research Institute, Ministry of Transport

1. Introduction

In order to solve some various problems of urban transportation such as traffic congestion, pollution and accidents, various kinds of people mover systems have been developed, and parts of some are in practical use in Japan. Though most people mover systems in existence use rubber tires and wheel guide rollers, there are several problems such as high operating and maintenance costs in comparison with conventional railways. In order to settle these problems, several new transportation systems driven by linear motors are being developed in Japan and are partly in practical use. Generally speaking, linear motor driven systems have magnetic suspensions because of many merits of contactless systems. However, in Japan, many new linear driven systems with contact are being developed.

This paper describes some technical characteristics of new urban transportation systems driven by linear motors in Japan with not only magnetically levitated suspensions but also other suspensions such as air or mechanical. Moreover, we denote several evaluation items for urban transportation systems and show the comparison results according to these evaluation indices. Receiving these results, we propose technical evaluation method for new urban transportation systems and show an example to introduce magnetically levitated transportation systems of HSST in new region by using this method.

2. Development of magnetically levitated transportation systems in Japan

In Japan, as you know, big project of superconducting magnetic levitated vehicles (JR Maglev) has been proceeding in Yamanashi test track since 1996, but other urban transportation systems with linear motors are being developed for several kinds of urban needs for example, steep slope or steep curve.

This section describes the developing status of these transportation systems.

2.1 Super high speed systems (JR Maglev) ¹⁾

The magnetically levitated system using superconducting magnets aims at extremely high speed of 500 km/h in revenue service for intercity transportation such as Tokyo-Osaka. This system has reached the running tests on Yamanashi Maglev Test Line and realized the maximum speed of 550 km/h in December 1997. It is continuing to undergo several safety and reliability tests.

Figure 1 shows the outline and location of priority section in Yamanashi test line, and main specifications of the priority section are shown in Table 1.

Main tests are executed in this priority section, and after some verification of safety, Japanese government will judge the possibility of practical services. Considering these circumstances, final test

line will be constructed as the part of the revenue line from Tokyo to Osaka.

Figure 2 shows the outline and main specifications of test vehicle MLX01.

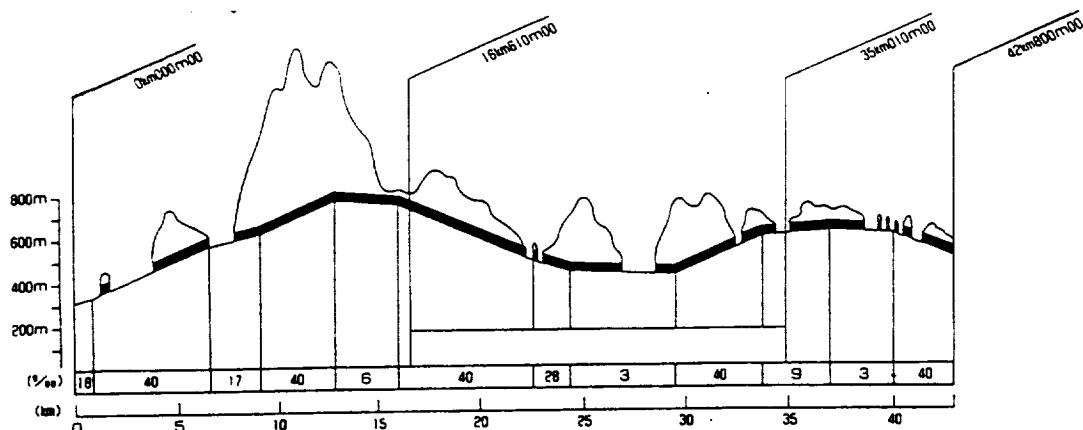


Figure 1 Outline and location of priority section in Yamanashi Test Line

Table 1 Specifications of the priority section of the Yamanashi Test Line

Length	Priority section 18.4 km , Tunnel section 16.0 km Open section 2.4 km
Maximum speed	550 km/h (operating speed 500 km/h)
Minimum curve radius	8000 m
Maximum gradient	4 %
Distance between the centers of adjacent guideways	5.8 m
Passing	Relative speed is 1000 km/h
Main facilities	Control center, Substation , Test embarkation platform , Train depot
Turnout apparatus	High speed turnout , Low speed turnout

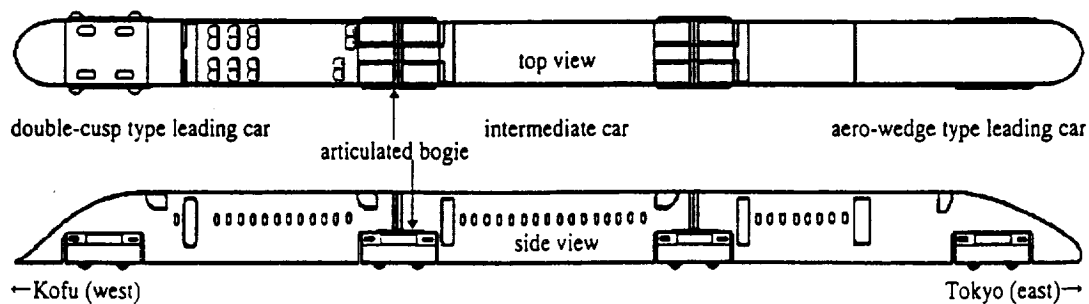


Fig.2 Outline and main specification of test vehicle MLX01

Figure 3 shows the outline and general diagram of truck suspension. The truck on which the superconducting magnets are mounted serves to transmit the propulsive and levitational force generated by the magnets to the vehicle. It is also fitted with landing gear and guide wheel needed when running at low speeds generally below 150 km/h , and with hydraulic apparatus that raises and lowers these wheels. Moreover apparatus for cooling the superconducting magnets are mounted. Also, various measures to improve cruising comfort , such as the double suspension spring and the vibration control devices, are incorporated on same trucks.

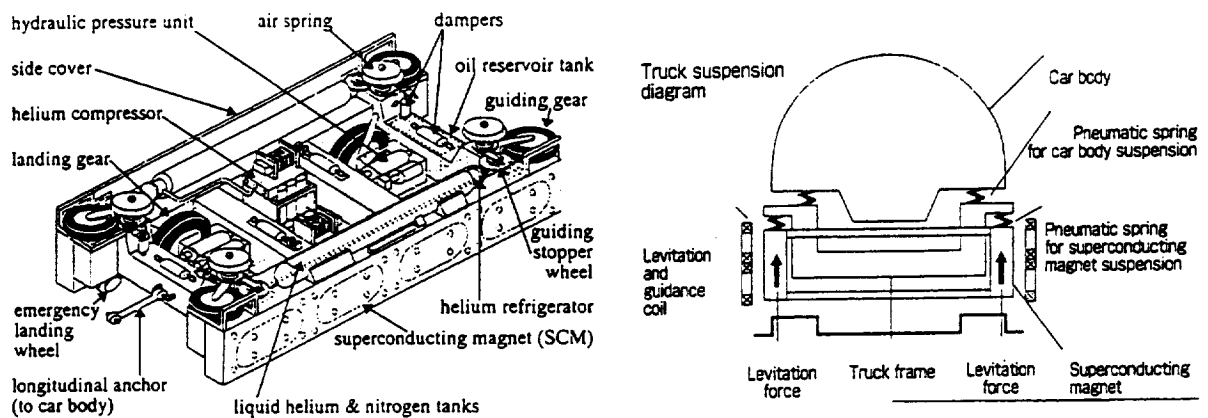


Fig.3 Outline and general diagram of truck suspension

Figure 4 shows the sample measurements of displacements between the truck and guideway at low speed. When the vehicle speed is lowered to about 100 km/h, an indication of instability is the gradual increase in the amplitudes of the vibrations of the lateral displacements between the truck and guideway. For the fundamental vehicle running tests on the Yamanashi Maglev Test Line , the speed at which the vehicle commences levitation was set to be 135 km/h for the straight guideway sections , and 150 km/h for the curved guideway sections.

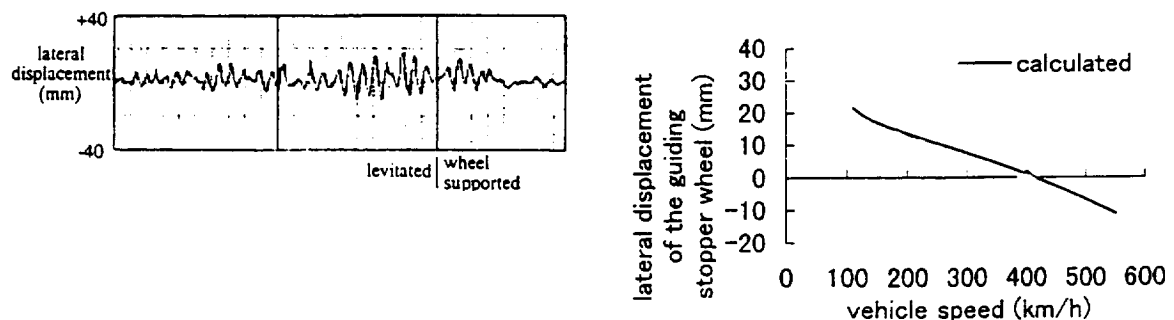


Fig.4 Sample measurements of the displacements between the truck and guideway at low speeds

2.2 Urban transportation systems

In Japan, according to several needs considering specific characteristics of urban problems, some new transportation systems driven by linear motors are being developed and are partly in practical use. In this section, some magnetically levitated transportation systems are denoted in technical viewpoints, and other systems are taken up for the sake of comparison.

2.2.1 Normal conducting magnetic levitation vehicle systems HSST²⁾

HSST that has been developed since 1974 is a magnetically levitated vehicle (maglev) transportation system using electromagnetic suspension (EMS) and short stator linear induction motors. Ministry of Transport of Japan has clarified its safety and practicality for revenue services through several test results in Nagoya test track.

Figure 5 shows the outline of test line in Nagoya and figure 6 shows the outline of HSST vehicles.

As HSST has developed for satisfying urban transportation demands, it aimed at a maximum speed of 100 km/h and comfortable riding performances because of levitation.

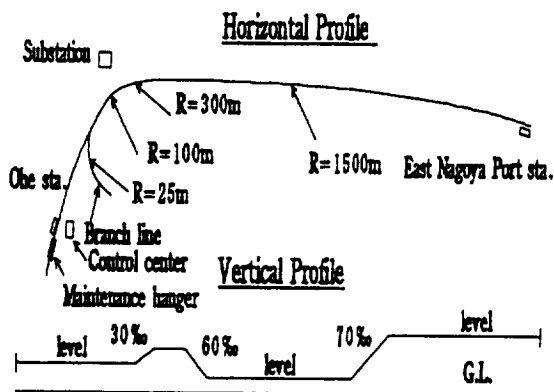


Fig. 5 Outline of test line in Nagoya

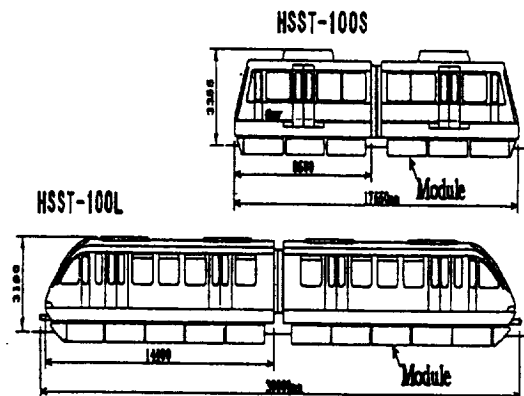


Fig.6 Outline of HSST vehicles

Table 2 shows several main specifications of HSST vehicles and figure 7 shows the cross section of the car body. Moreover, it is shown the cross section of the module that is the main element for controlling levitation and propulsion in figure 8.

Since HSST-100S was developed as the same size of standard rubber tire transportation systems (generally speaking as people mover) in Japan, length of car is restricted 8.5 m by Japanese standards for medium transportation demands such as 8,000 ~ 20,000 people per peak one hour. On the contrary, HSST-100L has been designed to realize larger transportation demands.

Table 2 Major specifications of HSST vehicles

Items	HSST-100S	HSST-100L
Length of end car	8.5 m	14.4 m
Width of car	2.6 m	2.5 m
Vehicle weight		
Empty	10 ton	15 ton
Full load	15 ton	25 ton
Passenger number (at peak hour)	44 (67)	68 (110)
Max speed	100 km/h	100 km/h
Acceleration	4.5 km/h/s	4.5 km/h/s
Number of module	6 /car	10 /car
Magnetic gap of levitation	8 mm	8 mm
Lateral suspension system	Hydraulic control	Mechanical control
Number of Linear Induction Motors	6 LIMs/car	10 LIMs/car

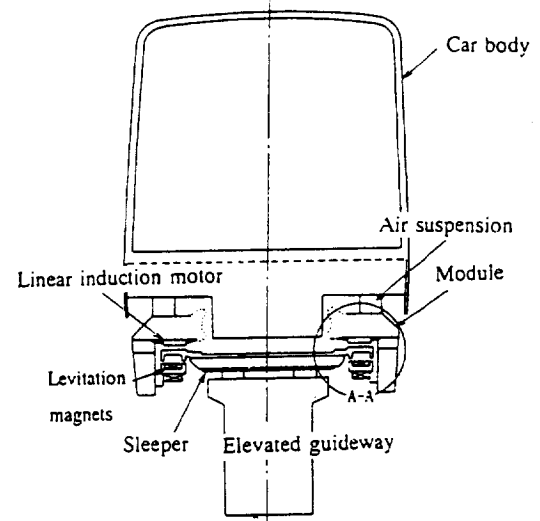


Fig.7 Cross section of car body

The relation between the fluctuation of levitation gap and vehicle speed is shown in figure 9. In this figure, levitation gap is defined as the length between levitation magnet and rail. It can be seen that the fluctuation of gap is proportion to the root of speed and no probability of contact between magnets and rail can be expected because the normal levitation gap is 8 mm. At 100 km/h with full load, the fluctuation of gap in RMS was 0.9 mm in average.

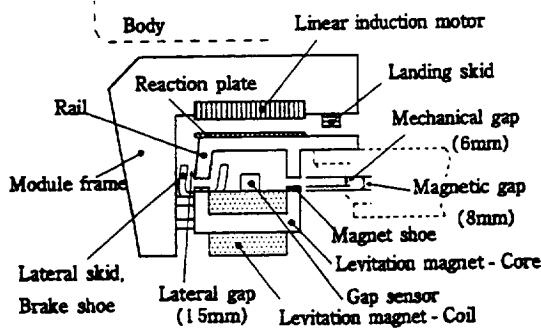


Fig. 8 The cross section of module

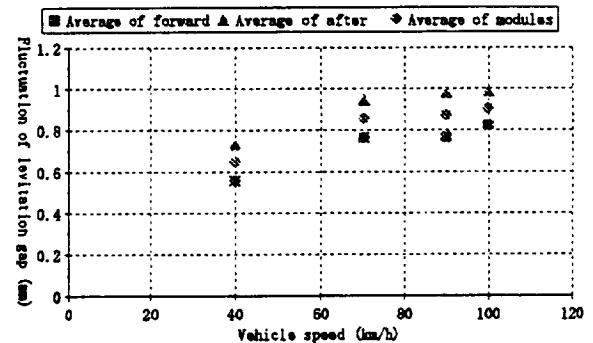


Fig. 9 Fluctuation of levitation gap

Presently, construction plan has been proceeding in east side of Nagoya that connects 11 km between subway station and suburban areas. HSST-100L system is now preparing for revenue service with continuing durability running tests in test line.

2.2.2 Permanent magnet levitation system³⁾

Formerly, M-bahn system has operated in west Berlin in 1989 and this system has characteristics in levitation with permanent magnets and propulsion with linear synchronous motors of primary side on ground type. However, this system is not perfect contactless but supported by wheel with mechanical system for compensating for the load variation from empty to full conditions. Though this system vanished unfortunately in Germany for the sake of several political reasons, it has been studied in Japan

as the short trip urban transportation systems utilizing high economic performance such as 0 energy for levitation.

This section introduces the Japanese study status for easy transportation system with permanent magnet levitation .

Figure 10 shows the outline of simple vehicle with permanent magnet levitation in the experimental line and gap control mechanism is shown in figure 11. As gap between permanent magnet on the vehicle and iron core of primary coil on the ground is controlled mechanically with the weight through link mechanism, vertical wheels do not support the normal load. The role of these wheels are to support the temporary load change such as running through on the joints in the track. You can see the relation between gap and load. That is to say , according to increasing loads, gap is gradually smaller mechanically.

Figure 12 shows the example of running results in the test line of about 50m. Running of this system is controlled automatically by computers that has running patterns and orders driving currents on the ground side.

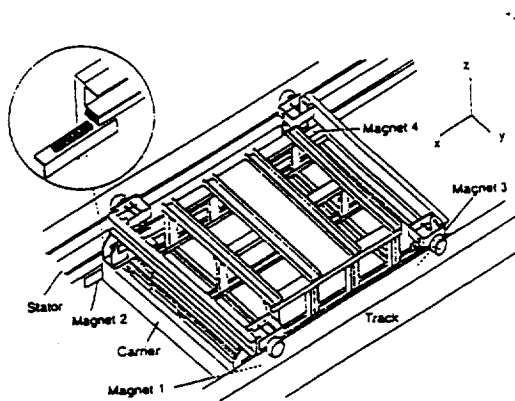


Fig. 10 Outline of test vehicle

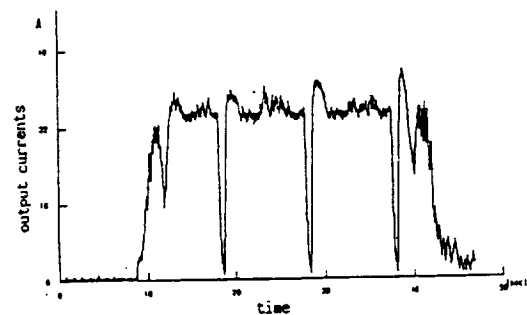


Fig.12 Example of running results

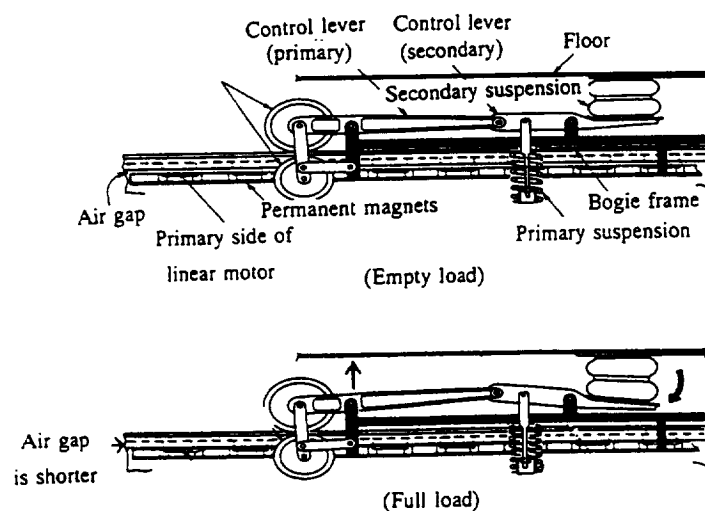


Fig. 11 Outline of gap control mechanism

2.2.3 Aerodynamic levitation system³⁾

It is well known that the aerodynamic levitation system such as OTIS shuttle has quietness inside and outside vehicle. In Japan, rope driven system was realized in Narita airport by OTIS and now, linear motor driven system is refining in test line also by OTIS.

This section describes the characteristics of aerodynamic levitation transportation systems driven by linear motors.

Figure 12 shows the outline of vehicle and suspension system.

This system is driven by linear induction motors with primary side on vehicle like HSST, but has characteristics in air suspension that supports the vehicle through air pads without perfect levitation. The distances between road surface and air pads are within 0.1 mm or 0 mm that is contact. But the system was designed for this contact between air pads and road surface and has no problems from the viewpoint of running and wear. No contacts are realized in other parts such as linear motors (primary coils and reaction plate) or brake skids (skid and road surface). Figure 13 shows the relation of gap and speed at some parts of vehicle.

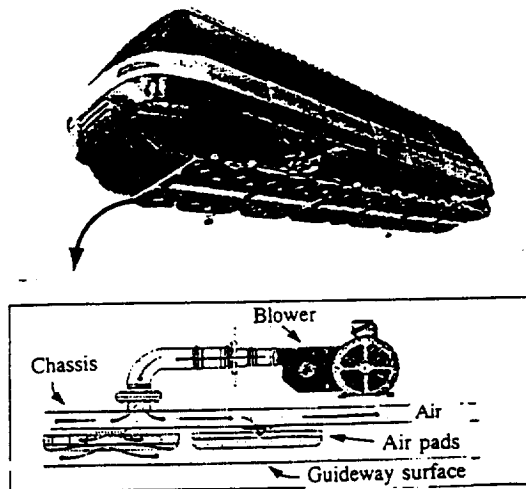


Fig.12 Outline of vehicle and air suspension

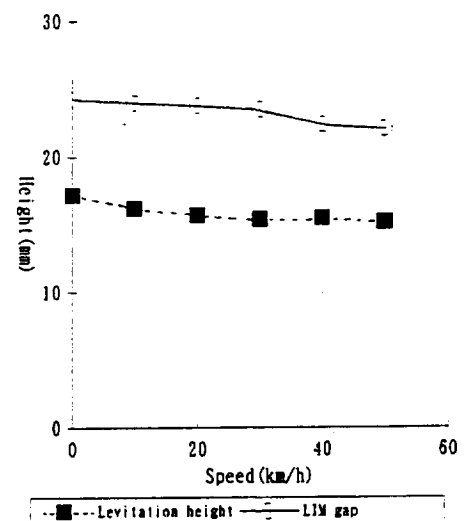


Fig.13 Relation of gap and speed

It is shown that levitation height is on the decrease in proportion with speed, but margins for contacts have secured enough. Presently, several tests are executed under the directions of technical committee in Railway Electrical Engineering Association of Japan at test line of about 450m. It realized maximum speed of 55 km/h and secured low noise characteristics inside and outside vehicle.

2.2.4 Other systems for urban transportation

1) Linear metro system⁵⁾

In Japan, in big cities, though subway systems are popularized for eliminating road traffic congestions, many subjects such as large financial costs and long term planning are pointed out by local government sides that generally operate subway systems. For these reasons, linear metro was developed for realizing low construction costs under the instructions of Ministry of Transport.

Figure 14 shows the section of linear metro system. According to this figure you can see the small cross section because of flatness of linear motor. It can be realized to be about 70 % of diameter of tunnel in comparison with conventional subway.

This system has characteristics of using wheel and rail for supporting vehicles like conventional railways. Moreover, truck can be easily improved to have simple steering functions because of flatness of linear motor without steering link. The outline of truck is shown in figure 15 and it can run smoothly on steep curve by this structure. Since Table 3 shows the comparison of mechanical dynamic gap between primary coil and reaction plate of design values and running results, it can be judged that the standard gap of 12 mm is appropriate.

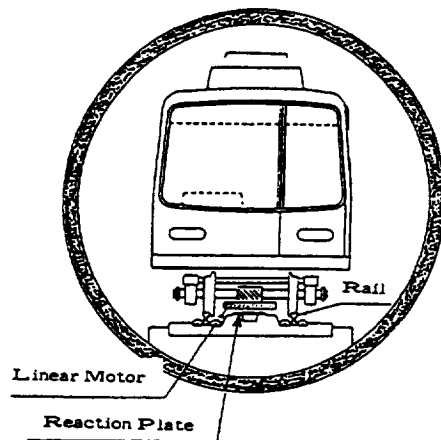


Fig.14 Section of linear metro system

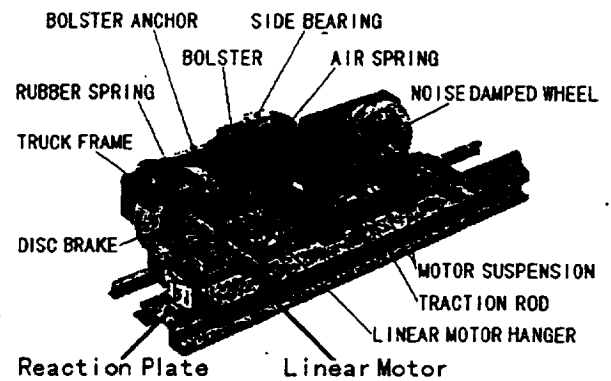


Fig.15 Outline of bogie truck

Table 3 Comparison of gap between designs and results

(Unit:mm)

Items for causing gap fluctuations		Design value	Measurement results	
			Straight line	Curve line
Setting error of linear motor coils		1 . 0	1 . 0	1 . 0
Deflection of support and linear motor coils		0 . 5	0 . 9	0 . 7
Wheel wearing up to maintenance		1 . 0	1 . 0	1 . 0
Gap margin	Deflection by temperature	3 . 5	0 . 4	0 . 4
	Others		—	—
	deflection of reaction plate		0 . 7	1 . 1
Deflection of reaction plate		0 . 5		
Setting error of reaction plate		2 . 0	2 . 0	2 . 0
Rail sinking		0 . 5	0 . 3	0 . 7
Fall on rail joint		1 . 0	(1 . 0)	(1 . 0)
Rail wearing up to maintenance		2 . 0	2 . 0	2 . 5
Total amount		12 . 0	9 . 3	10 . 4

2) Sky rail system⁶⁾

This system has developed for transporting people who live on the top of mountain hills at steep gradient districts to the railway stations that are located on the flat spaces in short trips. This system has characteristics in driving by rope and linear motors with primary side on ground. Though vehicles are suspended by the elevated girders like suspended monorail with wheels (vertical and guide), they are driven by rope between stations and by linear induction motors with primary side on ground at the station areas. Figure 16 shows the outline of sky rail systems. It is interesting that vehicles are accelerated by linear motors at the station and grasp the rope with synchronous speed and are pulled by rope between stations and at the next station edge detach the rope and are decelerated by linear motor and stopped automatically. This system has just started as practical use in Hiroshima districts in 1998 on 1.3 km length.

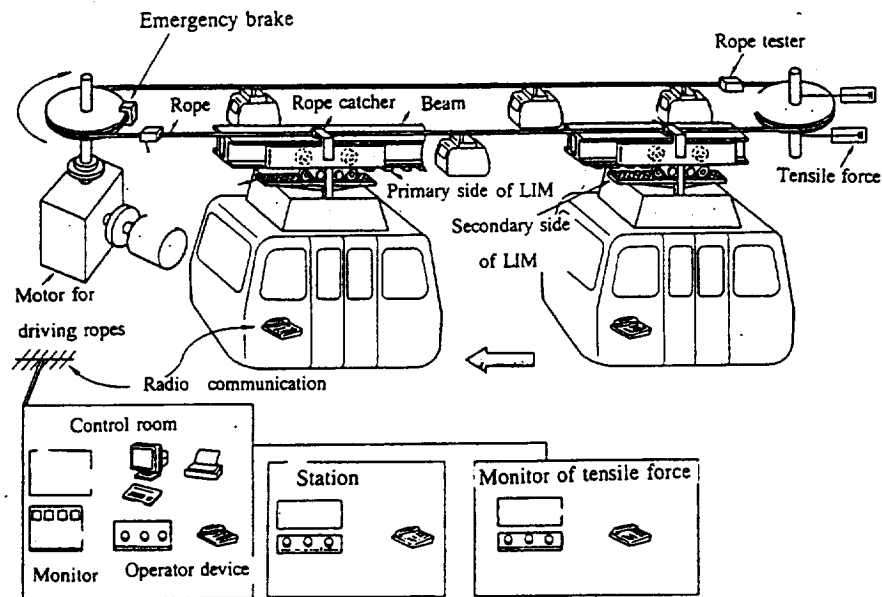


Fig.16 The outline of skyrail

3. Evaluation of urban levitated transportation systems

As you know, many new urban transportation systems are developing and some are in partly practical use. However, it is not said that the best solution to solve urban transportation problems is to prepare in Japan. It is said that some systems that are developed by each manufacturer are introduced somewhere by plausible reasons. In the section, it is denoted to evaluate these systems objectively in the viewpoints of technical, energy, and environmental sides.

3.1 Technical evaluation

As technical items that can be evaluated for maglev systems are taken up various topics, it is difficult to say that these systems are prior to conventional railways. For example, figure 17 shows the comparison of riding comfort between maglev systems and other urban transportation systems. As you understand by this figure, it is clear that magnetic suspensions have secured good riding comforts. The running resistance of

several urban transportation systems are shown in figure 18.

You can find the profitability of levitated or linear motor driven systems in comparison with conventional railways. Through these comparisons , the characteristics of maglev systems are confirmed.

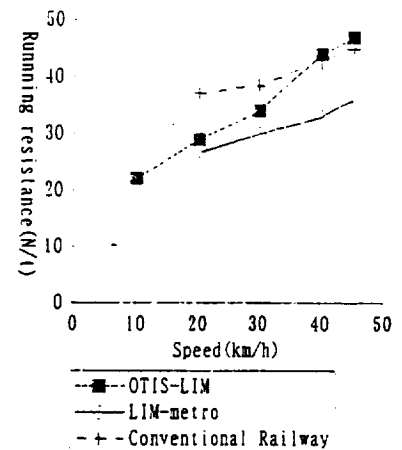
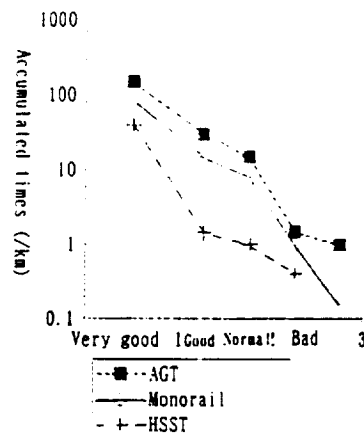


Fig.17 Riding comforts of transportation systems Fig.18 Running resistances of transportation systems

3.2 Evaluation on environment

It is supposed for maglev systems to be silent in and outside vehicles because of non-contact and non adhesion drive. It is one of the most important merits to develop maglev systems in Japan for urban transportation systems. This is only realized by using magnetic or aerodynamic suspensions. Figure 19 shows the example of noise characteristics outside vehicle. According to this result, it is easily understood that levitation systems are friendly on noise environment. Moreover, it is natural for these electric railway systems including levitation systems to be superior to other transportation systems such as automobiles and buses.

3.3 Evaluation on energy

Levitation systems need extra energy for levitation, except for those using permanent magnets and high temperature superconducting magnets, beside propulsion energy. Moreover, in most cases, linear motors are used for levitation systems because of flatness and separate constructions. Therefore, it is supposed that levitation systems consume more energy for driving vehicles because of gap of linear motors. Figure 20 shows the running energy consumptions of several transportation systems with distances between stations. Generally speaking, energy consumption decreases in proportion to distances between stations. Though considering this tendency, it must be said that levitated systems need much more energy than conventional railway systems.

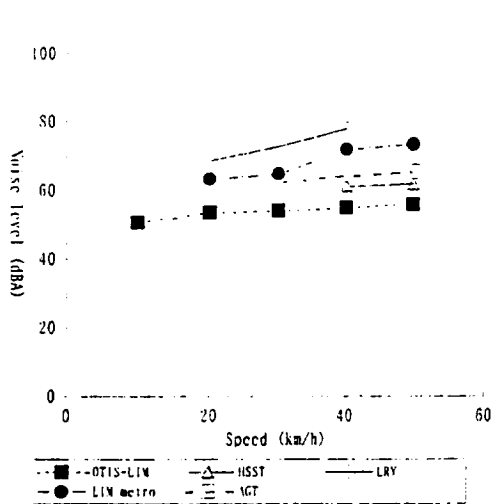


Fig.19 Noise characteristics outside vehicles

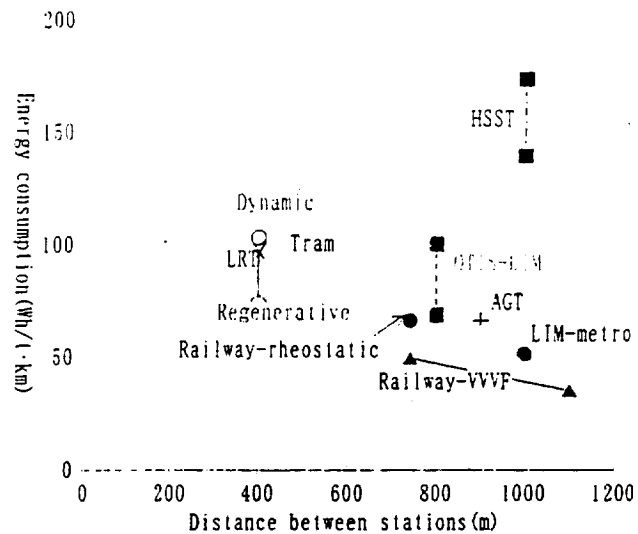


Fig.20 Energy consumptions of transportation systems

3.4 Synthetic evaluation

Above mentioned, levitated vehicles have several features in comparison with conventional railways . Some of these are merits and others are demerits. We must choose the proper transportationsystems by synthetic judgements. As one of the evaluation techniques, we propose new evaluation method using applied AHP (Analytic Hierarchy Process). Figure 21 shows the calculation example of this method. This example shows the traffic demand changes after introducing several systems instead of bus systems at present stage. According to this calculation, maglev system (HSST) has secured top priority to introduce.

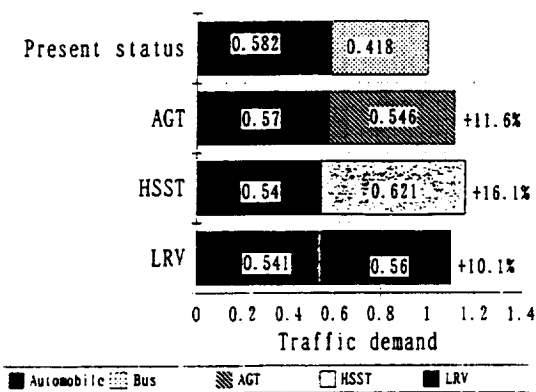


Fig.21 Example of results for evaluation transportation systems on traffic demand

4 . Scenario to be practical uses of maglev systems in Japan

Presently, no maglev systems have revenue services in Japan. But, linear motor driven systems that are the first step to realize levitation systems are in practical use in some districts in Japan. And several types

linear motors such as primary side on vehicle and ground are used. Namely, the foundation of practical use for maglev systems are arranged at this present stage. Receiving these trends, in the near future, the construction plan will be finally fixed to realize maglev system of HSST for urban transportation systems on Aichi prefecture. This construction plan was decided by committee through the above evaluation method. Moreover, environment assessments are starting for construction of HSST line from airport to railway station in Hiroshima districts. In Japan, for new urban transportation systems, it seems to proceed steadily in realizing practical use. At first, linear metro systems that have linear motors with wheel and rail are practical uses because of easy control of support and guidance. Secondly, aerodynamic systems such as OTIS that are supported by air and guided by wheels are realized because of easy levitation. And finally, perfect levitation systems that are supported and guided by magnetic suspensions will be introduced after many kinds of technical verifications step by step for public transports.

5. Conclusions

In Japan, maglev systems are developed for two purposes. One is for a **super high speed** and large capacity transportation system and the other is for urban transportation systems. For urban transportation systems it does not always follow that magnetically levitated vehicles are the only solutions. In Japan, to conquer the subjects of urban transportation problems and to turn public transportation systems from automobiles, magnetically levitated vehicles systems have been developing for the sake of low noise and low costs such as construction costs and maintenance costs. It was gradually successful to introduce new urban transportation systems in Japan. From automated people mover supported by rubber tires and guide wheels, thorough linear motor driven systems supported and guided by wheels and rails like conventional railways, supported only by aerodynamics and finally maglev systems are to have revenue service. According to these flows, it will be expected for high temperature superconducting magnets levitation systems to develop as urban transportation systems.

References

- 1) Yoshioka et al. 「 Results of running tests and characteristics of the dynamics of the MLX01 Yamanashi Maglev Test Line vehicles 」 The 15th international conference on magnetically levitated systems and linear drives April, 1998
- 2) Tanaka et al. 「 The results of running test of the HSST- 100L vehicle 」 The 15th international conference on magnetically levitated systems and linear drives April, 1998
- 3) Masada et al. 「 Linear drive technologies and its' applications 」 published by Ohm co. 1991
- 4) KIM, Peter 「 Otis hover transit system 」 The 15th international conference on magnetically levitated systems and linear drives April, 1998
- 5) Teraoka, S 「 Adoption of linear motor propulsion system for subway 」 The 15th international conference on magnetically levitated systems and linear drives April, 1998
- 6) Mizuma et al. 「 Several urban transportation systems 」 The journal of the institute of electrical engineers of Japan, Vol.119 No.3 March, 1999

linear motors such as primary side on vehicle and ground are used. Namely the foundation of practical use for maglev systems are arranged at this present stage. Receiving these trends, in the near future, the construction plan will be finally fixed to realize maglev system of HSST for urban transportation systems on Aichi prefecture. This construction plan was decided by committee through above this evaluation method. Moreover, environment assessments are starting for construction HSST line from airport to railway station on Hiroshima districts. In Japan, for new urban transportation systems it seems to proceed steadily in realizing practical use. At first, linear metro systems that have linear motors with wheel and rail are practical uses because of easy control of support and guidance. Secondly, aero dynamic systems such as OTIS that are supported by air and guided by wheels are realized because of easy levitation. And finally, perfect levitation systems that are supported and guided by magnetic suspensions will be introduced after many kinds of technical verifications step by step for public transports.

5. Conclusions

In Japan, maglev systems are developed for two purposes. One is for super high speed and large capacity transportation system and the other is for urban transportation systems. For urban transportation systems it does not always follow that magnetically levitated vehicles are only solutions. In Japan, to conquer the subjects of urban transportation problems and to turn public transportation systems from automobiles, magnetically levitated vehicles systems have been developing for the sake of low noise and low costs such as construction costs and maintenance costs. It was gradually successful to introduce new urban transportation systems in Japan. From automated people mover supported by rubber tires and guide wheels, thorough linear motor driven systems supported and guided by wheels and rails like conventional railways, supported only by aero dynamics and finally maglev systems are to have revenue service. According to these flows, it will be expected for high temperature superconducting magnets levitation systems to develop as urban transportation systems

References

- 1) Yoshioka et al. 「 Results of running tests and characteristics of the dynamics of the MLX01 Yamanashi Maglev Test Line vehicles 」 The 15th international conference on magnetically levitated systems and liner drives April,1998
- 2) Tanaka et al. 「 The results of running test of the HSST- 100L vehicle 」 The 15th international conference on magnetically levitated systems and liner drives April,1998
- 3) Masada et al. 「 Linear drive technologies and its' applications 」 published by Ohm co. 1991
- 4) KIM, Peter 「 Otis hovair transit system 」 The 15th international conference on magnetically levitated systems and liner drives April,1998
- 5) Teraoka ,S 「 Adoption of linear motor propulsion system for subway 」 The 15th international conference on magnetically levitated systems and liner drives April,1998
- 6) Mizuma et al. 「 Several urban transportation systems 」 The journal of the institute of electrical engineers of Japan, Vol.119 No.3 March, 1999

CONCRETE GUIDEWAYS FOR MAGLEV VEHICLES

Robert F. Mast
BERGER/ABAM Engineers Inc.
Federal Way, Washington

James S. Guarre
BERGER/ABAM Engineers Inc.
Federal Way, Washington

Michael W. LaNier
BERGER/ABAM Engineers Inc.
Federal Way, Washington

SUMMARY

This paper discusses parameters of concrete guideway beams for Maglev systems. Concrete beam parameters discussed include beam cross section, beam stiffness, vehicle/guideway dynamic interaction, constructed geometric accuracy of vehicle/guideway interface surfaces, maintaining geometric accuracy of vehicle/guideway interface surfaces, deflection stability, and choice of optimum span length. Two methods of providing and maintaining required geometric accuracy of vehicle/guideway interface surfaces are also discussed. One method uses good modern construction techniques; the other method reaches outside the box to develop an automated production facility through an extensive research and development effort. Typical costs are provided for concrete Maglev guideway beams. Potential cost savings are also presented to show the result of automating concrete beam production.

INTRODUCTION

Scope of Paper

Guideway beams for Maglev vehicles are a significant part of the Maglev transportation system. Guideway beams support vertical and lateral vehicle loads, guide the vehicles, and house the subsystems that operate the vehicle system. Furthermore, Maglev vehicle guideways are even more critical elements of the complete system than in other transportation systems since tolerance control and deflection control are system features provided by guideway structures. Maglev guideways are key components to a Maglev system since 50 to 70 percent of the cost of the system is attributed to the guideway. This paper will limit its discussion to dual-lane guideway beams for high-speed (> 300 kph) aerial Maglev guideways. "At-grade" guideways

In EDS, conductive coils are provided in the guideway levitation surface. Repulsive magnetic forces are produced when coils in the vehicle move past coils in the guideway. This force is generated as the vehicle moves relative to the guideway levitation surface, and when the speed of the vehicle reaches “take-off” speed, the force is sufficient to support the vehicle. Guidance is provided by lateral guidance rails similar to EMS. Propulsion is also often provided by LIMs or LSMs. Slide surfaces are provided to “land” the vehicle when approaching stations or when a failure in the magnetic levitation systems occurs. An important feature of guideways for an EDS is that guideway materials within a certain distance of the vehicle coils must have specific magnetic characteristics and/or be non-conducting to prevent interference with the system operation. A schematic diagram of a Maglev EDS is shown on Figure 2.

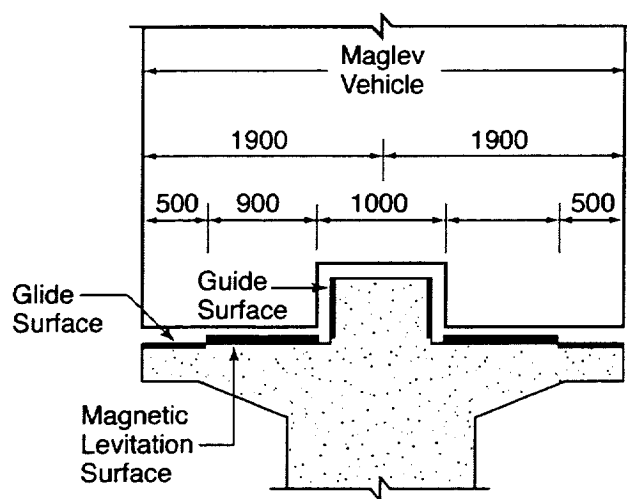


Figure 2. EDS vehicle/guideway interface.

Dimensions shown on Figures 1 and 2 are not intended to be representative of any particular Maglev vehicle system.

CONCRETE GUIDEWAY PARAMETERS

Beam Cross Section

Typical concrete guideway beam cross sections are shown on Figure 3. These beam cross sections are capable of supporting vehicle static and dynamic loads, and are also designed to house Maglev subsystems. Box beam cross sections are often used for aesthetic appeal and greater torsional strength. Open sections are less costly to produce using current methods. Also

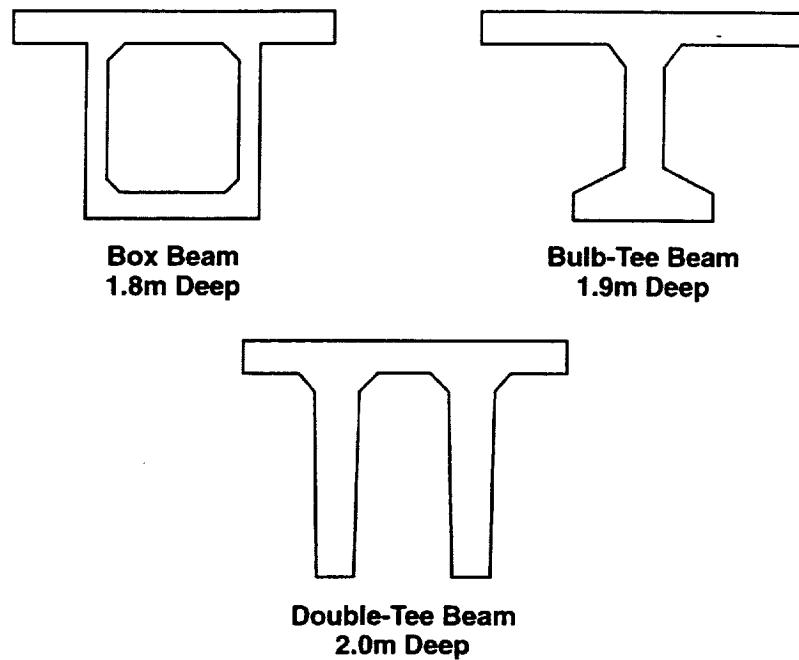


Figure 3. EMS guideway cross sections for 30m spans.

for open sections, intermediate span diaphragms, located at approximately the 1/4 points of the span, would be required to couple beams supporting each lane of the dual-lane guideway.

Guideway beams for Maglev systems will generally span from support to support. Longer span beams can be achieved using other methods, such as segmental construction techniques.

Construction Materials

Concrete guideway beams for EMS would use conventional concrete, reinforcing steel, and prestressing steel materials. As the use of composite materials in civil engineering facilities progresses, the use of composite materials in conjunction with concrete should be explored. The use and benefits of lightweight or semi-lightweight concrete should also be explored.

Concrete guideways for EDS would use non-magnetic and/or non-conductive materials for a distance of approximately 1 meter from the magnetic levitation surface. This is required to prevent interference with the operation of system. These materials can include nitronic stainless steel or carbon reinforcing elements. Conventional concrete, reinforcing steel, and prestressing steel would be used in the remainder of the guideway beam cross section. Similar materials have been used in magnetic silencing facilities for the U.S. Navy. Design and fabrication of this guideway beam will impose unique material selection challenges for vertical reinforcing components.

Beam Stiffness and Vehicle/Guideway Dynamic Interaction

Beam stiffness or deflection due to vehicle loads is important for efficient and comfortable operation of a Maglev system. In the vertical direction, this interaction is often controlled by limiting the vertical deflection generated by the Maglev Vehicle to 1/4000 of the span length.

Vehicle/guideway dynamic interaction is controlled by limiting the vertical deflection as discussed above or by separating the crossing frequency (CF in spans per second) of a span, vehicle velocity divided by span length, and the natural frequency of the guideway beam (SF). The basic structural frequency for a single span or for a series of equal multiple spans is expressed as

$$SF = \frac{\Pi}{2L^2} \sqrt{\frac{EI}{m}}$$

L = span length

E = dynamic modulus of elasticity

I = vertical moment of inertia

m = mass per unit length

Studies², for point vehicles, have shown that multiple-span structures reach maximum dynamic amplification at a CF/SF = 2 and also have shown that there is little or no dynamic amplification at CF/SF ratios less than 1.0. Single-span structures reach peak dynamic amplification at a CF/SF = 1.2 with significant dynamic amplification at CF/SF ratios from 0.6 to 3.0. See Figure 4. This would indicate that for the same beam bending stiffness, same span length, and same vehicle velocity, beams with 60 percent of the beam bending stiffness can be used with multiple span structures and still limit dynamic vehicle/guideway amplification to acceptable levels.

Lateral Deflections

Lateral deflections of guideway beams are also critical parameters. Lateral deflections are controlled primarily by the stiffness of supporting columns and foundations. Discussion of these guideway components is outside the scope of this paper.

Constructed Geometric Accuracy of Vehicle/Guideway Interface Surfaces

The constructed geometric accuracy of vehicle/guideway interface surfaces is critical to efficient, comfortable, and safe operation of Maglev Vehicles. These interface surfaces are shown on Figure 1 for EMS and on Figure 2 for EDS. Critical surfaces for EDS are the guideway

ferromagnetic rails, the horizontal guidance surfaces, and the gliding surfaces. The same interface surfaces, but arranged in a different pattern are critical for EDS.

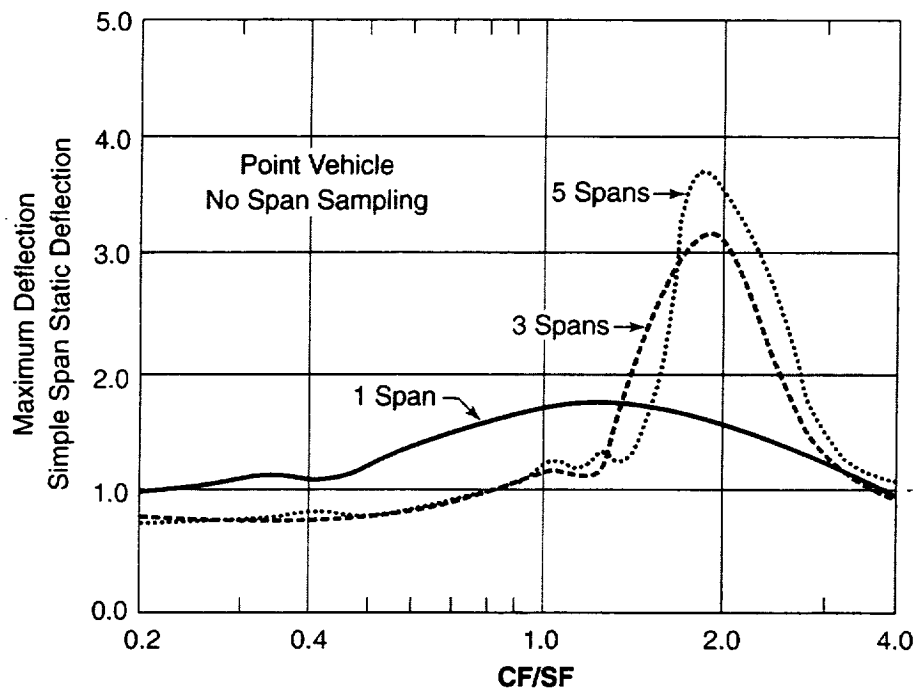


Figure 4. Dynamic to static deflection ratio vs. CF/SF ratio (from Reference 2)

There are fundamentally two basic approaches to providing and maintaining adequate interface tolerances.

Method 1

Manufacture concrete beams with conventional “industry standard” interface tolerance surfaces and mechanically attach horizontal guide surfaces, levitation/propulsion surfaces, and gliding surfaces. These interface surfaces have sometimes been packaged into pre-assembled modular units to minimize the amount of field assembly required. Generally, these surfaces are secured to guideway beams through mechanical fasteners. See Figure 5.

Some discussion of “industry standard” interface tolerances is warranted. Concrete beams must be produced to accurate horizontal curvature, vertical profile, and superelevation so that Maglev modules can be economically attached to these beams. Special adjustable forms would be used to fabricate these beams. These type of forms have been used on past transit projects to fabricate complex geometry guideway beams^{3,4,5}.

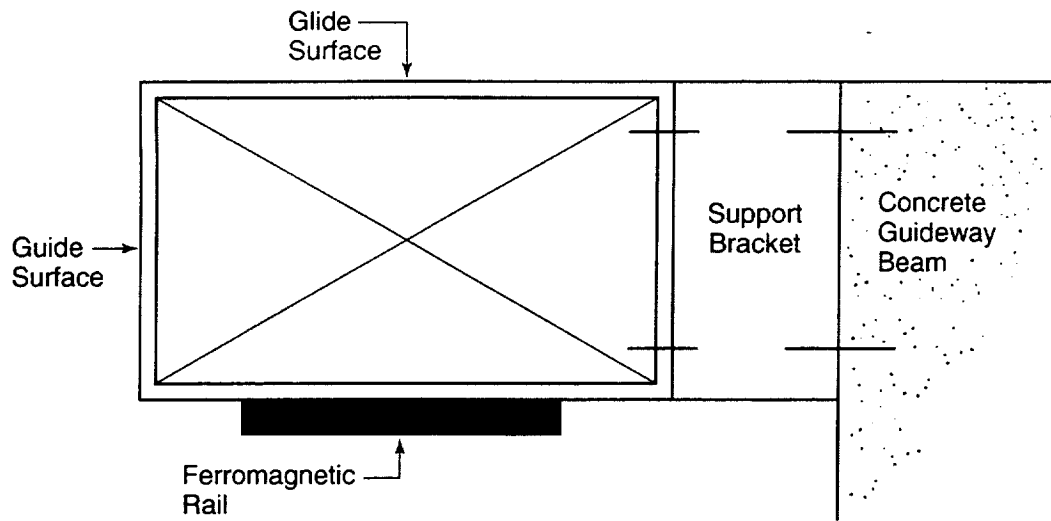


Figure 5. Modular Maglev Subsystem Assembly

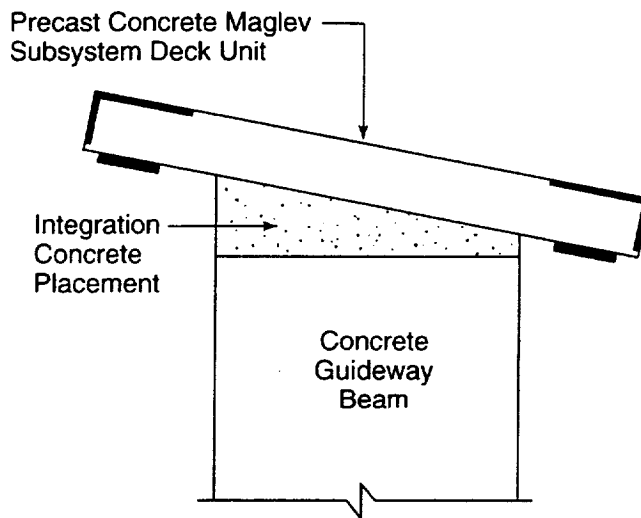


Figure 6. Use of precast concrete maglev subsystem deck unit.

A variation on this method is shown in Figure 6. The beam cross section is made up of bulb-tee, double-tee, or box beams supporting precast subsystem deck units. Precast deck slab units are fabricated to the true horizontal alignment, vertical profile, and superelevation of the spatial geometry. Special adjustable forms will be used for production of these deck units. Lengths of subsystem deck units will be multiples of ferromagnetic rail lengths and LIM secondary rail modules. Precast subsystem deck units are integrated with beams through cast-in-place closure pours. Precast concrete beams are cast as straight components. These beams chord across

horizontal curves. Superelevation is provided by varying the height of the integration concrete placement between the concrete girder and precast subsystem slab units.

Method 1, or variations thereof, have been used to construct most of the Maglev guideways to date. This method is used since it is an extrapolation of good modern construction practices.

Method 2

Manufacture concrete beams with accurate “custom tolerance” interface tolerance surfaces. Horizontal guide surfaces and/or assemblies, levitation/propulsion surfaces and modules, and glide surfaces are built into concrete beams at the beam production facility. This method would use computer-controlled machines that could configure a mold to a wide range of lengths, horizontal and vertical curvatures, and superelevations. The beam manufacturing process would be automated so that reinforcing steel, prestressing steel, and Maglev assemblies would be placed very accurately and reliably.

Developing such a process would take a substantial research and development (R&D) effort. This effort would entail marrying technologies of automated production of precast elements with precision surface production technology from the machine industry and could involve a National Aeronautics and Space Administration (NASA) scale R&D effort. This method could be a combination of concepts shown on Figures 5 and 6. However, the economics of Maglev systems and guideways warrant an investment of this scale. Possible economics and potential cost benefits of this method will be discussed in a subsequent section of this paper.

Maintaining Geometric Accuracy of Vehicle/Guideway Interface Surfaces

Maintenance of these critical interface tolerances is as important as initially providing them, since maintainability is an important consideration for a system that will have many hundreds of kilometers. Guideways should be designed to provide ways to continually maintain these interface tolerances.

Using Method 1 described above, maintenance of interface tolerances is achieved through continually monitoring and adjusting attachment fasteners. This relatively simple means of maintaining tolerances may also pose the biggest disadvantage to this method; that is attachments that can be adjusted to maintain tolerances can also get out of adjustment to allow deterioration of tolerances.

Maintaining tolerances using Method 2 would require a special machine that grinds interface surfaces to required tolerances. The machine could index off guideway global geometry measurements and levitation/propulsion surfaces, and grind horizontal guide surfaces and gliding

surfaces to achieve smoothness and relative dimensional tolerances to fractions of centimeters as required.

Maintenance of tolerances using either method, for Maglev systems of several hundred km in length, would require machines or a train of machines similar to maintenance equipment that is used by railroads to measure track alignment and profile, realign rails, retamp ballast, replace ties, etc. Maintenance equipment of this scale will be needed to make Maglev systems feasible, comfortable, and safe.

Deflection Stability

Deflection stability of critical Maglev interface surfaces (therefore of supporting concrete beams) is also a **key parameter**. Concrete guideways for aerial structures will be constructed using prestressed concrete beam elements. Generally, these beams will also be precast under factory controlled conditions. In addition to providing the manufacturing environment necessary for close tolerance fabrications, factory precasting beams that are components of long repetitive type structures is an economical approach to guideway construction. Prestressed concrete guideways utilize steel prestressing strands that are stressed to high prestress forces to counteract applied loads. However, prestressing forces shorten guideway concrete beams and also usually generate upward vertical deflections in these beams. Concrete, being an elastic-plastic material, also undergoes long-term deflections associated with these prestress forces due to concrete creep. Differential (varies throughout the guideway beam cross section) concrete shrinkage strains can also cause guideway vertical deflections. **All of these considerations must be addressed in a successful Maglev guideway design.**

Multiple-span guideway structures are better suited to maintaining deflection stability than single-span guideway structures. Strain effects, in multiple span guideways, are resisted by combinations of deflections and internal forces. Strain effects in single-span guideways primarily result in deflection while minimizing internal forces. Past efforts in dealing with deflection stability have considered continuous concrete guideways that are similar in principal to continuously welded rails for rail transportation systems. Guideways would be continuous between guideway anchor structures. These anchor structures would be capable to resisting the continuous guideway thermal force. Similar to thermal forces generated in continuously welded rails, this force would equal

$$= A_c E_c \alpha_c \Delta T$$

A_c = Area of concrete cross section

E_c = Elastic modulus of concrete

α_c = Thermal coefficient of concrete

ΔT = Temperature rise or temperature fall

Consideration has been given to use semi-lightweight concrete to reduce E_c and to reduce the thermal coefficient of concrete.

Typical dual-lane guideway beams would generate dual-lane guideway anchor forces equal to approximately 25,000 kN. Anchor structures would be provided every 2 to 3 km.

Optimum Guideway Span length

Selecting the optimum “system” guideway span length depends on many factors. The span length for guideway beams is an important parameter in limiting the live load deflection of the guideway beam. Live load deflection is

$$\Delta_{LL} = k W_{LL} \ell^4 / E_{dyn} I$$

If this deflection is less than 1/4000 of ℓ , then

$$\ell \leq (E_{dyn} I / 4000 W_{LL} k)^{\frac{1}{3}}$$

ℓ = Span length

k = deflection constant

E_{dyn} = Dynamic modulus of elasticity

I = Vertical moment of inertia

W_{LL} - Equivalent uniform vehicle load (vehicle + passengers)

The constant k depends on the structural configuration of the guideway. This constant can be reduced if the guideway beam is partially fixed at one or both ends. The modulus of elasticity is related to the square root of the compressive strength of the concrete. The dynamic modulus of elasticity is approximately 25 percent greater than the static modulus of elasticity computed in accordance with conventional formulae for determining this parameter. The vertical moment of inertia of the guideway beam is related to the cross section configuration and to the depth of the cross section. Increasing cross-section depth is the most effective way to increase this value. The equivalent uniform vehicle live load depends upon the weight and length of the Maglev Vehicle.

The optimum span length depends upon relative costs between guideway beams and guideway crossheads, columns, and foundations. The optimum span also depends upon the guideway configuration and upon limiting transport and erection weights of precast concrete beam components. This is especially important for guideway beams that are single elements spanning from support to support.

For purposes of this paper, a “system” span length of 30 m was selected. This typical span length has worked well on past projects and is at the upper end for conventional transport and erection weight and is long enough to span typical obstacles.

CONCRETE BEAM COSTS AND ECONOMICS

Past studies⁶ and projects⁵ provide the basis for the following discussion. This discussion will focus on the costs and cost savings potential of developing special Maglev guideway concrete beams. Total Maglev project costs include many other items. These items include guideway beam transport, guideway beam erection, guideway foundations, columns and crossheads, Maglev assemblies, Maglev vehicles, passenger stations, maintenance facilities, switches, power distribution facilities, right-of-way, right-of-way improvements, program management, engineering, and construction management.

The manufactured cost of 30-m concrete guideway beams using Method 1, FOB manufacturing facility, cost approximately \$50,000. The unit guideway beam cost per meter of dual-lane guideway would cost

$$= 2 * \$50,000 / 30.0 \text{ m} = \$3,333 \text{ per dual-lane meter}$$

At this unit cost, the total guideway beam cost for a 500-km long Maglev system equals \$1.67 billion.

The above manufacturing cost of guideway beams is broken out as follows.

Materials	\$ 24,000
Production Labor	12,000
Contingencies	3,600
Plant Overhead	5,400
General Overhead and Profit	<u>5,000</u>
Total	\$ 50,000

If guideway beams were produced in automated manufacturing facilities (Method 2), reasonable cost reduction targets are as follows.

Materials	\$ 22,000 - Size discount
Production Labor	3,000 - Production labor reduction
Contingencies	1,200 - Production risk reduction
Plant Overhead	3,000 - Prorated from above
General Overhead & Profit	<u>2,800 - Prorated from above</u>
Total	\$ 32,000

This reduced cost for guideway beams would result in a \$600 million savings in guideway beams alone for a 500-km-long Maglev system. This savings is an indication of the R&D investment that would be available to develop specialized production facilities and machines to manufacture concrete Maglev guideway beams and achieve the objectives of the Method 2 approach.

This research and development effort could be undertaken by a consortium of companies each bringing special skills and knowledge to the endeavor. Centralized fabrication facilities could be located in regions throughout the country, or alternatively the specialized machines could be transported to facilities close to project sites.

CONCLUSION

Concrete guideway beams offer several advantages for Maglev systems. Concrete guideways are inherently stiff and have a high unit mass. These features cost-effectively reduce loads resulting from vehicle/guideway dynamic interaction. Concrete guideway beams will last for many years with very little maintenance. Incorporation of composite reinforcing materials into concrete guideway beams will further enhance this benefit. Concrete Maglev guideway beams also offer good possibilities to capture the benefits resulting from being manufactured in automated factories. Significant cost savings could accrue to Maglev systems making them a more economical mode of transportation in the 21st century.

REFERENCES

1. Cai, Y. and Chen, S.S., "Dynamic Characteristics of Magnetically Levitated Vehicle Systems", reprinted from 1997 American Society of Mechanical Engineers, ASME Reprint No AMR 225, Applied Mechanics Rev Volume 50, No. 11, part 1, November 1997.
2. American Iron and Steel Institute, "Steel Structures for Mass Transit," approximately 1975.
3. Mast, R.F. and Dolan, C.W., "Walt Disney World Monorail Designed for Smooth Riding," ASCE Civil Engineering Magazine, March 1972.
4. Josten, M.G., Painter, W.L., Jr. and Guarre, J.S., "Precast Prestressed Concrete Structure Provides Solution of Getty Center Tram Guideway," PCI Journal, May-June 1995.
5. Lowe, P., "Manufacture and Installation of Prestressed Concrete Guideway Beams for the Vancouver ALRT," American Concrete Institute, SP 93-19, 1986.
6. ABAM Engineers Inc., "ICTS Development Program – Summary Report," prepared for Metro Canada Limited, 15 April 1981.

Session 13 -- Applications 2

Chairman: Paul E. Allaire
University of Virginia (UVA)

SIMULATION OF WIND TUNNEL FORCES USING MAGNETIC SUSPENSION TECHNOLOGY

R.Ralph Sinno

Department of Civil Engineering
Mississippi State University

Thomas Price

Bert Nail

Department of Electrical and Computer Engineering
Mississippi State University
Mississippi State, MS 39762

Jason Melton

SUMMARY

Forces experienced by metal roofs under high wind conditions vary as a function of both time and space. Modeling a roof structure subdivided into segments or nodes accommodates spatial variation, for which magnetic suspended actuators are made to generate time-tailored forces equivalent to the wind-induced forces. In this study, each node consists of an induced electromagnetic actuator, an electronic control board, and a load cell for verification of the force produced. Short duration wind gust and the effect of such impulsive loading on a metal roof panel and the overall structural system are poorly incorporated in the present state-of-the-art in structural analysis and design. A full-scale testing facility for metal building roof components, now in operation at Mississippi State University, provides realistic forces that approximate those produced by high velocity winds from wind tunnel models.

INTRODUCTION

High velocity wind on relatively flat roofs of low-rise buildings exerts uplift pressures that are potentially destructive and hazardous to human life. Tests performed in wind tunnels on small modules, 1/50 scale, confirm the dynamic nonuniformity of hurricane wind loadings. Although wind loading is known to be nonuniform and unsteady, uniform static loading is the only currently available method of simulating high velocity wind loading for engineering analysis, design and research.

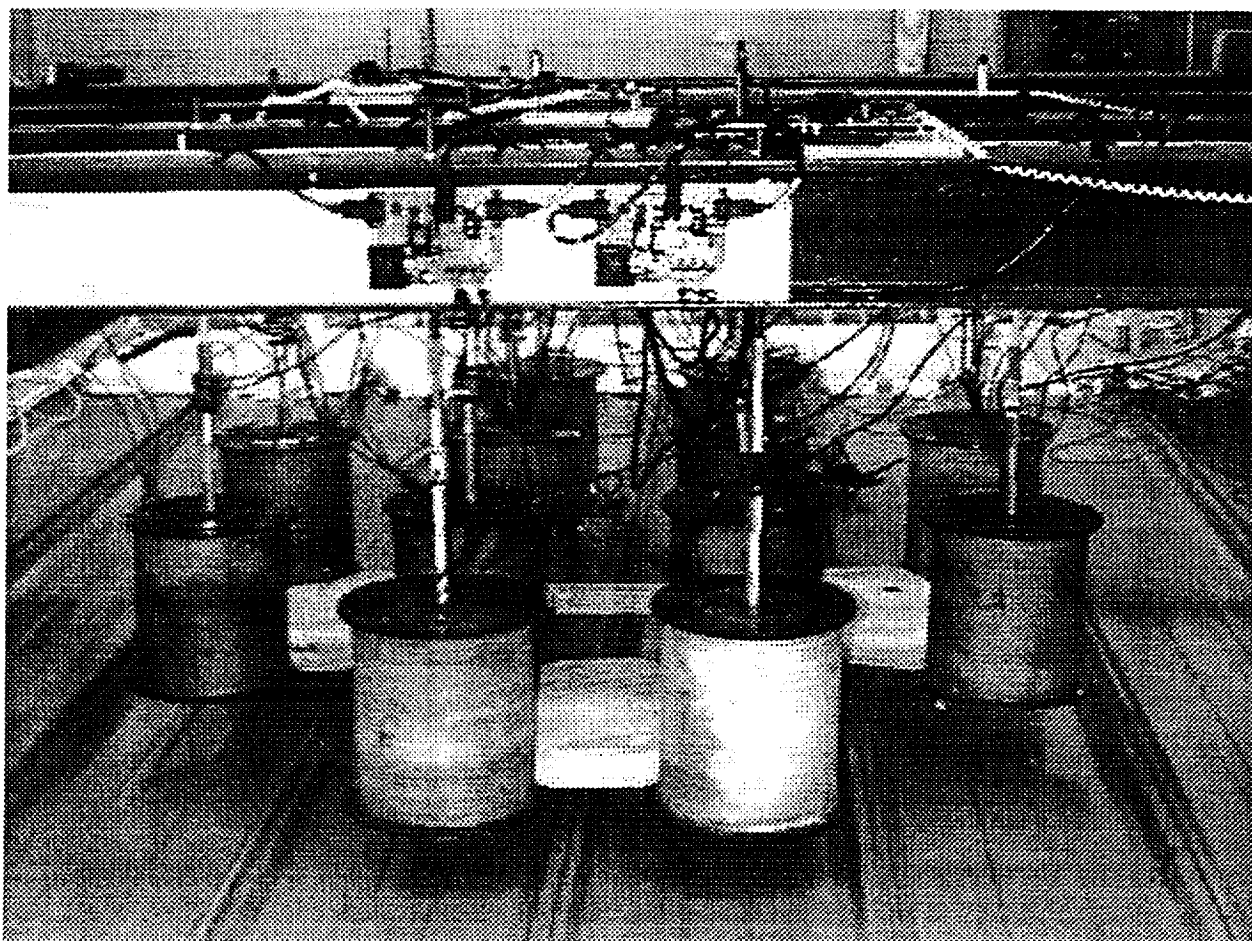


Figure 1. Wind Simulation Test Setup.

Metal building construction is presently the fastest growing segment in the low rise building construction industry. The primary lateral and dynamic loading on these buildings is caused by high velocity wind. The present design procedure of using the uniform uplift forces on metal roofs is highly questionable, and unrealistic from an engineering point of view. Analyzing and designing metal buildings for the true spectrum of dynamic, spatially variable wind loading, as recorded from wind tunnel testing programs, represents a significant advance in the state of knowledge in the metal building industry. The ongoing research at Mississippi State to establish a testing program that utilizes the true wind loadings is expected to open new and exciting options in innovations, analysis and design.

In this research, nonuniform dynamic forces are produced using induced intensive electromagnetic fields. An individually controlled, magnetized grid of nodal points is electronically monitored and controlled to produce dynamic electromagnetic suction forces (Figure 1). The induced electromagnetic forces are then adjusted to any given or randomly generated suite of nonuniform dynamic wind loading. Extensive research on the efficacy and optimization of the induced electromagnetic forces in the grid system has been investigated. Significant technical challenges have been overcome to generate the needed pressure intensity within the time and space criteria imposed by the physics of the underlying problem. The test set-up being developed will be used at a later date

to investigate the failure modes and cause of failure of light gauge metal roofs, and to develop simplified analysis and design procedures to be used by the metal building industry.

BACKGROUND

The effects of wind loading have taken an increasingly important role in the design of metal buildings. The goal is to better prevent loss of life and to lessen property losses. Hurricanes Hugo (1989), Iniki (1992) and Andrew (1992), which struck Puerto Rico and South Carolina; Hawaii; and Southern Florida respectively, demonstrated the importance of considering wind loads in the design and construction of typical metal buildings. Some of the current research areas are probabilistic assessment of wind speeds, translation of wind speeds into loads through wind tunnel testing, validation of this translation through full-scale testing, and documentation of damage and economic assessment of construction techniques. The aim of this type of research is to allow increased testing of building response to this type of load, and to improve the safety and efficiency of building designs [1].

The research presented here involves full-scale testing. Wind load forces generated from wind tunnel testing by the University of Western Ontario [2] are recreated on a full-scale model. A roof testing system based on magnetic actuators and embedded processors has been developed, and is currently operational in a multi-magnet configuration. The system is generating realistic forces such as those experienced by a metal roof structure under high wind velocity conditions. The techniques for controlling the nodes and measuring the results are described herein. The process that is used to calibrate magnetically generated forces and wind tunnel data is especially interesting and is described in some detail. The results for the single magnet configuration are shown and the expansion of the process to account for multiple magnets is presented.

TEST APPARATUS

Forces experienced by a metal roof under high wind conditions vary widely, both as a function of time, and as a function of position. Subdividing a roof structure into segments or nodes (See Figure 1) accommodates positional variation, for which actuators generate time-tailored forces equivalent to the forces of nature. Each node consists of the actuator, an electronic control board for the electromagnet, and a load cell for verification of the force produced. This is shown in Figure 2.

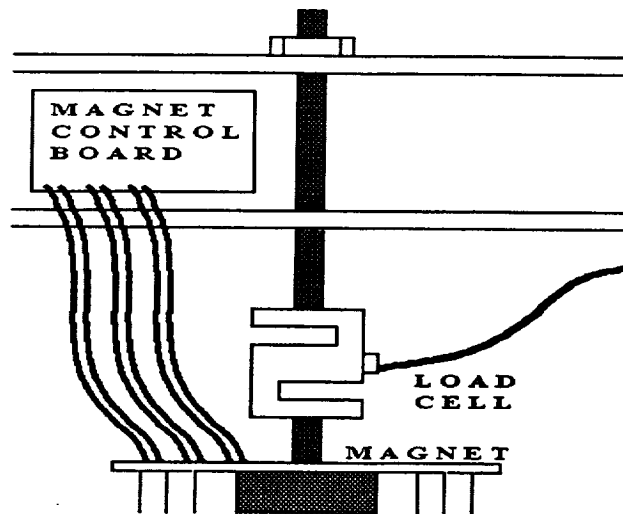


Figure 2. Elements of a Node.

The most noticeable part of each node is the actuator – an electromagnet, which consists of three coils to be powered selectively from a three-phase 208-volt source (Figures 1 and 2). This is also most interesting from a control perspective, since it embodies strong elements of nonlinearly, and cross coupling between neighboring nodes. The electromagnets are approximately 11 inches in diameter and 13 inches high, weigh about 270 pounds, and can exert forces in excess of 300 pounds on a thin sheet of metal at a distance of 1 inch. This does not sound impressive until compared to a commercial lift magnet tested to 14,000 pounds – that magnet only achieved a force of about 30 pounds on a thin sheet at the same distance. Any combination of the three magnet coils can be energized to provide a wide variation of force, with peak power near 4 KW. The control of these closely coupled magnets, highly nonlinear with gap distance, to achieve forces matching the wind tunnel data, is the thrust of this paper.

The completed system is to have 36 nodes, which must be closely synchronized and centrally commanded. Zero crossing detectors on each electronics board are connected to one phase of the AC power, thus establishing 120 Hz pulses as a time base. Each control board groups the time base into frames of 6 pulses, which matches the 20 Hz wind tunnel sampling time.

Simple commands (start, stop, ...) are daisy-chained through optoisolators on each magnet control board as current signals to diminish noise. Phone cables are used for command signal interconnection between nodes for reconfiguration ease. Commands from the central controller are first daisy-chained through beam controller boards, and they relay the information in another daisy chain to the magnet control boards. All units operate from the same time base for synchronization, and any problem in connection is easily noticeable since an entire daisy-chained group will fail. The daisy chain arrangement is shown in Figure 3.

On each magnet control board is a Microchip PIC16F84 8-bit microcontroller, a Microchip 24AA65 I²C serial eeprom (8k x 8), three Crydom solid state relays and a Harris CA3059 zero-voltage switch used to create the 120 pulses per second time frame. The forces for each 1/20th frame are stored in the serial eeprom, which has an identical pin-out for a wide range of memory sizes, for

easy memory upgrade. The solid-state relays allow selected activation of the three-phase magnet windings. The PIC16F84 is the brains of the board, responsible for deciphering commands, retrieving the drive data for the next frame and turning on the appropriate magnet coils.

SINGLE NODE CONTROL

The first step in the control process is to create a method for matching the force from a single node to the wind tunnel forces. After the solution for one node is found, it can be extended to include multiple nodes.

This process is accomplished in 3 steps. In the first step, the desired force time history is converted to driving voltages for the electromagnet, specifying what coils are driven on and for what duration. A test run of the apparatus is then run, generating three arrays of data, the desired force from wind tunnel data (W), measured magnet force response (R), and actual commanded force (A). The results of this step are shown in Figure 4.

Step 2 involves two calculations, to determine the relationships between 1) R and A, and 2) W and A.

First, the magnet force is written as a function of the command voltage, its time derivative, and its integral

$$R = f \left(A, \dot{A}, \int A dt \right)$$

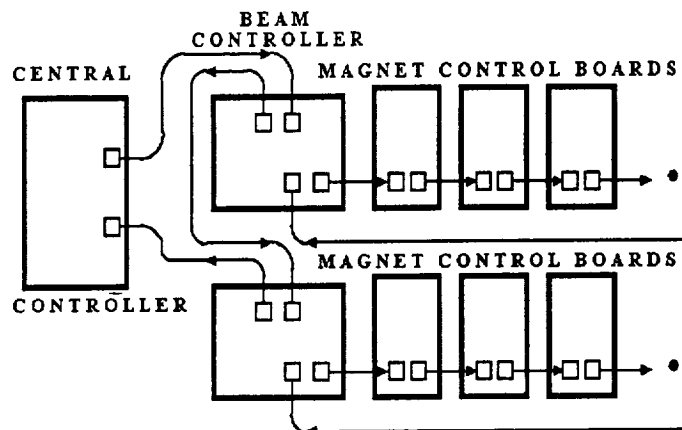


Figure 3 Schematic View of the Command Structure.

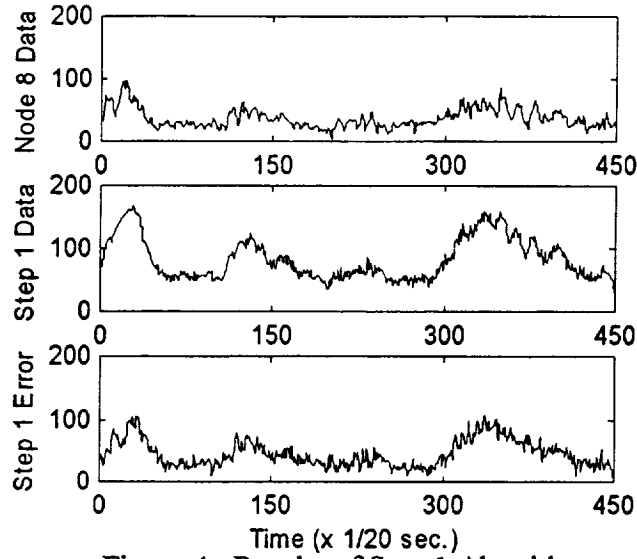


Figure 4. Results of Step 1 Algorithm

At time t_k we posit a relationship between magnet force and command voltage that can be written as a linear time-domain convolution

$$R_k = aA_k + bA_{k-1} + cA_{k-2} + \varphi$$

We can calculate optimal values of the constants a , b , c , ... by minimizing a performance measure J given by

$$J = \sum (aA_k + bA_{k-1} + cA_{k-2} + \varphi - R_k)^2$$

This implies

$$\frac{\partial J}{\partial a} = \frac{\partial J}{\partial b} = \varphi = 0$$

The derivatives of J are evaluated at each time in the time history, providing an overdetermined set of equations for the constants, which is solved using a least squares technique.

The second calculation in step 2 is used to enforce the requirement that $R = W$ at all times t_i in the time history. We define a matrix M as

$$M = \begin{bmatrix} a & b & c & d & e & \varphi \\ 0 & a & b & c & d & \varphi \\ 0 & 0 & a & b & c & \varphi \\ 0 & 0 & 0 & a & b & \varphi \\ \varnothing & \varnothing & \varnothing & \varnothing & \varnothing & \varphi \\ 0 & 0 & 0 & 0 & 0 & a \end{bmatrix}$$

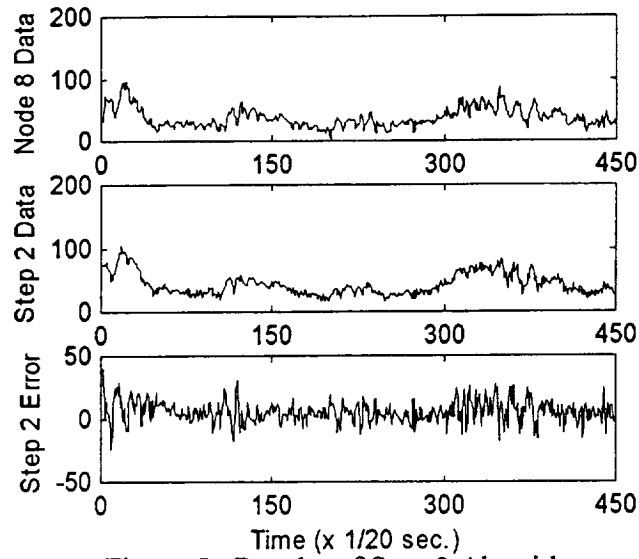


Figure 5. Results of Step 2 Algorithm

and define Wr as the row reversal of W_i , and likewise Ar as the row reversal of A_i . Solving the following equation

$$Ar = M^{-1}Wr$$

yields Ar . If Ar is then row reversed, the drive data for the magnet is obtained. Finally, a modified set of constants a , b , c , ... is computed as described above, and another cycle of the testing apparatus is performed. The results of the second calibration step are shown in Figure 5.

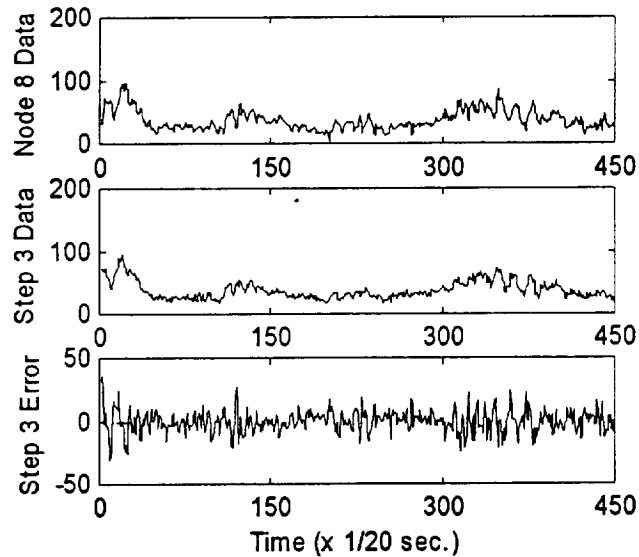


Figure 6. Results of Step 3 Algorithm

In the third and final calibration step, the peaks of the wind tunnel data are achieved. Another algorithm searches through the wind tunnel force data for significant changes between two adjacent samples. It then backs up no more than 20 points and increases their values to account for the magnet rise time. Once this step is completed, the algorithm in the first step is run again and a final cycle of the test apparatus is performed. The results of step 3 are shown in Figure 6.

MULTI-NODE CONTROL

The multi-magnet approach is similar to the single magnet approach, except that additional terms are added to account for the effects of the adjacent magnets. The procedure for four magnets is reflected in the equations:

$$R1 = f\left(A1, \dot{A1}, \int A1dt, W2, W3, W4\right)$$

$$R1_x = aA1_x + bA1_{x-1} + cA1_{x-2} + \phi + rW2_x + sW3_x + tW4_x$$

$$J = \sum (aA1_x + bA1_{x-1} + cA1_{x-2} + \phi - R1_x)^2$$

$$C = \begin{bmatrix} A1_1 & 0 & 0 & \phi & W2_1 & W3_1 & W4_1 \\ A1_2 & A1_1 & 0 & \phi & W2_2 & W3_2 & W4_2 \\ A1_3 & A1_2 & A1_1 & \phi & W2_3 & W3_3 & W4_3 \\ \text{⋮} & \text{⋮} & \text{⋮} & \phi & \text{⋮} & \text{⋮} & \text{⋮} \\ A1_n & A1_{n-1} & A1_{n-2} & \phi & W2_n & W3_n & W4_n \end{bmatrix}$$

$$\begin{bmatrix} a \\ b \\ c \\ \phi \\ r \\ s \\ t \end{bmatrix} = (C^T C)^{-1} C^T R1$$

$$R1_x = W1_x$$

$$M = \begin{bmatrix} a & b & c & d & e & & r & s & t \\ 0 & a & b & c & d & & 0 & r & s \\ 0 & 0 & a & b & c & & 0 & 0 & t \\ 0 & 0 & 0 & a & b & & 0 & 0 & 0 \\ 0 & 0 & 0 & 0 & a & & 0 & 0 & 0 \\ & & & & & \ddots & & & \\ & & & & & & & & \ddots \end{bmatrix}$$

$$A/r = M^{-1}(W1r - rW2r - sW3r - tW4r)$$

Finally, the drive data for A/r magnet is obtained by row reversing A/r .

Figure 7 shows a comparison of the force induced in one magnet in the actuator array, and the target wind tunnel force time history. The degree of reproduction is considered to be outstanding for practical purposes of testing a full-scale metal roof.

CONCLUSION

The force exerted by an electromagnet on a thin metal roofing material is highly nonlinear with gap distance, and adjacent magnet nodes exhibit significant cross coupling. Full-scale metal roof tests require force profiles to match wind tunnel results, with all nodes synchronized to account for the spatial effects of high velocity winds. The approach described has proven capable of achieving the desired functions both temporally and spatially.

The techniques for adapting the actuator drive to accommodate the nonlinearity of gap distance and the influence of neighboring actuators are extremely effective and the mathematics are widely applicable to similar control problems involving coupling and nonlinearity. The actuators are possibly applicable to specialized applications such as dynamic loading, fatigue testing, etc.

One limitation of the technique is the offline processing required. Although it is conceivable that this could be done in real-time, it was unnecessary for this application since the target trajectory was known from the outset.

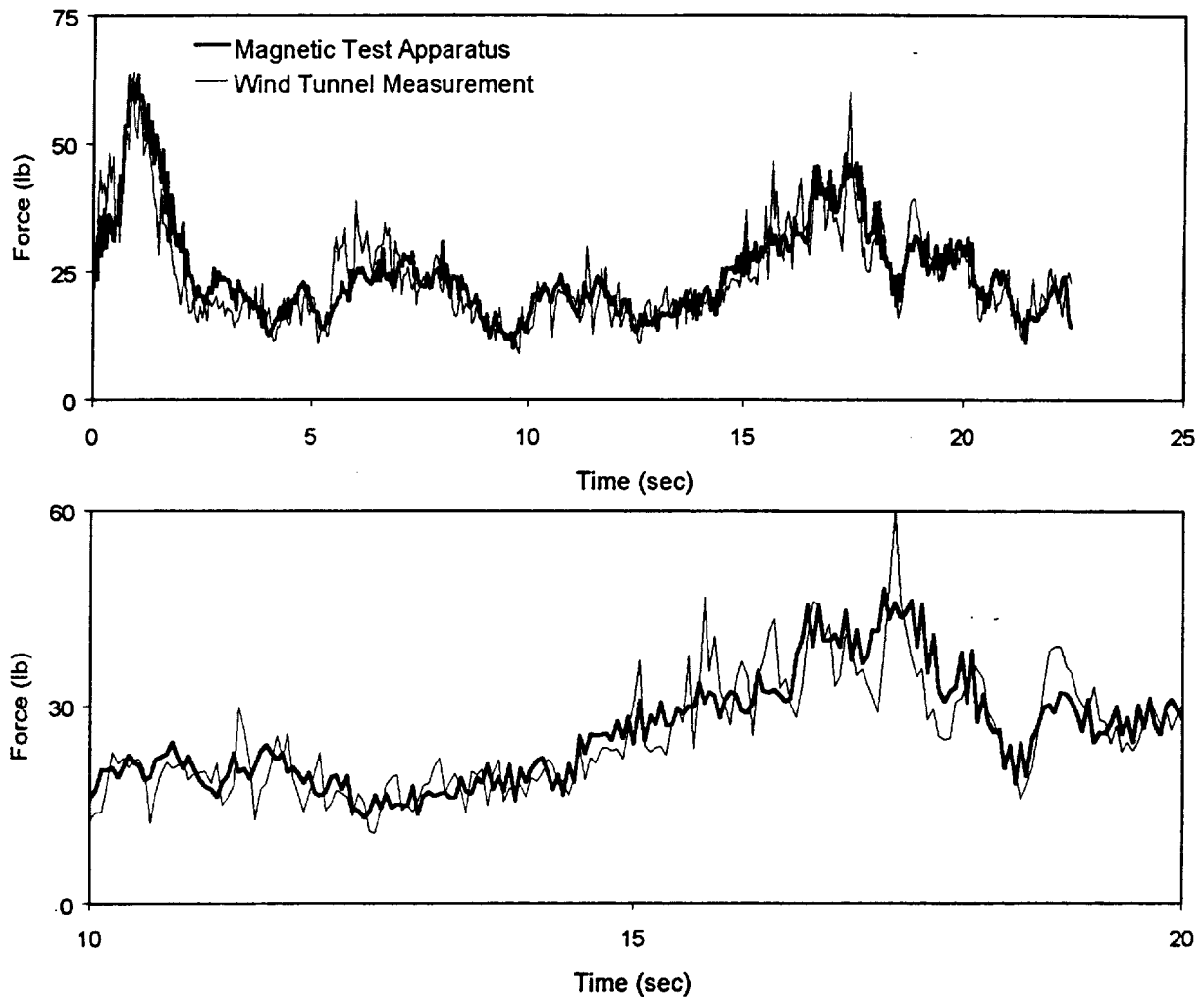


Figure 7. Comparison of Roof Forces Induced in Wind Tunnel and by Magnetic Test Apparatus

ACKNOWLEDGEMENTS

The authors thank the Metal Building Manufacturers Association (MBMA), American Iron and Steel Institute (AISI) and the Metal Constructors Association (MCA) for providing the funding for this research. They also thank Tim Stults for his work on the electronics and structure; Robert Lewis for his work with the load cells; and Mark Maupin for his work on the structure.

REFERENCES

- [1] K.C. Mehta and R. D. Marshall, *Guide to the Use of Wind Load Provisions of ASCE 7-95*, (Virginia: the American Society of Civil Engineers, 1998).
- [2] D. Surry, T. C. E. Ho, and G. R. Lythe, Simulation Requirements for Roof Wind Loads Near the Corners of Low Buildings with Low-Slope Roofs, ASCE Structures Congress '99, New Orleans, LA, April 19-22, 1999.

HIGH-Tc SUPERCONDUCTING ACCELEROMETER

Shigeharu Enkyo* and Atushi Nakajima**

*Flight Systems Research Center, National Aerospace Laboratory

Tel:+81-422-40-3363, Fax:+81-422-40-5314, E-mail:enkyo@nal.go.jp

**Space Project Research Center, National Aerospace Laboratory

Tel:+81-422-40-3715, Fax:+81-422-40-3149, E-mail:nakajima@nal.go.jp

7-44-1 Jindaiji-higashi-machi, Chofu-shi, Tokyo 182-8522, Japan

Abstract

Ultra-high resolution accelerometer is required in completing the high precision airplane inertial navigation system employing a gravity gradiometer which compensates the geodetic induced error and is also required in micro-g environment in space. The resolution of the conventional accelerometer is limited in the order of $10^{-6}g_E$. On the contrary, superconducting accelerometer has the potential of $10^{-12}g_E$. In National Aerospace Laboratory (NAL), a principle model of a high-Tc superconducting accelerometer operated at the liquid nitrogen temperature (77K) was designed, manufactured and evaluated and some of the characteristics are described in this paper.

1. Introduction

Ultra-high resolution accelerometers are required in the field of aerospace for detecting micro-g environment. An accelerometer consists of a proof mass and elastic coils. Superconducting accelerometer also has the same construction. Paik[1] has developed superconducting accelerometers and pointed out that the potential sensitivity is estimated with an order of $10^{-12}g_E/\text{Hz}^{1/2}$ (where $g_E=9.8\text{ms}^{-2}$ Earth gravity) under 50Hz frequency range and Hoffman[2] has proposed superconducting fluxgradient accelerometer whose sensitivity is expected to be $9 \times 10^{-20}(\Delta f)^{-1/2}\text{m}$, where Δf is the bandwidth of the amplifier. The sensitivity capability is almost the same as that of Paik.

A principle model of a high-Tc superconducting accelerometer operated at the liquid nitrogen temperature(77K) is developed and preliminary results are obtained.

2. Experimental Model

NAL has studied a high-Tc superconducting accelerometer for aerospace application. Fig.1 shows the constitution of the trial manufactured superconducting accelerometer. They are permanent magnet(instead of superconducting coil for easy construction) for magnetic flux supply, superconducting proof mass(inertia mass) which is fixed to the inertial frame, SQUID(Super-conducting Quantum Interference Device) magnetometer for detecting the magnetic flux variation and superconducting magnetic shield vessel. The material of this superconductor is YBCO($\text{YBa}_2\text{Cu}_3\text{O}_{7-y}$) with 92K critical temperature. Proof mass and permanent magnet are arranged and cooled in a liquid

nitrogen filled vessel which shields the external magnetic fluxes. If an acceleration(Δg) acts on this accelerometer, the distance(x) between the proof mass supported with a hinge and permanent magnet is deviated from its normal position with a small distance(Δx), which causes a small flux change($\Delta \phi$) induced by the permanent magnet. $\Delta \phi$ is detected by the SQUID magnetometer and converted to the output voltage(Δv).

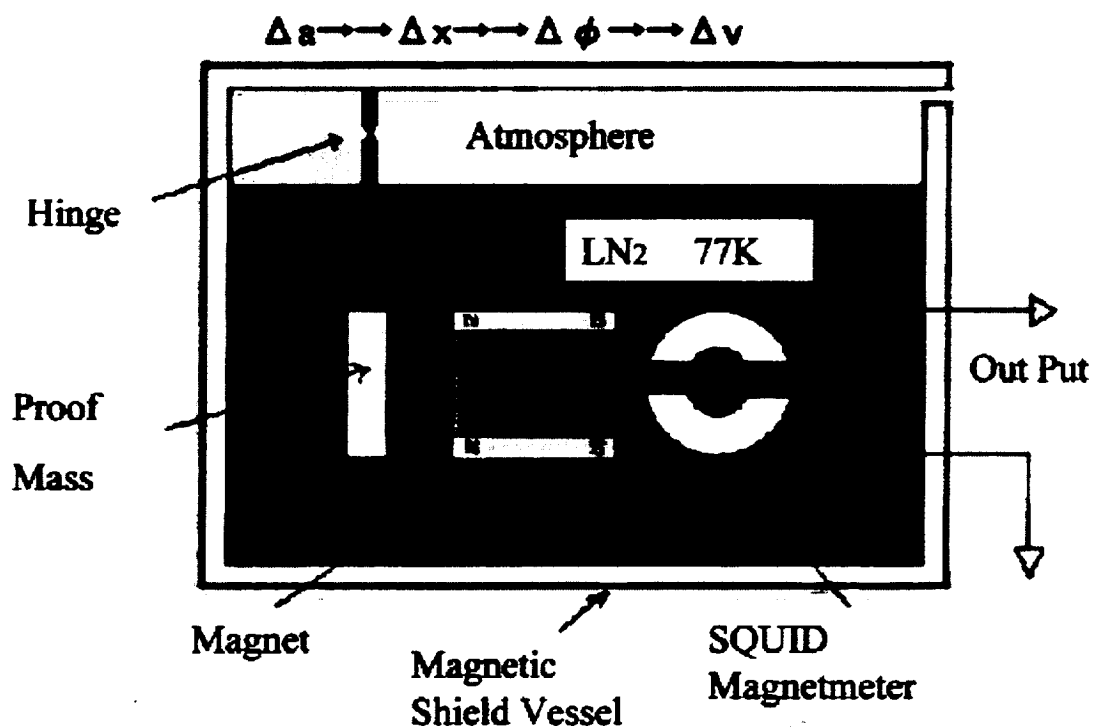
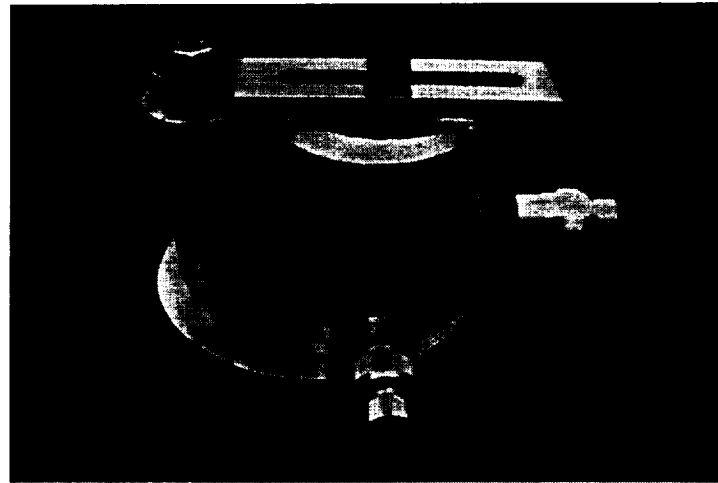


Fig.1 Conceptual Model of experimental high-Tc superconducting accelerometer



160 dia. \times 225 mm
Dimension of the accelerometer

Fig.2 Trial-manufactured Experimental Model

The manufactured model is shown in Fig.2. The proof mass is supported by the left-side pole and the distance between the proof mass and permanent magnet is positioned by adjusting the two micrometers shown in this figure for the determination of the high sensitivity position

3. Preliminary Experimental Data

Fig.3 shows the measured output voltage versus input acceleration. The linearity

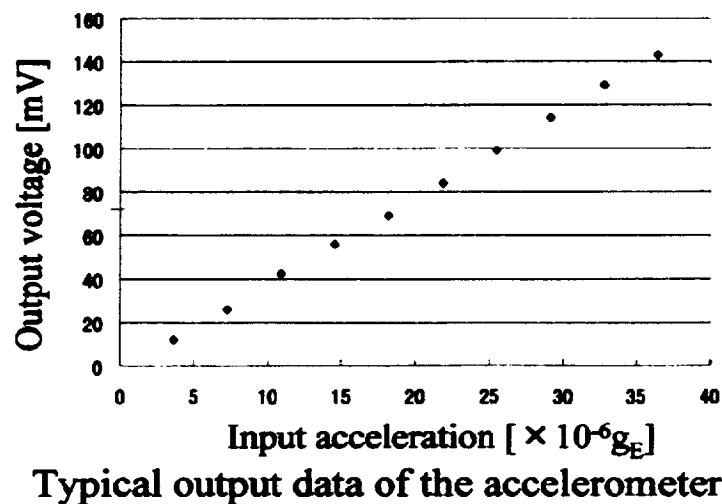


Fig. 3 Measured Acceleration Linearity

is obtained in the range of $10^{-6} g_E$ order. The measurement under this level is limited by the accelerator itself at this time. The sensitivity $10^{-7} g_E$ order will be expected by the improvements of the measured system.

4. Concluding Remarks

High-Tc superconducting accelerometer was designed and manufactured for aerospace applications. From the evaluations of the principle model, the potential capability for detecting low-level acceleration by applying the high-Tc superconductors was confirmed. Magnetic flux analysis is ongoing for the improvement of sensitivity and the optimization of the mechanical arrangement. Miniaturization of the system is necessary for practical use in aerospace applications.

References

- [1] H.J.Paik: Superconducting tunable-diaphragm transducer for sensitive acceleration measurements. J.of Appl.Phys.Vol.47, No.3, pp.1168-1178, 1976
- [2] A.W Hoffman et.al.: Fluxgradient accelerometer; Test on a working model. Rev.Sci.Instrum. Vol.47, No.12, pp1441-1444, 1976

Design of a Hermetically Sealed Chemical Pump With Magnetic Bearings

J. Sobotzik, A. Hantke, R. Nordmann
Darmstadt University of Technology
Department of Mechanical Engineering
Petersenstraße 30, D-64287 Darmstadt, Germany
sobotzik@mesym.tu-darmstadt.de
hantke@mesym.tu-darmstadt.de

S. Brodersen, J. Gröschel, B. Köhler
KSB AG
D-91357 Pegnitz, Germany

ABSTRACT

Increasing demands for environmental protection and severe anti-pollution regulations have led to an extended market for hermetically sealed pumps, e.g. so called canned-motor pumps. The usually installed medium-lubricated hydrodynamic bearings reach their limits of operation if the medium has very poor lubrication characteristics and/or contains gas. Also temperature shocks or bearing overloads may damage such conventional bearing arrangements. Active magnetic bearings seem to be an interesting alternative in such a case. The focus of this study is the possibility to integrate magnetic bearings to one-stage chemical pumps which are available typically in the range of 2 kW to 15 kW. Not only the design of one suspension system is the objective, but the comparison of conventional radial/axial magnetic bearing designs and conical bearing shapes. The influence of the stainless-steel can inside the stator and around the rotor is calculated numerically for static conditions. A test rig is introduced which allows the evaluation of the static calculations and the quantification of power losses caused by Eddy current effects in the can.

INTRODUCTION

The strict application of anti-pollution laws has enforced the development and optimization of hermetically sealed chemical pumps. Fig.1 shows the cross-section of a standard one-stage chemical pump with canned motor drive.

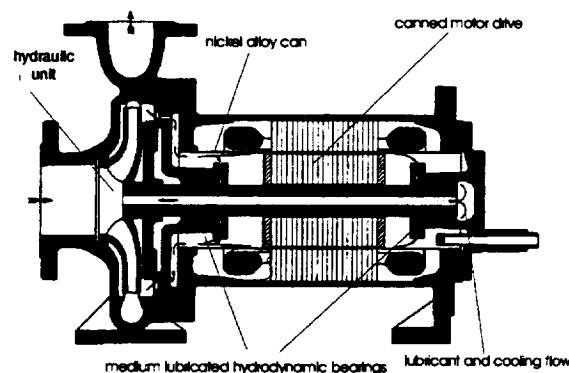


Fig. 1: Cross section of a standard canned motor pump [Neum-94]

To separate the fluid-filled regions from the dry ones of the pump, this design uses a stiff, thin (approx. 0.3 mm), coaxial housing of antimagnetic and highly corrosion-resistant material (stainless steel or nickel alloy), the can, as shown in fig.2. A photograph of a rotor can is shown in fig.3.

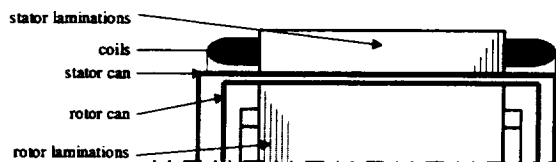


Fig. 2: Principle setup of a canned Motor

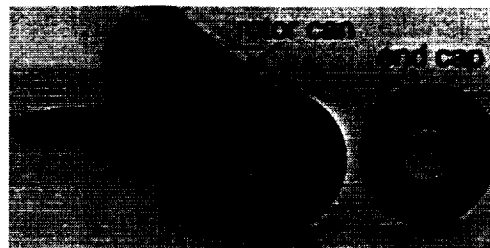


Fig. 3: Cylindrical can with two caps

The usually applied hydrodynamic bearings are located inside this can, in the fluid-filled region. Therefore they are designed as medium-lubricated bearings, often realised with very hard, highly abrasion-resistant materials, e.g. silicon-carbide (SiC). Even such advanced bearing designs reach their limit if the fluid gets very poor lubrication characteristics, extremely low viscosity or the risk of cavitation. In addition, frequent start-ups and run-downs, sudden variations in temperature and transport of abrasive solids limit the lifetime of conventional bearings. Bearing failures have been reported as one of the common problems in hermetically sealed pumps [Voll-93]. One reason to start the present research activities has been the lately published articles about the future perspectives of pump development [Neum-94, Hergt-99]. The application of active magnetic bearings as an alternative has been outlined especially for chemical pumps. Publications about successful designs for such machines are already available. In 1989, Allaire et al. [Allaire-89] reported about the design and realization of a 15 kW canned motor pump equipped with magnetic bearings. He used two 8-pole radial magnetic bearings and two single-acting thrust bearings to support the pump rotor. The two radial bearings have different geometries corresponding to the required bearing loads. Pump performance and vibration levels before and after the installation of the magnetic bearing system have been measured and compared at various locations on the pump casing. In the outlook, the installation of a similar pump in a chemical plant to determine the pump performance for several years was mentioned. A similar project with a 37 kW pump was reported by Marscher et al. [Marscher-91] in 1991. In this pump, a hydraulic balancing device has been applied to reduce the remaining hydraulic axial thrust and to renounce an active axial bearing. One year later, in 1992, Hanson et al. [Hanson-92] described the development of magnetic bearings fitted to a canned motor pump with a motor power of about 93 kW. Two identical radial and one double-acting thrust bearing have been utilized to support the pump rotor. Beside the pump characteristics and rotordynamics, the cooling requirements have been specified and the benefits of magnetic bearings for diagnosis purposes have been pointed out. Gempp et al. [Gempp-96] published the introduction of a bearingless 1.5 kW motor and 3-phase AC bearings for a small canned chemical pump. Due to the bearingless motor, only one additional radial bearing is installed beside a double-acting thrust bearing.

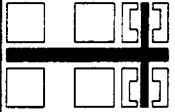
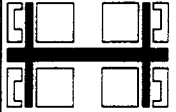
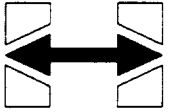
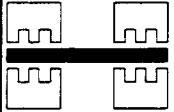
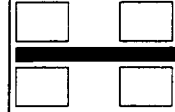
To leverage active magnetic bearings to become a competitive element in commercial canned motor pumps, the additional investments and especially the life-cycle costs have to be reduced. The present study focuses on the comparison of different geometrical bearing designs. Conical and teeth pole contour bearings are investigated by means of their practicability, especially by means of installation efforts, and the possible reduction of electronic hardware. The investigation of the influence of the can on the magnetic circuit will enable the necessary enlargement of the bearing load capability. For this purpose, a test rig to realize rundown tests with different bearing configurations is designed.

MAGNETIC BEARING DESIGN

A selection of the different targets which have been defined at the beginning of the study is listed below:

- The compatibility with existing commercial pumps will ensure the realization of a laboratory test installation with justifiable effort.
- Diameters of rotor and stator parts have to be similar to the motor diameter to use continuous cans and to avoid the necessity of complicated welded joints on the thin material.
- The pump design should be modular, which means that an easy exchange of different bearing geometries without modifications on hydraulic and drive units should be ensured.
- To simplify the assembly of the pump, it is desirable to balance the pump rotor with mounted laminations and can, and to insert it without any dismantling into the pump housing.
- The shaft length extension should be kept as small as possible to preserve the conditions for a dynamically stiff rotor.

To respect all these requirements, a set of principle arrangements of magnetic bearings mounted on a rotor with an overhung load are compared in table 1. The comparison has been carried out for a pump bearing with a load ratio (f_{rad}/f_{ax}) of about 1.25.

<i>Version</i>	<i>A</i>	<i>B</i>	<i>C</i>	<i>D</i>	<i>E</i>
	2 Radial bearings, 1 double-acting axial bearing 	2 Radial bearings, 2 single-acting axial bearings 	2 conical shaped bearings 	2 teeth pole contour bearings 	conventional hydrodynamic bearings 
adequate radial load capacity	available, depending on diameter, length	available, depending on diameter, length	available, depending on diameter, length, conical angle,	available, depending on diameter, length	not available with critical fluid parameters
adequate axial load capacity	available, depending on diameter	available, depending on diameter	available, reasonable only for high force ratios (radial/axial)	only available for very high force ratios (radial/axial)	not available with critical fluid parameters
bearing diameter = motor diameter	possible	possible	diameter not constant	possible	not necessary
conditions for dynamically stiff rotor design	fulfilled	fulfilled	fulfilled	fulfilled	fulfilled
assembly without rotor dismantling	possible without additional restrictions	possible, if outer diameter of axial and inner diameter of radial bearing are identical	possible	possible	possible
shaft length extension	1,15	1,2	1,1	?	1,0 (original length)

<i>Version</i>	<i>A</i>	<i>B</i>	<i>C</i>	<i>D</i>	<i>E</i>
shaft weight extension	1,65	1,55	1,4	?	1,0 (original weight)
installation of can	stator and rotor can have to be assembled and welded out of different parts	can may have a constant diameter, if outer diameter of axial bearing and inner diameter of radial bearing are identical	stator and rotor can have to be manufactured and installed with conical shape	possible, in principle, influence of axial force development not yet clarified	standard procedure

Table 1: Comparison of different bearing configurations

The estimated performance of each design is evaluated. Two designs, version B and C are selected as the most promising ways to realize a future prototype pump.

The main reason for version B is the possibility to install the rotor after the balance procedure without the need of dismantling. A simple can geometry for stator and rotor is sufficient for this configuration. In principle, the rotor can only has to be extended if both radial bearings have identical diameters. This is also valid for the stator can, if easy disassembly of the pump is not required. If the disassembly is necessary, e.g. for a scheduled test pump, the continuous can can be replaced with three discrete cans. A diameter similar to the motor can diameter and equal length are required. Radial and axial bearing geometry can be designed with validated calculation methods. The decentralized control is not expected to be complicated because interactions between the different degrees of freedom are of minor order. The shaft length extension factor is slightly higher than for version A with a double-acting axial bearing, but this disadvantage is compensated by the easier installation procedure.

On one hand, version C requires additional effort to install the can around a conical shaped lamination. But, on the other hand, it enables the reduction of hardware components because the axial and the radial force development is coupled via the conical angle. Therefore, no additional thrust bearing is required. The coupling may complicate the design of a decentralized control for the system. The shaft length extension is only about 10 % for the given load ratio and conical angle. The calculation of the optimum conical angle has been described by Lähtenmäki [Lähten-98]. The shaft length extension strongly depends on the load ratio, because this relation leads to the selected conical angle.

Version D, namely teeth contour pole bearings, seem to be an interesting idea. Their design has been introduced by Canders et al. [Canders-97]. Unfortunately, so far, no publications about measurements to verify the calculations have been found. Nevertheless, the teeth pole stator contour bearings will only be an alternative if axial loads are negligible to the radial loads.

MAGNETIC FORCE CALCULATION

Static forces

In the design phase of the electromagnets, the static magnetic forces have first been calculated analytically, as it is described in [SchTr-93]. The static force losses caused by the stainless steel cans have to be estimated. Therefore, the airgap used in the calculation is increased by the thickness of 2 cans (rotor and stator can). The nominal airgap, required by the minimum circulation flow to ensure an adequate cooling flow for the motor, is about 0.4 mm. The resulting airgap with two cans is 1.0 mm. The results of this analytical calculation are compared with results derived from a numerical calculation with the FE-

software FLUX2D [FLUX2D-98]. The numerical calculations have been performed under consideration of the material properties of the can material, table 2.

Material	<i>ISO NiMo16Cr16Ti (UNS N06455)</i>
Density	8600 kg/m ³
Relative Permeability at 0.3 T (approx.)	40
Specific Resistance at 373 K	1,3 10 ⁻⁶ Ωm

Table 2: Material properties of nickel alloy can

To receive comparable results in the analytic and the numeric calculation, material properties and magnet geometries have been kept identical. The coil current density and the winding density in the coils are similar to the ones of the asynchronous motor drive. Calculation results are shown in comparison in table 3. Fig. 4 and fig. 5 illustrate the results of the numerical calculation. The numerical results without consideration of the can material properties are performed under the assumption of an airgap of 1*10⁻³ m. With the can integrated, the nominal airgap decreases to 0.4*10⁻³ m, the remaining 0.6*10⁻³ m are filled with the can material. The slightly higher relative permeability of the nickel alloy can explain the higher calculated magnetic force in comparison with a similar gap filled with air.

	<i>Analytical calculation</i>	<i>Numerical Calculation</i>	<i>Numerical Calculation under consideration of can material properties</i>
airgap	1*10 ⁻³ m	1*10 ⁻³ m	0.4*10 ⁻³ m
can thickness	–	–	2 x 0.3*10 ⁻³ m
stray fluxes	not considered	calculated	calculated
inhomogeneity of flux distribution	not considered	calculated	calculated
nonlinear material properties	B/H curve	B/H curve	B/H curve
estimated max. force	100%	84%	90%

Table 3: Comparison of analytic and numeric calculation

Beside the force characteristics, the temperature distribution inside the pump will be determined. The calculations will be based on a finite–element model of the pump under consideration of heat transfer between fluid, asynchronous motor drive and bearings. If the cooling based on convection is not sufficient, an additional external cooling loop will be added to the pump to enable the operation of the bearings with satisfiable high coil current densities.

Dynamic Effects, Eddy Current Losses

The electric properties of the can material will influence the required power to support the pump rotor. Static force reduction in comparison to a magnetic bearing with identical geometry but without a can has been elucidated in the previous paragraph. As a second important factor, the developed Eddy currents in the can should be contemplated. For canned asynchronous motor drives the losses caused by the can are reported as about 10–15 % of nominal power [Neum-94, Vetter-98]. To quantify the Eddy current losses experimentally it has been decided to design a handy test rig to perform measurements with different magnetic bearing configurations.

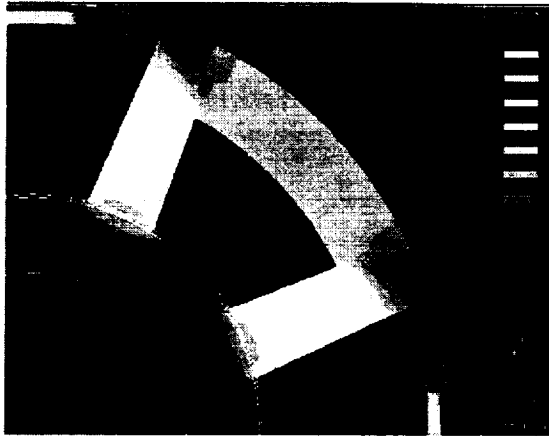


Fig. 4: Numerical results without considering the can

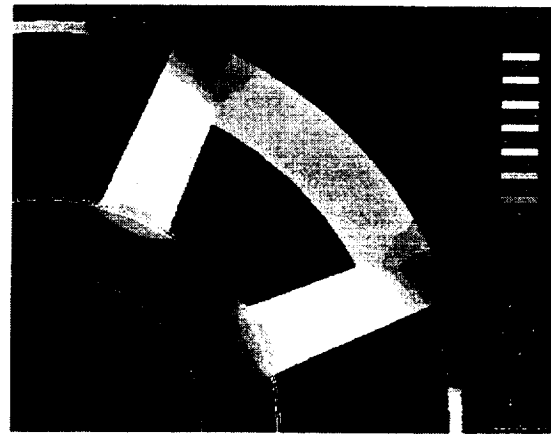


Fig. 5: Calculation considering the can

RUN DOWN TEST RIG

Measurements performed with magnet configurations with and without cans have to be compared to quantify the losses. Two different principle possibilities to measure the Eddy current losses have been conceivable. First, the torque loss could be determined by integrating a torque measurement device in a motor driven thread with an electromagnetic actuator. The selection of the correct measurement range for such a torque metering system would be difficult if the order of the loss moment is unknown, but the losses can be measured at different shaft speeds, if a speed controlled drive unit is available. Secondly, the losses may be derived by performing run down tests of a shaft with an electromagnetic actuator. Kasarda et al. [Kasarda-97] have compared measurements of rotor losses of homopolar with heteropolar bearing designs. Interesting results of these tests have been documented, and therefore it has been decided to design a test rig with a related functionality. To minimize the required effort, the test shaft should be supported by roller bearings. Very precise aerospace bearings are able to operate at high speeds with minimized friction losses, table 4.

<i>bearing type</i>	<i>B71907E.TPA.P4.UL</i>
inner/outer diameter	$35 \cdot 10^{-3} / 55 \cdot 10^{-3} \text{ m}$
rotary speed limit, oil breathed	26 000 rpm
friction losses at maximum speed	$< 38 \cdot 10^{-3} \text{ Nm}$

Table 4: data of exemplary roller bearings

Because the shaft is supported in roller bearings, no control loop is needed for the electromagnetic devices, only a current supply is required. The coil current has to be adjustable and recordable. The magnetic force will be measured by Hall sensors mounted on the pole shoes. The calibration of these Hall sensors has to be performed by external load cells to reach a sufficient accuracy, discussed in Knopf et al. [Knopf-98]. A test shaft of 0.3 m length will be accelerated to 12 000 rpm by a 2 kW AC-Servo drive. This drive unit is joint to the test shaft by a disconnectable friction coupling. When the targeted operational speed is reached, the shaft will be manually declutched and the run down curve will be registered. The test rig is presented in fig.6.

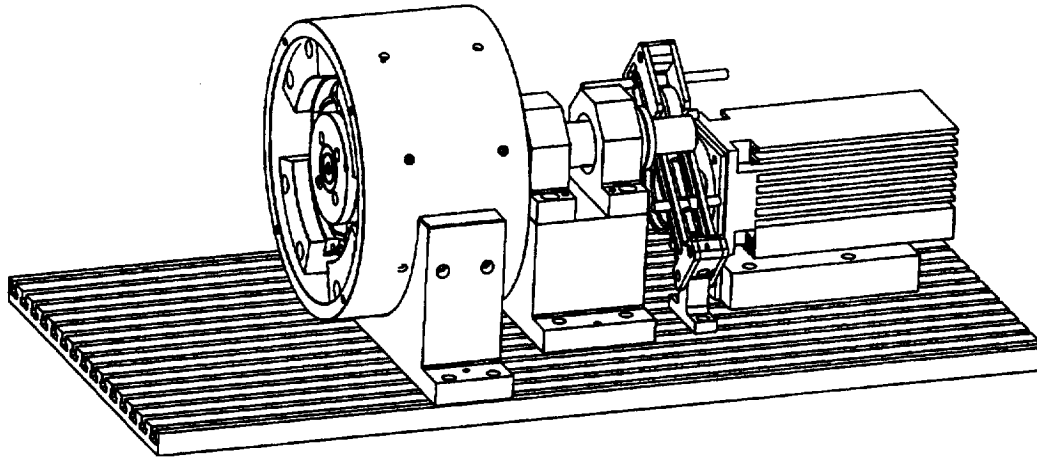


Fig. 6: Test rig for run down tests with different magnet designs

Run down time is depending on the rotors moments of inertia, on roller bearing and air friction and on the deceleration moments produced by the electromagnetic circuit. Due to comparison of different run down times realized with different magnetic circuit configurations, the losses caused by Eddy current and hysteresis can be quantified. The air drag is expected to be nearly constant in all configurations. The sum of mechanical losses may be estimated by subtraction of measurements with and without activated electromagnets. Scheduled measurement configurations are listed below in table 5.

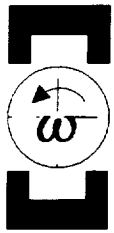





<i>radial heteropolar bearing</i>	<i>canned radial heteropolar bearing</i>	<i>radial homopolar bearing</i>	<i>canned radial homopolar bearing</i>	<i>conical shaped bearing</i>	<i>canned conical shaped bearing</i>
					

Table. 5: Different magnetic bearing configurations

Because of geometrical aspects, conical shaped bearings in homopolar configuration have been disregarded. The geometrical properties of the test magnets shown in fig.7 are listed in table 6 beside the assumed and calculated magnetic data.

The evaluation of the test results will hopefully lead to an optimal bearing design for canned-motor pumps by means of rotor power and magnetic suspension losses. In addition to the run down tests, flux density measurements by means of Hall sensors are planned. The Hall sensors will be placed in the airgap of the electromagnets or between the laminations and the can. Flux density measurement results should enable the validation of the numerically calculated magnetic fields.

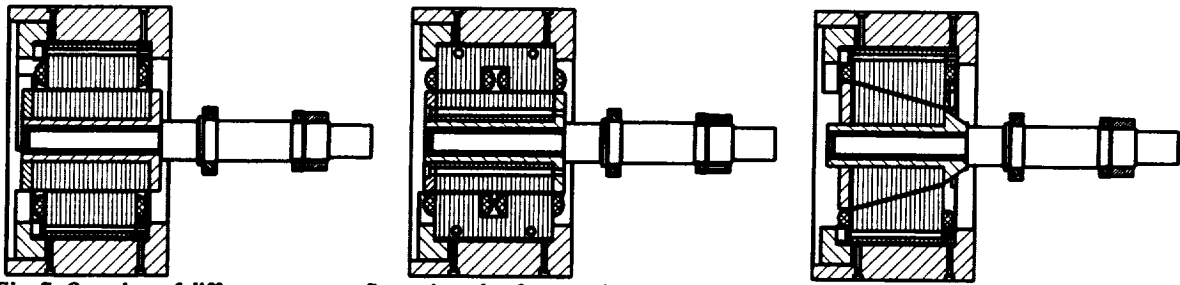


Fig. 7: Overview of different rotor configurations for the run-down test rig

	<i>radial heteropolar magnet</i>	<i>radial homopolar magnet</i>	<i>conical shaped magnet</i>
inner diameter	95 mm	95 mm	72 – 120 mm
outer diameter	180 mm	180 mm	180 mm
pole area	1290 mm ²	1290 mm ²	1290 mm ²
nominal air gap	1 mm	1 mm	1 mm
flux density B_{max}	1,4 T	1,4 T	1,4 T
coil area A_{coil}	310 mm ²		
conical angle			15 °
calculated radial force	2000 N	2000 N	1250 N
calculated axial force	–	–	380 N

Table 6: design properties of test magnets

POSITION MEASUREMENT

For the exact control of the rotor, its position has to be measured and fed back. Therefore sensors have to be integrated in a location where the collocation conditions are fulfilled. The target of a sensor selection process would be ideally a sensor which is placed in the center of the magnetic bearing.

The selection of possible sensor systems is one of the major tasks in the design process of a canned pump with magnetic bearings. Standard proximity probes are not qualified for this application because of the rough environmental conditions, temperature and aggressiveness of the process fluid. In principle there are three possibilities to meet this difficulty, see fig. 8.

A corrosion resistant sensor with a stainless steel housing may be utilized. An additional sealing has to prevent any fluid leakage. The corrosion resistant sensor may be, e.g. an inductive or an Eddy current type. To use sensors with a conventional housing, an in the can integrated ceramic shielding would be helpful. An installation close to the magnetic bearings is possible if the ceramic ring diameter is identical to the stator. Another possibility is to install a ceramic plate, like a small bent disk. It can be used as a kind of window in the metallic can. Both the corrosion resistant sensor and the ceramic shielded sensor would fulfil the conditions for hermetically sealed pumps, only the static sealings are necessary.

If the measurement has to be performed through the can, Eddy current, inductive and Hall sensors represent three possible principles. Utilizing Eddy current or inductive sensors, the high signal attenuation has to be taken into account. Hall sensors enable the measurement of the flux density directly between the pole surface and the stator can.

In coherence with an additionally coinstantaneous available parameter, e.g. the measured current in the magnetic coils, the flux density could be utilized to calculate the air gap in the magnetic circuit and hence the rotor position.

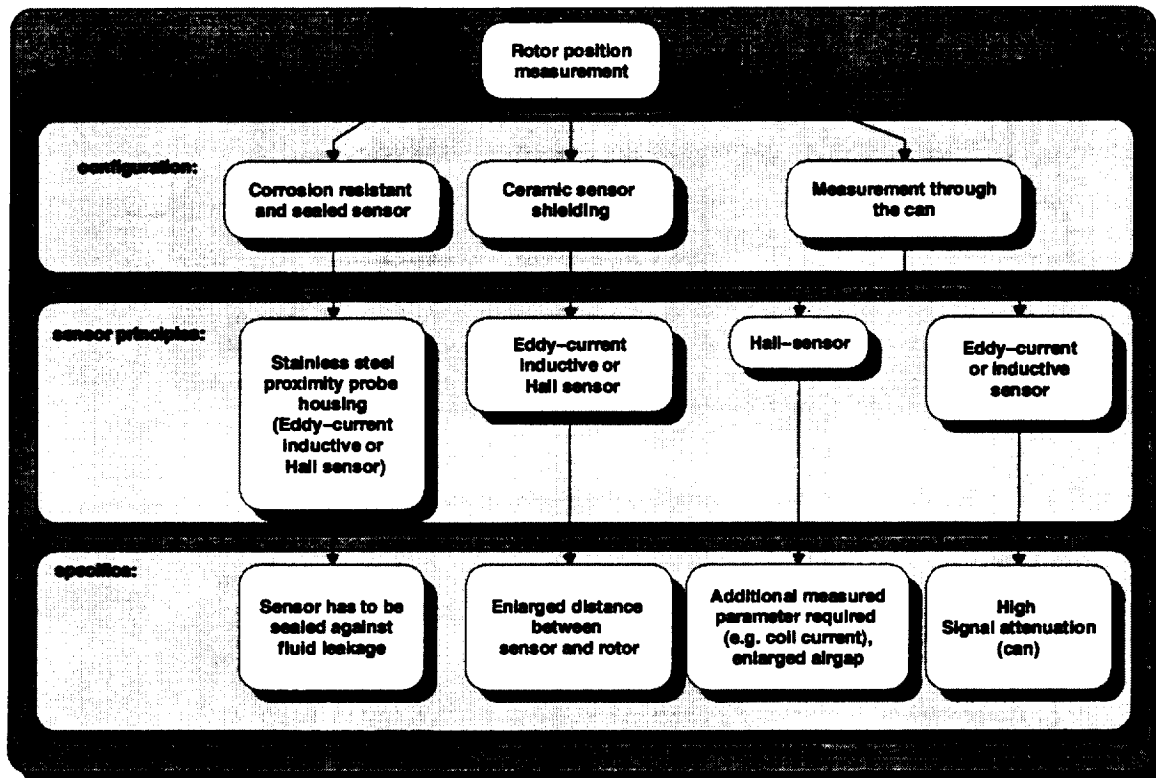


Fig. 8: Rotor position measurement in canned pumps

The design of a future test pump should enable the integration and testing of different sensor principles. At the moment, Hall sensors seem to be the most elegant way for the position measurement. Their advantage is the possibility of a position measurement directly where the force is acting on the rotor. Their first disadvantage is the additional effort to calculate the position out of flux density and, e.g. the coil current. The second disadvantage is the required enlargement of the airgap which leads to a significant reduction of the maximum bearing force. The signal processing must be performed fast enough to satisfy the dynamic characteristics of the entire system.

PUMP PROTOTYPE

In the near future a widespread test program will be executed. Measurements on different magnet configurations are scheduled to get information about their individual behaviour. There will be the examination of force development and force losses by means of Eddy currents and hysteresis effects. At least conventional radial bearings in combination with two single-acting axial bearings (see fig. 9) and conical shaped bearings (see fig. 10) will be tested and compared with each other. At this moment these

two alternatives seem to be the most attractive configurations to reach a satisfiable system performance with acceptable effort. In parallel the numerical calculations will be validated and updated. The two pump configurations will be installed in the laboratories of the University of Darmstadt and run in a lab testloop under nearly real conditions. The prototypes will be equipped with sensor systems to record all interesting mechanical, electrical, thermal and process data.

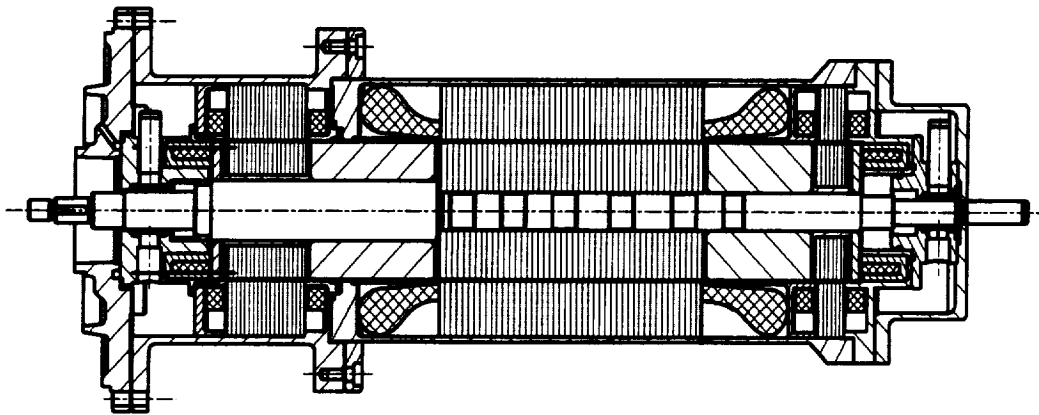


Fig. 9: Canned motor pump with two radial and two single-acting axial bearings

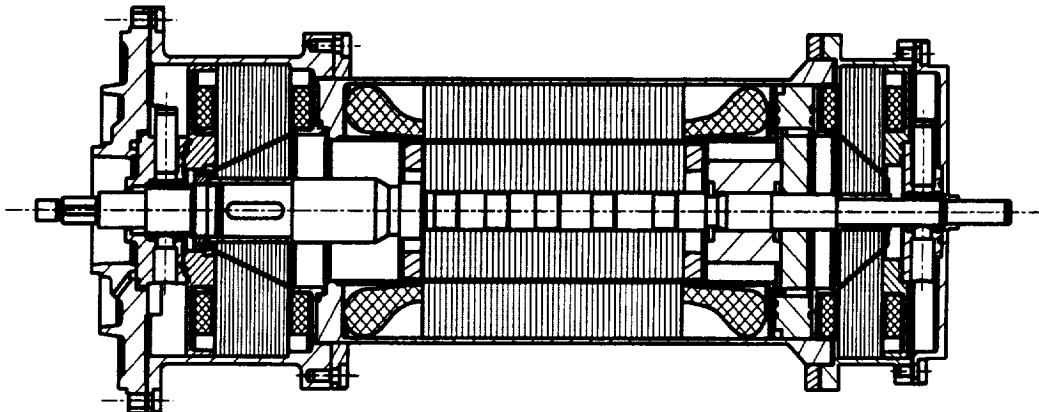


Fig. 10: Canned pump with two conical shaped bearings

The design of the test pumps enables the integration of different sensor concepts. Especially the ceramic sensor shielding and the integration of Hall sensors are scheduled. The ceramic shielding will be realized as a concentric ring next to the magnetic bearing. An even better solution for the future would be the entire substitution of the metallic can through a ceramic one (e.g. ZrO_2). Such ceramics are already used to build shieldings for permanent magnetic couplings in mag-drive pumps, the second design alternative for a hermetically sealed pump. By the time they are available with an acceptable thickness they will reduce can losses to nearly zero. They would enable the use of a wide range of different sensor principles. Also they provide interesting characteristics as backup bearing materials.

SIMULATION OF THE CLOSED-LOOP SYSTEM

Before the realization of the prototype pump, a nonlinear time domain based simulation model of the pump with two different bearing configurations has been developed. The first one has two radial bearings and a double acting axial bearing, the second consists of two conical shaped bearings. Fig. 11 shows the MatrixX simulation model of the canned pump. The block *External Forces* describes one possible set of hydraulic forces acting on the rotor. The overall hydraulic force in a pump consists of a static part which is variable in direction and value depending on the operation conditions and a dynamic part which depends on the rotational speed, number of impeller blades, etc..

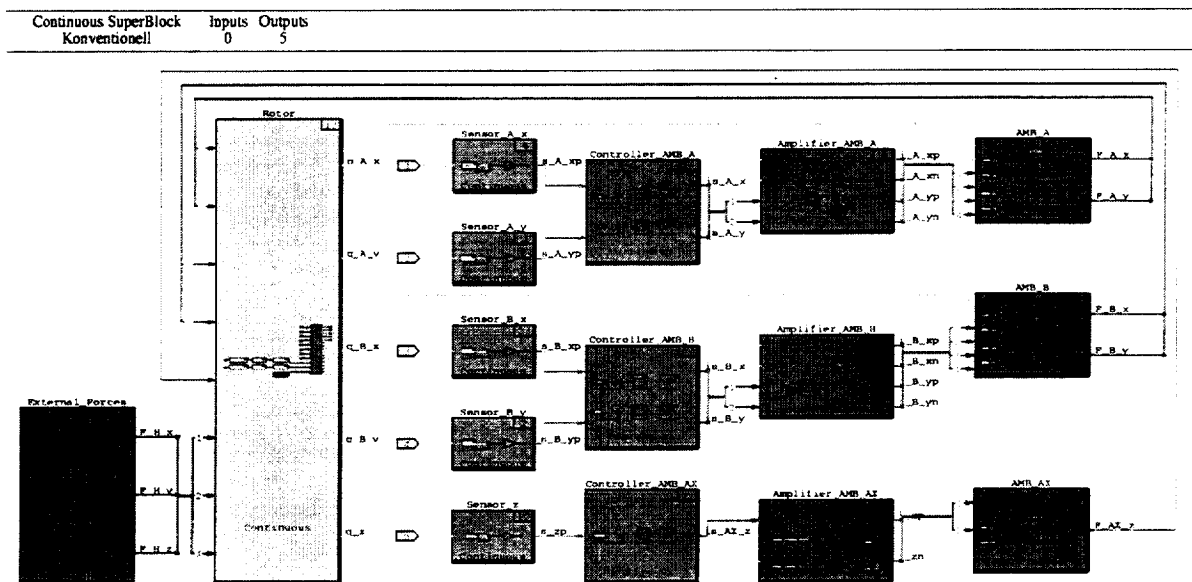


Fig. 11: Model of a AMB system with two radial and one double-acting axial bearing

In a first step the sum of static and dynamic hydraulic forces have been assumed as one harmonic force rotating with shaft speed. The rotor is modelled as a rigid body system, an acceptable simplification because its first bending mode eigenfrequency (approx. 275 Hz) is clearly above the frequencies of the dynamic excitations (1. assumption: 50 Hz). The displacements are measured by sensors, which have at this state of the simulation a P characteristic, in five degrees of freedom to be fed forward to the controller. The PID-Controllers set the required currents for the amplifiers which have a PT1 performance and are limited to 70 VDC and 10 A. The absolute magnetic bearing force depends on this current and the actual position of the rotor. The closed loop system allows the prediction of the system performance especially an estimation of the rotor displacements in the magnetic bearings considering the mechanical and process forces. The external hydraulic and mechanical forces and the resulting magnetic bearing forces acting on the rotor are shown in fig. 12. Fig. 13 displays the simulated rotor displacements at the bearing locations. This simulation model helps to select the optimum hardware to reach a satisfactory system performance for the given loads and operation conditions.

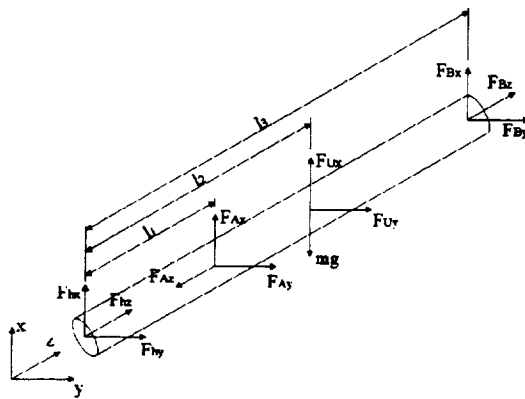


Fig. 12: The on the pump rotor acting forces

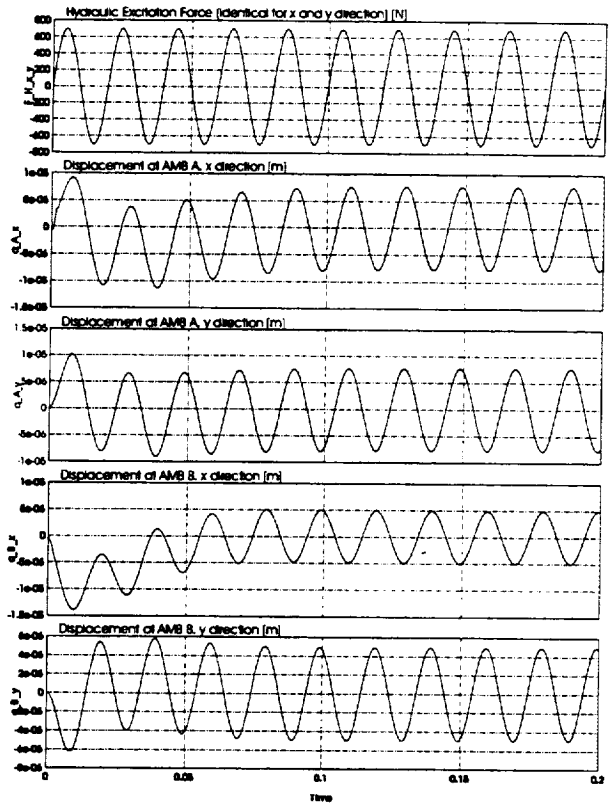


Fig. 13: Simulation results; displacements in the AMB's

SUMMARY

Magnetic bearings for hermetically sealed pumps have been introduced years ago. Despite increasing demands for these machines the magnetic bearing technology has not yet been leveraged in chemical pumps. The relatively high costs and the additional effort to integrate magnetic bearings have decelerated adequate developments.

First steps to a systematic approach to an enhanced design of a canned motor pump with active magnetic bearings have been introduced. Different bearing configurations and applicable sensor principles have been compared. In completion of analytical and numerical calculations, the design of a run down test rig to quantify Eddy current and hysteresis losses has been quantified. A conventional design with two radial and two single-acting axial bearings and a design with conical shape bearings have been presented as the most attractive solutions under consideration of pump specific and manufacturing aspects.

Two prototype pumps are scheduled by the Institute of Mechatronic Systems for the next time. The aim of this study is to introduce new ideas for the development of hermetic sealed pumps with magnetic bearings.

ACKNOWLEDGEMENT

The Institute of Mechatronic Systems at the Darmstadt University of Technology would like to thank the KSB AG, Germany, for financing and supporting the basic examinations in this studies. Also the provision of FE–software by SIMEC, Germany, is gratefully mentioned.

REFERENCES

- Voll–93 Vollmüller, H., Fischer, K.: Canned Motor and Magnetically Coupled Pumps Applications, Operations and Maintenance in a Chemical Plant, Pump Symposium, Texas A&M University, Texas, USA, 1993
- Neum–94 Neumaier, R.: Hermetische Pumpen, Verlag Faragallah, Sulzbach, Germany, 1994
- Hergt–99 Hergt, P.: Pump Research and Development: Past, Present and Future, Journal of Fluids Engineering, June 1999
- Allair–89 Allaire, P. E., McDonald, J. P.: Design, Construction and Test of Magnetic Bearings in an Industrial Canned Motor Pump, World Pumps, Sep. 1989
- Marscher–91 Marscher, W. D., Jen, C.: Development of an Active Magnetic Bearing for a 50 HP Canned Motor Pump, ROMAC '91 Magnetic Bearings and Dry Gas Seals, International Conference and Exhibition, University of Virginia, USA, 1991
- Hanson–92 Hanson, L., Imlach, J.: Development of a Magnetic Bearing API Process Pump with a Canned Motor, 9th International Pump Symposium, Texas A&M University, USA, 1992
- Gempp–96 Gempp, T., Schöb, R.: Design of a Beringless Canned Motor Pump, 5th International Symposium on Magnetic Bearings, Kanazawa, Japan, 1996
- Lähteen–98 Lähteenmäki, J. K., Lantto, E. J. : Optimization of the Conical Angle of Cone-shaped Active Magnetic Bearings, Proceedings of the Sixth Int. Symp. on Magnetic Bearings, MIT, Cambridge, USA, 1998
- Canders–97 Canders, W.–R., Lee, W. L. : Integrated Radial and Axial Low Cost Magnetic Bearings, Proceedings of MAG '97, Industrial Conf. and Exhib. on Magnetic Bearings, Alexandria, USA, 1997
- FLUX2D–98 FLUX2D: CAD Package for Electromagnetic and Thermal Analysis using Finite Elements, CEDRAT, Meylan Cedex, France, cedrat@cedrat-grenoble.fr
- Vetter–98 Vetter, G. (Editor): Leckfreie Pumpen, Verdichter und Vakuumpumpen, Vulkan Verlag, Essen, Deutschland, 1998

- SchTr-93 Schweitzer, G.; Traxler, A.; Bleuler, H.: **Magnetlager, Grundlagen, Eigenschaften und Anwendungen berührungsfreier, elektromagnetischer Lager**, Springer-Verlag, Berlin, Germany, 1993
- Vetter-98 Vetter, G. (editor): **Leckfreie Pumpen, Verdichter und Vakuumpumpen**, Vulkan-Verlag, Essen, Germany, 1998
- Kasarda-97 Kasarda, M. E. F., Allaire, P. E., et al.: **Comparison of Measured Rotor Power Losses in Homopolar and Heteropolar Magnetic Bearings**, Proceedings of MAG '97, Industrial Conf. and Exhib. on Magnetic Bearings, Alexandria, USA, 1997
- Knopf-98 Knopf, E., Nordmann, R.: **Active Magnetic Bearings for the Identification of Dynamic Characteristics of Fluid Bearings**, 6th Int. Symp. on Magnetic Bearings, Massachusetts Institute of Technology, Cambridge, USA, 1998

Session 14 -- Controls 3

Chairman: Hideo Sawada
National Aerospace Laboratory (NAL)

ADAPTIVE MODEL FOLLOWING CONTROL METHOD FOR ACTIVELY CONTROLLED MAGNETIC BEARING MOMENTUM WHEEL

Y.-C. Xie

C.O.E. research fellow of Institute of Space and Astronautical Science (ISAS) on leaving from
Beijing Institute of Control Engineering, P. R. China

H. Sawada, T. Hashimoto, and K. Ninomiya

Institute of space and Astronautical Science, 3-1-1 Yoshinodai, Sagamihara, 229-8510, Japan

ABSTRACT

For the active control of magnetic bearing momentum wheels that could be used as actuators of high-accuracy spacecraft attitude control system, an adaptive model following control method is presented in this paper. This method is featured by adaptive bandwidth-regulation mechanism, controller with logical derivative, new nutation damping network, and non-linearity compensator. Thus it is convenient to make compromise between fast dynamic response and active-vibration suppression at harmonic frequencies of the wheel rotation. The robust stability of this method is analyzed and digital simulation is carried out. Simulation results show that this method has great capability of active-vibration suppression, good dynamic response, and satisfactory nutation damping of the wheel rotor for a large range of wheel rotational speed.

INTRODUCTION

For the high-accuracy attitude control of spacecraft, Magnetic Bearing Momentum Wheel (MBMW) is being investigated as an actuator because of its merits of low disturbance characteristics [1, 2] and gimballability when a suitable active controller is used. In this context, the active control of MBMW means to make the rotor spin around its principal axis of inertia to achieve low disturbance input while being able to tilt the principal axis of inertia for attitude control of spacecraft. This has to be done with adequate nutation damping of the wheel rotor. The performance requirements for the active control system of MBMW are usually as follows:

- (1) Good active-vibration suppression of inevitable sensor errors. Since the band-limited white noise is easy to be suppressed by using a low pass filter, the components to be suppressed by means of active-

vibration suppression are mainly those disturbance components with harmonic frequencies of the wheel rotation. In [2] Active-Vibration Suppression (AVS) is defined, which means to enable the rotor to rotate about its principle axis of inertia and suppress all the resulting noise components from the whirling and wobbling sensor surface without affecting suspension stability. This term is adopted through this paper.

- (2) Robustness against electromagnetic non-linearity.
- (3) Good disturbance suppression against wheel external environmental disturbance torques.
- (4) Robustness against wheel rotational speed in a large range.

In previous literature, considering the non-linearity of electromagnets, Nam et al. [1] applied the H_∞ robust control method to the active control of MBMW, but only a fixed rotational speed is considered. Without thinking of the non-linearity of electromagnets, Bichler [2] proposed a Model Following Control (MFC) method and indicated that this method has superior capability of active-vibration suppression for a large range of wheel rotational speed. However, this method is based on a special observer to realize active-vibration suppression, thus its response to fast externally impressed torques and movements is slow. If external environmental disturbance torques which have been mentioned already exist, large overshoot and small nutation of the wheel rotor will be excited when wheel rotational speed is low. Therefore, in order to solve the above problems and to realize the active control of MBMW with non-linear electromagnets, an Adaptive Model Following Control (AMFC) method is proposed in this paper.

In this new method, first an adaptive mechanism is inserted into the above model following control method. This adaptive mechanism can adaptively regulate the bandwidth of a special observer based on on-line characteristic identification so as to improve system dynamic response if needed. Second, logical derivative [3] is applied to the controller design to reduce overshoot further. Third, a new nutation damping method that can automatically adjust the gain of nutation damping according to wheel speed is introduced in order to obtain consistent nutation damping rate for different wheel speed. Finally, a non-linearity compensator is put forward to overcome electromagnetic non-linearity. Consequently, the adaptive model following control method is suitable for the active control of MBMW.

In this paper, the mathematical model of MBMW is introduced first. Then the adaptive model following control method is presented. Since the closed-loop system is a nonlinear and time-varying system, the robust stability of this method is analyzed from the engineering viewpoint. To verify the effectiveness of this new method, digital simulation is carried out and the possible application of this method to the active control of MBMW for spacecraft attitude control is discussed at the end.

MBMW

Although the control method presented in this paper could be applied to any actively controlled MBMW, the authors select a specific type of MBMW and apply the method to the control of this kind of wheel.

Octa-Electromagnet-Type Active Magnetic Bearing Momentum Wheel

For future three-axis spacecraft attitude control, Octa-Electromagnet-Type Active Magnetic Bearing Momentum Wheel (OETA-MBMW), which is a kind of five-degree of freedom MBMW, is developed in ISAS [1, 4]. OETA-MBMW is composed of eight electromagnets whose attractive forces have components both in axial and in radial direction so that it may serve to reduce size and weight. Eight gap sensors are symmetrically installed with tilts so as to measure the rotor displacements in three directions and gimballing angles around two axes vertical to the wheel rotational axis. The cross section of this kind of OETA-MBMW is shown in Fig. 1.

Wheel Dynamics

In describing the rotational motion of the MBMW, rotational coordinate systems are used as shown in Fig. 2, in which coordinate system $X_0Y_0Z_0$ is considered as spacecraft's attitude reference coordinate system while $X_wY_wZ_w$ a wheel-body coordinate. $X_0Y_0Z_0$ changes so slowly in inertial space that it can be considered as an inertial coordinate system for the present purpose. Angles ϕ_w , θ_w and φ_w are the Euler angles in X-Z-Y transformation from $X_0Y_0Z_0$ to $X_wY_wZ_w$. For the simplicity of motion derivation, spin-free coordinate system $X_{2w}Y_{2w}Z_{2w}$ is used to describe the dynamic motion of MBMW [1].

Suppose that the selected coordinates are on the principal axes, the gimballing angles of MBMW are small, the wheel is rigid and symmetric about its rotational axis, and the wheel rotational speed varies so slowly with time that it can be considered as constant [1]. Then the linearized dynamic model of MBMW in gimballing axes can be expressed as follows.

$$\begin{cases} \ddot{\phi}_w - \sigma\Omega\dot{\phi}_w = (T_x + T_{dx})/J_w \\ \ddot{\phi}_w + \sigma\Omega\dot{\phi}_w = (T_z + T_{dz})/J_w \end{cases} \quad (1)$$

In (1), $\sigma = J_{yw}/J_w$ is the ratio of moments of inertia. J_{wx} , J_{wy} and J_{wz} are inertial moments of the wheel in X_w , Y_w and Z_w axis, respectively, and $J_{wx} = J_{wz} = J_w$ can safely be assumed. $\Omega = \dot{\theta}_w$ is wheel rotational speed. T_x and T_z are electromagnetic torques. T_{dx} and T_{dz} are external environmental disturbance torques including those due to eddy current loss, ohmic loss and those exerted from the spacecraft body on which the physical space-environmental torque acts.

According to experimental data, the model of electromagnet can be modeled as accurately as follows [4].

$$\begin{cases} T_x = k_m \phi_g^2 \left(\frac{V_b + v_\phi}{\phi_g - \phi} \right)^2 - k_m \phi_g^2 \left(\frac{V_b - v_\phi}{\phi_g + \phi} \right)^2 \\ T_z = k_m \phi_g^2 \left(\frac{V_b + v_\phi}{\phi_g - \phi} \right)^2 - k_m \phi_g^2 \left(\frac{V_b - v_\phi}{\phi_g + \phi} \right)^2 \end{cases} \quad (2)$$

In (2), k_m is electromagnetic gain, ϕ_g and ϕ_g are nominal electromagnetic gaps, ϕ and ϕ are electromagnetic gaps, and satisfy $|\phi| < \phi_g$, $|\phi| < \phi_g$. If we neglect the attitude motion of spacecraft, then $\phi = \phi_w$ and $\phi = \phi_w$. V_b is a constant representing bias voltage applied to electromagnets, v_ϕ and v_ϕ are control commands or control voltages, and satisfy $|v_\phi| < V_b$, $|v_\phi| < V_b$.

According to (2) we know that the non-linearity of electromagnets is proportional and inversely proportional in the second order for voltage-input and the gimbaling angles of the wheel, respectively. Although, in order to overcome this kind of electromagnetic non-linearity, a constant pre-magnetization bias voltage V_b is added, the electromagnetic torque-output is still not pure linear function of control voltage-input. By using Taylor expansion, the first-order approximation of (2) can be expressed in (3).

$$\begin{cases} T_x = k_{EM} v_\phi + k_{N\phi} \phi \\ T_z = k_{EM} v_\phi + k_{N\phi} \phi \end{cases} \quad (3)$$

Where $k_{EM} = 4k_m V_b$, $k_{N\phi} = 4k_m V_b^2 / \phi_g$, $k_{N\phi} = 4k_m V_b^2 / \phi_g$.

Gap Sensors

Following sensor noises of MBMW are considered in gap sensor model according to wheel mechanism [4].

- (1) Sensor noise resulting from the electric noise components of gap sensors is modeled as white noise (ζ_ϕ, ζ_ϕ) whose frequency band is limited to the controller's sampling frequency.
- (2) Harmonic sensor noises caused by imbalance of rotor, i.e. the geometric axis of rotor is not coincident with the principal axis of inertia, and mechanical imperfections of the rotating part are modeled with the harmonic signals of wheel rotational speed shown as follows.

$$\begin{cases} n_\phi = \sum_{i=1}^{N_i} c_i \sin(i * \theta_w + \theta_i) \\ n_\phi = \sum_{i=1}^{N_i} c_i \sin(i * \theta_w + \theta_i + \pi / 2) \end{cases} \quad (4)$$

In (4), N_h is the number of harmonics, c_i is the amplitude of harmonics, and θ_i is initial angle. As a result, the model of gap sensors can be expressed in (5).

$$\begin{cases} \tilde{\phi}_w = \phi_w + \sum_{i=1}^{N_h} c_i \sin(i * \theta_w + \theta_i) + \zeta_o \\ \tilde{\phi}_w = \phi_w + \sum_{i=1}^{N_h} c_i \sin(i * \theta_w + \theta_i + \pi / 2) + \zeta_o \end{cases} \quad (5)$$

ADAPTIVE MODEL FOLLOWING CONTROL METHOD

AMFC method is proposed based on MFC method [2], thus it keeps the basic structure of MFC method and inherits MFC's advantages. However, AMFC method is superior to MFC method because of its adaptive mechanism for AVS, controller with logical derivative, new nutation damping strategy and non-linearity compensator.

The block diagram of the AMFC closed-loop system for the active control of the rotor-tilt-loops of MBMW is shown in Fig. 3. In Fig. 3, the right part enclosed by dash-line frame represents the plant to be controlled, i.e. MBMW, while the other left part represents AMFC's control loop.

The block of AMF-AVS in Fig. 3 is demonstrated in Fig. 4. In Figure 4, *integrator I* and *integrator II* are standard integrators. *Low pass filter* is a first-order low pass filter that can be represented as $\frac{a}{s+a}$, where a is positive real number. k_{11} , k_{12} , k_{21} and k_{22} are observer coefficients, *Gain* represents the gain coefficient of the plant to be controlled from electromagnet input to rotor output. For the plant discussed in this paper, *Gain* equals to k_{EM0}/J_{w0} , where k_{EM0} and J_{w0} represent the nominal values of k_{EM} and J_w , respectively. In the following parts of this paper, the variable with subscript 0 also denotes the nominal value of this variable. *Adaptive mechanism* automatically determines when k_{21} and k_{22} should be switched on or switched off so that the bandwidth of AMF-AVS observer is regulated adaptively. In fact, the AMF-AVS loop in Fig. 4 can be considered as a special adaptive observer of rotor movements.

In Fig. 3, *gyro-decoupling* network uses the same decoupling network proposed in [5], which is depicted in (6).

$$\begin{cases} u_{rx} = -\sigma_0 \Omega_0 \frac{1}{s} u_z \\ u_{rz} = \sigma_0 \Omega_0 \frac{1}{s} u_x \end{cases} \quad (6)$$

Where, u_x and u_z are the inputs of the *gyro-decoupling* network while u_{rx} and u_{rz} the outputs.

In Fig. 3, *Controller* can be designed as single-input and single-output controller because of the effect of *gyro-decoupling* network. *Nutation damping* network is used to damp down the nutation

deteriorated by AMF-AVS and wheel external environmental disturbance torques. *Non-linearity compensator* is employed to compensate electromagnetic non-linearity.

In the following sections, adaptive mechanism of AMF-AVS, controller with logical derivative, new nutation damping strategy and non-linearity compensator will be explained in detail.

Adaptive Mechanism of AMF-AVS

In [2], to control the faster externally impressed stator movements, a *limit switch* is used to quicken the convergence of AVS observer by detecting the difference of the rotor real position and the observer output. If the difference exceeds half of the nominal gap, a second stronger feedback is turned on to force the observer output immediately to the real position to prevent a touch down of the rotor. The block diagram of AVS of MFC method is shown in Fig. 5. In fact, this kind of limit switch can not control the faster externally impressed stator movements. The reason is that the limit switch works only after the difference exceeds half of the nominal gap, and even in this case stronger feedback in observer tends to result in larger controller output than the input voltage limit of the electromagnets, which means this effort is in vain. Furthermore, even if the second stronger feedback works, the low noise quality of AVS is reduced because unfiltered sensor signal is introduced directly into the control system. In order to solve this problem and to make a good compromise between fast convergence of observer and satisfactory active-vibration suppression in the whole gap range, adaptive bandwidth-regulation method is proposed to replace the limit switch of MFC for AVS.

The main idea of the adaptive bandwidth-regulation method is to broaden the observer bandwidth when fast convergence is needed, for example when large overshoot occurs in gimbaling angles, and to reduce the observer bandwidth when active-vibration suppression is the main purpose, for example at the steady state. Moreover, in this method the saturation non-linearity of the input voltage of electromagnets is also considered. The adaptive bandwidth-regulation is based on on-line characteristic identification.

As defined in Fig. 4, y_lpf is the output of AMF-AVS low-pass filter. Define the average value of y_lpf in one wheel rotational period as y_ave . y_ave is refreshed every one wheel rotational period. The rule for determining when k_{21} and k_{22} should be turned on/off is depicted as follows.

Rule 3.1.

If $|y_ave| > \delta_1$ and $|y_ave| < \delta_2$,
then k_{21} and k_{22} are switched on,
else k_{21} and k_{22} are switched off.

In Rule 3.1, δ_1 is named as steady-state threshold, and is determined according to the index of steady state and the amplitude of sensor noises. δ_2 is named as saturation threshold, and is determined according to the input voltage limit of electromagnets and controller.

Rule 3.1 means that if the average difference of the observer output and the rotor position is much

larger than the sensor noises and smaller than the saturation threshold, which can make sure the controller output is less than the input voltage limit, the bandwidth of AMF-AVS observer is broadened. This kind of bandwidth regulation can make the observer output follow the rotor position quickly and effectively. Therefore the adaptive bandwidth-regulation method can improve system dynamic response while active-vibration suppression is guaranteed.

Controller with Logical Derivative

Logical derivative was proposed in [3] to improve system dynamic response, especially to reduce system overshoot. The controller with logical derivative is designed in such a way. First design a Proportional- Integral-Derivative (PID) controller, then modify the derivative coefficient according to a certain logical rule.

After introducing logical derivative the controller for single-axis gimbaling control is designed as follows.

$$u = k_p e + k_i \int e dt + k'_d \dot{e}. \quad (7)$$

In (7), u is controller output, e is the difference between position command and AMF-AVS observer output,

$$\begin{cases} k'_d = k_d & \text{if } (e\dot{e} \leq 0 \text{ or in steady state}) \\ k'_d = k_{logic} k_d & \text{else} \end{cases}$$

k_p , k_i and k_d are PID coefficients, k'_d is logical derivative coefficient, k_{logic} is the modifying coefficient for logical derivative and $k_{logic} \geq 1$. As discussed above, If $|e| < \delta_s$ is satisfied continuously for more than N_s sampling periods then we say that system is 'in steady state'. Where δ_s is the required steady state error and N_s is positive integer.

In the transient process, suitable k_{logic} leads to high controller bandwidth and phase lead, thus logical derivative can improve system dynamic response. However, in the steady state, the controller with logical derivative becomes a standard PID controller, hence logical derivative doesn't affect the stability of the whole control system [3].

Nutation Damping

In this paper, a new nutation damping strategy is proposed to damp down the nutation deteriorated by AMF-AVS and wheel external environmental disturbance torques. The nutation damping cross coupling network for tilt loops is shown as follows.

$$\begin{cases} u_{n1} = -\frac{k_{nut}}{k_{EM0}} J_{w0} \Omega_0 \frac{\kappa s^2}{s^2 + \kappa s + (\sigma_0 \Omega_0)^2} \cdot \frac{b}{s+b} \tilde{\phi}_w \\ u_{n2} = -\frac{k_{nut}}{k_{EM0}} J_{w0} \Omega_0 \frac{\kappa s^2}{s^2 + \kappa s + (\sigma_0 \Omega_0)^2} \cdot \frac{b}{s+b} \tilde{\phi}_w \end{cases} \quad (8)$$

In (8) $\frac{\kappa s^2}{s^2 + \kappa s + (\sigma_0 \Omega_0)^2}$ is a bandwidth filter, and κ is a positive real number. $\frac{b}{s+b}$ is a low pass filter, and b is a positive real number. k_{nut} is nutation damping gain and $k_{nut} > 0$.

The advantage of this nutation damping method is that the declining rate of nutation damping is independent of wheel rotational speed because the parameters of the nutation-damping network are functions of wheel rotational speed. In addition, by choosing a suitable nutation-damping gain, this nutation damping method is easy to realize nutation damping for MBMW with large time delay.

Non-linearity Compensator

According to (3), a compensator for making up for electromagnetic non-linearity in the tilt loops is designed as follows.

$$\begin{cases} u_{cx} = -\frac{k_{N0}}{k_{EM0}} \phi_e \\ u_{cz} = -\frac{k_{N0}}{k_{EM0}} \varphi_e \end{cases} \quad (9)$$

In (9), u_{cx} and u_{cz} are the non-linearity compensator outputs while ϕ_e and φ_e are the non-linearity compensator inputs or the observer outputs.

ROBUST STABILITY

According to the above two sections, we know that the closed-loop system containing the plant to be controlled, i.e. MBMW itself, and AMFC's control loop is nonlinear and time varying. Therefore, the following robust stability analysis follows an engineering method.

The AMFC only has its observer adaptively switched between two groups of parameters. One group of parameters is $[k_{11} \ k_{12} \ k_{21_off} \ k_{22_off}]^T = K_1$, the other group of parameters is $[k_{11} \ k_{12} \ k_{21_on} \ k_{22_on}]^T = K_2$. If characteristic variable $|y_ave|$ is larger than a steady-state threshold δ_1 and smaller than a saturation

threshold δ_2 , then K_2 is switched on as observer parameters, otherwise K_1 is switched on. Since y_ave is the average value of y_lpf in one wheel rotational period, then y_lpf can be expressed as $y_lpf \approx y_ave + f(\Omega, 2\Omega, \dots)$, where $\Omega = 2\pi/T_w$ and T_w is wheel rotational period. Suppose that both the closed-loop system containing K_1 and the closed-loop system containing K_2 are exponentially stable. Define area $I = \{y_ave \mid |y_ave| \leq \delta_1\}$, area $II = \{y_ave \mid \delta_1 < |y_ave| < \delta_2\}$, and area $III = \{y_ave \mid |y_ave| \geq \delta_2\}$. Since $\delta_1 \ll \delta_2$, then the stability analysis in area I , II and III can be carried on equivalently and separately in area I and II , and area II and III . First consider the stability in area I and II . If at time $N_1 T_w$ (N_1 is an integer), $|y_ave| > \delta_1$ and K_2 is switched on, then an integer N_2 ($N_2 > N_1$) must exist so that at time $N_2 T_w$, $|y_ave| \leq \delta_1$ and the observer parameters are switched to K_1 . From time $N_2 T_w$, if $|y_ave|$ keeps smaller than δ_1 , then it will converge to zero and the amplitude of $f(\Omega, 2\Omega, \dots)$ will converge too. After time $N_2 T_w$, if $|y_ave|$ is larger than δ_1 again, then it must become smaller at another time $N_3 T_w$ ($N_3 > N_2$, N_3 is an integer). If K_1 and K_2 are designed suitably, then after several times switches, the closed-loop system will converge to steady state. By the same kind of discussion, the stability in area II and III can also be analyzed if the saturation non-linearity does not make system unstable. As a result, If K_1 , K_2 , δ_1 , δ_2 and controller are designed reasonably, after finite times of switches the closed-loop system will enter steady state. In simulation, only one to three times switches occurred.

According to the transfer function of the closed-loop system, the exponential stability and robustness of the closed-loop system including K_1 and the closed-loop system including K_2 are analyzed separately. For the MBMW whose parameters are listed in Table 1, and the AMFC's control loop whose parameters are as listed in Table 2, the robust stability range of J_w , k_{EM} , $k_{N\phi}$, $k_{N\phi}$, Ω , and σ as a whole, i.e. $[J_w/J_{w0} \ k_{EM}/k_{EM0} \ k_{N\phi}/k_{N\phi0} \ k_{N\phi}/k_{N\phi0} \ \Omega/\Omega_0 \ \sigma/\sigma_0] = \Sigma/\Sigma_0 [1 \ 1 \ 1 \ 1 \ 1]$, is demonstrated in Table 3. Considering the time delay in electromagnets, which is modeled as $\frac{1}{\tau s + 1}$, where τ is time constant and $\tau = 0.01$ sec, the robust stability range of J_w , k_{EM} , $k_{N\phi}$, $k_{N\phi}$, Ω , and σ as a whole is demonstrated in Table 4.

For case H in Table 3, the root loci of the closed-loop system with respect to Σ/Σ_0 is demonstrated in Fig. 6, respectively. In Fig. 6, asterisks show the positions of the poles of the closed-loop system when J_w , k_{EM} , $k_{N\phi}$, $k_{N\phi}$, Ω , and σ reach their nominal values, i.e. $\Sigma/\Sigma_0 = 1$.

Table 1 parameters of MBMW

J_w	σ	k_{EM}	$k_{N\phi}(k_{N\phi})$	V_b	N_s	ϕ_r	φ_r	c_1, c_3, c_5	c_2, c_4, c_6
0.0129 kgm ²	1.85	0.0448Nm/V	3.4225Nm	0.8V	6	0.6deg	0.6deg	0.004deg	0.0005deg

Table 2 parameters of AMFC's control loop

κ	h	$k_p, gain$	$k_i, gain$	$k_d, gain$	k_{11}	k_{12}	k_{21}	k_{22}	a	k_{anti}	k_{logit}	δ_1	δ_2
32	10	121.2	150	15.64	1	2	0/20	0/5	25	k_{EM0}	5	10^{-5}	0.0035

Table 3 robust stability range of AMFC when $\tau = 0$ sec

Case	k_{11}	k_{12}	k_{21}	k_{22}	σ	r (rpm)	Σ/Σ_0
A	1	2	20	5	1.6	1000	0.7 ~ 1.24
B	↓	↓	↓	↓	↓	6000	0.6 ~ 1.25
C	↓	↓	↓	↓	1.85	1000	0.7 ~ 1.24
D	↓	↓	↓	↓	↓	6000	0.6 ~ 1.25
E	↓	↓	0	0	1.6	1000	0.6 ~ 1.47
F	↓	↓	↓	↓	↓	6000	0.4 ~ 1.47
G	↓	↓	↓	↓	1.85	1000	0.5 ~ 1.47
H	↓	↓	↓	↓	↓	6000	0.4 ~ 1.47

Table 4 robust stability range of AMFC when $\tau = 0.01$ sec

Case	A	B	C	D	E	F	G	H
Σ/Σ_0	0.7 ~ 1.03	0.6 ~ 1.0	0.7 ~ 1.02	0.6 ~ 1.0	0.6 ~ 1.03	0.4 ~ 1.0	0.6 ~ 1.02	0.4 ~ 1.0

SIMULATION

The AMFC method, MFC method [2], and H_∞ control method [1] are simulated for comparison. Both AMFC and MFC use the same kind of non-linearity compensator proposed in this paper. The parameters of MBMW are listed in Table 1. The parameters of AMFC's control loop are as listed in Table 2. MFC has the same parameters as AMFC except for adaptive mechanism, logical derivative, and nutation damping. The H_∞ controller is an eighth-order controller. The characteristics of electromagnetic non-linearity are shown in Fig. 7. In simulation, a step external environmental disturbance whose amplitude is 0.0005Nm is inserted in φ_w channel. The simulation results are shown in Fig. 8(a, b)~ Fig. 12(a, b).

Fig. 8(a, b) ~ Fig. 11(a, b) show the true values of the gimbaling angles when MFC/AMFC control method is used and when the wheel rotational speed is 1000rpm and 6000rpm, respectively. Fig. 12(a, b) show the true values of the gimbaling angles when H_∞ / AMFC control method is used and when the wheel rotational speed is 4000rpm.

Simulation results show that both AMFC method and MFC method are robust against wheel

rotational speed in a large range and have much better active-vibration suppression compared with H_∞ control method, although by using H_∞ control method almost no overshoot occurs. However, compared with MFC method, AMFC method keeps much smaller overshoot and shorter settling time for different wheel rotational speed and different position commands. Simulation results also show that the new nutation damping method is very effective for a large range of wheel rotational speed.

Although in simulation the AMFC method is only applied to a specific MBMW, the AMFC method is easy to be applied to any kind of actively controlled MBMWs. Furthermore, the AMFC method is also easy to realize in practical engineering. Applying the AMFC method to a prototype actively controlled MBMW owned by ISAS is being considered.

CONCLUSION

In this paper adaptive model following control method is presented. This method relies on adaptive bandwidth-regulation mechanism, controller with logical derivative, new nutation damping network and non-linearity compensator. Consequently this method is convenient to make compromise between dynamic response and active-vibration suppression at harmonic frequencies of the wheel rotation, and to damp nutation of the wheel rotor while keeping the closed-loop system stable.

Study results show that this method has great capability of active-vibration suppression, good dynamic response, and satisfactory nutation damping for a large range of wheel rotational speed. The robustness of this method with respect to system uncertain parameters is also strong. Therefore it is easy and possible to realize high-accuracy spacecraft attitude control by using the MBMW controlled by the AMFC method. Now, applying the MBMW controlled by the AMFC method to spacecraft attitude control is being considered.

ACKNOWLEDGEMENTS

The authors would like to express their honest thanks to Prof. I. Nakatani, Prof. T. Kubota (both of ISAS) and Dr. M. Inoue of Mitsubishi Electric Corporation for their useful comments.

REFERENCES

- [1] M.-R. Nam, T. Hashimoto and K. Ninomiya. Design of H_∞ Attitude Controllers for Spacecraft Using

- a Magnetically Suspended Momentum Wheel. European Journal of Control (1997), 3:114-124.
- [2] U. J. Bichler. A Low Noise Magnetic Bearing Wheel for Space Application. 2nd International Symposium on Magnetic Bearing, July 12-14, 1990, Tokyo, Japan, 1-8.
- [3] Yong-Chun Xie, Hong-Xin Wu, Zhen-Duo Lu. The All-Coefficient Adaptive Control Method and Its Application in Spacecraft Attitude Control. Space Technology, Vol.16, No.5/6, pp.331-336, 1996.
- [4] Myeong-Ryong Nam, Studies on the Attitude Control System for Spacecraft Employing a Magnetically-Suspended Momentum Wheel, Doctoral Dissertation, University of Tokyo, 1997.
- [5] U. Bichler, T. Eckardt, A 3(5) Degree of Freedom Electro-dynamic Bearing Wheel for 3-axis Spacecraft Attitude Control Applications, proceedings of the First International Symposium on Magnetic Bearings, ETH Zurich, June 6-8, 1988.

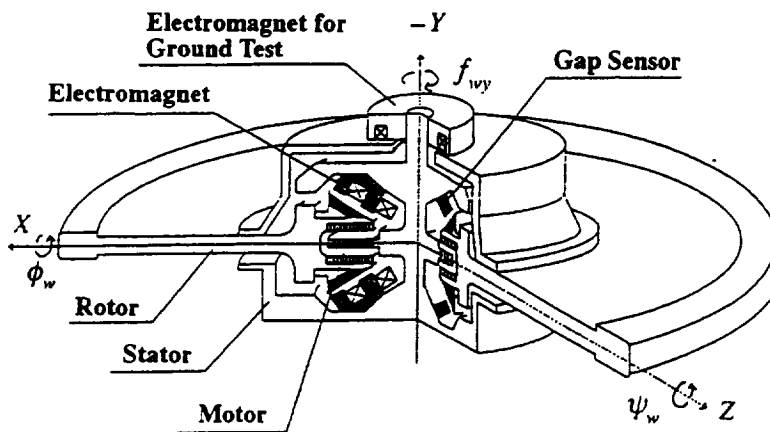


Fig. 1 Cross section of Octa-Electromagnet-Type Active Magnetic Bearing Momentum Wheel

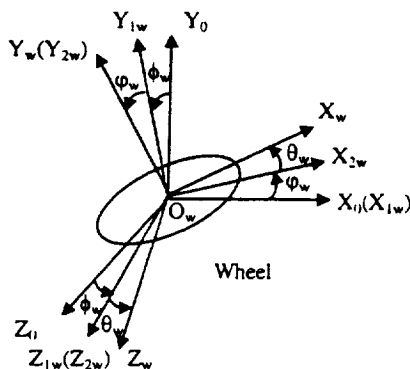


Fig. 2 Coordinate systems of MBMW

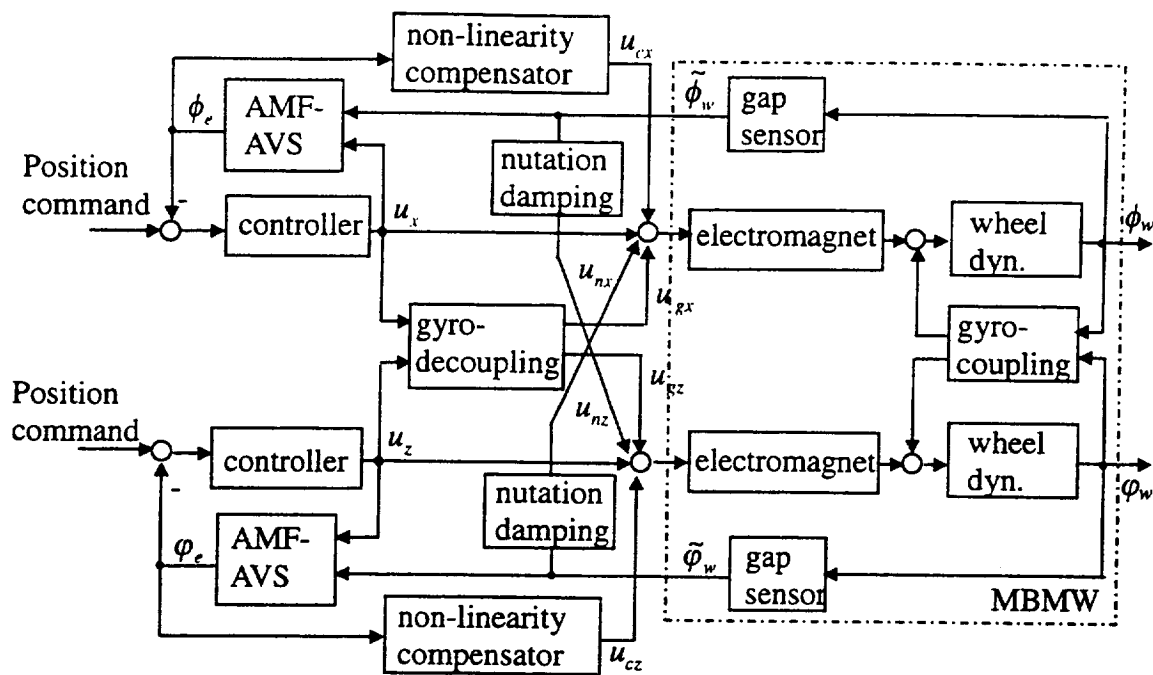


Fig. 3 AMFC in the tilt loops of MBMW

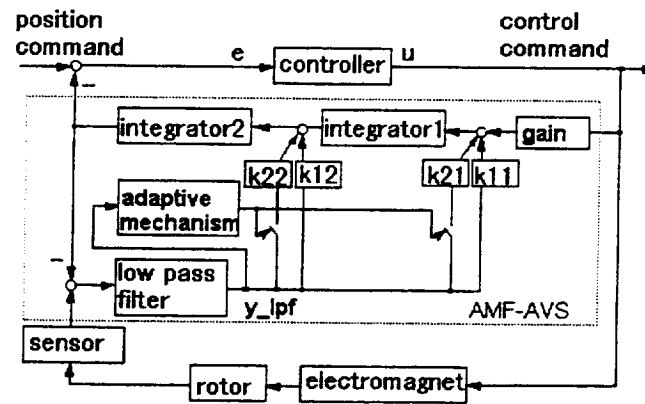


Fig. 4 Block diagram of AMF- AVS of AMFC

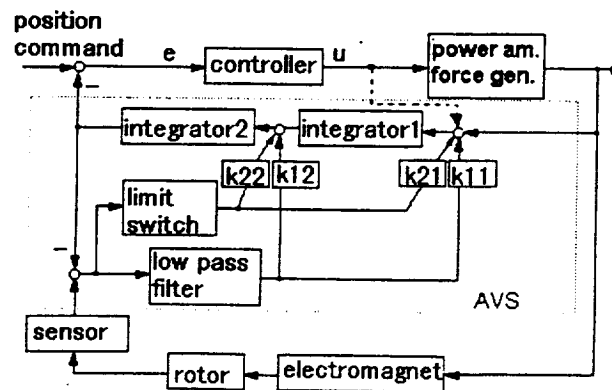


Fig. 5 Block diagram of AVS of MFC

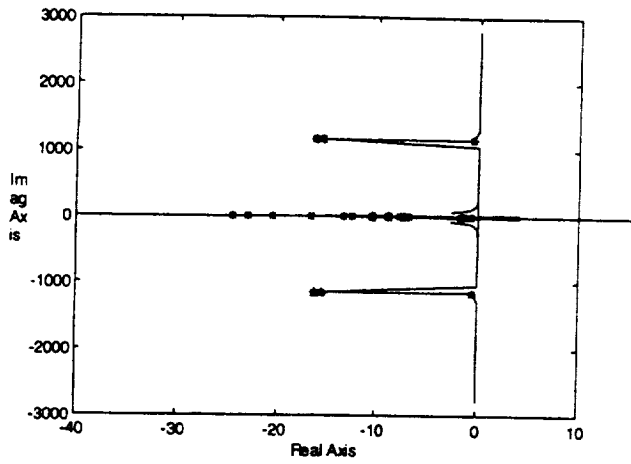


Fig. 6 Root locus of the closed-loop system with respect to Σ/Σ_0
(case H, $\Sigma/\Sigma_0 \in [0.25, 1.55]$)
(critical points: $\Sigma/\Sigma_0 = 0.34, 1.47$)

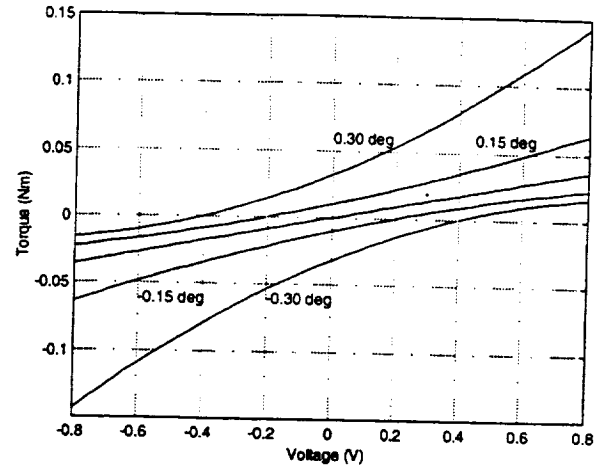
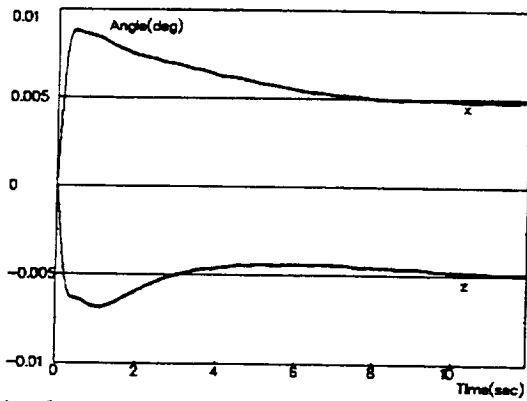
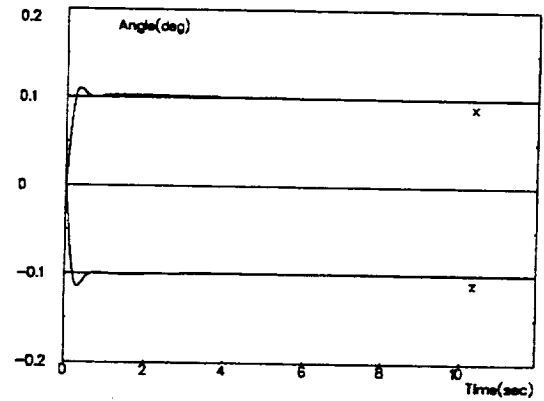


Fig. 7 Characteristics of electromagnetic non-linearity

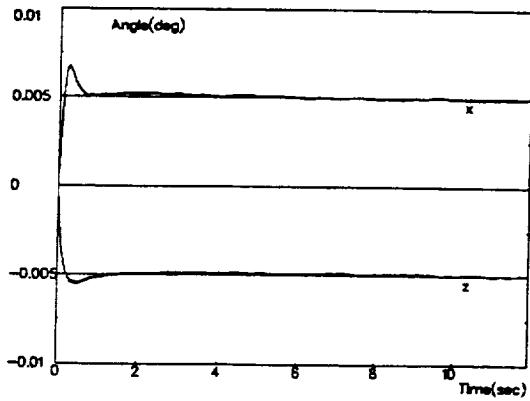


(a) when position commands are $\pm 0.005\text{deg}$

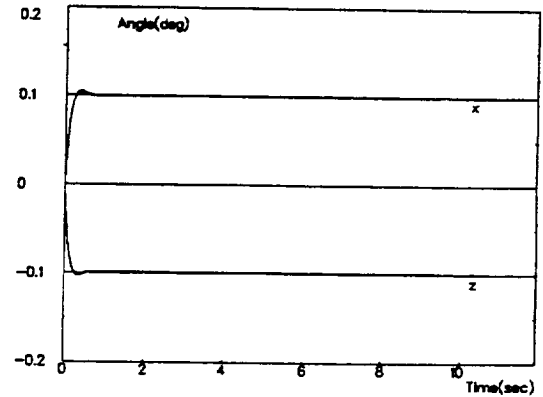


(b) when position commands are $\pm 0.1\text{deg}$

Fig. 8 Simulation results of MFC method (1000rpm)

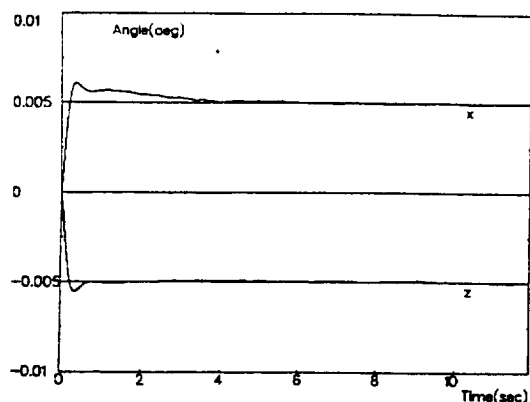


(a) when position commands are $\pm 0.005\text{deg}$

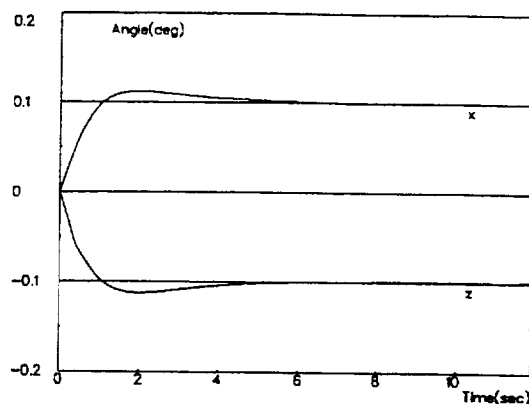


(b) when position commands are $\pm 0.1\text{deg}$

Fig. 9 Simulation results of AMFC method (1000rpm)

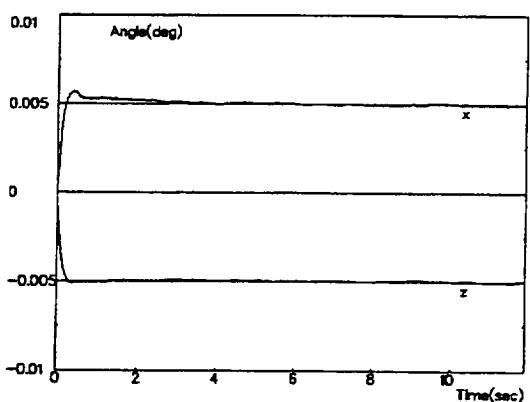


(a) when position commands are $\pm 0.005\text{deg}$

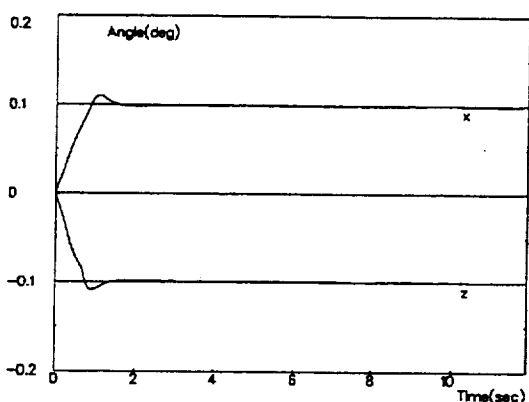


(b) when position commands are $\pm 0.1\text{deg}$

Fig. 10 Simulation results of MFC method (6000rpm)

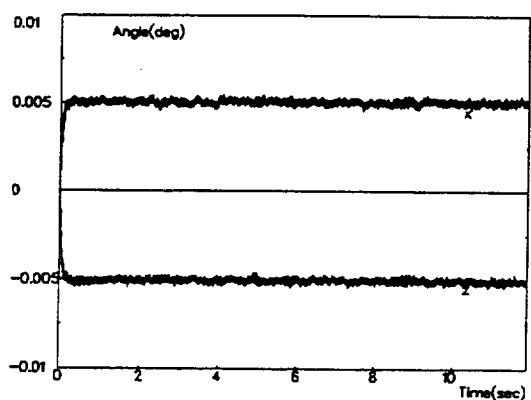


(a) when position commands are $\pm 0.005\text{deg}$

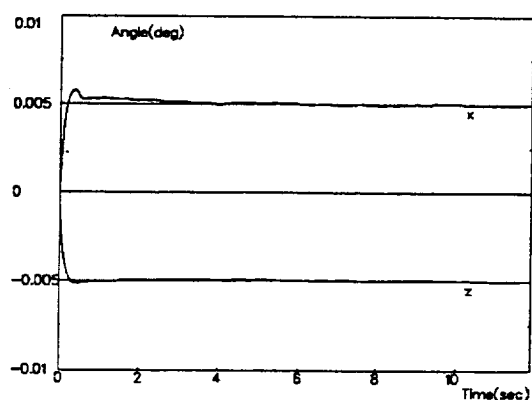


(b) when position commands are $\pm 0.1\text{deg}$

Fig. 11 Simulation results of AMFC method (6000rpm)



(a) H_∞ control method



(b) AMFC method

Fig. 12 Simulation results (4000rpm)

ACHIEVABLE ROBUSTNESS COMPARISON OF POSITION SENSED AND SELF-SENSING MAGNETIC BEARING SYSTEMS*

Nancy Morse Thibeault[†] Roy Smith[‡] Brad Paden[§] James Antaki[¶]

ABSTRACT

Two options for the control of a magnetic bearing system are considered and compared for achievable robustness. The first of these, the position sensed configuration, uses a measurement of the position of the rotor for feedback. The second configuration, the self-sensing configuration, attempts to achieve closed-loop stability and robustness using only a measurement of the electromagnet coil currents. We derive limits, independent of the choice of linear, time-invariant controller, on the achievable robustness in each case. We also consider how these limits change with changing bearing physical parameters as well as closed-loop system bandwidth and controller relative degree. Finally, we consider an example magnetic bearing system in order to determine the magnitude of these bounds for a real system.

*The authors would like to sincerely thank the McGowan Center for Artificial Organ Development and Magnetic Moments, LLC, for their financial support of this research. This work was also supported in part by NSF Grant ECS-9634498.

[†]Department of Mechanical Engineering, University of California at Santa Barbara, Santa Barbara, CA 93106-5070, nancy@engineering.ucsb.edu

[‡]Department of Electrical and Computer Engineering, University of California at Santa Barbara, Santa Barbara, CA 93106-2040, roy@ece.ucsb.edu

[§]Magnetic Moments LLC., 5733C Hollister Ave., Goleta, CA 93117, bpaden@mmsb.com

[¶]University of Pittsburgh, 420 Center for Biotechnology and Bioengineering, 300 Technology Dr., Pittsburgh, PA 15219, antaki@pittsburg.nb.upmc.edu

1 INTRODUCTION

Commonly used sensors, for the purpose of controlling a magnetic bearing system, are position sensors and current sensors. Position measurement is attractive because it provides direct information on the system property which is typically most important to regulate, the rotor position. However, achieving closed-loop stability by current measurement alone (known as the self-sensing bearing configuration) is desirable because of the low cost and simplicity of current sensors. Attracted by these potential benefits, many researchers have studied and implemented magnetic bearings using the self-sensing configuration [1]-[5]. However, these investigations have typically shown this configuration to yield low robustness to system unmodeled dynamics [1]-[6]. In the following development, we will offer an explanation of these findings by showing that the self-sensing configuration is particularly limited in its achievable robustness for any internally stabilizing, linear, time-invariant (LTI) controller. We show that these robustness limitations increase further with constraints placed on the closed-loop system bandwidth and controller relative degree. We will also investigate how the choice of magnetic bearing system parameters affects these robustness limits. In addition, we derive bounds on achievable robustness for the position sensed magnetic bearing configuration; however, we show that these bounds are typically much less restrictive than in the self-sensing case.

2 BASIC MAGNETIC BEARING SYSTEM MODEL

The system we will consider is the two-pole, single degree-of-freedom magnetic bearing shown in Figure 1. This system represents the fundamental building block for many more complicated magnetic bearing systems, and, as such, it offers the essential design challenges associated with magnetic bearings without unnecessary complexity. For our model derivation, we will make the following assumptions about our system. We assume that the levitated bar moves in only one degree-of-freedom, the x direction. In addition, we do not allow for any rotation or bending of the bar. This leads us to conclude that the gap lengths G_1 and G_2 must be the same when measured from either pole of the given electromagnet. The point at which $G_1 = G_2$, centered between the electromagnets, is an unstable equilibrium point; thus, active feedback control is required to achieve stability about this point. A list of the bearing system parameters is included in Table 1.

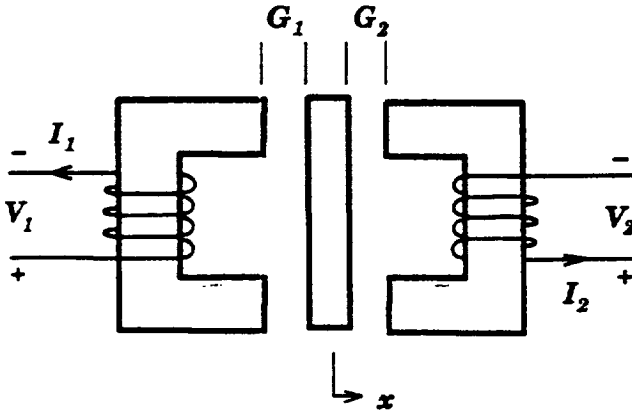


Figure 1: Two Electromagnet Magnetic Bearing System

A linearization of the bearing dynamics about

Symbol	Description
μ_0	Permeability of air
N	The number of turns in each coil
A_g	Gross sectional area of the air gap
m	Mass of the bar
G_0	The nominal gap value
R	The resistance of each coil
I_0	The bias current
V_0	The bias voltage
L	The coil inductance $L = \frac{\mu_0 N^2 A_g}{2G_0}$
k_I	The current force constant $k_I = \frac{2I_0}{mG_0}$
k_x	The position force constant $k_x = k_I \frac{I_0}{G_0}$

Table 1: Magnetic Bearing Parameters

the operating point

$$\begin{bmatrix} x & \dot{x} & I_1 & I_2 & \dot{I}_1 & \dot{I}_2 \end{bmatrix}^T = \begin{bmatrix} 0 & 0 & I_0 & -I_0 & 0 & 0 \end{bmatrix}^T, \quad (1)$$

where I_0 is a constant bias current, and making the following definitions $I_c := (I_1 + I_2)/2$ and $V_c := (V_1 + V_2)/2$, yields the linearized bearing system model:

$$\ddot{x} = k_x x + k_I I_c \quad (2)$$

$$\dot{I}_c = -\frac{R}{L} I_c - \frac{I_0}{G_0} \dot{x} + \frac{1}{L} V_c. \quad (3)$$

For this system there are several choices of measured outputs. In this paper we will analyze and compare two measurement configurations. The first uses a measurement of the rotor position x . We will refer to this as the Position Measurement (PM) configuration. Another output option is to measure the current I_c . We refer to this as the Current Measurement (CM) (or Self-Sensing) configuration. Transfer function representations of the PM and CM configurations, respectively, are given

below.

$$y_{PM}(s) = x(s) = \frac{\frac{k_x}{l}}{s^3 + \frac{R}{l}s^2 - \frac{R}{l}k_x} V_c(s) \quad (4)$$

$$y_{CM}(s) = I_c(s) = \frac{\frac{1}{l}(s^2 - k_x)}{s^3 + \frac{R}{l}s^2 - \frac{R}{l}k_x} V_c(s) \quad (5)$$

Both of these transfer functions are controllable and observable and share the characteristic equation $s^3 + \frac{R}{l}s^2 - \frac{R}{l}k_x$ which has one real, unstable pole which we will denote p_0 , and two other stable poles. The CM configuration, a SISO system, has a real, non-minimum phase (NMP) zero located at $s = \sqrt{k_x}$ which we denote z_0 . The PM system has no finite transmission zeros.

We next consider the closed-loop system with P , representing the magnetic bearing system in either the PM or CM configuration, in feedback with the controller, C . This closed-loop system has a loop gain of $L = PC$ along with sensitivity and complementary sensitivity functions S and T as follows:

$$S(s) := \frac{1}{1 + L(s)} \quad T(s) := \frac{L(s)}{1 + L(s)}. \quad (6)$$

From this we see that the poles of L are zeros of S and the zeros of L are zeros of T . Therefore, the following relationships hold: $S(p_0) = 0$, $T(p_0) = 1$. In the CM configuration, the following relationships also hold: $S^{CM}(z_0) = 1$, and $T^{CM}(z_0) = 0$.

In the following development, we will investigate certain limits on the achievable sensitivity and complementary sensitivity reduction which result from the interpolation conditions on S and T given above. Additional constraints on S and T can be derived by considering their behavior at high frequencies. For practical systems, $L(j\omega) \rightarrow 0$ as $\omega \rightarrow \infty$. Thus, $S = \frac{1}{1+L(s)} \rightarrow 1$ and $T = \frac{L(s)}{1+L(s)} \rightarrow 0$ as $\omega \rightarrow \infty$. In fact, not only are the magnitudes

of S and T bounded at high frequencies but also the rate of convergence of each is bounded, the rate bound depending on the relative degree of L . These high frequency constraints on S and T can provide additional robustness and performance limits for our magnetic bearing system as we will show in the development that follows. The following constraint, adapted from [10], will be imposed upon our magnetic bearing system to determine the effect of such high frequency affects as finite closed-loop system bandwidth and non-zero controller relative degree on the achievable robustness of our system.

Constraint 1 *Let ω_c be equal to the desired bandwidth of T and let k be a non-negative integer equal to the relative degree of L . Then given $\rho \in \mathbb{R}$, $1 \geq \rho > 0$, let S and T be constrained in high frequencies as follows:*

$$|S(j\omega) - 1| = |T(j\omega)| \leq \rho \left(\frac{\omega_c}{\omega} \right)^k \quad \forall \omega \geq \omega_c. \quad (7)$$

In the analysis that follows, we will employ the \mathcal{H}_∞ system norm which is defined for a stable, LTI, SISO system $G(s)$ as follows:

$$\|G\|_\infty := \sup_{\omega \in \mathbb{R}} |G(j\omega)|.$$

3 MEASURES OF ROBUSTNESS

We now introduce two measures of robustness based on the sensitivity and complementary sensitivity functions. We will use these robustness measures in the following development to bound the achievable robustness of our various system configurations.

A classical measure of robustness for SISO systems is the distance from the Nyquist plot of

the system loop transfer function L to the critical point $(-1, 0)$. This distance is exactly $\frac{1}{\|S\|_\infty}$. Therefore, large values of $\|S\|_\infty$ imply poor robustness for SISO systems.

Similarly, constraints of the form $\|T(s)\|_\infty \geq \beta$ are directly linked to classical gain and phase margin ideas of robustness for both MIMO and SISO systems. The block diagram of Figure 2 represents our magnetic bearing system model P , perturbed as $P(1 + \Delta)$ where Δ is an unknown, norm bounded perturbation. The transfer function seen by Δ , an output multiplicative uncertainty in the plant, is simply $-T$. Thus, from the small gain theorem [13],

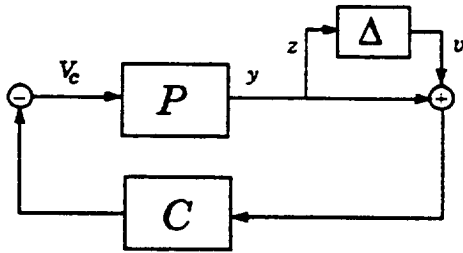


Figure 2: Bearing System with Output Multiplicative Perturbation

we have the following result.

Remark 2: Output Multiplicative Stability Margin *The system of Figure 2 is guaranteed to remain stable for all unknown bounded systems Δ such that*

$$\|\Delta\|_\infty < \frac{1}{\|T\|_\infty} \quad (8)$$

and there exists a destabilizing LTI system Δ satisfying:

$$\|\Delta\|_\infty = \frac{1}{\|T\|_\infty}. \quad (9)$$

4 ROBUSTNESS LIMITS OF THE PM CONFIGURATION

4.1 SENSITIVITY BOUNDS

The PM system is a SISO system with an unstable pole. Therefore, the following integral constraint on the sensitivity function holds [9]:

$$\int_0^\infty \log |S^{\text{PM}}(j\omega)| d\omega = \pi p_0. \quad (10)$$

Since $p_0 \in \mathbb{R}$, $p_0 > 0$, this constraint tells us that for some frequency range, $|S^{\text{PM}}(j\omega)| > 1$. Thus,

$$\|S^{\text{PM}}\|_\infty > 1. \quad (11)$$

If we constrain S^{PM} at high frequencies as given in Constraint 1, the peak magnitude of S^{PM} overall increases. The following theorem characterizes this phenomenon more precisely.

Theorem 3 *Consider P to be the linear model of our PM magnetic bearing system given in (4) with unstable pole p_0 . Assume C is an LTI, internally stabilizing controller for our system in feedback as shown in Figure 2. Denote the sensitivity function for this closed-loop system as S^{PM} defined as in (6) and assume that the high frequency bounds of Constraint 1 apply. Then the following bound holds:*

$$\|S^{\text{PM}}\|_\infty \geq e^{\left[\frac{\pi p_0}{\omega_c} - \frac{1}{\omega_c} \int_{\omega_c}^\infty \log \left[\rho \left(\frac{\omega}{\omega_c} \right)^k + 1 \right] d\omega \right]}.$$

Proof: The proof combines the procedure outlined in the proof of Theorem 3 of [9] with the high frequency constraint analysis of [10].

Note that the bound derived above on $\|S^{\text{PM}}\|_\infty$ requires the condition that $k \geq 2$. However, since k is the relative degree of L and P^{PM} itself has a relative degree of 3, this condition is always satisfied.

4.2 COMPLEMENTARY SENSITIVITY BOUNDS

Since our PM magnetic bearing system is an unstable, minimum-phase system, we may use Lemma A.1 of [9], to deduce the following bound:

$$\|T^{\text{PM}}\|_{\infty} > 1 \quad (12)$$

Note: To derive this bound, we make the assignment $f(s) = T^{\text{PM}}(s)$ in Lemma A.1 of [9] and employ the fact that $T^{\text{PM}}(p_0) = 1$.

With the application of high frequency constraints on T , its lower bound will increase further as shown in the following theorem.

Theorem 4 Consider P to be the linear model of our PM magnetic bearing system given in (4) and p_0 its unstable pole. Assume C is an LTI, internally stabilizing controller for our system connected as shown in Figure 2. Denote the closed-loop complementary sensitivity function as T^{PM} defined as in (6) and assume that the high frequency bounds of Constraint 1 apply. Then if we define

$$\begin{aligned} \phi_c &:= \tan^{-1}(\omega_c/p_0) \\ \alpha &:= \frac{\pi/2}{\phi_c} \\ Cl_2(\theta) &:= -\int_0^{\theta} \log\left(2 \sin \frac{z}{2}\right) dz \\ I(\phi_c) &:= Cl_2(2\phi_c) + Cl_2(\pi - 2\phi_c) \end{aligned}$$

where Cl_2 is the Clausen integral [11], the following bound results:

$$\|T^{\text{PM}}\|_{\infty} \geq \left(\frac{1}{\rho}\right)^{(\alpha-1)} \left[\left(\frac{p_0}{\omega_c}\right)^{(\alpha-1)} e^{\frac{I(\phi_c)}{2\phi_c}}\right]^k.$$

Proof: The proof of this result combines the analysis of Theorem 2 of [10] with that of Equation (12) above. ■

5 ROBUSTNESS LIMITS OF THE CM CONFIGURATION

5.1 SENSITIVITY BOUNDS

Through the application of Poisson's integral formula, Freudenberg and Looze [9] derive the following bound on the sensitivity function of any linear, time-invariant system, such as our linearized bearing system in the CM configuration, with an unstable pole p_0 and a NMP zero z_0 that is stabilized by a linear, time-invariant controller.

$$\|S^{\text{CM}}\|_{\infty} \geq \left| \frac{p_0 + z_0}{p_0 - z_0} \right| \quad (13)$$

Notice that this bound becomes infinite as p_0 and z_0 approach each other.

If we constrain S^{CM} at high frequencies as given in Constraint 1, then we obtain the following bound on the sensitivity function which, as we will show later using a practical example, can be a more restrictive bound than Equation (13).

Theorem 5 Consider P to be the linear model of our CM magnetic bearing system given in (5) and C to be an LTI, internally stabilizing controller for our system in feedback as shown in Figure 2. Denote the sensitivity function for this closed-loop system as S^{CM} defined as in (6) and assume that the high frequency bounds of Constraint 1 apply. Let p_0 and z_0 denote the RHP pole and zero of P , respectively. Then if we define

$$\begin{aligned} \beta &:= \frac{\pi/2}{\psi_c} \\ \psi_c &:= \tan^{-1}(\omega_c/z_0) \\ d\theta_{z_0}(\omega) &:= \frac{z_0}{z_0^2 + \omega^2} d\omega, \end{aligned}$$

the following bound holds:

$$\|S^{\text{CM}}\|_{\infty} \geq \left| \frac{p_0 + z_0}{p_0 - z_0} \right|^{\beta} e^{\left[-\frac{1}{\psi_c} \int_{-\infty}^{\infty} \log\left[\rho\left(\frac{\omega}{z_0}\right)^k + 1\right] d\theta_{z_0}(\omega)\right]}.$$

Proof: The proof is a simple modification of Theorem 1 of Freudenberg and Looze [9]. ■

5.2 COMPLEMENTARY SENSITIVITY BOUNDS

Bounds on complementary sensitivity can be derived using similar techniques. From Looze and Freudenberg [10], we have for our CM configuration:

$$\|T^{CM}\|_{\infty} \geq \left| \frac{z_0 + p_0}{z_0 - p_0} \right|. \quad (14)$$

Additionally, Looze and Freudenberg [10] show that high frequency limitations on the magnitude and convergence rate of T^{CM} further constrain the achievable complementary sensitivity reduction. If we bound T^{CM} at high frequencies as shown in Constraint 1, we obtain the following bound on the achievable $\|T^{CM}\|_{\infty}$.

Theorem 6 Consider P to be the linear model of our CM magnetic bearing system given in (5) and C to be an LTI, internally stabilizing controller for our system connected as shown in Figure 2. Denote the closed-loop complementary sensitivity function as T^{CM} defined as in (6) and assume that the high frequency bounds of Constraint 1 apply. Let p_0 and z_0 denote the RHP pole and zero of P , respectively. Then if we define

$$\begin{aligned} \phi_c &:= \tan^{-1}(\omega_c/p_0) \\ \alpha &:= \frac{\pi/2}{\phi_c} \\ Cl_2(\theta) &:= -\int_0^{\theta} \log\left(2 \sin \frac{z}{2}\right) dz \\ I(\phi_c) &:= Cl_2(2\phi_c) + Cl_2(\pi - 2\phi_c) \end{aligned}$$

where Cl_2 is the Clausen integral [11], the fol-

lowing bound results:

$$\|T^{CM}\|_{\infty} \geq \left(\left| \frac{z_0 + p_0}{z_0 - p_0} \right| \right)^{\alpha} \left(\frac{1}{\rho} \right)^{(\alpha-1)} \times \left[\left(\frac{p_0}{\omega_c} \right)^{(\alpha-1)} e^{\frac{I(\phi_c)}{2\phi_c}} \right]^k.$$

Proof: This proof closely parallels that given in Theorem 2 of [10]. ■

Notice the similarity of these bounds with the PM bounds given in Section 4. For the CM bounds, the term $\left| \frac{z_0 + p_0}{z_0 - p_0} \right|$ replaces the quantity 1 in the PM bounds. Thus, the CM bounds are typically much larger than the PM bounds.

6 DESIGN IMPLICATIONS

In order to give realistic numerical values to the robustness and performance limitations derived above, we evaluate them for a real magnetic bearing system. For this purpose, we consider the MBC500 magnetic bearing system [8] which has the parameter values given in Table 2. For a magnetic bearing system with these parameter values, the unstable pole and non-minimum phase zero are, respectively,

$$p_0 = 248.55 \text{ rad/sec} \quad z_0 = 295.73 \text{ rad/sec.}$$

μ_0 : $4\pi \times 10^{-7} \frac{\text{Wb}}{\text{A}\cdot\text{m}}$	R : 2.2 ohms
N : 220 turns	I_0 : 0.5 A
A_g : $4.84 \times 10^{-5} \text{ m}^2$	L : 3.68 mH
m : 0.1315 kg	k_f : $7.00 \times 10^4 \frac{\text{mm}}{\text{A}\cdot\text{s}^2}$
G_0 : 0.4 mm	k_x : $8.74 \times 10^4 \frac{1}{\text{s}^2}$

Table 2: MBC500 Magnetic Bearing Parameter Values

Table 3 below contains an evaluation of the bounds on $\|S\|_\infty$ and $\|T\|_\infty$ given in Equations (11), (12), (13) and (14) for both magnetic bearing configurations assuming no high frequency constraints on $S(j\omega)$ and $T(j\omega)$ and given the parameter values specified in Table 2. In addition, it gives a value of $\|S\|_\infty$ and $\|T\|_\infty$ which has been achieved by solving a μ -Synthesis design and optimizing either $\|S\|_\infty$ or $\|T\|_\infty$. Notice that the lower bound values and the achieved norms differ by only a small amount for each configuration. This indicates that the lower bounds capture accurately the fundamental system properties that are limiting the achievable sensitivity or complementary sensitivity reduction in each configuration.

	CM Bearing	PM Bearing
$\ S\ _\infty$ Lower Bound	11.538	1
$\ T\ _\infty$ Lower Bound	11.538	1
$\ S\ _\infty$ Achieved	11.578	1.0235
$\ T\ _\infty$ Achieved	11.564	1.0349

Table 3: Upper and Lower Bounds on $\|S\|_\infty$ and $\|T\|_\infty$ for each Configuration

6.1 ROBUSTNESS LIMIT EVALUATIONS

6.1.1 PM CONFIGURATION: All magnetic bearings in the PM configuration stabilized by an LTI controller satisfy the following bounds:

$$\|S^{PM}\|_\infty \geq 1 \quad \text{and} \quad \|T^{PM}\|_\infty \geq 1 \quad (15)$$

as we showed in Equations (11) and (12). Furthermore, the sensitivity and complementary

sensitivity bounds of the PM configuration are affected by high frequency magnitude constraints of the type given in Constraint 1 as shown in Theorems 3 and 4. Figures 3 and 4 show how these lower bounds on $\|S^{PM}\|_\infty$ and $\|T^{PM}\|_\infty$ are affected by choice of ω_c , ρ and k . Notice that the most significant factor leading to high sensitivities is the closed-loop bandwidth ω_c . The highest bounds occur when low ω_c is combined with high k or low ρ values. This is simply the classic "water bed" effect.

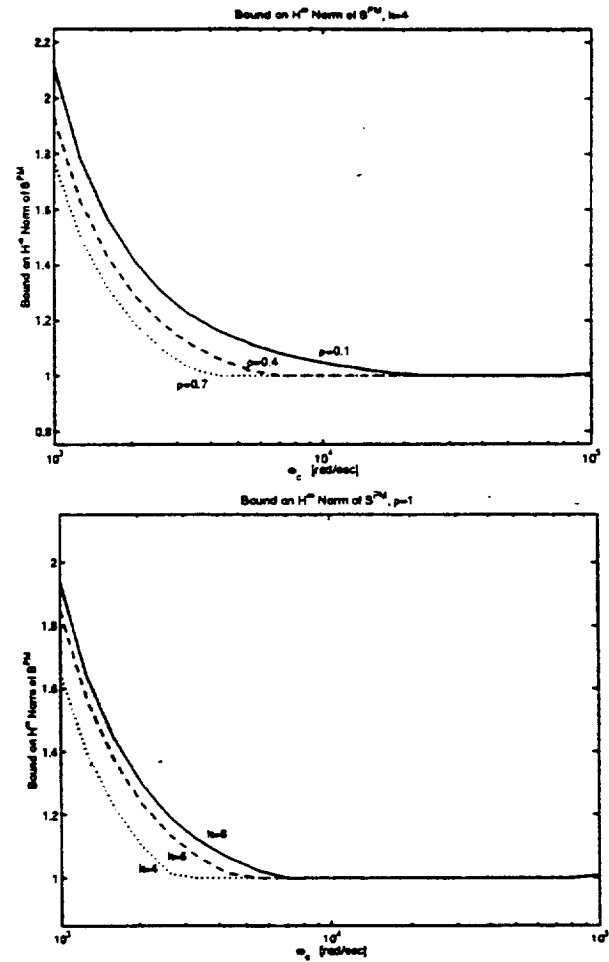


Figure 3: Bound on PM Configuration $\|S^{PM}\|_\infty$ for Varying ω_c , ρ and k

6.1.2 CM CONFIGURATION: The plots given in Figure 5 show how the

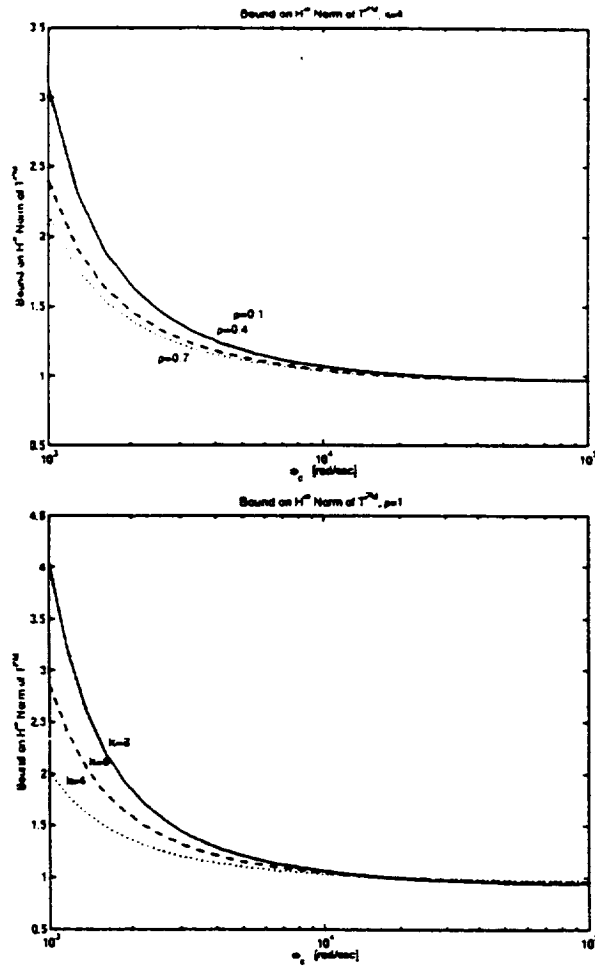


Figure 4: Bound on PM Configuration $\|T^{PM}\|_{\infty}$ for Varying ω_c , ρ and k

bound on $\|S^{CM}\|_{\infty}$ in Theorem 5 for the CM system varies with different values of ω_c , ρ and k . Similarly, Figure 6 shows how the bound on $\|T^{CM}\|_{\infty}$ from Theorem 6 varies as we change ω_c , ρ and k . Again, the largest factor affecting peaks in S^{CM} and T^{CM} in Figures 5 and 6 is low closed-loop bandwidth ω_c . In addition, combining low ω_c with small values of ρ or high values of k produce especially high peaks. This has important implications for controller design. A primary reason for choosing the CM configuration is the low cost associated with having no position sensor. However, if high bandwidth is required in order to achieve acceptable robustness and

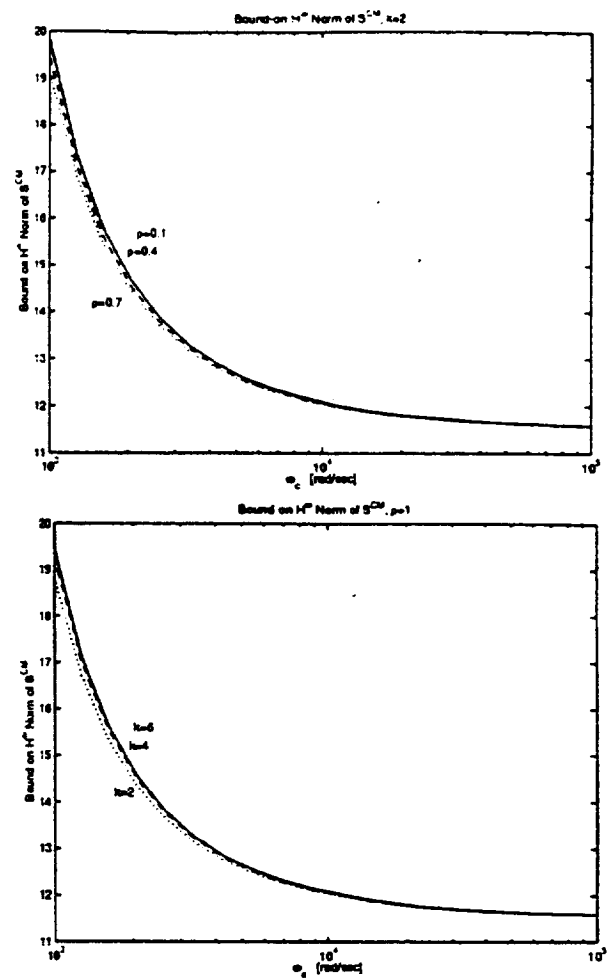


Figure 5: Bound on CM Configuration $\|S^{CM}\|_{\infty}$ for Varying ω_c , ρ and k

performance, then the configuration may cease to be a low cost option.

We now consider the effect of varying the bearing system parameters on the sensitivity and complementary sensitivity bounds. We first make the observation that in the CM case, both $\|S^{CM}\|_{\infty}$ and $\|T^{CM}\|_{\infty}$ are bounded by the same quantity. Define

$$B_{CM} := \left| \frac{p_0 + z_0}{p_0 - z_0} \right|. \quad (16)$$

From equations (13) and (14) we see that $\|S^{CM}\|_{\infty} \geq B_{CM}$ and $\|T^{CM}\|_{\infty} \geq B_{CM}$. Figure 7 shows how this lower bound on both

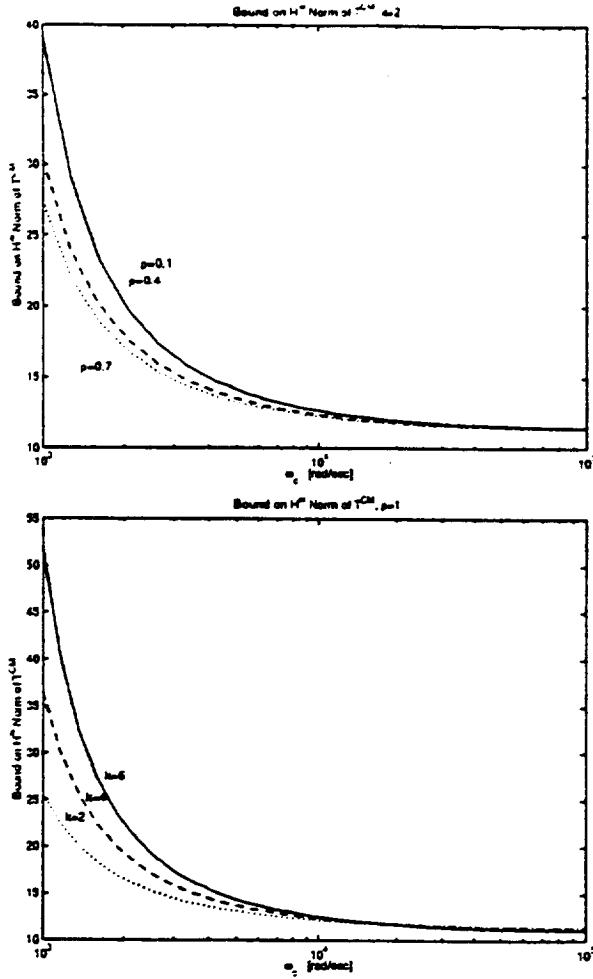


Figure 6: Bound on CM Configuration $\|T^{CM}\|_{\infty}$ for Varying ω_c , ρ and k

$\|S^{CM}\|_{\infty}$ and $\|T^{CM}\|_{\infty}$ in the CM case varies as the system parameters R , I_0 , G_0 , m , and $N^2 A_g$ vary. Each plot varies only one parameter at a time, spanning a range of $\pm 50\%$ of its nominal MBC500 bearing system value, while holding the other parameters fixed at the value used in the MBC500 bearing system.

All magnetic bearing systems have some inefficiency due to eddy currents, hysteresis, flux leakage, etc. For practical magnetic bearing systems, a constant γ called a derating factor, multiplying the force dynamics as shown below, is used to account for this loss in the sys-

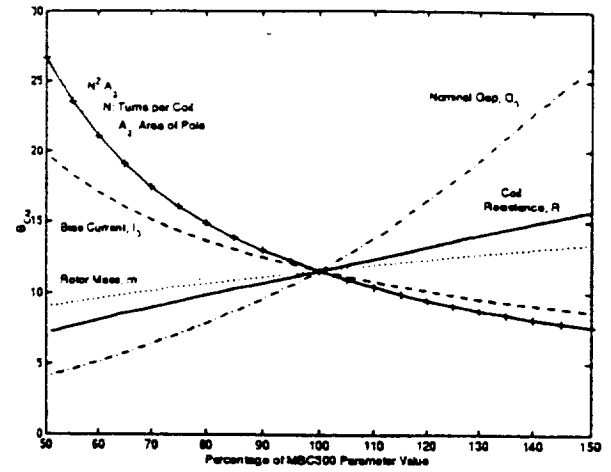


Figure 7: Bound on CM Configuration $\|S^{CM}\|_{\infty}$ and $\|T^{CM}\|_{\infty}$ for Varying Bearing Parameters R , I_0 , G_0 , m , and $N^2 A_g$

tem.

$$\ddot{x} = \gamma(k_x x + k_f I_c) \quad (17)$$

Figure 8 shows how the bound on $\|S^{CM}\|_{\infty}$ and $\|T^{CM}\|_{\infty}$ varies as γ varies from 0.5 to 1. Typical values for this derating factor are 0.6 or 0.7. Note from Figure 8 that for the MBC500 bearing system in the CM configuration, a derating factor of 0.6 causes a 21% increase in B_{CM} from its underrated value.

All of the plots in Figures 7 and 8 consider only one parameter varying at a time; however, to get an accurate view of the best and worst that the sensitivity and complementary sensitivity bounds can be in the CM case, we must vary all of the parameters simultaneously. Varying R , I_0 , G_0 , m , $N^2 A_g$ and γ simultaneously within the ranges plotted in Figures 7 and 8 we find the following best and worst case bounds, respectively:

$$B_{CM} = 2.0445 \quad \text{and} \quad B_{CM} = 337.22. \quad (18)$$

Now considering B_{CM} as a bound on $\|S^{CM}\|_{\infty}$, in the case of $B_{CM} = 2.0445$, the Nyquist plot

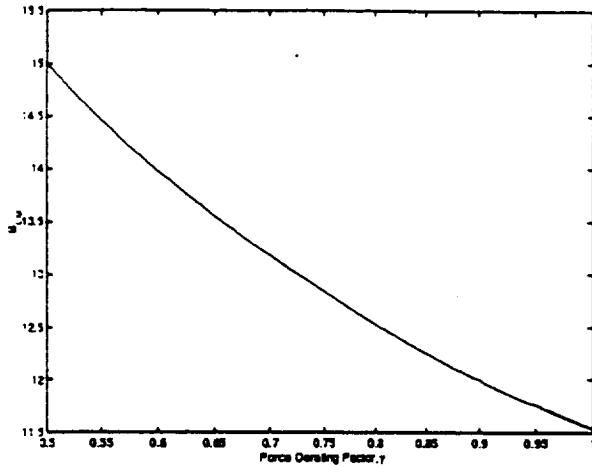


Figure 8: Bound on CM Configuration $\|S^{CM}\|_{\infty}$ and $\|T^{CM}\|_{\infty}$ for Varying Derating Factor, γ

for this system passes with a ball of radius $\frac{1}{2.0445} \approx 0.5$ of the critical point. The Nyquist plot associated with the CM system of bound $B_{CM} = 337.22$, however, passes within a ball of radius $\frac{1}{337.22} \approx 0.003$ of the critical point representing very poor robustness. Thus, the choice of the bearing dimensions and other physical properties can be critical to the achievable robustness of the controlled system when using the CM configuration.

7 CONCLUSION

The CM magnetic bearing configuration, although lower in cost and simpler to build than a PM bearing system, suffers from lower robustness to modeling uncertainties. The above analysis shows theoretically the reasons for reduced robustness in the CM case, that is, a near unstable pole/zero cancelation which causes the rotor position to be nearly unobservable in this configuration. In fact, limits have been given, which can be computed for any bearing system under consideration, which bound the robustness achievable by any linear controller in feedback with the linearized

bearing model in the CM configuration. We have shown, by considering the MBC500 bearing system as a typical example, that the difference in these limits between the CM and PM configurations can be significant.

However, we also saw in (18) and Figures 7 and 8 that the robustness limitations for the CM configuration can vary significantly with changing bearing physical parameters and system properties such as closed-loop system bandwidth and controller relative degree. Using the analysis provided above, a magnetic bearing designer can use constraints on the physical properties of a given bearing system along with available controller bandwidth information, and closed-loop robustness requirements to determine if the CM configuration is a viable control option for a given application.

ACKNOWLEDGMENT

The authors would like to thank Jim Freudenberg, University of Michigan at Ann Arbor, for helpful discussions related to this research.

References

- [1] Vischer, D. and H. Bleuler, "A New Approach to Sensorless and Voltage Controlled AMBs Based on Network Theory Concepts," Proceedings of the Second International Symposium on Magnetic Bearings, July 12-14, 1990, pp. 301-306.
- [2] Bleuler, H., D. Vischer, G. Schweitzer, A. Traxler and D. Zlatnik, "New Concepts for Cost-Effective Magnetic Bearing Control," Automatica, Vol. 30, No. 5, 1994, pp. 871-876.
- [3] Mizuno, T., H. Bleuler, H. Tanaka, H. Hashimoto, F. Harashima, H. Ueyama, "Industrial Application of Position Sensorless Active

Magnetic Bearings." Electrical Engineering in Japan, Vol. 117, No. 5, 1996, pp. 124-133.

[4] Mohamed, A. M, F. Matsumura, T. Namerikawa, J. Lee, "Modeling and Robust Control of Self-Sensing Magnetic Bearings with Unbalance Compensation," Proceedings of the 1997 IEEE International Conference on Control Applications, October 1997, pp. 586-594.

[5] Noh, M. D., E. H. Maslen, "Self-Sensing Magnetic Bearings Using Parameter Estimation," IEEE Transactions on Instrumentation and Measurement, Vol. 46, No. 1, February 1997, pp. 45-50.

[6] Kucera, L. "Robustness of Self-Sensing Magnetic Bearing," Magnetic Bearings Industrial Conference, Alexandria, USA, 1997. Also available on the web: <http://www.ifr.mavt.ethz.ch/ifr.html>.

[7] Havre, K. and S. Skogestad, "Effect of RHP Zeros and Poles on Performance in Multivariable Systems," Proceedings of the UKACC International Conference on Control '96, Exeter, UK, Sept. 1996, pp. 491-496.

[8] Paden, B., N. Morse, and R. Smith, "Magnetic Bearing Experiment for Integrated Teaching and Research Laboratories," Proceedings of the 1996 IEEE International Conference on Control Applications, Dearborn, MI, Sept. 15-18, 1996, pp. 421-425.

[9] Freudenberg, J. S. and D. P. Looze, "Right Half Plane Poles and Zeros and Design Tradeoffs in Feedback Systems," IEEE Transactions on Automatic Control, Vol. AC-30, No. 6, June 1985.

[10] Looze, D. P. and J. S. Freudenberg, "Limitations of Feedback Properties Imposed by Open-Loop Right Half Plane Poles," IEEE Transactions on Automatic Control, Vol. 36, No. 6, June 1991.

[11] Prudnikov, A. B., Yu A. Brychkov, and O. I. Marichev, *Integral and Series, Volume I: Elementary Functions*, New York, Gordon and

Breach, 1986, Translated from *Inegraly i ryady*, Moscow, Nauka.

[12] Gómez, G. I. and G. C. Goodwin, "Integral Constraints on Sensitivity Vectors for Multivariable Systems," Automatica, Vol. 32, No. 4, pp.499- 518, 1996.

[13] Zhou, Kemin, J. Doyle, and K. Glover, *Robust and Optimal Control*, Printice Hall, 1996, pp. 217-219.

ADAPTIVE COMPENSATION OF SENSOR RUNOUT FOR MAGNETIC BEARINGS WITH UNCERTAIN PARAMETERS: THEORY AND EXPERIMENTS

Joga D. Setiawan Ranjan Mukherjee

Department of Mechanical Engineering
Michigan State University
East Lansing, MI 48824-1226

Eric H. Maslen
Department of Mechanical and Aerospace Engineering
University of Virginia
Charlottesville, VA 22903

SUMMARY

The problem of sensor runout in magnetic bearing systems has been largely overlooked due to similarities with mass unbalance in creating periodic disturbances. While the effect of mass unbalance can be significantly reduced, if not eliminated, through rotor balancing, sensor runout disturbance is unavoidable since it originates from physical nonconcentricity between rotor and stator. Sensor runout is also caused by nonuniform electrical and magnetic properties around the sensing surface. To improve performance of magnetic bearings, we present an adaptive algorithm for sensor runout compensation. It guarantees asymptotic stability of the rotor geometric center and on-line feedforward cancellation of runout disturbances using persistent excitation. Some of the advantages of our algorithm include simplicity of design and implementation, stability, and robustness to plant parameter uncertainties. The stability and robustness properties are derived from passivity of the closed-loop system. Numerical simulations are presented to demonstrate efficacy of the algorithm and experimental results confirm stability and robustness for large variation in plant parameters.

I. INTRODUCTION

Active magnetic bearings have a number of advantages over conventional bearings. These advantages include elimination of lubrication system, friction free operation, operation capability at temperature extremes and at higher rpm, reduced power consumption, and adjustable stiffness and damping characteristics achieved through active control of bearing forces. The bearing forces are also used for cancelling periodic disturbances, which, common in rotating machinery, cause vibration, degrade performance, and sometimes lead to instability.

The dominant sources of periodic disturbance in magnetic bearings are mass unbalance and sensor runout. Mass unbalance results from lack of alignment between the geometric axis and the principal axis of inertia, and results in an unbalance force synchronous with rotor angular speed. Mass unbalance can be significantly reduced in industrial applications, if not completely eliminated, by rotor balancing. In comparison, sensor runout is unavoidable since it results from manufacturing imperfections in the magnetic bearing assembly. Specifically, sensor runout disturbance originates from lack of concentricity of the sensing surface, and non-uniform electrical

or magnetic properties around the sensing surface. Unlike mass unbalance, sensor runout also generates disturbance at multiple harmonics of angular speed. Despite differences between mass unbalance and sensor runout disturbances, the control objective for their compensation is often similar. Stabilization of the rotor about the geometric center, which is the objective for sensor runout compensation, is often the objective for unbalance compensation.

Though few researchers (Setiawan, et al., 1999) have addressed the problem of compensation of combined unbalance and sensor runout disturbances, there exists a large volume of research on compensation of individual disturbances. Some of the early work on unbalance compensation has been based on insertion of a notch filter in the control loop (Batty, 1988). The drawback of this approach stems from negative phase of the notch transfer function which can reduce stability margin of the closed-loop system and lead to instability (Knospe, 1991; Bleuler, et al., 1994; Na and Park, 1997). Another approach for periodic disturbance cancellation is adaptive feedforward control (Shafai, et al., 1994; Hu and Tomizuka, 1993), where fourier coefficients of the disturbance are continually estimated and used for cancellation. These adaptive controllers, operationally bear resemblance to the notch filters (Na and Park, 1997) and can result in instability, if designed without considering the underlying structure of the system. To preserve stability of the closed-loop system, Herzog, et al. (1996) developed the generalized notch filter and Na and Park (1997) proposed variation of the least mean square algorithm. For improved performance in disk drives, Sacks, et al. (1996) modified the feedforward controller to remove oscillations from the transient response for faster parameter convergence. Other approaches that compensate unbalance while ensuring stability include adaptive auto-centering (Lum, et al., 1996) and output regulation with internal stability (Matsumura, et al., 1990). Both these approaches achieve rotor stabilization about the center-of-mass.

Though unbalance compensation has been widely studied with the objective of stabilization about the mass center, most users and vendors push for geometric centering accepting that the real objective is to avoid seal or aero tip collisions. While geometric center stabilization has been addressed by a few researchers (Hisatani and Koizumi, 1994; Song and Mukherjee, 1996), both problems were investigated by Reinig and Desrochers (1986) and Mizuno and Higuchi (1990). These results indicate stabilization about mass center or geometric center can be achieved through cancellation of disturbance in the current signal or the displacement signal, respectively. In a general and experimental approach for disturbance attenuation (Knospe, et al., 1996; 1997), any form of rotor vibration that can be measured, can be attenuated using pseudo-inverse of the pre-computed influence coefficient matrix. The stability and performance of the algorithm in the presence of uncertainties were investigated, and experimental results were used to demonstrate effectiveness. The method decouples the problem into two independent control tasks, and while it has been demonstrated to work successfully, there is no theoretical basis for stability of the two interacting processes. Some of the other approaches employed for unbalance compensation include robust control designs (Fujita, et al., 1993; Rutland, et al., 1994), Q-parameterization control (Mohamed et al., 1997), and neural networks (Paul, et al., 1997).

In this paper we address the problem of sensor runout compensation with the objective of rotor stabilization about the geometric center. This problem was recently investigated by Kim and Lee (1997), where the open-loop influence coefficient method (Knospe, et al., 1997) was used to suppress vibration at the fundamental frequency and at higher harmonics. Our approach to the problem is based on traditional adaptive control designs (Narendra and Annaswamy, 1989)

that guarantee both plant stability and convergence of unknown parameters in the persistency of excitation. While such methods based on Lyapunov stability theory have found applications for stepper motors (Chen and Paden, 1993), they have not been used for the control of magnetic bearings. To this end we design a simple, yet robust, adaptive feedforward controller for rotor stabilization in the presence of sensor runout disturbances. The salient features of our controller include simplicity of design and implementation, closed-loop estimation and cancellation of sensor runout harmonics, asymptotic stability of the complete system, and robustness to significant variation in plant parameters. The robustness of our algorithm does not require separate control action; it is an artifact of passivity of the closed-loop system. Such inherent robustness provides advantages over state-space approaches based on deterministic models. In such approaches the disturbance harmonics are modeled using linear oscillators and estimated with an observer. In the presence of parameter uncertainty, asymptotic stability of the observer is not guaranteed.

This paper is organized as follows. The mathematical model of the magnetic bearing with sensor runout is presented in section II. The sensor runout compensation scheme is presented in section III along with simulation results. The robustness of the closed-loop system to variation in plant parameters is mathematically established in section IV. Simulation results presented in this section indicate that large variation in parameters can be tolerated. Experimental results are presented in section V. These results verify that asymptotic stability of the plant and sensor runout compensation remain unaffected by significant variation in plant parameters.

II. MODEL OF MAGNETIC BEARING WITH SENSOR RUNOUT

Consider the magnetically levitated rigid rotor in Fig.1. The rotor has two degrees of freedom along the x and y axes; the displacements along these axes are measured by non-contact gap sensors. The dynamics of the rotor along these axes, which are both inclined at 45° with the horizontal, are decoupled but similar. Along the x axis, one may write

$$m\ddot{x} = F - m\bar{g}, \quad \bar{g} \triangleq g/\sqrt{2} \quad (1)$$

where m is the mass of the rotor, x is the rotor position, F is the magnetic force, and g is the acceleration due to gravity. The magnetic force can be expressed as (Siegwart, 1992)

$$F = k \left[\left(\frac{i_{10} + I}{l - x} \right)^2 - \left(\frac{i_{20} - I}{l + x} \right)^2 \right] \quad (2)$$

where k is the magnetic force constant, l is the nominal air gap, i_{10} , i_{20} are the bias currents in the top and bottom electromagnets, and I is the control current. By linearizing Eq.(2) about $x = 0$, $I = 0$, Eq.(1) can be written as

$$m\ddot{x} = K_s x + K_c I, \quad K_s \triangleq 2k(i_{10}^2 + i_{20}^2)/l^3, \quad K_c \triangleq 2k(i_{10} + i_{20})/l^2 \quad (3)$$

where K_s and K_c are the magnetic stiffness and actuator gain of the magnetic bearing, respectively. The true location of the rotor geometric center is not available for a magnetic bearing with sensor runout. Instead, the gap sensors provide the signal x_s ,

$$x_s = x + d \quad (4)$$

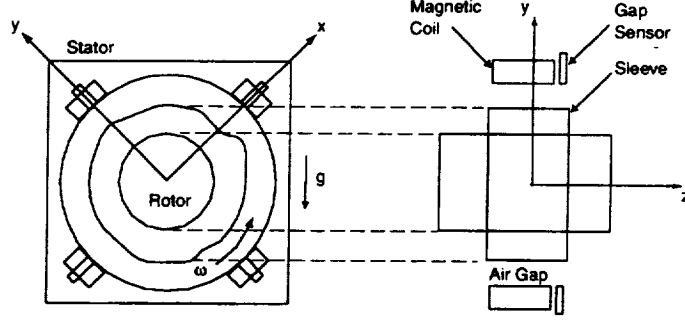


Figure 1. A magnetic bearing system with sensor runout.

where, d , the sensor runout disturbance, can be expressed by the Fourier series

$$d = a_0 + \sum_{i=1}^n a_i \sin(i\omega t) + b_i \cos(i\omega t) \quad (5)$$

In the above expression, ω is the rotor angular speed, n is the number of harmonics, a_0 is the DC component, and $a_i, b_i, i = 1, 2, \dots, n$, are the harmonic Fourier coefficients. The effect of runout can be inferred from the block diagram of the magnetic bearing control system in Fig.2. Unless compensated, runout will seriously degrade performance of the system. Specifically, it will cause undesirable rotor vibration and may ultimately result in failure.

III. SENSOR RUNOUT COMPENSATION SCHEME

III-A. ADAPTIVE SENSOR RUNOUT COMPENSATION (ASRC)

We present an adaptive controller for stabilization of the rotor geometric center to the origin through estimation and feedforward cancellation of sensor runout. We propose the controller to have the structure shown in Fig.2, where \bar{x} is the estimated rotor geometric center, and \bar{d} is the estimated sensor runout, defined as

$$\bar{x} = x_s - \bar{d}, \quad \bar{d} \triangleq \bar{a}_0 + \sum_{i=1}^n \bar{a}_i \sin(i\omega t) + \bar{b}_i \cos(i\omega t) \quad (6)$$

In the above expression, \bar{a}_0 is the estimated value of a_0 , and \bar{a}_i, \bar{b}_i are estimated values of a_i, b_i , respectively, for $i = 1, 2, \dots, n$. Using Eqs.(4) and (6), \bar{x} can also be expressed as

$$\bar{x} = x + \tilde{d} \quad (7)$$

where, \tilde{d} , the error in the estimate of sensor runout disturbance, is given by the relation

$$\tilde{d} \triangleq (d - \bar{d}) = Y^T \tilde{\phi} \quad (8)$$

The regressor vector Y , and the vector of parameter estimation errors $\tilde{\phi}$, are defined as follows

$$Y \triangleq [1 \quad \sin(\omega t) \quad \cos(\omega t) \quad \sin(2\omega t) \quad \cos(2\omega t) \quad \dots \quad \sin(n\omega t) \quad \cos(n\omega t)]^T \quad (9)$$

$$\tilde{\phi} \triangleq [\tilde{a}_0 \quad \tilde{a}_1 \quad \tilde{b}_1 \quad \tilde{a}_2 \quad \tilde{b}_2 \quad \dots \quad \tilde{a}_n \quad \tilde{b}_n]^T \quad (10)$$

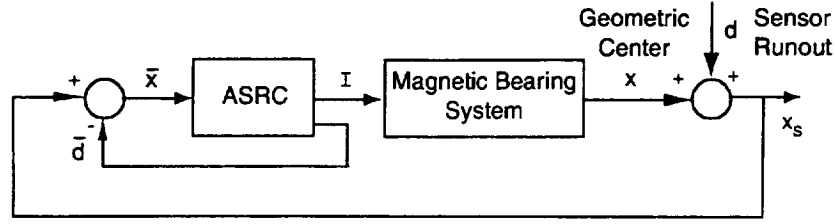


Figure 2. Block diagram of magnetic bearing system with sensor runout.

where $\tilde{a}_0 \triangleq (a_0 - \bar{a}_0)$, and $\tilde{a}_i \triangleq (a_i - \bar{a}_i)$, $\tilde{b}_i \triangleq (b_i - \bar{b}_i)$, $i = 1, 2, \dots, n$. For estimation and cancellation of sensor runout, and stabilization of the rotor geometric center, we propose the control action

$$I = -\frac{1}{K_c} (K_s \bar{x} + m \lambda \dot{\bar{x}} + c \bar{e}), \quad \bar{e} \triangleq (\dot{\bar{x}} + \lambda \bar{x}) \quad (11)$$

along with the adaptation law

$$\dot{\tilde{\phi}} = \Gamma Y_m \bar{e} \quad (12)$$

where $\Gamma \in R^{(2n+1) \times (2n+1)}$ is a matrix of adaptation gains, Y_m is a regressor vector, defined as

$$\Gamma \triangleq \text{diag}(\gamma_0, \gamma_1, \gamma_1, \gamma_2, \gamma_2, \dots, \gamma_n, \gamma_n), \quad Y_m \triangleq K_s Y - m \ddot{Y} \quad (13)$$

and c , λ , and γ_i , $i = 0, 1, 2, \dots, n$ are positive constants.

From the definition of Y and Y_m in Eqs.(9) and (13), we can establish

$$\dot{Y}^T \Gamma Y_m = 0, \quad Y^T \Gamma \dot{Y}_m = 0 \quad (14)$$

Also, we define

$$\Delta \triangleq Y^T \Gamma Y_m = \sum_{i=0}^n \gamma_i (K_s + m i^2 \omega^2) \quad (15)$$

and choose adaptation gains $\gamma_0, \gamma_1, \dots, \gamma_n$ to guarantee $0 < \Delta < 1$. Substituting Eq.(11) into Eq.(3), the dynamics of the controlled rotor can be described by

$$m \ddot{x} = -K_s \tilde{d} - m \lambda \dot{\bar{x}} - c \bar{e}$$

Using the relation $\ddot{x} = \ddot{\bar{x}} + \ddot{\tilde{d}}$ from Eq.(7), and $\dot{\bar{e}} = \dot{\bar{x}} + \lambda \bar{x}$ from Eq.(11), the above equation can be rewritten as

$$m \dot{\bar{e}} = m \ddot{\tilde{d}} - K_s \tilde{d} - c \bar{e}$$

Substituting Eq.(8) and then using the relations in Eq.(14) and (15), we get

$$m(1 - \Delta) \dot{\bar{e}} = -Y_m^T \tilde{\phi} - c \bar{e}$$

The closed loop system dynamics can now be described by

$$\dot{\bar{x}} = -\lambda \bar{x} + \bar{e} \quad (16a)$$

$$\dot{\bar{e}} = -\frac{1}{m(1 - \Delta)} (Y_m^T \tilde{\phi} + c \bar{e}) \quad (16b)$$

$$\dot{\tilde{\phi}} = \Gamma Y_m \bar{e} \quad (16c)$$

The following observations can now be made with respect to the closed-loop system.

Theorem 1:

Consider the sub-system described by Eqs.(16b) and (16c). For this system, $(\bar{e}, \tilde{\phi}) \equiv (0, 0)$ is an asymptotically stable equilibrium.

Proof: From Eqs.(16b) and (16c) first notice that $(\bar{e}, \tilde{\phi}) = (0, 0)$ implies $(\dot{\bar{e}}, \dot{\tilde{\phi}}) = (0, 0)$. Therefore, $(\bar{e}, \tilde{\phi}) \equiv (0, 0)$ is an equilibrium point. To show that this equilibrium is asymptotically stable, we define the continuously differentiable, positive definite function

$$V(\bar{e}, \tilde{\phi}) = \frac{1}{2}m(1 - \Delta)\bar{e}^2 + \frac{1}{2}\tilde{\phi}^T \Gamma^{-1} \tilde{\phi}, \quad 0 < \Delta < 1 \quad (17)$$

The derivative of V can be computed as

$$\dot{V} = m(1 - \Delta)\bar{e}\dot{\bar{e}} + \tilde{\phi}^T \Gamma^{-1} \dot{\tilde{\phi}}$$

Using Eqs.(16b) and (16c), we get

$$\dot{V} = -c\bar{e}^2 \leq 0 \quad (18)$$

Since V is positive definite and \dot{V} is negative semi-definite, we conclude $(\bar{e}, \tilde{\phi}) \equiv (0, 0)$ is stable. In addition, since \dot{V} is uniformly continuous, we use Barbalat's lemma (Khalil, 1996) to deduce $\dot{V} \rightarrow 0$ as $t \rightarrow \infty$. This implies $\bar{e} \rightarrow 0$ as $t \rightarrow \infty$. By differentiating Eq.(16b), we can show that $\ddot{e} = \ddot{e}(t, \tilde{\phi}, \bar{e})$ is bounded. This implies that $\dot{\bar{e}}$ is uniformly continuous. Since $\bar{e} \rightarrow 0$ as $t \rightarrow \infty$, we once again use Barbalat's lemma (Khalil, 1996) to deduce $\dot{\bar{e}} \rightarrow 0$ as $t \rightarrow \infty$. Knowing $\bar{e}, \dot{\bar{e}} \rightarrow 0$ as $t \rightarrow \infty$, we can conclude from Eq.(16b)

$$Y_m^T \tilde{\phi} \rightarrow 0 \quad (19)$$

It can be shown that there exist positive constants α_1, α_2 , and δ , such that

$$\alpha_2 I \geq \int_t^{t+\delta} Y_m Y_m^T d\tau \geq \alpha_1 I$$

where I is the identity matrix. Therefore Y_m is a persistently exciting signal (Khalil, 1996). This implies from Eq.(19) that $\tilde{\phi} \rightarrow 0$, as $t \rightarrow \infty$. Knowing $\bar{e}, \tilde{\phi} \rightarrow 0$, as $t \rightarrow \infty$, we can now assert that $(\bar{e}, \tilde{\phi}) \equiv (0, 0)$ is an asymptotically stable equilibrium. This concludes our proof.

Lemma 1:

The origin of the closed-loop system in Eq.(16), $(\bar{x}, \bar{e}, \tilde{\phi}) \equiv (0, 0, 0)$, is an asymptotically stable equilibrium point.

Proof: The closed loop system in Eq.(16) is an interconnected system of the form

$$\dot{z}_1 = f_1(t, z_1, z_2) \quad (20a)$$

$$\dot{z}_2 = f_2(t, z_2) \quad (20b)$$

where $z_1 \triangleq \bar{x}$, and $z_2 \triangleq (\bar{e} \quad \tilde{\phi}^T)^T$ are the state variables of the two sub-systems. We know from Theorem 1 that $z_2 = 0$ is an asymptotically stable equilibrium of the sub-system in Eq.(20b). Also, $\dot{z}_1 = f_2(t, z_1, 0)$ has an asymptotically stable equilibrium point at $z_1 = 0$. This can be readily established from Eqs.(20b) and (16c). Using the asymptotic stability theorem for cascaded systems (Khalil, 1996), we conclude $(\bar{x}, \bar{e}, \tilde{\phi}) \equiv (0, 0, 0)$, is an asymptotically stable equilibrium.

Theorem 2:

The coordinate $(x, \dot{x}, \tilde{\phi}) \equiv (0, 0, 0)$ is a stable equilibrium point for the closed loop system defined by Eqs.(3), (11), and (12).

Proof: Using Eqs.(7), (8), (11), (12), and (15), we can show that at $(x, \dot{x}, \tilde{\phi}) \equiv (0, 0, 0)$, we have

$$\tilde{d} = Y^T \tilde{\phi} = 0, \quad \bar{x} = x + \tilde{d} = 0, \quad \dot{\tilde{d}} = (\dot{Y}^T \tilde{\phi} + Y^T \dot{\tilde{\phi}}) = Y^T \Gamma Y_m \bar{e} = \Delta \bar{e} = \Delta(\dot{x} + \lambda \bar{x}) = \Delta \dot{x}$$

Also, at $(x, \dot{x}, \tilde{\phi}) \equiv (0, 0, 0)$, $\dot{\tilde{d}} = (\dot{x} - \dot{x}) = \dot{x}$. Comparing with the expression for $\dot{\tilde{d}}$ above, we have $\dot{\tilde{d}} = \dot{x} = 0$, since $\Delta \neq 1$. From Eqs.(3), (11), and (12), it follows that $(\dot{x}, \ddot{x}, \dot{\tilde{\phi}}) = (0, 0, 0)$. Therefore, $(x, \dot{x}, \tilde{\phi}) \equiv (0, 0, 0)$ is an equilibrium point. The fact that $(x, \dot{x}, \tilde{\phi}) \equiv (0, 0, 0)$ is asymptotically stable can now be deduced from

- (a) $(\bar{x}, \bar{e}, \tilde{\phi}) \equiv (0, 0, 0)$ is an asymptotically stable equilibrium (follows from Lemma 1),
- (b) the transformation matrix P that maps $(\bar{x}, \bar{e}, \tilde{\phi})$ to $(x, \dot{x}, \tilde{\phi})$

$$\begin{pmatrix} x \\ \dot{x} \\ \tilde{\phi} \end{pmatrix} = \begin{pmatrix} & & \\ P & & \\ & & \end{pmatrix} \begin{pmatrix} \bar{x} \\ \bar{e} \\ \tilde{\phi} \end{pmatrix}, \quad P \triangleq \begin{pmatrix} 1 & 0 & -Y^T \\ -\lambda & (1 - \Delta) & -\dot{Y}^T \\ 0 & 0 & E \end{pmatrix}$$

- where $E \in R^{(2n+1) \times (2n+1)}$ is the identity matrix, is well defined and upper bounded, and
- (c) the inverse transformation P^{-1} exists, and $\|P^{-1}\|$ is also upper bounded.

Theorem 2 establishes that the adaptive controller proposed herein guarantees stabilization of the rotor geometric center through identification and cancellation of sensor runout disturbance.

III-B. SIMULATION RESULTS

Simulation results are presented here to demonstrate effectiveness of the adaptive controller, discussed in the previous section. Though the controller was designed using a linearized model of the plant, we use the nonlinear plant model to simulate the real situation. The bearing parameters, which include rotor mass, magnetic force constant, nominal air gap, bias currents, magnetic stiffness, and actuator gain, were assumed to be the ones in our experimental hardware. These values can be referenced from table 1 in section V. The Fourier coefficients of sensor runout disturbance were assumed to be $a_0 = 10$, $a_1 = 67.615$, $b_1 = 18.117$, $a_2 = 7.071$, $b_2 = 7.071$

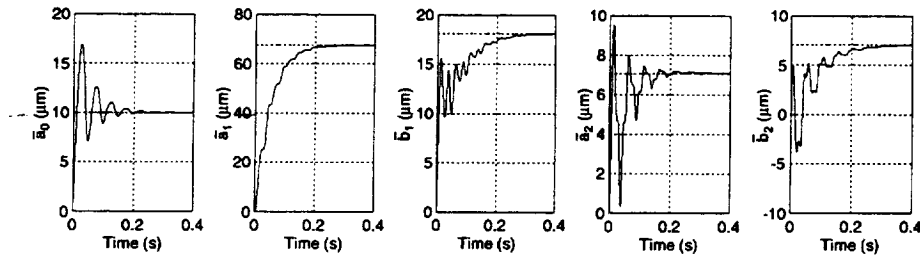


Figure 3. Estimated parameters of sensor runout; true values are shown with dashed lines.

where the units are in micrometers. Higher harmonics of the disturbance were assumed absent. The rotor initial conditions were assumed to be $x(0) = -1.0 \times 10^{-4}$ and $\dot{x}(0) = 0.0$, respectively, in SI units. The angular velocity of the rotor was assumed to be 1200 rpm. The simulation results for

error gains $\lambda = 400 \text{ s}^{-1}$, and $c = 1200 \text{ kg/s}$, and adaptation gains $\Gamma = \text{diag}(1, 2, 2, 1, 1, 0.5, 0.5) \times 10^{-7} m/N$, are shown in Figs.3 and 4. These figures indicate that estimation of runout is successfully completed within 0.3 secs, and the rotor geometric center is effectively stabilized to the origin.

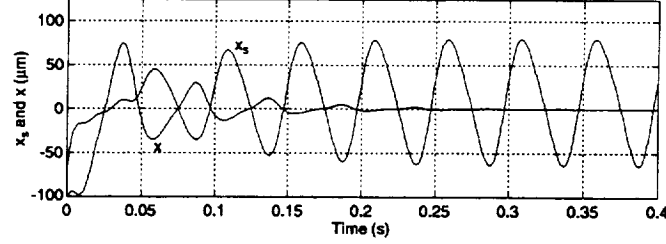


Figure 4. Stabilization of rotor geometric center in the presence of sensor runout.

IV. ROBUSTNESS TO UNCERTAIN PLANT PARAMETERS

IV-A. STRICT PASSIVITY OF CLOSED LOOP SYSTEM

In this section we establish that the adaptive sensor runout compensation (ASRC) scheme is robust to uncertainties and/or variation in plant parameters. Specifically, we show that ASRC guarantees stabilization of rotor geometric center and exact cancellation of sensor runout in the absence of exact knowledge of rotor mass, m , magnetic stiffness, K_s , and actuator gain, K_c . To this end, we estimate the values of these parameters to be \bar{m} , \bar{K}_s , and \bar{K}_c , respectively, and modify our control action and adaptation law in Eqs.(11) and (12), as follows

$$I = -\frac{1}{\bar{K}_c} (\bar{K}_s \bar{x} + \bar{m} \lambda \dot{\bar{x}} + c \bar{e}) \quad (21)$$

$$\dot{\bar{\phi}} = \Gamma \bar{Y}_m \bar{e}, \quad \bar{Y}_m \triangleq \bar{K}_s Y - \bar{m} \ddot{Y} \quad (22)$$

Substitution of Eq.(21) in Eq.(3) indicates that the closed-loop system takes the form

$$m \ddot{\bar{x}} + \frac{K_c}{\bar{K}_c} (\bar{m} \lambda + c) \dot{\bar{x}} + \left[\frac{K_c}{\bar{K}_c} (\bar{K}_s + c \lambda) - K_s \right] \bar{x} = m \ddot{\bar{d}} - K_s \bar{d} \quad (23)$$

Using Eqs.(8), (13) and (22), the right hand side of Eq.(23) can be simplified as follows

$$\begin{aligned} m \ddot{\bar{d}} - K_s \bar{d} &= m \left(\ddot{Y}^T \bar{\phi} + 2 \dot{Y}^T \dot{\bar{\phi}} + Y^T \ddot{\bar{\phi}} \right) - K_s Y^T \bar{\phi} \\ &= -Y_m^T \bar{\phi} + m \left[2 \dot{Y}^T \Gamma \bar{Y}_m \bar{e} + Y^T \Gamma \left(\dot{Y}_m \bar{e} + \bar{Y}_m \dot{\bar{e}} \right) \right] \end{aligned}$$

Using the identities $\dot{Y}^T \Gamma \bar{Y}_m = 0$, $Y^T \Gamma \dot{\bar{Y}}_m = 0$, we get

$$m \ddot{\bar{d}} - K_s \bar{d} = -Y_m^T \bar{\phi} + m \bar{\Delta} \dot{\bar{e}}, \quad \bar{\Delta} \triangleq Y^T \Gamma \bar{Y}_m = \sum_{i=0}^n \gamma_i (\bar{K}_s + \bar{m} i^2 \omega^2) \quad (24)$$

Substituting Eq.(24) into Eq.(23), we get the closed-loop system dynamics

$$M \ddot{\bar{x}} + C \dot{\bar{x}} + K \bar{x} = -Y_m^T \bar{\phi} \quad (25)$$

where M , C , and K , are defined as follows

$$M \triangleq m(1 - \bar{\Delta}), \quad C \triangleq \frac{K_c}{\bar{K}_c}(\bar{m}\lambda + c) - m\lambda\bar{\Delta}, \quad K \triangleq \left[\frac{K_c}{\bar{K}_c}(\bar{K}_s + c\lambda) - K_s \right] \quad (26)$$

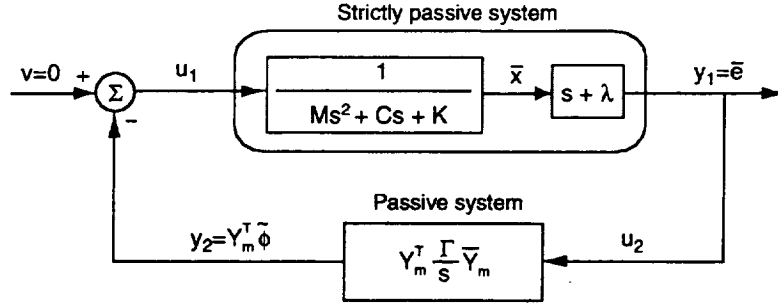


Figure 5. Block diagram of closed-loop system in the presence of uncertainty.

The closed loop system, described by the dynamics of the rotor in Eq.(25) and the adaptation law in Eq.(22) is represented by the block diagram in Fig.5, which is a feedback inter-connection of two linear systems. The following observations can be made regarding these linear systems.

Lemma 1: The linear system in the forward path in Fig.5, defined by the transfer function

$$G(s) = \frac{s + \lambda}{Ms^2 + Cs + K}$$

is strictly passive if $M, C, K > 0$, and $C - \lambda M > 0$.

Proof: If $M, C, K > 0$, $G(s)$ is Hurwitz. Furthermore, if $C - \lambda M > 0$, we have

$$G(j\omega) + G(-j\omega) > 0, \quad G(\infty) = 0, \quad \lim_{\omega \rightarrow \infty} \omega^2 [G(j\omega) + G(-j\omega)] > 0$$

Therefore, $G(s)$ is strictly positive real (Khalil, 1996). The Kalman-Yakubovich-Popov lemma can now be used (Khalil, 1996) to show that $G(s)$ is strictly passive.

Lemma 2: The linear system in the feedback path of Fig.5 is passive.

Proof: The adaptation law in Eq.(22) can be written as

$$\ddot{\tilde{a}}_0 = \gamma_0 \bar{K}_s \bar{e}, \quad \ddot{\tilde{a}}_i = \gamma_i [\bar{K}_s + \bar{m}i^2\omega^2] \sin(i\omega t) \bar{e}, \quad \ddot{\tilde{b}}_i = \gamma_i [\bar{K}_s + \bar{m}i^2\omega^2] \cos(i\omega t) \bar{e}, \quad i = 1, 2, \dots, n$$

Using these relations, and defining

$$\rho_i = \frac{K_s + mi^2\omega^2}{\gamma_i(\bar{K}_s + \bar{m}i^2\omega^2)}$$

for $i = 0, 1, 2, \dots, n$, we can express the net energy flow into the system as

$$\begin{aligned} \int_0^t y_2 u_2 dt &= \int_0^t \mathbf{Y}_m^T \tilde{\boldsymbol{\phi}} \bar{e} dt = K_s \int_0^t \tilde{a}_0 \bar{e} dt + \sum_{i=1}^n (K_s + mi^2\omega^2) \int_0^t [\tilde{a}_i \sin(i\omega t) \bar{e} + \tilde{b}_i \cos(i\omega t) \bar{e}] dt \\ &= \rho_0 \int_0^t \tilde{a}_0 \dot{\tilde{a}}_0 dt + \sum_{i=1}^n \rho_i \int_0^t [\tilde{a}_i \dot{\tilde{a}}_i + \tilde{b}_i \dot{\tilde{b}}_i] dt \\ &= \frac{\rho_0}{2} [\tilde{a}_0^2(t) - \tilde{a}_0^2(0)] + \sum_{i=1}^n \frac{\rho_i}{2} [\tilde{a}_i^2(t) + \tilde{b}_i^2(t) - \tilde{a}_i^2(0) - \tilde{b}_i^2(0)] \\ &= W[\tilde{\boldsymbol{\phi}}(t)] - W[\tilde{\boldsymbol{\phi}}(0)] \end{aligned} \quad (27)$$

where $W[\tilde{\phi}(t)]$ is a positive definite energy storage function given by the relation

$$W[\tilde{\phi}(t)] \triangleq \frac{1}{2} \tilde{\phi}^T M \tilde{\phi}, \quad M \triangleq \text{diag}(\rho_0, \rho_1, \rho_1, \rho_2, \rho_2, \dots, \dots, \rho_n, \rho_n)$$

From Eq.(27) we claim passivity (Khalil, 1996).

We now present our final result with the help of the following theorem.

Theorem 3: (Asymptotic stability and robustness)

The control and adaptation laws in Eqs.(21) and (22) guarantee asymptotic stability of the equilibrium $(x, \dot{x}, \tilde{\phi}) \equiv (0, 0, 0)$ of the magnetic bearing system in Eq.(3) in the presence of uncertainty in rotor mass, m , magnetic stiffness, K_s , and actuator gain, K_c , provided the error and adaptation gains are chosen to satisfy $M, C, K > 0$, and $C - \lambda M > 0$.

Proof: Through proper choice of the error gains c, λ , and adaptation gains γ_i , $i = 0, 1, 2, \dots, n$, we can easily guarantee $M, C, K > 0$, and $C - \lambda M > 0$. Using Lemmas 1 and 2, we can then conclude that the closed-loop system is a feedback interconnection of a strictly passive system and a passive system. Using the passivity theorem from the appendix (Krstić, et al., 1995) we claim $(\bar{x}, \dot{\bar{x}}, \tilde{\phi}) \equiv (0, 0, 0)$ is globally uniformly stable, and $\bar{x}, \dot{\bar{x}} \rightarrow 0$ as $t \rightarrow \infty$.

Now, to show $(x, \dot{x}, \tilde{\phi}) \equiv (0, 0, 0)$ is an asymptotically stable equilibrium, we first need to show that $(x, \dot{x}, \tilde{\phi}) \equiv (0, 0, 0)$ is an equilibrium. This can be verified using Eqs.(3), (8), (21), and (22), and is left to the reader. The fact that $(x, \dot{x}, \tilde{\phi}) \equiv (0, 0, 0)$ is stable follows from

- (a) $(\bar{x}, \dot{\bar{x}}, \tilde{\phi}) \equiv (0, 0, 0)$ is globally uniformly stable,
- (b) the transformation matrix $P(t)$ that maps $(\bar{x}, \dot{\bar{x}}, \tilde{\phi})$ to $(x, \dot{x}, \tilde{\phi})$ is well defined and $\|P\|$ is upper bounded, and
- (c) the inverse transformation P^{-1} exists, and $\|P^{-1}\|$ is also upper bounded.

Finally, we prove $(x, \dot{x}, \tilde{\phi}) \rightarrow (0, 0, 0)$ as $t \rightarrow \infty$. Since $\bar{x}, \dot{\bar{x}} \rightarrow 0$, $\bar{e} \rightarrow 0$. Also, from Fig.5 we claim $u_1 = y_2 \rightarrow 0$. This is true since the mass-spring-damper system in Fig.5 cannot have zero output for nonzero input. Since Y_m^T is persistently exciting, as discussed in the proof of theorem 1, $y_2 = 0$ implies $\tilde{\phi} = 0$, and $\tilde{d} = Y^T \tilde{\phi} = 0$. Also, $\dot{\tilde{d}} = (\dot{Y}^T \tilde{\phi} + Y^T \dot{\tilde{\phi}}) = Y^T \dot{\tilde{\phi}} = Y^T \Gamma Y_m \bar{e} = 0$. We conclude the proof by simply showing $x \triangleq (\bar{x} - \tilde{d}) \rightarrow 0$ and $\dot{x} \triangleq (\dot{\bar{x}} - \dot{\tilde{d}}) \rightarrow 0$.

IV-B. SIMULATION RESULTS

To demonstrate robustness of the adaptive controller to parameter uncertainties, we present simulation results using the nonlinear model of our magnetic bearing. The nominal parameter values were assumed to be the ones in our experimental hardware; these values can be referenced from table 1 in section V. The nominal values, along with the error and adaptation gains, satisfy the asymptotic stability conditions in theorem 3, namely

$$M = 1.94 > 0, \quad C = 1.97 \times 10^3 > 0, \quad K = 4.8 \times 10^5 > 0, \quad (C - \lambda M) = 1.2 \times 10^3 > 0 \quad (28)$$

The above values in SI units, which were computed from the expressions in Eq.(26), support the simulation results in Figs.3 and 4. To demonstrate robustness, we over-estimate the uncertain parameters, namely, rotor mass, magnetic stiffness, and actuator gain, by 100%. The Fourier coefficients of sensor runout, rotor initial conditions, angular velocity, error gains, and adaptation

gains were chosen as in section III-B. The results in Figs.6 and 7 indicate sensor runout is exactly estimated and the rotor geometric center is successfully stabilized to the origin. These results can be independently asserted from the conditions for asymptotic stability in theorem 3, namely

$$M = 1.44 > 0, \quad C = 1.18 \times 10^3 > 0, \quad K = 2.4 \times 10^5 > 0, \quad (C - \lambda M) = 0.6 \times 10^3 > 0 \quad (29)$$

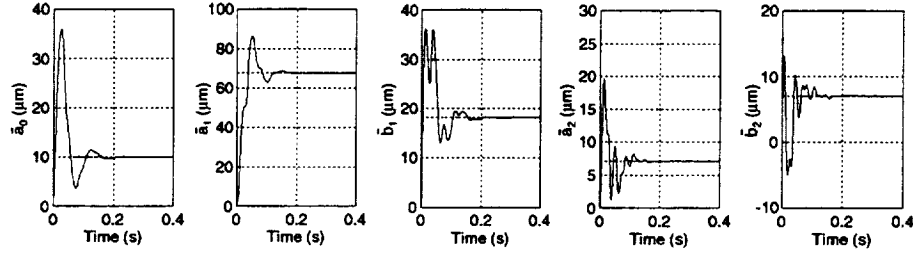


Figure 6. Sensor runout estimation for uncertain plant; true values shown in dashed lines.

A comparison of Figs.3 and 6 and Figs.4 and 7 indicates that the closed-loop system with 100% over-estimated parameters has better transient response than the closed-loop system with known parameters. This only indicates that the same set of error gains and adaptation gains will not necessarily result in the same performance of different systems. It is obvious from the values of M , C , K in Eqs.(28) and (29) that parameter uncertainty changes the forward path transfer function in Fig.5. The time-varying feedback in Fig.5 also changes due to uncertainty.

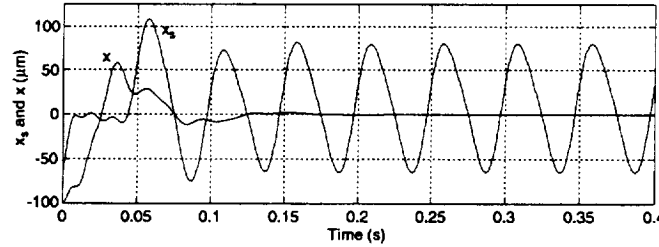


Figure 7. Stabilization of rotor for uncertain plant in the presence of sensor runout.

V. EXPERIMENTAL RESULTS

In this section we present experimental data to validate the theoretical results presented in sections III and IV. The parameters of the bearing and rotor assembly are as follows:

Table 1. Magnetic Bearing Test Rig Parameters

Parameter	Value
rotor mass, m	2.43 kg
electromagnetic force constant, k	$2.82 \times 10^{-6} \text{ Nm}^2/\text{A}^2$
nominal air gap, l	$0.508 \times 10^{-3} \text{ m}$
top coil bias current, I_{10}	2.41 A
bottom coil bias current, I_{20}	2.06 A
actuator gain, K_c	97.71 N/A
magnetic stiffness, K_s	$4.33 \times 10^5 \text{ N/m}$

The adaptive controller was implemented in Matlab/SimulinkTM environment and downloaded to a Digital Signal Processor (DSP) board, manufactured by DSpace. The DSP board, sampling approximately at 13 KHz, was used to control the rotor along both bearing axes, independently. The runout disturbance was assumed to be comprised of two harmonics in addition to the DC component. Under this computation load, the DSP allowed us to store ten signals, five per axis, in real time. For the x axis we stored the estimated position, \bar{x} , current, I_x , and the DC component and estimated Fourier coefficients of the first harmonic, \bar{a}_{0x} , \bar{a}_{1x} , \bar{b}_{1x} . The estimated coefficients of the second harmonic were found to be negligible but could not be stored due to DSP limitations. The sensor signal, x_s , was regenerated from stored data \bar{x} , \bar{a}_{0x} , \bar{a}_{1x} , and \bar{b}_{1x} , using Eq.(6). Since the second harmonic coefficients were used in the computation of \bar{x} , regeneration of x_s from \bar{x} in the absence of these coefficients lacks some accuracy. Our choice of real-time signals for the y axis was exactly the same as that for the x axis.

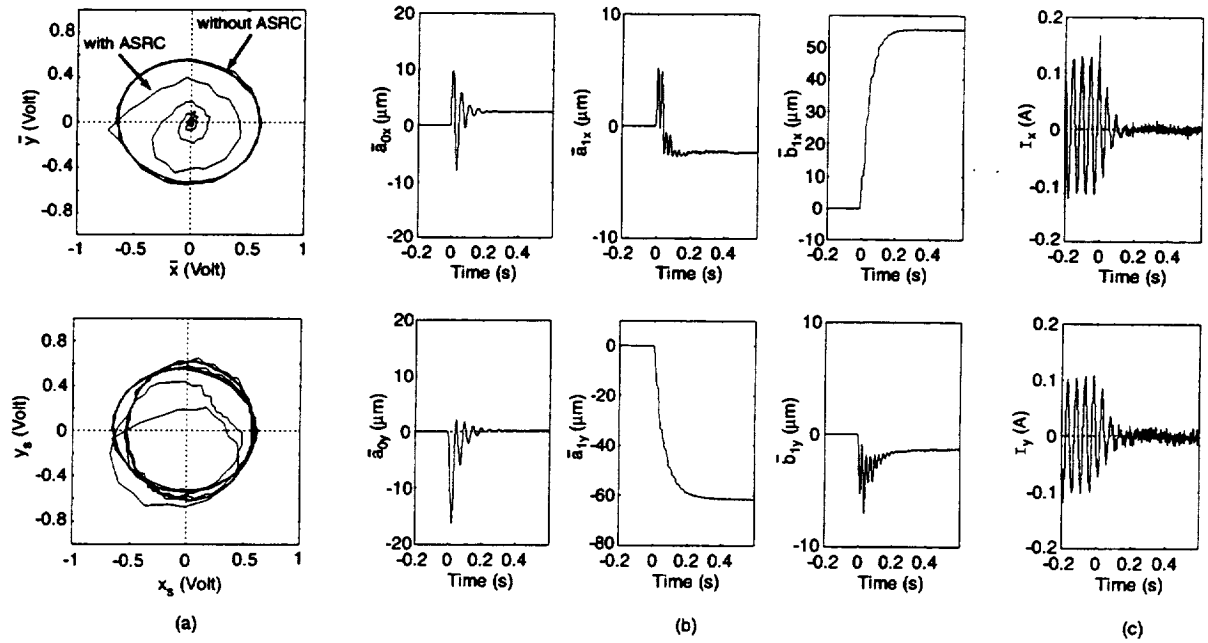


Figure 8. Trajectory of (a) estimated rotor geometric center and regenerated sensor signals, scale 1 V = 50 μm (b) estimated Fourier coefficients of sensor runout, and (c) control currents, with and without ASRC. The controller used known plant parameter values.

The electromagnets were driven by switching power amplifiers, product of Advanced Motion Control, operating with 1.6 KHz bandwidth. To ensure negligible effects due to unbalance, the rotor was well balanced and spun at the relatively low rpm of 1200. This speed is 20 times less than the first critical speed of the rotor, and guarantees negligible effects due to flexibility, which was not considered in our model. The error and adaptations gains of the adaptive controller, given by Eqs.(11) and (21), were chosen as

$$\lambda = 400 \text{ s}^{-1}, \quad c = 1200 \text{ kg/s}, \quad \Gamma = \text{diag}(1.0, 1.7, 1.7, 1.5, 1.5) \times 10^{-7} \text{ m/N} \quad (30)$$

In controller implementation, the derivative of the estimated position signal, $\dot{\hat{x}}$, was numerically computed using the transfer function $2500s/(s + 2500)$. This eliminates potential problems arising from infiltration of wideband noise into the sensor signal.

Controller using known plant parameters We first present experimental results based on control and adaptation laws in Eqs.(11) and (12). In the control law, the values of m , K_s , and K_c were taken from Table 1. The trajectory of the estimated rotor geometric center (\bar{x}, \bar{y}) and regenerated trajectory of geometric center provided by the position sensors (x_s, y_s) are shown in Fig.8 (a). These trajectories indicate that while the sensors continue to provide geometric center positions corrupt with runout disturbance, their estimated values are stabilized to the origin with ASRC. It is seen from Fig.8 (b) that estimation of Fourier coefficients of runout are completed in 0.3 seconds. In the same time, sinusoidal variation in the control currents vanish in Fig.8 (c). These zero steady-state control currents imply stabilization of rotor geometric center to the origin in the absence of mass unbalance. Indeed, we can verify from Eq.(3) that the rotor would become unstable if this was not the case. We ensured negligible mass unbalance effects in our experiments through rotor balancing and by spinning the rotor at low rpm. Knowing that the rotor geometric center has stabilized to the origin, runout disturbance was obtained from the Fourier coefficients in Fig.8 (b). The trajectories of x_s, y_s in Fig.8 (a) also provide this information.

Controller using larger plant parameter values To demonstrate the robustness of ASRC to parameter uncertainty, we used control and adaptation laws in Eqs.(21) and (22). The parameter values \bar{m} , \bar{K}_s , and \bar{K}_c in the control law were chosen to be 25% larger than the values of m , K_s , and K_c , respectively, provided in Table 1. The results obtained from our experiments are shown in Fig.9. These results indicate that runout is eliminated and the rotor geometric center is successfully stabilized to the origin despite error in the model used to construct the controller.

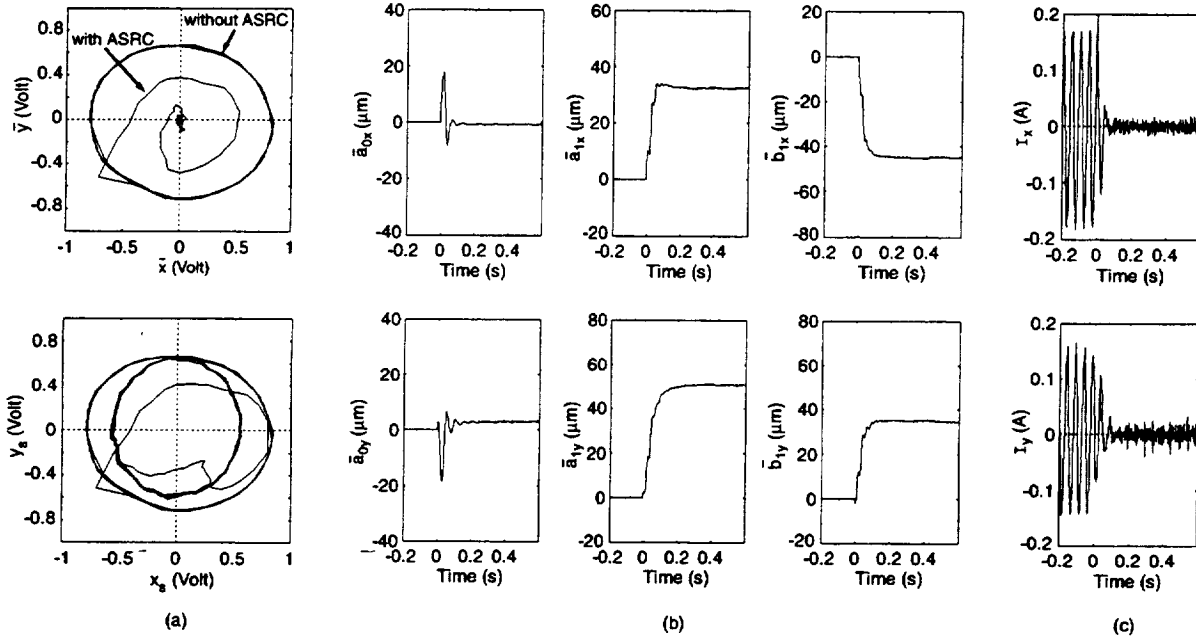


Figure 9. Trajectory of (a) estimated rotor geometric center and regenerated sensor signals, scale $1\text{ V} = 50\text{ }\mu\text{m}$, (b) estimated Fourier coefficients of sensor runout, and (c) control currents, with and without ASRC. To demonstrate robustness 25% larger parameter values were used.

VI. CONCLUSION

This paper presents a simple, yet robust, algorithm for adaptive compensation of sensor runout in active magnetic bearings. The algorithm is based on a rigid rotor model with no mass unbalance and assumes the angular speed of the rotor to be known and constant. Using powerful tools such as Lyapunov stability, persistency of excitation, and passivity, the algorithm is shown to guarantee perfect cancellation of runout harmonics and stabilization of the rotor geometric center. Through modeling, estimation, and cancellation of the DC component of runout, the algorithm generates the equivalent action of integral feedback for elimination of steady state errors. The algorithm is also robust to significant variation in plant parameters that include rotor mass, magnetic stiffness, and actuator gain. The effectiveness of our algorithm is validated through numerical simulations, as well as experiments. We present experimental data that confirm stabilization of the geometric center of a rotor with negligible mass unbalance effects, even when the modelled plant parameters are quite different. As compared to existing results on compensation of periodic disturbances, our algorithm has the combined advantages of simplicity of design and implementation, closed-loop estimation and cancellation of disturbances, stability of the overall system, and importantly, robustness to parameter variation. Our algorithm can also be used for compensation of mass unbalance, but in such applications the rotor will be stabilized about its inertial center. Our future work will address the important problem of combined mass unbalance and sensor runout compensation with rotor stabilization about the geometric center.

ACKNOWLEDGEMENT

The authors thank Dr. Hassan Khalil for his useful comments and suggestions.

REFERENCES

- [1] Batty, R., 1988, "Notch filter control of magnetic bearings", MS Thesis, Massachusetts Institute of Technology, Cambridge, MA.
- [2] Bleuler, H., Gahler, C., Herzog, R., Larssonneur, R., Mizuno, T., Siegwart, R., and Woo, S. -J., 1994, "Application of digital signal processors for industrial magnetic bearings", IEEE Transactions on Control Systems Technology, Vol.2, No.4, pp.280-289.
- [3] Chen, D., and Paden, B., 1993, "Adaptive linearization of hybrid step motors: Stability analysis", IEEE Transactions on Automatic Control, Vol.38, No.6, pp.874-887.
- [4] Fujita, M., Hatake, K., and Matsumura, F., 1993, "Loop shaping based robust control of a magnetic bearing", IEEE Control Systems, pp.57-65.
- [5] Herzog, R., Buhler, P., Gahler, C., and Larssonneur, R., 1996, "Unbalance Compensation using generalized notch filters in multivariable feedback of magnetic bearings", IEEE Transactions on Control Systems Technology, Vol.4, No.5, pp.580-586.
- [6] Hisatani, M., and Koizumi, T., 1994, "Adaptive filtering for unbalance vibration suppression", 4th ISMB, ETH Zurich, Switzerland.
- [7] Hu, J., and Tomizuka, M., 1993, "A new plug-in adaptive controller for rejection of periodic disturbances", ASME J. of Dyn. Sys., Meas., and Cont., 115, pp.543-546.

- [8] Khalil, H., 1996, "Nonlinear Systems", 2nd Ed., Prentice Hall, Upper Saddle River, NJ 07458.
- [9] Kim, C. -S., and Lee, C. -W., "In situ runout identification in active magnetic bearing system by extended influence coefficient method", IEEE/ASME Trans. on Mechatronics, 2(1), pp.51-57.
- [10] Knospe, C. R., 1991, "Stability and performance of notch filters for unbalance response", Proc. ISMST, NASA Langley Research Center, Hampton, VA.
- [11] Knospe, C. R., Hope, R. W., Tamer, S. M., and Fedigan, S. J., 1996, "Robustness of adaptive unbalance control of rotors with magnetic bearings", J. of Vibration and Control, 2, pp.33-52.
- [12] Knospe, C. R., Tamer, S. M., and Fedigan, S. J., 1997, "Robustness of adaptive rotor vibration control to structured uncertainty", ASME JDSMC, 119, pp.243-250.
- [13] Krstic, M., Kanellakopoulos, I., and Kokotovic, P., 1995, "Nonlinear and adaptive control design", Wiley Interscience, New York, NY.
- [14] Lum, K. -Y., Coppola, V., and Bernstein, D., 1996, "Adaptive autocentering control for an active magnetic bearing supporting a rotor with unknown mass imbalance", IEEE Transactions on Control Systems Technology, Vol.4, No.5, pp.587-597.
- [15] Matsumura, F., Fujita, M., and Okawa, K., 1990, "Modeling and control of magnetic bearing systems achieving a rotation around the axis of inertia", 2nd ISMB, Tokyo, Japan, pp.273-280.
- [16] Mizuno, T., and Higuchi, T., 1990, "Design of magnetic bearing controllers based on disturbance estimation", Proc. 2nd Int. Symp. on Magnetic Bearings, Tokyo, Japan, pp.281-288.
- [17] Mohamed A. M., Matsumura, M., Namerikawa, T., and Lee, J., 1997, "Q-parameterization control of vibrations in a variable speed magnetic bearing", Proc. 1997 IEEE Int. Conf. on Control Applications, Hartford, CT.
- [18] Na, H. -S., and Park, Y., 1997, "An adaptive feedforward controller for rejection of periodic disturbances", Journal of Sound and Vibration, 201(4), pp.427-435.
- [19] Narendra, K. S., and Annaswamy, A. M., 1989, "Stable adaptive systems", Prentice Hall, Englewood Cliffs, NJ 07632.
- [20] Paul, M., Hoffman, W., and Steffani, H. F., 1998, "Compensation for unbalances with aid of neural networks", 6th ISMB, Cambridge, MA.
- [21] Reining, K. D., and Desrochers, A. A., 1986, "Disturbance accomodating controllers for rotating mechanical systems", ASME J. of Dyn. Sys., Meas., and Cont., 108, pp.24-31.
- [22] Rutland, N. K., Keogh, P. S., and Burrows, C. R., 1994, "Comparison of controller designs for attenuation of vibration in a rotor bearing system under synchronous and transient conditions", 4th ISMB, ETH Zurich, Switzerland, pp.107-112.
- [23] Sacks, A., Bodson, M., and Khosla, P., "Experimental results of adaptive periodic disturbance cancellation in a high performance magnetic disk drive", ASME JDSMC, 118, pp.416-424.
- [24] Setiawan, J. D., Mukherjee, R., Maslen, E. H., and Song, G., 1999, "Adaptive compensation of sensor runout and mass unbalance in magnetic bearing systems", Proc. IEEE/ASME Int. Conf. on Advanced Intelligent Mechatronics, Atlanta, GA, September 1999.
- [25] Shafai, B., Beale, S., Larocca, P., and Cusson, E., 1994, "Magnetic bearing control systems and adaptive forced balancing", IEEE Control Systems, 14, pp.4-13.
- [26] Siegwart, R., 1992, "Design and applications of active magnetic bearings for vibration control", Von Karman Inst. Fluid Dyn. Lec. Series 1992-06, Vibration and Rotor Dynamics.
- [27] Song, G., and Mukherjee, R., 1996, "Integrated adaptive robust control of active magnetic bearings", IEEE Int. Conf. on System, Man, and Cybernetics, Beijing, China.

Session 15 -- Magnetic Bearings 2

Chairman: Anthony S. Kondoleon
The Charles Stark Draper Lab

DESIGN OF A MINIMUM CURRENT MAGNETIC BEARING

C. Klesen, R. Nordmann, U. Schönhoff

Darmstadt University of Technology, Department of Mechatronics,
Petersenstr. 30, 64287 Darmstadt, Germany
e-mail: klesen@mesym.tu-darmstadt.de

ABSTRACT

Current consumption of active magnetic bearings is an essential factor for the running costs and particularly for the acquisition costs. The maximum value of the needed current defines the size of the power amplifier, the diameter of the windings and the size of the slots etc. For the same lifting capacity, size and costs can be reduced significantly by reduction of the current.

This paper analyses the current consumption systematically. At first it shows how the bias current pre-magnetization can be replaced by permanent magnets. Different constructions are discussed. Furthermore, a control strategy will be presented, which minimizes the DC currents necessary for the support of static loads. The avoidance of currents caused by imbalance compensation has already been discussed in former papers. **All three measures together are usable to reduce the current consumption of AMBs significantly. Solely the transient currents are still required.**

INTRODUCTION

One criteria to qualify and compare active magnetic bearings is the load capacity in relation to the volume. It is mainly limited by two parameters:

- the losses in the windings
- saturation of the iron in the magnetic circuit

The saturation is a material specific parameter. It can be increased a little by variation of the material. A reduction of percentage of silicon in the iron core material increases the saturation flux density but decreases the specific resistance and causes higher eddy current losses. Materials that include cobalt are very expensive and have a low specific resistance but a saturation density of more than 2T can be reached. Hence the effect of saturation can not be reduced significantly by changing the material without increasing the cost dramatically, the cross-sectional area of the iron has to be enlarged. If the cross-sectional area of the iron is enlarged, there is less space for the copper of the windings. This means less total ampere-turns and less force. **The optimal design can only be found iterative. The total ampere-turns are**

also limited by the specific current density. Because of the cooling conditions, it mostly can not be increased to more than $5-7 \text{ A/mm}^2$.

Reduction of the **power consumption** is the only thing that can be done to increase the load capacity of an AMB at the same volume **overall. Thus, the lifetime cost can be reduced.**

The total power consumption of an magnetic bearing consists of static currents, dynamic and transient currents. Static currents are

- the bias current for premagnetization
- a DC current caused by static loads like the weight of the rotor

the dynamic and transient components are

- a current synchronous to the rotation frequency, caused by unbalance
- transient currents, caused by lifting of the rotor, changes of loads and other transient disturbance forces.

In many cases, the static components have a bigger **share of** the total power consumption than the dynamic ones. If there are mainly static loads, $0.05-0.1 \text{ W/N}$ losses are produced because of ohms resistance in the windings[4][5].

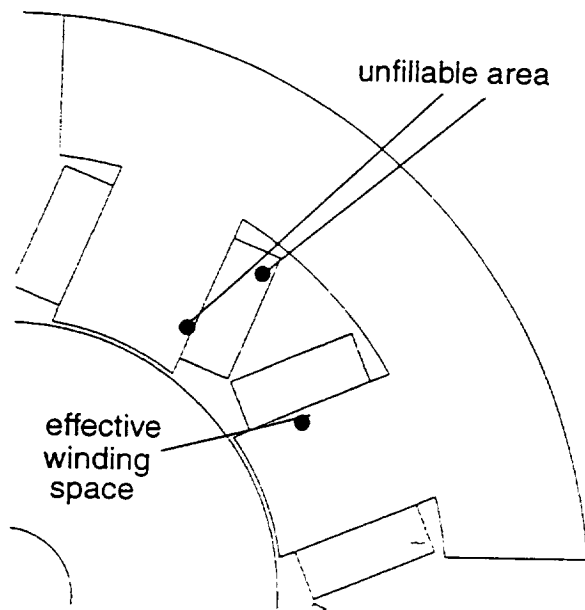


figure 1 Winding space of an AMB

As **already mentioned**, the total ampere-turns depend on the volume that can be filled with copper. As can be seen in *figure 1*, there is some space needed in the slot for isolation and due to the round wire, a bulk factor has to be considered. There is also an area which can not be filled with windings, because the windings are coiled first and than put to the iron core as a unit. Thus, the effective winding space is limited to 75-80% of the slot space [2]. Magnetic bearings with plates from three-phase-motors are coiled slot by slot. Therefore, the whole slot can be filled up with windings and there is nearly no empty space left. This is the reason for higher total ampere-windings of this construction, the effective winding space is more than 90% of the slot space. Together with the availability of this plates, this was the main reason to use this kind of plates in the constructions studied.

All of the named parameters have an influence on the current consumption and load capacity, but do not reduce current consumption as much as the implementation of permanent magnets (PM) does. They can substitute the whole flux generated by the static current. This is mainly the premagnetization, but also static loads can be supported by the permanent magnets. The first is discussed detail in the following three sections, the later is discussed in the section zero DC-current control. **Inbalance** can invoke large

amplitudes of harmonic current synchronous to the rotational speed. The reduction of this current by means of unbalance compensation is well known (Herzog et al. [6]). Applying this three measures,

- the **permanent magnetic** premagnetization,
- the zero DC-current control and
- the unbalance compensation,

current will only be needed for dynamic and transient forces and to stabilize the system. Thereby the load capacity per volume relation is significantly increased.

IMPLEMENTATION OF PERMANENT MAGNETS

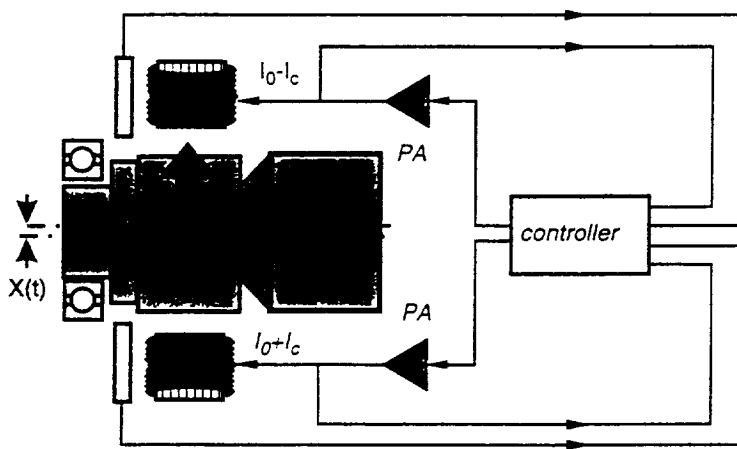


figure 2 principle arrangement of an magnetic bearing

This means that a bias current I_0 is driven through both opposite coils of one axis. A positive control current I_c results in a positive force, a negative current results in a negative force for this axis. This arrangement also linearizes the bearing but always needs a bias current which is half of the maximum current, no matter how big the load is.

The constant flux generated by the bias current can also be realized by the implementation of a permanent magnet. This constant flux can be reduced or enlarged depending on the sign of the control current. This results in higher load capacity.

Figure 2 shows the principle arrangement of an magnetic bearing without permanent magnet. There is at least one position sensor to measure the distance between rotor and stator. The position controller drives the current commands to the power amplifier. This allows the rotor to levitate in the desired position. Electromagnetical actuators can only deliver forces in one direction, no matter in which direction the current is driven through the coils. To guarantee correct working of the position control at acceptable dynamic performance, both force directions are needed.

This can be reached by a differential drive of the opposite coils of one axis.

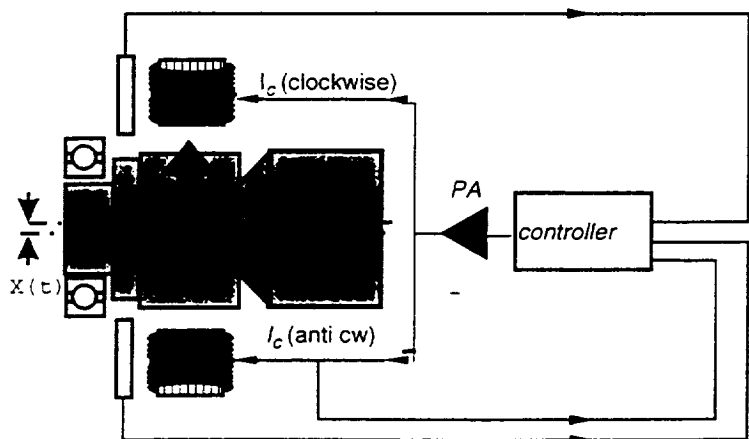


figure 3 principle arrangement of an magnetic bearing with permanent magnet

figure 4 finite element calculation of the example shown in figure 5 with small leakage

For coplanar bearings, an easy analytical model can be used to calculate the forces because the flux only flows in two dimensions. *Figure 5* shows the equivalent circuit for coplanar bearing neglecting the non-linearity of the materials.

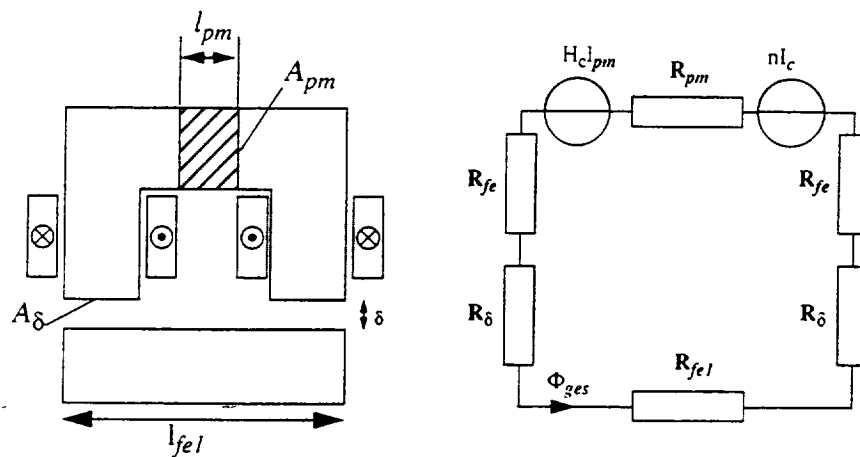


figure 5 equivalent circuit of a coplanar bearing

$$\oint \vec{H} d\vec{s} = \iint \vec{S} d\vec{A} \quad (1)$$

596

$$\sum Hl = nI + H_c \cdot l_{pm} \quad (2)$$

Together with

$$B_{\delta} \cdot A_{\delta} = B_{Fe} \cdot A_{Fe} \cdot S_{Fe} = B_{pm} \cdot A_{pm} \cdot S_{pm} \quad (3)$$

and

$$B_{\delta} = H_{\delta} \mu_0, \quad B_{Fe} = H_{Fe} \mu_0 \mu_{Fe}, \quad B_{pm} = H_{pm} \mu_0 \mu_{pm}, \quad R_{\delta} = \frac{\delta}{\mu_0 A_{\delta}}, \quad R_{fe} = \frac{l_{fe}}{A_{\delta} \mu_0 \mu_{fe}} \quad \text{and}$$

$$R_{pm} = \frac{l_{pm}}{A_{pm} \mu_{pm} \mu_0} \quad \text{the force can be calculated by the following equation}$$

$$F_B(I_c, B_{pm}) = \frac{A_{\delta} (2\mu_0 n I_c + B_{pm} l_{pm})^2}{\mu_0 \left(2\delta + \frac{A_{\delta}}{A_{pm} \cdot L_{pm}} \cdot \frac{l_{pm}}{\mu_{pm}} + \frac{A_{\delta}}{A_{Fe} \cdot L_{Fe}} \cdot \frac{l_{Fe}}{\mu_{Fe}} \right)^2} \quad (4)$$

A_{δ} is the cross-sectional area of the air gap δ , A_{pm} the cross-sectional area, L_{pm} the leakage factor of this area and l_{pm} the length of the permanent magnet, l_{Fe} the middle length of the whole iron with the relative permeability μ_{Fe} and the flux density B_{pm} of the permanent magnet, n is the number of windings for each coil and I_c the current. As (4) shows, the force can be **increased** with positive currents and can be reduced with negative currents. This is the same effect that can be realized with a bias current in the windings.

Measurements and comparisons with 2D-FE-calculations have shown that the force error of this method can be less than 15%. Depending on the current, the maximum flux density in the iron core and the eccentricity of the rotor, the error can be reduced to 6% by implementation of the geometry specific leakage factor. Less leakage can be seen in *figure 4*, which is without current in the coil then in *figure 6* which is with weakening of the field.

The realization of this kind of bearing is described in COPLANAR DESIGN.

Much more difficult is the calculation of the non-coplanar type. The flux generated by the permanent magnet flows in the r - z -plane, the flux generated by the coils in the r - ϕ -plane. This means, that a 3D-problem has to be solved.

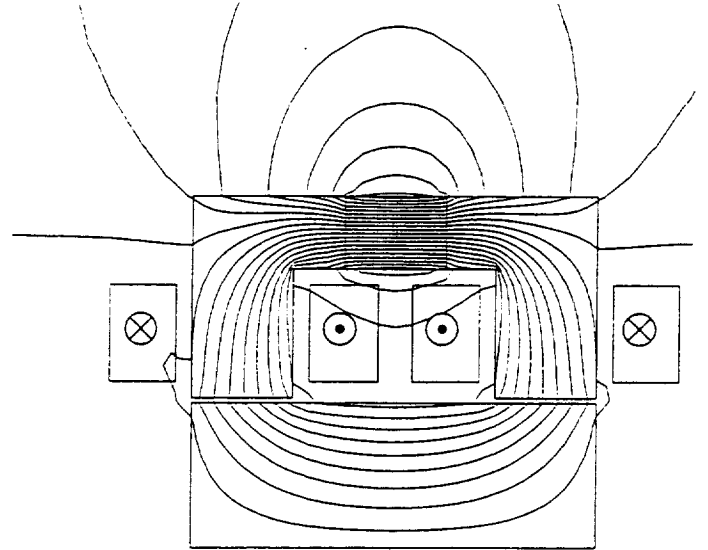


figure 6 massive leakage due to high current density

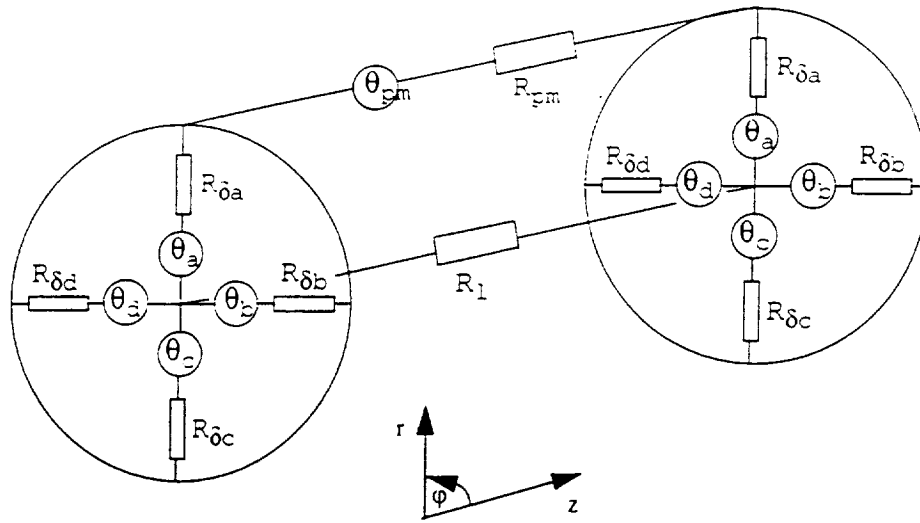


figure 7 equivalation circuit neglecting the resistance of the iron

The simplest model neglecting the resistance of iron, scattering and non-linear effects is shown in figure 7, where R_l is the resistance of the isolation of the laminations. Such a model is already explained in [1]. The model becomes difficult to calculate and to evaluate considering the nonlinearities and scattering. Another method is to compute the flux in the air gap generated by the coils in the r - ϕ -plane and the flux generated by the permanent magnet in the r - z -plane separately. The addition of the flux vectors delivers the resulting flux in the air gap and the force can be calculated. The error of this calculation is bigger than 40% in some cases. One reason for this massive error is the other operating point of the B-H-curve if the two fluxes are considered separately. Better results can be expected, if the inner and outer boundary condition is set to dirichlét. This method allows to consider the bias flux as normal flux at the inner and outer boundary. The 3d- finite element method is the only way to get good results. However this method is very time intensive and difficult to handle.

COPLANAR DESIGN

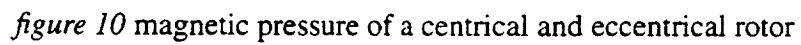
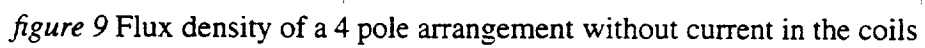
Figure 8 shows possible arrangements of coplanar bearings. The bias flux of the permanent magnets can be realized by axial, tangential or radial polarisation of the permanent magnet. It can be implemented in the stator with polar or cylindric flux direction. An implementation in the rotor is also possible. The most common arrangement is version b).

The coplanar as well as the non-coplanar type of bearing can be realized in 3-pole arrangement as well as in 4-pole arrangement [7]. In opposition to bearings biased by coils, the 3-pole version with permanent magnet does not have the advantage, that one power amplifier can be economized. Experimental studies of three pole bearings without permanent magnets have pointed out that this system has a tendency to become **unstable**.

	axial polarisation	tangential polarisation	radial polarisation
flux direction polar magnet in the stator		b)	c)
flux direction cylindric magnet in the stator	d)		f)
flux direction cylindric magnet in the rotor	g)		

figure 8 Arrangements of coplanar bearings

The reason is the electromagnetic coupling of the axis and due to the accuracy of the fixed point DSP controller the inaccurate coordinate-transformation for the three force axis in the 2 dimensional plane. Figure 9 shows a 4 pole arrangement with two permanent magnets per pole. The plates are of an eight pole AC-motor with 0.25 kW and have the number IEC 80/6-8.80. The outer diameter is 120mm, the inner diameter is 80 mm with an air gap of 0.6 mm. The permanent magnets are made of $\text{Sm}_2\text{Co}_{17}$ with an energy density of 225 kJ/m^3 and a remanence of 1.1 T.



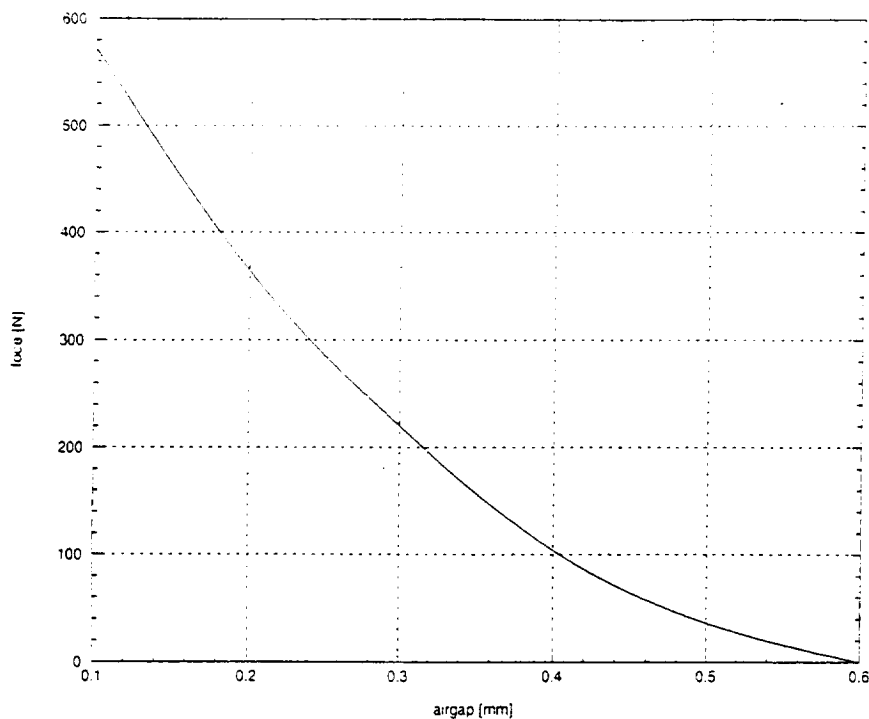


figure 11 rotor force without current

Figure 10 shows the force density that acts on the rotor surface. The force has the same size if the rotor is in central position. The resulting force is zero. If the rotor is moved in the direction x , a force results in the same direction.

Figure 11 shows the resulting force if there is no current in the windings.

The force characteristic becomes more linear, if a permanent magnet is implemented in every slot of the plate (variant A in figure 1).

Figure 1 shows some possible implementations of permanent magnets for a 3-pole bearing realized with plates of an AC-motor.

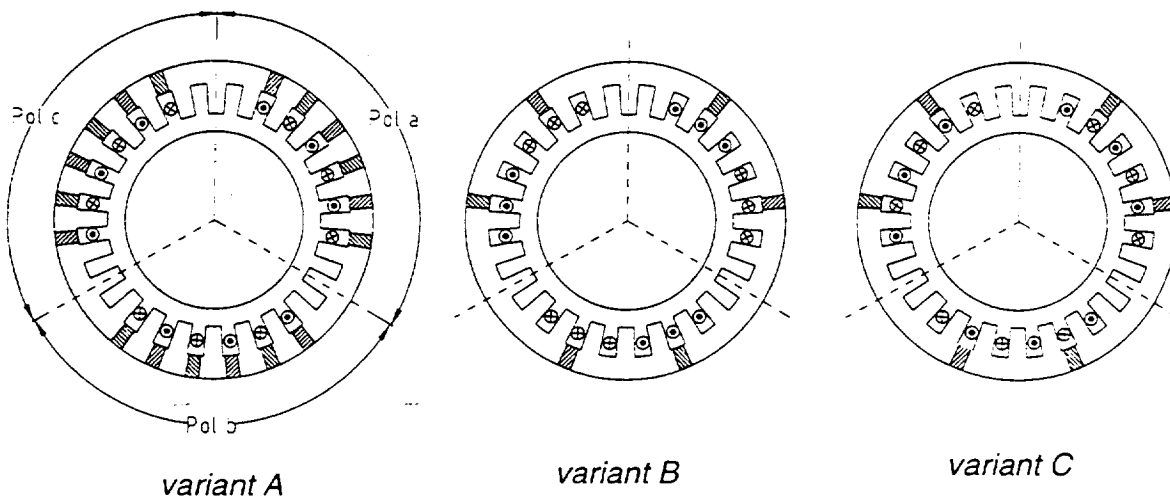


figure 1 some arrangements of a coplanar bearing of type b in figure 8

Figure 12 shows the results of the FE-calculation of variant A. There is a very good linearity between current and force. The disadvantage of this solution is the high force that still appears, when weakening the field of the permanent magnet. The reason is the high remanence of the permanent magnets. The curve becomes more steep, when the thickness of the magnets is reduced. However this reduction is limited by the stability against demagnetisation of the permanent magnets especially at high temperatures.

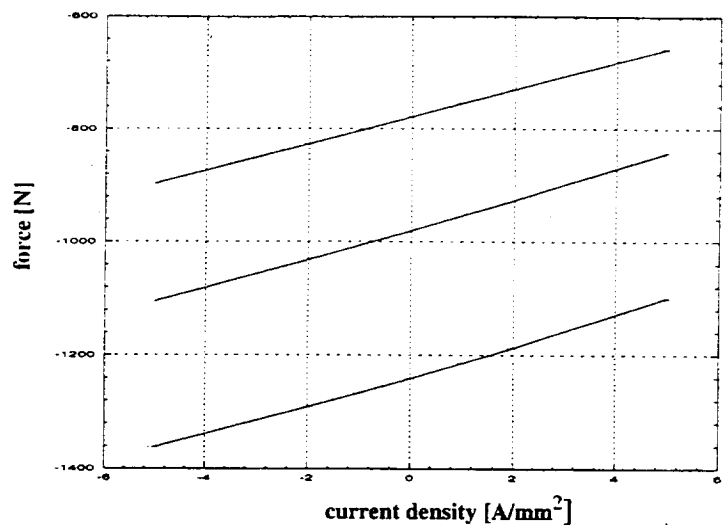


figure 12 characteristic diagram of one pole in figure 13

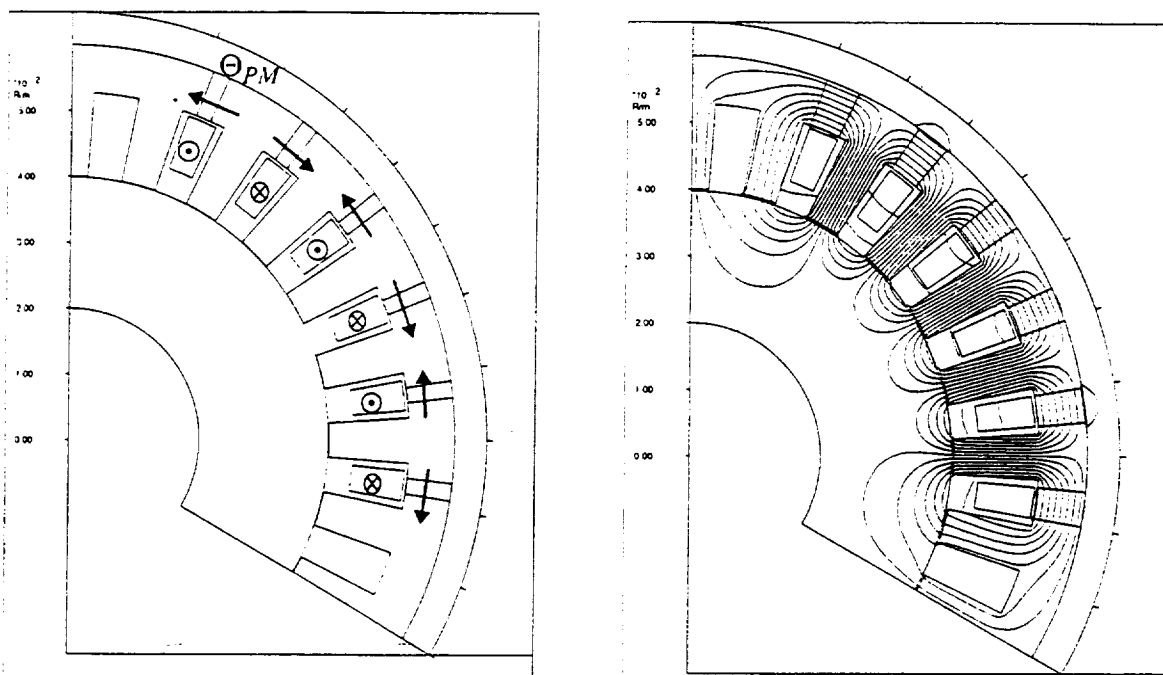


figure 13 computation of variant A with the FD- program *PROFI*

Figure 14 shows the curves for the variants B and C. The characteristic becomes much more nonlinear. The reason of this effect can be explained with the plots in figure 15. If the force is reduced by weakening the field of the permanent magnets, another flux path appears, that generates a force. This effect is bigger for variant C and leads to a bigger nonlinearity. Variant A is the auspicious design for a coplanar bearing with AC-motor-plates. It has a nearly linear characteristic and offers the largest surface for permanent magnets. This means highest forces without current. Beside the high cost for permanent magnets, the main disadvantage is the small current force ratio.

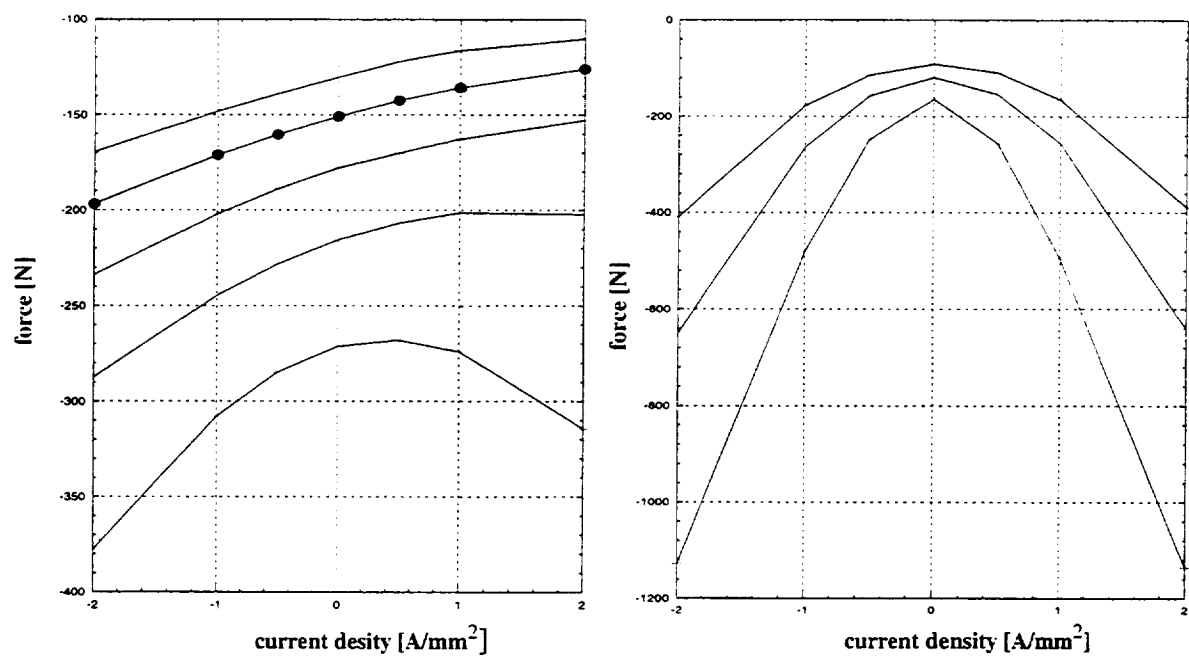


figure 14 characteristic curves of variants B and C

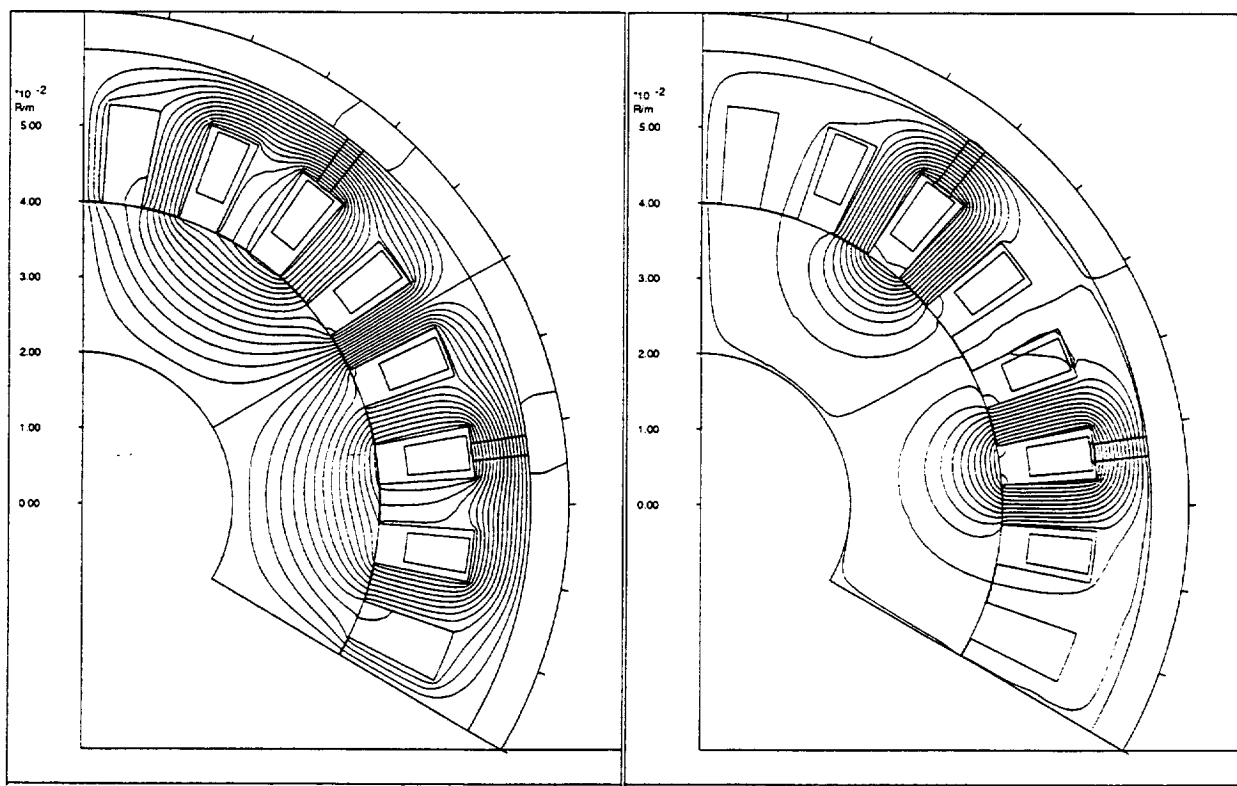


figure 15 fieldlines without current (l) and with weakening of field (r)

NON-COPLANAR BEARINGS

Figure 16 shows possible arrangements of non-coplanar bearings. The bias flux of the permanent magnets can be integrated in the rotor or the stator.

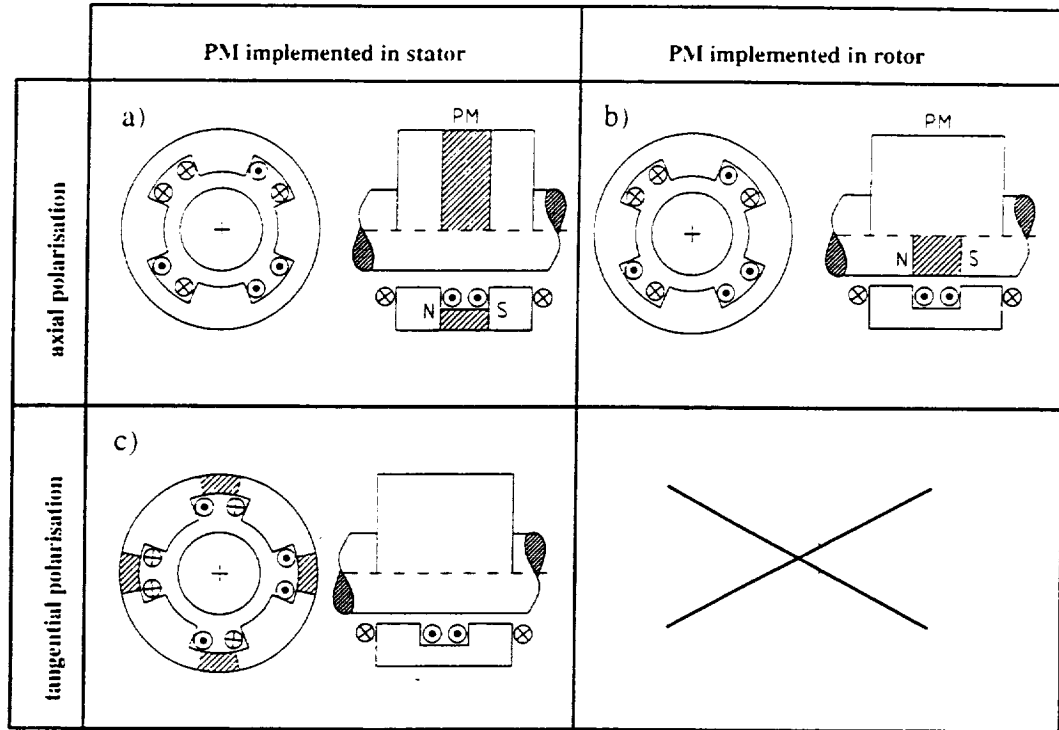


figure 16 arrangements of non-coplanar bearings

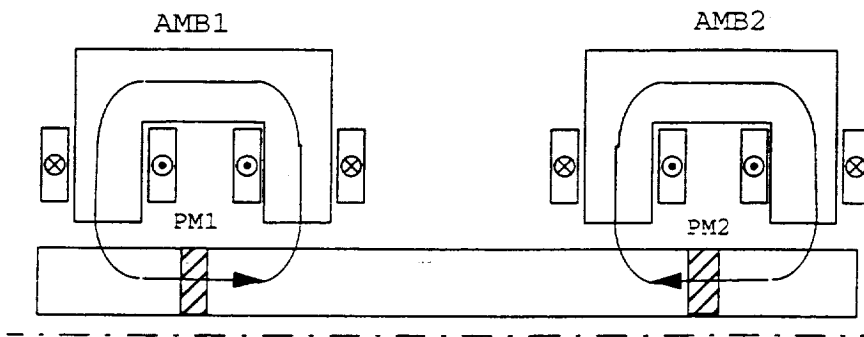


figure 17 arrangement with two bearings and two permanent magnets

Non-coplanar bearings have already been realized as 3 ([3],[7]) or 4 ([2]) pole magnetic bearings. It can be point out as a main technical advantage, that there is no additional resistance from the permanent magnets in the magnetic circuit. There is less current needed to generate the same coil flux as in coplanar bearings. However, the surface to implement permanent magnets is smaller than for coplanar bearings. This means less

forces without current but a better current force ratio. Most of the constructions prefer variant a) of figure 16. The permanent magnet, which has a thickness of 2 mm only, is very difficult to handle and to obtain for such an construction with permanent magnet in the stator when IEC 80/6-8.80-plates are used.

Beyond it, the surface of the permanent magnet in the rotor is almost **twice** as large as the surface in the stator. These are the main reasons, why an arrangement with permanent magnets in the rotor is preferred. *Figure 17* shows an arrangement with two bearings and one permanent magnet for each bearing. The disadvantage of such a construction is the need of two windings for every axis of the bearing. Thus, the specific load capacity decreases. Another possibility is shown in *figure 18*. The only stator modification, that has to be done is a housing for the two bearings that

is made of a ferromagnetic material. The rotor has to be made of two parts to allow the assembly of the permanent magnet disc. If the permanent magnet is made of two halves of a disk, only a slot has to be machined. In this case, the magnet should be fixed with a bandage.

As already mentioned, the force of a non-coplanar bearing can only be computed with the 3 dimensional finite element method. For a better oversight, *figure 19* shows only a quarter of the model of such a computation. The complete bearing is shown in *figure 20*. When we assume, that both bearings have the same load, only one bearing has to be computed, the other one can be considered by symmetry. This reduces the computation time. The length of the rotor is reduced to a minimum due to the same reason. The force generated in one bearing without current is shown in *figure 21*.

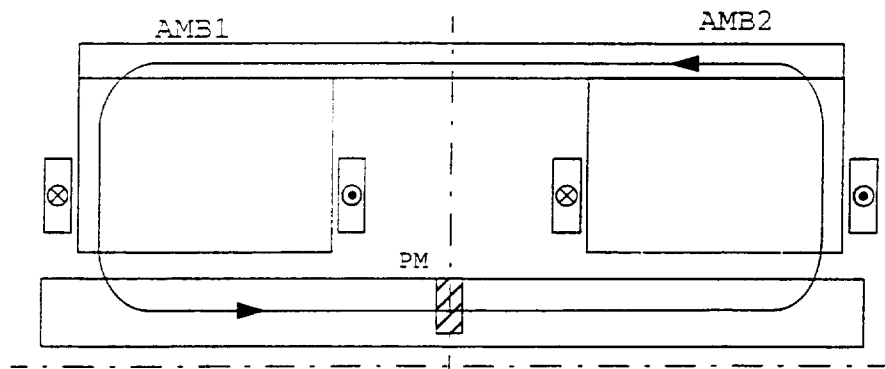


figure 18 arrangement with two bearings and one permanent magnet

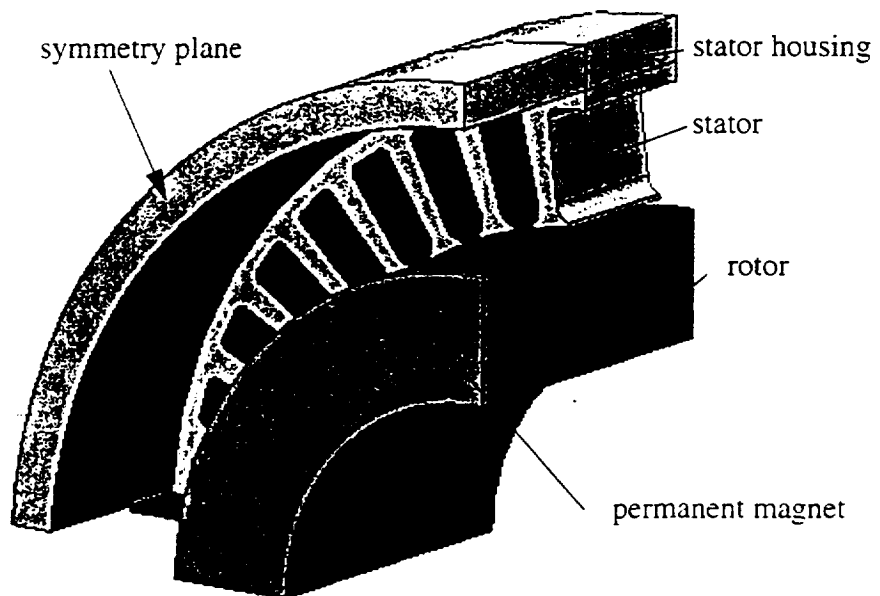


figure 19 one pole of the FE-model of the non-homopolar bearing

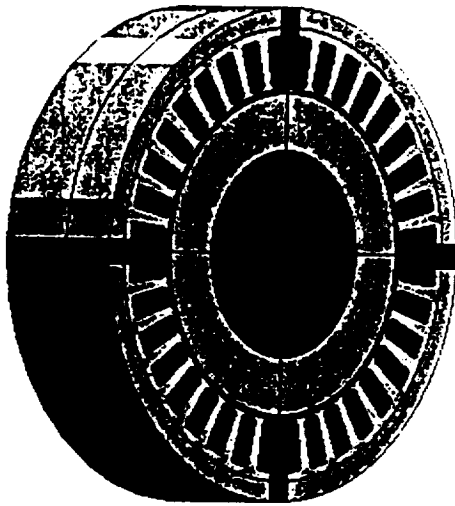


figure 20 model of one complete bearing

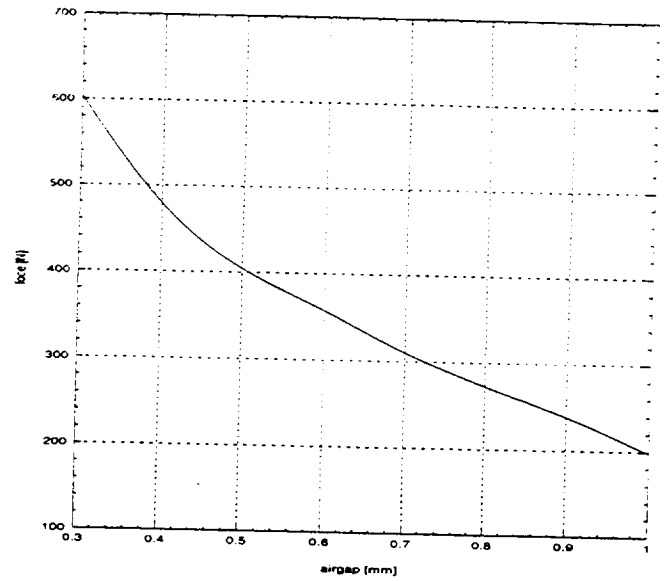


figure 21 loading capacity of one AMB without current

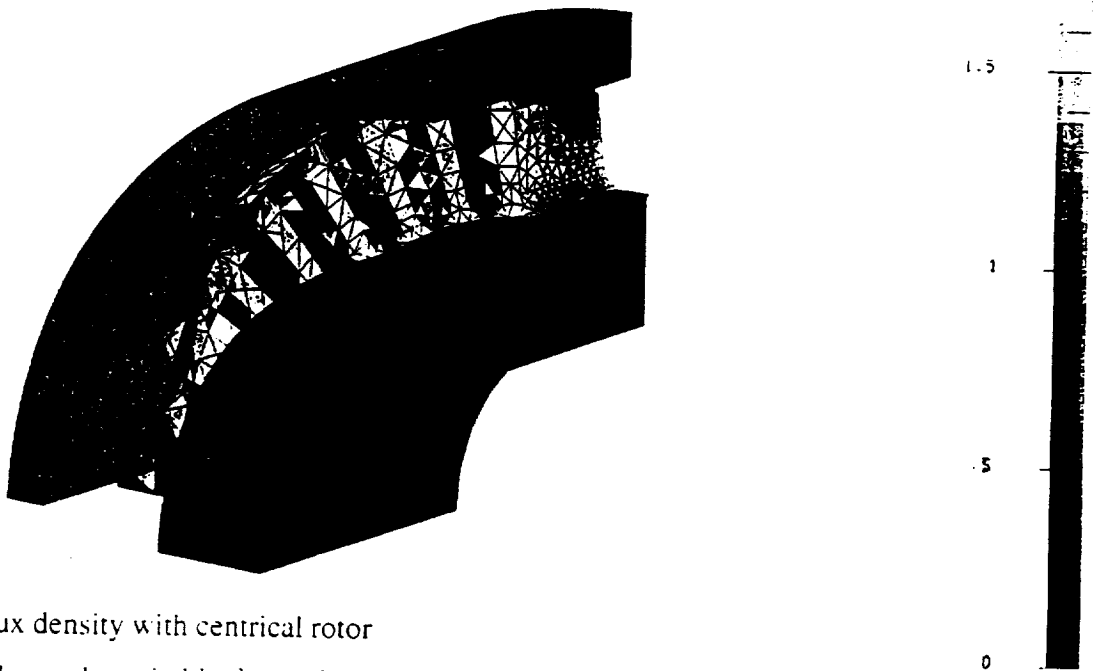


figure 22 flux density with central rotor

Figure 21 shows the suitable force characteristic of the non-coplanar bearing. It can deliver more than 500 N per bearing from one permanent magnet only. Although the coplanar bearing has a higher load

capacity than the noncoplanar type. The current force ratio of this bearing is higher. Thus, this bearing has a better performance, if the dynamic forces are higher than the static ones.

ZERO DC-CURRENT CONTROL

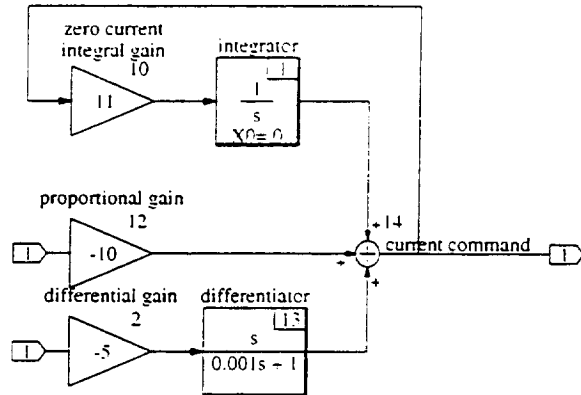


figure 23 modified PID controller scheme for zero DC-current

The usage of permanent magnets already reduces the DC-current significantly. But if the AMB has to support static loads like gravitational loads, a DC-current is still required. This depends on the common control strategy to keep the rotor in the centre of the bearing. As already mentioned, outside the centre of a permanent magnetic premagnetized AMB a position can be found, where the specific static force is supported by the permanent magnets without any current. To move the rotor to this position of force-equilibrium the static behaviour of the position control loop has to be changed. The current and not the position deviation has to become zero for $t \rightarrow \infty$. For the common PID-control this can be realised easily: The input to the integral

gain of the PID controller is no longer the position deviation, it now is the current. This scheme is shown in figure 23. Stability of the closed loop is reached by a positive sign of the integral feedback. A low gain is desired, because a high gain increases the compliance at low frequencies. If the gain is chosen small, the stability margin of the underlying PD-controller is not touched.

From a practical point of view the range of displacement should be limited in order to avoid contact with the stator and to keep a gap for excursions invoked by dynamic loads. If the rotor exceeds the limits, the control is switched to conventional PID-control with the limit as desired position.

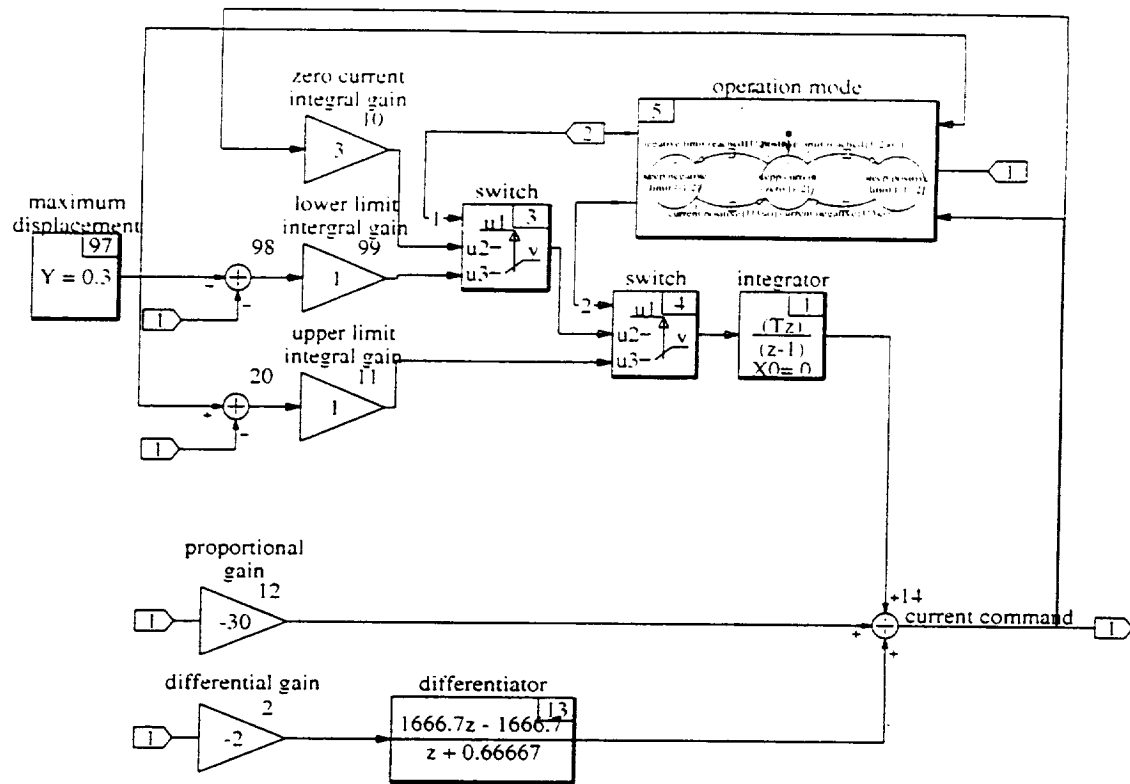


figure 24 controller scheme for zero DC-current with displacement limitation

Figure 24 shows the control scheme with displacement limitation. There are three operation modes: keeping the upper limit, keeping the lower limit and enforcing zero current.

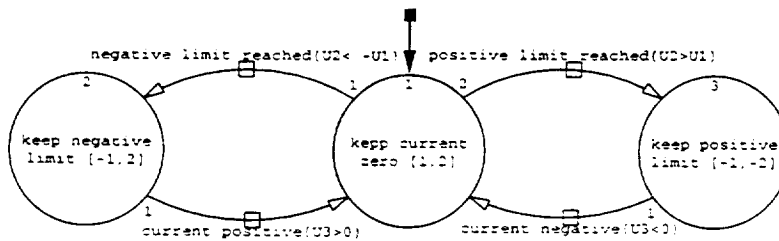


figure 25 controller operation mode switching for displacement limitation

For all three modes one integrator is used and only the feedback paths are switched to the input of the integrator to avoid unsteadiness of the current command. Figure 25 shows the three operation modes and their switching conditions.

Simulation results are shown in figure 26. The load is stepwise increased. As long as the limits are not exceeded the current returns to zero. When the limits are reached, the DC-current increases. The dynamic behaviour to the load steps is not affected by the switching between the operation modes.

The developed control scheme allows static displacement of the rotor within a given range to minimize the DC-current consumption. It has to be checked for each application, whether displacement of the rotor

is tolerable and if so, which range can be allowed. The control strategy can also be combined with other controller types than PID. Stability and performance has to be checked for both operation modes, conventional integral gain and zero current integral gain.

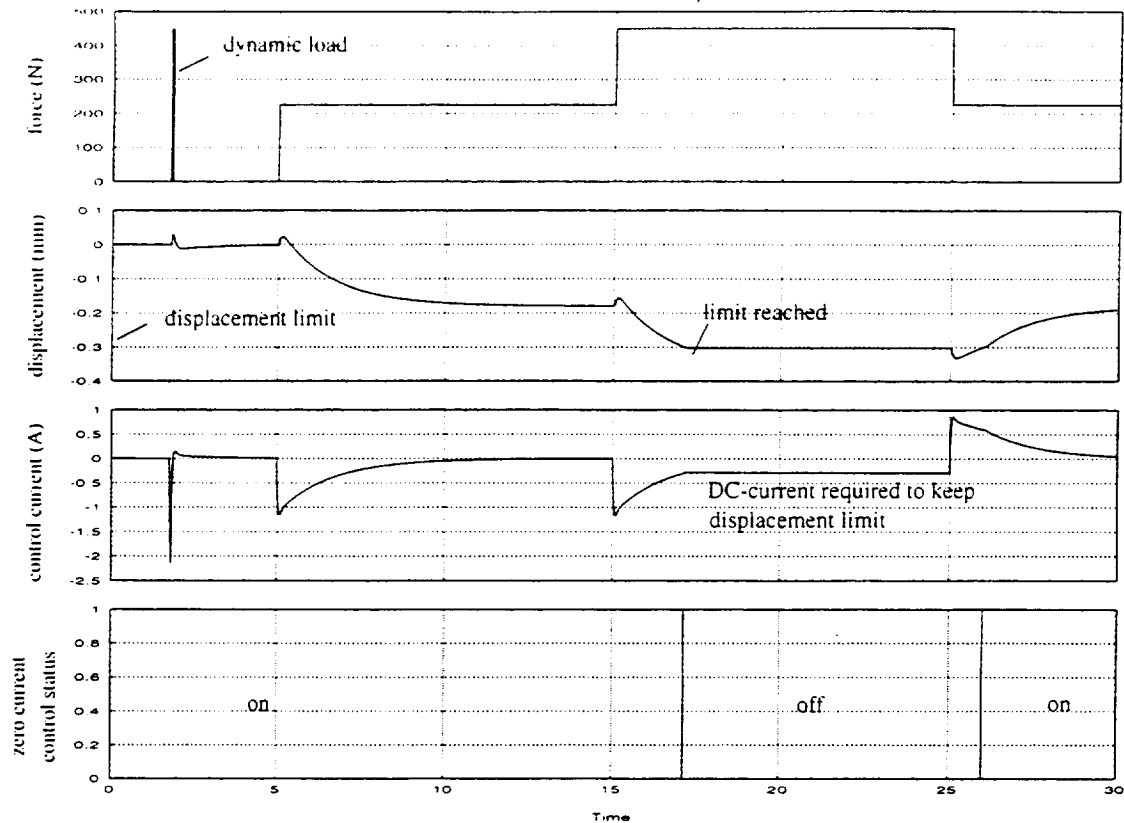


figure 26 operation of the zero DC-current control

CONCLUSION AND OUTLOOK

The power consumption of an AMB has been analysed first. The static currents can be reduced by the implementation of permanent magnets. The realisation of the two principal constructions of AMBs with permanent magnet coplanar and non-coplanar bearings, has been presented. The coplanar bearing delivers higher forces without current in the coils whereas the non-coplanar types have an higher current force ratio. The presented zero-dc-current-controller reduces the static current. This means higher load capacity and reduced life time costs. A coplanar bearing is the preferred construction, if there are mainly static forces. If the dynamic ones are predominantly, the non-coplanar type is the right choice.

These statements are based on simulations. Shortly the rotor with the permanent magnets will be finished and the two kinds of bearings can be compared in experiment.

ACKNOWLEDGEMENT

We would like to thank Mr. Jörg Buchwald for his support and Mr. Martin Ernst for the FE-3D-computation. Beyond it SIMEC GmbH, Germany for providing the software FLUX 3d of CEDRAT and PROFI Engineering GmbH, Germany for the preparation of the software PROFI 2d.

REFERENCES

- [1] Hsiao, F.-Z. / Ko, Dennil / Lee, A.-D.; „Analysis and Testing of Magnetic Bearing with Permanent Magnets for Bias“, JSME International Journal Series C, 1996, Vol. 39, No. 3, S. 586 - 596
- [2] Hsiao, F.-Z. / Fan, C.C. / Chieng, W. H. / Lee, A.-D.; „Optimum Magnetic Bearing Design Considering Performance Limitations“, JSME International Journal Series C, 1996, Vol. 39, No. 3, S. 586 - 596
- [3] Grbêsa, Boris; „Modeling of a Homopolar Beraing“, Intelligent Motion, May 1998 Proceedings
- [4] May, Hardo / Shalaby, Mahfooz / Weh, Herbert; „Berechnung von geregelten Permanent-Magneten für Tragen, Führen und Antriebsaufgaben“, etz-Archiv 1979, Heft 2, S. 63 - 67
- [5] Hübner, K. - D. / Kaupert, G. / Weh, Herbert; „Dynamisches Verhalten geregelter permanenterregter Tragsmagnete für Schnellbahnen“, etz-Archiv 1981, Band 3, Heft 10, S. 341 - 348
- [6] Herzog, R.; Bühler, P.; Gähler, C.; Larssonneur, R. (1996): Unbalance Compensation Using Generalized Notch Filters in the Multivariable Feedback of Magnetic Bearings. IEEE Trans. on Control System Technology 4(5), 580-586.
- [7] Sundermeier, R.; Konzeption und Simulation einer magnetischen Lagerung mit transversaler Flußführung und permanentmagnetischer Sammlerbauweise“, Diss. TU Braunschweig, 1992

INSIDE-OUT CONFIGURATION ACTIVE MAGNETIC BEARING ACTUATORS

M.A. Pichot, J.P. Kajs, R.J. Hayes, J.H. Beno, A. Ouroua, and B.M. Rech

University of Texas at Austin
Center for Electromechanics

ABSTRACT

The University of Texas Center for Electromechanics (UT-CEM) has designed active magnetic bearing actuators for use in a 5 MW flywheel alternator with a 700 lb (318 kg), 20,000 rpm rotor, under the sponsorship of the Department of Defense Combat Hybrid Power Systems (CHPS) program. Because this machine incorporates an unusual inside-out topology (i.e., the rotating portion of the flywheel is located outside the stationary components), unique inside-out configuration magnetic bearing actuators are required. Permanent magnet bias bearings were chosen for this application because of inherent low power requirements, low power losses, and nearly linear current stiffness and positional stiffness. To verify performance, a bearing test fixture was designed and built which permits static and dynamic force measurement. This paper discusses bearing requirements, actuator design, predicted performance, and compares theoretical versus measured bearing characteristics. A companion paper discusses control issues for this unique magnetic bearing system [1].

INTRODUCTION

The CHPS program seeks to produce a new class of hybrid-electric combat vehicles with significant advances in the areas of mobility, armaments, and defensive systems. One of the distinguishing features of these vehicles is that all major subsystems will be electrically driven, including a hybrid electric drive-train system, electric armaments and electromagnetic armor. An illustration for the vehicle concept appears in figure 1.

UT-CEM serves as a subcontractor in this project, with the task of developing a flywheel alternator to deliver pulsed power for weapons systems as well as load-leveling power for drive-train components. High power electrical loads for the alternator include the following weapons systems: an electrothermal-chemical (ETC) gun, high power lasers, and electromagnetic armor. The alternator also provides power for AC induction traction motors used for propulsion and for a fully active electromagnetic suspension system.

Since the flywheel alternator will be mounted onboard the vehicle, its weight and volume are of prime importance. Accordingly, the alternator is designed to maximize energy density and operate at high speed. Energy storage for this machine is 25 MJ at 20,000 rpm with an estimated alternator weight of 1,310 lb (595 kg). It provides up to 5 MW peak power for intermittent weapon systems loads and 350 kW continuous power for propulsion related loads.

This work was supported by the U.S. Defense Advanced Research Projects Agency under letter subcontract #4500152859.

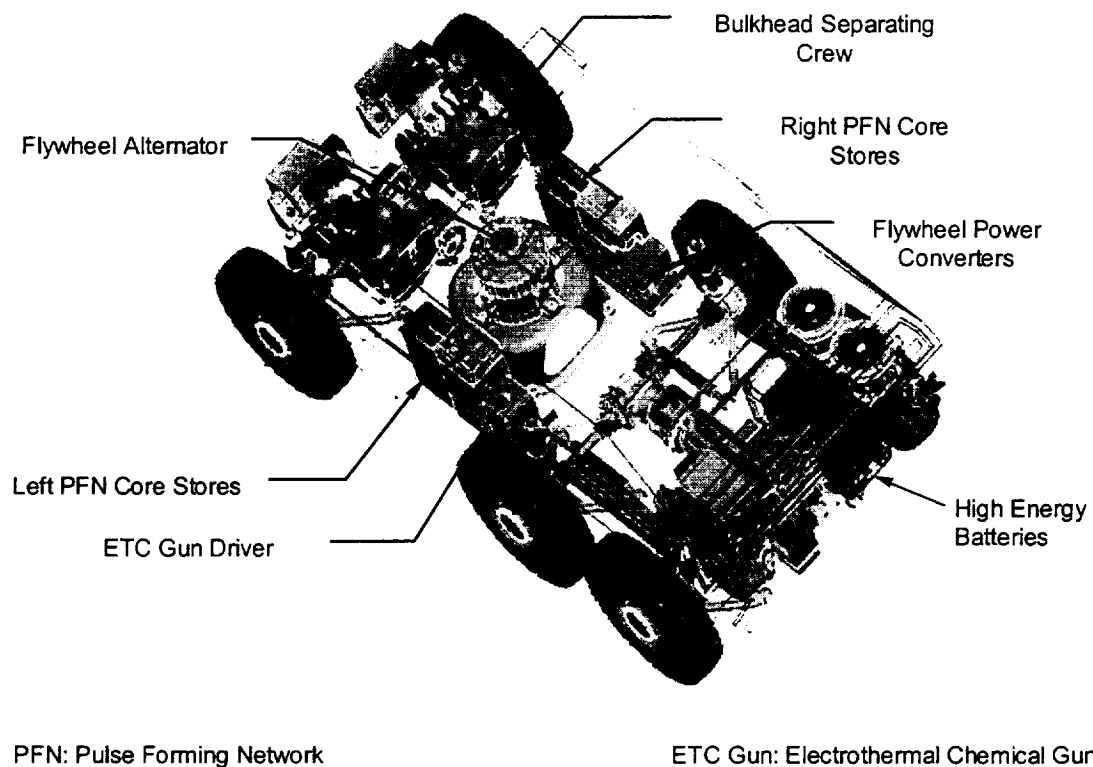


Figure 1. CHPS hybrid electric combat vehicle.

A cross-sectional view of the CHPS flywheel alternator is shown in figure 2 (note that the alternator is a vertical axis machine in the vehicle). The inside-out topology shown is very efficient in terms of maximizing energy stored per unit volume, but creates challenging bearing requirements. Rolling element bearings were first investigated for use in the CHPS machine, but proved unattractive for several reasons including: excessive rolling element bearing power loss and heat generation for this continuous duty machine, difficult lubrication and cooling because the rotor spins in a vacuum, and inadequate calculated bearing life.

For these reasons, a magnetic bearing system was selected over rolling element bearings, despite increased complexity. Since magnetic bearings are the only bearing type that appears compatible with the CHPS flywheel requirements, development of inside-out bearing actuators is viewed as essential to successful flywheel design.

BEARING SYSTEM REQUIREMENTS

The bearing system for the flywheel alternator must have sufficient capabilities to deal with rotor static and dynamic loads common to all high-speed machines. In addition, since mounted in a combat vehicle with off-road capabilities, terrain loads are transmitted through the vehicle suspension and will be present at the bearings. To reduce windage power losses, the alternator

rotor operates in a vacuum, necessitating a vacuum-compatible bearing system. Cooling oil is available in the stator shaft at 70-90°C. A summary of the magnetic bearing system requirements appears in table 1.

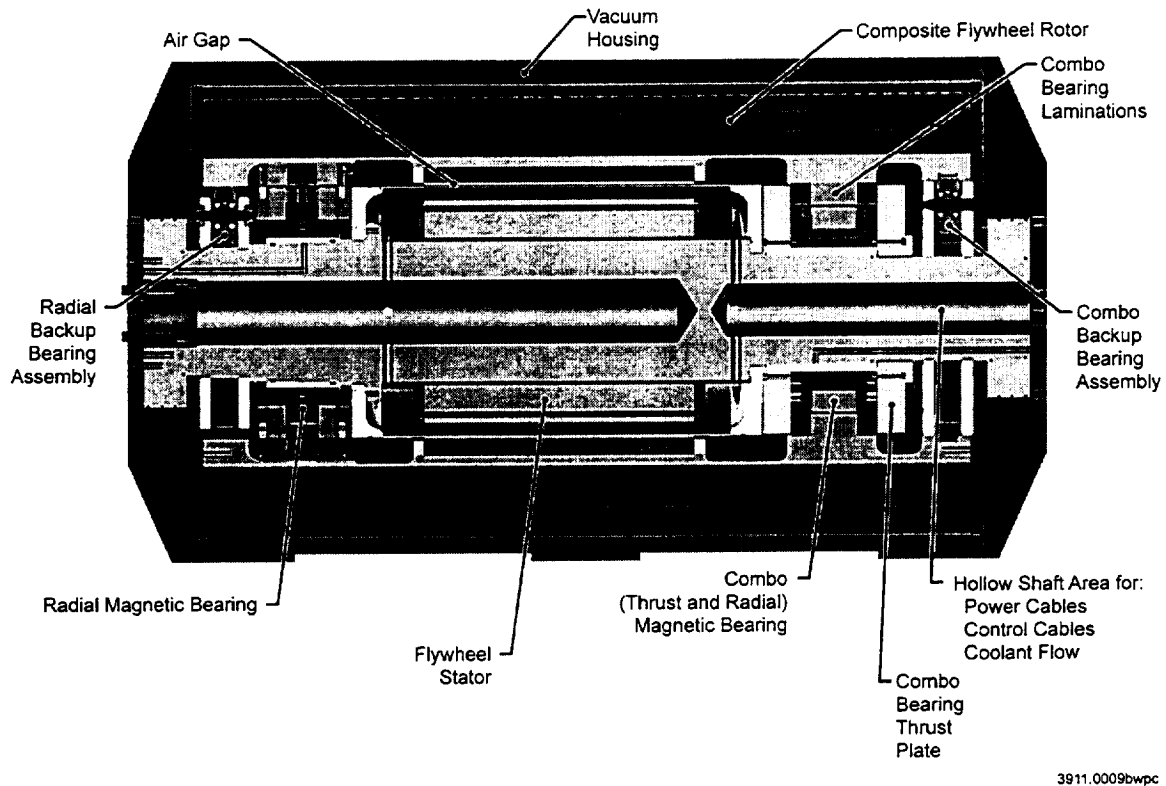


Figure 2. CHPS flywheel alternator.

Table 1. Magnetic Bearing System Requirements

Maximum Speed	20,000 rpm
Normal Operating Speed Range	15,000 – 20,000 rpm
Load Capacity	2g dynamic load capacity (plus 1g static load)
Maximum Power Loss	~100 W per bearing
Frequency Response	
Radial Actuators	Bandwidth at least 10X machine rotational frequency [1] Full load capacity at 2X machine rotational frequency
Thrust Actuator	Bandwidth of approximately 10 Hz desired
Backup Bearing Requirements	Provide support when magnetic bearings not levitated Shut down from full speed with magnetic bearing system inactive Provide support for short duration loads exceeding magnetic bearing load capacity (up to 8g maximum)

BEARING SYSTEM DESIGN

Magnetic Bearing Type

Permanent magnet bias homopolar (PMBH) magnetic bearings were selected for this application based on studies showing reduced power requirements and lower losses compared to heteropolar bearings [2]. An additional benefit of PMBH bearings is that control is simplified because of nearly linear current stiffness and positional stiffness characteristics.

Although PMBH bearings have been described in the literature previously [3], the CHPS machine presents an unusual application due to its inside-out topology. Since the rotational portion of the bearings is positioned outboard of the stator at a relatively large radius, bearing rotor laminations must withstand higher stresses than in conventional magnetic bearings. In addition, the magnetic air gap grows larger with increasing speed, instead of decreasing as in conventional configuration bearings. These factors complicate the bearing actuator design, and for our application, necessitate the use of unconventional bearing materials.

Bearing System Configuration

As shown in figure 2, the bearing configuration chosen consists of a radial magnetic bearing used on one end of the rotor and a combination bearing on the other. The radial bearing provides support in the radial direction only, while the combination bearing supports loads in both radial and axial directions. The advantage of this arrangement is that the combination bearing is significantly shorter in the axial direction than separate radial and thrust bearings, and allows the CHPS machine to be more compact than if separate bearings were used.

Also incorporated in the magnetic bearing system are backup bearings. These bearings provide support during nonoperational periods when the magnetic bearings are inactive, and provide a means to shut down the machine safely in the event of a magnetic bearing system failure. In addition, in the CHPS machine the backup bearings must occasionally provide additional support for short duration loads exceeding the magnetic bearing load capacity. Infrequent loads as high as $8g$ can be expected on combat vehicles from terrain shock loads transmitted through the vehicle suspension. It would be prohibitive to use bearing actuators with enough capacity to handle these loads (the bearings would be too large to be practical), so the backup bearings are required to accept these additional loads.

Bearing Design Process

The bearing design for this application is approached with an iterative process involving consideration of several system components, and takes the following form:

- Develop a model of the entire system to determine requirements (includes control and rotor dynamics modeling)
- Design baseline actuators (using design codes discussed later in this paper)

- Analyze system model including actuators, amplifiers, sensor dynamics, and control algorithms •
- Iterate system design until an acceptable design is identified

RADIAL BEARING ACTUATOR DESIGN

An illustration of the radial bearing actuator is shown in figure 3. The inside-out configuration is readily apparent in the fact that the outer part of the bearing includes the rotor lamination assembly, with the inner part of the bearing consisting of stator components. The radial bearing is 14.17 in. (36.0 cm) on the outside diameter with an overall length of 4.33 in. (11.0 cm), and a radial air gap 0.020 in. (0.051 cm) at rest. At 20,000 rpm, the radial air gap increases to 0.049 in. (0.125 cm).

In this bearing design, the bias field is established with neodymium-iron-boron (NdFeB) permanent magnets located in the center of the stator. The magnets are segmented and sandwiched between two solid stator iron components manufactured from low carbon steel. Stator laminations are fabricated from 0.014 in. (0.356 mm) thick M-19 silicon steel and include dovetail-shaped coil slots to reduce rotor lamination rotating losses. The stator laminations are assembled to the stator iron with an interference fit to provide high rigidity in the radial direction and for good mechanical integrity. A hydraulic fit is used for bearing stator assembly to the alternator shaft, providing an interference fit for high radial rigidity, but in a form that can be repeatedly reassembled. Each of the eight actuator coils is wound with 90 turns of No. 19 polyester coated copper magnet wire, with G-10 coil guides provided to simplify the winding process.

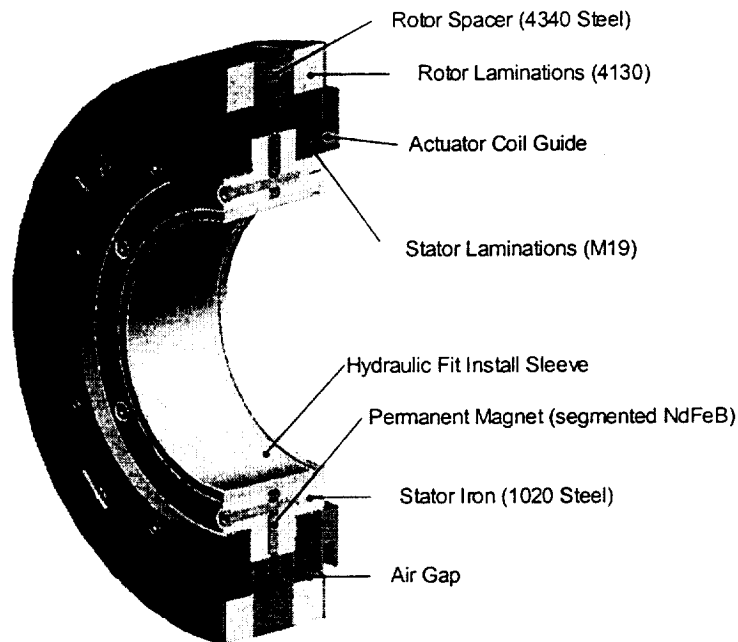


Figure 3. Radial bearing actuator.

From an electromagnetic point of view, silicon steel would also be a good choice for the rotor laminations; however, silicon steel does not have adequate mechanical properties to withstand induced rotor stresses and corresponding fatigue conditions. A structural grade steel (AISI 4130) was ultimately chosen for the rotor laminations for desirable strength and fatigue characteristics, despite less desirable electromagnetic properties.

COMBINATION BEARING ACTUATOR DESIGN

The CHPS combination bearing actuator is shown in figure 4. As with the radial bearing, the outer part of the bearing rotates with the flywheel rotor, with the stator bearing components assembled to the flywheel stator shaft. The combination bearing is 12.0 in. (30.5 cm) outside diameter with an overall length of 6.58 in. (16.7 cm), and radial and thrust air gaps 0.020 in. (0.051 cm) at rest. At 20,000 rpm, the radial air gap increases to 0.036 in. (0.091 cm). As discussed earlier, this bearing provides support in both radial and axial directions, eliminating the need for separate radial and thrust bearings. This is accomplished with separate actuator coils for the radial and axial directions, which generate forces in separate radial and thrust air gaps. As with the radial bearing, bias flux is provided with NdFeB permanent magnets, although in the combination bearing, the magnets are magnetized in the radial instead of the axial direction. The combination bearing also employs a hydraulic fit install sleeve and includes segmented wedges as shown; these devices permit assembly and disassembly into the CHPS flywheel topology.

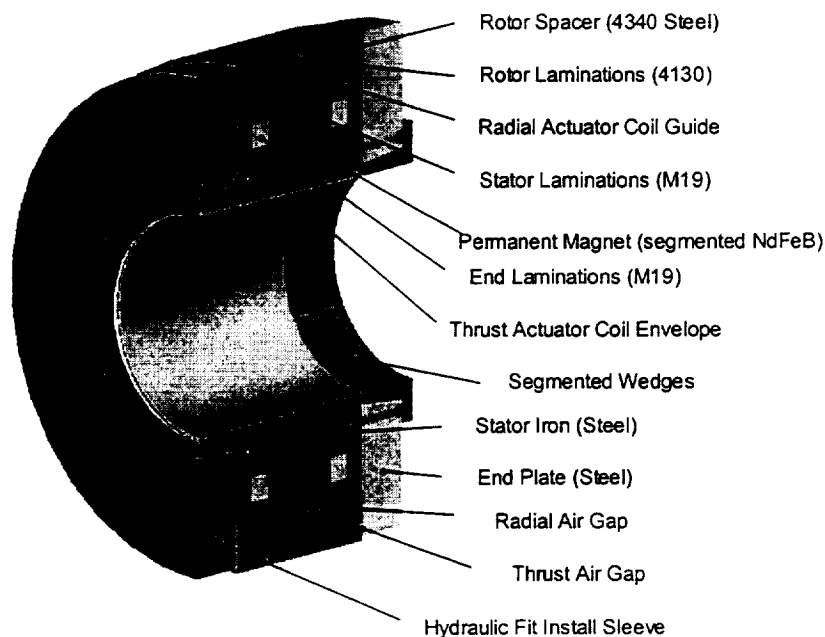


Figure 4. Combination bearing actuator.

Materials chosen for the combination bearing are similar to the radial bearing, with rotor laminations made from AISI 4130 steel, stator iron and end plate components made from low-carbon steel, and stator laminations fabricated from M-19 silicon steel. The combination bearing requires four radial actuator coils of 75 turns each, wound with No. 20 copper magnet wire. Two thrust actuator coils are required, each consisting of 190 turns of No. 20 magnet wire.

ACTUATOR ANALYSIS AND PREDICTED PERFORMANCE

A variety of analyses were performed in the design of the CHPS magnetic bearing actuators, including modeling of actuator electromagnetics, thermal response, mechanical stress and fatigue, and control system behavior. This paper will present results from the electromagnetic analysis, with control system modeling discussed in a companion paper [1].

For actuator electromagnetic analysis, a 1-D non-linear magnetic circuit code for inside-out actuators was developed at UT-CEM. It includes modeling of non-linear B-H characteristics and calculations necessary for sizing of coil conductors to meet required criteria of resistance, voltage, and current. Simplified thermal calculations are also provided for power loss and corresponding temperature rise estimates. Calculation turn-around time is fast, allowing the user to rapidly evaluate candidate bearing geometries during preliminary design optimization.

As a final check in the electromagnetic analysis, 3-D non-linear finite element analysis (FEA) is performed using *Opera-3D* software commercially available from Vector Fields Inc. Figure 5 shows example FEA meshes used for the radial and combination bearings. As shown in the figure, symmetry is used where appropriate to reduce computation time, and actuator coil geometry is accurately modeled.

Predicted bearing force versus DC current is shown in Figure 6 for the radial and combination bearings operating at 20,000 rpm. In-line and diagonal radial force curves are provided, where in-line forces are defined as being in the direction of the bearing poles, and diagonal forces in the direction of the coil slots (at 45° with respect to bearing poles).

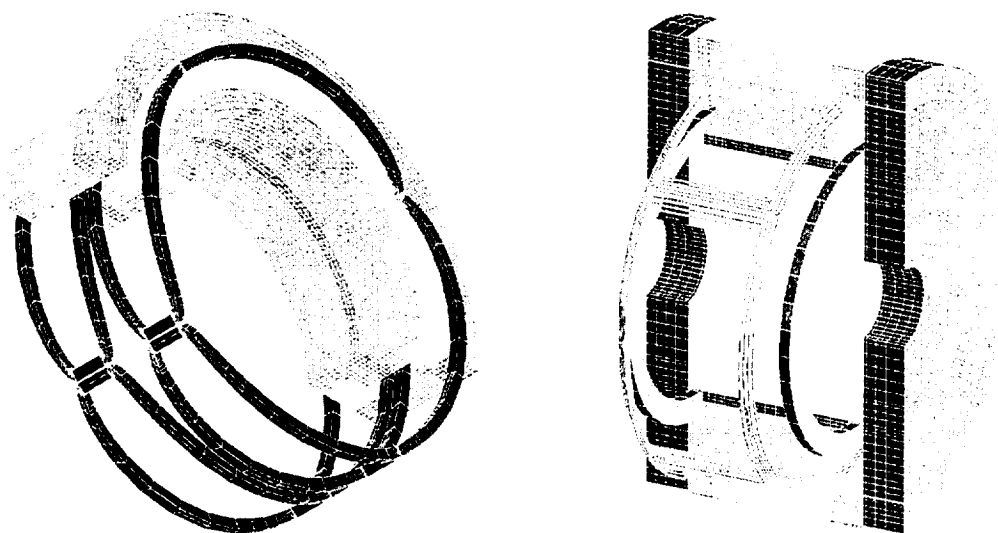


Figure 5. Radial and combination bearing FEA meshes.

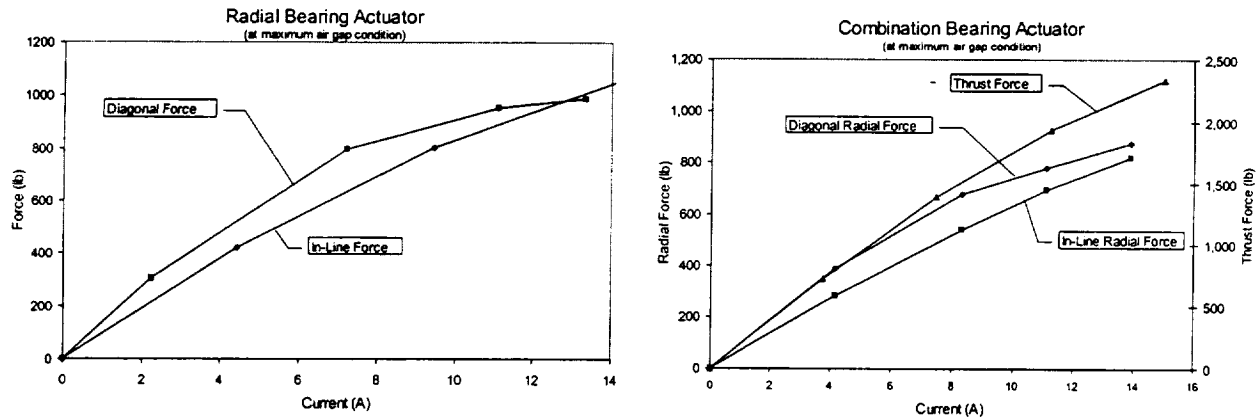


Figure 6. Predicted actuator force vs. DC current.

To simplify control, the actuators were designed to meet stated load capacity goals while operating on the linear part of the force versus current curve. Assuming equal distribution of the $2g$ dynamic load, this corresponds to a required radial force of 700 lb (3.11kN) per bearing. The thrust bearing requires sufficient capacity to support $2g$ dynamic plus $1g$ static load for this vertical axis machine, corresponding to 2,100 lb (9.34 kN).

BEARING TEST HARDWARE

To verify design and analysis codes, and provide first-hand experience with fabrication and operation of the inside-out bearing actuators, UT-CEM fabricated and assembled a radial bearing actuator for testing. To measure bearing characteristics, a non-rotational test fixture was designed and built which permits direct measurement of output force, displacement, coil temperature, and air gap flux density levels. The completed radial test bearing stator appears in figure 7.

An illustration of the radial bearing test fixture is shown in figure 8. The fixture includes a stator shaft that mimics the CHPS flywheel alternator shaft, and is equipped with the hydraulic seals and porting required to demonstrate a test hydraulic fit of the radial bearing onto the stator shaft. For measuring bearing output forces, eight strain-gauge type force transducers are provided; for measuring displacements of the bearing rotor with respect to stator, four eddy current type displacement sensors are used. Thin hall sensors were procured that allow direct measurement of magnetic air gap flux densities. The

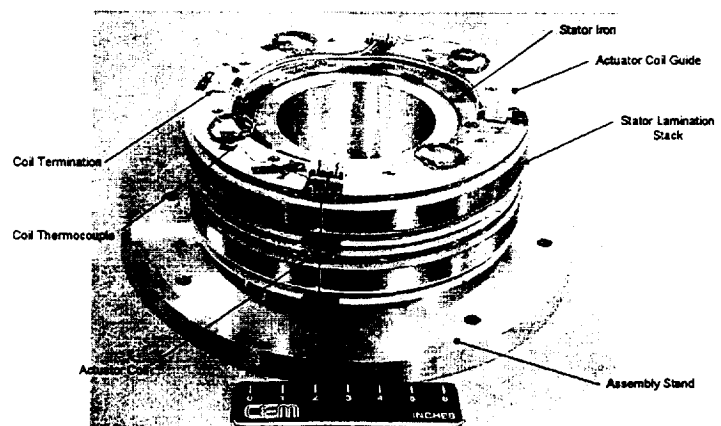


Figure 7. Radial test bearing stator.

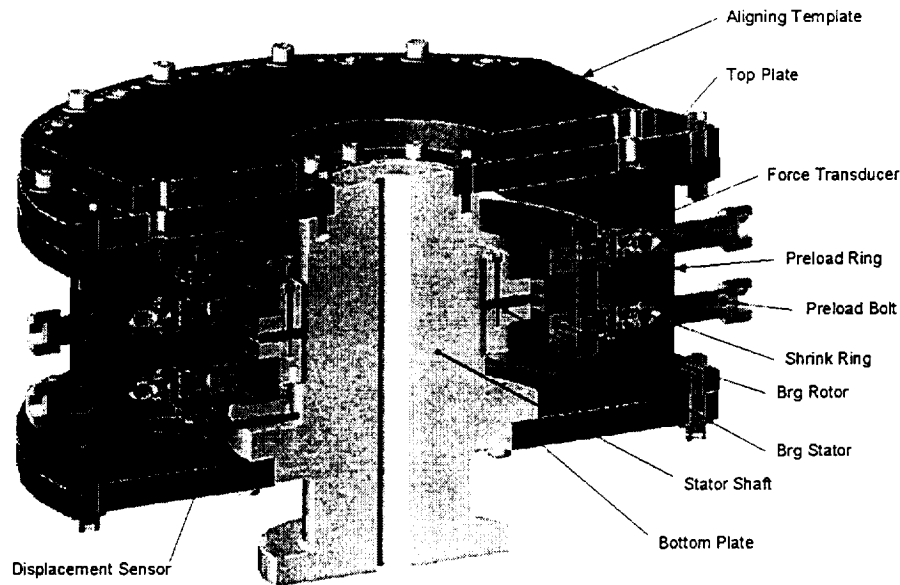


Figure 8. Radial bearing test fixture.

test fixture also includes provisions for magnetically centering and making prescribed displacements of the rotor with respect to the stator (useful for positional stiffness measurement).

Data collection and control for the bearing testing was done using PC-based control and data acquisition software. Amplifiers used are pulse width modulated type servo amplifiers (designed to drive brush-type DC motors) with 25 A nominal output current capability. The data acquisition system provides a control panel in which desired values are input, commands are sent out to the bearing amplifiers, and the resulting data from the force, displacement, and magnetic field sensors are digitized, displayed on screen, and if desired, written to a spreadsheet file for subsequent review.

This test setup allows measurement of the following bearing characteristics: actuator positional stiffness, air gap flux density distribution, AC and DC output force vs. input current, current stiffness transfer function, and actuator magnetic hysteresis. Photographs of the experimental setup are shown in figure 9.

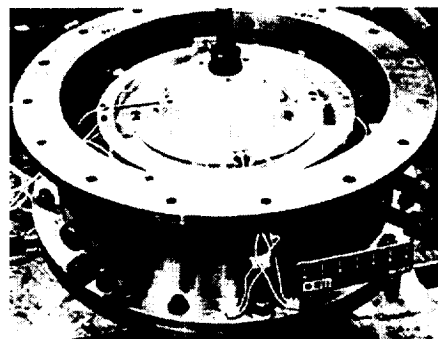
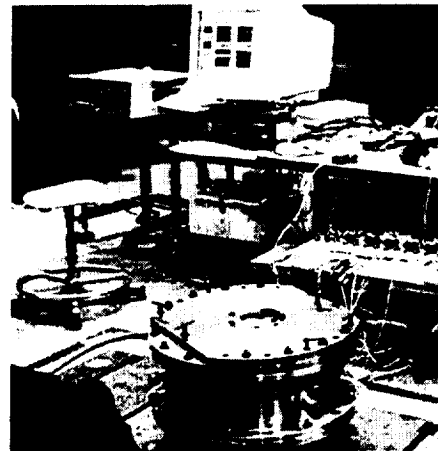


Figure 9. Bearing test experimental hardware.

TEST RESULTS

Before attempting bearing measurements, a test fixture calibration procedure was conducted to ensure accuracy and repeatability. This was done by inserting a small hydraulic cylinder and load cell into the fixture, applying known forces, and establishing a fixture calibration factor, which was thereafter used to adjust force data collected by the data acquisition system. Radial bearing actuator parameters were measured with an air gap corresponding to the zero-speed condition at room temperature. Results are summarized below.

Impedance Measurement

Measured actuator impedance is shown in figure 10. Predicted DC impedance is $1.4\ \Omega$ and $17\ \text{mH}$, which agrees well with the measured zero frequency characteristics.

Positional Stiffness Measurement

Predicted versus measured positional stiffness is shown in figure 11. Measured stiffness is $70\ \text{lb/mil}$ ($123\ \text{kN/cm}$), compared to $50\ \text{lb/mil}$ ($87.6\ \text{kN/cm}$) predicted by FEA, assuming a 93% lamination packing factor (PF). As expected, this actuator exhibits highly linear positional stiffness.

Output Force Measurement

Output force as a function of DC and AC actuator current is plotted in figures 12 and 13. Figure 12 shows predicted and measured DC bearing performance; measurements show that actual DC forces are substantially greater than predicted. Bearing design and initial force predictions were done based on a lamination PF of 93% (the packing factor predicted by the lamination vendor). Also plotted is the predicted

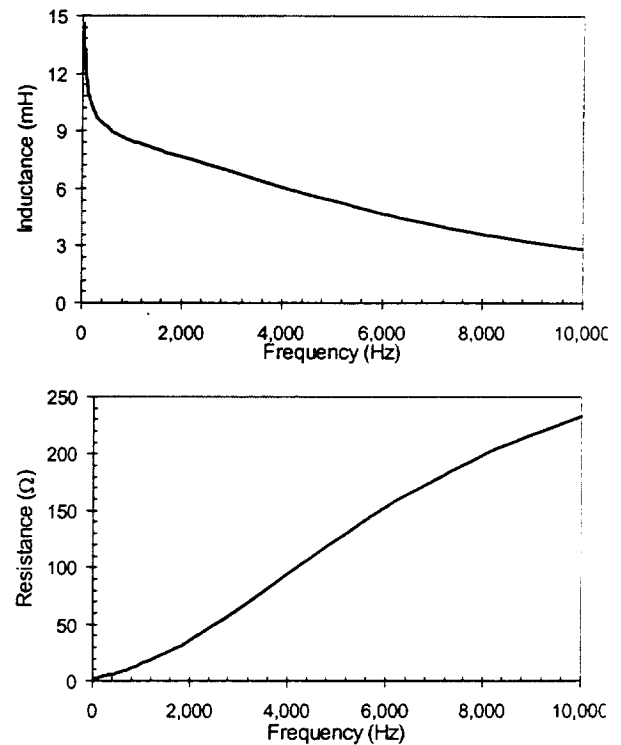


Figure 10. Measured actuator impedance.

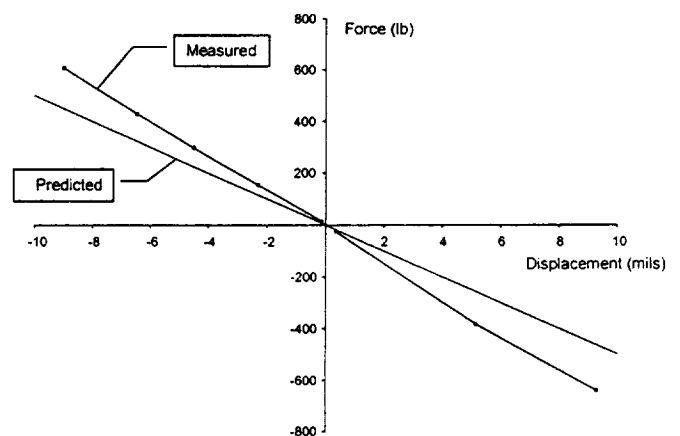


Figure 11. Positional stiffness, predicted vs. measured.

in-line force vs. current for 98% PF. As demonstrated in the figure, the predicted force output for this bearing is highly sensitive to the assumed PF.

To reconcile the difference between predicted and measured forces, Hall sensors were used to map the bias flux density distribution in the bearing air gap (see figure 14 regarding bias field prediction and measurement). New FEA was then done to determine whether an adjustment in PF would produce reasonable agreement with the measured field distribution. At 98% PF, good agreement was found for both the bias field distribution and for in-line radial force (the diagonal force FEA predictions are not yet complete). Further study is required to determine the actual PF and establish whether some other factors are responsible for the predicted versus measured force disparity.

In figure 13, force vs. current is plotted for DC current at 50 Hz. As seen by comparing figures 12 and 13, the current stiffness (force per unit current) is significantly greater

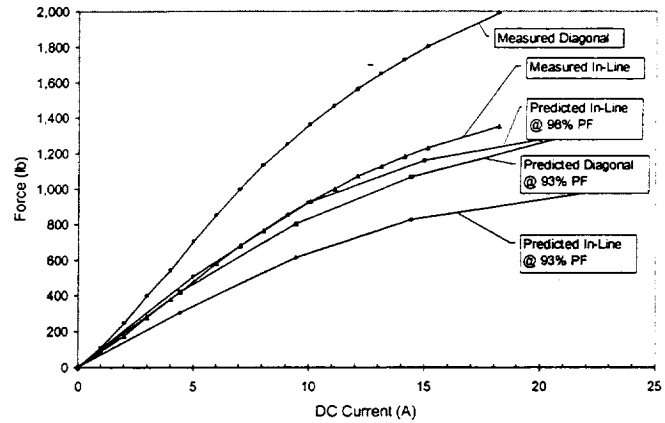


Figure 12. Actuator force vs. DC current, predicted vs. measured.

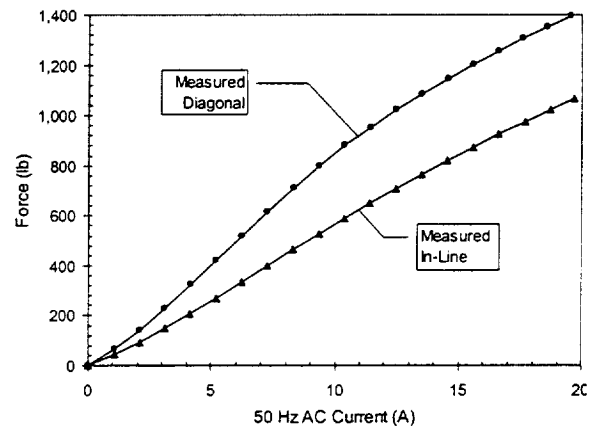


Figure 13. Measured actuator force vs. AC current.

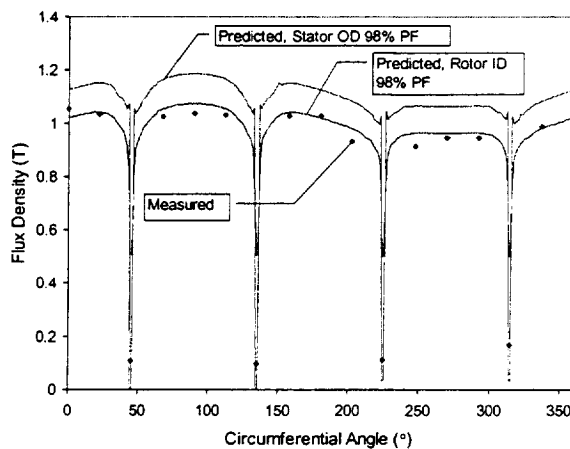
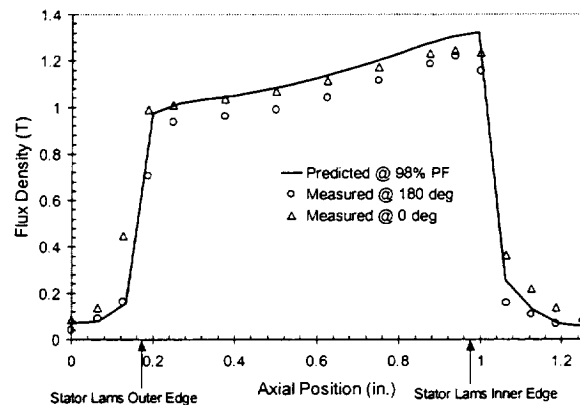


Figure 14. Air gap flux density distribution, predicted vs. measured.



for DC than for AC current input. This characteristic is confirmed in a transfer function plot presented later. Although AC current stiffness is less than at DC, the actuator still meets stated load capacity requirements, and exhibits nearly linear behavior.

Air Gap Flux Density Measurement

Hall sensors were inserted into the bearing air gap to directly measure the bias flux density distribution. Predicted and measured field distributions as a function of circumferential angle and axial length are plotted in figure 14. The predicted field levels are plotted for a 98% lamination packing factor, which gives good agreement with experimental results.

Transfer Function Measurement

Current stiffness magnitude and phase angle versus frequency are plotted in figure 15 for actuator currents of 1 and 5 A. Measurements were done for a maximum frequency of 200 Hz to avoid bearing fixture natural frequency modes above 200 Hz. Two transfer function plot characteristics are especially noteworthy: the current stiffness magnitude at DC is substantially greater than that measured above 50 Hz (also see figures 12 and 13), and a consistent 20° phase lag was measured between input current and output force. Knowledge of the phase lag is particularly valuable for accurate control system modeling. Magnetic hysteresis in the 4130 steel rotor lamination material may be responsible for the phase lag, and could be a consequence of choosing a structural steel for this component.

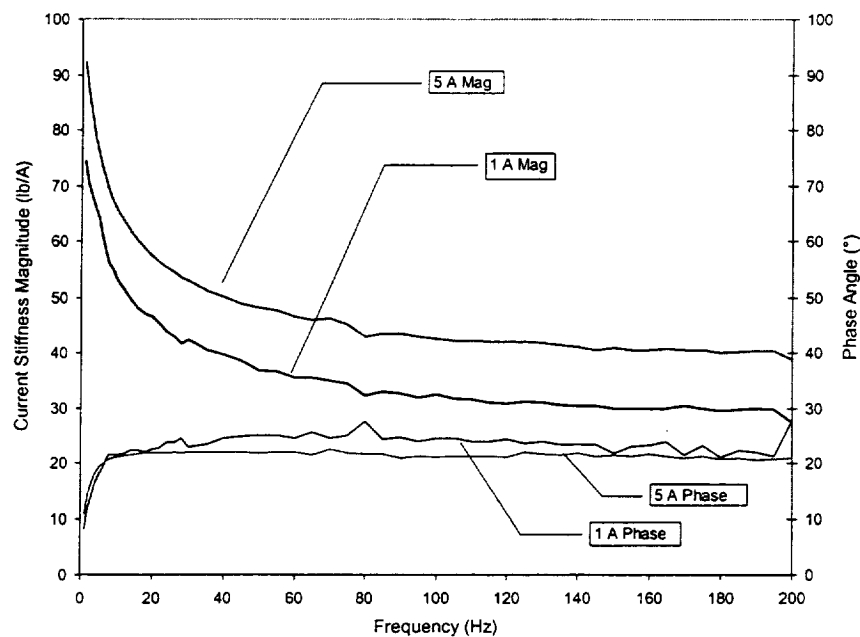


Figure 15. Measured actuator transfer function.

Magnetic Hysteresis Measurement

During bearing testing it was observed that the bearing force at zero current was not consistent, but appeared to depend on the current magnitude of the previous test. To test the hypothesis that this was hysteresis-induced behavior, a series of DC current pulses from zero to 18 A was input to the bearing, and the residual force recorded after each pulse was complete and current was re-zeroed. The resulting curve shown in figure 16 strongly suggests magnetic hysteresis behavior, and could explain the transfer function phase lag previously measured.

The most likely source of this behavior is the 4130 structural steel laminations; tests are currently underway to directly measure hysteresis characteristics for the 4130 and other materials used in the test bearing. If excessive, hysteresis would result in unacceptable bearing power losses and heating.

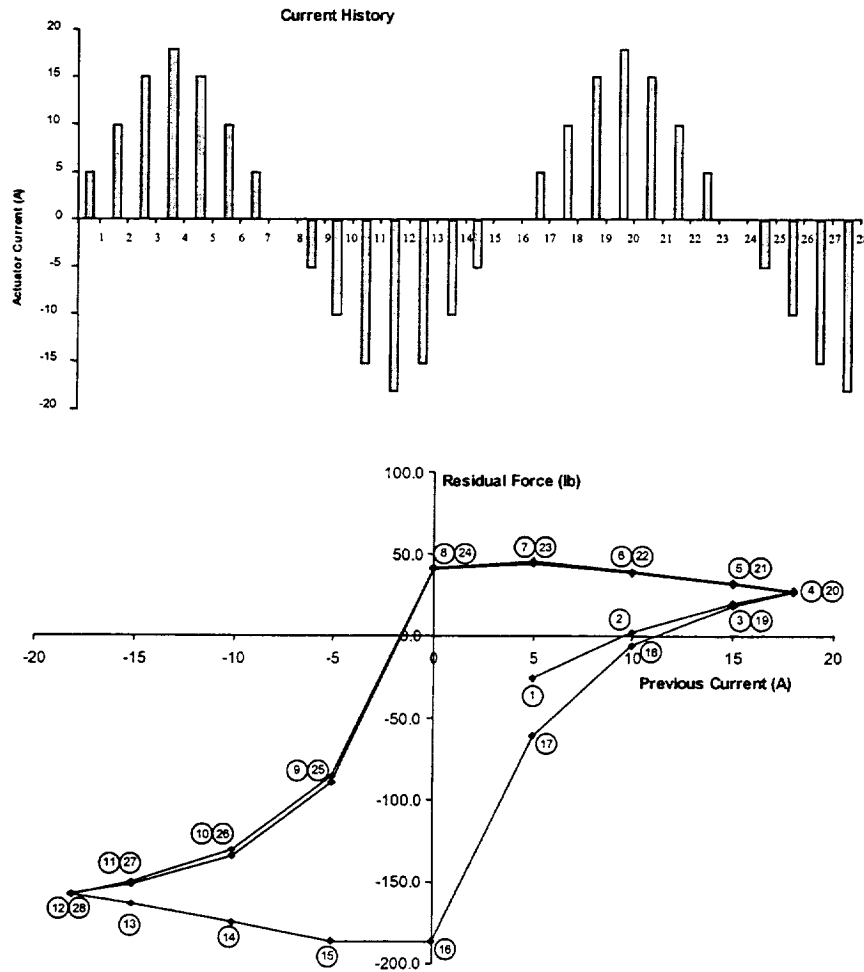


Figure 16. Residual force measurement.

CONCLUSIONS

Researchers from UT-CEM have designed inside-out configuration active magnetic bearing actuators for use in a flywheel alternator for a hybrid-electric combat vehicle. This is the first known application of magnetic bearing actuators incorporating an inside-out topology. A prototype radial bearing was successfully fabricated, assembled, and tested in a bearing test fixture that directly measures important bearing parameters. Although measured bearing parameters meet performance goals, further work is underway to fully understand bearing behavior. Knowledge gained from this work will permit more accurate electromagnetic and control system modeling, and is an important step in the successful implementation of inside-out bearing actuators.

ACKNOWLEDGEMENTS

The authors wish to thank Marilyn Freeman of DARPA for her support of this work. In addition, we want to acknowledge the contributions made by UT-CEM technicians Robert Arndt and Richard Rodriguez to the successful completion of this project. Finally, we wish to thank Vicki Heydron and Roy Pena for their assistance in the publication of this paper.

REFERENCES

1. G. Buckner, A. Palazzolo, J. Kajs, B. Murphy, and J. Beno, "Control System for Inside-Out Configuration Magnetic Bearings," 5th International Symposium on Magnetic Suspension Technology, Dec 1-3, 1999.
2. M. Kasarda, P. Allaire, P. Norris, C. Mastrangelo, and E. Maslen, "Experimentally Determined Rotor Power Losses in Homopolar and Heteropolar Magnetic Bearings," International Gas Turbine & Aeroengine Congress & Exhibition, Stockholm, Sweden, June 2-5, 1998, ASME Publication No.98-GT-317.
3. G. Schweitzer, H. Bleuler, and A. Traxler, *Active Magnetic Bearings: Basics, Properties, and Applications of Active Magnetic Bearings*, vdf Hochschulverlag AG an der ETH Zurich, 1994.

DEVELOPMENT AND TESTING OF A FOUR POLE MAGNETIC BEARING

Joe Imlach
Imlach Consulting Engineering
Anchorage, AK

SUMMARY

A 4 pole radial active magnetic bearing actuator has been developed, constructed, and tested. Among the anticipated characteristics of this configuration were: higher specific load capacity, lower power losses, and improved stability as compared to other heteropolar configurations. The theoretical basis of each of these aspects will be investigated, and some limitations of the design will be discussed. Testing of the new actuator verified that higher load capacities are achievable. Stability problems with the prototype, due to interaction with the power amplifiers, limited the ability of the testing to investigate actuator stability improvements.

INTRODUCTION

One of the major limitations of active magnetic bearing (AMB) systems is their relatively low specific load capacities. Specific load capacity, P , is generally defined as the load capacity of the bearing, F , divided by the bearing's projected area (rotor length, L , times rotor diameter, D).

$$P = \frac{F}{D * L} \quad (1)$$

While fluid film bearings typically have specific load capacities of more than 1.7 MN/mm^2 (250 psi), AMB's are more typically limited to $0.35 - 0.7 \text{ MN/mm}^2$ (50 - 100 psi). This limitation is due to two factors. First is the limitation of the flux carrying capacity of the magnetic material. The second factor is the efficiency with which the magnetic material can be used.

In the general case, the load capacity of an AMB in-line with an axis can be given by

$$F = \frac{B}{2\mu_0} (W_{pt} L) \quad (2)$$

where B is the nominal flux density in the magnetic gaps, W_{pt} is the total projected widths of the gap in the quadrant, and L is the length of the stator stack. An example geometry for an 8 pole

bearing illustrating these concepts is shown in Figure 1.

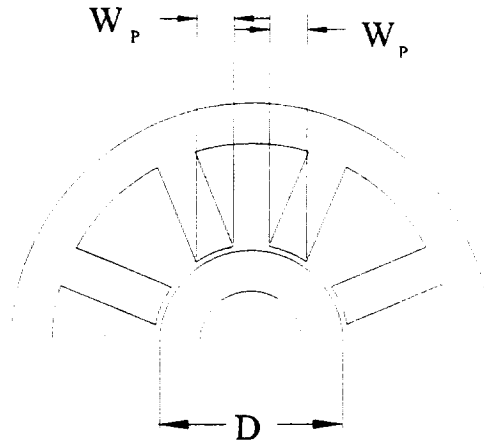


Figure 1: Eight pole bearing projected area.

By introducing a term for the bearing geometric efficiency, ξ , we can develop the following equations for this example:

$$\xi = \frac{2W_p}{D} \quad (3)$$

$$F = \xi \frac{B^2}{2\mu_0} DL \quad (4)$$

$$P = \xi \frac{B^2}{2\mu_0} \quad (5)$$

Equation 5 indicates clearly that the specific load capacity of an AMB is determined completely by the saturation flux density of the material and by the geometric efficiency of the bearing. Once the material is chosen, the saturation flux density is fixed. Selecting high flux materials (e.g. nickel and vanadium alloys) is usually associated with great increases in material costs. It is of interest, therefore, to determine ways to increase the specific load capacity, ξ .

From the example of figure 1 and equation 3, it is easy to see that the maximum value of geometric efficiency for a symmetric AMB is 0.707. Experience has shown that most real systems have values between 0.2 and 0.5. This limitation is due primarily to the space required for coils.

DEVELOPMENT OF A FOUR POLE BEARING

Again from figure 1, it can be seen that the slots between pole pieces, which are required for the placement of the coils, detracts from the geometric efficiency of the bearing. The wider the coil slots are, and the more coil slots there are, the less projected area is available for magnetic material adjacent the rotor. There are two basic ways to minimize the projected area required for the coils: the first is to minimize the coil width; and the second is to minimize the number of coils. Minimizing the coil width, if all other design parameters are held constant, results in a long thin coil and long pole pieces. This option is not always feasible due to space constraints and the increased flux leakage and dynamic problems associated with long pole pieces. The other alternative is to minimize the number of pole pieces.

Some work has been done (e.g. Grbesa [1]) that indicates that a minimum of three pole pieces is required for an AMB. This three pole configuration requires significant modifications to the control algorithms, and is not amenable to fault tolerant operation. It was postulated early in this project that a four pole bearing might not have either of these drawbacks, and would still allow a significant improvement to geometric efficiency. For this reason it was decided to investigate the performance characteristics of a four pole bearing. The basic geometry of this configuration is shown in figure 2. From this figure it is seen that one of the primary characteristics of this design is that the flux produced by one quadrant (i.e. the top pole) returns to

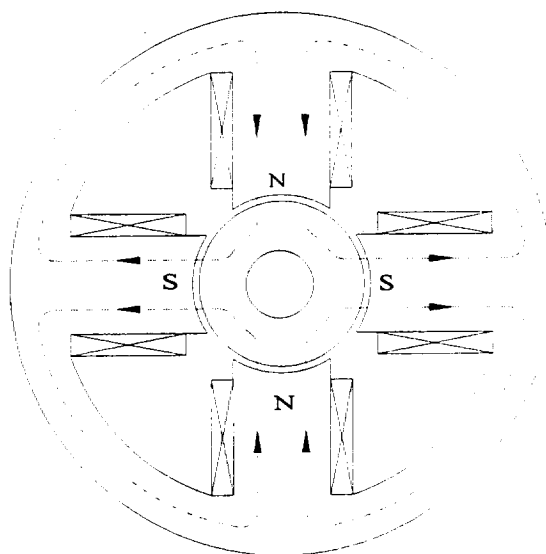


Figure 2: Basic four pole layout..

the stator through the two poles in the perpendicular axis (i.e. the horizontal axis). Another characteristic is that, assuming the total flux produced by the each axis remains constant, the control flux from the vertical axis will supply the bias flux to the horizontal axis, and vice versa. This is an important assumption, and in practice limits the performance of this configuration. This will be discussed further in the experimental results section.

Another characteristic of the bearing that can be developed from inspection is that the rotating power losses for this configuration should be lower than those of a corresponding eight pole bearing. Because the flux is split in the rotor, the rotor radial dimension needs to be only one half of the pole width. The configuration shown will, therefore, have approximately the same rotor volume as a corresponding eight pole bearing. There are, however, only half as many flux variations. Kasarda [2] has shown that the number of poles has a strong influence on rotor losses, while the orientation of the poles (NSNS vs NNSS) has a weak influence. The rotor losses for this configuration, therefore, may be comparable to a four pole homopolar bearing. This characteristic needs to be investigated experimentally.

The four pole bearing should also have a significantly different open loop stiffness behavior. In a standard heteropolar bearing, as the rotor is displaced towards the poles of one quadrant, all of the gaps in that quadrant decrease. Because the open loop stiffness, K_x , is inversely proportional to the sum of those gaps, its magnitude increases dramatically. This effect is due to the fact that the reluctance of the flux loops in the quadrant goes to zero as the gaps close (neglecting stator reluctance for illustrative purposes). In the four bearing, however, the flux loops all contain two perpendicular gaps. A vertical displacement, therefore, will close only one gap of the flux path, resulting in a smaller increase in the open loop stiffness magnitude. This

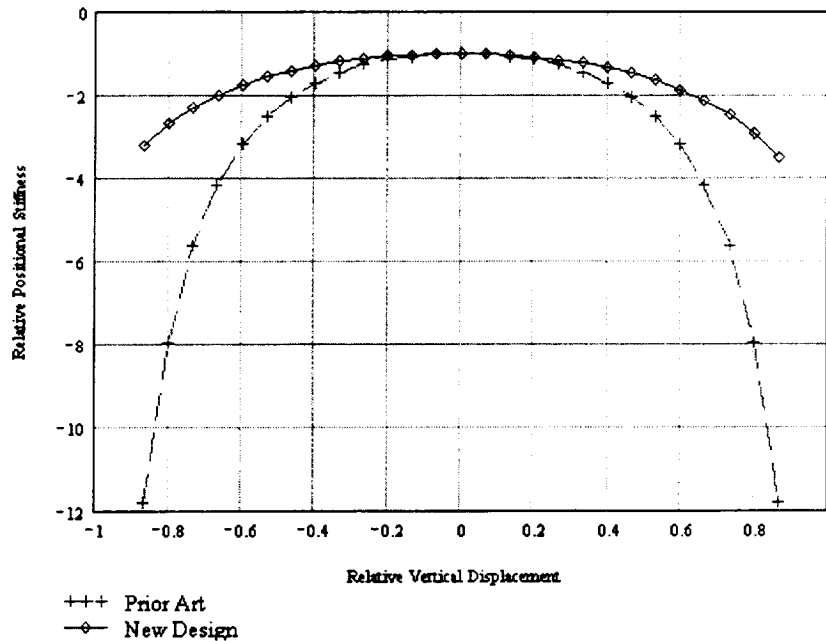


Figure 3: Comparison of open loop stiffness of 4 and 8 pole bearings

effect is illustrated in figure 3, which compares the normalized open loop stiffness of a four pole and an 8 pole bearing of the same basic size and load capacity.

Several things are evident from this plot. First is that the negative stiffness of a standard bearing increases dramatically with displacement. This increase, which must be compensated by the current stiffness and gain of the bearing, decreases the available stiffness of the bearing under large displacements. This contributes to bearing instability. Four pole bearings, however, should be tolerant of greater relative displacements without suffering adverse consequences, and should have a more uniform closed loop stiffness over the range of displacements.

Alternatively, the relative open loop stiffness of a four pole bearing at 50% relative displacement is comparable to that of an eight pole bearing at 33% relative displacement. If other design factors allow, this would allow a four pole bearing to operate with smaller gaps (e.g back-up bearing clearance of 66% magnetic gap, rather than 50% magnetic gap) than a similar eight pole bearing. This would in turn allow a reduced coil size and a further increase in geometric efficiency and specific load capacity. These benefits were deemed to be significant enough that a patent application for the technology was submitted [4]

One limitation that is evident in the four pole bearing is a limitation on its size. Because the rotor radial dimension must be at least as wide as half of the pole width, larger bearings become impractical. For example, a bearing with a 150 cm pole width would require a 75 cm thick radial rotor lamination and a 75 cm thick backiron section. This geometry would result in a very large rotor diameter, and would probably be better served by a 12 or 16 pole bearing (38 cm or 25 cm thick rotor respectively). This factor should be addressed on a case by case design basis.

EXPERIMENTAL VERIFICATION

A prototype of a four pole bearing was developed for a particular application. Due to outside limitations on the allowable, rotor and the stator diameters complete design freedom was not available. This makes the comparison more representative of real world applications. An eight pole bearing was already in use in this application, and was available for comparison. The relevant design parameters for both bearings are shown in table 1.

It is noted that, while the geometric efficiency of the four pole bearing does not approach the maximum theoretical value (70.7%), it represents a 40% improvement over that achievable with the 8 pole bearing in this specific design. This translates directly into a 26% increase in theoretical load capacity, on a reduced rotor diameter. Testing indicated that the actual increase in load capacity was even greater than predicted. This is potentially due to a reduction in fringing effects due to the larger pole sizes.

PARAMETER	4 Pole	8 Pole
Stator OD (cm)	7.160	7.160
Stator ID (cm)	3.206	3.506
Gap (cm)	0.038	0.038
Rotor OD (cm)	3.130	3.430
Rotor ID (cm)	1.905	2.327
Stack Length (cm)	1.270	1.270
Coil Turns	120	120
Wire Gauge (AWG)	23	23
Bias Current (Amps)	3.3	3.3
Geometric Efficiency (%)	39.1	28.0
Nominal Load Capacity (N)	92.5	73.4
Experimental Load Capacity (N)	111.2	62.3

Table 1. Comparison Data

Some problems were encountered in the testing of this bearing. It was noted that the 4 pole bearing was significantly more “noisy” (audible noise) than the comparable eight pole bearing, and that there was an instability mode in which the bearing position would “jump” approximately 10 microns, and then drift back to center. This effect was predicted by Meeker [3], in bearings which utilize a separate power amplifier (PA) to drive each coil. The effect is due to a singularity in the inductance matrix and is excited by the switching nature of the power amplifier. Due to the randomness of the timing of the PA switching, there exist states in which currents in all of the coils are increasing or decreasing at the same time. Because of the series nature of the flux paths, this leads to a change in current with no corresponding change in flux density (inductance matrix singularity). To the PA this represents a temporary zero inductance, leading to errors in current output. As indicated in [3], a decoupling ring placed in series with the bearing coils eliminated the instability and significantly reduced the bearing noise.

As stated earlier, one of the assumptions in the original bearing configuration was that the total flux in the bearing would remain constant. Clearly, the problems associated with the switching PA indicate that the configuration in which each coil is driven independently by this type of amplifier violates this assumption. Several potential solutions to this problem exist. One is the use of linear amplifiers in conjunction with four pole bearings. Another is the use of separate bias and control coils, with the control coils for each axis connected in series and driven with a bi-polar amplifier. A third potential solution is the inclusion of permanent magnet biasing in conjunction with the series bi-directional control coils. These are subjects of future work.

CONCLUSION

The characteristics of a four pole AMB with a unique winding configuration have been developed. Theoretically, this type of bearing should offer a significant increase in specific load capacity, reduced rotor power losses, and improved stability characteristics. Experimental work has verified the increase in specific load capacity. Because of the specific coil configuration developed in the prototype, the bearing was susceptible to instabilities caused by an interaction with the coils and the switching power amplifiers. This instability resulted in an increase in bearing audible noise and a tendency for the bearing rotor to “jump.” Potential solutions to this problem have been identified. One, the inclusion of a decoupling ring as suggested by Meeker [3], **resulted** in improved bearing performance. Other potential solutions, which do not require additional hardware, will be investigated in future research.

REFERENCES

- 1) Grbesa, B., “Low Loss and Low Cost Active Radial Homopolar Magnetic Bearing,” 6th International Symposium on Magnetic Bearings, Boston, MA, 1998.
- 2) Kasarda, M.E.F., The Measurement and Characterization of Power Losses in High Speed Magnetic Bearings, Doctoral Dissertation, University of Virginia, 1997.
- 3) Meeker, D.C., Optimal Solutions to the Inverse Problem in Quadratic Magnetic Actuators, Doctoral Dissertation, University of Virginia, 1996.
- 4) Imlach, J., “High Specific Load Capacity Radial Magnetic Bearing Actuator,” U.S. Patent #5,962,940, October 5, 1999.

Session 16 -- Controls 4

Chairman: Nancy Morse Thibeault
University of California at Santa Barbara (UCSB)

Integral Sliding Mode Controller for Magnetically Suspended Balance Beam : Theory and Experimental Evaluation

Jun-Ho Lee[†], Edgar F. Hilton[†], Xuerui Zhang[‡], Gang Tao[‡], Paul E. Allaire[†]

[†] Department of Mechanical and Aerospace Engineering, University of Virginia, Charlottesville, Virginia, 22903 USA. E-mail:jl7e@virginia.edu, efh4v@virginia.edu, pea@virginia.edu, respectively

[‡] Department of Electrical Engineering, University of Virginia, Charlottesville, Virginia, 22903 USA. E-mail:xz5d@virginia.edu, gt9s@ral.ee.virginia.edu, respectively

ABSTRACT

This paper deals with a sliding mode controller with integral compensation in a magnetic suspension system. The control scheme comprises an integral controller which is designed for achieving zero steady-state error under step disturbance input, and a sliding mode controller which is designed for enhancing robustness under plant parametric variations. A procedure is developed for determining the coefficients of the switching plane and integral control gain such that the overall closed-loop system has stable eigenvalues. A proper continuous design signal is introduced to overcome the chattering problem. The performance of a magnetically suspended balance beam using the proposed integral sliding mode controller is illustrated. Simulation and experimental results show that the proposed method is effective under the external step disturbance and input channel parameter variations.

INTRODUCTION

Electromagnetic bearings inherently have nonlinear properties [2]. With regard to such a nonlinear system, various controllers have been developed. The integral sliding mode control approach has been reported by a number of authors recently as a method of servo control [1],[6],[7]. The integral sliding mode control approach consists of two compensators: one uses an integral compensator for achieving a zero steady-state error under an external step disturbance force, and the other uses a sliding mode controller. Sliding mode controllers select a surface in phase space, typically a linear hypersurface, called the switching surface, and switch the control input on this surface. The control input is then chosen to guarantee that trajectories near the sliding surface are directed toward the surface via reaching conditions. Once the system is on the surface, the system closed-loop dynamics are completely governed by the equations which define the surface. The closed-loop dynamics will be insensitive to the parameter variations of the input channel and robustness is achieved [3],[4],[5].

The design problem of an integral sliding mode controller consists of three items. The first item is concerned with the design of a switching surface σ upon which desired dynamic behavior can be guaranteed for

the nominal system. The second item is concerned with the selection of a proper nonlinear control law to handle strong nonlinearities of the initial states of the magnetically suspended system. The third item is to select a proper integrator gain.

In this paper we apply an integral sliding mode control method to a magnetically suspended balance beam to achieve zero steady-state error under an external step disturbance and its insensitivity with respect to the parametric variations of the input channel. We first derive the linearized mathematical model with integrator of the magnetically suspended balance beam at the nominal point, and then construct the integral sliding mode controller using a pole placement method to a designed switching surface. Simulation and experimental results show that an integral sliding mode control design can achieve accurate tracking and is fairly robust to plant parameter variations and external load disturbances.

MATHEMATICAL MODEL

Fig. 1 shows the geometry of the symmetric balance beam with two magnetic bearings, and Table 1 shows each parameter of the balance beam. The balance beam shown in fig. 1 can be modeled by using

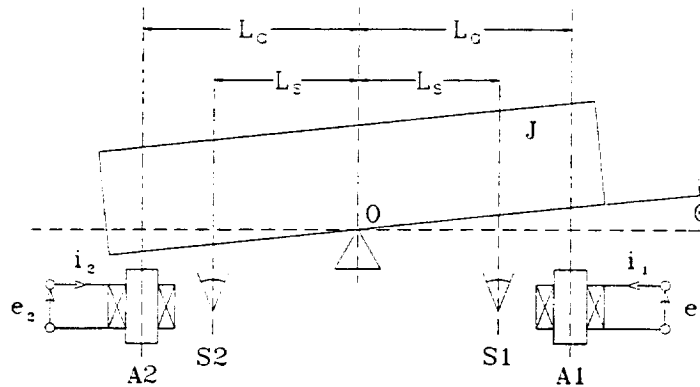


Figure 1: Symmetric balance beam on two magnetic bearings.

Table 1: Balance Beam Parameters

Parameter	Symbol	Value	Units
Angular Position	θ		rad
Half Bearing Span	L_a	1.1412	m
Mass Moment of Inertia about the Pivot Point	J	0.0948	kg/m ²
Coil Current in Bearing 1	i_1		A
Coil Current in Bearing 2	i_2		A
Control Voltage in Bearing 1	e_1		V
Control Voltage in Bearing 2	e_2		V
Coil Resistance	R	0.7	Ω
Coil Inductance	L	0.545	mH
Magnetic Bearing Open Loop Stiffness	K_s	2114	N/m
Actuator Current Gain	K_i	1.074	N/A
Steady Current	I	1	A
Steady Gap	G	380	μm

the second order dynamic equation and voltage equation.

$$J\ddot{\theta} = L_a(f_1 - f_2) + f_d \quad (1)$$

$$e' = Ri' + L \frac{di'}{dt} \quad (2)$$

where J is the mass moment of inertia about the pivot point, L_a is the half bearing span, f_1 is the electromagnetic attractive force in bearing 1, f_2 is the electromagnetic attractive force in bearing 2, f_d is the external disturbance force, R is the coil resistance, L is the coil inductance, $e' = e_1 - e_2$ is the control voltage difference, and $i' = i_1 - i_2$ is the instantaneous coil current difference. Eqs. (1) and (2) can be linearized by a Taylor series expansion about the operating point, $\theta = 0$, $e' = 0$, $i' = 0$. Eq. (3) shows the linearized state space equations of the balance beam.

$$\begin{aligned} \dot{x} &= Ax + Bu + f_d \\ y &= Cx \end{aligned} \quad (3)$$

where,

$$\begin{aligned} x &= \begin{bmatrix} \theta \\ \dot{\theta} \\ i' \end{bmatrix}, \quad A = \begin{bmatrix} 0 & 1 & 0 \\ \frac{2K_s L_a^2}{J} & 0 & \frac{K_i L_a}{J} \\ 0 & -2K_i \frac{1}{L} & -\frac{R}{L} \end{bmatrix}, \quad B = \begin{bmatrix} 0 \\ 0 \\ \frac{1}{L} \end{bmatrix} \\ C &= \begin{bmatrix} 1 & 0 & 0 \\ 0 & 1 & 0 \\ 0 & 0 & 1 \end{bmatrix}, \quad u = e' \end{aligned} \quad (4)$$

In order to include the integrator as a state variable into (3), we design the following block diagram shown

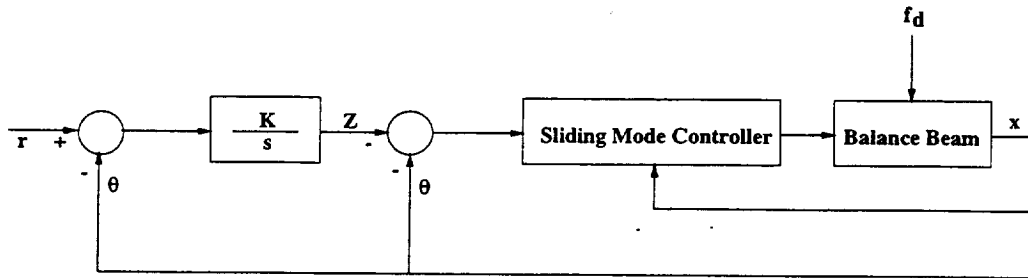


Figure 2: Block diagram of an integral-sliding-mode-controlled balance beam

in fig. 2. Here the integrator output Z is expressed as the difference between the integrated reference angular position r and integrated angular position θ written as:

$$Z = \int (r - \theta) dt \quad (5)$$

where $r = 0$. By using (5) we construct new state space equations including the integrator as a state variable.

CONTROLLER SYNTHESIS

In order to synthesize the integral sliding mode controller we write the state variables as $x = [Z \ \theta \ \dot{\theta} \ i']^T$, and get the following state space matrices.

$$A = \begin{bmatrix} 0 & -1 & 0 & 0 \\ 0 & 0 & 1 & 0 \\ 0 & \frac{2K_s L^2}{J} & 0 & \frac{K_i L_a}{J} \\ 0 & 0 & -2K_i \frac{1}{L} & -\frac{R}{L} \end{bmatrix}, \quad B = \begin{bmatrix} 0 \\ 0 \\ 0 \\ \frac{1}{L} \end{bmatrix}, \quad C = \begin{bmatrix} 0 & 0 & 0 & 0 \\ 0 & 1 & 0 & 0 \\ 0 & 0 & 1 & 0 \\ 0 & 0 & 0 & 1 \end{bmatrix} \quad (6)$$

Here, we can formulate the sliding mode state space equations by decomposing (6) such as:

$$\begin{bmatrix} \dot{x}_1 \\ \dot{x}_2 \end{bmatrix} = \begin{bmatrix} A_{11} & A_{12} \\ A_{21} & A_{22} \end{bmatrix} \begin{bmatrix} x_1 \\ x_2 \end{bmatrix} + \begin{bmatrix} B_1 \\ B_2 \end{bmatrix} u \quad (7)$$

where,

$$\begin{aligned} x_1 &= \begin{bmatrix} Z \\ \theta \\ \dot{\theta} \end{bmatrix}, \quad x_2 = i' \\ A_{11} &= \begin{bmatrix} 0 & -1 & 0 \\ 0 & 0 & 1 \\ 0 & \frac{2K_s L^2}{J} & 0 \end{bmatrix}, \quad A_{12} = \begin{bmatrix} 0 \\ 0 \\ \frac{K_i L_a}{J} \end{bmatrix}, \quad A_{21} = [0 \quad 0 \quad -2K_i \frac{1}{L}], \quad A_{22} = -\frac{R}{L} \\ B_1 &= \begin{bmatrix} 0 \\ 0 \\ 0 \end{bmatrix}, \quad B_2 = \frac{1}{L}, \quad u = e' \end{aligned} \quad (8)$$

Let the sliding mode surface be defined as $\sigma = Sx$.

$$\sigma = [S_1 \quad S_2] \begin{bmatrix} x_1 \\ x_2 \end{bmatrix} \quad (9)$$

If the system dynamics yield ideal sliding mode dynamics (9) equals zero or $\sigma = Sx = 0$. By using this property we can determine the equivalent linear control input from (9). x_2 becomes

$$x_2 = \frac{\sigma - S_1 x_1}{S_2} \quad (10)$$

Substituting (10) into (7) yields

$$\dot{x}_1 = (A_{11} - A_{12} S_2^{-1} S_1) x_1 + A_{12} S_2^{-1} \sigma \quad (11)$$

The sliding surface is defined as $\sigma = S_1 x_1 + S_2 x_2 = 0$. Eq. (11) becomes

$$\dot{x}_1 = (A_{11} - A_{12} S_2^{-1} S_1) x_1 = (A_{11} - A_{12} k) x_1 \quad (12)$$

where $k = S_2^{-1} S_1$. The location of poles of the sliding mode surface are obtained by selecting k . The equation for the sliding surface becomes $S = [S_1 \quad S_2] = [S_2 k \quad S_2] = S_2 [k \quad 1]$.

The sliding mode control input can be separated into the linear and nonlinear components as $u = u_l + u_{nl}$. The linear input can be selected by the following equations:

$$\dot{x} = Ax + Bu \quad (13)$$

$$\dot{\sigma} = S\dot{x} = 0 \quad (14)$$

From eq. (13), (14) we can get the equivalent linear control input as:

$$u = u_l = -(SB)^{-1}SAx \quad (15)$$

The sliding mode reaching condition, given by $\sigma\dot{\sigma} < 0$, brings the balance beam to the sliding surface. If the nonlinear control is given by $u_{nl} = -(SB)^{-1}\rho\text{sgn}(\sigma)$ where $\rho > 0$, $(SB)^{-1} = I$. The reaching condition becomes

$$\sigma\dot{\sigma} = -\rho\sigma\text{sgn}(\sigma) < 0 \quad (16)$$

The control input can then be written as

$$u = -(SB)^{-1}[SAx + \rho\text{sgn}(\sigma)] \quad (17)$$

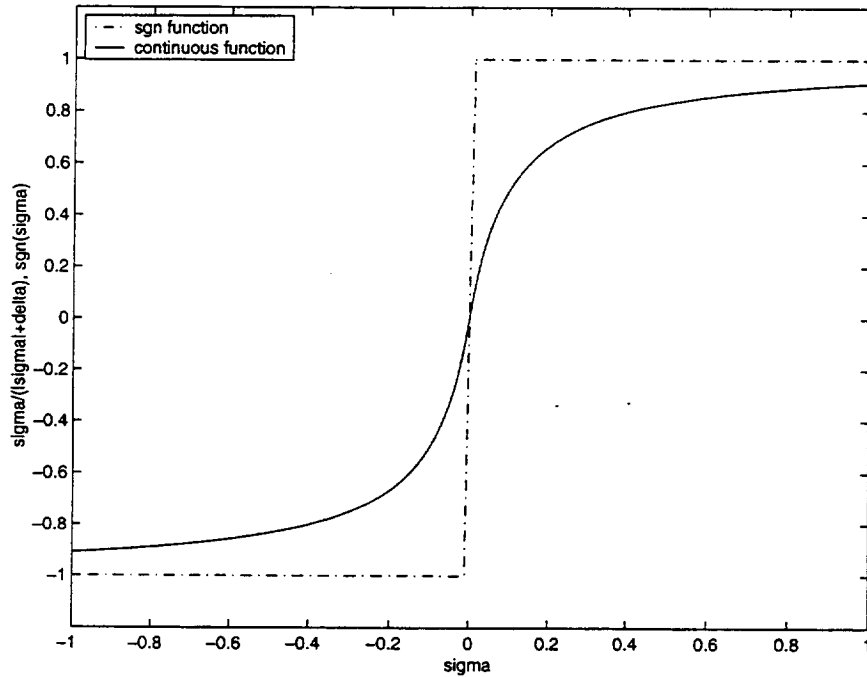


Figure 3: Sliding surface using discontinuous and continuous function

In practical terms such a nonlinear discontinuous control component is undesirable because the $\text{sgn}(\sigma)$

function may cause a chattering problem. So, the control effort is required to ensure σ or a neighborhood of σ is reached and maintained. Ideally, a control strategy is required to ensure that the system dynamics is both close to σ and as close as possible to the ideal sliding mode dynamics. With this point of view, modern design methods employ a continuous, usually nonlinear, control to ensure system dynamics within a region containing σ . Let the nonlinear control input be defined as the continuous function

$$u_{nl} = -\rho \frac{\sigma}{|\sigma| + \delta} \quad (18)$$

where δ is the boundary layer which is selected to reduce the chattering problem and ρ is a design parameter. Fig. 3 shows the relation between the discontinuous sgn function and continuous function. In this figure we can see that the slope of the continuous function depends upon δ . Fig. 4 shows the block diagram of the designed sliding mode controller connected to the integral compensator.

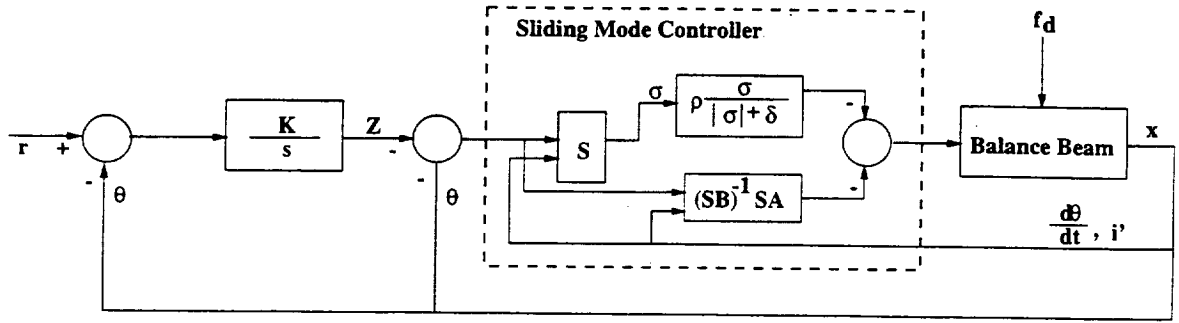


Figure 4: Block diagram of integral sliding mode control implementation

SIMULATION RESULTS

In order to show the effectiveness of the proposed controller we consider a comparison between the integral sliding mode controller and a simple integral state feedback controller. For making the parameter variations, we changed the nominal inductance value ($L = 7.2727 \times 10^{-4}[\text{H}]$) was changed from $0.1L$ to $10L$, where the nominal inductance is a function of nominal gap. The vector S which defines the sliding surface, design parameters of the nonlinear control components and linear component gain matrices $F_l = (SB)^{-1}SA$ are such as:

1. When the nominal inductance is applied ($x = [Z \ \theta \ \dot{\theta} \ i']^T$)

$$\begin{aligned} S &= [3.5174508 \times 10^5 \quad 9886.579 \quad 91.453 \quad 1.0] \\ F_l &= [0 \quad 395.9667 \quad 6.6511 \quad -0.5109] \\ \rho &= 10, \delta = 0.4 \end{aligned} \quad (19)$$

2. When 10 times of the nominal inductance is applied ($x = [Z \ \theta \ \dot{\theta} \ i']^T$)

$$\begin{aligned} S &= [3.5174508 \times 10^5 \quad 9886.579 \quad 91.453 \quad 1.0] \\ F_l &= [0 \quad 3959.666 \quad 71.362 \quad 1.190] \\ \rho &= 10, \delta = 0.4 \end{aligned} \quad (20)$$

3. When 0.1 times of the nominal inductance is applied($x = [Z \ \theta \ \dot{\theta} \ i]^T$)

$$S = [3.5174508 \times 10^5 \ 9886.579 \ 91.453 \ 1.0]$$

$$Fl = [0 \ 39.5967 \ 0.1800 \ -0.6811]$$

$$\rho = 10, \delta = 0.4$$

(21)

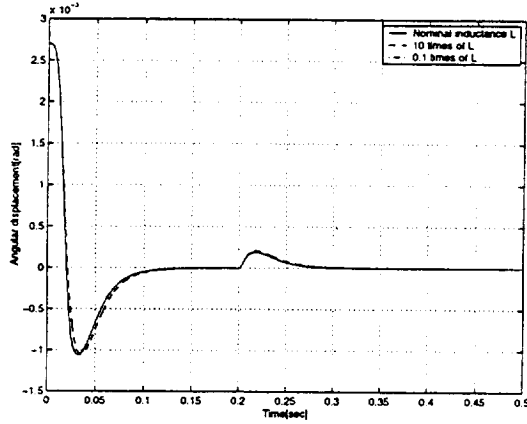


Figure 5: Evolution of angular displacement by integral sliding mode controller

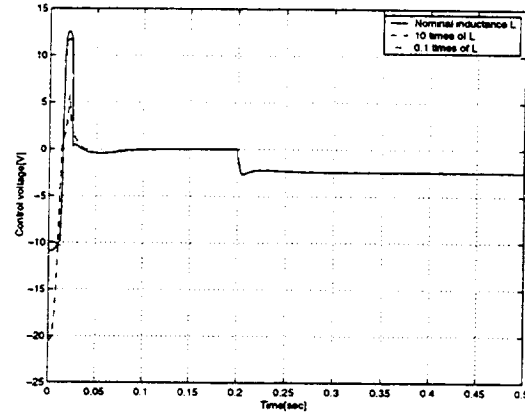


Figure 6: Evolution of control effort by integral sliding mode controller

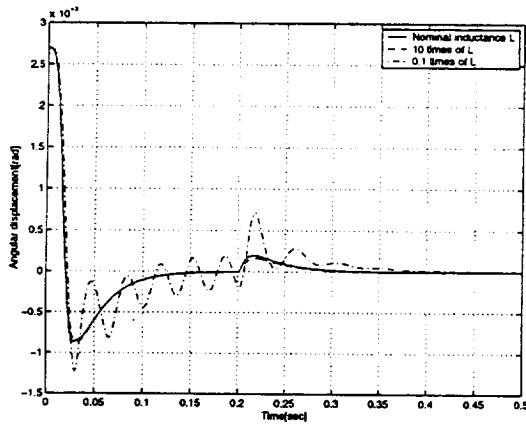


Figure 7: Evolution of angular displacement by integral state feedback controller

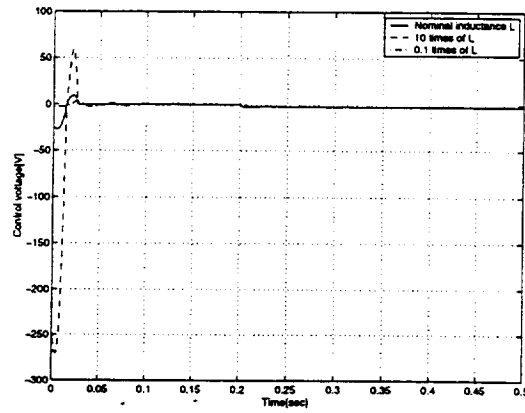


Figure 8: Evolution of control effort by integral state feedback controller

Fig. 5 - 8 show the simulation results under the parameter variations and the external step disturbance(0.2sec 1[N]). In fig. 5 the angular displacements are in close agreement, thereby illustrating the insensitivity to parameter variations. However fig. 6 shows significant difference in control effort. In fig. 7, 8 we can see the significant angular displacements and significant overshoot in control voltage which is controlled by the simple integral state feedback controller. This means that our proposed integral sliding mode controller is very robust over the parameter variations and external step disturbances.

EXPERIMENTAL SETUP

Fig. 9 shows the total experimental setup. Near the magnetic bearings of the balance beam there are two eddy-current type displacement sensors. The experimental machine is controlled by a digital control system that consists of 450 MHz Intel Pentium II Processor which is loaded with Real Time Linux OS (version Beta 16) running Real Time Control Laboratory (<http://www.people.virginia.edu/~efh4v>) [8], 12 bits A/D and D/A converters, LPF which has 1.2 kHz cutoff frequency. In our amplifier we use an H-bridge (4 HEXFETS, International Rectifier Co.) This amplifier operates on 20 kHz (much higher than the natural frequency of the balance beam) and ± 15 V power supply voltage.

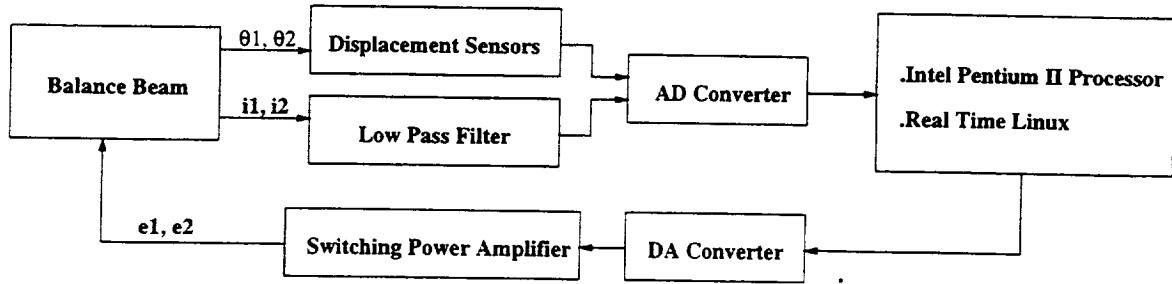


Figure 9: Block diagram of experimental setup

EXPERIMENTAL RESULTS

Fig. 10 - 15 show the gap deviations under the parametric variations and external load disturbance. In order to make the parametric variations the nominal inductance was changed from $2L$ to $0.5L$, where L is nominal inductance included in the A and B matrices. By changing this nominal inductance the system matrices A , B are changed. For the external load test a 500 g mass was added on the left side of the balance beam. Fig. 10, 12 and 14 show the initial state response when the same initial position is applied. In these figures we can see the close agreement in the transient response to the initial state even if there are parametric variations, which means good robustness of the proposed controller against the parametric variations. Fig. 11, 13 and 15 show the results of the load test. We loaded a 500 g mass at the first peak and unloaded the same mass at the second peak. From these figures we can see the almost same levitated states and the very small steady state error close to zero under the load, which means effective step disturbance rejections. For the implementation we used the following controller gain matrix and design parameters.

$$S = [15 \quad 13448.3 \quad 153.4 \quad 1.0]$$

$$\rho = 4.0, \delta = 0.4 \quad (22)$$

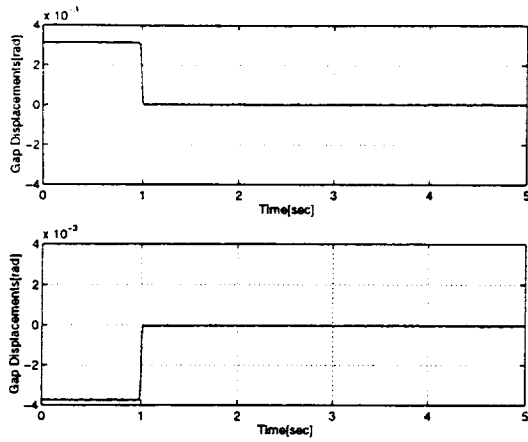


Figure 10: Initial state under the nominal inductance

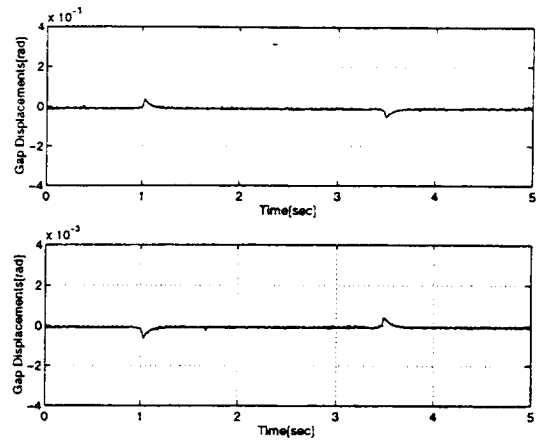


Figure 11: Load 500 g to left side under the nominal inductance

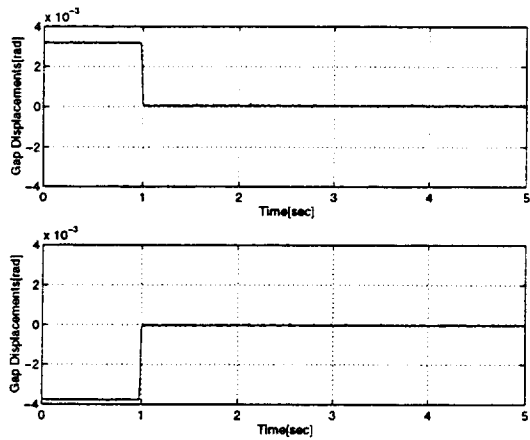


Figure 12: Initial state under two times of the nominal inductance

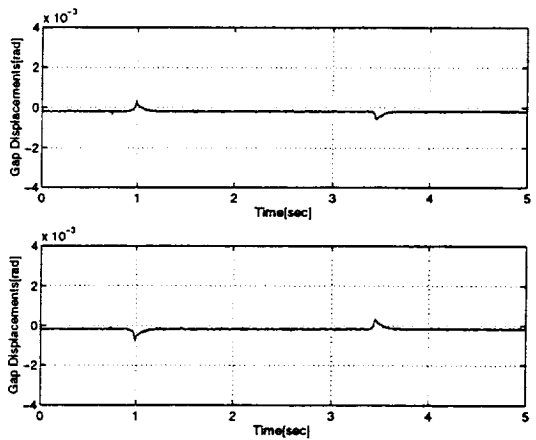


Figure 13: Load 500 g to left side under two times of the nominal inductance

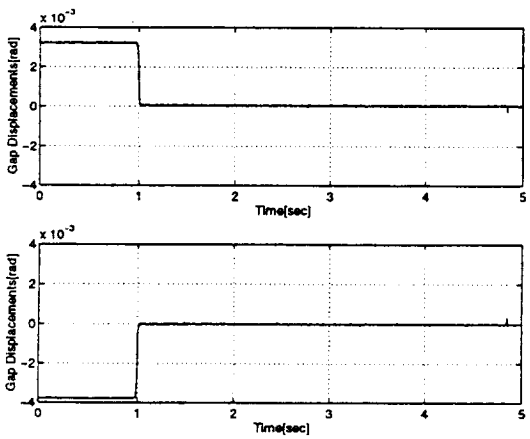


Figure 14: Initial state under 0.5 times of the nominal inductance

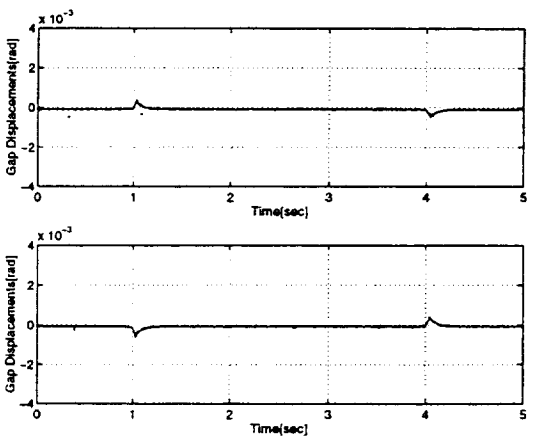


Figure 15: Load 500 g to left side under 0.5 times of the nominal inductance

CONCLUSIONS

This paper presents a method to control the angular displacement of a magnetically suspended balance beam with the parametric variations subject to initial start up conditions and a external step disturbance. To overcome the effect of the parametric variations and to reject the external step disturbance forces we used an integral sliding mode controller. First, we derived the mathematical model of the balance beam including an integral compensator, then we designed the linear and nonlinear control components. Next we showed the insensitivity of the controller response under the parametric variations and the disturbance rejection by simulations. Finally we proved the effectiveness of the integral sliding mode controller by experimentation. This paper does not directly consider plant uncertainties and sinusoidal disturbance forces, hence the next challenging issue is a new control algorithm to consider uncertainties and sinusoidal disturbance force rejection.

REFERENCES

1. P. E. Allaire and A. Sinha, "Robust Sliding Mode Control of a Planar Rigid Rotor System on Magnetic Bearings", *6th International Symposium on Magnetic Bearings, Cambridge, Mass, August 5-7, 1998*
2. S. Ueno, J. H. Lee, P. E. Allaire, Y. Okada, "Sliding Mode Control of Magnetic Bearings: Comparison of Sensed and Self Sensing Performance", *Proceedings on The American Society of Mechanical Engineering(ASME), Indianapolis, Indiana, June 7 - June 10, 1999.*
3. C. Edwards S. K. Spurgeon, "Sliding Mode Control-Theory and Application", *Taylor and Francis Ltd, 1998.*
4. K. Nonami, K. Den, "Sliding Mode Control-Design Theory of Nonlinear Robust Control(Japanese Version)", *Corona, Tokyo, 1994.*
5. S. K. Spurgeon, R. Davies, "A nonlinear control strategy for robust sliding mode performance in the presence of unmatched uncertainty", *INT. J. CONTROL, Vol. 57, No. 5, pp. 1107-1123, 1993.*
6. T. L. Chen, Y. C. Wu, "Integral variable structure control approach for robot manipulators", *IEE Proceedings-D, Vol. 138, No. 2, March, 1992*
7. T. L. Chen, Y. C. Wu, "Design of integral variable structure controller and application to electrohydraulic velocity servosystems", *IEE Proceedings-D, Vol. 138, No. 5, September, 1991*
8. E. Hilton, M. Humphrey, V. Stankovic and P. Allaire, "Real Time Control of a magnetic Bearing Suspension System for Flexible Rotors", *Proceedings of the 5th International Symposium on Magnetic Suspension Technology, Santa Barbara, CA, USA, December 1-3, 1999*

SELF-SYNCHRONOUS DETECTION METHOD FOR MAGNETIC SUSPENSION DIGITAL CONTROL

Shin-ichi Moriyama

Kyushu Institute of Technology, Kawazu 680-4, Iizuka, Fukuoka 820, Japan

Katsuhide Watanabe, Takahide Haga

Ebara Research Co., Ltd., Honfujisawa 4-2-1, Fujisawa, Kanagawa 251, Japan

ABSTRACT

This paper deals with a detection method for picking up the amplitude component from a differential signal between two inductive type sensors in magnetic suspension control. The amplitude detection, which corresponds to measuring the displacement of the suspended body, is automatically completed in the software of a digital controller because the differential signal is synchronized with the sampling cycle and can be directly fed to the A/D converter. Such a digital synchronous detection scheme is embodied for a magnetic suspension device in which an electromagnet itself is used as an inductive type sensor. The inductive sensing is performed with a carrier current superimposed on the original exciting current of electromagnet, but the carrier frequency becomes much lower than that chosen for usual inductive type sensors. Thus a deterioration of the frequency response in the displacement measurement is inevitable. Besides, since the original exciting current itself varies the inductance of the electromagnet somewhat, a lowering of the measurement accuracy is inevitable as well. The present approach, which is named the self-synchronous detection method, holds the response delay to a minimum and reduces the measurement error remarkably. As the result, stable control with a crossover frequency of 25 Hz is achieved with a carrier frequency of only 2 kHz.

INTRODUCTION

Magnetic suspension devices often require position sensors which are low cost and compact in size. For this reason, the inductive type sensor with laminated steel core is employed widely. This sensor is usually used as a pair of gap sensors to secure a linearity between the output of the sensor and the displacement of the suspended body, e.g., as two sensors inserted into the differential sensing system of Fig. 1. In this sensing system, the oscillator feeds a carrier signal v_0 to both the sensors and the resistors. When the suspended body shifts from the equilibrium position, there is a difference in inductance between the two sensors and consequently the differential signal v appears according to the unbalance quantity. Therefore, if only the amplitude component of v is picked up, the displacement will be easily estimated. But, in the amplitude detection, the carrier component of v has to be sufficiently eliminated, especially when utilizing a digital controller, because it may make the magnetic suspension control unstable. The simplest approach is to use a low pass filter, together with a multiplier for multiplying the differential signal by the carrier signal. In this case, however, the low

pass filter may bring a large time lag into the control system. The most advanced approach is to use a sample-and-hold circuit as a synchronous detector [1]. In this case, there is no need to eliminate the carrier component in the amplitude detection, but the detector becomes considerably complicated in composition and the unit cost of the sensor will increase.

The aforementioned problem may be settled by a synchronous detector which can be integrated well into a digital controller. In the sensing system, the differential signal is synchronized with the sampling cycle and can be directly fed to the A/D converter. The sign of the sampled data is reversed by each sampling cycle in the digital signal processor. This operation is equivalent to an amplitude detection for the differential signal. Therefore the hardware concerning amplitude detection is remarkably simplified. Though the fundamental idea of such a digital synchronous detection has been already proposed by the authors [1], the method is not yet established and the demonstration is left as a future subject. In this paper, a self-synchronous detection scheme is embodied for a magnetic suspension device in which an electromagnet itself is used as an inductive type sensor. The aim is to prove the strong points of the self-synchronous detection method. Though the conception of the sensorless control is based on the test signal injection method [2], the system construction is reconsidered from a different viewpoint because the materialization was not as easy as the authors thought originally.

SELF-SYNCHRONOUS DETECTION

Figure 2 shows a magnetic suspension device used in the present experiment. The arm is rotatable in a vertical plane while being supported at Point P. Electromagnet 3 is excited by a constant current so as to balance the attractive force with the gravitational force mg . On the other hand, Electromagnets 1 and 2 are excited by variable currents in order to keep the arm horizontal. Since they also are used as a pair of inductive type sensors, each exciting current must include a carrier component for sensing the arm displacement x . Since Electromagnets 1 or 2 has a large inductance, the carrier frequency becomes much lower than that chosen for usual inductive sensors. A lowering of the carrier frequency means a deterioration of the frequency response of the inductive sensing system. Therefore it is necessary to hold the deterioration to a minimum by some detection approach without low pass filter. In this point, it can be said that the device of Fig. 2 is a target suitable for clarifying the strong points of the self-synchronous detection method. Figure 3 shows a sensorless control system constructed for this device. The action is as follows.

The digital signal processor (DSP) produces a series of data in which the magnitude is constant and the sign alternates positive and negative. These data are outputted as a rectangular signal v_s through the left D/A converter (D/A 1). The signal v_s is applied to the oscillator through the band pass filter (BPF 1) with a quality factor of 10. As the result the oscillator generates a sinusoidal signal under a synchronization with the sampling cycle of DSP. The sinusoidal signal is converted to a carrier signal v_0 by the all pass filter (APF) with a phase lag ϕ_0 . The carrier signal, together with the synchronizing rectangular signal, is shown in Fig. 4. The sampling frequency f_s of DSP is set to 4 kHz and the resultant carrier frequency f_0 becomes 2 kHz. The oscillator has an amplitude

modulation function for examining the frequency response of this sensing system. But, if the purpose is only to produce a synchronized carrier signal, the oscillator is excluded because the output signal of BPF 1 can be regarded as a sinusoidal wave which is the most suitable for this sensing scheme. The carrier signal, together with a variable voltage command e , is supplied to the left power amplifier (PA 1) as a positive input signal and to the right power amplifier (PA 2) as a negative one. Since a dc voltage command e_0 is applied to PA 1 and PA 2 in common, the exciting currents of Electromagnets 1 and 2 can be approximately expressed as $i_1 = i_0 + i$ and $i_2 = i_0 - i$, respectively, if there is no carrier signal. Here i_0 is the bias current due to e_0 and i is the controlling current due to e . On the other hand, the contribution of v_0 appears as a carrier component superimposed on the exciting currents. The carrier component can be written as $s_1 = s_0 + s$ or $s_2 = -s_0 + s$, where s_0 is a carrier current at the equilibrium position and s is the unbalance quantity due to displacement.

The total currents of Electromagnets 1 and 2 are measured by means of the resistors and the buffer amplifiers (BA 1 & BA 2). The sum of the two total currents becomes $2(i_0 + s)$. Since the bias current i_0 in the addition signal is cut by the band pass filter (BPF 2) with a quality factor of 1, the output signal v of the instrument amplifier (IA) is due only to the unbalance quantity s . The signal v corresponds to the differential signal in this sensing system and can be directly fed to the left A/D converter (A/D 1). Therefore it is possible to sample the peak of v by adjusting the phase of v adequately with APF, as shown in Fig. 5. The peak detection is completed by reversing the sign of the sampled data by each sampling cycle in the DSP. Figure 6 shows a differential signal modulated with OSC and the peak detection result outputted by another D/A converter (D/A 3). On the other hand, the difference between the two total currents becomes $2(i + s_0)$. This subtraction signal can be directly fed to the right A/D converter (A/D 2) as well even if it includes the carrier current s_0 . The data about the controlling current i is obtained by adding the sampled value at a sampling cycle to that at the previous cycle because the contribution of s_0 is canceled by doing so. Figure 7 shows a subtraction signal produced with a sinusoidal voltage command e and the addition result outputted by another D/A converter (D/A 4). The data about the controlling current will become necessary when introducing a state feedback scheme into the control system.

SENSING / CONTROLLING PERFORMANCES

A relation between the peak detection output and the arm displacement can be examined by changing the position successively while supporting the arm by micrometers. The results are summarized in Fig. 8. Here the bias current i_0 is set to the value indicated in this figure and the controlling current i is kept zero. A series of data for each case of i_0 is good in linearity, but the slopes of the fitting lines are different and the resultant sensitivity decreases from 8 V/mm to 5 V/mm as increasing i_0 . This seems to be connected to a variation of inductance due to the exciting current. In general, the inductance of an electromagnet somewhat depends on the magnetic flux density in electromagnet core or in the suspended body and the dependence is stronger as the magnetic flux density approaches the saturation level. In this device, the magnetic flux density in the arm is closer to the saturation level and is roughly estimated to be 0.45 T at $x = 0$ mm and 0.6 T at $x = \pm 0.3$ mm in the

case $i_0 = 0.6$ A. Since the magnetic suspension control requires a bias current of 0.5 A at least, the exciting current will have a little influence on the inductance. The influence appears as an error in the displacement measurement. Figure 9 shows a relation between the peak detection output and the controlling current. Here the bias current is set to 0.5 A and the arm is fixed at the equilibrium position. From the negative slope, the error sensitivity is estimated to be 6 V/A. Since the detection sensitivity in the case $i_0 = 0.5$ A is 7 V/mm, the sensitivity ratio is close to 1 mm/A and cannot possibly be neglected. The error can be compensated with data about the controlling current, but it should be noted that the error sensitivity somewhat decreases as increasing the frequency of controlling current. So, in order to keep the compensation good over a wide frequency range, the current data was reformed according to an algorithm of a first-order low pass filter. Consequently it was possible to make the sensitivity ratio less than 0.01 mm/A in a frequency range up to 1 kHz.

The other performance in this sensing system is the frequency response to a variable displacement of the peak detection output, but it is difficult to measure the frequency response directly. So, by modulating the differential signal with OSC as shown in Fig. 6, let us indirectly estimate the frequency response. Here the modulating signal is fed to another A/D converter (A/D 3) and is outputted straight by another D/A converter (D/A 5) so as to exclude a time lag due to DSP itself from the frequency response. Figure 10 shows the transmission characteristic from the modulating signal output to the peak detection output. The gain cutoff frequency is about 1 kHz and the phase lag is about 5° at 100 Hz and increases to about 50° at 1 kHz. In this sensing system, since no low pass filter is employed, the response delay is due to the DSP and BPF 2 essentially. It is known that the effect of a band pass filter on the amplitude component of an amplitude-modulated wave is equivalent to a first-order lag element with a time constant $Q/\pi f_0$ [1]. In the case of BPF 2, the cutoff frequency of the first-order lag element becomes 1 kHz. The characteristic of Fig. 10 nearly accords with this theoretical expectation. Therefore, if the quality factor Q is reduced, the sensing performance seems to be improved further. It should be noted, however, that the differential signal is still not released from the controlling current. Strictly speaking, when there is no carrier signal, the total exciting currents should be expressed as $i_1 = i_0 + i + \Delta i$ and $i_2 = i_0 - i + \Delta i$, where Δi is the unbalance quantity of controlling current due to displacement. Since the addition signal in Fig. 3 is corrected as $2(i_0 + \Delta i + s)$, the unbalance quantity Δi may bring a new error into the displacement measurement. Considering this error and a deficiency of the aforementioned compensation, a regular limitation of frequency bandwidth due to BPF 2 seems to be necessary for the control system to work stably.

The feedback control in Fig. 3 is completed by producing the feedback signal e_f from the data about displacement according to an adequate control algorithm. In the present experiment, let us adopt the following algorithm in consideration for a voltage control of the electromagnet and a vibration mode of arm; a proportional and integral regulator, first-order high pass filter, band pass filter and band elimination filter. The frequency response of the digital controller is shown in Fig. 11. The phase margin is secured between 3 Hz and about 200 Hz for exciting the electromagnet and the sharp gain drop is set to about 400 Hz for preventing a vibration of the arm. By using this digital controller, stable control was achieved successfully. Figure 12 shows the frequency response to a

sinusoidal voltage command e of the feedback signal output e_f , that is, the open loop frequency response of this control system. This response was measured with the reference signal e_r in Fig. 3. From this response, it is found that the phase margin is about 15° at a crossover frequency of 25 Hz and the gain margin is about 12 dB in the neighborhood of 100 Hz.

CONCLUSION

The self-synchronous detection method proposed by the authors has been applied to a magnetic suspension device without position sensor. In the sensing system, a carrier current superimposed on the original exciting current of electromagnet is used for measuring the displacement of the suspended body. The carrier current has to be made of a carrier signal with a relatively low frequency. Thus a deterioration of the frequency response in the displacement measurement is inevitable. Besides, since the original exciting current itself varies the inductance of the electromagnet somewhat, a lowering of the measurement accuracy is inevitable as well. The present approach holds the response delay to a minimum by excluding low pass filters from the sensing system and reduces the measurement error remarkably by compensating the measurement result with the data about exciting current. Consequently, stable control with a crossover frequency of 25 Hz was achieved under a carrier frequency of only 2 kHz.

Though the self-synchronous detection method is premised on the use of digital controller, the application enables us to optimize the flexible function of digital controller simultaneously. Furthermore, since the sensorless control system constructed in this study is very simple in composition, it is possible to mount all the electronic circuits except the power amplifiers on the DSP board. This will be useful to improve the cost-performance ratio of digital controller further.

REFERENCES

- [1] S. Moriyama, K. Watanabe and T. Haga, "Inductive sensing system for active magnetic suspension control," in *Proc. 6th Int. Symp. Magn. Bearings*, pp. 529-537, Technomic Publishing Co., Inc., 1998.
- [2] K. K. Sivadasan, "Analysis of self-sensing active magnetic bearings working on inductance measurement principle," *IEEE Trans. Magn.*, vol. 32, pp. 329-334, 1996.

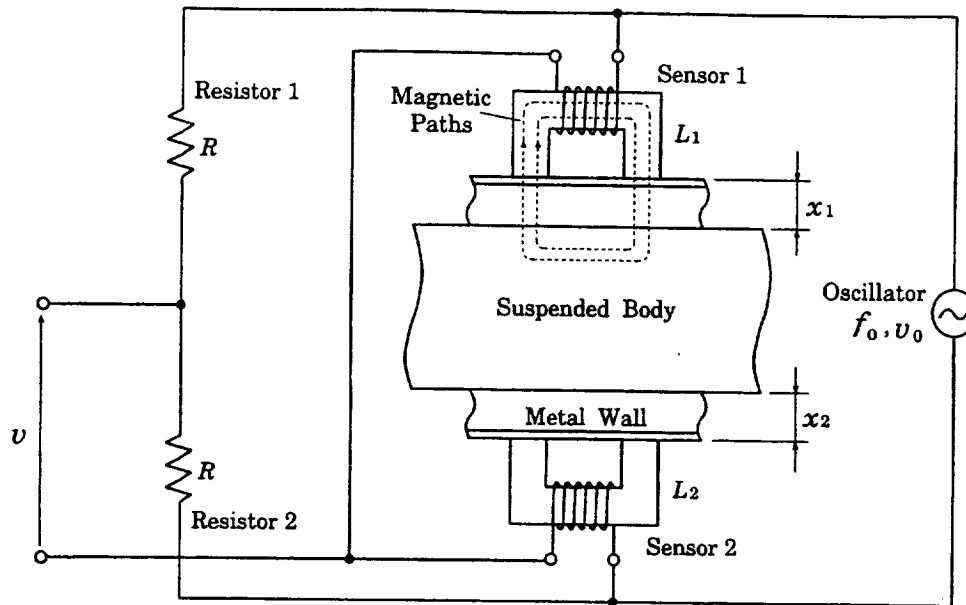


Fig. 1. Basic structure of inductive type sensors discussed in Ref. [1]. Though the metal wall is used for protecting the sensor, it is not the essential component for the inductive sensing system.

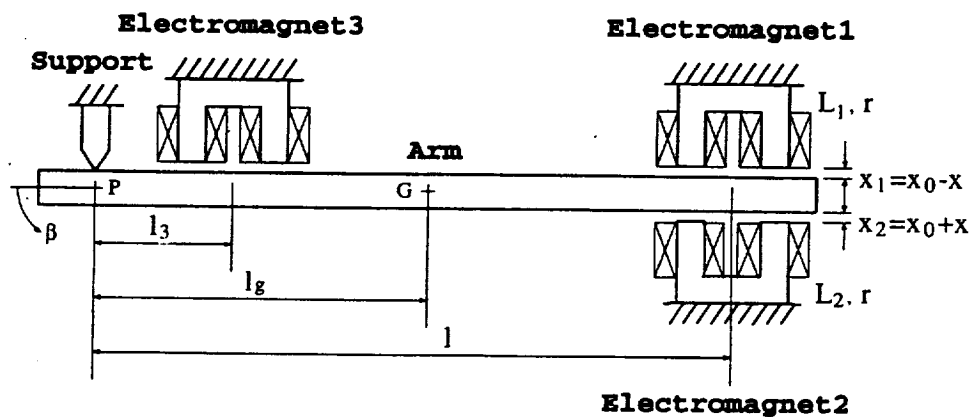


Fig. 2. A magnetic suspension device with one degree of freedom: $l = 193$ mm, $l_3 = 29$ mm, $l_g = 111$ mm, $x_0 = 1$ mm, -0.3 mm $\leq x \leq 0.3$ mm, $m = 1.3$ kg, $L_1, L_2 \sim 100$ mH, $r = 10$ Ω .

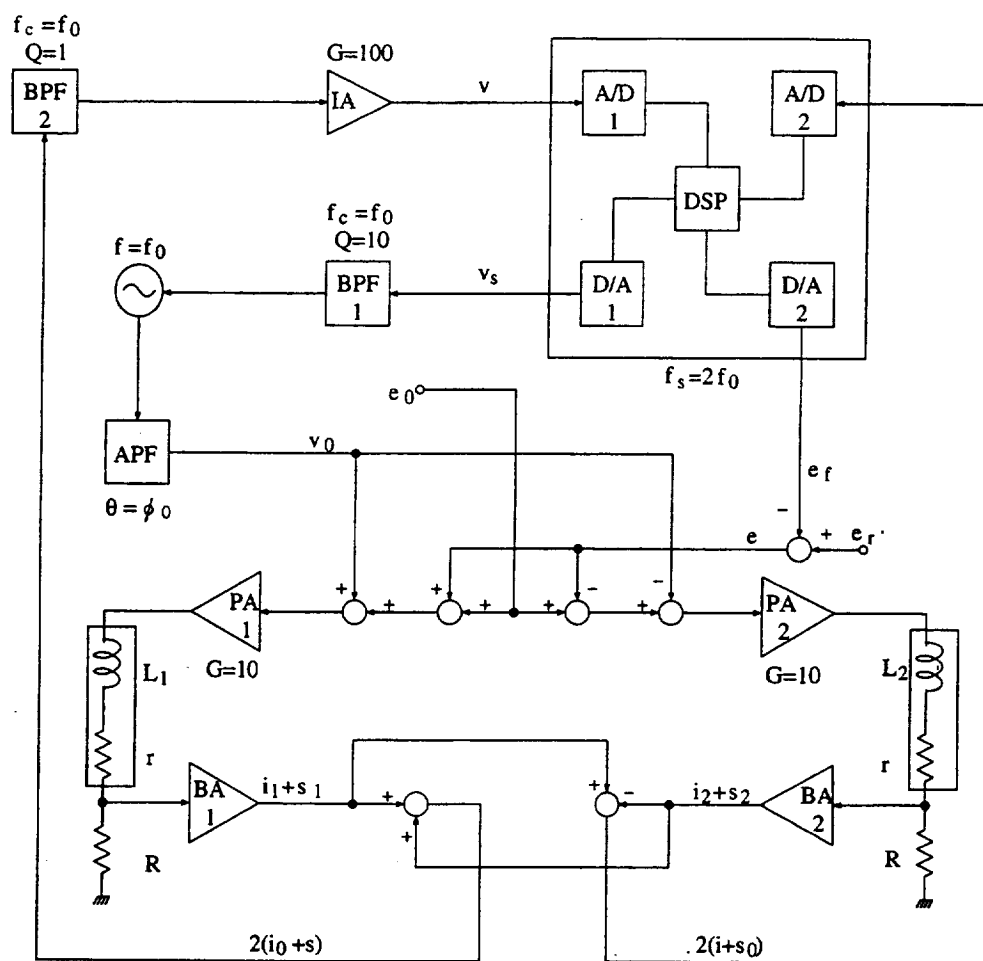


Fig. 3. Schematic diagram of a sensorless control system: $R = 4 \Omega$, $f_0 = 2 \text{ kHz}$, $f_s = 4 \text{ kHz}$. The DSP board used as a digital controller has five A/D converters and five D/A converters in reality.

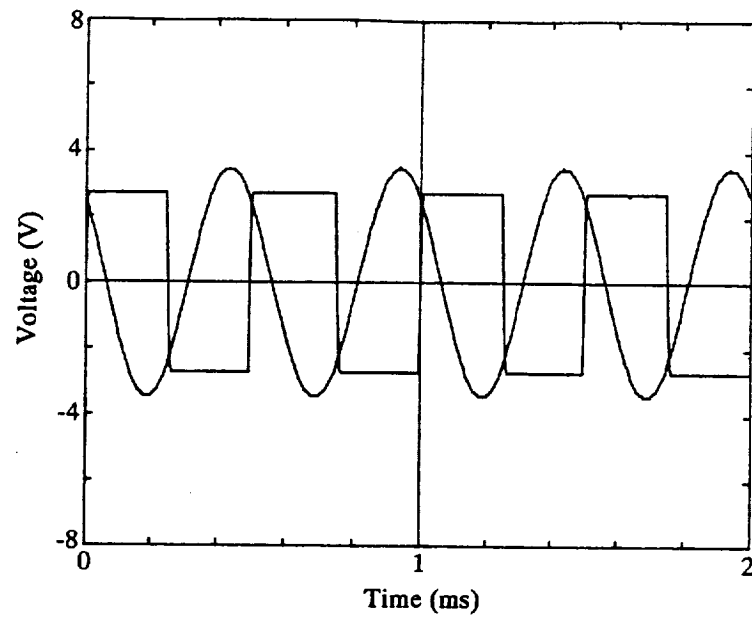


Fig. 4. A sinusoidal carrier signal and the synchronizing rectangular one. The phase difference between the two signals is equal to a phase lag given by APF.

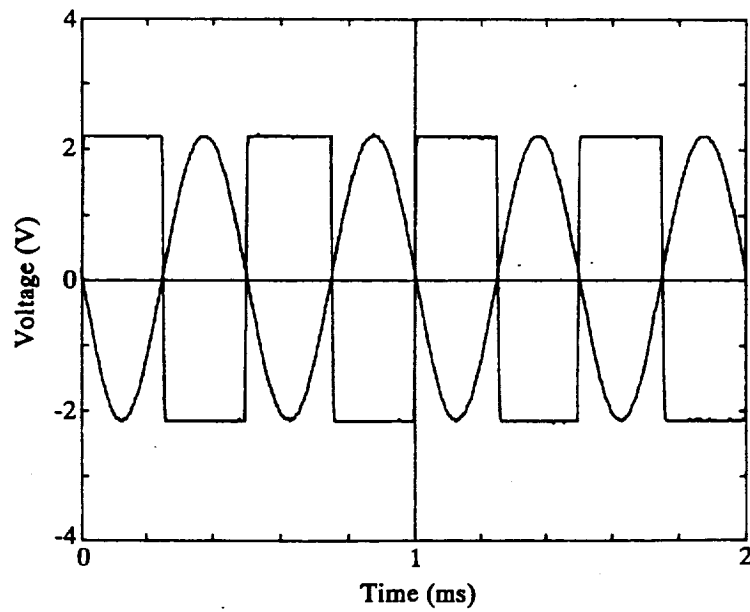


Fig. 5. A differential signal and the sampled data output (of D/A 3) when the arm is fixed at $x = 0.3$ mm.

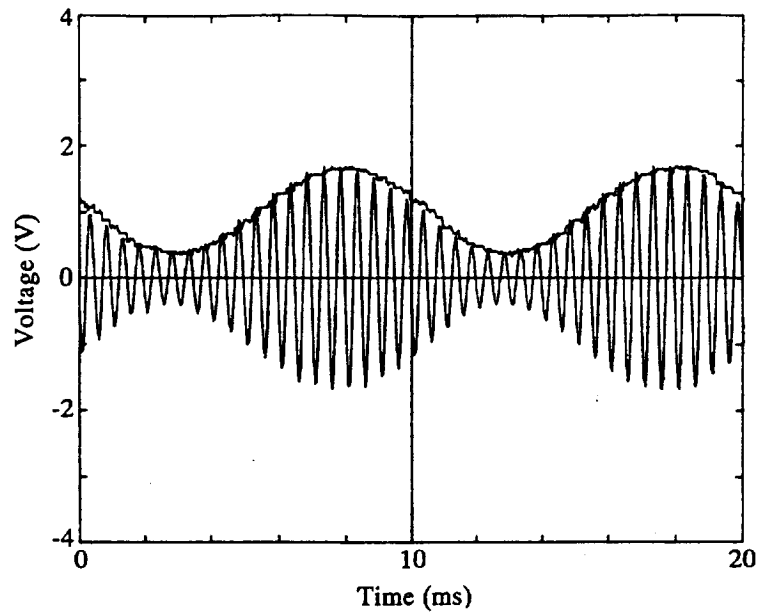


Fig. 6. An amplitude-modulated differential signal and the peak detection output (of D/A 3) when $x = 0.3$ mm. The modulating frequency is 100 Hz.

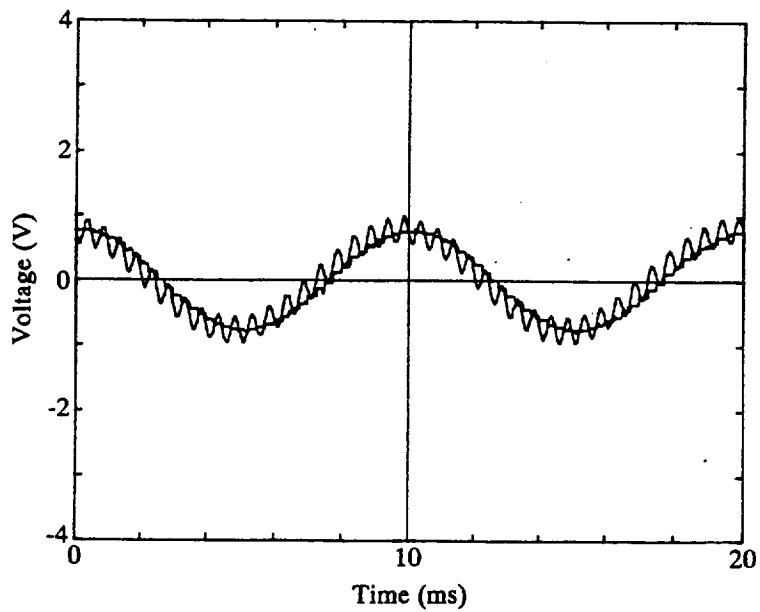


Fig. 7. A subtraction current signal and the output (of D/A 4) for the controlling current with a frequency of 100 Hz.

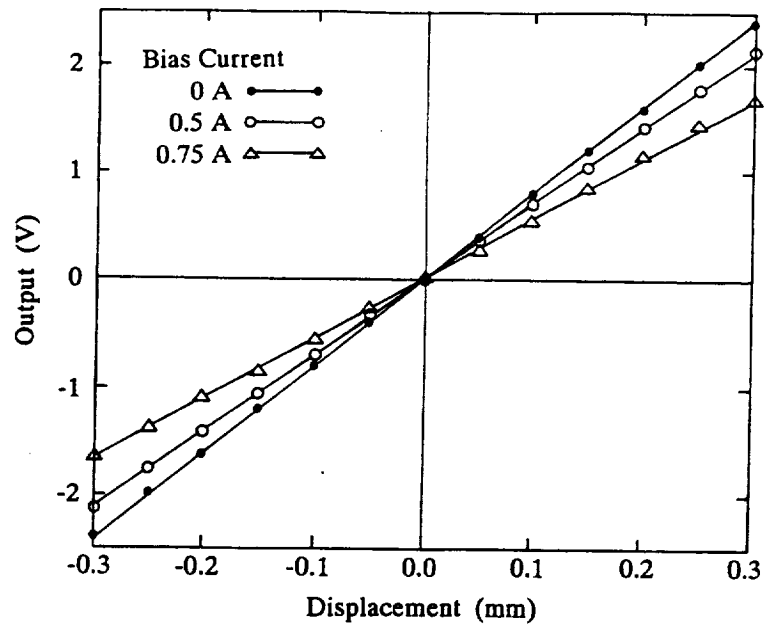


Fig. 8. Relation between the peak detection output (of D/A 3) and the arm displacement when $i = 0$ A. The arm displacement is measured by micrometers with a resolution of $10\text{ }\mu\text{m}$.

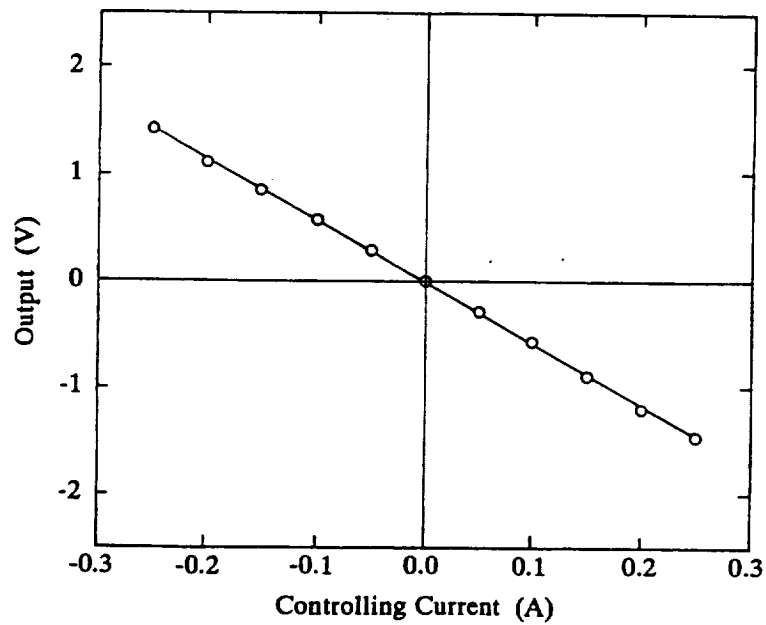


Fig. 9. Relation between the peak detection output (of D/A 3) and the controlling current when $i_0 = 0.5$ A and $x = 0$ mm.

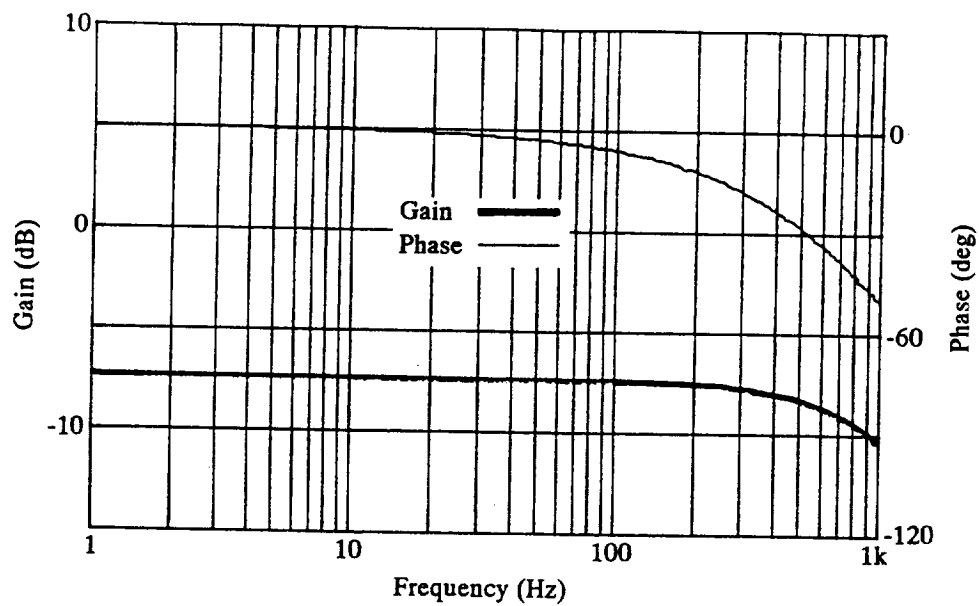


Fig. 10. Transmission characteristic from the modulating signal output (of D/A 5) to the peak detection output (of D/A 3) when $i_0 = 0$ A and $x = 0.3$ mm.

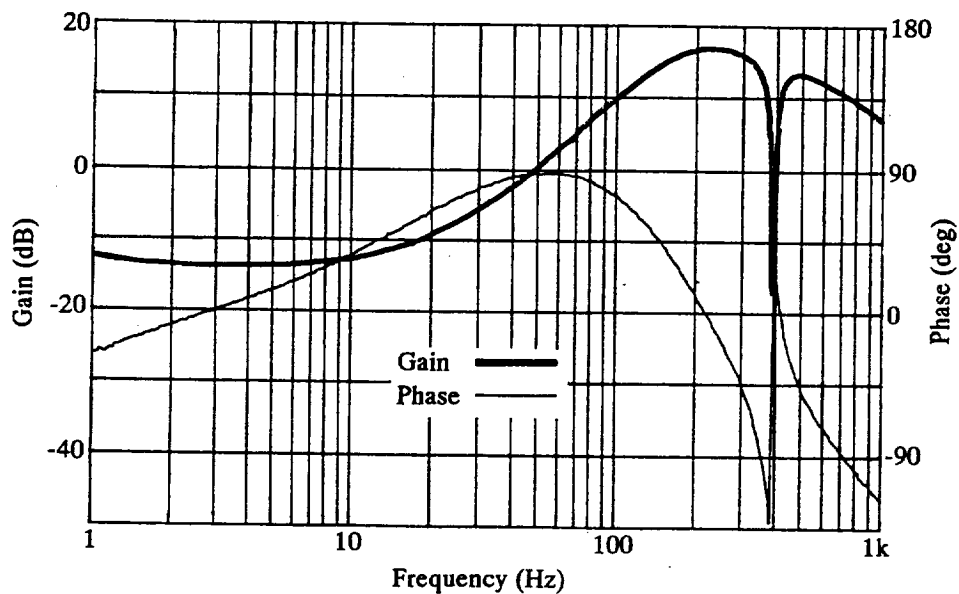


Fig. 11. Frequency response to a sinusoidal signal input (of A/D 1) of the feedback signal output (of D/A 2).

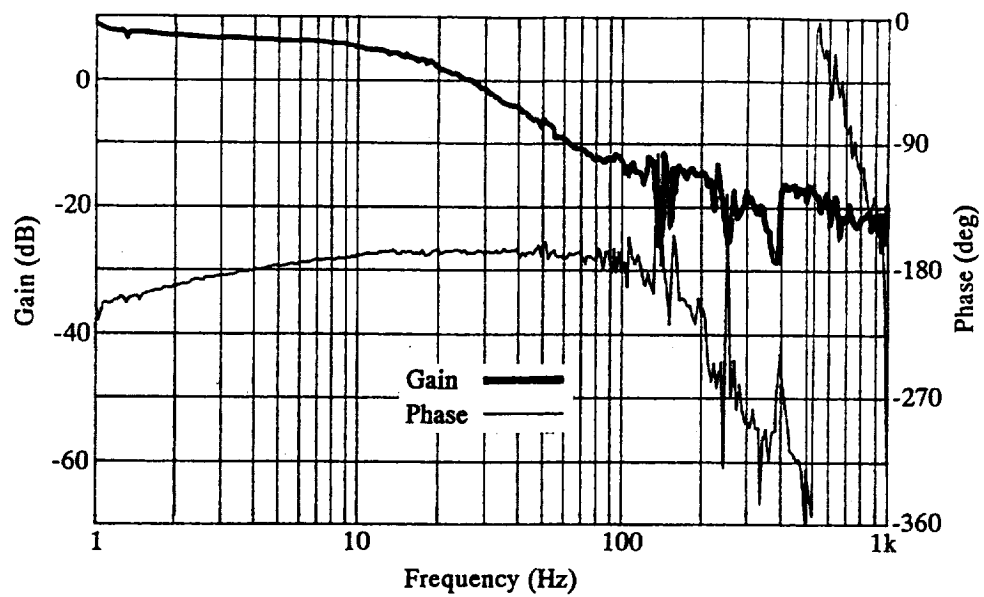


Fig. 12. Frequency response to a sinusoidal voltage command of the feedback signal output (of D/A 2). The arm is magnetically suspended by Electromagnets 1 and 2 with a bias current of 0.5 A.

Session 17 -- Magnetic Suspension In Wind Tunnels 2

Chairman: Nelson J. Groom
NASA Langley Research Center

Status of MSBS Study at NAL

Hideo SAWADA, Takashi KOHNO, and Tetsuya KUNIMASU
National Aerospace Laboratory
7-44-1 Jindaijihigashi-machi Chofu-shi, Tokyo, Japan

Applications: Wind tunnel model suspension systems

ABSTRACT

A superconductive solenoid model core was suspended successfully in the NAL 60-cm MSBS. The cryostat containing the solenoid is 600 mm long and its diameter is 87mm and the solenoid works at 4.2K. Its material is NbTi. Duration time of the permanent current mode is about 1 hour. According to several test results, the available time for wind tunnel tests is around 30 minutes for the system. The superconducting solenoid core has the same characteristics, up to 20A in coil current, in the MSBS as the permanent magnet core does. The model position sensing system was improved to be easy to use. An auto-calibration system was built. The lighting system was improved to light up with red and green lights respectively from upper and side ways in order to avoid the interference between lateral and longitudinal position components. The 60cm MSBS was installed in a low speed wind tunnel with a closed circuit. A cylindrical model and a cone-cylinder model were suspended at various flow speeds up to 28.5m/s without any extra motion compared with flow off.

Introduction

Magnetic Suspension and Balance Systems (MSBS) provide an ideal way of supporting a model for wind tunnel tests because the force to support the model is generated by the magnetic field which is controlled by the coils arranged outside the test section as shown in Figure 1. Any mechanical support system is not needed in the flow field. Then the support interference problem does not exist except for very special test conditions like hypersonic flow containing ionized atoms. Besides, it is very suitable to carry out difficult tests like dynamic tests. It is also much easier to change model attitude over a wide range by an MSBS than by a mechanical support system. These features of the MSBS will improve the tunnel data productivity. Many MSBSs have been built up to the 1970s but only a few are in operation presently.

The NAL 10-cm MSBS has been developed since 1985 and the 60-cm MSBS has been developed since 1993 at the National Aerospace Laboratory (NAL).¹ The 60-cm MSBS has the largest test section in the world in the sense of the dimensions as of present. The detail of research activity relating to the 10-cm MSBS at NAL must be referred to References 1) to 4).

In order to generate a large magnetic force balancing the aerodynamic load, both a strong magnetic field and large magnetic moment of the model core are needed. The superconductive solenoid core can be mounted inside a model and can generate much larger magnetic moment than permanent magnet cores. A small superconductive solenoid model core was designed and was suspended successfully in a MSBS at Southampton University supported by NASA.^{5,6} This was the only successful suspension of a superconductive solenoid until the suspension of the solenoid described in this paper. A new superconductive

solenoid model core was designed at NAL and was built by a manufacturer in 1997. The core was suspended in the 60-cm MSBS successfully in 1998. As far as the authors know, there was no procedure of safety handling superconductive solenoid model cores in MSBSs. Through the experience of suspending the core in the 60-cm MSBS, a safe handling procedure was developed.

The 60-cm MSBS was installed in an old low-speed wind tunnel at NAL. The tunnel has a closed circuit and is fan-driven. The maximum flow speed is about 28.5m/s and its pressure is ambient. The MSBS has been improved to be easy for researchers to use it. The model position sensing system can be calibrated automatically with a computer. A computer controls all of the MSBS in order to avoid wrong operations. Model position and coil current data sets for 16 seconds at any time during the operation can be stored. The system is still being improved to meet to user satisfaction. Two kinds of models were suspended in the tunnel and the results were examined to determine whether or not the MSBS was acceptable for wind tunnel testing.

SYMBOLS

(x,y,z)	... coordinate system, unit : mm, See Figure 1.
(ϕ,θ,ψ)	... rolling, pitching , and yawing angles of a model, unit : degree.
H	... magnetic field intensity, (H_x,H_y,H_z) .
M	... magnetic moment (Wb.m), (M_x,M_y,M_z) .
P[0] to P[5]	... ceiling sensing camera outputs, (counts).
P[6] to P[9]	... side sensing camera outputs, (counts).
P,Q,R,S,T	... see Eqn. (2).

Brief Description of the NAL 60-cm MSBS

The 60-cm MSBS consists of 8 electromagnets and 2 air cored coils. Four of the 8 electromagnets make a magnetic circuit with an iron ring perpendicular to the wind axis (x -axis). The other four also make a magnetic circuit with another iron ring as shown in Figure 2. Each has four pole-surfaces. The coils 1 to 4 are attached to the upstream iron ring. The coils 5 to 8 are attached to the downstream ring similarly. The coil currents can control the magnetic field surrounded by the four pole-surfaces in each ring. The four coils are always excited in pairs like a pair of coils, 1 and 3. The paired coils of (1, 3) and (5, 7) control H_z and its derivative with respect to x . Similarly, the paired coils of (2,4) and (6,8) control H_y and its derivative with respect to x . A pair of air cored coils, (0, 9) controls the derivative of H_x with respect to x . The distance between the poles of the coil pair is 640 mm. The specifications of the coils are listed in Table 1. Details of the NAL 60-cm MSBS are described in References 1 to 4 and 7.

We have two permanent cylindrical magnets magnetized along their axes for the 60-cm MSBS. One is 50 mm in diameter and 300 mm long and a TOKIN K-5 type Fe-Cr-Co magnet. The other is 55 mm in diameter and 280 mm long and is an Alnico5 magnet. Five coil drive units for the coil pairs range from -75 to 75 A at 60V. A bias coil for generating additional lifting force is driven by two constant current power units of 1500 W, which range from 0 to 100 A. The coils are cooled with ambient air and they can be operated for about 1 hour.

A model position sensing system for the NAL 60-cm MSBS has been developed at NAL. The principle of the system is the same for the NAL 10-cm MSBS. It is described in reference 1. Two model position sensing cameras are mounted at the side and upper side test section walls. The upper camera measures x , y coordinates and yaw angle, ψ of the model. The side camera measures z coordinate and pitch angle, θ . Each camera is connected to a computer and both measured data sets are gathered synchronously in a computer and the computer evaluates the model position with them and adjusts the coil currents. Large noise radiated from the power units affect the accuracy of the measured position significantly. All position data are modified with low pass filter of 10 Hz cut-off frequency before evaluating the model position.

coil #	turn number	dimensions	purposes
0,9	50	620 x 620	drag
1,3,5,7	97 + 97	200 x 200	lift, pitch moment
2,4,6,8	100	200 x 200	side force yawing moment, and rolling moment
coil drive units	60V, 75A	5 units	
bias coil drive units	1500 W	2 units	
model cores	50-x 300 cylindrical permanent magnet (Fe-Cr-Co)		
	55-x 280 cylindrical permanent magnet (Alnico5)		
control	5 degree of freedom except for rolling motion control		
	rolling motion : mechanical control with a fly wheel ⁸⁾		

Table 1 Specifications of the NAL 60-cm MSBS

In order to avoid model damage and personnel accident during initial suspension, the 60-cm MSBS has a model holding system. The system was designed to hold the model horizontally at the center of the test section as shown in Figures 2 and 5. The arm part of the system can be moved out from the test section completely after releasing the model. After moving out of the test section, the open space on the test section wall for motion can be closed with a removable window by hand. In order to confirm that the model is in balance, the model holding system is equipped with a balance. If the output from the balance becomes very small in its magnitude, it suggests that the model has been in near balance condition. The balance is accurate enough to monitor a model balance condition. Details of the model holding system and the monitoring system are in Reference 7.

A Superconductive Solenoid Core

A superconductive solenoid model core, shown schematically in Figure 3, was designed and built in 1997 by NAL and a manufacturing company. The cryostat is 600 mm long and 87mm in diameter. The solenoid is 300 mm long and 72 mm in outer diameter and 43mm in inner diameter and works in liquid helium at 4.2 K. The superconductive material is NbTi. The maximum magnetic moment is above 0.0057 Wb_m. Duration time of the permanent current mode is about 1 hour. The maximum storage of liquid helium is about 1 liter. Details are in Table 2.

All parts for the solenoid operation are installed completely inside a cylindrical region of 87 mm in diameter. This condition is necessary to install the cryostat into a wind tunnel model

easily. The vaporized gas from the liquid helium is exhausted through a slender pipe continuously at the present time. During the gas exhausting, aerodynamic forces cannot be measured because the flow around the model is disturbed by the exhausted gas jet. The mass of the cryostat is about 7.4 kg.

The magnetic moment, M_x , was measured with the 60-cm MSBS magnetic field and it is 0.0023 Wbm when the solenoid is excited at 20A. The cryostat was inserted into a thin cylinder of 91mm in its outer diameter to protect the cryostat shell from the model holding system. The mass of the whole model including the model mass is 8.7kg and the inertia moment about the gravity center is about 0.233kgm², which was evaluated by oscillation tests. Because the MSBS does not have rolling motion control capability as of present, a small thin plate of lead was attached inside the cylindrical model so that the helium gas exhaust pipe exit may be upwards in balance. The control constants were estimated with the constants of a permanent magnet model core.

Magnet		
Field achieved in test at 4.2K	Specified: 6.5 T	Actual: >6.5 T
Coil inductance:	Specified: N/A	Actual: ~7 H
Current density at 6.5T:	Specified: >25 kA/cm ²	Actual: 45.1 kA/cm ²
Calculated magnetic moment at 6.5T:	Specified: >0.0047 Wb.m	Actual: 0.0057 Wb.m
Magnet bore:	Specified: 35 mm	Actual: 43 mm
Overall diameter:	Specified: 75 mm	Actual: 72 mm
Overall length:	Specified: N/A	Actual: 348 mm
Winding length:	Specified: 300 mm	Actual: 300 mm
Distance from base to field center:	Specified: N/A	Actual: 156.5 mm
Cryostat		
Cryostat length:	Specified: 600 mm	Actual: 600 mm
Cryostat outside diameter:	Specified: 87 mm	Actual: 87 mm

Table 2 Superconductive solenoid model core specifications for the 60-cm MSBS

Handling and Operating Test Results of the Superconductive Solenoid Model Core.

It is necessary to estimate the procedure in detail for testing a model with the superconductive solenoid model core in the MSBS because only one example of suspending a small superconductive solenoid core in the small MSBS⁵⁾ was reported. After several tests, a testing procedure was built temporarily, which is subdivided into 62 steps. Fundamental sequential steps are listed in Table 3.

The coil temperature history is shown in Figure 7, which was monitored at the model suspension test in the 60-cm MSBS. The solenoid was excited at 20A. Parts of the temperature history during the model suspension are not depicted because the cables are disconnected during that time. At the first test in the figure, it took one hour and 43 minutes to cool down the solenoid and it took 16 minutes to build the permanent current mode to 20A and to disconnect all cables. Then the model was suspended in the MSBS for about 30 minutes. After holding the model by the holding system, we waited for quench phenomenon. When the quench happened, the solenoid temperature rose up suddenly as shown in the figure. Once quench happens, we must wait for an hour to achieve uniform temperature in the solenoid. In order to proceed to the next test, the solenoid was cooled again. It took about one

and a half-hour to cool it and store liquid helium inside the cryostat. After exciting the solenoid, the model was tested in the MSBS again. The model was held by the holding system at 10 minutes before expected quench time. Then the power unit sank the current passing through the solenoid safely. The cryostat was stood on a base to pour liquid helium into it. The solenoid was cooled soon again because heat was not generated by quench. The third test was also carried out safely as shown in this figure. If quench is avoided, model suspension tests of about 20 minutes duration could be carried out every 150 minutes. It took 30 minutes to cool down the solenoid with this procedure. It also took about 1 hour to store enough liquid helium inside the cryostat. The one-hour of the storing time was decided through several cool down test experiences. Then, there is some room to make the time shorter. The whole procedure listed in the Table 3 for suspending and holding and de-energizing the superconductive solenoid model core safely was confirmed by several tests.

-
1. get the 60-cm MSBS ready to suspend a model,
 2. stand the cryostat vertically on a base,
 3. connect coil temperature and liquid helium monitoring cables,
 4. disconnect the short bar on the solenoid ends,
 5. start measuring the coil temperatures and liquid helium level,
 6. start transferring liquid helium into the cryostat,
 7. wait until conditions are satisfied completely,
 8. finish transfer of liquid helium, (See Figure 4.),
 9. disconnect coil temperature and liquid helium monitoring cables,
 10. insert the cryostat into a model,
 11. connect coil temperature and liquid helium monitoring cables again,
 12. connect coil exciting cables,
 13. mount the model on the model holding system,
 14. hold the model strongly, (See Figure 5.)
 15. switch on a power unit for the solenoid,
 16. build permanent coil current mode,
 17. switch off the power unit,
 18. short the solenoid ends with the short bar,
 19. disconnect the coil exciting cables and monitoring cables,
 20. start operation of the 60-cm MSBS, (See Figure 6.)
 21. hold the model by the holding system before 10 minutes of quench phenomenon,
 22. stop operation of the MSBS,
 23. connect the monitoring cables,
 24. decide whether or not to continue sinking current procedure by the monitored coil temperatures,
 25. connect the coil exciting cables,
 26. switch on the power unit,
 27. disconnect the short bar,
 28. sink the coil current completely,
 29. switch off the power unit,
 30. disconnect all cables,
 31. release the model from the model holding system,
 32. pull out the cryostat from the model,
 33. stand the cryostat on a base,
 34. connect the monitoring cables,
 35. transfer liquid helium into the cryostat again if it needed,
-

Table 3 Handling procedure for the superconductive solenoid model core at the NAL 60-cm MSBS

The model with the superconductive solenoid model core was suspended successively in the NAL 60-cm MSBS as shown in Figure 8. The 20A current passed through the solenoid at the test. It was not necessary to tune up the control performance with the reduced control constants from the permanent magnet cores. The responses of model position change were acceptable as shown in Figure 9. Large differences in response and suspension performance did not appear between a permanent magnet core and the superconductive solenoid core at the time. In Figure 6, strings are shown in the figure, which have no tension and do not affect the suspension at all. The strings were attached to the model in order to avoid accidental drop directly against the test section wall. A picture of the suspended superconductive solenoid model core model without any strings is shown in Figure 8. The cryostat was out of order after the test and the coil temperature could not cool down with liquid helium. According to the manufacturing company's repair report, the cause was that the solenoid suspension rods inside the cryostat were broken which caused the thermal insulation performance to degrade significantly. It was repaired. The success of suspending the superconductive solenoid model core suggests the possibility of realizing larger sized MSBS by using the superconductivity technology. We are proceeding to design a 2m MSBS for a low speed wind tunnel.

Improved Model Position Sensing System

The model position sensing system at the NAL 60-cm MSBS was significantly improved in accuracy two years ago by adding another sensing camera in upper side of the model. However, the two cameras were connected to computers, respectively. One computer, which received the measured model position by the upper camera, controlled the lateral model motion. Similarly, the other computer, which gathered the model longitudinal model position with the side camera, controlled the longitudinal model motion. Only the x coordinate was corrected by measured model yaw angle. Practically, a model is lighted with four optical fiber illumination systems. The two systems light the model from the upper side and the other two systems light from the side. Then a part of the model surface is lit up more strongly than the other lighted parts from both ways. In order to avoid interference between the lateral and longitudinal measured data sets, the upper side model is lit up with red light with color filter sheets on the upper window and the side surface of the model is lit up with green light with a color filter sheet on the side window.

The two cameras are driven synchronously with one signal and the measured data sets are gathered into one computer at the same time. Then interference among the five model position components is corrected with following linear equations:

$$\begin{pmatrix} x \\ y \\ z \\ \theta \\ \psi \end{pmatrix} = \begin{pmatrix} +0.0680 & -0.0011 & +0.0001 & -0.0174 & -0.0009 \\ +0.0001 & -0.0646 & +0.0009 & +0.0009 & +0.0048 \\ -0.0001 & +0.0046 & +0.0527 & -0.0001 & +0.0002 \\ -0.0000 & -0.0000 & -0.0010 & +0.0349 & +0.0026 \\ +0.0000 & +0.0005 & +0.0004 & -0.0005 & -0.0367 \end{pmatrix} \begin{pmatrix} T \\ R \\ P \\ Q \\ S \end{pmatrix} + \begin{pmatrix} +39.59 \\ -76.80 \\ +70.88 \\ -1.05 \\ +0.68 \end{pmatrix} \quad \dots(1)$$

where

$$\begin{aligned}
 T &= \frac{(P[0] + P[1])}{2} \\
 R &= \frac{(P[2] + P[3] + P[4] + P[5])}{4} \\
 P &= \frac{(P[6] + P[7] + P[8] + P[9])}{4} \\
 Q &= \frac{(P[6] + P[7] - P[8] - P[9])}{4} \\
 S &= \frac{(P[2] + P[3] - P[4] - P[5])}{4}
 \end{aligned}
 \quad \dots (2)$$

The 60-cm MSBS was equipped with the 60-cm low-speed wind tunnel this spring. Aerodynamic tests will be carried out with various models in near future. The model position sensing system must be calibrated much more easily and often for each tested model. Then, an automatic calibration system was built as shown in Figure 10. A specially made calibration model, which has the same shape and surface condition as the aerodynamic test model, is positioned by a computer and its position measured automatically. The model is in very similar condition at the calibration test as the aerodynamic test model is suspended inside the test section. The calibration coefficient matrix and offsets are evaluated easily with the gathered data sets by the same computer on the spot. The simple relations between model position, T to S in Eqn. (2) and sensing camera outputs are depicted on the monitor of the computer during the calibration test. Then, if unexpected relations are observed, the test can be stopped anytime and the system can be adjusted again. The calibration coefficients and offsets used in the MSBS control program can also be changed with the new obtained coefficients and offsets on the spot. y and Ψ calibration test results are shown in Figures 11 and 12. As shown in Figure 12, the interference still remains larger than 2 degrees in Ψ . Another computer is placed by the control computer, which gathers the all measured model position data sets and a part of coil current data at the same speed as the control computer. When a special key is hit, the model position and coil currents are stored as a file on hard disk for about 16 seconds after the time.

Installation of the 60-cm MSBS at the 60-cm low speed wind tunnel

The NAL 60-cm MSBS was built in 1990 and operated successfully in 1993. The MSBS has been improved in its control and in its sensing system. But it has not been installed at a low speed wind tunnel because a low-speed wind tunnel with a 60cm x 60cm test section was not available. A very old wooden wind tunnel was proposed to use for the MSBS in 1998. Then the MSBS was moved to the tunnel in the spring. The tunnel had been used for boundary layer research and was modified to have a long test section of 2m. The long test section consists of two parts of 1m long. The main parts except its contraction and test section were made of wood. It is good for MSBS. Besides, the iron contraction is 1m upstream far from its downstream test section inlet. The MSBS replaced the downstream test section and is far from the iron contraction by 1m as shown in Figure 13. The upstream test section was made of aluminum alloy in its frame parts and transparent material in the other parts. The test section of the MSBS was made of wood and 1.2m long. A 15cm x 15cm sensing window is in a side and ceiling walls of the test section, respectively. A replaceable 15cm x 47cm window is in the other side wall for a model holding system going out of the test section. A

new collector was designed and installed to meet the new situation of this tunnel. The fan system was designed to be good up to 1500rpm but was limited up to 1000rpm because of fan belt oscillation trouble presently. Then the highest speed is 28.5m/s, which was measured 1m upstream from the MSBS test section inlet. A flow quality data set is not available yet.

The possible model incidence ranges up to 12.5 degrees because the drag coil current reaches around 65A at this model attitude without flow. In order to increase the maximum incidence beyond this value, drag coil current must be increased. The model, at the incidence of 12.5 degrees, is shown in Figure 14. A cylindrical model was tested at the incidence of 4 degree in the flow of 28m/s as shown in Figure 15. The model stayed at a position during the test without any additional motion.

One of the purposes of equipping the tunnel with the MSBS is to estimate the model support system interference in a new airship development project at NAL. The drag of airships consists of the friction drag and pressure drag. The two kinds of drags which are significantly affected are the boundary layer transition and flow separation. The flow is very complicated around the connecting sections between the model support and model itself. There is concern whether or not the simple subtraction method of evaluating the interference could be still available in this sensitive case. It is easy to estimate the model drag interference free case if the drag is measured with the MSBS.

A cone-cylinder model was tested at 0 incidence at speeds up to 28m/s in the tunnel as shown in Figure 16. The drag coil current was measured with respect to the flow speed. The result shows the averaged drag current changes in proportion with its dynamic pressure as shown in Figure 17. The measured model position shows that the model stayed at the same position during the test. However, this figure shows only the trends of the obtained data set but is not a valid aerodynamic data set at all because the flow has not been calibrated yet. Besides, the model surface was poor because the model was wrapped with a sheet of white paper. The figure shows only the availability of the 60-cm MSBS. A 6:1 ellipsoid model will be tested in the wind tunnel this fall. The model surface will be painted in white and will be aerodynamically smooth. Several tests conducted during this spring and fall show the MSBS works well in flow at the speeds up to 28m/s in the tunnel. The tunnel will be improved in its maximum speed next year.

Concluding Remarks

The superconductive solenoid model core designed and built by NAL and a manufacturing company was suspended successfully for about 30 minutes at the NAL 60-cm MSBS. The handling procedure of testing the solenoid model core was examined and confirmed as safe. The control performance of the core looks like those of the permanent magnet cores.

The control system of the MSBS was improved to be one computer control with two synchronously driven cameras of the model position sensing system. The position sensing system can be calibrated automatically with a control computer and the obtained calibration coefficients can be available quickly on the spot. The lighting system was also improved to light up with red and green lights respectively from upper and side ways in order to avoid the interference between lateral and longitudinal position components.

The 60-cm MSBS was installed in a low speed wind tunnel, of which flow speed is up to 28.5m/s and pressure is ambient. A cylindrical model and a cone-cylinder model were tested in the wind tunnel at various speeds including the maximum one. No motion was observed during the tests. Although several aerodynamic data sets were obtained, they are not valuable, except to demonstrate the availability of the MSBS, because the model surfaces were poor and any flow quality data sets are not available. After calibrating the flow and finishing model surface smoothly, valuable data sets will be obtained.

REFERENCES

1. H.Sawada, H.Kanda, and H.Suenaga : "the 10cm x 10cm Magnetic Suspension and Balance System at the National Aerospace Laboratory." AIAA 91-0397, 1991
2. H.Sawada and H.Suenaga : "Status of MSBS Study at NAL", NASA CP 3247, 1994, pp. 275-289
3. H.Sawada and H.Suenaga : "Magnetic Suspension and Balance Systems at NAL." Pacific International Conference on Aerospace Science and Technology, Conference Proceedings Vol. 2, 1993, pp. 1014-1021
4. H.Sawada, H.Suenaga and T.Kohno : "Status of MSBS Study at NAL in 1995." NASA CP 3336, 1996, pp. 505-519
5. C.P.Britcher : "Progress Toward Magnetic Suspension and Balance Systems for Large Wind Tunnels." Journal of Aircraft, Vol. 22, No. 4, April, 1995 pp. 264-269
6. J.Eskins : "Further Investigation into Calibration Techniques for a Magnetic Suspension and Balance System." NASA CR-178056, 1986
7. H.Sawada, T.Kohno and T.Kunimasu: "Superconductive Solenoid for the NAL 60cm MSBS" NASA CP-1998-207654, 1998, pp. 425-439
8. T.Kohno, H.Sawada and T.Kunimasu: "Roll Motion Restraint System for NAL 0.6m MSBS" NASA CP-1998-207654, 1998, pp. 141-150

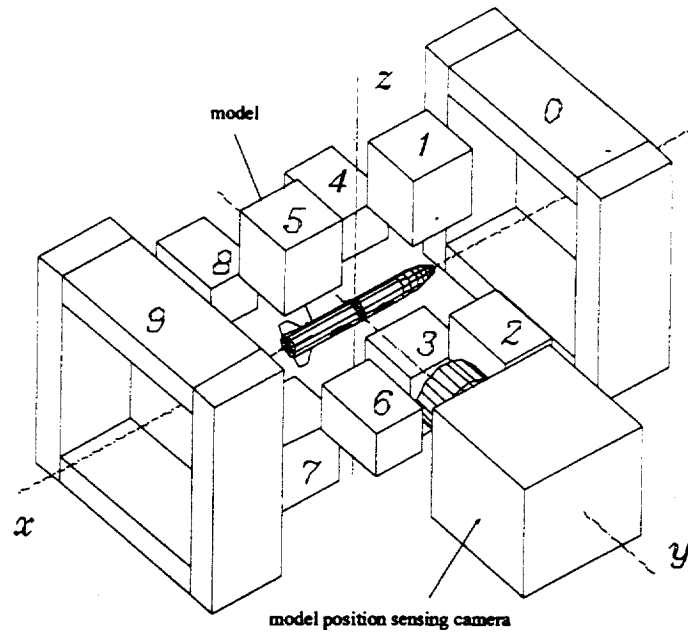


Figure 1 Coordinate system at the NAL 60-cm MSBS

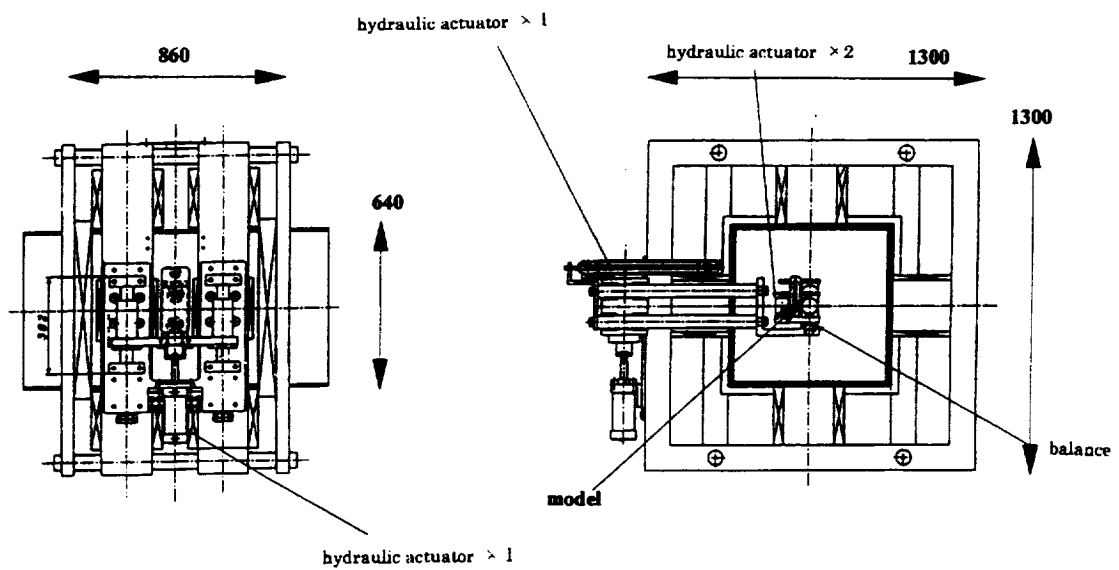


Figure 2 The NAL 60-cm MSBS and the model holding system

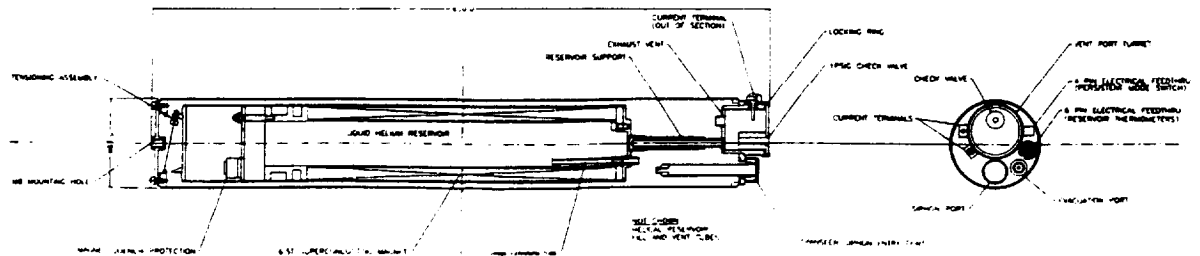


Figure 3 The NAL superconductive solenoid model core

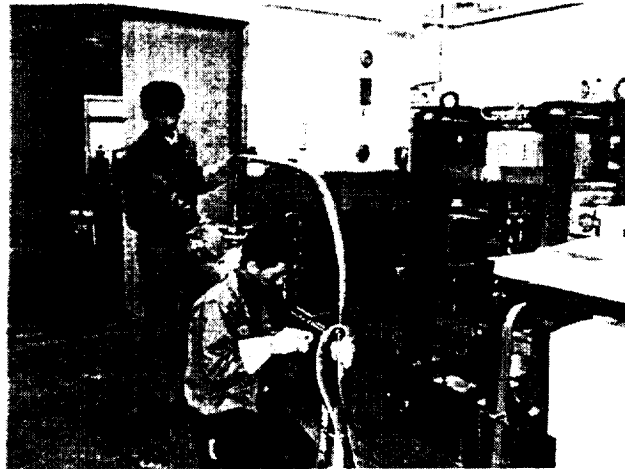


Figure 4 The NAL superconductive solenoid model core on a base

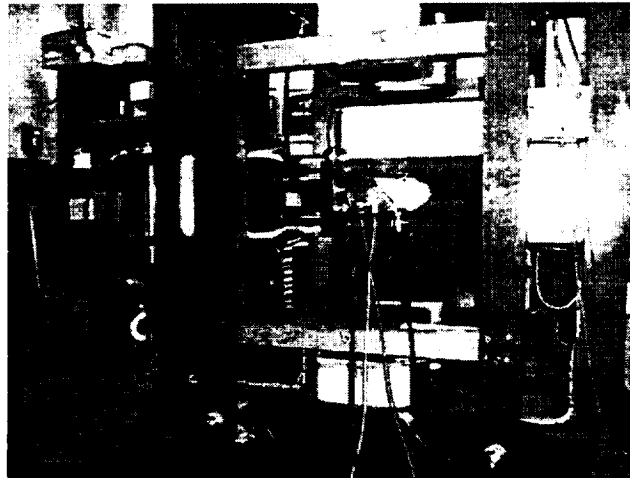


Figure 5 The NAL superconductive solenoid model core in the model holding system



Figure 6 The NAL superconductive solenoid model core suspended in the 60-cm MSBS

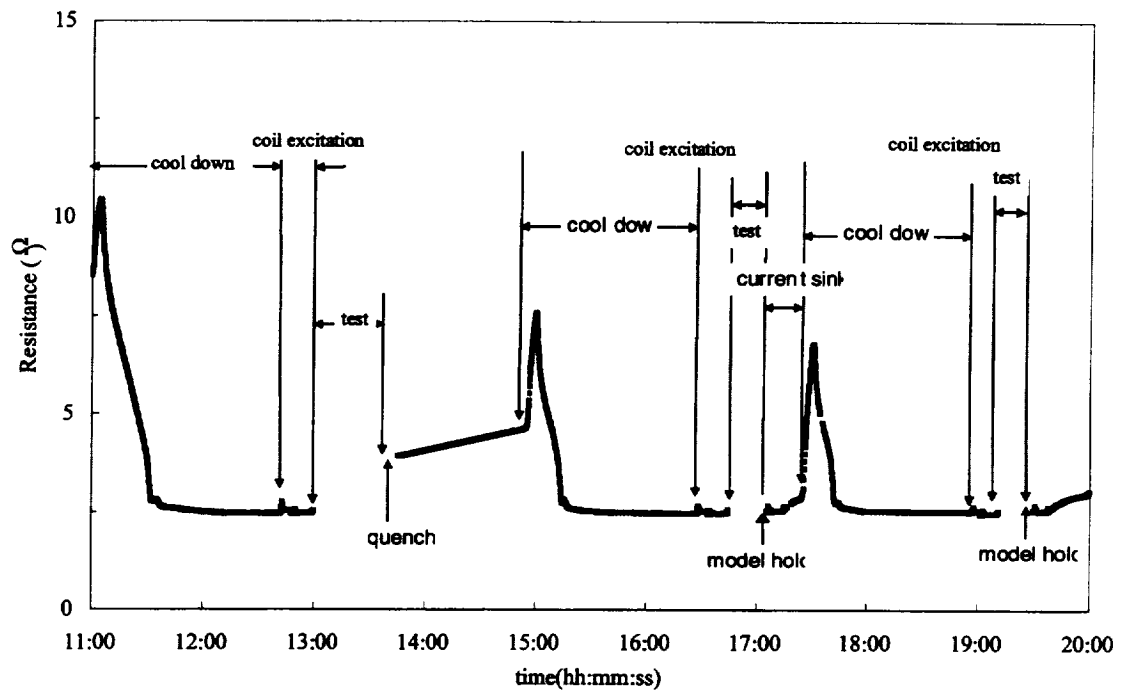


Figure 7. Time history of the superconductive solenoid temperature at the NAL 60-cm MSBS

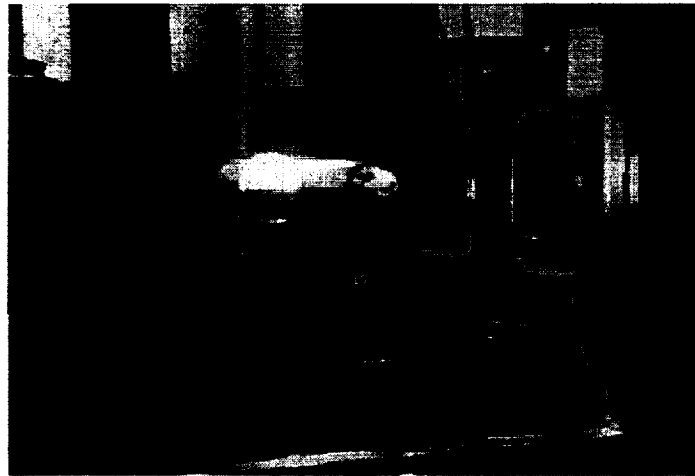


Figure 8. A superconducting solenoid model core suspended in the 60-cm MSBS

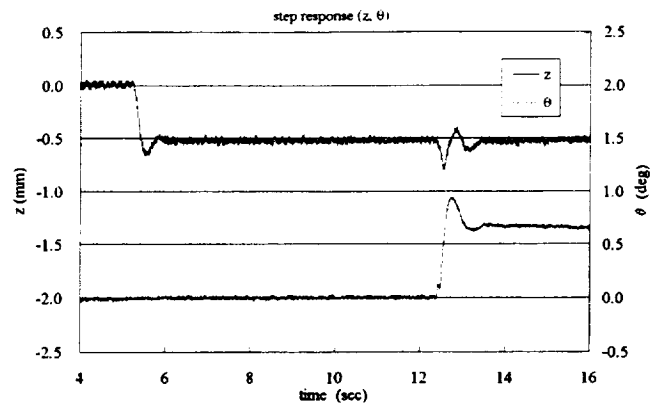


Figure 9. Step response of a superconductive solenoid model core at the NAL 60-cm MSBS



Figure 10. Auto-calibration system

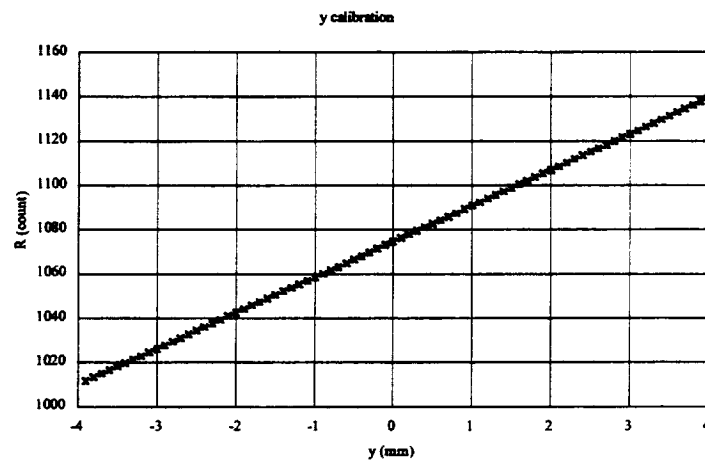


Figure 11 y calibration test results

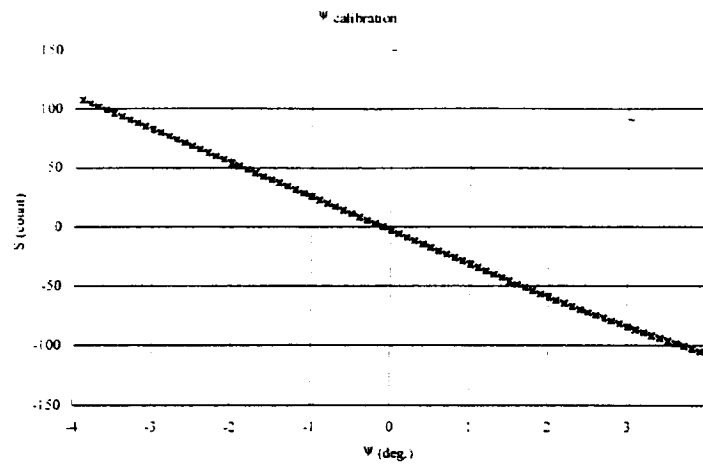


Figure 12 ψ calibration test results



Figure 13. The 60-cm MSBS installed in the 60-cm-low-speed-wind-tunnel
(A new collector is removed.)



Figure 14 A cylindrical model at the incidence of 12.5 degree



Figure 15 A cylindrical model at 4 degree incidence in the flow of 28m/s



Figure 16 A cone-cylinder model at zero incidence in the flow of 28m/s

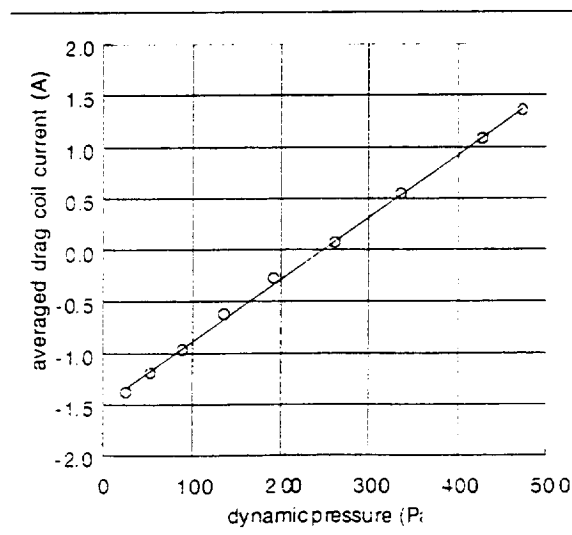


Figure 17 Relation between uniform flow dynamic pressure and drag coil current for the cone-cylinder model

Design of a Magnetic Suspension and Balance System for the Princeton/ONR High Reynolds Number Testing Facility

Dr. Colin P. Britcher[†], Dr. Oscar González[‡], Dr. Steven Gray[‡]

Old Dominion University

Dr. Alexander J. Smits

Department of Mechanical and Aerospace Engineering, Princeton University

Oscar Gomeiz[†], James E. Barkley[‡], Adeel Jafri[‡]

Old Dominion University, [†]Department of Aerospace Engineering,

[‡]Department of Electrical & Computer Engineering

Abstract

Princeton University is currently constructing a specialized wind tunnel, the Princeton/ONR High Reynolds number Testing Facility (HRTF) to be used for aero/hydrodynamic testing of submersible shapes. The facility will operate at very high pressures, up to 230 atmospheres, and relatively low velocities. Old Dominion University is responsible for the design and commissioning of a Magnetic Suspension and Balance System (MSBS) for use with the HRTF. The HRTF design and operational characteristics will be briefly described, then the paper will concentrate on the design challenges faced by the MSBS. The most unusual problems are related to the fact that the electromagnets will be located outside the wind tunnel pressure shell, with position sensing and other hardware inside. The test section is constructed of stainless steel, so eddy currents generated by unsteady magnetic fields are a serious concern. It is shown by analysis and confirmed by measurements that the system is practical, provided the eddy current effects are properly modeled and accounted for in the control system design. Due to restricted access to the interior of the tunnel, the position sensing and control systems must be configured so as to reliably suspend models for long periods of time, with a variety of aero/hydrodynamic tests conducted in sequence. This leads to a relatively conservative choice of system configuration and hardware. The general design of the MSBS will be presented and plans for completion, commissioning, calibration and operation of the facility will be reviewed.

Introduction

In the late 1980's, considerable interest was generated in the possibility of constructing an ultra-high Reynolds number wind tunnel dedicated to aero/hydrodynamic testing of submersibles. At the time, the leading proposal was an ultra-low temperature facility employing either gaseous or liquid helium as the test medium. From the outset, a Magnetic Suspension and Balance System (MSBS) was considered necessary in order to provide a test environment free of support interference. A publication derived from the proceedings of a Workshop which summarizes the position in 1989 is available [1]. Although a helium-based facility appeared feasible, the practical problems of operating

flow diagnostic and other instrumentation at extremely low temperatures was apparently a barrier to further progress.

In the early 1990's, a research program at Princeton University resulted in the development of an ultra-high Reynolds number pipe flow apparatus, now known as the Princeton/DARPA-ONR SuperPipe (Figure 1), which has provided turbulent pipe flow data at the highest Reynolds numbers achieved to date (38×10^6 based on diameter) [2-4]. The SuperPipe achieves ultra-high Reynolds numbers by utilizing air at normal temperatures, but extremely high pressures, up to 3500 psi (24 MPa; above 230 atmospheres). Since the proposed application is not Mach number constrained, this approach could be applied to the ultra-high Reynolds number wind tunnel.

In the mid-1990's, following two further Workshops [5,6], it was apparent that the high pressure approach seemed to provide the best near-term opportunity for construction of a pilot facility and a project was started at Princeton University, funded by the Office of Naval Research (ONR). The new facility would share certain infrastructure already in place for the SuperPipe. The task of design and construction of the MSBS was assigned to Old Dominion University. The HRTF will begin operation in late 1999 and the MSBS is scheduled to be delivered as a "turnkey" system in late 2000.

Generation of High Reynolds Numbers

The submersible application is distinct from the perhaps better-known aerospace problem in one very important respect. This is that the test Mach number is simply very low and does not need to be held to any specific value. It is easily seen that since :

$$Re = \frac{\rho VL}{\mu} \quad ; \quad q = \frac{1}{2} \rho V^2$$

- then for a gaseous test medium :

$$Re \propto \sqrt{qp} L$$

Thus it is seen that high Reynolds numbers can be achieved with modest dynamic pressures and physical scales by utilizing very high test pressures. An implication is that the test velocity will be quite low, since the rise in ρ is offset by allowing V^2 to decline. This results in very low test Mach numbers; also relatively modest power consumption for conventional fan-driven wind tunnel layouts.

Initial Development of the HRTF MSBS Design

The HRTF was specified as operating at a maximum pressure of 3500 psi, thereby remaining within the range already used for the SuperPipe. A representative test model

would be a 12:1 length-to-diameter ratio quasi-axisymmetric, low-drag model¹. The target length Reynolds number was around 1.8×10^8 . These requirements could be satisfied with a test section diameter of around 18 inches (0.46 m) and a flow velocity below 65 ft/s (20 m/s). In turn, the drive power requirements of such a facility would be comparable to those of the SuperPipe, permitting the use of common electrical drives and cooling systems.

A major design decision was whether to mount the MSBS electromagnets inside or outside the pressure shell. The pressure shell would be fabricated from stainless steel; relatively conductive, but non-magnetic. The former alternative was preferred for the MSBS, since it placed eddy currents induced in the pressure shell further away from the suspended model, while placing the electromagnets closer. However, the cost of the larger cross-section pressure shell required in the test section area proved prohibitive. Following some analysis of eddy current behavior, it was concluded that electromagnets mounted outside the pressure shell would be practical, as discussed more fully later. This configuration was therefore chosen. Model position sensor and other hardware would be located inside the pressure shell, so as to avoid a requirement for extensive viewing ports in the test section region². Figure 2 shows the HRTF layout. Note that an aerodynamic liner, not shown, is to be fitted inside the test section leg.

The pressure shell dimensions in the test section region were fixed at 24 inches outside diameter (0.61 m), nominally 19 inches inside diameter (0.48 m). The shell material was 304L stainless steel. Due to the unavailability of cast or drawn stainless steel pipe of these dimensions, the section was fabricated by rolling a plate, with a welded seam. For metallurgical reasons, the weld material was stainless steel with 10% ferrous addition. This results in the weld being weakly magnetic. Massive carbon steel flanges were attached to each end by welding. Figure 3 shows the dimensions of the test section, and the fabricated part is illustrated in Figure 4.

Dynamic Analysis

The critical issue arising from the choice of the placement of MSBS electromagnets outside the pressure shell is that of eddy currents induced in the stainless steel walls. A series of finite element models were developed using the magnetodynamic analysis package OPERA/ELEKTRA™ in order to provide preliminary estimates of the field attenuation and guidance for development of a dynamic model.

A simple finite element model of the test section pressure shell is shown in Figure 5, with a representative air-cored electromagnet located externally. ELEKTRA™ can solve the magnetodynamic problem either as a series of single frequency, quasi-steady problems, or as the time response to a prescribed electromagnet current transient. In both cases, only the electromagnet current is assumed, all other fields and currents are computed. Figure 6

¹An ellipsoid is currently used as the baseline geometry

²Optical position sensing is assumed, as discussed later

shows the computed magnitude and phase of the magnetic field on the axes of both the electromagnet and the test section (the nominal centroid of the suspended model). Also shown is the field development in response to a step change in electromagnet current. It should be noted that the reliability of these solutions decreases as the frequency increases, or at shorter times following the step, due to concentration of the eddy current near the surface of the conducting material - the "skin effect". These degradations can be alleviated to some extent by adjustments to the finite element mesh.

It is seen that a simple first-order lag provides an order-of-magnitude representation of the eddy current effects. Further, the time constant, around 0.009 seconds, is acceptable from a system dynamics point of view. Previous analysis [7, etc.] has shown that the form of the eddy current effect is perhaps more accurately described by a "half-order" pole³. As system development proceeds, more attention will be paid to development of high-fidelity dynamic models.

MSBS Design Synthesis

The initial design of the MSBS, particularly electromagnet sizing and placement, is driven by steady-state operating conditions. By incorporating substantial performance margins, in the electromagnet sizing, dynamic capability is introduced. The key issue affecting system dynamics is the provision of adequate power supply capacity. The system design procedure will be briefly reviewed here.

Test Section Cross-Section

Within the circular pressure shell, some allowance must be made for location of model position sensor and other hardware. Figure 7 illustrates one possible choice, giving a flow area of around 220 square inches (0.142 m²).

Model Size

With the flow area set, the model size can now be established based on a compromise between Reynolds number requirements (larger models) and test section blockage (smaller models). From other dimensions stated, we have :

Table 1 - Baseline Model Specifications

Length	35.4 in (0.9 m)	Volume	162 cu.in ($2.65 \times 10^{-3} \text{m}^3$)
Diameter	2.95 in (0.075 m)	Weight	45.6 lbs (202.8N)
Blockage	≈ 3%	C_D	0.1 to 0.3

³For instance, see also the paper by Fukata et al in this symposium

The estimated dynamic pressure in the HRTF is only 5.8 psi (40 kPa; < 0.4 atmospheres), so typical model aerodynamic drag loads are only of the order of 3.8 to 11.7 lbs (17 to 52 N). It is seen that the model deadweight is the dominant force in this application.

Magnetic Fields and Forces

A permanent magnet model core was chosen with a view to minimizing steady-state power consumption (i.e. no magnetizing coils needed). Taking the classical axial model magnetization and using the axis system shown in Figure 8, we have :

$$\vec{F} = \int_V \vec{M} \cdot \nabla \vec{B} dV \approx V \vec{M} \cdot \nabla \vec{B}_o \quad ; \quad \vec{T} = \int_V \vec{M} \times \vec{B} dV \approx V \vec{M} \times \vec{B}_o$$

$$\vec{M} = (0, 0, M_z) \quad (\text{see Figure 8})$$

$$F_x (\text{sideforce}) = V M_z B_{xz_o}$$

$$F_y (\text{vertical force}) = V M_z B_{yz_o}$$

$$F_z (\text{axial force}) = V M_z B_{zz_o}$$

$$T_x (\text{pitching moment}) = - V M_z B_{y_o}$$

$$T_y (\text{yawing moment}) = V M_z B_{x_o}$$

$$T_z (\text{rolling moment}) = 0$$

- where V is the magnetic core volume, M its magnetization and B the external magnetic flux. A subscript of o indicates evaluation at the model centroid. Rolling moment capability will be required, but will be addressed later, as is traditional practice. The target maximum force capability and corresponding nominal field and field gradient values are shown below, based on a "1 Tesla" magnetic core (i.e. $M_z = 796,000$ A/m). The drag and sideforce targets are twice the maximum expected steady-state aero/hydrodynamic forces. The vertical force target is the deadweight of the model, plus twice the maximum expected steady-state aero/hydrodynamic force. The aero/hydrodynamic moments are expected to be relatively small and hence a weak design driver. The sizing of the electromagnet array can now proceed.

Table 2 - Design Forces and Corresponding Field Gradients

F_x	106 N	B_{xz_o}	0.1 T/m
F_y	106 N	B_{yz_o}	0.3 T/m
F_z	308.8 N	B_{zz_o}	0.1 T/m

A baseline set of air-cored electromagnets has been developed, by trial-and-error, using the OPERA/TOSCA™ magnetostatic package. The general configuration follows the classical "+" arrangement and is shown in Figure 9. Considerable further refinements are to be expected prior to the design "freeze", such as the introduction of iron cores to the vertical and lateral electromagnets.

MSBS Control Law Design and Synthesis

The objective of the MSBS is to reliably suspend and position in six degrees of freedom a test model with a cylindrical permanent magnet core. In addition to regulating the position in six degrees of freedom, the system should also allow tracking of slow time-varying signals⁴. Due to restricted access to the interior of the tunnel, the control system must maintain the test model in suspension for long periods of time while a variety of aero/hydrodynamic tests are conducted in succession. These constraints place special requirements on the hardware as well as on the control law design. For example, the electromagnet coils will need a built-in cooling system, and the control law will need to be robust and able to regulate the disturbance effects of the aero/hydrodynamic tests being conducted. Additional constraints are imposed on the sensor system, which is inside the tunnel where the maximum pressure can reach 3500 psi. The sensor elements will need to be prepared to withstand the pressure, such as by venting enclosed air cavities. In this section, the plan for the design of the regulation and tracking control law is described.

Plant Model

For control purposes, the plant consists of the actuators and load, that is, ten suspension/control electromagnets, six (or more) power supplies, and the test model. The equations of motion of the cylindrical magnet inside the test model can be derived starting with the nonlinear torque and force equations developed in References 8-10. The torque and force equations will first need to be modified to properly include the effect of the eddy currents induced on the walls of the pressure shell as explained earlier. In addition, analytical models are being developed for the fields and their gradients acting on the permanent magnet that fit numerical data generated by the OPERA/TOSCA/ELEKTRA™ package. The plant model derivation will yield nonlinear equations that characterize the plant's response from the commanded power supply currents to the three displacement and three rotational outputs. These nonlinear equations are being derived for the design of nonlinear controllers. The nonlinear model will also be linearized to develop perturbation models for linear control design.

Sensor System

Initially, five laser light sheet sensors will be used to provide measurements for pitch and yaw angles, and longitudinal, lateral, and vertical displacements. These five degrees of freedom control are the only ones possible if the permanent magnet magnetization is along its axis and the magnet is cylindrical [9,10]. If other types of magnetizations are included, or if the magnet is made non-axisymmetric, then roll control is also possible. Several techniques are still being considered for the measurement of the roll angle; the technique to be used will depend on the test model. For example, X-shaped stern control surfaces of a submarine model can be used with shadow position sensors. The currently selected

⁴To simulate dynamic maneuvers

sensors are SUNX™ Model No. LA-511. Each sensor consists of an emitter and receiver element with side-view mirror attachments that bend the beam through 90°. The mirrors are needed to improve packaging of the sensors in the narrow space between the inside wall of the pressure shell and the flow liner, hence maximizing the flow area through the middle of the tunnel. The sensors are attached to rings that are fitted inside the tunnel. Each ring can hold one or two sensors. Figure 10 shows the front view of a ring with two sensors and a cylindrical three inch diameter model. This figure does not show the aerodynamic liner. This liner will have portholes to allow the light beams to pass. Since the laser beam width is 15 mm, with this configuration it is possible to measure ± 7.5 mm displacements in each direction. The sensors will be placed to give about a $\pm 5^\circ$ angle variation for pitch and yaw.

Controller Hardware

The hardware selected for the data acquisition and control is a dSpace™ Advanced Control Kit 1103 which includes a micro-controller board with a Motorola PowerPC, a TI DSP subsystem, and an integrated real-time software environment. The main advantage of the software is that it interfaces with Matlab™ and Simulink™ to simplify testing and analyzing control algorithms in real-time. The hardware includes 8 DACs (14 bit, 5 μ s settling time) and several ADCs, including 16 high performance ADCs (16 bit, 4 μ s conversion time). If necessary, the hardware can be used to implement high order controllers while maintaining sampling rates between 0.5-2 kHz. The dSpace software environment will also be used to develop a custom GUI interface for the production turnkey system.

Control Laws

The main goal for the control law is to robustly meet the regulation and tracking control specifications. The design will be very challenging because of the large-gap magnetic suspension requirement and the placement of the coils on the outside of the tunnel. This coil placement induces eddy currents, which add a layer of uncertainty, and will probably increase the coupling of the multivariable dynamics. Due to limited access to the inside of the tunnel and the high degree of uncertainty of the models, robustness will be emphasized over performance at first. Once the equipment is in operation and system identification gives models and uncertainty descriptions that are more accurate, then the control laws will be redesigned to have improved performance, trading-off robustness for performance. The initial control laws to be designed will be based on linear perturbation models. These include classical sequential loop closure and robust multivariable controllers. The nonlinear plant models that are being derived will permit the design of nonlinear controllers such as sliding mode controllers, which have well known robustness properties.

Discussion - Project Status

A significant analysis effort is underway to fully model the effect of the weakly magnetic test section weld. Following completion of this effort, the design presented will be refined, such as by inclusion of iron electromagnet cores, principally to minimize the steady-state power consumption and capital cost. The final specifications will then be frozen and hardware procurement started. It is currently planned to complete assembly of all major components in Summer 2000, with delivery to Princeton around the end of 2000. *(Authors note - shortly after the Symposium, the electromagnet configuration was changed to an "X" layout, as shown in Figure 11. This distributes the model deadweight more evenly across the electromagnet array)*

Acknowledgements

This work is supported by the Office of Naval Research, under Grant No. N00014-99-1-0298, by Princeton University under Grant No. 150-67555-1 and by NASA Langley Research Center under Cooperative Agreement No. SAA #450.

References

1. Donnelly, R. (ed.): High Reynolds number flows using liquid and gaseous helium - Proceedings of the 7th Oregon conference on low-temperature physics. Springer-Verlag, 1991.
2. Zagarola, M.V.; Smits, A.J.: Scaling of the mean velocity profile for turbulent pipe flow. *Physical Review Letters*, Vol.78, No.1, 1997.
3. Smits, A.J.; Zagarola, M.V.: The issue of roughness in the Princeton Superpipe experiment. *Physics of Fluids*, Vol. 9, 1977.
4. www.princeton.edu/~gasdyn/Facilities/Facilities.html#SuperPipe.
5. Donnelly, R. (ed.): Flow at ultra-high Reynolds and Rayleigh numbers - a status report - Proceedings of the international workshop on ultra-high Reynolds number flows, Brookhaven National Laboratory, June 1996. Springer-Verlag, 1998
6. ONR Workshop on needs for high Reynolds number facilities to design the next generation of sea and air vehicles. Arlington, VA, October 1997.
7. Britcher, C.P.: Eddy current influences on the dynamic behaviour of magnetic suspension systems. 4th International Symposium on Magnetic Suspension Technology, Gifu City, Japan, October 1997. NASA CP-1998-207654.
8. Covert, E.E.; Finston, M.; Vlajinac, M.; Stevens, T.: Magnetic suspension and balance systems for use with wind tunnels. *Progress in Aerospace Sciences*, Vol. 14, 1973.
9. Groom, Nelson J. and Britcher, Colin, P., Open-Loop Characteristics of Magnetic Suspension Systems Using Electromagnets Mounted in a Planar Array, NASA TP-3229, 1992.
10. Groom, Nelson J., Expanded Equations for Torque and Force on a Cylindrical Permanent Magnet Core in a Large-Gap Magnetic Suspension System, NASA TP-3638, 1997.

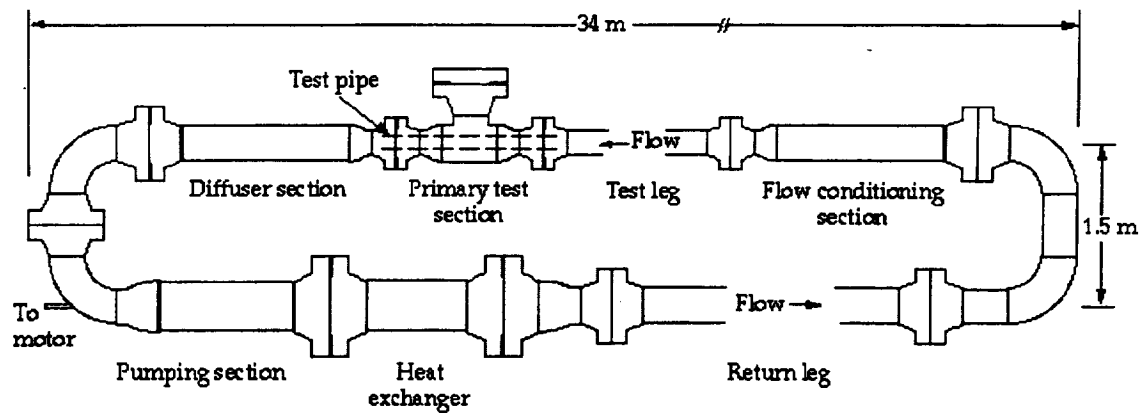


Figure 1 - The Princeton/DARPA-ONR SuperPipe

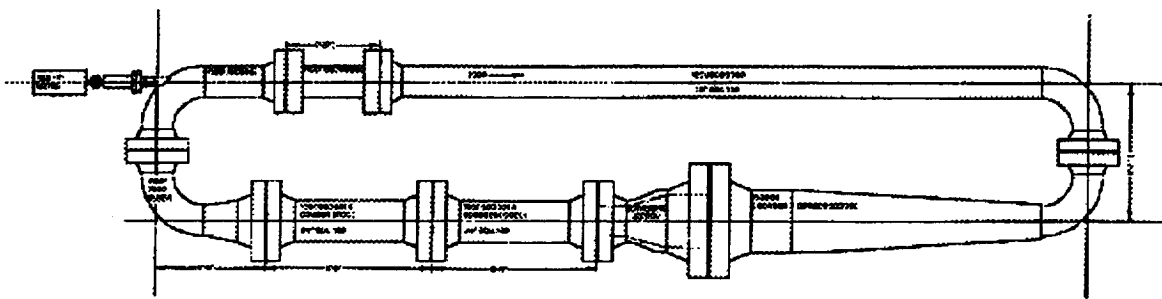


Figure 2 - The Princeton/ONR High Reynolds Number Test Facility (HRTF) Circuit

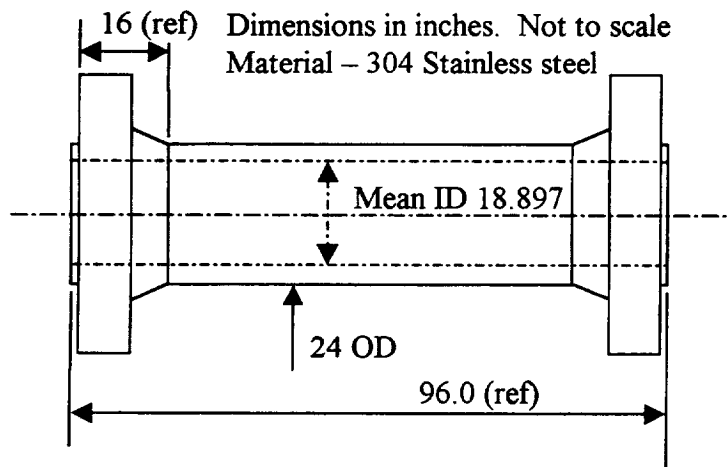


Figure 3 - The HRTF Test Section Schematic

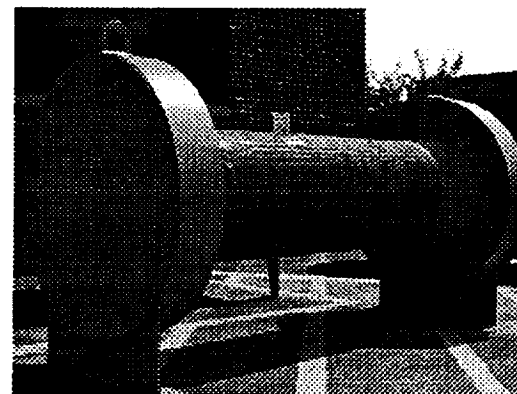


Figure 4 - The HRTF Test Section

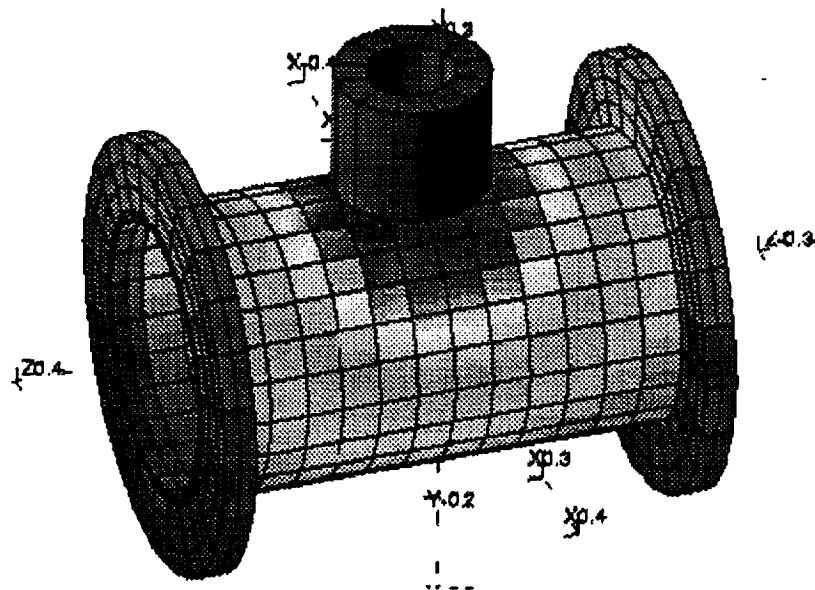
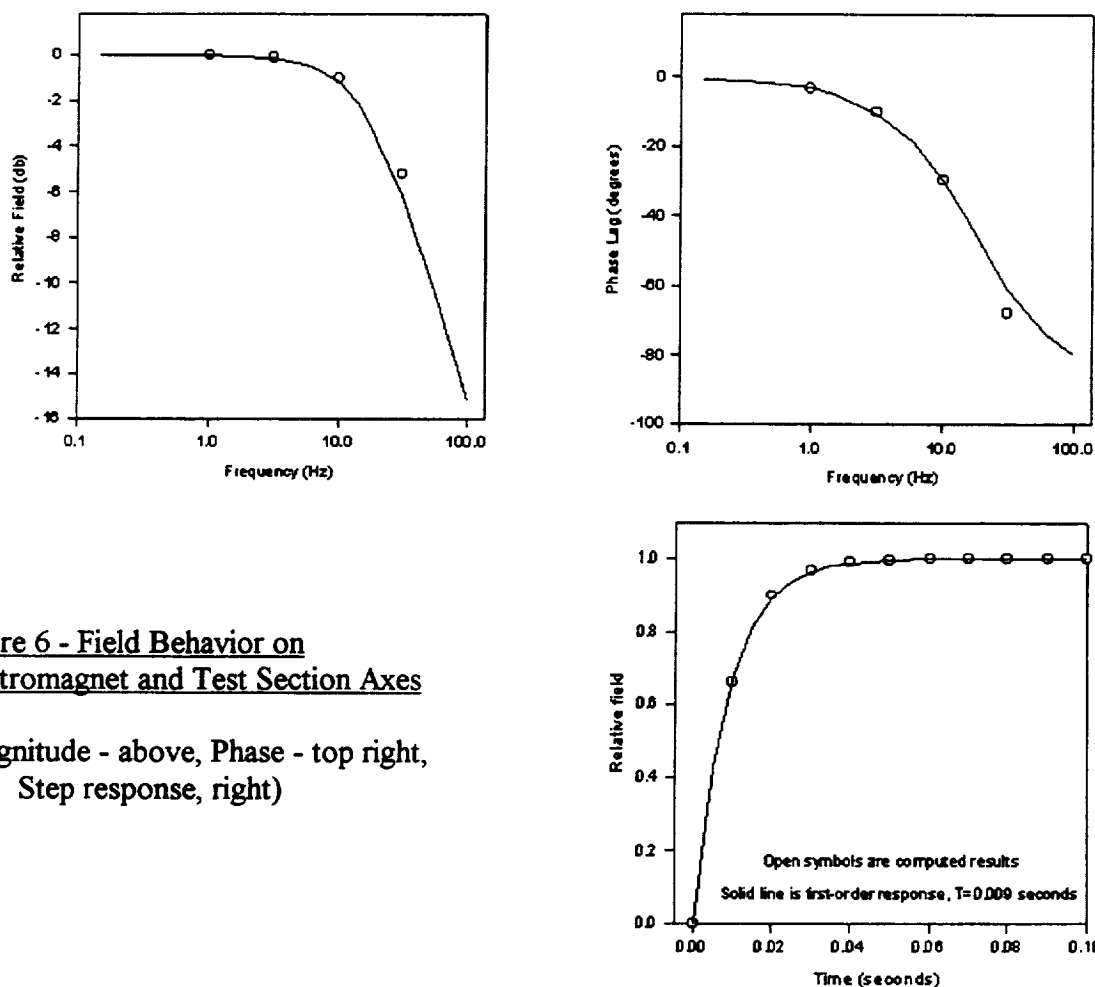


Figure 5 - Finite Element Model Representative of the HRTF Test Section
(Shaded contours represent eddy currents)



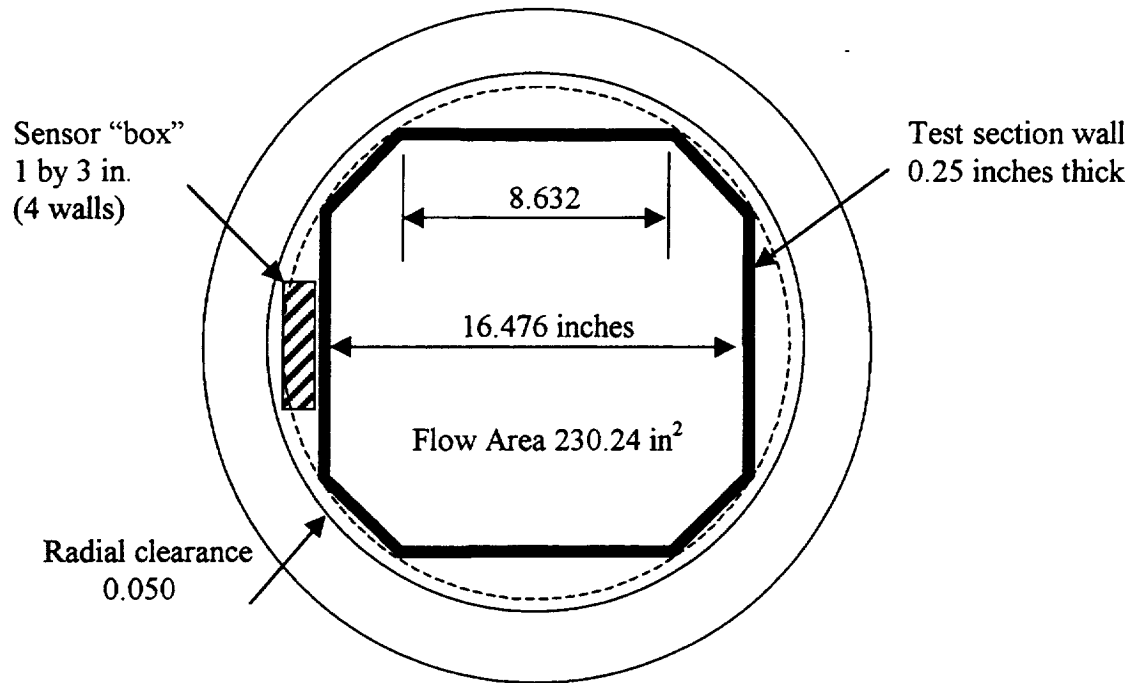


Figure 7 - Candidate Test Section Cross-Section

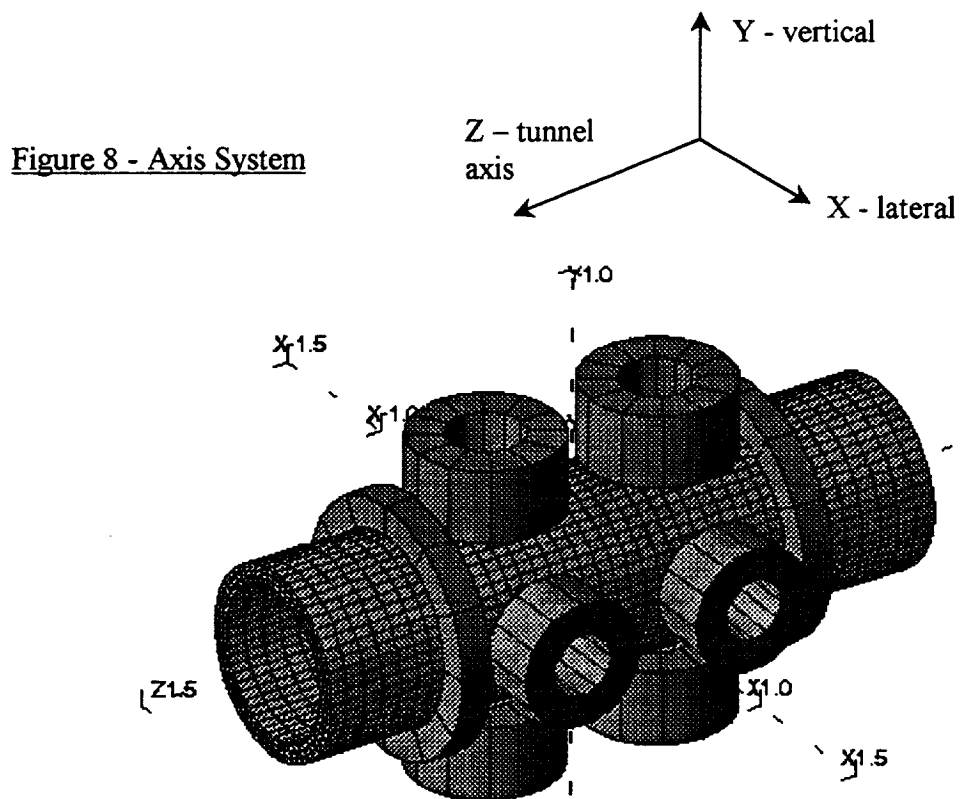


Figure 9 - Baseline Electromagnet Configuration ("+" layout)

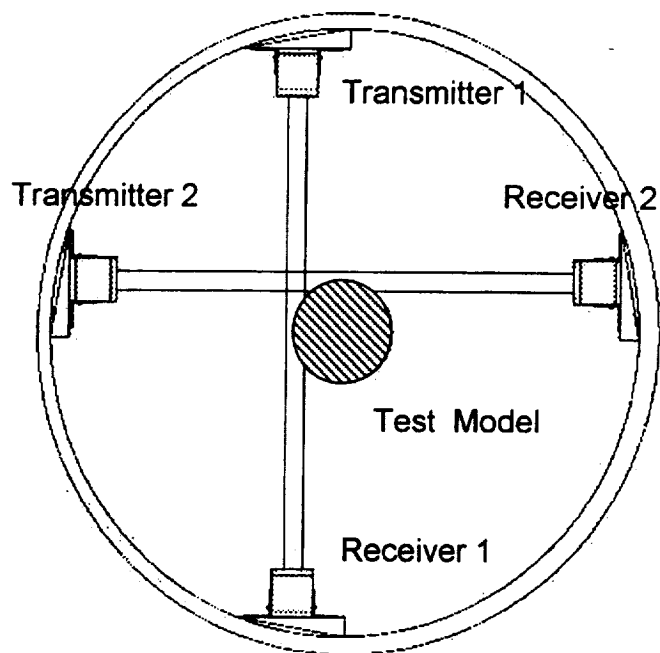


Figure 10 - Front View of the Sensor System - showing two sensors and a 3 in. dia. model.

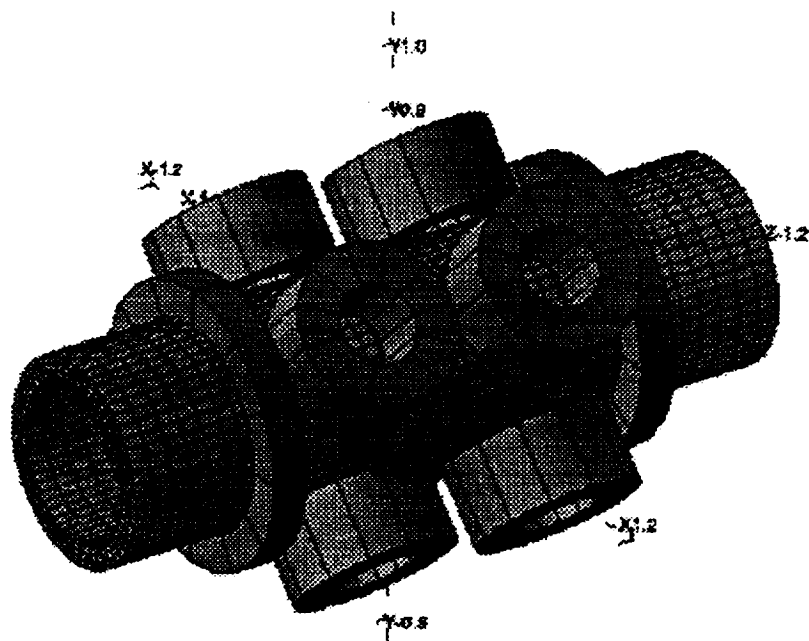


Figure 11 - Recently Modified Electromagnet Configuration ("X" layout)

Session 18 -- Modeling 3

Chairman: Dennis Smith
Honeywell

NEURAL NETWORK BASED FAULT DETECTION FOR FAULT TOLERANT CONTROL OF SYSTEMS WITH MULTIPLE MAGNETIC ACTUATORS AND SENSORS*

Matthew O. T. Cole, Patrick S. Keogh and Clifford R. Burrows
Department Of Mechanical Engineering
University of Bath
Bath BA2 7AY, UK.

SUMMARY

There is considerable interest in the improvement of fault tolerance in the design of active position and vibration control systems. In the creation of many magnetic actuator position or vibration control systems there exists potential for the inclusion of redundancy in the number of actuators and sensors used for control. This redundancy can provide improved tolerance to actuator or sensor related faults if, when a fault occurs, control of the system can be rapidly reconfigured to bypass control from a faulty component to the remaining healthy ones. To do this requires a system for the detection and identification of faults as and when they occur. The performance of modern computerised control hardware is now sufficient to allow such a system to run in real-time, in parallel to any digital control algorithm.

In this paper the development of a method for the detection and isolation of faults relating to control sensors and actuators is presented as a basis for the implementation of a fault tolerant control scheme. The method is based on the use of a neural network, operating in real time, for the detection of signal errors occurring in the plant inputs or outputs. The neural network is trained off-line using identification data taken from the plant and therefore does not require an accurate model of the plant dynamics.

Results are presented for the application of this method to an active magnetic bearing/rotor system, both in simulation and experiment. The issues of sensitivity to faults, speed of response and the effect of external disturbances on the reliability of the fault detection system are investigated and discussed. It is demonstrated that, through the implementation of a reconfigurable control scheme with a fault detection system, improved tolerance to sensor and actuator related faults can be achieved.

NOTATION

$A, B_{\alpha}, C_{\beta}, D_{\alpha}$	system state space matrices (subscripts α/β relate to inputs/outputs)
b	neural network bias vector
d, D	vector of direct rotor forces (time domain, Laplace domain)

* Work done under Engineering and Physical Sciences Research Council grant GR/L62238

e	neural network output error vector
f, F	system fault signal (time domain, Laplace domain)
$G_{r\beta}$	fault signal transfer function matrix from β to r
I	identity matrix
J	performance index for network training
j	$\sqrt{-1}$
n	plant identification signal vector
q	sensor noise signal vector
p, \bar{p}	vector of neural network fault detector inputs (with and without fault component)
r, R	fault detector residual (time domain, Laplace domain)
t	time variable
u, U	magnetic bearing control forces vectors (time domain, Laplace domain)
v, \bar{v}	vector of concurrent plant input and outputs (with and without fault component)
w	fault signal vector used for fault detector training
W	neural network weighting matrix
x	system state vector
y	vector of plant outputs
Ω	rotational frequency
Φ	set of detectable fault conditions
ω	angular frequency

INTRODUCTION

Fault detection and diagnosis have been recognised as issues of primary importance in modern process automation as they provide the prerequisites for fault tolerance, reliability, and security. For this reason there has been considerable development in the design of fault detection systems for various purposes and using a wide range of methods. Moreover, the fault detection system is a principal component of a reconfigurable control strategy and it is with this purpose that development of a fault detection scheme will be made. State estimation techniques have been widely studied in this field (ref. 1) and have proved to be successful in numerous cases where linear system theory can be applied to the dynamic modelling of the plant. Alternatively, parameter estimation is also a powerful method for the detection of faults in dynamic systems by on-line estimation of physical system parameters (ref. 2). This is a particularly important method for process plants (chemical processes, nuclear reactors, etc) where the plants often have slow dynamic behaviour, but process faults can cause sudden parameter variations that need to be estimated quickly. The important consideration in common with these methods is that they require a system model on which to base the fault detector design and as such are sensitive to the accuracy of the model. Also, they are applicable only to systems that can be represented by a linear model.

The main requirements for a fault detection and isolation scheme can be classified as either performance or robustness related. Performance criteria can include speed of detection, sensitivity to incipient faults, sensitivity to false alarms, missed fault detections and incorrect fault detections.

Robustness requirements can be defined with respect to unmodelled non-linearities or uncertain system dynamics, unknown disturbance and noise.

In this paper the approach of using fault detection observers will be briefly reviewed, outlining recent work on frequency domain design methods. Although this approach will not be implemented in this study, it serves as a useful comparison to the previously undeveloped approach of using neural network architectures for the parameterisation of fault detectors. The main reason for using the neural network approach to fault detection is that the available system model is unlikely to be sufficiently accurate for the design of a reliable fault detection observer, whereas the neural network approach is model free if training is performed using experimental measurements.

FAULT DETECTION OBSERVERS - BACKGROUND

The use of state estimation techniques for the generation of fault detection signals, or residuals, has been considered for systems with unknown inputs, where the objective is not only to decouple the effects of different faults on the observer output, but also minimise the effect of the unknown plant inputs, that might otherwise cause false fault detection.

Consider a general system model with the discrete time state space structure applicable to a linear system having multiple control actuators and measurement signals:

$$\begin{aligned}\mathbf{x}_{k+1} &= \mathbf{A}\mathbf{x}_k + \mathbf{B}_u\mathbf{u}_k + \mathbf{B}_d\mathbf{d}_k + \mathbf{B}_f\mathbf{f} \\ \mathbf{y}_k &= \mathbf{C}_y\mathbf{x}_k + \mathbf{D}_d\mathbf{d} + \mathbf{D}_u\mathbf{u} + \mathbf{D}_f\mathbf{f}\end{aligned}\tag{1}$$

where \mathbf{u} is the control force applied by the control actuators and \mathbf{d} is the system disturbance. The system input \mathbf{f} represent the effects of faults.

The unknown input fault detection observer (UIFDO) is based on the state space observer (or state estimator) techniques of Luenberger (ref. 3) and has the same basic structure. The observer inputs are the plant control inputs and plant outputs. The observer state space matrices are chosen so that a fault in the system produces a known residual output. However, the effects of different faults must be uncoupled so that individual faults can be isolated. A design method for producing an observer with these qualities from the plant equations given (1) was developed by Frank and Wunnenberg (ref. 1), who used the Kronecker canonical form of the system equations to produce a UIFDO. Other methods have been developed (ref. 4) for the design of optimal state space UIFDOs, but for most systems it is impossible to completely decouple the observer output from the effects of plant disturbances. Recent research has therefore considered a different approach to the UIFDO design, where the design objectives are specified in the frequency domain as performance and robustness bounds on the observer transfer functions. The frequency domain design of fault observers having the structure given by equation (2) has been proposed by Frank and Ding (ref. 5) using an H_∞ design specification. An enhancement of this technique (ref. 6) uses a mixed H_2/H_∞ specification for which a linear matrix inequality (LMI) formulation can be used to obtain a solution.

NEURAL NETWORK FAULT DETECTION

Artificial neural networks (ANNs) have been shown to have enormous potential in application to both system modelling and identification. Recent progression has naturally led to them being employed for control and fault detection purposes (ref. 7). The key properties of ANNs, making them attractive for application to fault detection problems, include:

- The ability to approximate non-linear functions over a finite interval using multi-layer neural networks.
- They can be trained directly from plant data without requiring any predefined model of the plant. On-line adaptation is also possible.
- They have an in-built ability for pattern recognition, whether from static data using feed-forward networks or from time series data using recurrent networks.
- They naturally have multiple inputs and outputs and therefore lend themselves to the modelling of multivariable systems.

Methodology

Although a variety of network architectures (both feedforward and recurrent) could be employed for the fault detection problem, probably the simplest feasible network architecture for a rotor/magnetic bearing system has a form corresponding to a series-parallel model:

$$\mathbf{r}_k = \mathbf{W}\mathbf{p}_k + \mathbf{b} \quad (2)$$

where $\mathbf{p}_k = [\mathbf{y}_{k-n}^T, \mathbf{u}_{k-n}^T, \dots, \mathbf{y}_k^T, \mathbf{u}_k^T]^T$. The addition of the bias vector \mathbf{b} allows the model to be linear about a non-zero operating point caused by, for example, an unknown static disturbance. The output \mathbf{r}_k is the fault detection signal, often required to be an estimate of the fault signal \mathbf{f} . This detection system has the form of a single linear feed-forward network. This model can be extended to the non-linear case, using a 2-layer network having overall transfer function

$$\mathbf{r}_k = \mathbf{W}_2 \tanh(\mathbf{W}_1 \mathbf{p}_k + \mathbf{b}_1) + \mathbf{b}_2 \quad (3)$$

Here the input layer is a pure linear neuron layer and the output layer neurons have a hyperbolic sigmoid transfer function, allowing the incorporation of some plant non-linearities into the model.

To overcome practical problems associated with training and speed of implementation, the network employed in this study was a single layer linear network. The computational complexity of this type of network is comparable with a linear state space observer algorithm of the same order. A schematic of the network is shown in figure 1. Function computation time is important when implementing the fault detector in real time and the size of the network employed has a direct influence on the maximum sample frequency that can be used for the fault detection algorithm.

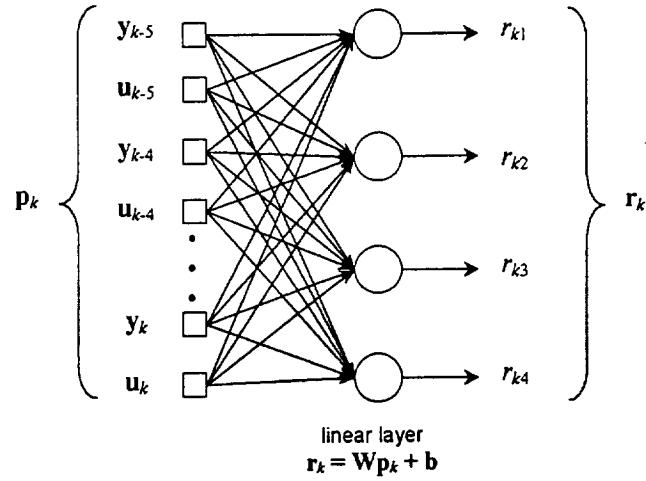


Figure 1 Network architecture for fault detection problem

Combined Plant/Fault Detector Dynamics

The dynamics of the neural network fault detector and plant can be described in state space form and combined to give an overall dynamic model of the system that includes the effects of faults, system disturbances and control inputs. The frequency response of the fault detection signal to these signals can then be written using transfer function matrix notation as:

$$\mathbf{R}(j\omega) = \mathbf{G}_{rf}(j\omega)\mathbf{F}(j\omega) + \mathbf{G}_{rd}(j\omega)\mathbf{D}(j\omega) + \mathbf{G}_{ru}(j\omega)\mathbf{U}(j\omega) \quad (4)$$

where \mathbf{G}_{ab} are the relevant transfer function matrices from b to a and can be derived from equations (1) and (2) as given in Cole *et al.* (ref. 8).

Written in terms of these transfer functions, the fault detector design objectives can be specified as:

- Approximate \mathbf{G}_{rf} to the identity matrix (\mathbf{I}) over a frequency range for which fault signals need to be detected so that \mathbf{r} is an approximation of \mathbf{f} over the bandwidth of detectable faults.
- Minimise a suitable norm of $\mathbf{G}_{rd}(j\omega)$ over the frequency range of expected disturbances.
- Minimise a suitable norm of $\mathbf{G}_{ru}(j\omega)$ over the frequency range of expected control signals.

The network can be trained using time series data taken from the real plant with a sum-squared error criteria to optimise the weighting and bias matrices. Plant data is obtained by applying test signals to the appropriate plant inputs and outputs. The choice of test signal, i.e. magnitude and spectral content will indirectly influence the level of optimisation with respect to the above design criteria.

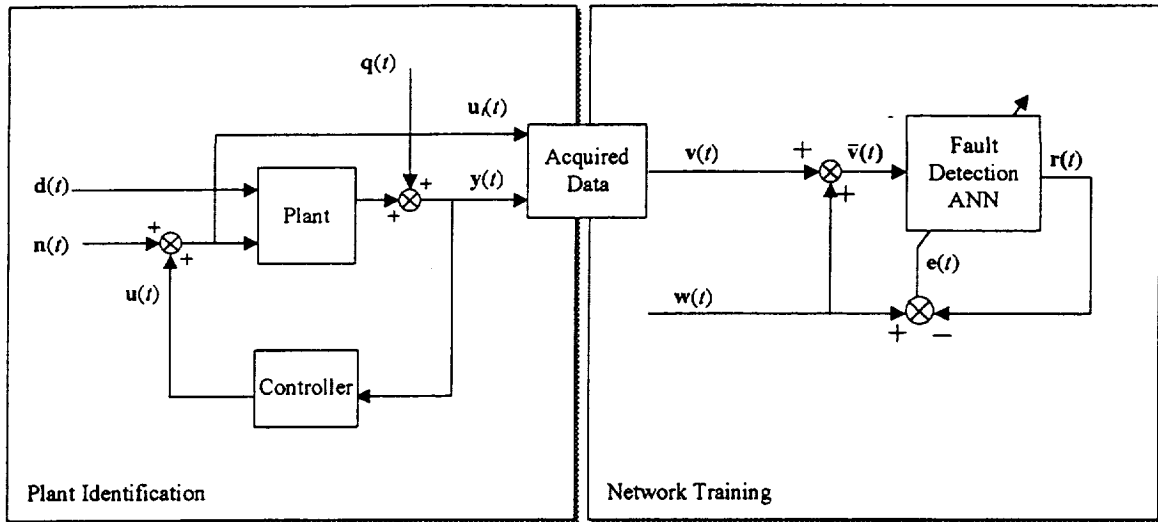


Figure 2 Plant identification and network training with simulated fault

NETWORK TRAINING

The training of the fault detector (FD) network is undertaken using the following strategy:

- (i) Obtain plant identification data by applying a (discrete time) input signal $n(t)$ to the plant input and acquiring corresponding output data.
- (ii) The plant data obtained from (i) is used for the training of the fault detector. A simulated fault signal is added to the plant data and the neural network is trained to produce an estimate of this fault signal.

Plant Identification

The system structure for plant identification is shown in figure 2. The form of the discrete input signal $n(t)$ used for the identification of the plant has an important influence on the design optimisation for the fault detector. Although the optimisation takes place in the time domain the frequency content of the identification signal should also be considered in terms of its design influence.

The choice of identification signal will depend on the nature of the faults being considered for detection. If the fault signal (f) is likely to be a band limited noise signal then, in order to minimise the effect of the control signal on the fault detector, a similar identification signal should be employed. If the desire is to produce a fault detector that is optimised for sudden fault occurrence, characterised by step changes in f , then a fixed step input signal is probably more suitable. In either case consideration should

be made to the steady state accuracy of the fault detector, as all fault signals are likely to have a DC component that needs to be accurately estimated for detection and diagnosis.

Fault Simulation

Acquired plant identification data can subsequently be used for the off-line training of the fault detection network. Defining a set of plant data with sample period T , $V = [v_0, v_1, \dots, v_k, \dots, v_s]$, where $v_k = v(kT)$, and a fault condition, as characterised by $f_k \in \Phi$, where Φ is the set of fault signals that are required to be detectable/identifiable. Φ should also include the no fault condition ($f_k = [0]$). An error signal w_k is generated that will embody the effect of these faults on the plant input-output pairs (v_k). This error signal w is added to the plant data v (figure 2) and the total signal \bar{v} used as the network input data set. The network is trained using the error signal w as the set of target vectors, which must be estimated by the network output vector, as defined by the equation:

$$r_k = W\bar{p}_k + b \quad (5)$$

where
$$\bar{p}_k = [v_{k-n}^T, v_{k-n+1}^T, \dots, v_k^T] \quad \text{and} \quad \bar{v}_k = v_k + w_k \quad (6)$$

The network output error is given by

$$e_k = r_k - w_k \quad (7)$$

and the network is optimised using a least squares criterion:

$$\min \left(J(W, b) = \sum_k \|e_k\|^2 \right) \quad (8)$$

Network training can be achieved using a standard back propagation method for the case of non-linear layers, or solved directly in the linear case. The ideal solution would completely filter out both the effects of plant disturbance and plant control input on the fault estimate. In general, however, the solution will be a compromise between minimising the effect of the plant disturbance and plant control input and maximising the accuracy of the fault estimate. The dependency on control input is important because it is desirable for the fault detector to be effective with any control algorithm (and therefore it should be decoupled from the control input). Also, a plant fault will obviously have an effect on the control input through the control feedback loop and therefore, for accurate estimation, the fault estimate must be independent of this signal.

The objective of the fault detector design is to produce a system that generates a set of signals that are an estimate of the predicted faults, as represented by the error signal $w(t)$. However, this signal must then be monitored for any significant excursion from zero and on occurrence of a fault give an interpretation upon which a suitable action can be made e.g. give an alarm or reconfigure the control to bypass the fault.

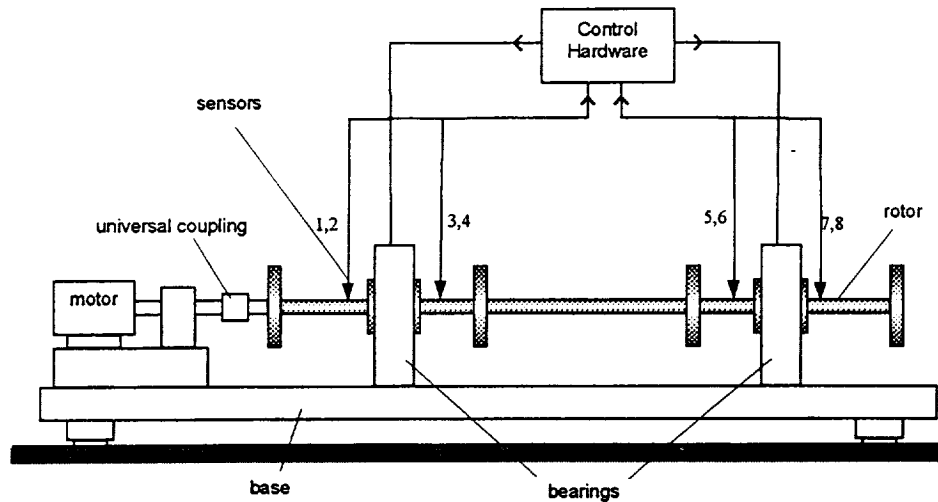


Figure 3 Schematic diagram of magnetic bearing/flexible rotor system
(rotor length 2 m, rotor mass 100 kg, shaft diameter 0.05 m)

The form that this signal post-processing takes will be dependent on the nature of the faults that need to be detected. However, it will generally embody some method for the comparison of signal magnitudes with a threshold signal, which indicates a fault when exceeded. The dynamics of the fault will also be an important consideration. For example, an additional detection criterion may be necessary for rapid detection of sudden faults which, by this fact, cannot be identified instantly, but still require some immediate corrective action.

SIMULATION RESULTS

The procedure for plant identification and fault detector design was investigated in a simulation study, in order to assess parameter choice in the fault detector design and various performance related effects. System models were created in Matlab (ref. 9), based on the experimental flexible rotor/ magnetic bearing rig shown schematically in figure 3, and the simulations carried out in the Simulink dynamic modelling environment. The rig itself consists of a two metre long rotor supported by two radial magnetic bearings. Eight displacement transducers measure the rotor displacement in four planes.

The simulation used a linear two-dimensional state space half model of the plant at zero rotational speed, incorporating translatory motion in one plane only (i.e. the y plane), including the first four rotor flexural modes. The model incorporated four displacement sensors (indexed 1, 3, 5 and 7), located inboard and outboard each of the two bearings with the two inner sensors (3 and 5) used to stabilise the plant with control feedback. Figure 4 shows the two singular values of the rotors transfer function matrix from control inputs to sensor measurements as a function of frequency. The first four natural frequencies of the rotors flexural modes are evident at 171 rad/s, 423 rad/s, 1075 rad/s and 1588 rad/s.

Typically, plant data was acquired over a ten second period, where the identification signal magnitude was selected to produce rotor displacement signals over the range ± 1 mm. Initially, the running speed of the plant was chosen to be 100 rad/s with sinusoidal forcing representing a single unbalance mass at one end of the rotor. Plant input-output data was acquired at a sample frequency of 100 Hz, giving a total data set of 1000 sample points. A signal to represent sensor noise q was added to the plant output, having a low frequency cut-off of 100 rad/s.

The fault signal w is added to the plant input-output data. This represents the effect of an error occurring in one of the plant measurement transducers or actuators. The fault detector is then trained to reproduce this signal given the original set of plant input-output data only.

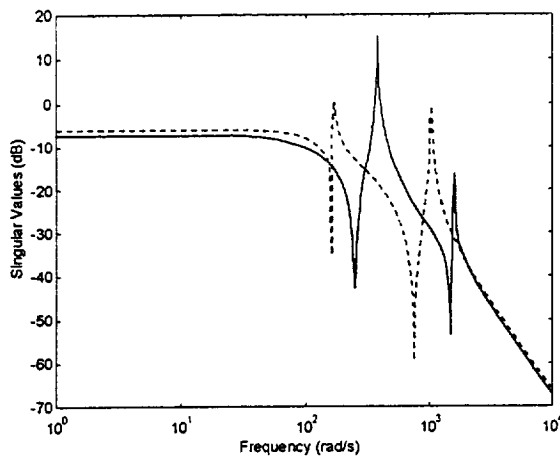


Figure 4 Singular values of (open loop) plant model transfer function at zero running speed

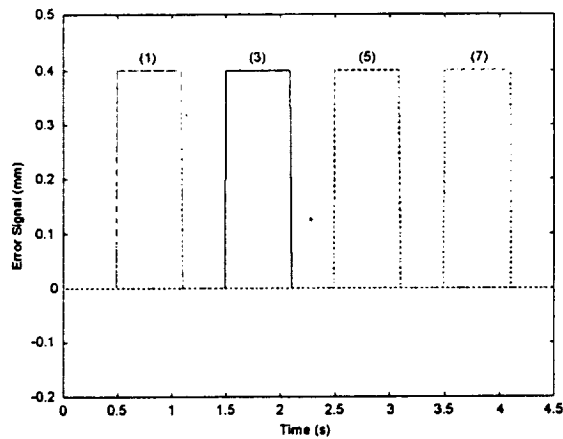


Figure 5 Sensor error signal for training/simulation. This signal is added to the actual sensor signal to simulate occurrence of a fault

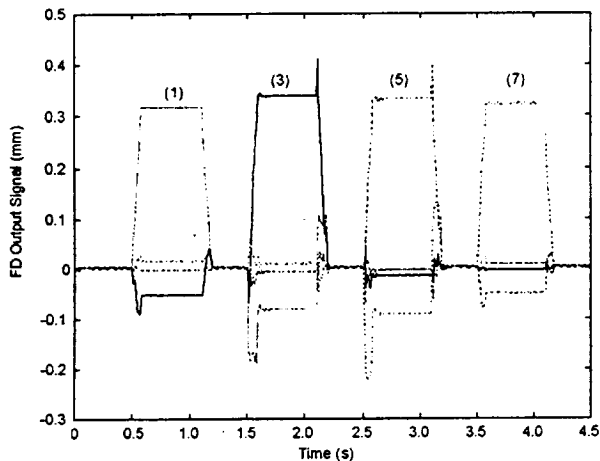


Figure 6 FD output signals for fault detector 1

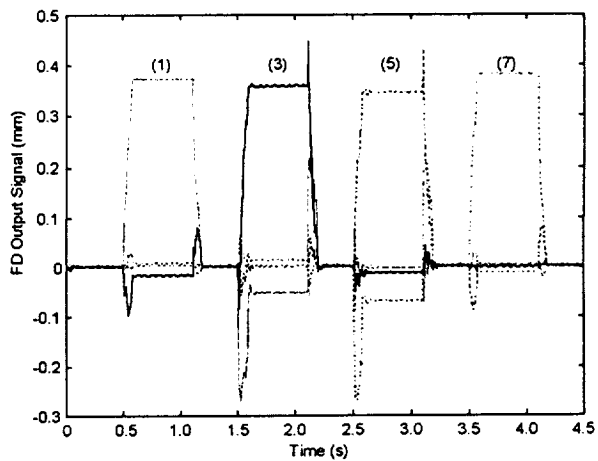


Figure 7 FD output signals for fault detector 2

Fault Detector Performance

In this simulation study, four different neural network fault detectors were generated using different identification and training data, summarised as follows:

Fault detector 1	Band limited white noise plant identification signal. Fault amplitude during training = 0.1 mm.
Fault detector 2	Band limited white noise plant identification signal. Fault amplitude during training = 0.2 mm.
Fault detector 3	Random step plant identification signal. RMS sensor noise = 0.05 mm. Fault amplitude during training = 0.2 mm.
Fault detector 4	Random step plant identification signal. RMS sensor noise = 0.01 mm. Fault amplitude during training = 0.2 mm.

The resulting network weighting and bias matrices can be implemented in simulation and the performance tested using a simulated fault error signal similar to that used in the training. The influence of training parameters, on the resulting network performance can be assessed from the time responses of the fault detector output $r(t)$ to various fault types. The results in figures 6, 7, 8 and 9 show the fault detector responses to an offset error occurring on each of the four sensors in turn over a four second period. The amplitude of the error is 0.4mm, as seen from figure 5.

Comparison of figures 6 and 7 shows a number of important characteristic features of the simulated outputs in which they differ from the desired responses. Firstly, there is the steady state performance of the network. This includes, not only the steady state accuracy of the error estimate for a particular sensor, but also the degree of spillover that effects the network outputs corresponding to the other three sensors. Accuracy during the no fault condition is also important for avoiding false alarms, during which the outputs should be close to zero. The transient response of the network to the step change in error should also be assessed, in terms of response time, overshoot and, again, the degree of spillover. Unlike in network training, the response for sensors 3 and 5 will differ to those for 1 and 7, as sensor 3 and 5 are used as control inputs while 1 and 4 are for fault monitoring only. Therefore, a fault acting on sensors 3 and 5 acts as a disturbance on the plant via the control feedback. One other consideration is the amplitude of the ripple on the FD signal due to synchronous disturbance.

Figures 6 and 7 show the response of two networks to the fault conditions. Both networks have been generated using plant identification signals consisting of band limited white noise. However the amplitude of error signal w used in the training differs. The results show that increasing the amplitude of the error signal improves the steady state performance, i.e. the mean deviation in the non-faulty sensor signals is reduced slightly. However, it has a detrimental effect on the transient response, i.e. large signal spikes now occur when the fault is activated.

Figures 8 and 9 show the results of network training from data generated with a random step signal at the controller input. Comparison with the results from the random noise signal generally show better performance, attributable to the fact that the training signal is specifically for a step type disturbance (as

caused by the step error signal). Comparison of figures 8 and 9 show how decreasing the noise level on the sensor signal has the same effect as increasing the error signal amplitude i.e. it improves the steady state performance, but degrades the peak transient response.

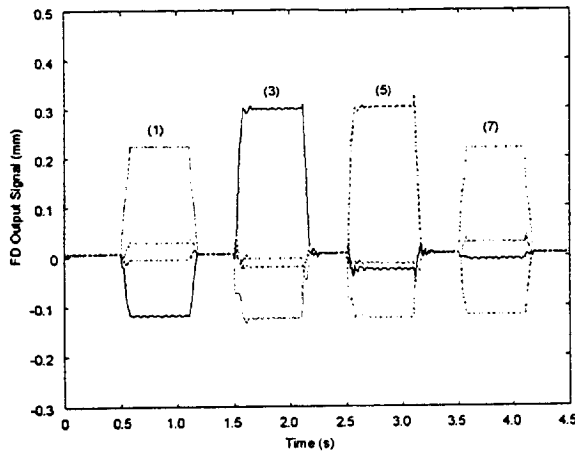


Figure 8 FD output signals for fault detector 3

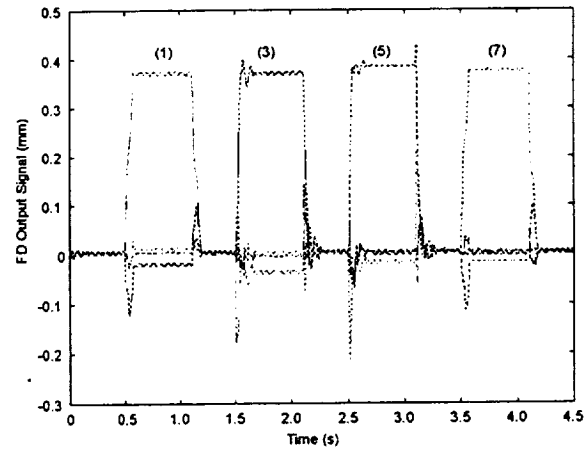


Figure 9 FD output signals for fault detector 4

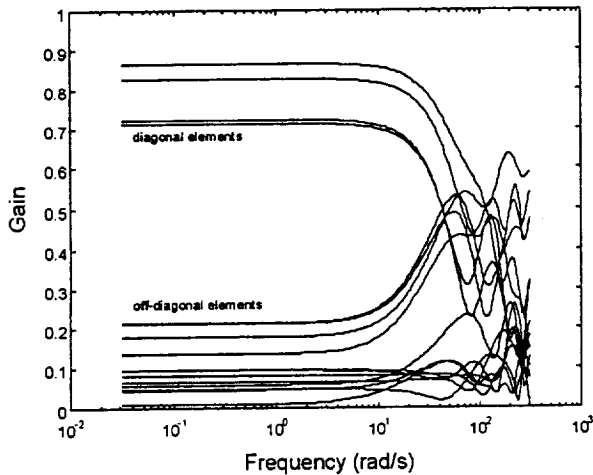


Figure 10 Magnitude of matrix elements of $G_A(j\omega)$ for fault detector 1 showing diagonal dominance up to the cross over frequency at 40 rad/s

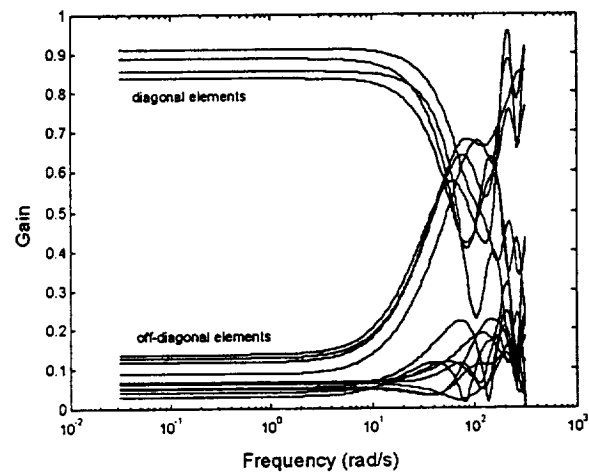


Figure 11 Magnitude of matrix elements of $G_A(j\omega)$ for fault detector 4 showing diagonal dominance up to the cross over frequency at 50 rad/s

It can be concluded from these results that the network solution is a trade-off between the transient response and state steady accuracy of the fault detection signal. The ability to influence these factors is provided through the choice of error signal (amplitude) used as the target set and the frequency spectrum of the plant identification signal used to generate the input set. Sensor noise also has an important influence on the resulting network performance, but is an intrinsic property of the real system and cannot easily be changed in practice. The exact nature of this behaviour can be seen through comparison of the frequency response matrices for the system $G_A(j\omega)$ and $G_{ru}(j\omega)$ (defined by equations (4)). Figures 10

and 11 show magnitudes of the elements of the frequency response matrix for $G_{rd}(j\omega)$ for two different fault detectors. At low frequencies the four diagonal elements are close to unity and the remaining elements are small, so the fault detector will give a good estimate of the error signal. However, above the cross over frequency (approximately 50 rad/s) the transfer function matrix is no longer diagonally dominant, and spillover occurs.

Plant Disturbance Changes

The effect of variations in plant disturbance on the FD network output, from either changing rotor speed, changes in unbalance, or possibly some other direct forcing disturbance such as rotor impact or mass loss, can be assessed through inspection of the frequency response matrix $G_{rd}(j\omega)$. Plots of the frequency dependent matrix elements amplitudes of $G_{rd}(j\omega)$ are shown in figure 12 and 13 corresponding to fault detectors 1 and 4. It is evident from the plots that the responses have been minimised close to the synchronous frequency of 100 rad/s.

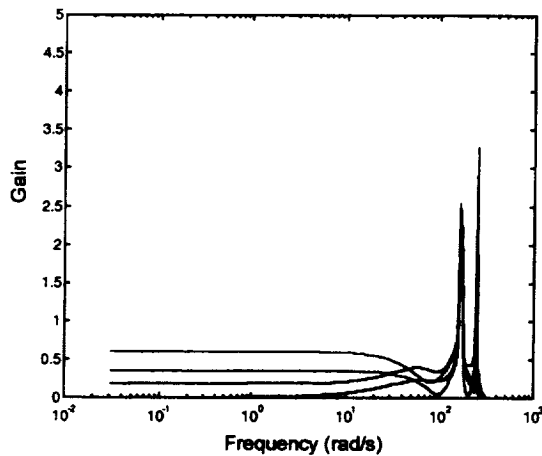


Figure 12 Magnitude of matrix elements of $G_{rd}(j\omega)$ for fault detector 1 showing minima at disturbance frequency (100 rad/s)

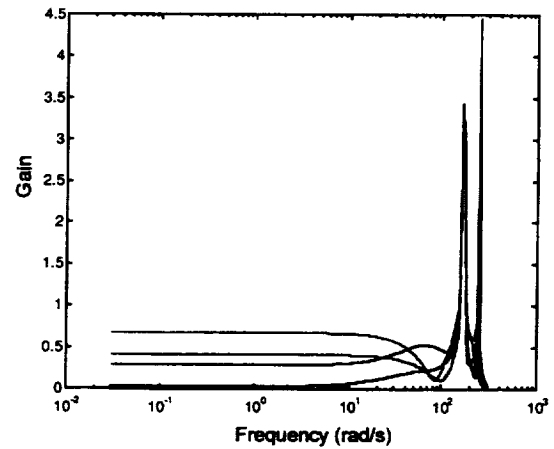


Figure 13 Magnitude of matrix elements of $G_{rd}(j\omega)$ for fault detector 4 showing minima at disturbance frequency (100 rad/s)

EXPERIMENTAL RESULTS

Experimental implementation of the neural network based fault detector has been used to demonstrate the performance capabilities and show how it can be used as a basis for a reconfigurable control system. In the experimental system, the fault detectors were implemented in software to run in real-time on a DSP system, used also for controller implementation. Fault detectors were trained using data taken from the rig during operation. These fault detectors were then tested by simulating a number of fault conditions on the rig. In this example the rotor is under steady operating conditions with a rotational speed of 88 rad/s prior to the onset of the fault. Figures 14 and 15 show the eight fault detector outputs (one corresponding to each sensor) when an offset error occurs on one of the sensors after one second. The responses differ

due to the fact that sensor 3 is being used for control feedback at the time whereas sensor 1 is used purely for condition monitoring purposes.

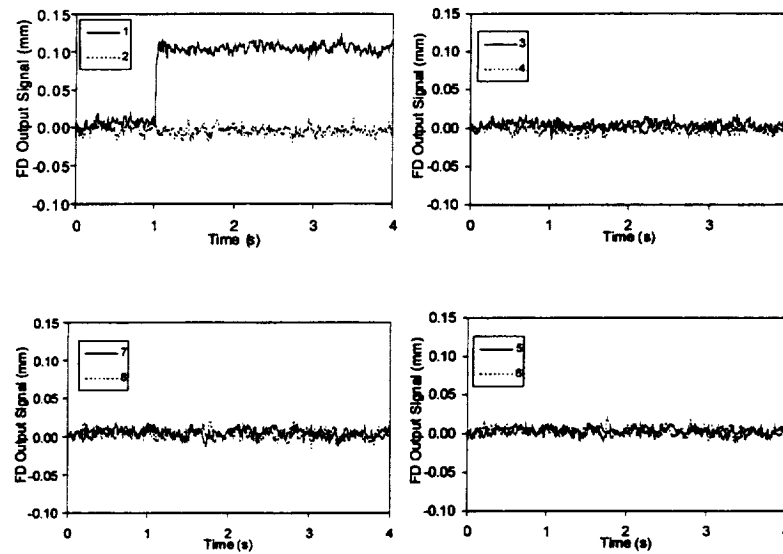


Figure 14 Fault detector output during fault on sensor 1 ($\Omega = 88$ rad/s)

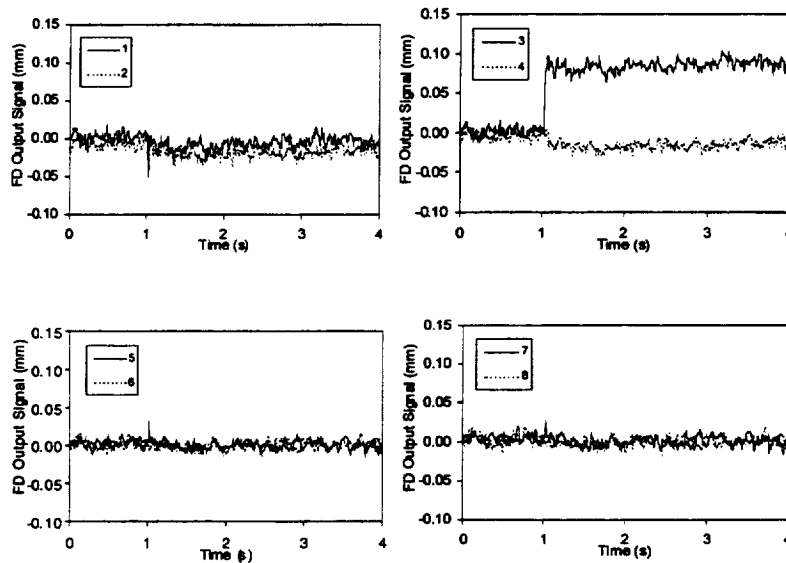


Figure 15 Fault detector output during fault on sensor 3 ($\Omega = 88$ rad/s)

The complete failure of a sensor may produce damaging behaviour, depending on the response of the rotor. Figure 16 shows the response of the rotor to a failure of sensor 3 while it is being used for control feedback. It can be seen that stability is lost and the rotor collides and remains in contact with the retainer bearing. Damage to the retainer bearings and/or rotor could result from prolonged contact at high running speed, or when interaction of the rotor and bearing involves large impact forces.

Automatic Control Reconfiguration

For the purposes of condition monitoring and automatic control configuration the fault detector has been combined with a post processor algorithm (ref. 10) that monitors and interprets the output from the fault detector. This is combined with some simple decision logic that provides the ability to reconfigure control or issue warnings when a fault is recognised. Figure 17 shows the response of the rotor to complete loss of sensor 3 (while being used for control feedback) when the automatic control reconfiguration is in operation. Comparison with figure 13 shows that the fault detector has enabled recognition of the fault and has invoked automatic reconfiguration of the control algorithm to bypass the faulty sensor. Although the speed of recognition is not sufficient to completely avoid collision of the rotor with the retainer bearing, the touchdown is brief and the rotor quickly returns to steady operation when control is switched to a healthy sensor.

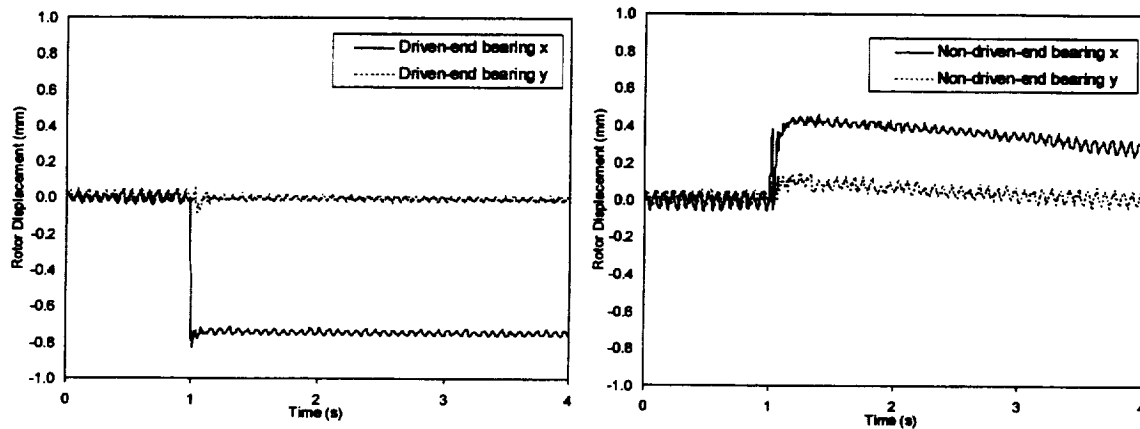


Figure 16 Measured rotor response during sensor 3 failure ($\Omega = 88$ rad/s)

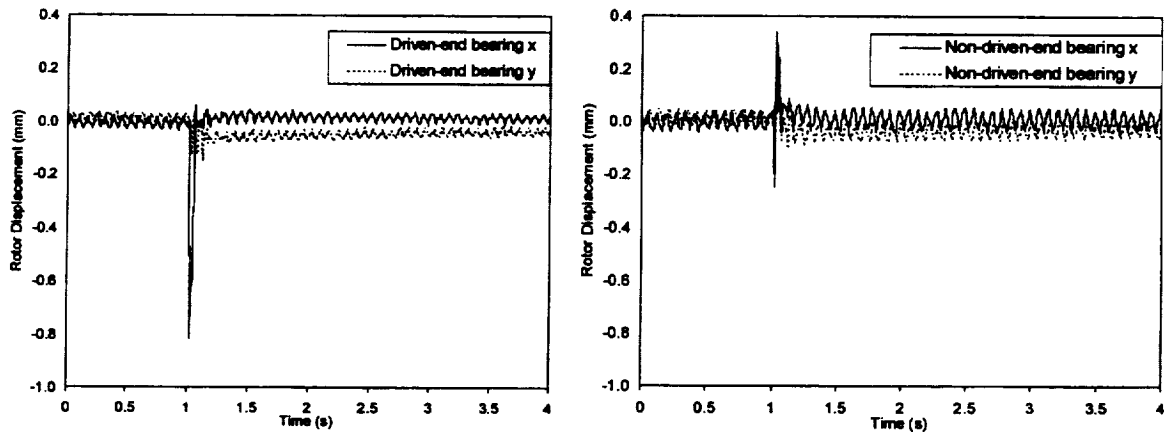


Figure 17 Measured rotor response during sensor 3 failure with automatic control reconfiguration ($\Omega = 88$ rad/s)

CONCLUSIONS

This study has shown how a method for fault detection, based on a neural network type architecture, can be applied to a dynamic system with multiple inputs and outputs. Application of the method to a magnetic bearing/flexible rotor system through simulation has shown that the performance of the fault detector is dependent on the plant input and output signal data used for the training of the network. Application to an experimental system was successful during tests to simulate faults occurring on any of the rotor displacement transducers. Tests demonstrated that it was possible to use the fault detector as the basis for a reconfigurable control system that could switch control algorithms on detection of a fault in order to bypass the failed component. The results indicated that the severity of damaging touchdowns with retainer bearings could be significantly reduced.

The ability of neural networks to give a non-linear mapping property suggest that further investigation would be worthwhile into the application of this method to strongly non-linear systems.

REFERENCES

1. Frank P.M, and Wunnenburg J.: Robust Fault Diagnosis Using Input Observer Schemes, *Fault Diagnosis in Dynamic Systems, Theory and Application*, Patton, R. Frank P. & Clark, R. eds., Prentice Hall International, 1989. pp. 47-98.
2. Isermann, R.: Process Fault Detection Diagnosis Based on Dynamic Models and Parameter Estimation Methods, *Fault Diagnosis in Dynamic Systems, Theory and Application*, Patton, R. Frank P. & Clark, R. eds., Prentice Hall International, 1989, pp. 253-291.
3. Luenberger, D.G.: An Introduction to Observers. *IEEE Trans. on Automatic Control*, vol. 16, 1971, pp. 596-602.
4. Fairmann, F.W., Mahil, S.S. and Luk, L.: Disturbance De-Coupled Observer Design via Singular Value Decomposition, *IEEE Transactions On Automatic Control*, vol. AC-29, no. 1, 1984.
5. Frank, P.M. and Ding, X.: Frequency Domain Approach to Optimally Robust Residual Generation and Evaluation for Model-Based Fault Diagnosis, *Automatica*, vol. 30, no.5, 1994, pp. 789-804.
6. Hou, M. and Patton, R.J.: An LMI Approach to H_2/H_∞ Fault Detection Observers. *UKACC Int. Conf. On Control*, IEE, 1996, pp. 305-309.
7. Maki, Y. and Loparo, K.A.: A Neural-Network Approach to Fault Detection and Diagnosis in Industrial Processes. *IEEE Trans. on Control Systems Technology*, vol. 5, no. 6, 1997, pp. 529-541.
8. Cole, M.O.T., Keogh P.S. and Burrows, C.R.: Fault Tolerant Control of Rotor/Magnetic Bearing Systems using Re-Configurable Control With Built-In Fault Detection. Submitted to *Proc. Instn. Mech. Engrs., Part C, Journal of Mechanical Engineering Science*, March 1999.
9. Mathworks Inc.: Matlab with Simulink.
10. Cole, M.O.T.: Fault Tolerant Control of Rotor/Magnetic Bearing Systems, PhD Thesis, University of Bath, May 1999.

POSSIBILITY OF EXISTENCE OF NON-LINEAR ELECTROMOTIVE FORCE (EMF)

Osamu Ide, Clean Energy Laboratory, Tokyo, Japan

ABSTRACT

It is well known that a conventional Faraday electromotive force (EMF) is proportional to the time derivative of the magnetic flux. The author made a prototype of a motor driven by the current discharged from the capacitor of an LC circuit and performed an investigation of its characteristics, experimentally and theoretically. The results – when motor drive units of a specific design are installed to drive the motor – confirm the phenomenon that unknown EMF components are created and that these can not be explained only with the conventional Faraday EMF model.

The unknown EMF is, for the most part, proportional to a function of the second-order time derivative of the magnetic flux applied. It is also evident that there is even a possibility of the existence of components that are dependent on the third-order, or higher, time derivatives of the magnetic flux applied. Furthermore, it must be noted that the direction of the EMF generated is always in the direction that accelerates the current flow discharged from the circuit.

INTRODUCTION

In a previous work¹ it is reported that a motor driven by the current discharged from an LC resonance circuit, indicates the creation of an anomalous EMF when the magnetic fields generated from the coil units which are composed of such motor drive units are set to repel each other (repulsion mode), together with the fact that the EMF created is in the direction to accelerate or encourage the discharged current. The results obtained in previous work suggest the existence of a positive EMF that is substantially different in nature from the conventionally known back-EMF. In addition, the results of a theoretical analysis which was done based on a computer simulation also support the assumption that this positive EMF is the result of some anomalous phenomenon that is outside the range that can be explained by the conventional Faraday's law.

In this paper, further experimental and theoretical investigation was made of the results obtained in the previous study.

In the previous study, the positive EMF was observed only when the magnetic fields generated from each motor driver unit composed of a pair of the single-coil units are set to repel each other. (Repulsion mode). A double-coil unit, which is somewhat different from the single-coil ones previously used in the design, was also used for this research. In all other respects the prototype motors were identical.

The motor prototype used in both studies has two sets of drive units, each of which is installed on the stator of the motor. Each drive unit is composed of a pair of driving coils with coaxial alignment in a face-to-face configuration so the pair sandwiches the rotor along the horizontal plane of the motor axis.

The circuit controller operates the driving coils so the magnetic fields generated will be in the opposite direction.

Each of the double-coil units making up the drive unit used in this study is composed of two coils, an inner coil and an outer coil, being connected in series with each other and sharing a common center, and has a total of three paramagnetic core plates that are made of Permalloy 45. One of the core plates is set in the common center position of the coil unit, and the other two are set in the spaces between the inner and outer coils. The motor using the double-coil units displays the existence of a positive EMF of a significantly higher voltage compared with the EMF values obtained in the previous study. It is also possible that a slight repulsion force exists between the inner and outer coils of the double-coil unit.

On the other hand, the theoretical equations used for the computer simulation and theoretical analysis were projected to a higher level of precision than in the case of the previous study. In that work, the computer-simulation analysis was made on the supposition that the inductance of the coil varies in approximation depending upon the position of the coils according to a first-order algebraic equation. However, such a first-order approximation is effective only when the motor's rotation speed is in the low range. It is speculated that, as the motor's rotation speed increases, the obtained inductance value to be input to the simulation equation would greatly deviate from the corresponding experimental values.

In contrast to that, this study features that a third-order equation for the time derivative of magnetic inductance should be introduced to replace the simple first-order equation used in the previous study. The introduction of the new, improved equation allows the calculated inductance values to very closely match the corresponding measured values. This, in turn, enables the author to perform a computer simulation on EMF with a higher degree of precision. Consequently, the theoretical analysis by the computer simulation resulted in substantially more precise EMF values compared with those of the previous case study, which is based simply on Faraday's law in an unmodified form. The accuracy of the theoretical analysis based on the new approximation equation indicates an improvement of nearly a hundred-fold.

Computer-simulation analysis based on the new equation was made also on the result of the previous study that used a single-coil type. The degree of deviation was represented by the difference of the values that were obtained in the experiment from the theoretical values.

The deviation between the experimental and theoretical values and the time derivative for the inductance were used to evaluate the level of unknown EMF that was generated. A very interesting result was obtained after performing this evaluation.

In the previous study in which single coils were used, the unknown positive EMF was observed only when the magnetic fields generated from a motor drive unit were in repulsion mode. However, in this study, a positive EMF – although it was less intense – was observed even when the magnetic fields from a drive unit are set in attraction mode. Thus, when a drive unit using the double-coil units is in repulsion mode, the anomalous EMF will appear more conspicuously for easier observation. Based on the above, it is speculated that such phenomenon could occur in any type of electromagnetic system, as well as that it might be too weak to be detected because the intensity level of such components is much lower compared to that for conventional Faraday EMF.

The intensity level of the unknown EMF also varies depending on the time derivative of inductance, indicating an upward curve of a nonlinear nature. The fact that a certain amount of order is observed in the obtained deviation data even after screening out statistical noise or measurement errors, means that the data obtained is a significant indication of the existence of the unknown factors. In other words, there is a possibility that there could be additional non-linear components that have not yet come to the attention of the academic community. The conventional Faraday EMF is only indicative of the linear component.

DESCRIPTION OF THE MOTOR PROTOTYPE USED FOR THE RESEARCH

The basic electrical circuit of the motor drive unit of the motor prototype is shown in Fig.1. Two motor drive units are installed on the motor prototype system used for the experiment. The current discharged from capacitor C , whose initial voltage is $+V_0$, runs through the components composing the circuit. Each motor drive unit installed on the stators is made up of a pair of coil units (L_1 , L_2).

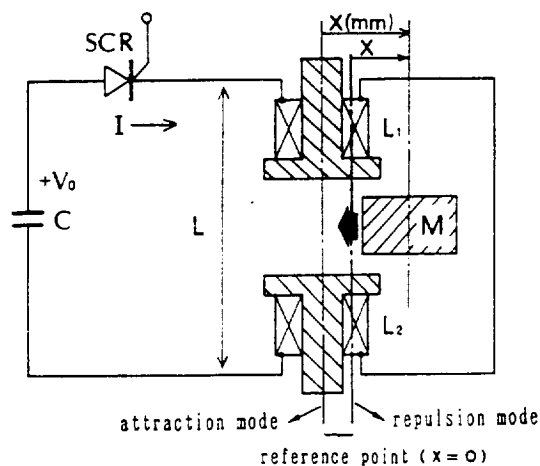


Fig. 1 The basic electrical circuit of a motor drive unit of the motor prototype

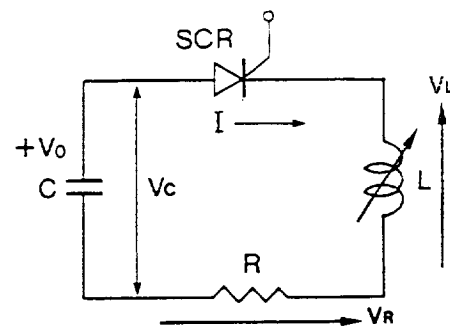


Fig. 2 The equivalent electrical circuit diagram of the motor prototype

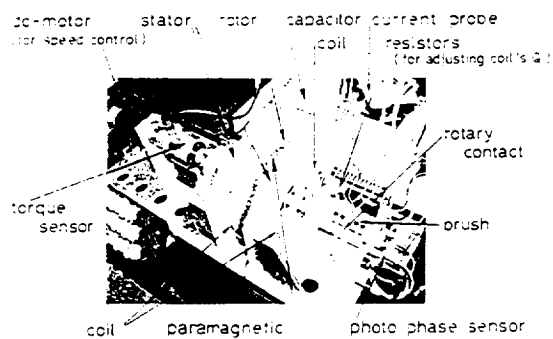


Fig. 3(a) A photograph of the whole view of the motor prototype system

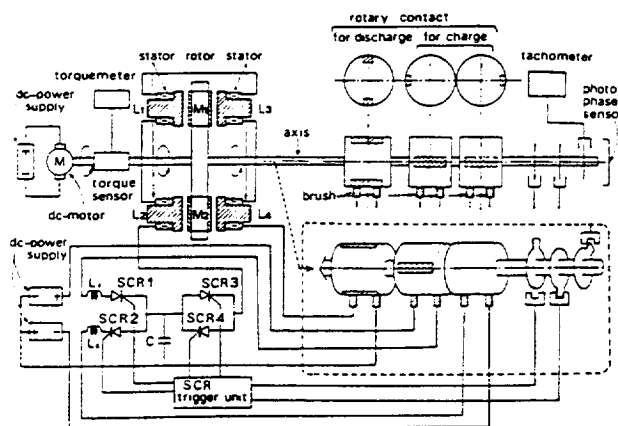


Fig. 3(b) An illustration of the configuration of the whole motor prototype system

A simplified circuit diagram that is equivalent to the circuit described above is shown in Fig. 2. The resultant value L of the inductance of L_1 and L_2 is intrinsically variable, because it is influenced by the position of core plates M on the rotor when the paramagnetic core plates are moved by the attraction force applied by the motor drive units.

A photograph and an illustration of the configuration of the whole motor prototype system used for experiment is shown in Fig. 3(a) and Fig. 3(b). The system is an embodiment of the circuit diagram shown in Fig. 1. It is a motor that allows continuous operation. Core plates M_1 and M_2 made of a paramagnetic substance Permalloy45 are installed on the rotor disk. The rotor disk is started by driving an auxiliary DC drive motor. The rotation rate can be set to a desired value over a wide range by setting the attached speed controller, and the rate is indicated on the tachometer.

Each motor drive unit is composed of a pair of the coil units, (L_1, L_2) or (L_3, L_4). The magnetic fields that are generated from each drive unit can be set to either attraction mode (N-S, N-S) or repulsion mode (N-S, S-N).

A set of rotary contact units installed on the axis of the rotor is used to switch the circuit for charging or discharging. It is set in series in the circuit of each mode. It is designed so that the SCR will become ON after the rotary contact units are set to ON; and so that the rotary contact circuit will become OFF after the SCR is set to OFF when the sign of the recharge voltage is reversed. In the result, the SCR is protected from malfunctioning.

Two motor drive units composed of four coil units are installed on the two stators of the motor. (Each coil unit has two coils.) The two paramagnetic cores M_1 and M_2 are installed at an interval of 180 degrees around the perimeter of the rotor disk which is installed between the two stators. See reference

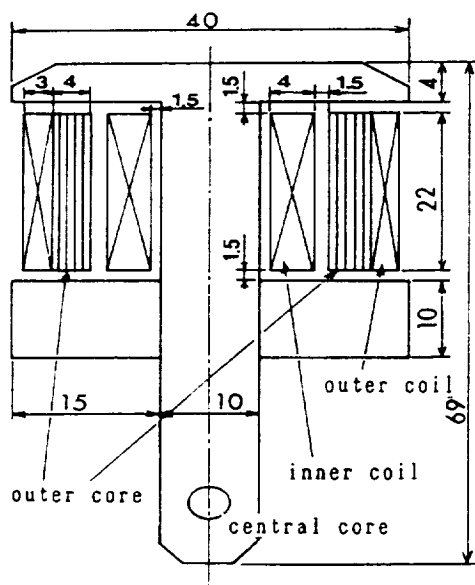


Fig. 4(a) A cross sectional view of the double-coil unit

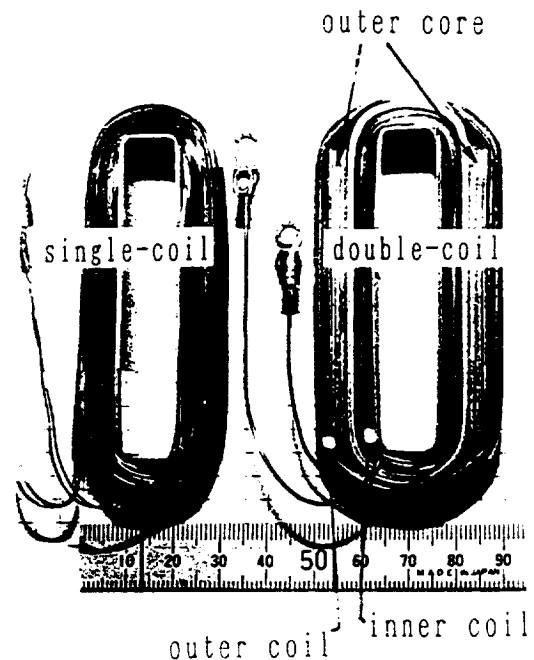


Fig. 4(b) Exterior views of a single-coil and a double-coil without their central cores

(1) for a detailed description on the positions of the coil units on the stator and of the paramagnetic cores on the rotor, since they are common to the previous study.

It is known that the values of the resultant inductance of the four coils L_1 , L_2 , L_3 and L_4 , will reach a maximum when the paramagnetic cores on the rotor are at a certain angle. The angle is called "the Reference Point". There is a slight difference in the position of the reference points between attraction mode and repulsion mode (Fig.1).

In this research, two types of motor drive unit were examined to compare their performance, one using the newly developed double-coil units, and the other using the single-coil units tested in the previous research. A cross sectional view and a plan view of the double-coil unit, are shown in **Fig. 4(a)** and **Fig.4(b)**.

The double-coil unit is composed of two coils, an inner coil and an outer coil. The magnetic fields generated from the two coils seem to repel each other, due to a design effect. It should be noted that two paramagnetic core plates of each double-coil unit are vertically installed in the spaces between the inner and outer coils. The core(s) of each coil are made of paramagnetic substance Permalloy 45 that is common to that of the rotor's cores .

The value Q of the double coil is intentionally set to a value equal to that of the single coil used in the previous research to check the effect of the newly-developed paramagnetic core plates inserted between the inner and outer coils. This means that the values of L and R of the two types of coil unit are approximately equal to the "discharge initiation point" which is described below.

EXPERIMENTAL METHOD

The relationship of the resultant inductance of all the coils existing to the position of the core plates, is shown in **Fig. 5**. Measurement of the inductance was done using a LCR meter. The values of the attraction force acting on the paramagnetic cores of the rotor were also measured so as to obtain the values to be used for reference.

From the curve to indicate the relationship between the resultant inductance (mH) and the relative position (mm) of the paramagnetic cores on the rotor's peripheral to the reference point, it can be seen that the resultant inductance of the coils gradually increases as the cores get closer to the coil units of the motor drive units under the influence of the attraction force applied. It is also known from the same curve that the value of the inductance will reach a maximum and that the torque acting on the rotor will become zero (gram meter) at the reference point ($x = 0$ mm). Incidentally, a back torque is generated if the core goes into a negative coordinate range by passing over the reference point.

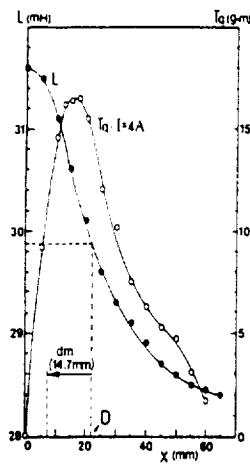


Fig. 5(a) Double coil (repulsion mode)

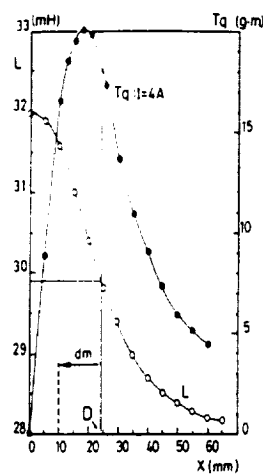


Fig. 5(b) Single coil (repulsion mode)

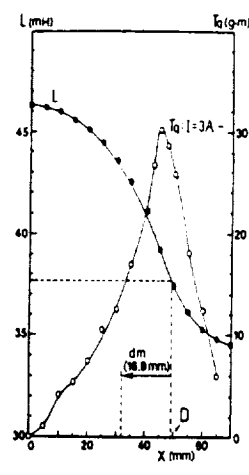


Fig. 5(c) Double coil (attraction mode)

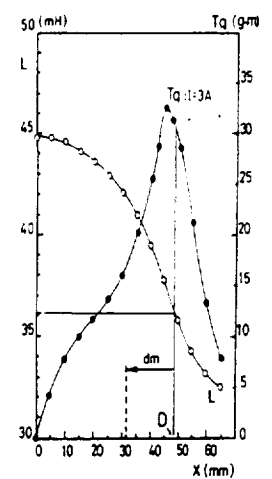


Fig. 5(d) Single coil (attraction mode)

dm: Maximum displacement of the rotor in the period of $T/2$

Fig. 5 The relationship of the resultant inductance of all the coils existing, and of the torque T_q to act on the rotor, to the position of the core plates [the distance of the rotor from the reference point]

Discharge from the capacitor will be initiated when the paramagnetic core reaches a certain point in the distance D (mm) from the reference point. The distance D is called the "discharge initiation point". This point is located near the position where it is observed that the maximum torque acts on the rotor. The discharge initiation point had been set to a position where the paramagnetic cores will never pass over the reference point during the discharging period of a half cycle $T/2$, even when the rotor reaches the maximum rotation speed required for the measurement. By taking such measures, it is impossible for the rotor to receive any back torque.

Fig. 6 shows the waveforms to represent the continuous changes of the discharge current and the capacitor voltage when the motor is in operation.

- (1) The capacitor is charged to a voltage $+V_0$ from the positive (+) terminal of a dc power source.
- (2) When the rotor core gets close enough to the stator core to raise the voltage to the level of the discharge initiation point, SCR3 will be set to ON to initiate a discharge from the capacitor for the period of a half cycle ($T/2$). Subsequently the capacitor will be recharged to voltage $-V_r$.

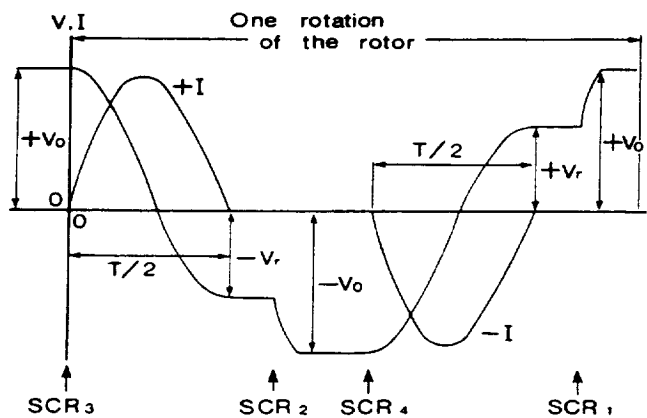


Fig. 6 The waveforms of the discharge current and voltage of the capacitor when the motor is in a continuous operation, with the action points of the SCRs

(3) SCR2 is set to ON, and the capacitor is charged to voltage $-V_0$ from the negative (-) terminal of a dc power source

(4) SCR4 and subsequently SCR1 are set to ON, and the equivalent steps will be performed likewise in the discharging process in the opposite direction.

Thus the positive and negative discharging processes are repeated alternately in each cycle.

The absolute values of $+V_r$ and $-V_r$ corresponding to the desired rotation rate n (rpm) of the rotor, were measured experimentally. Each desired rotation rate was reached by starting from a standstill.

In order to minimize the effect of measurement errors, measurements were made 16 times for each rotation rate, namely, eight measurements for each of the positive and negative discharge processes. The average value of the 16 data sets was adopted as the measured value for each rotation rate.

The capacitance C of the capacitor used was 15.87 micro F, and the initial charge voltage V_0 was set to ± 240 V. Measurement of the capacitor's voltage was done using a high impedance probe of 200 M ohms (dc - 15 kHz), and the intensity of the current was measured using a clamp-type probe. The waveforms to indicate the changes of the capacitor voltage and of the discharge current were continuously recorded using an oscilloscope with a digital memory. The measured data stored in the memory was then transmitted to a computer via a GP-IB mode line to be used as the input data for the theoretical analysis.

THEORETICAL ANALYSIS

A. The function of time on the inductance of the coil, to be derived from the approximation of the measured data

One of the major purposes of performing a theoretical analysis in this research is to derive a function for time from the inductance of the coil in the state that the rotor is moving. It is first necessary to derive a function for the position of the rotor (x) from the resultant inductance of the coil (L), based on the measured data.

Fig. 5 shows the measured data indicating the relationship of the inductance of the coil (L) to position of the rotor (x). Based on the data, an attempt was made to derive an equation simulating the ($L - x$) curve by means of theoretical analysis. In order to improve the level of precision, the assumption was made that L (mH) is a function of the 3rd order series of x (mm) for approximation (the equation (1)), instead of the straight line approximation (first order series) which was employed in the previous study.

$$L = A_0 + A_1x + A_2x^2 + A_3x^3 \quad (\text{mH}) \quad (1)$$

Where, x (mm): position of the rotor

A_0, \dots, A_3 : Approximate values of the coefficients calculated from the measured values ($L - x$)

The relationship of the speed of rotation v to the position of the rotor x , is given by the equation (2). The relationship of the rotation speed v to the rotation rate n is given by (3), considering that the radius of the rotor is 1000 mm.

$$x = D - vt \quad (\text{mm}) \quad (2)$$

$$v = (1000 \times n) / 60 \quad (\text{mm/s}) \quad (3)$$

Where,

D (mm): Discharge initiation point to mean at distance D from the reference point

v (mm/s): Rotation speed of the rotor (rotor's peripheral speed)

t (s): Time elapsed after the discharge is initiated

n (rpm): Rotation rate

The equation (4) of the inductance L as a function of time t. is derived from relationships (1), (2) and (3):

$$L = B_0 + B_1 t + B_2 t^2 + B_3 t^3 \quad [\text{H}] \quad (4)$$

Where,

$$B_0 = (A_1 + A_2 D + A_3 D^2 + A_4 D^3) \times 10^{-3}$$

$$B_1 = \{ (-A_2 - 2A_3 D - 3A_4 D^2) \times v \} \times 10^{-3}$$

$$B_2 = \{ (A_3 + 3A_4 D) \times v^2 \} \times 10^{-3}$$

$$B_3 = -A_4 v^3 \times 10^{-3}$$

The first order time derivative of the inductance (dL/dt) and the second order time derivative of the same are given by the relationships (5) and (6), respectively, being derived from the relation (4).

$$\frac{dL}{dt} = B_1 + 2B_2 t + 3B_3 t^2 \quad (\text{H/sec}) \quad (5)$$

$$\frac{d^2 L}{dt^2} = 2B_2 + 6B_3 t \quad (\text{H/sec}^2) \quad (6)$$

B. Equation to express the capacitor's voltage as a function of the elapsed time after discharge is initiated

The voltage V_L between the coil's two terminals (Fig. 2) is expressed by (7), which is derived from Faraday's law and relationships (4) and (5).

$$\begin{aligned} V_L &= \frac{d\Phi}{dt} = \frac{d(Li)}{dt} = L \left(\frac{di}{dt} \right) + \left(\frac{dL}{dt} \right) i \\ &= (B_0 + B_1 t + B_2 t^2 + B_3 t^3) \frac{di}{dt} + (B_1 + 2B_2 t + 3B_3 t^2) i \end{aligned} \quad (7)$$

Where, i (Ampere): Discharge current

The voltage between the capacitor's terminals V_c and the voltage between the terminals of the resistor composing of the circuit V_R , are given by (8) and (9), as functions of the capacitor C (Farad) and the discharge current i. (See Fig. 2).

$$V_c = \left(\frac{\int i dt}{C} \right) \quad (\text{Volt}) \quad (8)$$

$$V_R = Ri \quad (\text{Volt}) \quad (9)$$

The following relationship (10) is obtained based on Kirchhoff's law and relationships (7), (8) and (9).

$$V_c = V_L + V_R = \left(\frac{\int i dt}{C} \right) \\ = (B_0 + B_1 t + B_2 t^2 + B_3 t^3) \frac{di}{dt} + (B_1 + 2B_2 t + 3B_3 t^2 + R)i \quad (10)$$

METHOD OF EVALUATION

The unknown EMF (V_p) is expressed by (11), which is estimated from the recharged capacitor's voltage based on the assumption that an EMF other than Faraday's EMF exists.

$$V_p = [\text{Measured value of } V_r] - [\text{Theoretical value of } V_r] \quad (11)$$

Where, V_r : capacitor's recycle voltage shown in Fig. 6

It is absolutely necessary to obtain the curve to express the relationship between the unknown EMF (V_p) and the inductance's time derivative to use it as the basis for evaluation of the EMF. In order to do so, it is necessary to take the following steps:

- (a) Obtain the measured value of V_r corresponding to each rotation rate for experiment, first.
- (b) Calculate the theoretical values of V_r corresponding to each rotation rate for experiment, by solving the equation (10) for V_c . The solutions of the equation are obtained by performing the following substeps (b1), (b2) and (b3):
 - (b1) Calculate the value of resistance loss R from the values of V_0 and V_r measured at $n = 0$, and from the integrated value of the square of the current $\int i^2 dt$ curve (current value) which had been obtained by measurement.
 - (b2) Calculate the theoretical value of the capacitor's voltage V_c from the equation (10) using the Runge-Kutta method, while setting the initial conditions to $t = 0$, $V_c = V_0$ and $i = 0$, respectively.
 - (b3) Calculate the theoretical value of the recharged capacitor's voltage V_c to obtain the value of V_r at the time when the value i becomes zero again, after the discharge period for a half cycle is completed.
- (c) Calculate the values of the first-order time derivative (dL/dt) and the second-order time derivatives (d^2L/dt^2) of the inductance for each rotation rate which is measured for experiment, at the moment when the discharge process is completed ($t = T/2$), from (5) and (6).
- (d) Make graphs by plotting the values obtained in the above step (c) on the horizontal axis and the values V_p corresponding on the vertical axis. The graphs thus obtained are supposed to be the curves to represent the relationship of the unknown EMF to the inductance time derivatives of the first order and second order.

RESULTS

The results of the research are shown in **Fig. 7**, **Fig. 8** and **Fig. 9**. **Fig. 7** shows the curves indicating the dependency of the unknown EMF (V_p) upon the time derivative of the inductance (dL/dt). Both of the EMF curves obtained has a rising inclination of a non-linear nature, whether or not it is in attraction mode or repulsion mode, and regardless of whether it is a single-coil unit or a double-coil unit.

Fig. 8 and **Fig. 9** show the curves indicating the dependency of the unknown EMF (V_p) upon the second-order time derivative of the inductance of the coil (d^2L/dt^2). **Fig. 9** is an enlargement of the area near the origin of the x-axis shown in **Fig. 8**. Regardless of the conditions of the experiment, the curves obtained are rising curves of a non-linear nature, indicating patterns, which is significantly different from those shown in the **Fig. 7**.

The results obtained indicate that the EMF value V_p always stays in the positive range and never becomes negative. The sizes of the absolute values of V_p obtained were in the following order based on the experimental factors; (a) > (b) > (c) > (d) [case (a) is the largest, (d) the smallest]. Here, (a) the double-coil unit in repulsion mode, (b) single-coil unit in repulsion mode, (c) double-coil unit in attraction mode, (d) single-coil unit in attraction mode.

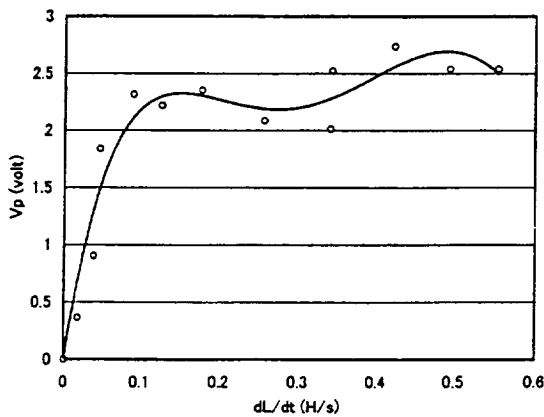


Fig. 7(a) Double coil (repulsion mode)

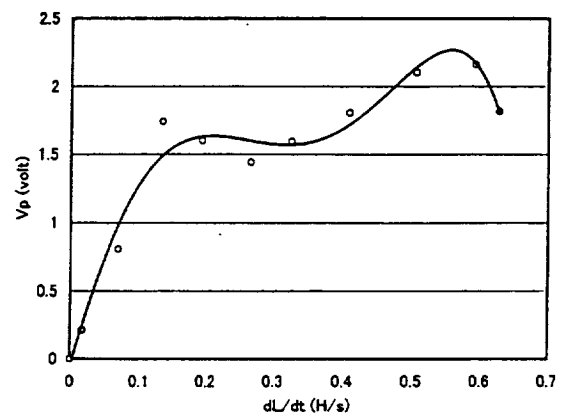


Fig. 7(b) Single coil (repulsion mode)

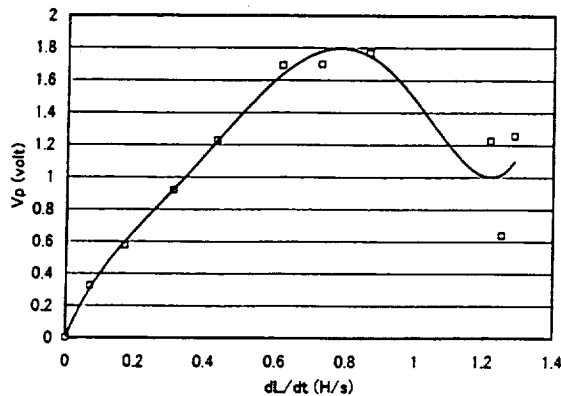


Fig. 7(c) Double coil (attraction mode)

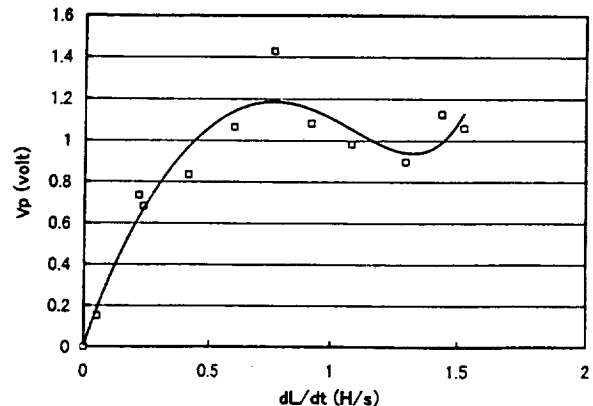


Fig. 7(d) Single coil (attraction mode)

Fig. 7 The dependency of the unknown EMF (V_p) upon the first-order time derivative of the inductance (dL/dt)

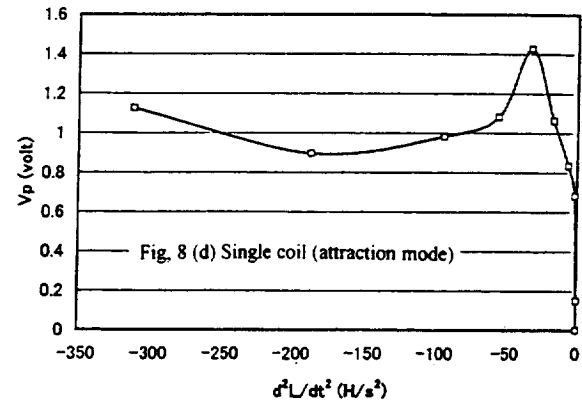
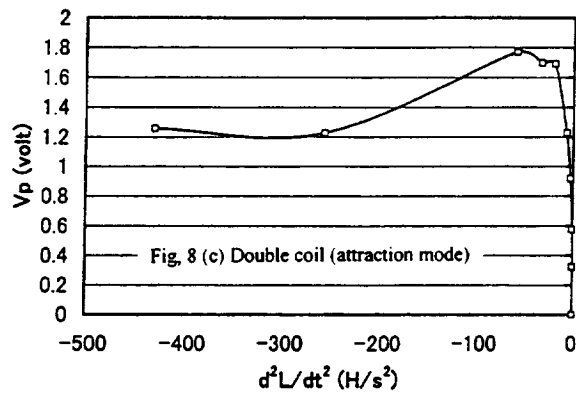
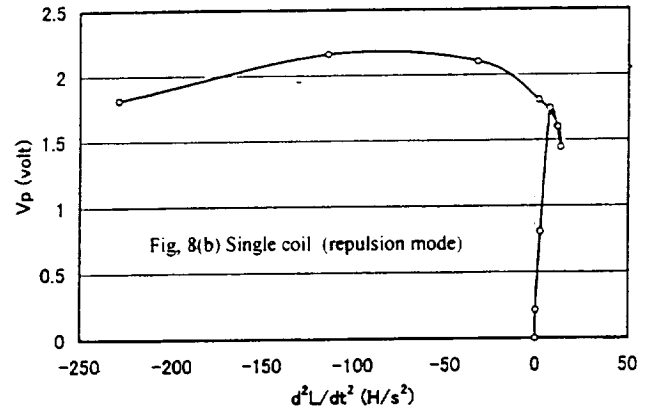
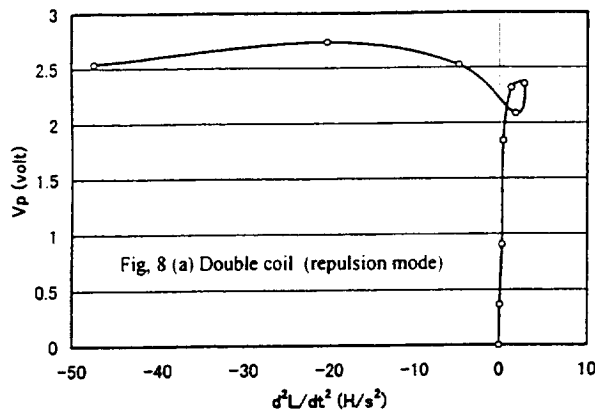


Fig.8 The dependency of the unknown EMF (V_p) upon the second-order time derivative of the inductance of the coil (d^2L/dt^2).

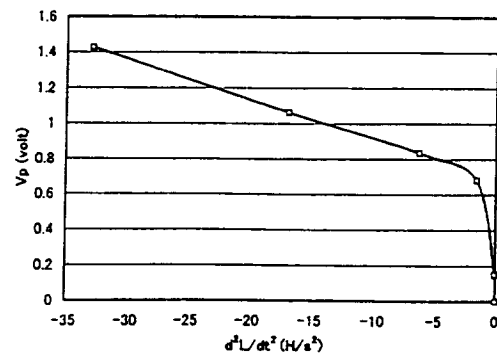
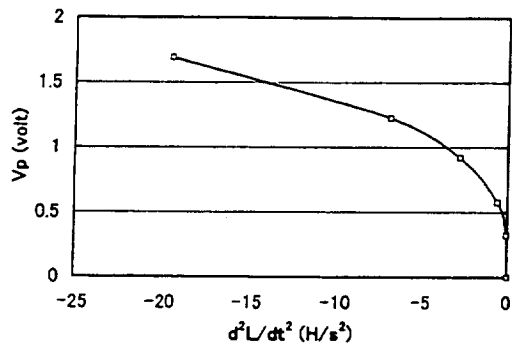
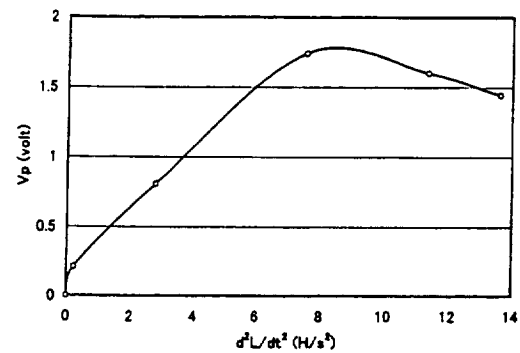
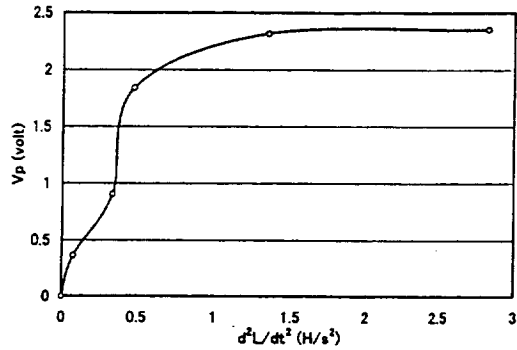


Fig. 9(c) Double coil (attraction mode)

Fig. 9(d) Single coil (attraction mode)

Fig. 9 An enlargement of the area near the origin of the x-axis shown in Fig. 8.

CONSIDERATIONS

There is a point that could be misunderstood with respect to this research. Let us consider an interpretation to introduce the possibility that the anomalous voltage (EMF) occurs because part of the kinetic energy of the rotor is converted into electrical energy. It is discussed in the following and proof is given that such an interpretation is wrong.

In order for the phenomenon of the above claim to occur, the rotor of the motor should rotate in the direction against the coil's attraction force during the capacitor's discharging process, under the conditions that an external force is being applied, while the system is in operation as a generator instead of a motor. However, it is obvious that the rotor can never be in such a condition under the circumstances of this experimental system. Consequently, it was confirmed that the rotor never receives a repulsion force during the said discharge process of the capacitor, while it could receive an attraction force.

If the rotor's rotation rate is very high and the rotor passes the reference point during the half cycle capacitor discharge process, back torque will occur and cause the rotor to be decelerated. In such a situation it is possible that the author's claim could be refuted. But the experimental hardware used in this research was designed such that it never passed the reference point as long as the rotation rate stays below a certain level assumed for the measurements. The maximum rotation rate was set to 400 rpm. The maximum rate was set to a desired value by adjusting the discharge initiation point of each double coil. The above discussion should be enough to make this clear.

Another example of a common misinterpretation of the anomalous EMF observed is the hypothesis that the resistance loss of the coil had been decreased by a certain degree at higher speeds of rotation. Possible factors for this loss of coil resistance, such as copper losses (due to the skin effect), eddy current losses and hysteresis losses were considered and examined. It is known that these losses increase, as the frequency of the discharged current becomes higher. However, in the case of this experiment, it was discovered that the inductance of each coil increases due to the displacement of the coils during the discharge process, so that the frequency of the current will become slightly lower. Consequently, the coil's resistance loss could be reduced by a very small degree.

However, it is hard to regard this as the real cause of the anomalous EMF in question. The reason is that, if it is the cause, the largest value of the anomalous voltage EMF would be observed in the attraction mode of the motor drive unit using single coils, in which the highest increase in the rate of inductance was observed (**Fig. 5**). However, the experimental results shown in **Fig. 7** and **Fig. 8** indicate an entirely opposite situation that the highest anomalous EMF is observed in the repulsion mode of the double coil, in which the lowest increase in the rate of inductance was observed. Therefore this hypothesis must also be turned down. Thus it is concluded that the only reasonable hypothesis remaining to effectively explain the anomalous phenomenon in question is to recognize the existence of an unknown EMF which is observed with the coils installed on each of the motor drive units of the motor. (Refer to (1))

Fundamentally, almost all aspects of this research are identical as those in the previous study described in reference (1) in terms of the experimental procedures and the experimental hardware system. The only difference in respect of the hardware system is the use of the motor drive unit composed of the

newly-developed double coils, in addition to the case when the motor drive unit composed of the single coils was used. The results of the research under such conditions confirmed that a positive EMF had occurred whether the motor drive units were in attraction mode or repulsion mode.

In addition to the results obtained in the previous study, further characteristics of the EMF were uncovered after performing theoretical analysis based on a computer simulation of a higher level of precision. The resulting data from the simulation was compared to the experimentally measured values for the four categories of the experimental conditions.

Generally speaking, given the supposition that the conventional hypothesis is correct, it could be considered that the difference (V_p) of the measured value from the theoretical value, which is calculated from the simulation, is due to measurement errors or noise. In that case, it is customary that the sign of the deviation values of the measured values V_p from the corresponding theoretical values vary randomly, both in a positive and a negative direction.

However, the opposite conclusions were reached through the experiments performed in this research. Namely, value V_p is always positive and has a tendency to increase in a certain relationship with the rotation rate. This fact implies that certain physical factors that are unknown or cannot be explained as yet, are involved with the observed phenomenon.

With respect to the motor used in this experiment, it is possible to express its rotation rate in terms of the time derivative of the inductance of the coil (dL/dt). As is indicated in Fig. 7, the unknown EMF (V_p) is proportional to a non-linear function of dL/dt .

If it should be subject to Faraday's EMF law, V_p must be proportional to a linear function of dL/dt , according to Equation (7). On the other hand, if in the reality it is of a non-linear nature, it should have second and/or higher order time derivatives according to equation (12).

$$\frac{d^2\Phi}{dt^2} = \frac{d^2(Li)}{dt^2} = L \frac{d^2i}{dt^2} + 2 \frac{dL}{dt} \times \frac{di}{dt} + i \frac{d^2L}{dt^2} \quad (12)$$

Furthermore, the measured values V_p versus the calculated second-order time derivatives of the inductance (d^2L/dt^2) are plotted in Fig. 8 and Fig. 9. The results show that all of the curves obtained have identical characteristics of an incremental tendency of a non-linear nature. Particularly in the case of attraction mode combined with the newly introduced double coils, beautiful curves were obtained from the mathematical standpoint, at any rate (Fig. 9(c)). This fact emphasizes that V_p is an unknown EMF having certain orderliness.

In addition, the fact that V_p is still in a non-linear relationship to the second order time derivatives of inductance d^2L/dt^2 , implies that even higher time derivatives of inductance are involved with the phenomenon in question.

Postulating from the above, there is a possibility that the general form of the EMF is represented by an infinite series composed of the higher order time derivatives of magnetic flux, as shown by the equation (13).

$$EMF = K_0 \Phi - K_1 \frac{d\Phi}{dt} + K_2 \frac{d^2\Phi}{dt^2} - K_3 \frac{d^3\Phi}{dt^3} + \dots + (-1)^n K_n \frac{d^n\Phi}{dt^n} \quad (13)$$

In (13), the only terms which are already acknowledged, are the first term $K_0\Phi$ corresponding to the unipolar induction and the second term ($K_1=1$) corresponding to the Faraday EMF which is familiar to us in the aspect of power generation. The other 3rd, 4th, 5th... terms remaining, correspond to those of the unknown EMF which are discovered and discussed in this study.

What is important is *that the phenomenon to indicate an anomalous EMF is observed even with a coil which is in a magnetically unsaturated state*. It is suspected that the higher time derivative components of the non-linear terms of the EMF exist in any electromagnetic system that is in operation to some extent. However, in the past research of this field these components had been assumed to be measurement errors or noise.

When recalling the fact that EMF is a physical phenomenon of nature, it seems more reasonable to think in that way that EMF has characteristics of a non-linear nature, instead of purely linear ones.

CONCLUSIONS

Phenomena in a motor driven by oscillating current generated from a circuit composed of a capacitor and a coil were studied. It was observed that the capacitor's voltage was reversed to the opposite polarity by a half cycle after the start of the discharging process. The reversed voltage was used as the reference value to make comparisons of the experimental data with the theoretically estimated values obtained according to Faraday's law by computer simulation. Experiments were performed in four categories by changing between single coils or double coils and changing the motor drive units between attraction and repulsion modes (the directions of the magnetic fields).

Consequently, the following conclusions were confirmed:

1. The absolute values of the measured data always exceed the corresponding theoretical values obtained from the Faraday's law model in each of the four cases. This suggests that a positive EMF be always created in the motor.
2. A much stronger positive EMF is observed when the drive units are in repulsion mode compared to attraction mode.
3. The positive EMF observed experimentally can be represented in the form of a non-linear function of the time derivative of the inductance.

REFERENCES

- 1 Osamu Ide, "Increased voltage phenomenon in a resonance circuit of unconventional magnetic configuration", *J. Appl. Phys.*, Vol. 77, No. 11 (1 June 1995).

ACKNOWLEDGEMENTS

The author would like to acknowledge that this research was made with the strong support of the Natural Group Inc. The computer programs to generate simulations performing the theoretical analysis were prepared by Mr. Koji Mishima and Mr. Takashi Maeza. The illustrations and graphs for this paper were prepared by Mr. Toshiyuki Horii and Mr. Syunsuke Suzuki. Incidentally, the English translation of the whole text was prepared by Mr. Eiichi Yamamoto at Yama Trans Co. Ltd.

REPORT DOCUMENTATION PAGE			Form Approved OMB No. 0704-0188	
Public reporting burden for this collection of information is estimated to average 1 hour per response, including the time for reviewing instructions, searching existing data sources, gathering and maintaining the data needed, and completing and reviewing the collection of information. Send comments regarding this burden estimate or any other aspect of this collection of information, including suggestions for reducing this burden, to Washington Headquarters Services, Directorate for Information Operations and Reports, 1215 Jefferson Davis Highway, Suite 1204, Arlington, VA 22202-4302, and to the Office of Management and Budget, Paperwork Reduction Project (0704-0188), Washington, DC 20503.				
1. AGENCY USE ONLY (Leave blank)	2. REPORT DATE July 2000	3. REPORT TYPE AND DATES COVERED Conference Publication		
4. TITLE AND SUBTITLE Fifth International Symposium on Magnetic Suspension Technology		5. FUNDING NUMBERS WU 522-17-51-01		
6. AUTHOR(S) Nelson J. Groom and Colin P. Britcher, Editors				
7. PERFORMING ORGANIZATION NAME(S) AND ADDRESS(ES) NASA Langley Research Center Hampton, VA 23681-2199		8. PERFORMING ORGANIZATION REPORT NUMBER L-18002		
9. SPONSORING/MONITORING AGENCY NAME(S) AND ADDRESS(ES) National Aeronautics and Space Administration Washington, DC 20546-0001		10. SPONSORING/MONITORING AGENCY REPORT NUMBER NASA/CP-2000-210291		
11. SUPPLEMENTARY NOTES Groom: Langley Research Center, Hampton, VA Britcher: Old Dominion University, Norfolk, VA				
12a. DISTRIBUTION/AVAILABILITY STATEMENT Unclassified-Unlimited Subject Category 18 Availability: NASA CASI (301) 621-0390			12b. DISTRIBUTION CODE	
13. ABSTRACT (Maximum 200 words) In order to examine the state of technology of all areas of magnetic suspension and to review recent developments in sensors, controls, superconducting magnet technology, and design/implementation practices, the Fifth International Symposium on Magnetic Suspension Technology was held at the Radisson Hotel Santa Barbara, Santa Barbara, California, on December 1-3, 1999. The symposium included 18 sessions in which a total of 53 papers were presented. The technical sessions covered the areas of bearings, controls, modeling, electromagnetic launch, magnetic suspension in wind tunnels, applications flywheel energy storage, rotating machinery, vibration isolation, and maglev. A list of attendees is included in the document.				
14. SUBJECT TERMS Magnetic bearings; Magnetic suspension; Large gap magnetic suspension; Small gap magnetic suspension; Maglev; Sensors; Control systems			15. NUMBER OF PAGES 691	
			16. PRICE CODE A99	
17. SECURITY CLASSIFICATION OF REPORT Unclassified	18. SECURITY CLASSIFICATION OF THIS PAGE Unclassified	19. SECURITY CLASSIFICATION OF ABSTRACT Unclassified	20. LIMITATION OF ABSTRACT UL	

[REDACTED]

